

UNIVERSITY OF OKLAHOMA

GRADUATE COLLEGE

DEVELOPMENT OF SYNTHETIC METHODOLOGIES FOR N- TO C-TERMINAL
CYCLIZATION OF PEPTIDOMIMETIC SMALL MOLECULES AND IN SILICO AND IN
VITRO STUDIES OF THE ROLE OF CYCLIZATION ON ANTIBACTERIAL AND
ANTIVIRAL ACTIVITIES

A THESIS

SUBMITTED TO THE GRADUATE FACULTY

In partial fulfillment of the requirements for the

Degree of

DOCTORATE IN PHILOSOPHY

By

QUENTIN PAUL AVILA

Norman, Oklahoma

2022

DEVELOPMENT OF SYNTHETIC METHODOLOGIES FOR N- TO C-TERMINAL
CYCLIZATION OF PEPTIDOMIMETIC SMALL MOLECULES AND IN SILICO AND IN
VITRO STUDIES OF THE ROLE OF CYCLIZATION ON ANTIBACTERIAL AND
ANTIVIRAL ACTIVITIES

A DISSERTATION APPROVED FOR THE
DEPARTMENT OF CHEMISTRY AND BIOCHEMISTRY

BY THE COMMITTEE CONSISTING OF

Dr. Helen Zgurskaya, Chair

Dr. Robert Cichewicz

Dr. Indrajeet Sharma

Dr. Cameron Siler

© Copyright by QUENTIN PAUL AVILA 2022

All Rights Reserved.

Acknowledgements

Since the first day I arrived in Oklahoma, I have been welcomed and supported by the Department of Chemistry and Biochemistry. In particular, Dr. Adam Duerfeldt has played a crucial role to bring me to this point. Through his mentorship, he taught me how to be a researcher and he transmitted his passion for medicinal chemistry.

I wish to thank the Department of Chemistry and Biochemistry and particularly my committee members, Dr. Zgurskaya, Dr. Cichewicz, Dr. Sharma and Dr. Siler for giving me the key to success as a graduate student, an organic chemist and a scientist.

I also wish to thank the Duerfeldt lab, Nate, Dinesh, Jessi, Yangxiong, Xiaoxheng, Ziwei, Cat and Katelyn for their friendship and team spirit. Inside the lab and beyond I found some true friends in Jessi and Eric Gardner. They have become my adopted family and no words can describe how essential they have been to help me become who I am now.

Oklahoma was not the place where I expected to find love, but meeting Cecilia was probably the best surprise of my life. She makes me a better man with her love and kind words, and she brings me so much joy. Finally, I want to thank my parents and my sister for their constant support and encouragements. One important lesson I have learn is that family matters above everything else.

Table of Content

Chapter 1 Antibacterial Resistance: a Silent Pandemic	1
1 Introduction	1
2 New Mindsets in Antibacterial Development	3
2.1 Disparate Membrane Polarity in Gram-Negatives	3
2.2 Chemical Space and Structural Uniqueness of Gram-Negative Actives.....	4
2.3 Enhanced Antibacterial Potency.....	4
2.4 Early Consideration of Combinatorial Therapy	5
2.5 Development of Narrow-Spectrum Therapeutics.....	5
2.6 Non-Traditional Approaches to Antibacterial Development.....	5
3 Recent Advances in the Development of Antibacterials Active in Gram-Negative Bacteria	6
Chapter 2 Synthesis of a Piperazinone ClpP Activator Library as a Tool for Enhancing	
Small Molecules Accumulation in Gram-Negative Bacteria	9
1 Introduction	11
2 Slow Uptake and Active Efflux: The Challenges of Bacterial Membrane.....	12
2.1 Passive Diffusion.....	12
2.2 Facilitated Diffusion and Active Transport via Outer Membrane Proteins.....	15
2.3 Efflux Pumps	17

3	Methods to Evaluate Antibacterial Activity	20
3.1	Chemical Modifications of Cells.....	21
3.2	Genetic Modifications of Cells.....	22
4	Methods to Determine Compound Permeation and Accumulation.....	24
4.1	Mass Spectrometry	24
4.2	Fluorescence	25
4.3	Electrophysiology and Liposome Swelling Assays	25
5	Recent Examples of Rational Approaches to Enhance Gram-Negative Accumulation....	27
5.1	Sulfamoyladenines	29
5.2	Oxazolidinones	32
5.3	Tetrahydropyran-Based Topoisomerase Inhibitors	34
5.4	Diverse Chemotype Analysis	35
6	Small-molecule Penetration & Efflux in Antibiotic-Resistant Gram-Negatives (SPEAR-GN) Project.....	37
7	Rational Design of the Piperazinone ClpP Activator Scaffold	39
8	Preparation of the Synthon for the Piperazinone Scaffold	47
8.1	Synthesis of the Piperazinone Core.....	47
8.2	Preparation of the Propargyl Piperazinone.....	53
8.3	Preparation of the Cyclohexylpropanoyl Piperazinone	54
9	Synthetic Efforts for the Piperazinone ClpP Library	56

9.1	Synthesis of Propargyl Piperazinone Amide Analogs.....	56
9.2	Synthesis of Propargyl Piperazinone Urea Analogs.....	58
9.3	Synthesis of Propargyl Piperazinone Sulfonamides Analogs	59
9.4	Synthesis of N-Alkyl Cyclohexylpropanoyl Piperazinones	60
10	Antibacterial Activity of the Piperazinone and <i>Seco</i> Libraries	83
11	Conclusion and Future Directions	99
12	Experimental Section.....	105
12.1	Preparation of the Piperazinone Core.....	105
12.2	Preparation of the Cyclohexylpropanoyl Piperazinone	109
12.3	Preparation of Propargyl Piperazinone Amides	114
12.4	Preparation of Propargyl Piperazinone Ureas	140
12.5	Preparation of Propargyl Piperazinone Sulfonamides.....	145
12.6	Preparation of N-alkyl Cyclohexylpropanoyl Piperazinones	152
13	Bibliography	192
Appendix (Chapter 2)		206
 Chapter 3 Computational Studies and Synthesis of Cyclized Small-Molecule ClpP		
Activators		376
1	Introduction	378
1.1	Bacterial Caseinolytic Protease P (ClpP)	379
1.2	Chemo-Activation of ClpP	382

2	Rationale for the Design of Optimized ADEP Derivatives.....	388
2.1	N- to C-terminal Cyclization to Improve Potency and Stability of ADEP Bioactive Fragment.....	388
2.2	Design of Analogs to Interrogate Alternate Substitutions of ADEP Bioactive Fragment.....	391
3	Computational Studies.....	396
3.1	Conformational analysis.....	396
3.2	Docking Studies.....	416
4	Synthetic Work to Generate <i>Seco</i> and Cyclized ClpP Activators	422
4.1	Synthesis of the <i>Seco</i> Analogs.....	422
4.2	Six-Membered Ring Analog Synthesis	427
4.3	Seven-Membered Ring Synthesis.....	431
4.4	Eight-membered ring synthesis	441
5	Evaluation of the Synthesized Compounds for ClpP Activation	446
6	Conclusion and Future Directions	449
7	Experimental Section.....	451
8	Bioactivity Evaluation.....	482
8.1	ClpP Protein Purification.....	482
8.2	FITC-Casein Degradation Assay.....	483
9	Bibliography	483

Chapter 4 Design and Synthesis of Peptidomimetic Non-Covalent SARS-CoV-2 Main

Protease Inhibitors	550
1 Introduction	551
2 Coronaviruses	552
3 Biochemistry and Replication Cycle of Coronavirus	554
4 Rationale for the Selection of SARS-CoV-2 Target	556
4.1 Repurposing Drugs to Treat COVID-19	556
4.2 Current Research to Target SARS-CoV-2	559
5 Design of SARS-CoV-2 Mpro Non-Covalent Inhibitors	571
5.1 Structural Analysis of Mpro Non-covalent Inhibitors	571
5.2 Structural Analysis of XChem Fragment Library	572
5.3 Design of SARS-CoV-2 Mpro Non-Covalent Inhibitor Chemotypes	579
5.4 Computational Studies the Piperazine Scaffold	584
6 Synthesis of the Library of Mpro Inhibitors	617
6.1 Synthesis of the Piperazine Mpro Inhibitors	617
6.2 Synthesis of the Piperazinone Mpro Inhibitors	620
6.3 Synthesis of the Peptidic Mpro Inhibitors	623
7 Conclusion and Future Directions	624
8 Experimental Section	625
9 Bibliography	638

List of Figures

Figure 2.1: Optimization of tetrahydropyran-based topoisomerase inhibitors for permeability and efflux susceptibility in <i>E. coli</i>	35
Figure 2.2: Piperazinone ClpP activator scaffold (2.24).	40
Figure 2.3: Structures of the <i>seco</i> (2.146) and piperazinone (2.147) analogs studied in Chapter 3.	97
Figure 2.4: The Venn diagram represents the motifs of oxazolidinone analogs 2.23 (a) identified as liabilities to efflux susceptibility (b) and outer membrane permeation (c) in <i>E. coli</i> , <i>A. baumannii</i> and <i>P. aeruginosa</i>	102
Figure 2.5: Diagram summarizing correlation between descriptors and efflux avoidance and outer membrane penetration in <i>P. aeruginosa</i> . ^{216, 217} Efflux avoidance describes compounds not susceptible to be effluxed. Outer membrane penetration describes compounds able to permeate the outer membrane. Descriptors on the side of the arrow positively correlates with efflux avoidance and/or outer membrane penetration. Descriptors on the opposite side of the arrow negatively correlates with efflux avoidance and/or outer membrane penetration. Descriptors inside the blue or red rectangle only correlates with efflux avoidance or outer membrane penetration, respectively. Descriptors inside the grey rectangle correlates with both efflux avoidance and outer membrane penetration.	104
Figure 2.6: Diagram summarizing correlation between descriptors and efflux avoidance and outer membrane penetration in <i>E. coli</i> . ^{75, 217-220} Efflux avoidance describes compounds not susceptible to be effluxed. Outer membrane penetration describes compounds able to permeate the outer membrane. Descriptors on the side of the arrow positively correlates with efflux avoidance and/or	

outer membrane penetration. Descriptors on the opposite side of the arrow negatively correlates with efflux avoidance and/or outer membrane penetration. Descriptors inside the blue or red rectangle only correlates with efflux avoidance or outer membrane penetration, respectively. Descriptors inside the grey rectangle correlates with both efflux avoidance and outer membrane penetration.105

Figure 3.1: Structure of tetradecameric *Escherichia coli* ClpP. (a) Distal and (b) apical views (PDB: 1TYF).380

Figure 3.2: Structure of *E. coli* ClpXP complex. (a) Distal and (b) apical views of ClpX alone, (c) apical view of ClpP alone and (d) distal view of hexameric ClpX and heptameric ClpP complex (PDB: 1TYF).382

Figure 3.3: Apical view (a) and 2D diagram (b) of the co-crystal structure of ADEP 1 (3.1) bound to ClpP (PDB: 3PTI).384

Figure 3.4: Structures of ClpP activators......388

Figure 3.5: Structure of ADEP 2 (3.23)388

Figure 3.6: Rationale for the N- to C-terminal cyclization (a) and structures of the six- (3.25), seven- (3.26), eight-membered ring (3.27) and pyrazinone (3.28) ClpP activators (b).390

Figure 3.7: Structures of the para-Bromo (3.38) and tyrosyl seco (3.39) analogs.394

Figure 3.8: Structures of N-methyl *seco* (3.40) and toluyl-urea piperazinone (3.41) analogs. ...395

Figure 3.9: Structure of ureadepsipeptide (3.42).....396

Figure 3.10: Bioactive conformational ensemble pipeline using analog 3.24 as example.....399

Figure 3.11: Superimposed analogs 3.24 (green), 3.25 (yellow), 3.26 (violet), 3.27 (pink) and 3.28 (blue). The core (a.), propargyl (b.), 3,5-difluorobenzyl (c.) and heptenoyl (d. and e.) are highlighted in licorice and the rest of the structure is represented in lines.400

Figure 3.12: Conformational ensemble of analogs 3.24 (a.), 3.25 (b.), 3.26 (c.), 3.27 (d.) and 3.28 (e.). The conformer representative of the most populated cluster is shown in dark gray licorice, and the conformers representative of the less populated cluster are depicted in green lines.404

Figure 3.13: Histogram of dihedral angles of the propargyl group in analogs 3.24 (yellow), 3.25 (green), 3.26 (blue), 3.27 (orange) and 3.28 (purple). The dihedral angle was measured for the atoms C22-C21-N1-C2 (labeled in red) and displayed in a 3D representation of 3.25 as an example.407

Figure 3.14: Histogram of dihedral angles of the 3,5-difluorophenylalanine backbone in analogs 3.24 (yellow), 3.25 (green), 3.26 (blue), 3.27 (orange) and 3.28 (purple). The dihedral angle was measured for the atoms N1-C2-C3-N26 (labeled in red) and displayed in a 3D representation of 3.27 as an example. The red line in the histogram indicates the dihedral angle of the backbone bond of the cocrystal structure of ADEP 4 (3.2) bound to *S. aureus* ClpP (PDB: 6TTZ).409

Figure 3.15: Histogram of dihedral angles of the 3,5-difluorobenzyl group in analogs 3.24 (yellow), 3.25 (green), 3.26 (blue), 3.27 (orange) and 3.28 (purple). The dihedral angle was measured for the atoms C2-C3-C6-C7 (labeled in red) and displayed in a 3D representation of 3.25 as an example. The red line in the histogram indicates the dihedral angle of the backbone bond of the cocrystal structure of ADEP 4 (3.2) bound to *S. aureus* ClpP (PDB: 6TTZ).411

Figure 3.16: Histogram of dihedral angles of the heptenoyl tail in analogs 3.24 (yellow), 3.25 (green), 3.26 (blue), 3.27 (orange) and 3.28 (purple). The dihedral angle was measured for the atoms C18-C20-C24-C25 (labeled in red) and displayed in a 3D representation of 3.25 as an example. The red line in the histogram indicates the dihedral angle of the backbone bond of the cocrystal structure of ADEP 4 (3.2) bound to *S. aureus* ClpP (PDB: 6TTZ).413

Figure 3.17: Histogram of dihedral angles of the heptenoyl amide in analogs 3.24 (yellow), 3.25 (green), 3.26 (blue), 3.27 (orange) and 3.28 (purple). The dihedral angle was measured for the atoms C3-N26-C37-O38 (labeled in red) and displayed in a 3D representation of 3.25 as an example. The red line in the histogram indicates the dihedral angle of the backbone bond of the cocrystal structure of ADEP 4 (3.2) bound to <i>S. aureus</i> ClpP (PDB: 6TTZ).	414
Figure 3.18: 2D protein-ligand interactions diagrams of ADEP 4 (3.2) and analogs 3.16, 3.24, 3.25, 3.26, 3.27 and 3.28.	417
Figure 3.19: 2D protein-ligand interactions diagrams of compounds 3.38 – 3.41.	421
Figure 3.20: Structures of eight-membered fused-ring derivatives.	441
Figure 3.21: Fluorescence results from the FITC- β -casein degradation assay of compounds 3.24 – 3.28, 3.40 and 3.41 with BsClpP. Negative control = DMSO. Positive control = 3.16 (100 μ M). The blue bars represent the fluorescence at 250 μ M and the orange bars represent the fluorescence at 500 μ M.	447
Figure 3.22: Fluorescence results from the FITC- β -casein degradation assay of compounds 3.24, 3.38 and 3.39 with BsClpP. Negative control = DMSO. Positive control = 3.16 (100 μ M). The blue bars represent the fluorescence at 250 μ M and the orange bars represent the fluorescence at 500 μ M.	448
Figure 4.1: Antivirals under investigation for SARS, MERS and COVID-19.	558
Figure 4.2: SARS-CoV-2 RdRp inhibitors under investigation.	561
Figure 4.3: SARS-CoV-2 PLpro inhibitors under investigation.	564
Figure 4.4: Mpro monomer. Domain 1 in green, Domain 2 in cyan and Domain 3 in yellow. ...	565
Figure 4.5: Structure of dimeric SARS-CoV-2 Mpro. The catalytic dyad is circled in black highlighting Cysteine 145 in green and Histidine 41 in marine blue (PDB: 1UK4).	565

Figure 4.6: SARS-CoV-2 Mpro active site pocket. (a) Representative example of SARS-CoV-2 protein substrate. (b) Surface representation of the active site of SARS-CoV-2 Mpro bound to a protein substrate. ⁵⁷ (c) Summary table of SARS-CoV-2 Mpro residues for each subsite of the binding pocket. (bb) = backbone.	566
Figure 4.7: General structure of covalent SARS-CoV-2 Mpro inhibitors.....	567
Figure 4.8: Reversible covalent SARS-CoV-2 Mpro inhibitors. The functional groups in red are the warheads.	568
Figure 4.9: Non-covalent SARS-CoV-2 Mpro inhibitors.	569
Figure 4.10: Pfizer’s reversible covalent SARS-CoV-2 Mpro inhibitors.	570
Figure 4.11: 2D ligand interaction diagram of the co-crystal structure of ML188 (4.28) in SARS-CoV Mpro (PDB: 3V3M) and 4.29 in SARS-CoV-2 Mpro (PDB: 7KX5).	572
Figure 4.12: Representation of the rationale for the design of the urea scaffold 4.59 from XChem-0397 (4.56).	581
Figure 4.13: Representation of the rationale for the design of the tyrosine scaffold 4.60 from XChem-0967 (4.58).....	581
Figure 4.14: Representation of the rationale for the design of the piperazine scaffold (4.61) from XChem-1093 (4.55).....	582
Figure 4.15: Representation of the rationale for the design of the peptidomimetic scaffold (4.65) from 4.29.	584
Figure 4.16: 2D ligand interaction diagram of the co-crystal structure of TG-0205221 (4.79) with SARS-CoV Mpro (PDB: 2GX4).	597
Figure 4.17: Superposition of the monobenzylated piperazine series docked to SARS-CoV-2 Mpro. The 3D representation of the binding poses of 4.104 (left, orange), 4.105 (left, yellow),	

4.106 (right, cyan), 4.107 (right, green) in SARS-CoV-2 Mpro (PDB: 3V3M) was predicted by Glide.601

Figure 4.18: Superimposition of the monobenzylated piperazinone series docked to SARS-CoV-2 Mpro. The 3D representation of the binding poses of 4.108 (left, orange), 4.109 (left, yellow), 4.110 (right, cyan), 4.111 (right, green) in SARS-CoV-2 Mpro (PDB: 3V3M) was predicted by Glide.604

Figure 4.19: Structural representations of 4.113 in SARS-CoV-2 Mpro pocket. The 2D ligand interaction diagram is on the left and, on the right, the 3D representation of the binding pose of 4.113 in SARS-CoV-2 Mpro (PDB: 3V3M) was predicted by Glide. The blue circle highlights the α -carbon of the piperazinone.609

List of Tables

Table 2.1: World Health Organization priority pathogens list (2017). These pathogens were ranked based on their related mortality, prevalence of resistance, 10-year trend of resistance, transmissibility, preventability in hospital and community settings, treatability and current pipeline. ²	11
Table 2.2: Accumulation of sulfamoyladenosines in <i>E. coli</i> and statistically significant physicochemical correlations. LogD = calc n-octanol/water partition coefficient (pH = 7.4); LogP = calc n-octanol/ water partition coefficient; ALogPs = calc n-octanol/water partition coefficient (Tetko); relPSA = topological polar surface area + surface area; ALogpS = calc aqueous solubility (Tetko).	31
Table 2.3: MIC values and calculated physicochemical properties of C-ring oxazolidinone analogs. *, pKa of acidic group present. **, pKa of protonated basic group present (cpKa column).	33
Table 2.4: Comparison of Deoxynybomycin (2.20) and Amino-deoxynybomycin (2.21) spectrum of activity.....	36
Table 2.5: Structures of the chemotypes under investigation of the SPEAR-GN project.....	38
Table 2.6: Fragments and C-terminus derivatives of ADEP and MIC in <i>B. subtilis</i>	41
Table 2.7: Derivatives of ADEP and MIC in <i>B. subtilis</i>	43
Table 2.8: Antibacterial activity of ADEP 1 (2.38) and its optimized congeners ADEP 2 (2.39) and ADEP 4 (2.40).	44
Table 2.9: Metabolic stability, casein degradation and MIC in <i>S. aureus</i> of amide (2.41, 2.42, 2.44 and 2.46) and urea (2.43, 2.45 and 2.47) ADEP 4 analogs.	46
Table 2.10: Summary of DMP oxidation/cyclization conditions optimization.....	48

Table 2.11: Summary of conditions screened for the oxidation/cyclization of 2.51. * The Boc group of intermediate 2.51 was removed first using TFA in DCM.....	50
Table 2.12: Alternative synthetic route to the cyclic enamine intermediate 2.52 and summary of conditions screened for the acetal deprotection/cyclization.	52
Table 2.13: Summary of the conditions screened for propargylation of the piperazinone amide 2.62.	54
Table 2.14: Summary of the preparation of propargyl piperazinone amide analogs. Under each moiety, the compound number and yield are reported. * indicates that compound 2.69 was synthesized via propargylation of 2.67	58
Table 2.15: Summary of the preparation of propargyl piperazinone urea analogs. Under each moiety, the compound number and yield are reported.	59
Table 2.16: Summary of the preparation of propargyl piperazinone sulfonamide analogs. Under each moiety, the compound number and yield are reported.....	60
Table 2.17: Summary of PTC N-alkylation conditions of cyclohexylpropanoyl piperazinones...63	
Table 2.18: Summary of photoinduced, copper-catalyzed N-alkylation conditions of cyclohexylpropanoyl piperazinones 2.67.	67
Table 2.19: Screening of the photoinduced, copper-catalyzed N-alkylation conditions between unreactive alkyl halides and the uncyclized intermediate 2.61.	68
Table 2.20: Summary of conditions screened for the aminolytic ring-opening of ethylene oxide with benzylamine 2.136. The benzylamine was recovered under these conditions.	75
Table 2.21: Summary of conditions screened for the aminolytic ring-opening of ethylene oxide with phenylalanine methyl ester 2.138. The phenylalanine methyl ester was recovered under these conditions.	75

Table 2.22: Summary of conditions screened for the aminolytic ring-opening of ethylene oxide with phenylalanine methyl ester 2.138 using ionic liquids. The phenylalanine methyl ester was recovered under these conditions.77

Table 2.23: Summary of conditions screened for the aminolytic ring-opening of ethylene oxide with phenylalanine methyl ester 2.138 using metal-salen complexes 2.140. The phenylalanine methyl ester was recovered under these conditions.77

Table 2.24: Conditions tested for the reduction of the Weinreb amide cyclohexylpropanoyl piperazinone 2.115 to the aldehyde 2.144 analog.81

Table 2.25: Conditions tested for the N-alkylation of cyclohexylpropanoyl piperazinone with chloroacetonitrile.81

Table 2.26: MIC values of propargyl piperazinone and *seco* analogs in wild-type (WT), porinated (Pore), efflux-deficient (Δ) and porinated/efflux-deficient (Δ Pore) *E. coli* and *A. baumannii*. The *seco* analogs denoted by the compound number followed by s (#s) were synthesized by Quentin Gibault.87

Table 2.27: MIC values of propargyl piperazinone and *seco* analogs in wild-type (WT), porinated (Pore), efflux-deficient (Δ) and porinated/efflux-deficient (Δ Pore) *P. aeruginosa*. The *seco* analogs denoted by the compound number followed by s (#s) were synthesized by Quentin Gibault.90

Table 2.28: MIC values of cyclohexylpropanoyl piperazinone and *seco* analogs in wild-type (WT), porinated (Pore), efflux-deficient (Δ) and porinated/efflux-deficient (Δ Pore) *E. coli* and *A. baumannii*. The *seco* analogs denoted by the compound number followed by s (#s) were synthesized by Katelyn Stevens¹ and Quentin Gibault².93

Table 2.29: MIC values of cyclohexylpropanoyl piperazinone and <i>seco</i> analogs in wild-type (WT), porinated (Pore), efflux-deficient (Δ) and porinated/efflux-deficient (Δ Pore) <i>P. aeruginosa</i> . The <i>seco</i> analogs denoted by the compound number followed by s (#s) were synthesized by Katelyn Stevens ¹ and Quentin Gibault ²	96
Table 2.30: Antibacterial activity of ADEP 4 (2.40) against Gram-negative bacteria. * <i>E. coli lptD-4213</i> is a mutant strain with a compromised outer membrane.	98
Table 3.1: Antibacterial activity of ADEP 1 (3.1) and ADEP 4 (3.2). * Resistant phenotype of clinical isolates: penicillin-resistant <i>Streptococcus pneumoniae</i> 665, vancomycin-resistant <i>Enterococcus faecium</i> L 4001 and methicillin-resistant <i>Staphylococcus aureus</i> NRS 119.	385
Table 3.2: Derivatives of ADEP and MIC in <i>B. subtilis</i>	386
Table 3.3: SAR study of the fluorination of the ADEP phenylalanine in Gram-positive bacteria.	392
Table 3.4: SAR study of the substitution of the ADEP phenylalanine in Gram-positive bacteria.	393
Table 3.5: The number of rotatable bonds and the predicted globularities of analogs 3.24, 3.25, 3.26, 3.27 and 3.28.	397
Table 3.6: Root-mean square deviation (RMSD), weighted average RMSD and weighted standard deviation of the conformational ensemble of analogs 3.24 – 3.28.	406
Table 3.7: Summary of the docking score, protein-ligand interactions and RMSD between the <i>N</i> -heptenoyl 3,5-difluorophenylalanine fragment of ADEP 4 (3.2) and corresponding fragments in compounds 3.16, 3.24 – 3.28, 3.38 – 3.41.	419
Table 3.8: Acidic conditions screened for the synthesis of the cyclized intermediate 3.65.	433

Table 3.9: Synthetic route and acidic conditions screened for the synthesis of the cyclized intermediate 3.71.	436
Table 3.10: Conditions screening for aza-Michael addition between the amine 3.46' and acrylonitrile.....	439
Table 3.11: Conditions screened for the cyclization of 3.75 into the 1,4-diazepan-2-one 3.76.	440
Table 3.12: Acidic conditions screened for the synthesis of the cyclized intermediate 3.83.	442
Table 3.13: Summary of the acidic conditions screened for the synthesis of the cyclized intermediate 3.88.	444
Table 3.14: Dose-response comparison of the <i>seco</i> analogs 3.16 and 3.24 for FITC- β -casein degradation with BsClpP and EcClpP.	449
Table 3.15: Summary of the dihedral angles of the conformer ensemble of analog 3.24.	489
Table 3.16: Summary of the dihedral angles of the conformer ensemble of analog 3.25.	489
Table 3.17 Summary of the dihedral angles of the conformer ensemble of analog 3.26.	490
Table 3.18 Summary of the dihedral angles of the conformer ensemble of analog 3.27.	491
Table 3.19: Summary of the dihedral angles of the conformer ensemble of analog 3.28.	492
Table 3.20: Fluorescence measured for FITC-casein degradation assay with BsClpP, and DMSO (negative control) and compounds 16 (positive control), 23, 25, 26, 27, 28, 38, 39, 40 and 41. Each fluorescence presented is the average fluorescence for a triplicate. Fluorescence was monitored via an i-TECAN Infinite M200 plate reader (excitation: 485 nm; emission: 538 nm; gain: 120). ...	493
Table 3.21: Fluorescence measured for FITC-casein degradation assay with BsClpP and EcClpP, and DMSO (negative control), ADEP (positive control) and compound 16. Each fluorescence presented is the average fluorescence for a triplicate. Fluorescence was monitored via an i-TECAN Infinite M200 plate reader (excitation: 485 nm; emission: 538 nm; gain: 120).....	494

Table 3.22: Fluorescence measured for FITC-casein degradation assay with BsClpP and EcClpP, and DMSO (negative control), ADEP (positive control) and compound 23. Each fluorescence presented is the average fluorescence for a triplicate. Fluorescence was monitored via an i-TECAN Infinite M200 plate reader (excitation: 485 nm; emission: 538 nm; gain: 120).....	495
Table 4.1: XChem crystallographic hits excluded from our structural analysis. The fragments XChem-0161 (4.37), -0195 (4.38), -0354 (4.39), -0395 (4.40), -0946 (4.41) and -0091 (4.42) are represented in the 2D interaction diagram.....	574
Table 4.2: Summary of the binding subsites of the 16 XChem hits. * denotes the binding of fragments in S1' without interacting with the backbone of Gly143 via hydrogen bonding. ** denotes the binding of fragments in S3 without interacting with the backbone of Glu166 via hydrogen bonding.	575
Table 4.3: 2D ligand interaction diagrams of the co-crystal structure of XChem-0072 (4.43), -0104 (4.44), -0305 (4.45), -0387 (4.46), -0874 (4.47), -1077 (4.48) and -1249 (4.49) in SARS-CoV-2 Mpro (S2 subsite).	576
Table 4.4: 2D ligand interaction diagram of the co-crystal structure of XChem-0107 (4.50), -0426 (4.51), -0540 (4.52), -0678 (4.53), -0995 (4.54) and -1093 (4.55) in SARS-CoV-2 Mpro (S1 subsite).....	578
Table 4.5: 2D ligand interaction diagram of the co-crystal structure of XChem-0397 (4.56), -0434 (4.57) and -0967 (4.58) in SARS-CoV-2 Mpro.	578
Table 4.6: Probability of Mpro inhibition of know Mpro inhibitors predicted by 'SARS – Balanced'.....	587
Table 4.7: Probability of Mpro inhibition of XChem-fragment predicted by 'SARS – Balanced'.	588

Table 4.8: Structural representation of compound XChem-1093 (4.55) in SARS-CoV-2 Mpro pocket. The 2D ligand interaction diagram of the binding pose of 4.55 in SARS-CoV-2 Mpro (PDB: 3V3M) was predicted by Glide.	589
Table 4.9: Structural representation of compound 4.66 in SARS-CoV-2 Mpro pocket. The 2D ligand interaction diagram of the binding pose of 4.66 in SARS-CoV-2 Mpro (PDB: 3V3M) was predicted by Glide.	590
Table 4.10: Structural representation of compound 4.67 in SARS-CoV-2 Mpro pocket. The 2D ligand interaction diagram of the binding pose of 4.67 in SARS-CoV-2 Mpro (PDB: 3V3M) was predicted by Glide.	591
Table 4.11: Structural representation of compound 4.68 in SARS-CoV-2 Mpro pocket. The 2D ligand interaction diagram of the binding pose of 4.68 in SARS-CoV-2 Mpro (PDB: 3V3M) was predicted by Glide.	592
Table 4.12: Structural representation of compound 4.69 in SARS-CoV-2 Mpro pocket. The 2D ligand interaction diagram of the binding pose of 4.69 in SARS-CoV-2 Mpro (PDB: 3V3M) was predicted by Glide.	593
Table 4.13: Superposition of 4.66 and 4.70 docked to SARS-CoV-2 Mpro. On the right, the 3D representation of the binding poses of 4.66 (green) and 4.70 (orange) in SARS-CoV-2 Mpro (PDB: 3V3M) were predicted by Glide.	595
Table 4.14: Summary of the docking studies of the aryl piperazine series in SARS-CoV-2 Mpro (PDB: 3V3M). The docking score and protein-ligand interactions were predicted by Glide and SARS – Balanced model predicted the probability of Mpro inhibition. The binding poses of the ligands were considered not adequate (No binding) when the pyridyl group was not engaged in a H-bond with His163.	596

Table 4.15: Summary of the docking studies of the amino acid piperazine series in SARS-CoV-2 Mpro (PDB: 3V3M). The docking score and protein-ligand interactions were predicted by Glide and SARS – Balanced model predicted the probability of Mpro inhibition. The binding poses of the ligands were considered not adequate (No binding) when the pyridyl group was not engaged in a H-bond with His163. * The absolute stereochemistry of the chiral center of each analog is indicated by R or S.599

Table 4.16: Summary of the docking studies of the monobenzylated piperazine series in SARS-CoV-2 Mpro (PDB: 3V3M). The docking score and protein-ligand interactions were predicted by Glide and SARS – Balanced model predicted the probability of Mpro inhibition. * The absolute stereochemistry of the chiral center of each analog is indicated by R or S.600

Table 4.17: Summary of the docking studies of the monobenzylated piperazinone series in SARS-CoV-2 Mpro (PDB: 3V3M). The docking score and protein-ligand interactions were predicted by Glide and SARS – Balanced model predicted the probability of Mpro inhibition. * The absolute stereochemistry of the chiral center (denoted by *) of each analog is indicated by R or S at the end of the name.603

Table 4.18: Summary of the docking studies of the unsubstituted piperazinone series in SARS-CoV-2 Mpro (PDB: 3V3M). The docking score and protein-ligand interactions were predicted by Glide and SARS – Balanced model predicted the probability of Mpro inhibition.608

Table 4.19: Summary of the docking studies of the substituted piperazinone series in SARS-CoV-2 Mpro (PDB: 3V3M). The docking score and protein-ligand interactions were predicted by Glide and SARS – Balanced model predicted the probability of Mpro inhibition. * The absolute stereochemistry of the chiral center (denoted by *) of each analog is indicated by R or S at the end of the name.612

Table 4.20: Summary of the docking studies of the substituted peptidic series in SARS-CoV-2 Mpro (PDB: 3V3M). The docking score and protein-ligand interactions were predicted by Glide and SARS – Balanced model predicted the probability of Mpro inhibition. * The absolute stereochemistry of the chiral center (denoted by *) of each analog is indicated by R or S at the end of the name.614

Table 4.21: Summary of the library of compounds to synthesize.616

Table 4.22: Synthetic route for 4.70 from Boc-piperazine.620

List of Schemes

Scheme 2.1: Structures of the ClpP activator piperazinone scaffolds with the fixed moieties.	46
Scheme 2.2: Synthetic route to the cyclic enamine intermediate 2.52.	47
Scheme 2.3: Oxidation mechanism of a primary alcohol 2.53 into an aldehyde 2.56 by DMP (a) and acetoxyiodinane oxide 2.58 preparation (b).	49
Scheme 2.4: Proposed synthetic route for the piperazinone 2.59': retrosynthetic route for the piperazinone 2.59' using a phthalimide group (a) and synthetic steps for 2.59' (b).	51
Scheme 2.5: Hydrogenation conditions used to access the piperazinone 2.59.	52
Scheme 2.6: TFA-promoted Boc deprotection of the propargyl piperazinone 2.62'.	54
Scheme 2.7: Synthetic route for 3-cyclohexylpropanoic acid 2.66.	54
Scheme 2.8: Synthetic route for the cyclohexylpropanoyl piperazinone 2.67.	55
Scheme 2.9: Synthetic route for the cyclohexylpropanoyl piperazinone 2.67 in a higher yield. ...	56
Scheme 2.10: Synthetic route for the propargyl piperazinone amide analogs via amide coupling (a.) and acylation (b.).	57
Scheme 2.11: Synthetic route for the propargyl piperazinone urea analogs.	58
Scheme 2.12: Synthetic route for the propargyl piperazinone sulfonamide analogs.	59
Scheme 2.13: Conditions (a) and proposed mechanism (b) for photoinduced, copper-catalyzed N-alkylation with unactivated secondary alkyl halides.	64
Scheme 2.14: Proposed retrosynthetic route for N-alkylated cyclohexylpropanoyl piperazinones 2.49.	69
Scheme 2.15: Attempt at photoinduced, copper-catalyzed N-alkylation of 2.121 with 2-bromo-1,1-dimethoxyethane.	70

Scheme 2.16: Synthetic route to pyridopyrazine-1,6-dione 2.125 via TBD-mediated lactone-to-lactam conversion (a) and proposed mechanism (b).	71
Scheme 2.17: Retrosynthetic route for N-alkylated Cyclohexylpropanoyl Piperazinones via lactone-to-lactam conversion.....	72
Scheme 2.18: Proposed synthetic route for the synthesis N-alkylated piperazinones 2.133 via lactone-to-lactam conversion.....	72
Scheme 2.19: Retrosynthetic route for N-alkylated cyclohexylpropanoyl piperazinones 2.49 via an aminolytic ring-opening of ethylene oxide.....	73
Scheme 2.20: Photoinduced copper-catalyzed synthesis of compound 2.115.	79
Scheme 2.21: Retrosynthetic route for analogs 2.141 from the Weinreb amide cyclohexylpropanoyl piperazinone.....	79
Scheme 2.22: Retrosynthetic route for analogs 2.143 from the Weinreb amide cyclohexylpropanoyl piperazinone.....	80
Scheme 2.23: Synthetic route for the tetrazole cyclohexylpropanoyl piperazinone 2.141....	82
Scheme 2.24: Synthetic route for the Boc ethylamine cyclohexylpropanoyl piperazinone 2.143.	83
Scheme 3.1: Synthesis of (<i>E</i>)-hept-2-enoic acid (3.45) via Knoevenagel condensation.....	422
Scheme 3.2: Synthetic route of the propargyl ester analog 3.16.	423
Scheme 3.3: Synthetic route for the <i>seco</i> analogs 3.24 and 3.38.	424
Scheme 3.4: Synthetic route for tyrosyl <i>seco</i> analog 3.39.	425
Scheme 3.5: Synthetic route for the N-terminus methylated <i>seco</i> analog 3.40.....	426
Scheme 3.6: Synthetic route for the six-membered ring analog 3.25.....	428
Scheme 3.7: Synthesis of the <i>para</i> -tolyl-urea piperazinone analog 3.41.	429

Scheme 3.8: Synthetic route for the pyrazinone analog 3.28.	430
Scheme 3.9: Proposed retrosynthetic scheme for seven-membered ring 3.26 (a), ring-closure from the 3,5-difluorophenylalanine N-terminus approach (b) and ring-closure from the 3,5-difluorophenylalanine C-terminus approach (c).....	432
Scheme 3.10: Proposed mechanism for the formation of the enamine intermediates 3.56 and 3.65.	434
Scheme 3.11: Synthetic route to the 3,5-difluorophenylalanine 1,4-diazepanone 3.73.	437
Scheme 3.12: Synthetic route to the 1,4-diazepan-2-one precursor 3.75.	439
Scheme 3.13: Synthetic route to the seven-membered ring analog 3.26.....	440
Scheme 3.14: Synthetic route for the propargylated eight-membered ring precursor 3.86.....	443
Scheme 3.15: Synthetic route for the eight-membered ring analog 3.27.	445
Scheme 4.1: Retrosynthetic analysis of the piperazine scaffold 4.61.	583
Scheme 4.2: Rationale for the design of the amino acid piperazine series (4.80) from TG-0205221 (4.79).	597
Scheme 4.3: Retrosynthetic route of piperazine scaffold from piperazinone.....	602
Scheme 4.4: Synthetic route for the piperazine analog 4.66.	617
Scheme 4.5: Retrosynthetic analysis of the piperazine scaffold 4.183.	618
Scheme 4.6: Synthetic route for the diphenylalanine 4.186 (a) and dibenzyl diketopiperazine (b).	619
Scheme 4.7: Synthetic routes for 4.70 from methylpiperazine.	620
Scheme 4.8: Retrosynthetic schemes for the piperazinone scaffold.	621
Scheme 4.9: Synthetic route for the preparation of 4.198.....	621

Scheme 4.10: Synthetic route to the substituted piperazinone scaffold 4.194. The N-terminus protecting group (denoted by X) is either Boc or Cbz group.	623
Scheme 4.11: Synthetic route to the substituted piperazinone scaffold 4.208. The N-terminus protecting group (denoted by X) is either Boc or Cbz group.	624

Chapter 1 Antibacterial Resistance: a Silent Pandemic

1 Introduction

In a 2015 Ted Talk, Bill Gates cautioned about the fragility of our global system against pathogens and prophesized about life-altering pandemics: “When I was a kid, the disaster we worried about most was a nuclear war. ... If anything kills over 10 million people in the next few decades, it's most likely to be a highly infectious virus rather than a war. Not missiles, but microbes. Now, part of the reason for this is that we've invested a huge amount in nuclear deterrents. But we've actually invested very little in a system to stop an epidemic. We're not ready for the next epidemic.”¹ In December 2019, an outbreak of a novel coronavirus (SARS-CoV-2) in Wuhan, Hubei Province, China would spread across China and, in the span of a few weeks, would be present globally leading the World Health Organization (WHO) to proclaim a public health emergency of international concern. The trajectory this novel coronavirus would take echoed Bill Gates’ ominous warning and exposed the unpreparedness of our governments to address such a crisis.

After two year that brought more than 470 million cases and six million deaths worldwide, we are seemingly gaining control over the COVID-19 crisis through a global vaccination campaign, although new variants continue to arise. The last years have clearly illustrated the negative societal consequences of an infectious pandemic.

The emergence of multiple drug-resistant bacteria across the world represents an additional, yet more silent pandemic that has been years in the making as “superbugs” are now responsible for ~700,000 deaths a year.^{2, 3} Far from being unexpected, the growing crisis was

foreseen by Alexander Fleming in 1945 as he warned that “self-medication and all its abuses” would lead to select for resistant bacteria. Antibacterial resistance reduces the ability to control infectious disease, increases the cost of health care, augments the risk of innovative medical procedures, and threatens international trade, travel, and economic stability. The need for new antibacterials to treat resistant pathogens is indisputable, urgent, and global.

It is well understood that bacteria employ a multitude of resistance mechanisms to evade antibiotic exposure, including target modification (e.g., upregulation, downregulation, or structural modification), enzymatic drug inactivation, membrane modification, and efflux pump overexpression.⁴ While target modification and enzymatic degradation tend to be drug-class specific, alteration of membrane permeability and/or efflux potential directly affects the efficacy of a larger spectrum of antibacterials. A major barrier to the development of novel antibacterials able to overcome the issues of penetration and efflux in Gram-negative pathogens is our inability to employ typical medicinal chemistry structure-activity relationship (SAR) approaches to address these challenges. Traditional SAR on bacterial targets is possible and can increase potency; however, there is no roadmap for SAR to address permeation or efflux liabilities. As a result, while potent chemotypes can often be identified for new targets, developing them into viable leads with whole-cell antibacterial activity, let alone therapeutics, has proven challenging.⁴⁻⁸ The rational modification of hits and/or leads to address organism uptake and efflux deficiencies remains one of the most significant enigmas in drug development. Unlike the guidelines available for mammalian targets,⁹⁻¹¹ no comparable set of rules has been developed to guide the structural optimization of antibacterials. As such, no systematic approach exists to address the disconnects between compound efficacy in biochemical vs. whole-cell assays and *in vitro* vs. *in vivo*. Recent advances in the understanding of permeation factors and efflux biology and in the development of

new assay platforms and computational tools has now set a foundation for rational antibacterial development.⁷

2 New Mindsets in Antibacterial Development

Historically, antibacterial discovery/development has focused upon targeting enzymes/pathways that are essential to the organism, conserved across numerous species, and lack significant mammalian homology. Our inability to keep pace with bacterial resistance development and identify novel therapeutically relevant drug classes and targets has led to a discovery void.¹² As such, researchers have ventured into new concepts and approaches to fill the need for new Gram-negative antibacterials. Key topics that inform these initiatives are briefly highlighted below.

2.1 Disparate Membrane Polarity in Gram-Negatives

In order to access the cytoplasm, antibacterials must traverse the two membranes of Gram-negatives that differ greatly in chemical composition and polarity. This disparate membrane polarity has caused some to question whether it is possible to rationally design compounds capable of traversing both.^{5, 6} Compounds that rely on porin-mediated diffusion through the outer membrane (OM) tend to be polar and thus risk being trapped in the periplasm due to an inability to traverse the lipophilic inner membrane. Chemotypes that exhibit amphipathic properties, enabling passive diffusion across the OM, however, are more likely to also traverse the inner membrane and are better candidates for traditional medicinal chemistry campaigns.^{13, 14} While

disparate membrane polarity may present a challenge to cytoplasmic targets, it is not prohibitive to antibacterial development in general, as some very successful chemotypes (e.g., β -lactams) target essential processes in the periplasm and only require passage through the OM.

2.2 Chemical Space and Structural Uniqueness of Gram-Negative Actives

Although the general belief is that Gram-negative antimicrobials typically exhibit different structural and physicochemical properties compared to other drug classes, this does not apply in all cases. If, for example, β -lactams that permeate through pores and aminoglycosides that permeate by disrupting the structure of the OM are excluded, agents with activity against Gram-negative bacteria closely mimic “typical” drug-like structures.⁵ The structural diversity of Gram-negative active compounds provides a unique opportunity in drug discovery to pursue diverse chemotypes that exhibit a wide range of molecular properties.

2.3 Enhanced Antibacterial Potency

Historically, potency has not been emphasized as heavily in antibacterials as in therapeutics used to treat non-infectious conditions. This is largely because many antibacterials target enzymes/pathways that are non-existent or non-homologous to mammalian entities. Placing more focus on potency or emphasizing mechanistic efficiency (e.g., DNA cleavage vs. enzyme inhibition) during the discovery stages may provide avenues to mitigate organismal defense mechanisms.¹⁵ A recent kinetic modeling study,¹⁶ however, predicts a paradoxical relationship between the potency of a compound and its efflux. The more potent a compound, the more

efficiently it is removed from the cell by efflux pumps, because efflux is most effective at low intracellular concentrations of compounds.

2.4 Early Consideration of Combinatorial Therapy

Recent perspectives highlight the benefit of multi-targeted antibacterials. While developing new chemical entities that exhibit multiple modes of action represents one avenue of exploiting the benefit of polypharmacology, combinatorial chemotherapy should not be dismissed. In particular, combinations that enable penetration across the OM or inhibit multidrug efflux pumps could be beneficial.¹⁷ If considered early enough in the discovery phase, pharmacokinetics, pharmacodynamics, and synergism for combination therapy can be monitored throughout the evaluation process rather than retrospectively.

2.5 Development of Narrow-Spectrum Therapeutics

With the rapid rise of molecular diagnostics and the trajectory of medicine moving towards personalized and definitive treatments, there is potential future utility for organism-specific therapies. While the value in broad-spectrum antibacterials will persist, the ability to address specific pathogens will help mitigate the complications caused by broad-spectrum or “shotgun” approaches.¹⁸

2.6 Non-Traditional Approaches to Antibacterial Development

The verdict is still out on whether targeting virulence is a viable strategy for clearing infection.^{4, 19, 20} Nonetheless, this approach is revealing important information about both bacterial and human physiology and is worthy of continued pursuit. Likewise, the field of enzyme/pathway activation is rapidly gaining traction as a therapeutically promising avenue.²¹⁻²³ Despite the impact of traditional approaches, the current dire times call for creative, novel, and paradigm-shifting strategies, which will only arise from “outside-the-box” approaches.

3 Recent Advances in the Development of Antibacterials Active in Gram-Negative Bacteria

Faced with the pressing need for discovery of new antibacterials with activity against Gram-negative pathogens, new methods for assessment of antibacterial activity and for measuring compound permeation and accumulation have been developed. Several foundational studies have revealed that structure-accumulation relationships exist and can be implemented in medicinal chemistry campaigns. However, both retrospective and predictive approaches indicate that it is unlikely that general “Lipinski- type” permeation rules will be developed for Gram-negative accumulation. Rather, attention will likely need to be devoted to each specific chemotype and pathogen of interest. As more is learned about bacterial biology, it is becoming apparent that new kinetic and computational data analysis and machine learning are imperative to addressing the complexity of rational antibacterial drug design and development. In this regard, **Chapter 2** reviews recent advances in rational antibacterial discovery and presents my synthetic work for a library of piperazinone Caseinolytic protease P (ClpP) activators. The antibacterial activity of this library of chemically diverse analogs in genetically modified Gram-negative bacteria (*Escherichia*

coli, *Acinetobacter baumannii* and *Pseudomonas aeruginosa*) set the stage for the establishment of predictive models and strategies to enhance the accumulation of small molecules in Gram-negative bacteria. In **Chapter 3**, the SAR of the ClpP activator scaffold is expanded to manipulate the size of the piperazinone (six-membered ring) core to a diazepanone (seven-membered ring) and diazocanone (eight-membered ring), assessing the effect of ring size and corresponding conformation on activity. The impact of the structural constraint of a cyclized peptidomimetic scaffold was analyzed *in silico* and *in vitro* to provide insight. Finally, **Chapter 4** covers the *in silico* design of SARS-CoV-2 Main protease inhibitors, along with the synthetic work to generate a preliminary library of compounds.

1. Gates, B. The next outbreak? We're not ready. https://www.ted.com/talks/bill_gates_the_next_outbreak_we_re_not_ready/transcript?language=en#t-38410.
2. Resistance, I. C. G. o. A., No time to wait: Securing the future from drug-resistant infections. **2019**.
3. Balasegaram, M., Learning from COVID-19 to Tackle Antibiotic Resistance. *ACS Infect Dis* **2021**, 7 (4), 693-694.
4. Lewis, K., Platforms for antibiotic discovery. *Nat Rev Drug Discov* **2013**, 12 (5), 371-87.
5. Silver, L. L., A Gestalt approach to Gram-negative entry. *Bioorg Med Chem* **2016**, 24 (24), 6379-6389.
6. Silver, L. L., Challenges of antibacterial discovery. *Clin Microbiol Rev* **2011**, 24 (1), 71-109.
7. Nikaido, H., Prevention of drug access to bacterial targets: permeability barriers and active efflux. *Science* **1994**, 264 (5157), 382-8.
8. Walsh, C. T.; Wencewicz, T. A., Prospects for new antibiotics: a molecule-centered perspective. *J Antibiot (Tokyo)* **2014**, 67 (1), 7-22.
9. Lipinski, C. A.; Lombardo, F.; Dominy, B. W.; Feeney, P. J., Experimental and computational approaches to estimate solubility and permeability in drug discovery and development settings. *Advanced Drug Delivery Reviews* **1997**, 23 (1-3), 3-25.
10. Veber, D. F.; Johnson, S. R.; Cheng, H. Y.; Smith, B. R.; Ward, K. W.; Kopple, K. D., Molecular properties that influence the oral bioavailability of drug candidates. *J Med Chem* **2002**, 45 (12), 2615-23.
11. Over, B.; Matsson, P.; Tyrchan, C.; Artursson, P.; Doak, B. C.; Foley, M. A.; Hilgendorf, C.; Johnston, S. E.; Lee, M. D. t.; Lewis, R. J.; McCarren, P.; Muncipinto, G.; Norinder, U.; Perry, M. W.; Duvall, J. R.; Kihlberg, J., Structural and conformational determinants of macrocycle cell permeability. *Nat Chem Biol* **2016**, 12 (12), 1065-1074.

12. Aminov, R. I., A brief history of the antibiotic era: lessons learned and challenges for the future. *Front Microbiol* **2010**, *1*, 134.
13. Nikaido, H.; Thanassi, D. G., Penetration of lipophilic agents with multiple protonation sites into bacterial cells: tetracyclines and fluoroquinolones as examples. *Antimicrob Agents Chemother* **1993**, *37* (7), 1393-9.
14. Zgurskaya, H. I.; Lopez, C. A.; Gnanakaran, S., Permeability Barrier of Gram-Negative Cell Envelopes and Approaches To Bypass It. *ACS Infect Dis* **2015**, *1* (11), 512-522.
15. Kohanski, M. A.; Dwyer, D. J.; Collins, J. J., How antibiotics kill bacteria: from targets to networks. *Nat Rev Microbiol* **2010**, *8* (6), 423-35.
16. Westfall, D. A.; Krishnamoorthy, G.; Wolloscheck, D.; Sarkar, R.; Zgurskaya, H. I.; Rybenkov, V. V., Bifurcation kinetics of drug uptake by Gram-negative bacteria. *PLoS One* **2017**, *12* (9), e0184671.
17. Melander, R. J.; Melander, C., The Challenge of Overcoming Antibiotic Resistance: An Adjuvant Approach? *ACS Infect Dis* **2017**, *3* (8), 559-563.
18. Jernberg, C.; Lofmark, S.; Edlund, C.; Jansson, J. K., Long-term impacts of antibiotic exposure on the human intestinal microbiota. *Microbiology (Reading)* **2010**, *156* (Pt 11), 3216-3223.
19. Heras, B.; Scanlon, M. J.; Martin, J. L., Targeting virulence not viability in the search for future antibacterials. *Br J Clin Pharmacol* **2015**, *79* (2), 208-15.
20. Clatworthy, A. E.; Pierson, E.; Hung, D. T., Targeting virulence: a new paradigm for antimicrobial therapy. *Nat Chem Biol* **2007**, *3* (9), 541-8.
21. Conlon, B. P.; Nakayasu, E. S.; Fleck, L. E.; LaFleur, M. D.; Isabella, V. M.; Coleman, K.; Leonard, S. N.; Smith, R. D.; Adkins, J. N.; Lewis, K., Activated ClpP kills persisters and eradicates a chronic biofilm infection. *Nature* **2013**, *503* (7476), 365-70.
22. Mike, L. A.; Dutter, B. F.; Stauff, D. L.; Moore, J. L.; Vitko, N. P.; Aranmolate, O.; Kehl-Fie, T. E.; Sullivan, S.; Reid, P. R.; DuBois, J. L.; Richardson, A. R.; Caprioli, R. M.; Sulikowski, G. A.; Skaar, E. P., Activation of heme biosynthesis by a small molecule that is toxic to fermenting *Staphylococcus aureus*. *Proc Natl Acad Sci U S A* **2013**, *110* (20), 8206-11.
23. van Rensburg, J. J.; Fortney, K. R.; Chen, L.; Krieger, A. J.; Lima, B. P.; Wolfe, A. J.; Katz, B. P.; Zhang, Z. Y.; Spinola, S. M., Development and validation of a high-throughput cell-based screen to identify activators of a bacterial two-component signal transduction system. *Antimicrob Agents Chemother* **2015**, *59* (7), 3789-99.

Chapter 2 Synthesis of a Piperazinone ClpP Activator Library as a Tool for Enhancing Small Molecules Accumulation in Gram-Negative Bacteria

Abstract

Among the different mechanisms of resistance in Gram-negative bacteria, the permeability barrier of the outer membrane and efflux pumps represent a significant challenge to address as they synergize to reduce accumulation of most antibiotics. As no predictive model of the structural and physicochemical properties governing efflux susceptibility and outer membrane permeability has been developed, there is a pressing need for strategies to enhance the accumulation of small molecules in Gram-negative bacteria. The Small-molecule Penetration & Efflux in Antibiotic-Resistant Gram-Negatives (SPEAR-GN) project takes a multidisciplinary approach to develop a class- and activity-independent model for antibiotic permeability by building small-molecule libraries. For my contribution to this project, I conducted the synthesis of a library centered around a piperazinone scaffold which is derived from the natural product acyldepsipeptide (ADEP), a potent activator of bacterial caseinolytic protease P (ClpP). The N- to C-terminal cyclization of the ADEP pharmacophore, *N*-heptenoyl 3,5-difluorophenylalanine, was hypothesized to constraint the conformation of the scaffold and improve its metabolic stability. From an optimized three-step synthetic route to produce the piperazinone core, I generated a library of 48 chemically diverse piperazinone analogs, for which I investigated and optimized different methodologies such as N-alkylation of secondary amides with inactivated alkyl halides using phase-transfer catalysis, photoinduced copper catalysis and synthetic handles. In parallel to the piperazinone library, Quentin Gibault and Katelyn Stevens generated a set of uncyclized or *seco* analogs to examine the

role of the cyclization on antibacterial activity and accumulation in Gram-negatives. The Zgurskaya lab evaluated the antibacterial activity of the library by measuring the minimum inhibitory concentration (MIC) in isogenic strain sets of wild-type, hyperporinated, efflux-deficient, and doubly compromised (i.e., hyperporinated and efflux-deficient) *E. coli*, *P. aeruginosa*, and *A. baumannii*. The promising biological results set the stage for future LC/MS accumulation studies and will lead to the identification of physicochemical properties or motifs governing efflux susceptibility and outer membrane permeability in the *seco* and piperazinone libraries.

1 Introduction

In 2016, the Wellcome Trust supported Review on Antimicrobial Resistance estimated that death from antibiotic resistance could reach 10 million lives annually by 2050.¹ Subsequently, in 2017, the World Health Organization (WHO) published a priority pathogens list (**Table 2.1**) as a signal to researchers world-wide that advancements in antibiotic research are crucial to the longevity of our species. Such predictions and prioritizations emphasize the urgency to develop new antibiotics or methods capable of treating antimicrobial resistant infections.² Bacterial pathogens emphasized by the WHO are resistant either to the most frequently prescribed antibiotics (e.g., β -lactams, macrolides, fluoroquinolones) or last resort antibacterial treatments (e.g., vancomycin).³ Of particular concern, is the growing number of Gram-negative bacteria on this list, as they represent a critical challenge to drug development, due to increased mechanisms of inherent resistance.

Priority Level	Pathogen (Gram staining)	Antibiotic Resistance
Critical	<i>Acinetobacter baumannii</i> (-)	Carbapenem
	<i>Pseudomonas aeruginosa</i> (-)	Carbapenem
	<i>Enterobacteriaceae</i> (-)	Carbapenem Cephalosporin (3 rd generation)
High	<i>Enterococcus faecium</i> (+)	Vancomycin
	<i>Staphylococcus aureus</i> (+)	Methicillin Vancomycin
	<i>Helicobacter pylori</i> (-)	Clarithromycin
	<i>Campylobacter</i> (-)	Fluoroquinolone
	<i>Salmonella spp.</i> (-)	Fluoroquinolone
	<i>Neisseria gonorrhoeae</i> (-)	Cephalosporin (3 rd generation) Fluoroquinolone
Medium	<i>Streptococcus pneumoniae</i> (+)	Penicillin
	<i>Haemophilus influenza</i> (-)	Ampicillin
	<i>Shigella spp.</i> (-)	Fluoroquinolone

Table 2.1: World Health Organization priority pathogens list (2017). These pathogens were ranked based on their related mortality, prevalence of resistance, 10-year trend of resistance,

transmissibility, preventability in hospital and community settings, treatability and current pipeline.²

The rational modification of antibacterials to address uptake and efflux deficiencies remains one of the most significant barriers to medicinal chemistry. Unlike the Lipinski rules of 5⁴ or permeability guidelines for eukaryotic targets,⁵ no comparable set of rules has been developed to guide the structural optimization of antibacterials. As such, no systematic approach to address the disconnect between compound efficacy in recombinant and *in vivo* assays exists. It is well understood that bacteria employ a multitude of resistance mechanisms to evade antibiotic exposure, which include target modification (e.g., upregulation, downregulation or structural modification), enzymatic drug inactivation, membrane permeability alteration, and efflux pump overexpression.⁶ While, target modification and enzymatic degradation tend to be class specific, organismal alteration of permeability and/or efflux potential directly affects the efficacy of a large spectrum of antibacterials. Recent advances in the understanding of permeation factors, efflux biology, assay development and computational tools has now set in motion the pursuit of guidelines capable of directing medicinal chemistry efforts and providing a rational approach to lead optimization.⁷

2 Slow Uptake and Active Efflux: The Challenges of Bacterial Membrane

2.1 Passive Diffusion

2.1.1 Gram-Positive Bacteria

Gram-positive bacteria exhibit a cell envelope consisting of an external peptidoglycan layer and an internal phospholipid bilayer. The peptidoglycan layer is made of alternating units of N-

acetylglucosamine and N-acetylmuramic acid layers crosslinked by pentapeptide chains (varying between species). Composed of repeating units of ribitol or glycerol units linked by phosphodiester, lipoteichoic acids are covalently linked to a glycolipid on the outer face of phospholipid bilayer and traverse the peptidoglycan layer to the cell surface. The teichoic acid polymers give the cell envelope a net negative charge. Beneath the peptidoglycan layer is the plasma membrane consisting of an inner and outer leaflets of phospholipids.⁸⁻¹⁰

Due to the relative simplicity compared to Gram-negative bacteria, the cell wall of Gram-positive bacteria is permeable to wide range of antibiotics (up to 57 kDa), generally bacterial resistance in Gram-positive microbes arises from phenomena other than cell wall exclusion mechanisms.^{11, 12}

2.1.2 Gram-Negative Bacteria

Gram-negative bacteria differ significantly from Gram-positives regarding the composition of the cellular envelope. In addition to the peptidoglycan layer and the inner membrane, Gram-negative bacteria display an asymmetric outer membrane (OM) comprised of an inner leaflet that is composed of phospholipids and an outer leaflet consisting of a high lipopolysaccharide (LPS) content.

The structure of LPS can be divided in three parts: lipid A, a central oligosaccharide core, and O-antigen. Lipid A is a glucosamine disaccharide unit that resides in the inner leaflet of the OM and is phosphorylated at the 1 and 4' positions. The disaccharide backbone is N- and O-acylated with 3-hydroxymyristic acid, which is itself O-acylated with palmitic acid to an extent that varies between bacterial species. The central core of LPS is a complex oligosaccharide divided

into an inner and outer domain. The inner domain is linked to lipid A by several 3-deoxy-D-manno-2-octulosonate (KDO) residues functionalized with heptose moieties. In a species dependent fashion, the heptose residues can be substituted by phosphate, pyrophosphate, phosphorylethanolamine, or different saccharide. The outer core consists of hexose residues further functionalized with saccharide or alanine residues. At the outermost part of LPS is the O-antigen, which is composed of repeating units of oligosaccharides ranging from 1 to 40 monosaccharides. The structural integrity of the OM is rather unique, as it relies on divalent cation interactions rather than covalent cross-linking.¹³⁻¹⁵

The OM itself confers Gram-negative bacteria multiple layers of inherent resistance, especially to exogenous substances. For instance, increased lipid A acylation enhances the rigidity of the lipid core, thus lowering the permeability of small hydrophobic antibiotics.¹⁶ Additionally, structural modifications to the O-antigen alters antibiotic susceptibility. Bacterial species lacking O-antigen side chains, exhibit a deep rough phenotype, which indirectly promotes permeability to hydrophobic antibacterials.¹⁷ The highly charged nature of the outer surface of LPS precludes or slows the passage of hydrophobic antibiotics through the envelope. However, polycationic antibacterials such as aminoglycosides, polymyxins and polycationic peptides can permeate across the OM by interacting with divalent cation binding sites on the LPS surface. Due to high affinity within these sites, they competitively displace the divalent cations and cause a distortion of the OM structure. This “self-promoted uptake” pathway is postulated to account for efficacy of these antibacterials against *P. aeruginosa*. As one may infer, resistance to polycationic molecules arises from the modification of lipid A to contain positively charged aminoarabinose, which exhibits a low phosphate content and reduces the overall negative charge of the surface. This phenomenon has been observed in *Salmonella enterica* or *Burkholderia cepacia*.^{18, 19}

2.2 Facilitated Diffusion and Active Transport via Outer Membrane Proteins

Although the major roles of the Gram-negative OM are to protect the organism from environmental threats and provide structural scaffolding, the organisms must be able to compensate for the significantly reduced uptake of nutrients and essential solutes as a result of the increased envelope complexity. To address this, Gram-negatives incorporate proteins to regulate the influx of molecules into the bacterial cell through facilitated diffusion. Embedded in the OM, these proteins act as channels and are generally organized into trimers of water-filled β -barrels. These OM proteins, also called porins, can be separated into two main categories: specific and non-specific porins (**Table S2.1**). Porin selectivity arises from the highly polar constriction region at the center of the β -barrels formed by the internal loop 3.²⁰ The charge distribution within this eyelet, positively charged residues on one side (Arginine, Lysine) and negatively charged residues on the other (Aspartic acid, Glutamic acid), induces a transversal electric field, which orients polar water molecules. To permeate through the constriction region, solutes need to displace polarized water molecules, a phenomenon only enabled by polar molecules. Non-polar molecules, however, fail to displace polar water molecules and thus are not capable of diffusing through porins. Amphiphilic and hydrophilic solutes are capable to form hydrogen bonds and salt bridges with the eyelet residues; these interactions are stronger than those with water molecules. Therefore, these polar molecules bind more favorably to the charged residues than water and displace them from the constriction region.^{21, 22}

Although general porins allow a large range of molecular size (>600 Da) to permeate, some porin families exhibit unique ionic affinities. For example, the OmpC and OmpF families favor

cation diffusion whereas the PhoE family shows a preference for anionic passage.²³ Higher levels of selectivity have also been observed in some porin families. For instance, the maltoporin LamB family only allows maltodextrin-like molecules to pass due to the presence and specific orientation of aromatic and charged residues within the channel that specifically complement the maltodextrins.²⁴

Unlike the relatively low selectivity exhibited by the aforementioned open channels that, for the most part, lack specific substrate recognition domains, active transport porins require a high binding affinity between molecules and a specific protein site. These gated porins comprise the TonB-dependent receptor family. In addition to the β -barrels anchored in the OM, three proteins (TonB, ExbD and ExbB) embedded in the cytoplasmic membrane are involved in the energy transfer. Upon binding and recognition of the substrate, conformational changes in TonB, induced by the proton motive force across the cytoplasmic membrane, results in interaction of the TonB subunit with the OM transporter. In allosteric fashion, this interaction causes the release of the substrate from the binding site, enabling it to traverse the channel to reach the periplasm.²⁵

Gram-negative bacteria use this energy-coupled transport system to scavenge essential nutrients from the environment. This is exemplified in iron acquisition, during which secreted secondary metabolites called siderophores bind to ferric ions and then operate through active transport porins to deliver iron intracellularly (**Table S2.1**).²⁵ The uptake of vitamin B12 occurs in a similar fashion via the BtuB OM protein.²⁶

Within Gram-negative bacteria, *P. aeruginosa* is unique as the lack of general porins OmpC and OmpF results in an extremely effective defense barrier. *P. aeruginosa* has evolved to possess a large number of specific porins to counteract the significant general permeability barrier. Porins utilized by *P. aeruginosa* include the major porin, OprF, responsible for the uptake of

relatively large molecules (about 1.5 kDa),²⁷ OprD and OprB (homologs of LamB) for 50 kDa and 180 Da respectively.^{28, 29} Furthermore, a set of 35 TonB-dependent receptors (e.g., FpvA, FptA, PfeA, PirA, HasR, PhuR, OptI) specific to *P. aeruginosa* are employed by the organism to transport iron across the cell wall.³⁰

With such complex regulation of nutrient and solute transport, one is tempted to assume that taking advantage of this system in antibacterial drug development should be a trivial objective. However, we know this to not be the case, as bacteria constantly control the type and expression level of porins and exhibit the capability to evolve through protective mutations. As an example, in addition to enzymatic inactivation via β -lactamases, porin expression in Gram-negative bacteria directly affects the permeation of β -lactams. The amphiphilic nature of these antibiotics makes them good substrates for non-specific porins. As such, loss of OmpC or OmpK36 results in a decrease in β -lactam susceptibility. Likewise, in *P. aeruginosa*, OprD deficiency or residue mutation in the OprD eyelet results in carbapenem-resistance.³¹ Similarly, β -lactam diffusion is impaired when mutations in OmpF eyelet occur, as the mutated residues protrude into the channel and preclude the antibiotic from passing into the periplasm. Moreover, OmpF-deficient strains have been shown to be resistant to fluoroquinolones in *E. coli* and *P. aeruginosa*.³²⁻³⁵

2.3 Efflux Pumps

Despite the cell envelope and selective porins, noxious substances still manage to reach the bacterial cytoplasm and cause harm to the cell. Throughout bacterial species, a variety of export systems exist and are capable of expelling a broad range of molecules out of the cytoplasm and periplasm. Anchored in the membrane, these efflux pumps act in synergy with the permeability

barrier provided by the cell wall, to significantly decrease the intracellular concentration of antibacterials. Inner membrane transporters can be divided into five families: (1) ATP-binding cassette (ABC) superfamily; (2) Resistance-nodulation-division (RND) superfamily; (3) Major facilitator superfamily (MFS); (4) Multidrug and toxic compound extrusion (MATE) family; and (5) Small multidrug resistance (SMR) family.^{36, 37}

ABC transporter efflux pumps (**Table S2.2**) are generally composed of four protein domains: two membrane-spanning domains (MSDs) responsible for substrate translocation and two nucleotide-binding domains (NBDs), which provide energy to the transporter via ATP hydrolysis. The four domains are fused together within the inner membrane, however, in Gram-negative species additional OM facilitators are necessary to export substances from the periplasm (e.g., TolC). Drug efflux begins with substrate recognition on the cytoplasmic face of the transporter, via high-affinity binding of the substrate. Promoted by the drug binding, the closure of NBD allows for ATP hydrolysis which, in turn, triggers a conformational switch in the MSD that unidirectionally transports the molecule across the membrane. Upon ATP hydrolysis, the NBDs reopen, and the substrate diffuses from the outer face of the transporter into the extracellular environment.³⁸

Unlike ABC transporters that use ATP hydrolysis as a driving force, RND, MFS, MATE and SMF transporter families efflux drugs with proton or sodium motive force. The RND superfamily (**Table S2.3**) is notably widespread in Gram-negative bacteria, these efflux pump systems have been extensively studied, AcrAB-TolC (in *E. coli*) and MexAB-OprM (in *P. aeruginosa*) are well-known in particular. These export systems are channel-tunnel-dependent efflux pumps and form trans-envelope tripartite complexes: the inner membrane transporter (e.g.,

AcrB and MexB), the periplasmic membrane fusion protein (MFP) (e.g., AcrA and MexA) and the OM tunnel (e.g., TolC and OprM).^{36, 37}

In AcrAB-TolC, the homotrimer AcrB is embedded in the inner membrane and extends to the periplasm. Driven by proton motive force, AcrB goes through a cycle of conformational changes to export drugs. The MFP AcrA assembles into a hexameric structure on the surface of AcrB and forms a tunnel engaged in a highly flexible complex with TolC. The OM transporter TolC is a homotrimer consisting of three domains: the channel on the outer surface of the cell wall; the tunnel connected to the periplasm and an equatorial domain strapped around the mid-section of the tunnel. Unless activated, the periplasmic entrance remains in a closed conformation, where six aspartate residues assemble to form a 4 Å pore. AcrB substrate-dependent conformational changes are believed to initiate transition in AcrA conformation to open TolC. This trans-envelope complex allows *E. coli* to expel a variety of substrates from the cytoplasm and the periplasm through TolC. The efflux pump MexAB-OprM is homologous to AcrAB-TolC in structure and function.^{36, 37, 39, 40}

The MFS transporters (**Table S2.4**) consist of two transmembrane domains surrounding a substrate translocation pore, drug efflux is driven by electrochemical gradients. In Gram-negative bacteria, the export system functions as a tripartite complex with the transmembrane transporter, an MFP, and an OM channel (e.g., EmrAB-TolC and EmrKY-TolC in *E. coli*).^{36, 37} The MATE transporters (**Table S2.5**) are thought to use sodium or proton motive force to efflux substrates, however their function is still unclear.^{37, 41, 42} The SMR transporters (**Table S2.6**) function as homodimers of a small four-transmembrane protein, however they are limited to substrate efflux into the periplasm.³⁷

Bacteria have managed to set up an elaborate line of defense against antibiotics by precluding them from entering the cell with a poorly permeable membrane and by expelling them with efflux pumps. The synergy of these mechanisms of resistance embodies many challenges to efficiently treat bacterial infections: (1) Distinguishing the respective influence of outer/inner membrane penetration and active efflux on antibiotic accumulation and establishing methods to measure them; (2) Identifying the resistance mechanisms (i.e., OM composition, types of porins and efflux pumps) in each bacterial species and their respective effect on compound accumulation; (3) Developing models to predict the structural and physicochemical properties favorable and/or liable to the permeability barrier and efflux, and designing compounds based on these models. Hereafter, I highlight the existing bioassays and strategies used in antibiotic research, discuss their limitations and how the field can be improved upon.

3 Methods to Evaluate Antibacterial Activity

Historically, the determination of a compound's minimum inhibitory concentration (MIC), the lowest concentration that inhibits bacterial growth, has been the standard method to evaluate antibacterial activity. Extension of MIC assays, to include subsequent dilution and growth monitoring, provides a means to determine both if a compound is bactericidal or bacteriostatic and, if bactericidal, reveals the minimum bactericidal concentration (MBC). Typically, these MIC/MBC assays are run in broth microdilution formats amenable to the rapid evaluation of a series of compounds over a large dose range against a panel of bacteria. While meaningful and informative in nature, the degree of permeation, efflux, susceptibility to enzymatic degradation, and intracellular concentration for a given compound cannot be extracted from traditional

MIC/MBC assays, unless the antibacterial activities of compounds are compared between sets of genetically or chemically modified strains that overproduce or deplete the target, overproduce or deplete the efflux capacity, contain modifications in the OM that change the permeability barrier of the cells, etc.^{43, 44} When combined with morphological and metabolomics profiles, the MIC/MBC assays can provide an in-depth characterization of the intracellular activity of compounds.⁴⁵⁻⁴⁷

3.1 Chemical Modifications of Cells

It is well understood that antibiotic efflux significantly decreases the efficacy of antibacterials by expelling the active compound prior to target engagement.^{37, 48} Consequently, a negative result in MIC assays does not indicate if the compound is inactive due to lack of target engagement or because of active efflux from the cell. If genetic manipulation is not an option (often the case with clinical multidrug resistant isolates), efflux pump inhibitors (EPIs) can be combined with antibiotics to determine the contribution of efflux to the activities of compounds. Several classes of EPIs have been described, with some acting directly on specific efflux pumps and inhibiting various steps in a transporter's cycle (e.g., PA β N, NMP, ABI_PP, reserpine).^{37, 49-52} Due to high levels of selectivity exhibited by certain EPIs, they represent effective chemical tools to identify efflux pumps involved in antibiotic resistance and to elucidate the susceptibility of compounds of interest to efflux.⁵³⁻⁶¹ However, this approach has limited utility, especially for screening campaigns, as efflux pumps that interact with new chemotypes are rarely known.^{54, 56, 61-65} Furthermore, in many cases, pump-specific EPIs cannot penetrate across the OM of

“impermeable” species such as *P. aeruginosa* or *Burkholderia spp.* and fail to potentiate the activity of antibiotics because they cannot reach the targeted transporter.

EPIs that are non-specific and disrupt the proton motive force required for efflux (e.g., CCCP, phenothiazine) are also broadly used in analyses of antibiotic permeation and activity. However, these compounds are highly hydrophobic and accumulate in lipid bilayers, modifying lipid packing and membrane fluidity. As a result, permeation increases not only due inhibition of efflux pumps but also due to increased passive diffusion across lipid bilayers.

The Gram-negative OM itself precludes the entry of most molecules into bacterial cells.^{13-15, 66} Permeabilizing agents, however, can be used in combination with antibiotics to increase passive diffusion. Agents such as ethylenediaminetetraacetic acid (EDTA), polymyxin B nonapeptide (PMBN) derivatives,¹⁴ pyridinium zinc phthalocyanine (PPC)⁶⁷ and pentamidine⁶⁸ act on the OM by disrupting lipopolysaccharide (LPS) organization and are commonly used to artificially increase membrane permeability. Nevertheless, the ability of these agents to permeabilize the OM of Gram-negatives is inconsistent, as compound-induced permeation efficiency depends on the LPS architecture.⁶⁹⁻⁷³

3.2 Genetic Modifications of Cells

Beyond chemical manipulation of bacterial permeation and efflux, gene-editing quickly is becoming the gold-standard approach for characterization of antibacterial activities and mechanisms of action. Unlike chemical methods, gene manipulation ensures a more targeted approach regarding efflux and permeation within specific organisms. Several approaches have reshaped the field of antibacterial drug discovery and target evaluation, including gene knock-out

of efflux or porin components,^{50, 74-77} plasmid-borne efflux gene introduction,⁷⁸ and gene knock-outs of enzymes involved in cell wall biosynthesis.⁷⁹ Furthermore, experimental approaches have been developed to alter the permeability barrier of the Gram-negative OM. For example, a hyperporinated *E. coli* cell line has been developed by introducing genetically modified gated FhuA channels that lack the plug and extracellular loops, thereby creating large open pores that allow a wide range of substrates to permeate through the OM.⁴⁴ This provides an opportunity to determine the contributions of active efflux and/or the OM to the activities of antibiotics, enabling systematic SAR analyses for active efflux and/or permeation across the OM. To study the role of specific porins on antibiotic permeation a whole-cell assay called Titrable Outer Membrane Permeability Assay System (TOMAS) was recently developed. This platform allows for MIC determination in *E. coli* and *P. aeruginosa* mutants (lacking OmpA, OmpC and OmpF porins) under differing levels of OprD porin expression.⁷⁶ Parallel growth studies in wild-type, efflux-deficient, and membrane-compromised strains provides a means to extract permeation and efflux profiles of antibacterial leads, thus yielding insightful information that can be leveraged in SAR campaigns.

In summary, MIC/MBC determinations on wild-type pathogenic strains are insufficient to define the antibacterial activity of new chemical entities. In fact, in many cases, MIC/MBC assays can be misleading and result in the over-prioritization or neglect of viable hits/leads. Although the chemical and genetic approaches discussed herein provide additional information about the permeation and efflux profiles of new hits/leads, these studies are organism specific. Furthermore, for non-traditional antibacterial approaches (e.g., anti-virulence, enzyme/pathway activation), MIC/MBC determinations are often irrelevant, as the desired effect may not be tied to bacterial growth or survival, but rather to pathogenic traits. Taken together, the incorporation of assays

capable of determining physicochemical profiles for permeation, accumulation, and susceptibility to efflux early on in the discovery phase have high value in the efficiency of antibacterial development.

4 Methods to Determine Compound Permeation and Accumulation

Analytical methods can be paired with genetic mutants to allow for the intracellular localization of compounds to be quantified in bacterial cells. Several detection methods have been developed, including radiometry,^{52, 80-83} intrinsic fluorescence⁸⁴ and fluorescent probes,^{81, 82, 85-93} Raman spectroscopy,⁹⁴ enzyme kinetics (e.g., β -lactamase, peptidases),⁹⁵⁻⁹⁸ ToF-SIMS⁹⁹ and LC-MS/MS.^{82, 100-103} Among these, MS- and fluorescence-based techniques are the most broadly used and versatile.

4.1 Mass Spectrometry

LC-MS/MS is becoming established as the gold-standard in efflux and permeation measurements due to its broad applicability, high accuracy and versatility.^{82, 103-105} However, the method also has certain limitations, as cells must be separated from the external solution without any loss of the intracellular compound. Most common techniques utilize vacuum filtration, centrifugation, or growth on filters to achieve separation. Depending on the properties of compounds, significant experimental error can be present due to non-specific binding to filter, plastic tubes, or cell surfaces. The assay described by Zhou and co-workers eliminates washing steps by measuring changes in concentration of compounds in supernatants, while taking into

consideration the non-specific binding of drug on the cell surface.¹⁰³ This method is practical for compounds that accumulate and stay inside the cells by binding to an abundant high affinity target. For many other compounds, such depletion of compound from the supernatants will be very small and difficult to measure. An alternative approach is to determine relative changes in intracellular concentration by using sets of genetically modified strains with varying efflux capacities and OM permeabilities. Recent advances in a single cell imaging MS and untagged metabolomics further expand the applications of MS in drug accumulation analyses.^{106, 107}

4.2 Fluorescence

The uptake of environment-sensitive dyes can be used to compare and analyze differences in permeability barriers in laboratory and clinical isolates and in genetically altered variants.^{50, 54, 80, 97, 108-114} The fluorescence of these dyes is enhanced when they bind to membranes, proteins or nucleic acids. Time-dependent changes in fluorescence provide kinetic information about permeation, efflux, and intracellular accumulation. Such assays are of high throughput and can be adapted to microfluidics and microscopy for single-cell analyses. The fluorescence enhancement of the probe is often specific to cellular compartments, enabling assessment of intracellular localization.

4.3 Electrophysiology and Liposome Swelling Assays

The liposome swelling assay represents the most straightforward method to extract permeation rates through porins. Conceptually, this assay leverages the osmotic imbalance caused

by the diffusion of compounds through artificial lipid bilayer vesicles with or without incorporated porins. To restore balance the liposomes swell, and ultimately the vesicles burst and release pre-loaded dyes or polymers that can then be quantified. Penetration rate is determined from turbidity or fluorescence changes. This method allows for the evaluation of permeability in a simplified, more malleable model of living cells. Artificial liposomes, however, lack the structural complexity of Gram-negative bacteria, and the purification/reconstitution of porins can be a challenging task; thus, the translational value of these assays for clinically relevant pathogens is limited.^{97, 100, 115-118}

To specifically evaluate porin-mediated uptake of compounds, electrophysiology approaches on lipid bilayers artificially impregnated with porins are frequently employed. Passage of a compound of interest from one side of the bilayer to the other is quantified by ion current fluctuations due to molecular diffusion through a single channel. High-resolution ion-current fluctuation analysis allows for the determination of the permeation rate of compounds and the identification of porin substrates. Although the accuracy of this technique has been improved, the stability of the lipid bilayer can be easily disrupted by electrical and mechanical forces and thus the quality of the readings can be affected by ion current noise.^{23, 97, 100, 108, 115, 119, 120} Although useful, the method only provides relative porin permeation rates since it does not take into account passive diffusion across the lipid bilayer and translocation is indistinguishable from transient binding to the porin.¹²¹

Recently, optofluidic methods have been developed to provide a more accurate model for studying permeability across porins and lipid membranes. The assay measures the change in fluorescence intensity when the drug molecules and vesicles (liposomes/proteoliposomes) are mixed via a T-junction microfluidic chip. Currently, this method suffers from the variability of porin insertion into the vesicles, which prevents an accurate estimation of the flux per porin.^{116, 122}

The popularity of microfluidics, however, is expected to lead to improved experimental and quantification methods.

Advances in permeation, accumulation, and efflux quantification are finally providing detailed analyses of therapeutically relevant chemotypes (e.g., tetracyclines¹²³ and cephalosporins¹²⁴). The complexity and diversity of Gram-negative pathogens, however, will likely require organism and chemotype specific analyses to reveal useful SAR information. Paralleled evaluation of target engagement, cell accumulation, and susceptibility to efflux for individual chemotypes against specific pathogens has begun to pave the way for rational medicinal chemistry campaigns. When combined with MIC/MBC determinations, a clearer picture begins to unfold that provides direction for SAR. The examples that follow highlight recent approaches to enhance cell accumulation of promising hits/leads.

5 Recent Examples of Rational Approaches to Enhance Gram-Negative Accumulation

The aggregate effect of the variety and complexity of Gram-negative cell envelopes and efflux systems has limited the ability of medicinal chemists to develop general strategies to enhance accumulation and/or convert Gram-positive-only actives into broad-spectrum agents. However, some historic examples are known, notably the transformation of penicillin G into the broad-spectrum ampicillin, and the transformation of erythromycin into azithromycin.^{125, 126} These success stories, while small in number, provide proof-of-concept that rational approaches are possible.

In an effort to guide antibiotic research and facilitate rational SAR campaigns, a group of 147 antibacterial compounds, including both clinically approved entities and those still under

development, were analyzed for physicochemical trends that correlate with Gram-negative activity.¹²⁷ The study concluded that Gram-negative actives generally exhibit a MW<500 and a $\text{clogD}_{7.4} < -2.8$. However, 48 of the 147 (33%) compounds included in the analysis were penicillins, cepheids, and (carba)penems. The periplasmic locus of action of these compounds masks any revelation of properties necessary for cytoplasmic accumulation. As such, it is not surprising that while the results are compatible with porin architecture and have been corroborated by additional studies, there are molecules that fit these characteristics but do not accumulate in Gram-negative organisms.

A more recent study profiled more than 3,200 antibacterial compounds to identify trends that correlate with whole-cell activity against Gram-negative bacteria.¹²⁸ Overall, the results are consistent with the previous report, but further concluded that compounds with lower susceptibility to efflux are either (1) very polar and of low molecular weight or (2) zwitterionic and of high molecular weight. These trends do not discriminate between the compound permeation mode, or the type of transmembrane proteins involved in their efflux.

Thus far, attempts to identify optimal physicochemical properties for Gram-negative actives are empirical, retrospective in nature, often monopolized by a small number of chemotypes, and do not provide direct insight into addressing permeability or efflux susceptibility. The inability to produce a set of predictive “Lipinski-like” rules to guide antibacterial development, suggests that a more organism- or chemotype-specific approach may find more success in implementation. The following examples aim to highlight such approaches. The use of permeabilizing motifs,¹²⁹ siderophores,¹³⁰⁻¹⁴⁷ and permeable conjugates¹⁴⁸⁻¹⁵⁰ onto small molecules and natural products to enhance their Gram-negative activity¹⁵¹ have not been included; these approaches generally result

in mechanistic duality or active transport mechanisms and thus are not directly related to the manipulation of physicochemical properties for enhanced accumulation.

5.1 Sulfamoyladenosines

A systematic, prospective, and activity-independent platform has recently been developed to evaluate the accumulation of sulfamoyladenosine (AMS) analogs in Gram-negative, Gram-positive, and mycobacteria.¹⁰¹ LC-MS/MS accumulation quantification methods were combined with multivariate cheminformatic analyses to assess the effect of 20 structural and physicochemical properties on AMS accumulation in *E. coli*. Substitution on the sulfamate moiety (R group in **Table 2.2**) significantly influences intracellular accumulation with positive correlations noted for hydrophobicity (LogD, LogP, and ALogPs), ring content (Rings, RngAr, and RngSys), and size (MW and SA). Physicochemical properties identified as having a negative correlation on accumulation in *E. coli* include polarity (ALogpS and relPSA), ring complexity (RRSys), hydrogen bonding capacity (HBA and HBD), heteroatom counts (O and N) and rich 3D-topology. The study also determined the intracellular concentration of AMS analogs in *E. coli* in the presence of different EPIs (CCCP and Pa β N). These studies revealed no obvious correlation between physicochemical properties and susceptibility to proton-motive-force-driven efflux (Sal-AMS (**2.4**) and anthra-AMS (**2.3**), **Table 2.2**). Although dec-AMS (**2.7**) and 4-PhBz-AMS (**2.8**) exhibited higher accumulation in Pa β N pre-treated cells, this cannot be solely attributed to AcrAB-TolC inhibition, as Pa β N is known to enhance passive diffusion through an alternative mechanism by also permeabilizing the OM. This prototypical study demonstrates the value of incorporating cheminformatics analysis in antibacterial SAR campaigns.^{152, 153} The authors more recently

extended the strategy to engineer PqsA (anthranilyl-CoA synthetase) inhibitors with activity against *P. aeruginosa*.^{154, 155}

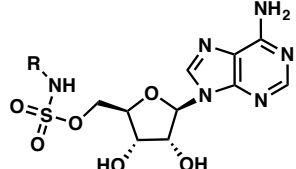
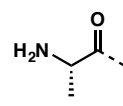
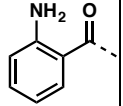
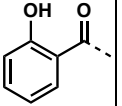
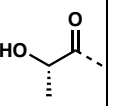
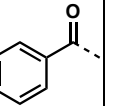
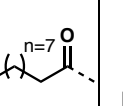
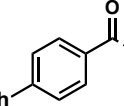
								
R		H						
Compound	L-Ala-AMS (2.1)	H-AMS (2.2)	Anthra-AMS (2.3)	Sal-AMS (2.4)	L-Lac-AMS (2.5)	Bz-AMS (2.6)	dec-AMS (2.7)	4-PhBz-AMS (2.8)
Intracellular concentration in <i>E. coli</i> (μM)	<0.05	25	25	35	51	80	99	185
Intracellular concentration in <i>E. coli</i> (μM) + 100 μM CCCP (fold increase)		25 (1)	75 (3)	130 (3.7)	51 (1)	140 (1.75)	200 (2)	310 (1.67)
Intracellular concentration in <i>E. coli</i> (μM) + 38 μM PaβN (fold increase)		25 (1)	25 (1)	35 (1)	51 (1)	80 (1)	600 (6)	405 (2.2)
logD	-3.91	-2.61	-1.89	-1.43	-3.85	-1.71	0.25	-0.07
LogP	-3.90	-2.61	-2.58	-2.11	-4.66	-2.41	-0.49	-0.76
AlogPs	-1.36	-1.26	-0.70	-0.44	-1.23	-0.35	1.37	1.25
relPSA	42	45	38	38	41	35	26	29
AlogpS	-1.96	-1.77	-2.40	-2.21	-1.87	-2.47	-3.26	-3.54

Table 2.2: Accumulation of sulfamoyladenines in *E. coli* and statistically significant physicochemical correlations. LogD = calc n-octanol/water partition coefficient (pH = 7.4); LogP = calc n-octanol/ water partition coefficient; ALogPs = calc n-octanol/water partition coefficient (Tetko); relPSA = topological polar surface area + surface area; AlogpS = calc aqueous solubility (Tetko).

5.2 Oxazolidinones

Oxazolidinones are an attractive therapeutic class for exemplifying rational approaches to engineer Gram-negative activity for several reasons: (1) The target (i.e., ribosomal 50S subunit) is clinically validated; (2) PK/PD and toxicity profiles of linezolid and tedezolid provide guidance for pre-clinical evaluation and compound risk mitigation; (3) Efficacy against Gram-negatives is observed when the OM is compromised; (4) The scaffold is synthetically tractable and analogs can be generated from a common intermediate; (5) The SAR is well-established and incorporates a structural component amenable to modification to manipulate physicochemical properties without detrimental effects to target engagement. The effect of charge, polarity, and hydrophobicity of this latter feature on antibacterial activity against *E. coli* has recently been explored.⁷⁵

The relative effects of structural modifications on OM permeability were revealed through MIC determinations both in the presence and absence of PMBN. Both the pKa of the pendant functional groups and their position on the ring (**Table 2.3**) play a role: derivatives containing functionalities that are polar and charged at physiological pH (e.g., DP-325 (**2.9**) and DP-326 (**2.11**)) exhibited enhanced permeation. Analogues exhibiting the best Gram-negative activity were calculated to exhibit significant zwitterionic character and were essentially unaffected by OM barriers. Zwitterionic antibiotics (e.g., fluoroquinolones, carbapenems) are known to preferentially utilize porins for permeation.^{22, 32, 33, 35, 98, 156-158}

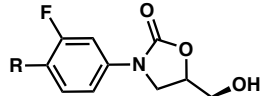
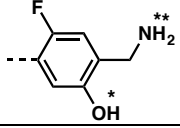
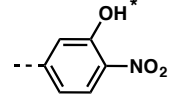
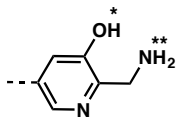
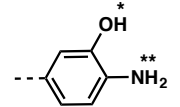
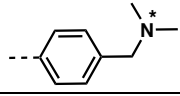
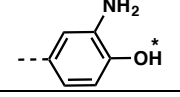
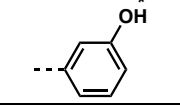
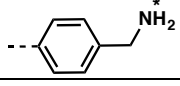
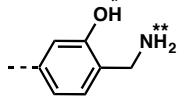
								
Cmpd	R	MIC ($\mu\text{g/ml}$) in <i>E. coli</i>			cpK _a	clogD	% ionized at pH 7.4	% zwitterion at pH 7.4
		Wild type	PMBN (Perm. Ratio)	ΔacrAB (Efflux ratio)				
DP-325 (2.9)		64	32 (2)	64 (1)	* 7.9 ** 10.2	0.2	99	26
DP-281 (2.10)		64	64 (1)	64 (1)	* 7.7	-2.2	32	
DP-326 (2.11)		51	32 (1.6)	32 (1.6)	* 7.3 ** 9.4	-0.3	99	57
DP-11 (2.12)		>64	32 (>2)	32 (>2)	* 10.0 ** 3.8	1.6		
DP-368 (2.13)		256	64 (4)	64 (4)	* 8.8	1.2	96	
DP-10 (2.14)		>64	64 (>2)	16 (>4)	* 10.0	1.6		
DP-23 (2.15)		>256	256 (>2)	45 (>6)	* >14	2.4	1	
DP-18 (2.16)		128	45 (2.8)	16 (8)	* 9.5	-0.2	99	
DP-19 (2.17)		84	32 (2.6)	8 (10.5)	* 8.0 ** 10.3	-0.1	99	18

Table 2.3: MIC values and calculated physicochemical properties of C-ring oxazolidinone analogs. *, pK_a of acidic group present. **, pK_a of protonated basic group present (cpK_a column).

To evaluate efflux susceptibility, the compounds were evaluated against wild-type and AcrAB efflux pump-deficient *E. coli*. Similar to requirements for permeability, both pK_a and location of the functional groups seem to play a role. As broad strategies, the authors suggest rational approaches should: (1) Use structural information to dictate the best location for molecular modification based on ligand-protein interactions (or lack thereof); (2) Utilize charge-carrying groups in SAR campaigns and leverage additive effects towards enhancing Gram-negative activity; (3) Be cognizant that preliminary efforts to minimize the impact of OM barriers may result in decreased on-target potency, so additional rounds of SAR employing biochemical and accumulation assays, run in parallel, are likely to be necessary.

5.3 Tetrahydropyran-Based Topoisomerase Inhibitors

While several non-fluoroquinolone bacterial type II topoisomerase inhibitors have been identified, few classes exhibit broad-spectrum activity. An SAR campaign towards expanding the spectrum of antibacterial activity of a tetrahydropyran-based scaffold to include efficacy against Gram-negatives was based upon the incorporation of a primary amine that would be charged at physiological pH and thus lower the clogD.¹⁵⁹⁻¹⁶¹ Compounds were evaluated against a panel of bacterial strains including drug-susceptible *S. aureus*, *E. coli*, and *P. aeruginosa* and drug resistant *A. baumannii*. Comparison with biochemical assays allowed for correlation of target engagement with whole-cell activity. Dibasic analogs including a primary amine instead of an alcohol in the linker domain led to improved Gram-negative whole-cell activity. The efflux susceptibility of the compounds was assessed by comparing the MICs between wild-type Gram-negatives and AcrAB- or TolC-deficient strains.¹⁶² The hydroxyl to amine substitution also reduced efflux by 92-fold,

demonstrating that the enhanced activity in Gram-negatives is likely due to the dual effect of increased permeation and decreased efflux. The mechanism of permeation is proposed to involve displacement of the divalent metal ions required for stabilization of the OM LPS layer, thus promoting self-uptake. From these studies two lead compounds were identified (**2.18** and **2.19**, **Figure 2.1**). Of the two, **2.19** exhibits a broader spectrum of utility, including MDR strains. Unfortunately, while the compounds in this series exhibit *in vivo* efficacy in Gram-negative murine infection models, they suffer from cardiotoxicity.

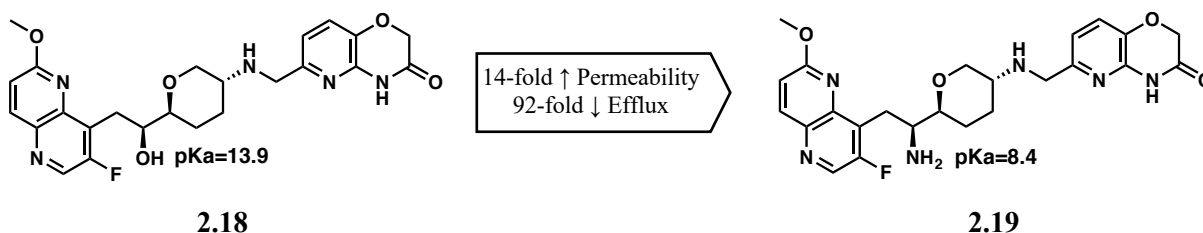


Figure 2.1: Optimization of tetrahydropyran-based topoisomerase inhibitors for permeability and efflux susceptibility in *E. coli*.

5.4 Diverse Chemotype Analysis

In an effort to set a more general foundation for predictive rules regarding antibacterial porin-mediated permeation, the accumulation of >180 diverse compounds in *E. coli* was determined via LC-MS/MS, and 297 molecular descriptors were assessed.¹⁶³ Four parameters governing the accumulation arose: (1) Flexibility: the number of rotatable bonds should be ≤ 5 ; (2) Globularity (a term used to describe the three-dimensionality of the structure) should be ≤ 0.25 (where benzene has globularity 0, and a sphere globularity 1);^{164, 165} (3) Amphiphilic moment: an increased distance between hydrophobic and hydrophilic portions of a molecule correlates to increased accumulation;¹⁶⁶ (4) The presence of at least one primary amine. Notably, charge,

molecular weight, and $\text{clogD}_{7.4}$ showed no correlative relationship with accumulation. The role of porins in accumulation was investigated through steered molecular dynamic simulations and revealed a key interaction between the requisite protonated amine and an aspartic acid residue within the constriction region that promotes translocation. As proof-of-concept that the identified parameters could be implemented in a rational fashion, an analog of deoxynybomycin (**2.20**), a Gram-positive-only antibiotic that satisfies the globularity and flexibility prerequisites, was selected for study. Introduction of a primary amine improved the accumulation in *E. coli* by ~4-fold (**Table 2.4**). Further evaluation of the new analog revealed antibacterial activity in *E. coli*, *A. baumannii*, *Klebsiella pneumoniae* and *Enterobacter cloacae* with accumulation heavily dependent on the presence of porins. The compound **2.21**, however, was less active against *P. aeruginosa*, indicative of the fact that *P. aeruginosa* porins are structurally unique and supporting the theory that chemotype and pathogen specific studies will likely be required in a case-by-case basis to guide SAR campaigns.

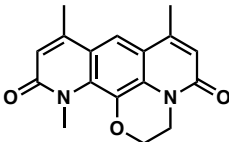
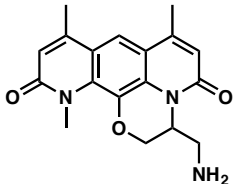
 Deoxynybomycin (6DNM) (2.20)		 Amino-Deoxynybomycin (6DNM-NH3) (2.21)					
Compound	Accumulation in <i>E. coli</i> nmol/10 ¹² CFUs	MIC in µg/mL					
		<i>S. aureus</i>	<i>E. coli</i>	<i>A. baumannii</i>	<i>K. pneumoniae</i>	<i>E. cloacae</i>	<i>P. aeruginosa</i>
6DNM (2.20)	298	0.06-1	>32	16->32	>32	>32	>32
6DNM-NH3 (2.21)	1,114	0.03-0.5	0.5-16	2-16	1-8	0.5-4	16

Table 2.4: Comparison of Deoxynybomycin (2.20) and Amino-deoxynybomycin (2.21) spectrum of activity.

Hereafter, I present my contributions to the Small-molecule Penetration & Efflux in Antibiotic-Resistant Gram-Negatives (SPEAR-GN) project, a collaborative research program working towards the establishment of predictive models and strategies to enhance the accumulation of small molecules in Gram-negative bacteria.

6 Small-molecule Penetration & Efflux in Antibiotic-Resistant Gram-Negatives (SPEAR-GN) Project

To convert Gram-positive antibiotics into Gram-negative-active compounds, the SPEAR-GN project takes a multidisciplinary approach involving expertise in organic synthesis/medicinal chemistry (i.e., Tan and Duerfeldt labs), bacterial biochemistry and microbiology (i.e., Zgurskaya lab), biophysical modeling (i.e., Rybenkov lab) and cheminformatics (i.e., Merck).

To set the stage for a class- and activity-independent model for antibiotic permeability, four distinct chemotypes were selected to build small-molecule libraries with diverse structural and physicochemical properties. Over 100 chemically diverse reactants were chosen to functionalize the four scaffolds (**Table 2.5**) and the resulting libraries bear the same moieties allowing cross-chemotype comparison to generate a robust predictive model. **Library 1:** Building upon the accumulation study in *E. coli* of a set of R1-substituted sulfamoyl-adenosine (AMS) analogs (**Section 5.1**), a more extensive library of AMS derivatives (**2.22, Table 2.5**) was synthesized by the Tan lab, containing three additional substitution sites (i.e., R², R³, R⁴). **Library 2:** As discussed in **Section 5.2**, modification of the *para*-position of the oxazolidinone B-ring (i.e., R on **2.23, Table 2.5**) can expand the antibacterial spectrum to Gram-negatives without disrupting binding to the ribosomal 50S subunit. To further this work, a library of oxazolidinones was

produced by the Duerfeldt lab (Ziwei Hu). **Libraries 3 and 4:** Derived from the natural product acyldepsipeptide (ADEP – **2.26**, **Table 2.6**), the piperazinone (**2.23**) and *seco* (**2.24**) scaffolds are targeted hypothesized activators of bacterial caseinolytic protease P (ClpP), an attractive new target upstream to diverse regulatory pathways in bacteria (See **Chapter 3** for more details).¹⁶⁷ Natural product ADEPs and synthetic relatives of this molecular family are bactericidal against Gram-positives but require co-administration of the membrane permeabilizer polymyxin B or efflux inhibition to exhibit activity against Gram-negatives.¹⁶⁸⁻¹⁷⁰ Therefore, the generation of the piperazinone (**2.23**, Quentin Avila) and *seco* (**2.24**, Quentin Gibault and Katelyn Stevens) libraries was conducted to not only hopefully broaden the activity of these scaffolds to include Gram-negative activity, but to also interrogate the role of the conformational constraint on penetration and efflux.

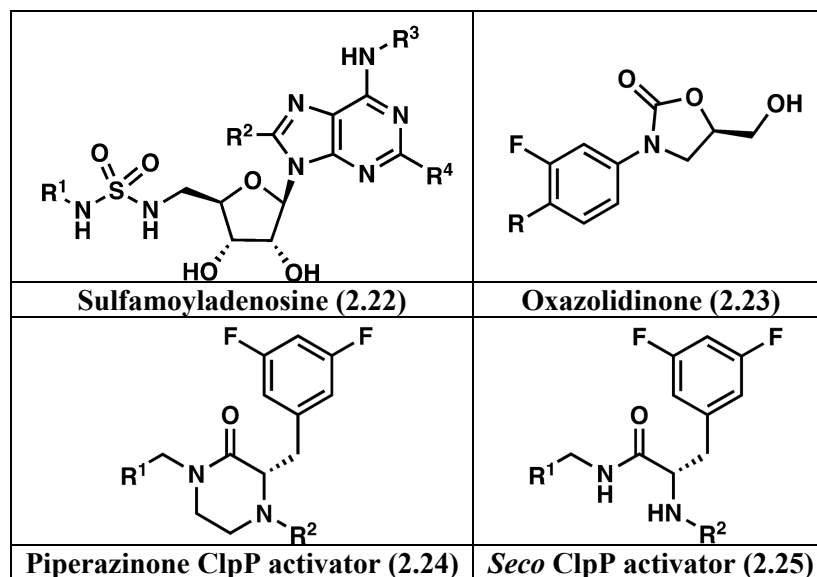


Table 2.5: Structures of the chemotypes under investigation of the SPEAR-GN project.

The Zgurskaya lab has pioneered an approach to distinguish the respective influence of outer/inner membrane penetration and active efflux on antibiotic accumulation by using unique

isogenic strain sets of wild-type, hyperporinated, efflux-deficient, and doubly compromised (i.e., hyperporinated and efflux-deficient) *E. coli*, *P. aeruginosa*, and *A. baumannii*. The contributions of the OM barrier and active efflux can be evaluated via both MIC determination and label-free LC-MS/MS detection for a quantitative evaluation of small-molecule accumulation in bacteria. The resulting data will serve to further develop a kinetic model for antibiotic penetration and efflux developed by the Rybenkov lab.

From Merck's machine learning and neural network approaches to QSAR (quantitative structure-activity relationship) modeling of pharmacological properties, predictive cheminformatic models for Gram-negative accumulation, penetration, and efflux will be established. This project will provide robust tools to enable medicinal chemistry campaigns in the field of antibacterial drug discovery to address this major threat to public health.

7 Rational Design of the Piperazinone ClpP Activator Scaffold

The piperazinone core **2.24** has two synthetic handles for substitution: the secondary amide (C-terminus of 3,5-difluorophenylalanine) and the secondary amine (N-terminus of 3,5-difluorophenylalanine) where chemically diverse moieties were installed, R¹ and R² respectively (**Figure 2.2**). Our approach to generate analogs was to functionalize one site while the other remained constant, hereafter I present our rationale for the selection of the piperazinone ring and the fixed moieties on both handles of the piperazinone core.

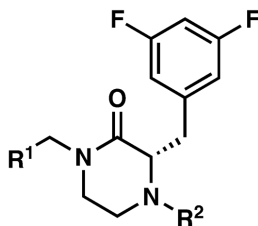


Figure 2.2: Piperazinone ClpP activator scaffold (2.24).

To determine the contribution of the ADEP (**2.26**) peptidolactone and side chains to the antibacterial activity, Sello J. K. et al. synthesized the fragments **2.27**, **2.28**, **2.29** and **2.30** (Table 2.6) and evaluated them in growth inhibition assays against the highly ADEP-susceptible wild-type *B. subtilis* AG174.¹⁶⁷ As presented in Table 2.6, a considerably weaker MIC was observed for the fragments than for the fully elaborated ADEP, upholding the natural product ADEPs and direct variants as the superior ClpP activating chemotype. Notably, the loss of bioactivity is the most significant for fragments **2.27** and **2.28**, suggesting that the *N*-acetyl-3,5-difluorophenylalanyl (**2.27**) and heptenoyl (**2.28**) moieties are necessary for ClpP activation. Although the partial (**2.29**) or complete (**2.30**) removal of the peptidolactone core led to an increase in MIC, the micromolar activity of these fragments further confirms that the *N*-heptenoyl-3,5-difluorophenylalanine core is the most bioactive fragment of ADEP. Thus, we chose to use the *N*-heptenoyl-3,5-difluorophenylalanine core (**2.29** and **2.30**) as starting points for developing a scaffold suitable to generating a library of analogs.

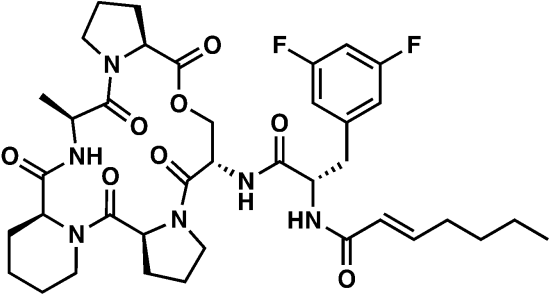
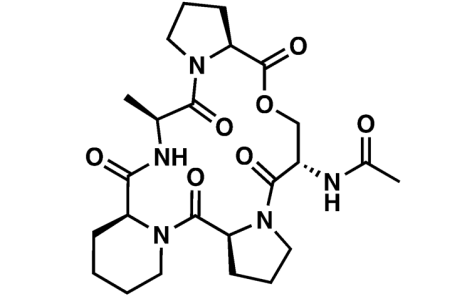
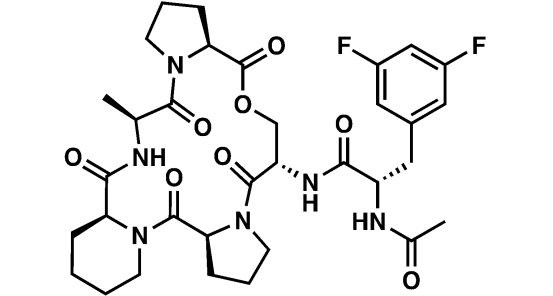
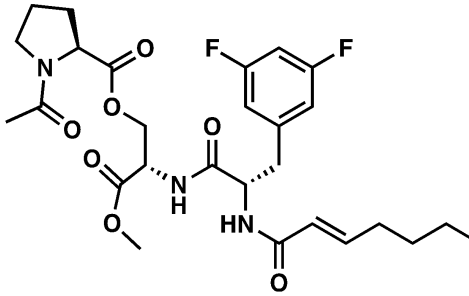
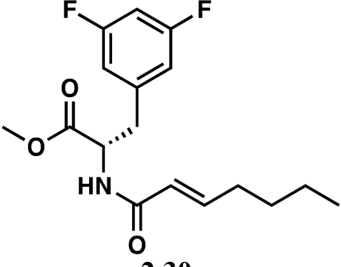
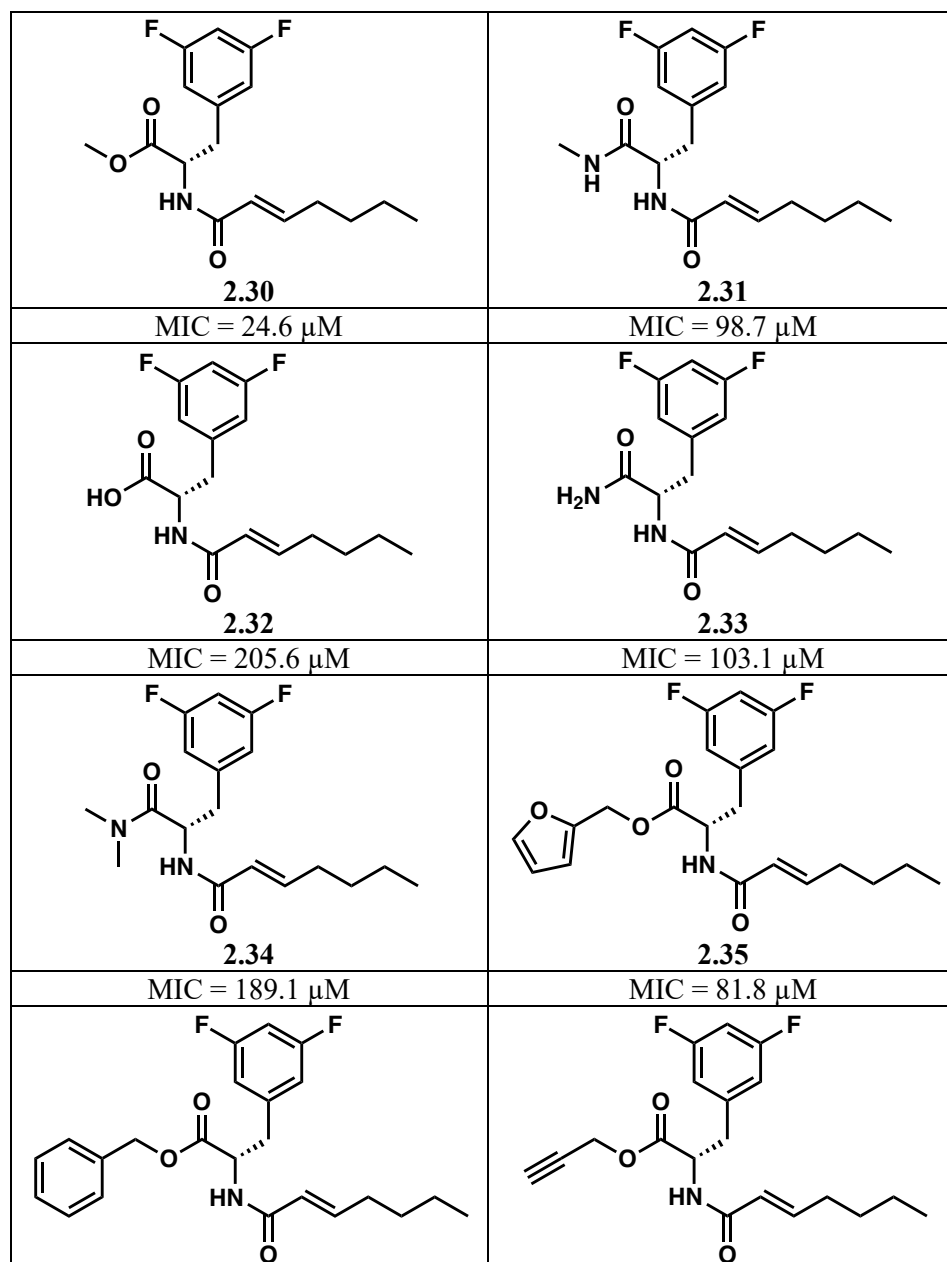
 <p style="text-align: center;">2.26</p>	 <p style="text-align: center;">2.27</p>
MIC = 21.1 nM	MIC > 253.2 μM
 <p style="text-align: center;">2.28</p>	 <p style="text-align: center;">2.29</p>
MIC > 185.9 μM	MIC = 58.0 μM
 <p style="text-align: center;">2.30</p>	
MIC = 24.6 μM	

Table 2.6: Fragments and C-terminus derivatives of ADEP and MIC in *B. subtilis*.

Building on the most active fragment **2.30**, Sello J. K. et al. used a positional scanning approach to identify moieties beneficial for ClpP activation on the C-terminus of *N*-acetyl-3,5-difluorophenylalanine core (**Table 2.7**). Although the linkage between *N*-acetyl-3,5-difluorophenylalanine and the peptidolactone is an amide bond, the carboxamide analogs (**2.31**, **2.33** and **2.34**) were surprisingly less potent than the methyl ester fragment **2.30**. Subsequently, three ester analogs were produced (**2.35**, **2.36**, **2.37**) and among them only the propargyl ester analog **2.37** surpassed **2.30** with a MIC = 5.7 μM. Not only was **2.37** the most potent ClpP activator

of the series, but it also binds more tightly to ClpP ($K_{app}=3.9 \mu\text{M}$; Hill coefficient: 1.6) compared to other fragments. Even though the lack of structural similarity between the propargyl moiety and the ADEP peptidolactone (**2.26**) prevents the rationalization for the potency of **2.37**, the propargyl group was selected as the fixed moiety in one library (**2.48**, Scheme 2.1) while varying the substitution on the amine.



2.36	2.37
MIC = 318.8 μ M	MIC = 5.7 μ M

Table 2.7: Derivatives of ADEP and MIC in *B. subtilis*.

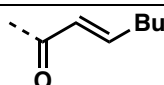
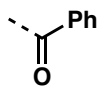
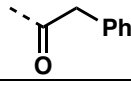
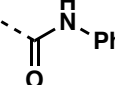
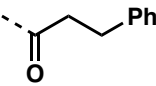
Optimization of the natural product ADEP 1 (**2.38**) by Brotz-Oesterhelt H. et al. led to ADEP 2 (**2.39**) and ADEP 4 (**2.40**) with improved antibacterial activity against a broad range of Gram-positive bacteria (**Table 2.8**), including multi-resistant clinical isolates (i.e., penicillin-resistant *Streptococcus pneumoniae* 665, vancomycin-resistant *Enterococcus faecium* L 4001 and methicillin-resistant *Staphylococcus aureus* NRS 119).¹⁶⁸ Consistent with Sello's conclusion that the *N*-heptenoyl-3,5-difluorophenylalanine is essential for activity, ADEP 4 (**2.40**) is the most active of this series and is identical to **2.26** apart from the methyl proline on the peptidolactone. ADEP 2 (**2.39**) displays comparable activity but bears a cyclohexylpropanoyl chain, suggesting some flexibility for the substitution and the state of conjugation on the 3,5-difluorophenylamine *N*-terminus. Although both ADEP 2 (**2.39**) and ADEP 4 (**2.40**) display nanomolar activity against Gram-positive pathogens, a lower clearance (CL) in mice was observed for ADEP 2 (**2.39**) than ADEP 4 (**2.40**), CL_{plasma} / CL_{blood}: 1.8 / 2.7 L/h*kg and 2.6 / 4.5 L/h*kg, respectively. As a Michael acceptor, the *N*-heptenoyl chain of ADEP4 (**2.40**) is likely more susceptible to metabolic degradation than the *N*-cyclohexylpropanoyl chain of ADEP2 (**2.39**). Therefore, the *N*-cyclohexylpropanoyl moiety represents a better candidate for a fixed aliphatic chain in the second library (**2.49**, **Scheme 2.1**). Stability was chosen as key prioritization to reduce possible intracellular degradation and/or reactivity that would complicate data analysis.

<p>ADEP 1 (2.38)</p>	<p>ADEP 2 (2.39)</p>		
	<p>R = </p>		
	<p>ADEP 4 (2.40)</p> <p>R = </p>		
Strain	IC ₅₀ (nM)		
	ADEP 1 (2.38)	ADEP 2 (2.39)	ADEP 4 (2.40)
<i>Bacillus subtilis</i> 168	278.2	62.6	13.0
<i>Streptococcus pneumoniae</i> 665	2,225.8	62.6	26.0
<i>Streptococcus pyogenes</i> Wacker	556.4	12.5	26.0
<i>Enterococcus faecalis</i> ICB 27159	556.4	≤ 12.5	≤ 13.0
<i>Enterococcus faecium</i> L 4001	556.4	25.0	≤ 13.0
<i>Staphylococcus aureus</i> NRS 119	8,764.0	500.7	65.0

Table 2.8: Antibacterial activity of ADEP 1 (2.38) and its optimized congeners ADEP 2 (2.39) and ADEP 4 (2.40).

In an effort to further improve metabolic stability of ADEP 4 (2.40), the Lee group explored different amides (i.e., 2.41, 2.42, 2.44 and 2.46, Table 2.9) and ureas (i.e., 2.43, 2.45, 2.47, Table 2.9) to replace the *N*-heptenoyl chain of ADEP4 (2.40). The result of their study is summarized in Table 2.9.¹⁷¹ Mouse microsomal studies substantiated the previous assumption of the low metabolic instability of ADEP4 (2.40), as it displays the lowest $t_{1/2}$ value of the series, 0.15 h. In addition to the amides exhibiting improved stability relative to ADEP 4 (2.40), the urea counterparts exhibited exceptionally higher stability, especially 2.47 which also maintained on-target activity. Although the authors did not explain the origin of the difference in metabolic stability between the amide and urea analogs, I hypothesized that this amide bond is susceptible to

peptidic cleavage. Taken together this data suggests that: (1) The acrylamide side chain is susceptible to metabolic degradation; (2) Replacement of acrylamide to amide alone is not sufficient to significantly improve metabolic stability. Therefore, replacing the heptenoyl group to the cyclohexylpropanoyl chain is not sufficient to decrease metabolic susceptibility, as 3,5-difluorophenylalanine N-terminus is likely still prone to peptidic cleavage. However, the ethylene bridge of the piperazinone is expected to provide conformational constraint and potentially decrease metabolic degradation, by shielding the amide bonds of the N- and C-termini of the 3,5-difluorophenylalanine.

Cmpd	R	Metabolic stability $t_{1/2}$ (hours) Mouse Liver Microsomes	Casein degradation (μM)		MIC in <i>S. aureus</i> (μM)		
			EC50	% Activation	ATCC 29213	USA 300 (MRSA)	USA 300 ΔClpP
ADEP 4 (2.40)		0.15	0.20	103	0.1	0.2	>25
2.41		0.19	Inactive	Inactive	>25	>25	>25
2.42		0.26	30.0	70.7	>25	>25	>25
2.43		1.01	0.61	68.8	3.1	3.1	>25
2.44		0.23	3.04	52.6	>25	25	>25

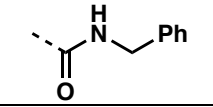
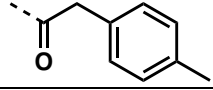
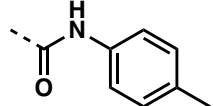
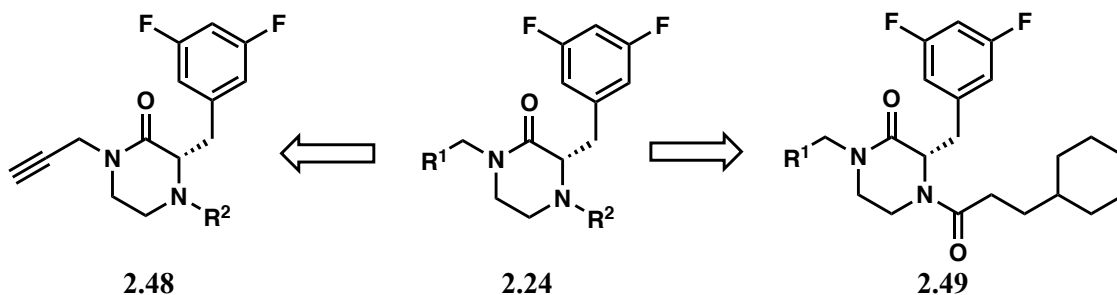
2.45		0.66	7.10	53.7	25	25	>25
2.46		1.42	8.84	63.4	25	25	>25
2.47		1.72	0.33	100.7	0.1	0.2	>25

Table 2.9: Metabolic stability, casein degradation and MIC in *S. aureus* of amide (2.41, 2.42, 2.44 and 2.46) and urea (2.43, 2.45 and 2.47) ADEP 4 analogs.

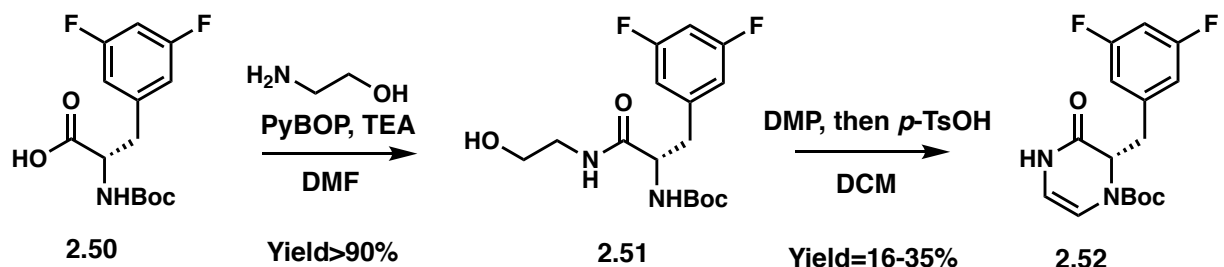
Even though ADEPs are the most potent ClpP activators, the synthesis of a library centered on the simplified bioactive fragment, 3,5-difluorophenylalanine, is more synthetically tractable. The propargyl (**2.48**, **Scheme 2.1**) and cyclohexylpropanoyl (**2.49**, **Scheme 2.1**) group were selected as fixed moieties for generating the library subsets due to their activity in relationship to ClpP activation and relative predicted metabolic stabilities. The piperazinone core was designed as a peptidomimetic analog of the ADEP bioactive fragment to increase the stability of the scaffold and, as discussed in **Chapter 3**, to investigate the role of the ring size on ClpP activation. Although the substitution of either propargyl or cyclohexylpropanoyl group is possibly deleterious for ClpP activation, the advantage of SPEAR-GN's approach is the capability of determining accumulation in Gram-negatives independently from the antibacterial activity of the compound.



Scheme 2.1: Structures of the ClpP activator piperazinone scaffolds with the fixed moieties.

8 Preparation of the Synthon for the Piperazinone Scaffold

8.1 Synthesis of the Piperazinone Core



Scheme 2.2: Synthetic route to the cyclic enamine intermediate 2.52.

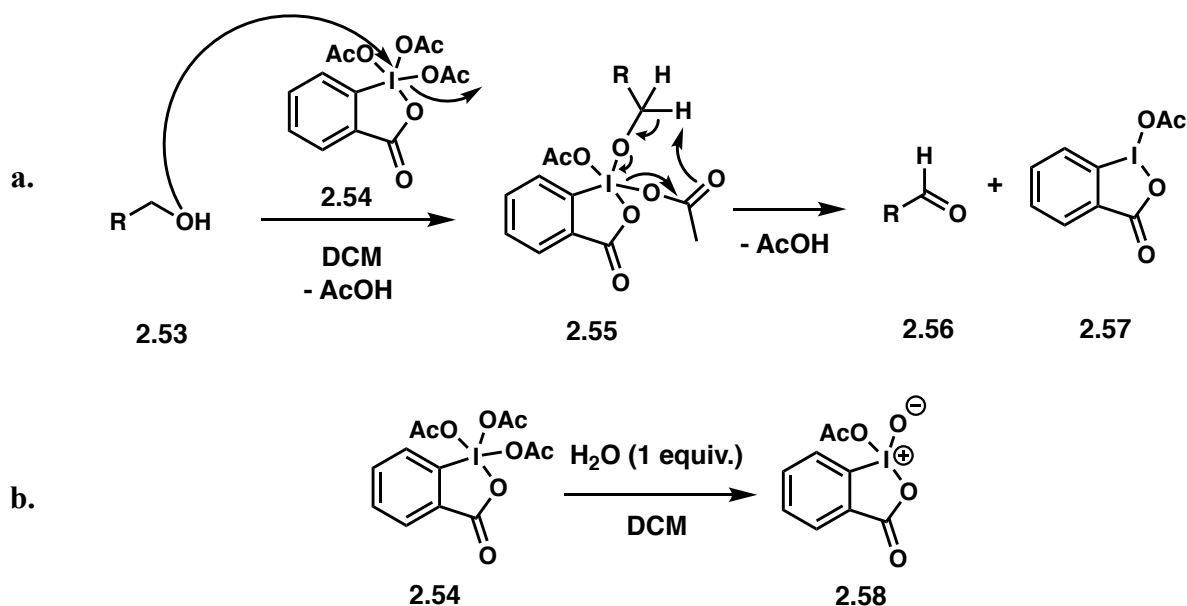
The amide coupling between Boc-3,5-difluorophenylalanine **2.50** and ethanolamine produced the intermediate **2.51** with typical yields above 90%. The six-membered ring was obtained by the oxidation of the primary alcohol into an aldehyde, by Dess-Martin periodinane (DMP) (Scheme 2.2) followed by the formation of an intramolecular iminium species between the newly made aldehyde and the Boc-protected amine. The subsequent addition of *para*-Toluenesulfonic acid (*p*-TsOH·H₂O) to the reaction mixture promoted the tautomerization of the iminium species to the cyclic enamine intermediate **2.52**. However, these conditions did not yield a significant amount of product (Entry 1, Table 2.10). Therefore, different reaction conditions were explored to optimize the formation of the enamine intermediate **2.52** (Table 2.10).

<p>2.51 \longrightarrow 2.52</p>			
Entry	Conditions		Yield
	DMP equivalents	Additives	

1	1.5	None	16-35 %
2	1.5	H ₂ O (1 eq)	51%
3	4	H ₂ O (1 eq) DCM/Toluene (2:1)	77%

Table 2.10: Summary of DMP oxidation/cyclization conditions optimization.

The Dess-Martin oxidation starts by a substitution on the hypervalent iodide of DMP (**2.54**, **Scheme 2.3a**) where the alcohol **2.53** displaces one of the acetate ions. Following the deprotonation on the α -carbon of the alcohol on the adduct **2.55**, the aldehyde **2.56** is produced along with the DMP by-product **2.57**. The reaction time of the Dess-Martin oxidation has been shown to be significantly decreased by the addition of one equivalent of water, which hydrolyzes DMP (**2.54**) into the acetoxyiodinane oxide intermediate (**2.58**, **Scheme 2.3b**). This partial hydrolysis increases the decomposition rate of this species due to the higher electron-donating ability of the water oxygen compared to the acetyl group.¹⁷² In the context of the formation of the cyclized intermediate **2.52**, addition of water to the reaction conditions only moderately improved the yield to 51% (**Entry 2**, **Table 2.10**). To further optimize the oxidation of the alcohol on intermediate **2.51**, two equivalents of DMP and one equivalent of water were dissolved in a 2:1 mixture of DCM and toluene (**Entry 3**, **Table 2.10**). Toluene was used with the goal to increase the solubility of DMP as it is insoluble in DCM. After three hours of stirring, two more equivalents of DMP were added as only partial conversion of the starting material was observed via TLC monitoring of the reaction. Although the yield increased to 77% under these conditions, the amount of DMP employed is impractical not only due to the cost of DMP (\$25-40/g) but also because the decomposition product **2.57** of DMP is difficult to separate from the product by flash chromatography.



Scheme 2.3: Oxidation mechanism of a primary alcohol 2.53 into an aldehyde 2.56 by DMP (a) and acetoxyiodinane oxide 2.58 preparation (b).

As such, different conditions were investigated to oxidize the alcohol to aldehyde (**Table 2.11**): (1) Fe(NO₃)₃/TEMPO catalyst system to induce imine formation (**2.52**);¹⁷³ (2) Manganese dioxide in combination with polymer-supported cyanoborohydride (PSCBH) was used in an attempt to execute a one-pot oxidant/reductant coupling to directly produce piperazinone **2.59**;¹⁷⁴ (3) A one-pot palladium-catalyzed coupling of alcohol and amine to obtain the free-amine piperazinone **2.59**.¹⁷⁵ However, no product formation was observed under any of these conditions, likely due to the inactivated nature of the primary alcohol of **2.51**. Literature precedent suggests that only benzylic, allylic or propargylic alcohols are reactive enough to undergo many of these transformations, an observation confirmed in these studies.

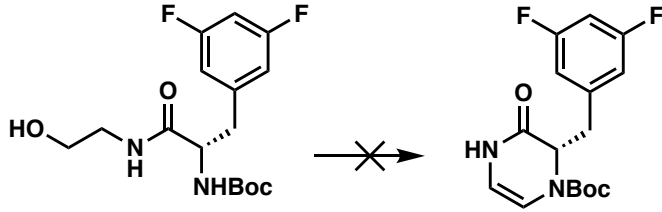
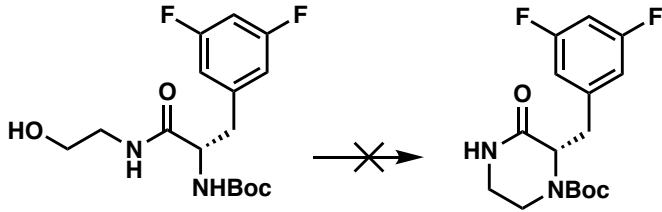
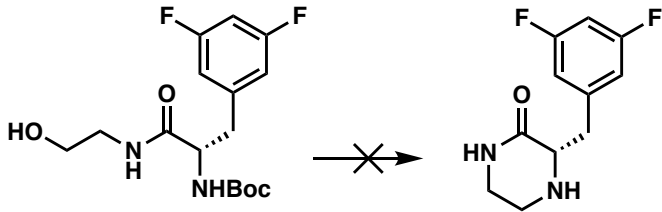
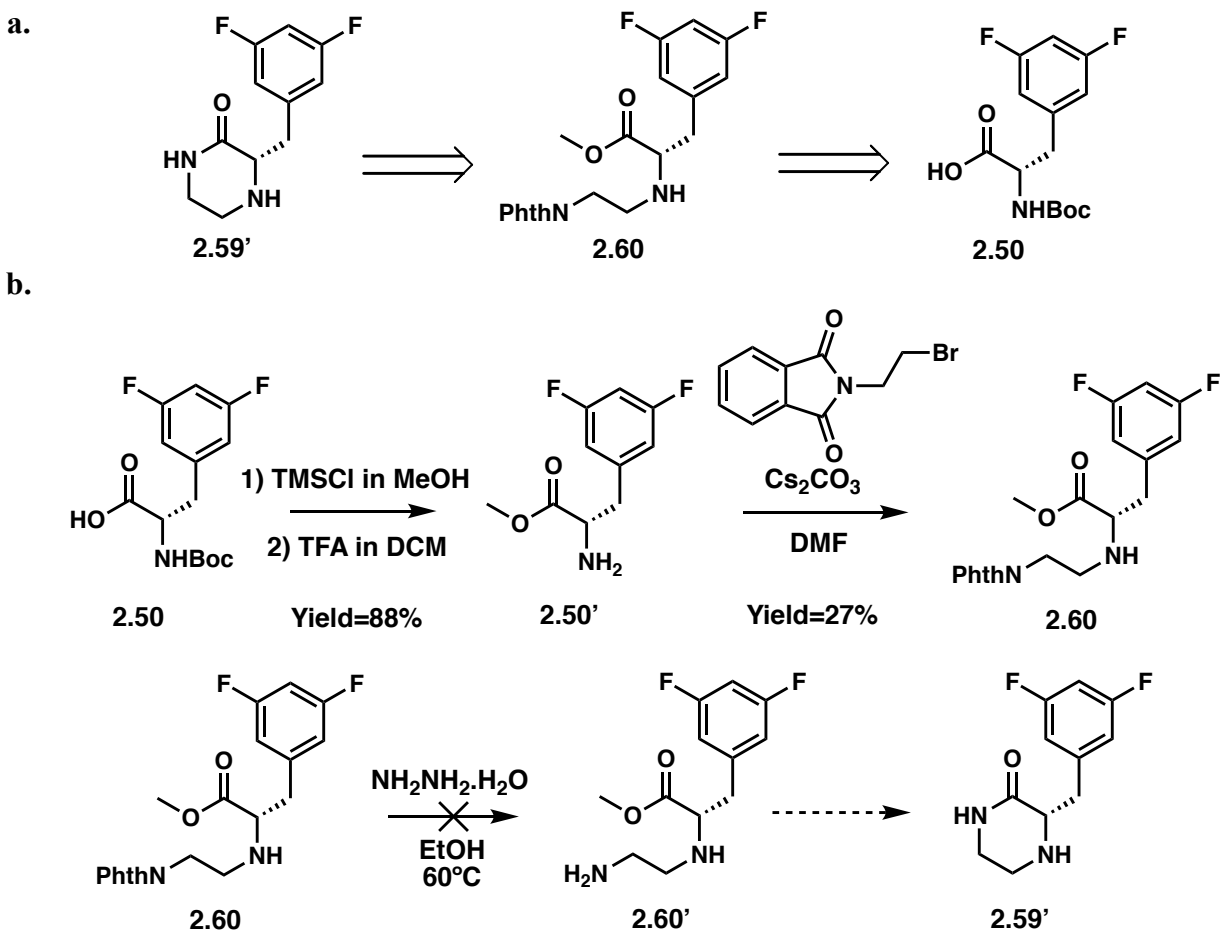
 2.51 2.52	
Conditions	Conversion observed
Fe(NO ₃) ₃ 9.H ₂ O (10 mol%) Tempo (10 mol%) KOH (20 mol%) in toluene @ 80°C	No (Starting material not recovered)
 2.51 2.59	
Conditions	Conversion observed
MnO ₂ , PSCBH in DCM @ 35°C	No (Starting material not recovered)
 2.51 2.59'	
Conditions	Conversion observed
Pd/AlO(OH) in heptane 95°C then H ₂ *	No (Starting material not recovered)

Table 2.11: Summary of conditions screened for the oxidation/cyclization of 2.51. * The Boc group of intermediate **2.51** was removed first using TFA in DCM.

Alternatively, I explored a route wherein the 3,5-difluorophenylalanine N-terminus is first alkylated with 2-bromoethylphthalimide (**2.60**, **Scheme 2.4**) and the deprotection of the phthalimide group was expected to lead to the cyclization of product **2.59'**. As depicted in **Scheme 2.4**, the Boc 3,5-difluorophenylalanine **2.50** was converted into the methyl ester 3,5-

difluorophenylalanine **2.50'** to access the *N*-ethylphthalimide intermediate **2.60**. However, this route failed to produce the piperazinone following the deprotection of the phthalimide group.



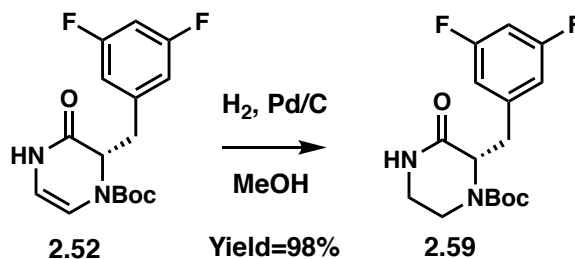
Scheme 2.4: Proposed synthetic route for the piperazinone **2.59': retrosynthetic route for the piperazinone **2.59'** using a phthalimide group (a) and synthetic steps for **2.59'** (b).**

Although the oxidation of a primary alcohol to aldehyde was not necessarily an efficient route, I knew from previous experience that once the aldehyde formed, it promptly reacted with the Boc-protected amine. Thus, an alternate functional group such as an acetal was predicted to be another way to access the aldehyde.¹⁷⁶ The amide coupling of **2.50** with aminoacetaldehyde dimethyl acetal afforded intermediate **2.61** in excellent yields (< 90%, **Table 2.12**). Conditions were screened to deprotect the acetal (**Table 2.12**) and the use of *p*-TsOH·H₂O (**Entry 7**, **Table**

2.12), in acetone at 45°C was the highest yielding. Finally, hydrogenation of the cyclic enamine intermediate **2.52** yielded the piperazinone synthon **2.59** in 98% yield (Scheme 2.5).

Entry	Conditions	Yield
1	70% TFA in H ₂ O	No reaction
2	Oxalic acid in THF/H ₂ O (4:1)	No reaction
3	Oxalic acid in THF/H ₂ O (4:1) @ 60°C	No reaction
4	LiBF ₄ (1.5 eq) in (wet) CH ₃ CN	No reaction
5	LiBF ₄ (20 eq) in (wet) CH ₃ CN	52%
6	<i>p</i> -TsOH·H ₂ O (1 eq) in acetone, 4 Å MS @ RT	No reaction
7	<i>p</i> -TsOH·H ₂ O (1 eq) in acetone, 4 Å MS @ 45°C	61-76%

Table 2.12: Alternative synthetic route to the cyclic enamine intermediate **2.52 and summary of conditions screened for the acetal deprotection/cyclization.**



Scheme 2.5: Hydrogenation conditions used to access the piperazinone **2.59.**

In summary, I developed a synthetic route of the piperazinone **2.59**, a synthon essential for the synthesis of the library, with an overall 57% yield, in three steps, and I optimized the cyclization step by employing an acetal that can be easily deprotected under mild acidic conditions.

8.2 Preparation of the Propargyl Piperazinone

To prepare the propargyl piperazinone synthon, the secondary amide needed to be propargylated, however the lower nucleophilicity of the amide nitrogen proved to make nucleophilic substitution less straight-forward than initially proposed. Although N-alkylation and O-alkylation are competing reactions, due to the ambident character of amides, N-alkylation is predominant as imidates are less thermodynamically stable and tend to hydrolyze or rearrange to the corresponding amides (Chapman rearrangement).¹⁷⁷ Furthermore, hard alkali (i.e., lithium, sodium, potassium) and tetraalkylammonium cations have been reported to promote N-alkylation¹⁷⁸ by coordinating with the oxygen while softer cations, such as silver, facilitate O-alkylation by associating with the nitrogen. O-alkylation becomes dominant in a π -conjugated system as aromatization is the driving force¹⁷⁹ or when reagents such as dimethyl sulfate,¹⁸⁰ diazomethane,¹⁸¹ or trialkyloxonium tetrafluoroborates (Meerwein's reagent)^{182, 183} are employed.

Nucleophilic substitution with propargyl bromide using bases such as potassium carbonate (K_2CO_3) or sodium hydride (NaH) failed to yield the propargylated product **2.62**, as shown in **Table 2.13**. Although typically used for N-alkylations, these conditions are not common for amides, based on the limited literature precedent. However, phase-transfer catalysis (PTC) represents a successful alternative, with milder and solvent-free conditions finding utility, particularly with lactams: a mixture of an amide, an alkyl halide in 50% excess and a catalytic amount of tetrabutylammonium bromide is absorbed on K_2CO_3 and potassium hydroxide (KOH) and then irradiated in a microwave.¹⁸⁴ As propargyl bromide is commercially available in a 80 wt. % in toluene, these solvent-free PTC conditions were adapted using dry toluene. Notably, KOH was not necessary for the propargylation to occur in 71% yield (**Table 2.13**). The propargyl

piperazinone **2.62** was then treated with trifluoroacetic acid (TFA) to reveal the secondary amine **2.62'** and allow for further functionalization (Scheme 2.6).

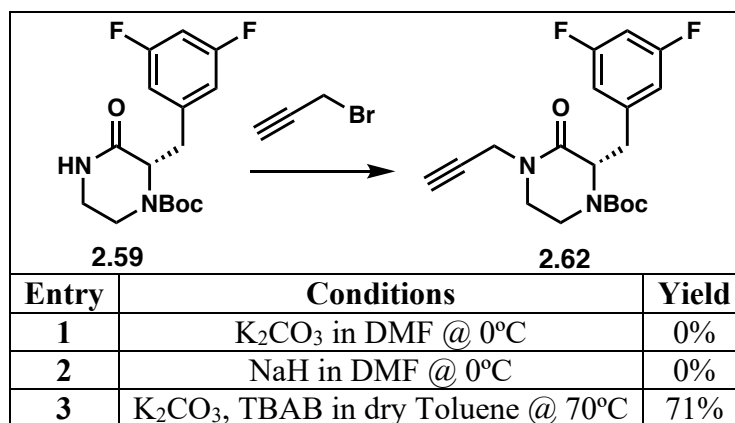
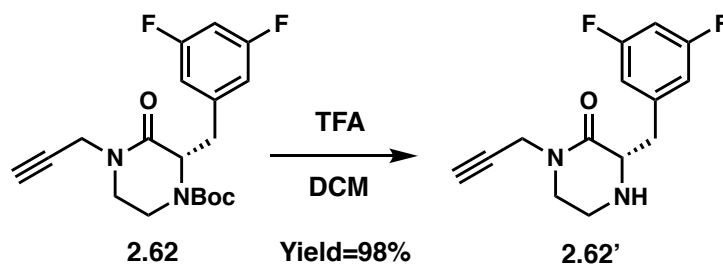
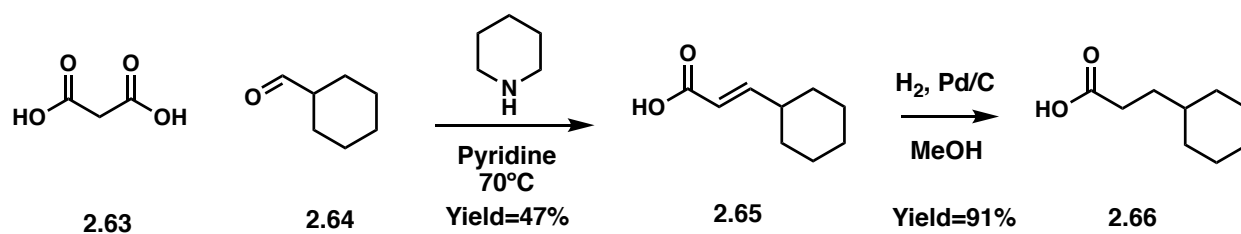


Table 2.13: Summary of the conditions screened for propargylation of the piperazinone amide **2.62**.



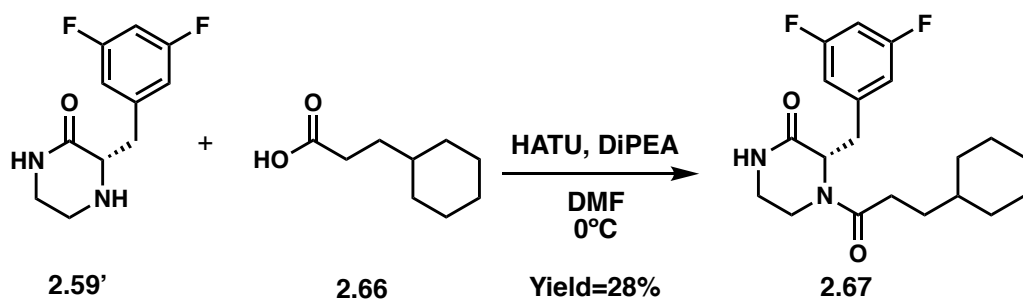
Scheme 2.6: TFA-promoted Boc deprotection of the propargyl piperazinone **2.62'**.

8.3 Preparation of the Cyclohexylpropanoyl Piperazinone



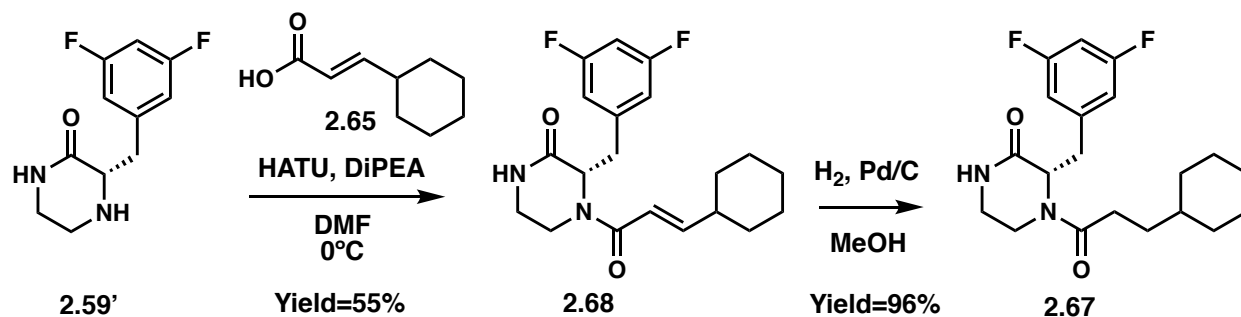
Scheme 2.7: Synthetic route for 3-cyclohexylpropanoic acid **2.66**.

The 3-cyclohexylpropanoic acid (**2.66**) was synthesized through a piperidine-catalyzed Knoevenagel condensation between malonic acid (**2.63**) and cyclohexanecarboxaldehyde (**2.64**) in pyridine at 70°C to produce (E)-3-cyclohexylacrylic acid (**2.65**) in 47% yield followed by hydrogenation using palladium on carbon (**Scheme 2.7**).



Scheme 2.8: Synthetic route for the cyclohexylpropanoyl piperazinone 2.67.

Following the removal of the Boc protecting group with TFA, the piperazinone **2.59'** was reacted with 3-cyclohexylpropanoic acid (**2.66**) in presence of HATU, DiPEA in DMF to prepare the cyclohexylpropanoyl piperazinone (**2.67**, **Scheme 2.8**) in 28% yield. Interestingly, the similar amide coupling of the Boc-protected piperazinone (**2.59'**) and (E)-3-cyclohexylacrylic acid (**2.65**) generated (E)-cyclohexylacryloyl piperazinone (**2.68**, **Scheme 2.9**) in 55% yield. Therefore, the synthetic route depicted in **Scheme 2.9** was used to prepare the cyclohexylpropanoyl piperazinone **2.67**.



Scheme 2.9: Synthetic route for the cyclohexylpropanoyl piperazinone 2.67 in a higher yield.

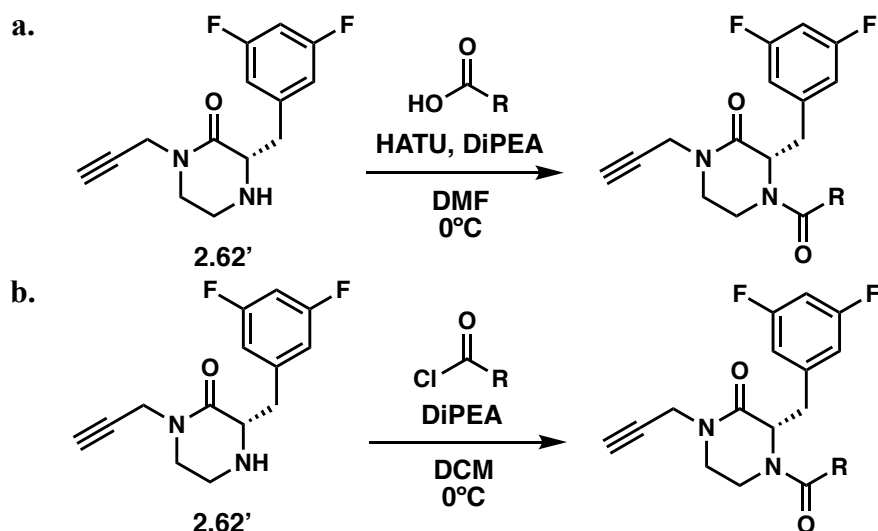
9 Synthetic Efforts for the Piperazinone ClpP Library

The development of synthetic routes for the piperazinone synthons (**2.62'** and **2.67**) enabled the production of 48 structurally diverse analogs (i.e., amides, sulfonamides, ureas, alkyl amides). My goal was to employ methodologies compatible with a majority of the reactants selected (i.e., carboxylic acids, acyl chlorides, sulfonyl chlorides, isocyanates, alkyl halides and alkyl amines) to produce 3-5 mg of products for antibacterial activity evaluation. My focus was not to optimize the conditions to improve the yield of each reaction, but to expand the scope of these methodologies to generate more analogs.

9.1 Synthesis of Propargyl Piperazinone Amide Analogs

The set of amide compounds were prepared using the propargyl piperazinone synthon (**2.62'**) following two procedures: (1) Amide coupling with substituted alkyl carboxylic acid using HATU and DiPEA in DMF (**Scheme 2.10a**); (2) Acylation with acyl chloride using DiPEA in

DCM (Scheme 2.10b). The synthesized propargyl piperazinone amide analogs and the yields are summarized in Table 2.14.



Scheme 2.10: Synthetic route for the propargyl piperazinone amide analogs via amide coupling (a.) and acylation (b.).

2.69	n/a*	2.70	53%	2.71	57%	2.72	44%
2.73	63%	2.74	62%	2.75	37%	2.76	74%
2.77	26%	2.78	67%	2.79	46%	2.80	n/a

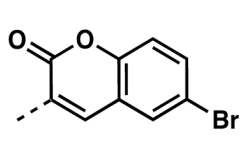
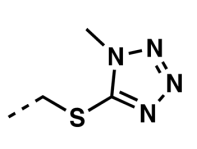
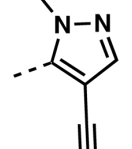
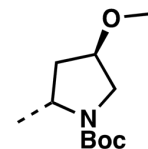
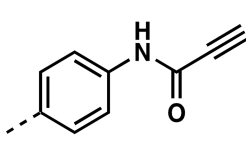
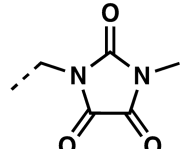
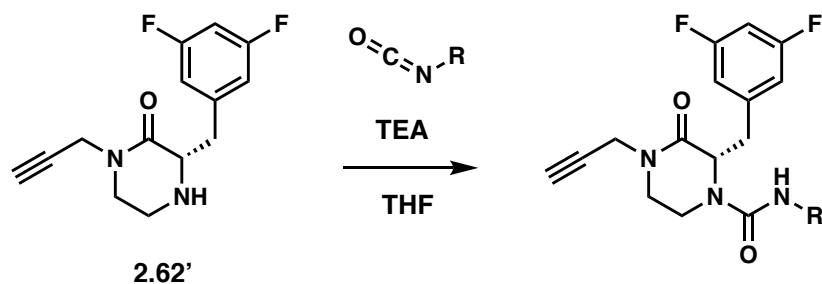
							
2.81	67%	2.82	78%	2.83	54%	2.84	50%
							
		2.85	23%	2.86			

Table 2.14: Summary of the preparation of propargyl piperazinone urea analogs. Under each moiety, the compound number and yield are reported. * indicates that compound **2.69** was synthesized via propargylation of **2.67**.

9.2 Synthesis of Propargyl Piperazinone Urea Analogs

The set of urea compounds were synthesized by reacting substituted isocyanates in presence of TEA in THF (**Scheme 2.11**). Use of a substoichiometric amount of isocyanates was necessary to prevent the formation of the isocyanate degradation by-product, which hindered the purifications of these compounds, as the resulting amines had a similar R_f as several of the products. The synthesized propargyl piperazinone urea analogs and the yields are summarized in **Table 2.15**.



Scheme 2.11: Synthetic route for the propargyl piperazinone urea analogs.

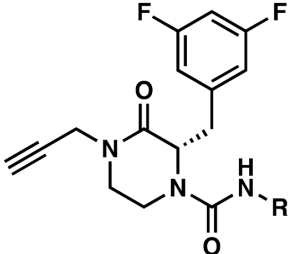
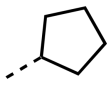
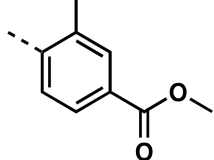
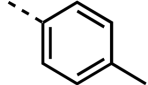
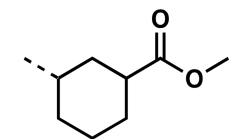
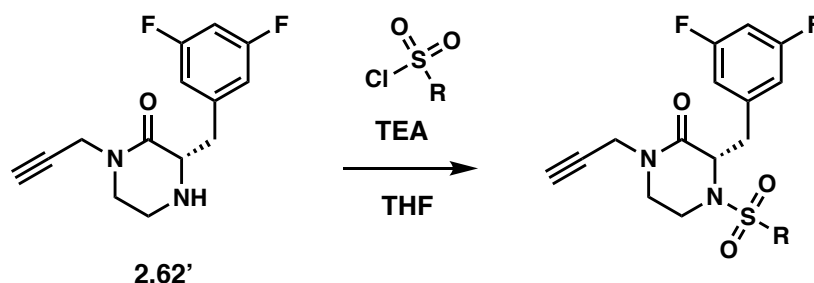
							
							
2.87	65%	2.88	80%	2.89	53%	2.90	44%

Table 2.15: Summary of the preparation of propargyl piperazinone urea analogs. Under each moiety, the compound number and yield are reported.

9.3 Synthesis of Propargyl Piperazinone Sulfonamides Analogs

The set of sulfonamide compounds were synthesized by reacting substituted sulfonyl chlorides in presence of TEA in THF (**Scheme 2.12**). The synthesized propargyl piperazinone sulfonamide analogs and the yields are summarized in **Table 2.16**.



Scheme 2.12: Synthetic route for the propargyl piperazinone sulfonamide analogs.

2.91	33%	2.92	57%	2.93	53%	2.94	57%	2.95	26%

Table 2.16: Summary of the preparation of propargyl piperazinone sulfonamide analogs.
Under each moiety, the compound number and yield are reported.

9.4 Synthesis of N-Alkyl Cyclohexylpropanoyl Piperazinones

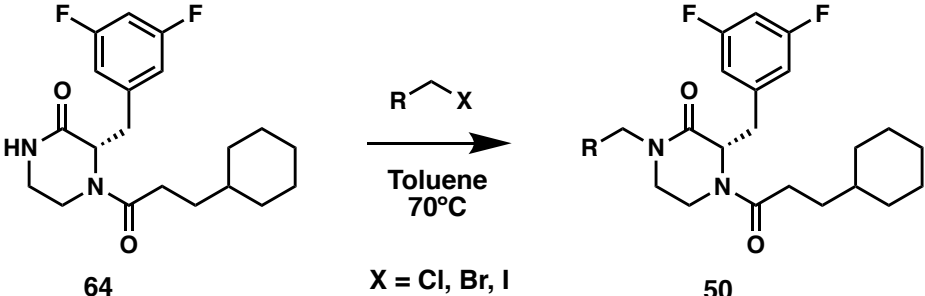
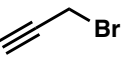
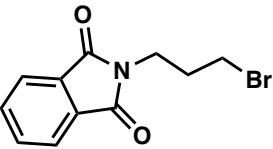
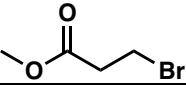
Among the library of chemically diverse reactants selected to functionalize the four scaffolds of the SPEAR-GN project, 35 alkyl halides (**Table S2.6**) and their amine homologs were employed to produce the subset of *N*-alkyl cyclohexylpropanoyl piperazinones and *N*-alkyl cyclohexylpropanoyl *seco* analogs, respectively. Although the functionalization of the propargyl piperazinone synthon (**2.62'**) was straight-forward (i.e., amide, sulfonamide and urea analogs), methodologies to *N*-alkylate amides compatible with the complete library of alkyl halides have yet to be reported. Hereafter, I present the different methodologies and synthetic strategies I investigated to generate the *N*-alkyl cyclohexylpropanoyl piperazinone analogs.

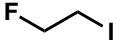
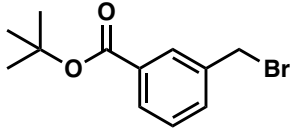
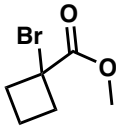
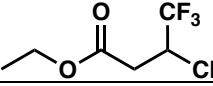
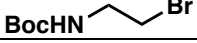
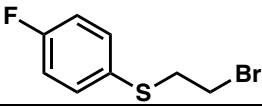
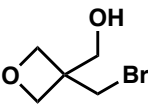
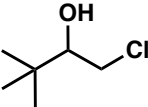
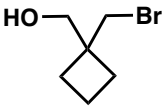
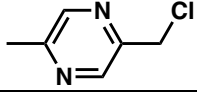
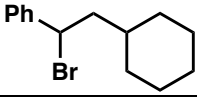
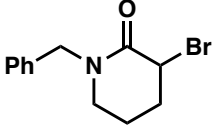
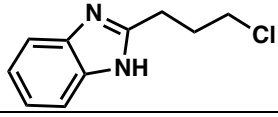
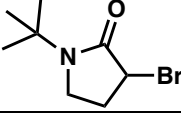
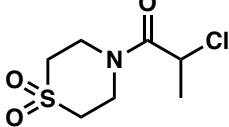
9.4.1 N-Alkylation of Secondary Amides

Although the propargylation of the secondary amide of the piperazinone core (**Entry 1**, **2.69**, **Table 2.17**) was achieved using PTC conditions, the *N*-alkylation using an alkyl halide

differing from propargyl bromide only worked for two other substrates in addition to propargyl bromide: methyl 4-bromobutanoate (**Entry 3, 2.96, Table 2.17**) and *tert*-butyl 3-(bromomethyl) benzoate (**Entry 5, 2.97, Table 2.17**). The selectivity of these conditions could not be rationalized. When investigating the propargylation of the piperazinone, KOH was not use, diverging from the reported literature. Thus, I hypothesized that returning to the original condition, by adding KOH, would improve the outcome of the N-alkylation and increase the substrate scope. However, no conversion was observed for the substrates tested under these new conditions (**Table 2.17**).

To further optimize the PTC conditions for N-alkylation, potassium carbonate was replaced by cesium carbonate (Cs_2CO_3) to determine if the “cesium effect” could be favorable.^{185, 186} However, combining tetrabutylammomium hydroxide (TBAOH) with Cs_2CO_3 was only productive in the N-alkylation with 3-bromo-1-(*tert*-butyl)pyrrolidin-2-one (**Entry 17, 2.98, Table 2.17**).

		Conditions (Yield %)			
Entry	Alkyl halide	Compound	K_2CO_3 TBAB	K_2CO_3 , KOH TBAB	Cs_2CO_3 TBAOH in H_2O
1		2.69	71		66
2			0	0	0
3		2.96	83		

4			0		
5		2.97	74		
6			0		0
7			0		0
8			0		
9				0	
10				0	
11				0	0
12					0
13				0	0
14				0	
15				0	
16				0	
17		2.98		0	50
18					0

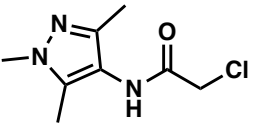
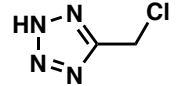
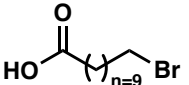
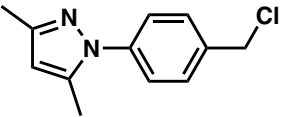
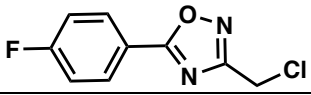
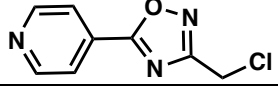
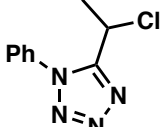
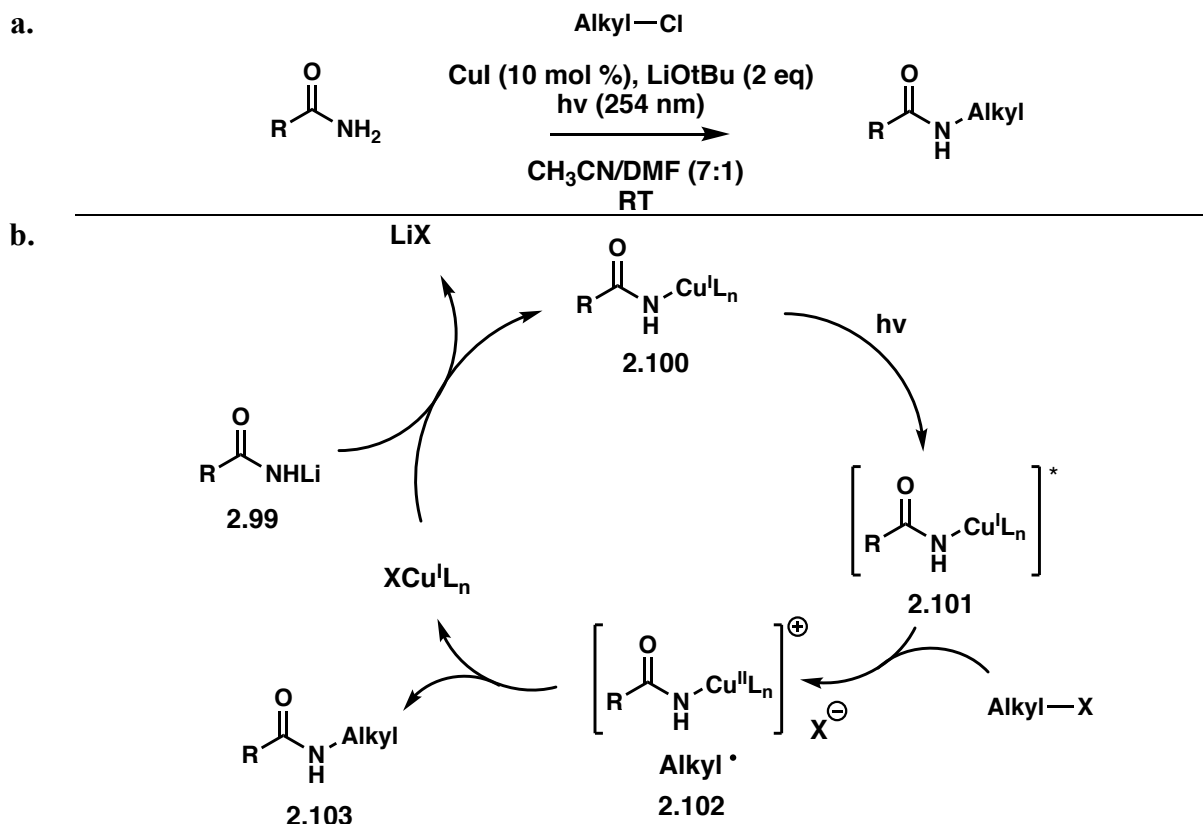
19					0
20					0
21					0
22					0
23					0
24					0
25					0

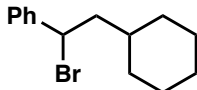
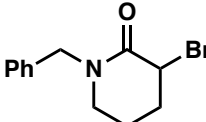
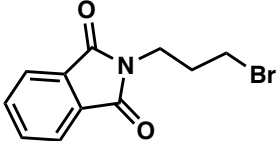

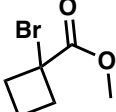
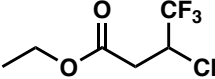
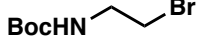
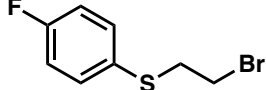
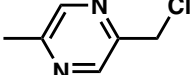
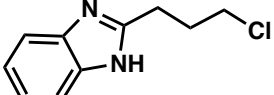
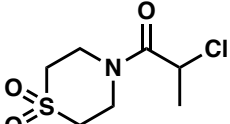
Table 2.17: Summary of PTC N-alkylation conditions of cyclohexylpropanoyl piperazinones.

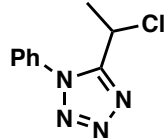
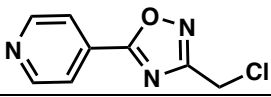
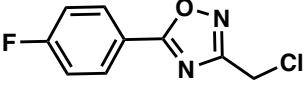
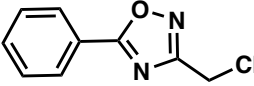
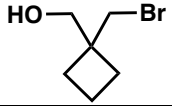
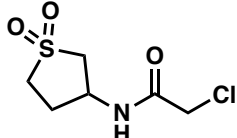
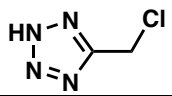
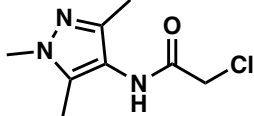
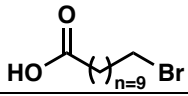
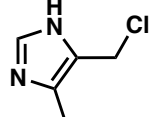
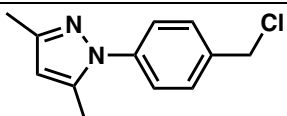
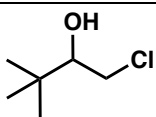
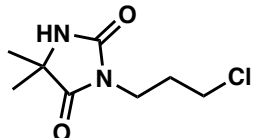
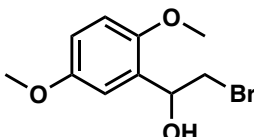
An alternative methodology for the N-alkylation of amides has been developed by the Fu group. It consists of a photoinduced, copper-catalyzed N-alkylation with inactivated secondary alkyl halides (**Scheme 2.13a**).¹⁸⁷ As depicted in **Scheme 2.13b**, the reaction mechanism was proposed to first form the copper(I)-amidate complex (**2.100**) which is converted into a photoexcited species (**2.101**) after irradiation. The reduction of alkyl halide generates an alkyl radical intermediate (**2.102**), and the catalyst is regenerated by the reductive elimination resulting in the N-alkylated amide (**2.103**).



Scheme 2.13: Conditions (a) and proposed mechanism (b) for photoinduced, copper-catalyzed N-alkylation with unactivated secondary alkyl halides.

These conditions were applied to the N-alkylation of the piperazinone and conversion in good yields were observed for a broader range of alkyl halides as summarized in **Table 2.18**. From these results, a selectivity for substrates with halogens alpha to an aryl group (**Entry 1, 9, 12, 14, 15 and 22**) and an acetamide (**Entry 2, 11, 17, 19, 26, 27 and 30**) arises. The non-reactive nature of several primary alkyl halides (**Entry 3, 4, 7, 16, 20, 23, 24 and 25**) is likely a consequence of their lower stability as radical species. In addition, certain functionalities on the substrate may interfere with the formation of the radical or lead to its instability: (1) Phthalimides (**Entry 3, Table 2.18**) are susceptible to photoirradiation leading to intramolecular reactions;¹⁸⁸ (2) Once deprotonated alcohols can coordinate with copper¹⁸⁹ and disrupt the catalytic cycle (**Scheme 2.13b**).

Entry	Alkyl halide	Compound Yield
1		2.104 58%
2		2.105 61%
3		0%
4		0%
5		0%
6		0%
7		0%
8		2.106 65%
9		2.107 58%
10		2.108 91%
11		2.109 90%

12		2.110 66%
13		0%
14		2.111 58%
15		2.112 63%
16		0%
17		2.113 62%
18		0%
19		2.114 57%
20		0%
21		0%
22		2.115 83%
23		0%
24		0%
25		0%

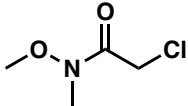
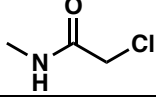
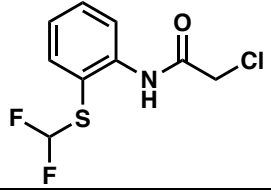
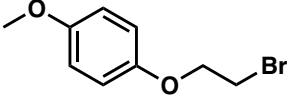
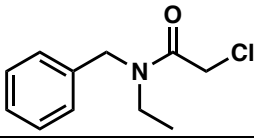

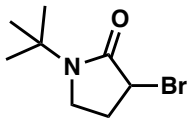
26		2.116 64%
27		2.117 54%
28		0%
29		2.118 75%
30		2.119 88%
31		0%
32		0%

Table 2.18: Summary of photoinduced, copper-catalyzed N-alkylation conditions of cyclohexylpropanoyl piperazinones 2.67.

Furthermore, it is possible that the piperazinone hinders the generation of the copper(I)-amidate complex. To test this hypothesis the uncyclized amide intermediate **2.61** was reacted with alkyl halides under the photoinduced, copper-catalyzed conditions (**Table 2.19**). However, no conversion was observed, possibly refuting the deleterious role of the piperazinone in the N-alkylation.

2.61		
Entry	Alkyl halide	Yield
1		0%
2		0%

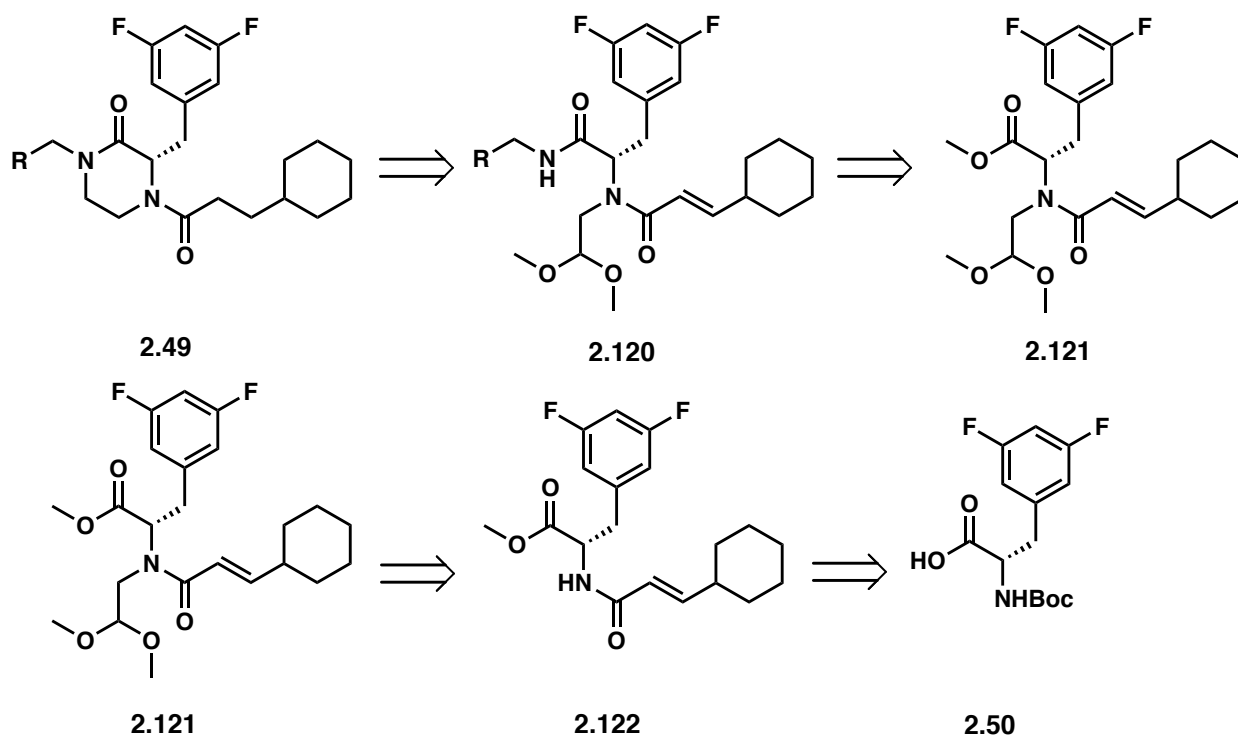
Table 2.19: Screening of the photoinduced, copper-catalyzed N-alkylation conditions between unreactive alkyl halides and the uncyclized intermediate **2.61**.

9.4.2 Alternative Approaches to Synthesize N-alkylated Cyclohexylpropanoyl Piperazinones

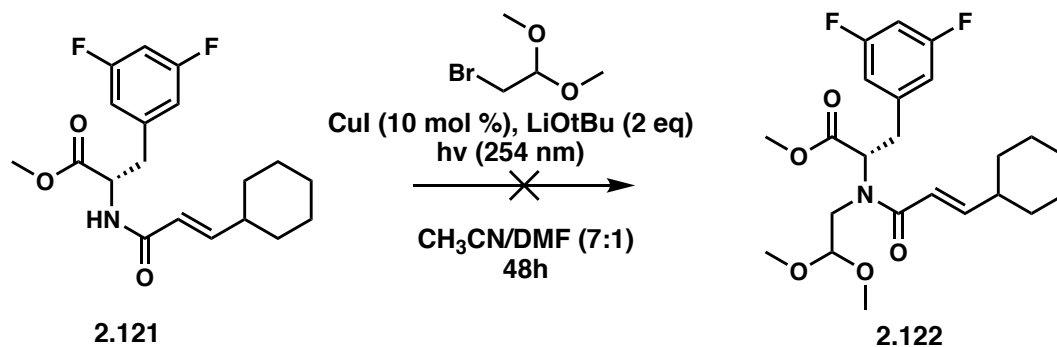
9.4.2.1 Cyclization Strategies of *Seco* Analogs

Although PTC and photoinduced copper-catalyzed N-alkylation conditions were compatible with 19 out of the 35 alkyl halides and led to the generation of the corresponding analogs, the remaining *N*-alkyl cyclohexylpropanoyl piperazinones required different synthetic approaches to be accessed. Since the amine homologs of the alkyl halides were available, I hypothesized that the cyclization step could be achieved after the amidation of the 3,5-difluorophenylalanine C-terminus and would circumvent the lack of reactivity for the alkyl halide substrates. Therefore, I investigated different synthetic handles that could be installed on either the C- or N-terminus of 3,5-difluorophenylalanine and elicit the formation of the piperazinone.

First, I proposed the N-alkylation of a *N*-acyl 3,5-difluorophenylalanine **2.122** using 2-bromo-1,1-dimethoxyethane to set the stage for the formation of the piperazinone **2.49** following the amidation with an alkyl amine on the C-terminus (**2.120**), as shown in the retrosynthetic analysis in **Scheme 2.14**. But the N-alkylation with 2-bromo-1,1-dimethoxyethane was not compatible with the photoinduced copper-catalyzed conditions (**Scheme 2.15**), as no conversion was observed and the starting material **2.61** was recovered.

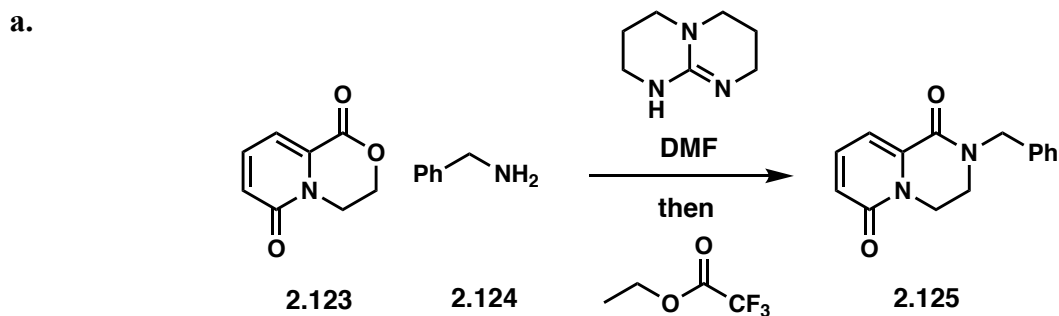


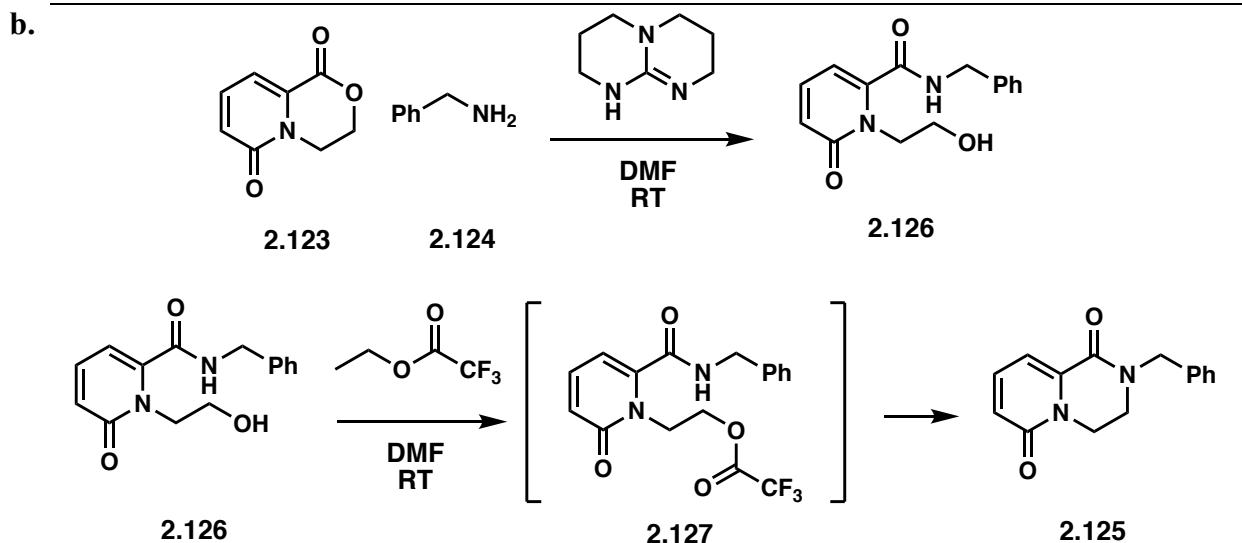
Scheme 2.14: Proposed retrosynthetic route for N-alkylated cyclohexylpropanoyl piperazinones 2.49.



Scheme 2.15: Attempt at photoinduced, copper-catalyzed N-alkylation of 2.121 with 2-bromo-1,1-dimethoxyethane.

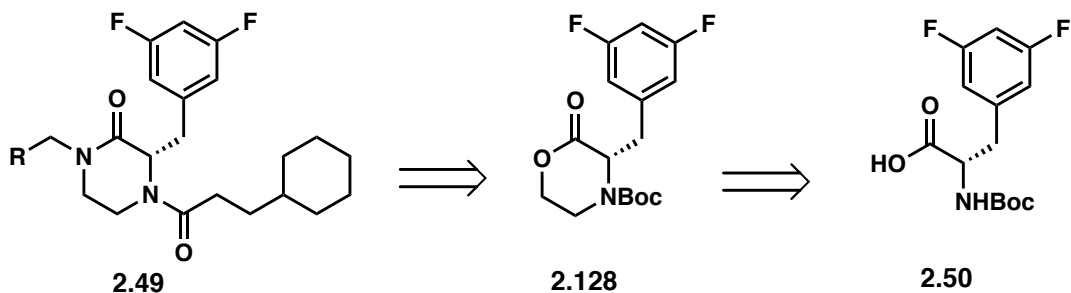
Rankic A. D. et al. developed a mild lactone-to-lactam conversion for the synthesis of pyridopyrazine-1,6-diones (**2.125**) utilizing 1,5,7-triazabicyclo[4.4.0]dec-5-ene (TBD), as shown in **Scheme 2.16a**.¹⁹⁰ The lactone ring opening and amidation is mediated by TBD acting as a bifunctional nucleophilic organocatalyst and leads to the formation of intermediate **2.126** (**Scheme 2.16b**).¹⁹¹ Following the addition of ethyl trifluoroacetate (ETFA), TBD induces transesterification between the **2.126** and ETFA, and subsequent intramolecular N-alkylation produces the lactam **2.125**.



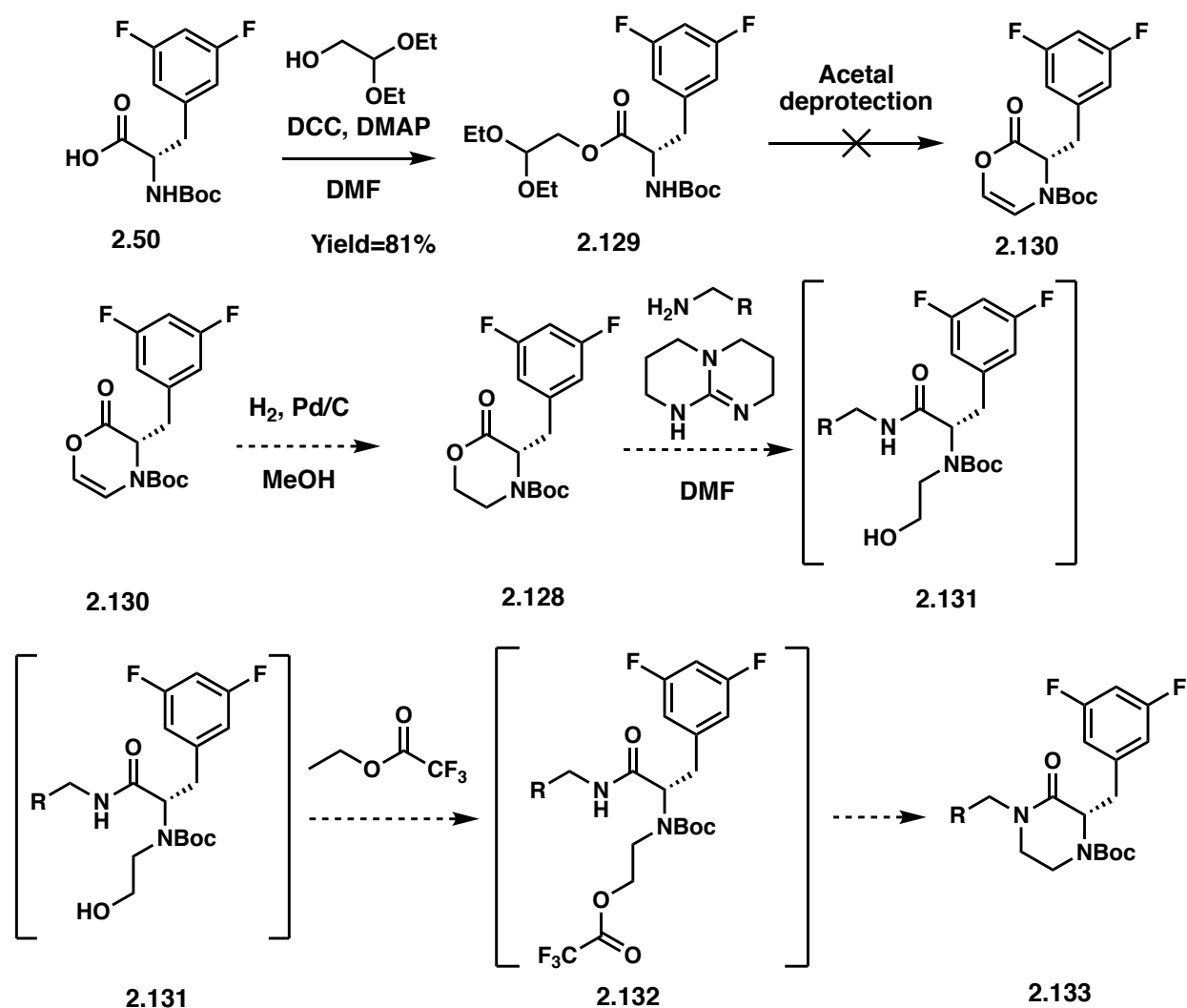


Scheme 2.16: Synthetic route to pyridopyrazine-1,6-dione **2.125** via TBD-mediated lactone-to-lactam conversion (a) and proposed mechanism (b).

As an alternative to the N-alkylation of the cyclohexylpropanoyl piperazinone **2.67**, I envisioned to emulate this lactone-to-lactam route to access the piperazinone from a morpholinone synthon **2.128**, allowing for a divergent synthetic approach as pictured in **Scheme 2.17**. To prepare the morpholinone core **2.118**, I proposed the formation of the ester **2.129** (**Scheme 2.18**), from Boc-3,5-difluorophenylalanine **2.50** with 2,2-diethoxyethan-1-ol. Similar to the piperazinone synthesis, the deprotection of the acetal was expected to promote the cyclization/enamine formation and, once reduced, the product would be reacted with TBD, an alkyl amine and ETFA to obtain the substituted piperazinone **2.133** (**Scheme 2.18**).



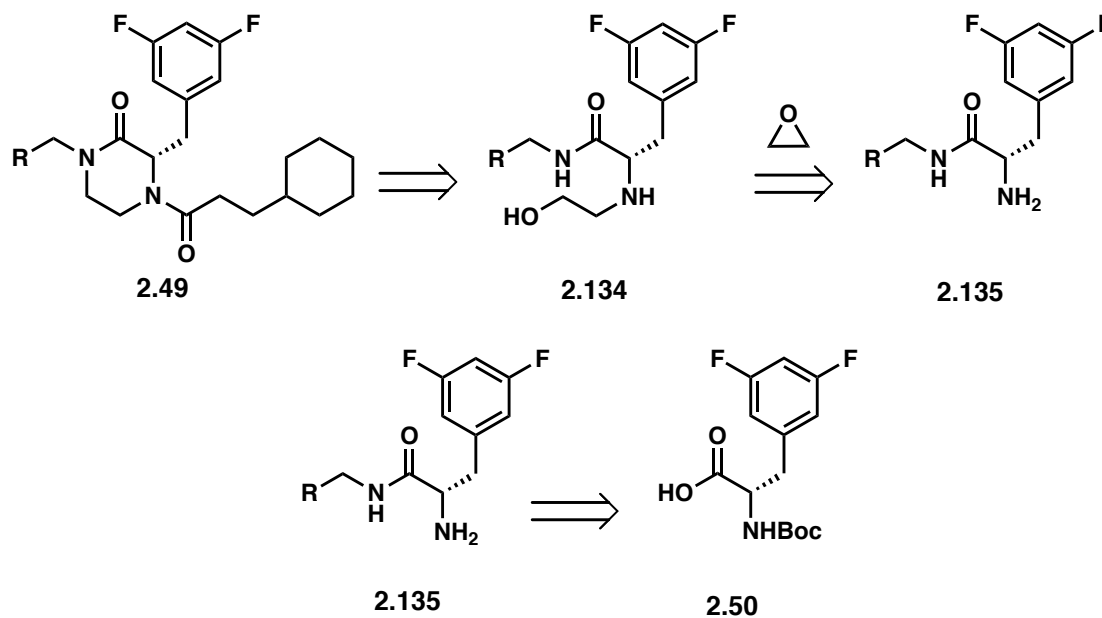
Scheme 2.17: Retrosynthetic route for N-alkylated Cyclohexylpropanoyl Piperazinones via lactone-to-lactam conversion.



Scheme 2.18: Proposed synthetic route for the synthesis of N-alkylated piperazinones 2.133 via lactone-to-lactam conversion.

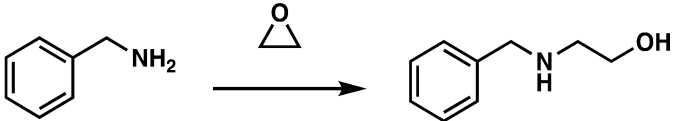
The esterification of Boc-3,5-difluorophenylalanine **2.50** with 2,2-diethoxyethan-1-ol using DCC and DMAP in DMF produced intermediate **2.129** in 81% yield. However, all attempts to remove the acetal and invoke cyclization under acidic conditions failed to produce the dihydromorpholinone **2.130**. Notably, the scarcity of literature precedent for the preparation of dihydromorpholinone **2.130** or morpholinone **2.128**, especially from amino acids, suggest that these heterocycles are not easily accessed.¹⁹²⁻¹⁹⁴

Informed by the pitfalls of the lactone-to-lactam route, I proposed a route involving an aminolytic ring-opening of ethylene oxide to access the β -amino alcohol intermediate **2.134** as depicted in the retrosynthetic analysis in **Scheme 2.19**.



Scheme 2.19: Retrosynthetic route for N-alkylated cyclohexylpropanoyl piperazinones **2.49** via an aminolytic ring-opening of ethylene oxide.

The high price of Boc-3,5-difluorophenylalanine (\$115/g) prohibits its use for the screening of conditions. Therefore, to determine adequate conditions for the aminolytic ring-opening of ethylene oxide, benzylamine (**2.136**) was first chosen for its similar nucleophilic character compared to the 3,5-difluorophenylalanine free amine. In addition, its UV active character would allow for straight-forward monitoring of reaction progress by TLC. As presented in **Table 2.20**, a variety of conditions for aminolytic ring-opening of epoxides were screened: (1) Solvents such as nitromethane (CH_3NO_2) (**Entry 1 and 2**),¹⁹⁵ ethanol (EtOH)¹⁹⁶ (**Entry 5 and 6**) and tetrahydrofuran (THF) (**Entry 3, 4, 7-17**); (2) Temperatures (i.e., 25°C and 40°C); (3) Acid-catalyzed conditions (i.e., acetic acid (AcOH), *p*-TsOH, water) (**Entry 7-10**); (4) Base-catalyzed conditions (i.e., TEA, sodium acetate (NaOAc)) (**Entry 14-17**); (5) In presence of water (**Entry 11-13**). No conversion to benzylaminoethanol (**2.137**) was observed under these conditions. In addition, monitoring of the reaction by TLC was unsuitable, as benzylamine spots proved to be very streaky.

				
Entry	Conditions			Conversion Observed
	Reagent	Solvent	Temperature	
1		CH_3NO_2	RT	No
2		CH_3NO_2	40°C	No
3		THF	RT	No
4		THF	40°C	No
5		EtOH	RT	No
6		EtOH	40°C	No
7	AcOH (1 eq)	THF	RT	No
8	AcOH (10 eq)	THF	RT	No
9	AcOH (10 eq)	THF	40°C	No
10	<i>p</i> -TsOH·H ₂ O (1 eq)	THF	RT	No
11	H ₂ O (2 eq)	THF	RT	No
12	H ₂ O (10 eq)	THF	RT	No
13	H ₂ O (10 eq)	THF	40°C	No
14	TEA (1 eq)	THF	RT	No
15	TEA (1 eq)	THF	40°C	No

16	NaOAc (1 eq)	THF	RT	No
17	NaOAc (1 eq)	THF	40°C	No

Table 2.20: Summary of conditions screened for the aminolytic ring-opening of ethylene oxide with benzylamine 2.136. The benzylamine was recovered under these conditions.

Phenylalanine methyl ester (**2.138**) was instead selected as a better candidate to identify conditions for the aminolytic ring-opening of ethylene oxide due to its closer structural similarity with 3,5-difluorophenylalanine. Two approaches to the formation of **2.139** were attempted and the different conditions screened are summarized in **Table 2.21**: (1) Different bases were employed (**Entry 2-8**) to increase the nucleophilicity of **2.138**; (2) Reagents (**Entry 9-12**) such as Lewis acids (i.e., Zinc chloride (ZnCl₂), Lithium triflate (LiOTf))¹⁹⁷, trimethylsilyl triflate (TMSOTf)¹⁹⁸ and DMAP¹⁹⁹ were used to activate ethylene oxide.

Conditions				Conversion Observed
Entry	Reagent	Solvent	Temperature	
1		CH ₃ NO ₂	50°C	No
2	NaOtBu (2 eq)	THF	RT	No
3	TEA (2 eq)	THF	RT	No
4	NaOCH ₃ (1 eq)	THF	RT	No
5	NaOEt (2 eq)	THF	RT	No
6	NaOAc (2 eq)	THF	RT	No
7	LiHMDS (1 eq)	THF	-78°C	No
8	LiHMDS (2 eq)	THF	-78°C	No
9	ZnCl ₂ (1 eq)	THF	0°C	No
10	LiOTf (2 eq)	THF	RT	No
11	TMSOTf (1 eq)	THF	RT	No
12	DMAP (1 eq)	THF	RT	No

Table 2.21: Summary of conditions screened for the aminolytic ring-opening of ethylene oxide with phenylalanine methyl ester 2.138. The phenylalanine methyl ester was recovered under these conditions.

Another approach employed to catalyze the ring opening of epoxide was the use of ionic liquids and organic salts. The Gao group developed a methodology to prepare 3-aryl-2-oxazolidinones via an ionic liquid-catalyzed reaction between anilines, ethylene oxide and carbon dioxide (CO₂).²⁰⁰ In an analogous manner, the Calo group was able to generate cyclic carbonates from CO₂ and ethylene oxide in tetrabutylammonium salts.²⁰¹ These conditions were applied to the aminolytic ring-opening of ethylene oxide using 1-Butyl-3-methylimidazolium chloride (BmimCl) and TBAB (**Entry 1-3, Table 2.22**). As the desired product **2.139** was not formed, diazabicyclo[5.4.0]undec-7-ene (DBU) was introduced as a catalytic base because it has been shown to synergize with ionic liquids by activating ethylene oxide and amines cooperatively through hydrogen bonding (**Entry 4-8, Table 2.22**).²⁰² However, the addition of DBU also failed to produce **2.139**. A possible explanation for the failure of these conditions is the low vapor pressure of ethylene oxide (0.15 MPa). Contrary to my attempts with this methodology, the Gao group used pressurized vessels (2.5 MPa), possibly preventing the vaporization of ethylene oxide. In addition, they reported lower yields for aliphatic amines such as benzylamine and cyclohexylamine.²⁰⁰

Conditions				Conversion Observed
Entry	Ionic liquid	Base	Temperature	
1	BmimCl (4 eq)		RT	No
2	BmimCl (4 eq)		60°C	No
3	TBAB (2 eq)		RT	No
4	BmimCl (8 eq)	DBU (0.5 eq)	RT	No

5	BmimCl (8 eq)	DBU (0.5 eq)	130°C	No
6	TBAB (8 eq)	DBU (0.5 eq)	RT	No
7	TBAB (8 eq)	DBU (0.5 eq)	130°C	No
8	TBAB (4 eq), BmimCl (4 eq)	DBU (0.5 eq)	130°C	No

Table 2.22: Summary of conditions screened for the aminolytic ring-opening of ethylene oxide with phenylalanine methyl ester 2.138 using ionic liquids. The phenylalanine methyl ester was recovered under these conditions.

Metal-salen complexes **2.140** represent an interesting class of catalysts capable of increasing the reactivity of ring-opening reactions by coordinating to the epoxide oxygen. Mn-, Co- and Cr-salen complexes were evaluated for their aminolytic reactivity with ethylene oxide, as summarized in **Table 2.23**, but these conditions also failed to generate the β -amino alcohol phenylalanine **2.139**.²⁰³⁻²⁰⁵

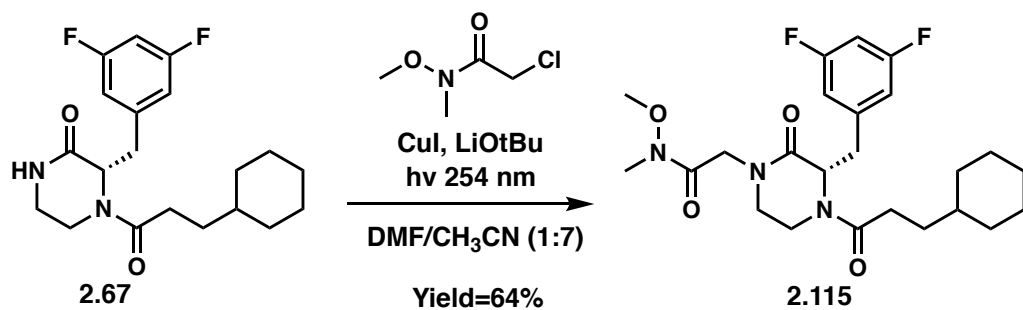
2.138		2.139	2.140	
Entry	Conditions			Conversion Observed
	Catalyst M =	Solvent	Temperature	
1	MnCl	Toluene	RT	No
2	MnCl	Toluene	RT	No
3	MnCl	DCM	RT	No
4	Co	Et ₂ O	RT	No
5	CrCl	Et ₂ O	RT	No
6	CrCl	DCM	RT	No
7	CrCl	DCM	0°C	No

Table 2.23: Summary of conditions screened for the aminolytic ring-opening of ethylene oxide with phenylalanine methyl ester 2.138 using metal-salen complexes 2.140. The phenylalanine methyl ester was recovered under these conditions.

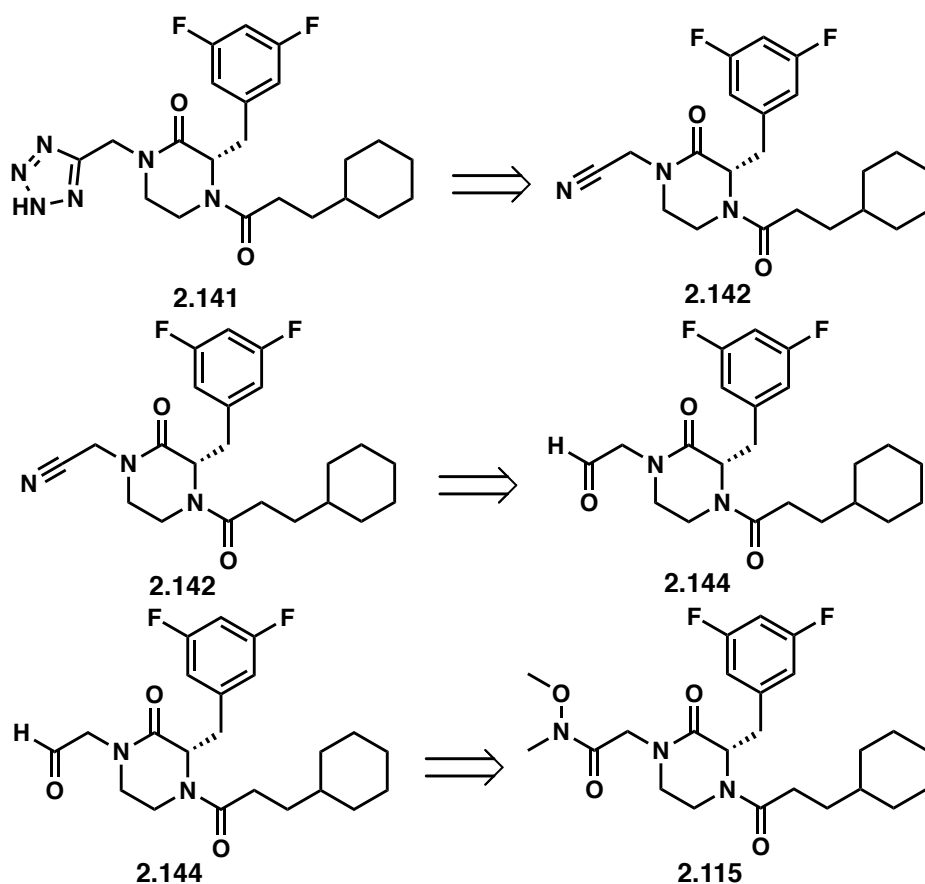
Taken together these results suggest that ethylene oxide is not ideal for aminolytic ring opening conditions and the limited amount of literature precedent supports this observation.²⁰⁶⁻²⁰⁸ Apart for the aforementioned ionic liquid methodology, substituted epoxides are more commonly used than ethylene oxide. Frequent use of ethylene oxide in polymerization reactions indicates that ethylene oxide might have oligomerized under exposure to the conditions I used. The volatility of ethylene oxide (Boiling point: 10.7°C) is an additional factor that renders its use less practical.

9.4.3 Weinreb Amide and Nitrile as Synthetic Handles

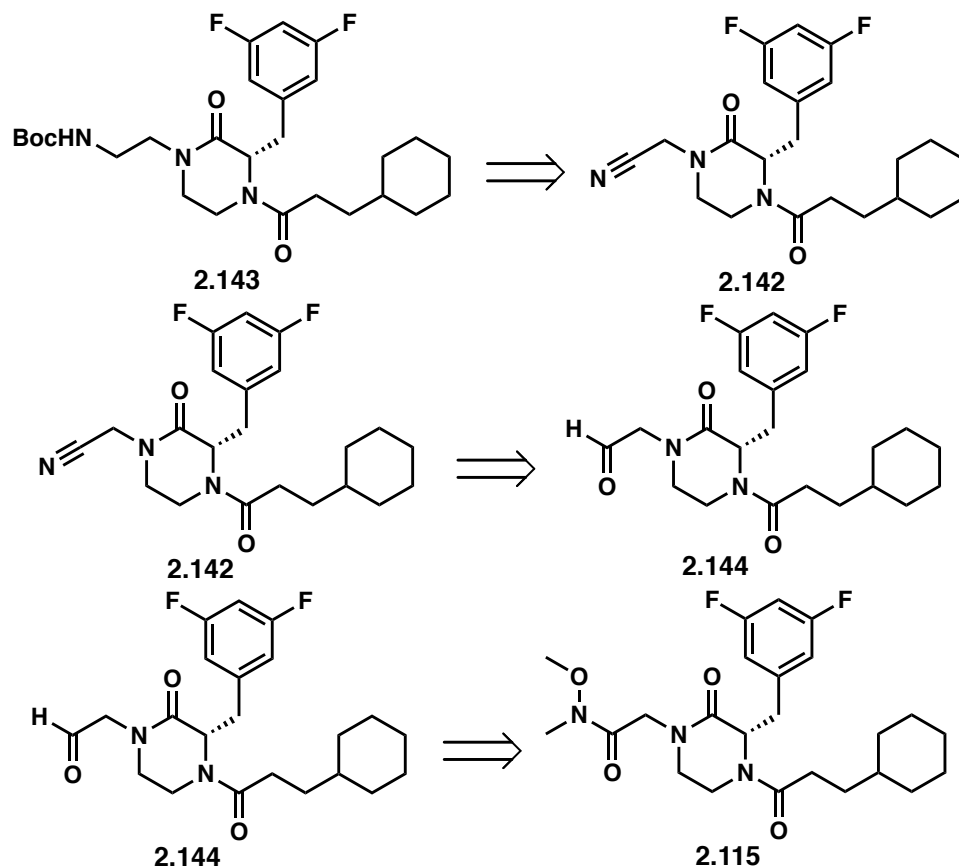
As previously described, functionalization of amides remains challenging and the limited scope of alkyl halides that are compatible with current N-alkylation methodologies calls for alternative approaches. Considering the photoinduced copper-catalyzed preparation of the Weinreb amide piperazinone analog **2.115** (Scheme 2.20) in good yield (64%), I hypothesized that this common synthetic handle can be leveraged to access different functionalities such as tetrazole **2.141** and Boc-protected amine **2.143** as depicted in the retrosynthetic analysis in Scheme 2.21 and 2.22, respectively. Initially, these target molecules (**2.141** and **2.143**) were to be generated from corresponding alkyl halides, but this new approach would allow access through **2.115**, thus capitalizing on the established method to access multiple analogs. Following the reduction of the Weinreb amide **2.115** to an aldehyde **2.144**, I envisioned the transformation of this resulting intermediate into a nitrile group **2.142**. From this nitrile piperazinone **2.142**, tetrazole **2.141** and Boc-protected **2.143** analogs could be obtained.



Scheme 2.20: Photoinduced copper-catalyzed synthesis of compound 2.115.



Scheme 2.21: Retrosynthetic route for analogs 2.141 from the Weinreb amide cyclohexylpropanoyl piperazinone.



Scheme 2.22: Retrosynthetic route for analogs 2.143 from the Weinreb amide cyclohexylpropanoyl piperazinone.

Although lithium aluminum hydride (LiAlH_4) is commonly employed to reduce Weinreb amides to aldehydes, it can also reduce amides, preventing its use in the context of this synthetic route. More selective reducing agent, diisobutylaluminum hydride (DIBAL-H) (**Entry 1, Table 2.24**) and a *t*-butoxy derivative of DIBAL-H, lithium diisobutyl-*t*-butoxyaluminum hydride (LDBBA) (**Entry 2, Table 2.24**) were tested.²⁰⁹ When employed on the Weinreb amide piperazinone, these conditions produced complex mixtures of products making this route not synthetically practical.

Entry	Conditions	Yield
1	DIBAL-H in toluene @ -78°C	n/a
2	LDBBA	n/a

Table 2.24: Conditions tested for the reduction of the Weinreb amide cyclohexylpropanoyl piperazinone 2.115 to the aldehyde 2.144 analog.

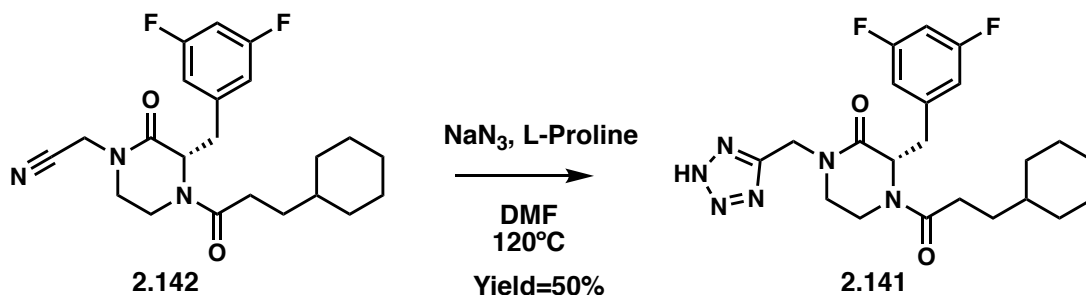
Even though the Weinreb amide appears not to be a suitable synthetic handle, the acetonitrile piperazinone intermediate **2.142** proposed in the retrosynthetic analysis was considered as a better candidate as less steps were expected to prepare tetrazole **2.141** and Boc-protected **2.143** analogs.

Entry	Conditions	Yield
1	TBAOH in H ₂ O, Cs ₂ CO ₃ in Toluene @ 70°C	No reaction
2	TBAB, Cs ₂ CO ₃ , H ₂ O in Toluene @ 70°C	No reaction
3	TBAB, Cs ₂ CO ₃ in dry Toluene @ 70°C	No reaction
4	CuI, LiOtBu, hν in CH ₃ CN/DMF	29-41%

Table 2.25: Conditions tested for the N-alkylation of cyclohexylpropanoyl piperazinone with chloroacetonitrile.

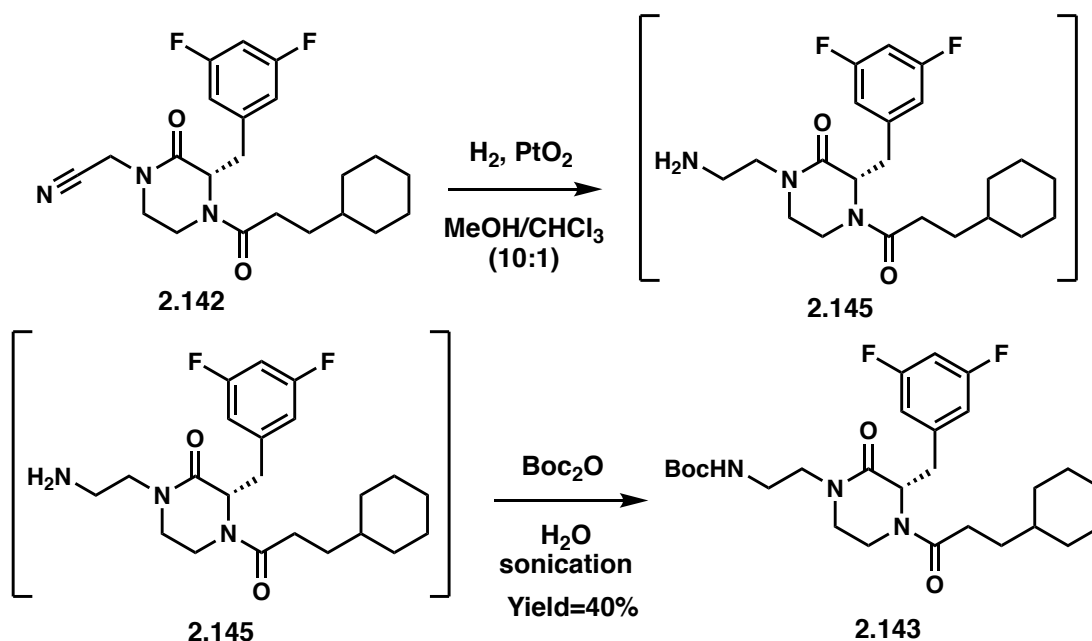
Different conditions for the N-alkylation of amides with chloroacetonitrile were screened but no conversion was observed with the PTC conditions with TBAOH (**Entry 1, Table 2.25**).

TBAOH has been shown to catalyze hydration of nitriles as tetrabutylammonium coordinates with the nitrile-nitrogen.²¹⁰ So, I made the decision to substitute TBAOH with TBAB with the expectation of preventing hydration. However, the presence of water likely led to the same outcome (**Entry 2, Table 2.25**). Water-free PTC conditions with only TBAB and Cs₂CO₃ in dry toluene were tested and also failed to generate product, suggesting that tetrabutylammonium coordination with the nitrile group promotes degradation of chloroacetonitrile (**Entry 3, Table 2.25**). However, the photoinduced copper-catalyzed N-alkylation conditions did produce the acetylnitrile piperazinone intermediate **2.142** in moderate yields (**Entry 4, Table 2.25**). The low conversion was likely due to the coordination of copper(I) to the nitrile contributing to the degradation of chloroacetonitrile.²¹¹



Scheme 2.23: Synthetic route for the tetrazole cyclohexylpropanoyl piperazinone 2.141.

From the acetylnitrile piperazinone intermediate **2.142**, the tetrazole cyclohexylpropanoyl piperazinone **2.141** was synthesized via a L-proline catalyzed [3+2] cycloaddition reaction with sodium azide (NaN₃) in 50% yield (**Scheme 2.23**).²¹² The Boc-protected ethylamine cyclohexylpropanoyl piperazinone **2.143** was generated by a hydrogenation catalyzed by platinum oxide (PtO₂) of **2.142** to access the ethylamine cyclohexylpropanoyl piperazinone **2.145** followed by a Boc protection in water (Yield=40%, **Scheme 2.24**).



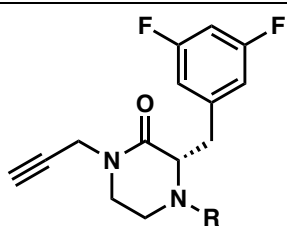
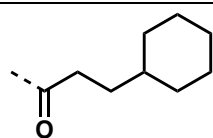
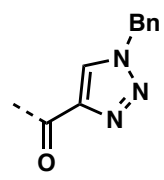
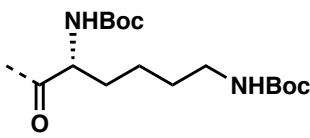
Scheme 2.24: Synthetic route for the Boc ethylamine cyclohexylpropanoyl piperazinone 2.143.

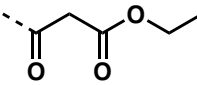
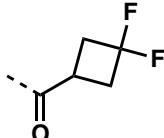
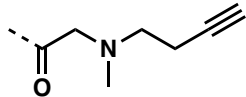
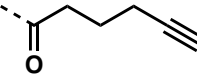
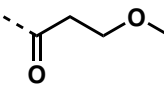
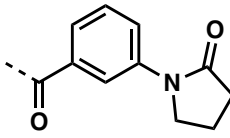
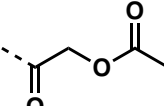
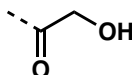
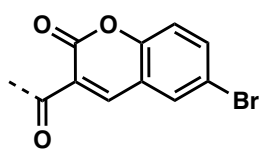
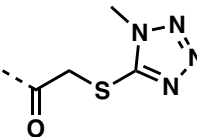
In summary, the N-alkylation routes (i.e., PTC and photoinduced copper catalysis) of the cyclohexylpropanoyl piperazinone afforded 19 analogs (**2.96 – 2.98**, **2.104 – 2.119**) bearing a wide range of functionalities (e.g., carbonyls, (hetero)aromatic rings, aliphatic substituents). Although I was not able to identify synthetic handles or methodologies to form the piperazinone following the amidation of the 3,5-difluorophenylalanine C-terminus, I leveraged the nitrile functionality to access two more analogs (**2.141** and **2.143**).

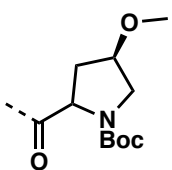
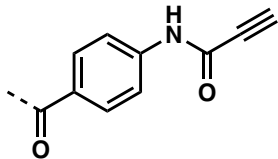
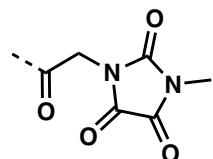
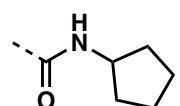
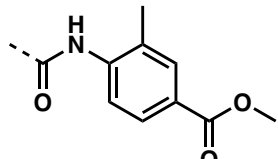
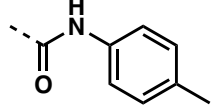
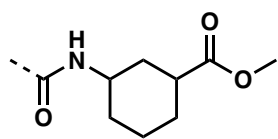
10 Antibacterial Activity of the Piperazinone and *Seco* Libraries

The synthetic work accomplished by Quentin Gibault, Katelyn Stevens and I resulted in 28 *seco* and 48 piperazinone analogs, setting up the stage for the evaluation of their antibacterial

activity. MICs for each analog were determined by the Zgurskaya lab for both the piperazinone library and the *seco* library (synthesized by Quentin Gibault and Katelyn Stevens) against three Gram-negative bacteria (i.e., *E. coli*, *A. baumannii* and *P. aeruginosa*). Wild-type and isogenic mutants (i.e., porinated (Pore), efflux-deficient (Δ) and porinated/efflux-deficient (Δ -Pore)) of the three species were used to determine the contributions of active efflux and OM permeability barriers on the activities of compounds. The MIC values are compiled in **Table 2.26** and **2.27** (propargyl piperazinone analogs) and **Table 2.28** and **2.29** (cyclohexylpropanoyl piperazinone analogs).

		MIC (μ M)							
		<i>E. coli</i>				<i>A. baumannii</i>			
R	Compound	WT	Pore	Δ	Δ Pore	WT	Pore	Δ	Δ Pore
	2.69	>100	>100	>100	>100	>100	>100	>100	>100
	2.70	>100	50	>100	50	>100	100	>100	100
	2.70s	>100	>100	>100	100	>100	>100	>100	>100
	2.71	>100	>100		50	>100	>100	>100	100
	2.71s	>100	>100	>100	100	>100	>100	>100	100

	2.72	>100	100	>100	100	>100	>100	>100	>100
	2.73	>100	100	>100	100	>100	>100	>100	>100
	2.74	>100	>100	>100	100	>100	>100	>100	>100
	2.75	>100	100	>100	100	>100	>100	>100	100
	2.77	>100	>100	>100	>100	>100	>100	>100	>100
	2.77s	>100	>100	>100	100	>100	>100	>100	>100
	2.78	>100	>100	>100	>100	>100	>100	>100	>100
	2.78s	>100	>100	>100	100	>100	>100	>100	>100
	2.79	>100	100	>100	100	>100	>100	>100	>100
	2.80	>100	>100	>100	>100	>100	>100	>100	>100
	2.81	>100	>100	>100	>100	>100	>100	>100	>100
	2.81s	>100	>100	>100	100	>100	>100	>100	>100
	2.82	>100	50	100	50	>100	>100	>100	100
	2.82s	>100	>100	>100	100	>100	>100	>100	100

	2.84	>100	>100	>100	>100	>100	>100	>100	>100
	2.84s	>100	>100	>100	100	>100	>100	>100	100
	2.85	>100	>100	>100	>100	>100	>100	>100	>100
	2.85s	>100	>100	>100	100	>100	>100	>100	100
	2.86	>100	>100	>100	>100	>100	>100	>100	>100
	2.86s	>100	>100	>100	>100	>100	>100	>100	>100
	2.87	>100	>100	>100	>100	>100	>100	>100	>100
	2.87s	>100	>100	>100	>100	>100	>100	50	25
	2.88	>100	>100	>100	>100	>100	>100	>100	>100
	2.89	>100	>100	>100	>100	>100	>100	>100	>100
	2.89s	>100	>100	>100	>100	>100	>100	100	100
	2.90	>100	>100	>100	>100	>100	>100	>100	>100
	2.90s	>100	>100	>100	>100	>100	>100	>100	>100

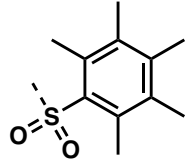
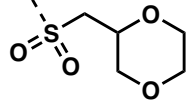
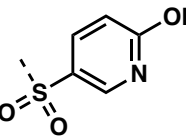
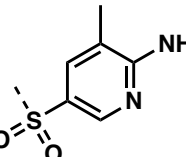
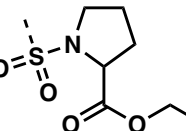
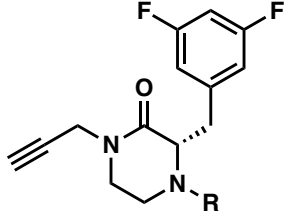
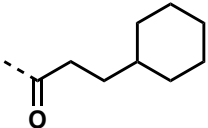
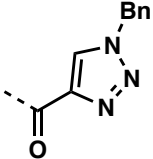
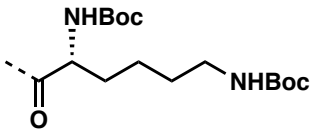
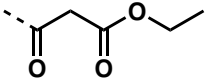
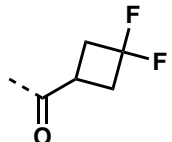
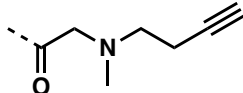
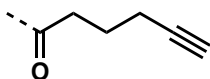
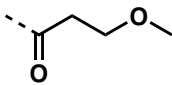
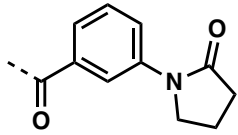
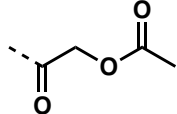
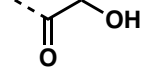
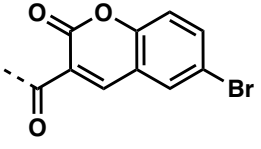
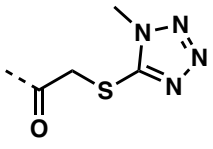
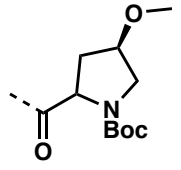
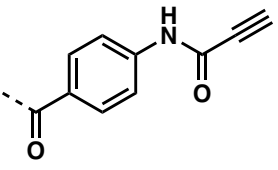
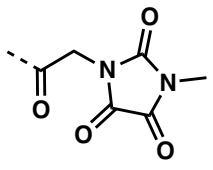
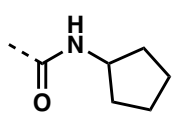
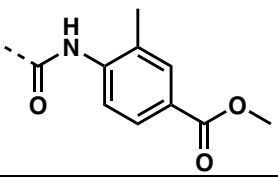
	2.91	>100	100	100	50	>100	>100	100	100
	2.92	>100	>100	>100	>100	>100	>100	>100	>100
	2.93	>100	>100	>100	>100	>100	>100	>100	>100
	2.93s	>100	>100	>100	100	>100	>100	>100	>100
	2.94	>100	>100	>100	>100	>100	>100	>100	>100
	2.95	>100	>100	>100	>100	>100	>100	>100	>100

Table 2.26: MIC values of propargyl piperazinone and *seco* analogs in wild-type (WT), porinated (Pore), efflux-deficient (Δ) and porinated/efflux-deficient (Δ Pore) *E. coli* and *A. baumannii*. The *seco* analogs denoted by the compound number followed by s (#s) were synthesized by Quentin Gibault.

		MIC (μ M)			
		<i>P. aeruginosa</i>			
R	Compound	WT	Pore	Δ	Δ Pore
	2.69	>100	>100	>100	>100
	2.70	>100	>100	>100	>100

	2.70s	>100	>100	>100	>100
	2.71	>100	>100	>100	50
	2.71s	>100	>100	>100	>100
	2.72	>100	>100	>100	>100
	2.73	>100	>100	>100	>100
	2.74	>100	>100	>100	>100
	2.75	>100	>100	>100	>100
	2.77	>100	>100	>100	>100
	2.77s	>100	>100	>100	>100
	2.78	>100	>100	>100	>100
	2.78s	>100	>100	>100	>100
	2.79	>100	>100	>100	>100
	2.80	>100	>100	>100	>100

	2.81	>100	>100	>100	>100
	2.81s	>100	>100	>100	>100
	2.82	>100	>100	100	100
	2.82s	>100	>100	>100	100
	2.84	>100	>100	>100	>100
	2.84s	>100	>100	>100	100
	2.85	>100	>100	>100	>100
	2.85s	>100	>100	>100	>100
	2.86	>100	>100	>100	>100
	2.86s	>100	>100	>100	100
	2.87	>100	>100	>100	>100
	2.87s	>100	>100	>100	100
	2.88	>100	>100	>100	>100
	2.89	>100	>100	>100	>100

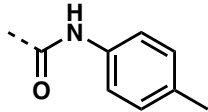
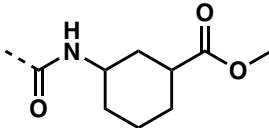
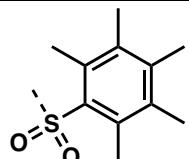
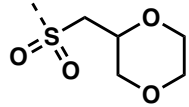
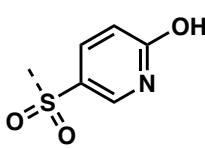
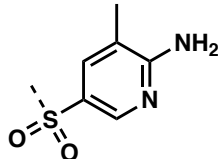
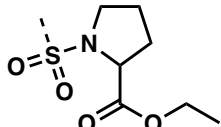
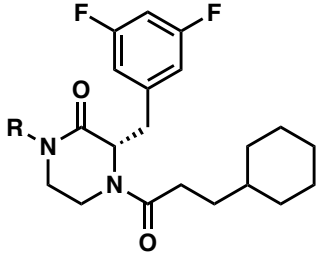
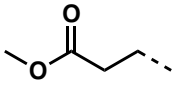
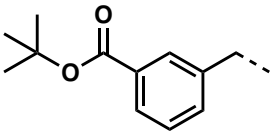
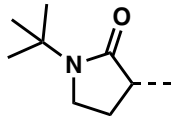
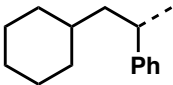
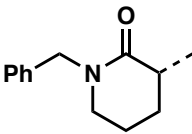
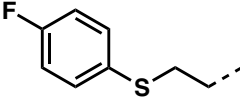
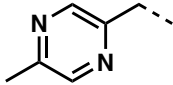
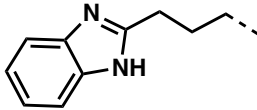
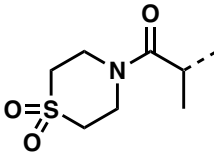
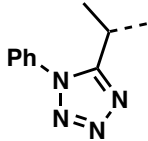
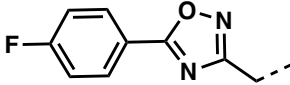
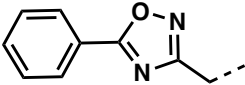
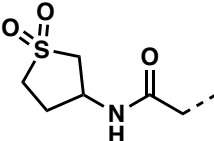
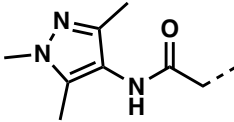
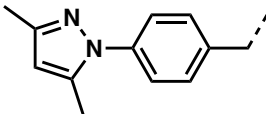
	2.89s	>100	>100	>100	50
	2.90	>100	>100	>100	>100
	2.90s	>100	>100	>100	100
	2.91	>100	>100	>100	50
	2.92	>100	>100	>100	>100
	2.93	>100	>100	>100	>100
	2.93s	>100	>100	>100	>100
	2.94	>100	>100	>100	>100
	2.95	>100	>100	>100	>100

Table 2.27: MIC values of propargyl piperazinone and *seco* analogs in wild-type (WT), porinated (Pore), efflux-deficient (Δ) and porinated/efflux-deficient (Δ Pore) *P. aeruginosa*. The *seco* analogs denoted by the compound number followed by s (#s) were synthesized by Quentin Gibault.

	MIC (μM)	
	<i>E. coli</i>	<i>A. baumannii</i>

R	Compound	WT	Pore	Δ	Δ Pore	WT	Pore	Δ	Δ Pore
H	2.67	>100	>100	100	100				
	2.96	>100	>100	>100	>100	>100	>100	>100	>100
	2.97	>100	>100	>100	100	>100	>100	>100	>100
	2.97s ¹	>100	>100	>100	>100	>100	>100	>100	>100
	2.98	>100	>100	>100	>100	>100	>100	>100	>100
	2.104	>100	>100	>100	>100	>100	>100	>100	>100
	2.104s ¹	>100	>100	>100	>100	>100	>100	>100	>100
	2.105					>100	>100	>100	25
	2.105s ²	>100	>100	>100	25	>100	>100	>100	25
	2.106	>100	>100	>100	>100	>100	>100	>100	>100
	2.107					>100	>100	100	100
	2.107s ²	>100	>100	>100	>100	>100	>100	>100	>100
	2.108					>100	>100	100	100

	2.108s¹	>100	>100	>100	>100	>100	>100	>100	>100
	2.109	>100	>100	>100	>100	>100	>100	>100	>100
	2.110	>100	>100	>100	>100	>100	>100	>100	>100
	2.110s¹	>100	>100	>100	>100	>100	>100	>100	>100
	2.111	>100	>100	>100	>100	>100	>100	>100	>100
	2.111s¹	>100	>100	>100	>100	>100	>100	>100	>100
	2.112	>100	>100	>100	>100	>100	>100	>100	>100
	2.112s¹	>100	>100	>100	>100	>100	>100	>100	>100
	2.113	>100	>100	>100	>100	>100	>100	>100	>100
	2.113s¹	>100	>100	>100	>100	>100	>100	>100	>100
	2.114	>100	>100	>100	>100	>100	>100	>100	>100
	2.114s¹	>100	>100	>100	>100	>100	>100	>100	>100
	2.115					>100	>100	>100	>100
	2.115s¹	>100	>100	>100	>100	>100	>100	>100	>100

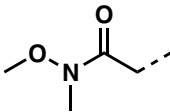
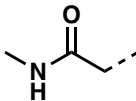
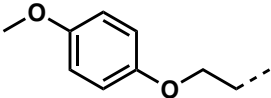
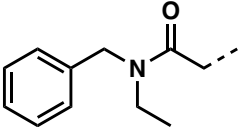

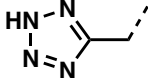
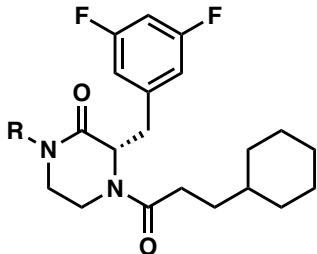
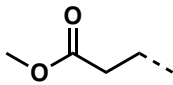
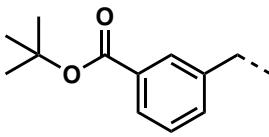
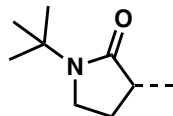
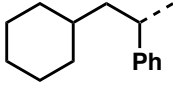
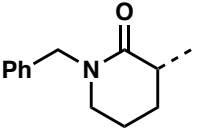
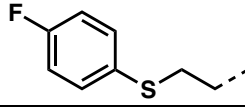
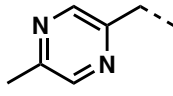
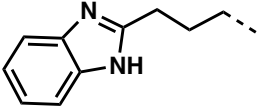
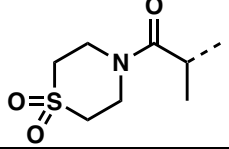
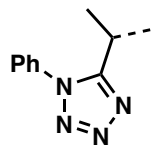
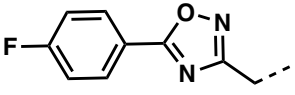
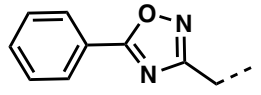
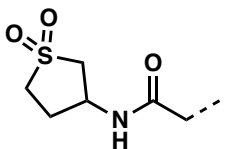
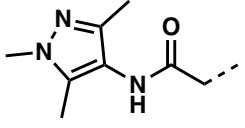
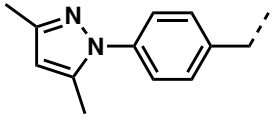
	2.116	>100	>100	>100	>100	>100	>100	>100	>100
	2.116s¹	>100	>100	>100	>100	>100	>100	>100	>100
	2.117	>100	>100	>100	>100	>100	>100	>100	>100
	2.117s¹	>100	>100	>100	>100	>100	>100	>100	>100
	2.118	>100	>100	>100	>100	>100	>100	>100	>100
	2.119	>100	>100	>100	>100	>100	>100	>100	>100
	2.119s¹	>100	>100	>100	>100	>100	>100	>100	>100
	2.143	>100	>100	>100	>100	>100	>100	>100	>100
	2.141	>100	>100	>100	>100	>100	>100	>100	>100
	2.141s¹	>100	>100	>100	>100	>100	>100	>100	>100

Table 2.28: MIC values of cyclohexylpropanoyl piperazine and *seco* analogs in wild-type (WT), porinated (Pore), efflux-deficient (Δ) and porinated/efflux-deficient (Δ Pore) *E. coli* and *A. baumannii*. The *seco* analogs denoted by the compound number followed by s (#s) were synthesized by Katelyn Stevens¹ and Quentin Gibault².

	MIC (μM)
	<i>P. aeruginosa</i>

R	Compound	WT	Pore	Δ	Δ Pore
H	2.67				
	2.96	>100	>100	>100	>100
	2.97	>100	>100	>100	100
	2.97s ¹	>100	>100	>100	>100
	2.98	>100	>100	>100	>100
	2.104	>100	>100	>100	>100
	2.104s ¹	>100	>100	>100	>100
	2.105				
	2.105s ²	>100	>100	>100	25
	2.106	>100	>100	>100	>100
	2.107				
	2.107s ²	>100	>100	>100	100
	2.108				

	2.108s¹	>100	>100	>100	>100
	2.109	>100	>100	>100	>100
	2.110	>100	>100	>100	>100
	2.110s¹	>100	>100	>100	>100
	2.111	>100	>100	>100	>100
	2.111s¹	>100	>100	>100	>100
	2.112	>100	>100	>100	>100
	2.112s¹	>100	>100	>100	>100
	2.113	>100	>100	>100	>100
	2.113s¹	>100	>100	>100	>100
	2.114	>100	>100	>100	>100
	2.114s¹	>100	>100	>100	>100
	2.115				
	2.115s¹	>100	>100	>100	>100

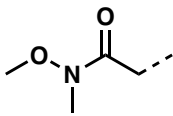
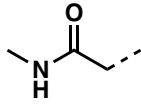
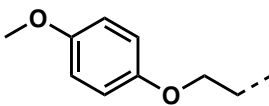
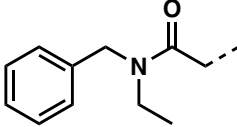

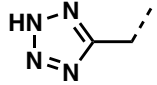
	2.116	>100	>100	>100	>100
	2.116s¹	>100	>100	>100	>100
	2.117	>100	>100	>100	>100
	2.117s¹	>100	>100	>100	>100
	2.118	>100	>100	>100	>100
	2.119	>100	>100	>100	>100
	2.119s¹	>100	>100	>100	>100
	2.143	>100	>100	>100	>100
	2.141	>100	>100	>100	>100
	2.141s¹	>100	>100	>100	>100

Table 2.29: MIC values of cyclohexylpropanoyl piperazinone and *seco* analogs in wild-type (WT), porinated (Pore), efflux-deficient (Δ) and porinated/efflux-deficient (Δ Pore) *P. aeruginosa*. The *seco* analogs denoted by the compound number followed by s (#s) were synthesized by Katelyn Stevens¹ and Quentin Gibault².

None of the compounds tested were active against the wild-type strains but a small number of analogs displayed low to moderate activity in the isogenic mutants: **2.87s** (Table 2.26 and 2.27), **2.105** and **2.105s** (Table 2.28 and 2.29) were the most active with 25 μ M in Δ -Pore *A. baumannii*, Δ -Pore *A. baumannii*, and Δ -Pore *E. coli*, *A. baumannii* and *P. aeruginosa*, respectively. In general,

porinated (Pore) and porinated/efflux-deficient (Δ -Pore) of *E. coli* were the most susceptible and *P. aeruginosa* was the least susceptible.

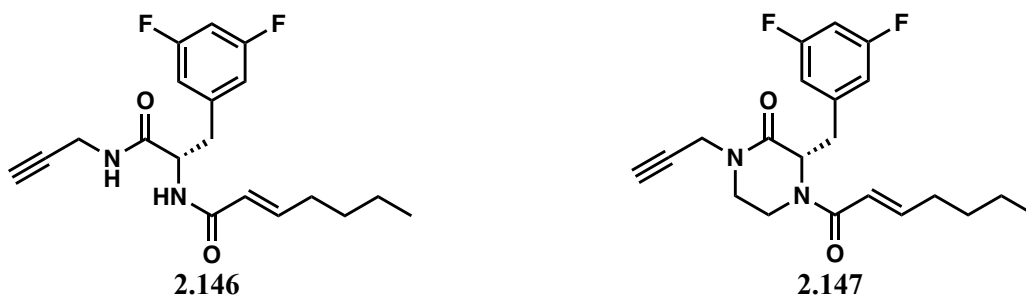


Figure 2.3: Structures of the *seco* (2.146) and piperazinone (2.147) analogs studied in Chapter 3.

The computational studies conducted in **Chapter 3** demonstrated that: (1) The piperazinone core adopts a different conformation relative to its *seco* counterpart; (2) The piperazinone core is less flexible; (3) The orientation of the appended moieties differs between piperazinone and *seco* scaffold. These conformational differences between the *seco* (2.146) and piperazinone (2.147) analogs are expected to translate to the *seco* and piperazinone libraries, thus, potentially influencing the efflux susceptibilities and OM permeabilities. Future LC-MS/MS accumulation studies will provide the data necessary to interrogate the role of conformational constraint on penetration and efflux of these compounds. In addition, I determined that 2.146 activates ClpP in a fluorescence-based assay and that 2.147 is likely inactive because the cyclization abolishes a critical hydrogen bond with ClpP. It is worth noting that a majority of *seco* compounds (i.e., 2.77s, 2.78s, 2.81s, 2.84s, 2.85s, 2.86s, 2.87s, 2.89s, 2.90s and 2.93s) displayed antibacterial activity against the isogenic mutants and their piperazinone congeners were inactive. Although the difference in activity between the libraries may reflect the effect of cyclization on

ClpP activation, further investigations are needed to determine (1) if the *seco* and piperazinone libraries activate ClpP and (2) if the antibacterial activity observed is due to ClpP on-target activity.

 ADEP 4 (2.40)	
Bacterial species	MIC (μM)
<i>Neisseria meningitidis</i>	0.081
<i>Neisseria gonorrhoeae</i>	0.162
<i>E. coli</i>	>166
<i>E. coli</i> <i>lptD-4213</i> *	>166
<i>P. aeruginosa</i>	>166

Table 2.30: Antibacterial activity of ADEP 4 (2.40) against Gram-negative bacteria. * *E. coli* *lptD-4213* is a mutant strain with a compromised outer membrane.

When evaluated against Gram-negative bacteria (**Table 2.30**) ADEP 4 (**2.40**) displayed nanomolar antibacterial activity against *N. meningitidis* and *N. gonorrhoeae*, but no activity against *E. coli* and *P. aeruginosa*.²¹³ It is worth noting that compromising the OM (*E. coli* *lptD-4213*) did not confer ADEP 4 (**2.40**) with antibacterial activity. However, Brotz-Oesterhelt H. et al. demonstrated that an efflux pump mutant (ΔacrA) *E. coli* strain was susceptible to ADEP 1 (**2.38**) when co-administered with polymyxin B.¹⁶⁸ Although some compounds of the *seco* and piperazinone libraries were active in efflux-deficient and porinated *E. coli* (**Tables 2.26** and **2.28**), the micromolar activities observed could be due to on-target activity or off-target effects and/or general toxicity. The lack of literature precedent of antibacterial activity for the ADEP chemotype against *A. baumannii* and *P. aeruginosa* makes it difficult to know if these species should be

expected to be responsive to ClpP activation. Thus the activity observed for some of the *seco* and piperazinone analogs may or may not be due to ClpP-mediated mechanisms. Further studies are needed to verify target engagement of these chemotypes and elucidate the mechanisms of growth inhibition.

Even though the current MIC results does allow us to determine the contribution of the efflux and OM barriers on the antibacterial activity of the compounds, future LC/MS accumulation studies will lead to the identification of physicochemical properties or motifs governing efflux susceptibility and OM permeability in the *seco* and piperazinone libraries.

11 Conclusion and Future Directions

In conclusion, I developed a robust three-step synthetic route to produce the piperazinone core from commercially available building blocks in an overall 57% yield. From the piperazinone synthons, I generated a library of 48 chemically diverse piperazinone analogs, for which I explored and optimized different methodologies such as N-alkylation of secondary amides with inactivated alkyl halides using phase-transfer catalysis, photoinduced copper catalysis and synthetic handles. My synthetic efforts laid the groundwork for the synthesis of new generations of piperazinone analogs. In addition, the chemical and structural space covered by the piperazinone library offers the opportunity to study the potential of the scaffold beyond ClpP activation, as the piperazinone core can be found in bromodomain inhibitors²¹⁴, dipeptidyl peptidase-4 inhibitors²¹⁵ or protein geranylgeranyltransferase-I inhibitors¹⁷⁶ for example.

Although the evaluation of my library for antibacterial activity against the wild-type and isogenic mutants (i.e., porinated, efflux-deficient and porinated/efflux-deficient) of *E. coli*, *A.*

baumannii and *P. aeruginosa* did not result in significant insights into the contributions of the efflux and outer membrane barriers on their activity, future LC-MS/MS accumulation studies will complement MIC data. This highlights the strength of the activity-independent approach of the SPEAR-GN project and opens the door for the study of any scaffold without the requirement of antibacterial activity.

Interestingly, *seco* compounds exhibited antibacterial activity in isogenic mutants not observed in their piperazinone counterparts, likely suggesting that cyclization impacts whole-cell activity. Therefore, studying the piperazinone library in parallel to the *seco* library offers the opportunity to investigate the effect of conformational constraint and the related physicochemical properties changes on efflux susceptibilities and OM permeabilities. Furthermore, comparison of the two libraries would provide insights into the effect of cyclization on metabolic stability and ClpP activation, enabling the design of more potent ClpP activators.

As mentioned previously, the Duerfeldt lab (Ziwei Hu) generated a library of oxazolidinone analogs (**2.23**, **Figure 2.4a**) and the Zgurskaya lab determined MICs in the wild-type and isogenic mutants (i.e., porinated (Pore), efflux-deficient (Δ) and porinated/efflux-deficient (Δ -Pore)) of the same three bacterial strains. By comparing the ratios Pore/ Δ -Pore and Δ / Δ -Pore representing the contribution of efflux and outer membrane barrier, respectively, on compound accumulation, this study led to the identification of species-specific motifs liable to efflux susceptibility (**Figure 2.4b**) and outer membrane permeation (**Figure 2.4c**). These results demonstrate that a portion of a chemotype can be modified and lead to changes in efflux and permeation in Gram-negative bacteria. Although the impact of these moieties on efflux and permeation have only been identified for the oxazolidinone scaffold, this study opens the door for the discovery of motifs (positively and negatively) modulating efflux and permeation across

c.

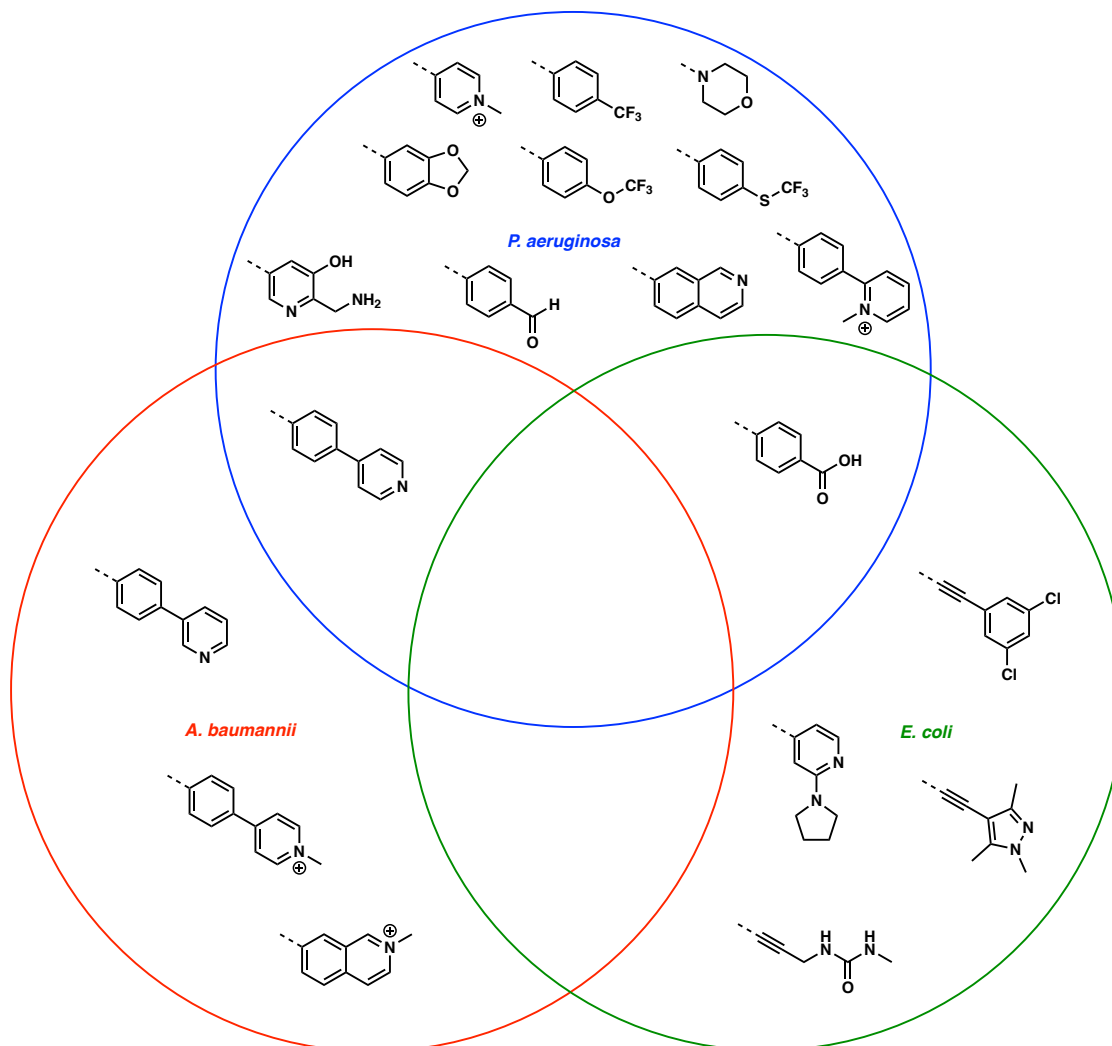


Figure 2.4: The Venn diagram represents the motifs of oxazolidinone analogs 2.23 (a) identified as liabilities to efflux susceptibility (b) and outer membrane permeation (c) in *E. coli*, *A. baumannii* and *P. aeruginosa*.

Even if no study to correlate physicochemical properties, and efflux and permeation was reported for the oxazolidinone library, such correlations are not obvious considering that each intersection of the Venn diagrams in **Figure 2.4b** and **2.4c** contains motifs with varying degrees of hydrophobicity and polarity, motifs with hydrogen bond donors and acceptors, and formal charges. Although a model between physicochemical descriptors and efflux and permeation might be generated, often a physicochemical descriptor-guided design of compounds can be challenging

as no straightforward correlation has been established so far between functional groups and descriptors. In **Figure 2.5** and **2.6**, I organized descriptors identified in the oxazolidinone study and more generally in literature, respectively as positively or negatively correlating with efflux avoidance and/or OM penetration in *P. aeruginosa* and *E. coli*. Although useful, these descriptors are global and determining the structural features necessary to alter them to promote efflux avoidance and outer membrane penetration remains difficult.

Furthermore, physicochemical descriptor-guided approaches to design Gram-negative active compounds are often built on models using 2D physicochemical descriptors of compounds compiled in formats losing significant structural information such as SMILES. The advantage of these approaches is that large libraries can be analyzed in a non-computationally expensive fashion, but I postulate that the decrease in accuracy and complexity of the resulting models prevent any consequential findings.

An ideal model cannot consider the OM and efflux pumps as a black box but need to acknowledge the multiple pathways a compound uses to penetrate the OM and the range of efflux pumps in each Gram-negative bacteria. For example, a compound crossing the OM via passive diffusion will require different physicochemical and structural properties than to a compound using porin-mediated diffusion. Fortunately, the combination of Merck's data scientists and the Rybenkov lab can help develop models encompassing the intricacies of efflux and OM permeation by using 3D descriptors and data science tools (e.g., machine learning), and kinetic model of compound accumulation, respectively.

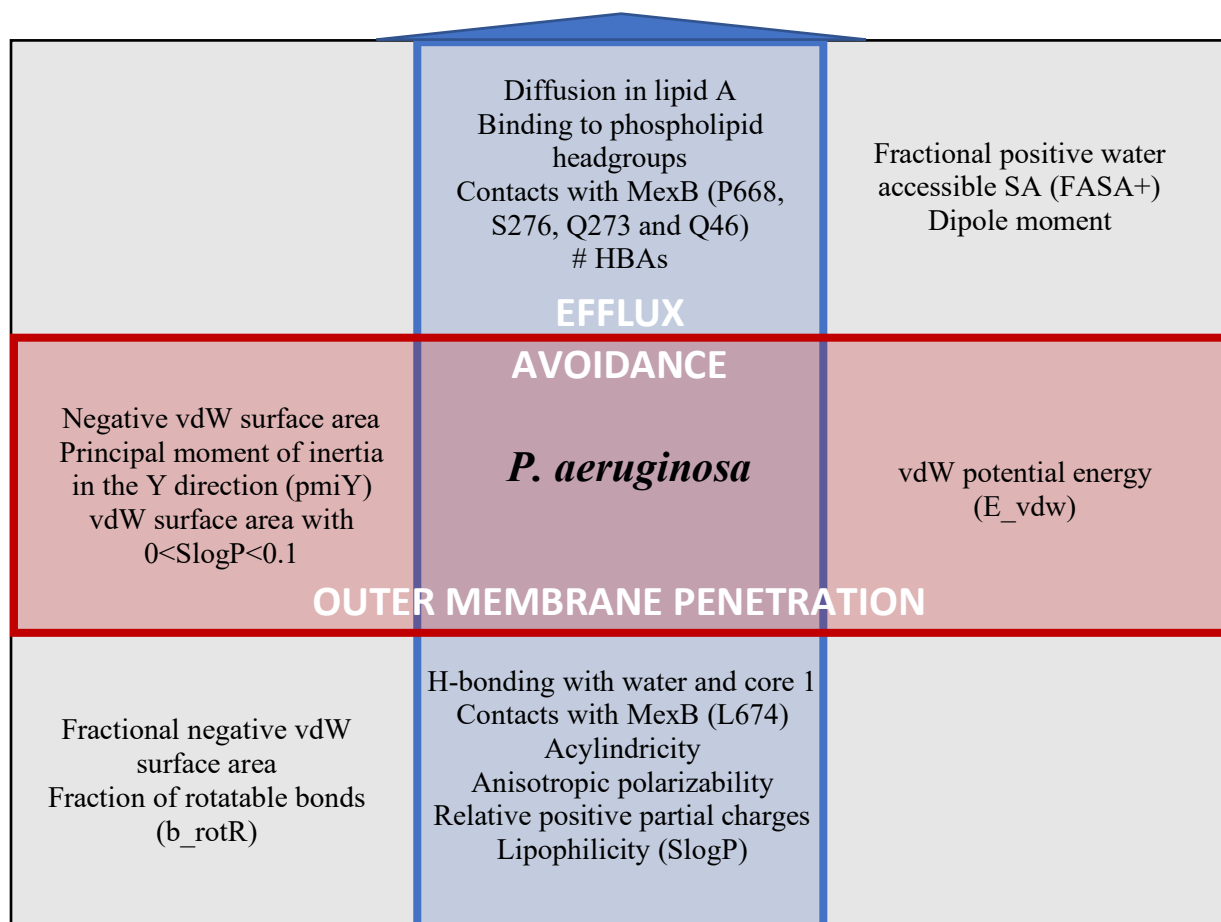


Figure 2.5: Diagram summarizing correlation between descriptors and efflux avoidance and outer membrane penetration in *P. aeruginosa*.^{216, 217} Efflux avoidance describes compounds not susceptible to be effluxed. Outer membrane penetration describes compounds able to permeate the outer membrane. Descriptors on the side of the arrow positively correlates with efflux avoidance and/or outer membrane penetration. Descriptors on the opposite side of the arrow negatively correlates with efflux avoidance and/or outer membrane penetration. Descriptors inside the blue or red rectangle only correlates with efflux avoidance or outer membrane penetration, respectively. Descriptors inside the grey rectangle correlates with both efflux avoidance and outer membrane penetration.

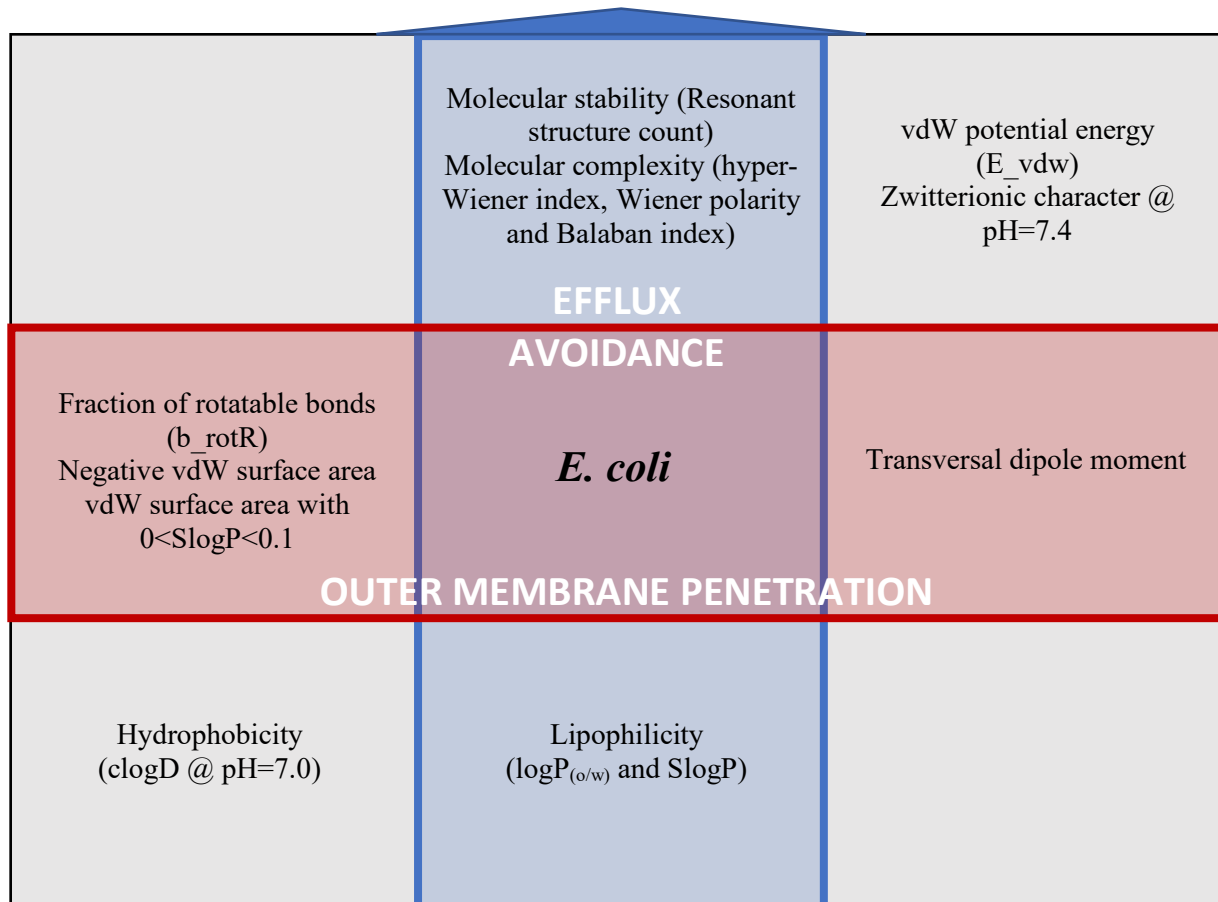
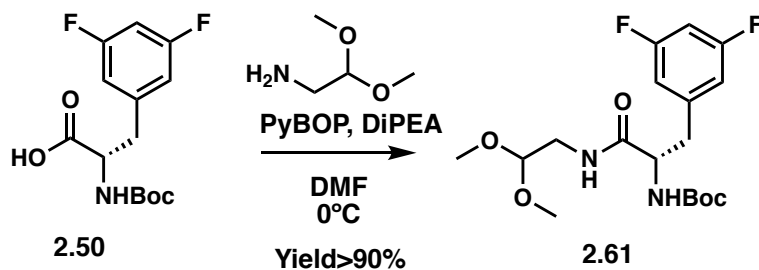


Figure 2.6: Diagram summarizing correlation between descriptors and efflux avoidance and outer membrane penetration in *E. coli*.^{75, 217-220} Efflux avoidance describes compounds not susceptible to be effluxed. Outer membrane penetration describes compounds able to permeate the outer membrane. Descriptors on the side of the arrow positively correlates with efflux avoidance and/or outer membrane penetration. Descriptors on the opposite side of the arrow negatively correlates with efflux avoidance and/or outer membrane penetration. Descriptors inside the blue or red rectangle only correlates with efflux avoidance or outer membrane penetration, respectively. Descriptors inside the grey rectangle correlates with both efflux avoidance and outer membrane penetration.

12 Experimental Section

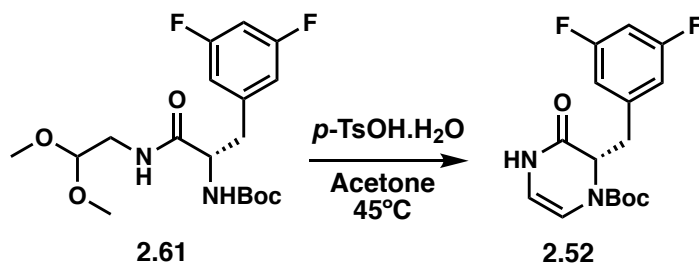
12.1 Preparation of the Piperazinone Core

tert-butyl (S)-(3-(3,5-difluorophenyl)-1-((2,2-dimethoxyethyl)amino)-1-oxopropan-2-yl)carbamate (2.61):



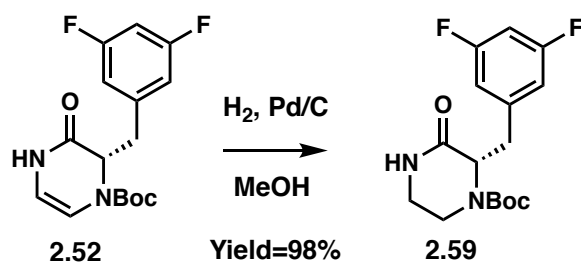
In a vial, Boc-3,5-difluorophenylalanine **2.50** (100 mg; 0.33 mmol), aminoacetaldehyde dimethyl acetal (80 μ L; 0.66 mmol) and 175 μ L of DiPEA were dissolved in 4 mL of dry DMF. After cooling down the solution to 0°C (ice bath), PyBOP (259 mg; 0.498 mmol) was added and the reaction mixture was stirred and let warm to room temperature (RT) overnight. The reaction was quenched with water (10 mL) and washed with a saturated solution of sodium bicarbonate (NaHCO₃) (20 mL) and the organic layer was extracted with ethyl acetate (EtOAc) (3 times). The organic layers were combined, washed with brine before being dried over sodium sulfate (Na₂SO₄) and filtered. The filtrate was concentrated in vacuo and purified by flash column chromatography (Silica gel, 20-50% EtOAc in hexane (Hex)) to yield **2.61** (114 mg; Yield=90%) as a white solid. ¹H NMR (500 MHz, Acetonitrile-*d*₃) δ 6.90 (dd, *J* = 4.0 Hz, 2H), 6.84 (tt, *J* = 9.5, 2.0 Hz, 1H), 6.75 (s, 1H), 5.64 (d, *J* = 8.6 Hz, 1H), 4.35 (t, *J* = 5.4 Hz, 1H), 4.31 (td, *J* = 8.8, 5.4 Hz, 1H), 3.34 (d, *J* = 3.9 Hz, 6H), 3.33 – 3.23 (m, 2H), 3.13 (dd, *J* = 14.0, 5.4 Hz, 1H), 2.85 (dd, *J* = 13.9, 9.1 Hz, 1H), 1.37 (s, 9H); ¹³C NMR (126 MHz, Acetonitrile-*d*₃) δ 171.0, 163.7, 161.8, 155.3, 142.4, 112.5, 102.3, 101.5, 79.1, 55.2, 53.4, 40.7, 37.6, 27.5.

***tert*-butyl (*S*)-2-(3,5-difluorobenzyl)-3-oxo-3,4-dihydropyrazine-1(2*H*)-carboxylate (**2.52**):**



The amide intermediate **2.61** (114 mg; 0.29 mmol), $p\text{-TsOH}\cdot\text{H}_2\text{O}$ (50 mg; 0.29 mmol) and 4Å molecular sieves were dissolved in 15 mL of acetone and stirred for 4h at 45°C . The crude was filtered through a celite plug and purified by flash column chromatography (Silica gel, 20-50% EtOAc in Hex) to yield **2.52** (57 mg; Yield=61%) as a white solid. ^1H NMR (400 MHz, Chloroform- d) δ 8.01 (d, $J = 24.5$ Hz, 1H), 6.74 – 6.63 (m, 3H), 6.25 (dd, $J = 84.7, 5.8$ Hz, 1H), 5.57 (dt, $J = 91.3, 5.3$ Hz, 1H), 4.91 (dt, $J = 63.8, 6.8$ Hz, 1H), 3.04 – 2.83 (m, 2H), 1.45 – 1.23 (m, 9H). ^{13}C NMR (101 MHz, Chloroform- d) δ 166.4, 164.1, 161.6, 151.6, 140.1, 112.6, 108.7, 107.2, 102.4, 82.0, 60.3, 35.6, 27.9.

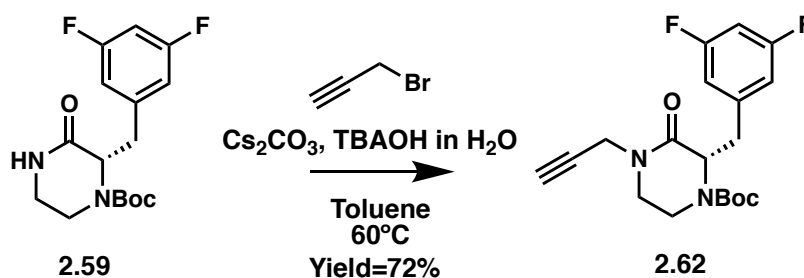
***tert*-butyl (*S*)-2-(3,5-difluorobenzyl)-3-oxopiperazine-1-carboxylate (**2.59**):**



In a sealable vial, **2.52** (57 mg; 0.18 mmol) and 50 mg of palladium on carbon (Pd/C) was dissolved in 10 mL of methanol. A balloon of hydrogen was connected to the sealed vial and the reaction mixture was stirred overnight. The crude was concentrated under nitrogen flow and filtered through a celite plug. The filtrate was concentrated in vacuo and purified by flash column

chromatography (Silica gel, 40-60% EtOAc in Hex) to yield **2.59** (57 mg; Yield=98%) as a clear oil. ^1H NMR (400 MHz, Chloroform-*d*) δ 7.01 (s, 1H), 6.77 – 6.62 (m, 3H), 4.72 (d, J = 8.0 Hz, 1H), 4.23 – 4.04 (m, 1H), 3.45 – 3.33 (m, 1H), 3.22 (dd, J = 13.7, 4.6 Hz, 1H), 3.15 – 3.05 (m, 2H), 2.88 – 2.75 (m, 1H), 1.32 (s, 9H). ^{13}C NMR (101 MHz, Chloroform-*d*) δ 169.8, 164.2, 161.7, 153.5, 141.4, 112.7, 102.2, 80.9, 58.1, 41.3, 37.1, 28.0.

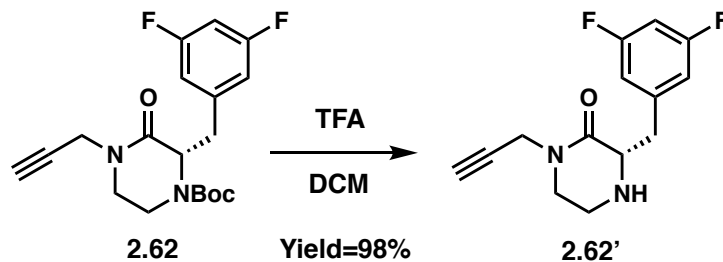
tert-butyl (S)-2-(3,5-difluorobenzyl)-3-oxo-4-(prop-2-yn-1-yl) piperazine-1-carboxylate (**2.62**):



In a 20 mL vial, the piperazinone **2.59** (57 mg; 0.18 mmol), Cs_2CO_3 (115 mg; 0.35 mmol), TBAOH (1M) in H_2O (102 μL ; 0.35 mmol) were dissolved in 10 mL of toluene at 60°C . Then the propargyl bromide solution 80 wt.% in toluene (57 μL ; 0.52 mmol) was added to the reaction mixture and stirred overnight at 60°C . The reaction washed with a saturated solution of NaHCO_3 (20 mL) and the organic layer was extracted with EtOAc (3 times). The organic layers were combined, washed with brine before being dried over Na_2SO_4 and filtered. The filtrate was concentrated in vacuo and purified by flash column chromatography (Silica gel, 20-50% EtOAc in Hex) to yield **2.62** (46 mg; Yield=72%) as a clear oil. ^1H NMR (400 MHz, Chloroform-*d*) δ 6.77 – 6.62 (m, 3H), 4.75 (s, 1H), 4.40 (dd, J = 17.3, 2.6 Hz, 1H), 4.11 (dd, J = 17.3, 2.5 Hz, 1H), 3.52 – 3.42 (m, 1H), 3.28 – 3.19 (m, 2H), 3.18 – 3.08 (m, 2H), 2.96 – 2.85 (m, 1H), 2.24 (t, J = 2.5 Hz, 1H), 1.33 (s, 9H). ^{13}C NMR

(101 MHz, Chloroform-*d*) δ 167.0, 164.2, 164.1, 161.7, 161.6, 153.4, 141.5, 141.4, 112.7, 112.6, 112.5, 102.5, 102.2, 102.0, 80.9, 77.5, 72.6, 45.7, 35.9, 28.0.

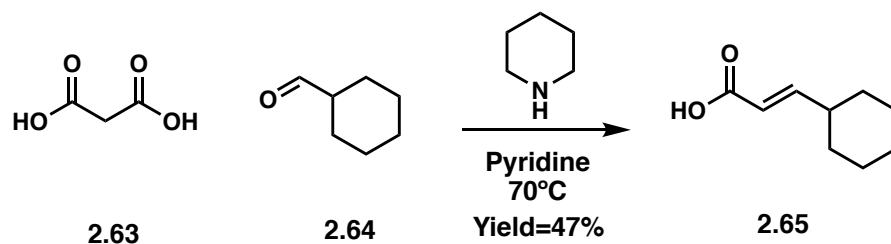
(*S*)-3-(3,5-difluorobenzyl)-1-(prop-2-yn-1-yl)piperazin-2-one (2.62'):



In a 3-dram vial, the propargyl piperazinone **2.62** (46 mg; 0.13 mmol) was dissolved in 5 mL of DCM and 1 mL of TFA was added. The reaction mixture was stirred for 3h. After concentration under N₂ flow, the reaction washed with a saturated solution of NaHCO₃ (20 mL) and the organic layer was extracted with EtOAc (3 times). The organic layers were combined, washed with brine before being dried over Na₂SO₄ and filtered. The filtrate was concentrated in vacuo and purified by flash column chromatography (Silica gel, 0-4% MeOH in DCM) to yield **2.62'** (45 mg; Yield=98%) as a yellow oil. ¹H NMR (400 MHz, Chloroform-*d*) δ 6.83 – 6.73 (d, 2H), 6.66 (tt, *J* = 9.1, 2.4 Hz, 1H), 4.24 (d, *J* = 2.5 Hz, 2H), 3.61 (dd, *J* = 9.4, 3.6 Hz, 1H), 3.47 (td, *J* = 11.1, 10.6, 4.6 Hz, 1H), 3.36 (m, 2H), 3.15 (ddd, *J* = 12.7, 4.6, 3.0 Hz, 1H), 2.98 (ddd, *J* = 12.7, 10.2, 4.2 Hz, 1H), 2.87 (dd, *J* = 13.9, 9.4 Hz, 1H), 2.22 (t, *J* = 2.6 Hz, 1H). ¹³C NMR (101 MHz, Chloroform-*d*) δ 168.5, 164.3, 161.7, 142.4, 112.3, 112.1, 102.2, 78.1, 72.2, 60.2, 47.4, 41.9, 38.0, 35.8.

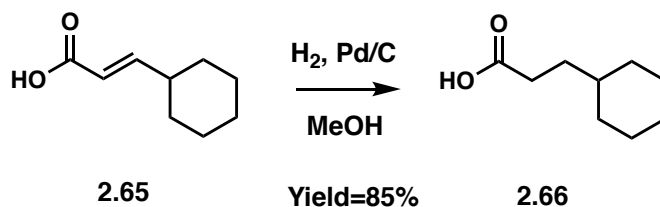
12.2 Preparation of the Cyclohexylpropanoyl Piperazinone

(E)-3-cyclohexylacrylic acid (2.65):



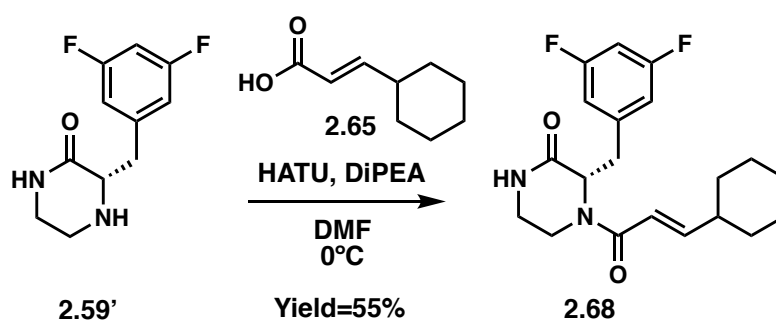
In a vial, malonic acid **2.63** (500 mg; 4.8 mmol), cyclohexanecarboxaldehyde **2.64** (647 mg; 5.8 mmol) and piperidine (60 μ L; 0.6 mmol) are dissolved in pyridine (5 mL). The reaction is stirred @ 75°C overnight. The reaction was quenched with 10 mL of concentrated HCl (12 M) in an ice bath. The reaction washed with a saturated solution of copper acetate (20 mL) and the organic layer was extracted with EtOAc (3 times). The organic layers were combined, washed with brine before being dried over Na₂SO₄ and filtered. The filtrate was concentrated in vacuo and purified by flash column chromatography (Silica gel, 0-1 % MeOH in DCM) to yield **2.65** (348 mg; Yield=47%) as a clear oil. ¹H NMR (400 MHz, Chloroform-*d*) δ 7.03 (dd, *J* = 15.8, 6.8 Hz, 1H), 5.78 (dd, *J* = 15.8, 1.4 Hz, 1H), 2.23 – 2.11 (m, 1H), 1.77 (td, *J* = 9.0, 8.2, 3.4 Hz, 4H), 1.69 (d, *J* = 13.4 Hz, 1H), 1.38 – 1.23 (m, 2H), 1.23 – 1.11 (m, 3H). ¹³C NMR (101 MHz, Chloroform-*d*) δ 170.9, 156.9, 118.0, 77.3, 76.9, 76.6, 40.5, 31.6, 25.6.

3-cyclohexylpropanoic acid (2.66):



In a sealable vial, **2.65** (100 mg; 0.65 mmol) and 50 mg of palladium on carbon (Pd/C) was dissolved in 10 mL of methanol. A balloon of hydrogen was connected to the sealed vial and the reaction mixture was stirred overnight. The crude was concentrated under nitrogen flow and filtered through a celite plug. The filtrate was concentrated in vacuo and purified by flash column chromatography (Silica gel, 0-1 % MeOH in DCM) to yield **2.66** (86 mg; Yield=85%) as a clear oil. ¹H NMR (300 MHz, Chloroform-*d*) δ 10.69 (s, 1H), 2.34 – 2.17 (m, 2H), 1.94 – 1.77 (m, 3H), 1.77 – 1.54 (m, 4H), 1.54 – 1.31 (m, 3H), 1.31 – 1.10 (m, 3H).

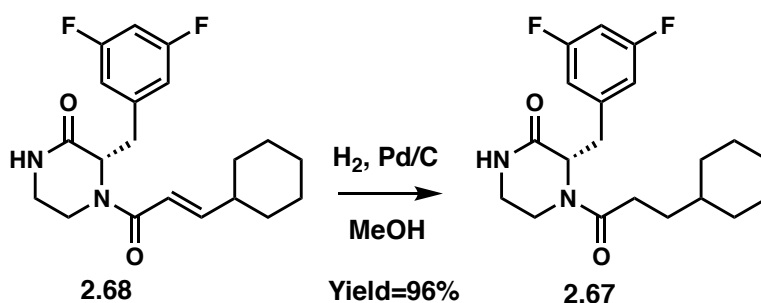
(*S,E*)-4-(3-cyclohexylacryloyl)-3-(3,5-difluorobenzyl)piperazin-2-one (2.68):



In a vial, the piperazinone **2.59'** (86 mg; 0.38 mmol), (*E*)-3-cyclohexylacrylic acid **2.65** (117 mg; 0.76 mmol) and 270 μL of DiPEA were dissolved in 4 mL of dry DMF. After cooling down the solution to 0°C (ice bath), HATU (289 mg; 0.76 mmol) was added and the reaction mixture was stirred and let warm to RT overnight. The reaction was quenched with water (10 mL) and washed with a saturated solution of NaHCO₃ (20 mL) and the organic layer was extracted with EtOAc (3 times). The organic layers were combined, washed with brine before being dried over Na₂SO₄ and filtered. The filtrate was concentrated in vacuo and purified by flash column chromatography (Silica gel, 1-8% MeOH in DCM) to yield **2.68** (76 mg; Yield=55%) as a yellow oil. ¹H NMR (400 MHz, Chloroform-*d*) δ 7.44 – 7.39 (m, 1H), 7.21 – 7.13 (m, 0H), 6.87 (dd, *J* = 15.5, 6.8 Hz,

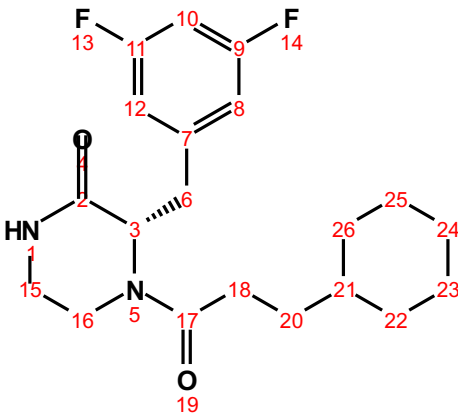
0H), 6.79 – 6.62 (m, 3H), 6.09 (d, $J = 15.1$ Hz, 0H), 5.45 (d, $J = 15.1$ Hz, 0H), 5.21 (dt, $J = 26.4$, 5.2 Hz, 1H), 4.75 (dd, $J = 13.7$, 4.0 Hz, 1H), 4.59 (dd, $J = 9.7$, 3.6 Hz, 0H), 4.48 (dd, $J = 9.5$, 3.6 Hz, 0H), 3.73 (dd, $J = 61.9$, 13.5 Hz, 1H), 3.47 – 3.32 (m, 1H), 3.33 – 3.18 (m, 2H), 3.18 – 3.06 (m, 1H), 2.94 – 2.71 (m, 1H), 2.38 – 2.24 (m, 0H), 2.13 (s, 0H), 2.01 – 1.86 (m, 1H), 1.81 – 1.52 (m, 5H), 1.52 – 1.42 (m, 1H), 1.35 – 1.22 (m, 1H), 1.22 – 1.06 (m, 2H), 0.97 – 0.79 (m, 2H), 0.79 – 0.68 (m, 0H).

(S)-4-(3-cyclohexylpropanoyl)-3-(3,5-difluorobenzyl)piperazin-2-one (2.67):



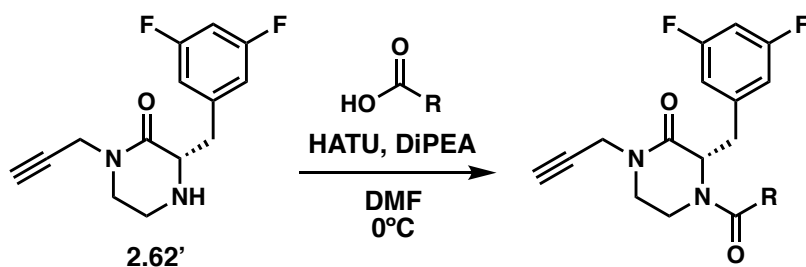
In a sealable vial, **2.68** (76 mg; 0.21 mmol) and 50 mg of palladium on carbon (Pd/C) was dissolved in 10 mL of methanol. A balloon of hydrogen was connected to the sealed vial and the reaction mixture was stirred overnight. The crude was concentrated under nitrogen flow and filtered through a celite plug. The filtrate was concentrated in vacuo and purified by flash column chromatography (Silica gel, 0-10 % MeOH in DCM) to yield **2.67** (74 mg; Yield=96%) as a yellow oil. ^1H NMR (500 MHz, $\text{DMSO}-d_6$) δ 8.13 – 8.03 (m, 1H), 7.14 – 6.96 (m, 2H), 6.84 (dt, $J = 9.7$, 4.8 Hz, 1H), 4.90 (t, $J = 6.7$ Hz, 1H), 3.78 (dd, $J = 13.9$, 3.6 Hz, 1H), 3.26 – 3.17 (m, 1H), 3.17 – 3.11 (m, 1H), 3.11 – 2.94 (m, 3H), 2.32 (ddd, $J = 15.5$, 9.1, 6.4 Hz, 1H), 2.17 (ddd, $J = 15.3$, 9.1, 6.1 Hz, 1H), 1.68 – 1.50 (m, 5H), 1.47 – 1.36 (m, 1H), 1.33 – 1.14 (m, 2H), 1.14 – 0.97 (m, 2H), 0.92 (td, $J = 9.9$, 5.5 Hz, 1H), 0.86 – 0.72 (m, 1H), 0.67 (ddq, $J = 18.8$, 11.6, 7.2, 5.5 Hz, 1H). ^{13}C

NMR (101 MHz, DMSO-*d*₆) δ 171.6, 168.6, 168.0, 163.8, 163.6, 161.2, 142.9, 142.8, 113.4, 113.1, 112.8, 102.5, 102.2, 102.0, 59.5, 55.4, 41.2, 39.5, 37.1, 37.0, 36.2, 34.9, 33.0, 32.6, 32.3, 30.4, 29.4, 26.6, 26.2, 26.1.

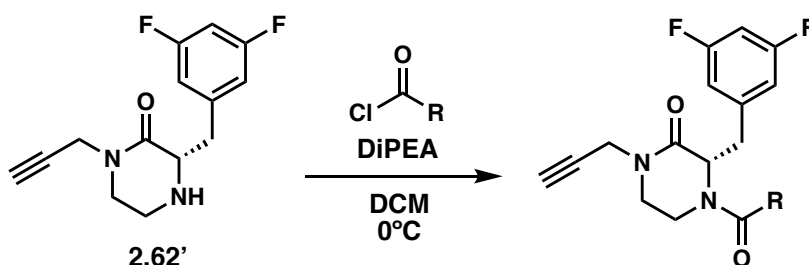


Position	δ C, type	δ H	<i>J</i> (Hz)	COSY
2	168.0 – 168.6			
3	55.4 – 55.9, CH	4.45 – 4.94 (m)		6
6	34.8 – 39.9, CH ₂	2.96 – 4.42 (m)		3, 15
7	142.8 – 142.9			
8	112.8 – 113.4, CH	6.80 – 7.07 (m)		10
9	161.2 – 163.8			
10	102.2, CH	6.99 – 7.13 (m)		8, 12
11	161.2 – 163.8			
12	112.8 – 113.4, CH	6.80 – 7.07 (m)		10
15	40.5 – 41.2, CH ₂	3.02 – 3.25 (m)		3, 15
16	36.2 – 37.0, CH ₂	3.04 – 3.19 (m)		16
17	171.6			
18	30.4, CH ₂	2.12 – 2.37 (m)		20
20	29.3 – 32.6, CH ₂	0.88 – 2.05 (m)		18
21	37.0 – 37.1, CH	0.88 – 1.12 (m)		
22	33.0, CH ₂	0.61 – 1.67 (m)		21, 23
23	26.1 – 26.2, CH ₂	1.02 – 1.69 (m)		22
24	26.6, CH ₂	1.02 – 1.69 (m)		23, 25
25	26.1 – 26.2, CH ₂	1.02 – 1.69 (m)		26
26	33.0, CH ₂	0.61 – 1.67 (m)		21, 25

12.3 Preparation of Propargyl Piperazinone Amides



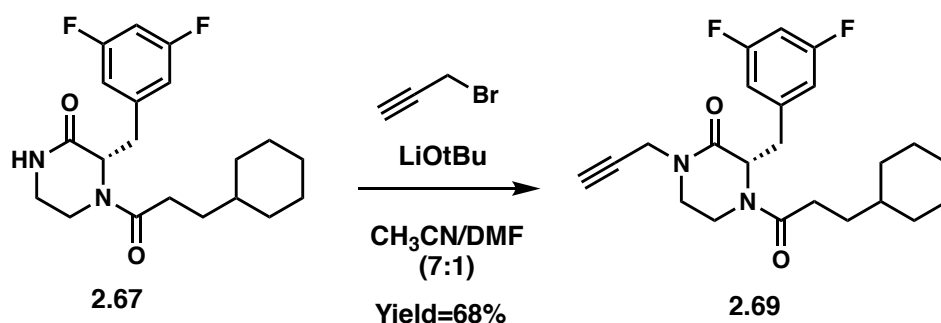
Amide coupling procedure (A1): In a vial, 1.1 equivalent of propargyl piperazinone **2.62'**, one equivalent of the acid and three equivalents of DiPEA were dissolved in 4 mL of dry DMF. After cooling down the solution to 0°C (ice bath), 1.5 equivalent of HATU was added and the reaction mixture was stirred and let warm to RT overnight. The reaction was quenched with water (10 mL) and washed with a saturated solution of NaHCO₃ (20 mL) and the organic layer was extracted with EtOAc (3 times). The organic layers were combined, washed with brine before being dried over Na₂SO₄ and filtered. The filtrate was concentrated in vacuo and purified by flash column chromatography.



Acylation procedure (A2): In a vial, 1.1 equivalent of propargyl piperazinone **2.62'** and three equivalents of DiPEA were dissolved in 4 mL of dry DCM. After cooling down the solution to 0°C (ice bath), one equivalent of acyl chloride was added and the reaction mixture was stirred and

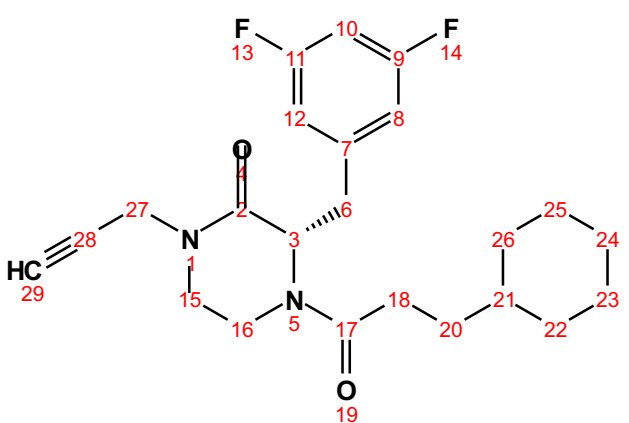
let warm to RT overnight. The reaction was quenched with water (10 mL) and washed with a saturated solution of NaHCO₃ (20 mL) and the organic layer was extracted with EtOAc (3 times). The organic layers were combined, washed with brine before being dried over Na₂SO₄ and filtered. The filtrate was concentrated in vacuo and purified by flash column chromatography.

(S)-4-(3-cyclohexylpropanoyl)-3-(3,5-difluorobenzyl)-1-(prop-2-yn-1-yl) piperazin-2-one (2.69):



In a vial, the piperazinone **2.67** (24 mg; 0.07 mmol) and LiOtBu (39 mg; 0.26 mmol) were dissolved in a 4 mL mixture of CH₃CN and DMF (7:1) and stirred for 10 mins. Then the propargyl bromide solution 80 wt.% in toluene (12 μL; 0.13 mmol) was added to the reaction mixture and stirred overnight at RT. The reaction was quenched with 10 mL of H₂O and washed with a saturated solution of NaHCO₃ (20 mL) and the organic layer was extracted with EtOAc (3 times). The organic layers were combined, washed with brine before being dried over Na₂SO₄ and filtered. The filtrate was concentrated in vacuo and purified by flash column chromatography (Silica gel, 0-5% MeOH in DCM) to yield **2.69** (18 mg; Yield=68%) as a clear oil. ¹H NMR (500 MHz, DMSO-*d*₆) δ 7.14 – 7.03 (m, 1H), 7.02 (d, *J* = 8.3 Hz, 1H), 6.87 (d, *J* = 7.6 Hz, 1H), 5.01 (dd, *J* = 8.2, 5.6 Hz, 1H), 4.63 (dd, *J* = 8.8, 5.6 Hz, 0H), 4.49 (d, *J* = 13.8 Hz, 0H), 4.29 – 4.12 (m, 2H), 4.04 – 3.90 (m, 1H), 3.46 (td, *J* = 11.6, 4.1 Hz, 1H), 3.40 – 3.33 (m, 1H), 3.33 – 3.28 (m, 1H), 3.29

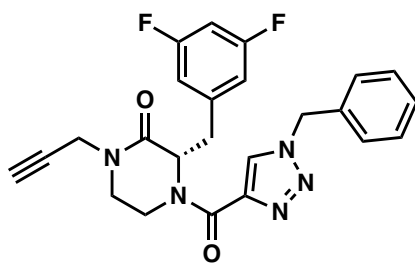
– 3.22 (m, 1H), 3.22 – 3.04 (m, 2H), 2.37 – 2.27 (m, 1H), 2.25 – 2.15 (m, 1H), 2.07 – 1.97 (m, 0H), 1.66 – 1.56 (m, 4H), 1.45 – 1.36 (m, 1H), 1.32 – 1.01 (m, 5H), 0.95 – 0.88 (m, 1H), 0.88 – 0.72 (m, 1H), 0.72 – 0.63 (m, 1H). ¹³C NMR (101 MHz, DMSO-*d*₆) δ 171.6, 171.5, 166.8, 166.3, 163.7, 163.6, 161.6, 161.3, 161.2, 142.5, 142.4, 142.3, 113.5, 113.3, 113.1, 113.0, 112.9, 102.7, 102.6, 102.3, 102.1, 79.2, 75.2, 75.1, 59.5, 55.3, 55.1, 46.4, 45.6, 39.5, 39.2, 37.1, 36.9, 36.8, 36.2, 35.6, 35.4, 34.6, 33.0, 32.9, 32.6, 32.2, 30.1, 29.2, 29.0, 26.6, 26.5, 26.2, 26.1, 25.6, 25.3.



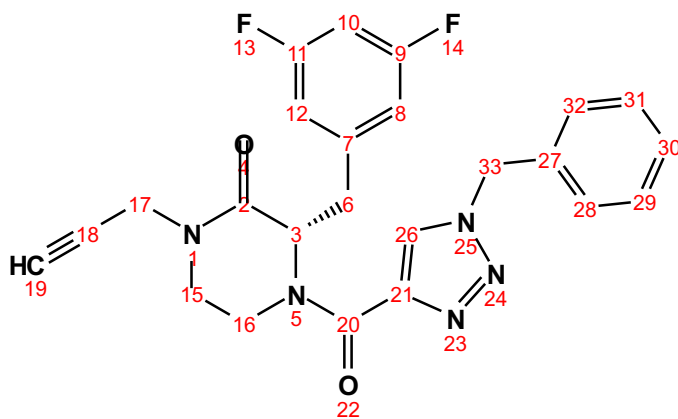
Position	δ C, type	δ H	<i>J</i> (Hz)
2	166.3 – 166.8		
3	55.3 – 59.5, CH	4.60 – 5.05 (m)	
6	34.6 – 39.5, CH ₂	3.13 – 4.52 (m)	
7	142.3 – 142.5		
8	112.9 – 113.5, CH	6.83 – 7.06 (m)	
9	161.2 – 163.7		
10	102.1 – 102.7, CH	6.99 – 7.13 (m)	
11	161.2 – 163.7		
12	112.9 – 113.5, CH	6.83 – 7.06 (m)	
15	45.6 – 46.4, CH ₂	3.22 – 3.51 (m)	
16	36.2 – 36.8, CH ₂	3.05 – 3.22 (m)	
17	171.5 – 171.6		
18	30.1, CH ₂	2.15 – 2.37 (m)	
20	29.0 – 32.2, CH ₂	0.88 – 2.06 (m)	
21	36.9 – 37.1, CH	0.89 – 1.10 (m)	
22	32.9 – 33.0, CH ₂	0.63 – 1.66 (m)	

23	25.3 – 26.2, CH ₂	1.02 – 1.68 (m)	
24	26.5 – 26.6, CH ₂	1.02 – 1.68 (m)	
25	25.3 – 26.2, CH ₂	1.02 – 1.68 (m)	
26	32.9 – 33.0, CH ₂	0.63 – 1.66 (m)	
27	35.4 – 35.6, CH ₂	4.12 – 4.29 (m)	
28	79.2		
29	75.1 – 75.2	3.24 (m)	

(S)-4-(1-benzyl-1*H*-1,2,3-triazole-4-carbonyl)-3-(3,5-difluorobenzyl)-1-(prop-2-yn-1-yl)piperazin-2-one (2.70):



Procedure A1 (10 mg; yield=53%). ¹H NMR (500 MHz, DMSO-*d*₆) δ 8.67 – 8.54 (m, 1H), 8.33 (s, 0H), 7.42 – 7.26 (m, 5H), 7.02 (t, *J* = 9.7 Hz, 1H), 6.94 (d, *J* = 7.8 Hz, 1H), 6.82 (t, *J* = 9.7 Hz, 0H), 6.73 (d, *J* = 7.8 Hz, 1H), 6.13 (dd, *J* = 9.8, 4.8 Hz, 0H), 5.59 (d, *J* = 35.1 Hz, 2H), 5.12 (t, *J* = 6.9 Hz, 0H), 5.02 (d, *J* = 10.5 Hz, 1H), 4.56 (d, *J* = 13.7 Hz, 0H), 4.29 (dd, *J* = 27.7, 17.4 Hz, 1H), 4.16 (dd, *J* = 17.4, 2.5 Hz, 1H), 3.59 – 3.46 (m, 1H), 3.46 – 3.43 (m, 1H), 3.38 – 3.32 (m, 1H), 3.27 (s, 1H), 3.26 – 3.21 (m, 2H), 3.21 – 3.14 (m, 1H). ¹³C NMR (101 MHz, DMSO-*d*₆) δ 166.3, 163.7, 163.4, 161.3, 161.1, 159.7, 159.4, 143.1, 143.0, 142.3, 141.7, 135.9, 135.8, 129.7, 129.5, 129.3, 129.2, 128.8, 128.7, 128.6, 128.4, 113.3, 113.2, 112.9, 110.0, 102.8, 102.5, 102.3, 102.0, 79.2, 75.3, 75.2, 59.2, 56.3, 53.5, 53.3, 46.6, 45.5, 40.3, 37.4, 36.2, 35.6, 35.5.

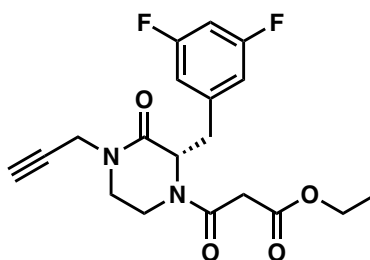


Position	δC , type	δH	J (Hz)
2	166.3		
3	56.3 – 59.2, CH	5.10 – 6.17 (m)	
6	35.5 – 40.3, CH ₂	3.29 – 4.59 (m)	
7	141.7 – 142.3		
8	112.9 – 113.3, CH	6.69 – 6.99 (m)	
9	161.1 – 163.7		
10	102.0 – 102.8, CH	6.79 – 7.04 (m)	
11	161.1 – 163.7		
12	112.9 – 113.3, CH	6.69 – 6.99 (m)	
15	45.5 – 46.6, CH ₂	3.14 – 3.29 (m)	
16	36.2 – 37.4, CH ₂	3.32 – 3.22 (m)	
17'	35.6, CH ₂	4.16 (dd)	17.4, 2.5
17''	35.6, CH ₂	4.29 (dd)	27.7, 17.4
18	79.2		
19	75.2 – 75.3, CH	3.27 (s)	
20	159.4 – 159.7		
21	143.0 – 143.1		
26	129.5 – 129.7, CH	8.31 – 8.63 (m)	
27	135.8 – 135.9		
28	128.4 – 129.3, CH	7.25 – 7.43 (m)	
29	128.4 – 129.3, CH	7.25 – 7.43 (m)	
30	128.4 – 129.3, CH	7.25 – 7.43 (m)	
31	128.4 – 129.3, CH	7.25 – 7.43 (m)	
32	128.4 – 129.3, CH	7.25 – 7.43 (m)	
33	53.3 – 53.5, CH ₂	5.59 (d)	35.1

8	39.9, CH ₂	3.03 – 4.44 (m)	
9	142.2 – 142.4		
10	113.1 – 113.3, CH	6.81 – 6.99 (m)	
11	102.4, CH	6.92 – 7.05 (m)	
12	161.3 – 163.8		
13	113.1 – 113.3, CH	6.81 – 6.99 (m)	
15	161.3 – 163.8		
17	35.7, CH ₂	4.08 – 4.28 (m)	
18	77.8		
19	74.8		
20	171.4		
21	50.9, CH	4.25 – 4.31 (m)	
23	31.2, CH ₂	1.45 – 1.54 (m)	
25	23.0, CH ₂	1.17 – 1.37 (m)	
26	29.7, CH ₂	1.28 – 1.49 (m)	
27	40.4, CH ₂	2.72 – 2.92 (m)	
29	156.0		
32	78.7 – 79.0		
33	28.6 – 28.8	1.37 (s)	
34	28.6 – 28.8	1.37 (s)	
35	28.6 – 28.8	1.37 (s)	
36	156.0		
39	78.7 – 79.0		
40	28.6 – 28.8	1.37 (s)	
41	28.6 – 28.8	1.37 (s)	
42	28.6 – 28.8	1.37 (s)	

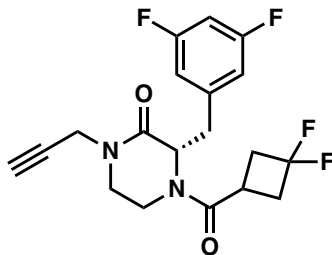
ethyl (*S*)-3-(2-(3,5-difluorobenzyl)-3-oxo-4-(prop-2-yn-1-yl)piperazin-1-yl)-3-oxopropanoate

(2.72):

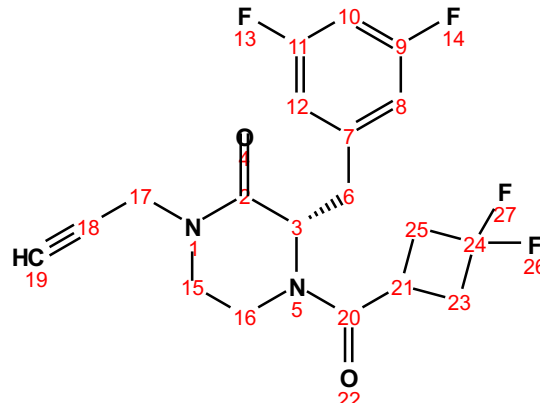


Procedure A2 (12 mg; yield=44%). ^1H NMR (500 MHz, Chloroform-*d*) δ 6.77 (d, J = 7.3 Hz, 2H), 6.69 (tt, J = 9.1, 2.4 Hz, 1H), 5.19 – 5.11 (m, 1H), 4.77 (dd, J = 13.9, 4.2 Hz, 0H), 4.51 – 4.39 (m, 1H), 4.24 (q, J = 7.1 Hz, 1H), 4.19 – 4.07 (m, 2H), 3.66 (dt, J = 13.9, 3.4 Hz, 1H), 3.54 (ddd, J = 24.4, 12.0, 4.1 Hz, 1H), 3.49 (s, 1H), 3.45 – 3.34 (m, 1H), 3.33 – 3.22 (m, 1H), 3.22 – 3.13 (m, 1H), 3.01 – 2.83 (m, 2H), 2.27 (dt, J = 15.9, 2.6 Hz, 1H), 1.31 (t, J = 7.1 Hz, 2H), 1.28 – 1.21 (m, 1H). ^{13}C NMR (126 MHz, Chloroform-*d*) δ 167.0, 166.4, 164.1, 160.8, 142.3, 112.9, 102.5, 77.3, 73.0, 72.7, 61.9, 61.8, 56.7, 45.5, 45.2, 42.2, 41.4, 39.9, 36.3, 36.0, 35.8, 35.7, 14.1.

(S)-3-(3,5-difluorobenzyl)-4-(3,3-difluorocyclobutane-1-carbonyl)-1-(prop-2-yn-1-yl)piperazin-2-one (2.73):

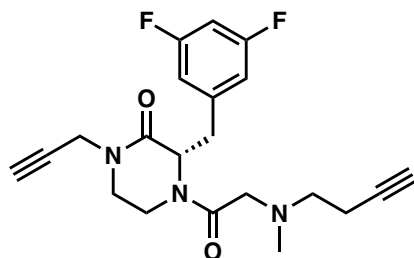


Procedure A2 (17 mg; yield=63%). ^1H NMR (500 MHz, DMSO-*d*₆) δ 7.15 – 6.98 (m, 1H), 6.94 – 6.86 (m, 2H), 5.00 – 4.93 (m, 1H), 4.70 (dd, J = 9.4, 4.4 Hz, 0H), 4.49 – 4.42 (m, 0H), 4.34 – 4.05 (m, 2H), 3.86 – 3.79 (m, 1H), 3.50 – 3.41 (m, 1H), 3.36 – 3.28 (m, 3H), 3.28 – 3.20 (m, 3H), 3.20 – 3.07 (m, 2H), 2.86 – 2.60 (m, 1H), 2.44 – 2.23 (m, 1H), 2.06 – 1.96 (m, 0H). ^{13}C NMR (101 MHz, DMSO-*d*₆) δ 170.5, 166.4, 166.0, 163.8, 163.6, 161.3, 161.2, 142.3, 142.2, 142.1, 122.7, 120.0, 119.9, 117.2, 113.6, 113.4, 113.2, 113.1, 113.0, 112.9, 102.8, 102.7, 102.4, 102.2, 79.2, 75.2, 59.1, 55.7, 46.3, 45.4, 39.1, 38.6, 38.4, 38.1, 37.5, 37.3, 37.0, 36.2, 35.6, 35.5, 24.6, 24.5, 24.4, 24.3.



Position	δC , type	δH	J (Hz)
2	166.0 – 166.4		
3	55.7 – 59.1, CH	4.67 – 5.01 (m)	
6	39.1, CH ₂	3.27 – 3.87 (m)	
7	142.1 – 142.3		
8	112.9 – 113.6, CH	6.87 – 7.05 (m)	
9	161.2 – 163.8		
10	102.2 – 102.8, CH	7.01 – 7.14 (m)	
11	161.2 – 163.8		
12	112.9 – 113.6, CH	6.87 – 7.05 (m)	
15	45.4 – 46.3, CH ₂	3.21 – 3.50 (m)	
16	36.2, CH ₂	3.08 – 3.19 (m)	
17	35.5 - 35.6, CH ₂	4.05 – 4.34 (m)	
18	79.2		
19	75.2, CH	3.25 (m)	
20	170.5		
21	24.3 – 24.6, CH	3.21 – 3.30 (m)	
23	38.1 – 38.6, CH ₂	2.24 – 2.85 (m)	
24	117.2 – 122.7		
25	37.0 – 37.5, CH ₂	2.62 – 3.23 (m)	

(S)-4-(N-(but-3-yn-1-yl)-N-methylglycyl)-3-(3,5-difluorobenzyl)-1-(prop-2-yn-1-yl)piperazin-2-one (2.74):

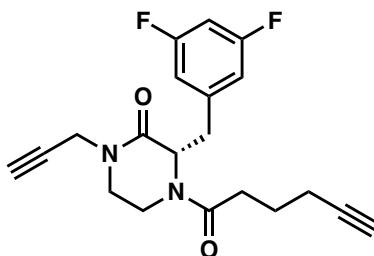


Procedure A1 (14 mg; yield=62%). ^1H NMR (500 MHz, $\text{DMSO-}d_6$) δ 7.12 (tt, $J = 9.4, 2.4$ Hz, 0H), 7.08 – 6.95 (m, 2H), 6.95 – 6.85 (m, 1H), 4.99 (dd, $J = 8.3, 5.5$ Hz, 1H), 4.93 (t, $J = 7.1$ Hz, 0H), 4.43 (d, $J = 13.9$ Hz, 0H), 4.30 – 4.10 (m, 3H), 3.59 – 3.47 (m, 1H), 3.41 – 3.30 (m, 1H), 3.29 – 3.03 (m, 5H), 2.95 – 2.82 (m, 0H), 2.73 (dt, $J = 19.7, 2.7$ Hz, 1H), 2.47 – 2.40 (m, 2H), 2.38 – 2.27 (m, 0H), 2.27 – 2.21 (m, 2H), 2.20 – 2.11 (m, 1H), 2.02 (d, $J = 5.9$ Hz, 3H). ^{13}C NMR (101 MHz, $\text{DMSO-}d_6$) δ 168.7, 166.7, 166.2, 163.8, 163.7, 161.4, 161.2, 142.5, 142.4, 142.3, 113.5, 113.1, 113.0, 112.9, 102.6, 102.4, 102.1, 83.5, 79.2, 75.0, 72.1, 72.0, 59.8, 59.1, 58.8, 55.8, 55.7, 55.6, 46.5, 45.6, 41.6, 37.1, 36.3, 35.6, 35.5, 35.2, 16.7.

Position	δC , type	δH	J (Hz)
2	45.6 – 46.5, CH_2	3.23 – 3.56 (m)	
3	36.3 – 37.1, CH_2	3.09 – 3.19 (m)	
5	55.6, CH	4.96 – 5.03 (m)	
6	166.2 – 166.7		
8	39.3, CH_2	3.34 – 4.21 (m)	

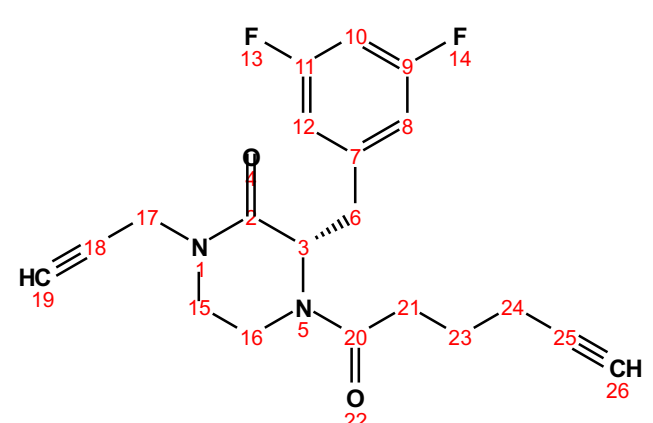
9	142.3 – 142.5		
10	112.9 – 113.5, CH	6.88 – 7.02 (m)	
11	102.1 – 102.6, CH	6.98 – 7.15 (m)	
12	161.2 – 163.8		
13	112.9 – 113.5, CH	6.88 – 7.02 (m)	
15	161.2 – 163.8		
17	35.2 – 35.6, CH ₂	4.10 – 4.30 (m)	
18	79.2		
19	75.0		
20	168.7		
21	59.8, CH ₂	3.09 – 3.26 (m)	
24	41.6, CH ₃	2.02 (d)	5.9
25	55.8, CH ₂	2.40 – 2.47 (m)	
26	16.7, CH ₂	2.12 – 2.29 (m)	
27	83.5		
28	72.0 – 72.1		

(S)-3-(3,5-difluorobenzyl)-4-(hex-5-ynoyl)-1-(prop-2-yn-1-yl)piperazin-2-one (2.75):



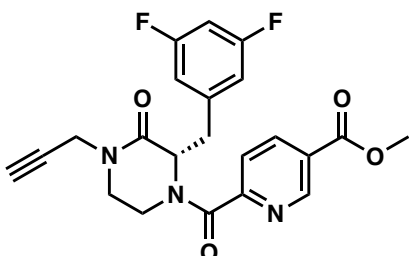
Procedure A1 (5 mg; yield=37%). ¹H NMR (500 MHz, DMSO-*d*₆) δ 7.11 (t, *J* = 9.6 Hz, 0H), 7.03 (td, *J* = 9.5, 4.7 Hz, 1H), 6.99 (d, *J* = 7.6 Hz, 1H), 6.91 – 6.85 (m, 1H), 5.06 – 4.96 (m, 1H), 4.63 – 4.56 (m, 0H), 4.47 (d, *J* = 13.6 Hz, 0H), 4.31 – 4.08 (m, 2H), 3.92 (d, *J* = 14.0 Hz, 1H), 3.53 – 3.42 (m, 1H), 3.41 – 3.30 (m, 1H), 3.30 – 3.23 (m, 2H), 3.21 – 3.00 (m, 2H), 2.71 (dt, *J* = 31.3, 2.5 Hz, 1H), 2.36 (q, *J* = 7.0 Hz, 1H), 2.24 – 2.06 (m, 1H), 2.07 – 1.89 (m, 2H), 1.65 – 1.41 (m, 2H), 1.34 – 1.26 (m, 0H). ¹³C NMR (101 MHz, DMSO-*d*₆) δ 170.8, 170.6, 166.7, 166.1, 163.8, 163.6, 161.3, 161.2, 142.5, 142.4, 113.5, 113.3, 113.1, 113.0, 112.9, 110.0, 102.9, 102.6, 102.4,

102.1, 84.4, 84.2, 79.2, 75.2, 75.1, 71.9, 71.8, 59.4, 55.8, 55.5, 46.3, 45.6, 39.5, 36.9, 36.3, 35.6, 35.5, 34.8, 31.3, 30.5, 24.1, 22.5, 17.6, 17.5.



Position	δC , type	δH	J (Hz)
2	166.1 – 166.7		
3	55.5 – 59.4, CH	4.58 – 5.03	
6	39.5, CH ₂	3.35 – 3.95 (m)	
7	142.4 – 142.5		
8	112.9 – 113.5, CH	6.85 – 7.02	
9	161.2 – 163.8		
10	102.1 – 102.9, CH	7.00 – 7.14	
11	161.2 – 163.8		
12	112.9 – 113.5, CH	6.85 – 7.02	
15	45.6 – 46.3, CH ₂	3.24 – 3.50 (m)	
16	36.3 – 36.9, CH ₂	3.06 – 3.21 (m)	
17	35.5	4.08 – 4.31 (m)	
18	79.2		
19	75.1 – 75.2		
20	170.6 – 170.8		
21	30.5 – 31.3, CH ₂	2.11 – 2.42 (m)	
23	24.1, CH ₂	1.44 – 1.59 (m)	
24	17.5 – 17.6, CH ₂	1.91 – 2.08 (m)	
25	84.2 – 84.4		
26	71.8 – 71.9		

methyl (S)-6-(2-(3,5-difluorobenzyl)-3-oxo-4-(prop-2-yn-1-yl)piperazine-1-carbonyl)nicotinate (2.76):



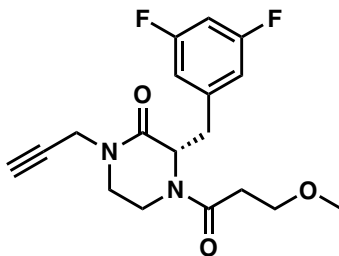
Procedure A1 (22 mg; Yield=74%). ¹H NMR (500 MHz, DMSO-*d*₆) δ 9.01 (dd, *J* = 44.6, 2.1 Hz, 1H), 8.30 (ddd, *J* = 110.5, 8.1, 2.2 Hz, 1H), 7.56 (d, *J* = 8.1 Hz, 1H), 7.09 – 6.99 (m, 1H), 6.96 (tt, *J* = 9.4, 2.3 Hz, 1H), 6.60 (d, *J* = 6.3 Hz, 1H), 5.40 – 5.07 (m, 1H), 4.69 – 4.62 (m, 1H), 4.37 – 4.15 (m, 2H), 3.90 (d, *J* = 2.2 Hz, 3H), 3.83 – 3.76 (m, 0H), 3.59 – 3.36 (m, 3H), 3.29 – 3.19 (m, 2H), 3.18 – 2.99 (m, 1H). ¹³C NMR (101 MHz, DMSO-*d*₆) δ 166.3, 166.0, 165.9, 165.6, 165.1, 164.9, 163.9, 163.8, 163.7, 161.4, 161.2, 156.9, 155.9, 149.5, 148.4, 142.1, 142.0, 141.5, 138.8, 138.3, 126.7, 126.4, 124.2, 123.7, 113.4, 113.3, 113.2, 113.1, 113.0, 103.1, 102.8, 102.6, 102.3, 79.2, 79.1, 75.4, 75.2, 59.8, 56.0, 53.1, 46.4, 45.6, 41.1, 36.9, 36.1, 35.7, 35.6, 35.4.

Position	δ C, type	δ H	<i>J</i> (Hz)
2	36.1 – 36.9, CH ₂	3.00 – 3.30 (m)	

3	45.6 – 46.4, CH ₂	3.20 – 3.57 (m)	
5	56.0 – 59.8, CH	5.10 – 5.39 (m)	
6	166.0 – 166.3		
8	35.4 – 41.1, CH ₂	3.37 – 4.69 (m)	
9	141.5 – 142.1		
10	113.0 – 113.4, CH	6.57 – 7.05 (d)	6.3
11	102.3 – 103.1	6.93 – 7.09 (tt)	9.4, 2.3
12	161.2 – 163.9		
13	113.0 – 113.4	6.57 – 7.05 (d)	6.3
15	161.2 – 163.9		
17	35.6 – 35.7, CH ₂	4.15 – 4.37 (m)	
18	75.2 – 75.4		
19	79.1 – 79.2		
20	164.9 – 165.1		
21	155.9 – 156.9		
24	148.4 – 149.5, CH	8.95 – 9.08 (d)	2.1
25	126.4 – 126.7		
26	138.3 – 138.8, CH	8.16 – 8.44 (dd)	8.1, 2.2
27	123.7 – 124.2, CH	6.99 – 7.60 (d)	8.1
28	165.6 – 165.9		
31	53.1, CH ₃	3.90 (d)	2.2

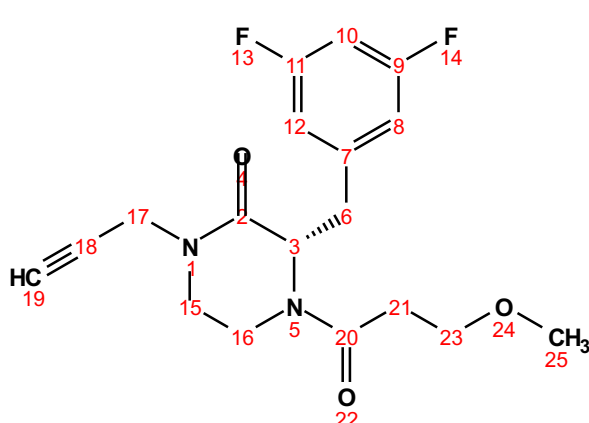
(S)-3-(3,5-difluorobenzyl)-4-(3-methoxypropanoyl)-1-(prop-2-yn-1-yl)piperazin-2-one

(2.77):



Procedure A1 (8 mg; yield=26%). ¹H NMR (500 MHz, DMSO-*d*₆) δ 7.15 – 7.01 (m, 1H), 7.01 – 6.97 (m, 1H), 6.91 – 6.83 (m, 1H), 5.00 – 4.93 (m, 1H), 4.69 (dt, *J* = 7.8, 3.1 Hz, 0H), 4.48 – 4.42 (m, 0H), 4.27 – 4.12 (m, 2H), 4.02 – 3.92 (m, 1H), 3.52 – 3.40 (m, 2H), 3.39 – 3.33 (m, 1H), 3.32

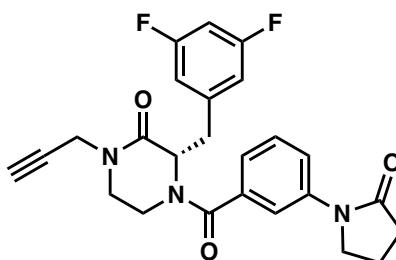
– 3.19 (m, 3H), 3.20 – 3.16 (m, 3H), 3.12 – 3.07 (m, 3H), 3.05 – 2.95 (m, 0H), 2.58 – 2.52 (m, 1H), 2.38 (dt, $J = 15.7, 6.9$ Hz, 0H), 1.72 (dt, $J = 15.5, 6.2$ Hz, 0H). ^{13}C NMR (101 MHz, DMSO- d_6) δ 169.8, 169.6, 166.7, 166.6, 166.2, 164.0, 163.9, 163.8, 163.6, 161.5, 161.4, 161.3, 161.2, 142.5, 142.4, 142.3, 142.2, 113.5, 113.4, 113.3, 113.1, 113.0, 112.9, 103.0, 102.8, 102.7, 102.5, 102.4, 102.1, 79.2, 75.1, 68.6, 59.4, 58.4, 58.3, 55.8, 55.6, 46.3, 45.6, 39.9, 36.9, 36.2, 35.6, 35.5, 35.0, 33.0, 32.1, 31.1.



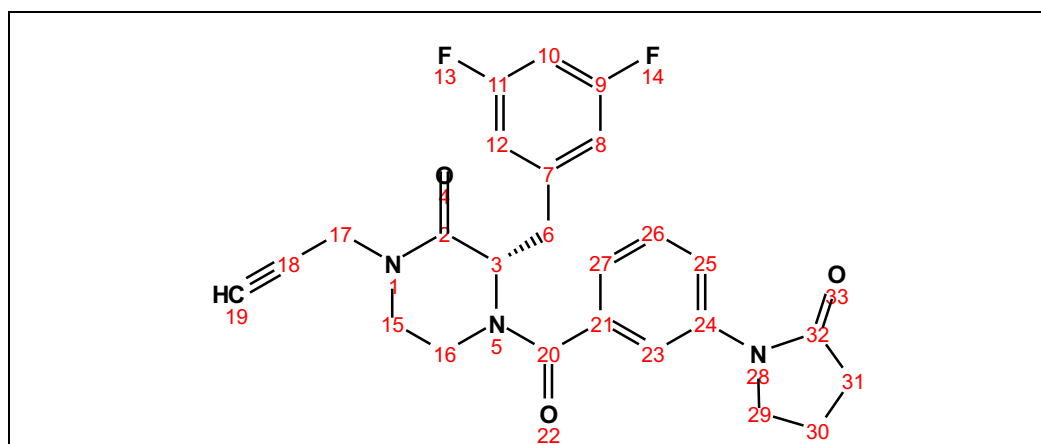
Position	δC , type	δH	J (Hz)
2	166.2 – 166.7		
3	55.6 – 59.4, CH	4.66 – 5.00	
6	35.0 - 39.9, CH ₂	2.97 – 4.48 (m)	
7	142.4 – 142.5		
8	112.9 – 113.5, CH	6.83 – 7.03	
9	161.2 – 164.0		
10	102.1 – 103.0, CH	7.01 – 7.14	
11	161.2 – 164.0		
12	112.9 – 113.5, CH	6.83 – 7.03	
15	45.6 – 46.3, CH ₂	3.20 – 3.50 (m)	
16	36.2 – 36.9, CH ₂	3.07 – 3.23 (m)	
17	35.5 – 35.6, CH ₂	4.12 – 4.27 (m)	
18	79.2		
19	75.1		
20	169.6 – 169.8		
21	32.1 – 33.0, CH ₂	1.70 – 2.59 (m)	

23	68.6, CH ₂	3.21 – 3.47 (m)	
25	58.3 – 58.4, CH ₂	3.07 – 3.22 (m)	

(S)-3-(3,5-difluorobenzyl)-4-(3-(2-oxopyrrolidin-1-yl)benzoyl)-1-(prop-2-yn-1-yl)piperazin-2-one (2.78):

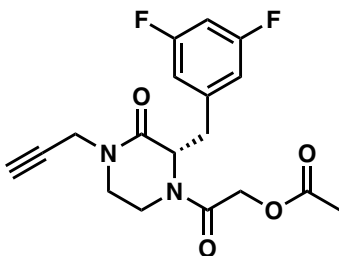


Procedure A1 (8 mg; yield=67%). ¹H NMR (500 MHz, DMSO-*d*₆) δ 7.80 – 7.73 (m, 1H), 7.48 (s, 1H), 7.47 – 7.38 (m, 1H), 7.30 (s, 0H), 7.17 (s, 0H), 7.12 – 7.00 (m, 2H), 6.95 – 6.90 (m, 1H), 6.66 (s, 1H), 5.20 – 5.12 (m, 1H), 4.64 – 4.50 (m, 0H), 4.32 (d, *J* = 17.4 Hz, 1H), 4.11 (dd, *J* = 17.3, 2.6 Hz, 1H), 3.88 – 3.76 (m, 2H), 3.66 – 3.56 (m, 1H), 3.45 – 3.35 (m, 2H), 3.36 – 3.14 (m, 4H), 2.52 (s, 2H), 2.06 (p, *J* = 7.6 Hz, 2H). ¹³C NMR (101 MHz, DMSO-*d*₆) δ 174.5, 169.1, 166.2, 163.9, 163.7, 161.4, 161.3, 142.2, 140.1, 135.9, 129.4, 121.9, 120.7, 117.4, 113.3, 113.1, 102.6, 79.2, 75.2, 60.2, 55.4, 48.3, 46.4, 41.5, 36.3, 35.6, 32.7, 17.8.



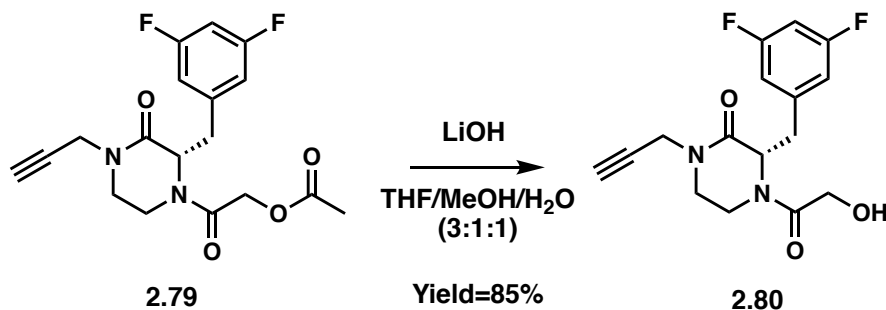
Position	δC , type	δH	J (Hz)
2	166.2		
3	55.4, CH	5.15 (m)	
6	41.5, CH ₂	3.37 – 3.64 (m)	
7	142.2		
8	113.1 – 113.3, CH	7.00 – 7.10	
9	161.3 – 163.9		
10	102.6, CH	7.03 – 7.12	
11	161.3 – 163.9		
12	113.1 – 113.3, CH	7.00 – 7.10	
15	46.4, CH ₂	3.19 – 3.44 (m)	
16	36.3, CH ₂	3.19 – 3.32 (m)	
17'	35.6, CH ₂	4.32 (d)	17.4
17''	35.6, CH ₂	4.11 (dd)	17.3, 2.6
18	79.2		
19	75.2		
20	169.1		
21	135.9		
23	117.4, CH	7.45 – 7.52 (m)	
24	140.1		
25	121.9, CH	6.89 – 6.97 (m)	
26	129.4, CH	7.39 – 7.47 (m)	
27	120.7, CH	7.73 – 7.81 (m)	
29	48.3, CH ₂	3.76 – 3.88 (m)	
30	17.8, CH ₂	2.06 (p)	7.6
31	32.7, CH ₂	2.47 – 2.54 (m)	
32	174.5		

(S)-2-(2-(3,5-difluorobenzyl)-3-oxo-4-(prop-2-yn-1-yl) piperazin-1-yl)-2-oxoethyl acetate
(2.79):



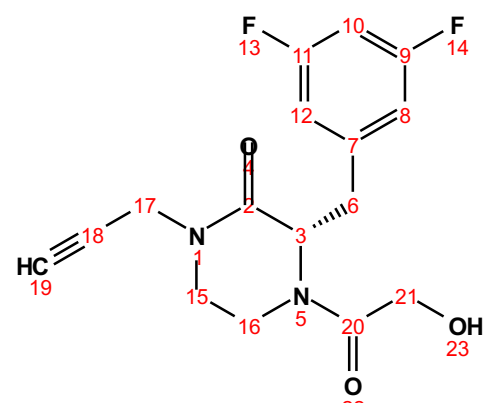
Procedure A2 (8 mg; yield=46%). $^1\text{H NMR}$ (500 MHz, Chloroform-*d*) δ 6.82 – 6.67 (m, 3H), 5.11 (t, J = 4.9 Hz, 1H), 4.75 – 4.65 (m, 2H), 4.52 – 4.36 (m, 2H), 4.10 (dt, J = 17.5, 4.4 Hz, 1H), 3.85 (d, J = 14.3 Hz, 0H), 3.56 – 3.50 (m, 1H), 3.50 – 3.29 (m, 2H), 3.29 – 3.20 (m, 1H), 3.20 – 3.12 (m, 0H), 2.94 – 2.76 (m, 1H), 2.31 – 2.25 (m, 1H), 2.17 (d, J = 41.7 Hz, 3H).

(S)-3-(3,5-difluorobenzyl)-4-(2-hydroxyacetyl)-1-(prop-2-yn-1-yl)piperazin-2-one (2.80):



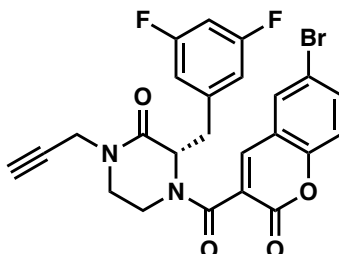
In a vial, **2.79** (4 mg; 0.011 mmol) and 2 mg of lithium hydroxide (LiOH) was dissolved in 5 mL of a mixture of THF, MeOH and H₂O (3:1:1). After stirring for 10h @ RT, the reaction was quenched with 1N HCl solution (2 mL) and washed with H₂O (20 mL) and the organic layer was extracted with EtOAc (3 times). The organic layers were combined, washed with brine before being dried over Na₂SO₄ and filtered. The filtrate was concentrated in vacuo and purified by flash column chromatography (Silica gel, 0-10% MeOH in DCM) to yield **2.80** (3 mg; Yield=85%) as a clear oil. $^1\text{H NMR}$ (500 MHz, DMSO-*d*₆) δ 7.16 – 7.01 (m, 1H), 6.99 (d, J = 7.5 Hz, 1H), 6.92 – 6.87 (m, 1H), 6.82 (d, J = 8.7 Hz, 0H), 4.92 (t, J = 6.6 Hz, 1H), 4.77 (t, J = 5.7 Hz, 1H), 4.64 (t, J

= 5.8 Hz, 0H), 4.56 (d, $J = 8.4$ Hz, 0H), 4.42 (d, $J = 13.6$ Hz, 0H), 4.31 – 4.21 (m, 0H), 4.19 (t, $J = 3.0$ Hz, 1H), 4.17 – 4.06 (m, 1H), 4.06 – 3.97 (m, 1H), 3.89 – 3.76 (m, 1H), 3.54 – 3.45 (m, 1H), 3.31 – 3.20 (m, 2H), 3.21 – 3.10 (m, 2H). ^{13}C NMR (101 MHz, DMSO- d_6) δ 170.7, 166.5, 163.6, 161.4, 142.3, 113.1, 112.9, 102.5, 79.2, 75.1, 60.7, 60.0, 58.5, 56.0, 46.1, 38.7, 36.9, 36.2, 35.5, 35.2.



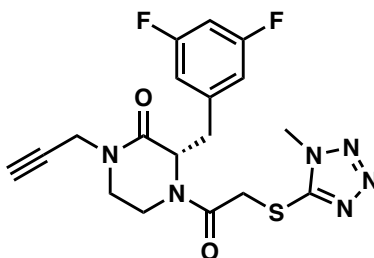
Position	δC , type	δH	J (Hz)
2	166.5		
3	56.0 – 58.5, CH	4.55 – 4.95 (m)	
6	35.2 – 38.7, CH ₂	3.23 – 4.45 (m)	
7	142.3		
8	112.9 – 113.1, CH	6.85 – 7.02	
9	161.4 – 163.6		
10	102.5, CH	7.01 – 7.14	
11	161.4 – 163.6		
12	112.9 – 113.1, CH	6.85 – 7.02	
15	46.1, CH ₂	3.20 – 3.53 (m)	
16	36.2 – 36.9, CH ₂	3.08 – 3.21 (m)	
17	35.5, CH ₂	4.13 – 4.30 (m)	
18	79.2		
19	75.1		
20	170.7		
21	60.0 – 60.7, CH ₂	3.97 – 4.16 (m)	

(S)-4-(6-bromo-2-oxo-2H-chromene-3-carbonyl)-3-(3,5-difluorobenzyl)-1-(prop-2-yn-1-yl)piperazin-2-one (2.81):



Procedure A1 (9 mg; yield=67%). ¹H NMR (500 MHz, Acetonitrile-*d*₃) δ 7.87 (d, 1H), 7.78 (td, *J* = 8.6, 2.4 Hz, 2H), 7.64 (d, *J* = 2.3 Hz, 0H), 7.33 (dd, *J* = 20.6, 8.8 Hz, 1H), 7.04 – 6.95 (m, 1H), 6.91 – 6.84 (m, 1H), 6.84 – 6.77 (m, 1H), 5.17 – 5.11 (m, 1H), 4.71 – 4.64 (m, 0H), 4.38 – 4.34 (m, 0H), 4.33 – 4.25 (m, 2H), 4.17 (dd, *J* = 17.4, 2.6 Hz, 1H), 3.70 (d, *J* = 13.5 Hz, 1H), 3.62 (td, *J* = 11.9, 4.6 Hz, 0H), 3.52 (t, *J* = 11.8 Hz, 1H), 3.47 – 3.41 (m, 0H), 3.20 – 3.09 (m, 3H), 2.57 (dt, *J* = 25.6, 2.5 Hz, 1H). ¹³C NMR (126 MHz, Acetonitrile-*d*₃) δ 165.8, 163.8, 163.2, 161.8, 157.7, 153.1, 141.4, 141.0, 135.3, 131.1, 131.0, 125.6, 120.2, 118.5, 116.6, 113.1, 112.9, 102.2, 102.0, 78.1, 72.5, 72.3, 60.3, 56.2, 45.9, 45.3, 41.7, 36.1, 35.4, 29.9.

(S)-3-(3,5-difluorobenzyl)-4-(2-((1-methyl-1H-tetrazol-5-yl)thio)acetyl)-1-(prop-2-yn-1-yl)piperazin-2-one (2.82):

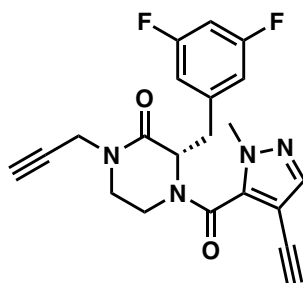


Procedure A1 (17 mg; yield=78%). ^1H NMR (400 MHz, Chloroform-*d*) δ 6.86 – 6.63 (m, 3H), 5.12 (t, J = 5.3 Hz, 1H), 4.76 – 4.64 (m, 1H), 4.56 (dd, J = 17.4, 2.5 Hz, 0H), 4.47 – 4.43 (m, 1H), 4.41 (d, J = 2.6 Hz, 0H), 4.36 – 4.31 (m, 1H), 4.15 – 3.99 (m, 2H), 3.98 – 3.88 (m, 3H), 3.95 – 3.91 (m, 0H), 3.60 – 3.50 (m, 1H), 3.49 – 3.40 (m, 0H), 3.40 – 3.30 (m, 2H), 3.28 – 3.17 (m, 1H), 3.11 – 2.99 (m, 1H), 2.99 – 2.89 (m, 0H), 2.30 – 2.24 (m, 1H). ^{13}C NMR (101 MHz, Chloroform-*d*) δ 166.1, 165.6, 165.2, 164.9, 164.2, 164.1, 161.7, 161.6, 153.4, 140.6, 112.7, 112.5, 103.2, 102.9, 102.7, 102.4, 77.1, 73.0, 72.9, 60.7, 60.4, 57.0, 45.4, 45.0, 41.8, 41.5, 37.8, 36.6, 36.4, 36.3, 36.0, 35.8, 35.1, 33.6, 33.5.

Position	δC , type	δH	J (Hz)
2	164.9 – 165.2		
3	57.0 – 60.7, CH	4.70 – 5.17 (m)	
6	36.0 – 41.8, CH ₂	2.92 – 4.73 (m)	
7	140.8		
8	112.5 – 122.7, CH	6.70 – 6.84	
9	161.6 – 164.2		
10	102.4 – 103.2, CH	6.65 – 6.72	
11	161.6 – 164.2		
12	112.5 – 122.7, CH	6.70 – 6.84	
15	45.0 – 45.4, CH ₂	3.22 – 3.60 (m)	
16	36.3 – 37.8, CH ₂	3.21 – 3.44 (m)	
17	35.8, CH ₂	4.15 – 3.99 (m)	
18	72.9 – 73.0		

19	77.1	2.21 – 2.28 (m)	
20	165.6 – 166.1		
21	36.6 – 41.5, CH ₂	4.31 – 4.48 (m)	
24	153.4		
29	33.5 – 33.6, CH ₃	3.89 – 4.00	

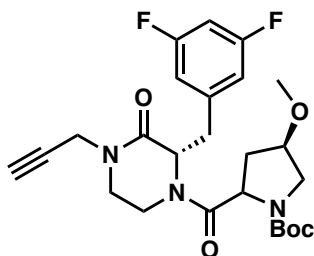
(S)-3-(3,5-difluorobenzyl)-4-(4-ethynyl-1-methyl-1H-pyrazole-5-carbonyl)-1-(prop-2-yn-1-yl)piperazin-2-one (2.83):



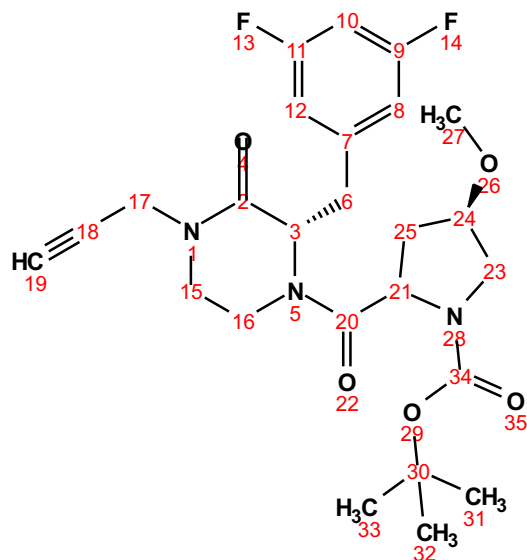
Procedure A1 (16 mg; yield=54%). ¹H NMR (500 MHz, DMSO-*d*₆) δ 7.68 (d, *J* = 15.0 Hz, 1H), 7.12 (t, *J* = 9.6 Hz, 0H), 7.03 (td, *J* = 14.6, 14.1, 8.5 Hz, 2H), 6.94 – 6.86 (m, 1H), 6.78 (d, *J* = 7.5 Hz, 0H), 5.20 (dd, *J* = 8.4, 5.1 Hz, 0H), 5.00 – 4.92 (m, 0H), 4.68 – 4.56 (m, 1H), 4.45 (d, *J* = 13.8 Hz, 0H), 4.36 – 4.09 (m, 2H), 3.90 – 3.83 (m, 0H), 3.74 – 3.67 (m, 0H), 3.66 – 3.58 (m, 1H), 3.58 – 3.39 (m, 1H), 3.38 – 3.30 (m, 2H), 3.30 – 3.29 (m, 1H), 3.28 – 3.26 (m, 1H), 3.26 – 3.20 (m, 2H), 3.20 – 3.14 (m, 1H), 3.14 – 2.98 (m, 2H). ¹³C NMR (101 MHz, DMSO-*d*₆) δ 168.9, 166.7, 166.2, 165.8, 163.9, 163.8, 163.6, 161.4, 161.2, 159.7, 142.5, 141.8, 141.3, 140.7, 113.5, 113.4, 113.3, 113.2, 113.1, 112.9, 112.8, 103.0, 102.4, 101.7, 101.5, 85.5, 84.8, 79.2, 79.0, 75.5, 75.3, 75.2, 75.1, 74.4, 61.4, 60.2, 56.2, 55.8, 55.5, 46.5, 46.2, 45.6, 41.4, 38.1, 37.5, 36.9, 36.5, 36.3, 35.6, 35.5, 34.7.

Position	δC , type	δH	J (Hz)
2	165.8 – 166.2		
3	55.5 – 61.4, CH	4.57 – 5.23 (m)	
6	34.7– 41.4, CH ₂	3.00 – 4.48 (m)	
7	142.5		
8	112.8 – 113.5, CH	6.75 – 7.08 (m)	
9	161.2 – 163.9		
10	102.4 – 103.0, CH	7.00 – 7.15 (m)	
11	161.2 – 163.9		
12	112.8 – 113.5, CH	6.75 – 7.08 (m)	
15	45.6 – 46.5, CH ₂	3.22 – 3.57 (m)	
16	36.2 – 36.9, CH ₂	3.06 – 3.32 (m)	
17	35.5 – 35.6, CH ₂	4.09 – 4.36 (m)	
18	74.4 – 75.5		
19	79.0		
20	166.7 – 168.9		
21	141.8		
23	101.5 – 101.7		
24	140.7 – 141.3		
27	79.2		
28	37.5 – 38.1, CH ₃	3.09 – 3.65 (m)	
29	84.8 – 85.5		

tert-butyl (4*R*)-2-((*S*)-2-(3,5-difluorobenzyl)-3-oxo-4-(prop-2-yn-1-yl)piperazine-1-carbonyl)-4-methoxypyrrolidine-1-carboxylate (2.84):

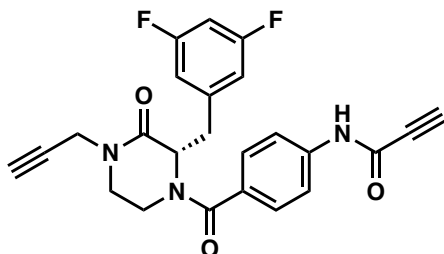


Procedure A1 (8mg; yield=50%). ¹H NMR (500 MHz, DMSO-*d*₆) δ 7.20 – 6.97 (m, 2H), 6.93 (d, *J* = 7.7 Hz, 1H), 6.88 (d, *J* = 7.7 Hz, 1H), 4.93 (dt, *J* = 25.2, 6.3 Hz, 1H), 4.81 (dt, *J* = 29.1, 6.1 Hz, 0H), 4.72 – 4.57 (m, 1H), 4.49 – 4.36 (m, 1H), 4.32 – 4.08 (m, 2H), 4.04 (dq, *J* = 16.6, 6.0, 5.4 Hz, 1H), 3.95 (s, 1H), 3.87 (d, *J* = 13.1 Hz, 1H), 3.54 – 3.44 (m, 1H), 3.42 (d, *J* = 10.6 Hz, 1H), 3.37 (dd, *J* = 10.9, 4.7 Hz, 1H), 3.34 – 3.28 (m, 1H), 3.28 – 3.23 (m, 2H), 3.21 (d, *J* = 5.7 Hz, 1H), 3.19 – 3.14 (m, 1H), 3.10 (d, *J* = 6.0 Hz, 2H), 3.03 (dt, *J* = 15.7, 6.1 Hz, 0H), 2.37 – 2.16 (m, 1H), 1.91 (dq, *J* = 14.8, 5.9, 5.4 Hz, 0H), 1.39 (d, *J* = 6.5 Hz, 2H), 1.32 (d, *J* = 5.7 Hz, 2H), 1.30 – 1.02 (m, 4H). ¹³C NMR (101 MHz, DMSO-*d*₆) δ 172.9, 172.2, 171.5, 171.0, 168.9, 166.7, 166.5, 166.2, 165.9, 163.8, 163.8, 163.6, 161.4, 161.3, 161.2, 154.0, 142.5, 142.4, 113.6, 113.4, 113.3, 113.1, 113.0, 112.9, 112.8, 112.6, 102.8, 102.7, 102.4, 102.2, 79.6, 79.5, 79.3, 79.2, 79.1, 79.0, 78.7, 78.2, 77.7, 75.5, 75.2, 75.1, 75.0, 60.3, 60.2, 56.8, 56.6, 56.3, 56.2, 55.9, 55.8, 55.5, 55.4, 53.9, 53.1, 52.2, 52.0, 51.6, 46.2, 46.1, 45.6, 40.5, 37.4, 36.9, 36.3, 36.2, 36.1, 35.6, 35.5, 34.7, 29.4, 29.1, 28.5, 28.3.



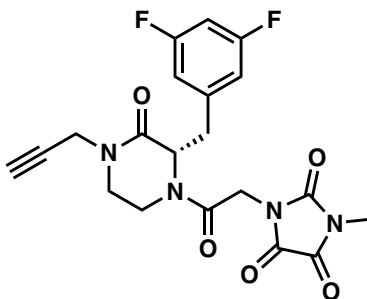
Position	δC , type	δH	J (Hz)
2	165.9 – 166.7		
3	55.5 – 56.8, CH	4.81 – 5.00 (m)	
6	34.7 – 40.5, CH ₂	3.00 – 4.49 (m)	
7	142.4 – 142.5		
8	112.6 – 113.6, CH	6.85 – 7.12 (m)	
9	161.2 – 163.8		
10	102.2 – 103.8, CH	6.99 – 7.17 (m)	
11	161.2 – 163.8		
12	112.6 – 113.6, CH	6.85 – 7.12 (m)	
15	45.6 – 46.2, CH ₂	3.12 – 3.54 (m)	
16	36.3 – 37.4, CH ₂	3.05 – 3.25 (m)	
17	35.5 – 35.6, CH ₂	4.09 – 4.32 (m)	
18	75.0 – 75.5		
19	79.2 – 79.3		
20	168.9 – 172.9		
21	55.4 – 60.3, CH	4.57 – 4.70 (m)	
23	52.0	3.22 – 3.51 (m)	
24	77.7 – 79.1, CH	3.94 – 3.97 (m)	
25	34.7 – 36.1, CH ₂	1.06 – 2.32 (m)	
27	55.8 – 56.3, CH ₃	3.07 – 3.26 (m)	
30	79.5 – 79.6		
31, 32, 33	28.3 – 29.4, CH ₃	1.21 – 1.44 (m)	
34	154.0		

(S)-N-(4-(2-(3,5-difluorobenzyl)-3-oxo-4-(prop-2-yn-1-yl) piperazine-1-carbonyl)phenyl) propiolamide (2.85):



Procedure A1 (7 mg; yield=23%). ¹H NMR (500 MHz, DMSO-*d*₆) δ 10.97 (s, 1H), 7.59 (s, 2H), 7.17 (s, 2H), 7.01 (dd, *J* = 20.6, 9.6 Hz, 3H), 5.10 (s, 1H), 4.45 (s, 1H), 4.33 – 4.21 (m, 2H), 4.11 – 4.04 (m, 1H), 3.69 – 3.57 (m, 1H), 3.44 – 3.29 (m, 3H), 3.27 – 3.08 (m, 2H). ¹³C NMR (126 MHz, DMSO-*d*₆) δ 174.9, 166.4, 163.6, 161.7, 150.3, 142.8, 140.0, 130.9, 128.2, 119.8, 113.4, 113.2, 102.5, 79.3, 78.7, 78.2, 77.1, 75.4, 55.8, 46.5, 41.6, 35.6, 31.8.

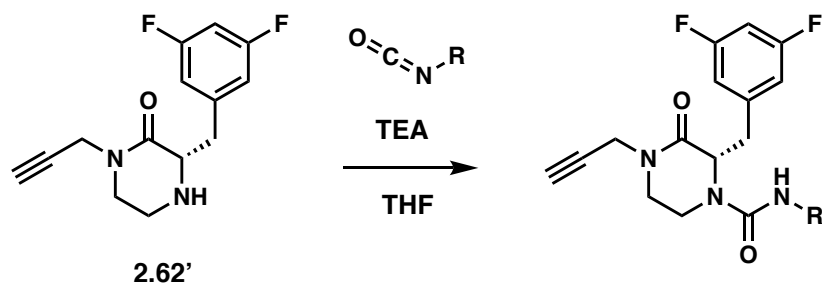
(S)-1-(2-(2-(3,5-difluorobenzyl)-3-oxo-4-(prop-2-yn-1-yl) piperazin-1-yl)-2-oxoethyl)-3-methylimidazolidine-2,4,5-trione (2.86):



Procedure A1 (15 mg; yield=79%). ¹H NMR (500 MHz, Chloroform-*d*) δ 6.79 – 6.65 (m, 3H), 5.14 (t, *J* = 5.2 Hz, 1H), 4.73 – 4.61 (m, 1H), 4.46 (ddd, *J* = 32.3, 17.3, 2.6 Hz, 1H), 4.17 – 4.05 (m, 1H), 4.06 – 3.93 (m, 1H), 3.77 – 3.65 (m, 1H), 3.53 – 3.42 (m, 1H), 3.38 – 3.25 (m, 1H), 3.26

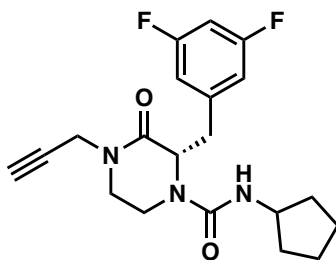
– 3.15 (m, 2H), 2.98 – 2.88 (m, 1H), 2.78 (dd, $J = 19.0, 4.7$ Hz, 3H), 2.30 – 2.25 (m, 1H). ^{13}C NMR (126 MHz, Chloroform- d) δ 169.1, 168.2, 166.3, 165.3, 164.0, 163.9, 162.0, 161.9, 158.5, 140.8, 140.7, 140.6, 113.9, 112.8, 112.6, 112.6, 112.5, 112.4, 103.2, 102.9, 102.7, 102.5, 77.1, 73.0, 72.9, 59.0, 56.6, 45.4, 45.3, 42.1, 41.3, 40.0, 37.8, 36.5, 36.1, 35.9, 27.3.

12.4 Preparation of Propargyl Piperazinone Ureas



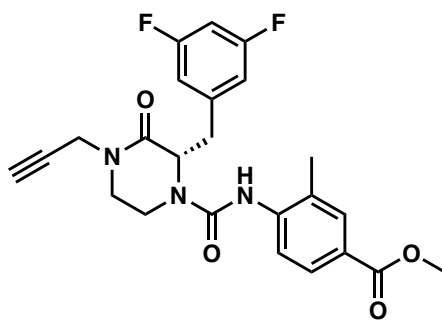
In a vial, one equivalent of propargyl piperazinone **2.62'** and three equivalents of TEA were dissolved in 4 mL of dry THF. The 0.8 equivalent of isocyanate was added and the reaction mixture was stirred overnight. The reaction was quenched with water (10 mL) and washed with a saturated solution of sodium bicarbonate (20 mL) and the organic layer was extracted with EtOAc (3 times). The organic layers were combined, washed with brine before being dried over Na_2SO_4 and filtered. The filtrate was concentrated in vacuo and purified by flash column chromatography.

(S)-N-cyclopentyl-2-(3,5-difluorobenzyl)-3-oxo-4-(prop-2-yn-1-yl) piperazine-1-carboxamide (2.87):



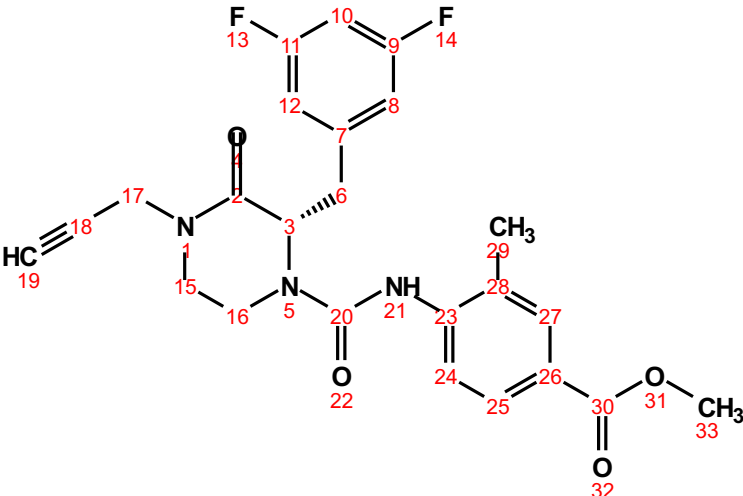
11 mg; Yield = 64%. ^1H NMR (400 MHz, Chloroform-*d*) δ 6.84 – 6.75 (m, 2H), 6.73 (td, J = 8.9, 4.4 Hz, 1H), 4.44 – 4.33 (m, 2H), 4.22 (ddt, J = 13.8, 4.0, 1.8 Hz, 1H), 4.11 (dd, J = 17.3, 2.6 Hz, 1H), 3.86 (h, J = 6.8 Hz, 1H), 3.71 – 3.46 (m, 2H), 3.34 (dd, J = 13.6, 3.7 Hz, 1H), 3.24 (ddd, J = 12.0, 3.7, 2.3 Hz, 1H), 3.09 – 2.97 (m, 2H), 2.25 (t, J = 2.5 Hz, 1H), 1.91 – 1.72 (m, 2H), 1.50 (qd, J = 7.7, 6.5, 2.6 Hz, 4H), 1.12 (dt, J = 14.4, 7.1 Hz, 1H), 0.88 (dq, J = 13.6, 7.2 Hz, 1H). ^{13}C NMR (101 MHz, Chloroform-*d*) δ 166.4, 164.4, 162.0, 156.3, 141.8, 112.6, 102.8, 77.4, 72.8, 60.3, 52.3, 45.5, 37.6, 37.1, 36.0, 33.3, 23.5.

methyl (*S*)-4-(2-(3,5-difluorobenzyl)-3-oxo-4-(prop-2-yn-1-yl) piperazine-1-carboxamido)-3-methylbenzoate (2.88):



9.7 mg; yield=71%. ^1H NMR (500 MHz, DMSO-*d*₆) δ 8.79 (s, 0H), 8.18 (s, 1H), 8.12 (d, J = 8.6 Hz, 0H), 7.80 (d, J = 2.2 Hz, 0H), 7.76 (dd, J = 8.6, 2.2 Hz, 0H), 7.74 (s, 0H), 7.72 (d, J = 2.1 Hz, 1H), 7.67 (dd, J = 8.3, 2.1 Hz, 1H), 7.20 (d, J = 8.4 Hz, 1H), 7.02 (tt, J = 9.4, 2.4 Hz, 1H), 6.96 (d, J = 6.9 Hz, 2H), 4.99 – 4.92 (m, 1H), 4.23 (ddd, J = 28.2, 17.4, 2.5 Hz, 2H), 4.14 (d, J = 3.6 Hz,

0H), 3.81 (d, $J = 3.9$ Hz, 3H), 3.53 (td, $J = 11.1, 4.4$ Hz, 1H), 3.42 – 3.29 (m, 3H), 3.26 (t, $J = 2.5$ Hz, 1H), 3.25 – 3.12 (m, 2H), 2.34 (s, 0H), 2.04 (s, 3H). ^{13}C NMR (101 MHz, DMSO- d_6) δ 166.9, 166.5, 163.9, 163.7, 161.4, 161.3, 154.3, 142.8, 142.5, 132.5, 131.5, 128.1, 127.4, 125.5, 124.9, 113.2, 113.0, 102.7, 102.4, 102.1, 79.3, 75.1, 57.5, 52.3, 52.2, 46.0, 38.0, 36.6, 35.6, 18.5, 18.1.

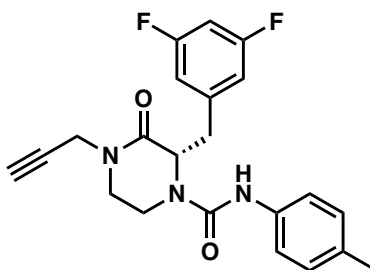


Position	δC , type	δH	J (Hz)
2	166.5		
3	57.5, CH	4.92 – 4.99 (m)	
6	38.0, CH ₂	3.33 – 4.20 (m)	
7	142.8		
8	113.0 – 113.2, CH	6.96 (d)	6.9
9	161.3 – 163.9		
10	102.1 – 102.7, CH	7.02 (tt)	9.4, 2.4
11	161.3 – 163.9		
12	113.0 – 113.2, CH	6.96 (d)	6.9
15	46.0, CH ₂	3.29 – 3.58 (m)	
16	36.6, CH ₂	3.12 – 3.25 (m)	
17	35.6, CH ₂	4.23 (ddd)	28.2, 17.4, 2.5
18	79.3		
19	75.1, CH	3.26 (t)	2.5
20	154.3		
21		8.18 (s)	
23	142.5		

24	124.9, CH	7.20 (d)	8.4
25	127.4 – 128.1, CH	7.64 – 7.78 (m)	
26	125.5		
27	131.5, CH	7.70 – 7.82 (m)	
28	132.5		
29	18.1 – 18.5, CH ₃	2.01 – 2.36 (m)	
30	166.9		
33	52.2 – 52.3, CH ₃	3.81 (d)	3.9

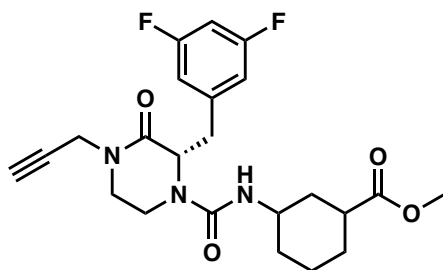
(S)-2-(3,5-difluorobenzyl)-3-oxo-4-(prop-2-yn-1-yl)-N-(p-tolyl)piperazine-1-carboxamide

(2.89):

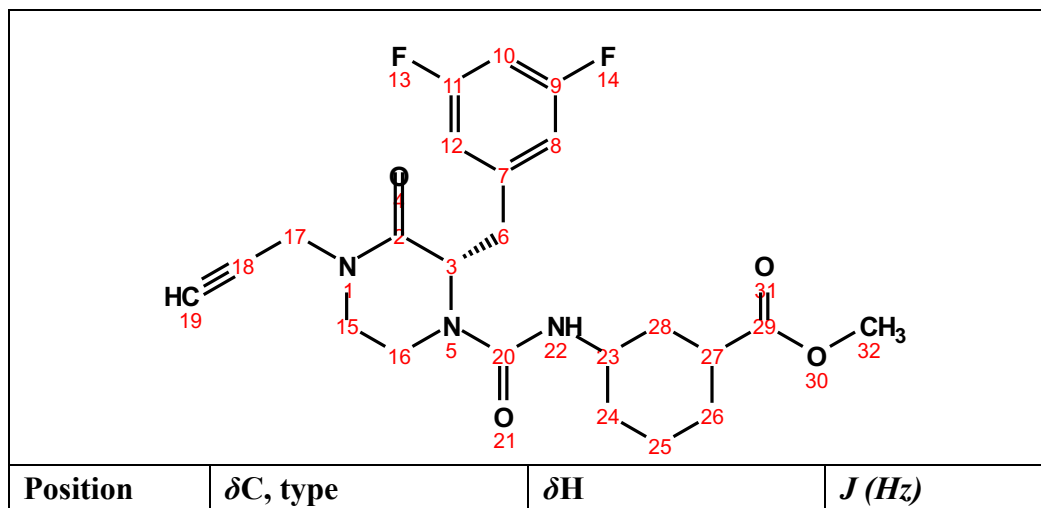


11 mg; yield=53%. ¹H NMR (500 MHz, Chloroform-*d*) δ 7.05 (d, *J* = 8.0 Hz, 2H), 6.97 (t, *J* = 9.0 Hz, 2H), 6.89 – 6.81 (m, 2H), 6.74 (tt, *J* = 9.4, 3.2 Hz, 1H), 5.89 (d, *J* = 40.0 Hz, 1H), 4.67 (td, *J* = 8.8, 3.7 Hz, 1H), 4.43 (dt, *J* = 17.4, 3.3 Hz, 1H), 4.31 – 4.23 (m, 1H), 4.13 (dd, *J* = 17.4, 2.5 Hz, 1H), 3.61 (td, *J* = 11.5, 4.0 Hz, 1H), 3.40 (ddd, *J* = 12.6, 8.4, 3.9 Hz, 1H), 3.29 (dt, *J* = 12.2, 3.0 Hz, 1H), 3.16 (ddd, *J* = 11.5, 8.7, 2.5 Hz, 1H), 3.09 (tt, *J* = 13.9, 3.2 Hz, 1H), 2.28 (s, 3H). ¹³C NMR (126 MHz, Chloroform-*d*) δ 166.27, 162.24, 135.49, 133.20, 129.42, 120.04, 112.64, 103.05, 77.30, 72.92, 60.21, 45.45, 37.55, 36.09, 20.72.

methyl 3-((S)-2-(3,5-difluorobenzyl)-3-oxo-4-(prop-2-yn-1-yl) piperazine-1-carboxamido) cyclohexane-1-carboxylate (2.90):

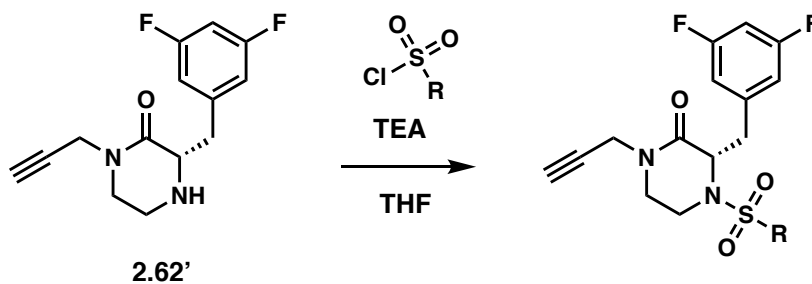


18 mg; yield=44%. ^1H NMR (500 MHz, $\text{DMSO-}d_6$) δ 7.10 – 6.95 (m, 1H), 6.92 – 6.84 (m, 2H), 6.21 – 6.13 (m, 1H), 5.99 – 5.91 (m, 0H), 4.87 (dt, $J = 31.8, 7.0$ Hz, 1H), 4.25 – 4.10 (m, 2H), 4.09 – 3.96 (m, 1H), 3.62 (s, 0H), 3.58 (s, 3H), 3.54 (d, $J = 7.2$ Hz, 0H), 3.41 – 3.27 (m, 2H), 3.26 – 3.19 (m, 2H), 3.19 – 3.10 (m, 1H), 3.11 – 3.03 (m, 2H), 2.73 – 2.65 (m, 0H), 2.58 – 2.54 (m, 0H), 2.38 – 2.26 (m, 1H), 1.81 (dd, $J = 37.7, 13.2$ Hz, 1H), 1.74 – 1.57 (m, 2H), 1.58 – 1.49 (m, 1H), 1.49 – 1.27 (m, 1H), 1.27 – 1.21 (m, 1H), 1.21 – 1.05 (m, 1H), 1.05 – 0.92 (m, 1H). ^{13}C NMR (101 MHz, $\text{DMSO-}d_6$) δ 175.5, 175.3, 175.2, 167.3, 167.2, 163.8, 163.6, 161.3, 161.2, 155.8, 155.6, 142.7, 142.6, 113.2, 113.1, 112.9, 102.5, 102.2, 102.0, 79.3, 75.0, 60.2, 57.1, 57.0, 56.9, 51.8, 51.7, 48.9, 48.8, 47.9, 46.0, 45.8, 42.0, 38.2, 37.2, 36.6, 35.6, 35.5, 33.1, 33.0, 32.4, 32.2, 31.2, 28.3, 27.8, 27.6, 24.2, 20.9, 20.8.



2	167.2 – 167.3		
3	56.9 – 57.1, CH	4.87 (dt)	31.8, 7.0
6	37.2, CH ₂	3.09 – 4.09 (m)	
7	142.6 – 142.7		
8	112.9 – 113.2, CH	6.84 – 6.92 (m)	
9	161.2 – 163.8		
10	102.2 – 102.5, CH	6.95 – 7.10 (m)	
11	161.2 – 163.8		
12	112.9 – 113.2, CH	6.84 – 6.92 (m)	
15	46.0, CH ₂	3.18 – 3.41 (m)	
16	36.6, CH ₂	3.03 – 3.13 (m)	
17	35.5, CH ₂	4.10 – 4.25 (m)	
18	79.3		
19	75.0	3.19 – 3.26 (m)	
20	155.6 – 155.8		
22		5.91 – 6.21 (m)	
23	38.2 – 42.0, CH	2.26 – 2.72 (m)	
24	31.2 – 32.4, CH ₂	0.95 – 1.67 (m)	
25	20.8 – 24.2, CH ₂	1.18 – 1.74 (m)	
26	27.6 – 28.3, CH ₂	1.06 – 1.83 (m)	
27	45.8 – 48.9, CH	3.26 – 3.61 (m)	
28	33.0 – 35.6, CH ₂	1.02 – 1.88 (m)	
29	175.2 – 175.5		
32	51.7 – 51.8, CH ₃	3.58 (s)	

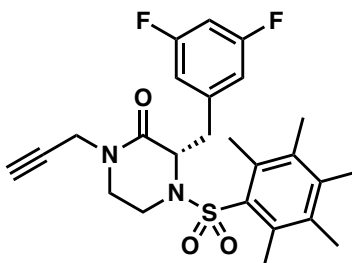
12.5 Preparation of Propargyl Piperazinone Sulfonamides



In a vial, 1.1 equivalent of propargyl piperazinone **2.62'** and three equivalents of TEA were dissolved in 4 mL of dry acetonitrile. The one equivalent of sulfonyl chloride was added and the

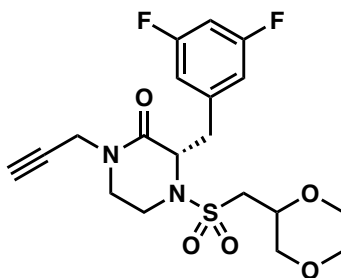
reaction mixture was stirred overnight. The reaction was quenched with water (10 mL) and washed with a saturated solution of sodium bicarbonate (20 mL) and the organic layer was extracted with ethyl acetate (3 times). The organic layers were combined, washed with brine before being dried over Na₂SO₄ and filtered. The filtrate was concentrated in vacuo and purified by flash column chromatography.

(S)-3-(3,5-difluorobenzyl)-4-((2,3,4,5,6-pentamethylphenyl)sulfonyl)-1-(prop-2-yn-1-yl)piperazin-2-one (2.91):



5mg; yield=33%. ¹H NMR (300 MHz, Chloroform-*d*) δ 6.72 (s, 1H), 6.44 – 6.30 (m, 2H), 4.69 (d, *J* = 17.0 Hz, 1H), 4.18 (d, *J* = 13.3 Hz, 2H), 3.98 (d, *J* = 16.8 Hz, 1H), 3.84 (td, *J* = 12.2, 4.5 Hz, 1H), 3.48 (d, *J* = 12.8 Hz, 1H), 3.38 (d, *J* = 12.1 Hz, 1H), 3.15 (d, *J* = 14.4 Hz, 1H), 2.92 – 2.77 (m, 1H), 2.34 (s, 6H), 2.28 (s, 1H), 2.25 (s, 3H), 2.15 (s, 6H). ¹³C NMR (101 MHz, Chloroform-*d*) δ 166.3, 163.9, 161.3, 161.1, 141.7, 141.0, 140.8, 135.5, 135.0, 112.7, 112.5, 111.6, 111.4, 102.0, 101.8, 101.4, 77.2, 72.8, 72.2, 63.0, 59.5, 47.5, 46.0, 44.7, 43.3, 37.8, 37.4, 35.9, 35.8, 35.2, 18.6, 17.9, 17.0.

(3S)-4-(((1,4-dioxan-2-yl)methyl)sulfonyl)-3-(3,5-difluorobenzyl)-1-(prop-2-yn-1-yl)piperazin-2-one (2.92):

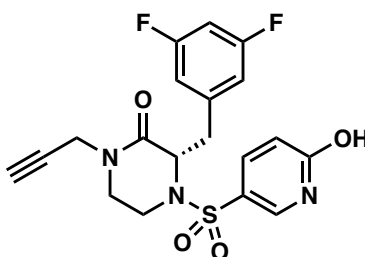


39 mg; yield=57%. ^1H NMR (400 MHz, Acetonitrile- d_3) δ 3.79 – 3.68 (m, 2H), 3.68 – 3.57 (m, 4H), 3.57 – 3.47 (m, 1H), 3.35 – 3.28 (m, 0H), 3.28 – 3.19 (m, 3H), 3.19 – 3.11 (m, 1H), 6.95 – 6.80 (m, 3H), 4.56 – 4.39 (m, 1H), 4.34 – 4.11 (m, 2H), 3.97 – 3.83 (m, 1H), 3.04 – 2.89 (m, 2H), 2.54 (d, J = 2.3 Hz, 1H). ^{13}C NMR (101 MHz, Acetonitrile- d_3) δ 166.3, 165.8, 164.1, 161.5, 142.0, 113.1, 113.0, 112.8, 112.7, 102.3, 102.1, 101.9, 101.6, 78.2, 78.1, 72.4, 70.8, 70.4, 69.0, 68.9, 66.0, 65.8, 59.6, 58.9, 53.9, 53.7, 45.6, 45.5, 39.4, 39.1, 38.3, 38.0, 35.5.

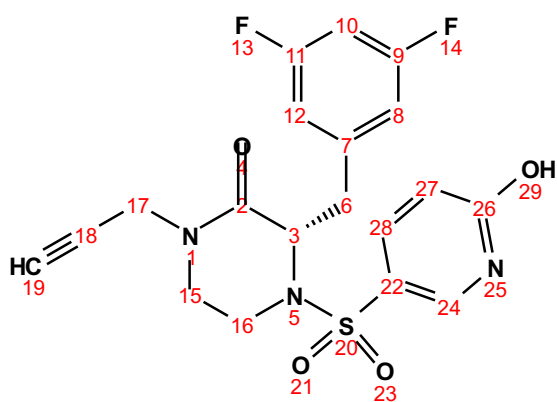
Position	δC , type	δH	J (Hz)	COSY
2	165.8 – 166.3			
3	58.9 – 59.6, CH	4.39 – 4.56 (m)		
6	39.1 – 39.4, CH ₂	3.23 – 3.78 (m)		
7	142.0			
8	112.7 – 113.1, CH	6.87 – 6.95 (m)		
9	161.5 – 164.1			
10	101.8 – 102.3, CH	6.84 – 6.90 (m)		

11	161.5 – 164.1			
12	112.7 – 113.1, CH	6.87 – 6.95 (m)		
15	45.5 – 45.6, CH ₂	3.15 – 3.71 (m)		
16	38.0 – 38.3, CH ₂	3.12 – 3.25 (m)		3
17	35.5, CH ₂	4.11 – 4.32 (m)		
18	78.1 – 78.2			
19	72.4			
22	53.7 – 53.9, CH ₂	2.89 – 3.04 (m)		24
24	70.4 – 70.7, CH	3.83 – 3.97 (m)		22, 25
25	68.9 – 69.0, CH ₂	3.15 – 3.68 (m)		24
27	65.8 – 66.0, CH ₂	3.48 – 3.74 (m)		
28	65.8 – 66.0, CH ₂	3.48 – 3.74 (m)		

(S)-3-(3,5-difluorobenzyl)-4-((6-hydroxypyridin-3-yl)sulfonyl)-1-(prop-2-yn-1-yl)piperazin-2-one (2.93):

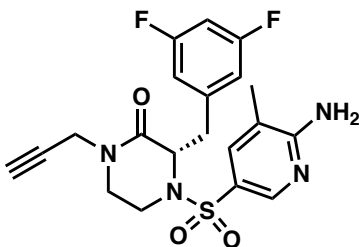


14 mg; yield=53%. ¹H NMR (500 MHz, Acetonitrile-*d*₃) δ 7.79 (d, *J* = 2.8 Hz, 1H), 7.27 (dt, *J* = 9.8, 2.2 Hz, 1H), 7.15 (s, 1H), 6.90 – 6.79 (m, 3H), 6.31 (d, *J* = 9.8 Hz, 1H), 4.42 (dd, *J* = 9.6, 4.2 Hz, 1H), 4.29 (dd, *J* = 17.3, 2.2 Hz, 1H), 4.09 – 4.03 (m, 1H), 3.91 – 3.80 (m, 1H), 3.56 – 3.43 (m, 2H), 3.34 – 3.09 (m, 3H), 2.53 – 2.48 (m, 1H). ¹³C NMR (126 MHz, Acetonitrile-*d*₃) δ 165.6, 163.7, 161.8, 161.4, 141.6, 139.1, 136.4, 127.7, 121.1, 117.0, 113.9, 112.8, 102.3, 102.1, 101.9, 78.0, 72.4, 59.1, 45.1, 38.6, 37.0, 35.4. HRMS (ESI+) *m/z* calcd for C₁₉H₁₇F₂N₃O₄S [M – H]⁺: 420.084, found 420.0829



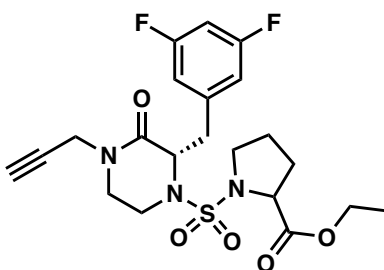
Position	δC , type	δH	J (Hz)
2	165.6		
3	59.1, CH	4.42 (dd)	9.6, 4.2
6	38.6, CH ₂	3.45 – 3.89 (m)	
7	141.6		
8	112.8 – 113.9, CH	6.82 – 6.90 (m)	
9	161.8 – 163.7		
10	101.9 – 102.3, CH	6.81 – 6.86 (m)	
11	161.8 – 163.7		
12	112.8 – 113.9, CH	6.82 – 6.90 (m)	
15	45.1, CH ₂	3.19 – 3.53 (m)	
16	37.0, CH ₂	3.09 – 3.26 (m)	
17	35.4, CH ₂	4.03 – 4.32 (m)	
18	78.0		
19	72.4, CH	2.48 – 2.53 (m)	
22	117.0		
24	139.1, CH	7.79 (d)	2.8
26	161.4		
27	121.1 – 127.7, CH	6.28 – 7.18 (m)	
28	136.4, CH	7.17 (dt)	9.8, 2.2

(S)-4-((6-amino-5-methylpyridin-3-yl)sulfonyl)-3-(3,5-difluorobenzyl)-1-(prop-2-yn-1-yl)piperazin-2-one (2.94):



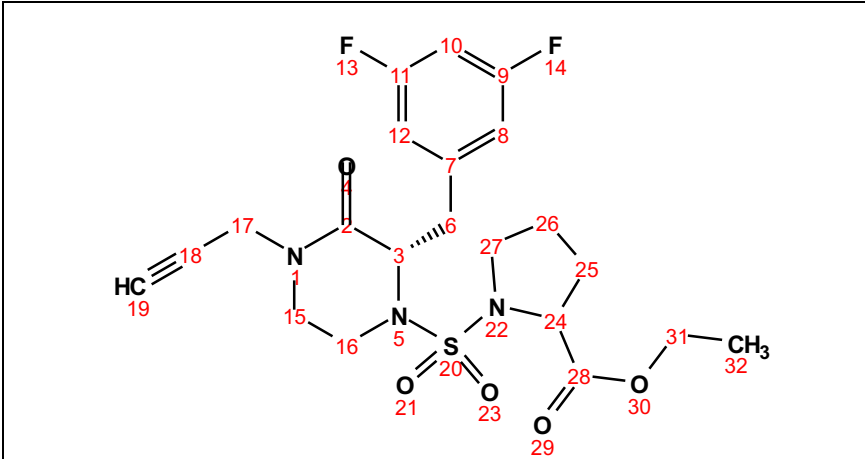
13 mg; yield=57%. ^1H NMR (400 MHz, Chloroform-*d*) δ 8.26 (d, $J = 2.3$ Hz, 1H), 7.36 (dd, $J = 2.4, 1.1$ Hz, 1H), 6.72 – 6.61 (m, 3H), 5.22 (s, 2H), 4.47 – 4.41 (m, 1H), 4.36 (dd, $J = 17.3, 2.5$ Hz, 1H), 4.00 (dd, $J = 17.3, 2.5$ Hz, 1H), 3.72 – 3.63 (m, 1H), 3.45 (ddd, $J = 12.3, 10.2, 4.3$ Hz, 1H), 3.33 – 3.19 (m, 2H), 3.18 – 3.06 (m, 2H), 2.22 (t, $J = 2.5$ Hz, 1H), 2.12 (s, 3H). ^{13}C NMR (101 MHz, Chloroform-*d*) δ 165.9, 161.6, 161.4, 159.7, 145.9, 140.4, 135.9, 123.8, 116.8, 112.8, 102.4, 77.2, 72.8, 58.9, 44.8, 39.9, 38.4, 35.8, 29.7, 16.8.

ethyl ((*S*)-2-(3,5-difluorobenzyl)-3-oxo-4-(prop-2-yn-1-yl)piperazin-1-yl)sulfonylprolinate (2.95):



6 mg; yield=26%. ^1H NMR (500 MHz, DMSO-*d*₆) δ 7.14 – 7.00 (m, 3H), 6.92 – 6.81 (m, 0H), 4.79 – 4.70 (m, 1H), 4.56 – 4.46 (m, 1H), 4.38 – 4.30 (m, 0H), 4.31 – 4.17 (m, 2H), 4.17 – 4.04 (m, 2H), 3.86 – 3.74 (m, 0H), 3.72 – 3.62 (m, 1H), 3.62 – 3.49 (m, 2H), 3.49 – 3.39 (m, 0H), 3.31 – 3.22 (m, 2H), 3.22 – 3.09 (m, 2H), 2.97 – 2.84 (m, 1H), 2.43 – 2.35 (m, 1H), 2.20 – 2.05 (m, 1H), 2.04 – 1.92 (m, 0H), 1.88 – 1.76 (m, 1H), 1.79 – 1.70 (m, 1H), 1.70 – 1.59 (m, 1H), 1.58 –

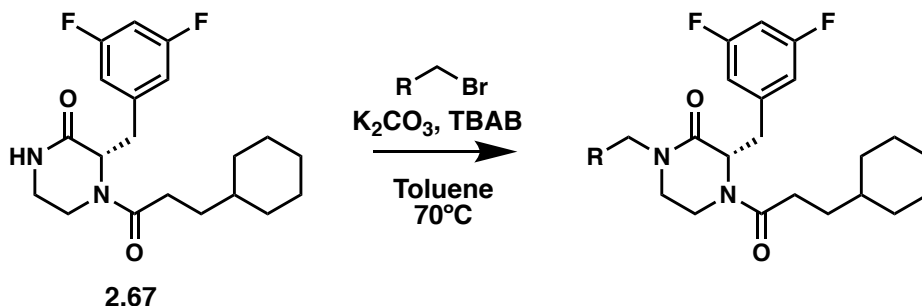
1.48 (m, 0H), 1.18 (dt, $J = 18.6, 7.1$ Hz, 3H). ^{13}C NMR (101 MHz, DMSO- d_6) δ 172.5, 172.3, 166.3, 166.2, 163.9, 161.3, 142.3, 113.4, 113.2, 102.5, 79.0, 75.2, 61.6, 61.3, 61.2, 60.8, 59.2, 59.0, 48.1, 47.2, 45.2, 38.7, 36.7, 35.6, 30.7, 24.9, 24.5, 14.4.



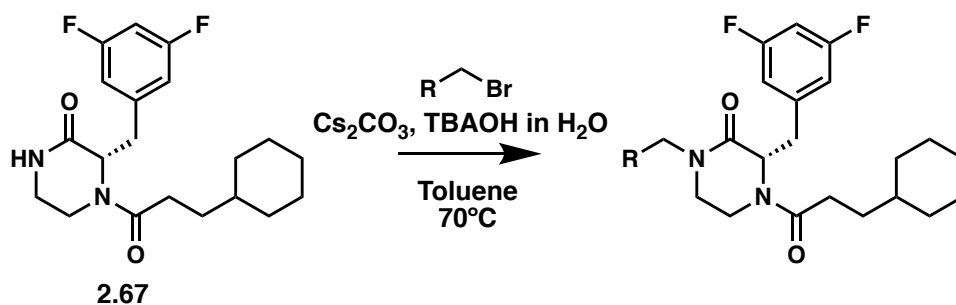
Position	δC , type	δH	J (Hz)
2	166.2 – 166.3		
3	59.0 – 59.2, CH	4.31 – 4.55 (m)	
6	38.7, CH ₂	3.24 – 3.70 (m)	
7	142.3		
8	113.2 – 113.4, CH	7.05 – 7.10 (m)	
9	161.3 – 163.9		
10	102.5, CH	7.01 – 7.10 (m)	
11	161.3 – 163.9		
12	113.2 – 113.4, CH	7.05 – 7.10 (m)	
15	45.2, CH ₂	3.24 – 3.70 (m)	
16	36.7, CH ₂	3.10 – 3.19 (m)	
17	35.6, CH ₂	4.15 – 4.28 (m)	
18	79.0		
19	75.2, CH		
24	60.8 – 61.6, CH	4.09 – 4.22 (m)	
25	30.7, CH ₂	1.77 – 2.18 (m)	
26	24.5 – 24.9, CH ₂	1.59 – 1.79 (m)	
27	47.2 – 48.1, CH ₂	2.37 – 2.95 (m)	
28	172.3 – 172.5		
31	61.2 – 61.3, CH ₂	4.05 – 4.15 (m)	

32	14.4	1.18 (dt)	18.6, 7.1
----	------	-----------	-----------

12.6 Preparation of N-alkyl Cyclohexylpropanoyl Piperazinones

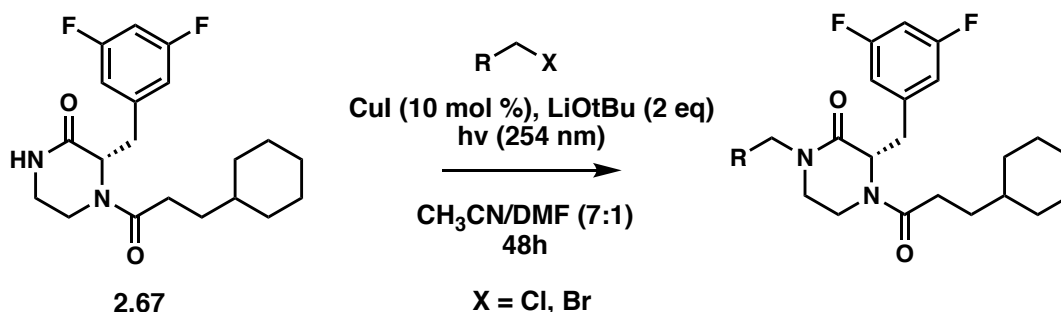


PTC N-alkylation procedure (N1): In a 20 mL vial, one equivalent of piperazinone **2.67**, two equivalents of K_2CO_3 and two equivalents of TBAB were dissolved in 10 mL of toluene at $70^\circ C$. Then 1.5 equivalent of alkyl bromide was added to the reaction mixture and stirred overnight at $70^\circ C$. The reaction washed with a saturated solution of $NaHCO_3$ (20 mL) and the organic layer was extracted with EtOAc (3 times). The organic layers were combined, washed with brine before being dried over Na_2SO_4 and filtered. The filtrate was concentrated in vacuo and purified by flash column chromatography.



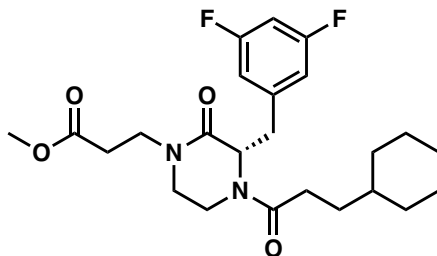
PTC N-alkylation procedure (N2): In a 20 mL vial, one equivalent of piperazinone **2.67**, two equivalents of Cs_2CO_3 and two equivalents of TBAOH in H_2O were dissolved in 10 mL of toluene

at 70°C. Then 1.5 equivalent of alkyl bromide was added to the reaction mixture and stirred overnight at 70°C. The reaction washed with a saturated solution of NaHCO₃ (20 mL) and the organic layer was extracted with EtOAc (3 times). The organic layers were combined, washed with brine before being dried over Na₂SO₄ and filtered. The filtrate was concentrated in vacuo and purified by flash column chromatography.



Photoinduced copper-catalyzed N-alkylation procedure (N3): A sealable vial containing one equivalent of piperazinone **2.67**, 10 mol% of CuI and two equivalents of LiOtBu was evacuated and back-filled with N₂ (3 cycles). A solution of two equivalent of alkyl halide in acetonitrile (2.7 mL) and DMF (0.4 mL) was then added to the vial. The reaction mixture was then stirred and irradiated with UVC lamp (254 nm) for 48h. The reaction was quenched with a solution of NH₄OH/NH₄Cl (5 mL) and washed with a saturated solution of NaHCO₃ (20 mL) and the organic layer was extracted with EtOAc (3 times). The organic layers were combined, washed with brine before being dried over Na₂SO₄ and filtered. The filtrate was concentrated in vacuo and purified by flash column chromatography.

methyl (S)-3-(4-(3-cyclohexylpropanoyl)-3-(3,5-difluorobenzyl)-2-oxopiperazin-1-yl) propanoate (2.96):

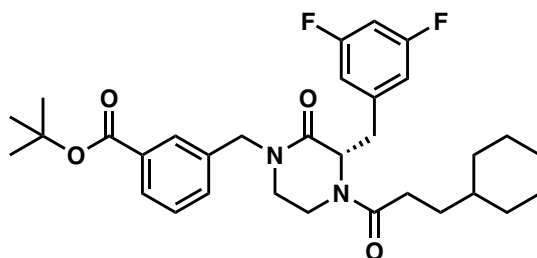


Procedure N1 (15 mg; yield=83%). ^1H NMR (500 MHz, $\text{DMSO-}d_6$) δ 7.13 – 6.99 (m, 2H), 6.86 – 6.78 (m, 1H), 4.93 – 4.87 (m, 1H), 4.61 (dd, $J = 10.7, 3.8$ Hz, 0H), 4.37 (d, $J = 13.6$ Hz, 0H), 3.96 – 3.89 (m, 1H), 3.60 – 3.56 (m, 3H), 3.65 – 3.54 (m, 1H), 3.54 – 3.44 (m, 1H), 3.45 – 3.35 (m, 1H), 3.30 – 3.25 (m, 1H), 3.25 – 3.18 (m, 1H), 3.18 – 3.13 (m, 2H), 3.13 – 3.01 (m, 2H), 2.62 – 2.50 (m, 3H), 2.03 – 1.95 (m, 0H), 1.91 – 1.83 (m, 0H), 1.68 – 1.61 (m, 1H), 1.61 – 1.48 (m, 2H), 1.47 – 1.41 (m, 2H), 1.36 – 1.19 (m, 4H), 1.17 – 0.96 (m, 2H), 0.46 (d, $J = 12.9$ Hz, 1H). ^{13}C NMR (101 MHz, $\text{DMSO-}d_6$) δ 174.3, 173.9, 172.1, 167.1, 166.7, 164.1, 163.7, 163.6, 161.6, 161.5, 161.3, 161.1, 142.5, 142.4, 142.3, 113.6, 113.4, 113.2, 113.1, 113.0, 112.9, 110.0, 102.5, 102.3, 102.0, 77.0, 59.1, 55.8, 55.2, 51.9, 47.6, 46.6, 43.4, 43.2, 39.7, 39.3, 37.1, 36.3, 35.6, 34.8, 31.9, 31.8, 31.7, 29.8, 29.5, 29.0, 28.8, 25.9, 25.8, 25.6, 25.4, 25.3, 25.2.

Position	δC , type	δH	J (Hz)
2	166.7 – 167.1		
3	55.2 – 59.1, CH	4.59 – 4.94 (m)	

6	34.8 – 39.7, CH ₂	3.10 – 4.40 (m)	
7	142.3 – 142.5		
8	112.9 – 113.6, CH	6.78 – 7.10 (m)	
9	161.1 – 164.1		
10	102.0 – 102.5, CH	7.00 – 7.12 (m)	
11	161.1 – 164.1		
12	112.9 – 113.6, CH	6.78 – 7.10 (m)	
15	36.3 – 37.1, CH ₂	3.02 – 3.23 (m)	
16	46.6 – 47.6, CH ₂	3.19 – 3.44 (m)	
17	172.1		
18	35.6, CH ₂	1.95 – 2.03 (m)	
20	29.8, CH ₂	0.97 – 1.48 (m)	
21	39.3, CH	1.83 – 2.57 (m)	
22	28.8 – 29.5, CH ₂	0.45 – 1.57 (m)	
23	25.2 – 25.6, CH ₂	1.19 – 1.68 (m)	
24	25.8 – 25.9, CH ₂	1.07 – 1.68 (m)	
25	25.2 – 25.6, CH ₂	1.19 – 1.68 (m)	
26	28.8 – 29.5, CH ₂	0.45 – 1.57 (m)	
27	43.2 – 43.4, CH ₂	3.43 – 3.62 (m)	
28	173.9 – 174.3		
29	31.7 – 31.9, CH ₂	2.50 – 2.62 (m)	
32	51.9, CH ₃	3.58 (d)	3.3

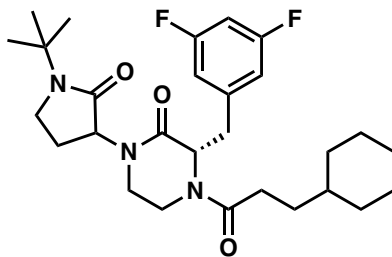
tert-butyl (S)-3-((4-(3-cyclohexylpropanoyl)-3-(3,5-difluorobenzyl)-2-oxopiperazin-1-yl)methyl)benzoate (2.97):



Procedure N1 (5 mg; yield=27%). ¹H NMR (500 MHz, DMSO-*d*₆) δ 7.84 – 7.74 (m, 2H), 7.50 – 7.44 (m, 2H), 7.11 (d, *J* = 8.3 Hz, 1H), 7.03 (t, *J* = 9.1 Hz, 1H), 6.85 (d, *J* = 7.7 Hz, 1H), 6.72 (d,

$J = 8.2$ Hz, 0H), 5.04 (t, $J = 6.8$ Hz, 1H), 4.82 – 4.65 (m, 1H), 4.59 – 4.36 (m, 1H), 4.02 – 3.90 (m, 1H), 3.36 (d, $J = 11.5$ Hz, 1H), 3.25 – 3.08 (m, 4H), 2.04 – 1.90 (m, 1H), 1.67 – 1.54 (m, 3H), 1.53 (d, $J = 3.6$ Hz, 10H), 1.51 – 1.35 (m, 2H), 1.35 – 1.13 (m, 3H), 1.14 – 0.94 (m, 2H), 0.91 – 0.78 (m, 2H), 0.47 (d, $J = 12.9$ Hz, 1H). ^{13}C NMR (101 MHz, DMSO- d_6) δ 174.0, 167.4, 167.0, 165.2, 161.1, 142.3, 137.9, 132.4, 132.3, 132.1, 129.4, 128.8, 128.5, 128.3, 113.2, 113.0, 110.0, 102.6, 102.3, 81.3, 70.9, 59.2, 55.3, 49.3, 47.0, 46.2, 44.0, 39.2, 37.1, 36.3, 34.6, 29.8, 29.4, 29.0, 28.2, 25.9, 25.6, 25.3.

(3S)-1-(1-(*tert*-butyl)-2-oxopyrrolidin-3-yl)-4-(3-cyclohexylpropanoyl)-3-(3,5-difluorobenzyl) piperazin-2-one (2.98):

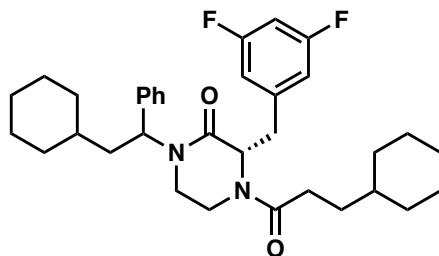


Procedure N2 (4 mg; yield=50%). ^1H NMR (400 MHz, DMSO- d_6) δ 7.11 – 6.98 (m, 2H), 6.88 (d, $J = 8.0$ Hz, 1H), 6.84 – 6.77 (m, 0H), 4.99 – 4.82 (m, 2H), 4.61 – 4.57 (m, 0H), 4.43 – 4.36 (m, 0H), 4.01 – 3.93 (m, 1H), 3.86 (d, $J = 13.2$ Hz, 1H), 3.74 – 3.65 (m, 1H), 3.51 – 3.30 (m, 1H), 3.29 – 3.02 (m, 2H), 2.97 (d, $J = 11.2$ Hz, 1H), 2.35 – 2.23 (m, 0H), 2.22 – 2.10 (m, 1H), 2.10 – 1.96 (m, 2H), 1.94 – 1.84 (m, 1H), 1.66 – 1.52 (m, 6H), 1.50 – 1.36 (m, 2H), 1.33 – 1.23 (m, 10H), 1.21 – 0.97 (m, 3H), 0.96 – 0.73 (m, 1H), 0.66 (s, 1H). ^{13}C NMR (101 MHz, DMSO- d_6) δ 171.4, 170.6, 167.5, 167.0, 163.0, 142.4, 113.2, 102.3, 59.7, 57.4, 55.7, 54.2, 44.0, 43.1, 42.0, 37.1, 36.9, 36.6,

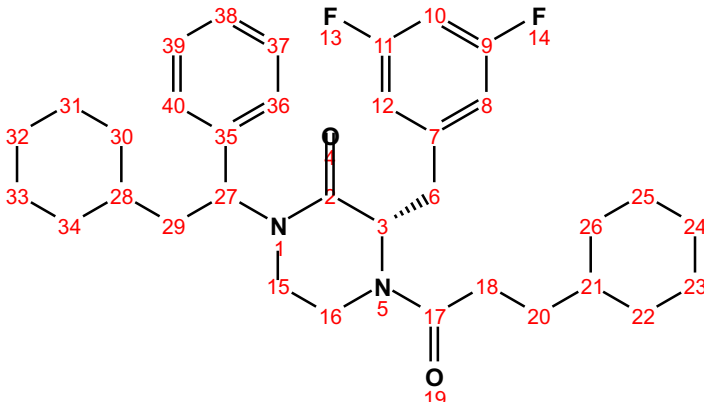
35.3, 33.0, 32.9, 32.5, 30.1, 29.5, 29.2, 27.5, 26.6, 26.5, 26.2, 26.1. HRMS (ESI+) m/z calcd for $C_{28}H_{39}F_2N_3O_3$ $[M + H]^+$: 504.30322, found 504.3039.

(3*S*)-1-(2-cyclohexyl-1-phenylethyl)-4-(3-cyclohexylpropanoyl)-3-(3,5-difluorobenzyl)

piperazin-2-one (2.104):



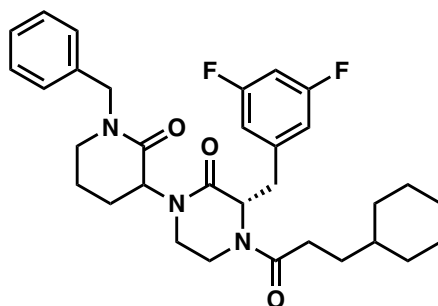
Procedure N3 (10 mg; yield=58%). 1H NMR (500 MHz, $DMSO-d_6$) δ 7.39 – 7.30 (m, 2H), 7.29 – 7.22 (m, 3H), 7.15 – 6.97 (m, 2H), 6.82 (ddd, $J = 18.8, 8.4, 2.3$ Hz, 1H), 5.88 – 5.81 (m, 1H), 4.94 (dt, $J = 33.2, 6.2$ Hz, 1H), 4.79 – 4.57 (m, 0H), 4.28 (dd, $J = 21.7, 13.6$ Hz, 1H), 3.80 – 3.58 (m, 1H), 3.25 – 3.00 (m, 3H), 2.81 – 2.65 (m, 1H), 2.63 – 2.52 (m, 0H), 2.33 – 2.18 (m, 1H), 2.18 – 1.97 (m, 1H), 1.92 – 1.81 (m, 1H), 1.81 – 1.69 (m, 1H), 1.70 – 1.53 (m, 8H), 1.53 – 1.35 (m, 1H), 1.35 – 1.18 (m, 2H), 1.18 – 0.95 (m, 11H), 0.95 – 0.60 (m, 2H). ^{13}C NMR (101 MHz, $DMSO-d_6$) δ 171.6, 171.5, 171.4, 167.0, 166.9, 166.7, 166.5, 163.8, 163.6, 161.3, 161.2, 142.5, 142.4, 140.0, 139.9, 139.4, 129.0, 128.9, 128.2, 128.0, 127.9, 127.8, 113.6, 113.3, 113.2, 113.0, 112.9, 102.7, 102.4, 102.2, 59.8, 59.6, 56.1, 55.9, 52.2, 52.1, 51.9, 40.9, 40.8, 40.7, 40.3, 37.4, 37.2, 37.1, 37.0, 36.9, 36.7, 36.5, 36.3, 36.1, 35.4, 34.4, 34.3, 34.2, 34.1, 33.6, 33.1, 33.0, 32.9, 32.6, 32.5, 32.4, 32.3, 30.3, 30.2, 29.5, 26.5, 26.3, 26.2, 26.1, 26.0, 25.9.



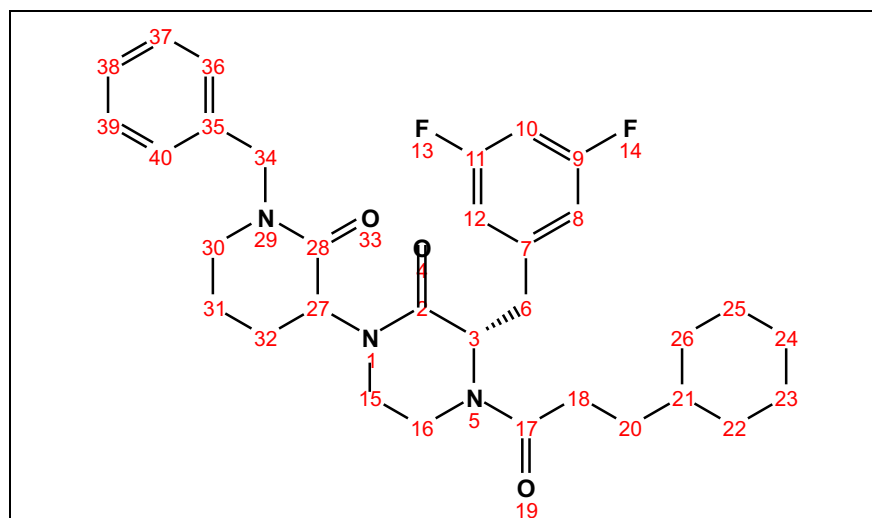
Position	δC , type	δH	J (Hz)
2	166.7 – 167.0		
3	55.9 – 59.8, CH	4.59 – 5.00 (m)	
6	35.4 – 40.9, CH ₂	3.09 – 4.33 (m)	
7	142.4 – 142.5		
8	112.9 – 113.6, CH	6.76 – 7.03 (m)	
9	161.2 – 163.8		
10	102.2 – 102.7, CH	7.03 – 7.11 (m)	
11	161.2 – 163.8		
12	112.9 – 113.6, CH	6.76 – 7.03 (m)	
15	36.5 – 37.4, CH ₂	3.09 – 3.23 (m)	
16	40.3 – 40.8, CH ₂	2.65 – 2.80 (m)	
17	171.4 – 171.6		
18	29.5 – 30.3, CH ₂	1.97 – 2.33 (m)	
20	33.6, CH ₂	0.97 – 1.68 (m)	
21	36.9 – 37.1, CH	1.00 – 1.07 (m)	
22	32.3 – 33.1, CH ₂	0.73 – 1.92 (m)	
23	25.9 – 26.3, CH ₂	1.02 – 1.68 (m)	
24	26.5, CH ₂	1.02 – 1.68 (m)	
25	25.9 – 26.3, CH ₂	1.02 – 1.68 (m)	
26	32.3 – 33.1, CH ₂	0.73 – 1.92 (m)	
27	51.9 – 52.2, CH	5.81 – 5.88 (m)	
28	34.1 – 34.4, CH	1.00 – 1.15 (m)	
29	36.1 – 36.5, CH ₂	1.71 – 1.80 (m)	
30	32.3 – 33.1, CH ₂	0.73 – 1.92 (m)	
31	25.9 – 26.3, CH ₂	1.02 – 1.68 (m)	
32	26.5, CH ₂	1.02 – 1.68 (m)	
33	25.9 – 26.3, CH ₂	1.02 – 1.68 (m)	

34	32.3 – 33.1, CH ₂	0.73 – 1.92 (m)	
35	139.4 – 140.0		
36	128.9 – 129.0, CH	7.28 – 7.36 (m)	
37	127.8 – 128.2, CH	7.21 – 7.32 (m)	
38	127.8 – 128.2, CH	7.21 – 7.32 (m)	
39	127.8 – 128.2, CH	7.21 – 7.32 (m)	
40	128.9 – 129.0, CH	7.28 – 7.36 (m)	

(3S)-1-(1-benzyl-2-oxopiperidin-3-yl)-4-(3-cyclohexylpropanoyl)-3-(3,5-difluorobenzyl) piperazin-2-one (2.105):



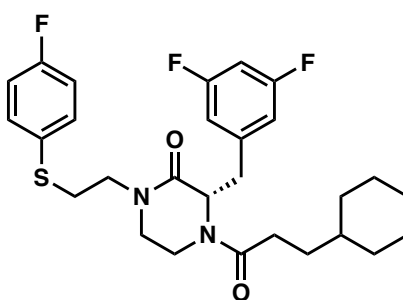
Procedure N3 (23 mg; yield=61%). ¹H NMR (500 MHz, DMSO-*d*₆) δ 7.33 (q, *J* = 7.5 Hz, 2H), 7.29 – 7.19 (m, 3H), 7.14 – 6.99 (m, 2H), 6.93 – 6.83 (m, 1H), 4.93 (td, *J* = 6.6, 3.8 Hz, 1H), 4.78 – 4.71 (m, 1H), 4.69 – 4.52 (m, 1H), 4.53 – 4.33 (m, 2H), 3.89 – 3.76 (m, 1H), 3.50 – 3.41 (m, 0H), 3.37 – 3.05 (m, 6H), 2.39 – 2.16 (m, 2H), 2.14 – 1.94 (m, 1H), 1.93 – 1.74 (m, 3H), 1.70 (p, *J* = 3.2 Hz, 1H), 1.67 – 1.52 (m, 4H), 1.52 – 1.41 (m, 1H), 1.38 – 1.02 (m, 4H), 1.02 – 0.89 (m, 1H), 0.88 – 0.74 (m, 1H), 0.74 – 0.63 (m, 1H). ¹³C NMR (101 MHz, DMSO-*d*₆) δ 171.6, 171.4, 170.0, 169.0, 167.3, 167.1, 166.8, 166.7, 164.0, 163.9, 163.7, 161.3, 161.2, 142.5, 138.2, 137.9, 137.8, 137.7, 128.9, 127.9, 127.8, 127.5, 127.4, 113.2, 113.0, 102.3, 59.7, 59.5, 55.9, 55.7, 50.0, 49.5, 47.4, 40.5, 37.3, 37.1, 36.9, 36.8, 36.7, 35.6, 33.1, 33.0, 32.9, 32.5, 32.4, 32.2, 30.3, 30.2, 29.3, 28.4, 26.6, 26.2, 26.1, 25.2, 23.1, 21.7, 21.6, 21.5.



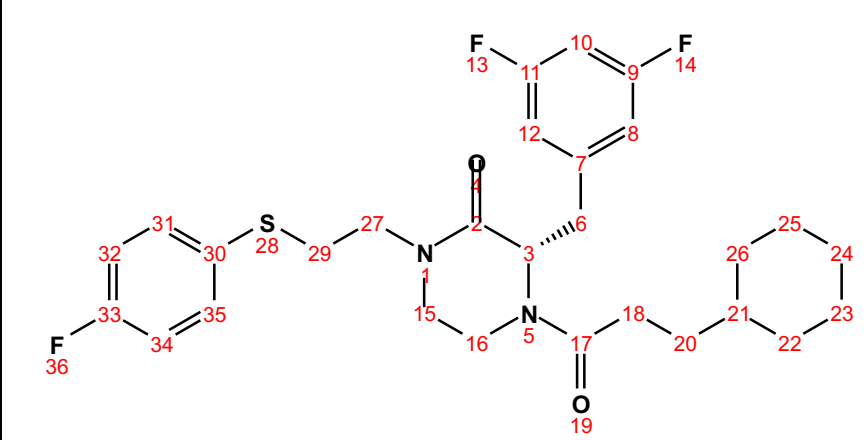
Position	δC , type	δH	J (Hz)
2	166.7 – 167.3		
3	55.7 – 55.9, CH	4.90 – 4.97 (m)	
6	35.6 – 40.5, CH ₂	3.09 – 4.41 (m)	
7	142.5		
8	113.0 – 113.2, CH	6.84 – 7.08 (m)	
9	161.2 – 164.0		
10	102.3, CH	7.00 – 7.13 (m)	
11	161.2 – 164.0		
12	113.0 – 113.2, CH	6.84 – 7.08 (m)	
15	36.7 – 37.3, CH ₂	3.07 – 3.24 (m)	
16	47.4, CH ₂	3.11 – 3.29 (m)	
17	171.4 – 171.6		
18	30.2 – 30.3, CH ₂	2.17 – 2.39 (m)	
20	29.3 – 32.5, CH ₂	0.93 – 2.34 (m)	
21	36.9 – 37.1, CH	0.93 – 1.16 (m)	
22	32.9 – 33.1, CH ₂	0.64 – 1.70 (m)	
23	25.2 – 26.2, CH ₂	1.03 – 1.69 (m)	
24	26.6, CH ₂	1.03 – 1.69 (m)	
25	25.2 – 26.2, CH ₂	1.03 – 1.69 (m)	
26	32.9 – 33.1, CH ₂	0.64 – 1.70 (m)	
27	59.5 – 59.7, CH	4.58 – 4.68 (m)	
28	169.0 – 170.0		
30	49.5, CH ₂	4.46 – 4.67 (m)	
31	21.5 – 23.1, CH ₂	1.67 – 1.93 (m)	
32	25.2, CH ₂	1.82 – 1.93 (m)	
34	50.0, CH ₂	4.41 – 4.65 (m)	

35	137.7 – 138.2		
36	128.9, CH	7.26 – 7.37 (m)	
37	127.4 – 127.9, CH	7.20 – 7.33 (m)	
38	127.4 – 127.9, CH	7.20 – 7.33 (m)	
39	127.4 – 127.9, CH	7.20 – 7.33 (m)	
40	128.9, CH	7.26 – 7.37 (m)	

(S)-4-(3-cyclohexylpropanoyl)-3-(3,5-difluorobenzyl)-1-(2-((4-fluorophenyl)thio)ethyl) piperazin-2-one (2.106):



Procedure N3 (7 mg; yield=65%). ¹H NMR (500 MHz, DMSO-*d*₆) δ 7.76 (dt, *J* = 10.3, 5.2 Hz, 0H), 7.48 – 7.41 (m, 2H), 7.18 (td, *J* = 8.9, 3.0 Hz, 2H), 7.14 – 6.96 (m, 2H), 6.87 – 6.81 (m, 1H), 4.92 (dd, *J* = 8.2, 5.3 Hz, 1H), 4.59 – 4.48 (m, 0H), 4.39 (d, *J* = 13.5 Hz, 1H), 3.83 (d, *J* = 14.2 Hz, 1H), 3.65 – 3.54 (m, 0H), 3.54 – 3.37 (m, 3H), 3.36 – 2.97 (m, 5H), 2.38 – 2.12 (m, 1H), 2.02 – 1.93 (m, 0H), 1.67 – 1.49 (m, 5H), 1.48 – 1.35 (m, 1H), 1.33 – 0.99 (m, 4H), 0.96 – 0.90 (m, 1H), 0.89 – 0.73 (m, 2H), 0.71 – 0.61 (m, 1H). ¹³C NMR (101 MHz, DMSO-*d*₆) δ 171.5, 171.4, 167.2, 166.7, 163.7, 163.6, 162.5, 161.6, 161.5, 161.3, 161.2, 160.1, 142.6, 142.5, 142.4, 131.2, 116.7, 116.5, 113.5, 113.3, 113.1, 112.9, 102.7, 102.3, 102.1, 59.5, 55.4, 47.3, 46.7, 46.7, 46.4, 40.0, 37.1, 37.0, 36.9, 36.3, 34.9, 33.1, 32.9, 32.8, 32.6, 32.2, 30.4, 30.3, 30.1, 29.2, 26.6, 26.5, 26.2, 26.1.

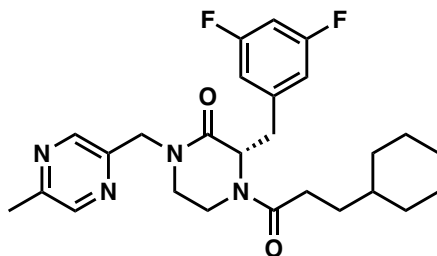


The chemical structure shows a central six-membered ring containing two nitrogen atoms (N1, N5) and one sulfur atom (S28). The ring is substituted with a carbonyl group (C2=O1), a methylene group (C3-CH2-6), and a piperidine ring (C15-16-17-18-20-21). Two fluorinated benzene rings are attached to the central ring at positions 30 and 31. The fluorinated ring at position 30 has fluorine atoms at positions 13 and 14, and carbons 7, 8, 9, 10, 11, 12. The fluorinated ring at position 31 has fluorine atoms at positions 33 and 34, and carbons 32, 35, 36. The piperidine ring has carbons 15, 16, 17, 18, 20, 21 and oxygen 19. The remaining carbons (22-26) form a cyclohexane ring attached to the piperidine ring at position 17.

Position	δC , type	δH	J (Hz)
2	166.7 – 167.2		
3	55.4 – 59.5, CH	4.51 – 4.95 (m)	
6	34.9 – 40.0, CH ₂	3.03 – 4.42 (m)	
7	142.4 – 142.6		
8	112.9 – 113.5, CH	6.81 – 7.03 (m)	
9	161.2 – 163.7		
10	102.1 – 102.7, CH	7.01 – 7.13 (m)	
11	161.2 – 163.7		
12	112.9 – 113.5, CH	6.81 – 7.03 (m)	
15	36.3 – 37.1, CH ₂	3.01 – 3.20 (m)	
16	47.3, CH ₂	3.19 – 3.46 (m)	
17	171.4 – 171.5		
18	29.2 – 32.6, CH ₂	0.90 – 2.03 (m)	
20	29.2 – 32.6, CH ₂	0.90 – 2.03 (m)	
21	36.9 – 37.0, CH	1.03 – 1.11 (m)	
22	32.8 – 33.1, CH ₂	0.63 – 1.66 (m)	
23	26.1 – 26.2, CH ₂	1.04 – 1.68 (m)	
24	26.5 – 26.6, CH ₂	1.04 – 1.68 (m)	
25	26.1 – 26.2, CH ₂	1.04 – 1.68 (m)	
26	32.8 – 33.1, CH ₂	0.63 – 1.66 (m)	
27	46.4 – 46.7, CH ₂	3.25 – 3.54 (m)	
29	30.4, CH ₂	3.07 – 3.18 (m)	
30	131.2		
31	131.2, CH	7.41 – 7.48 (m)	
32	116.5 – 116.7, CH	7.15 – 7.47 (m)	
33	160.1 – 162.5		
34	116.5 – 116.7, CH	7.15 – 7.47 (m)	

35	131.2, CH	7.41 – 7.48 (m)	
----	-----------	-----------------	--

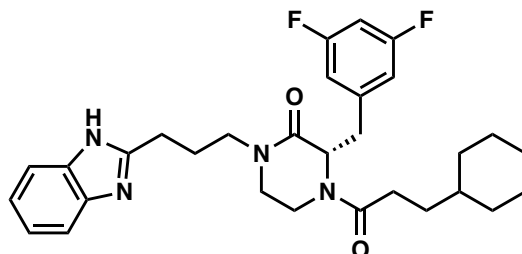
(S)-4-(3-cyclohexylpropanoyl)-3-(3,5-difluorobenzyl)-1-((5-methylpyrazin-2-yl)methyl) piperazin-2-one (2.107):



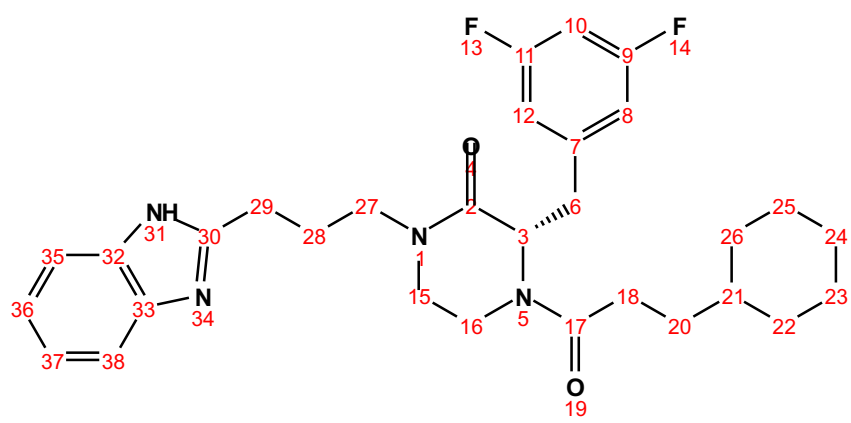
Procedure N3 (13 mg; yield=58%). ¹H NMR (500 MHz, DMSO-*d*₆) δ 8.48 – 8.42 (m, 1H), 8.10 – 8.04 (m, 1H), 7.15 – 6.95 (m, 2H), 6.90 – 6.79 (m, 1H), 5.04 – 4.96 (m, 1H), 4.90 (t, *J* = 6.7 Hz, 0H), 4.76 – 4.63 (m, 1H), 4.56 – 4.47 (m, 1H), 4.46 – 4.36 (m, 1H), 3.90 – 3.83 (m, 1H), 3.82 – 3.75 (m, 0H), 3.51 (td, *J* = 12.9, 4.2 Hz, 1H), 3.37 (td, *J* = 11.9, 4.4 Hz, 0H), 3.33 – 3.19 (m, 2H), 3.19 – 3.01 (m, 1H), 2.47 (s, 3H), 2.37 – 2.13 (m, 1H), 2.10 – 1.95 (m, 0H), 1.65 – 1.51 (m, 3H), 1.52 – 1.37 (m, 1H), 1.35 – 1.17 (m, 1H), 1.17 – 1.01 (m, 6H), 0.87 – 0.73 (m, 2H), 0.73 – 0.62 (m, 1H). ¹³C NMR (101 MHz, DMSO-*d*₆) δ 171.6, 171.5, 168.5, 168.0, 167.4, 167.0, 163.7, 163.6, 161.3, 161.2, 152.7, 149.4, 144.0, 143.0, 142.9, 142.5, 113.1, 112.9, 102.3, 59.5, 59.4, 58.0, 55.5, 55.3, 49.7, 49.5, 47.8, 47.2, 41.2, 37.1, 36.9, 36.3, 36.1, 33.0, 32.9, 32.6, 32.6, 32.3, 30.3, 30.1, 29.2, 26.6, 26.5, 26.2, 26.1, 21.2.

Position	δC , type	δH	J (Hz)
2	167.0 – 168.5		
3	55.3 – 59.5, CH	4.47 – 5.05 (m)	
6	35.0 – 41.2, CH ₂	3.02 – 4.46 (m)	
7	142.5		
8	112.9 – 113.1, CH	6.79 – 7.04 (m)	
9	161.2 – 163.7		
10	102.3, CH	6.99 – 7.14 (m)	
11	161.2 – 163.7		
12	112.9 – 113.1, CH	6.79 – 7.04 (m)	
15	36.1 – 37.1, CH ₂	3.05 – 3.25 (m)	
16	47.2 – 47.8, CH ₂	3.24 – 3.55 (m)	
17	171.5 – 171.6		
18	30.1 – 30.3, CH ₂	2.14 – 2.37 (m)	
20	29.2 – 32.6, CH ₂	0.90 – 2.09 (m)	
21	36.9 – 37.1, CH	0.90 – 1.12 (m)	
22	32.9 – 33.0, CH ₂	0.63 – 1.67 (m)	
23	26.1 – 26.2, CH ₂	1.02 – 1.69 (m)	
24	26.5 – 26.6, CH ₂	1.02 – 1.69 (m)	
25	26.1 – 26.2, CH ₂	1.02 – 1.69 (m)	
26	32.9 – 33.0, CH ₂	0.63 – 1.67 (m)	
27	49.5 – 49.7, CH ₂	4.49 – 4.77 (m)	
28	149.4		
29	142.9 – 143.0, CH	8.41 – 8.47 (m)	
31	152.7		
32	144.0, CH	8.44 – 8.49 (m)	
34	21.2, CH ₃	2.47 (s)	

(S)-1-(3-(1*H*-benzo[*d*]imidazol-2-yl)propyl)-4-(3-cyclohexylpropanoyl)-3-(3,5-difluorobenzyl) piperazin-2-one (2.108):



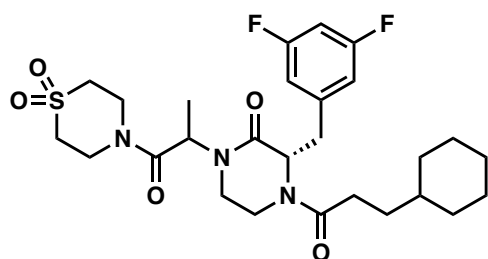
Procedure N3 (24 mg; yield=91%). ¹H NMR (500 MHz, DMSO-*d*₆) δ 8.10 – 8.04 (m, 1H), 7.53 (dd, *J* = 6.8, 2.0 Hz, 1H), 7.42 (dd, *J* = 7.1, 2.0 Hz, 1H), 7.18 – 7.10 (m, 2H), 7.10 – 7.01 (m, 1H), 7.01 – 6.96 (m, 1H), 6.89 – 6.82 (m, 1H), 4.91 (t, *J* = 6.7 Hz, 1H), 4.49 (dd, *J* = 9.4, 4.9 Hz, 0H), 4.39 (d, *J* = 13.1 Hz, 0H), 4.10 (t, *J* = 7.0 Hz, 2H), 3.79 (d, *J* = 13.0 Hz, 0H), 3.27 – 3.18 (m, 1H), 3.19 – 3.13 (m, 2H), 3.12 – 2.98 (m, 3H), 2.94 (t, *J* = 7.6 Hz, 2H), 2.63 (p, *J* = 7.3 Hz, 2H), 2.37 – 2.27 (m, 1H), 2.23 – 2.13 (m, 1H), 2.06 – 1.96 (m, 1H), 1.66 – 1.52 (m, 4H), 1.49 – 1.37 (m, 1H), 1.36 – 1.00 (m, 4H), 0.99 – 0.73 (m, 2H), 0.73 – 0.64 (m, 1H). ¹³C NMR (101 MHz, DMSO-*d*₆) δ 171.6, 168.5, 168.0, 163.7, 163.6, 161.7, 161.2, 148.8, 142.7, 132.7, 121.6, 121.4, 119.1, 113.5, 113.2, 113.1, 112.8, 110.5, 102.7, 102.3, 102.0, 59.4, 55.3, 42.9, 41.2, 40.5, 40.1, 37.1, 36.9, 36.8, 36.1, 34.7, 33.0, 32.9, 32.6, 32.3, 30.3, 29.3, 26.6, 26.5, 26.2, 26.1, 23.4.



Position	δC , type	δH	J (Hz)
2	168.0 – 168.5		
3	55.3 – 59.4, CH	4.46 – 4.94 (m)	
6	34.7 – 40.1, CH ₂	2.98 – 4.42 (m)	
7	142.7		
8	112.8 – 113.5, CH	6.82 – 7.03 (m)	
9	161.2 – 163.7		
10	102.0 – 102.7, CH	7.01 – 7.13 (m)	
11	161.2 – 163.7		
12	112.8 – 113.5, CH	6.82 – 7.03 (m)	
15	36.1 – 36.8, CH ₂	3.05 – 3.19 (m)	
16	40.5 – 41.2, CH ₂	3.02 – 3.25 (m)	
17	171.6		
18	30.3, CH ₂	2.14 – 2.37 (m)	
20	29.3 – 32.6, CH ₂	0.90 – 2.05 (m)	
21	36.9 – 37.1, CH	0.91 – 1.11 (m)	
22	32.9 – 33.0, CH ₂	0.64 – 1.67 (m)	
23	26.1 – 26.2, CH ₂	1.04 – 1.68 (m)	
24	26.5 – 26.6, CH ₂	1.04 – 1.68 (m)	
25	26.1 – 26.2, CH ₂	1.04 – 1.68 (m)	
26	32.9 – 33.0, CH ₂	0.64 – 1.67 (m)	
27	42.9, CH ₂	4.10 (t)	7.0
28	26.2, CH ₂	2.63 (p)	7.3
29	23.4, CH ₂	2.94 (t)	7.6
30	148.8		
31		8.04 – 8.10 (m)	
32	132.7		
33	142.7		

35	110.5, CH	7.42 (dd)	7.1, 2.0
36	121.4 – 121.6, CH	7.10 – 7.18 (m)	
37	121.4 – 121.6, CH	7.10 – 7.18 (m)	
38	119.1, CH	7.53 (dd)	6.8, 2.0

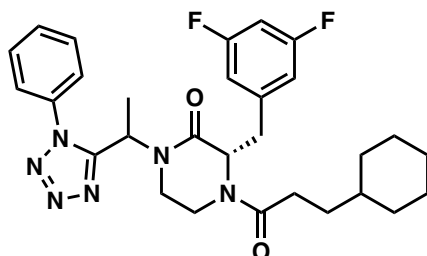
(3*S*)-4-(3-cyclohexylpropanoyl)-3-(3,5-difluorobenzyl)-1-(1-(1,1-dioxidothiomorpholino)-1-oxopropan-2-yl) piperazin-2-one (2.109):



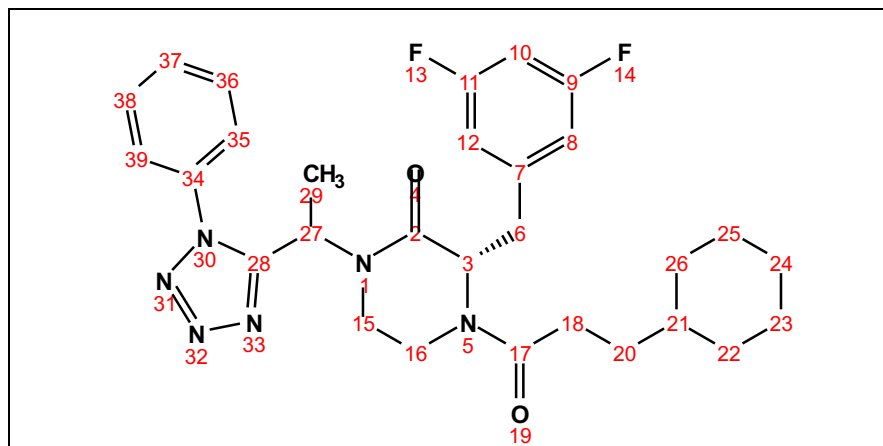
Procedure N3 (15 mg; yield=90%). ¹H NMR (500 MHz, DMSO-*d*₆) δ 7.15 – 6.95 (m, 2H), 6.84 (dt, *J* = 10.2, 4.8 Hz, 1H), 5.45 – 5.34 (m, 1H), 5.03 – 4.93 (m, 1H), 4.71 – 4.60 (m, 0H), 4.46 – 4.38 (m, 0H), 4.02 – 3.95 (m, 1H), 3.95 – 3.83 (m, 3H), 3.83 – 3.73 (m, 3H), 3.42 – 3.33 (m, 1H), 3.30 – 3.23 (m, 0H), 3.24 – 3.06 (m, 5H), 2.39 – 2.27 (m, 1H), 2.26 – 2.14 (m, 1H), 2.08 – 1.98 (m, 0H), 1.67 – 1.53 (m, 5H), 1.51 – 1.36 (m, 1H), 1.36 – 1.00 (m, 8H), 1.00 – 0.87 (m, 0H), 0.88 – 0.74 (m, 2H), 0.73 – 0.64 (m, 1H). ¹³C NMR (101 MHz, dmso) δ 171.5, 171.4, 170.3, 170.1, 169.8, 169.5, 169.4, 167.1, 166.8, 166.5, 166.4, 164.0, 163.9, 163.8, 163.7, 163.6, 161.6, 161.4, 161.3, 161.2, 161.1, 142.4, 142.3, 142.2, 113.6, 113.3, 113.2, 113.1, 113.0, 112.9, 102.8, 102.6, 102.5, 102.4, 102.2, 102.1, 77.0, 74.8, 59.5, 59.2, 56.2, 55.8, 55.6, 51.8, 51.6, 51.5, 51.4, 48.8, 48.6, 48.2, 43.6, 43.4, 42.6, 41.9, 41.8, 41.6, 41.0, 40.9, 40.8, 40.7, 40.1, 37.2, 37.1, 37.0, 36.9, 36.5, 36.4, 35.4, 35.0, 33.1, 32.9, 32.5, 32.2, 30.3, 30.1, 29.5, 29.3, 29.1, 26.6, 26.5, 26.2, 26.1, 17.1, 14.6, 14.5, 14.4.

Position	δC , type	δH	J (Hz)
2	166.4 – 167.1		
3	55.6 – 59.5, CH	4.61 – 5.03 (m)	
6	35.0 – 40.1, CH ₂	3.07 – 4.45 (m)	
7	142.2 – 142.4		
8	112.9 – 113.6, CH	6.80 – 7.03 (m)	
9	161.1 – 164.0		
10	102.1 – 102.8, CH	7.01 – 7.14 (m)	
11	161.1 – 164.0		
12	112.9 – 113.6, CH	6.80 – 7.03 (m)	
15	36.4 – 37.2, CH ₂	3.05 – 3.20 (m)	
16	51.4 – 51.8, CH ₂	3.00 – 3.43 (m)	
17	171.4 – 171.5		
18	30.1 – 30.3, CH ₂	2.14 – 2.39 (m)	
20	32.5, CH ₂	1.19 – 1.29 (m)	
21	37.0 – 37.1, CH	0.90 – 1.13 (m)	
22	32.9 – 33.1, CH ₂	0.62 – 1.67 (m)	
23	26.1 – 26.2, CH ₂	1.03 – 1.69 (m)	
24	26.5 – 26.6, CH ₂	1.03 – 1.69 (m)	
25	26.1 – 26.2, CH ₂	1.03 – 1.69 (m)	
26	32.9 – 33.1, CH ₂	0.62 – 1.67 (m)	
27	48.2 – 48.8, CH	5.34 – 5.45 (m)	
28	169.4 – 170.3		
29	14.4 – 17.1, CH ₃	1.12 – 1.26 (m)	
32	40.7 – 41.9, CH ₂	3.06 – 4.02 (m)	
33	42.6 – 43.6, CH ₂	3.10 – 3.95 (m)	
35	42.6 – 43.6, CH ₂	3.10 – 3.95 (m)	
36	40.7 – 41.9, CH ₂	3.06 – 4.02 (m)	

(3*S*)-4-(3-cyclohexylpropanoyl)-3-(3,5-difluorobenzyl)-1-(1-(1-phenyl-1*H*-tetrazol-5-yl)ethyl) piperazin-2-one (2.110):

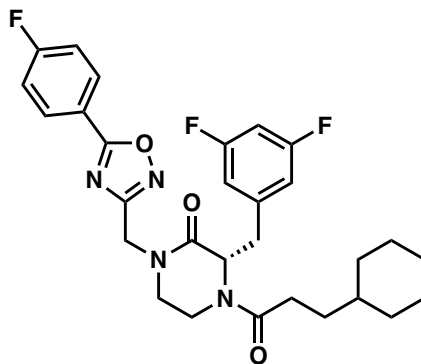


Procedure N3 (11 mg; yield=66%). ¹H NMR (500 MHz, DMSO-*d*₆) δ 7.70 – 7.47 (m, 5H), 7.13 – 6.96 (m, 1H), 6.93 – 6.81 (m, 1H), 6.74 (q, *J* = 7.5, 7.0 Hz, 1H), 6.02 – 5.78 (m, 1H), 4.82 – 4.75 (m, 0H), 4.50 – 4.43 (m, 1H), 4.38 – 4.08 (m, 1H), 3.76 – 3.63 (m, 1H), 3.26 – 3.09 (m, 1H), 3.09 – 2.58 (m, 3H), 2.29 – 1.95 (m, 2H), 1.68 – 1.50 (m, 5H), 1.49 – 1.33 (m, 1H), 1.33 – 0.96 (m, 9H), 0.96 – 0.71 (m, 1H), 0.71 – 0.58 (m, 0H). ¹³C NMR (101 MHz, DMSO-*d*₆) δ 171.2, 171.0, 166.7, 166.5, 166.0, 163.6, 161.1, 155.4, 155.3, 154.7, 142.3, 142.2, 133.9, 133.5, 131.3, 131.2, 131.0, 130.3, 130.1, 125.9, 125.4, 125.3, 113.0, 112.8, 110.0, 102.5, 102.4, 59.2, 55.0, 44.8, 44.7, 43.7, 43.4, 42.5, 42.4, 39.4, 37.1, 36.9, 36.8, 36.1, 34.6, 33.0, 32.9, 32.8, 32.4, 32.0, 29.9, 29.8, 29.5, 29.0, 26.5, 26.2, 26.1, 15.6, 15.3.

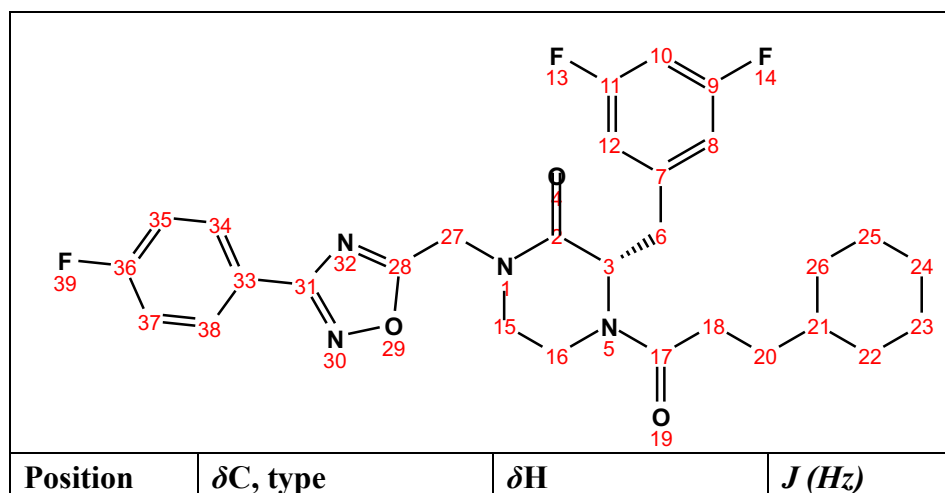


Position	δC , type	δH	J (Hz)
2	166.0 – 166.7		
3	55.0 – 59.2, CH	4.10 – 4.83 (m)	
6	34.6 – 39.4, CH ₂	2.71 – 4.32 (m)	
7	142.2 – 142.3		
8	112.8 – 113.0, CH	6.70 – 6.93 (m)	
9	161.1 – 163.6		
10	102.4 – 102.5, CH	6.97 – 7.11 (m)	
11	161.1 – 163.6		
12	112.8 – 113.0, CH	6.70 – 6.93 (m)	
15	36.1 – 36.8, CH ₂	2.66 – 3.03 (m)	
16	42.4 – 43.4, CH ₂	2.77 – 3.21 (m)	
17	171.0 – 171.4		
18	29.8 – 29.9, CH ₂	2.01 – 2.27 (m)	
20	29.0 – 32.4, CH ₂	0.81 – 1.29 (m)	
21	37.0 – 37.1, CH	0.87 – 1.09 (m)	
22	32.8 – 33.0, CH ₂	0.61 – 1.65 (m)	
23	26.1 – 26.2, CH ₂	1.01 – 1.68 (m)	
24	26.5, CH ₂	1.01 – 1.68 (m)	
25	26.1 – 26.2, CH ₂	1.01 – 1.68 (m)	
26	32.8 – 33.0, CH ₂	0.61 – 1.65 (m)	
27	43.7 – 44.8, CH	5.78 – 6.03 (m)	
28	154.7 – 155.4		
29	15.3 – 15.6, CH ₃	1.53 – 1.64 (m)	
34	133.5 – 133.9		
35	125.3 – 125.9, CH	7.51 – 7.70 (m)	
36	130.1 – 130.3, CH	7.48 – 7.65 (m)	
37	131.0 – 131.3, CH	7.55 – 7.64 (m)	
38	130.1 – 130.3, CH	7.48 – 7.65 (m)	
39	125.3 – 125.9, CH	7.51 – 7.70 (m)	

(S)-4-(3-cyclohexylpropanoyl)-3-(3,5-difluorobenzyl)-1-((5-(4-fluorophenyl)-1,2,4-oxadiazol-3-yl)methyl)piperazin-2-one (2.111):

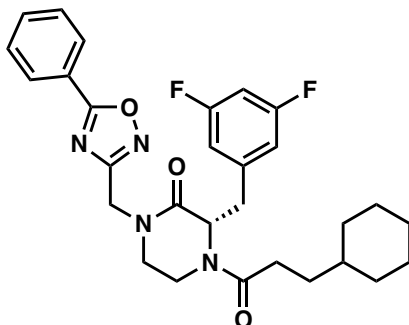


Procedure N3 (9 mg; yield=58%). ¹H NMR (500 MHz, DMSO-*d*₆) δ 8.14 (dd, *J* = 8.5, 5.6 Hz, 2H), 7.48 (t, *J* = 8.8, 1.9 Hz, 2H), 7.12 – 6.96 (m, 2H), 6.85 (h, *J* = 4.1 Hz, 1H), 5.03 (t, *J* = 6.6 Hz, 1H), 4.87 – 4.79 (m, 1H), 4.74 – 4.66 (m, 1H), 4.50 – 4.42 (m, 0H), 3.91 (dt, *J* = 13.8, 3.6 Hz, 1H), 3.57 (td, *J* = 11.6, 4.1 Hz, 1H), 3.51 – 3.41 (m, 1H), 3.41 – 3.25 (m, 1H), 3.22 – 3.10 (m, 2H), 2.38 – 2.28 (m, 1H), 2.27 – 2.17 (m, 1H), 2.04 (ddd, *J* = 15.5, 9.2, 5.6 Hz, 0H), 1.67 – 1.52 (m, 4H), 1.52 – 1.39 (m, 1H), 1.32 – 1.15 (m, 1H), 1.15 – 1.00 (m, 5H), 1.00 – 0.87 (m, 0H), 0.87 – 0.72 (m, 1H), 0.72 – 0.61 (m, 1H). ¹³C NMR (101 MHz, DMSO-*d*₆) δ 175.1, 171.7, 171.5, 167.9, 167.5, 167.1, 166.7, 164.2, 163.7, 163.6, 161.6, 161.3, 161.2, 142.3, 131.2, 131.2, 120.4, 117.4, 117.2, 113.6, 113.3, 113.2, 112.9, 102.7, 102.3, 102.1, 59.6, 55.6, 47.7, 47.1, 42.3, 42.0, 40.0, 37.0, 36.9, 36.3, 35.0, 33.0, 32.9, 32.6, 32.3, 30.2, 29.3, 26.5, 26.2, 26.1.

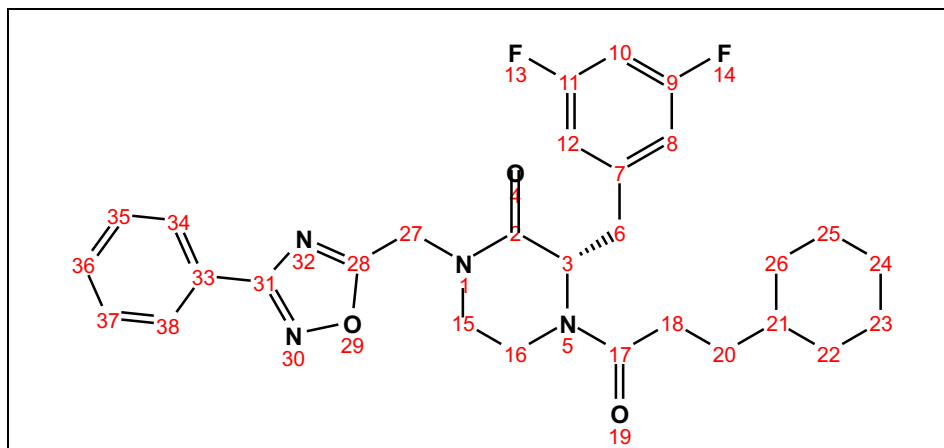


2	167.5 – 167.9		
3	55.6 – 59.6, CH	4.67 – 5.07 (m)	
6	35.0 – 40.1, CH ₂	3.12 – 4.50 (m)	
7	142.3		
8	112.9 – 113.6, CH	6.81 – 7.06 (m)	
9	161.2 – 163.7		
10	102.1 – 102.7, CH	6.97 – 7.12 (m)	
11	161.2 – 163.7		
12	112.9 – 113.6, CH	6.81 – 7.06 (m)	
15	36.3 – 37.0, CH ₂	3.09 – 3.23 (m)	
16	47.1 – 47.7, CH ₂	3.33 – 3.61 (m)	
17	171.5 – 171.7		
18	30.0, CH ₂	2.17 – 2.28 (m)	
20	29.3 – 32.6, CH ₂	0.92 – 2.08 (m)	
21	36.9 – 37.0, CH	0.91 – 1.12 (m)	
22	32.9 – 33.0, CH ₂	0.61 – 1.66 (m)	
23	26.1 – 26.2, CH ₂	1.02 – 1.66 (m)	
24	26.5, CH ₂	1.02 – 1.66 (m)	
25	26.1 – 26.2, CH ₂	1.02 – 1.66 (m)	
26	32.9 – 33.0, CH ₂	0.61 – 1.66 (m)	
27	42.0 – 42.3, CH ₂	4.66 – 4.79 (m)	
28	167.1		
31	175.1		
33	120.4		
34	131.2, CH	8.14 (dd)	8.5, 5.6
35	117.2 – 117.4, CH	7.48 (t)	8.8
36	164.2 – 166.7		
37	117.2 – 117.4, CH	7.48 (t)	8.8
38	131.2, CH	8.14 (dd)	8.5, 5.6

(S)-4-(3-cyclohexylpropanoyl)-3-(3,5-difluorobenzyl)-1-((5-phenyl-1,2,4-oxadiazol-3-yl)methyl)piperazin-2-one (2.112):

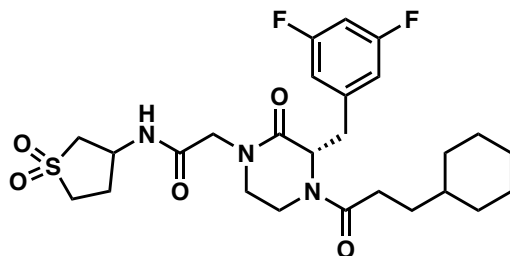


Procedure N3 (10 mg; yield=63%). ^1H NMR (500 MHz, $\text{DMSO-}d_6$) δ 7.98 (d, $J = 6.8$ Hz, 2H), 7.63 – 7.52 (m, 3H), 7.14 – 6.98 (m, 2H), 6.87 (h, $J = 4.1$ Hz, 1H), 5.06 (t, $J = 6.7$ Hz, 1H), 5.02 – 4.85 (m, 2H), 4.72 (d, $J = 7.5$ Hz, 0H), 4.53 – 4.45 (m, 0H), 3.96 (d, $J = 14.1$ Hz, 1H), 3.64 (td, $J = 11.6, 4.1$ Hz, 1H), 3.56 – 3.42 (m, 1H), 3.38 (ddd, $J = 14.5, 11.0, 3.7$ Hz, 1H), 3.28 – 3.17 (m, 1H), 3.13 (d, $J = 6.8$ Hz, 1H), 2.39 – 2.29 (m, 1H), 2.29 – 2.19 (m, 1H), 2.09 – 2.00 (m, 0H), 1.66 – 1.52 (m, 4H), 1.52 – 1.40 (m, 1H), 1.34 – 1.17 (m, 3H), 1.17 – 1.01 (m, 4H), 1.01 – 0.90 (m, 0H), 0.85 – 0.73 (m, 1H), 0.73 – 0.62 (m, 0H). ^{13}C NMR (101 MHz, $\text{DMSO-}d_6$) δ 176.7, 171.7, 171.6, 168.1, 167.9, 167.5, 164.0, 163.9, 163.7, 163.6, 161.6, 161.4, 161.3, 161.2, 142.4, 142.3, 142.2, 132.1, 129.7, 129.1, 127.5, 127.2, 126.4, 113.6, 113.4, 113.2, 113.1, 113.0, 112.9, 110.0, 102.8, 102.6, 102.4, 102.1, 59.6, 55.5, 48.3, 47.6, 43.2, 43.0, 37.1, 36.9, 36.8, 36.2, 35.0, 33.0, 32.9, 32.6, 32.3, 30.2, 29.3, 26.6, 26.5, 26.2, 26.1.



Position	δC , type	δH	J (Hz)
2	167.9 – 168.1		
3	55.5 – 59.6, CH	4.70 – 5.09 (m)	
6	35.0 – 40.1, CH ₂	3.20 – 4.53 (m)	
7	142.2 – 142.4		
8	112.9 – 113.6, CH	6.83 – 7.07 (m)	
9	161.2 – 164.0		
10	102.1 – 102.8, CH	6.99 – 7.13 (m)	
11	161.2 – 164.0		
12	112.9 – 113.6, CH	6.83 – 7.07 (m)	
15	36.2 – 36.8, CH ₂	3.10 – 3.24 (m)	
16	47.6 – 48.3, CH ₂	3.40 – 3.69 (m)	
17	171.6 -171.7		
18	30.2, CH ₂	2.19 – 2.29 (m)	
20	29.3 – 32.6, CH ₂	0.93 – 2.08 (m)	
21	36.9 – 37.1, CH	0.92 – 1.11 (m)	
22	32.9 – 33.0, CH ₂	0.63 – 1.66 (m)	
23	26.1 – 26.2, CH ₂	1.03 – 1.66 (m)	
24	26.5 – 26.6, CH ₂	1.03 – 1.66 (m)	
25	26.1 – 26.2, CH ₂	1.03 – 1.66 (m)	
26	32.9 – 33.0, CH ₂	0.63 – 1.66 (m)	
27	43.0 – 43.2, CH ₂	4.85 – 5.00 (m)	
28	167.5		
31	176.7		
33	126.4		
34	127.2 – 127.5, CH	7.95 – 8.02 (d)	6.8
35	129.1 – 129.7, CH	7.52 – 7.60 (m)	
36	132.1, CH	7.55 – 7.62 (m)	
37	129.1 – 129.7, CH	7.52 – 7.60 (m)	
38	127.2 – 127.5, CH	7.95 – 8.02 (d)	6.8

2-((*S*)-4-(3-cyclohexylpropanoyl)-3-(3,5-difluorobenzyl)-2-oxopiperazin-1-yl)-*N*-(1,1-dioxidotetrahydrothiophen-3-yl) acetamide (2.113):

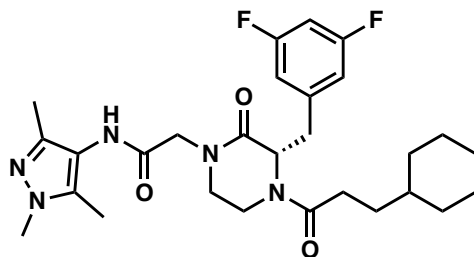


Procedure N3 (10 mg; yield=62%). ^1H NMR (500 MHz, $\text{DMSO-}d_6$) δ 8.45 (d, $J = 6.7$ Hz, 1H), 7.15 – 6.99 (m, 2H), 6.89 – 6.80 (m, 1H), 4.96 (d, $J = 7.4$ Hz, 1H), 4.64 – 4.56 (m, 0H), 4.50 – 4.37 (m, 2H), 4.11 – 3.93 (m, 2H), 3.93 – 3.82 (m, 1H), 3.52 – 3.32 (m, 2H), 3.32 – 3.18 (m, 2H), 3.20 – 3.02 (m, 3H), 2.91 – 2.83 (m, 1H), 2.43 – 2.24 (m, 2H), 2.24 – 2.14 (m, 1H), 2.09 – 1.94 (m, 1H), 1.66 – 1.53 (m, 5H), 1.48 – 1.38 (m, 2H), 1.34 – 1.16 (m, 1H), 1.17 – 1.01 (m, 2H), 0.97 – 0.89 (m, 1H), 0.87 – 0.73 (m, 1H), 0.72 – 0.64 (m, 1H). ^{13}C NMR (101 MHz, $\text{DMSO-}d_6$) δ 171.5, 171.4, 168.0, 167.9, 167.6, 167.1, 163.7, 163.6, 161.3, 161.1, 142.5, 113.6, 113.3, 113.1, 112.9, 102.3, 59.5, 55.7, 55.5, 50.8, 49.4, 48.3, 47.6, 46.2, 39.7, 37.1, 36.9, 36.5, 35.0, 33.0, 32.9, 32.8, 32.6, 32.2, 31.7, 30.2, 29.5, 29.3, 29.2, 29.1, 29.0, 28.7, 27.0, 26.6, 26.5, 26.2, 26.1, 25.5.

Position	δC , type	δH	J (Hz)
2	167.1 – 167.6		
3	55.5 – 59.5, CH	4.57 – 5.00 (m)	
6	35.0 – 39.7, CH_2	3.15 – 4.43 (m)	
7	142.5		

8	112.9 – 113.6, CH	6.83 – 7.06 (m)	
9	161.1 – 163.7		
10	102.3, CH	7.00 – 7.12 (m)	
11	161.1 – 163.7		
12	112.9 – 113.6, CH	6.83 – 7.06 (m)	
15	36.5 – 37.1, CH ₂	3.04 – 3.20 (m)	
16	47.6 – 48.3, CH ₂	3.19 – 3.50 (m)	
17	171.4 – 171.5		
18	30.2, CH ₂	2.16 – 2.36 (m)	
20	29.0 – 32.6, CH ₂	0.91 – 1.31 (m)	
21	36.9, CH	1.04 – 1.10 (m)	
22	32.8 – 33.0, CH ₂	0.65 – 1.66 (m)	
23	26.1 – 26.2, CH ₂	1.04 – 1.68 (m)	
24	26.5 – 26.6, CH ₂	1.04 – 1.68 (m)	
25	26.1 – 26.2, CH ₂	1.04 – 1.68 (m)	
26	32.8 – 33.0, CH ₂	0.65 – 1.66 (m)	
27	49.4, CH ₂	3.88 – 4.07 (m)	
28	167.9 – 168.0		
29		8.45 (d)	6.7
31	46.2, CH	4.39 – 4.50 (m)	
32	55.7, CH ₂	2.83 – 3.46 (m)	
34	50.8, CH ₂	3.11 – 3.32 (m)	
35	25.5, CH ₂	1.42 – 1.49 (m)	

(S)-2-(4-(3-cyclohexylpropanoyl)-3-(3,5-difluorobenzyl)-2-oxopiperazin-1-yl)-N-(1,3,5-trimethyl-1H-pyrazol-4-yl)acetamide (2.114):

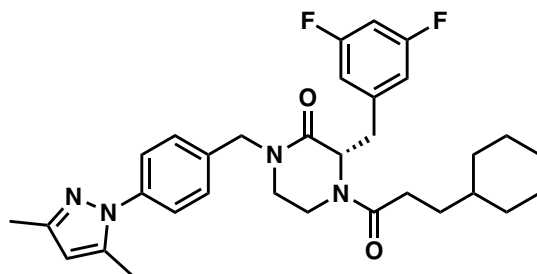


Procedure N3 (9 mg; yield=57%). ¹H NMR (500 MHz, DMSO-*d*₆) δ 9.06 (d, *J* = 9.0 Hz, 1H), 7.14 – 7.01 (m, 1H), 7.04 – 6.98 (m, 1H), 6.91 – 6.77 (m, 2H), 4.98 (t, *J* = 6.9 Hz, 1H), 4.64 – 4.58 (m, 0H), 4.46 – 4.40 (m, 0H), 4.22 – 4.01 (m, 2H), 3.91 – 3.81 (m, 1H), 3.77 – 3.57 (m, 2H), 3.60 (s, 2H), 3.57 – 3.45 (m, 1H), 3.43 – 3.32 (m, 0H), 3.32 – 3.23 (m, 1H), 3.23 – 3.12 (m, 1H), 3.12 – 3.03 (m, 1H), 2.37 – 2.27 (m, 0H), 2.25 – 2.14 (m, 1H), 2.14 – 2.01 (m, 3H), 2.01 – 1.84 (m, 3H), 1.67 – 1.53 (m, 5H), 1.48 – 1.39 (m, 1H), 1.33 – 0.99 (m, 3H), 0.96 – 0.88 (m, 1H), 0.87 – 0.74 (m, 2H), 0.72 – 0.61 (m, 1H). ¹³C NMR (101 MHz, DMSO-*d*₆) δ 171.4, 167.7, 167.3, 165.2, 163.7, 163.6, 161.3, 161.1, 142.6, 142.3, 142.1, 135.6, 134.4, 118.6, 115.2, 113.1, 112.9, 102.3, 59.5, 55.5, 55.4, 49.9, 48.4, 47.7, 40.1, 37.1, 36.9, 36.5, 36.4, 35.0, 33.0, 32.9, 32.8, 32.6, 32.2, 30.2, 26.6, 26.5, 26.2, 26.1, 11.6, 11.4, 9.5, 9.3.

Position	δ C, type	δ H	<i>J</i> (Hz)
2	165.2		
3	55.4 – 59.5, CH	4.59 – 5.01 (m)	
6	35.0 – 40.1, CH ₂	3.19 – 4.46 (m)	
7	142.1 – 142.3		
8	112.9 – 113.1, CH	6.83 – 7.06 (m)	
9	161.1 – 163.7		
10	102.3, CH	7.00 – 7.13 (m)	
11	161.1 – 163.7		
12	112.9 – 113.1, CH	6.83 – 7.06 (m)	

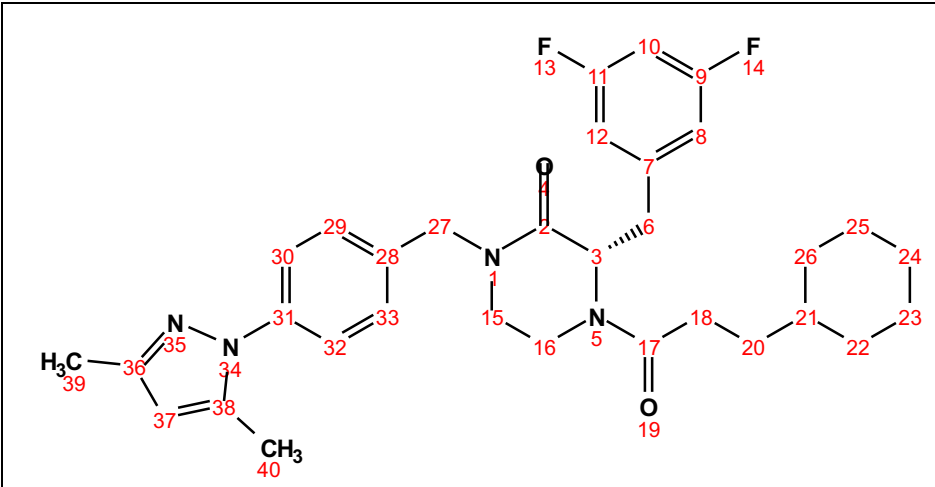
15	36.4 – 37.1, CH ₂	3.06 – 3.21 (m)	
16	47.7 – 48.4, CH ₂	3.25 – 3.57 (m)	
17	171.4		
18	30.2, CH ₂	2.17 – 2.36 (m)	
20	29.3 – 32.6, CH ₂	0.91 – 1.32 (m)	
21	36.9, CH	1.04 – 1.10 (m)	
22	32.8 – 33.0, CH ₂	0.64 – 1.67 (m)	
23	26.1 – 26.2, CH ₂	1.03 – 1.67 (m)	
24	26.5 – 26.6, CH ₂	1.03 – 1.67 (m)	
25	26.1 – 26.2, CH ₂	1.03 – 1.67 (m)	
26	32.8 – 33.0, CH ₂	0.64 – 1.67 (m)	
27	49.9, CH ₂	4.02 – 4.22 (m)	
28	167.3 – 167.7		
29		9.06 (d)	9.0
31	115.2 – 118.6		
32	142.6		
35	134.4 – 135.6		
36	9.3 – 9.5, CH ₃	1.98 – 2.14 (m)	
37	36.5, CH ₃	3.57 – 3.67 (m)	
38	11.4 – 11.6, CH ₃	1.90 – 2.03 (m)	

(S)-4-(3-cyclohexylpropanoyl)-3-(3,5-difluorobenzyl)-1-(4-(3,5-dimethyl-1H-pyrazol-1-yl)benzyl)piperazin-2-one (2.115):



Procedure N3 (16 mg; yield=83%). ¹H NMR (500 MHz, DMSO-*d*₆) δ 7.49 – 7.42 (m, 2H), 7.42 – 7.30 (m, 2H), 7.16 – 7.00 (m, 2H), 6.92 – 6.84 (m, 1H), 6.06 (s, 1H), 5.09 – 5.04 (m, 1H), 4.81 – 4.74 (m, 1H), 4.74 – 4.68 (m, 1H), 4.48 – 4.38 (m, 1H), 3.87 (d, *J* = 13.9 Hz, 0H), 3.39 (td, *J* =

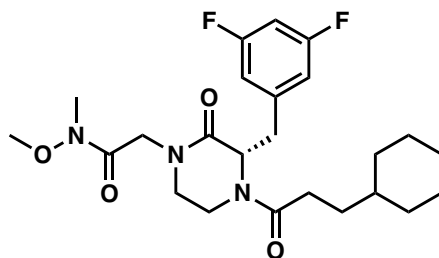
11.8, 4.2 Hz, 1H), 3.29 – 3.21 (m, 2H), 3.21 – 3.15 (m, 1H), 3.15 – 3.06 (m, 1H), 2.28 (s, 3H), 2.25 – 2.13 (m, 1H), 2.16 (s, 3H), 2.13 – 1.96 (m, 0H), 1.65 – 1.54 (m, 5H), 1.53 – 1.41 (m, 1H), 1.33 – 1.16 (m, 2H), 1.16 – 1.02 (m, 1H), 0.95 (q, $J = 12.2, 9.1$ Hz, 1H), 0.89 – 0.80 (m, 0H), 0.78 (d, $J = 11.5$ Hz, 2H), 0.74 – 0.63 (m, 1H). ^{13}C NMR (101 MHz, DMSO- d_6) δ 171.6, 171.5, 167.3, 166.9, 163.8, 163.6, 161.3, 161.2, 148.3, 142.6, 142.5, 139.5, 139.3, 135.9, 128.7, 128.6, 124.5, 113.6, 113.3, 113.2, 113.1, 113.0, 112.9, 107.6, 102.8, 102.7, 102.4, 102.1, 77.0, 59.5, 55.5, 49.3, 49.2, 46.7, 46.1, 40.1, 37.1, 36.9, 36.4, 34.9, 33.0, 32.9, 32.6, 32.3, 31.4, 30.1, 29.2, 26.5, 26.2, 26.1, 14.4, 13.8, 12.6.



Position	δC , type	δH	J (Hz)
2	166.9 – 167.3		
3	55.5 – 59.5, CH	4.68 – 5.09 (m)	
6	36.4 – 40.1, CH ₂	3.09 – 4.48 (m)	
7	142.5 – 142.6		
8	112.9 – 113.6, CH	6.85 – 7.06 (m)	
9	161.2 – 163.8		
10	102.1 – 102.8, CH	7.03 – 7.14 (m)	
11	161.2 – 163.8		
12	112.9 – 113.6, CH	6.85 – 7.06 (m)	
15	36.4 – 37.1, CH ₂	3.15 – 3.28 (m)	
16	46.1 – 46.7, CH ₂	3.08 – 3.45 (m)	

17	171.5 – 171.6		
18	30.1, CH ₂	2.17 – 2.36 (m)	
20	29.3 – 32.6, CH ₂	0.92 – 2.11 (m)	
21	36.9 – 37.1, CH	0.92 – 1.11 (m)	
22	32.9 – 33.0, CH ₂	0.65 – 1.65 (m)	
23	26.1 – 26.2, CH ₂	1.03 – 1.67 (m)	
24	26.5, CH ₂	1.03 – 1.67 (m)	
25	26.1 – 26.2, CH ₂	1.03 – 1.67 (m)	
26	32.9 – 33.0, CH ₂	0.65 – 1.65 (m)	
27	49.2 – 49.3, CH ₂	4.39 – 4.81 (m)	
28	139.3		
29	128.6 – 128.7, CH	7.29 – 7.46 (m)	
30	124.5, CH	7.41 – 7.49 (m)	
31	135.9		
32	124.5, CH	7.41 – 7.49 (m)	
33	128.6 – 128.7, CH	7.29 – 7.46 (m)	
36	148.3		
37	107.6, CH	6.06 (s)	
38	139.5		
39	12.6, CH ₃	2.28 (s)	
40	13.8, CH ₃	2.16 (s)	

(S)-2-(4-(3-cyclohexylpropanoyl)-3-(3,5-difluorobenzyl)-2-oxopiperazin-1-yl)-N-methoxy-N-methylacetamide (2.116):



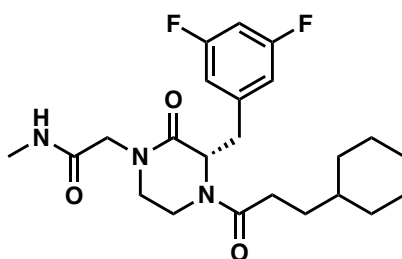
Procedure N3 (12 mg; yield=64%). ¹H NMR (500 MHz, DMSO-*d*₆) δ 7.14 – 6.98 (m, 2H), 6.91 – 6.83 (m, 1H), 4.96 (dd, *J* = 7.8, 5.7 Hz, 1H), 4.64 – 4.57 (m, 0H), 4.41 (dd, *J* = 13.2, 4.1 Hz, 0H), 4.35 – 4.20 (m, 2H), 3.87 (dt, *J* = 13.6, 3.7 Hz, 1H), 3.71 (s, 3H), 3.46 (td, *J* = 11.5, 4.0 Hz, 1H),

3.38 – 3.30 (m, 1H), 3.27 – 3.03 (m, 3H), 3.10 (s, 3H), 2.37 – 2.27 (m, 1H), 2.25 – 2.14 (m, 1H), 2.04 – 1.93 (m, 0H), 1.66 – 1.52 (m, 5H), 1.49 – 1.40 (m, 1H), 1.33 – 1.17 (m, 3H), 1.17 – 1.01 (m, 2H), 0.99 – 0.88 (m, 0H), 0.88 – 0.73 (m, 1H), 0.72 – 0.62 (m, 1H). ¹³C NMR (101 MHz, DMSO-*d*₆) δ 171.6, 171.5, 167.8, 167.3, 164.0, 163.9, 163.7, 163.6, 161.6, 161.4, 161.3, 161.1, 142.5, 142.4, 113.6, 113.3, 113.2, 112.9, 102.7, 102.5, 102.3, 61.6, 59.5, 55.4, 48.2, 47.6, 47.5, 37.1, 37.0, 36.9, 36.5, 35.1, 33.0, 32.9, 32.8, 32.6, 32.2, 30.2, 29.3, 26.6, 26.5, 26.2, 26.1.

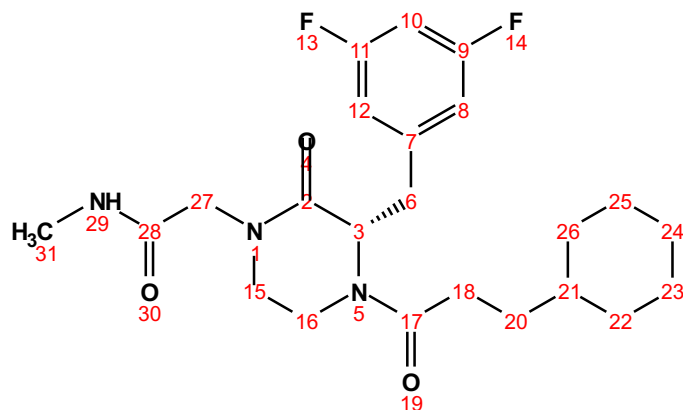
Position	δ C, type	δ H	<i>J</i> (Hz)
2	167.3		
3	55.4 – 59.5, CH	4.58 – 5.00 (m)	
6	35.1 – 40.0, CH ₂	3.16 – 4.44 (m)	
7	142.4 – 142.5		
8	112.9 – 113.6, CH	6.83 – 7.07 (m)	
9	161.1 – 163.9		
10	102.3 – 102.7, CH	6.99 – 7.13 (m)	
11	161.1 – 163.9		
12	112.9 – 113.6, CH	6.83 – 7.07 (m)	
15	36.5 – 37.0, CH ₂	3.05 – 3.20 (m)	
16	47.5 – 48.2, CH ₂	3.19 – 3.49 (m)	
17	171.5 – 171.6		
18	30.2, CH ₂	2.14 – 2.37 (m)	
20	29.3 – 32.6, CH ₂	0.90 – 2.02 (m)	
21	36.9 – 37.1, CH	0.90 – 1.13 (m)	
22	32.8 – 33.0, CH ₂	0.64 – 1.66 (m)	

23	26.1 – 26.2, CH ₂	1.04 – 1.67 (m)	
24	26.5 – 26.6, CH ₂	1.04 – 1.67 (m)	
25	26.1 – 26.2, CH ₂	1.04 – 1.67 (m)	
26	32.8 – 33.0, CH ₂	0.64 – 1.66 (m)	
27	47.6, CH ₂	4.20 – 4.35 (m)	
28	167.8		
32	32.2, CH ₃	3.10 (s)	
33	61.6, CH ₃	3.71 (s)	

(S)-2-(4-(3-cyclohexylpropanoyl)-3-(3,5-difluorobenzyl)-2-oxopiperazin-1-yl)-N-methylacetamide (2.117):

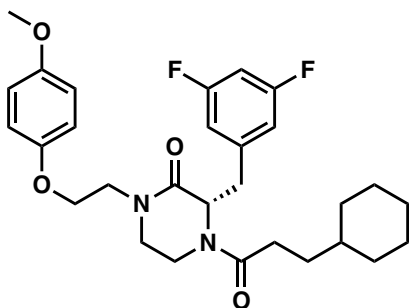


Procedure N3 (7 mg; yield=54%). ¹H NMR (500 MHz, DMSO-*d*₆) δ 7.89 – 7.82 (m, 1H), 7.14 – 6.97 (m, 2H), 6.90 – 6.80 (m, 1H), 5.00 – 4.93 (m, 1H), 4.61 – 4.55 (m, 0H), 4.44 – 4.28 (m, 0H), 4.04 – 3.80 (m, 3H), 3.76 – 3.66 (m, 0H), 3.52 – 3.40 (m, 1H), 3.40 – 3.32 (m, 1H), 3.26 – 3.03 (m, 3H), 2.61 – 2.57 (m, 3H), 2.37 – 2.27 (m, 1H), 2.24 – 2.14 (m, 1H), 2.05 – 1.94 (m, 0H), 1.68 – 1.53 (m, 5H), 1.46 – 1.36 (m, 1H), 1.33 – 0.98 (m, 4H), 0.98 – 0.73 (m, 2H), 0.72 – 0.62 (m, 1H). ¹³C NMR (101 MHz, DMSO-*d*₆) δ 171.5, 171.4, 168.2, 167.6, 167.1, 163.9, 163.7, 163.6, 161.6, 161.3, 161.1, 142.7, 142.6, 142.5, 113.5, 113.3, 113.1, 112.9, 102.7, 102.5, 102.3, 102.0, 59.5, 55.5, 55.3, 49.9, 49.7, 48.3, 47.6, 39.6, 37.1, 37.0, 36.9, 36.5, 34.9, 33.1, 32.9, 32.8, 32.6, 32.2, 30.2, 29.2, 26.6, 26.5, 26.2, 26.1, 25.9.



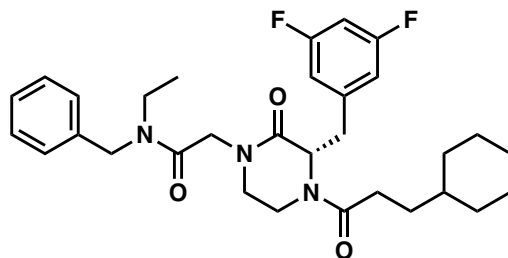
Position	δC , type	δH	J (Hz)
2	167.1 – 167.6		
3	55.3 – 59.5, CH	4.56 – 5.00 (m)	
6	34.9 – 39.6, CH ₂	3.19 – 4.44 (m)	
7	142.5 – 142.7		
8	112.9 – 113.5, CH	6.83 – 7.05 (m)	
9	161.1 – 163.9		
10	102.0 – 102.7, CH	7.00 – 7.13 (m)	
11	161.1 – 163.9		
12	112.9 – 113.5, CH	6.83 – 7.05 (m)	
15	36.5 – 37.1, CH ₂	3.05 – 3.20 (m)	
16	47.6 – 48.3, CH ₂	3.18 – 3.50 (m)	
17	171.4 – 171.5		
18	30.2, CH ₂	2.15 – 2.36 (m)	
20	29.2 – 32.6, CH ₂	0.90 – 1.31 (m)	
21	36.9, CH	1.05 – 1.10 (m)	
22	32.8 – 33.1, CH ₂	0.65 – 1.66 (m)	
23	26.1 – 26.2, CH ₂	1.05 – 1.68 (m)	
24	26.5 – 26.6, CH ₂	1.05 – 1.68 (m)	
25	26.1 – 26.2, CH ₂	1.05 – 1.68 (m)	
26	32.8 – 33.1, CH ₂	0.65 – 1.66 (m)	
27	49.7 – 49.9, CH ₂	3.81 – 4.04 (m)	
28	168.2		
29		7.82 – 7.89 (m)	
31	25.9, CH ₃	2.57 – 1.61 (m)	

(S)-4-(3-cyclohexylpropanoyl)-3-(3,5-difluorobenzyl)-1-(2-(4-methoxyphenoxy)ethyl) piperazin-2-one (2.118):



Procedure N3 (12 mg; yield=75%). ¹H NMR (600 MHz, Chloroform-*d*) δ 6.82 – 6.75 (m, 3H), 6.75 – 6.71 (m, 1H), 6.71 – 6.63 (m, 2H), 6.57 (tt, *J* = 8.9, 2.3 Hz, 1H), 5.12 (t, *J* = 5.3 Hz, 1H), 4.68 (dd, *J* = 13.9, 4.2 Hz, 0H), 4.48 – 4.43 (m, 0H), 4.14 – 4.02 (m, 2H), 3.79 – 3.66 (m, 5H), 3.62 – 3.55 (m, 1H), 3.51 (ddd, *J* = 12.3, 10.9, 3.8 Hz, 1H), 3.38 (ddd, *J* = 12.2, 4.1, 1.7 Hz, 1H), 3.33 – 3.16 (m, 2H), 3.05 (dd, *J* = 13.8, 9.5 Hz, 0H), 2.91 – 2.78 (m, 1H), 2.33 – 2.21 (m, 1H), 1.95 – 1.86 (m, 0H), 1.69 – 1.64 (m, 2H), 1.64 – 1.58 (m, 3H), 1.57 – 1.47 (m, 1H), 1.47 – 1.41 (m, 2H), 1.36 – 1.27 (m, 1H), 1.25 – 1.02 (m, 3H), 1.01 – 0.92 (m, 0H), 0.92 – 0.82 (m, 1H), 0.76 – 0.65 (m, 1H). ¹³C NMR (151 MHz, Chloroform-*d*) δ 172.2, 171.6, 167.4, 166.7, 164.0, 163.9, 163.6, 163.5, 162.3, 162.2, 162.0, 161.9, 154.1, 152.4, 152.3, 141.4, 141.3, 141.3, 140.8, 140.7, 115.2, 114.7, 112.6, 112.5, 112.4, 102.9, 102.8, 102.6, 102.4, 102.2, 102.1, 67.3, 66.7, 60.0, 56.2, 55.7, 48.9, 48.6, 47.7, 47.5, 41.4, 37.9, 37.3, 37.2, 36.4, 35.3, 33.0, 32.9, 32.8, 32.5, 32.0, 31.0, 29.7, 26.5, 26.4, 26.1.

(S)-N-benzyl-2-(4-(3-cyclohexylpropanoyl)-3-(3,5-difluorobenzyl)-2-oxopiperazin-1-yl)-N-ethylacetamide (2.119):



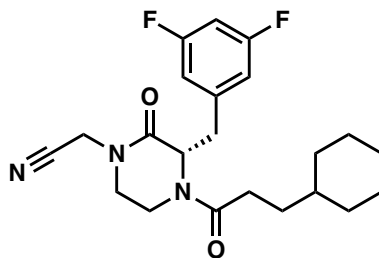
Procedure N3 (19 mg; yield=88%). ^1H NMR (500 MHz, $\text{DMSO-}d_6$) δ 7.38 (t, $J = 7.6$ Hz, 1H), 7.35 – 7.28 (m, 2H), 7.27 – 7.21 (m, 2H), 7.14 – 6.98 (m, 2H), 6.88 (td, $J = 8.2, 2.4$ Hz, 1H), 5.00 – 4.93 (m, 1H), 4.66 – 4.57 (m, 0H), 4.57 – 4.47 (m, 2H), 4.46 – 4.40 (m, 0H), 4.40 – 4.15 (m, 2H), 3.92 – 3.83 (m, 1H), 3.55 – 3.42 (m, 1H), 3.41 – 3.32 (m, 1H), 3.30 – 3.21 (m, 3H), 3.20 – 3.14 (m, 1H), 3.14 – 3.01 (m, 1H), 2.38 – 2.27 (m, 1H), 2.26 – 2.14 (m, 1H), 2.04 – 1.91 (m, 0H), 1.66 – 1.52 (m, 5H), 1.51 – 1.38 (m, 1H), 1.34 – 1.17 (m, 2H), 1.17 – 1.02 (m, 4H), 0.98 (t, $J = 7.1$ Hz, 1H), 0.96 – 0.90 (m, 0H), 0.89 – 0.73 (m, 2H), 0.73 – 0.62 (m, 1H). ^{13}C NMR (101 MHz, $\text{DMSO-}d_6$) δ 171.6, 171.4, 167.7, 167.4, 167.2, 167.1, 163.7, 163.6, 161.3, 161.1, 142.5, 138.4, 137.8, 129.1, 128.8, 128.0, 127.8, 127.4, 127.2, 113.2, 112.9, 102.7, 102.3, 59.6, 55.8, 55.5, 49.5, 48.6, 48.3, 48.2, 48.1, 48.0, 47.6, 41.2, 41.0, 40.1, 37.1, 36.9, 36.5, 36.4, 35.1, 33.0, 32.9, 32.8, 32.6, 32.2, 30.2, 29.3, 26.6, 26.5, 26.2, 26.1, 14.0, 13.0.

Position	δC , type	δH	J (Hz)
2	167.1 – 167.2		

3	55.5 – 59.6, CH	4.57 – 5.02 (m)	
6	35.1 – 40.1, CH ₂	3.18 – 4.46 (m)	
7	142.5		
8	112.9 – 113.2, CH	6.83 – 7.08 (m)	
9	161.1 – 163.7		
10	102.3 – 102.7, CH	6.99 – 7.13 (m)	
11	161.1 – 163.7		
12	112.9 – 113.2, CH	6.83 – 7.08 (m)	
15	36.4 – 37.1, CH ₂	3.03 – 3.23 (m)	
16	47.6 – 48.3, CH ₂	3.18 – 3.54 (m)	
17	171.4 – 171.6		
18	30.2, CH ₂	2.14 – 2.38 (m)	
20	29.3 – 32.6, CH ₂	0.90 – 2.02 (m)	
21	36.9 – 37.1, CH	0.90 – 1.14 (m)	
22	32.8 – 33.0, CH ₂	0.64 – 1.67 (m)	
23	26.1 – 26.2, CH ₂	1.04 – 1.68 (m)	
24	26.5 – 26.6, CH ₂	1.04 – 1.68 (m)	
25	26.1 – 26.2, CH ₂	1.04 – 1.68 (m)	
26	32.8 – 33.0, CH ₂	0.64 – 1.67 (m)	
27	48.1 – 48.6, CH ₂	4.16 – 4.40 (m)	
28	167.4 – 167.7	0.94 – 1.15 (m)	
31	48.0 – 49.5, CH ₂	4.45 – 4.59 (m)	
32	41.0 – 41.2, CH ₂	3.21 – 3.33 (m)	
33	13.0 – 14.0, CH ₃		
34	137.8 – 138.4		
35	128.8 – 129.1, CH	7.28 – 7.41 (m)	
36	127.2 – 128.0, CH	7.20 – 7.33 (m)	
37	127.2 – 128.0, CH	7.20 – 7.33 (m)	
38	127.2 – 128.0, CH	7.20 – 7.33 (m)	
39	128.8 – 129.1, CH	7.28 – 7.41 (m)	

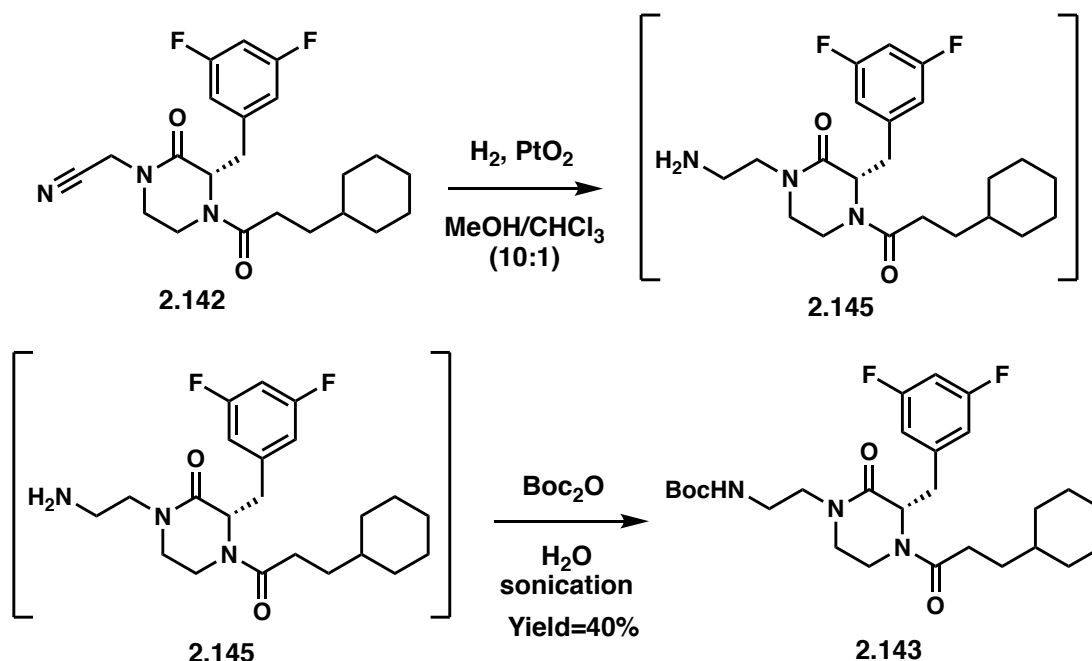
(S)-2-(4-(3-cyclohexylpropanoyl)-3-(3,5-difluorobenzyl)-2-oxopiperazin-1-yl)acetonitrile

(2.142):



Procedure N3 (11mg; yield=41%). ^1H NMR (500 MHz, Chloroform-*d*) δ 6.79 – 6.67 (m, 3H), 5.32 – 5.26 (m, 1H), 4.87 (d, J = 14.2 Hz, 0H), 4.58 (d, J = 9.8 Hz, 0H), 4.53 – 4.43 (m, 1H), 4.39 – 4.27 (m, 1H), 3.77 (d, J = 14.1 Hz, 0H), 3.64 – 3.50 (m, 1H), 3.38 – 3.32 (m, 1H), 3.31 – 3.18 (m, 2H), 3.16 – 2.93 (m, 2H), 2.38 – 2.26 (m, 1H), 2.00 – 1.90 (m, 0H), 1.75 – 1.53 (m, 4H), 1.53 – 1.42 (m, 2H), 1.40 – 1.30 (m, 1H), 1.31 – 1.06 (m, 5H), 1.01 (td, J = 8.3, 7.8, 4.2 Hz, 0H), 0.97 – 0.83 (m, 1H), 0.82 – 0.69 (m, 1H). ^{13}C NMR (126 MHz, Chloroform-*d*) δ 172.3, 171.7, 167.6, 166.9, 164.3, 164.2, 164.0, 163.9, 162.2, 162.0, 161.9, 140.7, 140.6, 140.2, 114.5, 114.3, 112.6, 112.5, 112.4, 103.3, 103.1, 103.0, 102.9, 102.7, 102.5, 60.2, 56.2, 47.1, 46.9, 40.6, 37.6, 37.3, 37.2, 36.4, 34.7, 34.6, 34.5, 33.1, 33.0, 32.9, 32.5, 32.0, 30.9, 29.7, 29.6, 26.5, 26.4, 26.1.

***tert*-butyl (S)-2-(4-(3-cyclohexylpropanoyl)-3-(3,5-difluorobenzyl)-2-oxopiperazin-1-yl)ethylcarbamate (2.143):**



In a sealable vial, **2.142** (10 mg; 0.025 mmol) and 20 mg of platinum(IV) oxide (PtO_2) were dissolved in 10 mL of a mixture of methanol and chloroform (10:1). A balloon of hydrogen was connected to the sealed vial and the reaction mixture was stirred overnight. The crude was concentrated under nitrogen flow, filtered through a celite plug and concentrated in vacuo.

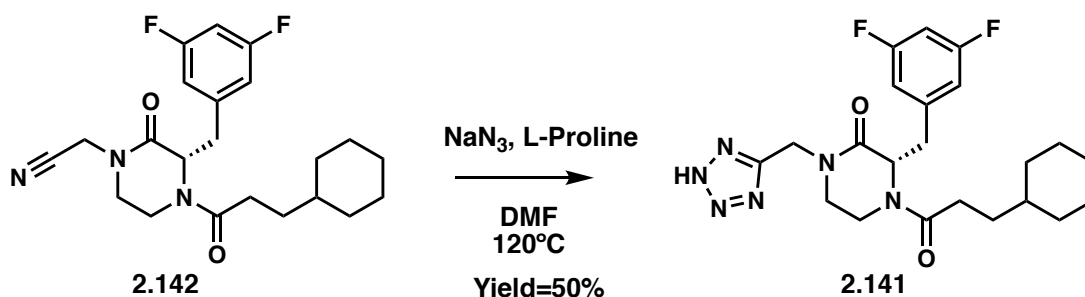
In a vial, the crude and Di-tert-butyl pyrocarbonate (50 mg; 0.23 mmol) were sonicated in 3 mL of H_2O overnight @ RT. The reaction was washed with a saturated solution of NaHCO_3 (20 mL) and the organic layer was extracted with EtOAc (3 times). The organic layers were combined, washed with brine before being dried over Na_2SO_4 and filtered. The filtrate was concentrated in vacuo and purified by flash column chromatography (Silica gel, 1-10% MeOH in DCM) to yield **2.143** (4 mg; yield=40%). ^1H NMR (500 MHz, $\text{DMSO}-d_6$) δ 7.14 – 6.94 (m, 1H), 6.91 – 6.88 (m, 1H), 6.87 – 6.79 (m, 1H), 6.65 (s, 1H), 4.94 – 4.88 (m, 1H), 4.54 – 4.48 (m, 0H), 4.44 – 4.37 (m, 0H), 4.04 – 3.73 (m, 1H), 3.48 – 3.40 (m, 1H), 3.41 – 3.15 (m, 3H), 3.15 – 2.99 (m, 5H), 2.35 – 2.26 (m, 1H), 2.22 – 2.13 (m, 1H), 2.04 – 1.92 (m, 1H), 1.67 – 1.48 (m, 5H), 1.50 – 1.40 (m, 1H), 1.35 (s, 9H), 1.32 – 0.96 (m, 3H), 0.95 – 0.86 (m, 1H), 0.87 – 0.73 (m, 1H), 0.73 – 0.61 (m, 1H).

^{13}C NMR (101 MHz, DMSO- d_6) δ 171.3, 167.2, 163.9, 163.6, 158.8, 156.7, 156.1, 142.8, 113.4, 113.0, 112.8, 102.2, 78.1, 55.8, 47.5, 47.4, 47.0, 40.3, 37.8, 37.1, 36.9, 36.6, 33.1, 32.9, 32.8, 32.5, 31.7, 30.1, 29.5, 29.3, 29.2, 29.1, 29.0, 28.7, 27.0, 26.6, 26.5, 26.2, 26.1.

Position	δC , type	δH	J (Hz)
2	167.2		
3	55.8, CH	4.88 – 4.94 (m)	
6	40.3, CH ₂	3.24 – 3.90 (m)	
7	142.8		
8	112.8 – 113.4, CH	6.81 – 7.04 (m)	
9	163.6 – 163.9		
10	102.2, CH	7.01 – 7.12 (m)	
11	163.6 – 163.9		
12	112.8 – 113.4, CH	6.81 – 7.04 (m)	
15	36.5 – 37.1, CH ₂	3.02 – 3.19 (m)	
16	47.4 – 47.5, CH ₂	3.16 – 3.47 (m)	
17	171.3		
18	30.1, CH ₂	2.14 – 2.37 (m)	
20	31.7 – 32.5, CH ₂	1.17 – 1.29 (m)	
21	36.9, CH	1.05 – 1.10 (m)	
22	32.8 – 33.1, CH ₂	0.77 – 1.65 (m)	
23	26.1 – 26.2, CH ₂	1.08 – 1.66 (m)	
24	26.5 – 26.6, CH ₂	1.08 – 1.66 (m)	
25	26.1 – 26.2, CH ₂	1.08 – 1.66 (m)	
26	32.8 – 33.1, CH ₂	0.77 – 1.65 (m)	

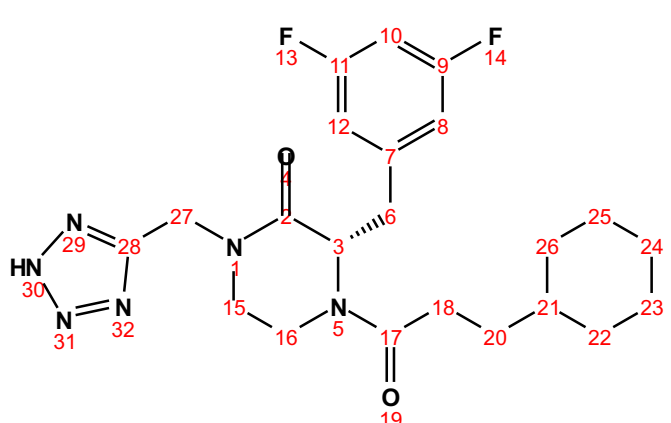
27	47.0, CH ₂	3.16 – 3.41 (m)	
28	37.8, CH ₂	3.04 – 3.13 (m)	
29		6.65 (s)	
30	156.1 – 158.8		
33	78.1		
34	28.7, CH ₃	1.32 – 1.41 (s)	
35	28.7, CH ₃	1.32 – 1.41 (s)	
36	28.7, CH ₃	1.32 – 1.41 (s)	

(S)-1-((2*H*-tetrazol-5-yl)methyl)-4-(3-cyclohexylpropanoyl)-3-(3,5-difluorobenzyl) piperazin-2-one (2.141):



In a vial, the piperazinone **2.142** (8 mg; 0.02 mmol), L-proline (2 mg; 0.02 mmol) and sodium azide (NaN_3) (3 mg; 0.04 mmol) were dissolved in 1 mL of DMF. The reaction mixture was stirred @ 120°C for 4h. The reaction was quenched with 2 mL of 1N HCl solution and washed with water (20 mL) and the organic layer was extracted with EtOAc (3 times). The organic layers were combined, washed with brine before being dried over Na_2SO_4 and filtered. The filtrate was concentrated in vacuo and purified by flash column chromatography (Silica gel, 1-10% MeOH in DCM) to yield **2.141** (4 mg; yield=50%). ¹H NMR (500 MHz, $\text{DMSO-}d_6$) δ 7.13 – 6.96 (m, 2H), 6.90 – 6.84 (m, 2H), 5.03 – 4.96 (m, 1H), 4.79 – 4.60 (m, 2H), 4.61 – 4.55 (m, 0H), 4.45 – 4.35 (m, 0H), 3.91 – 3.83 (m, 1H), 3.42 – 3.32 (m, 1H), 3.32 – 3.24 (m, 1H), 3.24 – 3.07 (m, 2H), 3.08 – 3.00 (m, 1H), 2.34 – 2.24 (m, 1H), 2.20 – 2.10 (m, 1H), 2.03 – 1.92 (m, 1H), 1.64 – 1.52 (m,

5H), 1.49 – 1.32 (m, 1H), 1.33 – 0.98 (m, 4H), 0.93 – 0.84 (m, 0H), 0.82 – 0.70 (m, 1H), 0.71 – 0.59 (m, 1H). ^{13}C NMR (101 MHz, DMSO- d_6) δ 171.5, 171.4, 166.8, 166.3, 164.0, 163.9, 163.7, 163.6, 161.6, 161.5, 161.3, 161.1, 156.3, 142.7, 142.6, 114.3, 113.5, 113.4, 113.3, 113.1, 113.0, 112.9, 110.0, 102.7, 102.4, 102.2, 101.9, 59.7, 55.8, 55.4, 46.9, 46.1, 41.4, 41.2, 39.6, 37.1, 37.0, 36.8, 36.5, 34.8, 33.0, 32.9, 32.8, 32.6, 32.2, 31.7, 30.1, 29.6, 29.5, 29.3, 29.2, 29.1, 29.0, 26.6, 26.5, 26.2, 26.1.



Position	δC , type	δH	J (Hz)
2	166.3 – 166.8		
3	55.4 – 59.7, CH	4.54 – 5.03 (m)	
6	34.8 – 39.6, CH ₂	3.14 – 4.43 (m)	
7	142.6 – 142.7		
8	112.9 – 113.5, CH	6.84 – 7.05 (m)	
9	161.1 – 164.0		
10	101.9 – 102.7, CH	6.97 – 7.11 (m)	
11	161.1 – 164.0		
12	112.9 – 113.5, CH	6.84 – 7.05 (m)	
15	36.5 – 37.0, CH ₂	3.01 – 3.23 (m)	
16	46.1 – 46.9, CH ₂	3.24 – 3.41 (m)	
17	171.4 – 171.5		
18	30.1, CH ₂	2.11 – 2.33 (m)	
20	29.0 – 32.6, CH ₂	0.84 – 2.01 (m)	
21	36.8 – 37.1, CH	0.87 – 1.08 (m)	
22	32.8 – 33.0, CH ₂	0.61 – 1.64 (m)	

23	26.1 – 26.2, CH ₂	1.02 – 1.65 (m)	
24	26.5 – 26.6, CH ₂	1.02 – 1.65 (m)	
25	26.1 – 26.2, CH ₂	1.02 – 1.65 (m)	
26	32.8 – 33.0, CH ₂	0.61 – 1.64 (m)	
27	41.2 – 41.4, CH ₂	4.61 – 4.78 (m)	
28	156.3		

13 Bibliography

- O'Neill, J., Tackling Drug-Resistant Infections Globally: Final Report and Recommendations. *The Review on Antimicrobial Resistance* **2016**.
- Tacconelli, E.; Magrini, N., Global priority list of antibiotic-resistant bacteria to guide research, discovery, and development of new antibiotics. *World Health Organization* **2017**, 1-7.
- Van Boeckel, T. P.; Gandra, S.; Ashok, A.; Caudron, Q.; Grenfell, B. T.; Levin, S. A.; Laxminarayan, R., Global antibiotic consumption 2000 to 2010: an analysis of Cross Mark 742 national pharmaceutical sales data. *Lancet Infectious Diseases* **2014**, *14* (8), 742-750.
- Lipinski, C. A.; Lombardo, F.; Dominy, B. W.; Feeney, P. J., Experimental and computational approaches to estimate solubility and permeability in drug discovery and development settings. *Advanced Drug Delivery Reviews* **1997**, *23* (1-3), 3-25.
- Veber, D. F.; Johnson, S. R.; Cheng, H.-Y.; Smith, B. R.; W., W. K.; Kopple, K. D., Molecular Properties That Influence the Oral Bioavailability of Drug Candidates. *J. Med. Chem.* **2002**, *45* (12), 2615-2623.
- Lewis, K., Platforms for antibiotic discovery. *Nat Rev Drug Discov* **2013**, *12* (5), 371-87.
- Nikaido, H., Prevention of drug access to bacterial targets: permeability barriers and active efflux. *Science* **1994**, *264* (5157), 382-388.
- Lambert, P. A., Cellular impermeability and uptake of biocides and antibiotics in Gram-positive bacteria and mycobacteria. *Journal of Applied Microbiology* **2002**, *92* (s1), 46S-54S.
- Malanovic, N.; Lohner, K., Gram-positive bacterial cell envelopes: The impact on the activity of antimicrobial peptides. *Biochim Biophys Acta* **2016**, *1858* (5), 936-46.
- Gentry, E. J., Antibiotics and Antimicrobial Agents. *Foye's Principles of Medicinal Chemistry: Wolters Kluwer Health*. **2012**, 1073-1124.
- Scherrer, R.; Gerhardt, P., Molecular sieving by the *Bacillus megaterium* cell wall and protoplast. *J Bacteriol* **1971**, *107* (3), 718-35.
- Russell, A. D., Bacterial resistance to disinfectants: present knowledge and future problems. *J Hosp Infect* **1999**, *43 Suppl*, S57-68.
- Denyer, S. P.; Maillard, J. Y., Cellular impermeability and uptake of biocides and antibiotics in Gram-negative bacteria. *J. Appl. Microbiol.* **2002**, *92* (s1), 35S-45S.
- Nikaido, H., Molecular Basis of Bacterial Outer Membrane Permeability Revisited. *Microbiol. Mol. Biol. Rev.* **2003**, *67* (4), 593-656.
- Delcour, A. H., Outer membrane permeability and antibiotic resistance. *Biochim. Biophys. Acta* **2009**, *1794* (5), 808-16.

16. Plesiat, P.; Nikaido, H., Outer membranes of gram-negative bacteria are permeable to steroid probes. *Mol Microbiol* **1992**, *6* (10), 1323-33.
17. Nikaido, H.; Vaara, M., Molecular basis of bacterial outer membrane permeability. *Microbiol. Rev.* **1985**, *49* (1), 1-32.
18. Hancock, R., The bacterial outer membrane as a drug barrier. *Trends in Microbiology* **1997**, *5* (1), 37-42.
19. Kumar, A.; Schweizer, H. P., Bacterial resistance to antibiotics: active efflux and reduced uptake. *Adv Drug Deliv Rev* **2005**, *57* (10), 1486-513.
20. Schulz, G. E., The structure of bacterial outer membrane proteins. *Biochimica et Biophysica Acta (BBA) - Biomembranes* **2002**, *1565* (2), 308-317.
21. Schulz, G. E., The Structures of General Porins. **2008**.
22. Scorciapino, M. A.; Acosta-Gutierrez, S.; Benkerrou, D.; D'Agostino, T.; Mallocci, G.; Samanta, S.; Bodrenko, I.; Ceccarelli, M., Rationalizing the permeation of polar antibiotics into Gram-negative bacteria. *J Phys Condens Matter* **2017**, *29* (11), 113001.
23. Pages, J. M.; James, C. E.; Winterhalter, M., The porin and the permeating antibiotic: a selective diffusion barrier in Gram-negative bacteria. *Nat. Rev. Microbiol.* **2008**, *6* (12), 893-903.
24. Schirmer, T., Structure-Function Relationships in Sugar-Specific Porins. **2005**, 169-181.
25. Braun, V.; Braun, M., Energy-Coupled Outer Membrane Iron Transporters. **2005**, 213-236.
26. Kadner, R. J.; Chimento, D. P.; Cadieux, N., Structural and Functional Aspects of the Vitamin B12 Receptor BtuB. **2005**, 237-258.
27. Nestorovich, E. M.; Sugawara, E.; Nikaido, H.; Bezrukov, S. M., Pseudomonas aeruginosa porin OprF: properties of the channel. *J Biol Chem* **2006**, *281* (24), 16230-7.
28. Li, H.; Luo, Y. F.; Williams, B. J.; Blackwell, T. S.; Xie, C. M., Structure and function of OprD protein in Pseudomonas aeruginosa: from antibiotic resistance to novel therapies. *Int J Med Microbiol* **2012**, *302* (2), 63-8.
29. Wylie, J. L.; Worobec, E. A., The OprB porin plays a central role in carbohydrate uptake in Pseudomonas aeruginosa. *J Bacteriol* **1995**, *177* (11), 3021-6.
30. Hancock, R. E. W.; Tamber, S., Porins of the Outer Membrane of Pseudomonas aeruginosa. **2005**, 61-77.
31. Epp, S. F.; Kohler, T.; Plesiat, P.; Michea-Hamzhepour, M.; Frey, J.; Pechere, J. C., C-terminal region of Pseudomonas aeruginosa outer membrane porin OprD modulates susceptibility to meropenem. *Antimicrob Agents Chemother* **2001**, *45* (6), 1780-7.
32. Lei, Y.; Sato, K.; Nakae, T., Ofloxacin-resistant Pseudomonas aeruginosa mutants with elevated drug extrusion across the inner membrane. *Biochemical and Biophysical Research Communications* **1991**, *178* (3), 1043-1048.
33. Piddock, L. J. V., Mechanism of quinolone uptake into bacterial cells. *J. Antimicrob. Chemother.* **1991**, *27* (4), 399-403.
34. Cohen, S. P.; Hooper, D. C.; Wolfson, J. S.; Souza, K. S.; McMurry, L. M.; Levy, S. B., Endogenous active efflux of norfloxacin in susceptible Escherichia coli. *Antimicrobial Agents and Chemotherapy* **1988**, *32* (8), 1187-1191.
35. Bryan, L. E.; Bedard, J., Impermeability to quinolones in gram-positive and gram-negative bacteria. *Eur. J. Clin. Microbiol. Infect. Dis.* **1991**, *10* (4), 232-239.
36. Andersen, C., Drug Efflux and Protein Export through Channel-Tunnels. **2005**, 139-167.
37. Li, X. Z.; Nikaido, H., Efflux-mediated drug resistance in bacteria: an update. *Drugs* **2009**, *69* (12), 1555-623.

38. Davidson, A. L.; Chen, J., ATP-binding cassette transporters in bacteria. *Annu Rev Biochem* **2004**, *73*, 241-68.
39. Zgurskaya, H. I.; Lopez, C. A.; Gnanakaran, S., Permeability Barrier of Gram-Negative Cell Envelopes and Approaches To Bypass It. *ACS Infect Dis* **2015**, *1* (11), 512-522.
40. Abdali, N.; Parks, J. M.; Haynes, K. M.; Chaney, J. L.; Green, A. T.; Wolloscheck, D.; Walker, J. K.; Rybenkov, V. V.; Baudry, J.; Smith, J. C.; Zgurskaya, H. I., Reviving Antibiotics: Efflux Pump Inhibitors That Interact with AcrA, a Membrane Fusion Protein of the AcrAB-TolC Multidrug Efflux Pump. *ACS Infect Dis* **2017**, *3* (1), 89-98.
41. Ogawa, W.; Minato, Y.; Dodan, H.; Onishi, M.; Tsuchiya, T.; Kuroda, T., Characterization of MATE-type multidrug efflux pumps from *Klebsiella pneumoniae* MGH78578. *PLoS One* **2015**, *10* (3), e0121619.
42. Radchenko, M.; Symersky, J.; Nie, R.; Lu, M., Structural basis for the blockade of MATE multidrug efflux pumps. *Nat Commun* **2015**, *6*, 7995.
43. Balouiri, M.; Sadiki, M.; Ibsouda, S. K., Methods for in vitro evaluating antimicrobial activity: A review. *J. Pharm. Anal.* **2016**, *6*, 71-79.
44. Krishnamoorthy, G.; Wolloscheck, D.; Weeks, J. W.; Croft, C.; Rybenkov, V. V.; Zgurskaya, H. I., Breaking the Permeability Barrier of *Escherichia coli* by Controlled Hyperporination of the Outer Membrane. *Antimicrob. Agents Chemother.* **2016**, *60* (12), 7372-7381.
45. Wong, W. R.; Oliver, A. G.; Linington, R. G., Development of antibiotic activity profile screening for the classification and discovery of natural product antibiotics. *Chem. Biol.* **2012**, *19* (11), 1483-95.
46. Nonejuie, P.; Burkart, M.; Pogliano, K.; Pogliano, J., Bacterial cytological profiling rapidly identifies the cellular pathways targeted by antibacterial molecules. *Proc. Natl. Acad. Sci. U.S.A.* **2013**, *110* (40), 16169-74.
47. Vincent, I. M.; Ehmann, D. E.; Mills, S. D.; Perros, M.; Barrett, M. P., Untargeted Metabolomics To Ascertain Antibiotic Modes of Action. *Antimicrob. Agents Chemother.* **2016**, *60* (4), 2281-91.
48. Andersen, C.; Hughes, C.; Koronakis, V., Protein export and drug efflux through bacterial channel-tunnels. *Curr. Opin. Cell Biol.* **2001**, *13* (4), 412-416.
49. Mamelli, L.; Petit, S.; Chevalier, J.; Giglione, C.; Lieutaud, A.; Meinel, T.; Artaud, I.; Pages, J. M., New antibiotic molecules: bypassing the membrane barrier of gram negative bacteria increases the activity of peptide deformylase inhibitors. *PLoS One* **2009**, *4* (7), e6443.
50. Opperman, T. J.; Kwasny, S. M.; Kim, H. S.; Nguyen, S. T.; Houseweart, C.; D'Souza, S.; Walker, G. C.; Peet, N. P.; Nikaido, H.; Bowlin, T. L., Characterization of a novel pyranopyridine inhibitor of the AcrAB efflux pump of *Escherichia coli*. *Antimicrob. Agents Chemother.* **2014**, *58* (2), 722-33.
51. Opperman, T. J.; Nguyen, S. T., Recent advances toward a molecular mechanism of efflux pump inhibition. *Front. Microbiol.* **2015**, *6*, 421.
52. Hasdemir, U. O.; Chevalier, J.; Nordmann, P.; Pages, J. M., Detection and prevalence of active drug efflux mechanism in various multidrug-resistant *Klebsiella pneumoniae* strains from Turkey. *J. Clin. Microbiol.* **2004**, *42* (6), 2701-6.
53. Sjuts, H.; Vargiu, A. V.; Kwasny, S. M.; Nguyen, S. T.; Kim, H. S.; Ding, X.; Ornik, A. R.; Ruggerone, P.; Bowlin, T. L.; Nikaido, H.; Pos, K. M.; Opperman, T. J., Molecular basis for inhibition of AcrB multidrug efflux pump by novel and powerful pyranopyridine derivatives. *Proc. Natl. Acad. Sci. U.S.A.* **2016**, *113* (13), 3509-14.

54. Abdali, N.; Parks, J. M.; Haynes, K. M.; Chaney, J. L.; Green, A. T.; Wolloscheck, D.; Walker, J. K.; Rybenkov, V. V.; Baudry, J.; Smith, J. C.; Zgurskaya, H. I., Reviving Antibiotics: Efflux Pump Inhibitors That Interact with AcrA, a Membrane Fusion Protein of the AcrAB-TolC Multidrug Efflux Pump. *ACS Infect. Dis.* **2017**, *3* (1), 89-98.
55. Lomovskaya, O.; Warren, M. S.; Lee, A.; Galazzo, J.; Fronko, R.; Lee, M.; Blais, J.; Cho, D.; Chamberland, S.; Renau, T.; Leger, R.; Hecker, S.; Watkins, W.; Hoshino, K.; Ishida, H.; Lee, V. J., Identification and characterization of inhibitors of multidrug resistance efflux pumps in *Pseudomonas aeruginosa*: novel agents for combination therapy. *Antimicrob. Agents Chemother.* **2001**, *45* (1), 105-16.
56. Pannek, S.; Higgins, P. G.; Steinke, P.; Jonas, D.; Akova, M.; Bohnert, J. A.; Seifert, H.; Kern, W. V., Multidrug efflux inhibition in *Acinetobacter baumannii*: comparison between 1-(1-naphthylmethyl)-piperazine and phenyl-arginine-beta-naphthylamide. *J. Antimicrob. Chemother.* **2006**, *57* (5), 970-4.
57. Ghisalberti, D.; Mahamoud, A.; Chevalier, J.; Baitiche, M.; Martino, M.; Pages, J. M.; Barbe, J., Chloroquinolines block antibiotic efflux pumps in antibiotic-resistant *Enterobacter aerogenes* isolates. *Int. J. Antimicrob. Agents* **2006**, *27* (6), 565-9.
58. Aparna, V.; Dineshkumar, K.; Mohanalakshmi, N.; Velmurugan, D.; Hopper, W., Identification of natural compound inhibitors for multidrug efflux pumps of *Escherichia coli* and *Pseudomonas aeruginosa* using in silico high-throughput virtual screening and in vitro validation. *PLoS One* **2014**, *9* (7), e101840.
59. Gholami, M.; Hashemi, A.; Hakemi-Vala, M.; Goudarzi, H.; Hallajzadeh, M., Efflux Pump Inhibitor Phenylalanine-Arginine Beta-Naphthylamide Effect on the Minimum Inhibitory Concentration of Imipenem in *Acinetobacter baumannii* Strains Isolated From Hospitalized Patients in Shahid Motahari Burn Hospital, Tehran, Iran. *Jundishapur J. Microbiol.* **2015**, *8* (10), e19048.
60. Bohnert, J. A.; Schuster, S.; Kern, W. V., Pimozide Inhibits the AcrAB-TolC Efflux Pump in *Escherichia coli*. *Open Microbiol. J.* **2013**, *7*, 83-6.
61. Li, X. Z.; Plesiat, P.; Nikaido, H., The challenge of efflux-mediated antibiotic resistance in Gram-negative bacteria. *Clin. Microbiol. Rev.* **2015**, *28* (2), 337-418.
62. Bina, X. R.; Philippart, J. A.; Bina, J. E., Effect of the efflux inhibitors 1-(1-naphthylmethyl)-piperazine and phenyl-arginine-beta-naphthylamide on antimicrobial susceptibility and virulence factor production in *Vibrio cholerae*. *J. Antimicrob. Chemother.* **2009**, *63* (1), 103-8.
63. Sanchez, P.; Le, U.; Martinez, J. L., The efflux pump inhibitor Phe-Arg-beta-naphthylamide does not abolish the activity of the *Stenotrophomonas maltophilia* SmeDEF multidrug efflux pump. *J. Antimicrob. Chemother.* **2003**, *51* (4), 1042-5.
64. Pages, J. M.; Masi, M.; Barbe, J., Inhibitors of efflux pumps in Gram-negative bacteria. *Trends Mol. Med.* **2005**, *11* (8), 382-9.
65. Jamshidi, S.; Sutton, J. M.; Rahman, K. M., An overview of bacterial efflux pumps and computational approaches to study efflux pump inhibitors. *Future Med. Chem.* **2016**, *8* (2), 195-210.
66. Hancock, R., The bacterial outer membrane as a drug barrier. *Trends Microbiol.* **1997**, *5* (1), 37-42.
67. Minnock, A.; Vernon, D. I.; Schofield, J.; Griffiths, J.; Parish, J. H.; Brown, S. B., Mechanism of uptake of a cationic water-soluble pyridinium zinc phthalocyanine across the outer membrane of *Escherichia coli*. *Antimicrob. Agents Chemother.* **2000**, *44* (3), 522-527.

68. Stokes, J. M.; MacNair, C. R.; Ilyas, B.; French, S.; Cote, J. P.; Bouwman, C.; Farha, M. A.; Sieron, A. O.; Whitfield, C.; Coombes, B. K.; Brown, E. D., Pentamidine sensitizes Gram-negative pathogens to antibiotics and overcomes acquired colistin resistance. *Nat. Microbiol.* **2017**, *2*, 17028.
69. Bolla, J. M.; Alibert-Franco, S.; Handzlik, J.; Chevalier, J.; Mahamoud, A.; Boyer, G.; Kiec-Kononowicz, K.; Pages, J. M., Strategies for bypassing the membrane barrier in multidrug resistant Gram-negative bacteria. *FEBS Lett.* **2011**, *585* (11), 1682-90.
70. Vaara, M., Agents That Increase the Permeability of the Outer-Membrane. *Microbiol. Rev.* **1992**, *56* (3), 395-411.
71. Shah, N. R.; Hancock, R. E.; Fernandez, R. C., Bordetella pertussis lipid A glucosamine modification confers resistance to cationic antimicrobial peptides and increases resistance to outer membrane perturbation. *Antimicrob. Agents Chemother.* **2014**, *58* (8), 4931-4.
72. Arroyo, L. A.; Herrera, C. M.; Fernandez, L.; Hankins, J. V.; Trent, M. S.; Hancock, R. E., The pmrCAB operon mediates polymyxin resistance in Acinetobacter baumannii ATCC 17978 and clinical isolates through phosphoethanolamine modification of lipid A. *Antimicrob. Agents Chemother.* **2011**, *55* (8), 3743-51.
73. Clifton, L. A.; Ciesielski, F.; Skoda, M. W.; Paracini, N.; Holt, S. A.; Lakey, J. H., The Effect of Lipopolysaccharide Core Oligosaccharide Size on the Electrostatic Binding of Antimicrobial Proteins to Models of the Gram Negative Bacterial Outer Membrane. *Langmuir* **2016**, *32* (14), 3485-94.
74. Fu, H. G.; Hu, X. X.; Li, C. R.; Li, Y. H.; Wang, Y. X.; Jiang, J. D.; Bi, C. W.; Tang, S.; You, X. F.; Song, D. Q., Design, synthesis and biological evaluation of monobactams as antibacterial agents against gram-negative bacteria. *Eur. J. Med. Chem.* **2016**, *110*, 151-63.
75. Takroui, K.; Cooper, H. D.; Spaulding, A.; Zucchi, P.; Koleva, B.; Cleary, D. C.; Tear, W.; Beuning, P. J.; Hirsch, E. B.; Aggen, J. B., Progress against Escherichia coli with the Oxazolidinone Class of Antibacterials: Test Case for a General Approach To Improving Whole-Cell Gram-Negative Activity. *ACS Infect Dis* **2016**, *2* (6), 405-26.
76. Iyer, R.; Sylvester, M. A.; Velez-Vega, C.; Tommasi, R.; Durand-Reville, T. F.; Miller, A. A., Whole-Cell-Based Assay To Evaluate Structure Permeation Relationships for Carbapenem Passage through the Pseudomonas aeruginosa Porin OprD. *ACS Infect. Dis.* **2017**.
77. Sulavik, M. C.; Houseweart, C.; Cramer, C.; Jiwani, N.; Murgolo, N.; Greene, J.; DiDomenico, B.; Shaw, K. J.; Miller, G. H.; Hare, R.; Shimer, G., Antibiotic susceptibility profiles of Escherichia coli strains lacking multidrug efflux pump genes. *Antimicrob. Agents Chemother.* **2001**, *45* (4), 1126-36.
78. Nishino, K.; Yamaguchi, A., Analysis of a complete library of putative drug transporter genes in Escherichia coli. *J. Bacteriol.* **2001**, *183* (20), 5803-12.
79. Wang, Z.; Wang, J.; Ren, G.; Li, Y.; Wang, X., Influence of Core Oligosaccharide of Lipopolysaccharide to Outer Membrane Behavior of Escherichia coli. *Mar. Drugs* **2015**, *13* (6), 3325-39.
80. Li, X. Z.; Zhang, L.; Nikaido, H., Efflux pump-mediated intrinsic drug resistance in Mycobacterium smegmatis. *Antimicrob. Agents Chemother.* **2004**, *48* (7), 2415-23.
81. Piddock, L. J. V.; Johnson, M. M., Accumulation of 10 Fluoroquinolones by Wild-Type or Efflux Mutant Streptococcus pneumoniae. *Antimicrob. Agents Chemother.* **2002**, *46* (3), 813-820.
82. Cai, H.; Rose, K.; Liang, L. H.; Dunham, S.; Stover, C., Development of a liquid chromatography/mass spectrometry-based drug accumulation assay in Pseudomonas aeruginosa. *Anal. Biochem.* **2009**, *385* (2), 321-5.

83. Diver, J. M.; Piddock, L. J. V.; Wise, R., The accumulation of five quinolone antibacterial agents by *Escherichia coli*. *J. Antimicrob. Chemother.* **1990**, *25* (3), 319-333.
84. Cinquin, B.; Maigre, L.; Pinet, E.; Chevalier, J.; Stavenger, R. A.; Mills, S.; Refregiers, M.; Pages, J. M., Microspectrometric insights on the uptake of antibiotics at the single bacterial cell level. *Sci. Rep.* **2015**, *5*, 17968.
85. Ricci, V.; Piddock, L., Accumulation of garenoxacin by *Bacteroides fragilis* compared with that of five fluoroquinolones. *J. Antimicrob. Chemother.* **2003**, *52* (4), 605-9.
86. Bensikaddour, H.; Fa, N.; Burton, I.; Deleu, M.; Lins, L.; Schanck, A.; Brasseur, R.; Dufrene, Y. F.; Goormaghtigh, E.; Mingeot-Leclercq, M. P., Characterization of the interactions between fluoroquinolone antibiotics and lipids: a multitechnique approach. *Biophys. J.* **2008**, *94* (8), 3035-46.
87. Nakashima, R.; Sakurai, K.; Yamasaki, S.; Nishino, K.; Yamaguchi, A., Structures of the multidrug exporter AcrB reveal a proximal multisite drug-binding pocket. *Nature* **2011**, *480* (7378), 565-9.
88. Asuquo, A. E.; Piddock, L. J. V., Accumulation and killing kinetics of fifteen quinolones for *Escherichia coli*, *Staphylococcus aureus* and *Pseudomonas aeruginosa*. *J. Antimicrob. Chemother.* **1993**, *31* (6), 865-880.
89. Bazile, S.; Moreau, N.; Bouzard, D.; Essiz, M., Relationships among antibacterial activity, inhibition of DNA gyrase, and intracellular accumulation of 11 fluoroquinolones. *Antimicrob. Agents Chemother.* **1992**, *36* (12), 2622-2627.
90. Bedard, J.; Wong, S.; Bryan, L. E., Accumulation of enoxacin by *Escherichia coli* and *Bacillus subtilis*. *Antimicrob. Agents Chemother.* **1987**, *31* (9), 1348-1354.
91. Mccaffrey, C.; Bertasso, A.; Pace, J.; Georgopapadakou, N. H., Quinolone Accumulation in *Escherichia-Coli*, *Pseudomonas-Aeruginosa*, and *Staphylococcus-Aureus*. *Antimicrob. Agents Chemother.* **1992**, *36* (8), 1601-1605.
92. Piddock, L. J. V.; Jin, Y. F.; Ricci, V.; Asuquo, A. E., Quinolone accumulation by *Pseudomonas aeruginosa*, *Staphylococcus aureus* and *Escherichia coli*. *J. Antimicrob. Chemother.* **1999**, *43* (1), 61-70.
93. Chapman, J. S.; Georgopapadakou, N. H., Routes of quinolone permeation in *Escherichia coli*. *Antimicrob. Agents Chemother.* **1988**, *32* (4), 438-442.
94. Heidari-Torkabadi, H.; Bethel, C. R.; Ding, Z.; Pusztai-Carey, M.; Bonnet, R.; Bonomo, R. A.; Carey, P. R., "Mind the Gap": Raman Evidence for Rapid Inactivation of CTX-M-9 beta-Lactamase Using Mechanism-Based Inhibitors that Bridge the Active Site. *J. Am. Chem. Soc.* **2015**, *137* (40), 12760-3.
95. Zimmermann, W.; Rosselet, A., Function of the Outer Membrane of *Escherichia coli* as a Permeability Barrier to Beta-Lactam Antibiotics. *Antimicrob. Agents Chemother.* **1977**, *12* (3), 368-372.
96. Nikaido, H.; Rosenberg, E. Y.; Foulds, J., Porin channels in *Escherichia coli*: studies with beta-lactams in intact cells. *J. Bacteriol.* **1983**, *153* (1), 232-40.
97. Sugawara, E.; Nikaido, H., OmpA is the principal nonspecific slow porin of *Acinetobacter baumannii*. *J. Bacteriol.* **2012**, *194* (15), 4089-96.
98. Kojima, S.; Nikaido, H., Permeation rates of penicillins indicate that *Escherichia coli* porins function principally as nonspecific channels. *Proc. Natl. Acad. Sci. U.S.A.* **2013**, *110* (28), E2629-34.

99. Tian, H.; Six, D. A.; Krucker, T.; Leeds, J. A.; Winograd, N., Subcellular Chemical Imaging of Antibiotics in Single Bacteria Using C60-Secondary Ion Mass Spectrometry. *Anal. Chem.* **2017**, *89* (9), 5050-5057.
100. Graef, F.; Gordon, S.; Lehr, C. M., Anti-infectives in Drug Delivery-Overcoming the Gram-Negative Bacterial Cell Envelope. *Curr. Top. Microbiol. Immunol.* **2016**, *398*, 475-496.
101. Davis, T. D.; Gerry, C. J.; Tan, D. S., General platform for systematic quantitative evaluation of small-molecule permeability in bacteria. *ACS Chem. Biol.* **2014**, *9* (11), 2535-44.
102. Bhat, J.; Narayan, A.; Venkatraman, J.; Chatterji, M., LC-MS based assay to measure intracellular compound levels in Mycobacterium smegmatis: linking compound levels to cellular potency. *J. Microbiol. Methods* **2013**, *94* (2), 152-8.
103. Zhou, Y.; Joubran, C.; Miller-Vedam, L.; Isabella, V.; Nayar, A.; Tentarelli, S.; Miller, A., Thinking outside the "bug": a unique assay to measure intracellular drug penetration in gram-negative bacteria. *Anal. Chem.* **2015**, *87* (7), 3579-84.
104. Mortimer, P. G. S.; Piddock, L. J. V., A comparison of methods used for measuring the accumulation of quinolones by Enterobacteriaceae, Pseudomonas aeruginosa and Staphylococcus aureus. *J. Antimicrob. Chemother.* **1991**, *28* (5), 639-653.
105. Liu, H. L.; Sabus, C.; Carter, G. T.; Du, C.; Avdeef, A.; Tischler, M., In vitro permeability of poorly aqueous soluble compounds using different solubilizers in the PAMPA assay with liquid chromatography/mass spectrometry detection. *Pharm. Res.* **2003**, *20* (11), 1820-1826.
106. Yang, J. Y.; Phelan, V. V.; Simkovsky, R.; Watrous, J. D.; Trial, R. M.; Fleming, T. C.; Wenter, R.; Moore, B. S.; Golden, S. S.; Pogliano, K.; Dorrestein, P. C., Primer on agar-based microbial imaging mass spectrometry. *J. Bacteriol.* **2012**, *194* (22), 6023-8.
107. Dunham, S. J.; Ellis, J. F.; Li, B.; Sweedler, J. V., Mass Spectrometry Imaging of Complex Microbial Communities. *Acc. Chem. Res.* **2017**, *50* (1), 96-104.
108. Masi, M.; Refregiers, M.; Pos, K. M.; Pages, J. M., Mechanisms of envelope permeability and antibiotic influx and efflux in Gram-negative bacteria. *Nat. Microbiol.* **2017**, *2*, 17001.
109. Husain, F.; Nikaido, H., Substrate path in the AcrB multidrug efflux pump of Escherichia coli. *Mol. Microbiol.* **2010**, *78* (2), 320-30.
110. Jin, J.; Hsieh, Y. H.; Cui, J.; Damera, K.; Dai, C.; Chaudhary, A. S.; Zhang, H.; Yang, H.; Cao, N.; Jiang, C.; Vaara, M.; Wang, B.; Tai, P. C., Using Chemical Probes to Assess the Feasibility of Targeting SecA for Developing Antimicrobial Agents against Gram-Negative Bacteria. *ChemMedChem* **2016**, *11* (22), 2511-2521.
111. Allam, A.; Maigre, L.; Alves de Sousa, R.; Dumont, E.; Vergalli, J.; Pages, J. M.; Artaud, I., New amphiphilic neamine conjugates bearing a metal binding motif active against MDR E. aerogenes Gram-negative bacteria. *Eur. J. Med. Chem.* **2017**, *127*, 748-756.
112. Coldham, N. G.; Webber, M.; Woodward, M. J.; Piddock, L. J., A 96-well plate fluorescence assay for assessment of cellular permeability and active efflux in Salmonella enterica serovar Typhimurium and Escherichia coli. *J. Antimicrob. Chemother.* **2010**, *65* (8), 1655-63.
113. Qian, C. D.; Wu, X. C.; Teng, Y.; Zhao, W. P.; Li, O.; Fang, S. G.; Huang, Z. H.; Gao, H. C., Battacin (Octapeptin B5), a new cyclic lipopeptide antibiotic from Paenibacillus tianmuensis active against multidrug-resistant Gram-negative bacteria. *Antimicrob. Agents Chemother.* **2012**, *56* (3), 1458-65.
114. Kaczmarek, F. M.; Dib-Hajj, F.; Shang, W.; Gootz, T. D., High-level carbapenem resistance in a Klebsiella pneumoniae clinical isolate is due to the combination of bla(ACT-1) beta-lactamase production, porin OmpK35/36 insertional inactivation, and down-regulation of the phosphate transport porin phoe. *Antimicrob. Agents Chemother.* **2006**, *50* (10), 3396-406.

115. Luckey, M.; Nikaido, H., Specificity of diffusion channels produced by lambda phage receptor protein of Escherichia coli. *Proc. Natl. Acad. Sci. U.S.A.* **1980**, *77* (1), 167-71.
116. Cama, J.; Schaich, M.; Al Nahas, K.; Hernandez-Ainsa, S.; Pagliara, S.; Keyser, U. F., Direct Optofluidic Measurement of the Lipid Permeability of Fluoroquinolones. *Sci. Rep.* **2016**, *6*, 32824.
117. Delcour, A. H., Solute uptake through general porins. *Front. Biosci.* **2003**, *8* (4), d1055-1071.
118. Yoshimura, F.; Nikaido, H., Diffusion of beta-Lactam Antibiotics Through the Porin Channels of Escherichia coli K-12. *Antimicrob. Agents Chemother.* **1985**, *27* (1), 84-92.
119. Mach, T.; Chimere, C.; Fritz, J.; Fertig, N.; Winterhalter, M.; Futterer, C., Miniaturized planar lipid bilayer: increased stability, low electric noise and fast fluid perfusion. *Anal. Bioanal. Chem.* **2008**, *390* (3), 841-6.
120. Winterhalter, M.; Ceccarelli, M., Physical methods to quantify small antibiotic molecules uptake into Gram-negative bacteria. *Eur. J. Pharm. Biopharm.* **2015**, *95* (Pt A), 63-7.
121. Mahendran, K. R.; Hajjar, E.; Mach, T.; Lovelle, M.; Kumar, A.; Sousa, I.; Spiga, E.; Weingart, H.; Gameiro, P.; Winterhalter, M.; Ceccarelli, M., Molecular basis of enrofloxacin translocation through OmpF, an outer membrane channel of Escherichia coli--when binding does not imply translocation. *J. Phys. Chem. B* **2010**, *114* (15), 5170-9.
122. Cama, J.; Bajaj, H.; Pagliara, S.; Maier, T.; Braun, Y.; Winterhalter, M.; Keyser, U. F., Quantification of Fluoroquinolone Uptake through the Outer Membrane Channel OmpF of Escherichia coli. *J. Am. Chem. Soc.* **2015**, *137* (43), 13836-43.
123. Thanassi, D. G.; Suh, G. S.; Nikaido, H., Role of outer membrane barrier in efflux-mediated tetracycline resistance of Escherichia coli. *J. Bacteriol.* **1995**, *177* (4), 998-1007.
124. Nagano, K.; Nikaido, H., Kinetic behavior of the major multidrug efflux pump AcrB of Escherichia coli. *Proc. Natl. Acad. Sci. U.S.A.* **2009**, *106* (14), 5854-8.
125. Brown, D. M.; Acred, P., "Penbritin"—A New Broad-spectrum Antibiotic. *BMJ Brit. Med. J.* **1961**, *2* (5246), 197-198.
126. Piscitelli, S. C.; Danziger, L. H.; Rodvold, K. A., Clarithromycin and azithromycin: new macrolide antibiotics. *Clin. Pharm.* **1992**, *11* (2), 137-52.
127. O'Shea, R.; Moser, H. E., Physicochemical properties of antibacterial compounds: implications for drug discovery. *J. Med. Chem.* **2008**, *51* (10), 2871-8.
128. Brown, D. G.; May-Dracka, T. L.; Gagnon, M. M.; Tommasi, R., Trends and exceptions of physical properties on antibacterial activity for Gram-positive and Gram-negative pathogens. *J. Med. Chem.* **2014**, *57* (23), 10144-61.
129. Yarlagadda, V.; Manjunath, G. B.; Sarkar, P.; Akkapeddi, P.; Paramanandham, K.; Shome, B. R.; Ravikumar, R.; Haldar, J., Glycopeptide Antibiotic To Overcome the Intrinsic Resistance of Gram-Negative Bacteria. *ACS Infect. Dis.* **2016**, *2* (2), 132-9.
130. Page, M. G., Siderophore conjugates. *Ann. N. Y. Acad. Sci.* **2013**, *1277*, 115-26.
131. Tan, L.; Tao, Y.; Wang, T.; Zou, F.; Zhang, S.; Kou, Q.; Niu, A.; Chen, Q.; Chu, W.; Chen, X.; Wang, H.; Yang, Y., Discovery of Novel Pyridone-Conjugated Monosulfactams as Potent and Broad-Spectrum Antibiotics for Multidrug-Resistant Gram-Negative Infections. *J. Med. Chem.* **2017**, *60* (7), 2669-2684.
132. Silley, P.; Griffiths, J. W.; Monsey, D.; Harris, A. M., Mode of Action of GR69153, a Novel Catechol-Substituted Cephalosporin, and Its Interaction with the tonB-Dependent Iron Transport System. *Antimicrob. Agents Chemother.* **1990**, *34* (9), 1806-1808.

133. Sykes, R. B.; Koster, W. H.; Bonner, D. P., The New Monobactams: Chemistry and Biology. *J. Clin. Pharmacol.* **1988**, *28* (2), 113-119.
134. Yue, W. W.; Grizot, S.; Buchanan, S. K., Structural Evidence for Iron-free Citrate and Ferric Citrate Binding to the TonB-dependent Outer Membrane Transporter FecA. *J. Mol. Biol.* **2003**, *332* (2), 353-368.
135. Schalk, I. J.; Mislin, G. L. A., Bacterial Iron Uptake Pathways: Gates for the Import of Bactericide Compounds. *J. Med. Chem.* **2017**.
136. McPherson, C. J.; Aschenbrenner, L. M.; Lacey, B. M.; Fahnoe, K. C.; Lemmon, M. M.; Finegan, S. M.; Tadakamalla, B.; O'Donnell, J. P.; Mueller, J. P.; Tomaras, A. P., Clinically relevant Gram-negative resistance mechanisms have no effect on the efficacy of MC-1, a novel siderophore-conjugated monocarbam. *Antimicrob. Agents Chemother.* **2012**, *56* (12), 6334-42.
137. Page, M. G.; Dantier, C.; Desarbre, E., In vitro properties of BAL30072, a novel siderophore sulfactam with activity against multiresistant gram-negative bacilli. *Antimicrob. Agents Chemother.* **2010**, *54* (6), 2291-302.
138. Kohira, N.; West, J.; Ito, A.; Ito-Horiyama, T.; Nakamura, R.; Sato, T.; Rittenhouse, S.; Tsuji, M.; Yamano, Y., In Vitro Antimicrobial Activity of a Siderophore Cephalosporin, S-649266, against Enterobacteriaceae Clinical Isolates, Including Carbapenem-Resistant Strains. *Antimicrob. Agents Chemother.* **2016**, *60* (2), 729-34.
139. Wencewicz, T. A.; Miller, M. J., Biscatecholate-monohydroxamate mixed ligand siderophore-carbacephalosporin conjugates are selective sideromycin antibiotics that target *Acinetobacter baumannii*. *J. Med. Chem.* **2013**, *56* (10), 4044-52.
140. Md-Saleh, S. R.; Chilvers, E. C.; Kerr, K. G.; Milner, S. J.; Snelling, A. M.; Weber, J. P.; Thomas, G. H.; Duhme-Klair, A. K.; Routledge, A., Synthesis of citrate-ciprofloxacin conjugates. *Bioorg. Med. Chem. Lett.* **2009**, *19* (5), 1496-8.
141. Ji, C.; Miller, M. J., Chemical syntheses and in vitro antibacterial activity of two desferrioxamine B-ciprofloxacin conjugates with potential esterase and phosphatase triggered drug release linkers. *Bioorg. Med. Chem.* **2012**, *20* (12), 3828-36.
142. Fardeau, S.; Dassonville-Klimpt, A.; Audic, N.; Sasaki, A.; Pillon, M.; Baudrin, E.; Mullie, C.; Sonnet, P., Synthesis and antibacterial activity of catecholate-ciprofloxacin conjugates. *Bioorg. Med. Chem.* **2014**, *22* (15), 4049-60.
143. Noel, S.; Gasser, V.; Pesset, B.; Hoegy, F.; Rognan, D.; Schalk, I. J.; Mislin, G. L., Synthesis and biological properties of conjugates between fluoroquinolones and a N³-functionalized pyochelin. *Org. Biomol. Chem.* **2011**, *9* (24), 8288-300.
144. Rivault, F.; Liebert, C.; Burger, A.; Hoegy, F.; Abdallah, M. A.; Schalk, I. J.; Mislin, G. L., Synthesis of pyochelin-norfloxacin conjugates. *Bioorg. Med. Chem. Lett.* **2007**, *17* (3), 640-4.
145. Ghosh, M.; Miller, M. J., Design, synthesis, and biological evaluation of isocyanurate-based antifungal and macrolide antibiotic conjugates: Iron transport-mediated drug delivery. *Bioorgan. Med. Chem.* **1995**, *3* (11), 1519-1525.
146. Ghosh, M.; Miller, P. A.; Mollmann, U.; Claypool, W. D.; Schroeder, V. A.; Wolter, W. R.; Suckow, M.; Yu, H.; Li, S.; Huang, W.; Zajicek, J.; Miller, M. J., Targeted Antibiotic Delivery: Selective Siderophore Conjugation with Daptomycin Confers Potent Activity against Multidrug Resistant *Acinetobacter baumannii* Both in Vitro and in Vivo. *J. Med. Chem.* **2017**.
147. Ghosh, M.; Miller, M. J., Synthesis and in vitro antibacterial activity of spermidine-based mixed catechol- and hydroxamate-containing siderophore—Vancomycin conjugates. *Bioorgan. Med. Chem.* **1996**, *4* (1), 43-48.

148. Gorityala, B. K.; Guchhait, G.; Goswami, S.; Fernando, D. M.; Kumar, A.; Zhanel, G. G.; Schweizer, F., Hybrid Antibiotic Overcomes Resistance in *P. aeruginosa* by Enhancing Outer Membrane Penetration and Reducing Efflux. *J. Med. Chem.* **2016**, *59* (18), 8441-55.
149. Cochrane, S. A.; Li, X.; He, S.; Yu, M.; Wu, M.; Vederas, J. C., Synthesis of Tridecaptin-Antibiotic Conjugates with in Vivo Activity against Gram-Negative Bacteria. *J. Med. Chem.* **2015**, *58* (24), 9779-85.
150. Deshayes, S.; Xian, W.; Schmidt, N. W.; Kordbacheh, S.; Lieng, J.; Wang, J.; Zarmer, S.; Germain, S. S.; Voyen, L.; Thulin, J.; Wong, G. C.; Kasko, A. M., Designing Hybrid Antibiotic Peptide Conjugates To Cross Bacterial Membranes. *Bioconjug. Chem.* **2017**, *28* (3), 793-804.
151. Klahn, P.; Bronstrup, M., Bifunctional antimicrobial conjugates and hybrid antimicrobials. *Nat. Prod. Rep.* **2017**.
152. Wenderski, T. A.; Stratton, C. F.; Bauer, R. A.; Kopp, F.; Tan, D. S., Principal component analysis as a tool for library design: a case study investigating natural products, brand-name drugs, natural product-like libraries, and drug-like libraries. *Methods Mol. Biol.* **2015**, *1263*, 225-42.
153. Stratton, C. F.; Newman, D. J.; Tan, D. S., Cheminformatic comparison of approved drugs from natural product versus synthetic origins. *Bioorg. Med. Chem. Lett.* **2015**, *25* (21), 4802-7.
154. Cisar, J. S.; Ferreras, J. A.; Soni, R. K.; Quadri, L. E.; Tan, D. S., Exploiting ligand conformation in selective inhibition of non-ribosomal peptide synthetase amino acid adenylation with designed macrocyclic small molecules. *J. Am. Chem. Soc.* **2007**, *129* (25), 7752-3.
155. Davis, T. D.; Mohandas, P.; Chiriach, M. I.; Bythrow, G. V.; Quadri, L. E.; Tan, D. S., Design, synthesis, and biological evaluation of alpha-hydroxyacyl-AMS inhibitors of amino acid adenylation enzymes. *Bioorg. Med. Chem. Lett.* **2016**, *26* (21), 5340-5345.
156. Vidal, S.; Bredin, J.; Pages, J. M.; Barbe, J., Beta-lactam screening by specific residues of the OmpF eyelet. *J. Med. Chem.* **2005**, *48* (5), 1395-400.
157. Danelon, C.; Nestorovich, E. M.; Winterhalter, M.; Ceccarelli, M.; Bezrukov, S. M., Interaction of zwitterionic penicillins with the OmpF channel facilitates their translocation. *Biophys. J.* **2006**, *90* (5), 1617-27.
158. Scorciapino, M. A.; D'Agostino, T.; Acosta-Gutierrez, S.; Mallocci, G.; Bodrenko, I.; Ceccarelli, M., Exploiting the porin pathway for polar compound delivery into Gram-negative bacteria. *Future Med. Chem.* **2016**, *8* (10), 1047-62.
159. Wiener, J. J.; Gomez, L.; Venkatesan, H.; Santillan, A., Jr.; Allison, B. D.; Schwarz, K. L.; Shinde, S.; Tang, L.; Hack, M. D.; Morrow, B. J.; Motley, S. T.; Goldschmidt, R. M.; Shaw, K. J.; Jones, T. K.; Grice, C. A., Tetrahydroindazole inhibitors of bacterial type II topoisomerases. Part 2: SAR development and potency against multidrug-resistant strains. *Bioorg. Med. Chem. Lett.* **2007**, *17* (10), 2718-22.
160. Surivet, J. P.; Zumbrunn, C.; Rueedi, G.; Hubschwerlen, C.; Bur, D.; Bruyere, T.; Locher, H.; Ritz, D.; Keck, W.; Seiler, P.; Kohl, C.; Gauvin, J. C.; Mirre, A.; Kaegi, V.; Dos Santos, M.; Gaertner, M.; Delers, J.; Enderlin-Paput, M.; Boehme, M., Design, synthesis, and characterization of novel tetrahydropyran-based bacterial topoisomerase inhibitors with potent anti-gram-positive activity. *J. Med. Chem.* **2013**, *56* (18), 7396-415.
161. Surivet, J. P.; Zumbrunn, C.; Rueedi, G.; Bur, D.; Bruyere, T.; Locher, H.; Ritz, D.; Seiler, P.; Kohl, C.; Ertel, E. A.; Hess, P.; Gauvin, J. C.; Mirre, A.; Kaegi, V.; Dos Santos, M.; Kraemer, S.; Gaertner, M.; Delers, J.; Enderlin-Paput, M.; Weiss, M.; Sube, R.; Hadana, H.; Keck, W.; Hubschwerlen, C., Novel tetrahydropyran-based bacterial topoisomerase inhibitors

- with potent anti-gram positive activity and improved safety profile. *J. Med. Chem.* **2015**, *58* (2), 927-42.
162. Surivet, J. P.; Zumbrunn, C.; Bruyere, T.; Bur, D.; Kohl, C.; Locher, H. H.; Seiler, P.; Ertel, E. A.; Hess, P.; Enderlin-Paput, M.; Enderlin-Paput, S.; Gauvin, J. C.; Mirre, A.; Hubschwerlen, C.; Ritz, D.; Rueedi, G., Synthesis and Characterization of Tetrahydropyran-Based Bacterial Topoisomerase Inhibitors with Antibacterial Activity against Gram-Negative Bacteria. *J. Med. Chem.* **2017**.
163. Richter, M. F.; Drown, B. S.; Riley, A. P.; Garcia, A.; Shirai, T.; Svec, R. L.; Hergenrother, P. J., Predictive compound accumulation rules yield a broad-spectrum antibiotic. *Nature* **2017**, *545* (7654), 299-304.
164. Kuenemann, M. A.; Bourbon, L. M.; Labbe, C. M.; Villoutreix, B. O.; Sperandio, O., Which three-dimensional characteristics make efficient inhibitors of protein-protein interactions? *J. Chem. Inf. Model.* **2014**, *54* (11), 3067-79.
165. Kuenemann, M. A.; Labbe, C. M.; Cerdan, A. H.; Sperandio, O., Imbalance in chemical space: How to facilitate the identification of protein-protein interaction inhibitors. *Sci. Rep.* **2016**, *6*, 23815.
166. Mannhold, R.; Berellini, G.; Carosati, E.; Benedetti, P., Use of MIF-based VolSurf Descriptors in Physicochemical and Pharmacokinetic Studies. *Molecular Interaction Fields: Applications in Drug Discovery and ADME Prediction* **2006**, *27*, 171-196.
167. Carney, D. W.; Compton, C. L.; Schmitz, K. R.; Stevens, J. P.; Sauer, R. T.; Sello, J. K., A simple fragment of cyclic acyldepsipeptides is necessary and sufficient for ClpP activation and antibacterial activity. *Chembiochem* **2014**, *15* (15), 2216-20.
168. Brotz-Oesterhelt, H.; Beyer, D.; Kroll, H. P.; Endermann, R.; Ladel, C.; Schroeder, W.; Hinzen, B.; Raddatz, S.; Paulsen, H.; Henninger, K.; Bandow, J. E.; Sahl, H. G.; Labischinski, H., Dysregulation of bacterial proteolytic machinery by a new class of antibiotics. *Nat Med* **2005**, *11* (10), 1082-7.
169. Conlon, B. P.; Nakayasu, E. S.; Fleck, L. E.; LaFleur, M. D.; Isabella, V. M.; Coleman, K.; Leonard, S. N.; Smith, R. D.; Adkins, J. N.; Lewis, K., Activated ClpP kills persisters and eradicates a chronic biofilm infection. *Nature* **2013**, *503* (7476), 365-70.
170. Dougan, D. A., Chemical activators of ClpP: turning Jekyll into Hyde. *Chem Biol* **2011**, *18* (9), 1072-4.
171. Griffith, E. C.; Zhao, Y.; Singh, A. P.; Conlon, B. P.; Tangallapally, R.; Shadrack, W. R.; Liu, J.; Wallace, M. J.; Yang, L.; Elmore, J. M.; Li, Y.; Zheng, Z.; Miller, D. J.; Cheramie, M. N.; Lee, R. B.; LaFleur, M. D.; Lewis, K.; Lee, R. E., Ureadepsipeptides as ClpP Activators. *ACS Infect Dis* **2019**, *5* (11), 1915-1925.
172. Meyer, S. D.; Schreiber, S. L., Acceleration of the Dess-Martin Oxidation by Water. *Journal of Organic Chemistry* **1994**, *59* (24), 7549-7552.
173. Zhang, E.; Tian, H.; Xu, S.; Yu, X.; Xu, Q., Iron-catalyzed direct synthesis of imines from amines or alcohols and amines via aerobic oxidative reactions under air. *Org Lett* **2013**, *15* (11), 2704-7.
174. Blackburn, L.; Taylor, R. J., In situ oxidation-imine formation-reduction routes from alcohols to amines. *Org Lett* **2001**, *3* (11), 1637-9.
175. Kwon, M. S.; Kim, S.; Park, S.; Bosco, W.; Chidrala, R. K.; Park, J., One-pot synthesis of imines and secondary amines by Pd-catalyzed coupling of benzyl alcohols and primary amines. *J Org Chem* **2009**, *74* (7), 2877-9.

176. Peng, H.; Carrico, D.; Thai, V.; Blaskovich, M.; Bucher, C.; Pusateri, E. E.; Sebti, S. M.; Hamilton, A. D., Synthesis and evaluation of potent, highly-selective, 3-aryl-piperazine inhibitors of protein geranylgeranyltransferase-I. *Org Biomol Chem* **2006**, *4* (9), 1768-84.
177. Stein, A. R.; Tan, S.-H., The Alkylation of Ambident Anions. IV. The Alkali Metal and Silver Salts of Formanilides. *Can. J. Chem* **1974**, *52*.
178. Levine, R.; Fernelius, W. C., The Chemistry of the Alkali Amides. *Chemical Reviews* **2002**, *54* (3), 449-573.
179. Breugst, M.; Mayr, H., Ambident reactivities of pyridone anions. *J Am Chem Soc* **2010**, *132* (43), 15380-9.
180. Petersen, S.; Tietze, E., Reaktionen Cyclischer Lactimäther mit Acylierten Hydrazinderivaten. *Chemische Berichte* **1957**, *90* (6), 909-921.
181. Bartels, G.; Hinze, R.-P.; Wullbrandt, D., Beiträge zur Kenntnis des chromophoren Systems der Corrine, VII. Notiz über die Reaktion von Diazoessigsäure-methylester mit Lactamen; eine Modellreaktion zur Cyclisierung von 5,6-Dioxo-monosecocorrinen. *Liebigs Annalen der Chemie* **1980**, *1980* (1), 168-170.
182. Meerwein, H.; Hinz, G.; Hofmann, P.; Kroning, E.; Pfeil, E., Über Tertiäre Oxoniumsalze, I. *Journal für Praktische Chemie* **1937**, *147* (10-12), 257-285.
183. Popov, K.; Somfai, P., Synthesis of Imidates: TFA-Mediated Regioselective Amide Alkylation Using Meerwein's Reagent. *J Org Chem* **2016**, *81* (8), 3470-2.
184. Bogdal, D., Fast Solvent-free Alkylation of Amides and Lactams under Microwave Irradiation. *Molecules* **1999**, *4* (12), 333-337.
185. Salvatore, R. N.; Nagle, A. S.; Jung, K. W., Cesium effect: high chemoselectivity in direct N-alkylation of amines. *J Org Chem* **2002**, *67* (3), 674-83.
186. Dijkstra, G.; Kruizinga, W. H.; Kellogg, R. M., An assessment of the causes of the "cesium effect". *The Journal of Organic Chemistry* **2002**, *52* (19), 4230-4234.
187. Do, H. Q.; Bachman, S.; Bissember, A. C.; Peters, J. C.; Fu, G. C., Photoinduced, copper-catalyzed alkylation of amides with unactivated secondary alkyl halides at room temperature. *J Am Chem Soc* **2014**, *136* (5), 2162-7.
188. Cho, D. W.; Mariano, P. S.; Yoon, U. C., Direct and indirect single electron transfer (SET)-photochemical approaches for the preparation of novel phthalimide and naphthalimide-based lariat-type crown ethers. *Beilstein J Org Chem* **2014**, *10*, 514-27.
189. Ryland, B. L.; McCann, S. D.; Brunold, T. C.; Stahl, S. S., Mechanism of alcohol oxidation mediated by copper(II) and nitroxyl radicals. *J Am Chem Soc* **2014**, *136* (34), 12166-73.
190. Rankic, D. A.; Stiff, C. M.; Am Ende, C. W.; Humphrey, J. M., Protocol for the Direct Conversion of Lactones to Lactams Mediated by 1,5,7-Triazabicyclo[4.4.0]dec-5-ene: Synthesis of Pyridopyrazine-1,6-diones. *J Org Chem* **2017**, *82* (23), 12791-12797.
191. Sabot, C.; Kumar, K. A.; Meunier, S.; Mioskowski, C., A convenient aminolysis of esters catalyzed by 1,5,7-triazabicyclo[4.4.0]dec-5-ene (TBD) under solvent-free conditions. *Tetrahedron Letters* **2007**, *48* (22), 3863-3866.
192. Kikelj, D.; Trstenjak, U.; Ilaš, J., Advances in the Synthesis of Morpholin-3-ones and Morpholin-2-ones. *Synthesis* **2012**, *44* (23), 3551-3578.
193. Yin, K. H.; Hsieh, Y. H.; Sulake, R. S.; Wang, S. P.; Chao, J. I.; Chen, C., Optimization of gefitinib analogues with potent anticancer activity. *Bioorg Med Chem Lett* **2014**, *24* (22), 5247-50.
194. Bardiot, D.; Thevissen, K.; De Brucker, K.; Peeters, A.; Cos, P.; Taborda, C. P.; McNaughton, M.; Maes, L.; Chaltin, P.; Cammue, B. P.; Marchand, A., 2-(2-oxo-morpholin-3-

- yl)-acetamide derivatives as broad-spectrum antifungal agents. *J Med Chem* **2015**, *58* (3), 1502-12.
195. Mohseni, S.; Bakavoli, M.; Morsali, A., Theoretical and experimental studies on the regioselectivity of epoxide ring opening by nucleophiles in nitromethane without any catalyst: nucleophilic-chain attack mechanism. *Progress in Reaction Kinetics and Mechanism* **2014**, *39* (1), 89-102.
196. Philippe, C.; Milcent, T.; Crousse, B.; Bonnet-Delpon, D., Non Lewis acid catalysed epoxide ring opening with amino acid esters. *Org Biomol Chem* **2009**, *7* (10), 2026-8.
197. Auge, J.; Leroy, F., Lithium trifluoromethanesulfonate-catalysed aminolysis of oxiranes. *Tetrahedron Letters* **1996**, *37* (43), 7715-7716.
198. Gala, D.; DiBenedetto, D. J., A rational approach to chiral α -hydroxy aryl ketones from chiral aryl epoxides via regioselective, stereo retentive oxidative epoxide opening: Its application to the synthesis of antifungal Sch 42427/SM 9164. *Tetrahedron Letters* **1994**, *35* (45), 8299-8302.
199. Hou, X.; Zhang, H.; Chen, B.-C.; Guo, Z.; Singh, A.; Goswami, A.; Gilmore, J. L.; Sheppeck, J. E.; Dyckman, A. J.; Carter, P. H.; Mathur, A., Regioselective Epoxide Ring Opening for the Stereospecific Scale-Up Synthesis of BMS-960, A Potent and Selective Isoxazole-Containing S1P1 Receptor Agonist. *Organic Process Research & Development* **2017**, *21*, 200-207.
200. Wang, B.; Elageed, E. H. M.; Zhang, D.; Yang, S.; Wu, S.; Zhang, G.; Gao, G., One-Pot Conversion of Carbon Dioxide, Ethylene Oxide, and Amines to 3-Aryl-2-oxazolidinones Catalyzed with Binary Ionic Liquids. *ChemCatChem* **2014**, *6* (1), 278-283.
201. Calo, V.; Nacci, A.; Monopoli, A.; Fanizzi, A., Cyclic carbonate formation from carbon dioxide and oxiranes in tetrabutylammonium halides as solvents and catalysts. *Org Lett* **2002**, *4* (15), 2561-3.
202. Wang, B.; Luo, Z.; Elageed, E. H. M.; Wu, S.; Zhang, Y.; Wu, X.; Xia, F.; Zhang, G.; Gao, G., DBU and DBU-Derived Ionic Liquid Synergistic Catalysts for the Conversion of Carbon Dioxide/Carbon Disulfide to 3-Aryl-2-oxazolidinones/[1,3]Dithiolan-2-ylidenephényl- amine. *ChemCatChem* **2016**, *8* (4), 830-838.
203. Jacobsen, E. N., Asymmetric catalysis of epoxide ring-opening reactions. *Acc Chem Res* **2000**, *33* (6), 421-31.
204. Bartoli, G.; Bosco, M.; Carlone, A.; Locatelli, M.; Massaccesi, M.; Melchiorre, P.; Sambri, L., Asymmetric aminolysis of aromatic epoxides: a facile catalytic enantioselective synthesis of anti-beta-amino alcohols. *Org Lett* **2004**, *6* (13), 2173-6.
205. Kantam, M. L.; Choudary, B. M.; Bharathi, B., Ring Opening of Oxiranes Catalyzed by Mn-Salen Immobilized Mesoporous Materials. *Synthetic Communications* **1999**, *29* (7), 1121-1128.
206. Ferris, W. V. Preparation of a N-alkylated rifampin. 2008.
207. Mastalerz, H.; Kadow, J. F. Preparation of 7-sulfur substituted paclitaxels as antitumor agents. 1998.
208. Deng, Q.; Ji, Q.-G.; Ge, Z.-Q.; liu, X.-F.; Yang, D.; Yuan, L.-J., Synthesis and biological evaluation of novel quinolin-2(1H)-one derivatives as potential antimicrobial agents. *Medicinal Chemistry Research* **2014**, *23* (12), 5224-5236.
209. An, J. S.; Shin, W. K.; An, D. K., Quantitative Synthesis of Aldehydes from Weinreb Amides Using Lithium Diisobutyl-t-Butoxyaluminum Hydride (LDBBA). *Bulletin of the Korean Chemical Society* **2015**, *36* (12), 2928-2931.

210. Veisi, H.; Maleki, B.; Hamelian, M.; Ashrafi, S. S., Chemoselective hydration of nitriles to amides using hydrated ionic liquid (IL) tetrabutylammonium hydroxide (TBAH) as a green catalyst. *Rsc Advances* **2015**, *5* (9), 6365-6371.
211. Rousselet, G.; Capdevielle, P.; Maumy, M., Copper(I)-induced addition of amines to unactivated nitriles: The first general one-step synthesis of alkyl amidines. *Tetrahedron Letters* **1993**, *34* (40), 6395-6398.
212. Telvekar, V.; Bhagat, S., l-Proline: An Efficient Organocatalyst for the Synthesis of 5-Substituted 1H-Tetrazoles via [3+2] Cycloaddition of Nitriles and Sodium Azide. *Synlett* **2018**, *29* (07), 874-879.
213. Goodreid, J. D.; Janetzko, J.; Santa Maria, J. P., Jr.; Wong, K. S.; Leung, E.; Eger, B. T.; Bryson, S.; Pai, E. F.; Gray-Owen, S. D.; Walker, S.; Houry, W. A.; Batey, R. A., Development and Characterization of Potent Cyclic Acyldepsipeptide Analogues with Increased Antimicrobial Activity. *J Med Chem* **2016**, *59* (2), 624-46.
214. Bradbury, R. H.; Callis, R.; Carr, G. R.; Chen, H.; Clark, E.; Feron, L.; Glossop, S.; Graham, M. A.; Hattersley, M.; Jones, C.; Lamont, S. G.; Ouvry, G.; Patel, A.; Patel, J.; Rabow, A. A.; Roberts, C. A.; Stokes, S.; Stratton, N.; Walker, G. E.; Ward, L.; Whalley, D.; Whittaker, D.; Wrigley, G.; Waring, M. J., Optimization of a Series of Bivalent Triazolopyridazine Based Bromodomain and Extraterminal Inhibitors: The Discovery of (3R)-4-[2-[4-[1-(3-Methoxy-[1,2,4]triazolo[4,3-b]pyridazin-6-yl)-4-piperidyl]phenoxy]ethyl]-1,3-dimethyl-piperazin-2-one (AZD5153). *J Med Chem* **2016**, *59* (17), 7801-17.
215. Kim, H. J.; Kwak, W. Y.; Min, J. P.; Lee, J. Y.; Yoon, T. H.; Kim, H. D.; Shin, C. Y.; Kim, M. K.; Choi, S. H.; Kim, H. S.; Yang, E. K.; Cheong, Y. H.; Chae, Y. N.; Park, K. J.; Jang, J. M.; Choi, S. J.; Son, M. H.; Kim, S. H.; Yoo, M.; Lee, B. J., Discovery of DA-1229: a potent, long acting dipeptidyl peptidase-4 inhibitor for the treatment of type 2 diabetes. *Bioorg Med Chem Lett* **2011**, *21* (12), 3809-12.
216. Mehla, J.; Mallocci, G.; Mansbach, R.; Lopez, C. A.; Tsivkovski, R.; Haynes, K.; Leus, I. V.; Grindstaff, S. B.; Cascella, R. H.; D'Cunha, N.; Herndon, L.; Hengartner, N. W.; Margiotta, E.; Atzori, A.; Vargiu, A. V.; Manrique, P. D.; Walker, J. K.; Lomovskaya, O.; Ruggerone, P.; Gnanakaran, S.; Rybenkov, V. V.; Zgurskaya, H. I., Predictive Rules of Efflux Inhibition and Avoidance in *Pseudomonas aeruginosa*. *mBio* **2021**, *12* (1).
217. El Zahed, S. S.; French, S.; Farha, M. A.; Kumar, G.; Brown, E. D., Physicochemical and Structural Parameters Contributing to the Antibacterial Activity and Efflux Susceptibility of Small-Molecule Inhibitors of *Escherichia coli*. *Antimicrob Agents Chemother* **2021**, *65* (4).
218. Spaulding, A.; Takroui, K.; Mahalingam, P.; Cleary, D. C.; Cooper, H. D.; Zucchi, P.; Tear, W.; Koleva, B.; Beuning, P. J.; Hirsch, E. B.; Aggen, J. B., Compound design guidelines for evading the efflux and permeation barriers of *Escherichia coli* with the oxazolidinone class of antibacterials: Test case for a general approach to improving whole cell Gram-negative activity. *Bioorg Med Chem Lett* **2017**, *27* (23), 5310-5321.
219. Cooper, S. J.; Krishnamoorthy, G.; Wolloscheck, D.; Walker, J. K.; Rybenkov, V. V.; Parks, J. M.; Zgurskaya, H. I., Molecular Properties That Define the Activities of Antibiotics in *Escherichia coli* and *Pseudomonas aeruginosa*. *ACS Infect Dis* **2018**, *4* (8), 1223-1234.
220. Ceccarelli, M.; Bodrenko, I.; Acosta Gutiérrez, S., Permeability Through Bacterial Porins Dictates Whole Cell Compound Accumulation. **2020**.

Appendix (Chapter 2)

Porin type	Characterized porin (PDB code)	Bacterial strain	Substrate
General porins	OmpC (2J1N)	<i>E. coli</i>	Various ¹
	OmpF (2OMF)	<i>E. coli</i>	Various ²
	PhoE (1PHO)	<i>E. coli</i>	Various ²
	OmpK36 (1OSM)	<i>K. pneumoniae</i>	Various ²
	OprF (4RLC)	<i>P. aeruginosa</i>	Various ³
	OmpA (1QJP)	<i>E. coli, A. baumannii</i>	Various ²
Specific porins	LamB (1MAL)	<i>E. coli, S. typhimurium</i>	Carbohydrates ²
	OprB (4GF4)	<i>P. aeruginosa</i>	Carbohydrates ³
	OprD (4FOZ)	<i>P. aeruginosa</i>	Basic amino acids, carbapenems ³
Transport porins	FhuA (1BY3)	<i>E. coli</i>	Ferrichrome ⁴
	FepA (1FEP)	<i>E. coli</i>	Ferric enterobactin ⁴
	FecA (1KMO)	<i>E. coli</i>	Ferric citrate ⁴
	BtuB (1NQH)	<i>E. coli</i>	Vitamin B ₁₂ ⁵

Table S2.1: Gram-negative porins and identified substrates.

Efflux pump system (PDB code)	Bacterial strain	Substrates	Ref.
MacAB-TolC (3FPP)	<i>E. coli</i> <i>S. enterica Typhimurium</i> <i>N. gonorrhoeae</i>	Macrolides (Erythromycin)	6-9

Table S2.2: ABC superfamily multidrug efflux transporters and reported substrates.

Efflux pump system (PDB code)			Bacterial strain	Substrates	Inhibitors	Ref.
Inner membrane transporter	Membrane fusion protein	Outer membrane protein				
AcrB (1IWG)	AcrA (2F1M)	TolC (1EK9)	<i>E. coli</i> , <i>S. enterica</i> <i>Typhimurium</i> <i>H. influenzae</i>	Chloramphenicol Minocycline Erythromycin Nalidixic acid Ciprofloxacin Norfloxacin Enoxacin Doxorubicin Novobiocin Rifampicin Trimethoprim Acriflavine Ethidium bromide Rhodamine 6G Crystal violet Tetraphenylphosphonium Benzalkonium Sodium dodecyl sulfate Deoxycholate Ampicillin Florfenicol Clotrimazole Puromycin Proflavine Methotrexate Tetraphenylarsonium chloride Dequalinum chloride Aminoglycoside Linezolid Lincomycin	Phenylalanine arginine β - naphthylamide (PA β N) Arylpiperazines: 1-(1- naphthylmethyl)- piperazine (NMP) NSC 60339 ABI_PP Pyridoquinoline Chloroquinolone Artesunate BSN-004 BSN-006 BSN-023 Pimozide Lanatoside C Diadzein	10-18
AcrB	AcrA	AcrR	<i>K. pneumoniae</i>	Acriflavine	NSC 60339	12, 14, 19-21

(1IWG)	(2F1M)			Chloramphenicol Ethidium bromide Erythromycin Nalidixic acid Norfloxacin Novobiocin Tetracyclines Tigecycline	NMP	
AcrF	AcrE	TolC (1EK9)	<i>E. coli</i> <i>S. enterica</i> <i>Typhimurium</i>	Doxorubicin Acridine Ethidium bromide Rhodamine 6G Sodium dodecyl sulfate Deoxycholate	PAβN	11, 22-24
AcrD (4R86)	AcrA (2F1M)	TolC (1EK9)	<i>E. coli</i> <i>S. enterica</i> <i>Typhimurium</i>	Amikacin Gentamicin Tobramycin Neomycin Naringenin Kanamycin Novobiocin Sodium dodecyl sulfate Deoxycholate Tetracycline	NSC 60339	14, 22, 24-27
MsdA	MsdB	MsdC/TolC	<i>S. enterica</i> <i>Typhimurium</i>	Deoxycholate Novobiocin Sodium dodecyl sulfate		6
MdtA	MdtBC	TolC (1EK9)	<i>E. coli</i> <i>S. enterica</i> <i>Typhimurium</i>	Deoxycholate Novobiocin Sodium dodecyl sulfate		6, 22
OqxB	OqxA		<i>E. coli</i> <i>K. pneumoniae</i>	Chloramphenicol Ciprofloxacin Ethidium bromide Olaquinox Fluoroquinolones		28
AdeB	AdeA	AdeC	<i>A. baumannii</i>	Amikacin	PAβN	29-33

				Gentamicin Kanamycin Netilmicin Tobramycin β -lactams Cephalosporins Nitrocefin Rifampicin Novobiocin Ethidium Bromide Tetracycline Erythromycin Chloramphenicol Trimethoprim Fluoroquinolones	NMP Carbonyl cyanide m- chlorophenylhydrazine (CCCP)	
AdeG	AdeF	AdeH	<i>A. baumannii</i>	Chloramphenicol Trimethoprim Ciprofloxacin Clindamycin	PA β N	34-36
AdeJ	AdeI	AdeK	<i>A. baumannii</i>	β -lactams Chloramphenicol Erythromycin Fluoroquinolones Fusidic acid Lincosamide Acridine Novobiocin Pyronine Rifampicin Safranin Sodium dodecyl sulfate Tetracyclines Trimethoprim		36, 37
CmeE	CmeD	CmeF	<i>Campylobacter jejuni</i>	Acridine Ampicillin Cetrimide	PA β N NMP CCCP	38-41

				Ethidium Bromide Polymyxin B Sodium dodecyl sulfate Triclosan	Reserpine Verapamil	
MexB (3W9I)	MexA (2V4D)	OprM (1WP1)	<i>P. aeruginosa</i>	Acriflavine Acridine orange Aminoglycosides β -lactams Macrolides Fluoroquinolones Novobiocin Sulfonamides Tetracyclines Lincomycin Chloramphenicol Tigecycline Triclosan	PA β N EA-371 α EA-371 δ ABI_PP Lanatoside C Diadzein	12, 18, 42, 43
MexD	MexC	OprJ (5AZS)	<i>P. aeruginosa</i>	Chlorhexidine Macrolides Fluoroquinolones Novobiocin Tetracyclines Lincomycin Chloramphenicol Penicillin	PA β N	12, 43, 44
MexF	MexE	OprN (5AZO)	<i>P. aeruginosa</i>	Chloramphenicol Fluoroquinolones Trimethoprim Tetracyclines	PA β N	12, 45, 46
MexN	MexM	OprM (1WP1)	<i>P. aeruginosa</i>	Chloramphenicol Thiamphenicol		47
MexQ	MexP	OpmE	<i>P. aeruginosa</i>	Macrolides Fluoroquinolones		47
MexW	MexV	OprM (1WP1)	<i>P. aeruginosa</i>	Acriflavine Chloramphenicol Ethidium bromide		48

				Erythromycin Fluoroquinolones Tetracyclines		
MexY	MexX	OprM (1WP1)	<i>P. aeruginosa</i>	Quinolones Macrolides Tetracyclines Cephalosporins Lincomycin Chloramphenicol Aminoglycosides Penicillins	PAβN Berberine	12, 43, 49
TriC	TriAB	OpmH	<i>P. aeruginosa</i>	Triclosan Sodium dodecyl sulfate		50

Table S2.3: RND superfamily multidrug efflux transporters and reported substrates and inhibitors.

Efflux pump system (PDB code)			Bacterial strain	Substrates	Inhibitors	Ref.
Inner membrane transporter	Membrane fusion protein	Outer membrane protein				
SmvA		OmpW	<i>S. enterica Typhimurium</i>	Acridine Erythromycin Quaternary ammonium Compounds Ethidium Bromide Malachite Green Pyronin B Methyl viologen		51, 52
Mef(B)			<i>E. coli</i>	Macrolides	PAβN	53
QepA			<i>E. coli</i>	Norfloxacin Ciprofloxacin Enrofloxacin		54
KmrA			<i>K. pneumoniae</i>	Kanamycin Norfloxacin Acridine	CCCP	55

				4',6-diamidino-2-phenylindole Ethidium bromide Bisbenzimidazole Tetraphenylphosphonium		
EmrB	EmrA	TolC	<i>E. coli</i> <i>S. enterica</i> <i>Typhimurium</i> <i>A. baumannii</i>	Deoxycholate Nalidixic acid Fluoroquinolones Novobiocin Thiolactomycin Colistin	Coumarin derivatives NMP PAβN	6, 12, 56-58

Table S2.4: MFS superfamily multidrug efflux transporters and reported substrates and inhibitors.^{11, 24, 42}

Efflux pump system	Bacterial strain	Substrates	Inhibitors	Ref.
AbeM	<i>A. baumannii</i>	Norfloxacin Ofloxacin Ciprofloxacin Gentamicin 4',6-diamino-2-phenylindol Triclosan Acriflavine Aminoglycosides Daunomycin Ethidium bromide Chloramphenicol Doxorubicin Fluoroquinolones Tetraphenylphosphonium Bisbenzimidazole Rhodamine 6G	CCCP	59
HmrM	<i>H. influenzae</i>	Norfloxacin Acriflavine Berberine Deoxycholate Daunomycin	CCCP	60

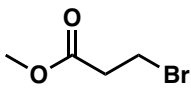
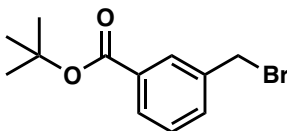
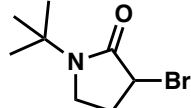
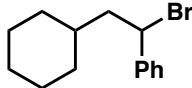
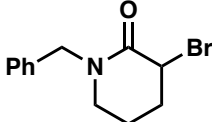
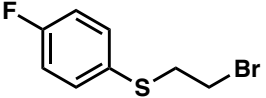
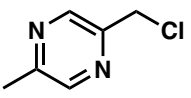
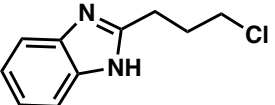
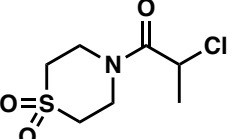
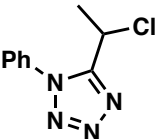
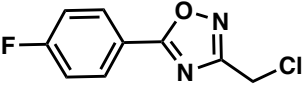
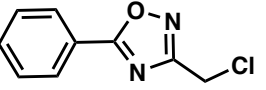
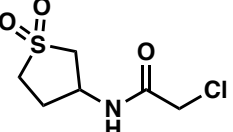
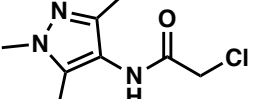
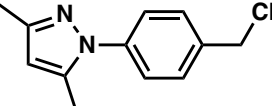
		4',6-diamidino-2-phenylindole Doxorubicin Ethidium bromide Bisbenzimidazole Tetraphenylphosphonium		
YdhE	<i>E. coli</i>	Chloramphenicol Fluoroquinolones Doxorubicin Ethidium bromide Tetraphenylphosphonium Rhodamine 6G Berberine Novobiocin Acriflavine	CCCP	61
NorM	<i>N. gonorrhoeae</i>	Chloramphenicol Fluoroquinolones Doxorubicin Ethidium bromide Tetraphenylphosphonium Rhodamine 6G Berberine Novobiocin Acriflavine	CCCP	62
MdtK	<i>S. enterica Typhimurium</i>	Acriflavine Doxorubicin Norfloxacin		6
PmpM	<i>P. aeruginosa</i>	Acriflavine Benzalkonium Ethidium bromide Fluoroquinolone Tetraphenylphosphonium		63

Table S2.5: MATE superfamily multidrug efflux transporters and reported substrates and inhibitors.

Efflux pump system	Bacterial strain	Substrates	Inhibitors	Ref.
AbeS	<i>A. baumannii</i>	Erythromycin	CCCP	64

		Novobiocin Amikacin Ciprofloxacin Norfloxacin Tetracycline Trimethoprim Acridine Acriflavine Benzalkonium Deoxycholate Sodium dodecyl sulfate		
MdtJI	<i>E. coli</i> <i>Shigella</i>	Deoxycholate Sodium dodecyl sulfate Spermidine		65, 66
EmrE (3B61)	<i>E. coli</i>	Acriflavine Ethidium bromide Benzalkonium		11, 67

Table S2.6: SMR superfamily multidrug efflux transporters and reported substrates and inhibitors.

				
N1	N1	N2	N3	N3
				
N3	N3	N3	N3	N3
				

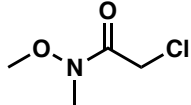
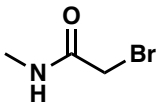
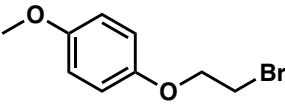
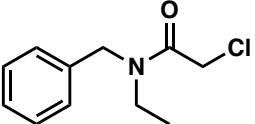
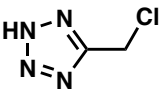
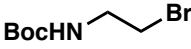
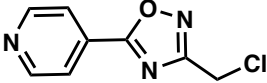
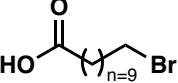
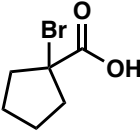
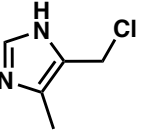
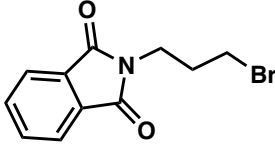
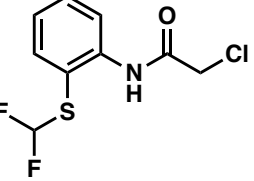
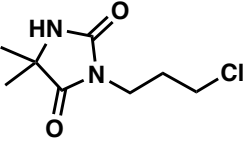
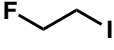
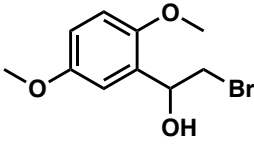
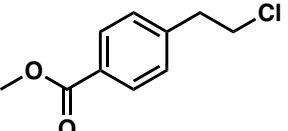
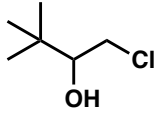
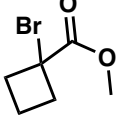
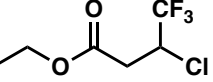
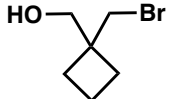
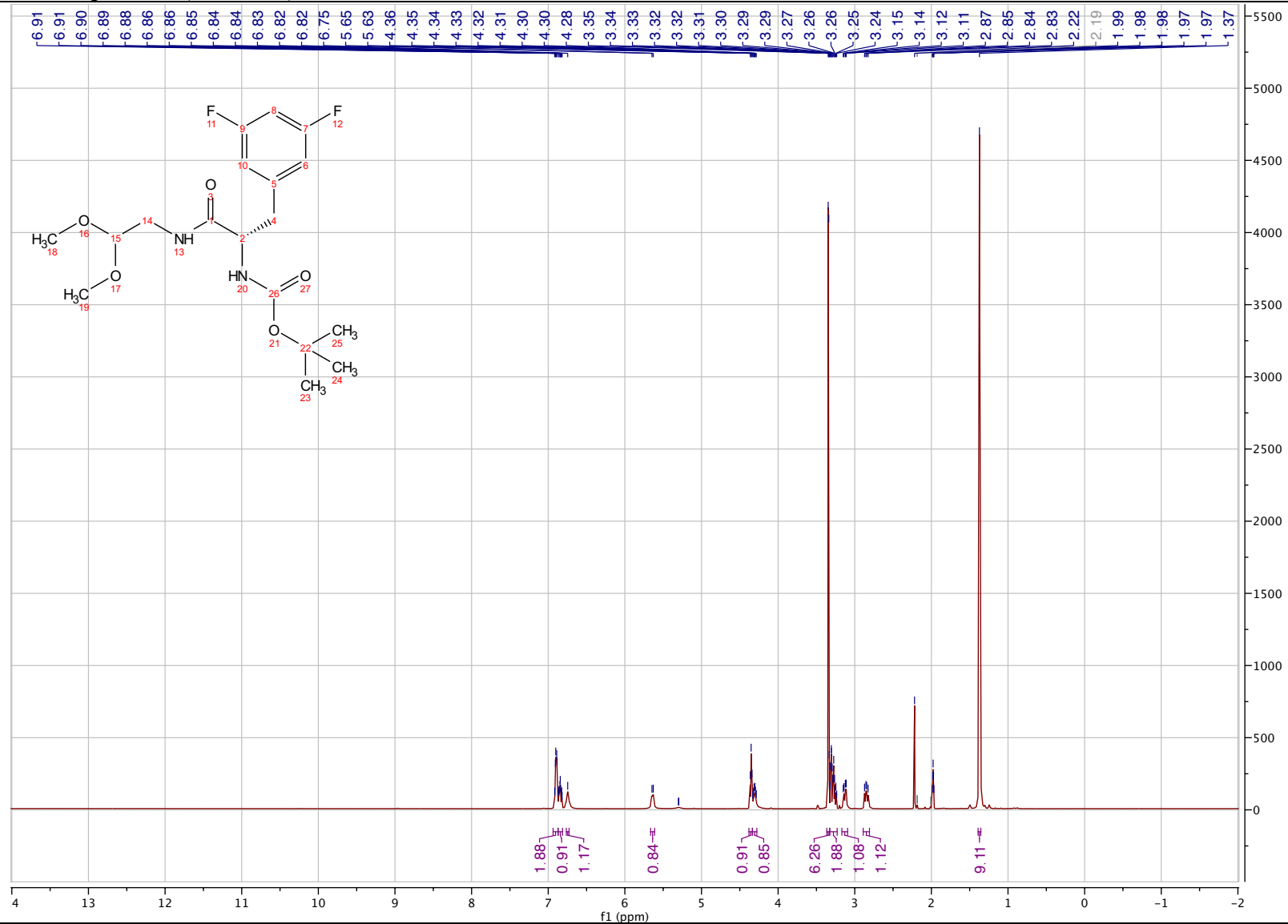
N3	N3	N3	N3	N3
				
N3	N3	N3	N3	N4
				
N4	n/a	n/a	n/a	n/a
				
n/a	n/a	n/a	n/a	n/a
				
n/a	n/a	n/a	n/a	n/a

Table S2.7: SPEAR-GN Alkyl halide list

Spectra

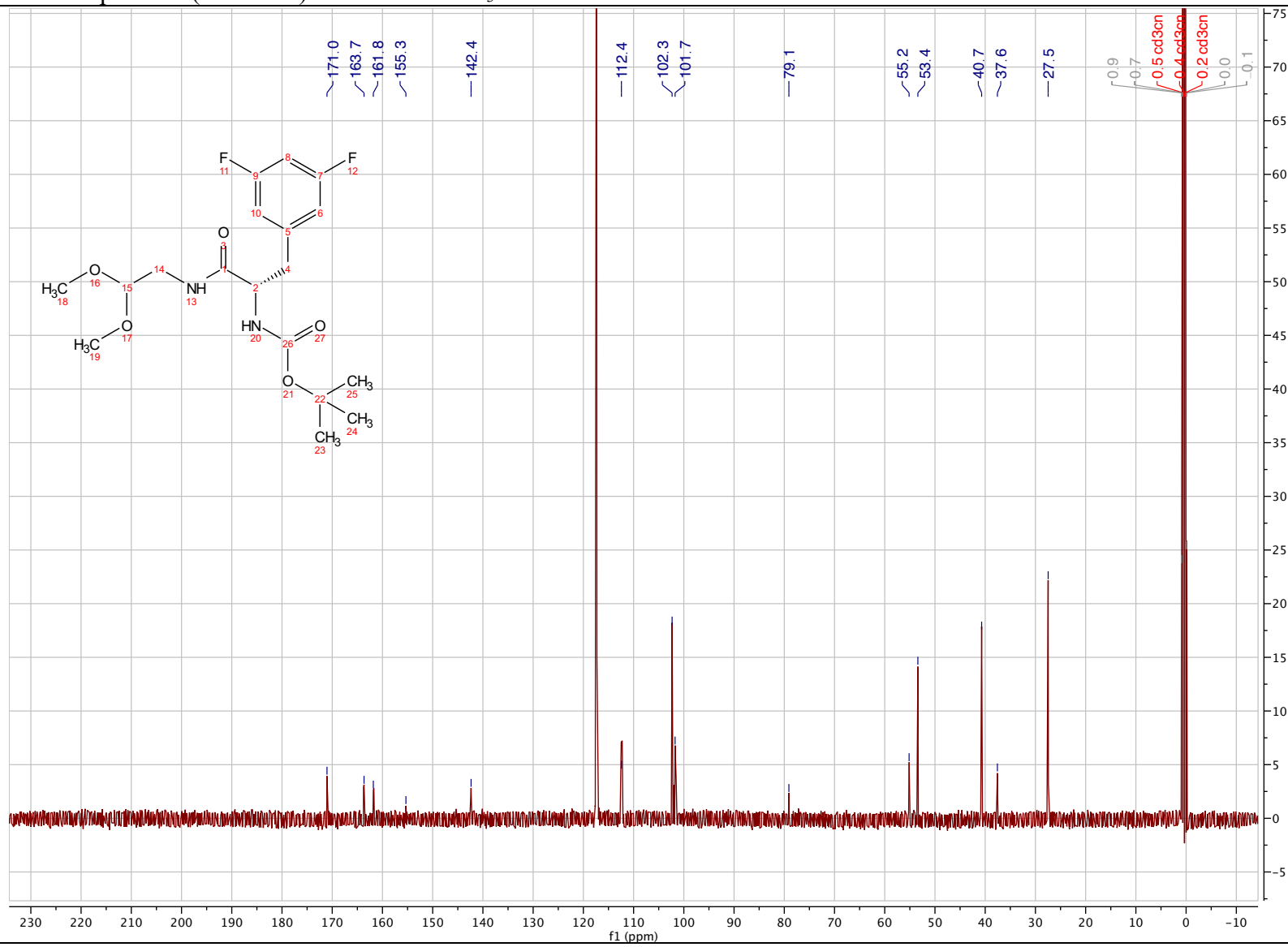
***tert*-butyl (S)-(3-(3,5-difluorophenyl)-1-((2,2-dimethoxyethyl)amino)-1-oxopropan-2-yl)carbamate (2.61)**

¹H NMR spectrum (500 MHz) in Acetonitrile-*d*₃



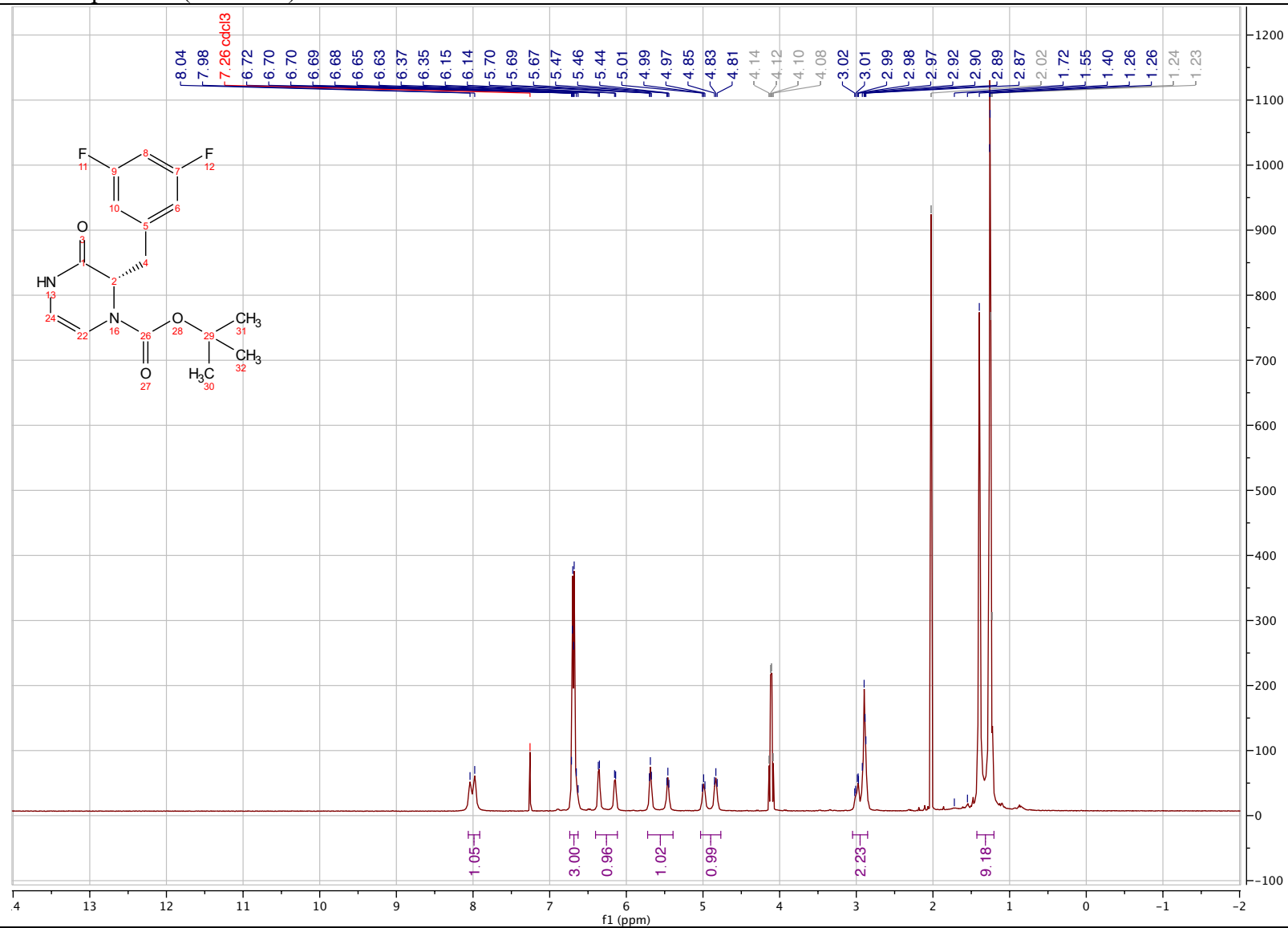
***tert*-butyl (*S*)-(3-(3,5-difluorophenyl)-1-((2,2-dimethoxyethyl)amino)-1-oxopropan-2-yl)carbamate (2.61)**

^{13}C NMR spectrum (126 MHz) in Acetonitrile- d_3



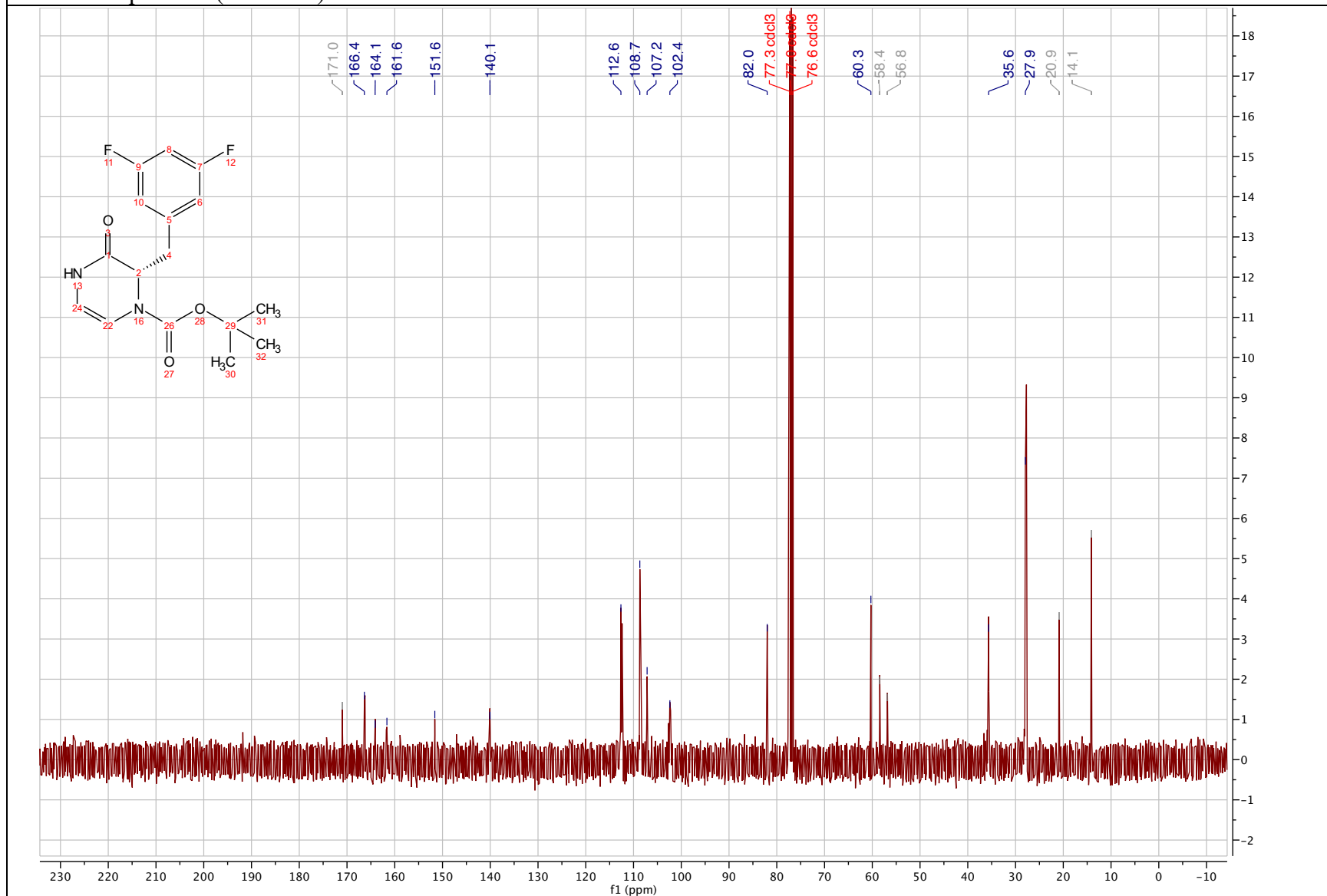
***tert*-butyl (S)-2-(3,5-difluorobenzyl)-3-oxo-3,4-dihydropyrazine-1(2*H*)-carboxylate (2.52)**

¹H NMR spectrum (400 MHz) in Chloroform-*d*



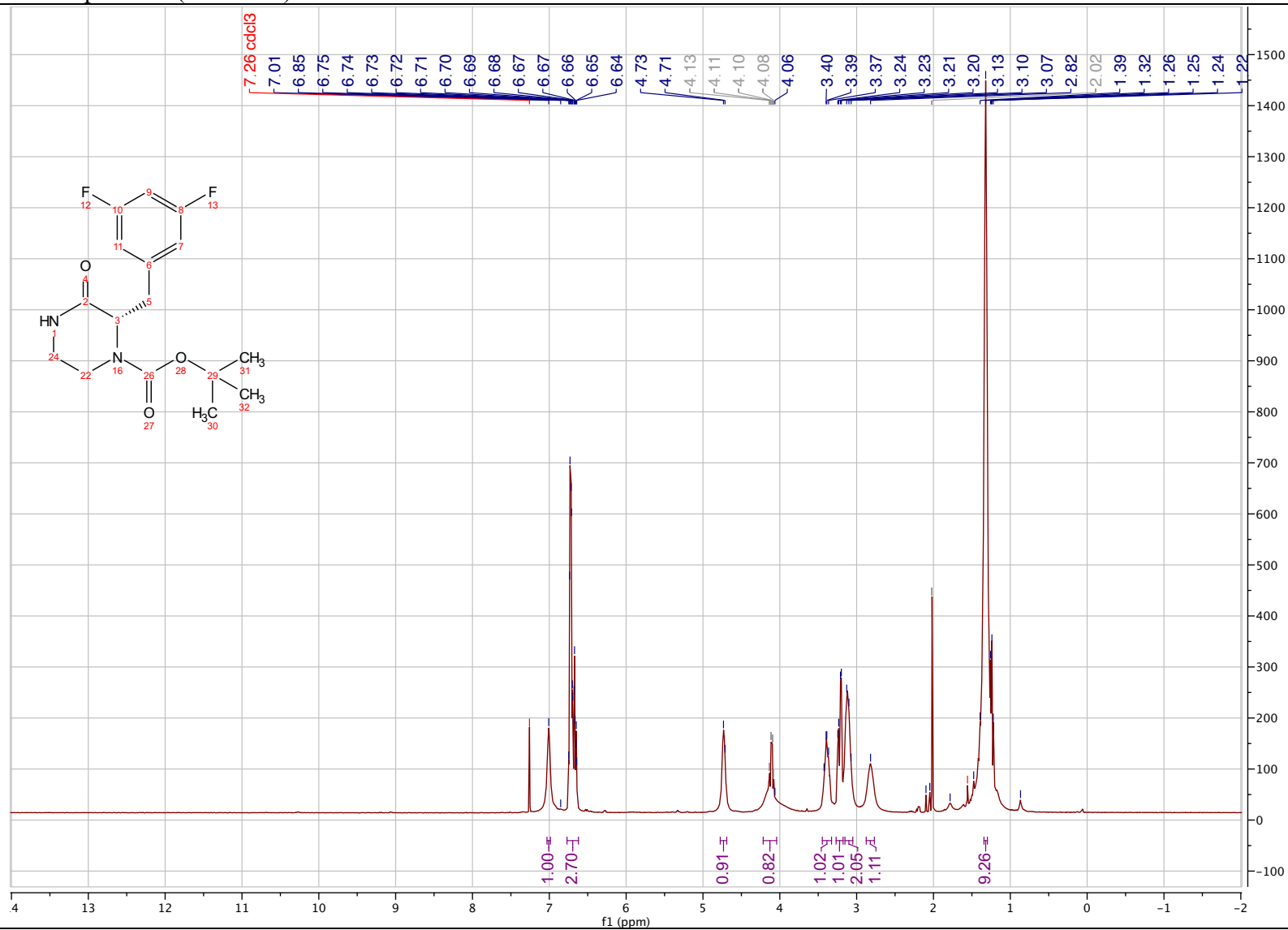
***tert*-butyl (*S*)-2-(3,5-difluorobenzyl)-3-oxo-3,4-dihydropyrazine-1(*2H*)-carboxylate (2.52)**

¹³C NMR spectrum (101 MHz) in Chloroform-*d*



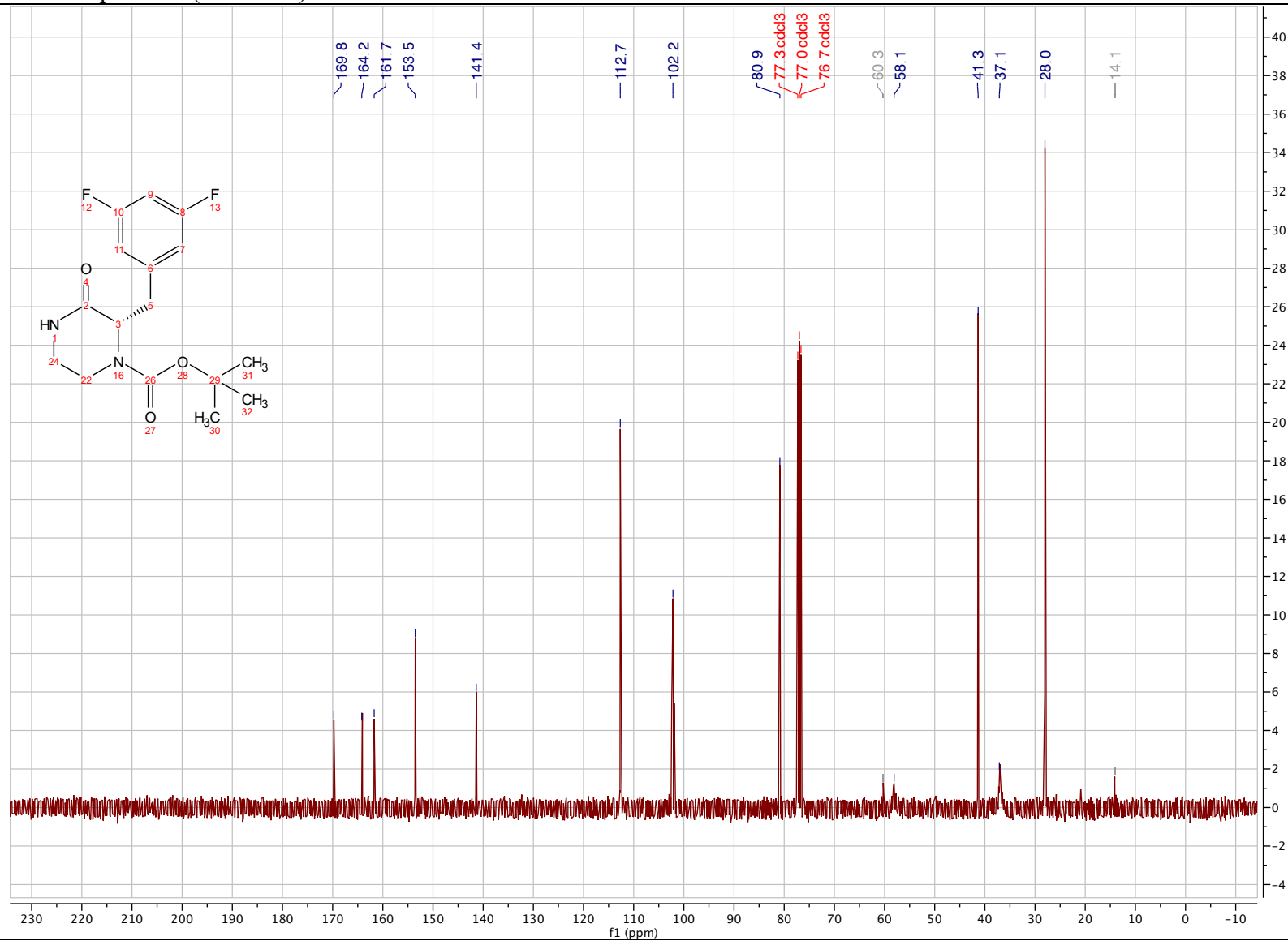
***tert*-butyl (S)-2-(3,5-difluorobenzyl)-3-oxopiperazine-1-carboxylate (2.59)**

¹H NMR spectrum (400 MHz) in Chloroform-*d*



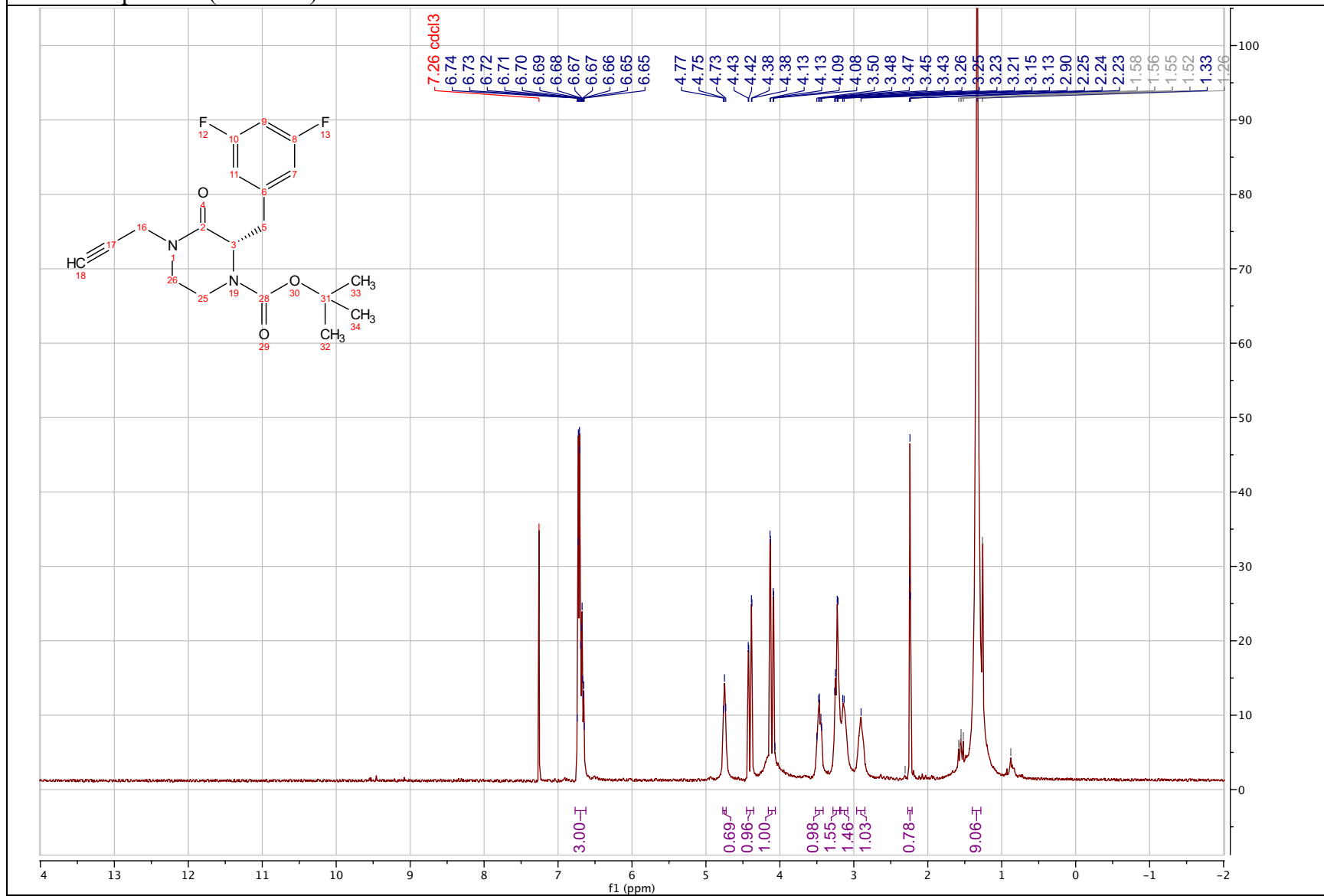
***tert*-butyl (S)-2-(3,5-difluorobenzyl)-3-oxopiperazine-1-carboxylate (2.59)**

^{13}C NMR spectrum (101 MHz) in Chloroform-*d*



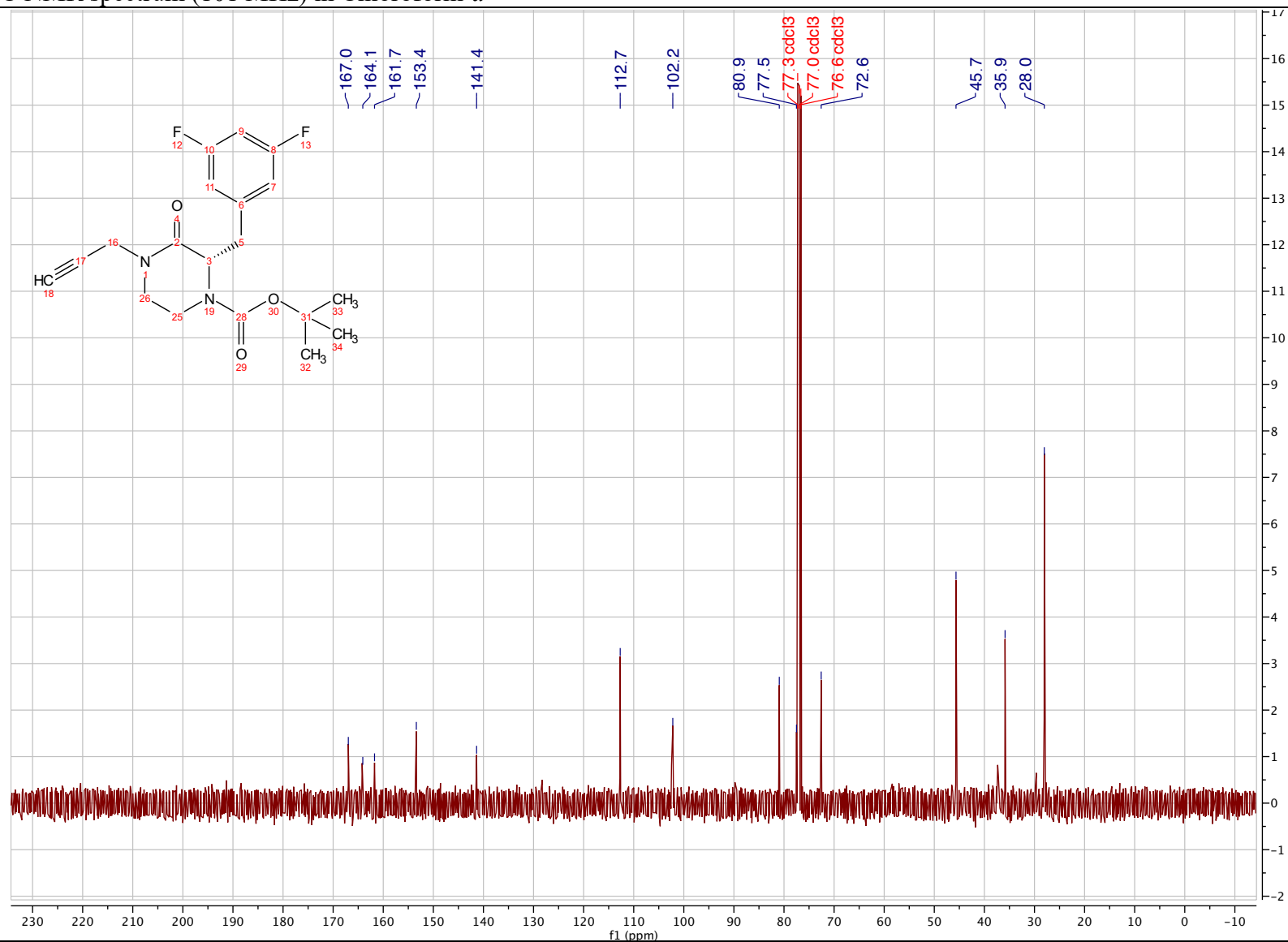
***tert*-butyl (*S*)-2-(3,5-difluorobenzyl)-3-oxo-4-(prop-2-yn-1-yl)piperazine-1-carboxylate (2.62)**

¹H NMR spectrum (400 MHz) in Chloroform-*d*



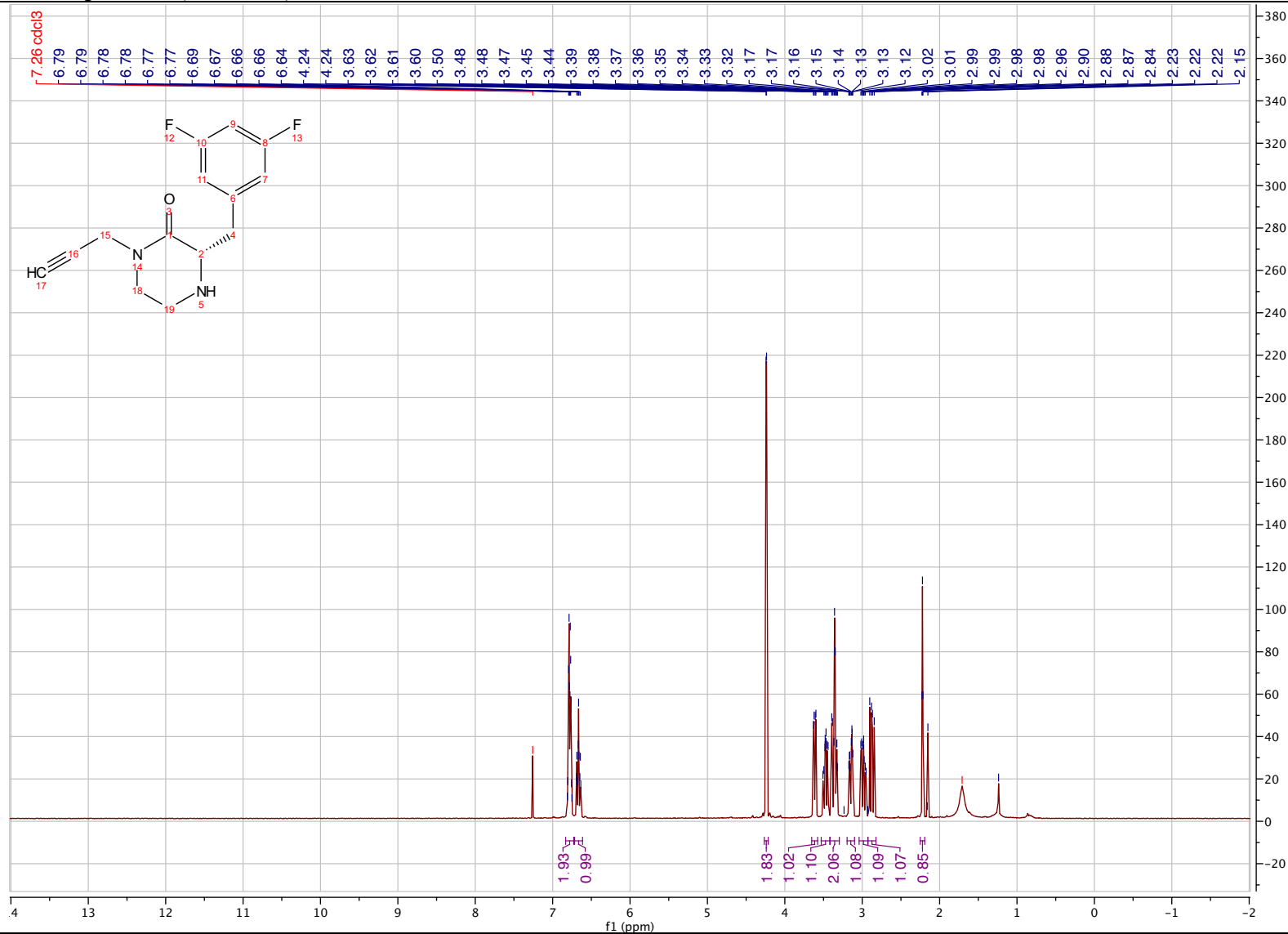
***tert*-butyl (*S*)-2-(3,5-difluorobenzyl)-3-oxo-4-(prop-2-yn-1-yl)piperazine-1-carboxylate (2.62)**

¹³C NMR spectrum (101 MHz) in Chloroform-*d*



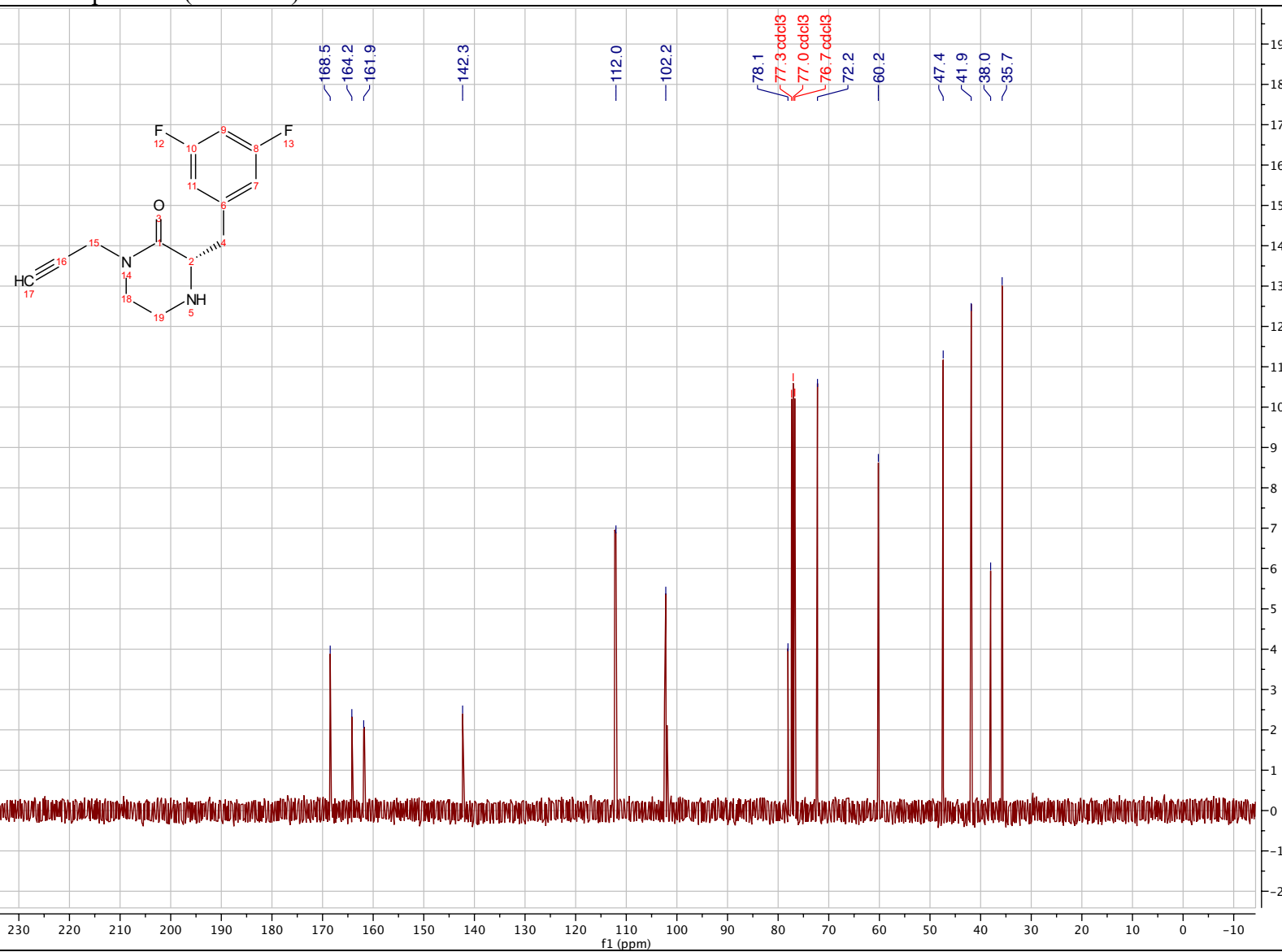
(S)-3-(3,5-difluorobenzyl)-1-(prop-2-yn-1-yl)piperazin-2-one (2.62')

¹H NMR spectrum (400 MHz) in Chloroform-*d*



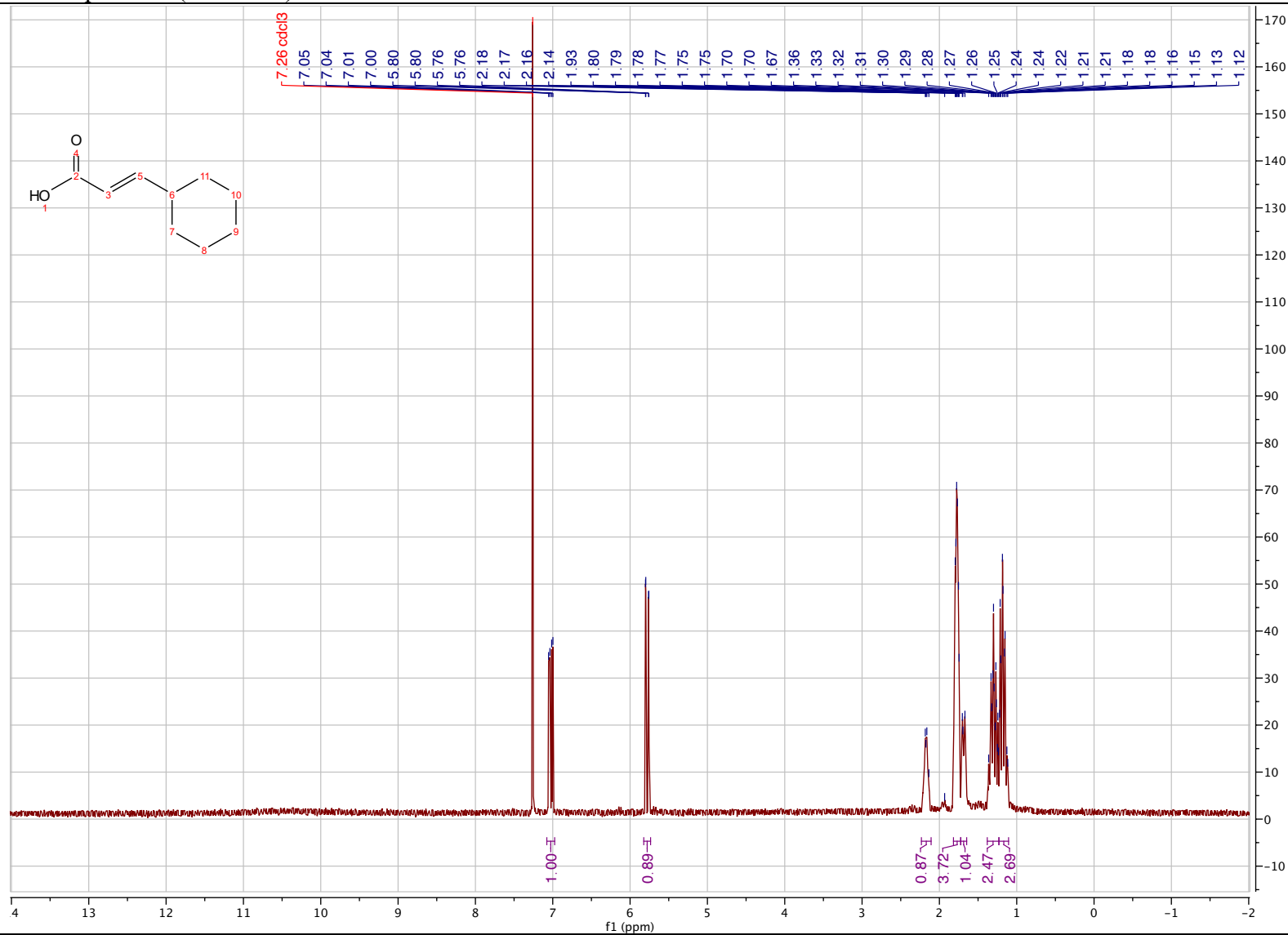
(S)-3-(3,5-difluorobenzyl)-1-(prop-2-yn-1-yl)piperazin-2-one (2.62')

¹³C NMR spectrum (101 MHz) in Chloroform-*d*



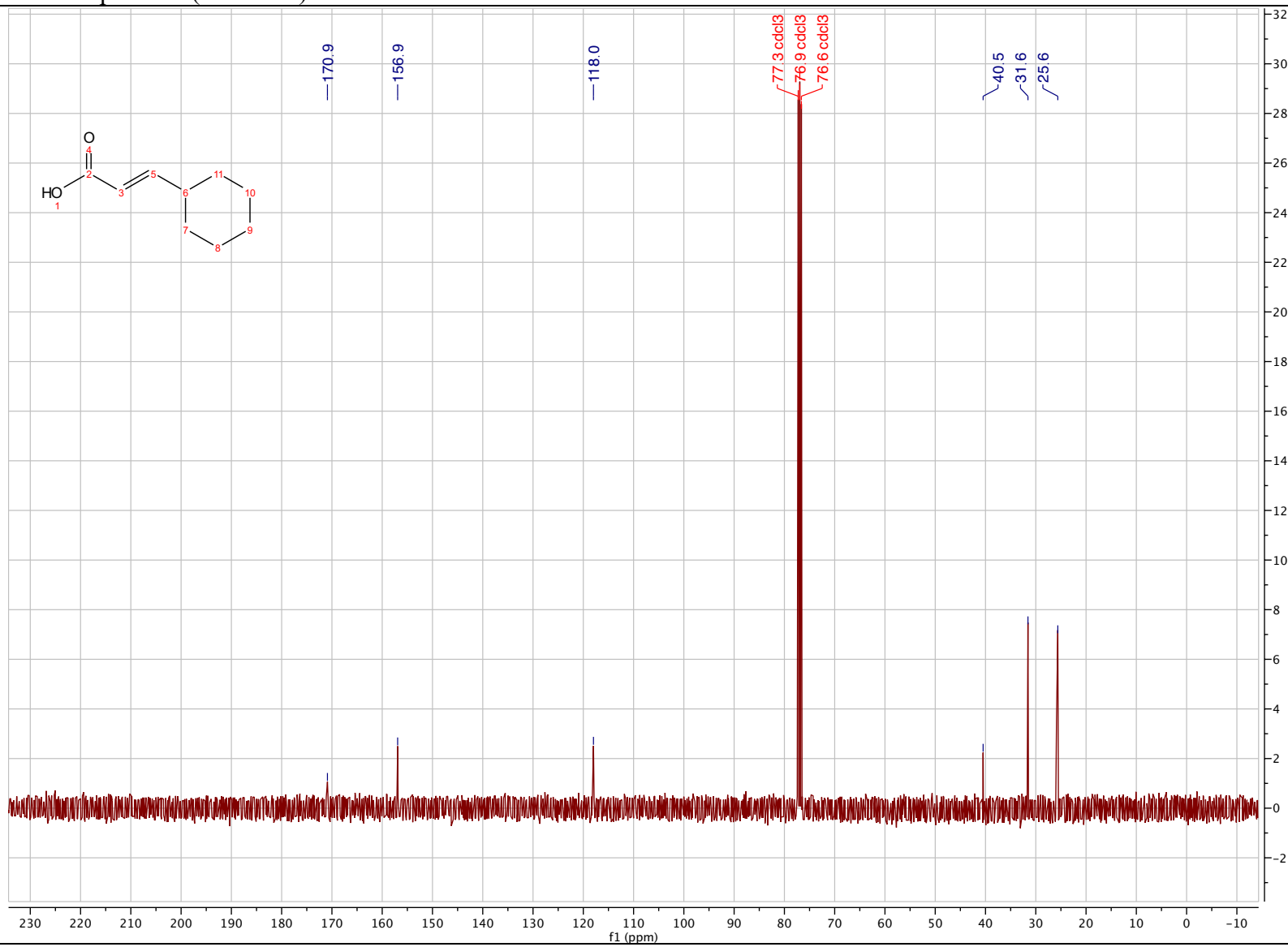
(E)-3-cyclohexylacrylic acid (2.65)

¹H NMR spectrum (400 MHz) in Chloroform-*d*



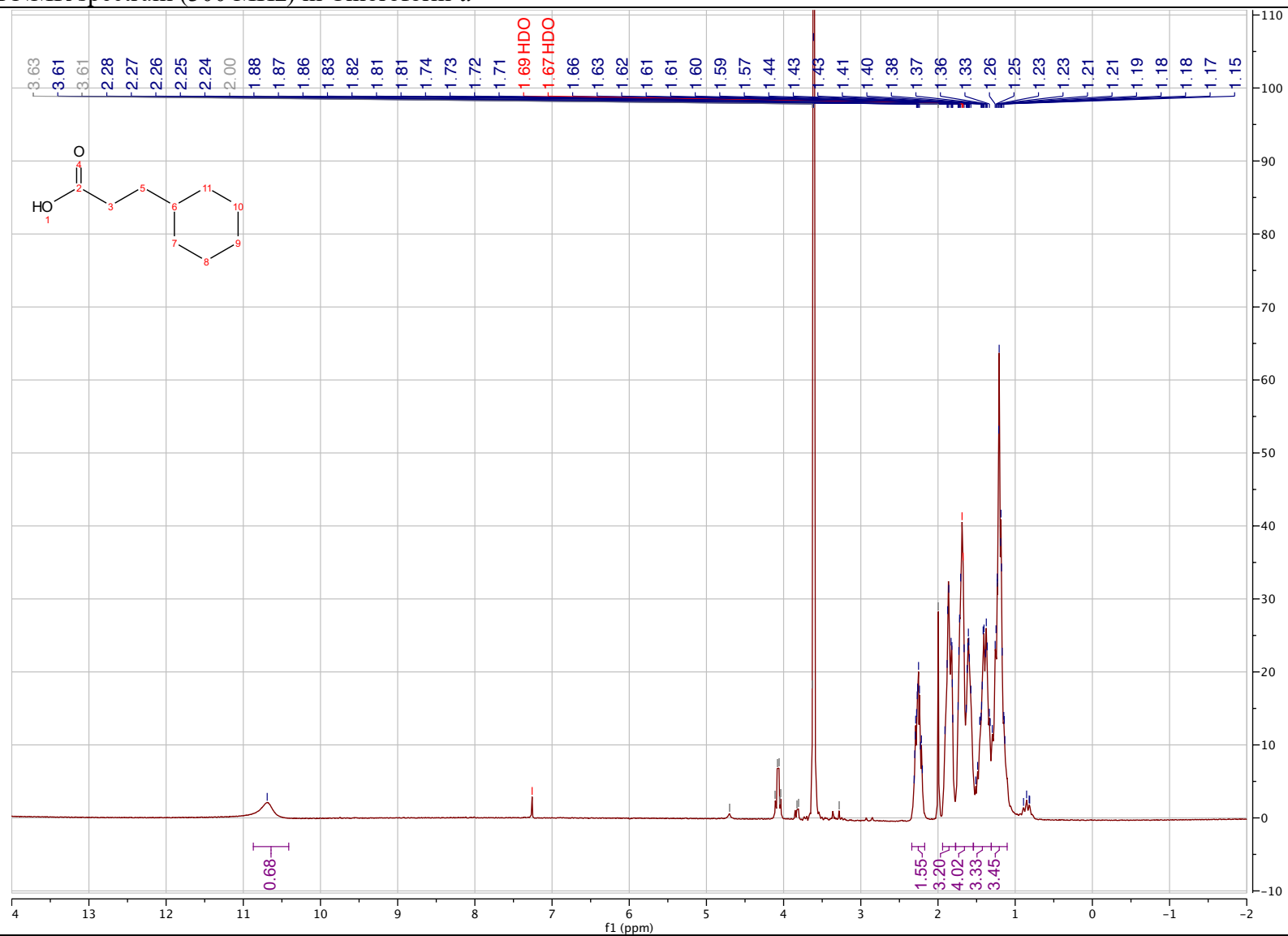
(E)-3-cyclohexylacrylic acid (2.65)

¹³C NMR spectrum (101 MHz) in Chloroform-*d*



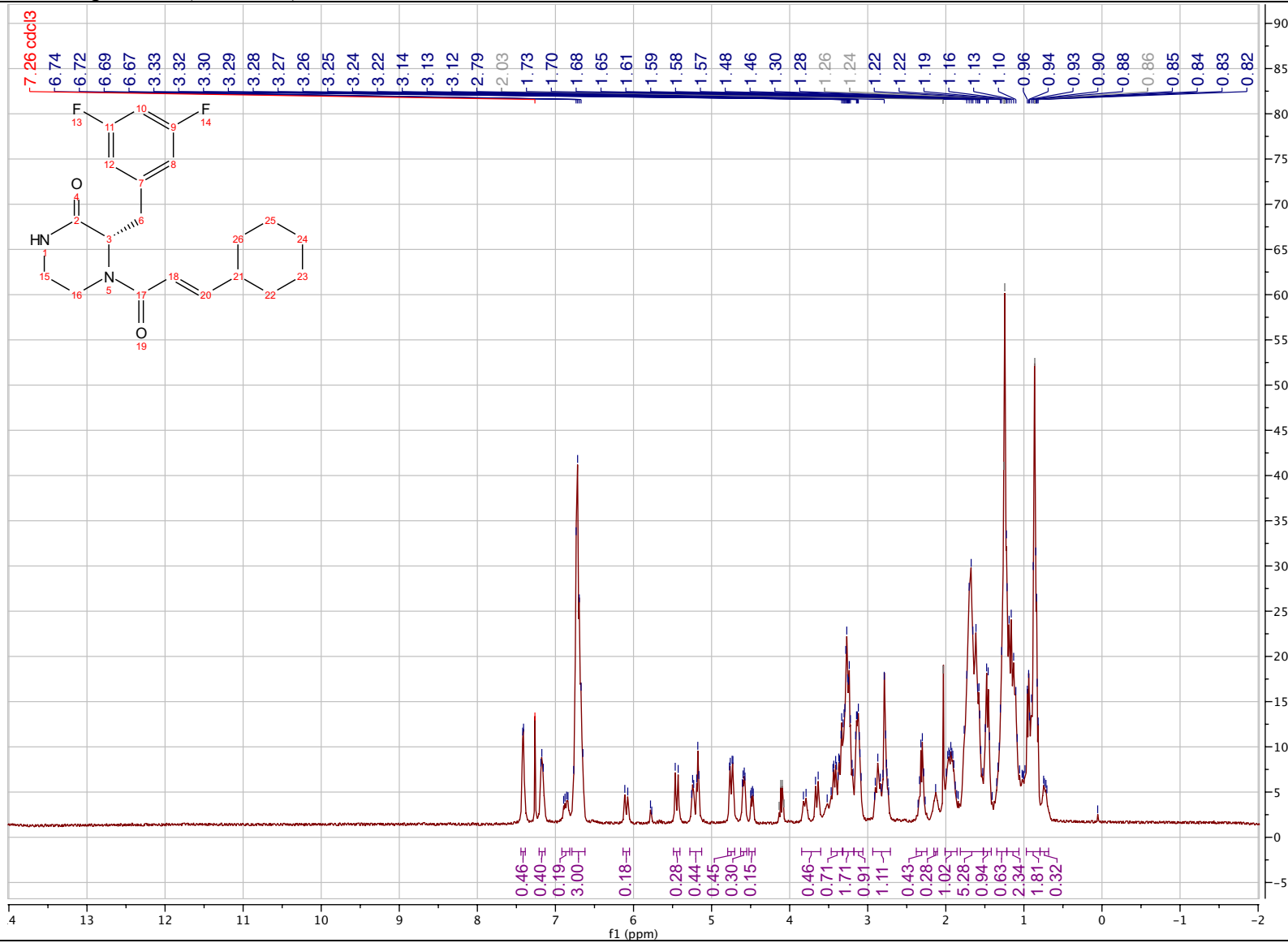
3-cyclohexylpropanoic acid (2.66)

¹H NMR spectrum (300 MHz) in Chloroform-*d*



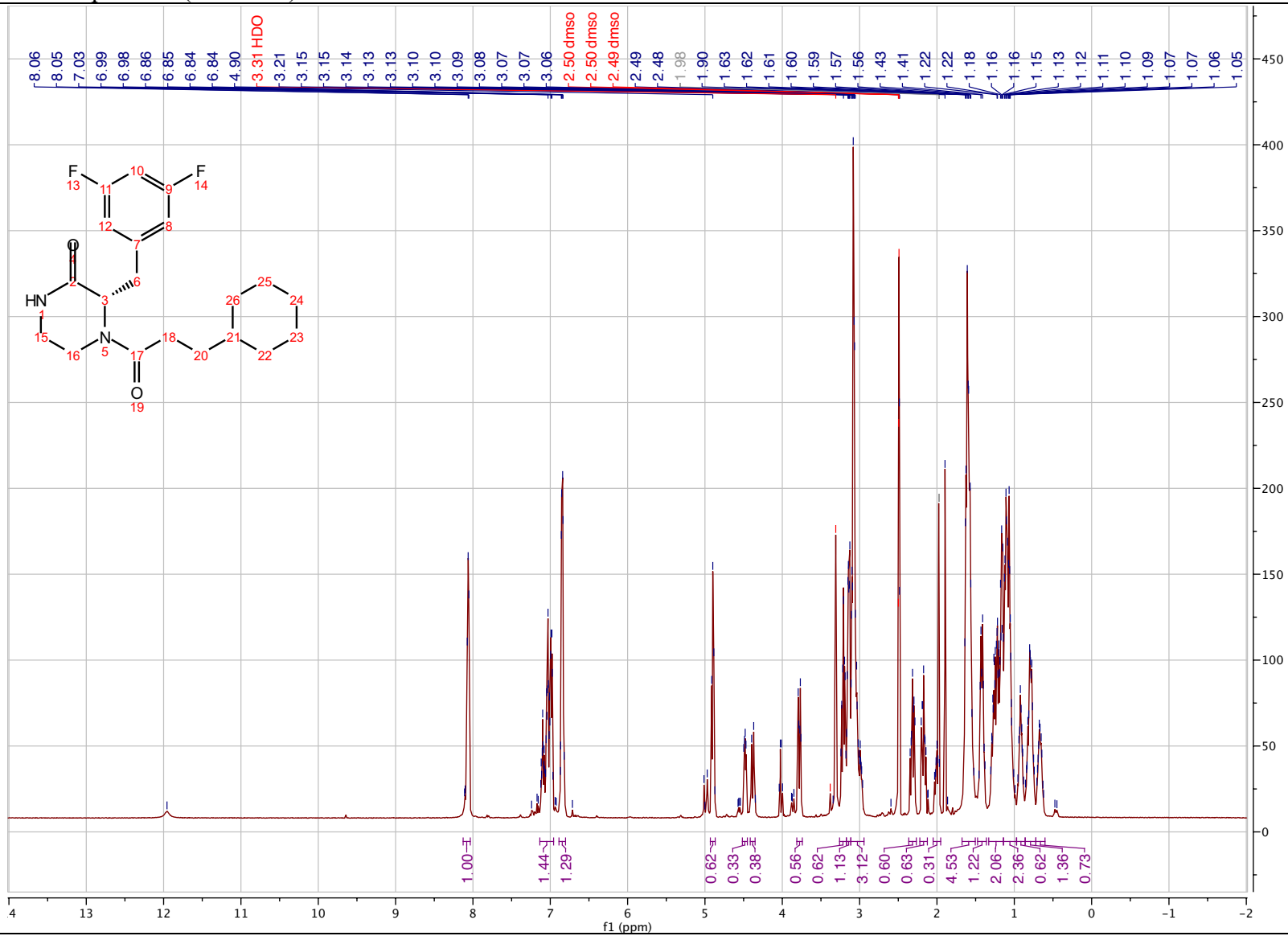
(*S,E*)-4-(3-cyclohexylacryloyl)-3-(3,5-difluorobenzyl)piperazin-2-one (2.68)

¹H NMR spectrum (400 MHz) in Chloroform-*d*



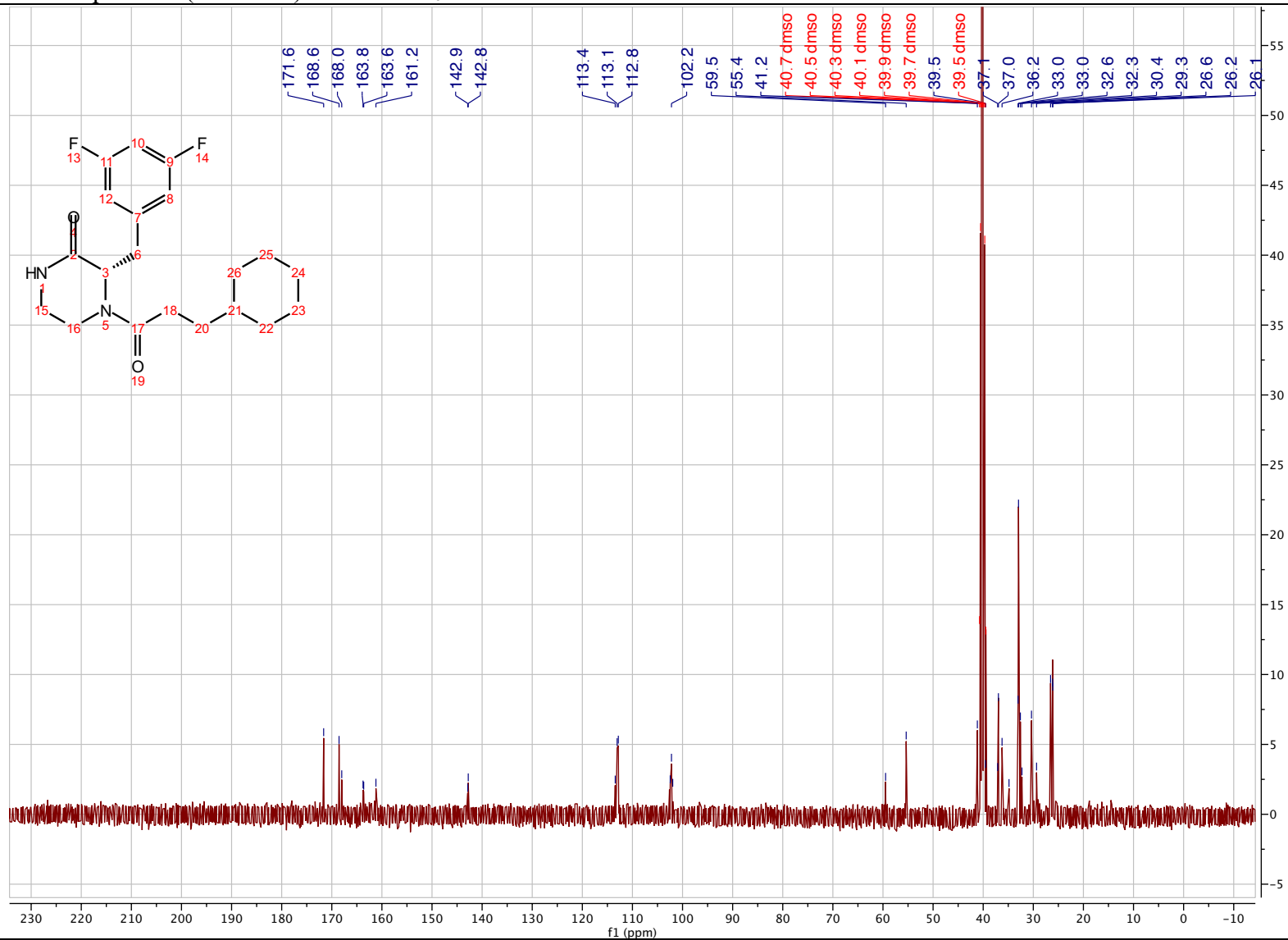
(S)-4-(3-cyclohexylpropanoyl)-3-(3,5-difluorobenzyl)piperazin-2-one (2.67)

¹H NMR spectrum (500 MHz) in DMSO-*d*₆



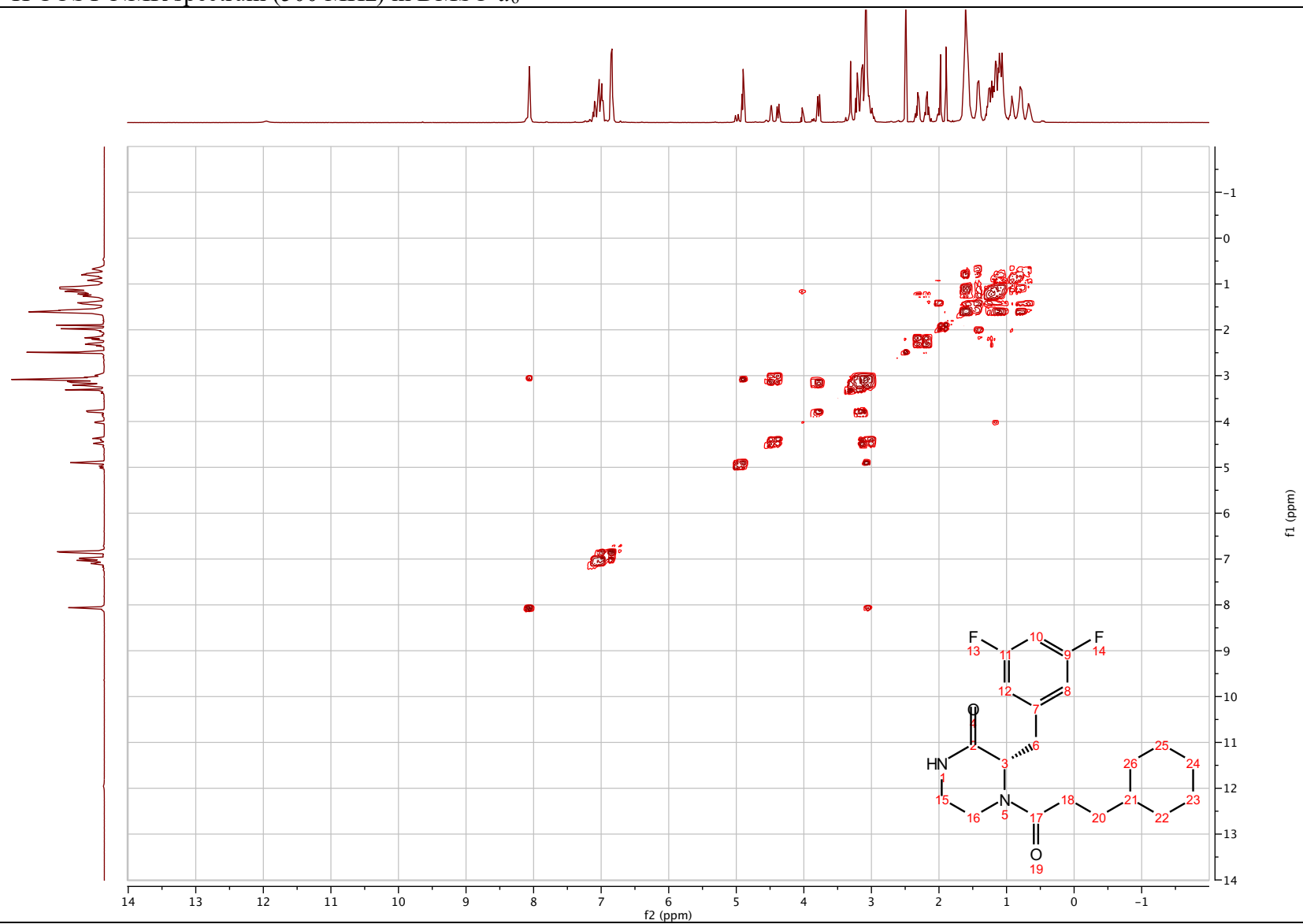
(S)-4-(3-cyclohexylpropanoyl)-3-(3,5-difluorobenzyl)piperazin-2-one (2.67)

^{13}C NMR spectrum (101 MHz) in $\text{DMSO-}d_6$



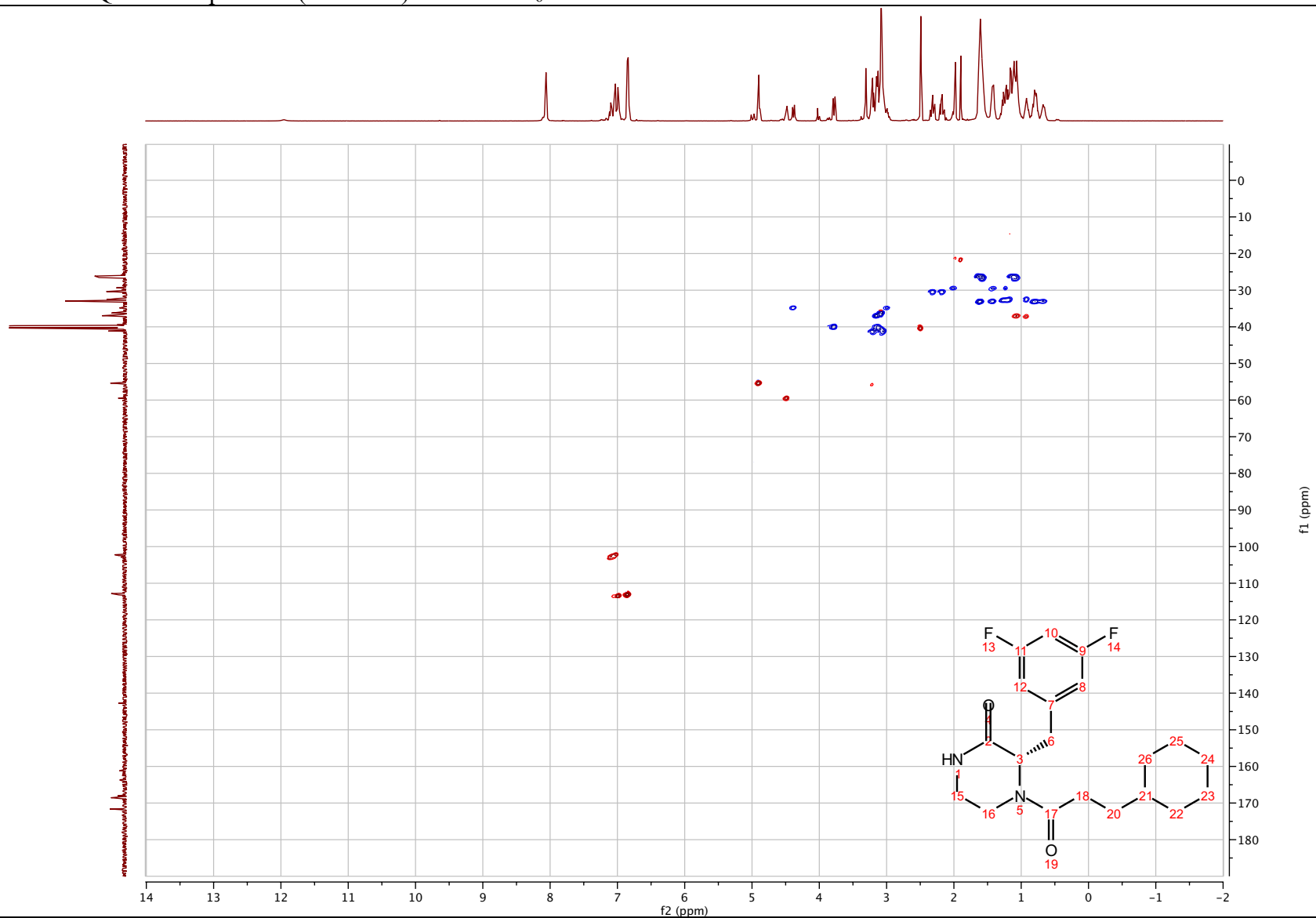
(S)-4-(3-cyclohexylpropanoyl)-3-(3,5-difluorobenzyl)piperazin-2-one (2.67)

^1H - ^1H COSY NMR spectrum (500 MHz) in $\text{DMSO-}d_6$



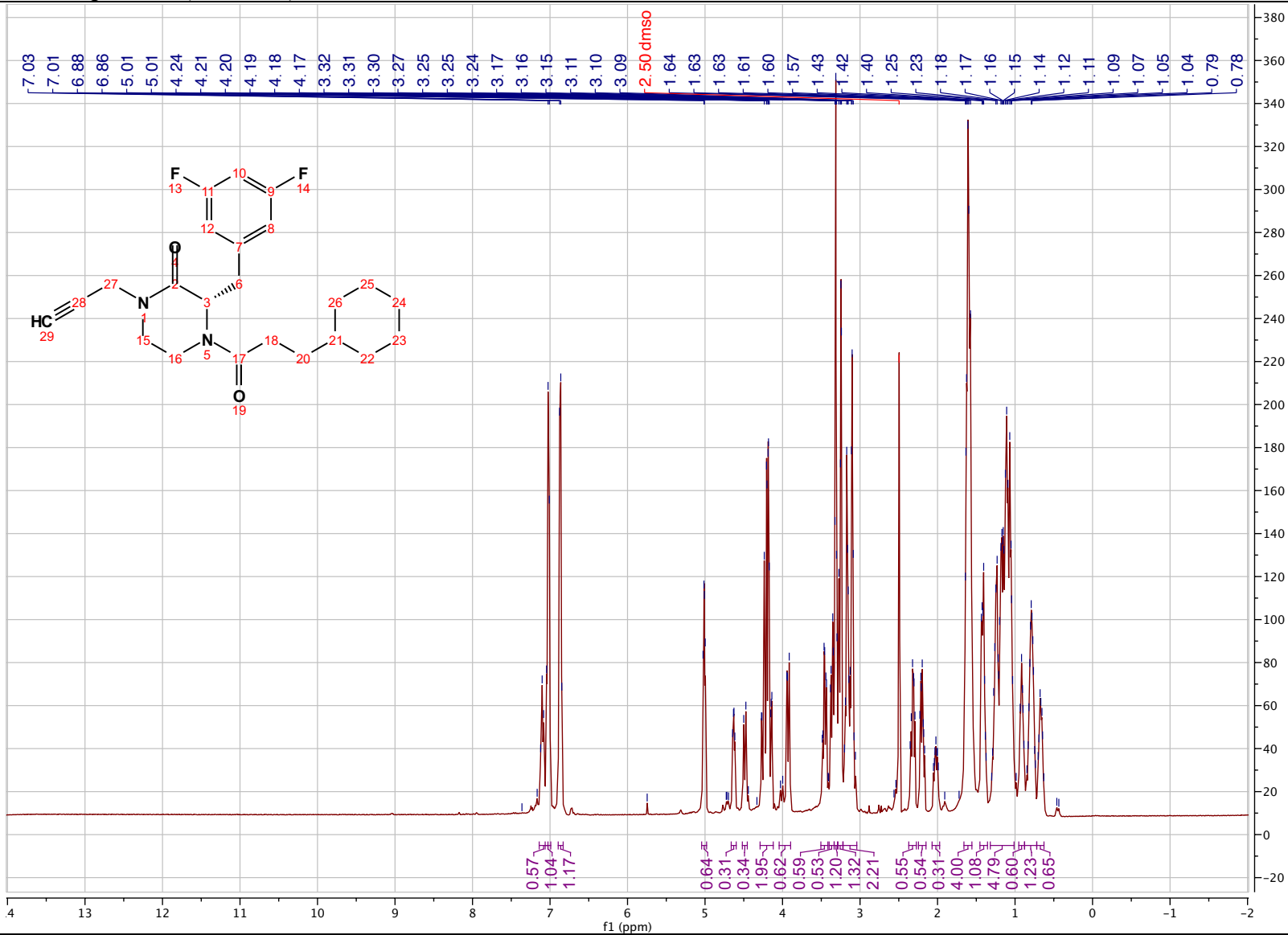
(S)-4-(3-cyclohexylpropanoyl)-3-(3,5-difluorobenzyl)piperazin-2-one (2.67)

^1H - ^{13}C HSQC NMR spectrum (500 MHz) in $\text{DMSO-}d_6$



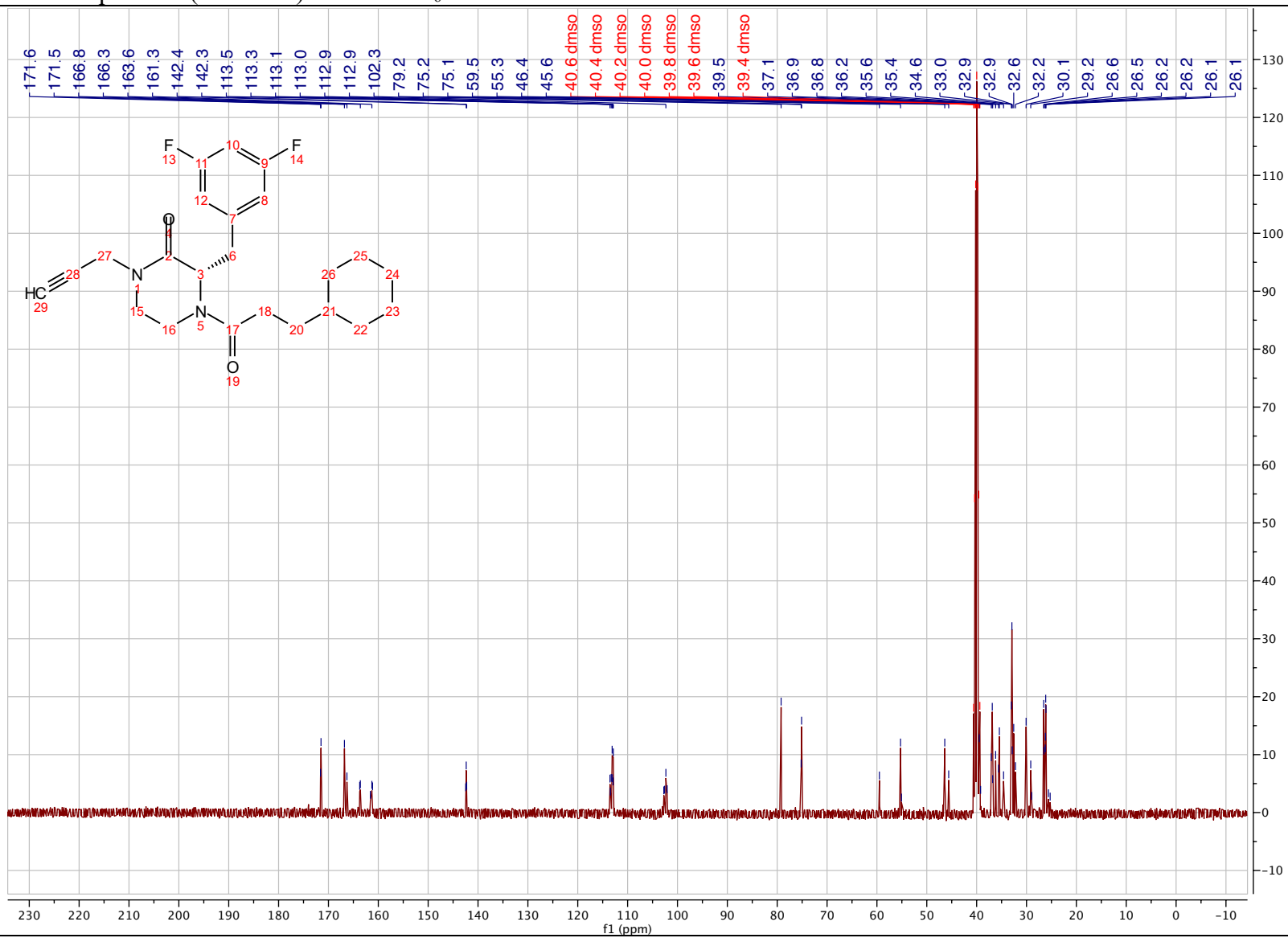
(S)-4-(3-cyclohexylpropanoyl)-3-(3,5-difluorobenzyl)-1-(prop-2-yn-1-yl)piperazin-2-one (2.69)

¹H NMR spectrum (500 MHz) in DMSO-*d*₆



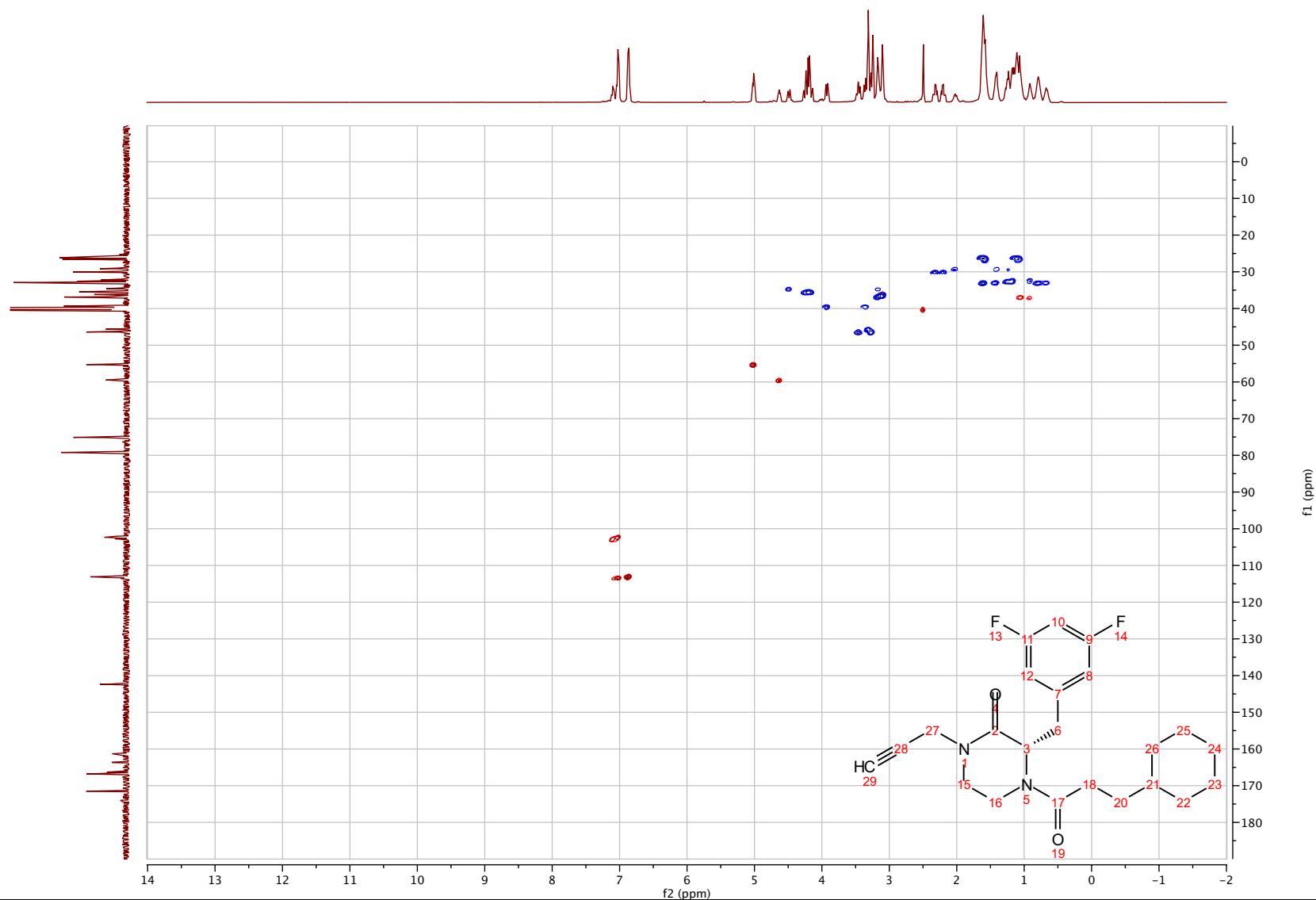
(S)-4-(3-cyclohexylpropanoyl)-3-(3,5-difluorobenzyl)-1-(prop-2-yn-1-yl)piperazin-2-one (2.69)

¹³C NMR spectrum (126 MHz) in DMSO-*d*₆



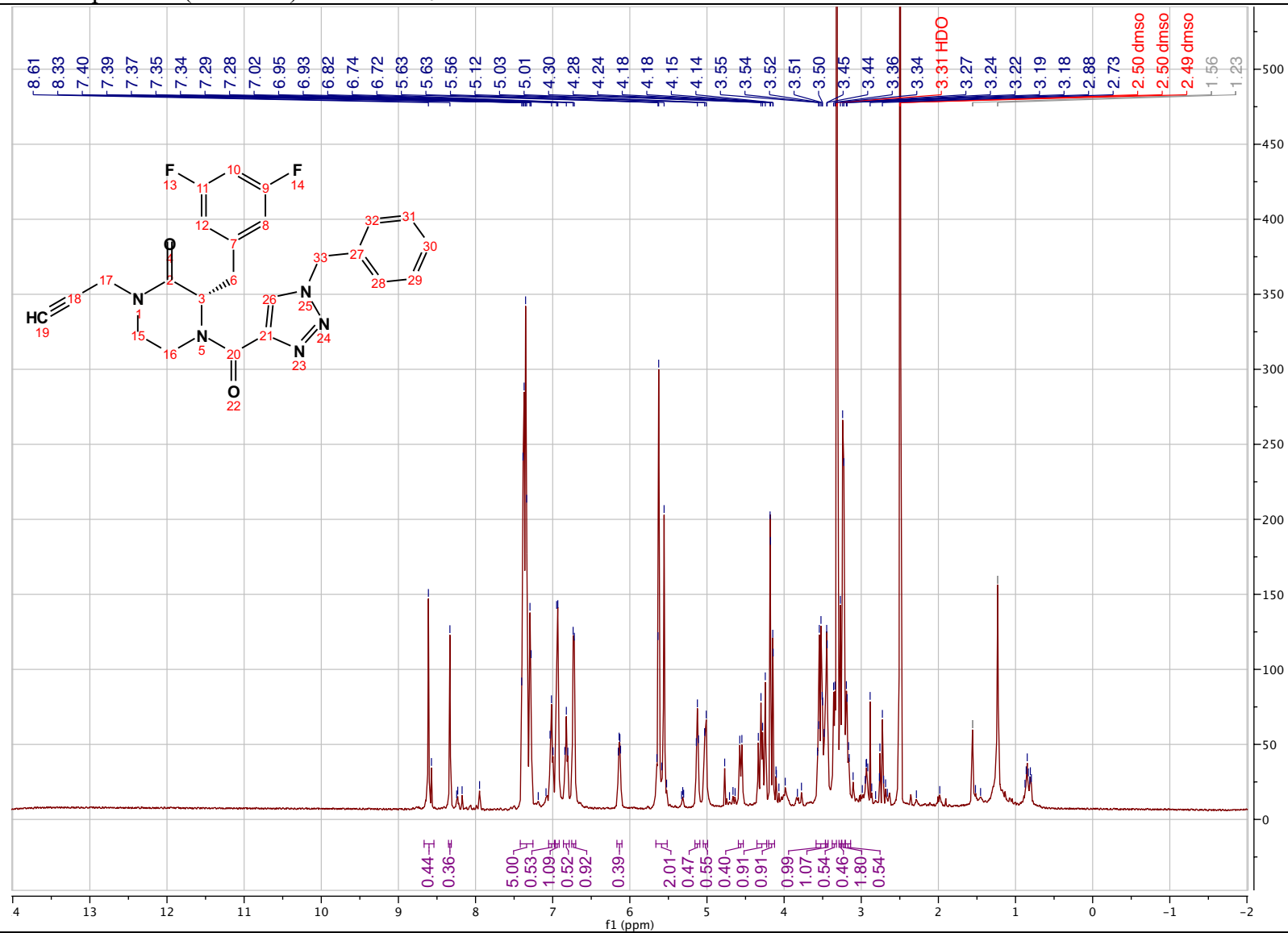
(S)-4-(3-cyclohexylpropanoyl)-3-(3,5-difluorobenzyl)-1-(prop-2-yn-1-yl)piperazin-2-one (2.69)

^1H - ^{13}C HSQC NMR spectrum (500 MHz) in $\text{DMSO-}d_6$



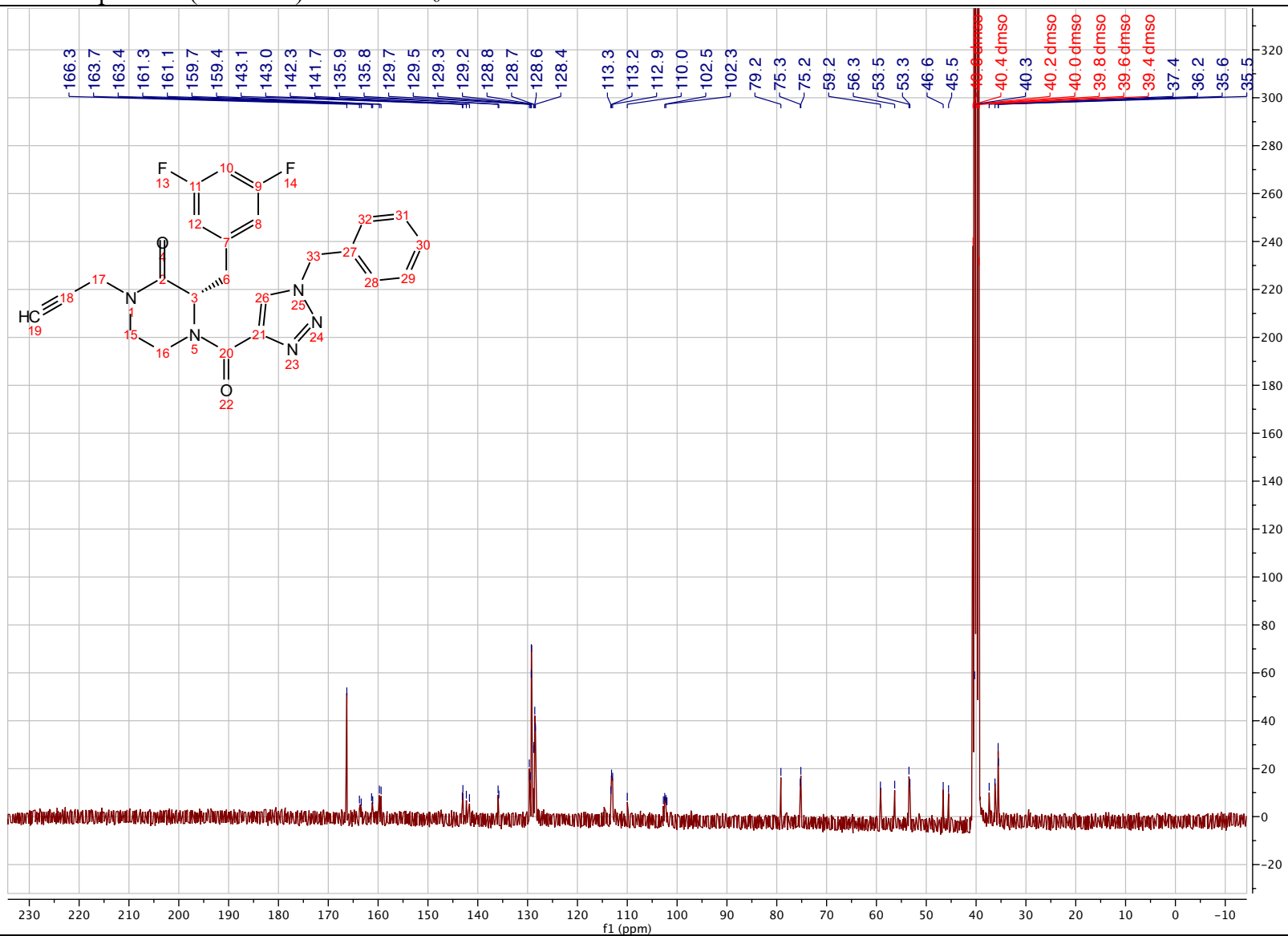
(S)-4-(1-benzyl-1H-1,2,3-triazole-4-carbonyl)-3-(3,5-difluorobenzyl)-1-(prop-2-yn-1-yl)piperazin-2-one (2.70)

¹H NMR spectrum (500 MHz) in DMSO-*d*₆



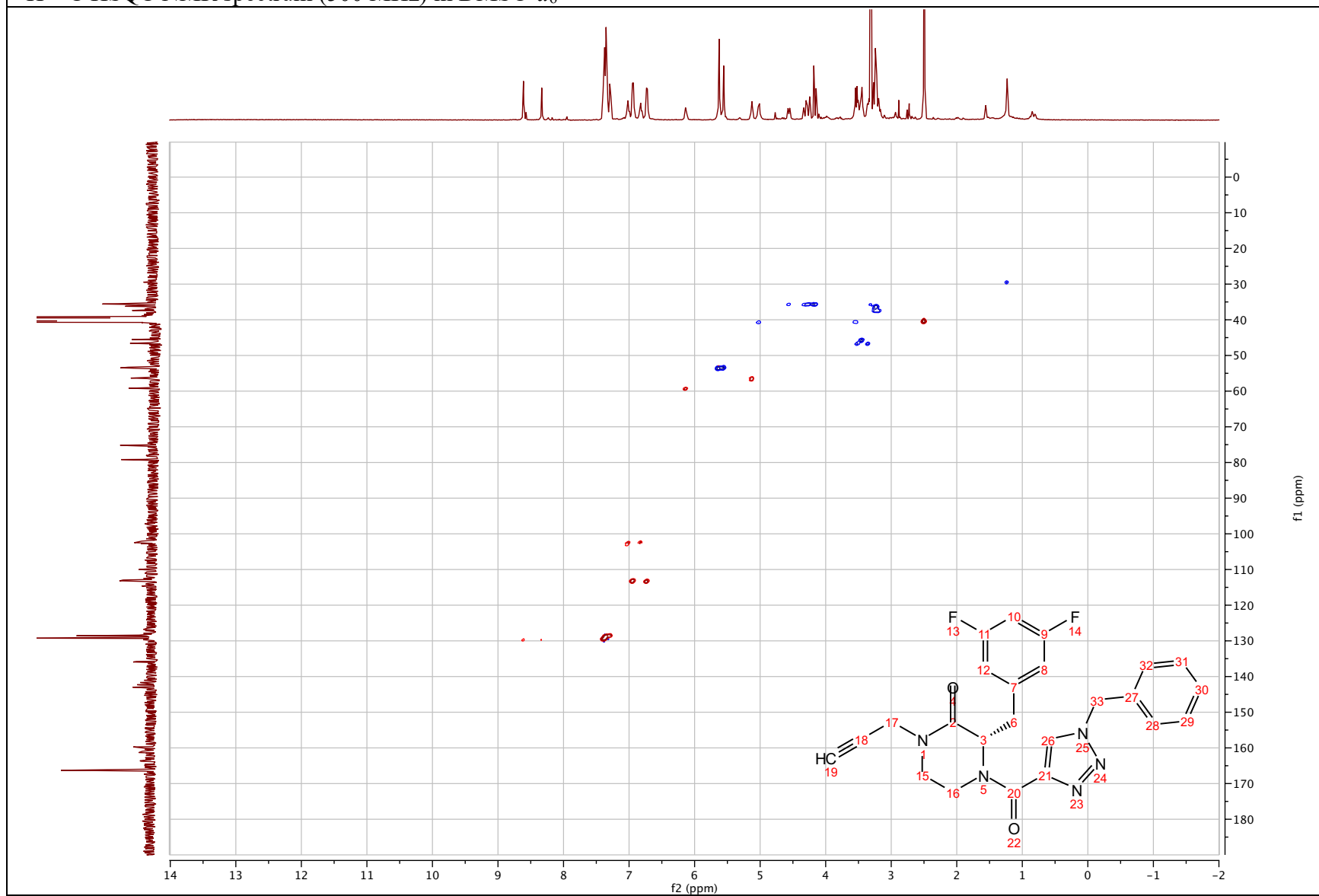
(S)-4-(1-benzyl-1H-1,2,3-triazole-4-carbonyl)-3-(3,5-difluorobenzyl)-1-(prop-2-yn-1-yl)piperazin-2-one (2.70)

¹³C NMR spectrum (101 MHz) in DMSO-*d*₆



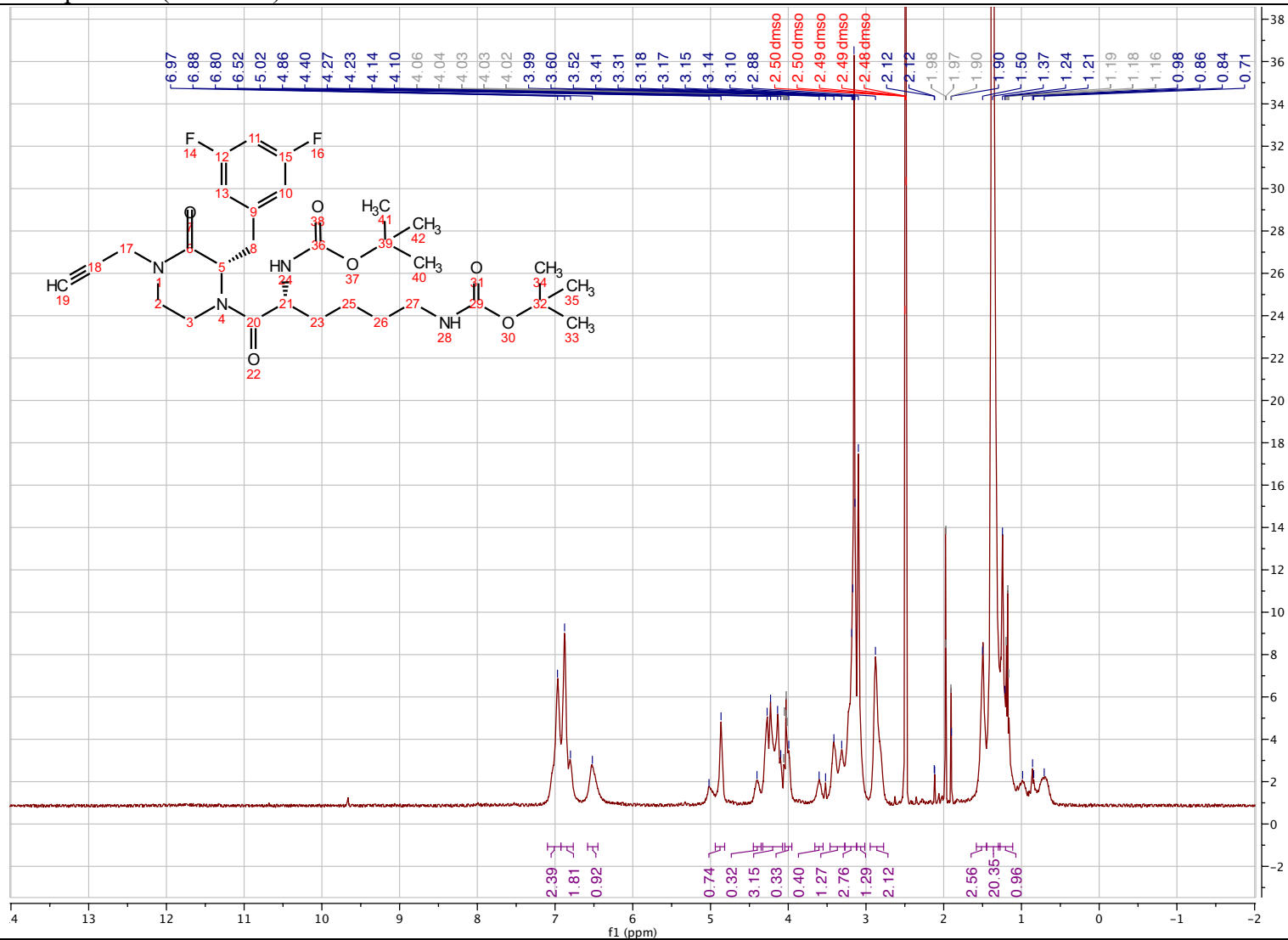
(S)-4-(1-benzyl-1*H*-1,2,3-triazole-4-carbonyl)-3-(3,5-difluorobenzyl)-1-(prop-2-yn-1-yl)piperazin-2-one (2.70)

^1H - ^{13}C HSQC NMR spectrum (500 MHz) in $\text{DMSO-}d_6$



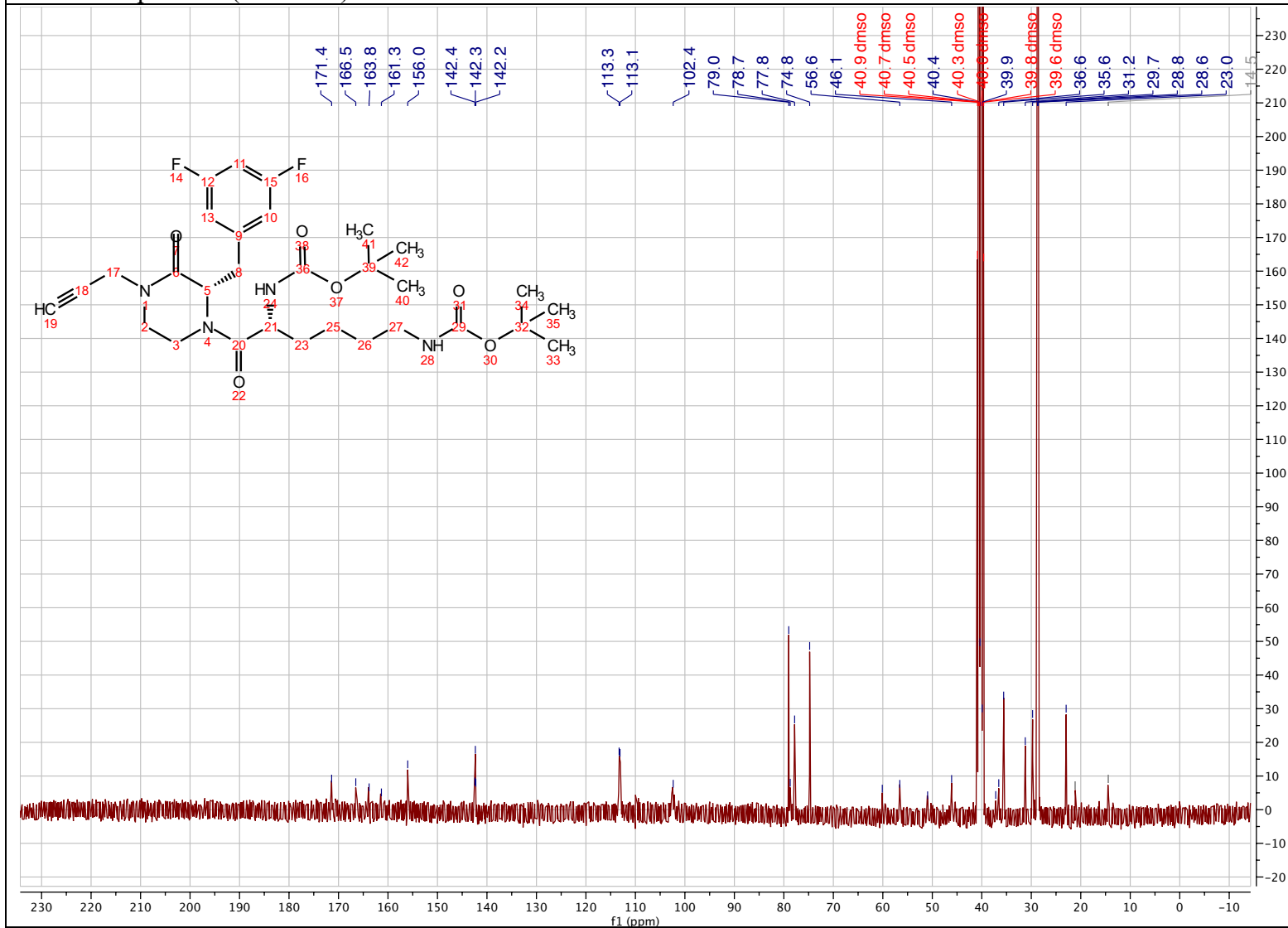
di-*tert*-butyl ((*R*)-6-((*S*)-2-(3,5-difluorobenzyl)-3-oxo-4-(prop-2-yn-1-yl)piperazin-1-yl)-6-oxohexane-1,5-diyl)dicarbamate
(2.71)

¹H NMR spectrum (500 MHz) in DMSO-*d*₆



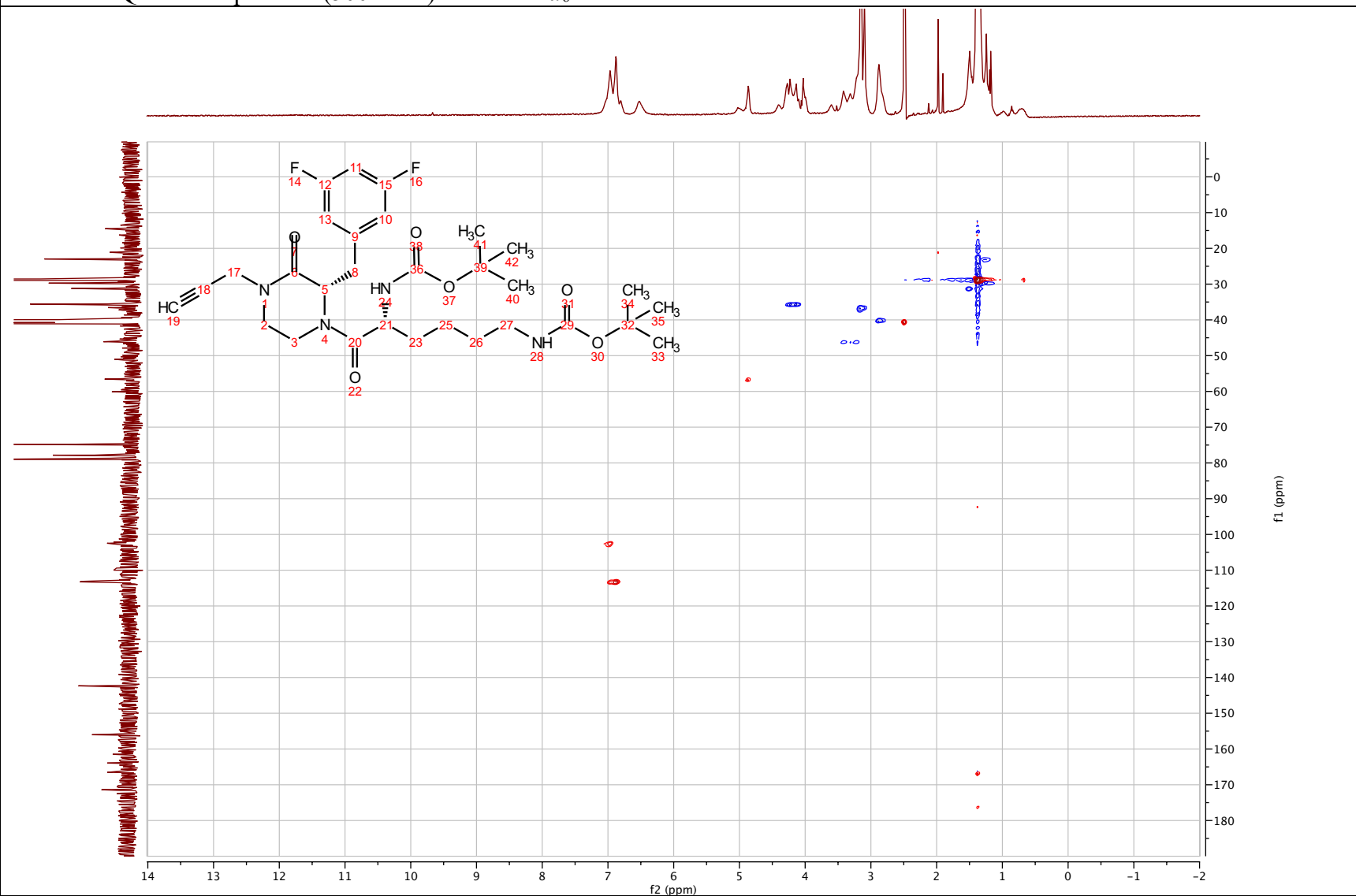
di-*tert*-butyl ((*R*)-6-((*S*)-2-(3,5-difluorobenzyl)-3-oxo-4-(prop-2-yn-1-yl)piperazin-1-yl)-6-oxohexane-1,5-diyl)dicarbamate
(2.71)

^{13}C NMR spectrum (101 MHz) in $\text{DMSO-}d_6$



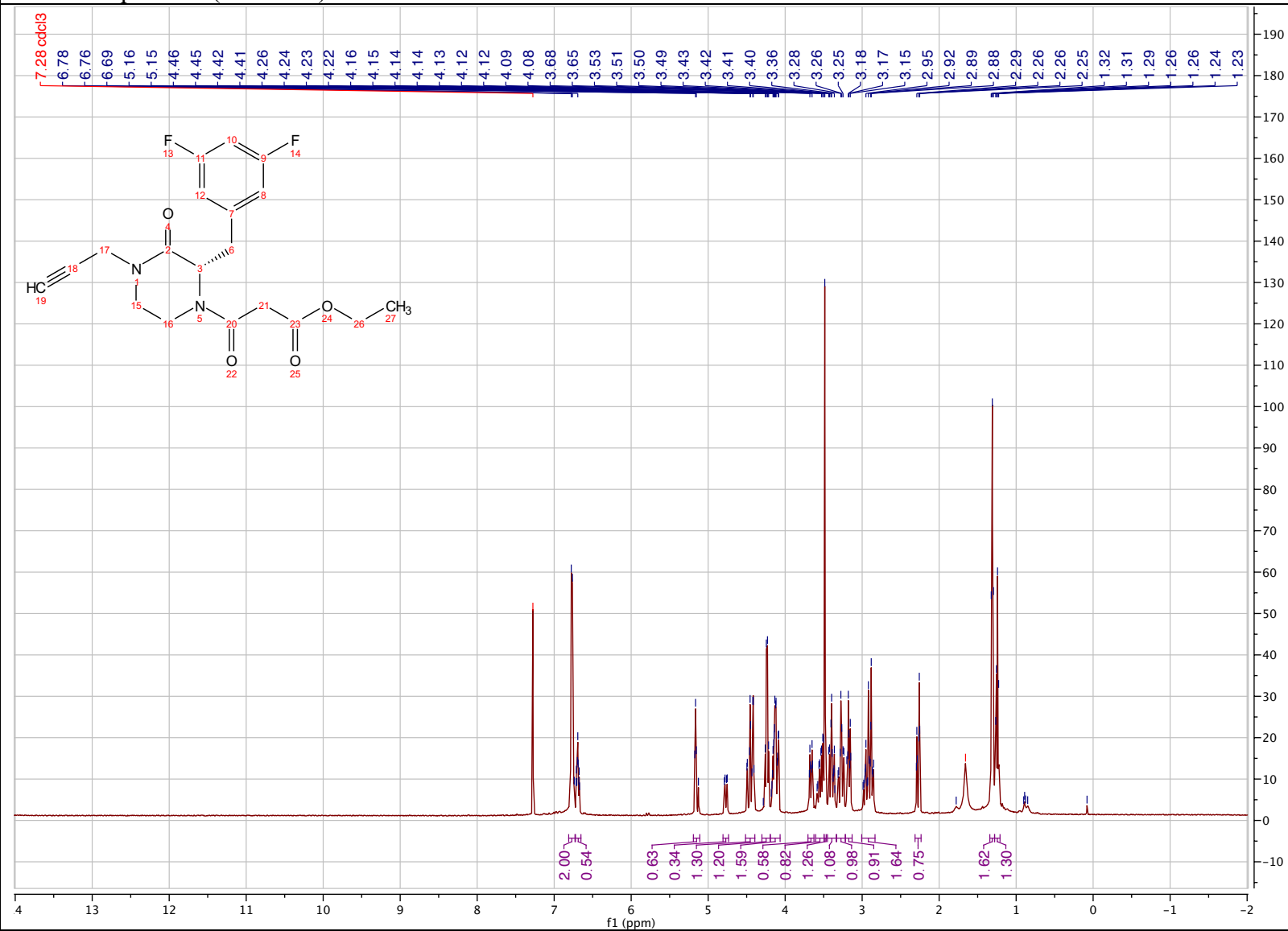
di-*tert*-butyl ((*R*)-6-((*S*)-2-(3,5-difluorobenzyl)-3-oxo-4-(prop-2-yn-1-yl)piperazin-1-yl)-6-oxohexane-1,5-diyl)dicarbamate
(2.71)

^1H - ^{13}C HSQC NMR spectrum (500 MHz) in $\text{DMSO-}d_6$



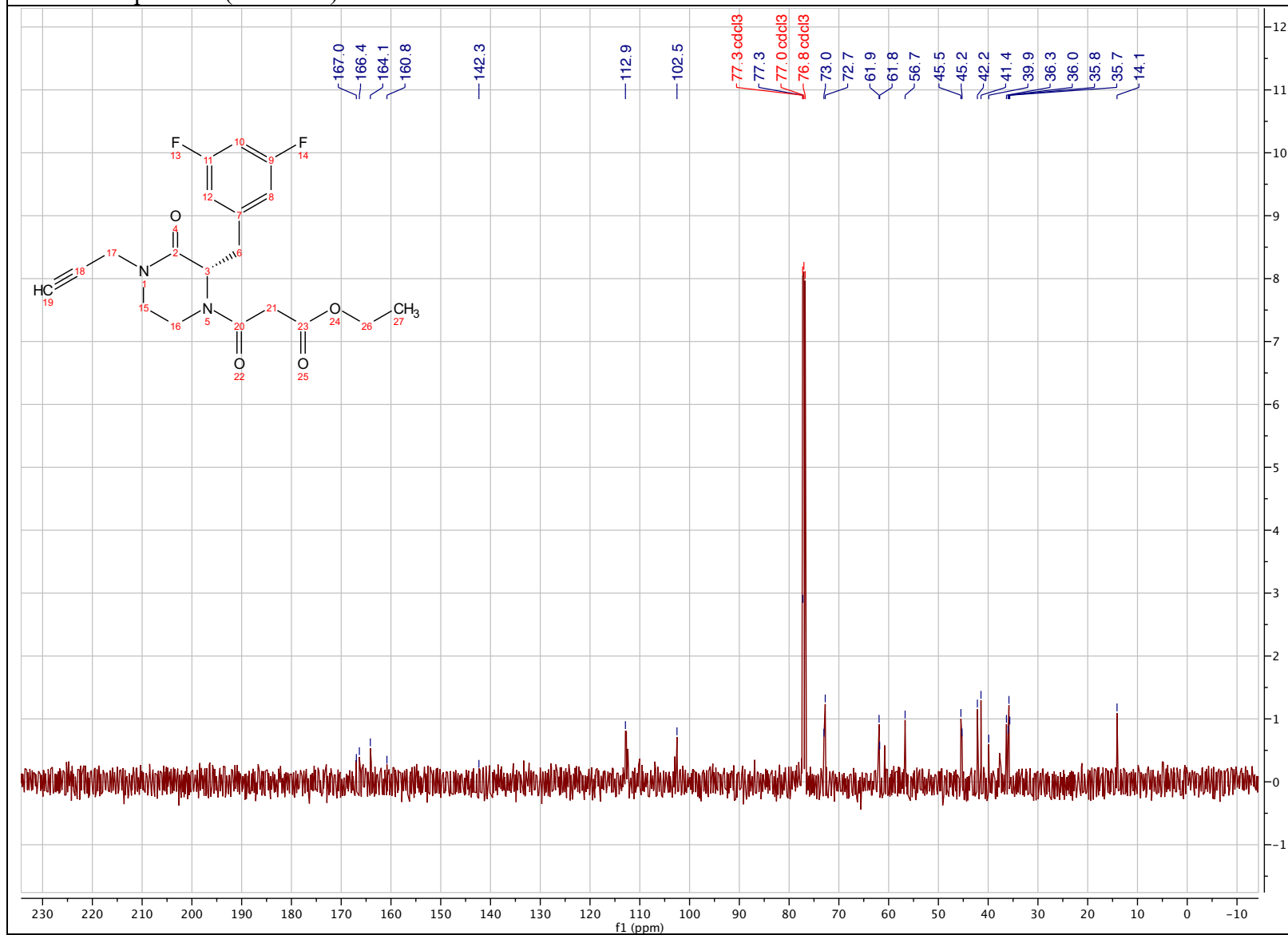
ethyl (S)-3-(2-(3,5-difluorobenzyl)-3-oxo-4-(prop-2-yn-1-yl)piperazin-1-yl)-3-oxopropanoate (2.72)

¹H NMR spectrum (500 MHz) in Chloroform-*d*



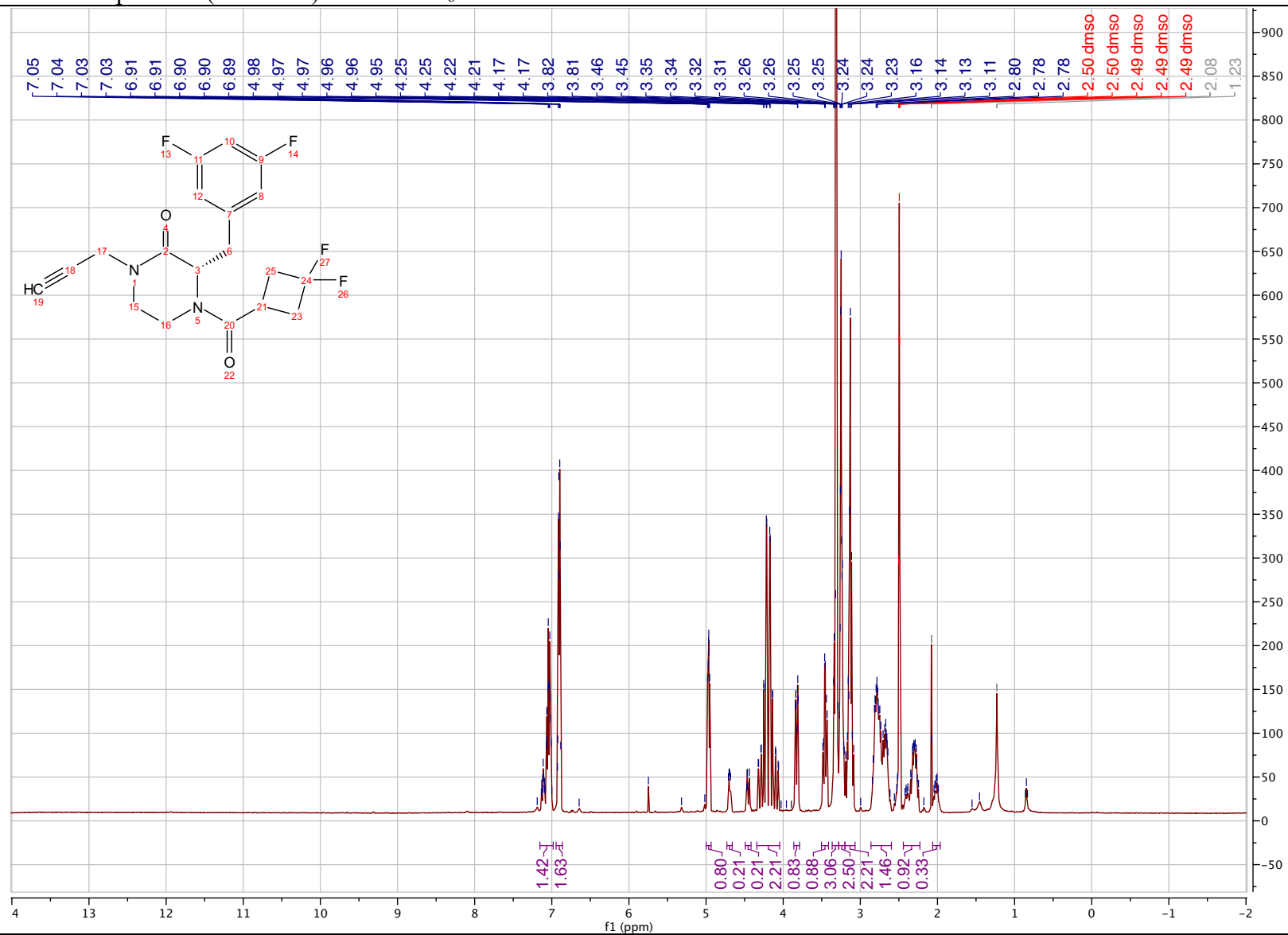
ethyl (S)-3-(2-(3,5-difluorobenzyl)-3-oxo-4-(prop-2-yn-1-yl)piperazin-1-yl)-3-oxopropanoate (2.72)

¹³C NMR spectrum (101 MHz) in Chloroform-*d*



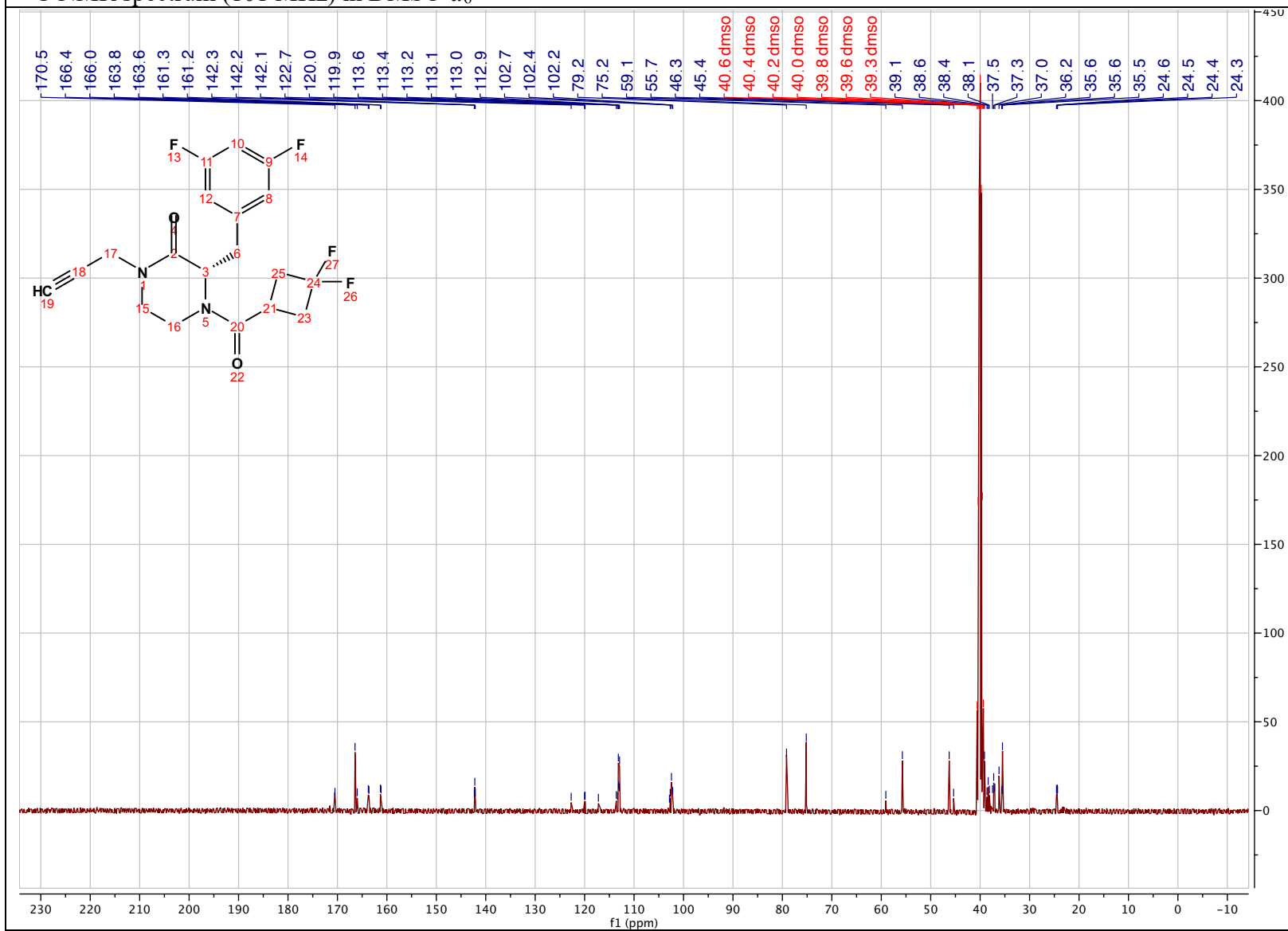
(S)-3-(3,5-difluorobenzyl)-4-(3,3-difluorocyclobutane-1-carbonyl)-1-(prop-2-yn-1-yl)piperazin-2-one (2.73)

¹H NMR spectrum (500 MHz) in DMSO-*d*₆



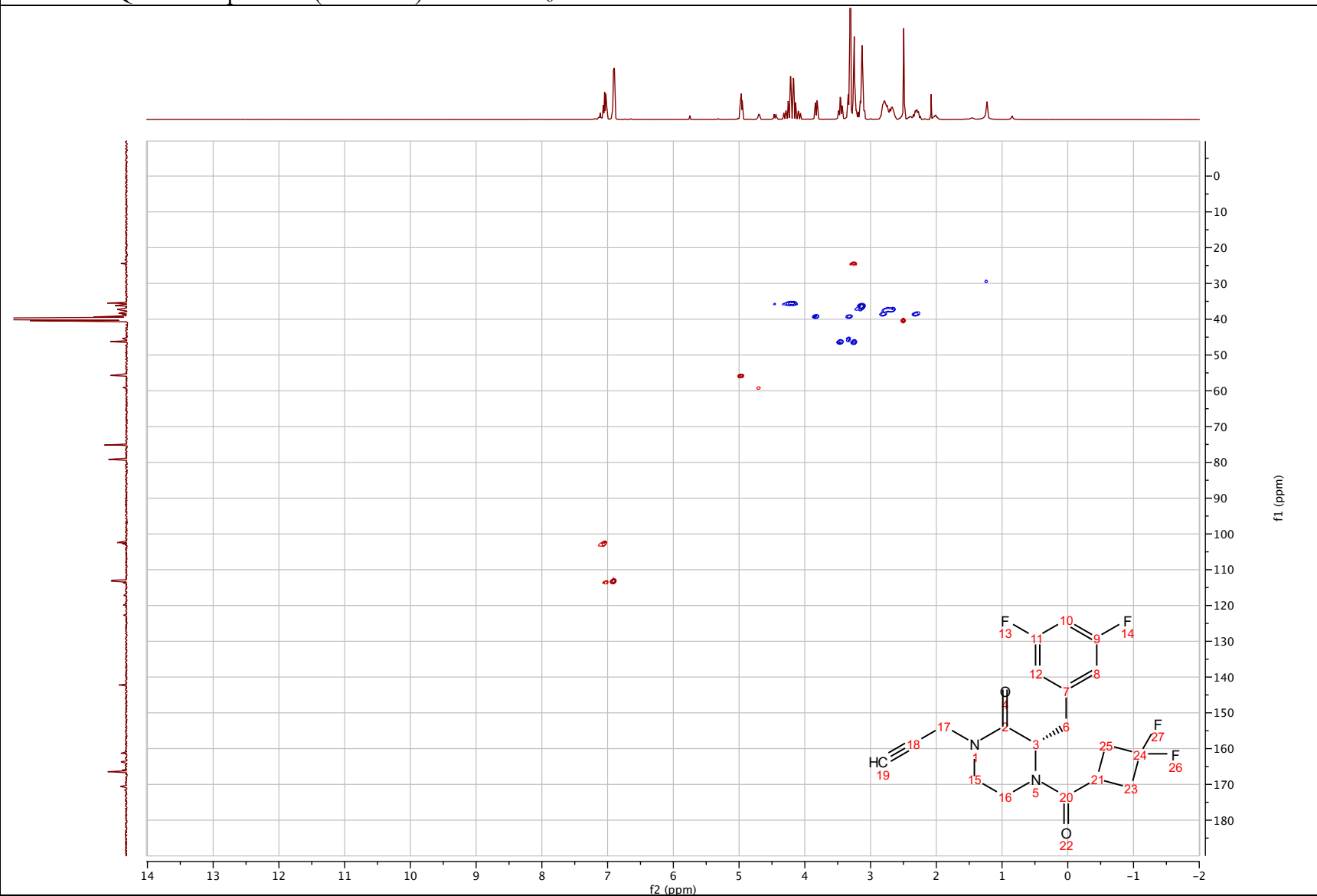
(S)-3-(3,5-difluorobenzyl)-4-(3,3-difluorocyclobutane-1-carbonyl)-1-(prop-2-yn-1-yl)piperazin-2-one (2.73)

¹³C NMR spectrum (101 MHz) in DMSO-*d*₆



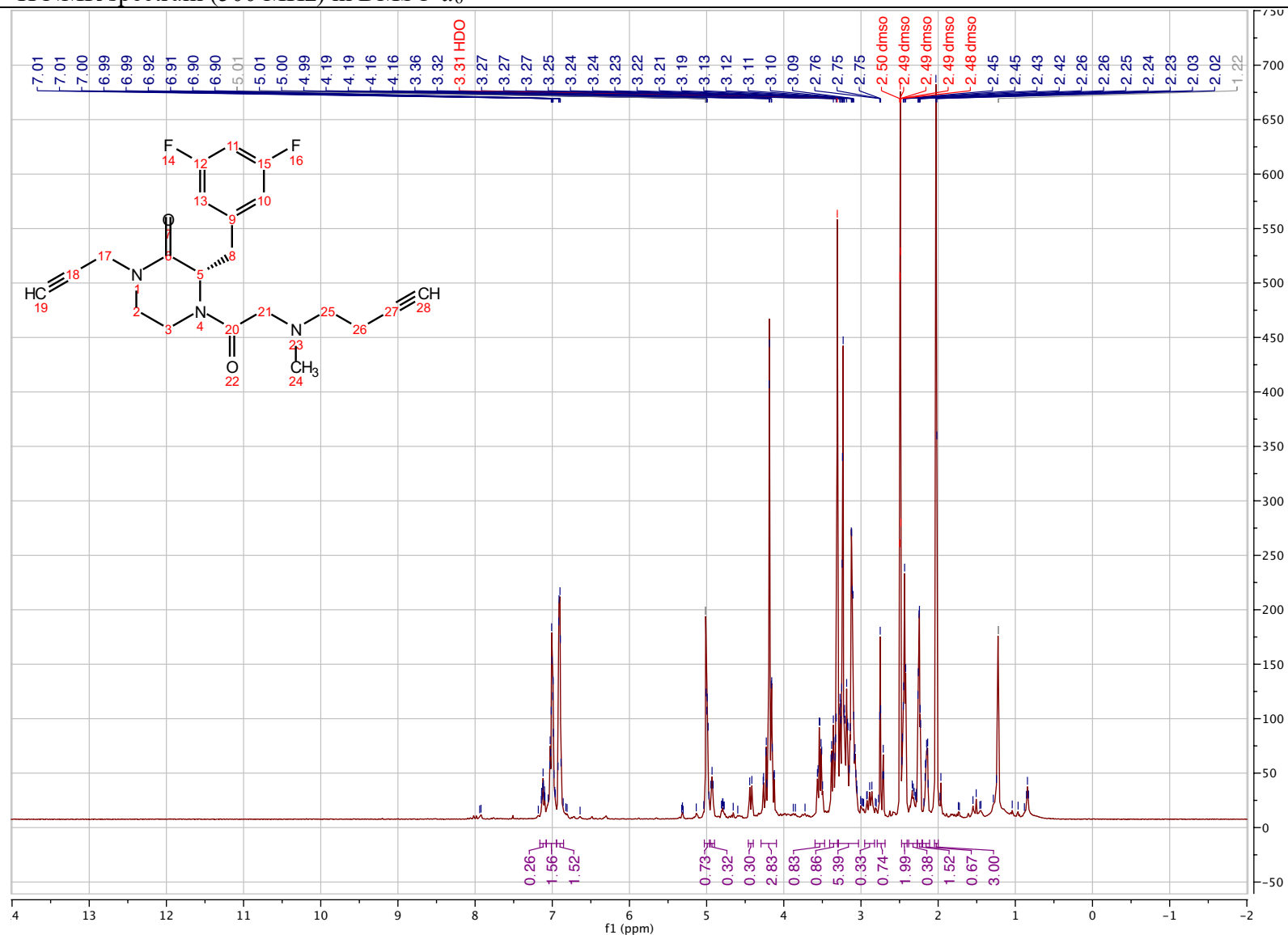
(S)-3-(3,5-difluorobenzyl)-4-(3,3-difluorocyclobutane-1-carbonyl)-1-(prop-2-yn-1-yl)piperazin-2-one (2.73)

^1H - ^{13}C HSQC NMR spectrum (500 MHz) in $\text{DMSO-}d_6$



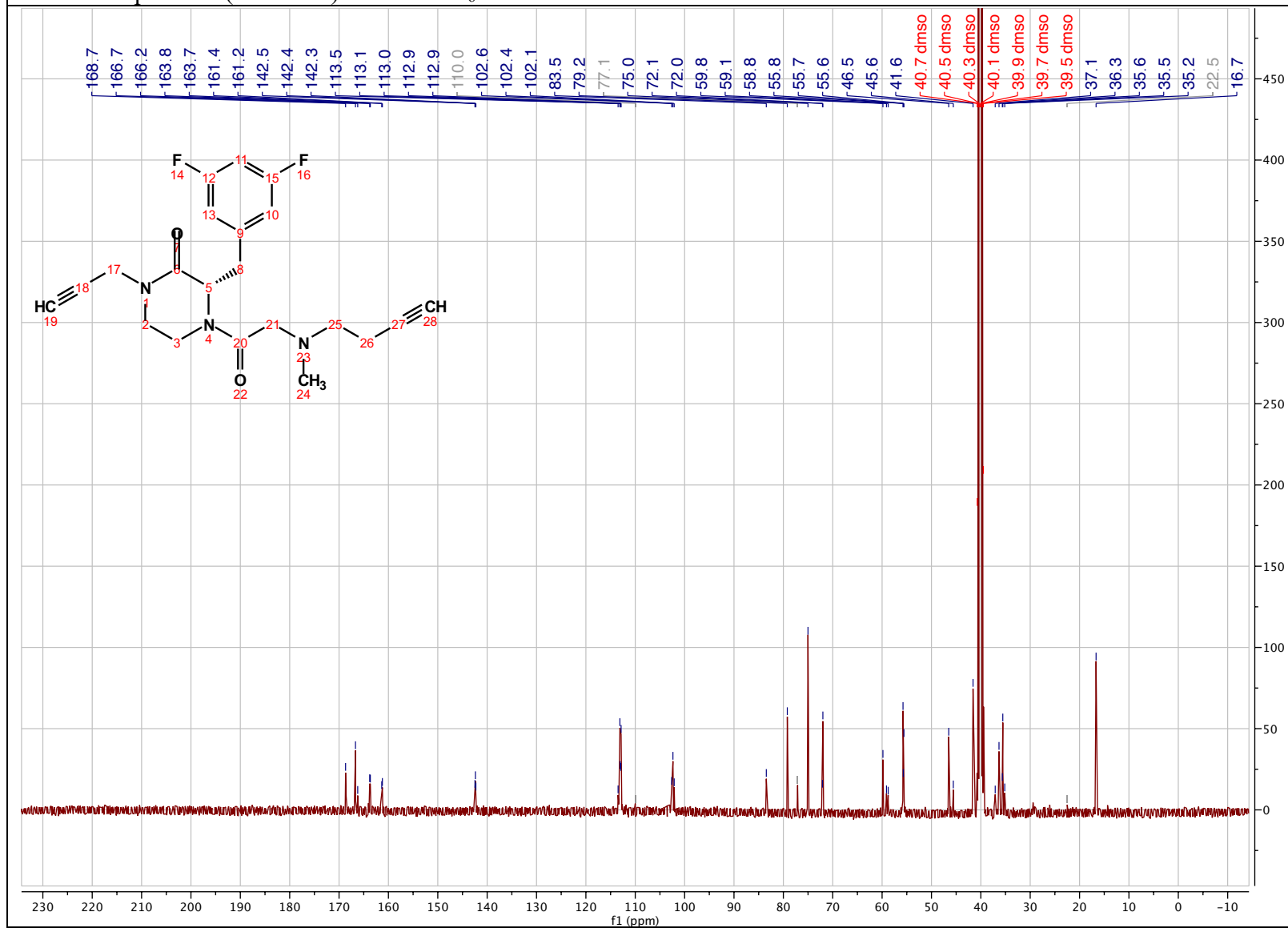
(S)-4-(N-(but-3-yn-1-yl)-N-methylglycyl)-3-(3,5-difluorobenzyl)-1-(prop-2-yn-1-yl)piperazin-2-one (2.74)

¹H NMR spectrum (500 MHz) in DMSO-*d*₆



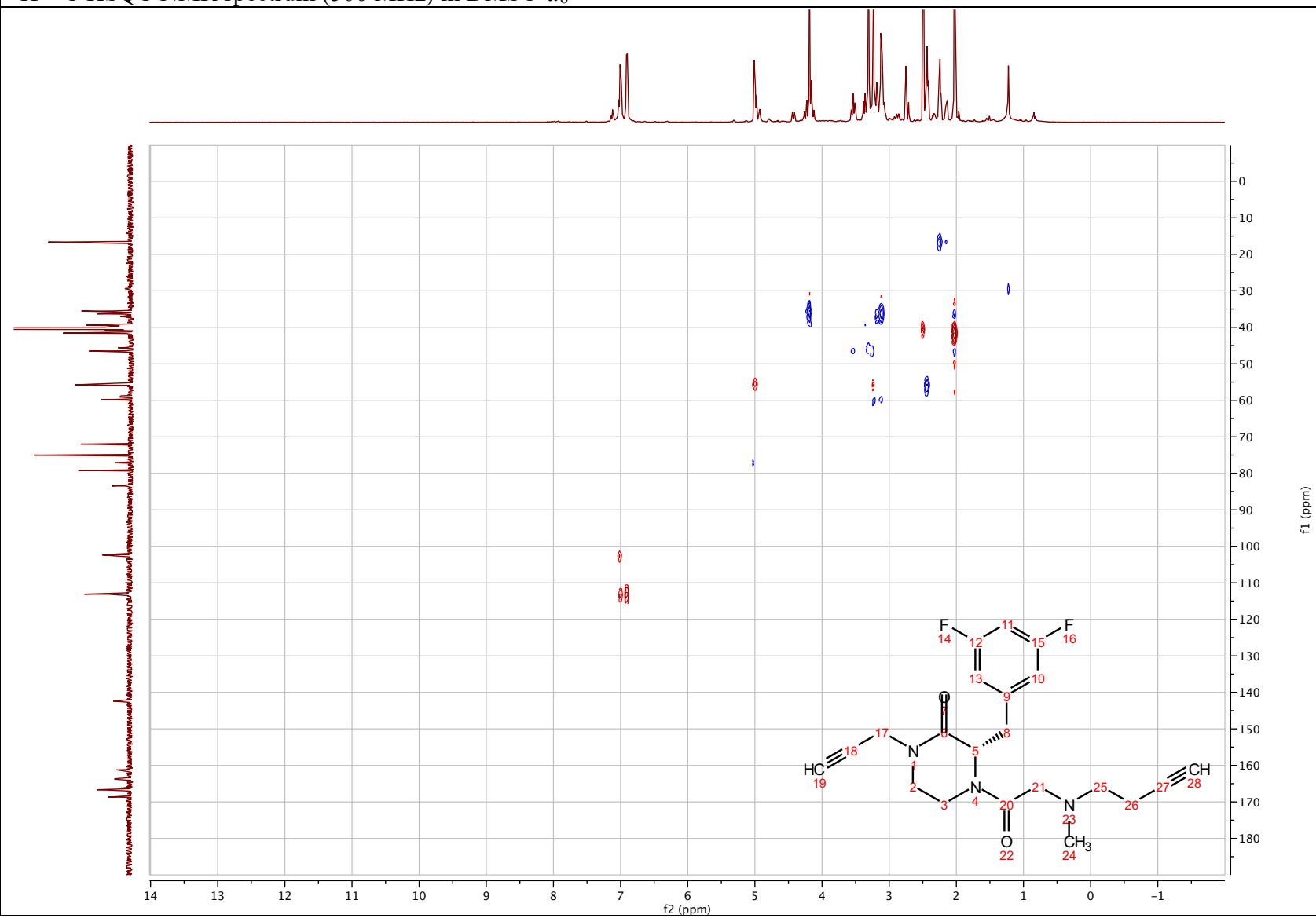
(S)-4-(N-(but-3-yn-1-yl)-N-methylglycyl)-3-(3,5-difluorobenzyl)-1-(prop-2-yn-1-yl)piperazin-2-one (2.74)

¹³C NMR spectrum (101 MHz) in DMSO-*d*₆



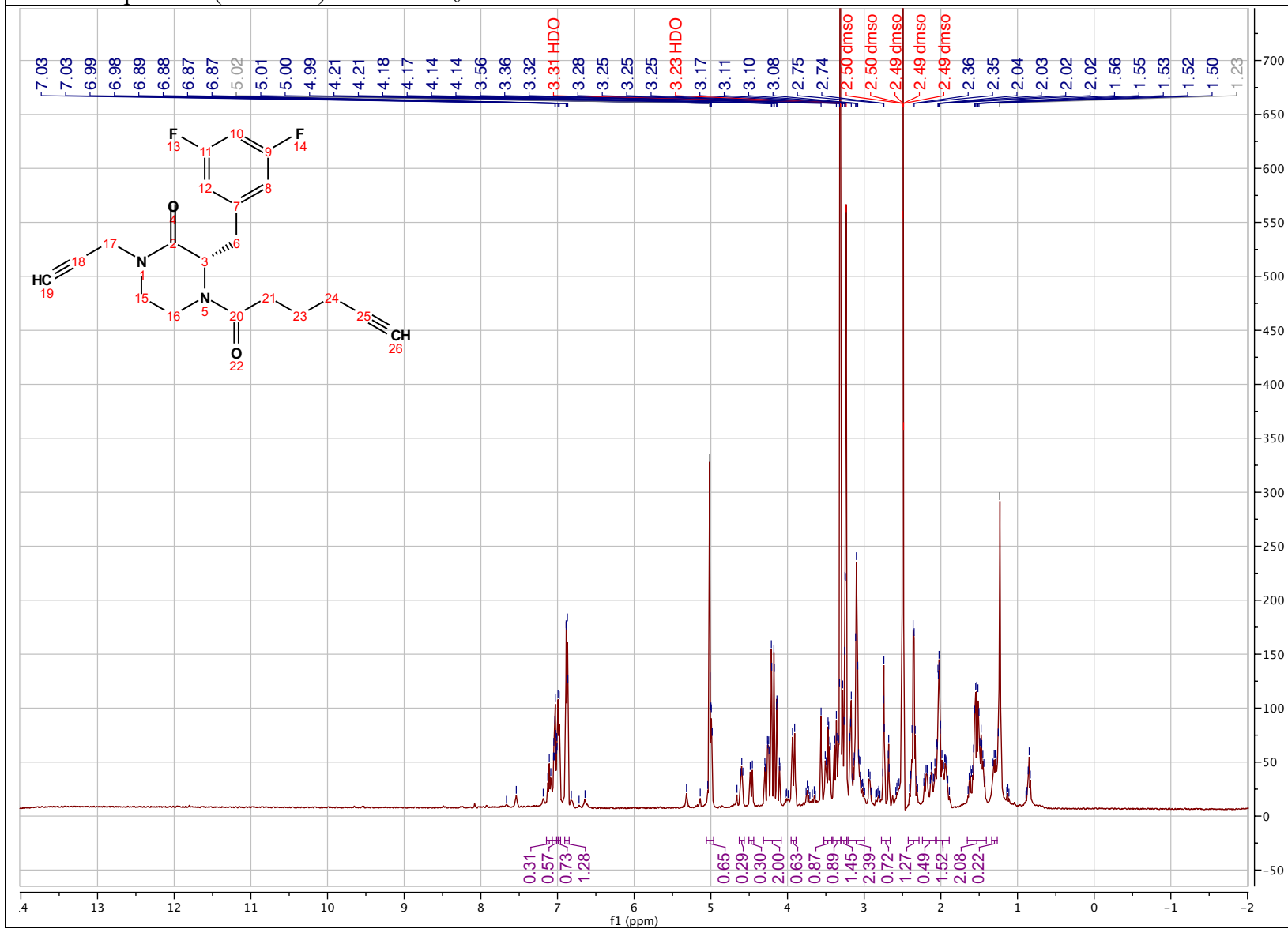
(S)-4-(N-(but-3-yn-1-yl)-N-methylglycyl)-3-(3,5-difluorobenzyl)-1-(prop-2-yn-1-yl)piperazin-2-one (2.74)

^1H - ^{13}C HSQC NMR spectrum (500 MHz) in $\text{DMSO-}d_6$



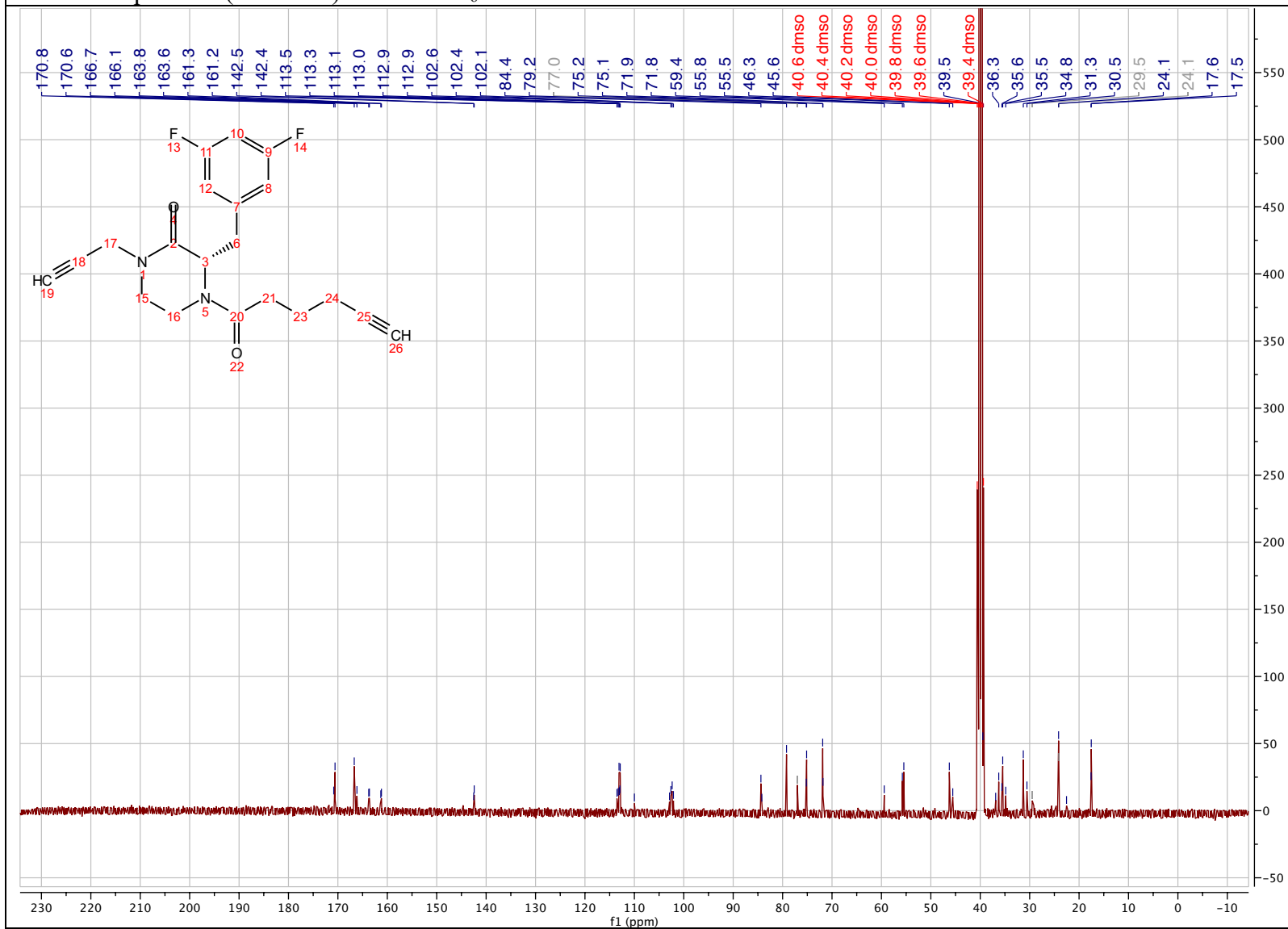
(S)-3-(3,5-difluorobenzyl)-4-(hex-5-ynoyl)-1-(prop-2-yn-1-yl)piperazin-2-one (2.75)

¹H NMR spectrum (500 MHz) in DMSO-*d*₆



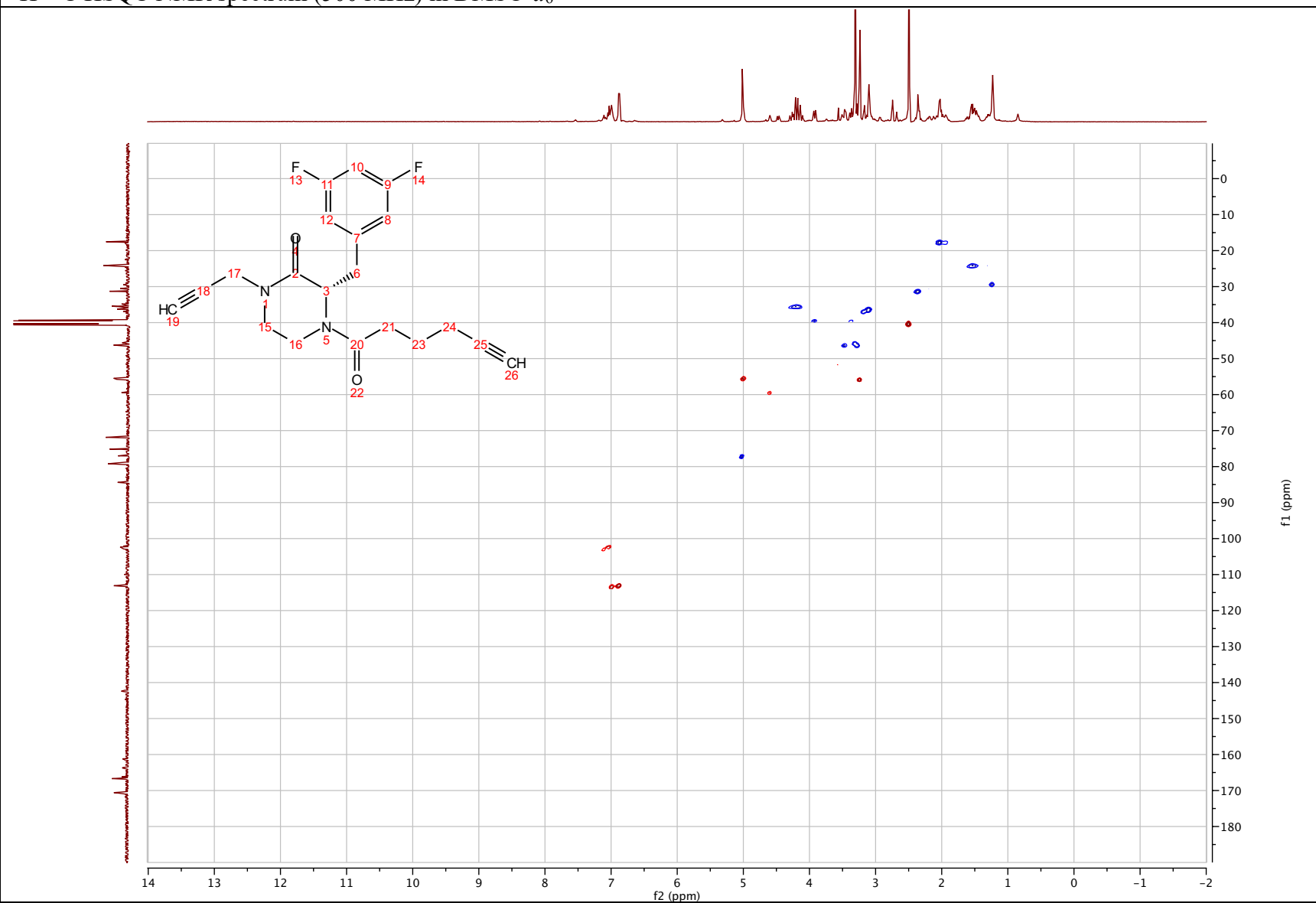
(S)-3-(3,5-difluorobenzyl)-4-(hex-5-ynoyl)-1-(prop-2-yn-1-yl)piperazin-2-one (2.75)

¹³C NMR spectrum (101 MHz) in DMSO-*d*₆



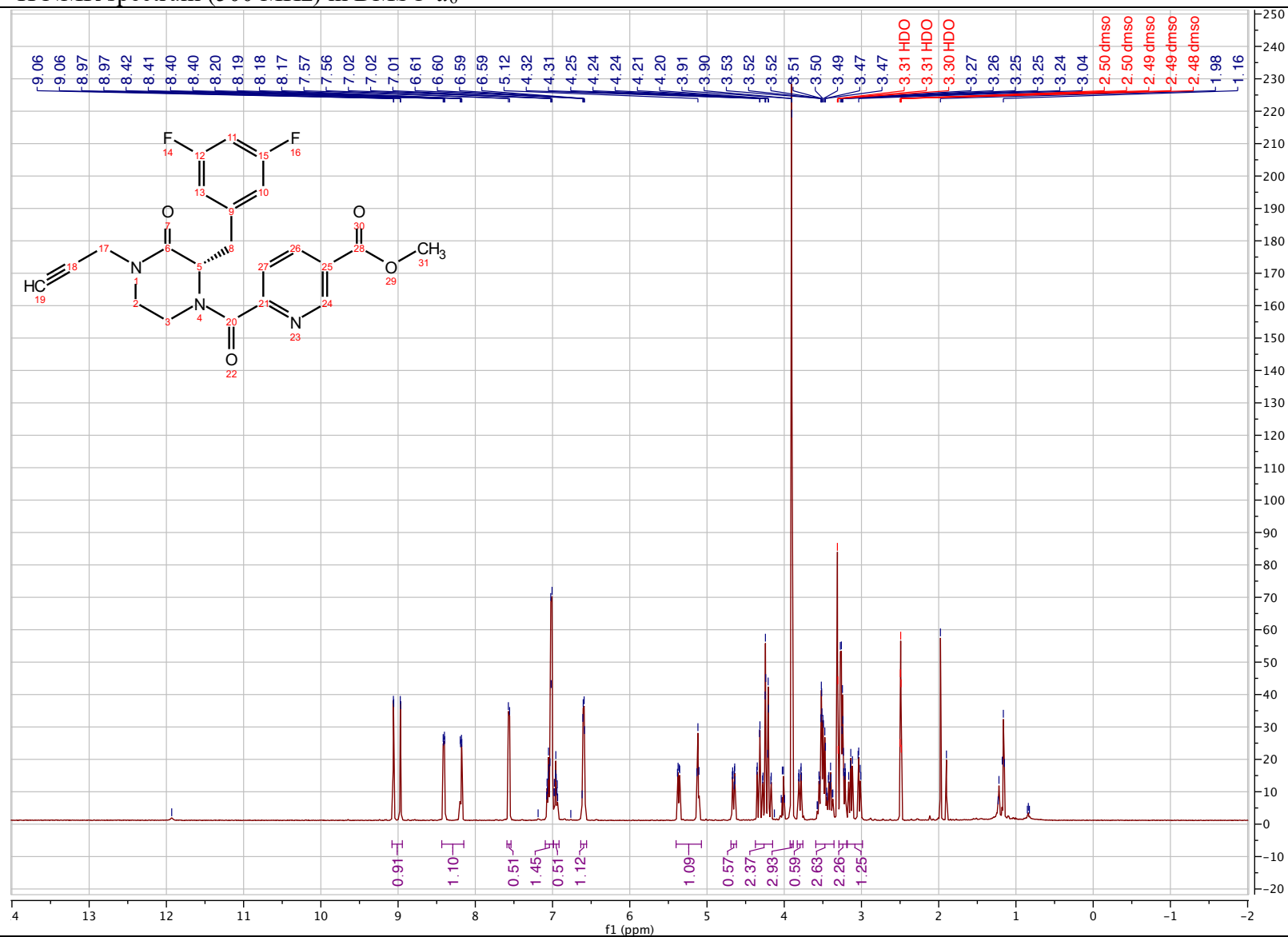
(S)-3-(3,5-difluorobenzyl)-4-(hex-5-ynyl)-1-(prop-2-yn-1-yl)piperazin-2-one (2.75)

^1H - ^{13}C HSQC NMR spectrum (500 MHz) in $\text{DMSO-}d_6$



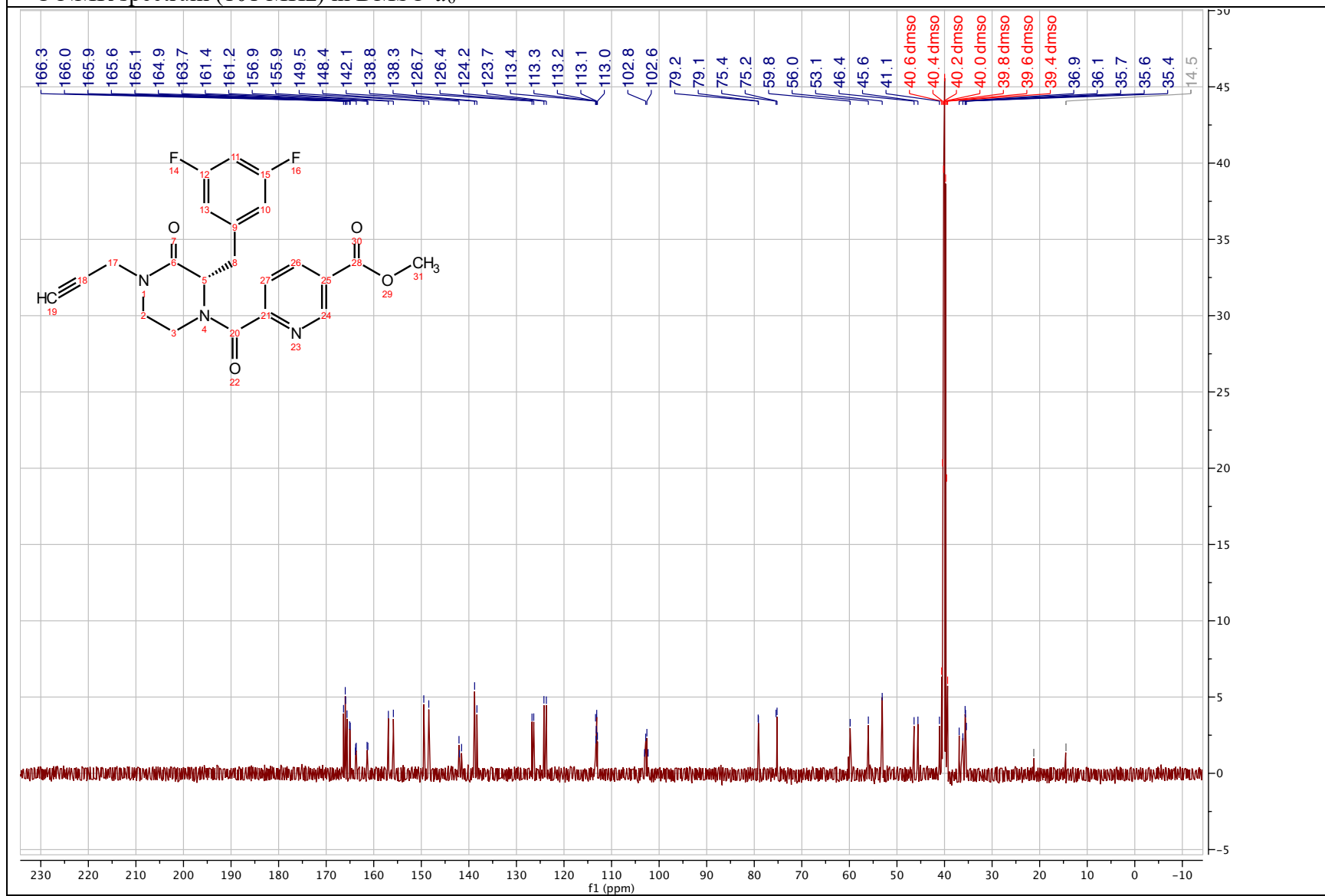
methyl (S)-6-(2-(3,5-difluorobenzyl)-3-oxo-4-(prop-2-yn-1-yl)piperazine-1-carbonyl) nicotinate (2.76)

¹H NMR spectrum (500 MHz) in DMSO-d₆



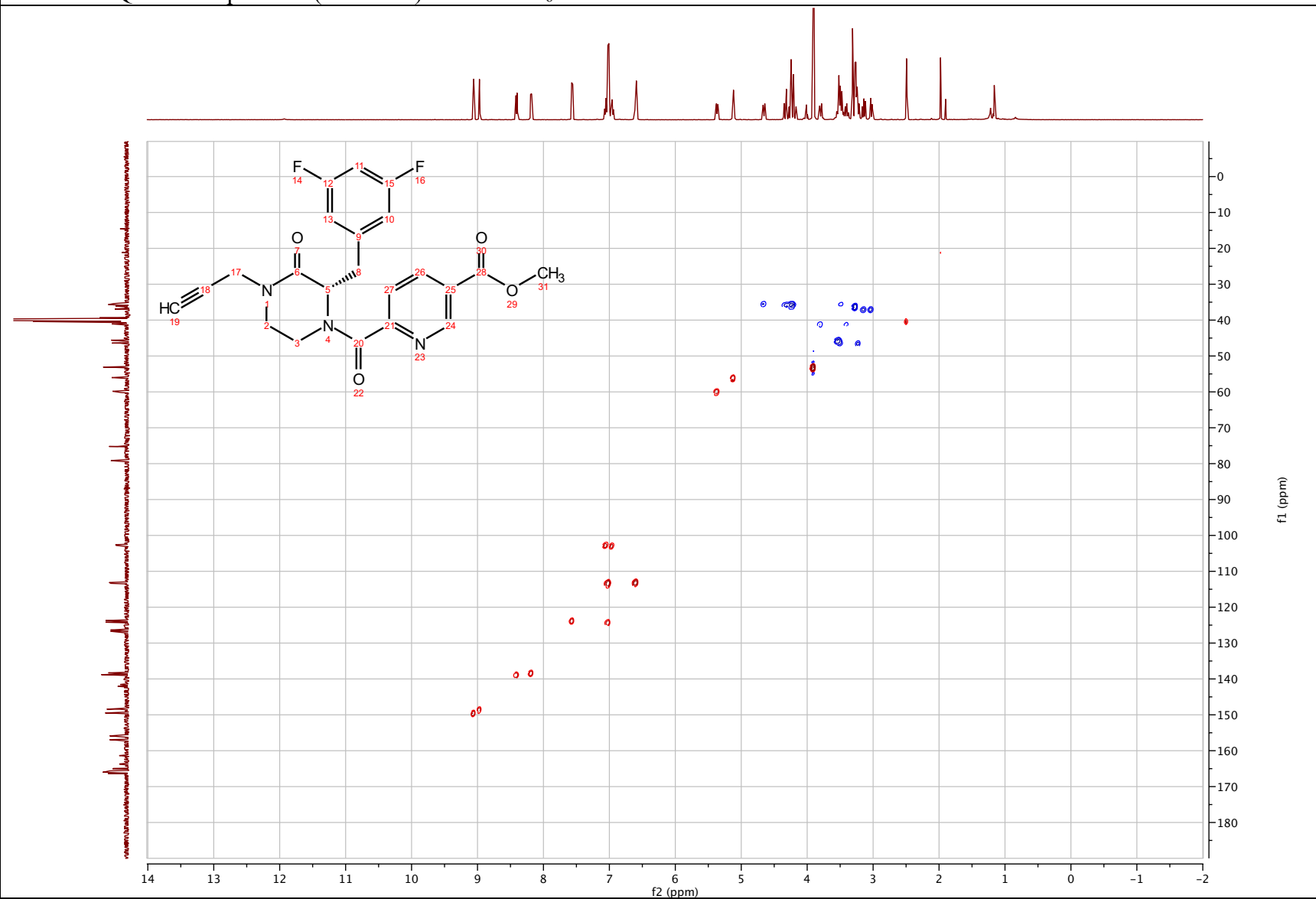
methyl (S)-6-(2-(3,5-difluorobenzyl)-3-oxo-4-(prop-2-yn-1-yl)piperazine-1-carbonyl) nicotinate (2.76)

¹³C NMR spectrum (101 MHz) in DMSO-d₆



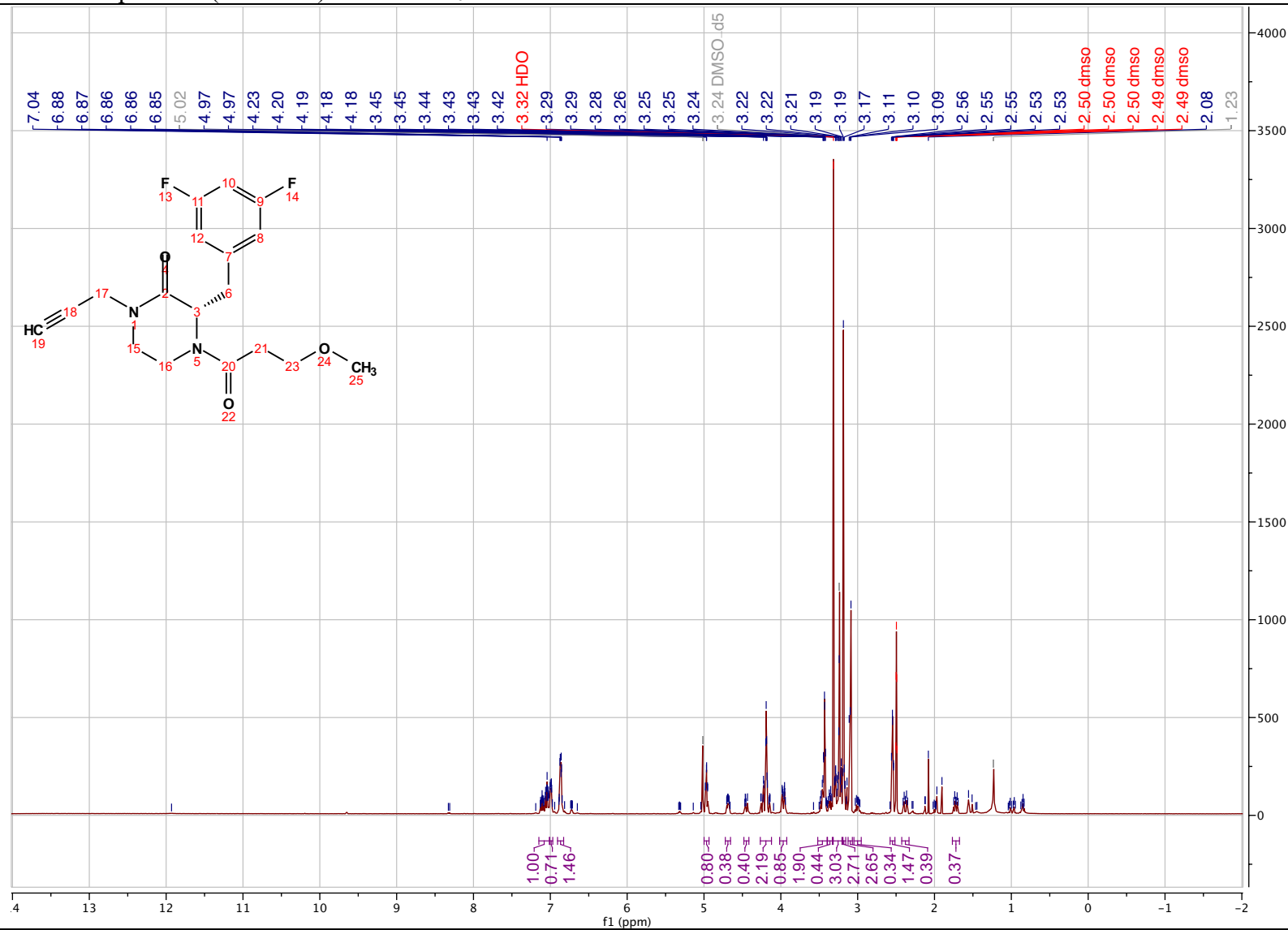
methyl (S)-6-(2-(3,5-difluorobenzyl)-3-oxo-4-(prop-2-yn-1-yl)piperazine-1-carbonyl) nicotinate (2.76)

^1H - ^{13}C HSQC NMR spectrum (500 MHz) in $\text{DMSO-}d_6$



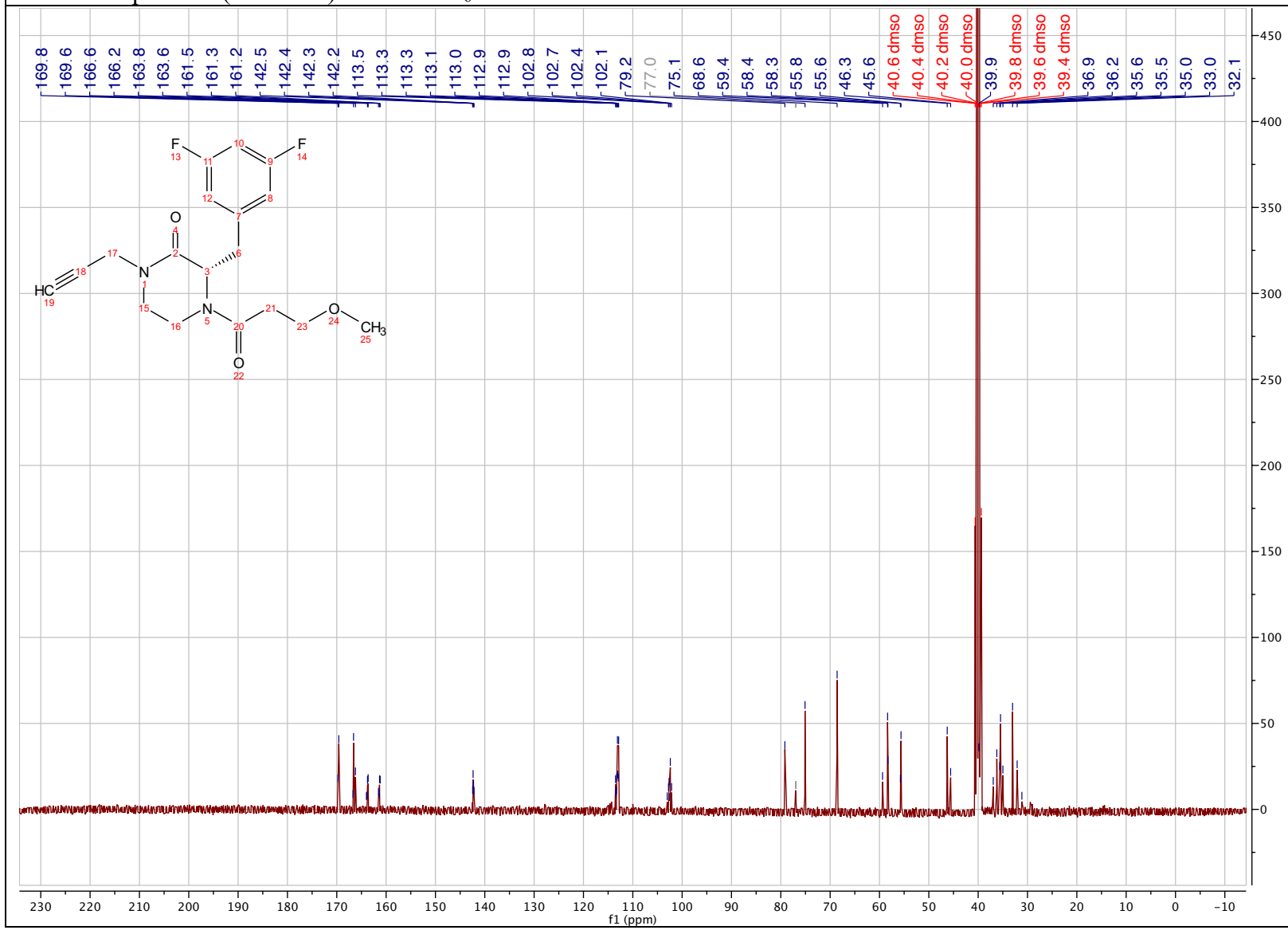
(S)-3-(3,5-difluorobenzyl)-4-(3-methoxypropanoyl)-1-(prop-2-yn-1-yl)piperazin-2-one (2.77)

¹H NMR spectrum (500 MHz) in DMSO-*d*₆



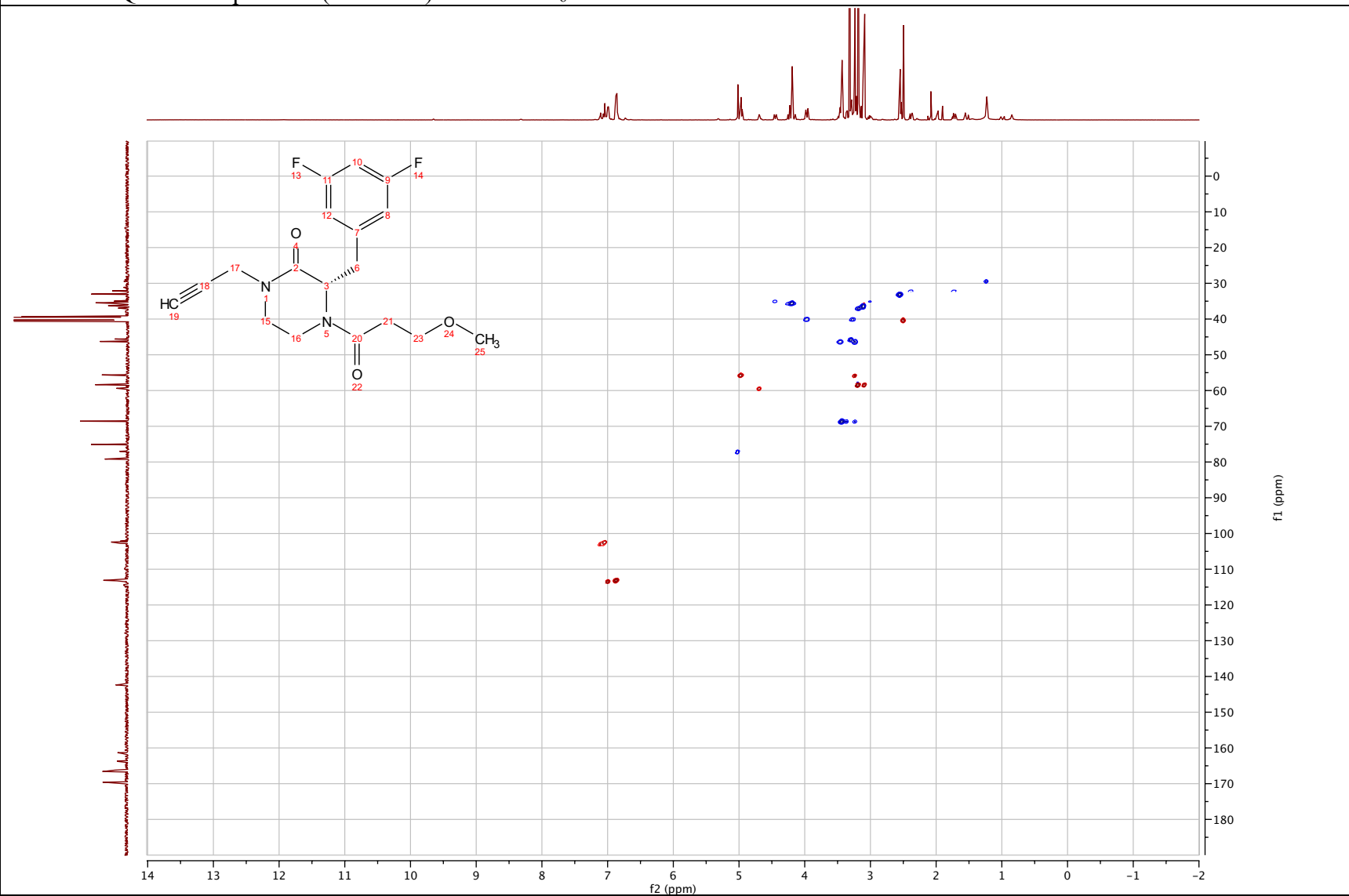
(S)-3-(3,5-difluorobenzyl)-4-(3-methoxypropanoyl)-1-(prop-2-yn-1-yl)piperazin-2-one (2.77)

¹³C NMR spectrum (101 MHz) in DMSO-*d*₆



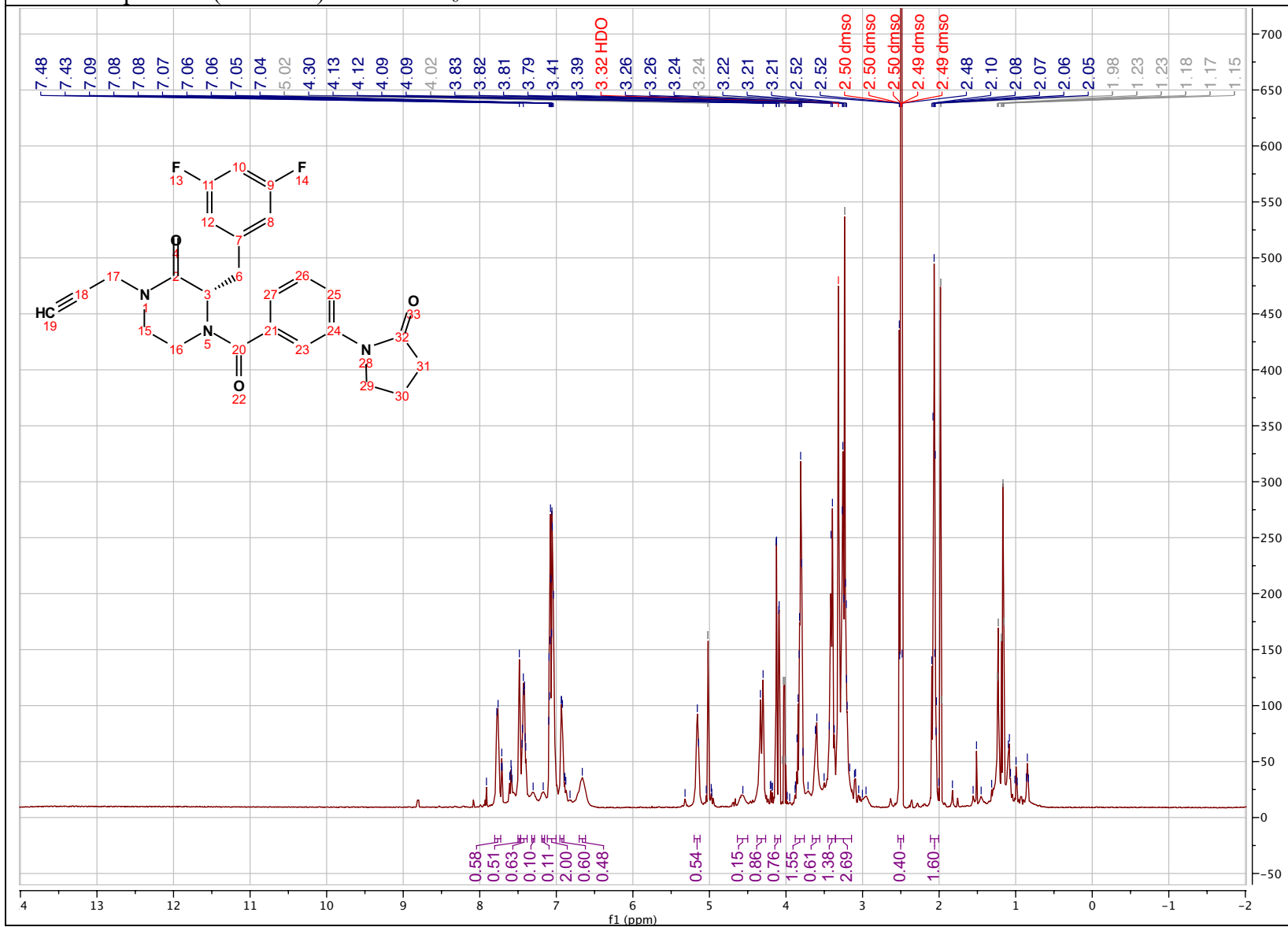
(S)-3-(3,5-difluorobenzyl)-4-(3-methoxypropanoyl)-1-(prop-2-yn-1-yl)piperazin-2-one (2.77)

^1H - ^{13}C HSQC NMR spectrum (500 MHz) in $\text{DMSO-}d_6$



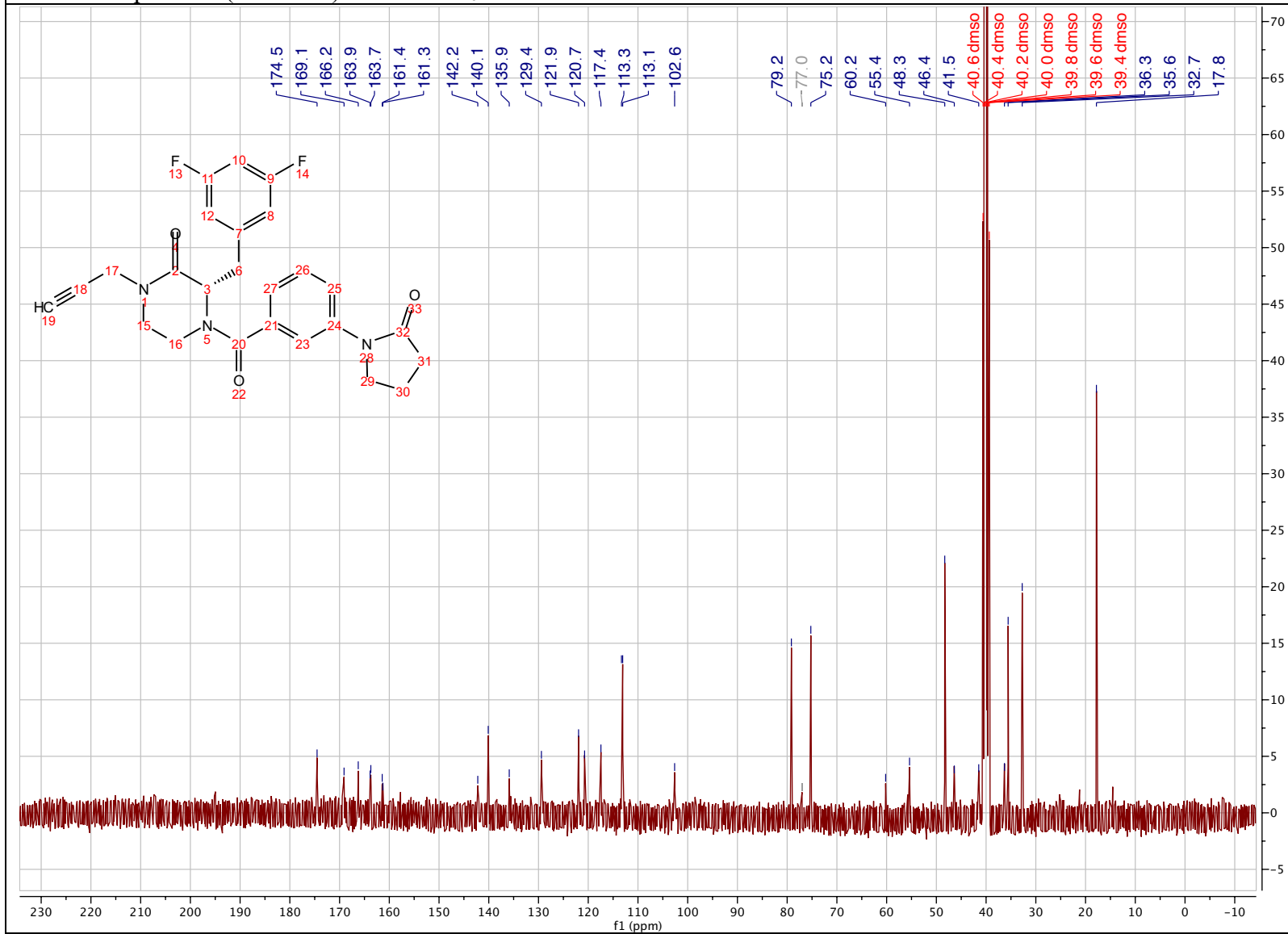
(S)-3-(3,5-difluorobenzyl)-4-(3-(2-oxypyrrolidin-1-yl)benzoyl)-1-(prop-2-yn-1-yl)piperazin-2-one (2.78)

¹H NMR spectrum (500 MHz) in DMSO-*d*₆



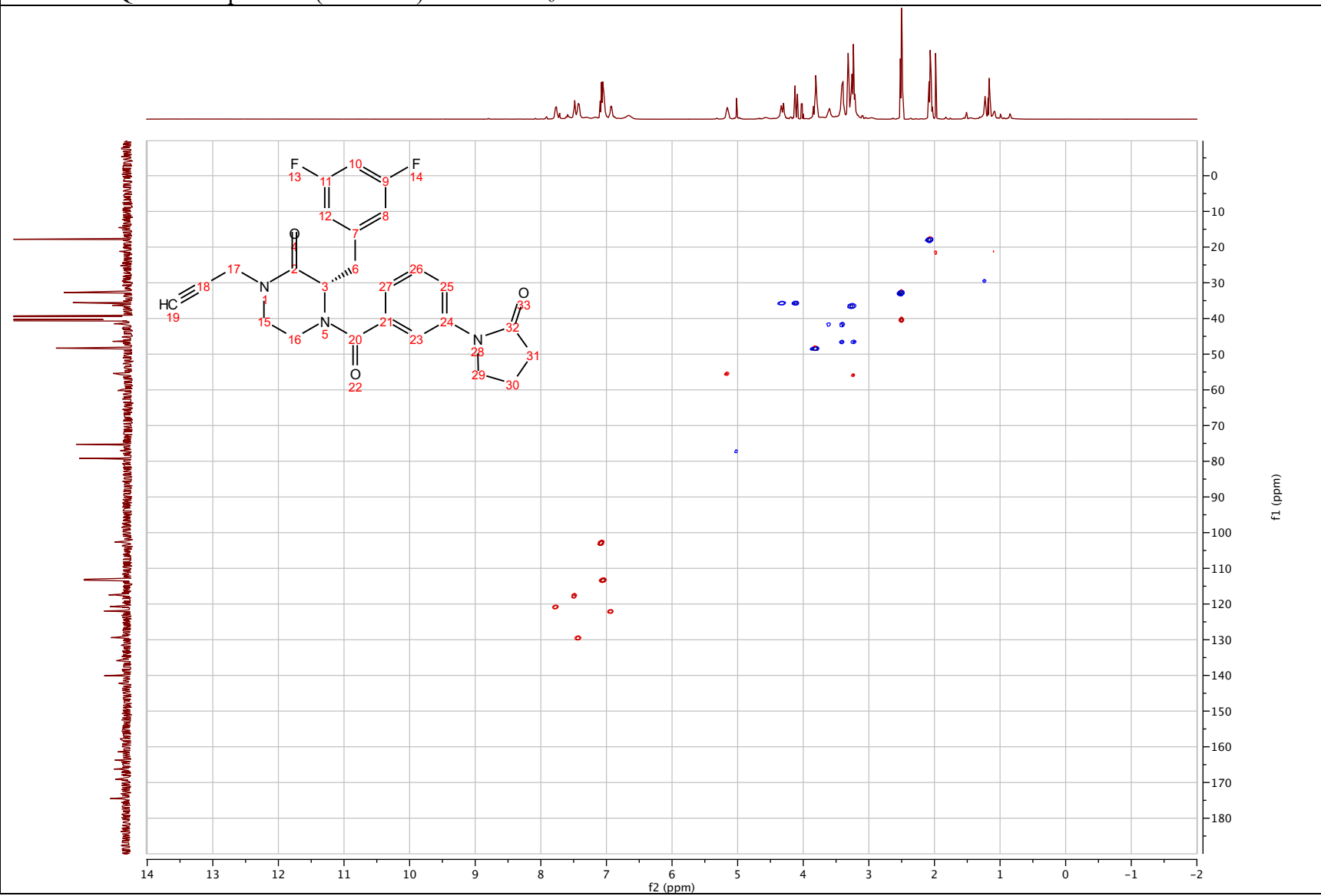
(S)-3-(3,5-difluorobenzyl)-4-(3-(2-oxopyrrolidin-1-yl)benzoyl)-1-(prop-2-yn-1-yl)piperazin-2-one (2.78)

^{13}C NMR spectrum (101 MHz) in $\text{DMSO-}d_6$



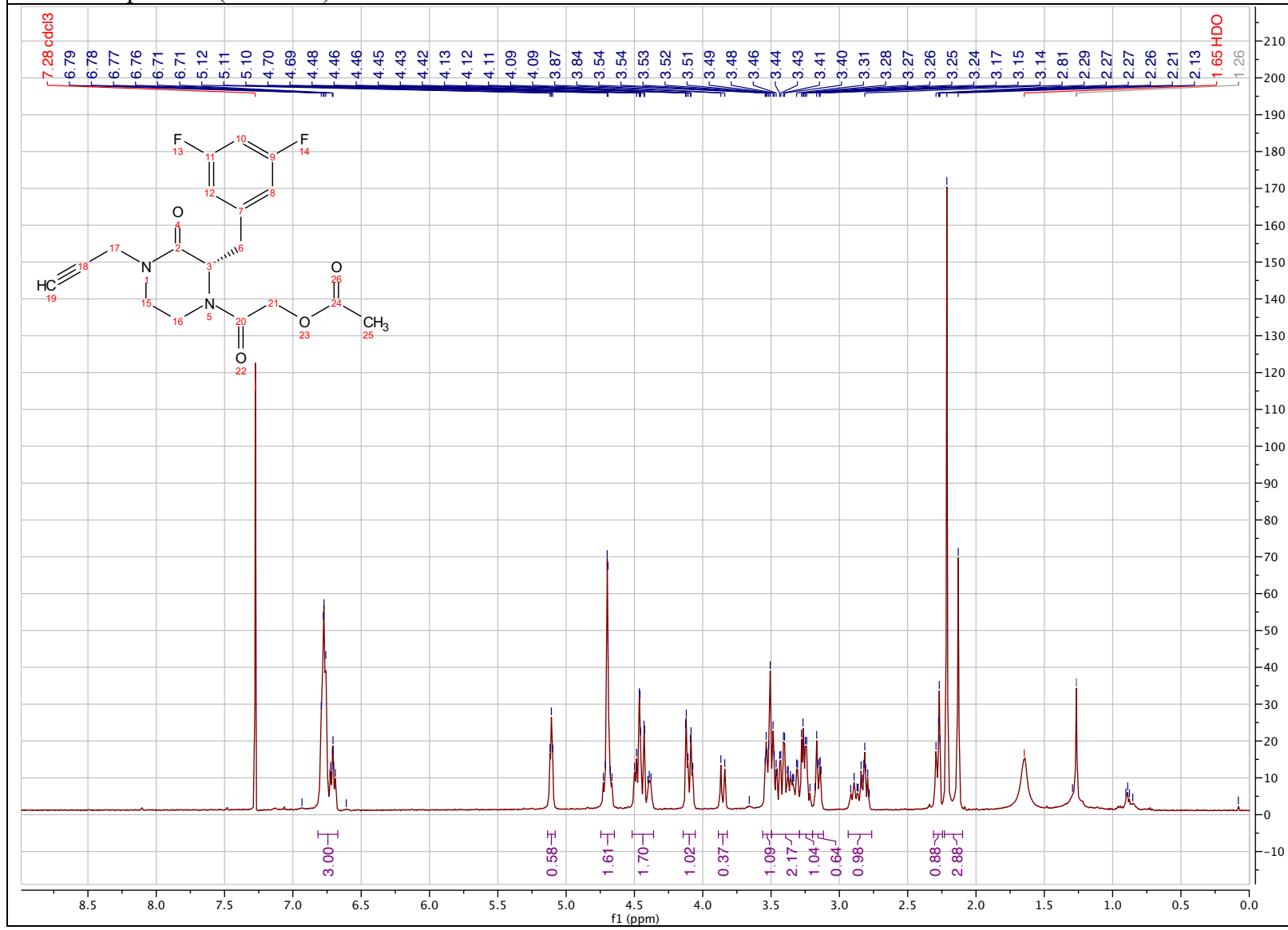
(S)-3-(3,5-difluorobenzyl)-4-(3-(2-oxopyrrolidin-1-yl)benzoyl)-1-(prop-2-yn-1-yl)piperazin-2-one (2.78)

^1H - ^{13}C HSQC NMR spectrum (500 MHz) in $\text{DMSO-}d_6$



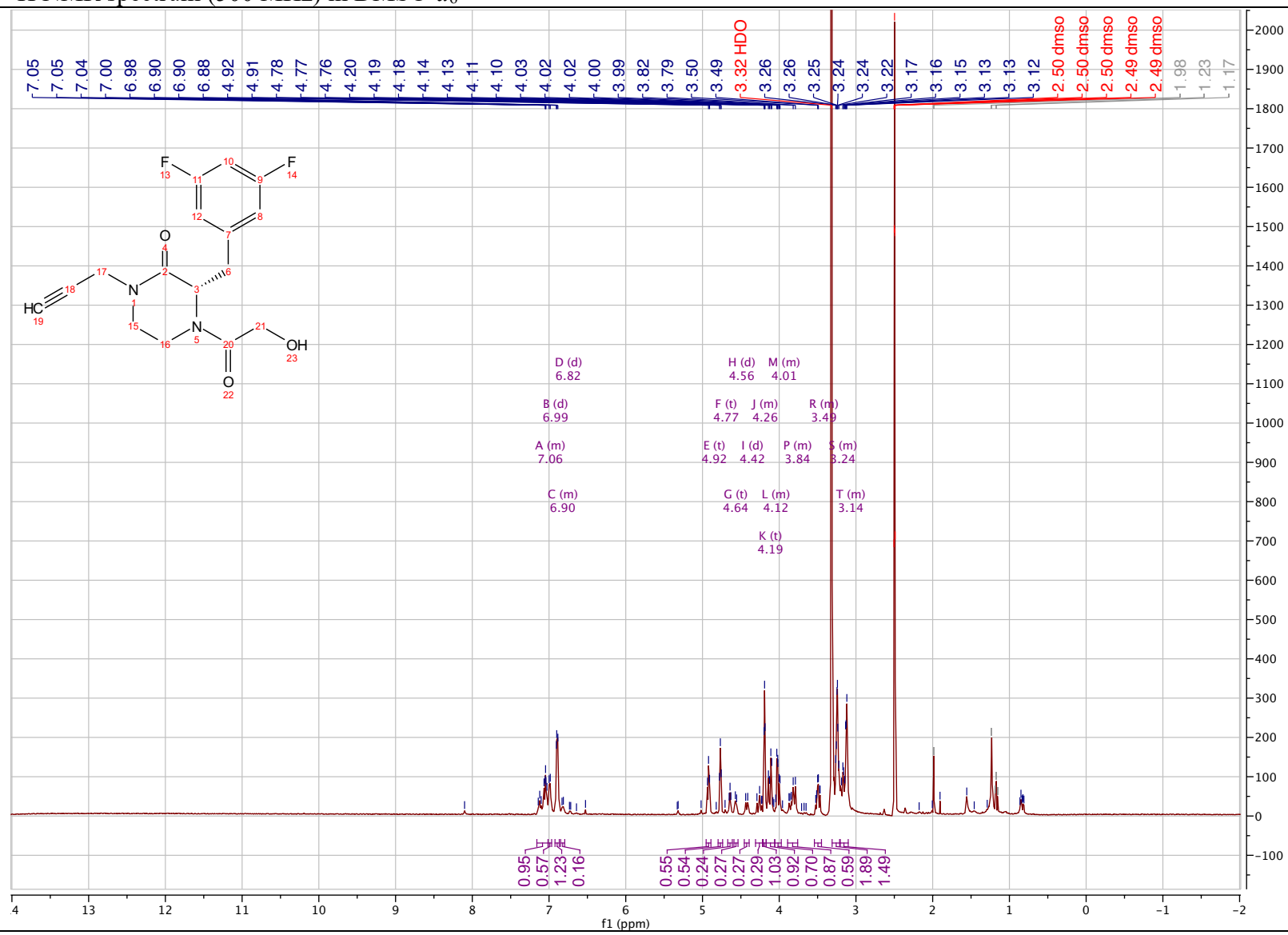
(S)-2-(2-(3,5-difluorobenzyl)-3-oxo-4-(prop-2-yn-1-yl)piperazin-1-yl)-2-oxoethyl acetate (2.79)

¹H NMR spectrum (500 MHz) in Chloroform-*d*



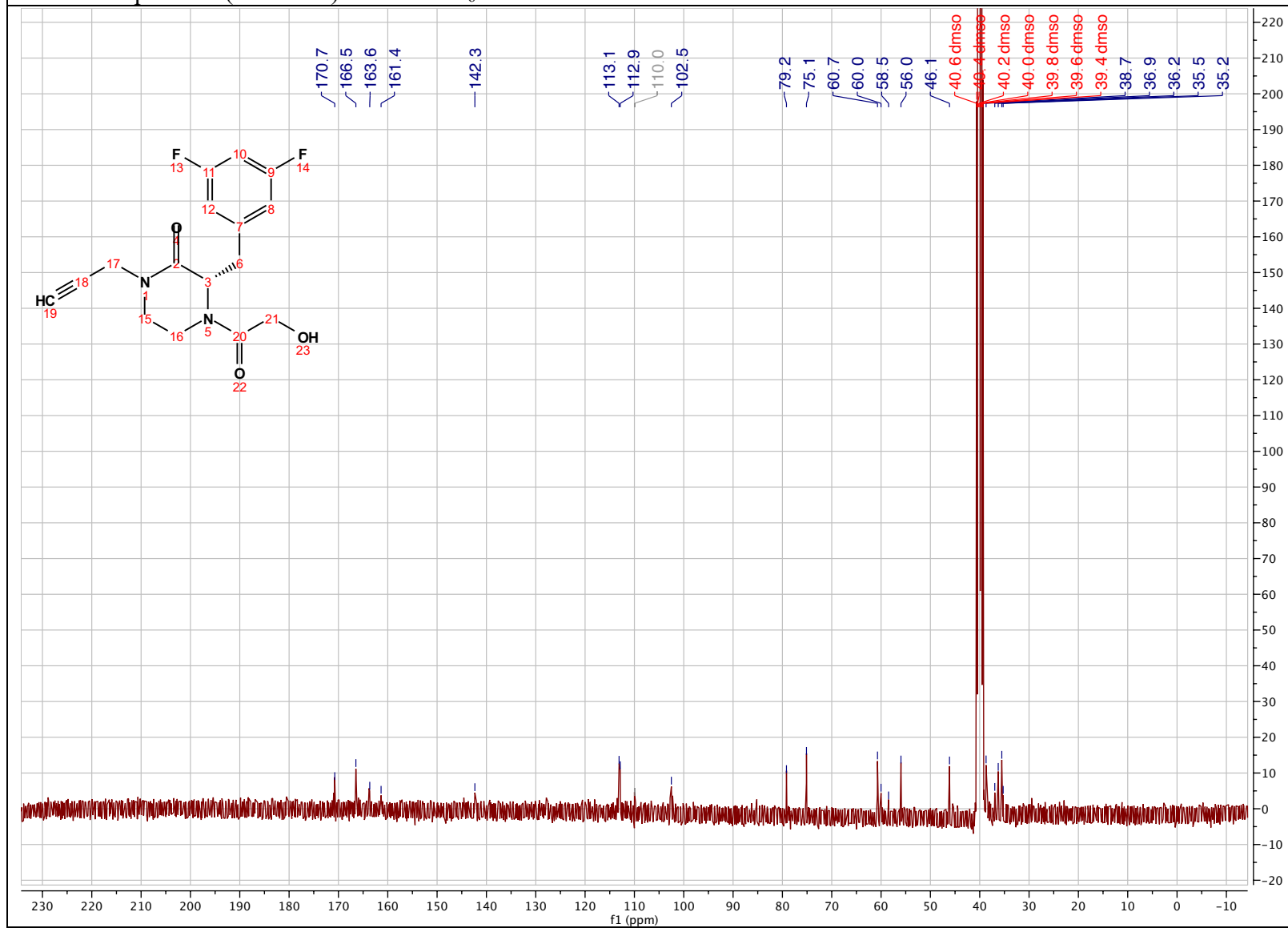
(S)-3-(3,5-difluorobenzyl)-4-(2-hydroxyacetyl)-1-(prop-2-yn-1-yl)piperazin-2-one (2.80)

¹H NMR spectrum (500 MHz) in DMSO-d₆



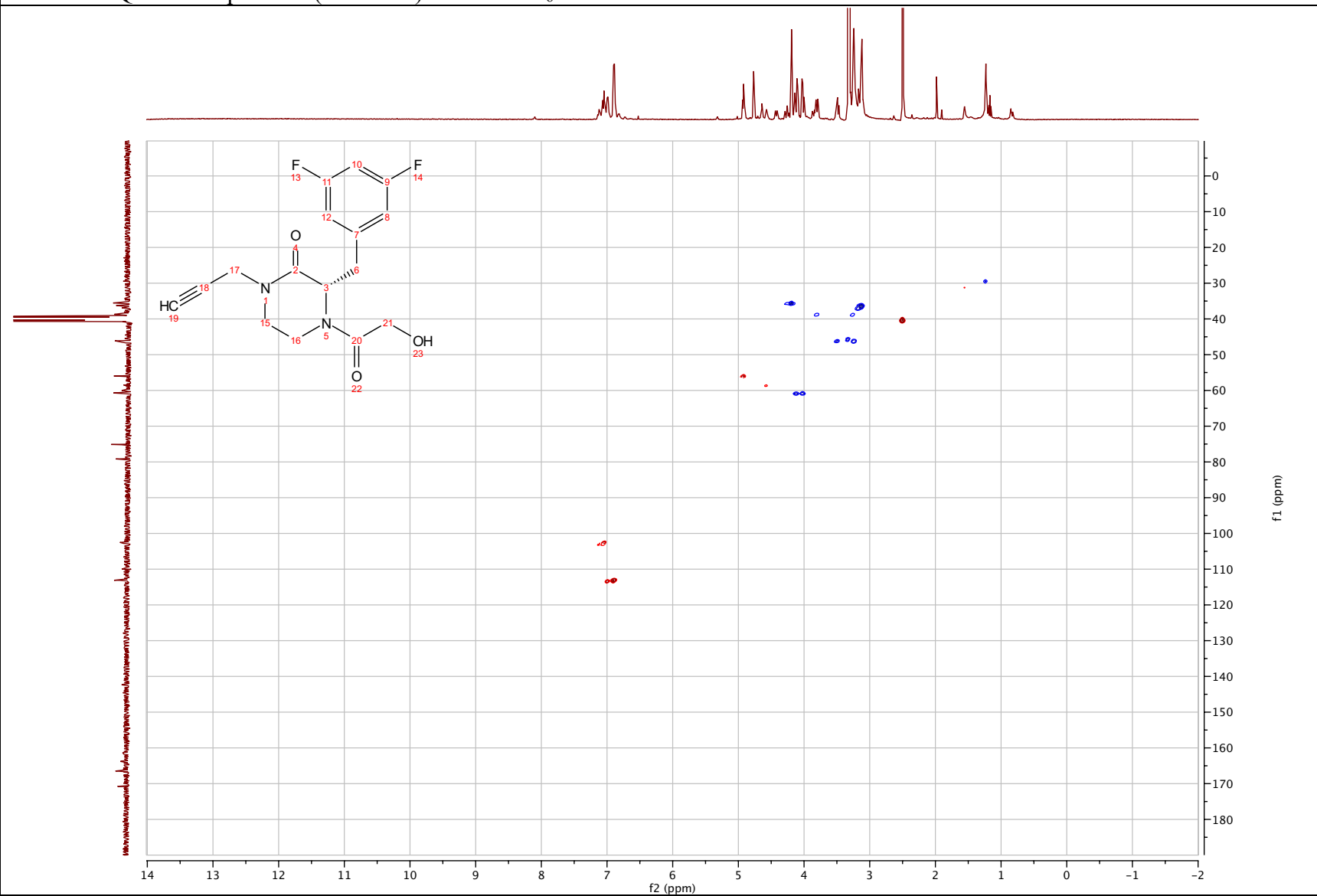
(S)-3-(3,5-difluorobenzyl)-4-(2-hydroxyacetyl)-1-(prop-2-yn-1-yl)piperazin-2-one (2.80)

¹³C NMR spectrum (101 MHz) in DMSO-*d*₆



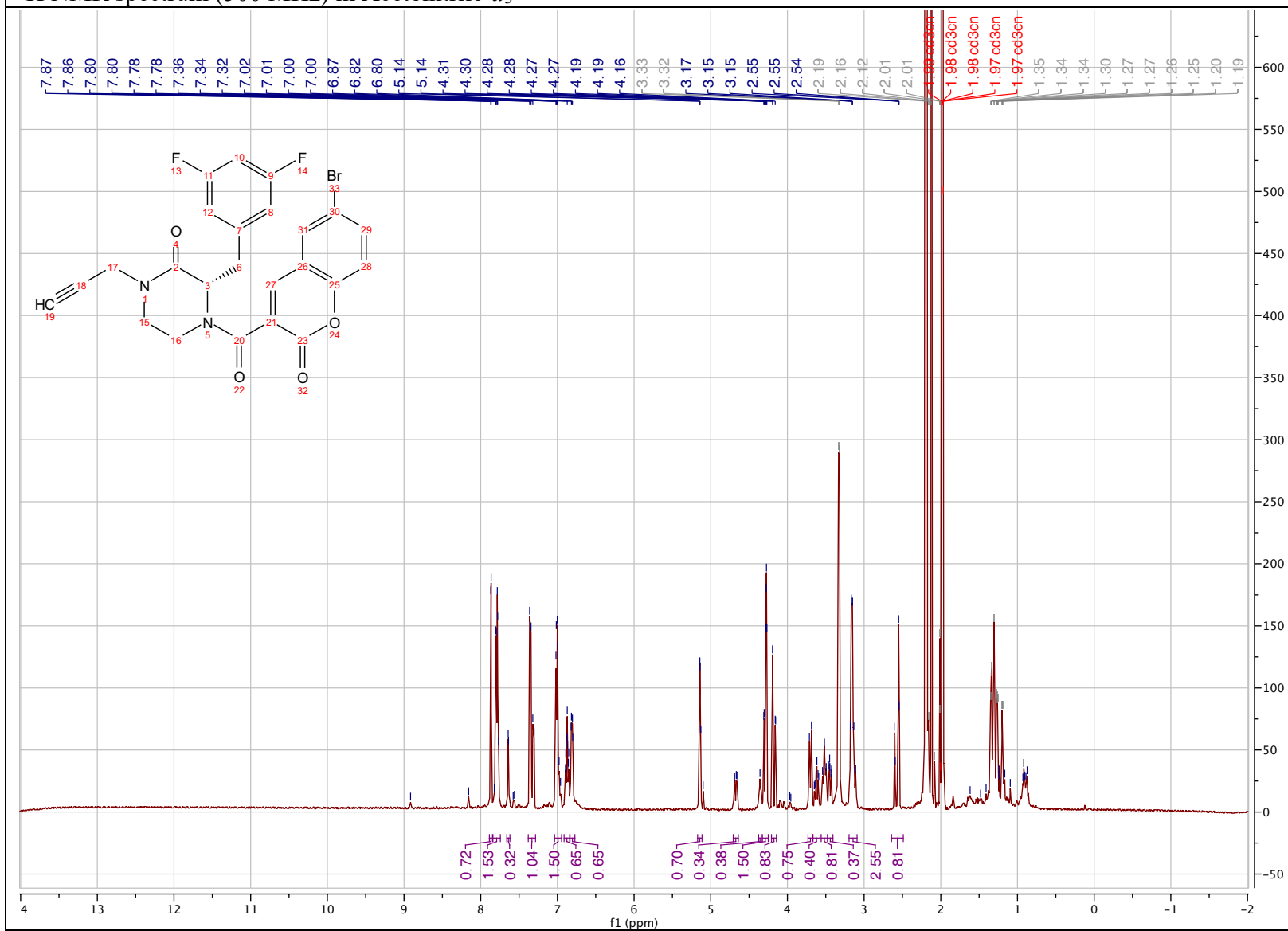
(S)-3-(3,5-difluorobenzyl)-4-(2-hydroxyacetyl)-1-(prop-2-yn-1-yl)piperazin-2-one (2.80)

^1H - ^{13}C HSQC NMR spectrum (500 MHz) in $\text{DMSO-}d_6$



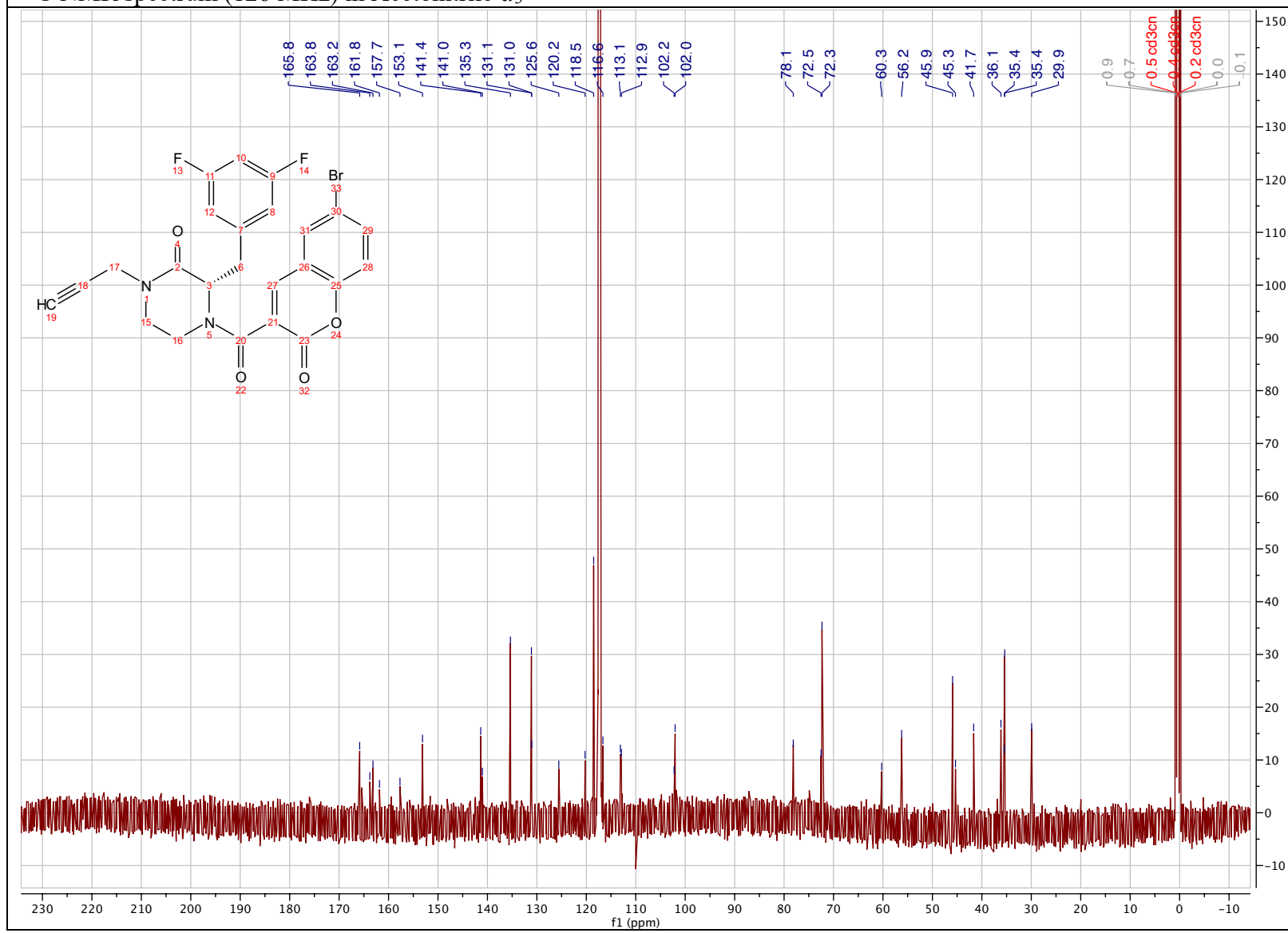
(S)-4-(6-bromo-2-oxo-2H-chromene-3-carbonyl)-3-(3,5-difluorobenzyl)-1-(prop-2-yn-1-yl)piperazin-2-one (2.81)

¹H NMR spectrum (500 MHz) in Acetonitrile-*d*₃



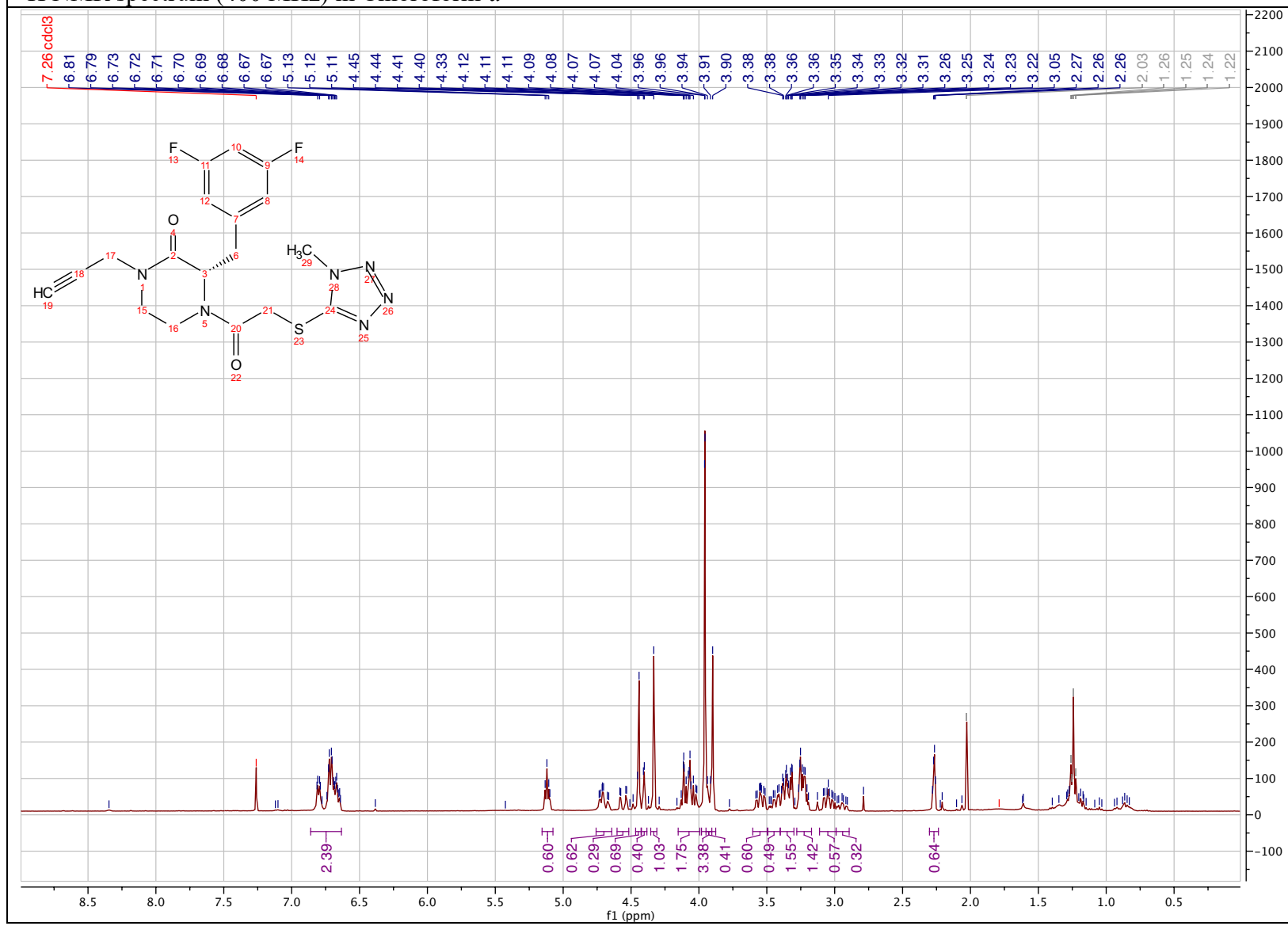
(S)-4-(6-bromo-2-oxo-2H-chromene-3-carbonyl)-3-(3,5-difluorobenzyl)-1-(prop-2-yn-1-yl)piperazin-2-one (2.81)

¹³C NMR spectrum (126 MHz) in Acetonitrile-*d*₃



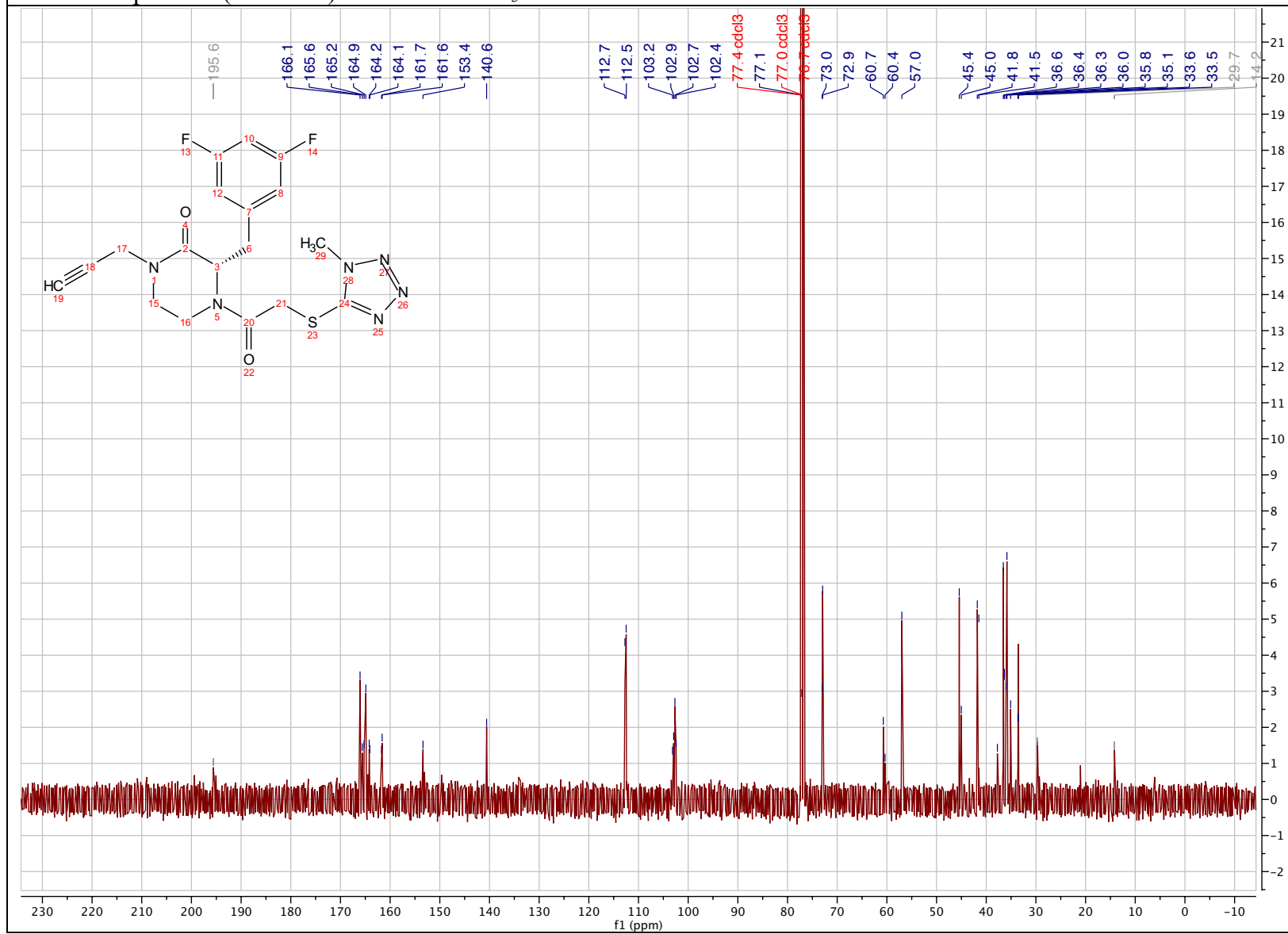
(S)-3-(3,5-difluorobenzyl)-4-(2-((1-methyl-1H-tetrazol-5-yl)thio)acetyl)-1-(prop-2-yn-1-yl)piperazin-2-one (2.82)

¹H NMR spectrum (400 MHz) in Chloroform-*d*



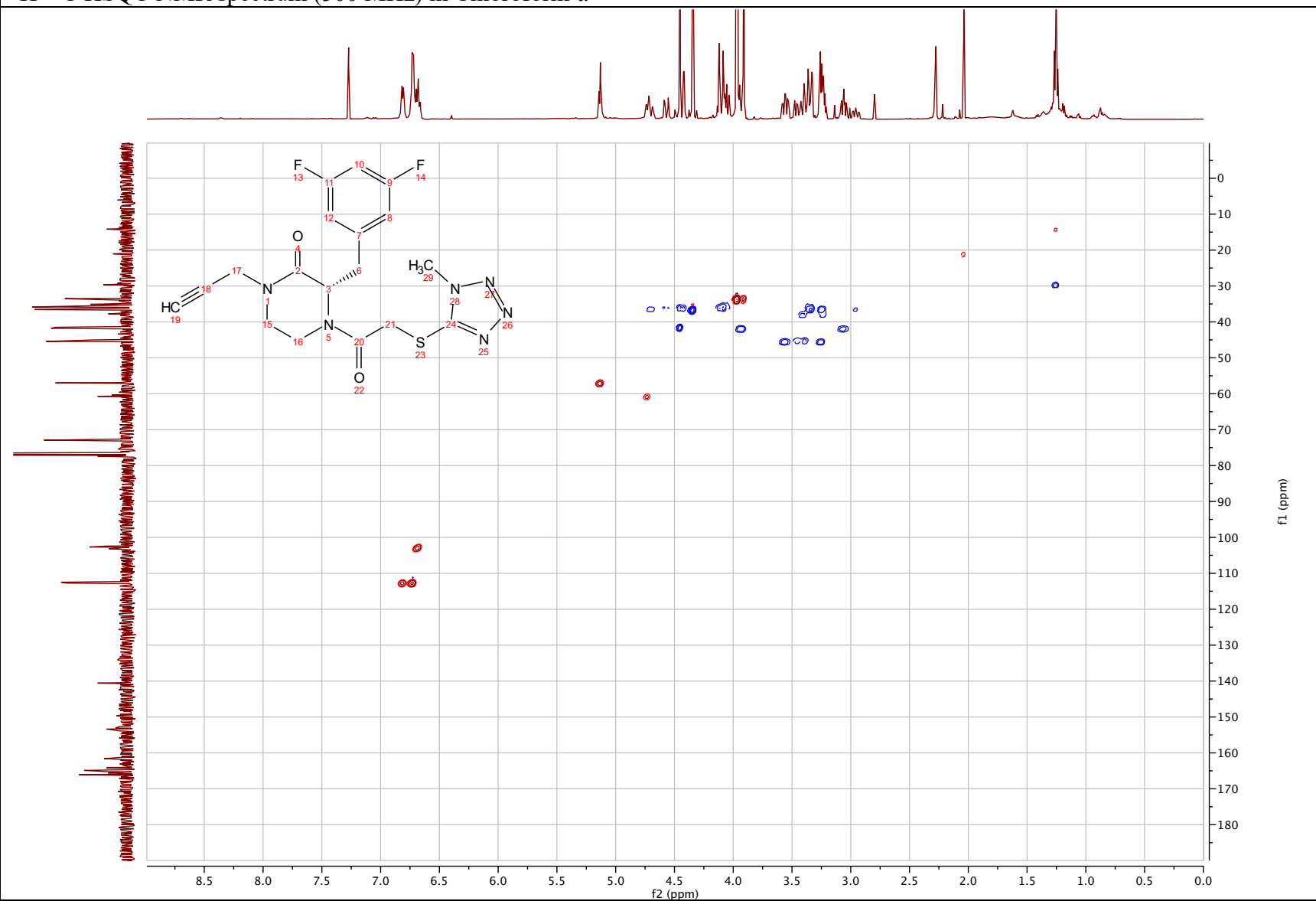
(S)-3-(3,5-difluorobenzyl)-4-(2-((1-methyl-1H-tetrazol-5-yl)thio)acetyl)-1-(prop-2-yn-1-yl)piperazin-2-one (2.82)

^{13}C NMR spectrum (126 MHz) in Acetonitrile- d_3



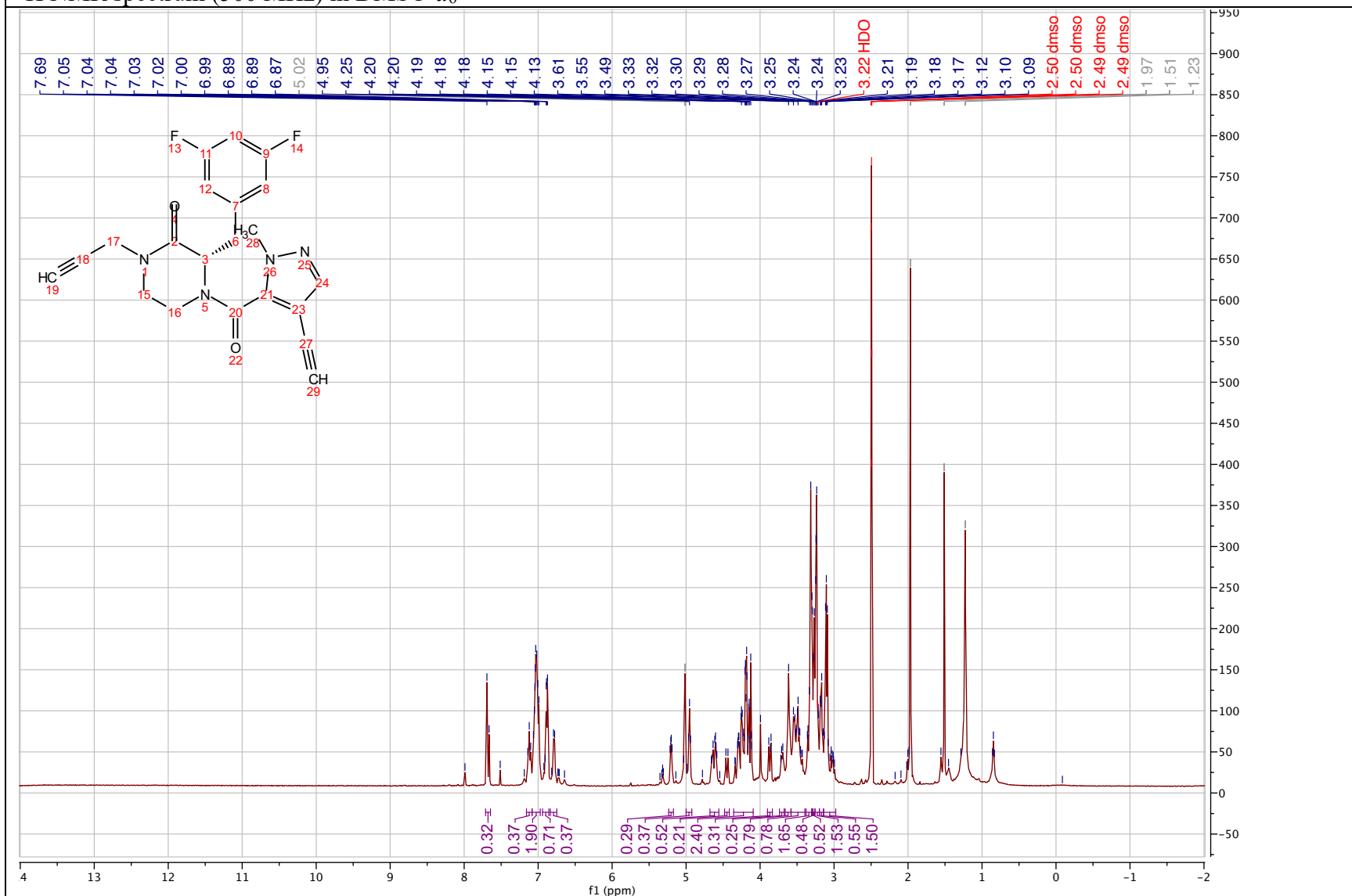
(S)-3-(3,5-difluorobenzyl)-4-(2-((1-methyl-1H-tetrazol-5-yl)thio)acetyl)-1-(prop-2-yn-1-yl)piperazin-2-one (2.82)

^1H - ^{13}C HSQC NMR spectrum (500 MHz) in Chloroform-*d*



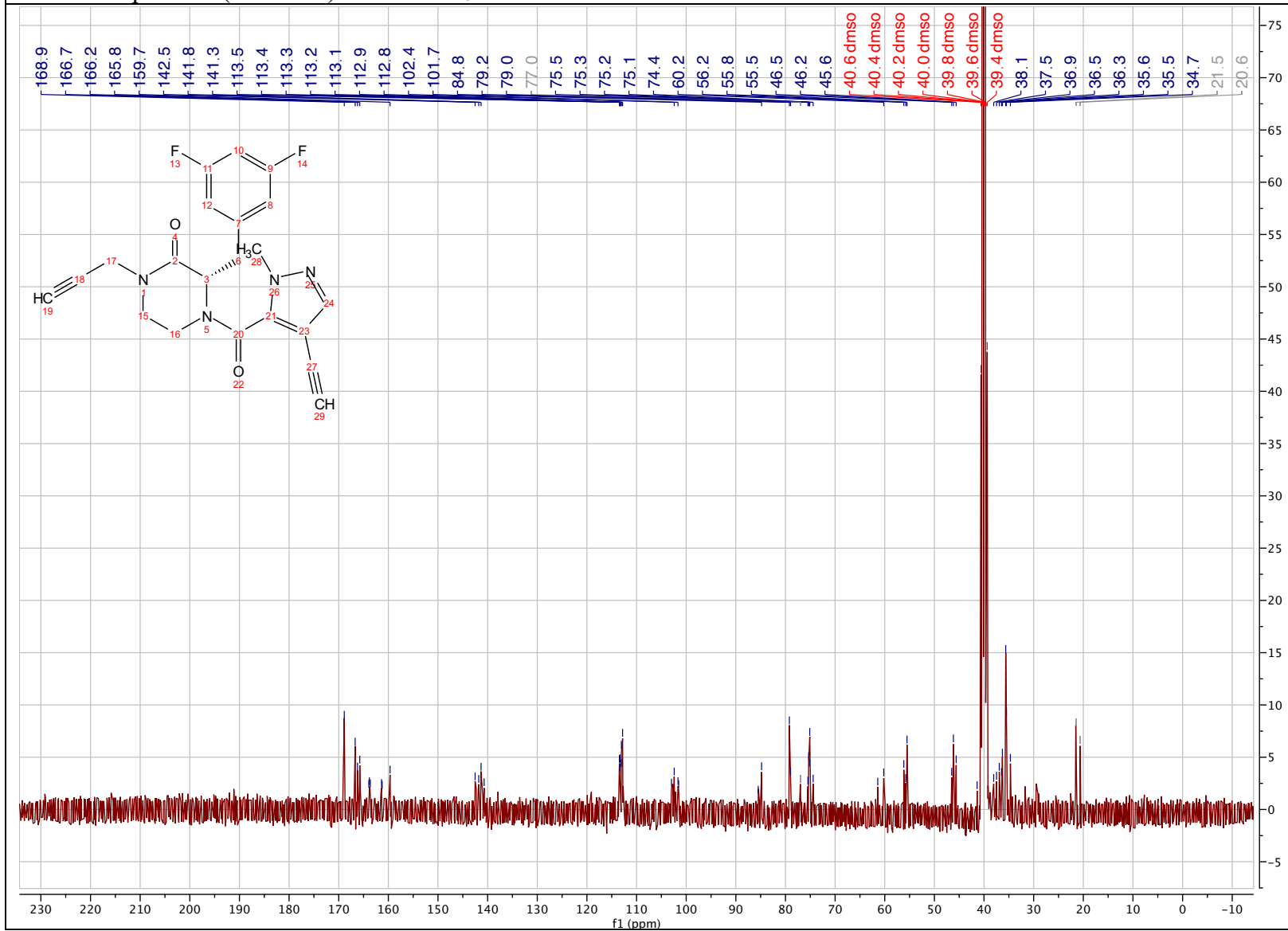
(S)-3-(3,5-difluorobenzyl)-4-(4-ethynyl-1-methyl-1H-pyrazole-5-carbonyl)-1-(prop-2-yn-1-yl)piperazin-2-one (2.83)

¹H NMR spectrum (500 MHz) in DMSO-*d*₆



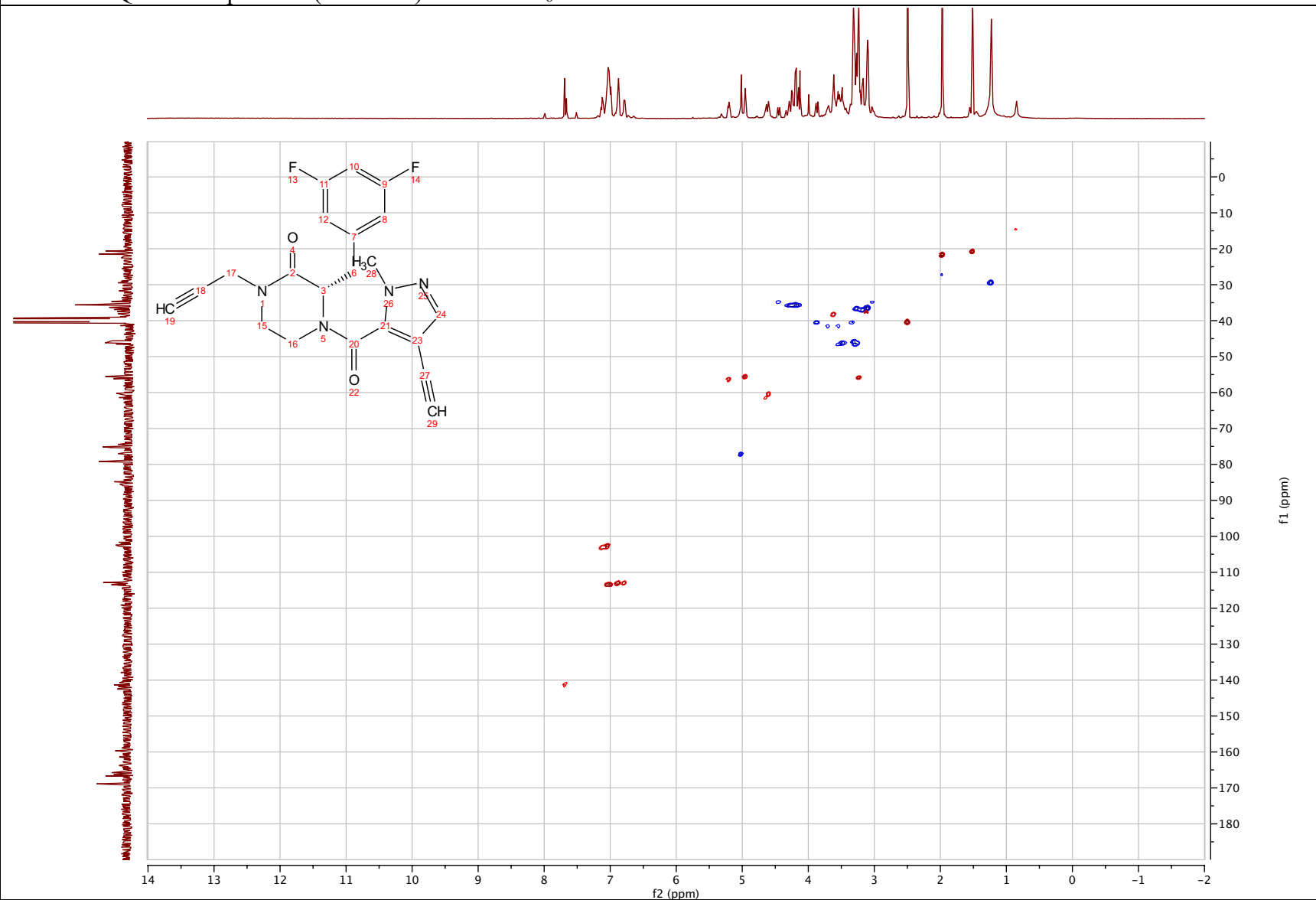
(S)-3-(3,5-difluorobenzyl)-4-(4-ethynyl-1-methyl-1H-pyrazole-5-carbonyl)-1-(prop-2-yn-1-yl)piperazin-2-one (2.83)

¹³C NMR spectrum (101 MHz) in DMSO-*d*₆



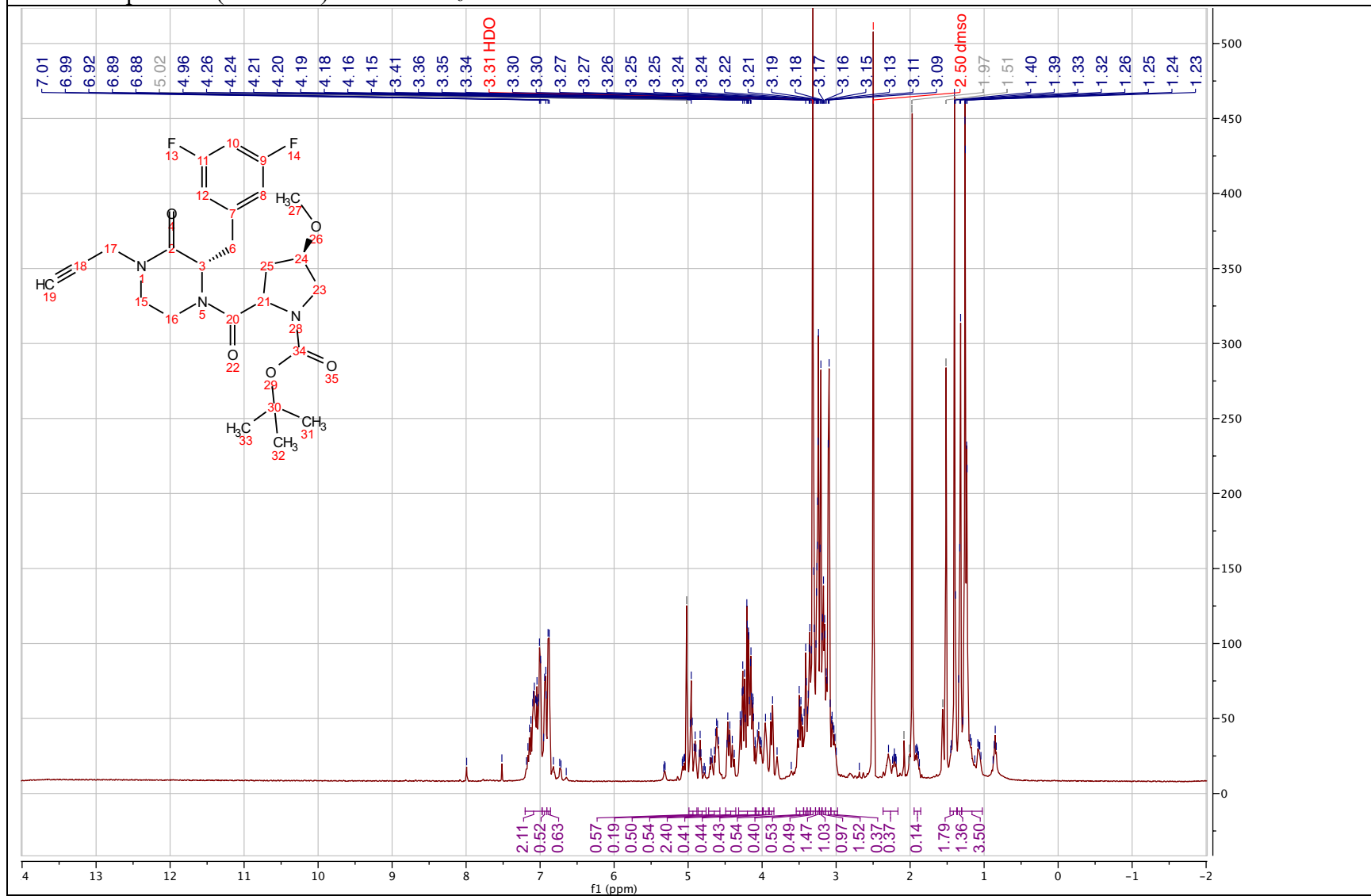
(S)-3-(3,5-difluorobenzyl)-4-(4-ethynyl-1-methyl-1H-pyrazole-5-carbonyl)-1-(prop-2-yn-1-yl)piperazin-2-one (2.83)

^1H - ^{13}C HSQC NMR spectrum (500 MHz) in $\text{DMSO-}d_6$



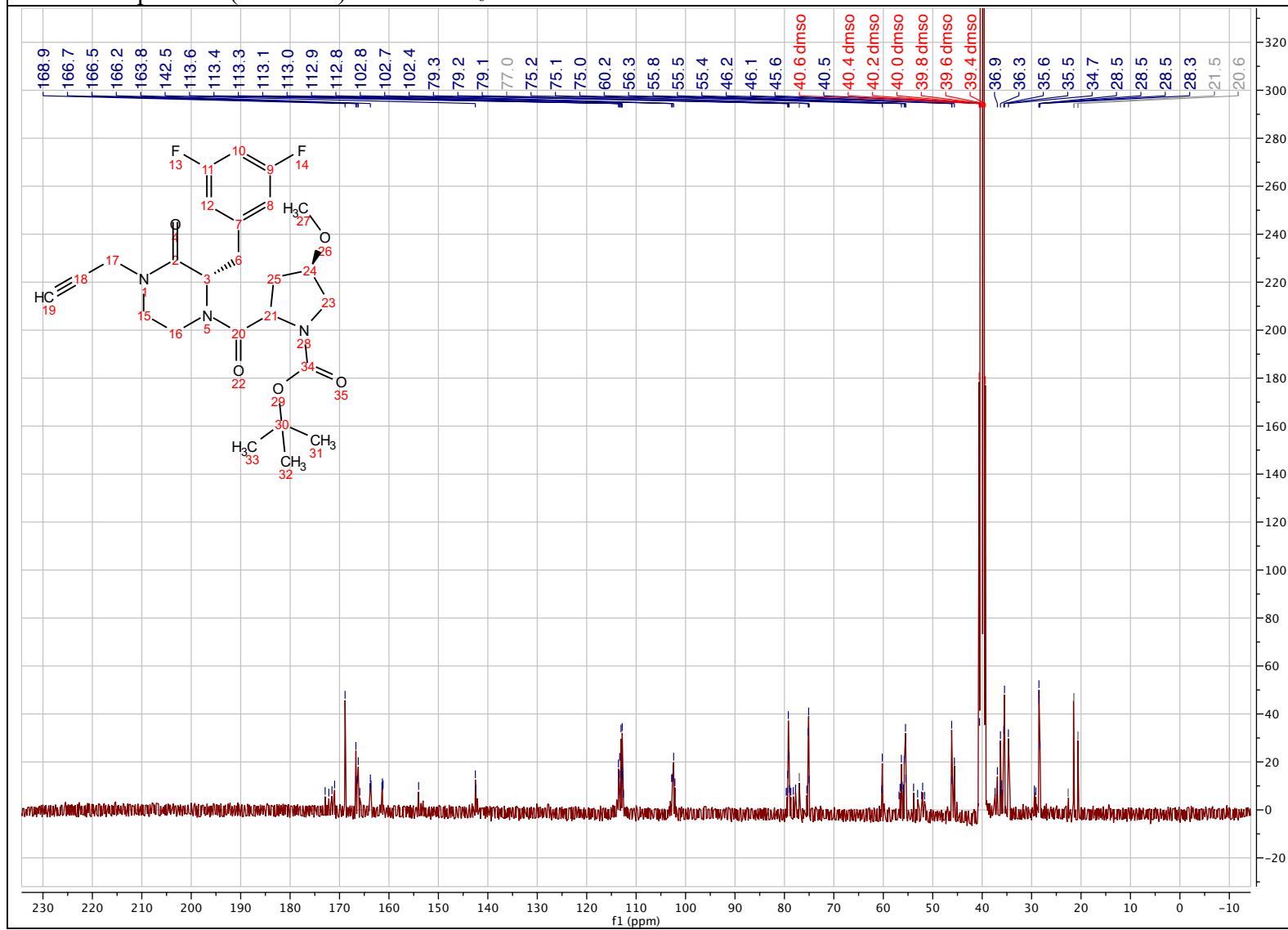
***tert*-butyl (4*R*)-2-((*S*)-2-(3,5-difluorobenzyl)-3-oxo-4-(prop-2-yn-1-yl)piperazine-1-carbonyl)-4-methoxypyrrolidine-1-carboxylate (2.84)**

¹H NMR spectrum (500 MHz) in DMSO-*d*₆



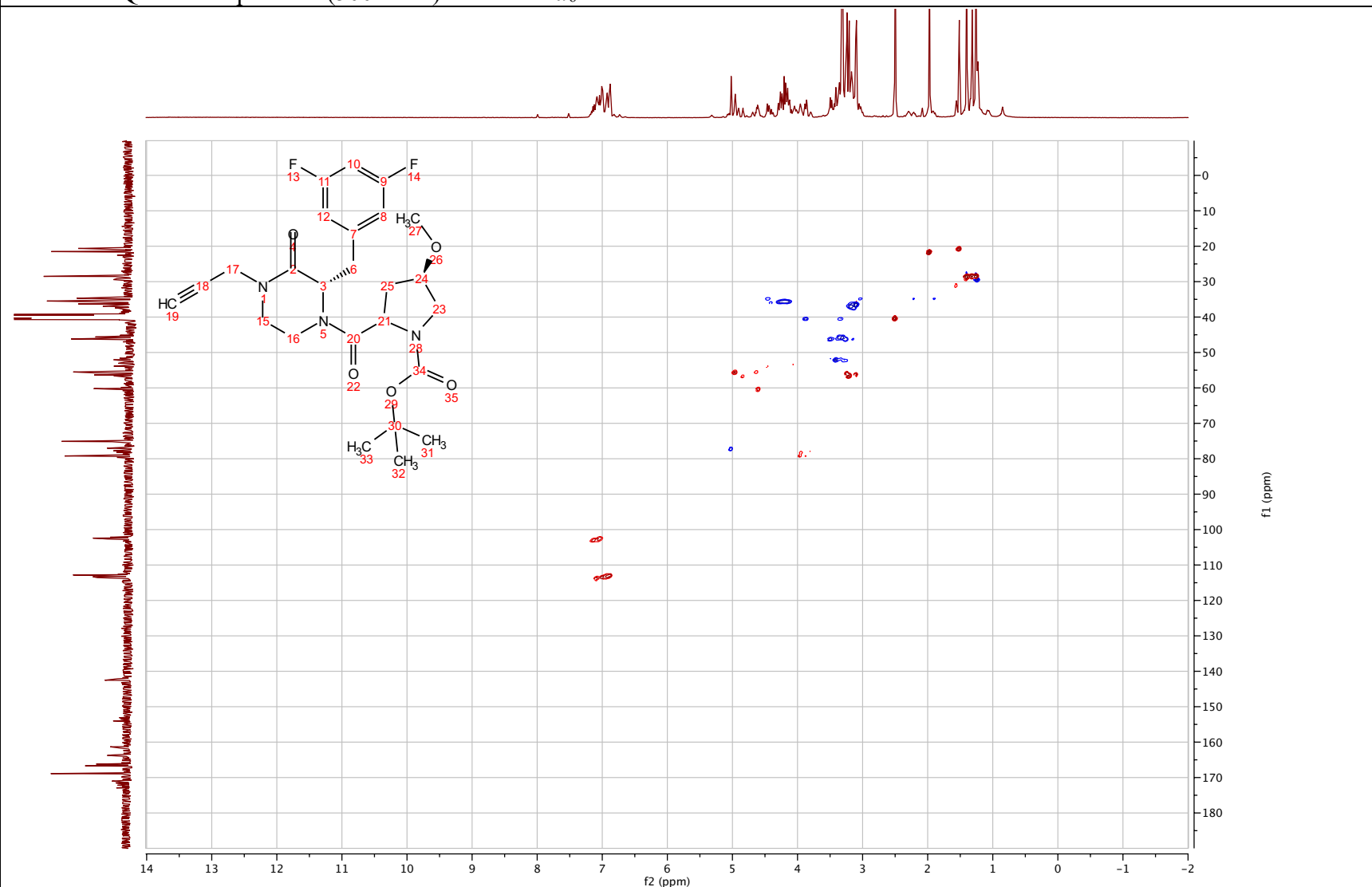
***tert*-butyl (4*R*)-2-((*S*)-2-(3,5-difluorobenzyl)-3-oxo-4-(prop-2-yn-1-yl)piperazine-1-carbonyl)-4-methoxypyrrolidine-1-carboxylate (2.84)**

^{13}C NMR spectrum (101 MHz) in $\text{DMSO-}d_6$



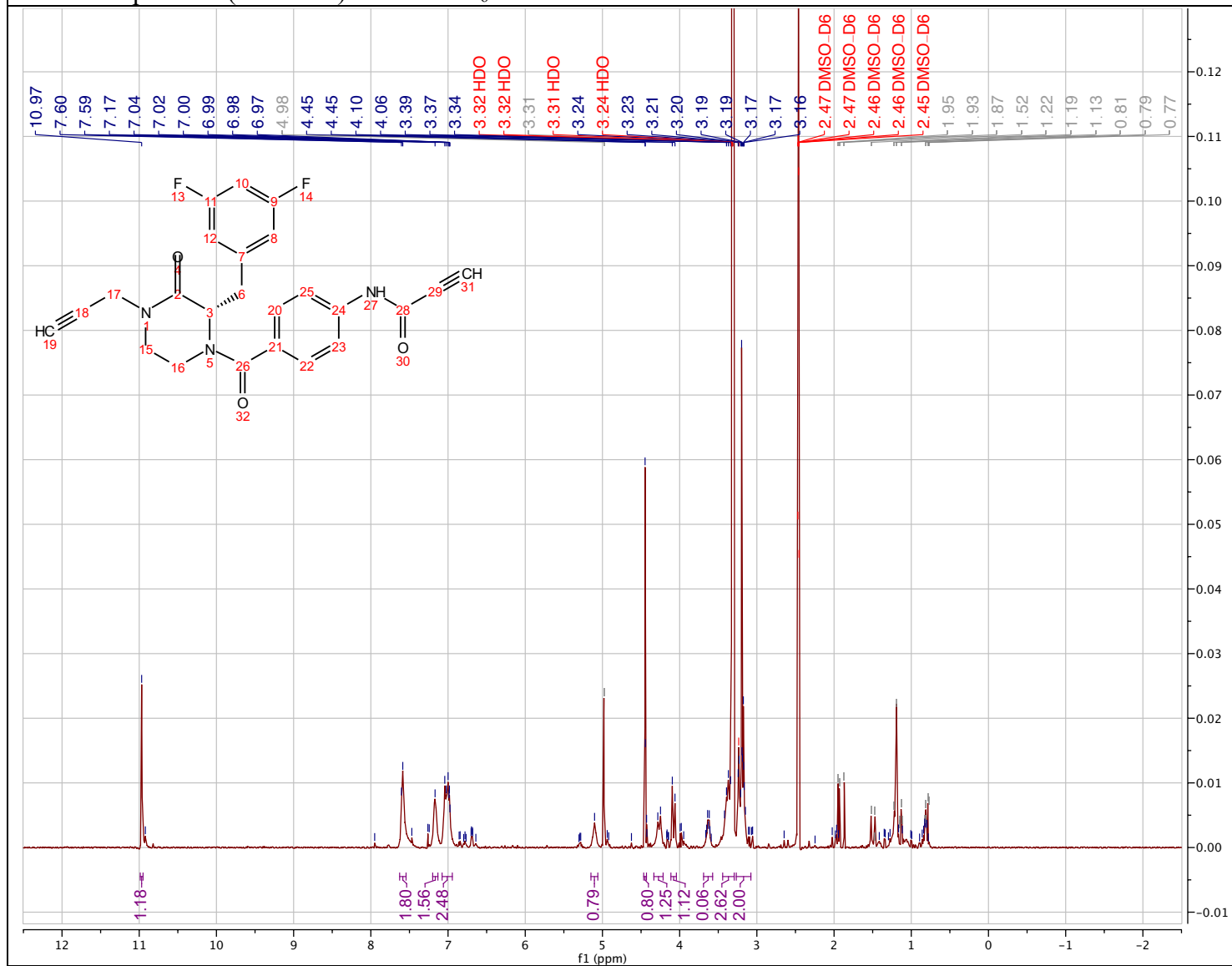
***tert*-butyl (4*R*)-2-((*S*)-2-(3,5-difluorobenzyl)-3-oxo-4-(prop-2-yn-1-yl)piperazine-1-carbonyl)-4-methoxypyrrolidine-1-carboxylate (2.84)**

^1H - ^{13}C HSQC NMR spectrum (500 MHz) in $\text{DMSO-}d_6$



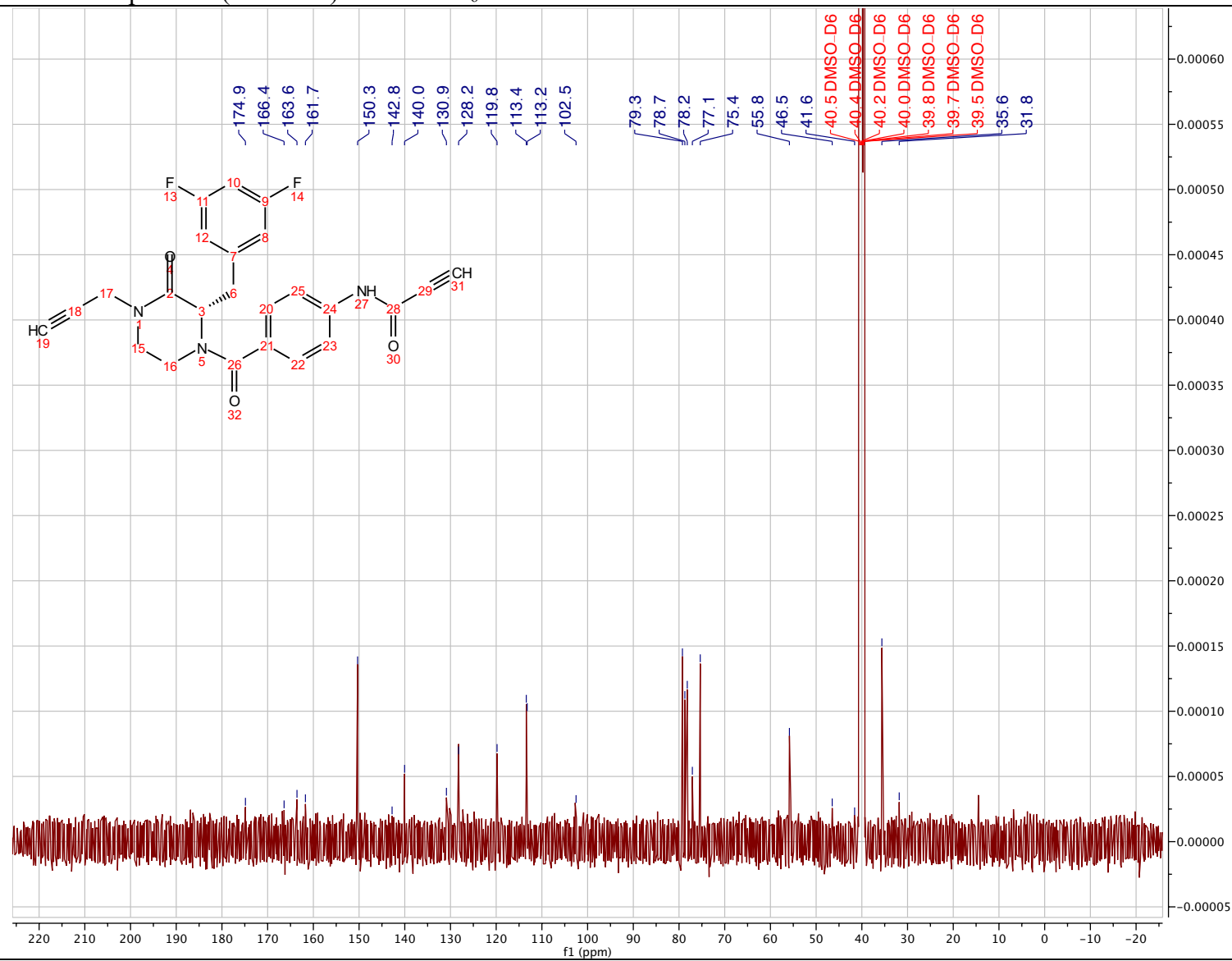
(S)-N-(4-(2-(3,5-difluorobenzyl)-3-oxo-4-(prop-2-yn-1-yl) piperazine-1-carbonyl)phenyl) propiolamide (2.85)

¹H NMR spectrum (500 MHz) in DMSO-d₆



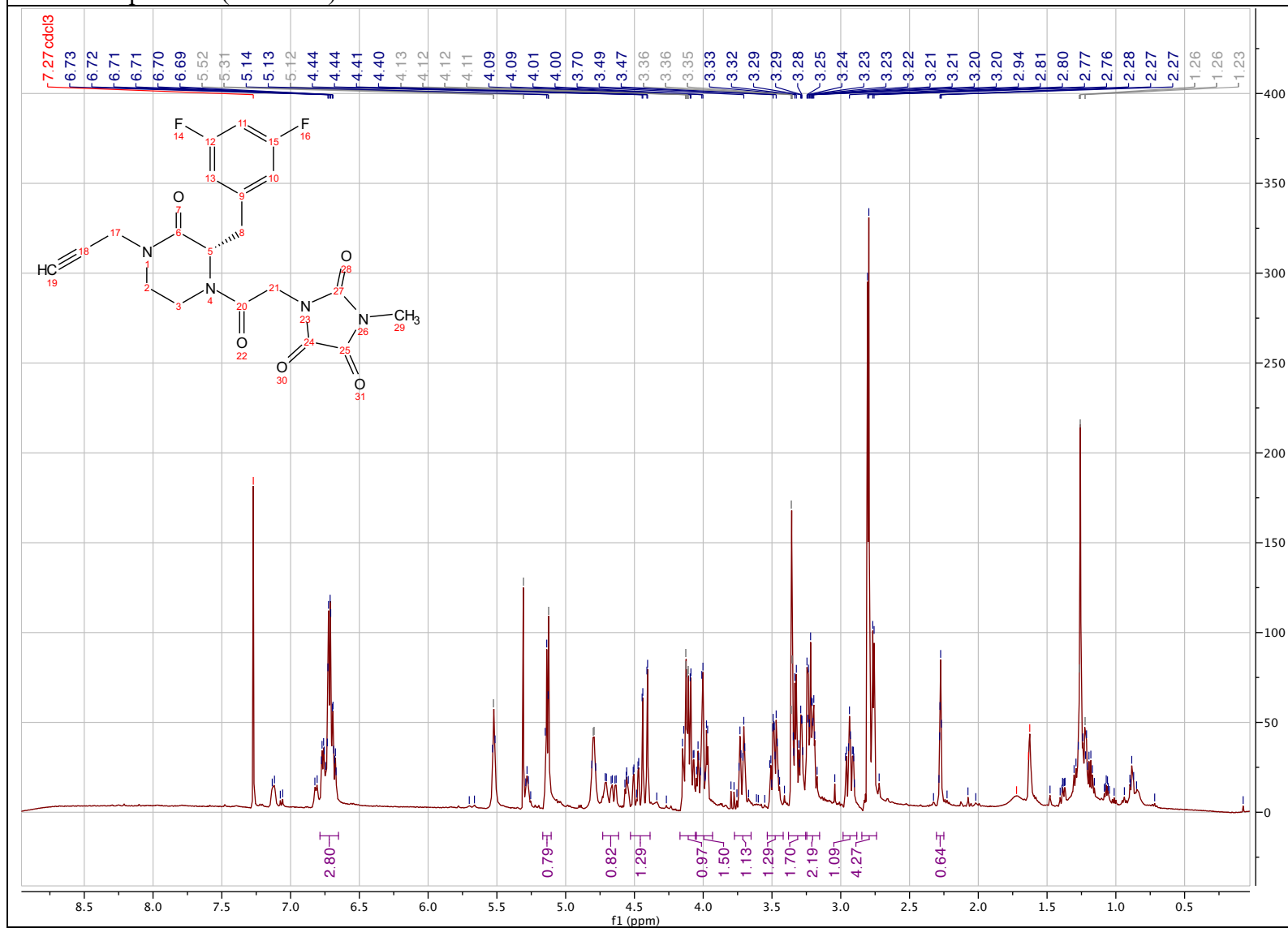
(S)-N-(4-(2-(3,5-difluorobenzyl)-3-oxo-4-(prop-2-yn-1-yl) piperazine-1-carbonyl)phenyl) propiolamide (2.85)

¹³C NMR spectrum (101 MHz) in DMSO-d₆



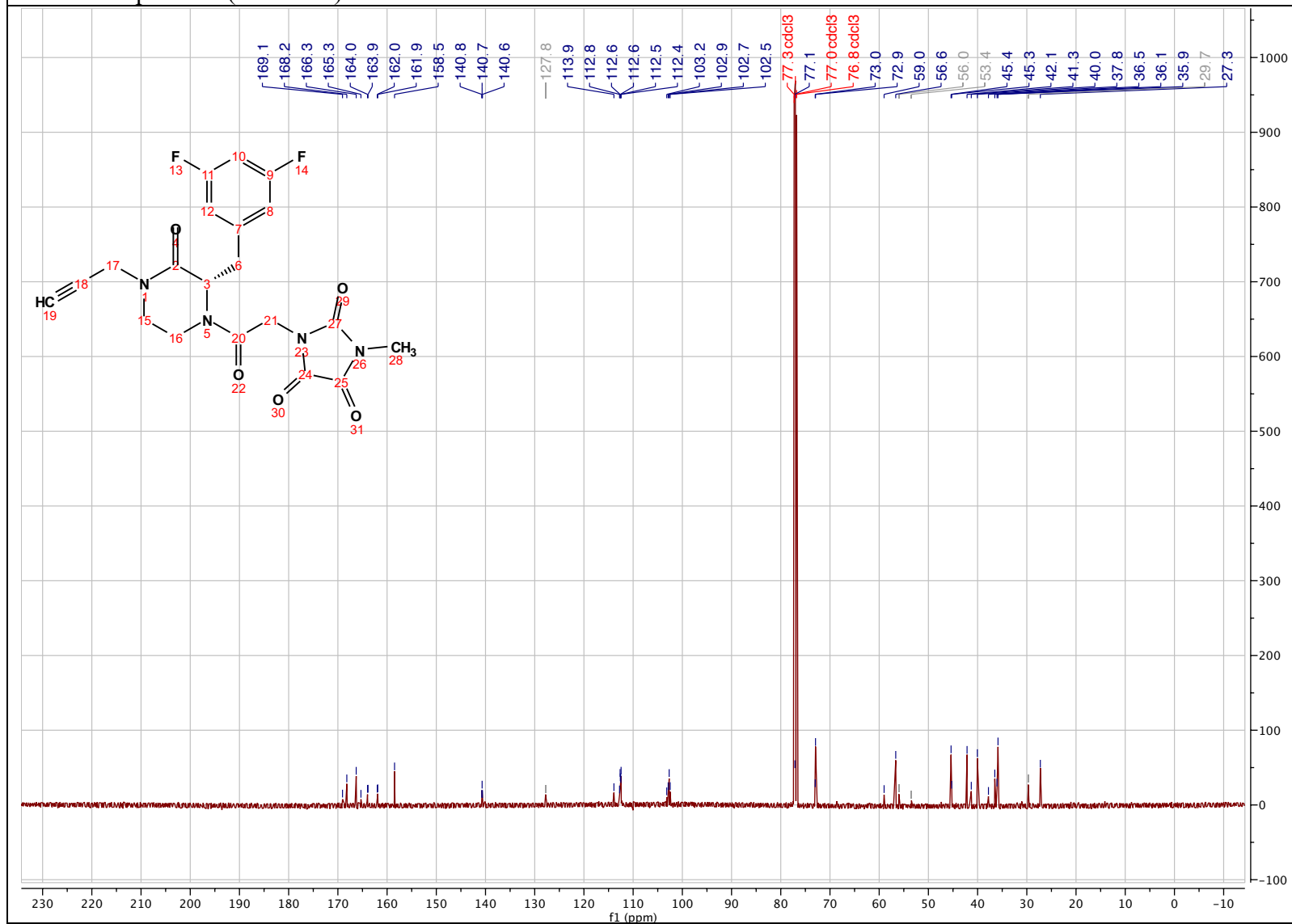
(S)-1-(2-(2-(3,5-difluorobenzyl)-3-oxo-4-(prop-2-yn-1-yl)piperazin-1-yl)-2-oxoethyl)-3-methylimidazolidine-2,4,5-trione (2.86)

¹H NMR spectrum (400 MHz) in Chloroform-*d*



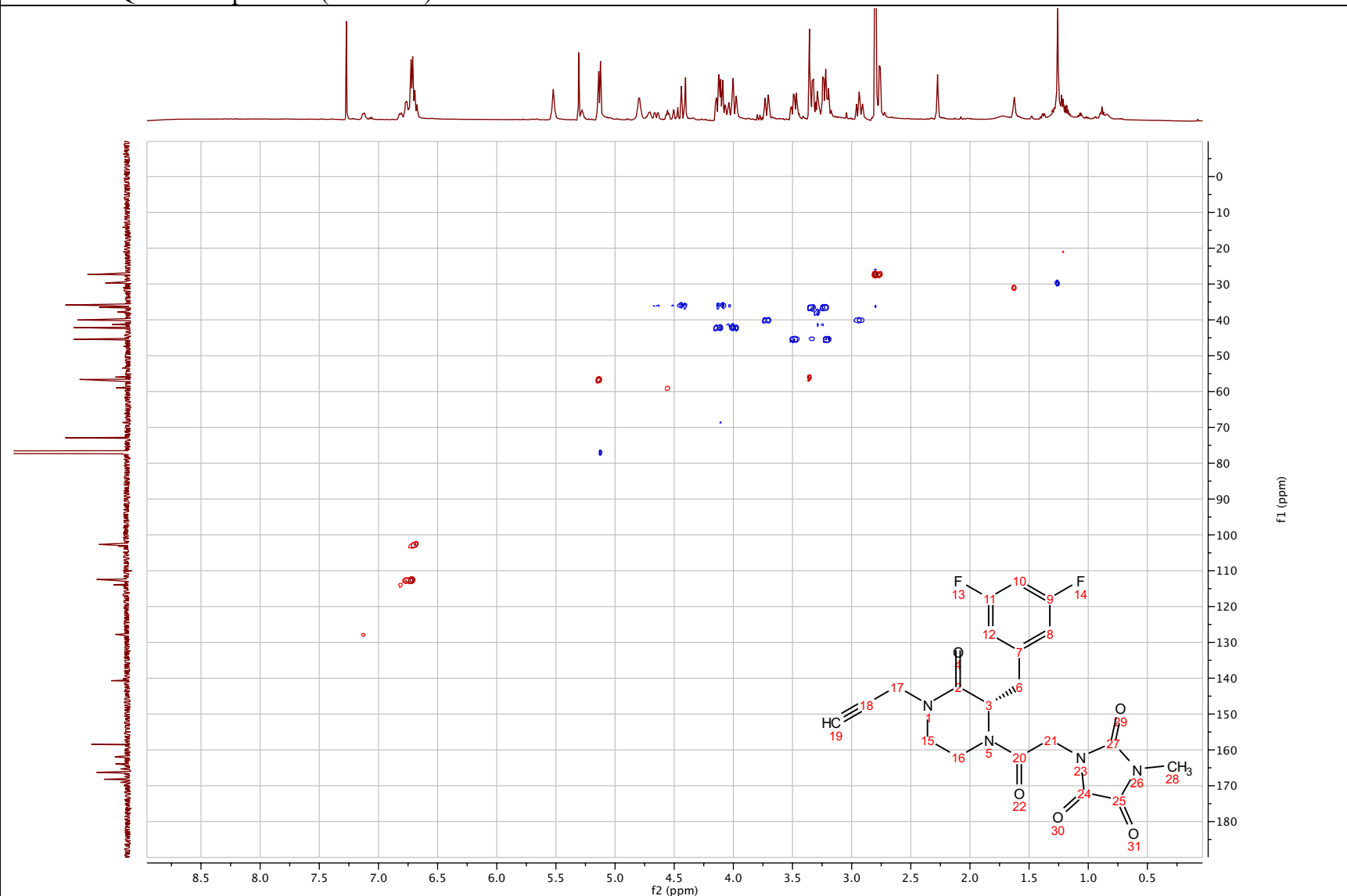
(S)-1-(2-(2-(3,5-difluorobenzyl)-3-oxo-4-(prop-2-yn-1-yl)piperazin-1-yl)-2-oxoethyl)-3-methylimidazolidine-2,4,5-trione (2.86)

¹³C NMR spectrum (126 MHz) in Chloroform-*d*



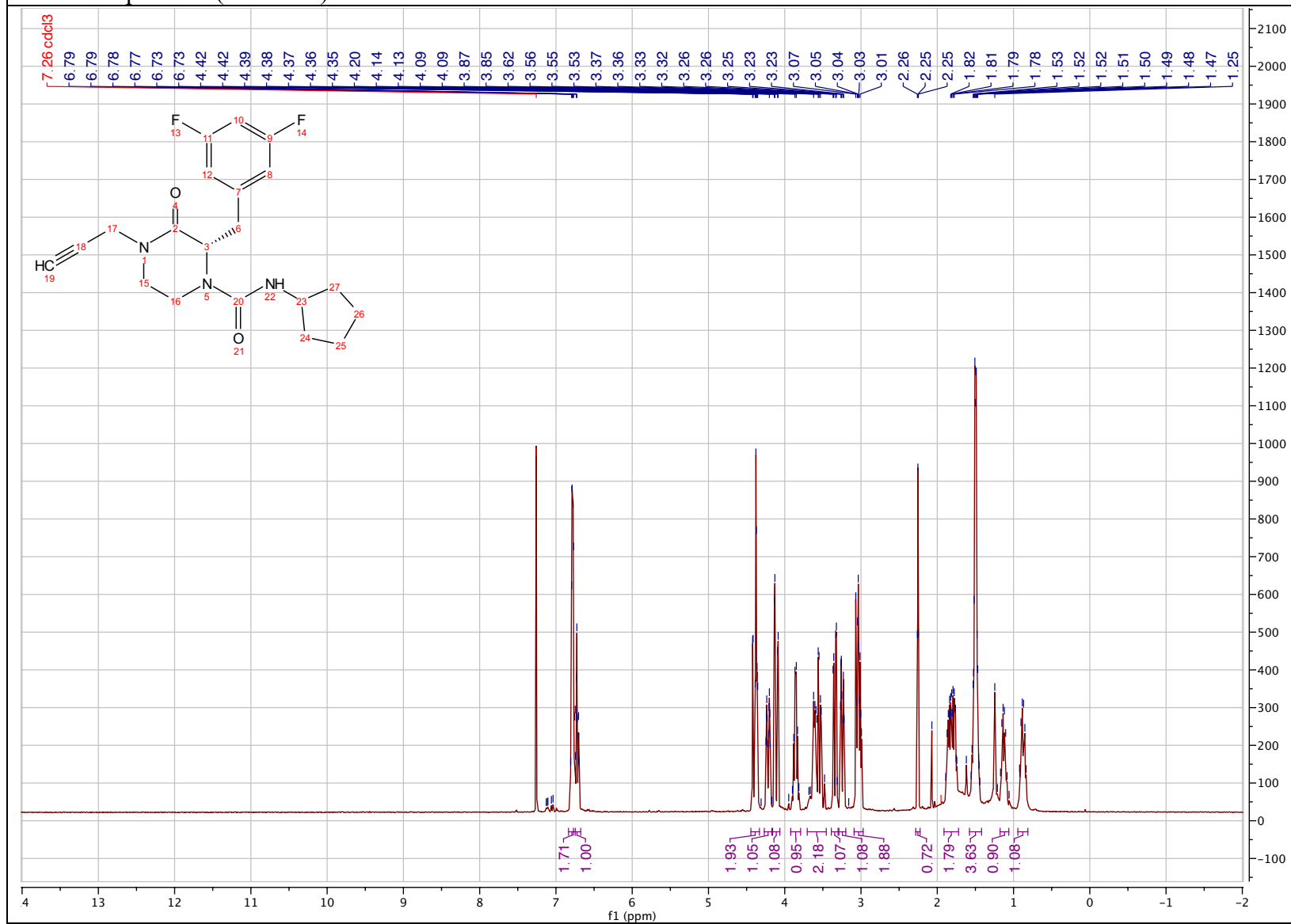
(S)-1-(2-(2-(3,5-difluorobenzyl)-3-oxo-4-(prop-2-yn-1-yl)piperazin-1-yl)-2-oxoethyl)-3-methylimidazolidine-2,4,5-trione (2.86)

^1H - ^{13}C HSQC NMR spectrum (500 MHz) in Chloroform-*d*



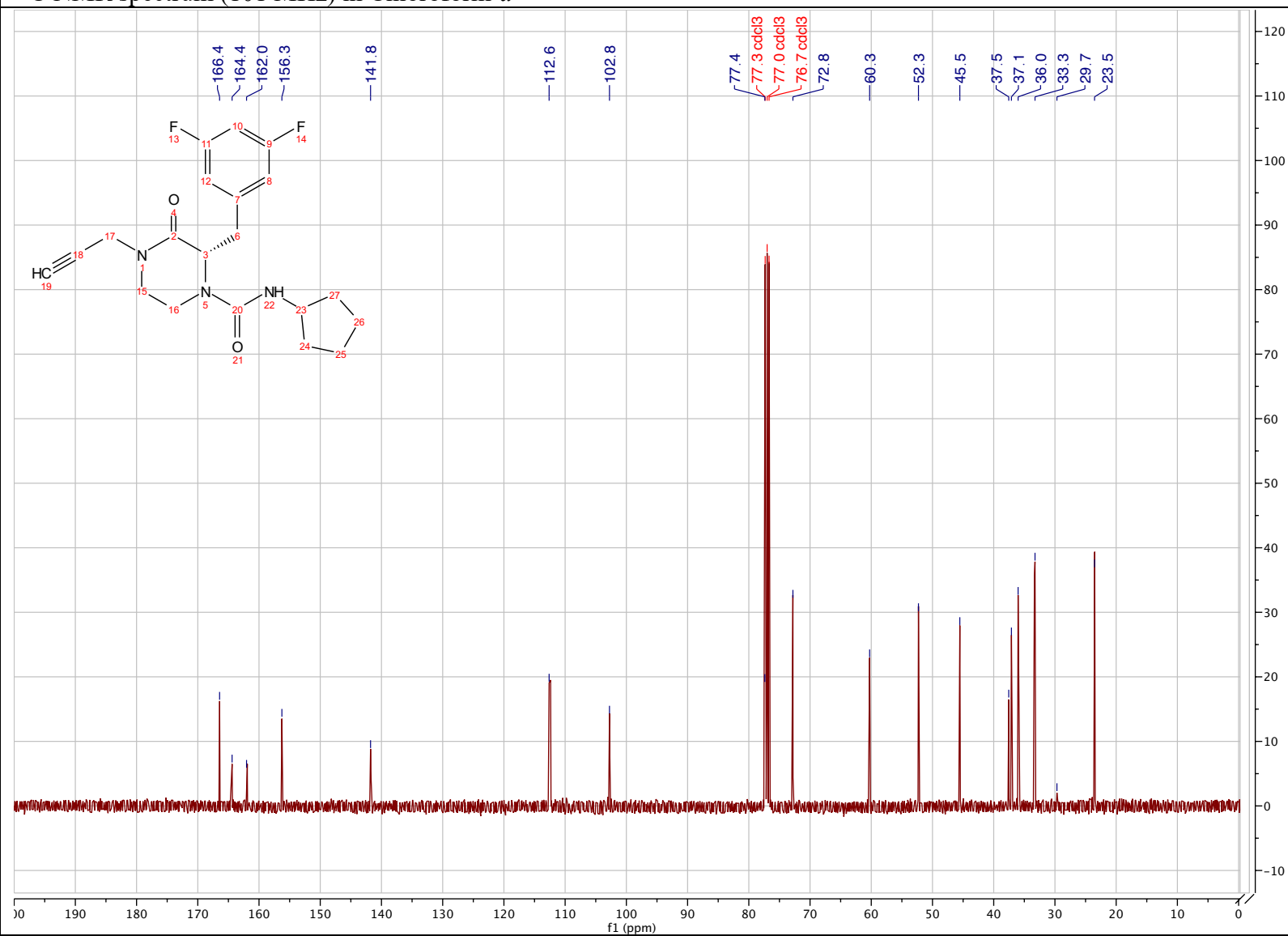
(S)-N-cyclopentyl-2-(3,5-difluorobenzyl)-3-oxo-4-(prop-2-yn-1-yl) piperazine-1-carboxamide (2.87)

¹H NMR spectrum (400 MHz) in Chloroform-*d*



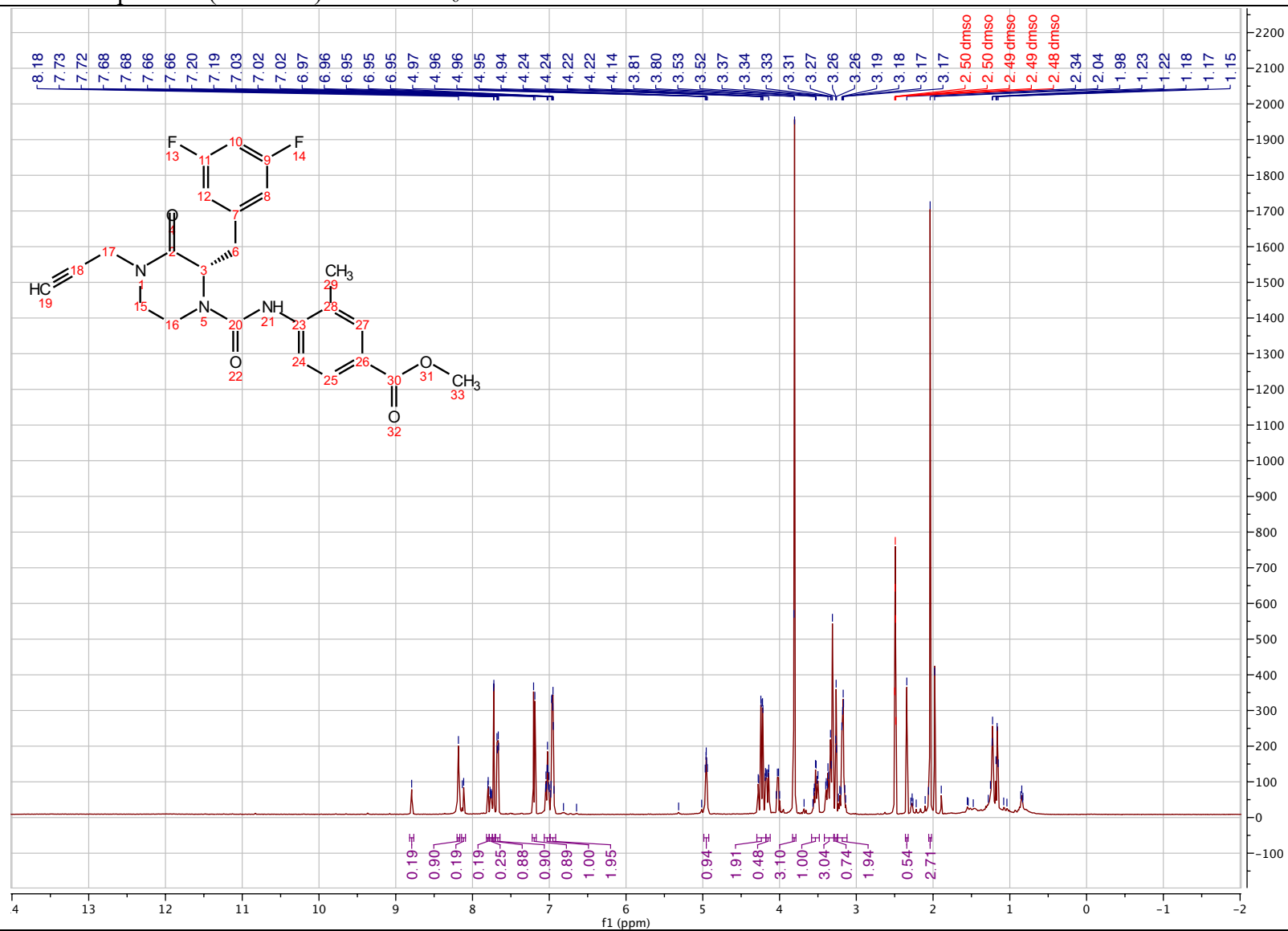
(S)-N-cyclopentyl-2-(3,5-difluorobenzyl)-3-oxo-4-(prop-2-yn-1-yl) piperazine-1-carboxamide (2.87)

¹³C NMR spectrum (101 MHz) in Chloroform-*d*



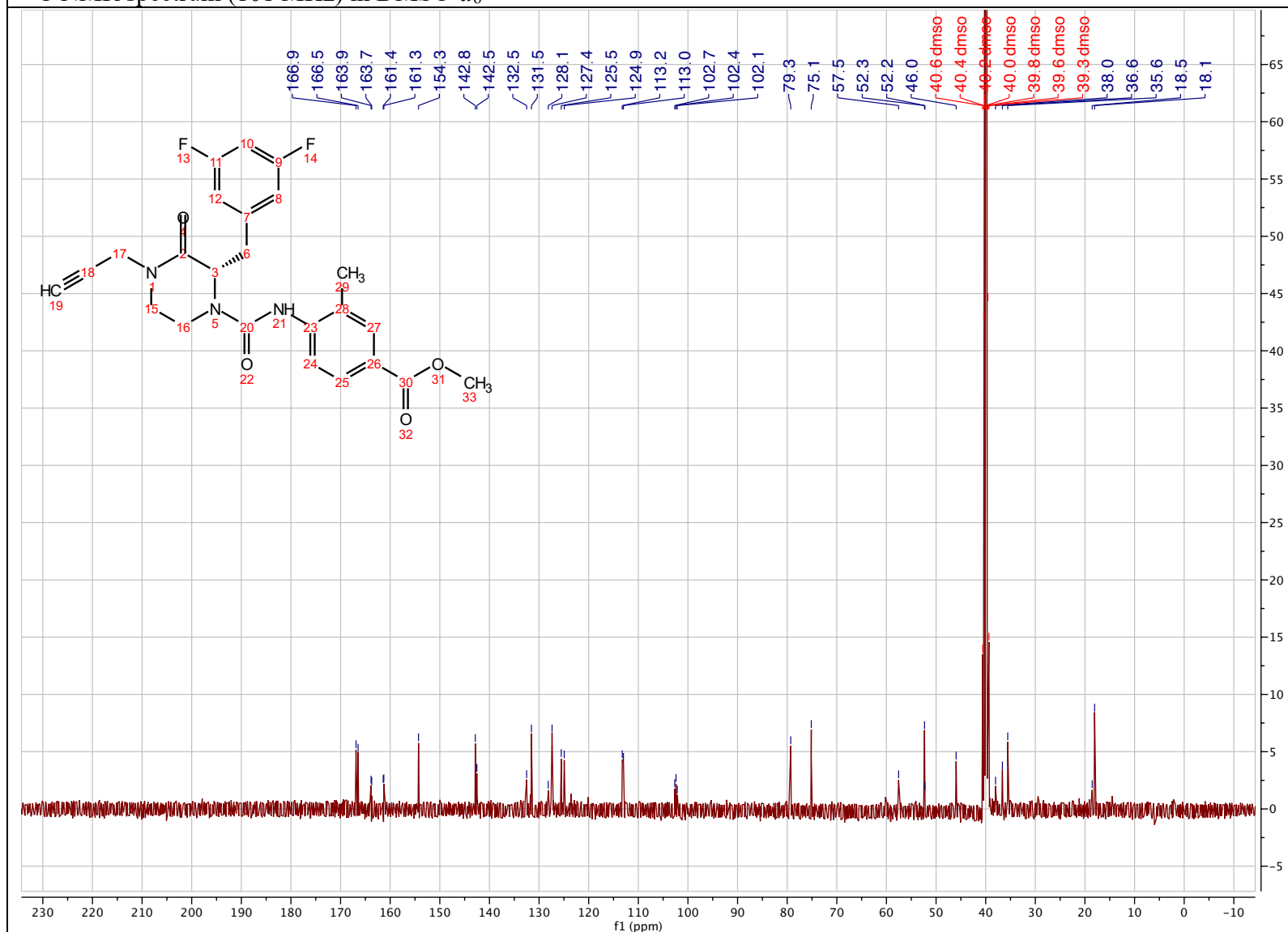
methyl (S)-4-(2-(3,5-difluorobenzyl)-3-oxo-4-(prop-2-yn-1-yl)piperazine-1-carboxamido)-3-methylbenzoate (2.88)

¹H NMR spectrum (500 MHz) in DMSO-*d*₆



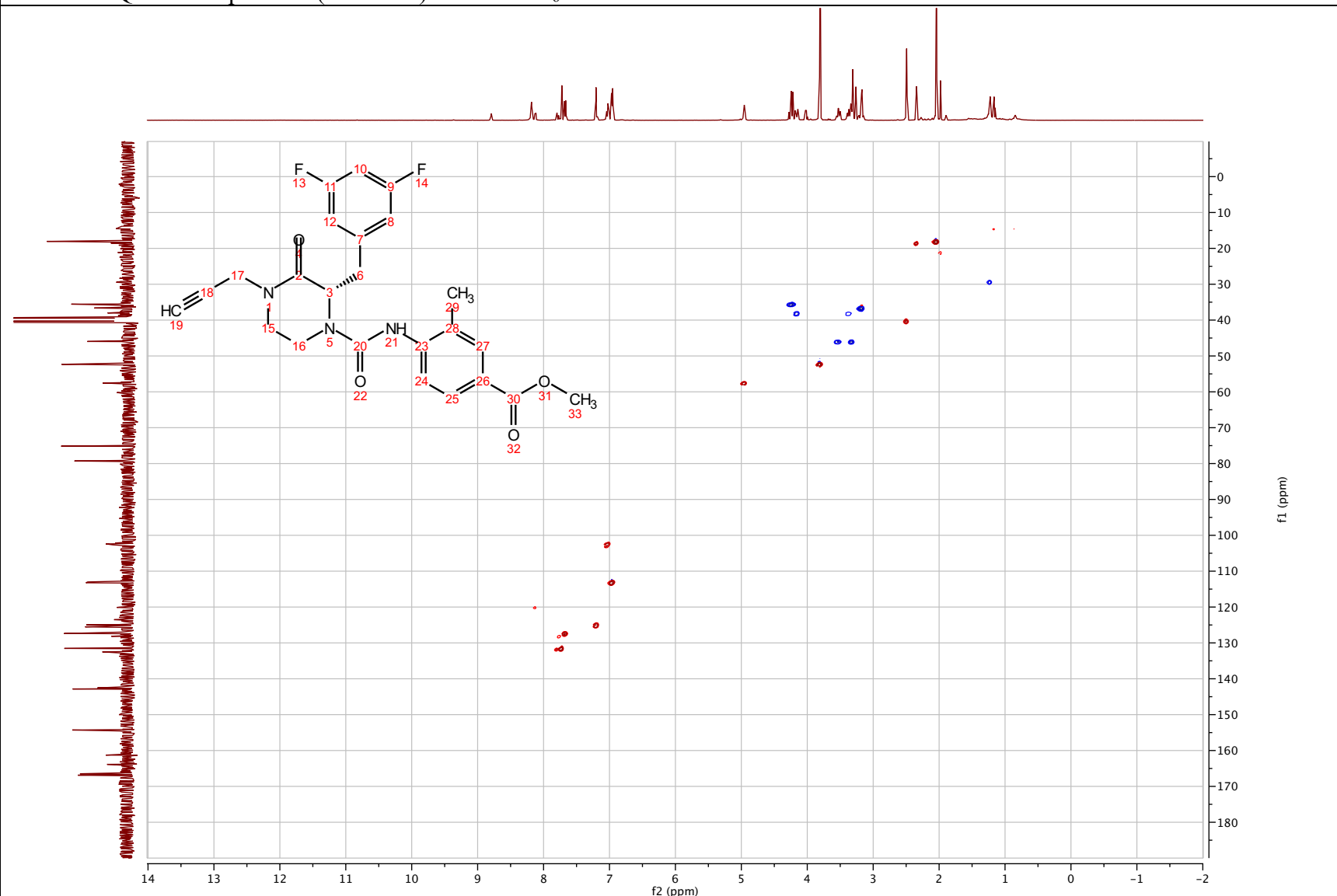
methyl (S)-4-(2-(3,5-difluorobenzyl)-3-oxo-4-(prop-2-yn-1-yl)piperazine-1-carboxamido)-3-methylbenzoate (2.88)

¹³C NMR spectrum (101 MHz) in DMSO-d₆



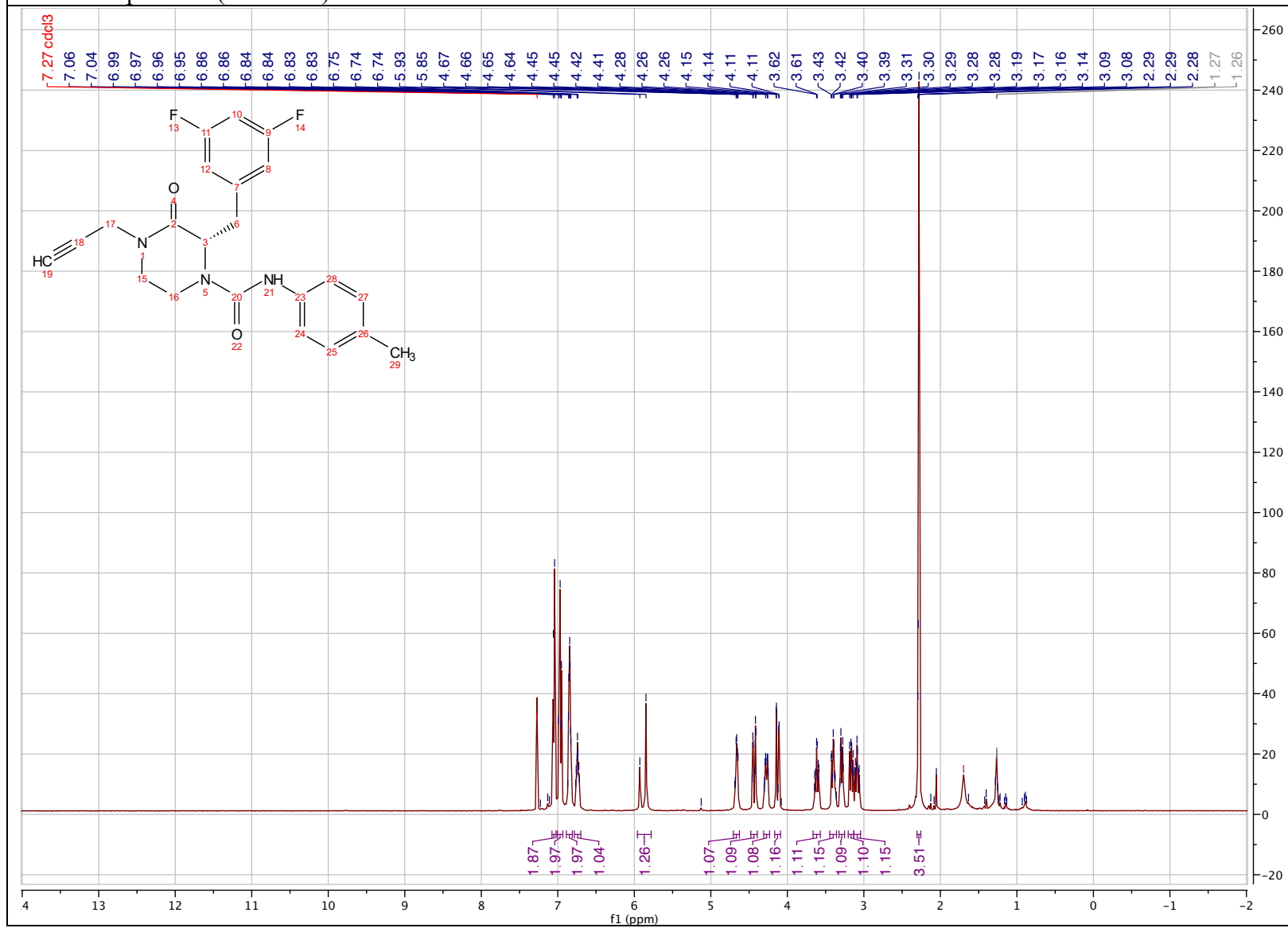
methyl (S)-4-(2-(3,5-difluorobenzyl)-3-oxo-4-(prop-2-yn-1-yl)piperazine-1-carboxamido)-3-methylbenzoate (2.88)

^1H - ^{13}C HSQC NMR spectrum (500 MHz) in $\text{DMSO-}d_6$



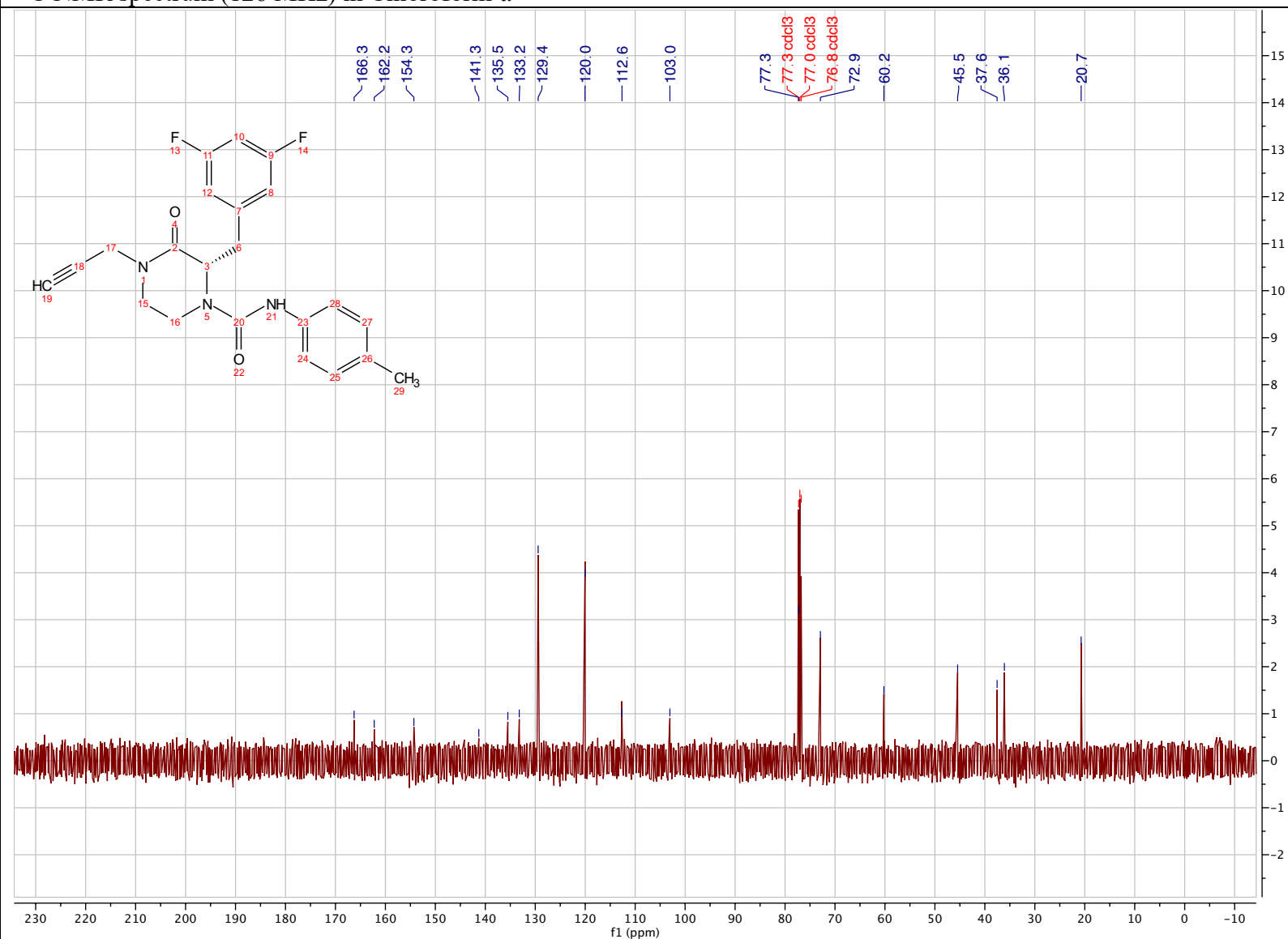
(S)-2-(3,5-difluorobenzyl)-3-oxo-4-(prop-2-yn-1-yl)-N-(p-tolyl)piperazine-1-carboxamide (2.89)

¹H NMR spectrum (500 MHz) in Chloroform-*d*



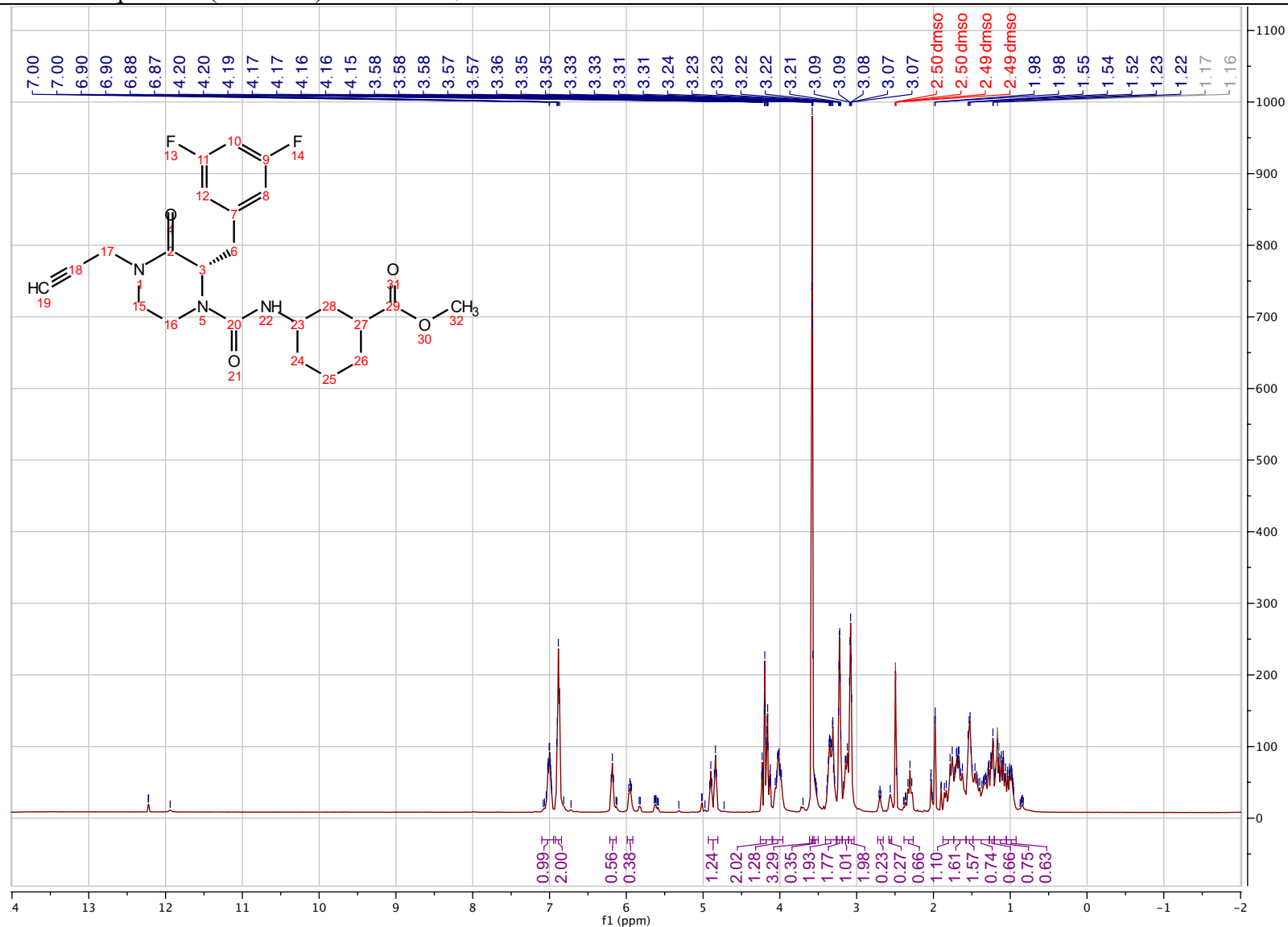
(S)-2-(3,5-difluorobenzyl)-3-oxo-4-(prop-2-yn-1-yl)-N-(p-tolyl)piperazine-1-carboxamide (2.89)

¹³C NMR spectrum (126 MHz) in Chloroform-*d*



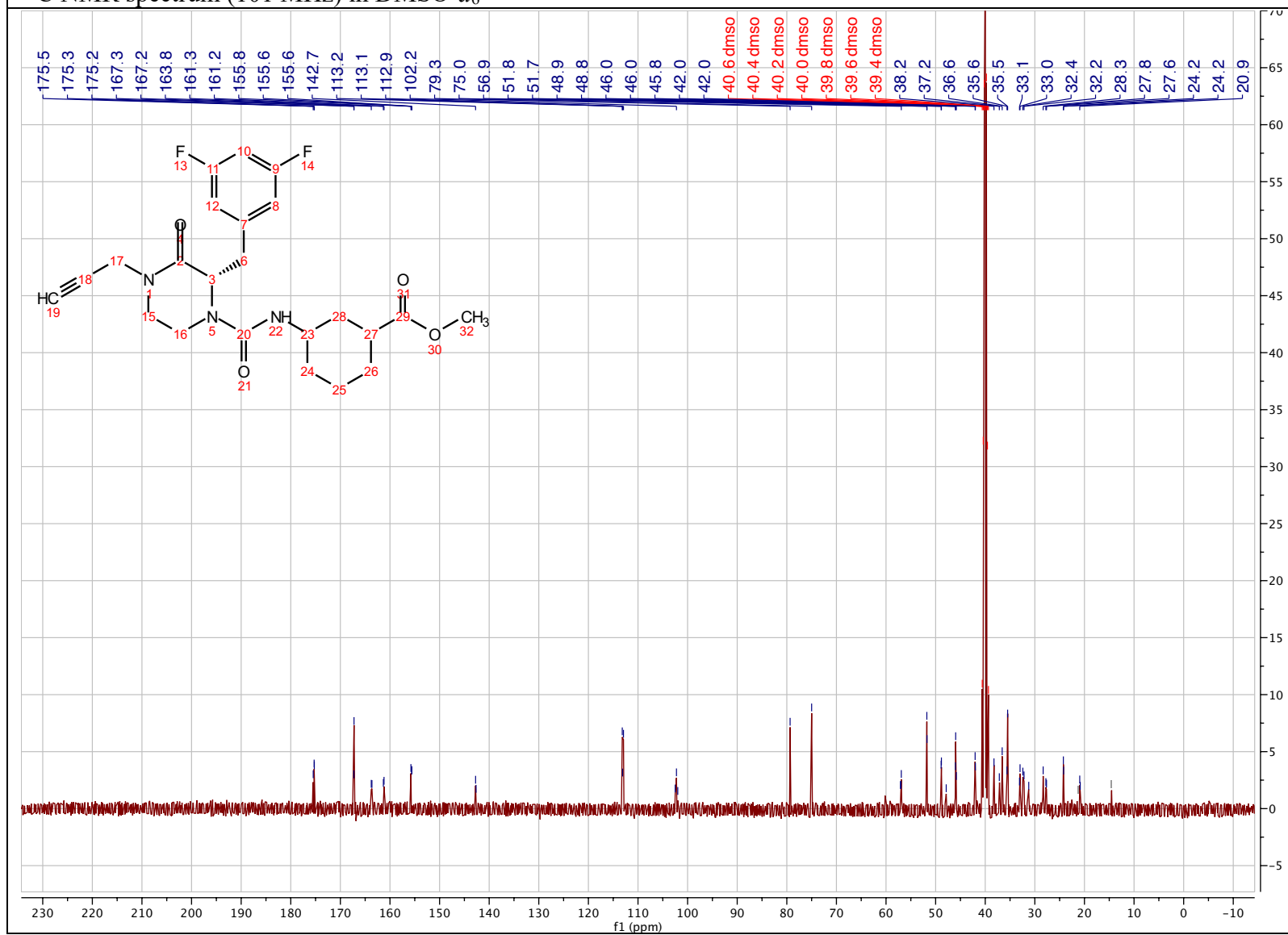
methyl 3-((S)-2-(3,5-difluorobenzyl)-3-oxo-4-(prop-2-yn-1-yl)piperazine-1-carboxamido)cyclohexane-1-carboxylate (2.90)

¹H NMR spectrum (500 MHz) in DMSO-d₆



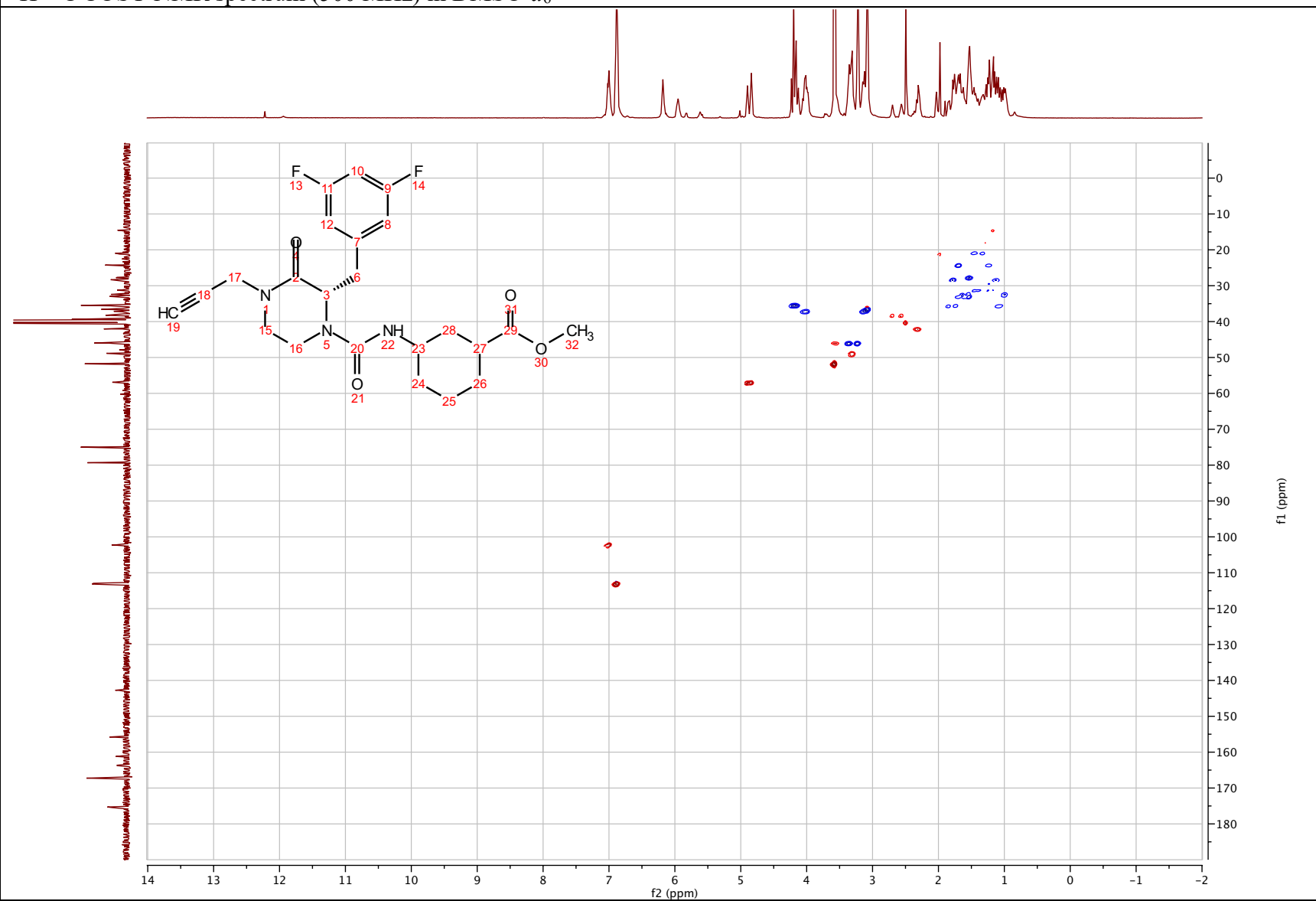
methyl 3-((S)-2-(3,5-difluorobenzyl)-3-oxo-4-(prop-2-yn-1-yl)piperazine-1-carboxamido)cyclohexane-1-carboxylate (2.90)

¹³C NMR spectrum (101 MHz) in DMSO-d₆



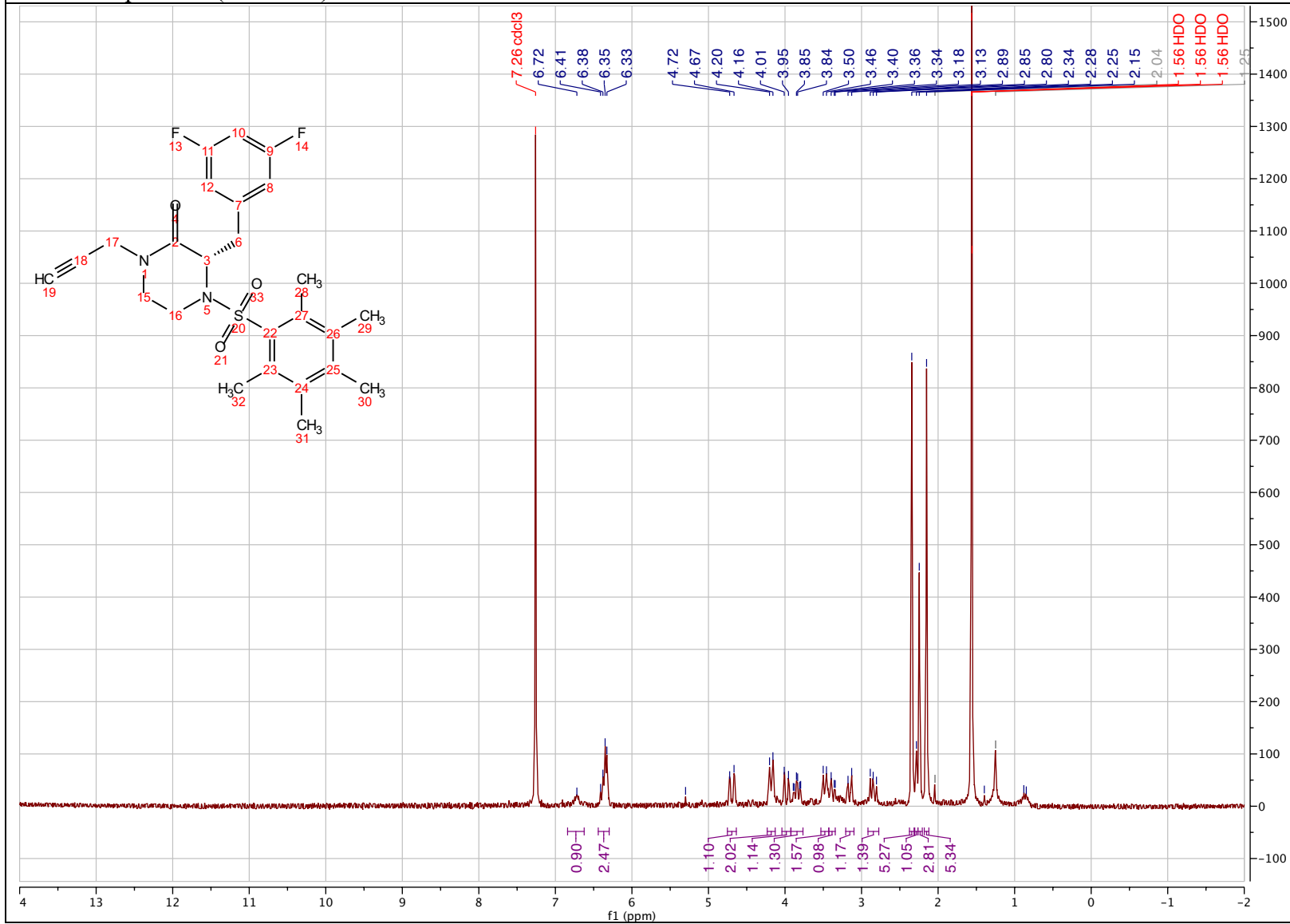
methyl 3-((*S*)-2-(3,5-difluorobenzyl)-3-oxo-4-(prop-2-yn-1-yl)piperazine-1-carboxamido)cyclohexane-1-carboxylate (2.90)

^1H - ^{13}C COSY NMR spectrum (500 MHz) in $\text{DMSO-}d_6$



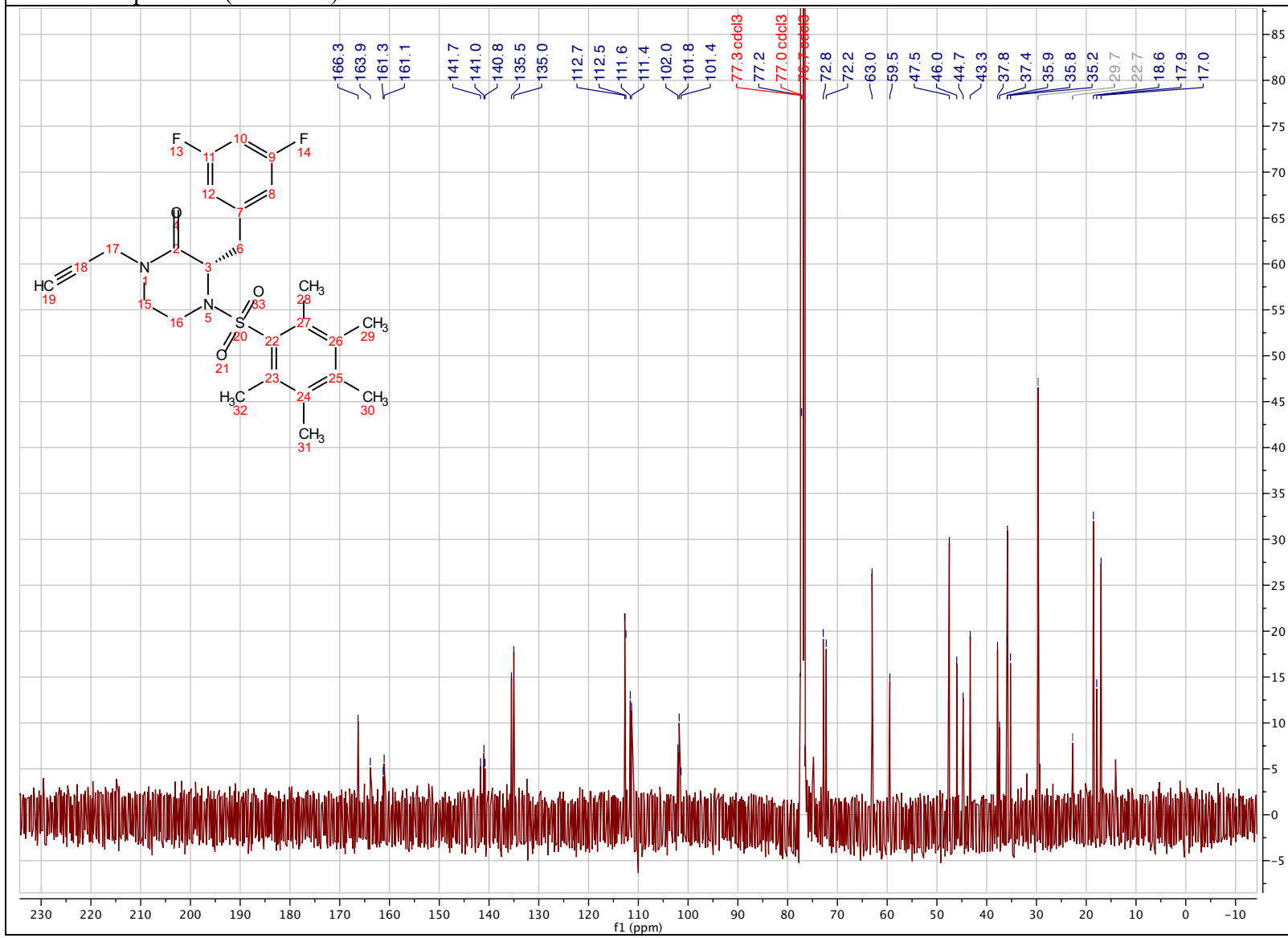
(S)-3-(3,5-difluorobenzyl)-4-((2,3,4,5,6-pentamethylphenyl)sulfonyl)-1-(prop-2-yn-1-yl)piperazin-2-one (2.91)

¹H NMR spectrum (300 MHz) in Chloroform-*d*



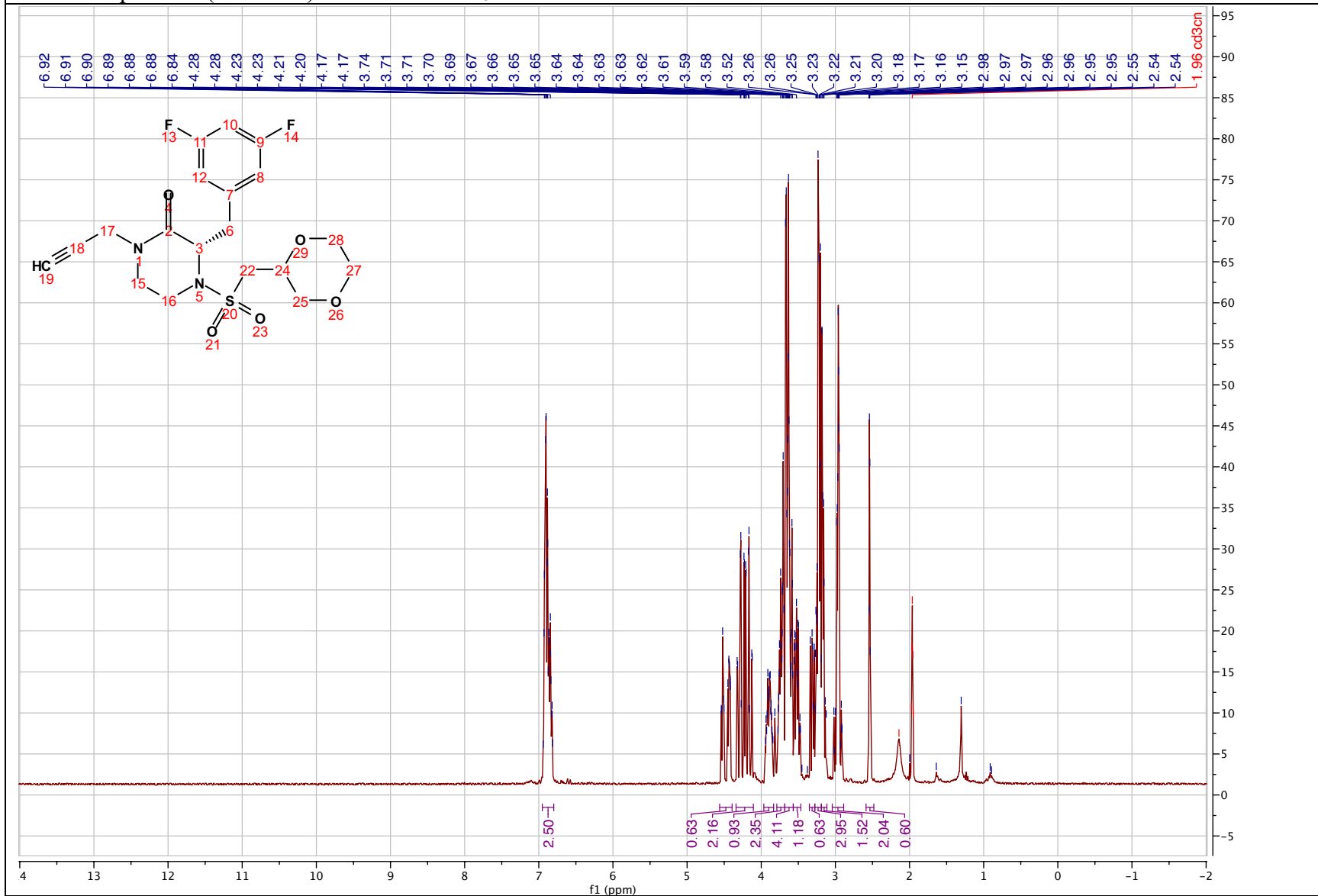
(S)-3-(3,5-difluorobenzyl)-4-((2,3,4,5,6-pentamethylphenyl)sulfonyl)-1-(prop-2-yn-1-yl)piperazin-2-one (2.91)

¹³C NMR spectrum (101 MHz) in Chloroform-*d*



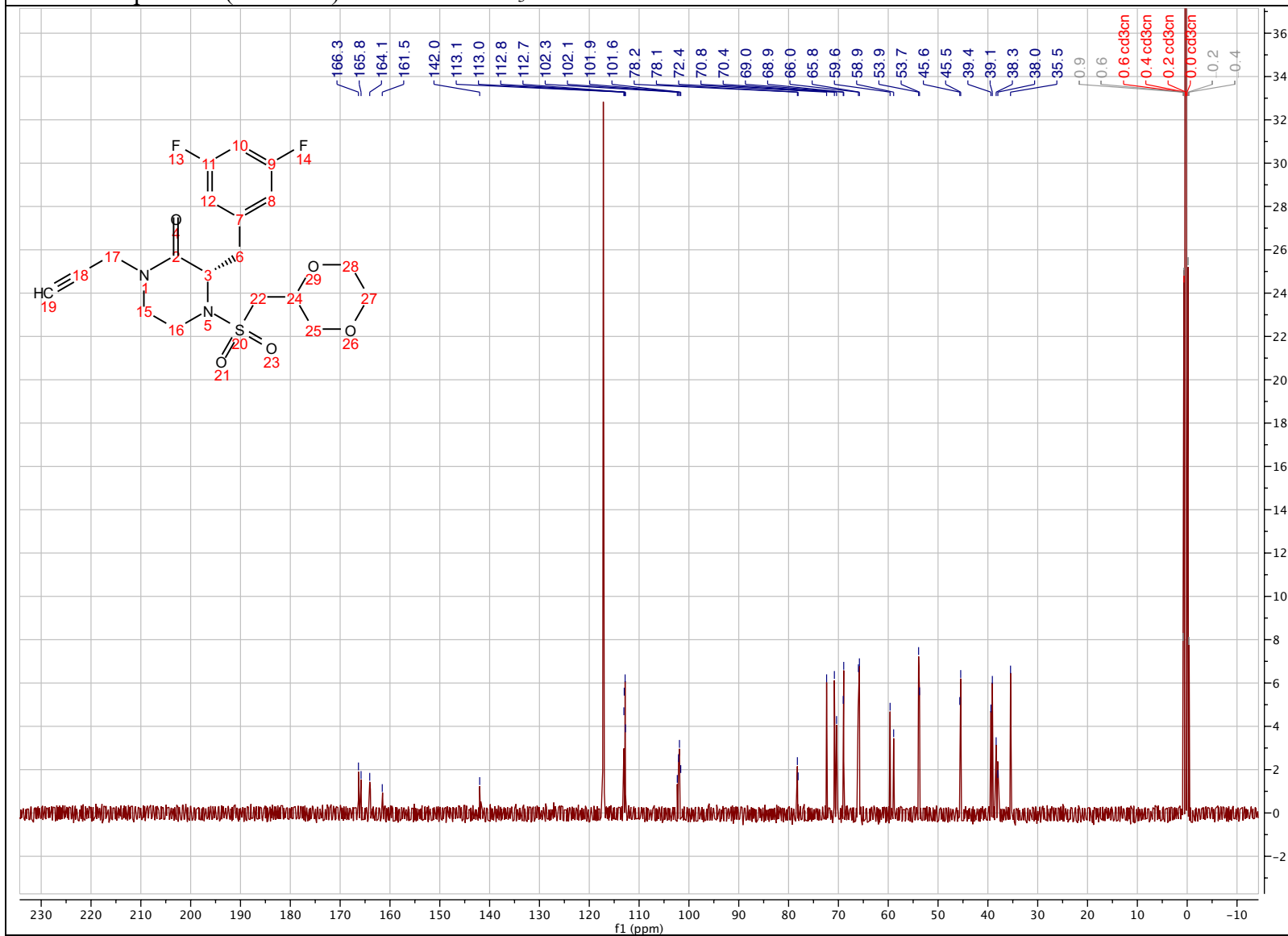
(3S)-4-(((1,4-dioxan-2-yl)methyl)sulfonyl)-3-(3,5-difluorobenzyl)-1-(prop-2-yn-1-yl)piperazin-2-one (2.92)

¹H NMR spectrum (400 MHz) in Acetonitrile-*d*₃



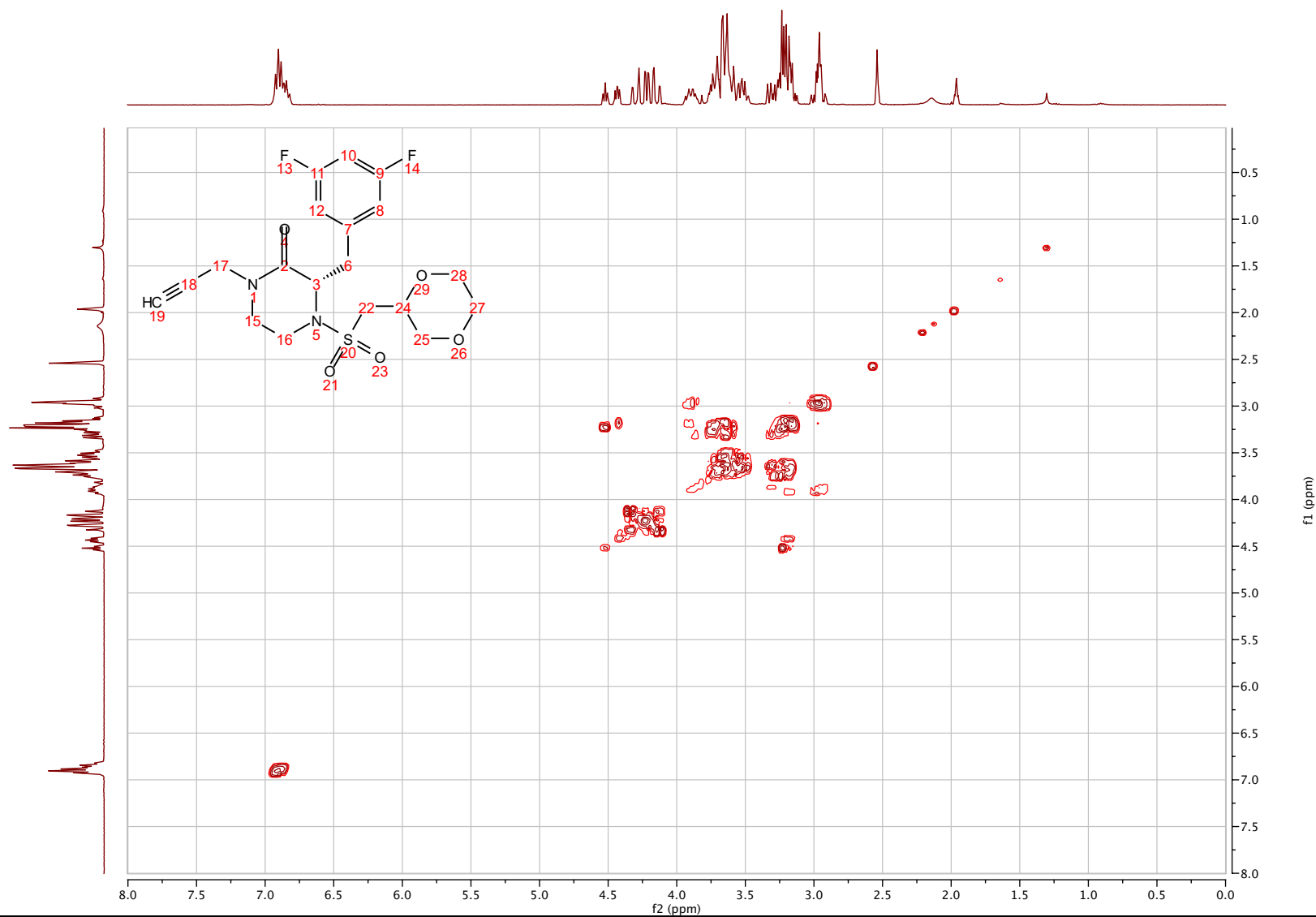
(3S)-4-(((1,4-dioxan-2-yl)methyl)sulfonyl)-3-(3,5-difluorobenzyl)-1-(prop-2-yn-1-yl)piperazin-2-one (2.92)

¹³C NMR spectrum (101 MHz) in Acetonitrile-*d*₃



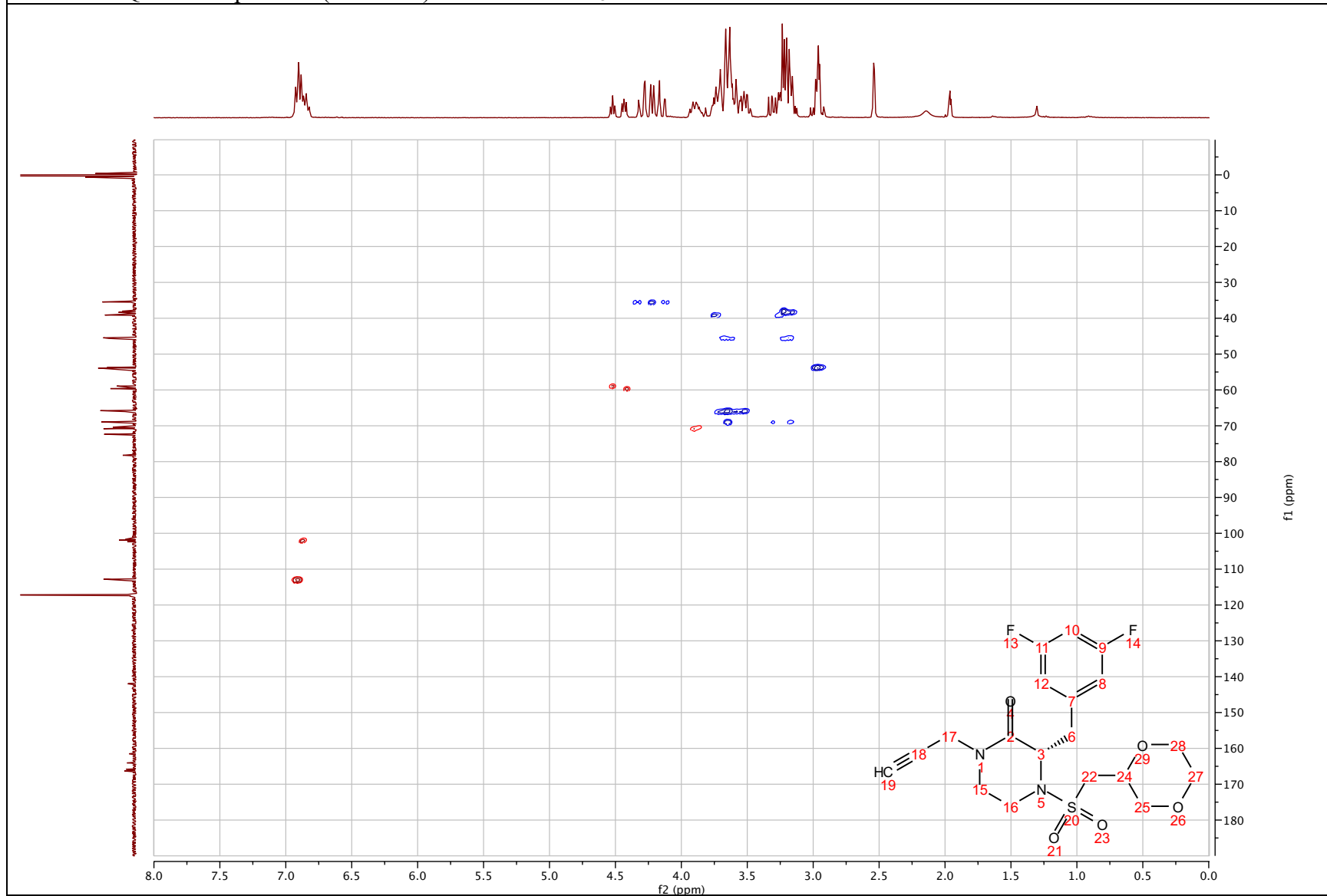
(3*S*)-4-(((1,4-dioxan-2-yl)methyl)sulfonyl)-3-(3,5-difluorobenzyl)-1-(prop-2-yn-1-yl)piperazin-2-one (2.92)

^1H - ^1H COSY NMR spectrum (500 MHz) in Acetonitrile- d_3



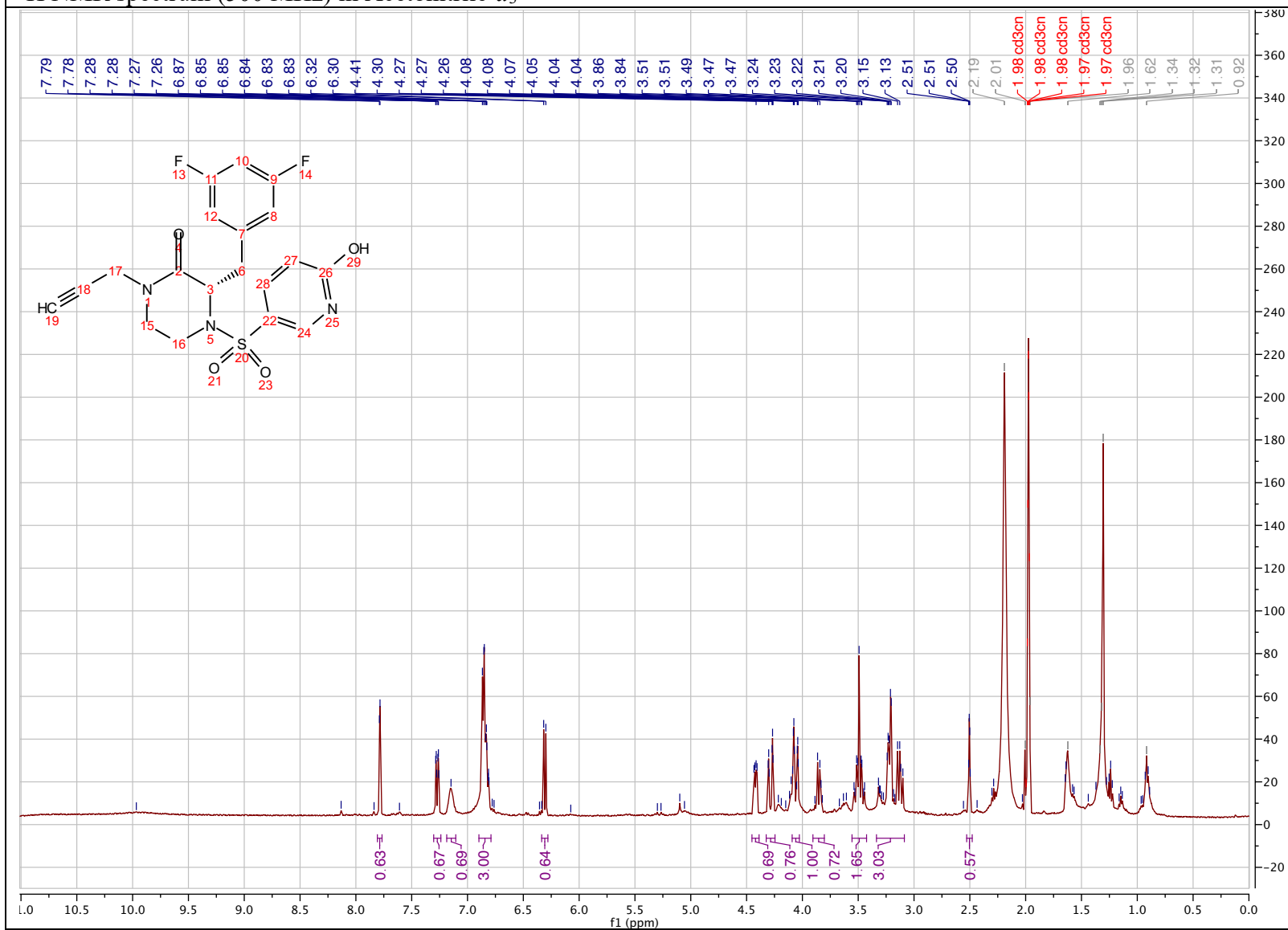
(3*S*)-4-(((1,4-dioxan-2-yl)methyl)sulfonyl)-3-(3,5-difluorobenzyl)-1-(prop-2-yn-1-yl)piperazin-2-one (2.92)

^1H - ^{13}C HSQC NMR spectrum (500 MHz) in Acetonitrile- d_3



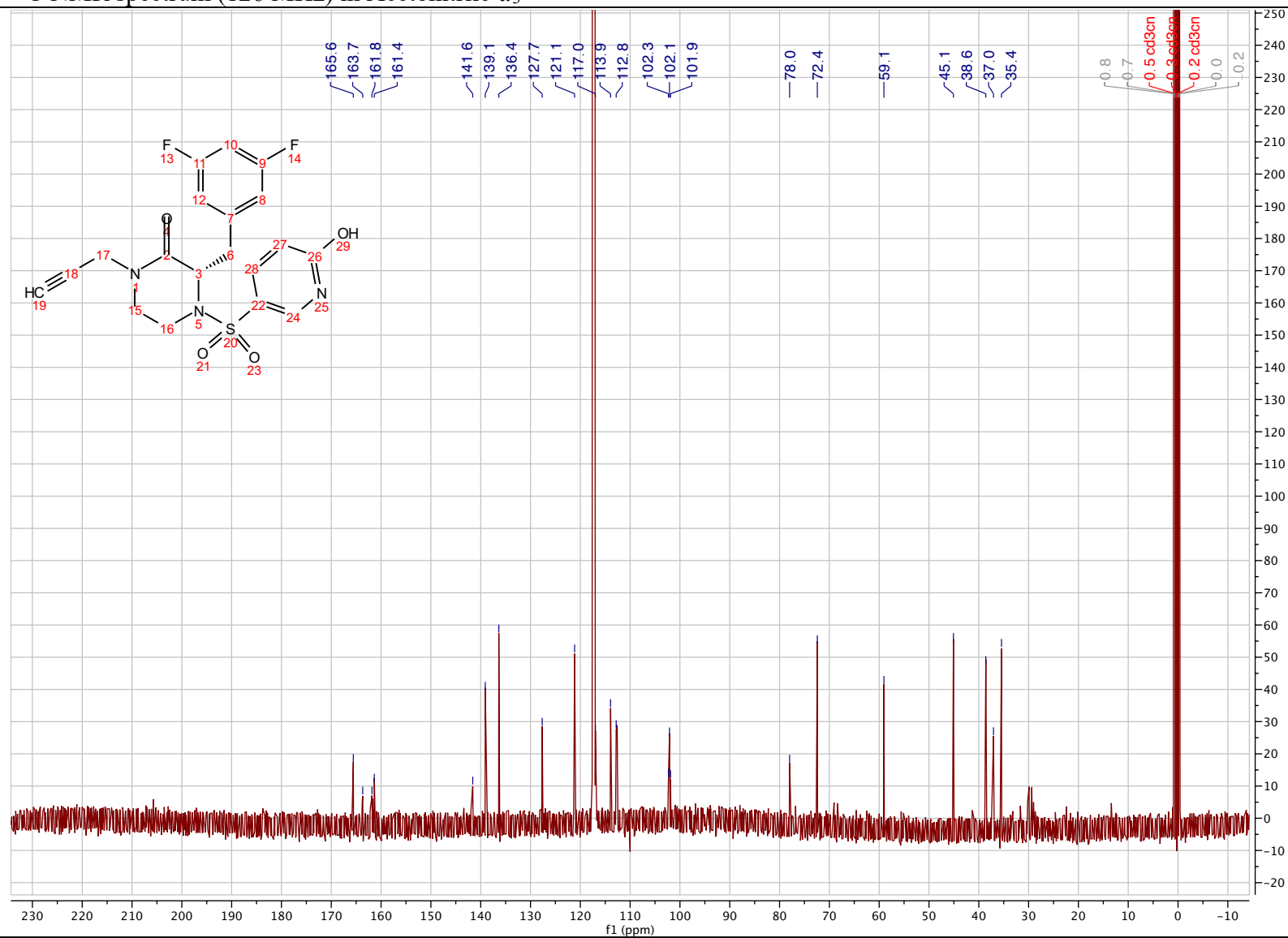
(S)-3-(3,5-difluorobenzyl)-4-((6-hydroxypyridin-3-yl)sulfonyl)-1-(prop-2-yn-1-yl)piperazin-2-one (2.93)

¹H NMR spectrum (500 MHz) in Acetonitrile-*d*₃



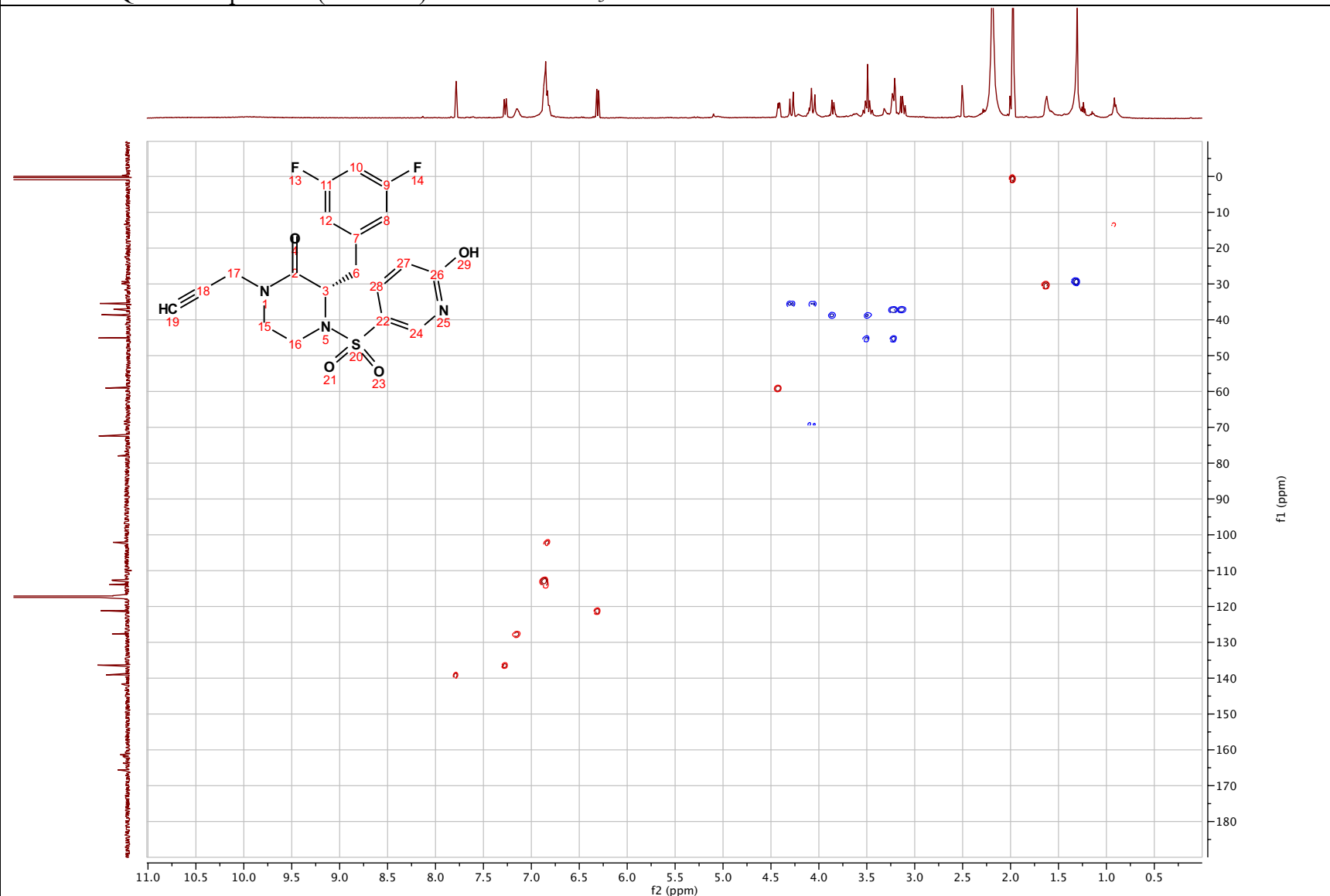
(S)-3-(3,5-difluorobenzyl)-4-((6-hydroxypyridin-3-yl)sulfonyl)-1-(prop-2-yn-1-yl)piperazin-2-one (2.93)

^{13}C NMR spectrum (126 MHz) in Acetonitrile- d_3



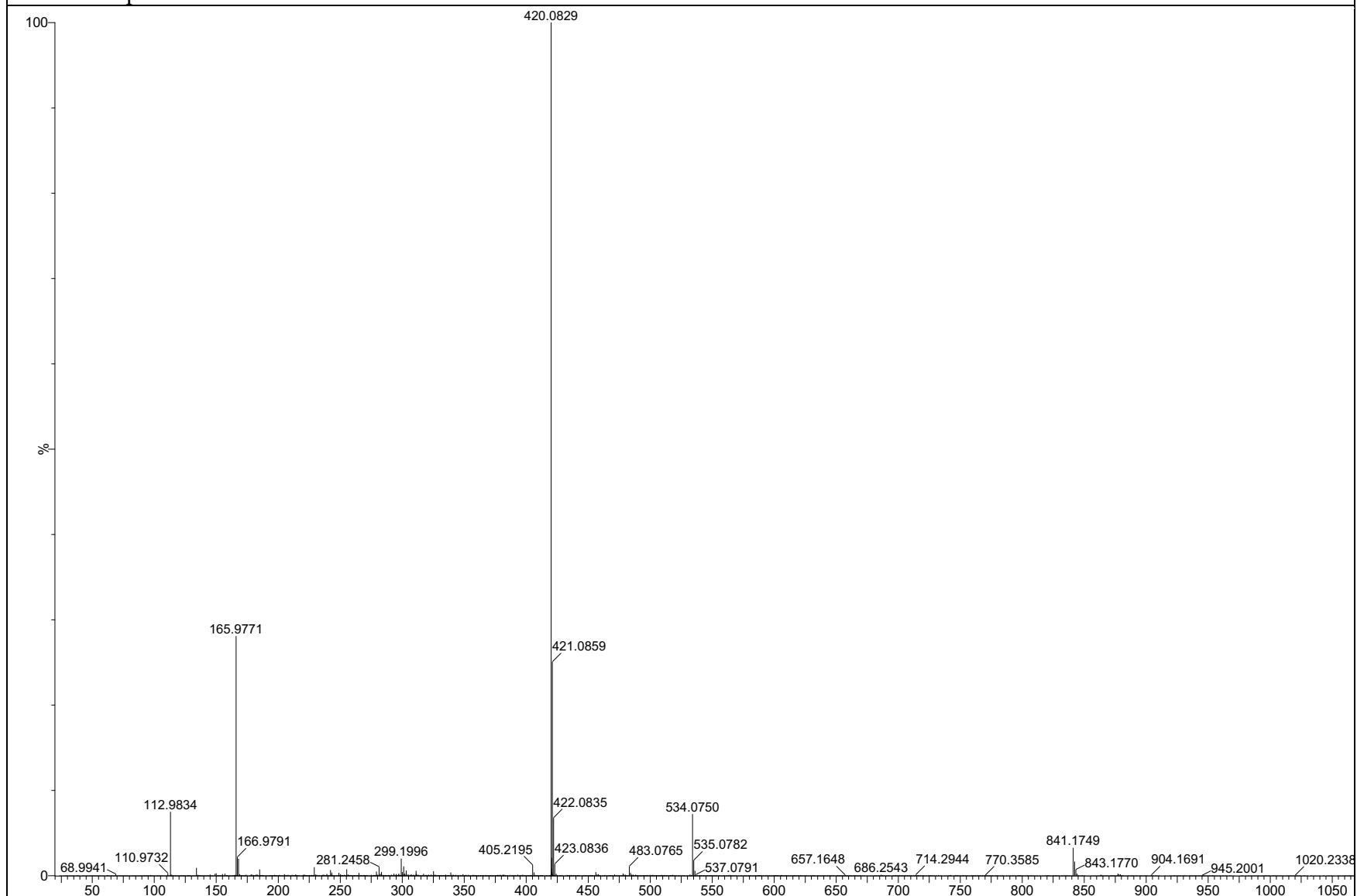
(S)-3-(3,5-difluorobenzyl)-4-((6-hydroxypyridin-3-yl)sulfonyl)-1-(prop-2-yn-1-yl)piperazin-2-one (2.93)

^1H - ^{13}C HSQC NMR spectrum (500 MHz) in Acetonitrile- d_3



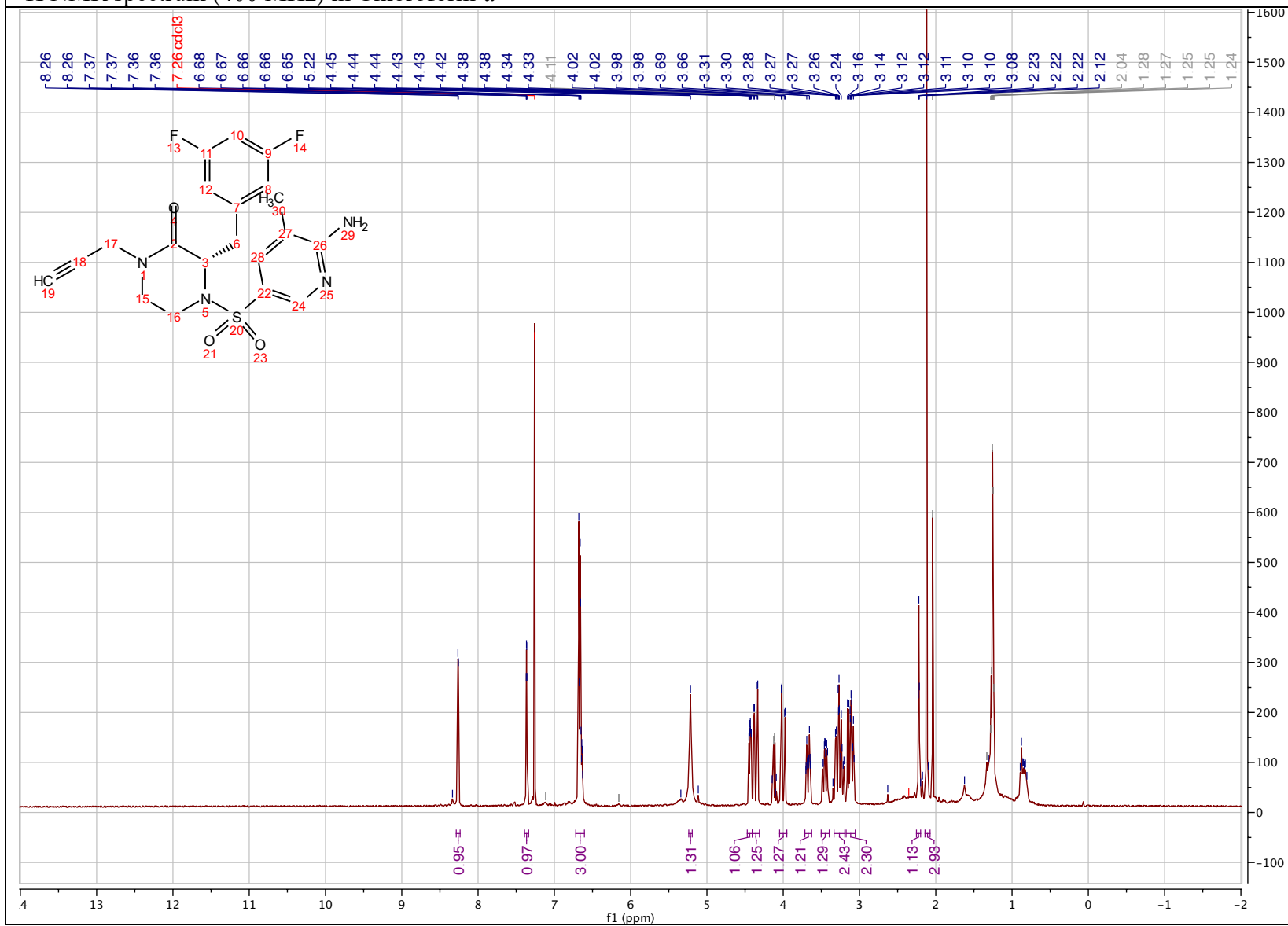
(S)-3-(3,5-difluorobenzyl)-4-((6-hydroxypyridin-3-yl)sulfonyl)-1-(prop-2-yn-1-yl)piperazin-2-one (2.93)

HRESI + spectrum



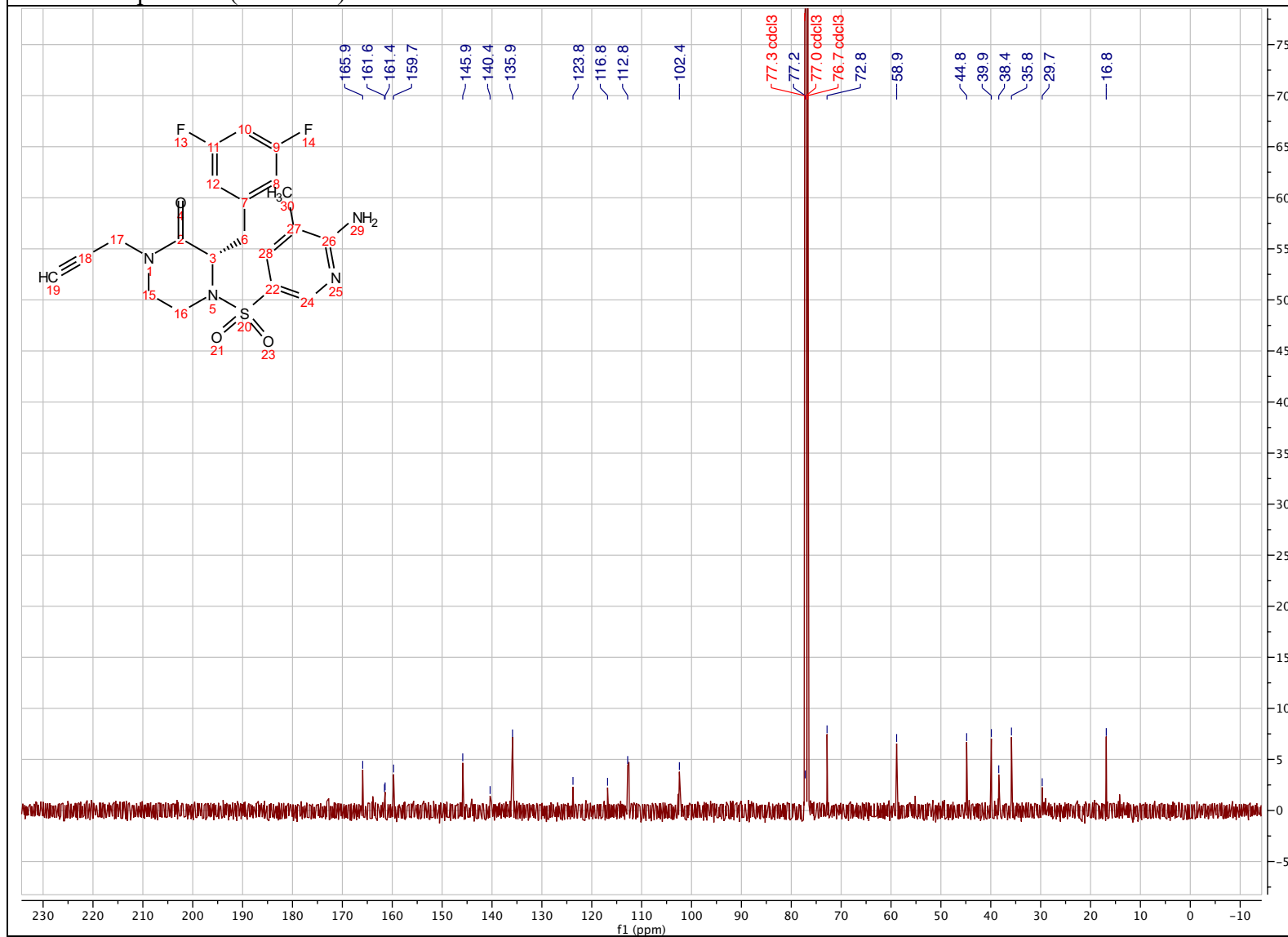
(S)-4-((6-amino-5-methylpyridin-3-yl)sulfonyl)-3-(3,5-difluorobenzyl)-1-(prop-2-yn-1-yl)piperazin-2-one (2.94)

¹H NMR spectrum (400 MHz) in Chloroform-*d*



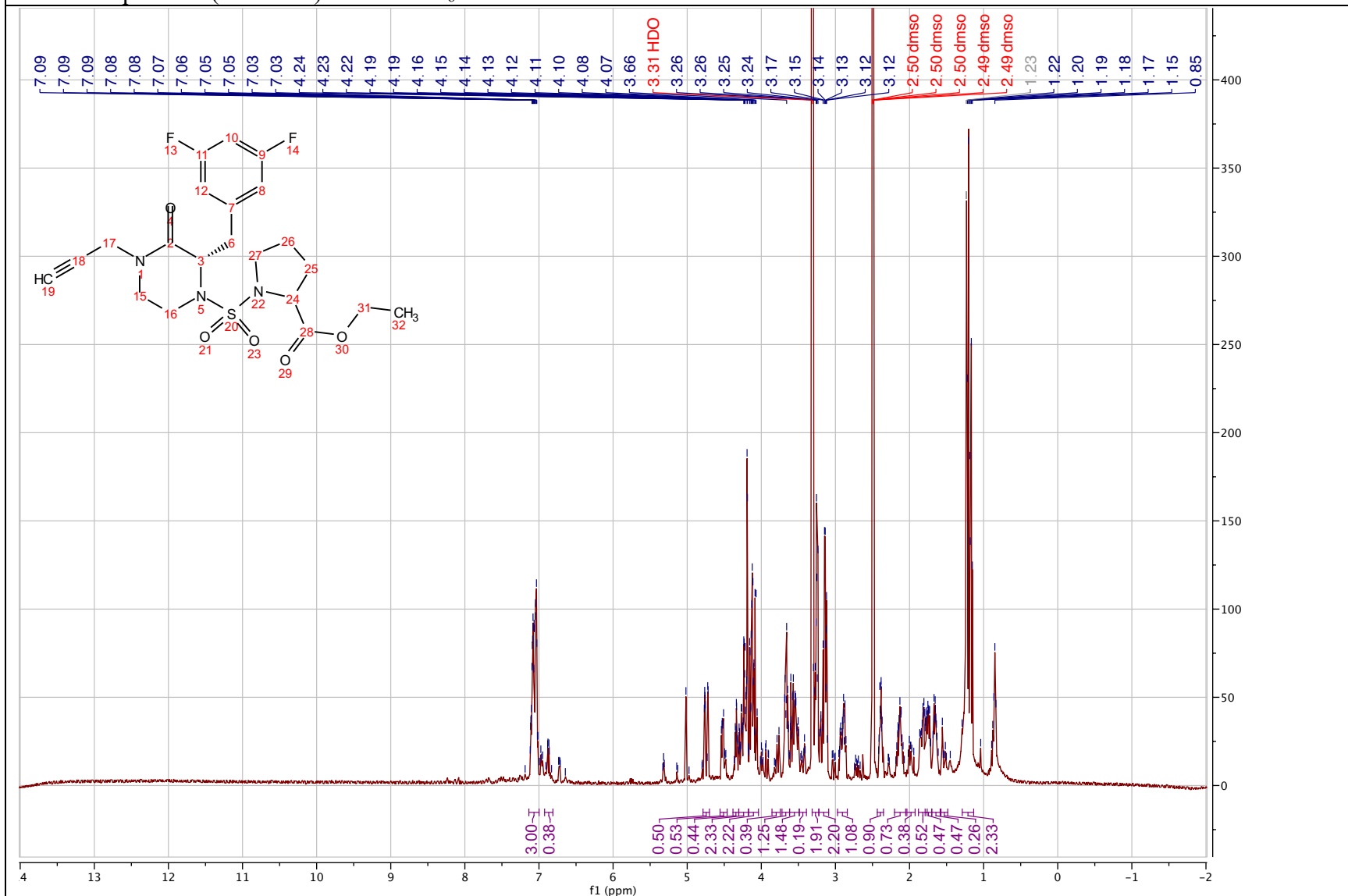
(S)-4-((6-amino-5-methylpyridin-3-yl)sulfonyl)-3-(3,5-difluorobenzyl)-1-(prop-2-yn-1-yl)piperazin-2-one (2.94)

¹³C NMR spectrum (101 MHz) in Chloroform-*d*



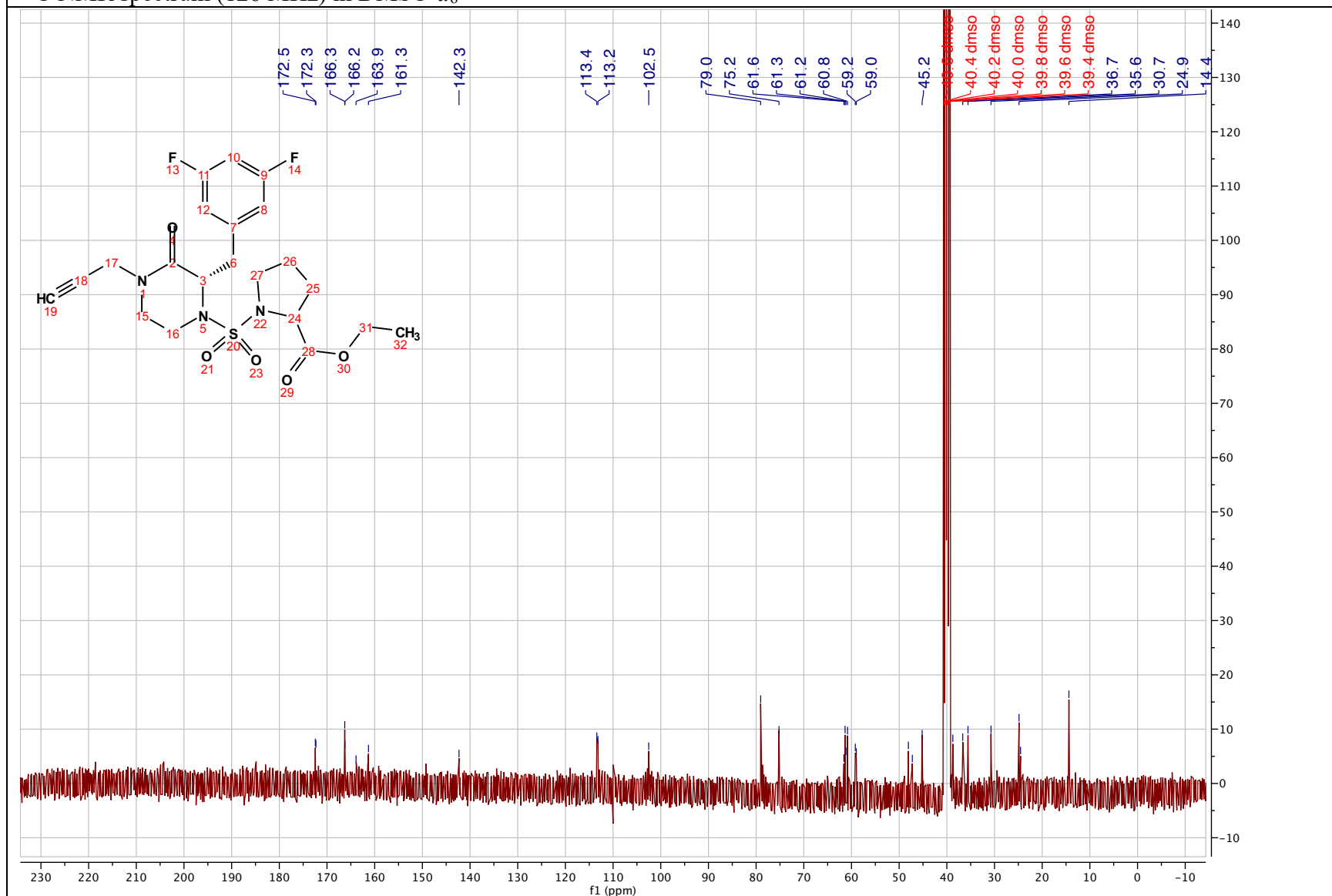
ethyl (((S)-2-(3,5-difluorobenzyl)-3-oxo-4-(prop-2-yn-1-yl)piperazin-1-yl)sulfonyl)prolinate (2.95)

¹H NMR spectrum (500 MHz) in DMSO-d₆



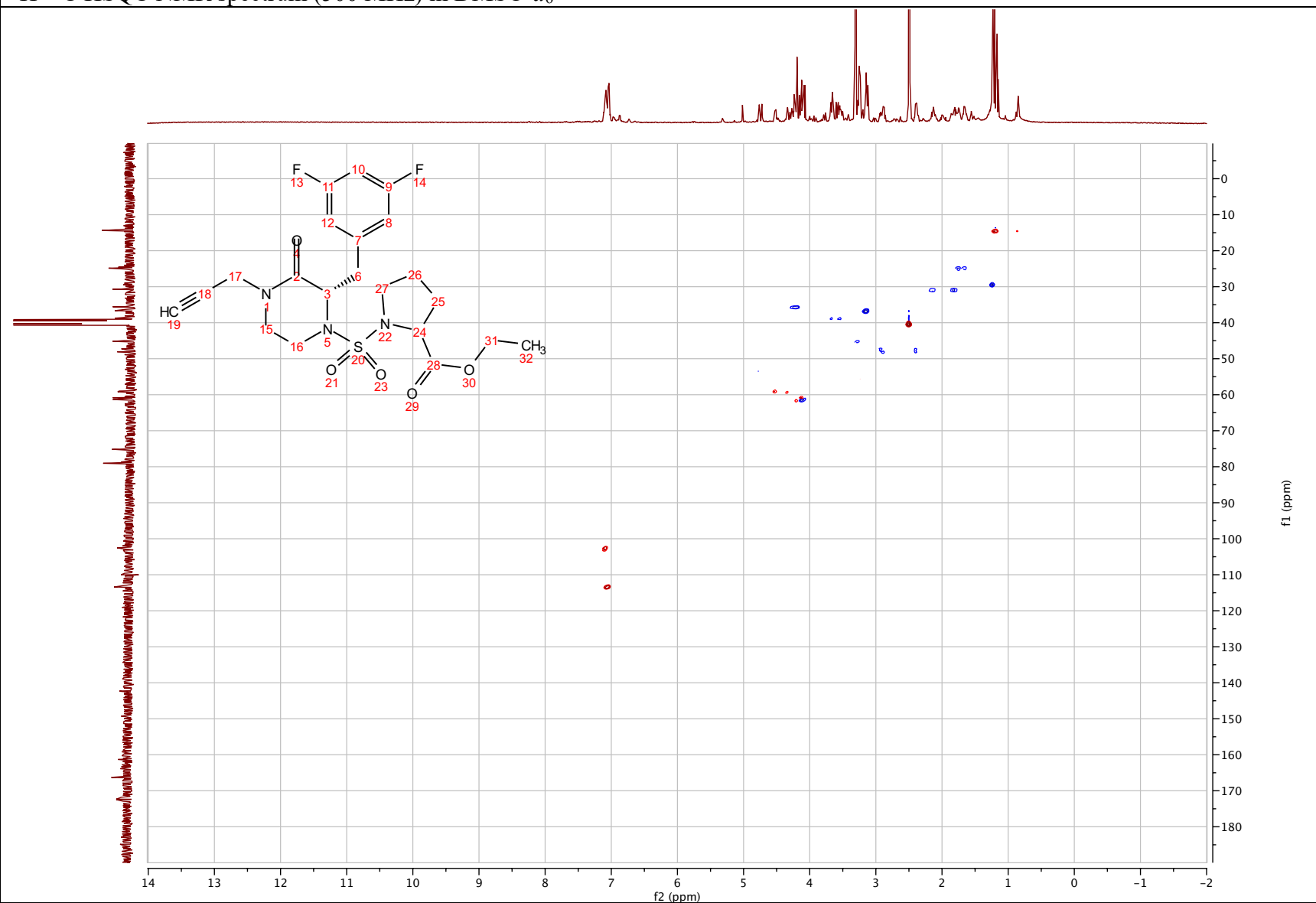
ethyl (((S)-2-(3,5-difluorobenzyl)-3-oxo-4-(prop-2-yn-1-yl)piperazin-1-yl)sulfonyl)prolinat (2.95)

¹³C NMR spectrum (126 MHz) in DMSO-d₆



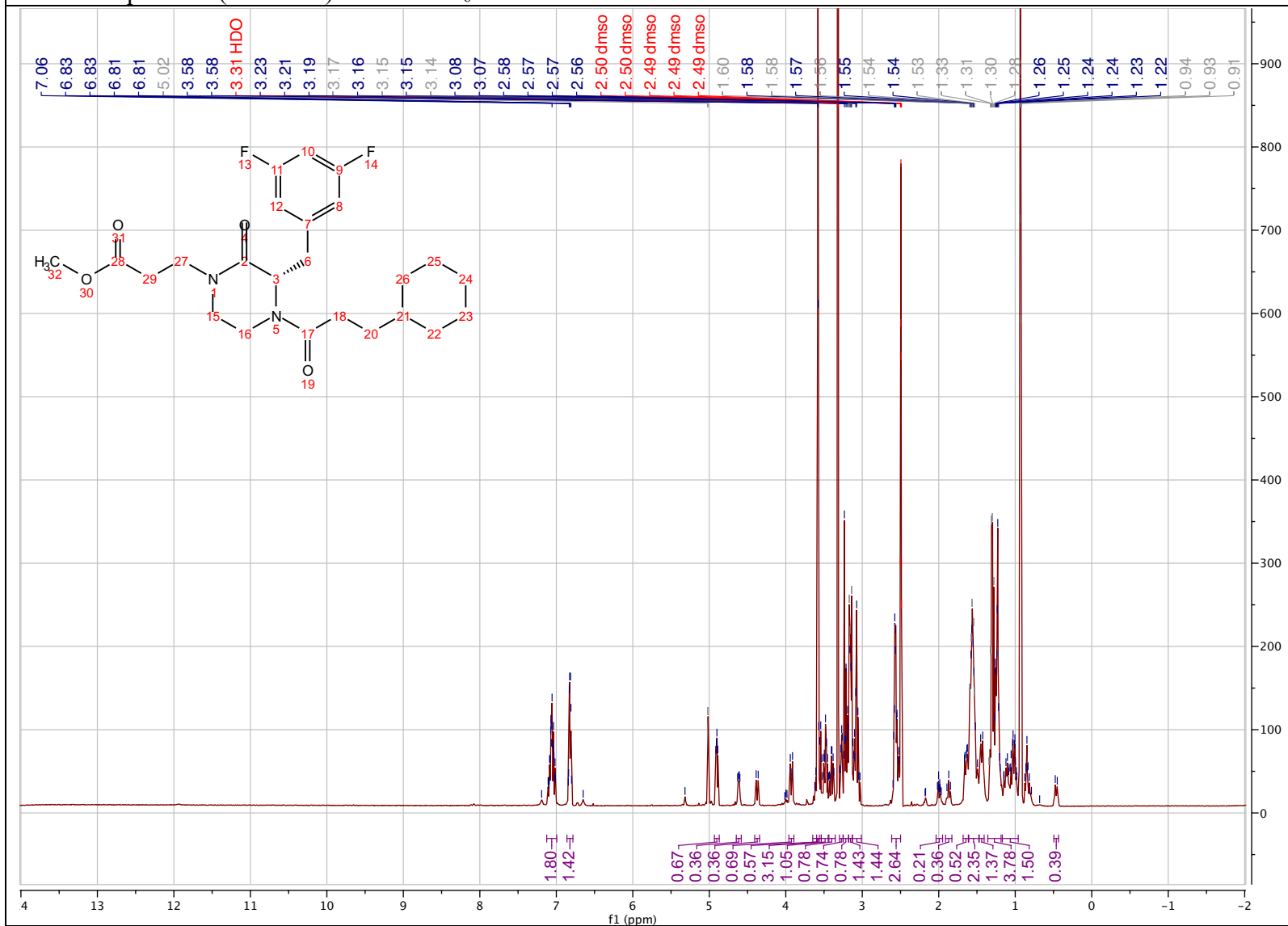
ethyl (((S)-2-(3,5-difluorobenzyl)-3-oxo-4-(prop-2-yn-1-yl)piperazin-1-yl)sulfonyl)prolinate (2.95)

^1H - ^{13}C HSQC NMR spectrum (500 MHz) in $\text{DMSO-}d_6$



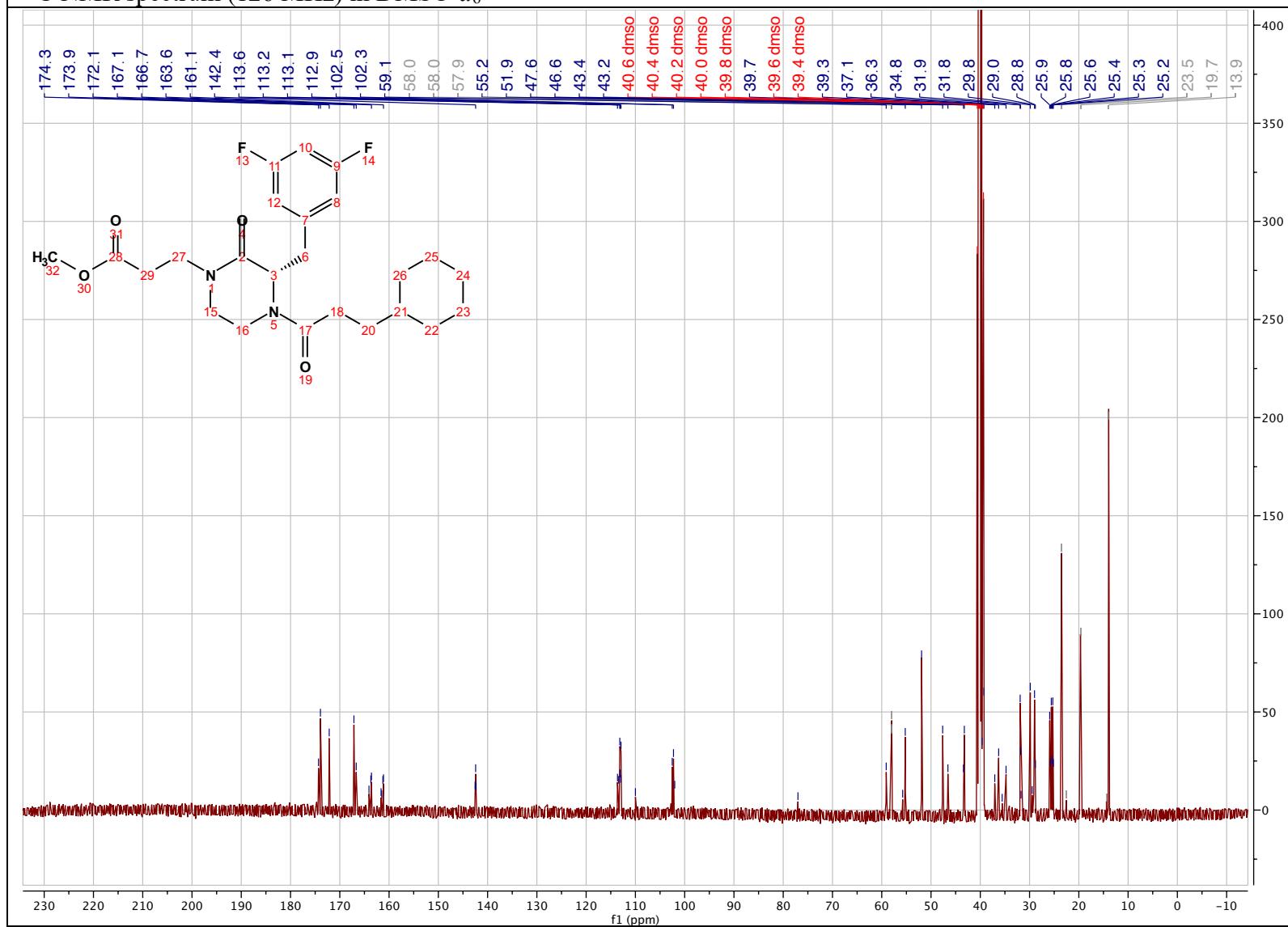
methyl (S)-3-(4-(3-cyclohexylpropanoyl)-3-(3,5-difluorobenzyl)-2-oxopiperazin-1-yl) propanoate (2.96)

¹H NMR spectrum (500 MHz) in DMSO-*d*₆



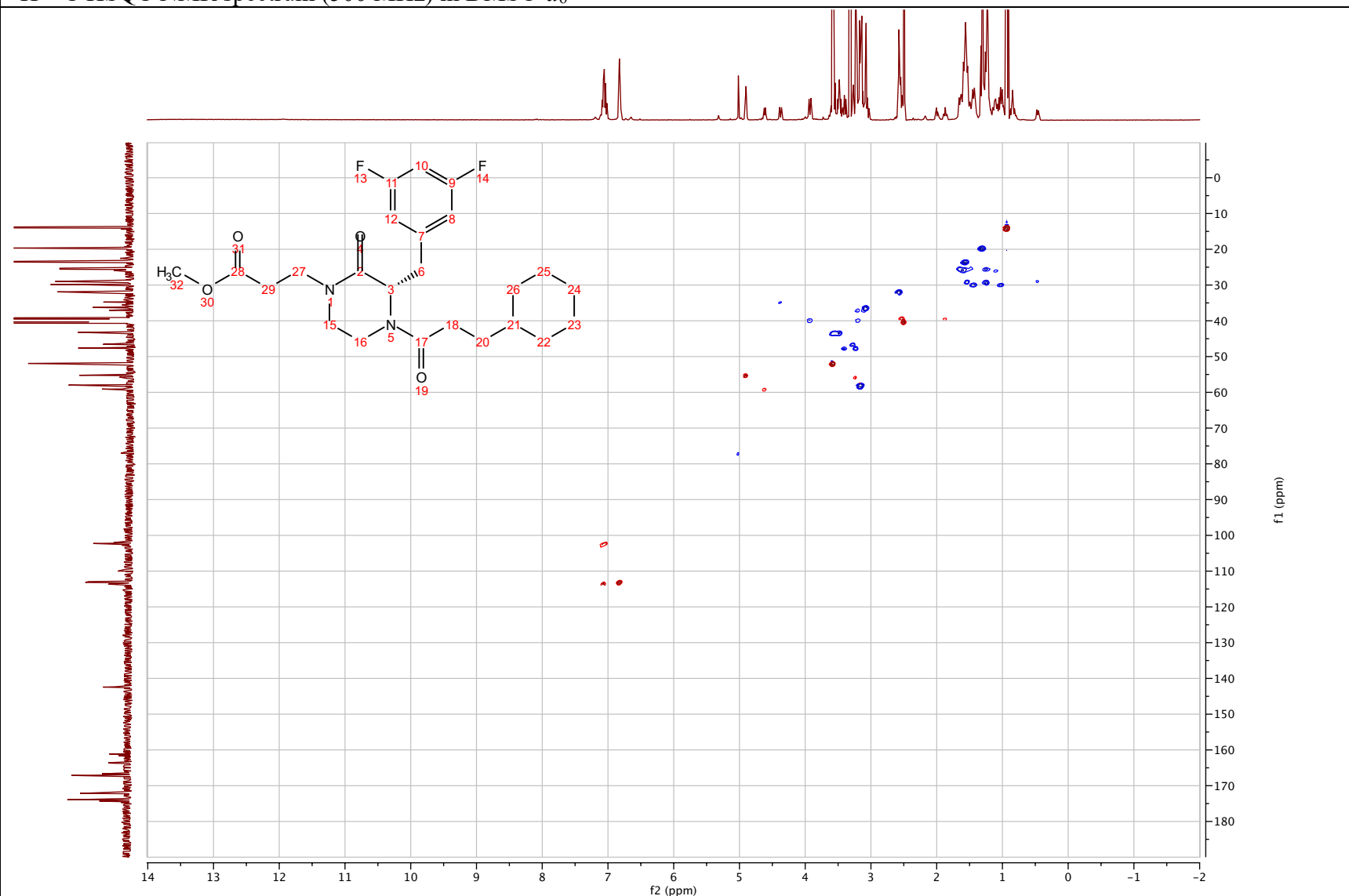
methyl (S)-3-(4-(3-cyclohexylpropanoyl)-3-(3,5-difluorobenzyl)-2-oxopiperazin-1-yl) propanoate (2.96)

¹³C NMR spectrum (126 MHz) in DMSO-*d*₆



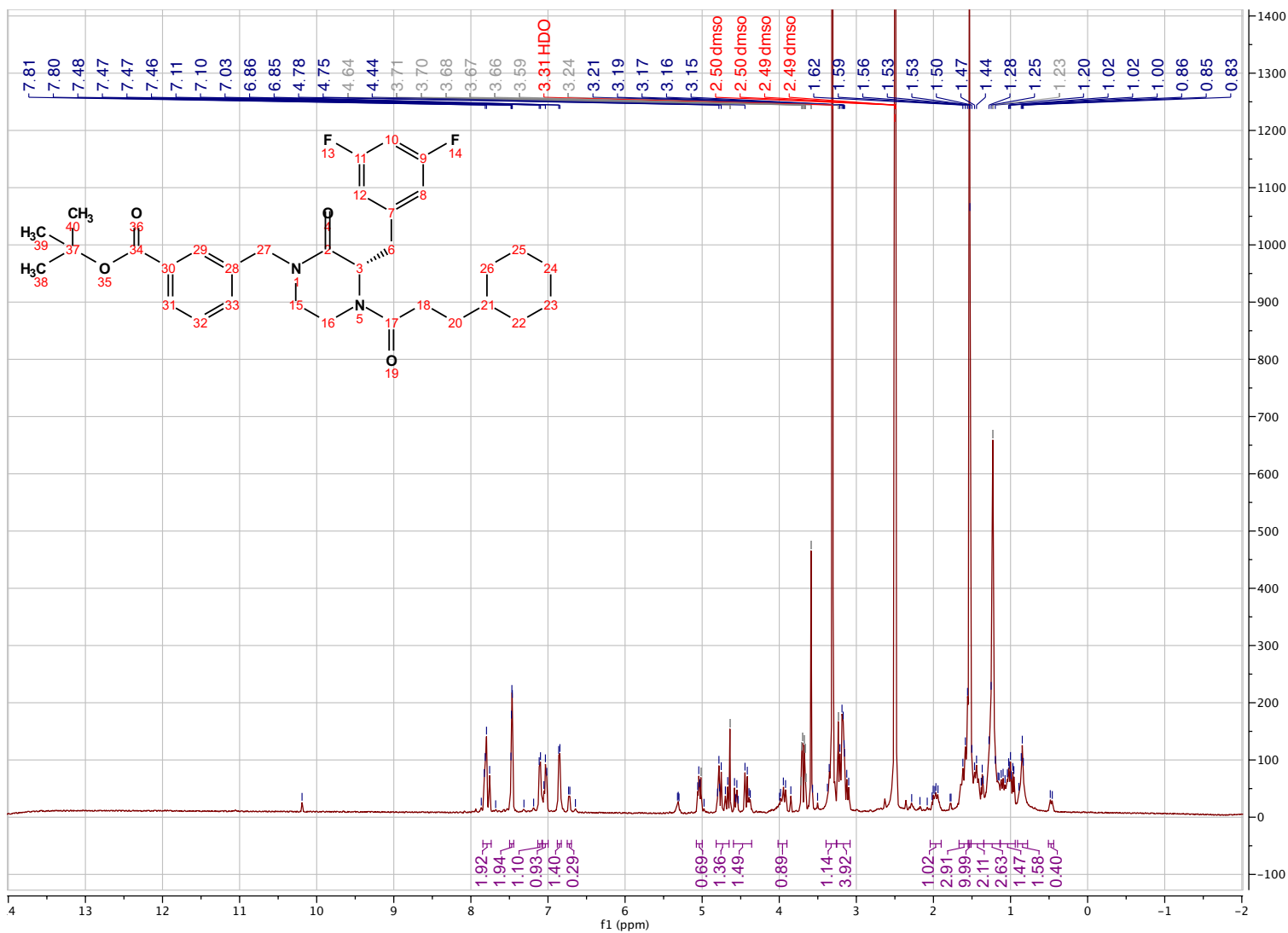
methyl (S)-3-(4-(3-cyclohexylpropanoyl)-3-(3,5-difluorobenzyl)-2-oxopiperazin-1-yl) propanoate (2.96)

^1H - ^{13}C HSQC NMR spectrum (500 MHz) in $\text{DMSO-}d_6$



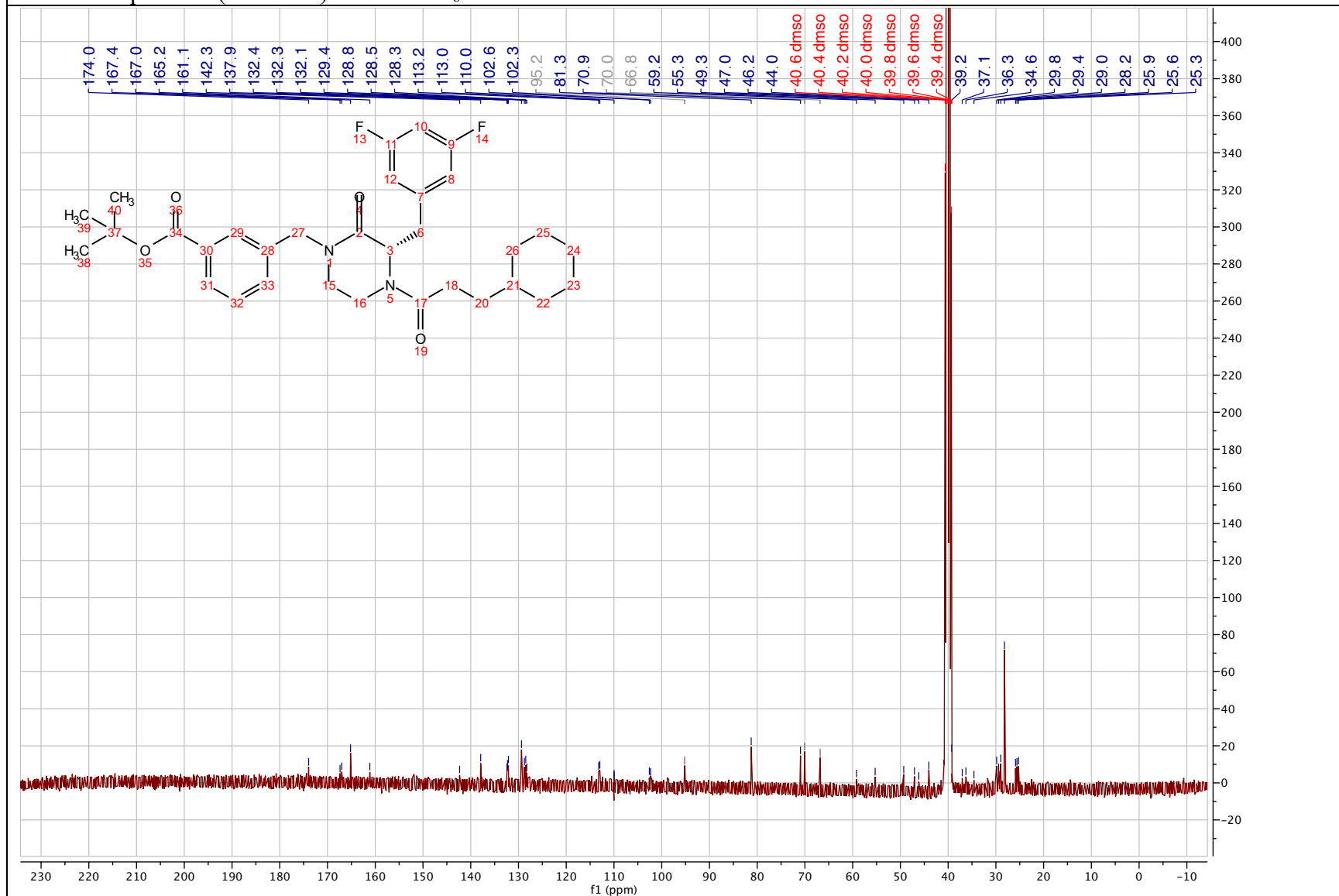
***tert*-butyl (*S*)-3-((4-(3-cyclohexylpropanoyl)-3-(3,5-difluorobenzyl)-2-oxopiperazin-1-yl)methyl)benzoate (2.97)**

¹H NMR spectrum (500 MHz) in DMSO-*d*₆



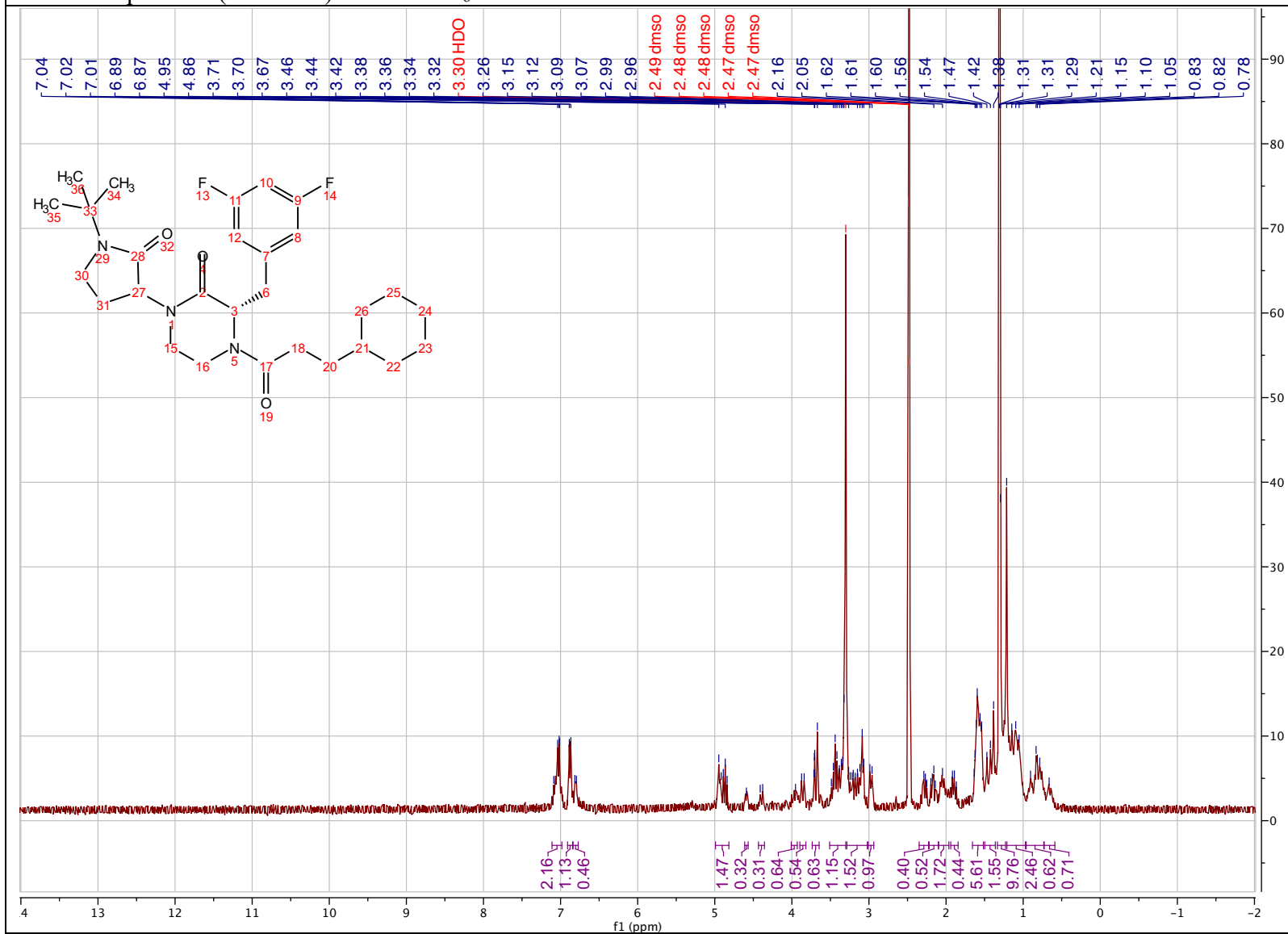
***tert*-butyl (*S*)-3-((4-(3-cyclohexylpropanoyl)-3-(3,5-difluorobenzyl)-2-oxopiperazin-1-yl)methyl)benzoate (2.97)**

¹³C NMR spectrum (126 MHz) in DMSO-*d*₆



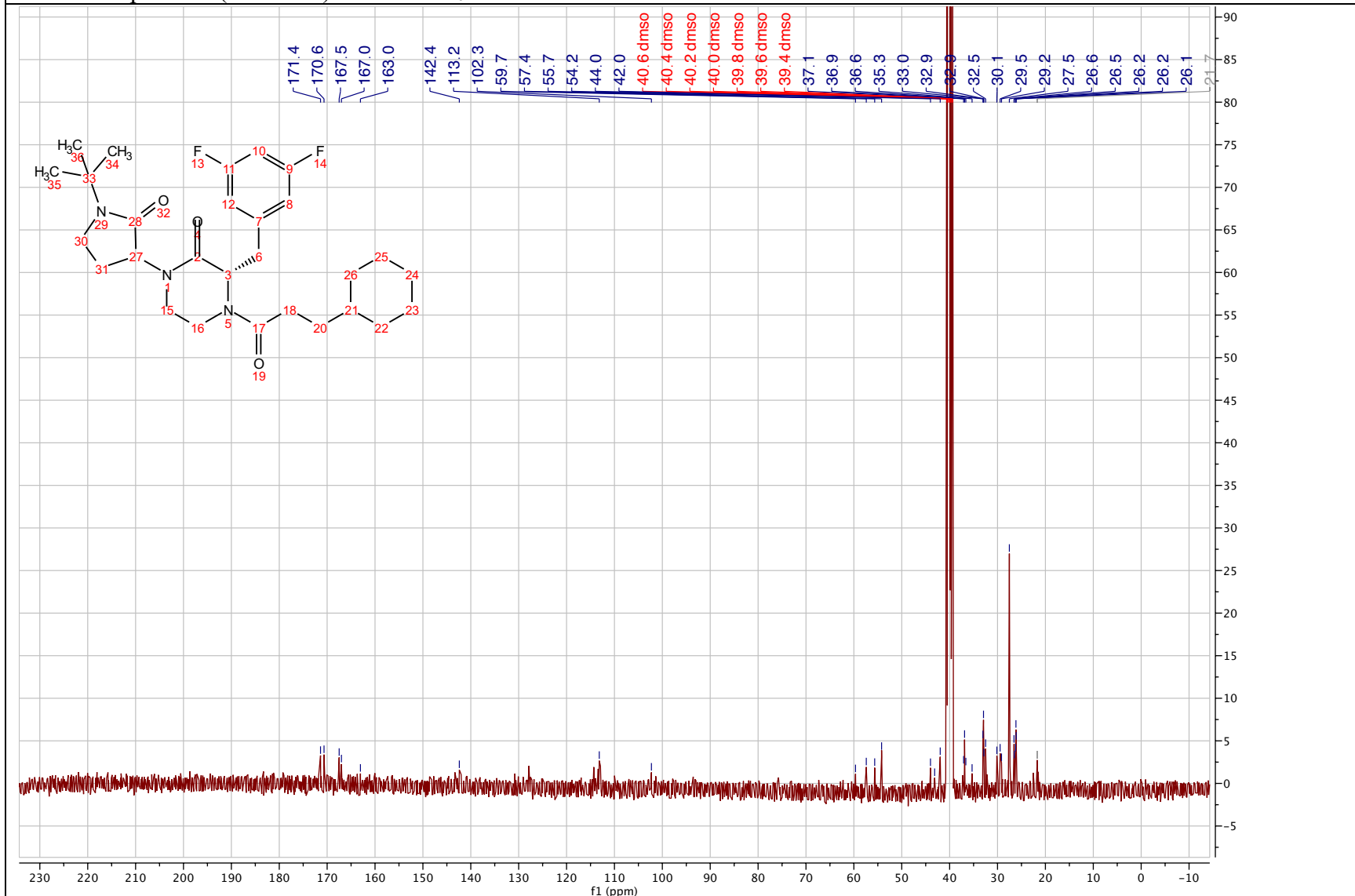
(3S)-1-(1-(*tert*-butyl)-2-oxopyrrolidin-3-yl)-4-(3-cyclohexylpropanoyl)-3-(3,5-difluorobenzyl) piperazin-2-one (2.97)

¹H NMR spectrum (500 MHz) in DMSO-*d*₆



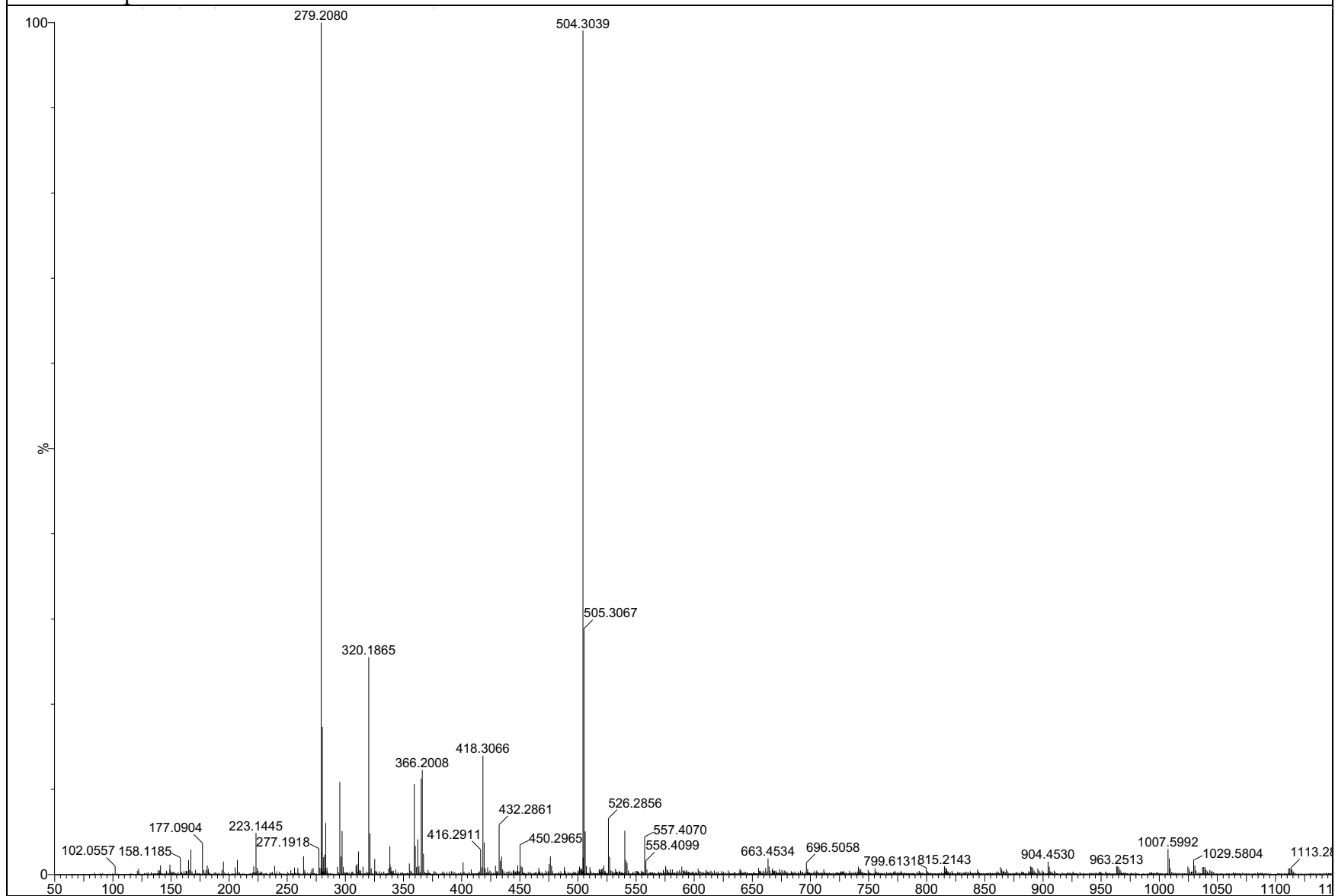
(3S)-1-(1-(*tert*-butyl)-2-oxopyrrolidin-3-yl)-4-(3-cyclohexylpropanoyl)-3-(3,5-difluorobenzyl) piperazin-2-one (2.97)

¹³C NMR spectrum (126 MHz) in DMSO-*d*₆



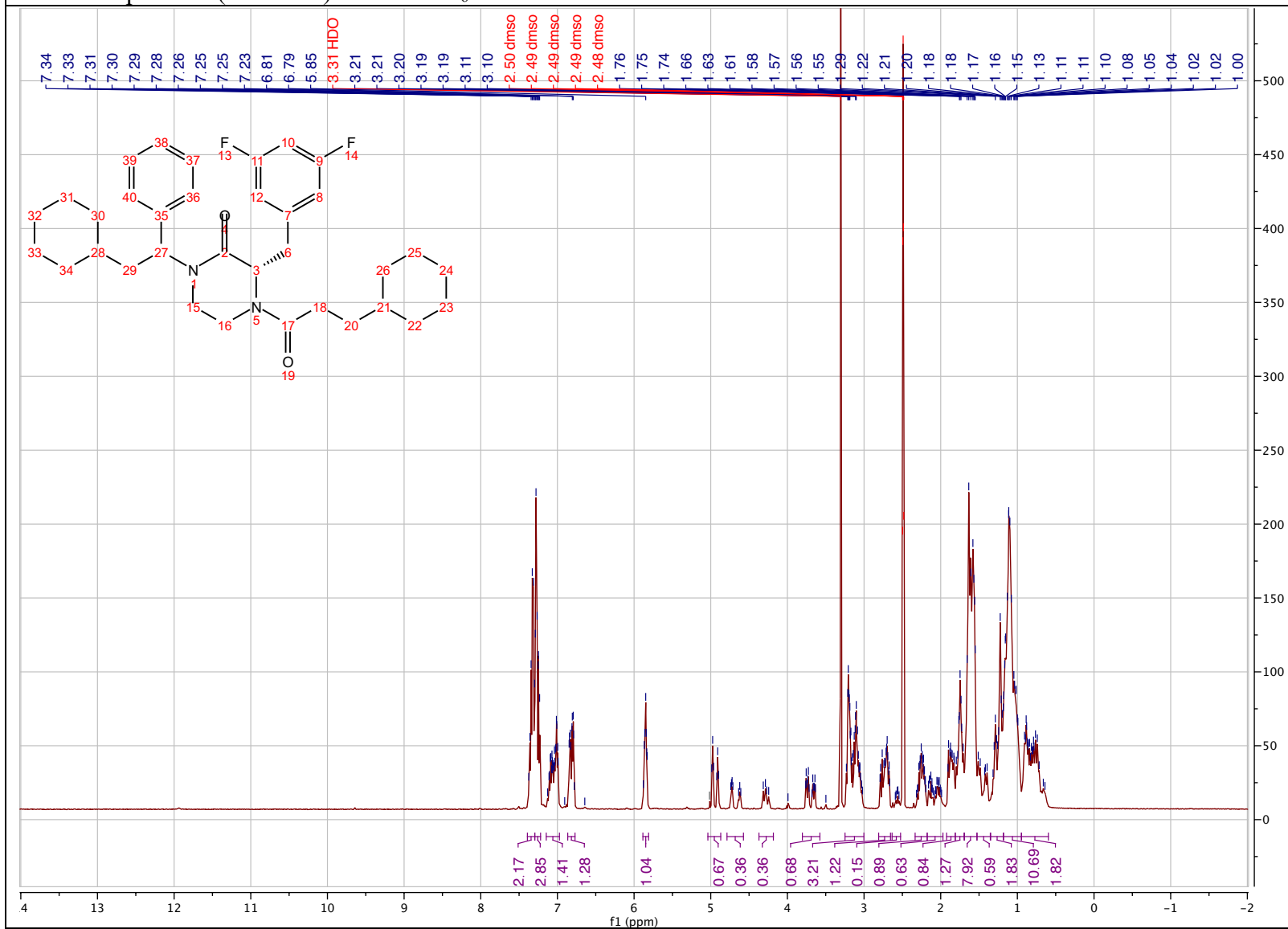
(3*S*)-1-(1-(*tert*-butyl)-2-oxopyrrolidin-3-yl)-4-(3-cyclohexylpropanoyl)-3-(3,5-difluorobenzyl) piperazin-2-one (2.97)

HRESI + spectrum



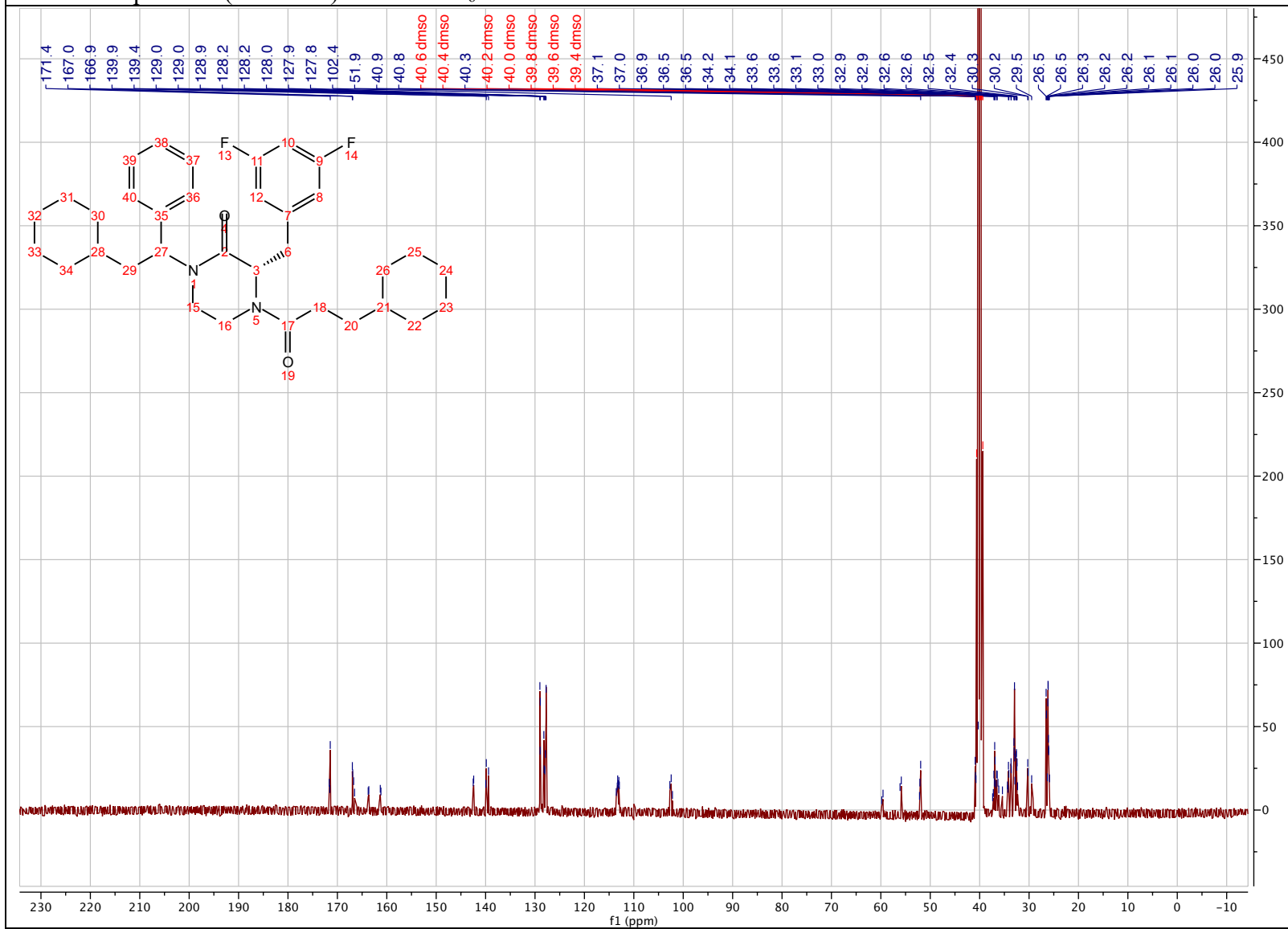
(3*S*)-1-(2-cyclohexyl-1-phenylethyl)-4-(3-cyclohexylpropanoyl)-3-(3,5-difluorobenzyl) piperazin-2-one (2.104)

¹H NMR spectrum (500 MHz) in DMSO-*d*₆



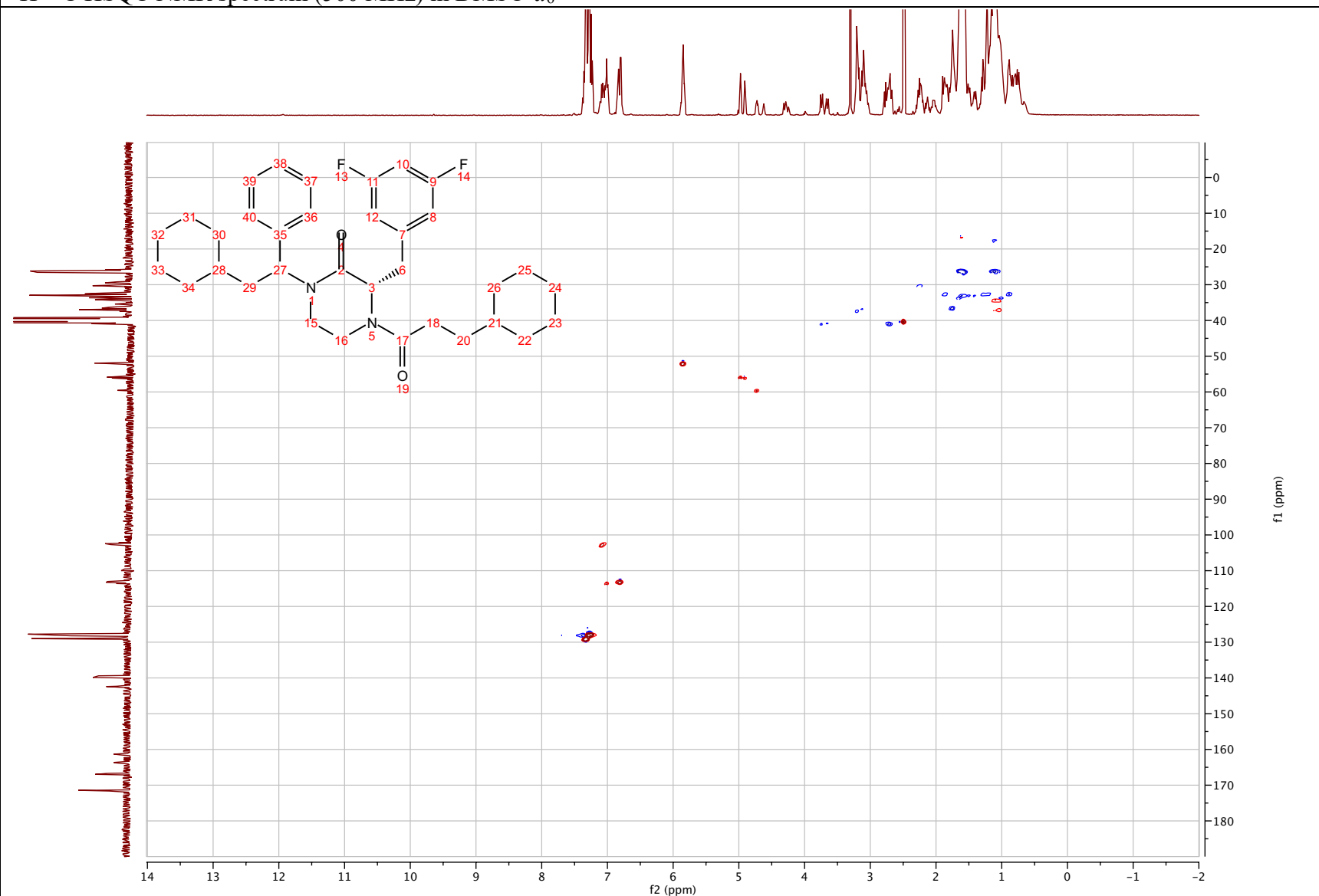
(3S)-1-(2-cyclohexyl-1-phenylethyl)-4-(3-cyclohexylpropanoyl)-3-(3,5-difluorobenzyl) piperazin-2-one (2.104)

¹³C NMR spectrum (101 MHz) in DMSO-*d*₆



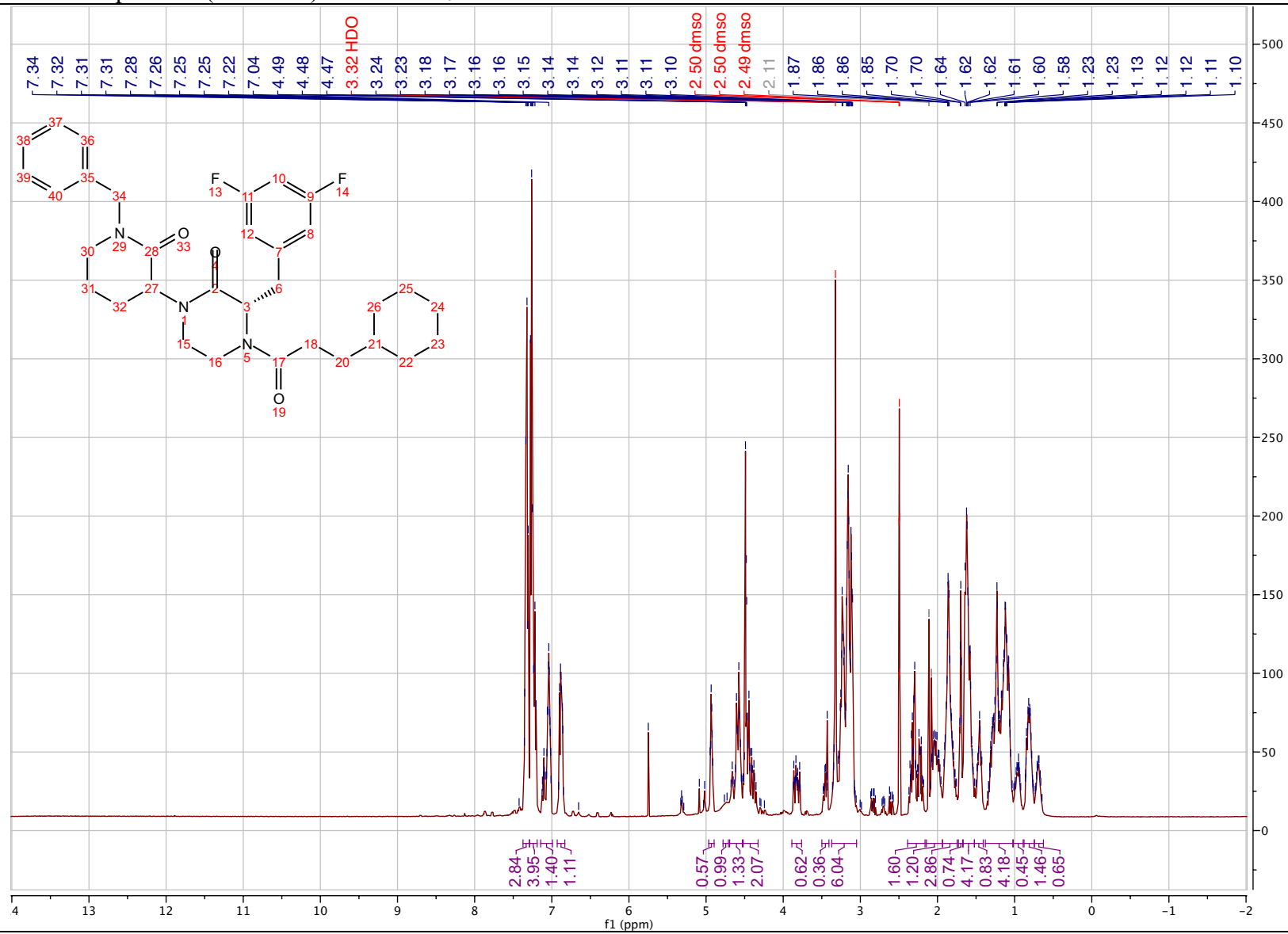
(3*S*)-1-(2-cyclohexyl-1-phenylethyl)-4-(3-cyclohexylpropanoyl)-3-(3,5-difluorobenzyl) piperazin-2-one (2.104)

^1H - ^{13}C HSQC NMR spectrum (500 MHz) in $\text{DMSO-}d_6$



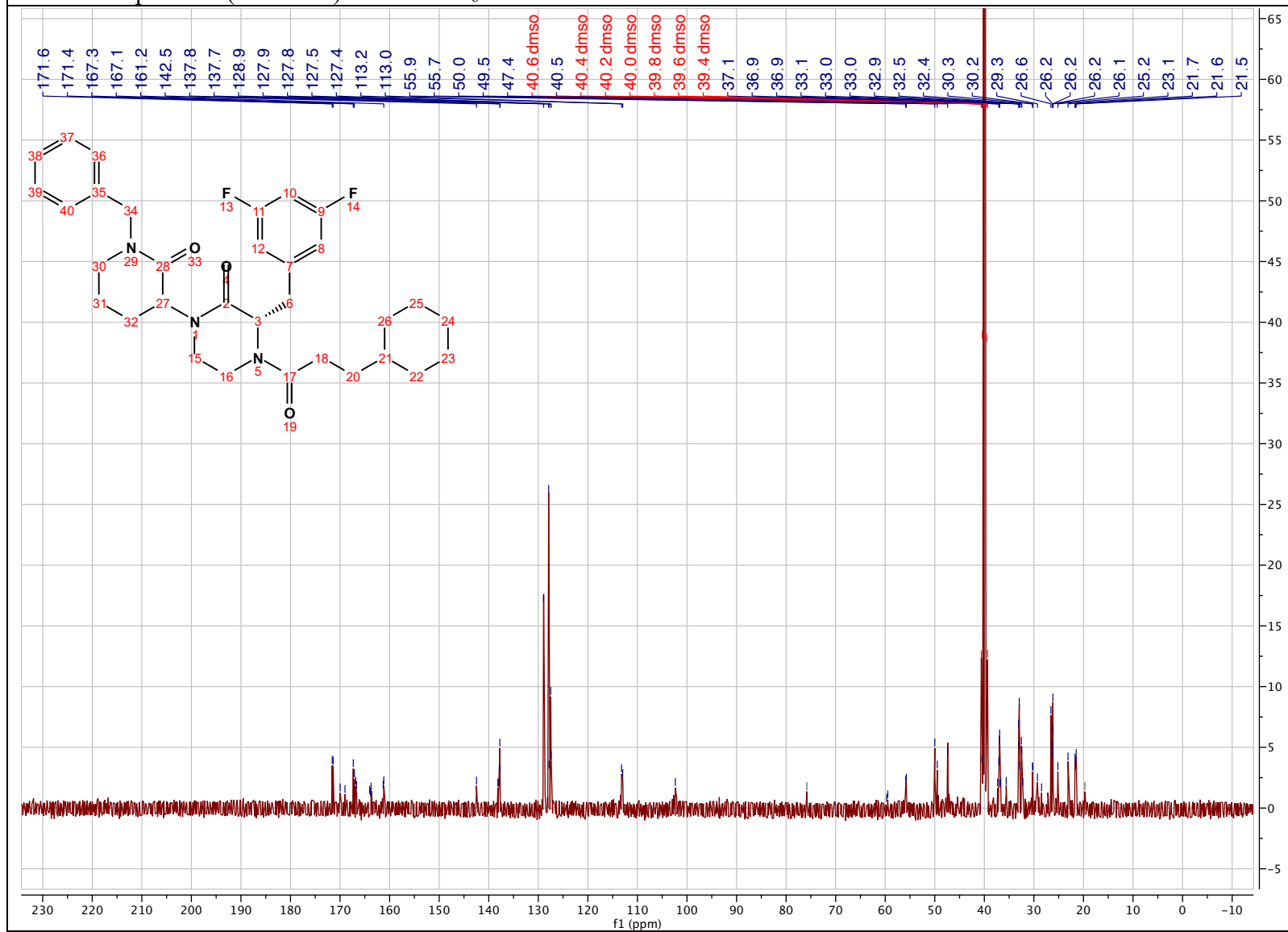
(3S)-1-(1-benzyl-2-oxopiperidin-3-yl)-4-(3-cyclohexylpropanoyl)-3-(3,5-difluorobenzyl) piperazin-2-one (2.105)

¹H NMR spectrum (500 MHz) in DMSO-*d*₆



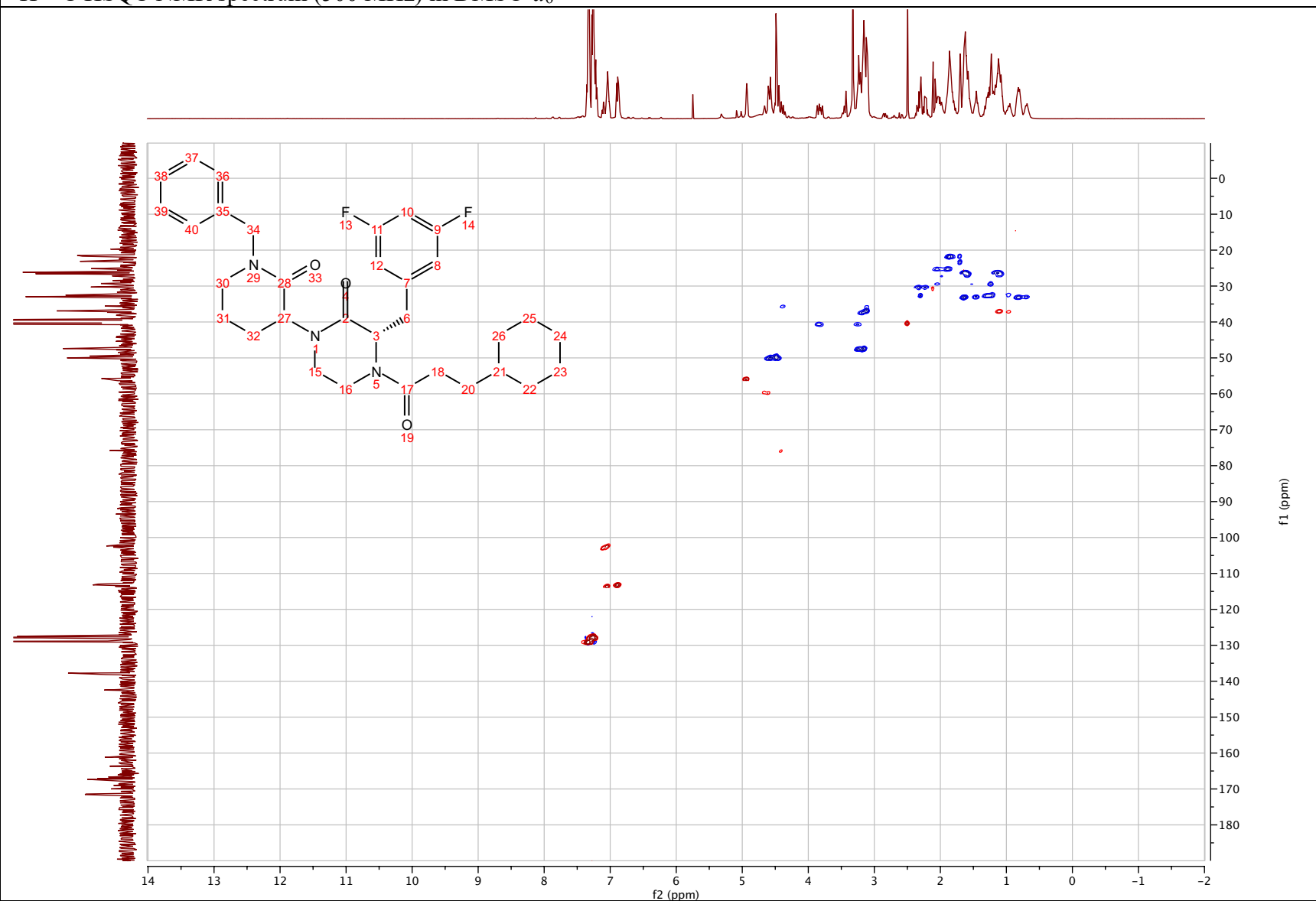
(3S)-1-(1-benzyl-2-oxopiperidin-3-yl)-4-(3-cyclohexylpropanoyl)-3-(3,5-difluorobenzyl) piperazin-2-one (2.105)

¹³C NMR spectrum (101 MHz) in DMSO-*d*₆



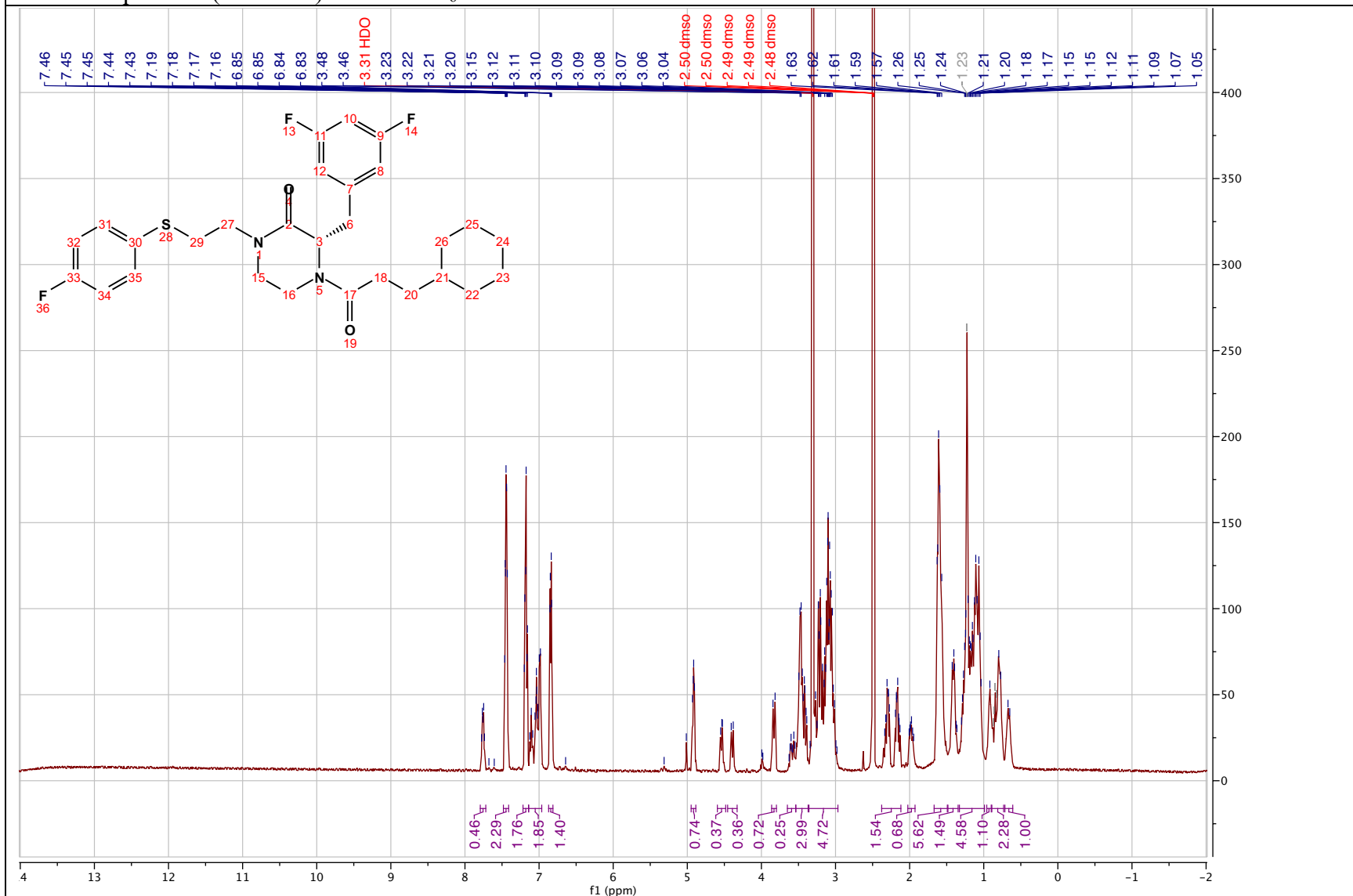
(3*S*)-1-(1-benzyl-2-oxopiperidin-3-yl)-4-(3-cyclohexylpropanoyl)-3-(3,5-difluorobenzyl) piperazin-2-one (2.105)

^1H - ^{13}C HSQC NMR spectrum (500 MHz) in $\text{DMSO-}d_6$



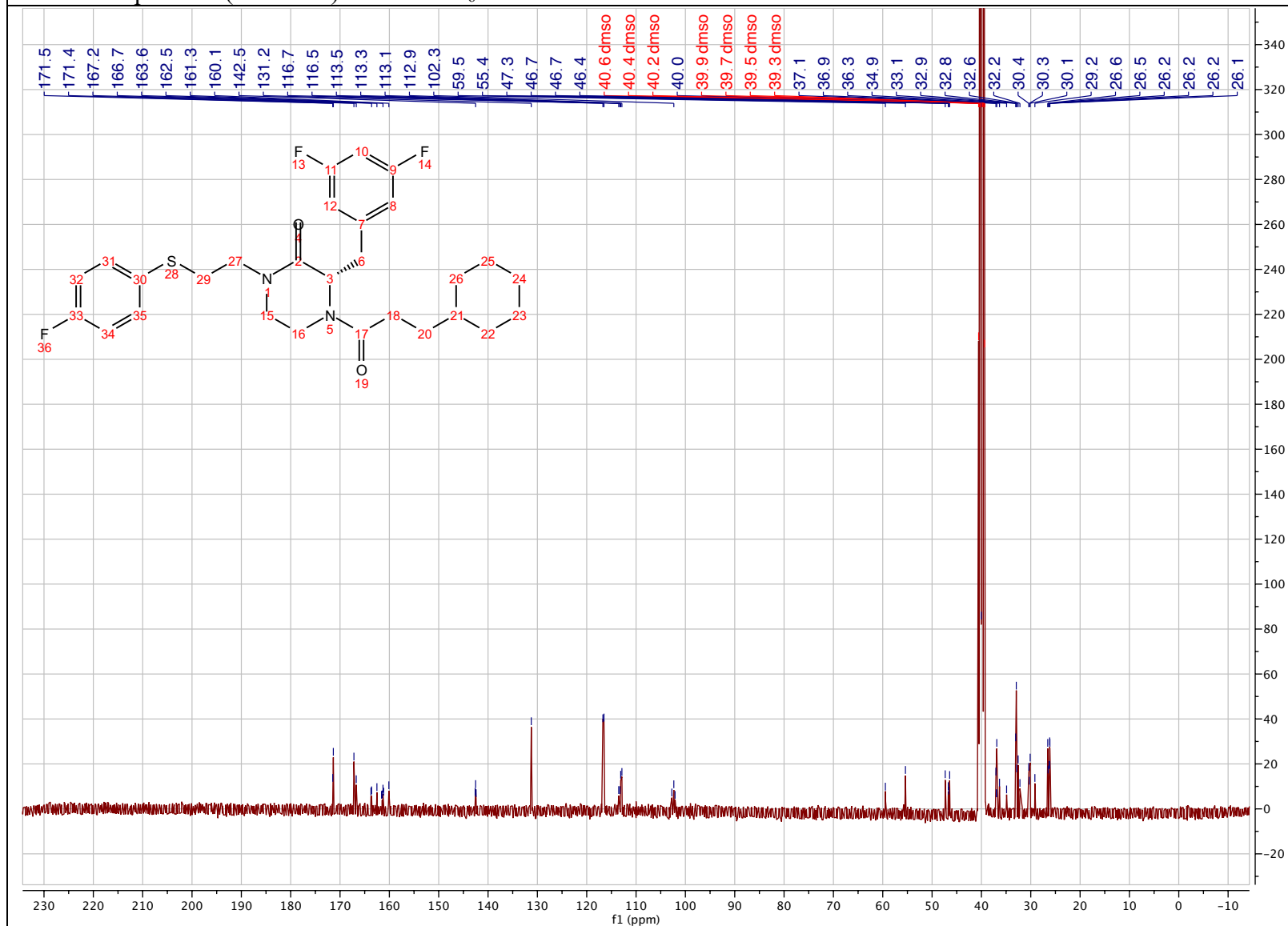
(S)-4-(3-cyclohexylpropanoyl)-3-(3,5-difluorobenzyl)-1-(2-((4-fluorophenyl)thio)ethyl) piperazin-2-one (2.106)

¹H NMR spectrum (500 MHz) in DMSO-*d*₆



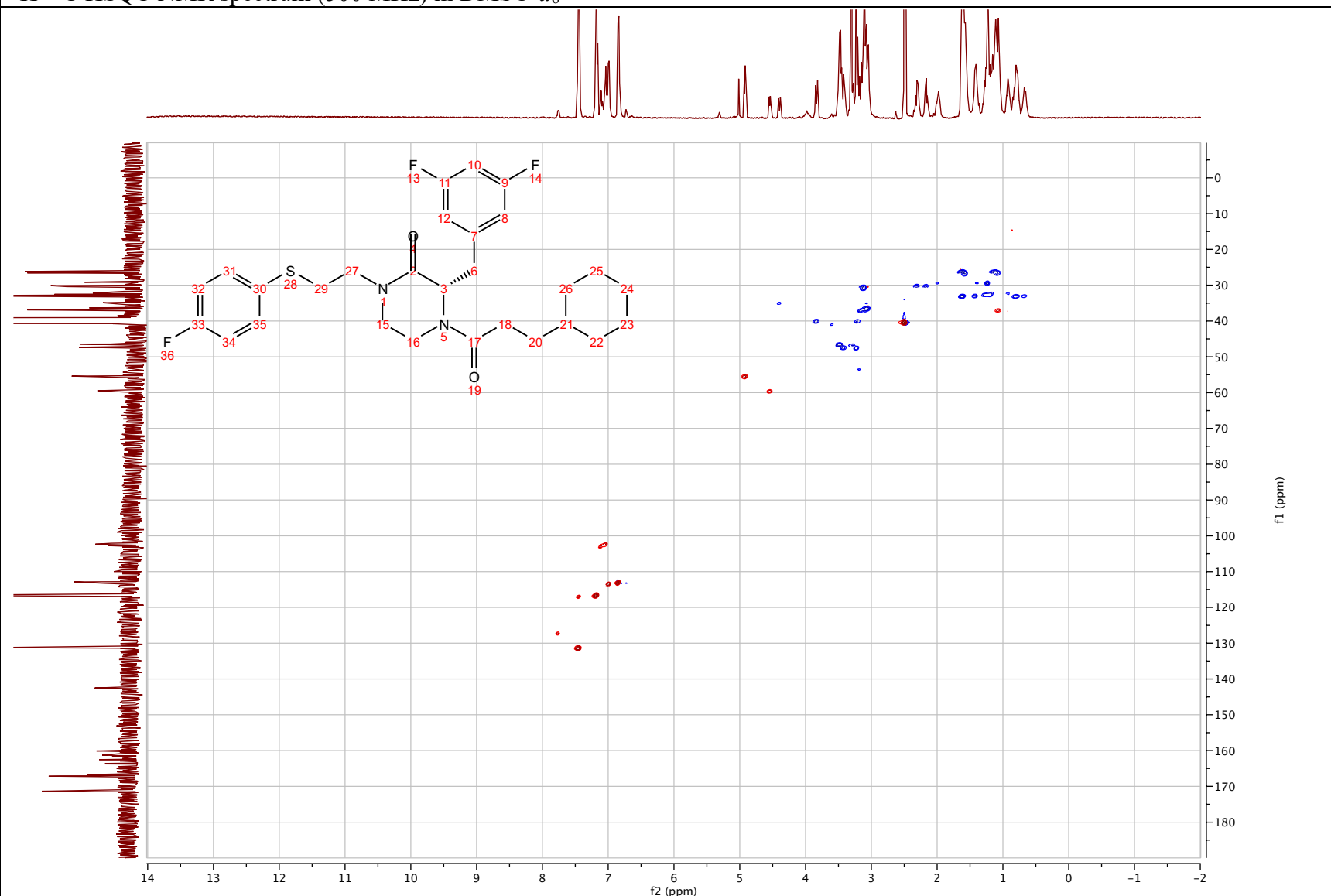
(S)-4-(3-cyclohexylpropanoyl)-3-(3,5-difluorobenzyl)-1-(2-((4-fluorophenyl)thio)ethyl) piperazin-2-one (2.106)

¹³C NMR spectrum (101 MHz) in DMSO-*d*₆



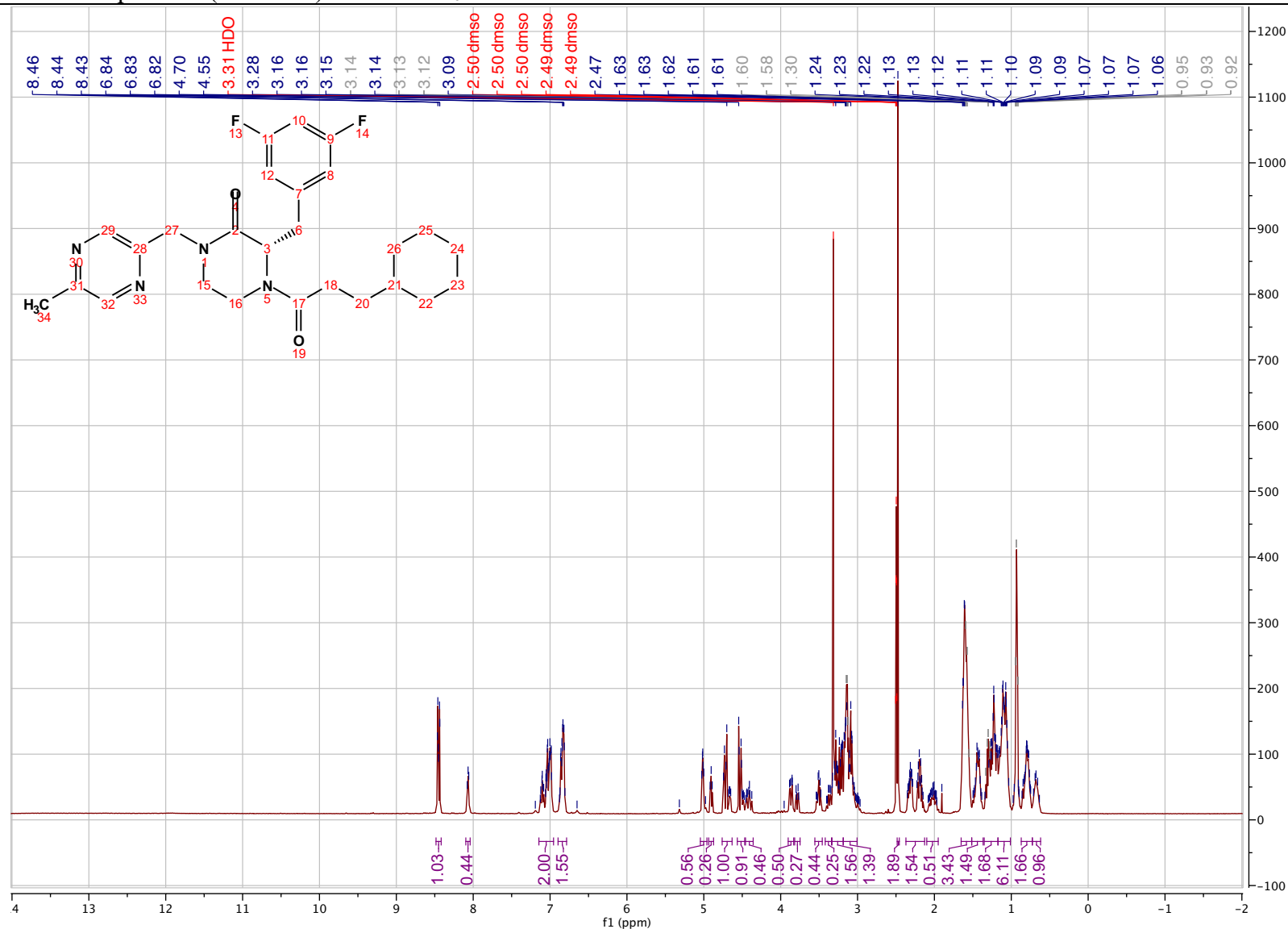
(S)-4-(3-cyclohexylpropanoyl)-3-(3,5-difluorobenzyl)-1-(2-((4-fluorophenyl)thio)ethyl) piperazin-2-one (2.106)

^1H - ^{13}C HSQC NMR spectrum (500 MHz) in $\text{DMSO-}d_6$



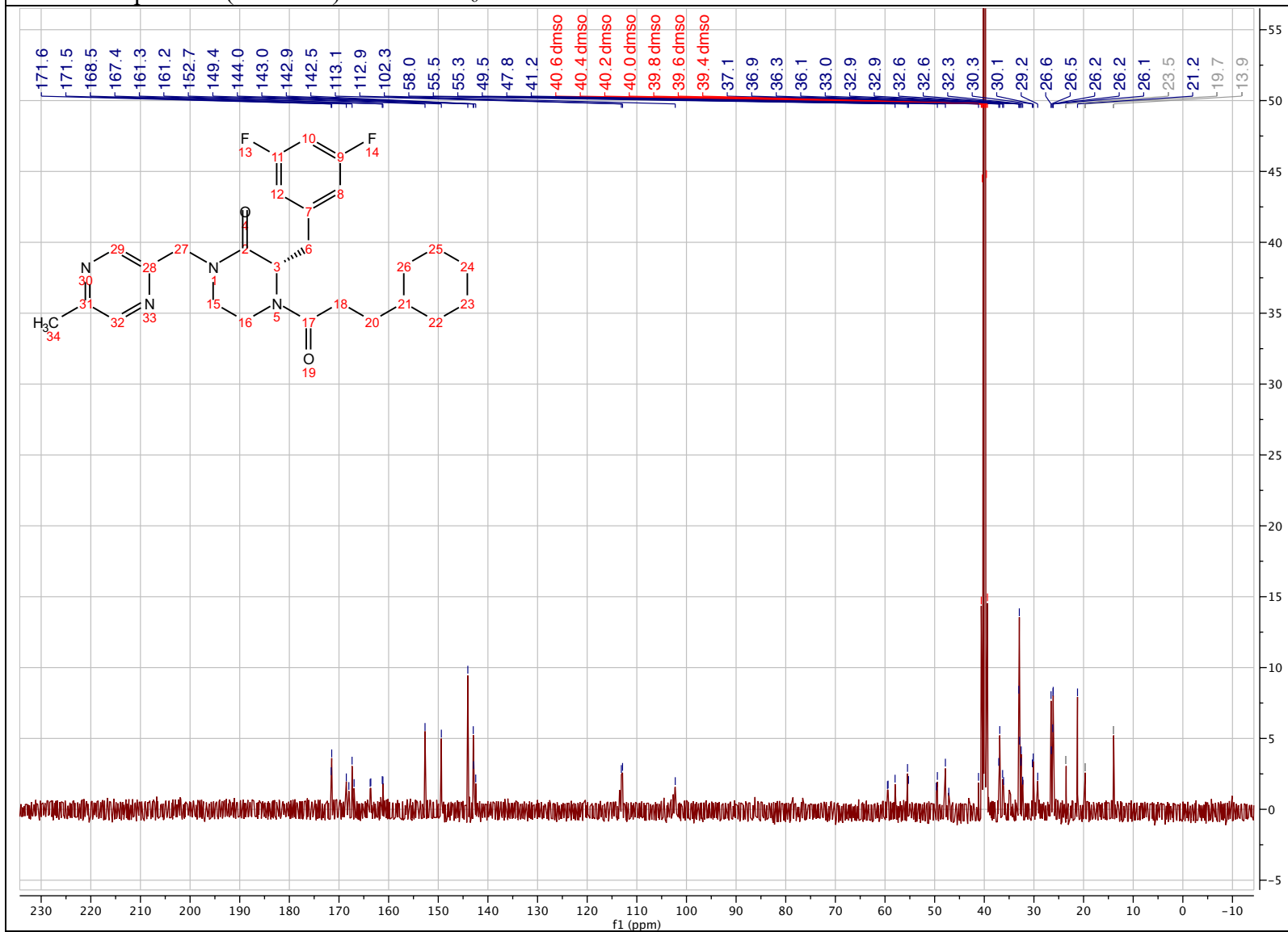
(S)-4-(3-cyclohexylpropanoyl)-3-(3,5-difluorobenzyl)-1-((5-methylpyrazin-2-yl)methyl) piperazin-2-one (2.107)

¹H NMR spectrum (500 MHz) in DMSO-*d*₆



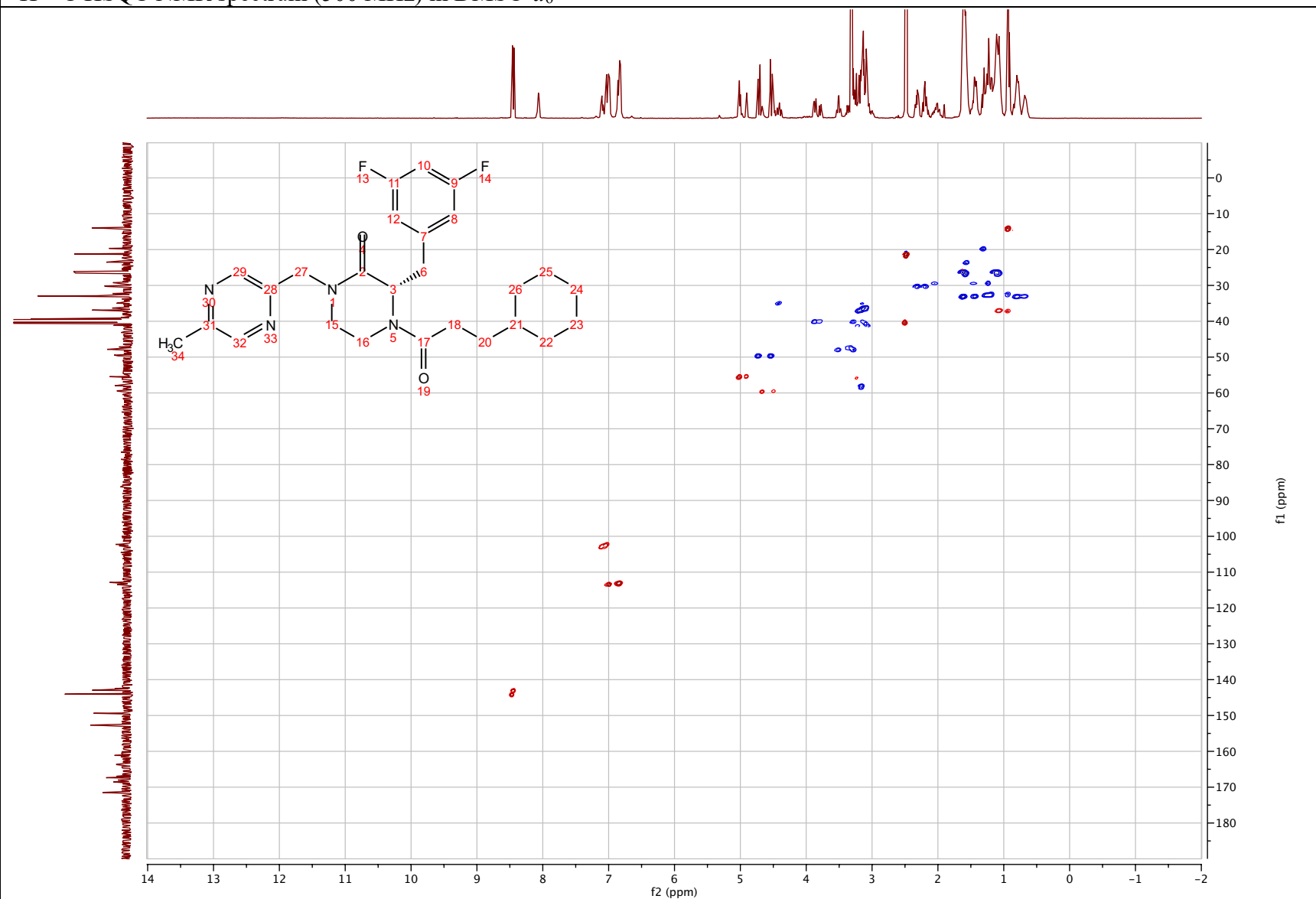
(S)-4-(3-cyclohexylpropanoyl)-3-(3,5-difluorobenzyl)-1-((5-methylpyrazin-2-yl)methyl) piperazin-2-one (2.107)

¹³C NMR spectrum (101 MHz) in DMSO-*d*₆



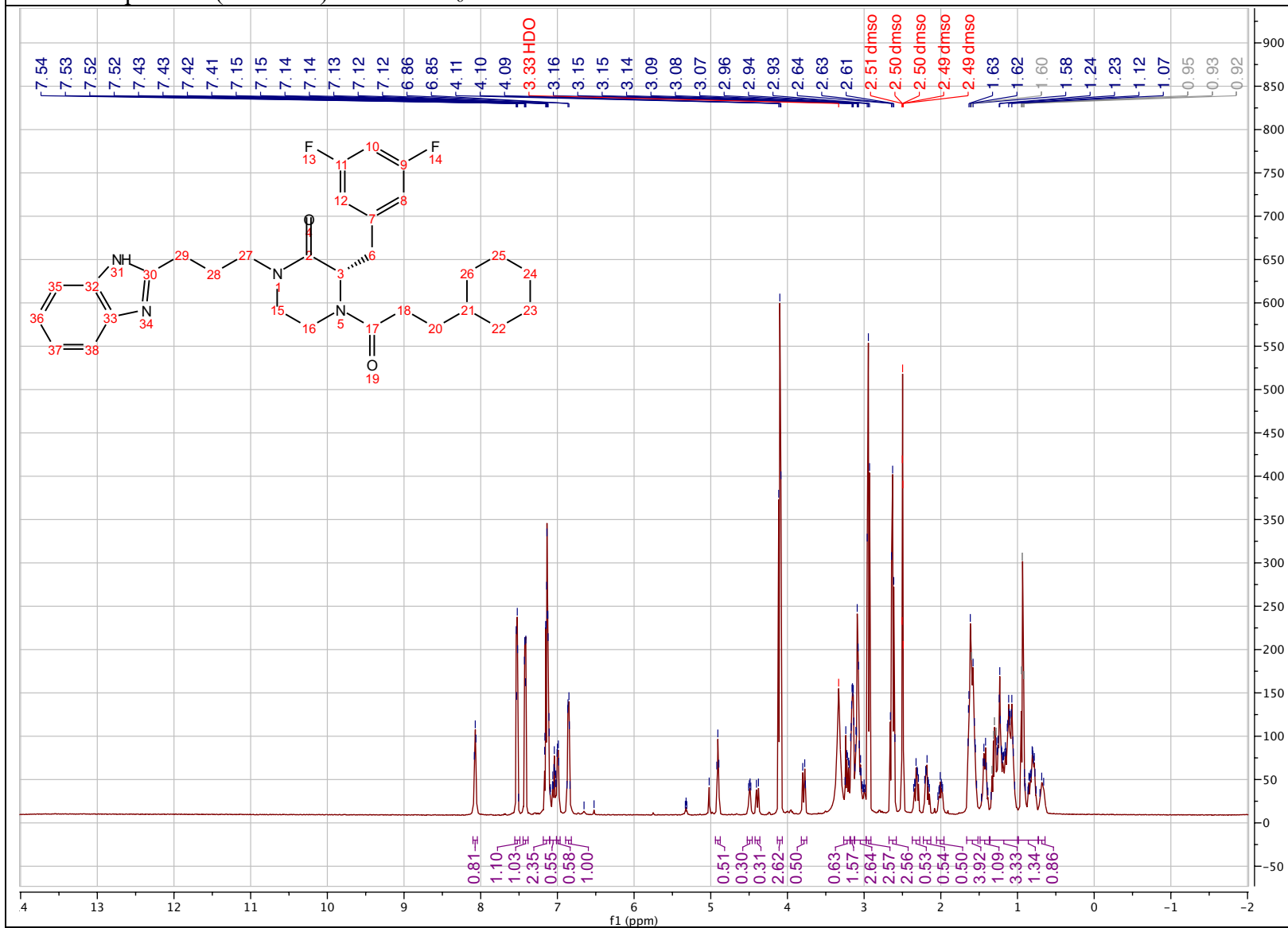
(S)-4-(3-cyclohexylpropanoyl)-3-(3,5-difluorobenzyl)-1-((5-methylpyrazin-2-yl)methyl) piperazin-2-one (2.107)

^1H - ^{13}C HSQC NMR spectrum (500 MHz) in $\text{DMSO-}d_6$



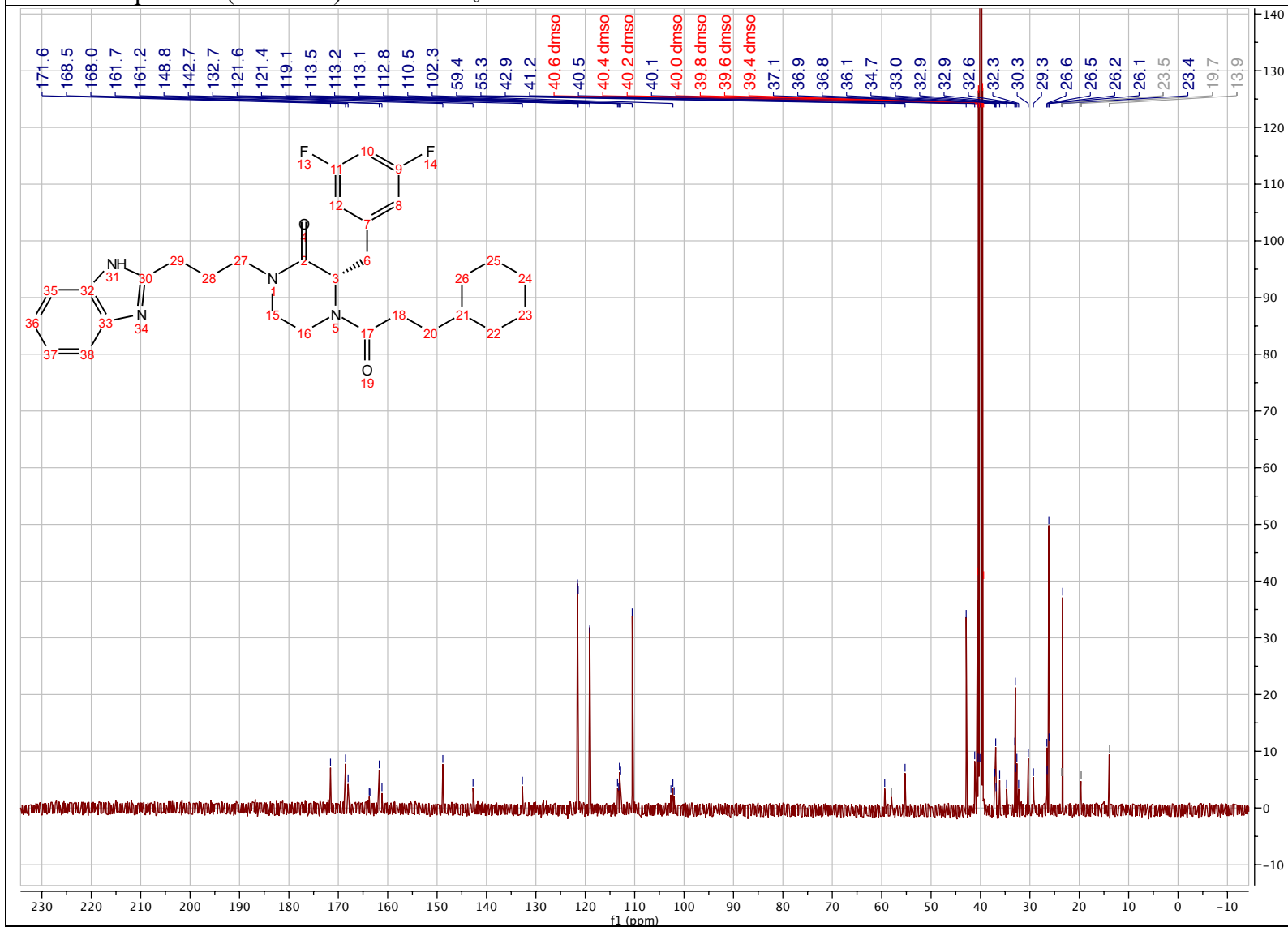
(S)-1-(3-(1H-benzo[d]imidazol-2-yl)propyl)-4-(3-cyclohexylpropanoyl)-3-(3,5-difluorobenzyl) piperazin-2-one (2.108)

¹H NMR spectrum (500 MHz) in DMSO-d₆



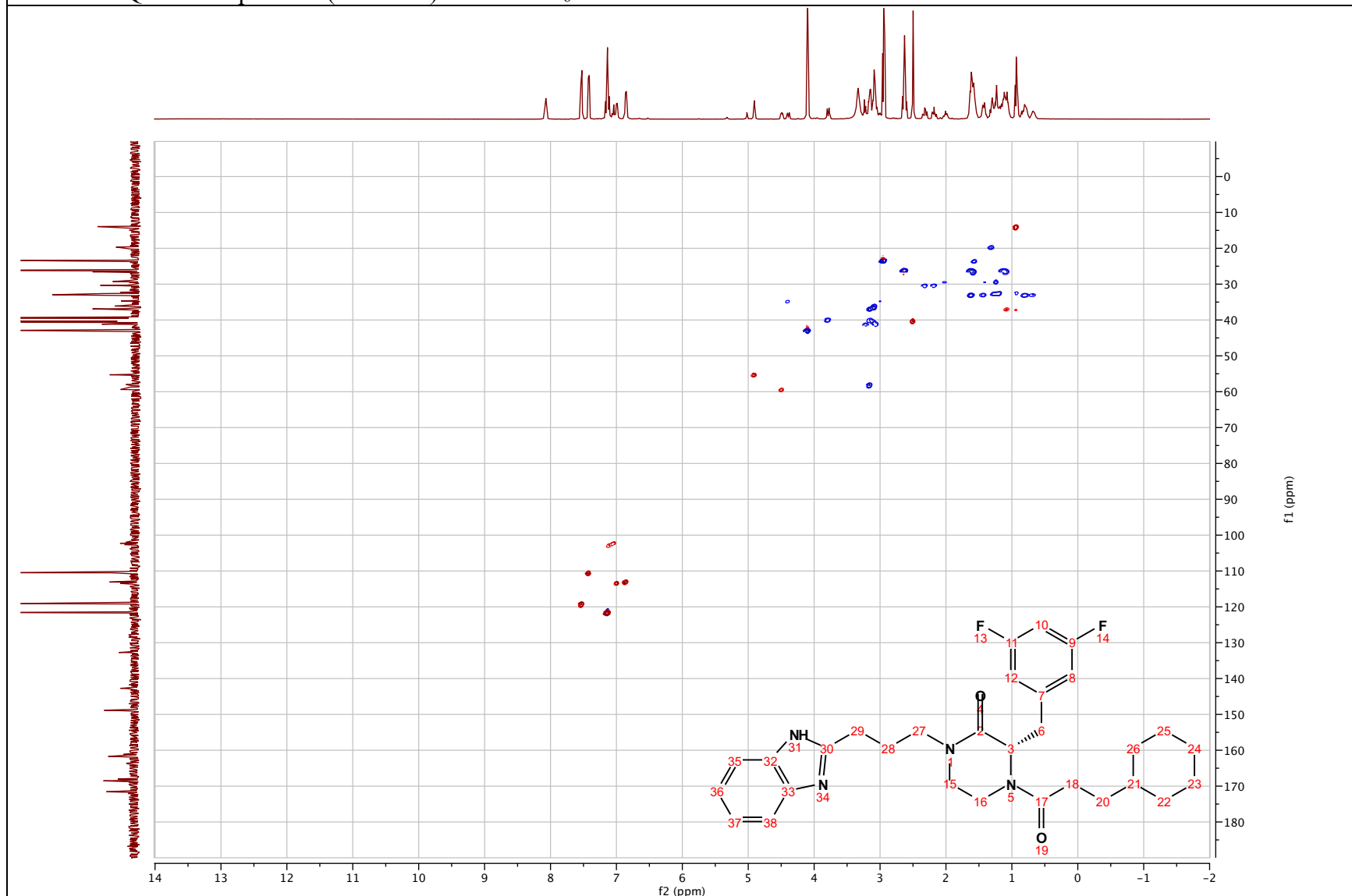
(S)-1-(3-(1H-benzo[d]imidazol-2-yl)propyl)-4-(3-cyclohexylpropanoyl)-3-(3,5-difluorobenzyl) piperazin-2-one (2.108)

¹³C NMR spectrum (101 MHz) in DMSO-d₆



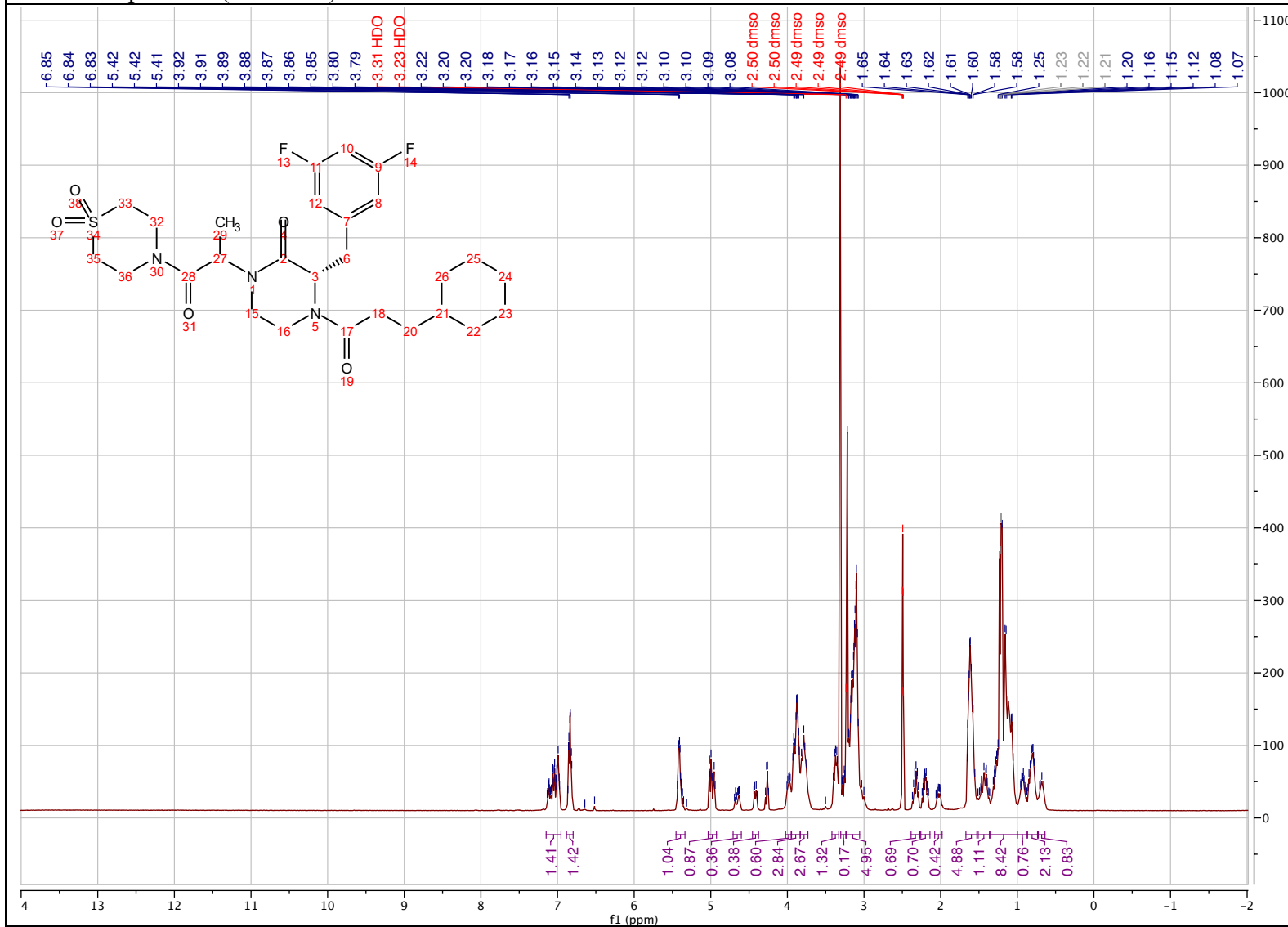
(S)-1-(3-(1H-benzo[d]imidazol-2-yl)propyl)-4-(3-cyclohexylpropanoyl)-3-(3,5-difluorobenzyl) piperazin-2-one (2.108)

^1H - ^{13}C HSQC NMR spectrum (500 MHz) in $\text{DMSO-}d_6$



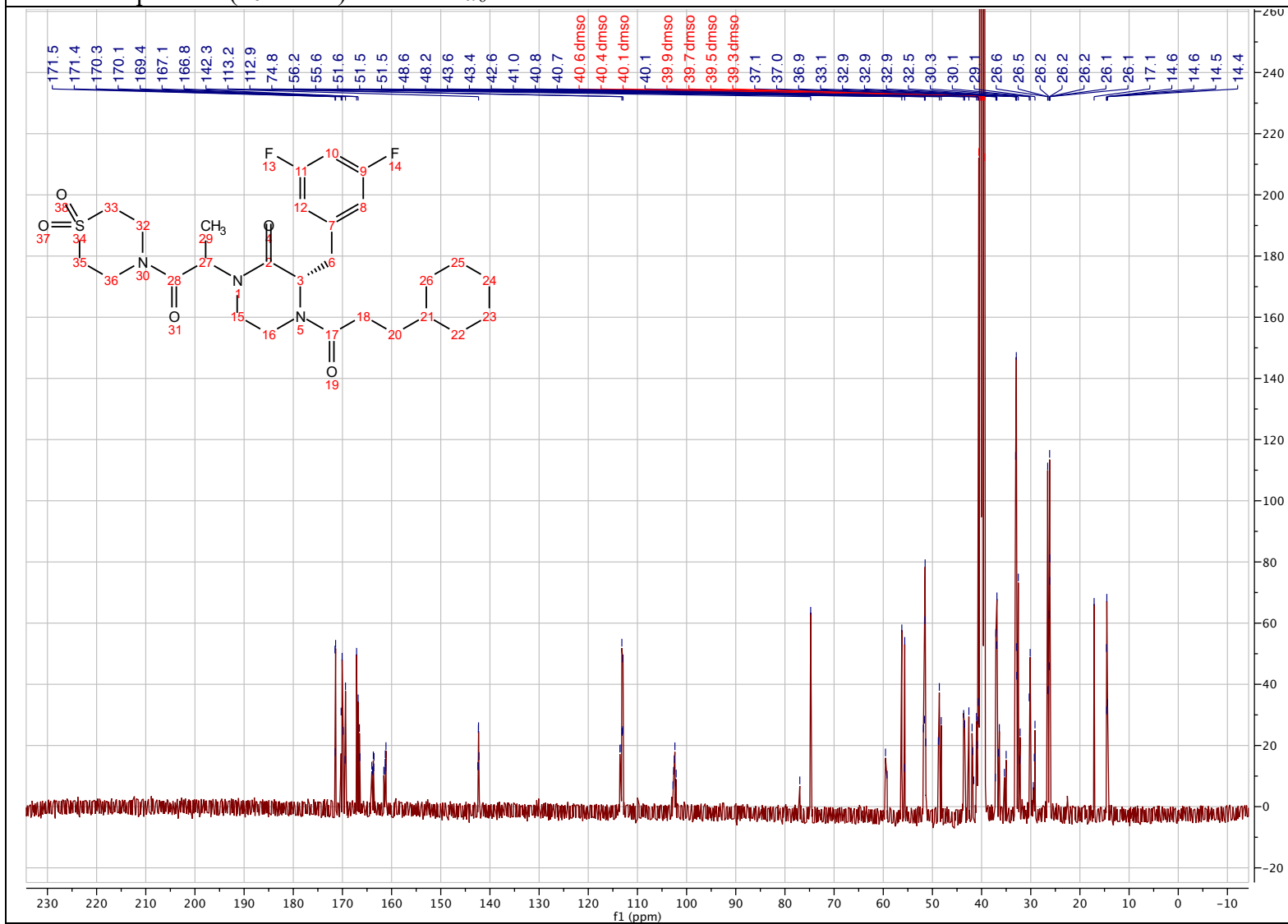
(3S)-4-(3-cyclohexylpropanoyl)-3-(3,5-difluorobenzyl)-1-(1-(1,1-dioxidothiomorpholino)-1-oxopropan-2-yl) piperazin-2-one (2.109)

¹H NMR spectrum (500 MHz) in DMSO-*d*₆



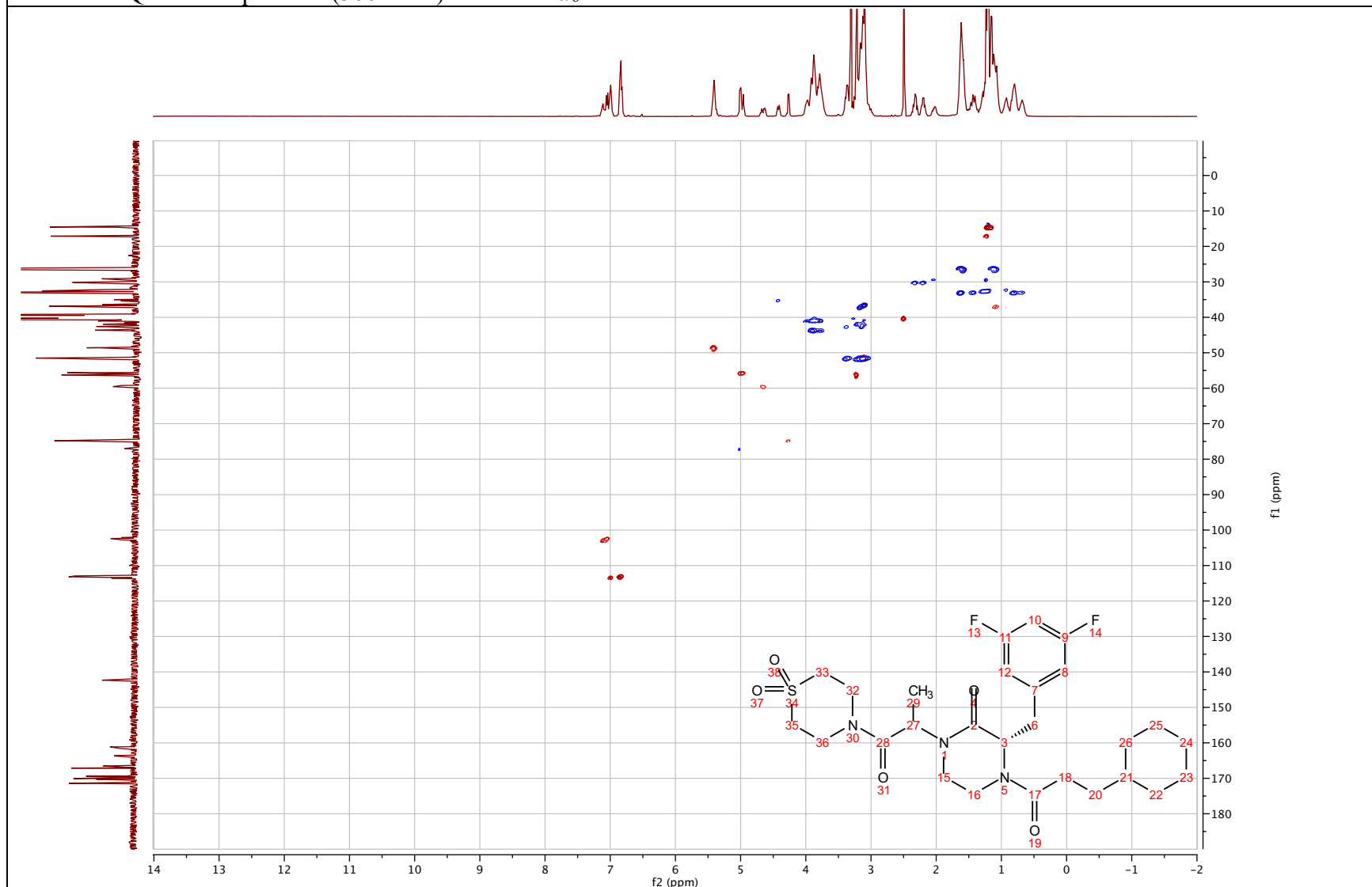
(3*S*)-4-(3-cyclohexylpropanoyl)-3-(3,5-difluorobenzyl)-1-(1-(1,1-dioxidothiomorpholino)-1-oxopropan-2-yl) piperazin-2-one
(2.109)

¹³C NMR spectrum (101 MHz) in DMSO-*d*₆



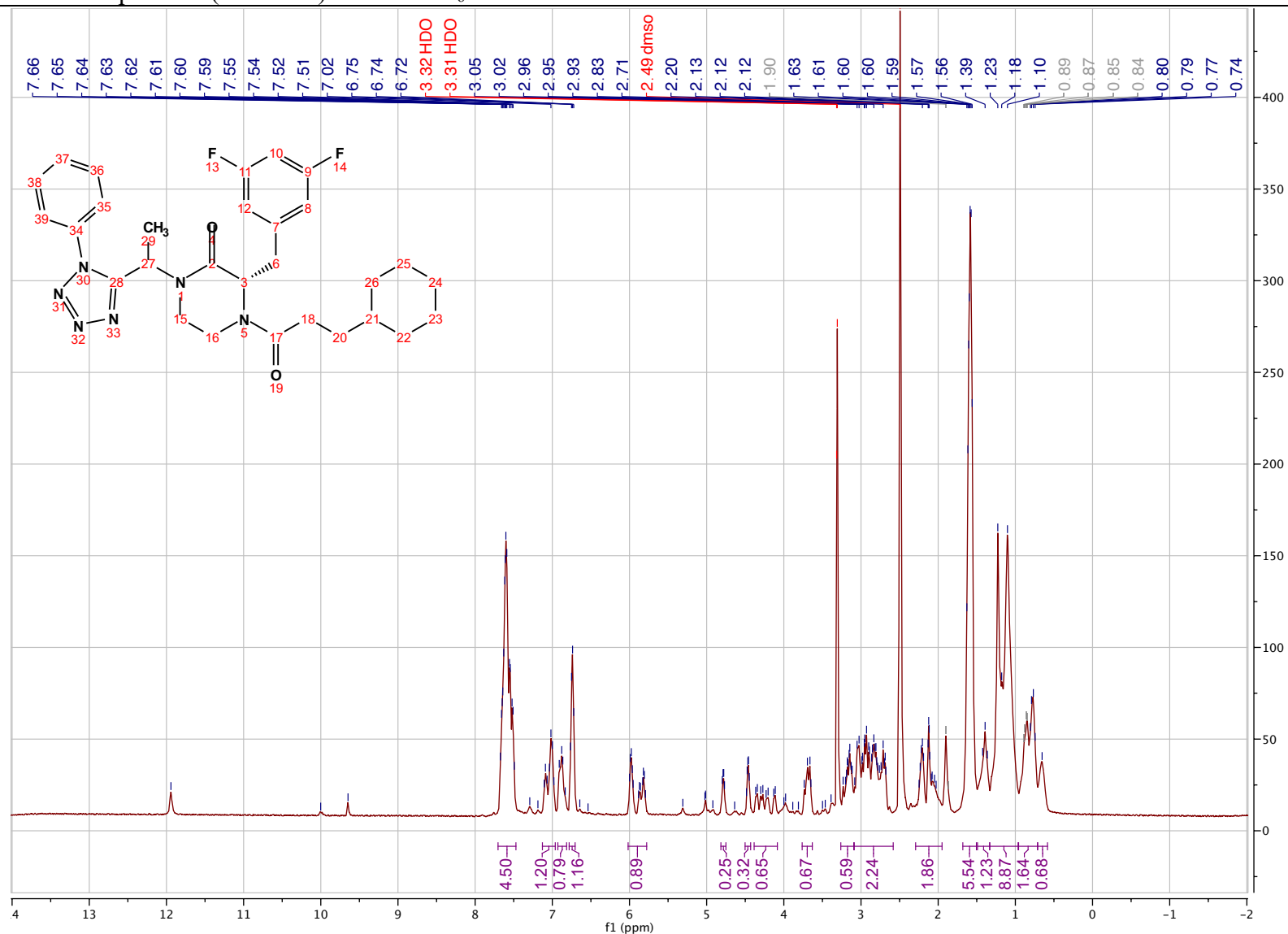
(3*S*)-4-(3-cyclohexylpropanoyl)-3-(3,5-difluorobenzyl)-1-(1-(1,1-dioxidothiomorpholino)-1-oxopropan-2-yl) piperazin-2-one
(2.109)

^1H - ^{13}C HSQC NMR spectrum (500 MHz) in $\text{DMSO-}d_6$



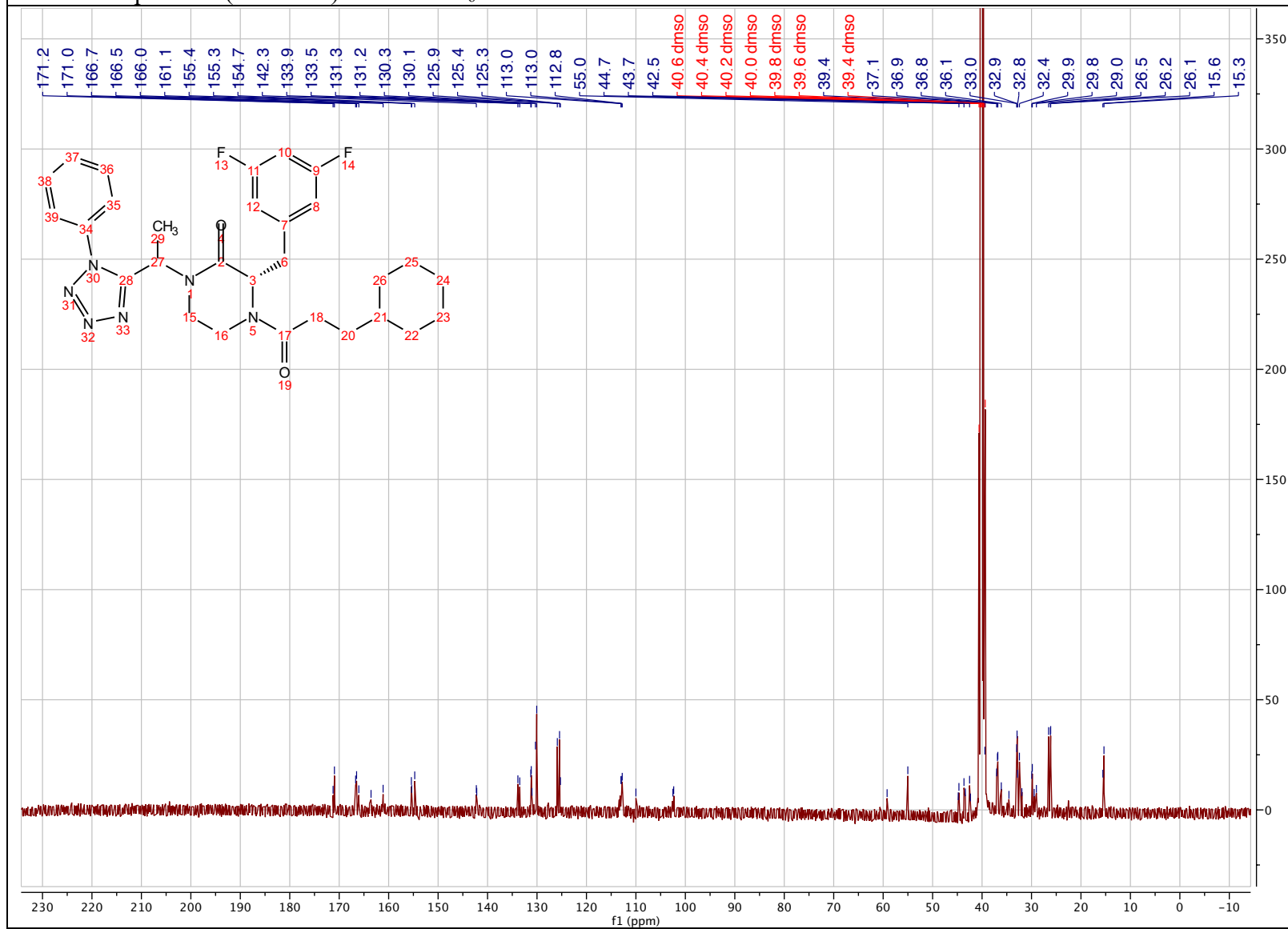
(3S)-4-(3-cyclohexylpropanoyl)-3-(3,5-difluorobenzyl)-1-(1-(1-phenyl-1H-tetrazol-5-yl)ethyl) piperazin-2-one (2.110)

¹H NMR spectrum (500 MHz) in DMSO-*d*₆



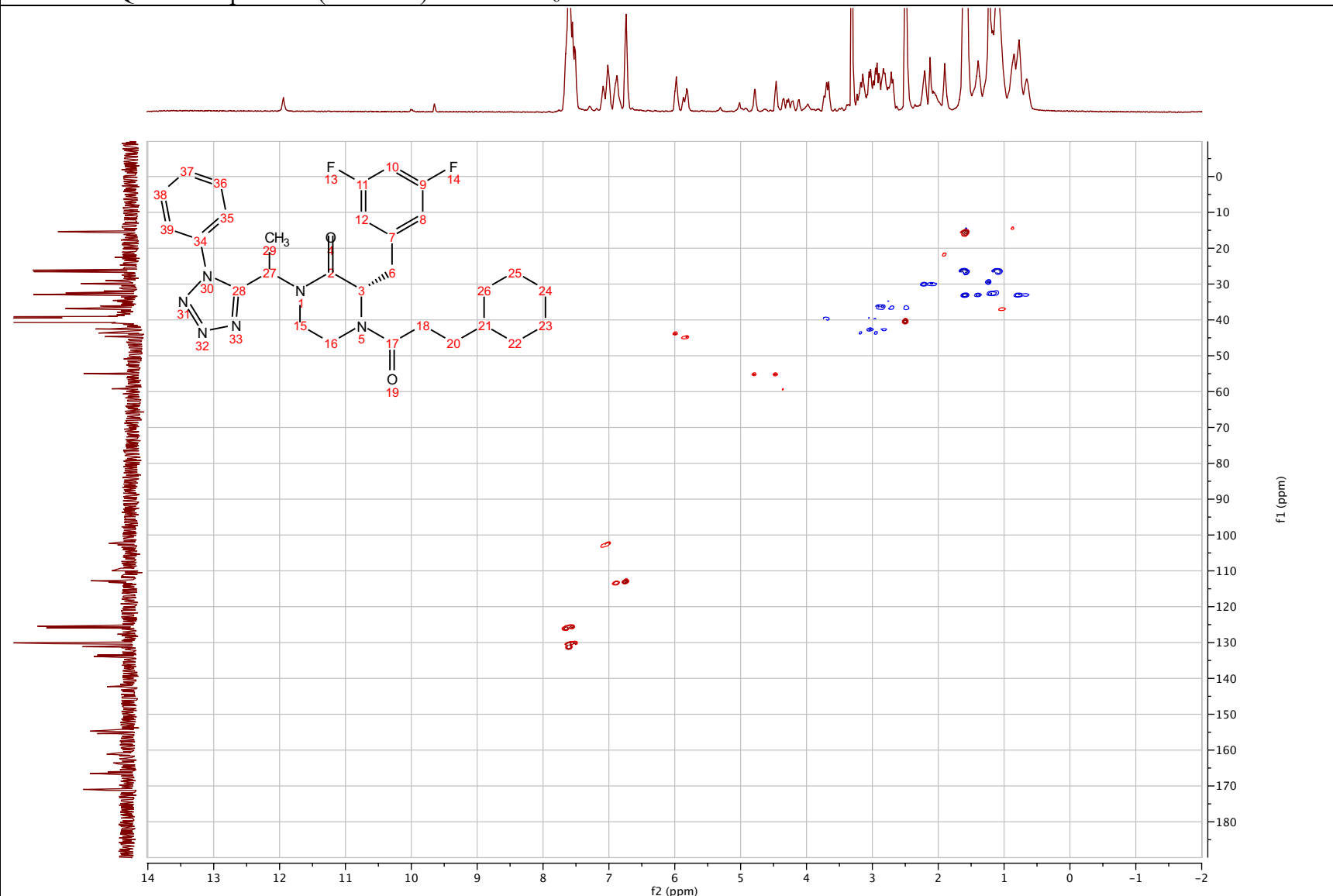
(3S)-4-(3-cyclohexylpropanoyl)-3-(3,5-difluorobenzyl)-1-(1-(1-phenyl-1H-tetrazol-5-yl)ethyl) piperazin-2-one (2.110)

¹³C NMR spectrum (101 MHz) in DMSO-*d*₆



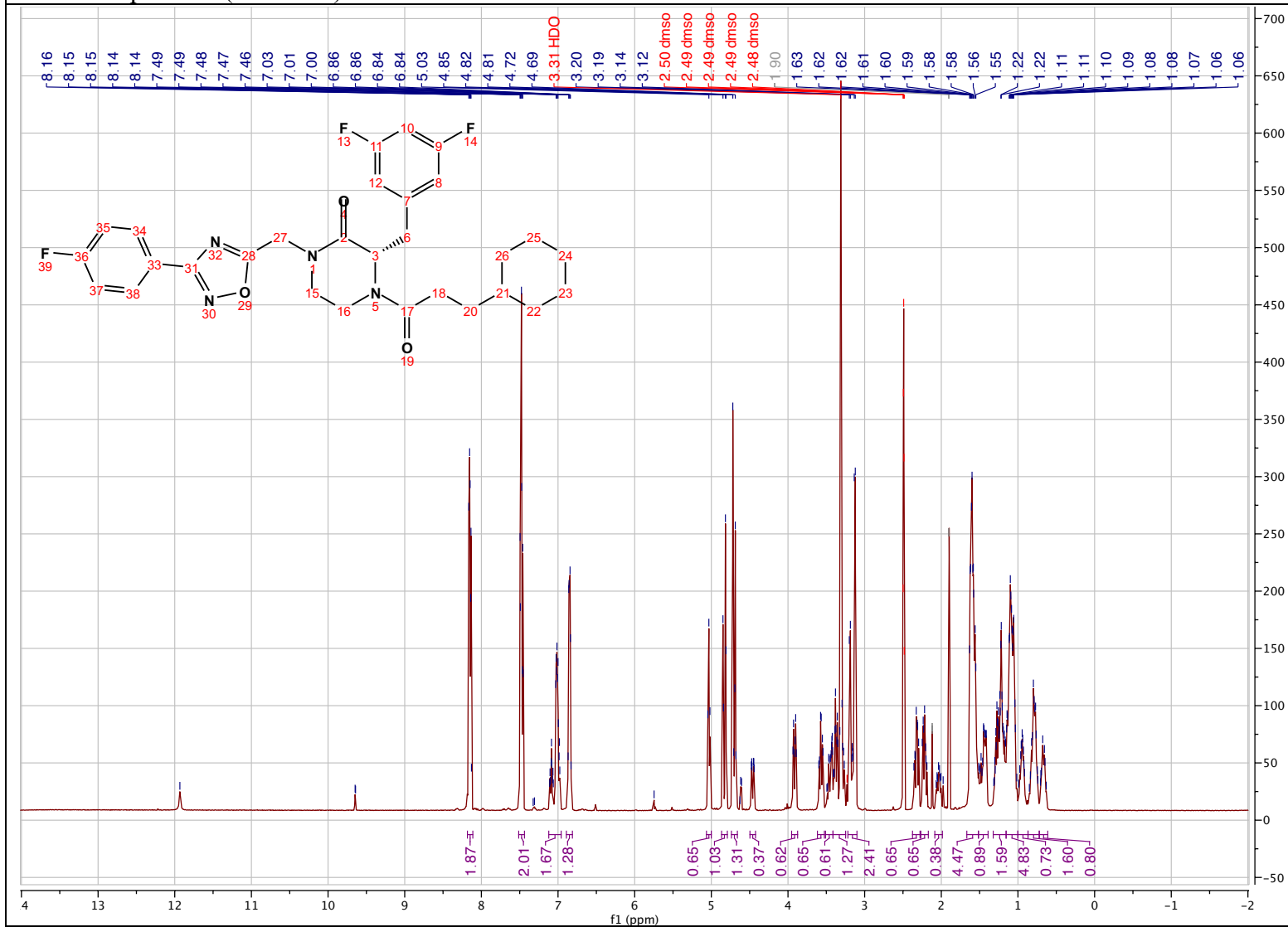
(3*S*)-4-(3-cyclohexylpropanoyl)-3-(3,5-difluorobenzyl)-1-(1-(1-phenyl-1*H*-tetrazol-5-yl)ethyl) piperazin-2-one (2.110)

^1H - ^{13}C HSQC NMR spectrum (500 MHz) in $\text{DMSO-}d_6$



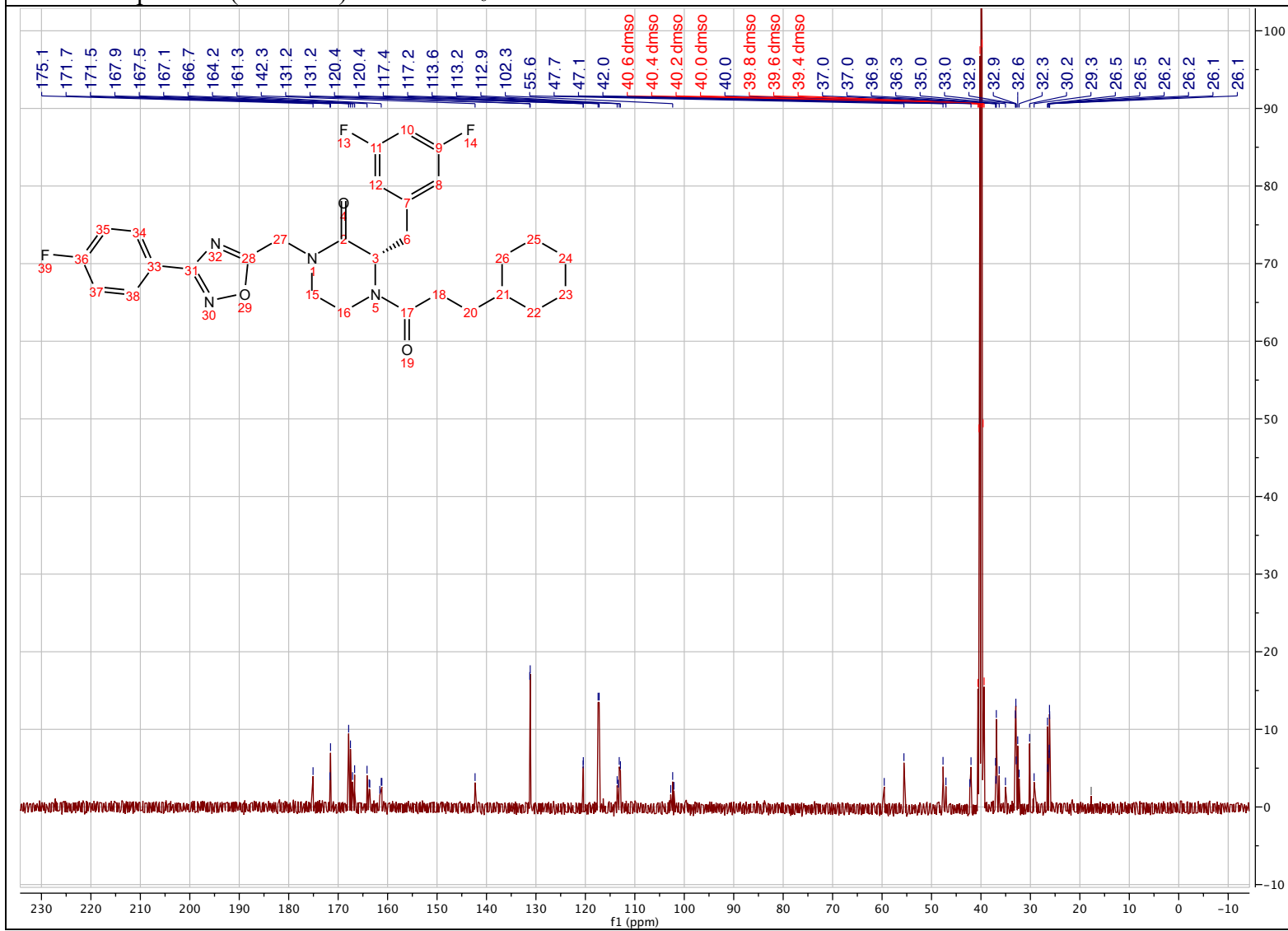
(S)-4-(3-cyclohexylpropanoyl)-3-(3,5-difluorobenzyl)-1-((5-(4-fluorophenyl)-1,2,4-oxadiazol-3-yl)methyl)piperazin-2-one
(2.111)

¹H NMR spectrum (500 MHz) in DMSO-*d*₆



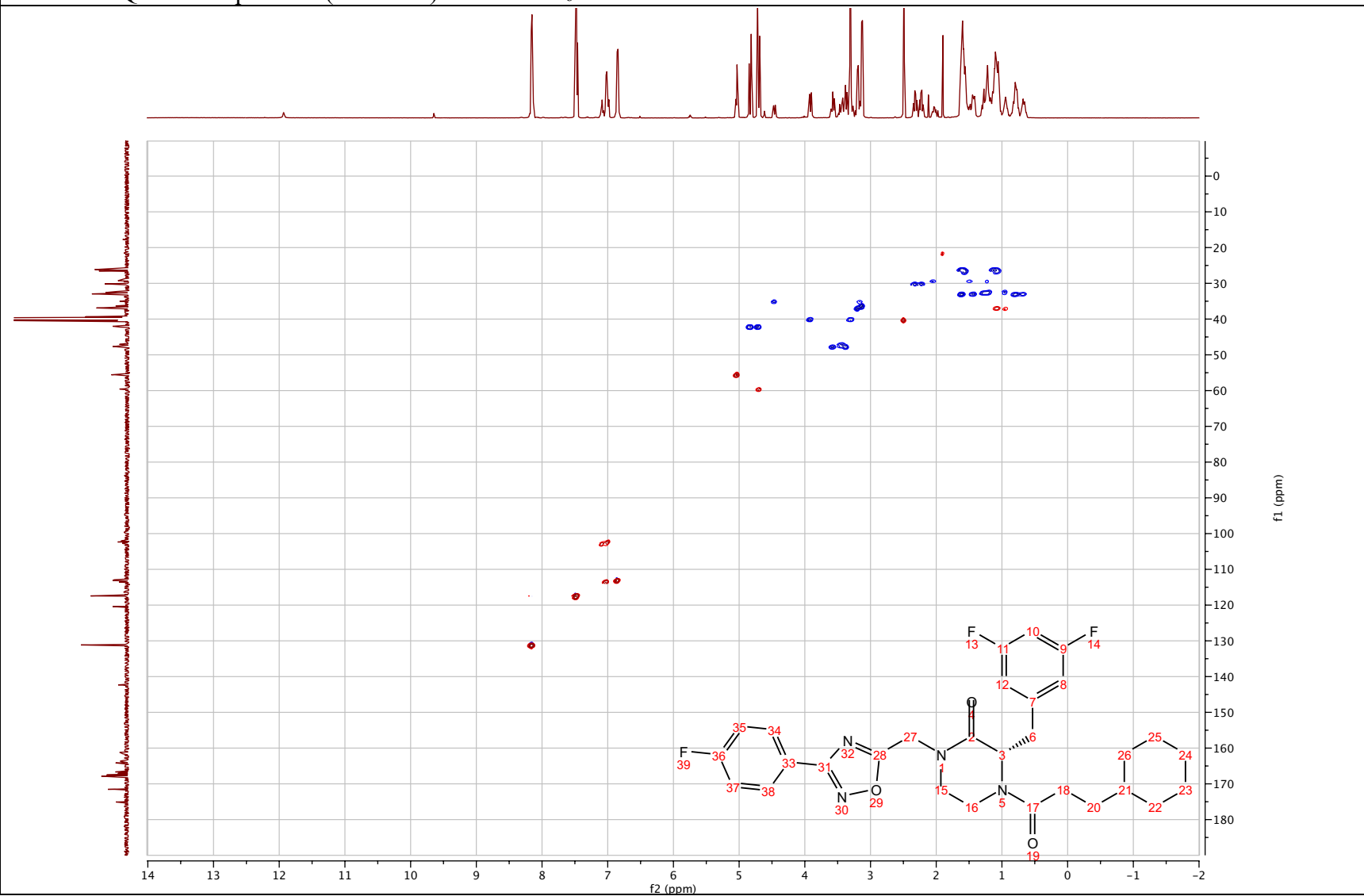
(S)-4-(3-cyclohexylpropanoyl)-3-(3,5-difluorobenzyl)-1-((5-(4-fluorophenyl)-1,2,4-oxadiazol-3-yl)methyl)piperazin-2-one
(2.111)

^{13}C NMR spectrum (101 MHz) in $\text{DMSO-}d_6$



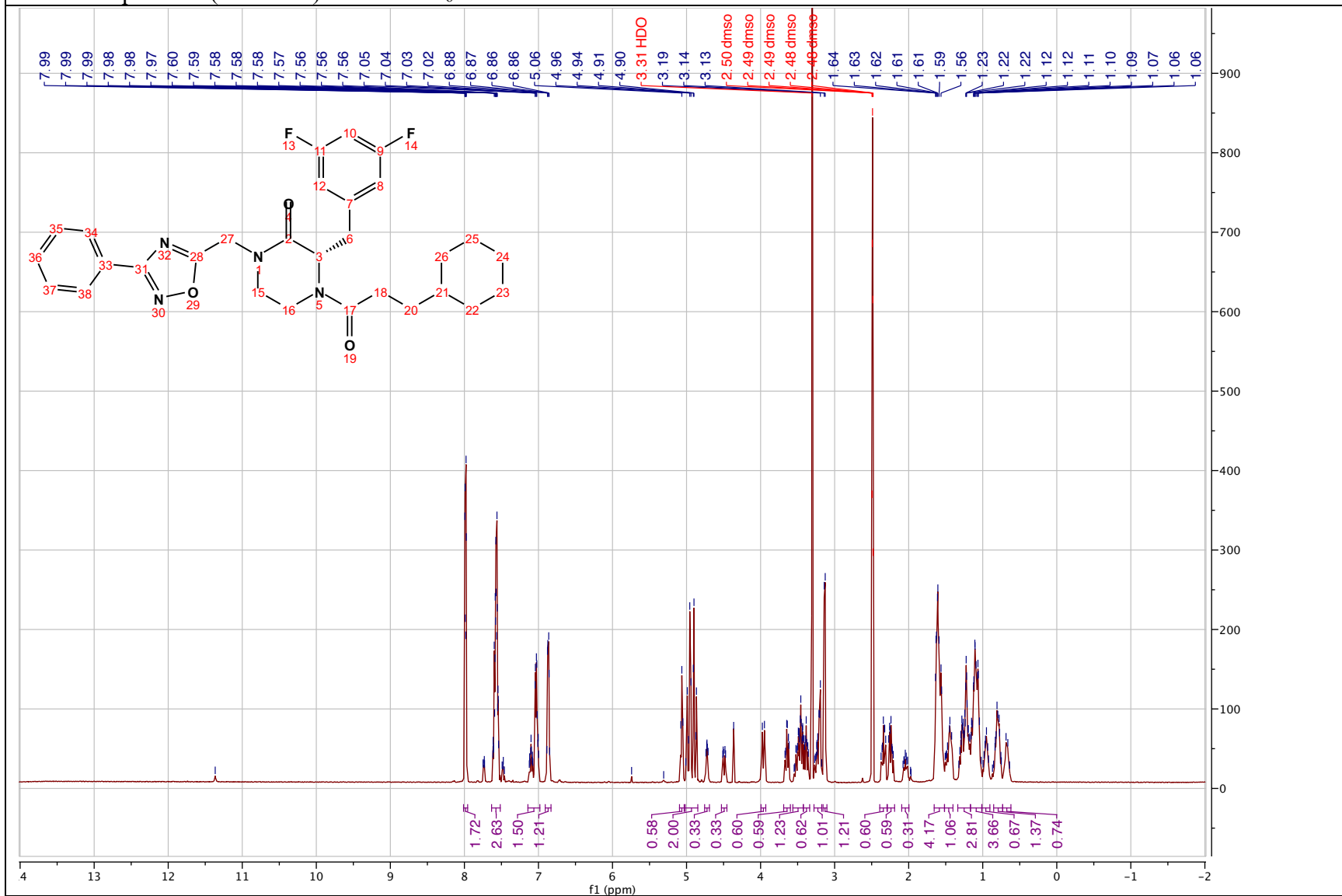
(S)-4-(3-cyclohexylpropanoyl)-3-(3,5-difluorobenzyl)-1-((5-(4-fluorophenyl)-1,2,4-oxadiazol-3-yl)methyl)piperazin-2-one
(2.111)

^1H - ^{13}C HSQC NMR spectrum (500 MHz) in $\text{DMSO-}d_6$



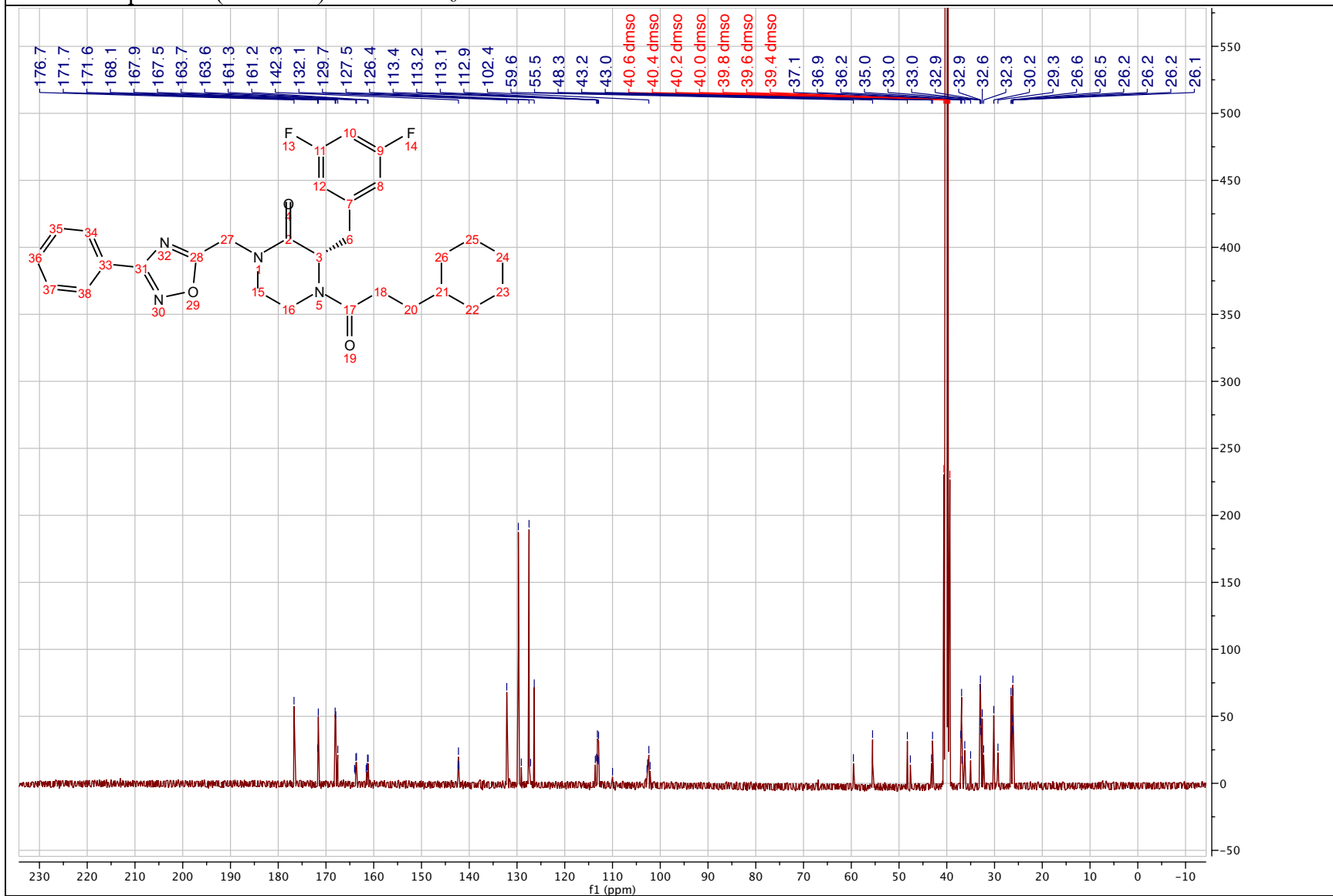
(S)-4-(3-cyclohexylpropanoyl)-3-(3,5-difluorobenzyl)-1-((5-phenyl-1,2,4-oxadiazol-3-yl)methyl)piperazin-2-one (2.112)

¹H NMR spectrum (500 MHz) in DMSO-*d*₆



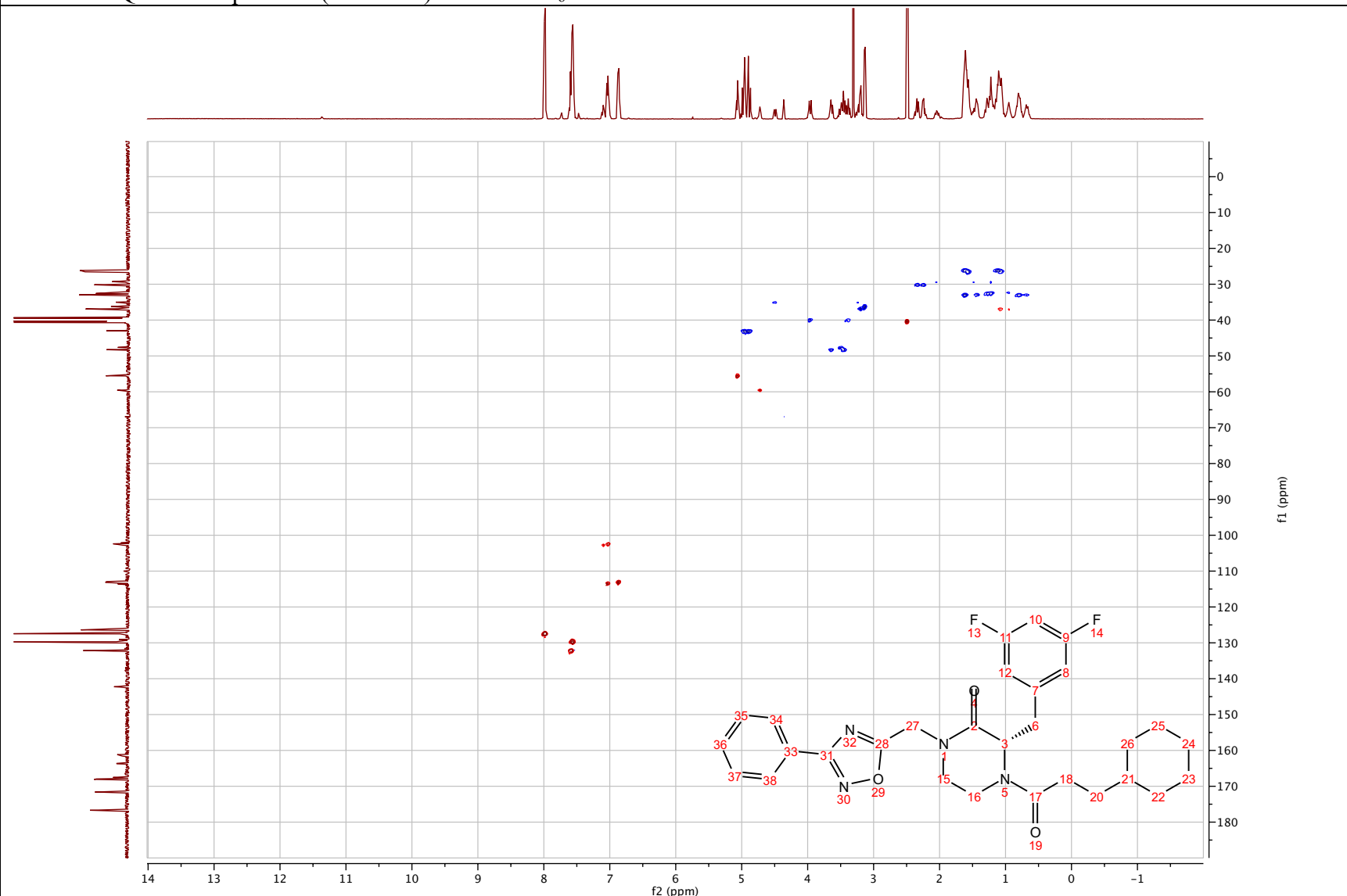
(S)-4-(3-cyclohexylpropanoyl)-3-(3,5-difluorobenzyl)-1-((5-phenyl-1,2,4-oxadiazol-3-yl)methyl)piperazin-2-one (2.112)

¹³C NMR spectrum (101 MHz) in DMSO-*d*₆



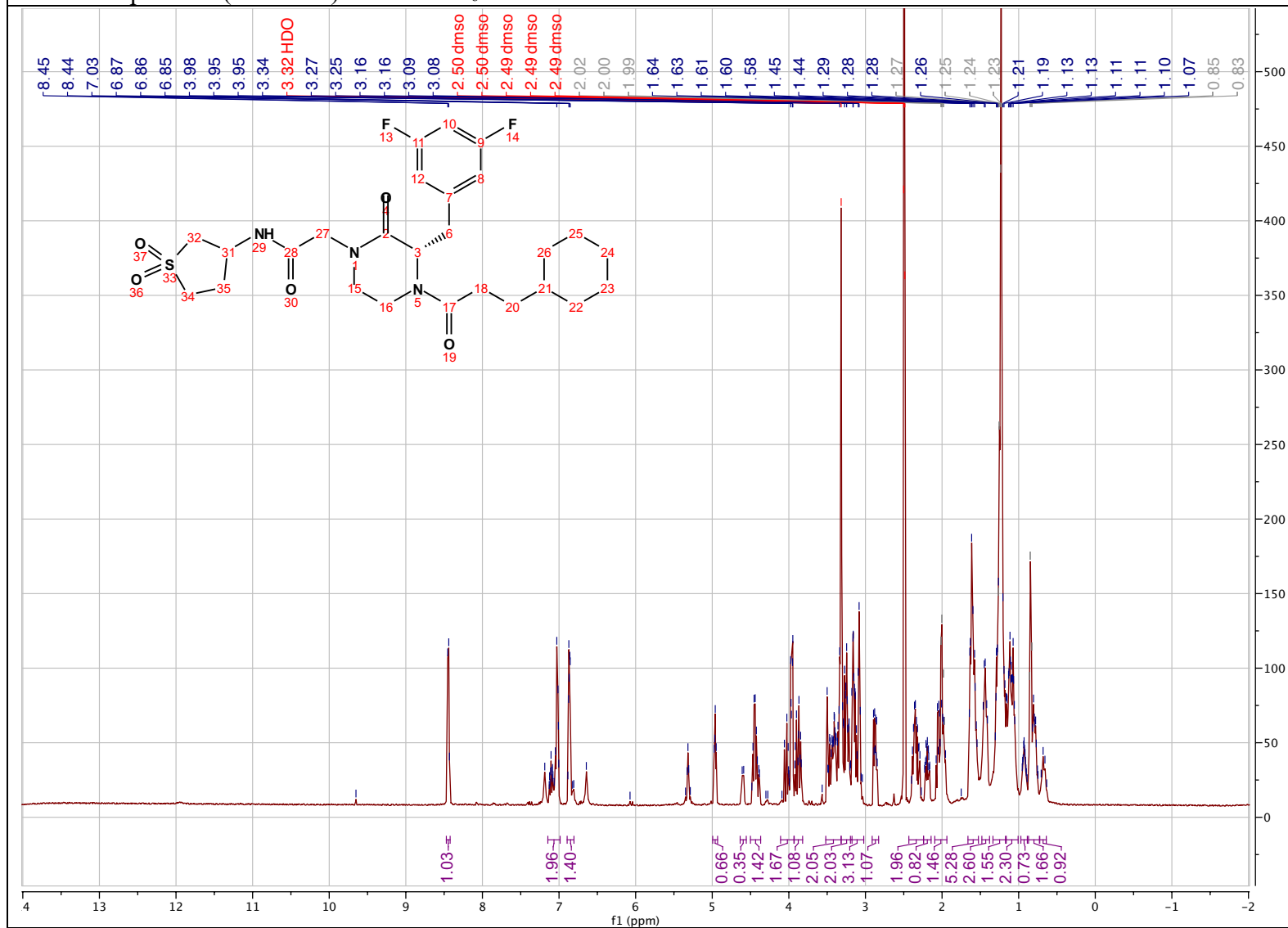
(S)-4-(3-cyclohexylpropanoyl)-3-(3,5-difluorobenzyl)-1-((5-phenyl-1,2,4-oxadiazol-3-yl)methyl)piperazin-2-one (2.112)

^1H - ^{13}C HSQC NMR spectrum (500 MHz) in $\text{DMSO-}d_6$



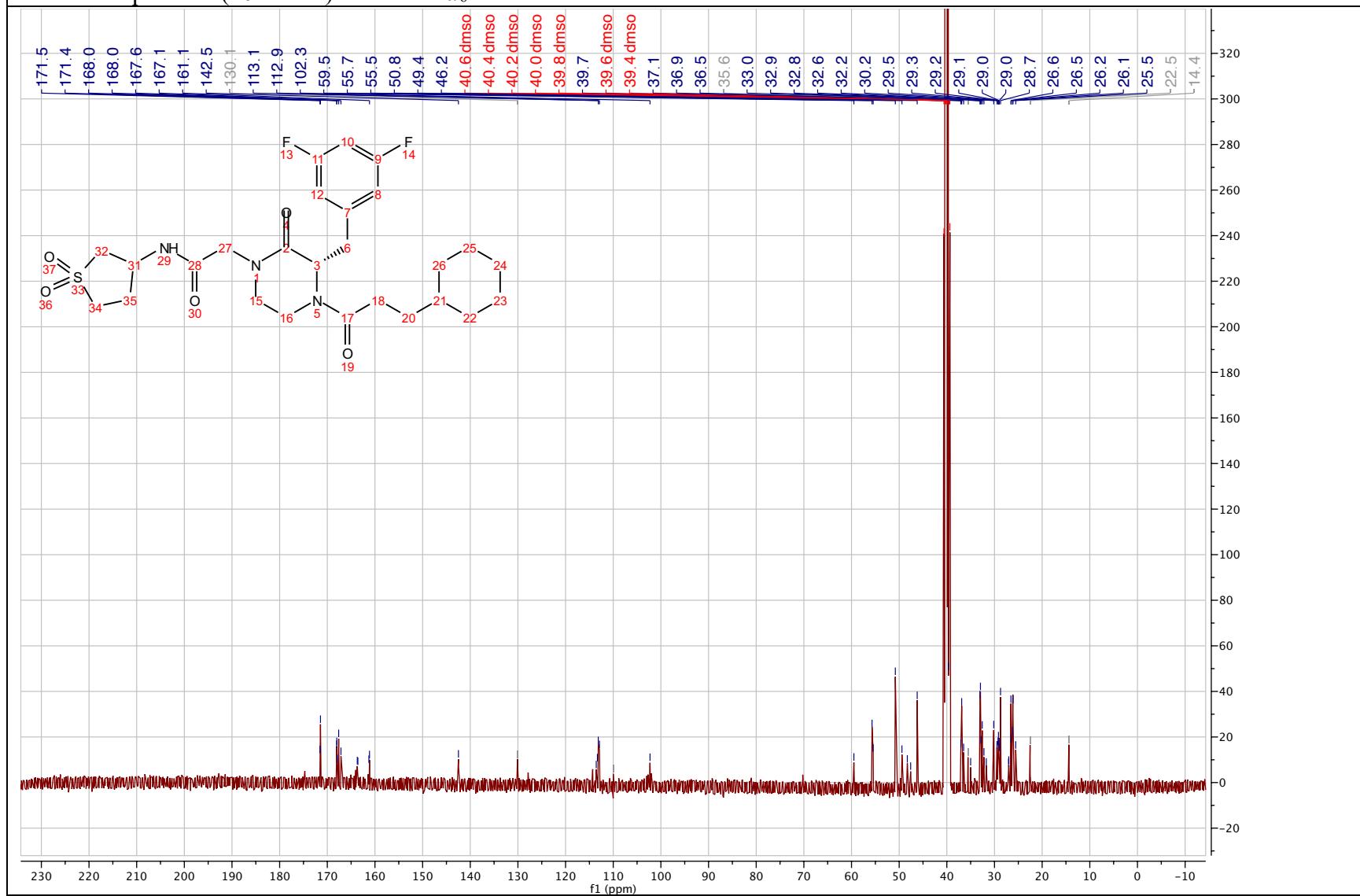
2-((*S*)-4-(3-cyclohexylpropanoyl)-3-(3,5-difluorobenzyl)-2-oxopiperazin-1-yl)-*N*-(1,1-dioxotetrahydrothiophen-3-yl)acetamide (2.113)

^1H NMR spectrum (500 MHz) in $\text{DMSO-}d_6$



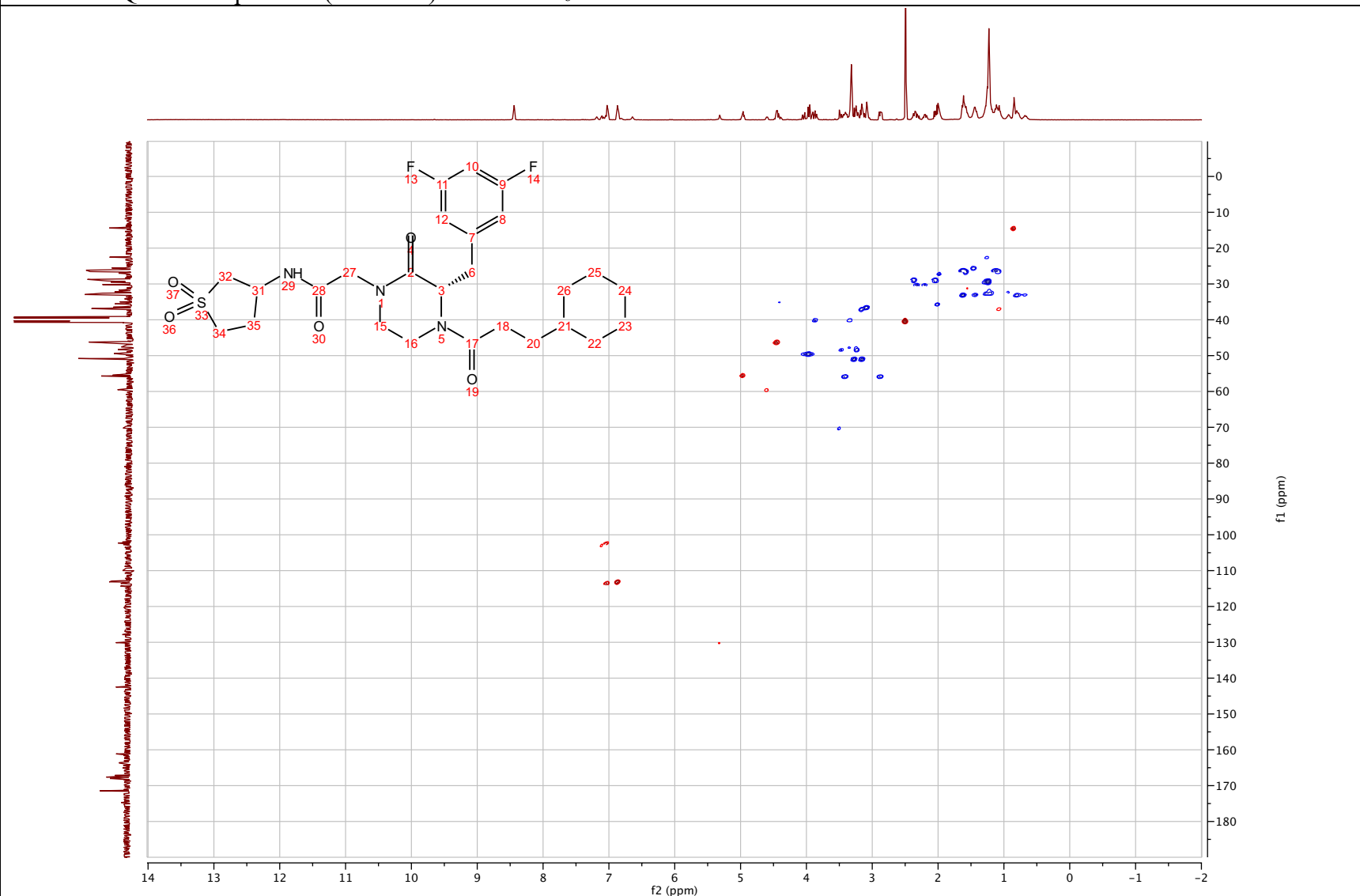
2-((S)-4-(3-cyclohexylpropanoyl)-3-(3,5-difluorobenzyl)-2-oxopiperazin-1-yl)-N-(1,1-dioxidotetrahydrothiophen-3-yl)acetamide (2.113)

¹³C NMR spectrum (101 MHz) in DMSO-*d*₆



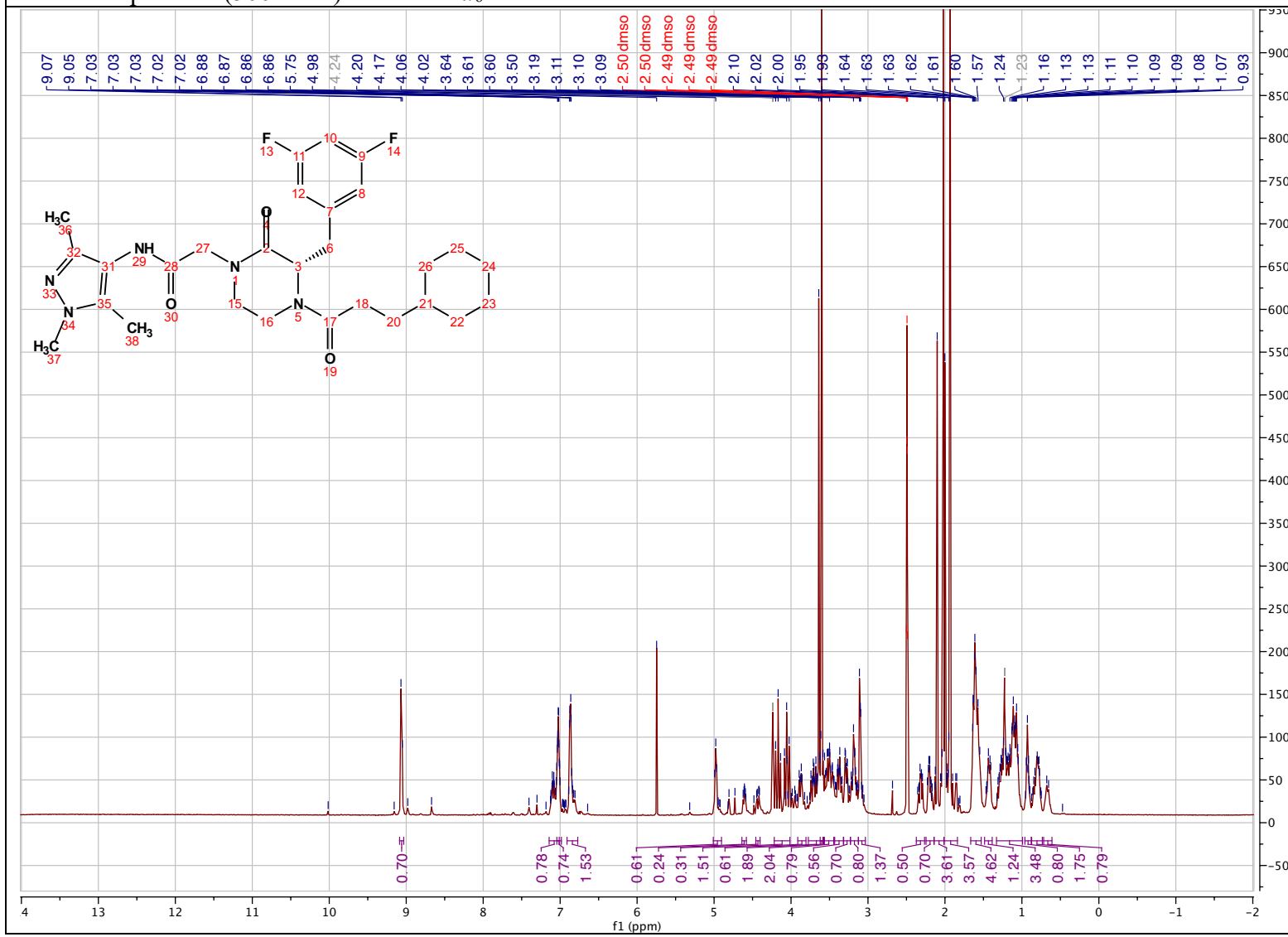
2-((*S*)-4-(3-cyclohexylpropanoyl)-3-(3,5-difluorobenzyl)-2-oxopiperazin-1-yl)-*N*-(1,1-dioxidotetrahydrothiophen-3-yl)acetamide (2.113)

^1H - ^{13}C HSQC NMR spectrum (500 MHz) in $\text{DMSO-}d_6$



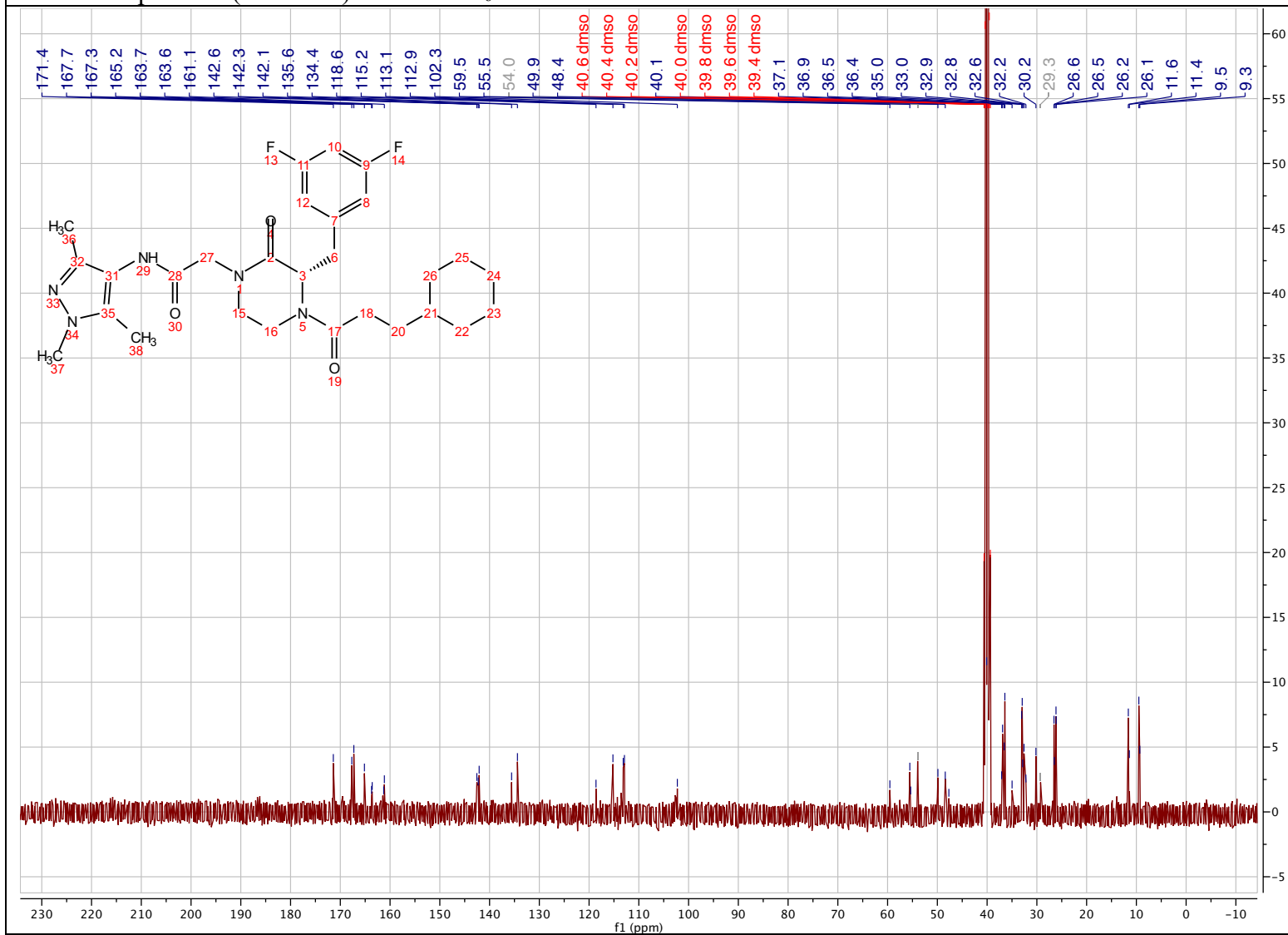
(S)-2-(4-(3-cyclohexylpropanoyl)-3-(3,5-difluorobenzyl)-2-oxopiperazin-1-yl)-N-(1,3,5-trimethyl-1H-pyrazol-4-yl)acetamide (2.114)

¹H NMR spectrum (500 MHz) in DMSO-*d*₆



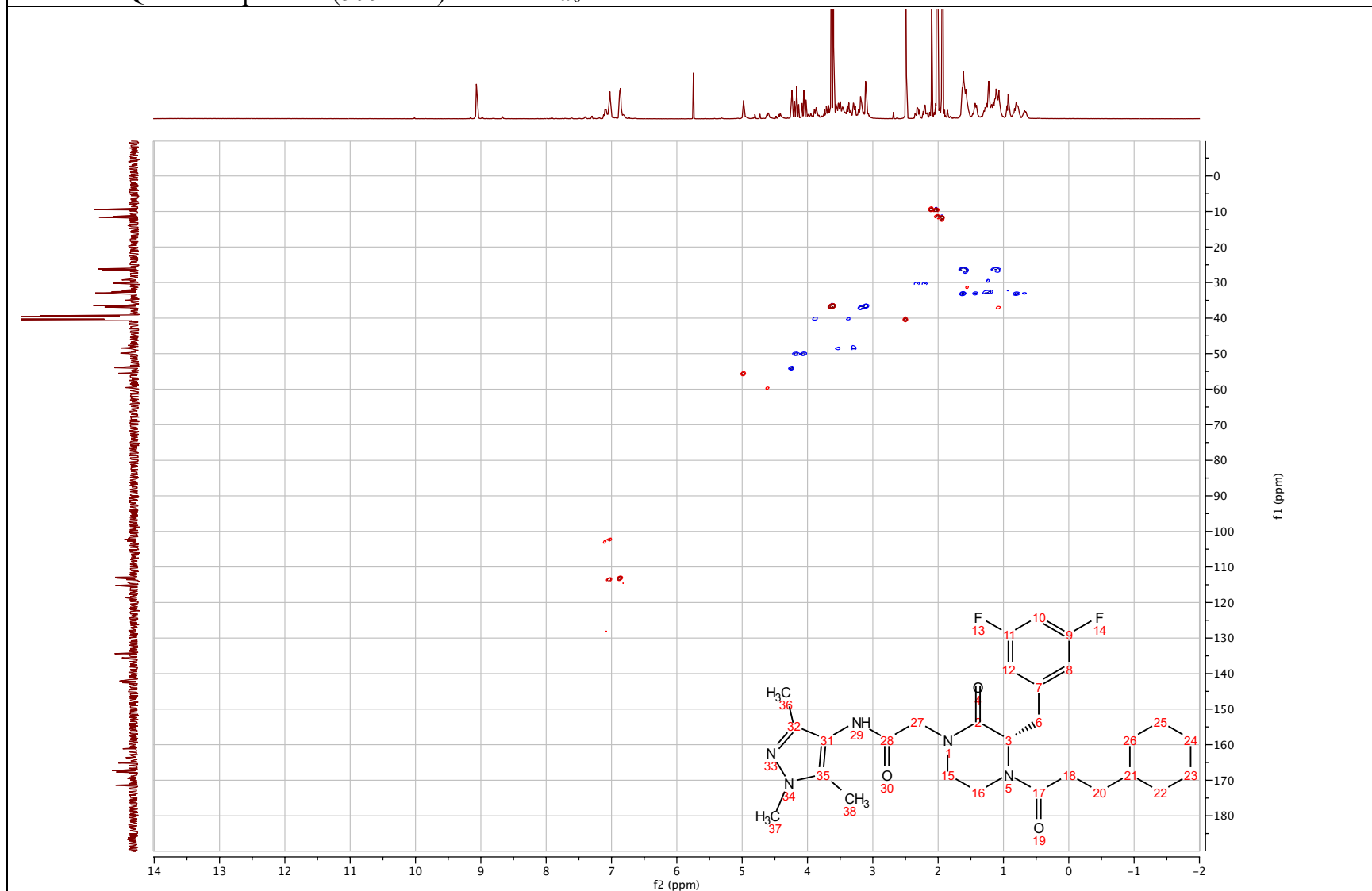
(S)-2-(4-(3-cyclohexylpropanoyl)-3-(3,5-difluorobenzyl)-2-oxopiperazin-1-yl)-N-(1,3,5-trimethyl-1H-pyrazol-4-yl)acetamide (2.114)

^{13}C NMR spectrum (101 MHz) in $\text{DMSO-}d_6$



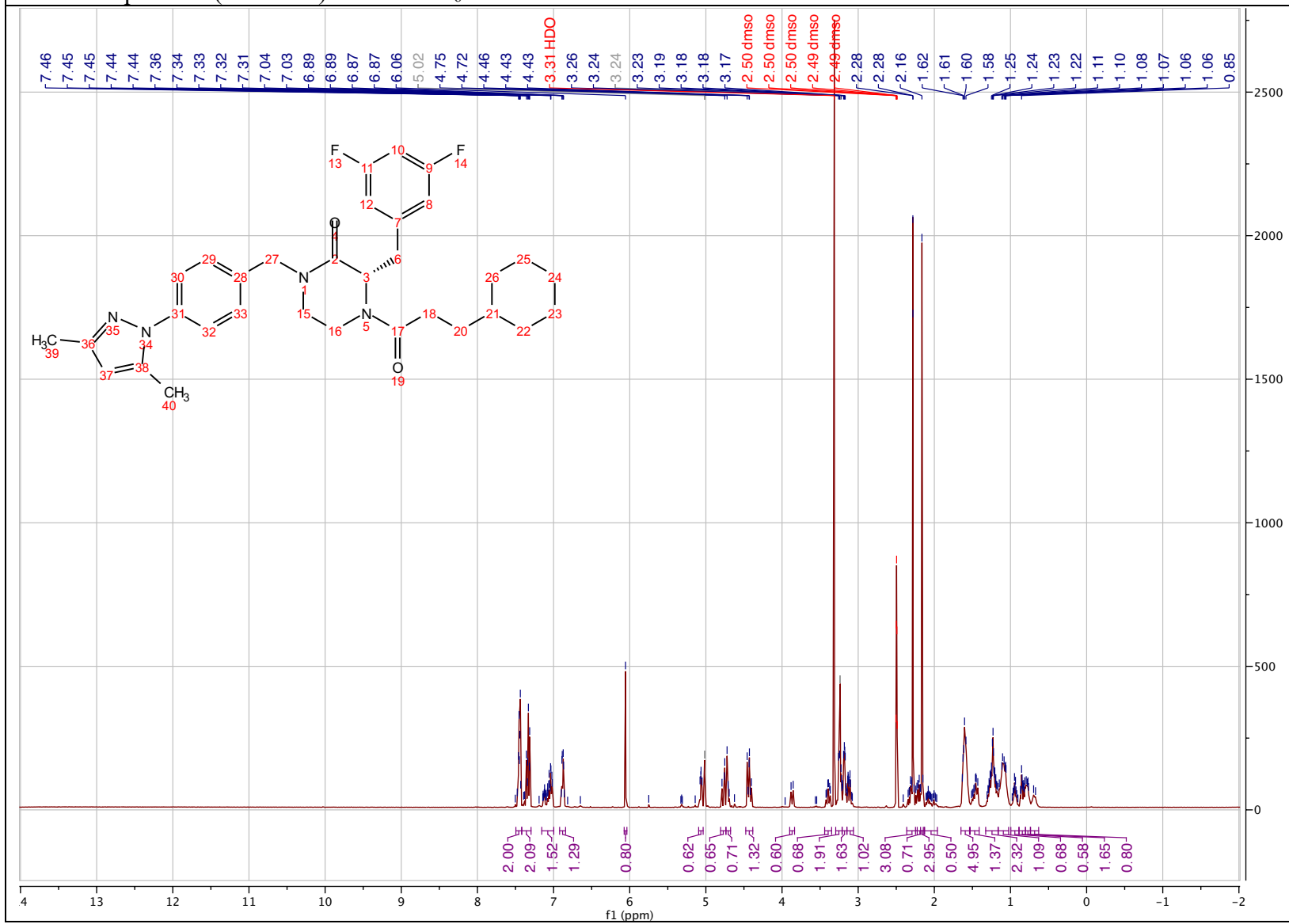
(S)-2-(4-(3-cyclohexylpropanoyl)-3-(3,5-difluorobenzyl)-2-oxopiperazin-1-yl)-N-(1,3,5-trimethyl-1H-pyrazol-4-yl)acetamide
(2.114)

^1H - ^{13}C HSQC NMR spectrum (500 MHz) in $\text{DMSO-}d_6$



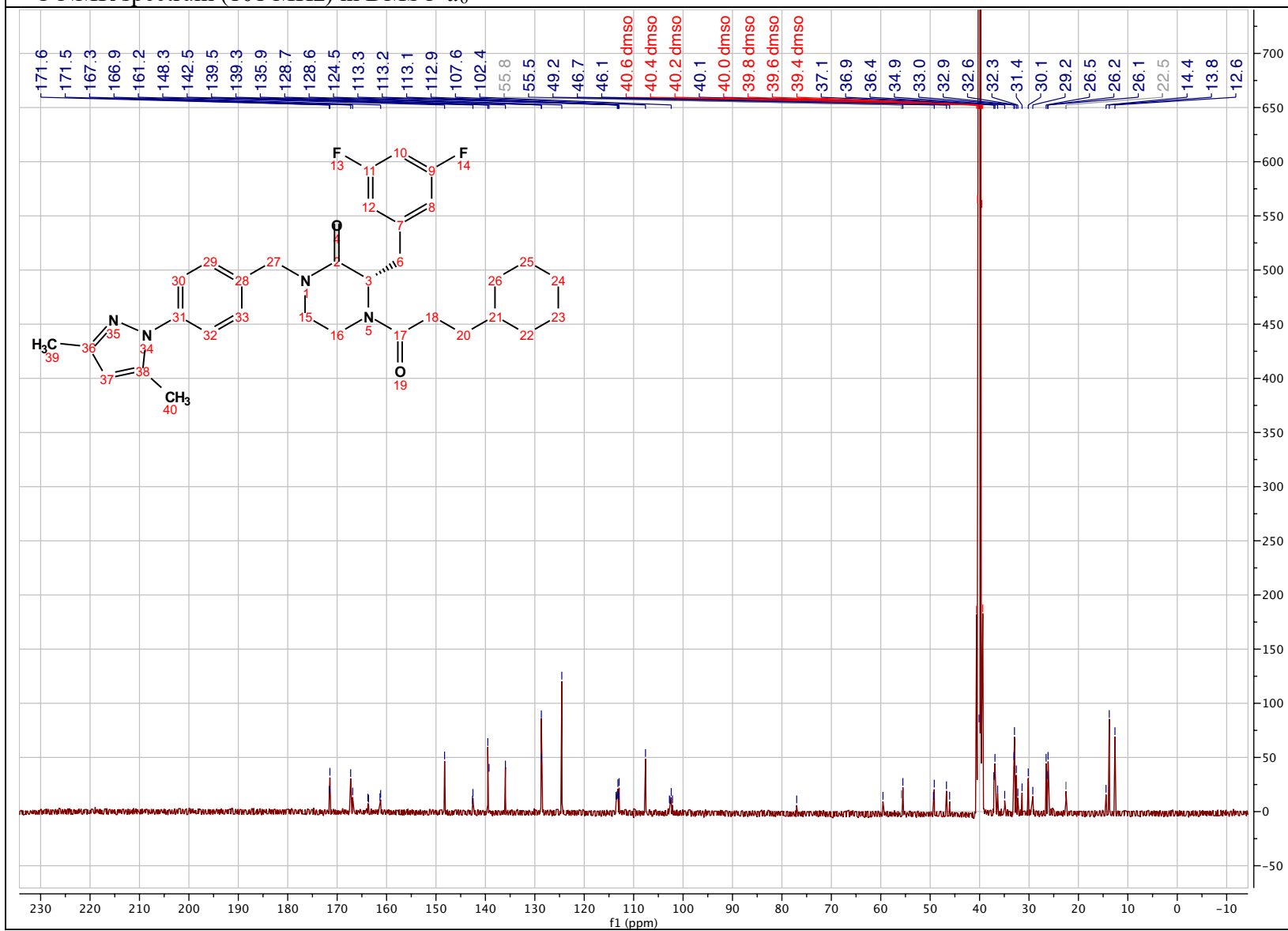
(S)-4-(3-cyclohexylpropanoyl)-3-(3,5-difluorobenzyl)-1-(4-(3,5-dimethyl-1H-pyrazol-1-yl)benzyl)piperazin-2-one (2.115)

¹H NMR spectrum (500 MHz) in DMSO-*d*₆



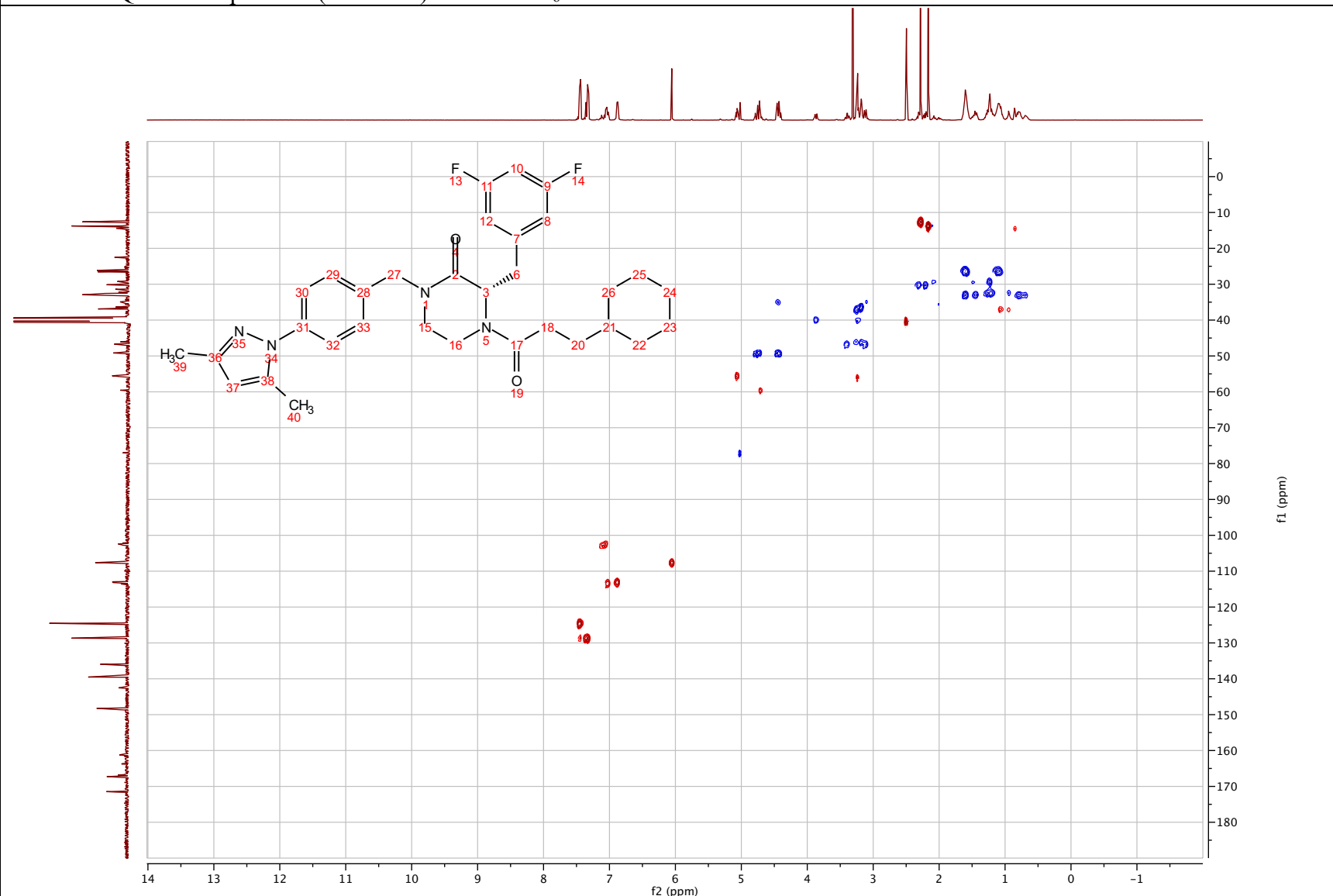
(S)-4-(3-cyclohexylpropanoyl)-3-(3,5-difluorobenzyl)-1-(4-(3,5-dimethyl-1H-pyrazol-1-yl)benzyl)piperazin-2-one (2.115)

¹³C NMR spectrum (101 MHz) in DMSO-*d*₆



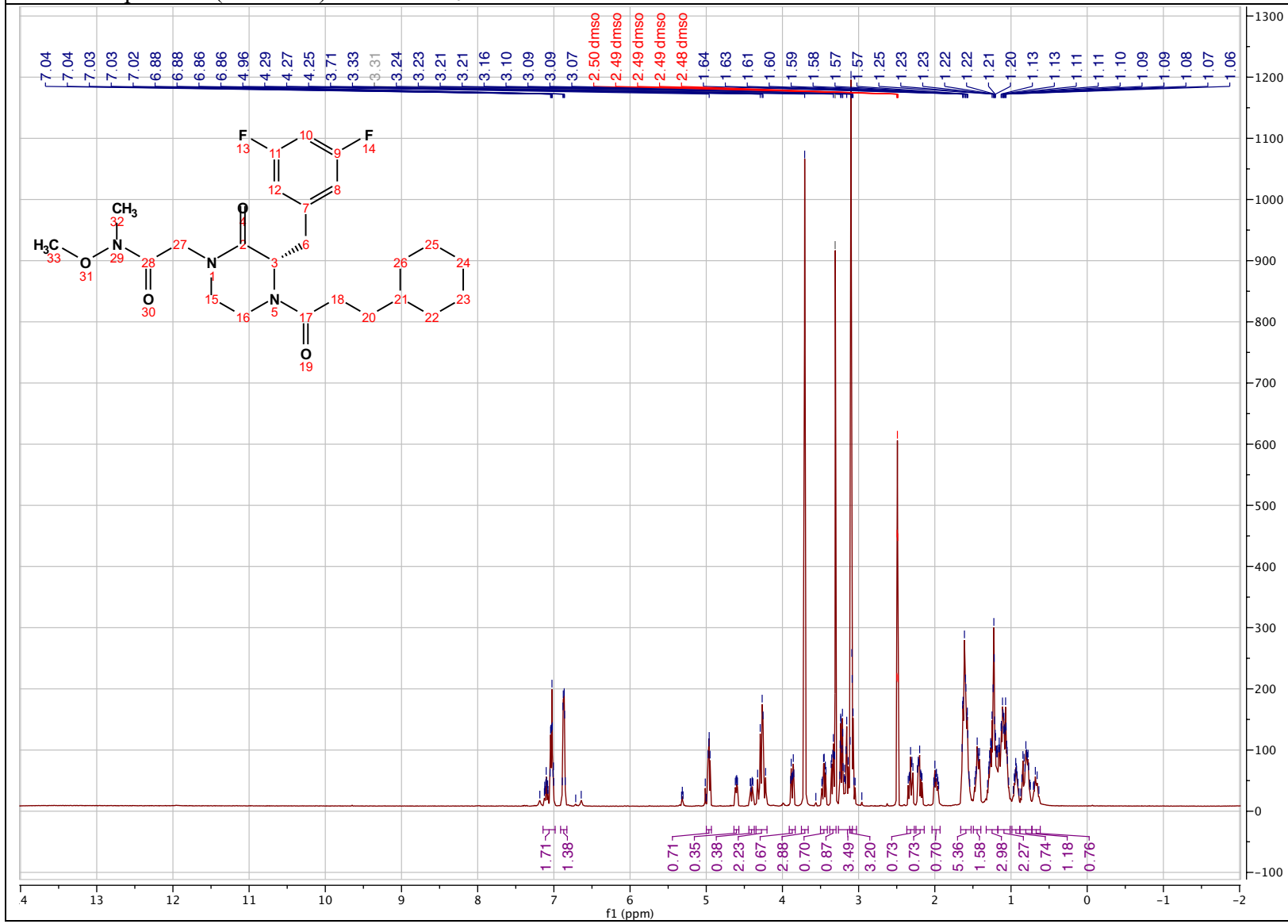
(S)-4-(3-cyclohexylpropanoyl)-3-(3,5-difluorobenzyl)-1-(4-(3,5-dimethyl-1H-pyrazol-1-yl)benzyl)piperazin-2-one (2.115)

^1H - ^{13}C HSQC NMR spectrum (500 MHz) in $\text{DMSO-}d_6$



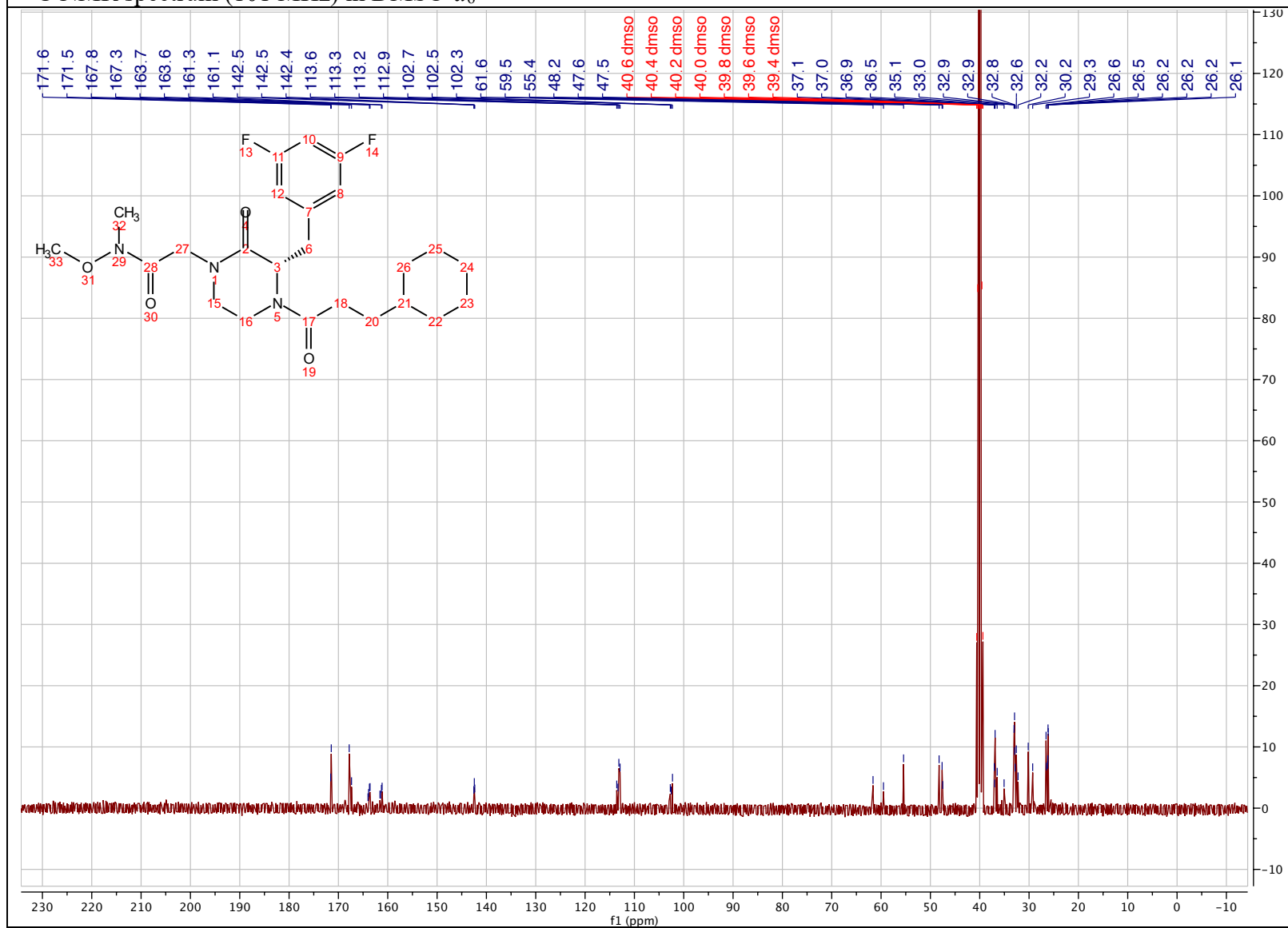
(S)-2-(4-(3-cyclohexylpropanoyl)-3-(3,5-difluorobenzyl)-2-oxopiperazin-1-yl)-N-methoxy-N-methylacetamide (2.116)

¹H NMR spectrum (500 MHz) in DMSO-*d*₆



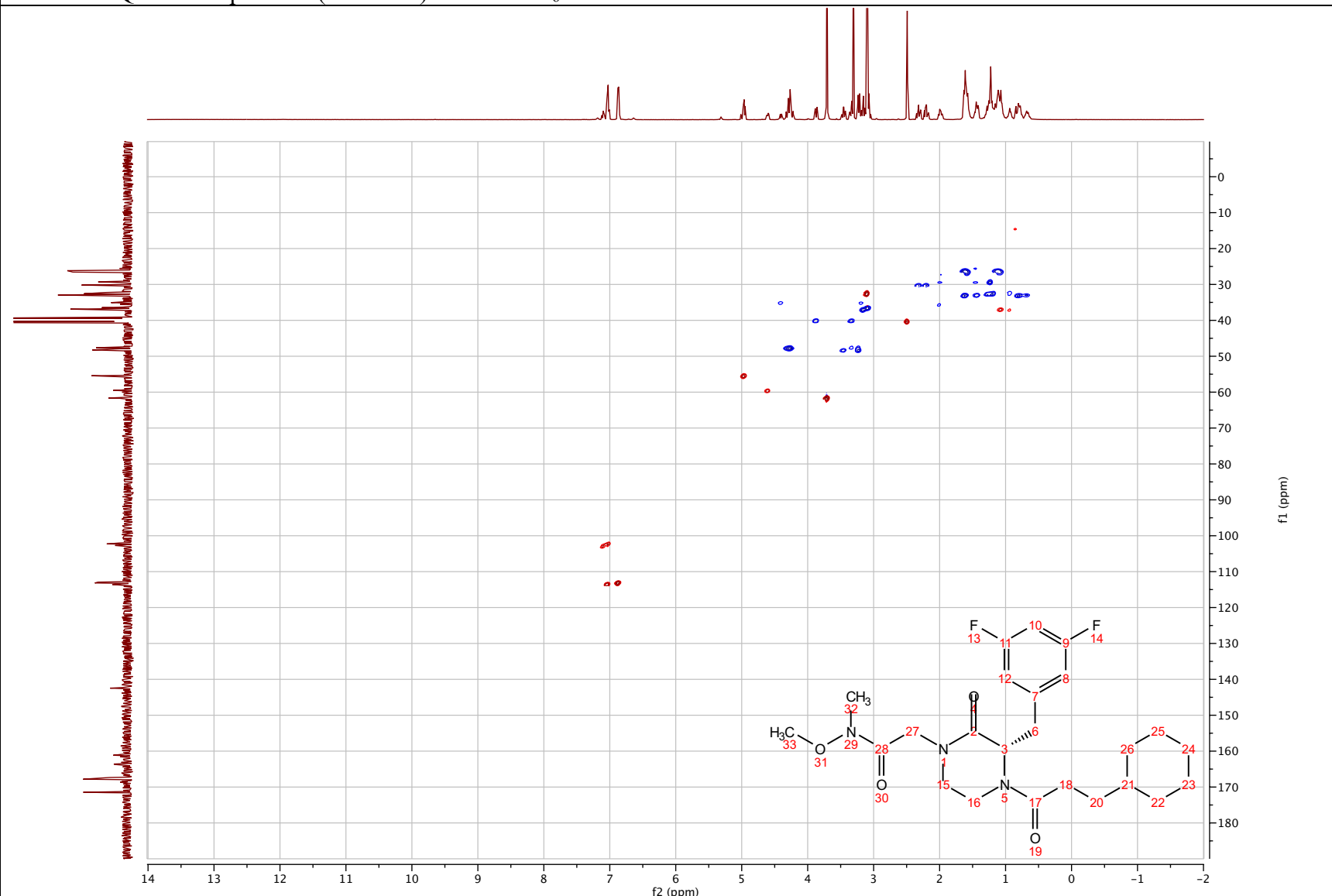
(S)-2-(4-(3-cyclohexylpropanoyl)-3-(3,5-difluorobenzyl)-2-oxopiperazin-1-yl)-N-methoxy-N-methylacetamide (2.116)

¹³C NMR spectrum (101 MHz) in DMSO-*d*₆



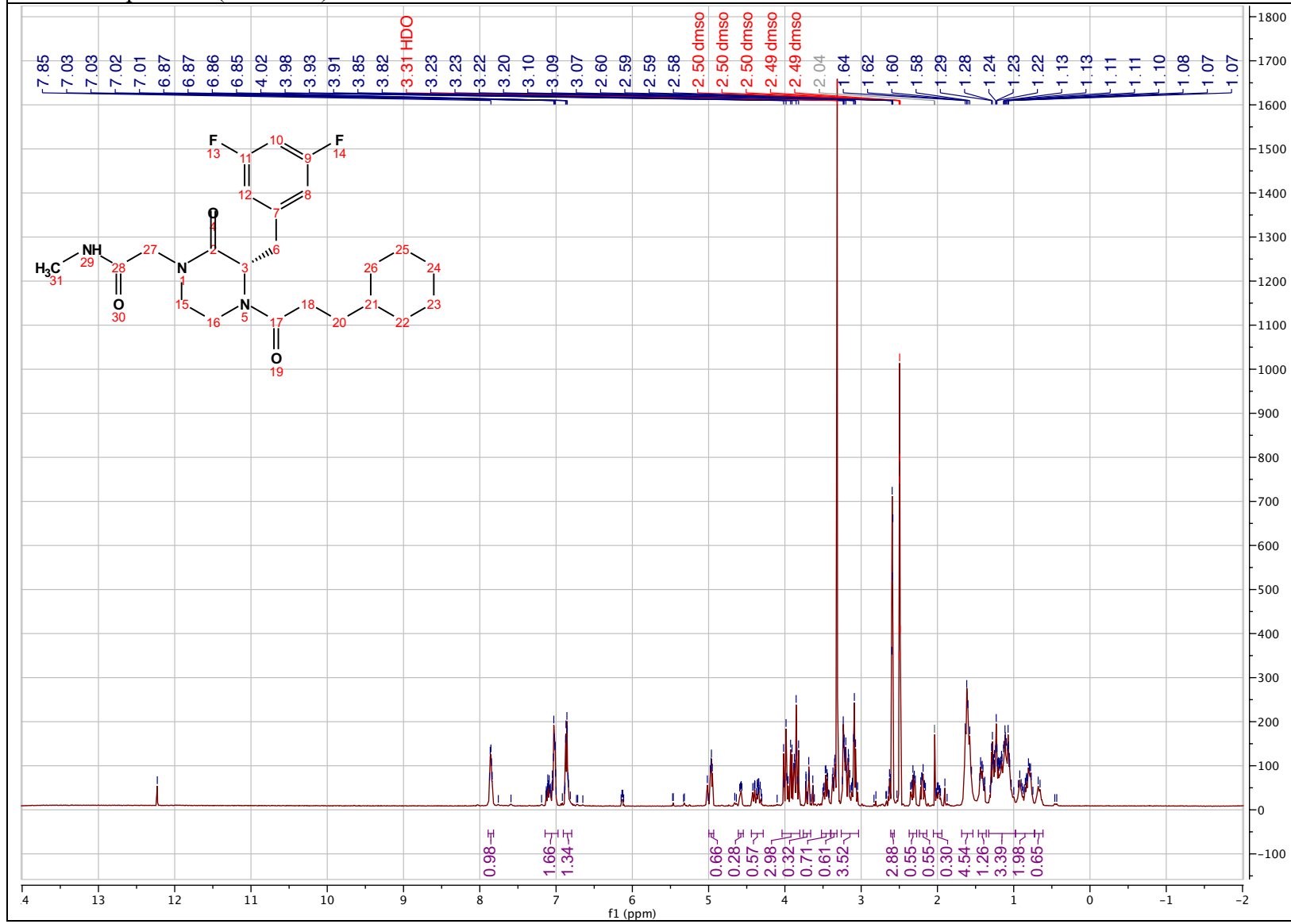
(S)-2-(4-(3-cyclohexylpropanoyl)-3-(3,5-difluorobenzyl)-2-oxopiperazin-1-yl)-N-methoxy-N-methylacetamide (2.116)

^1H - ^{13}C HSQC NMR spectrum (500 MHz) in $\text{DMSO-}d_6$



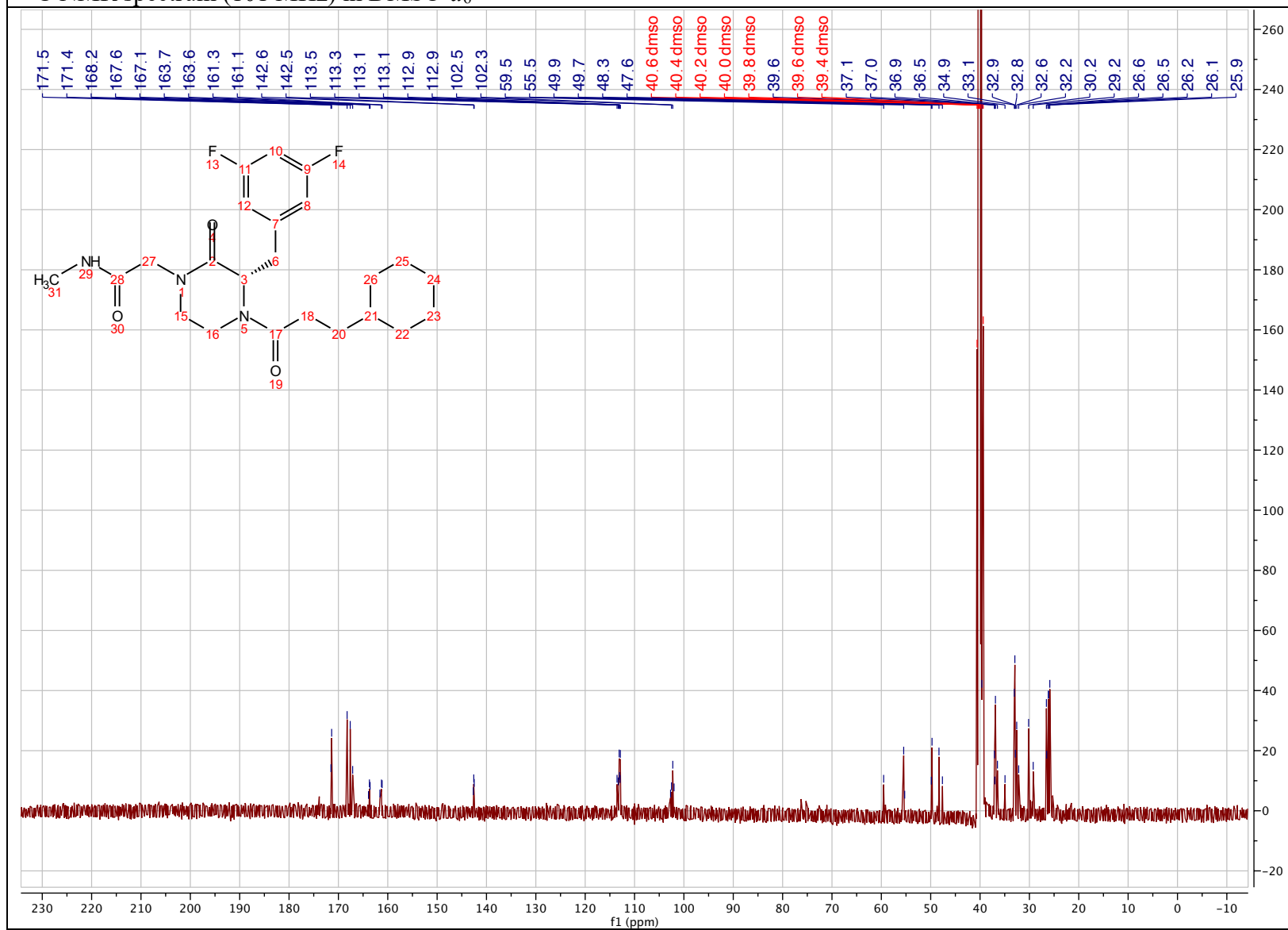
(S)-2-(4-(3-cyclohexylpropanoyl)-3-(3,5-difluorobenzyl)-2-oxopiperazin-1-yl)-N-methylacetamide (2.117)

¹H NMR spectrum (500 MHz) in DMSO-*d*₆



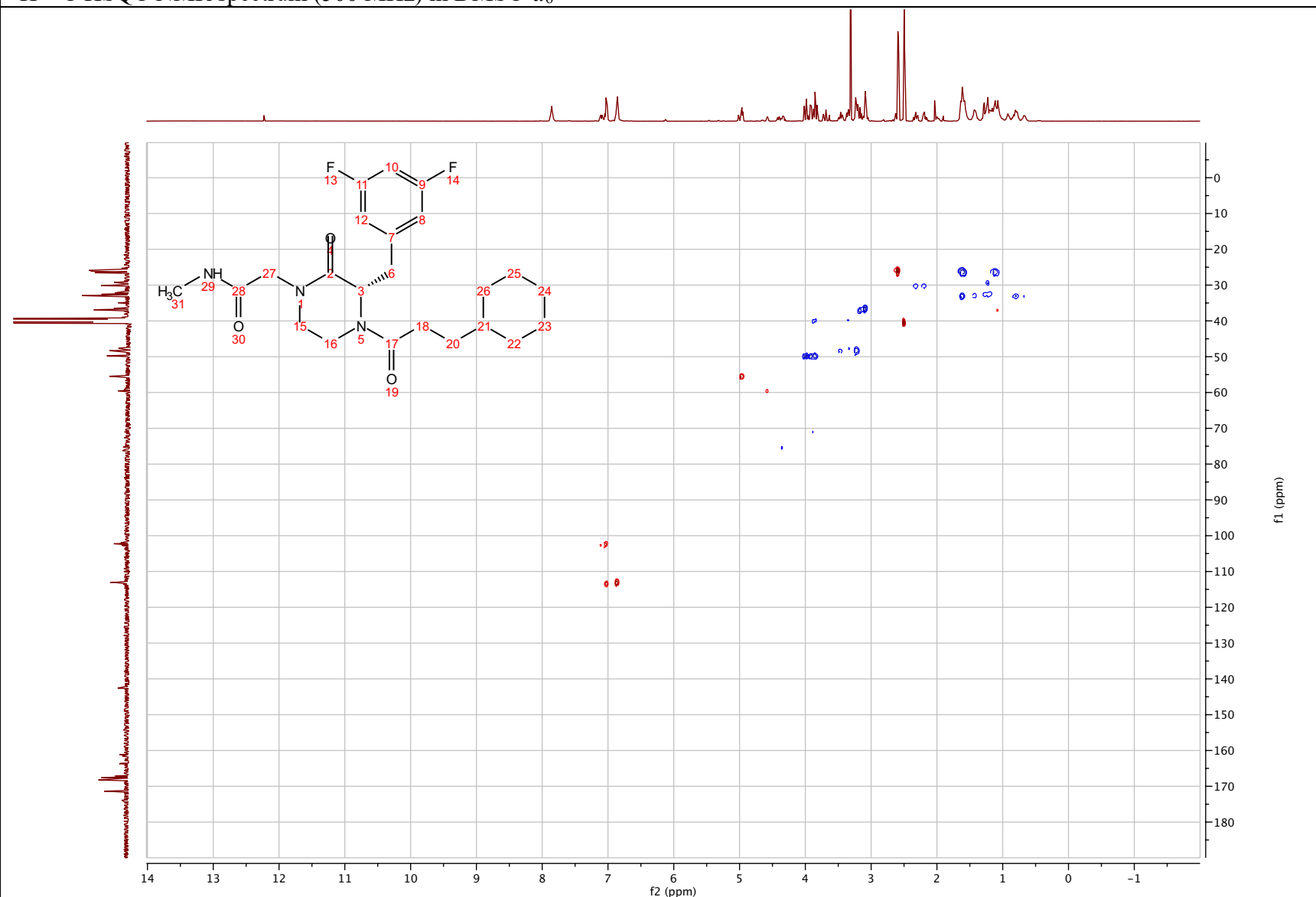
(S)-2-(4-(3-cyclohexylpropanoyl)-3-(3,5-difluorobenzyl)-2-oxopiperazin-1-yl)-N-methylacetamide (2.117)

¹³C NMR spectrum (101 MHz) in DMSO-*d*₆



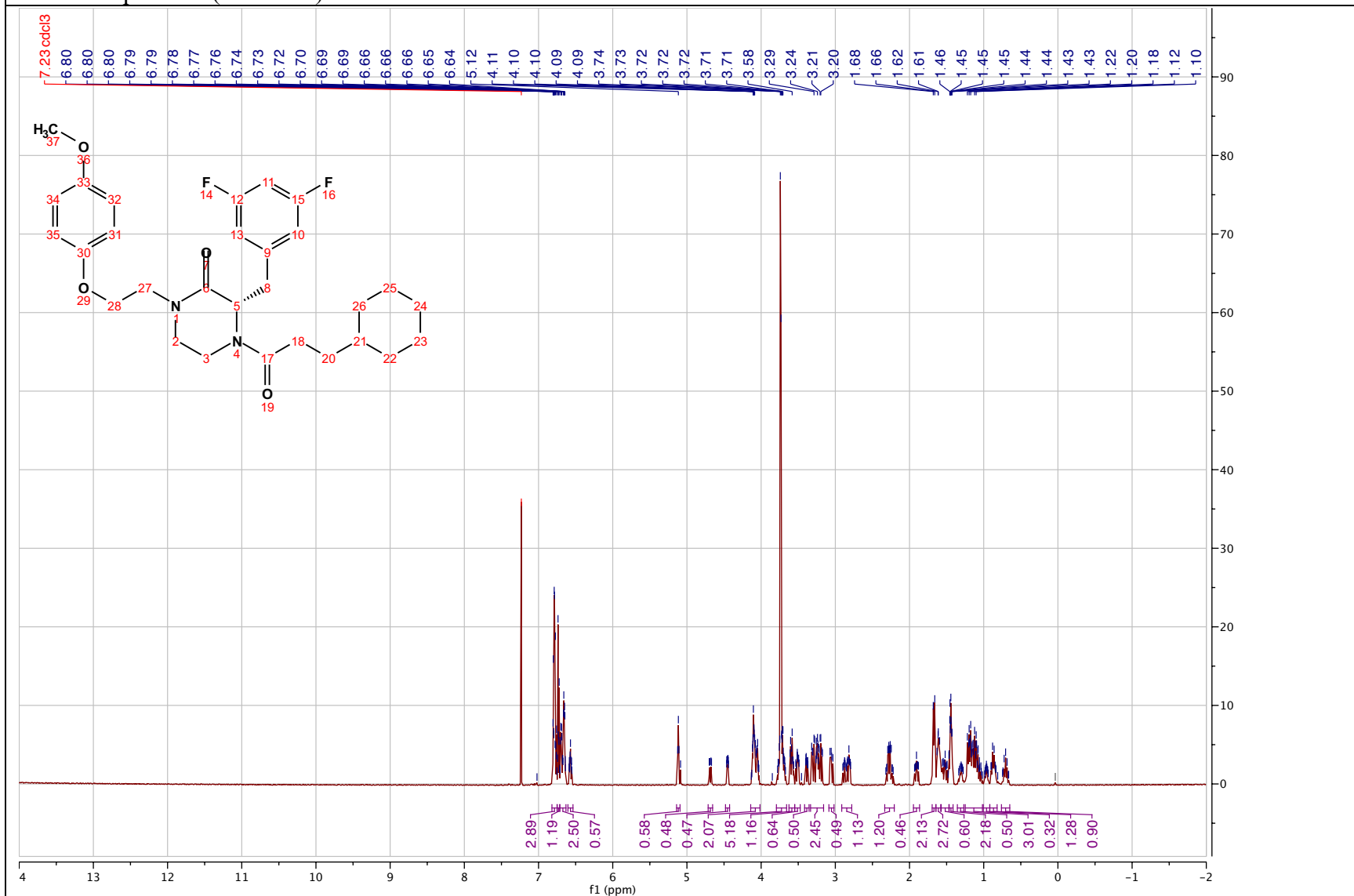
(S)-2-(4-(3-cyclohexylpropanoyl)-3-(3,5-difluorobenzyl)-2-oxopiperazin-1-yl)-N-methylacetamide (2.117)

^1H - ^{13}C HSQC NMR spectrum (500 MHz) in $\text{DMSO-}d_6$



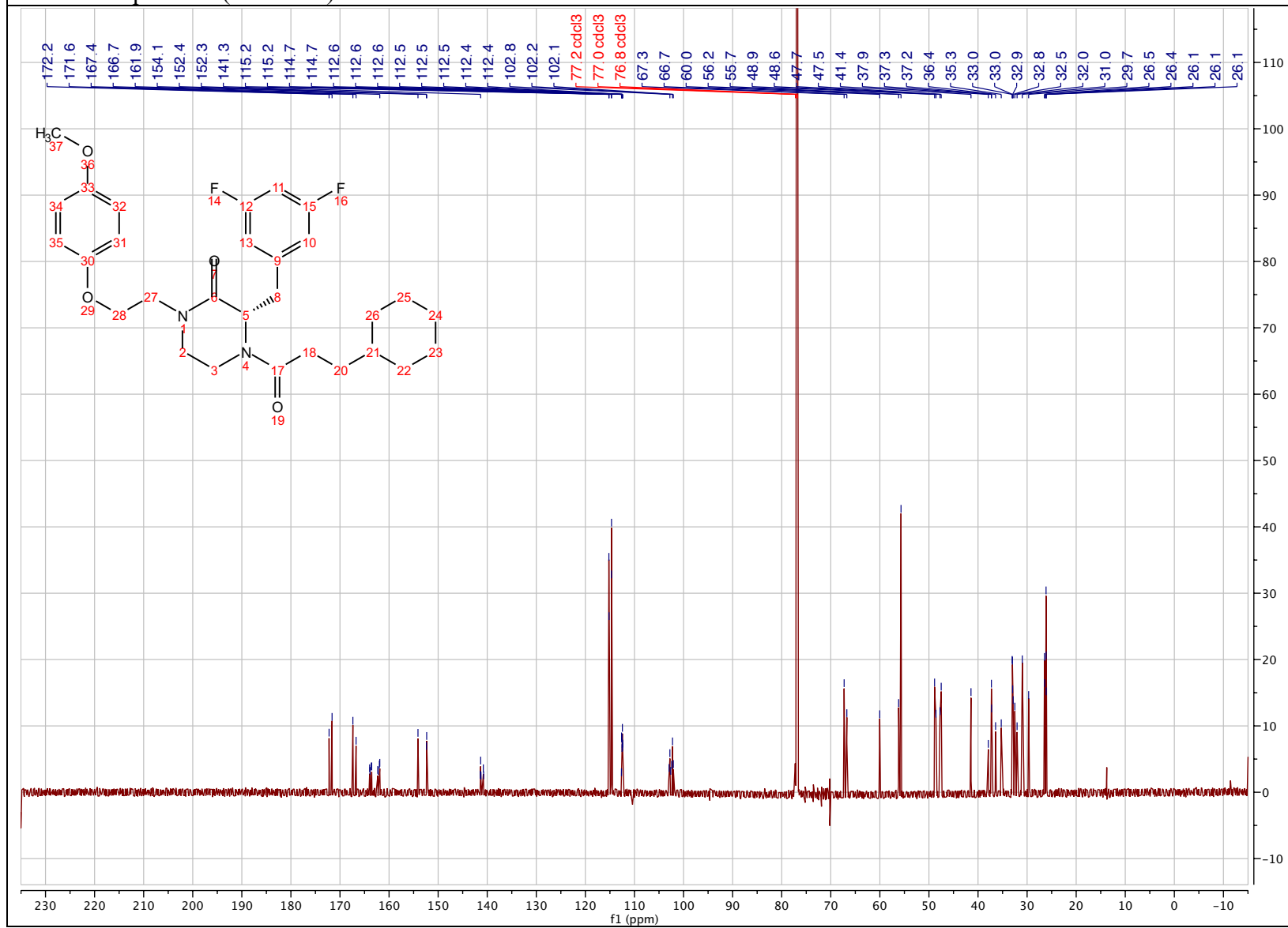
(S)-4-(3-cyclohexylpropanoyl)-3-(3,5-difluorobenzyl)-1-(2-(4-methoxyphenoxy)ethyl) piperazin-2-one (2.118)

¹H NMR spectrum (600 MHz) in Chloroform-*d*



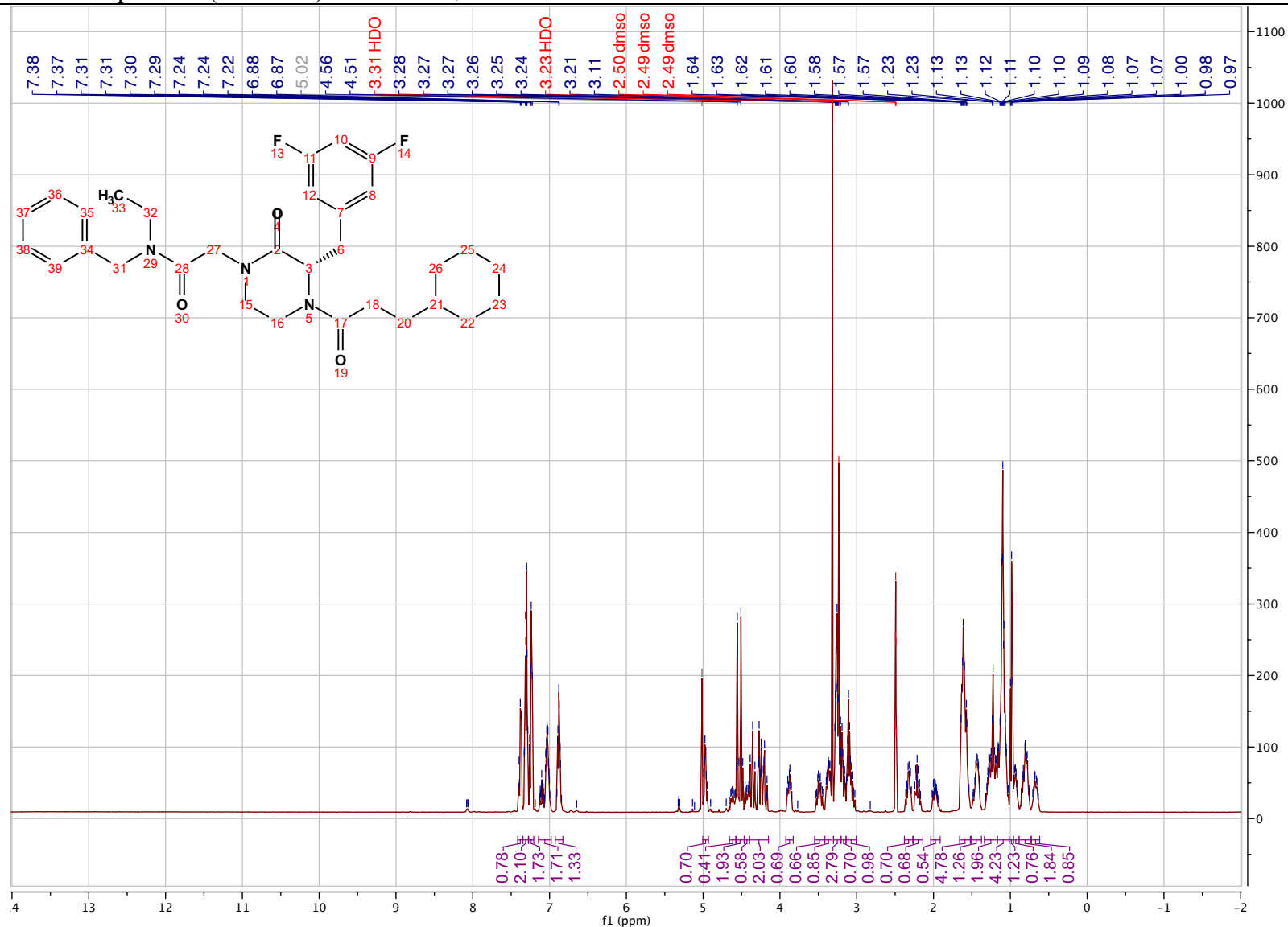
(S)-4-(3-cyclohexylpropanoyl)-3-(3,5-difluorobenzyl)-1-(2-(4-methoxyphenoxy)ethyl) piperazin-2-one (2.118)

¹³C NMR spectrum (151 MHz) in Chloroform-*d*



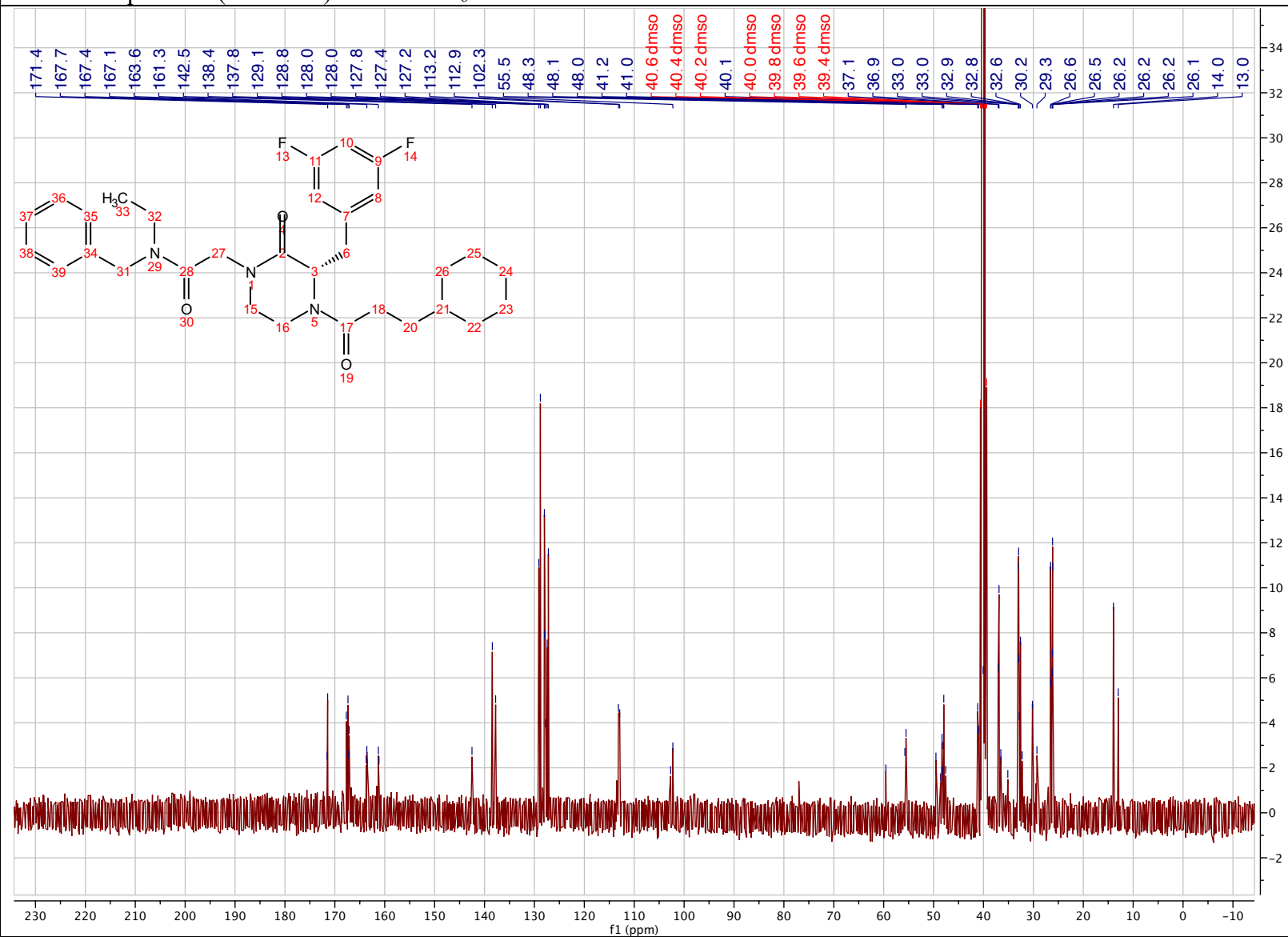
(S)-N-benzyl-2-(4-(3-cyclohexylpropanoyl)-3-(3,5-difluorobenzyl)-2-oxopiperazin-1-yl)-N-ethylacetamide (2.119)

¹H NMR spectrum (500 MHz) in DMSO-*d*₆



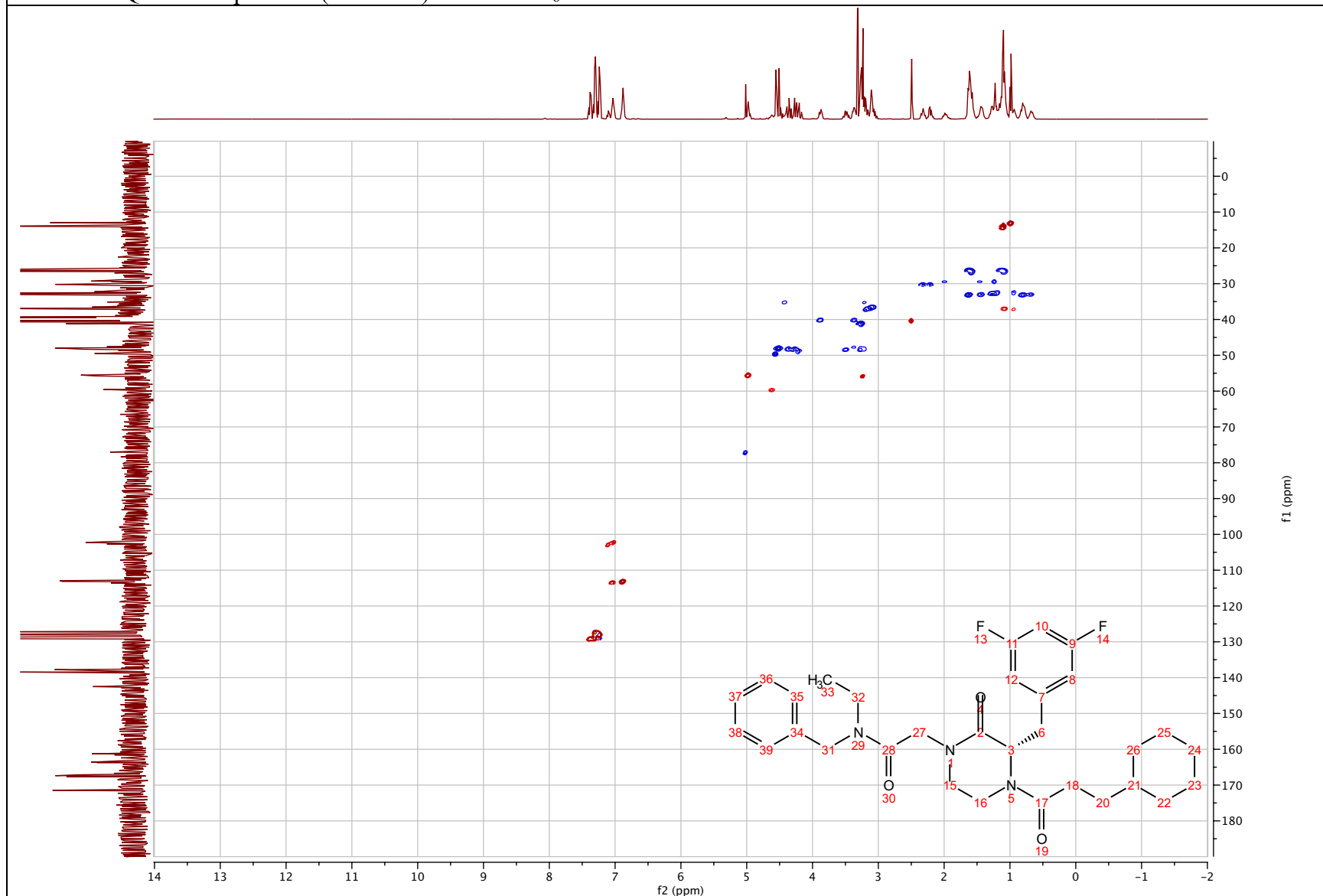
(S)-N-benzyl-2-(4-(3-cyclohexylpropanoyl)-3-(3,5-difluorobenzyl)-2-oxopiperazin-1-yl)-N-ethylacetamide (2.119)

¹³C NMR spectrum (101 MHz) in DMSO-*d*₆



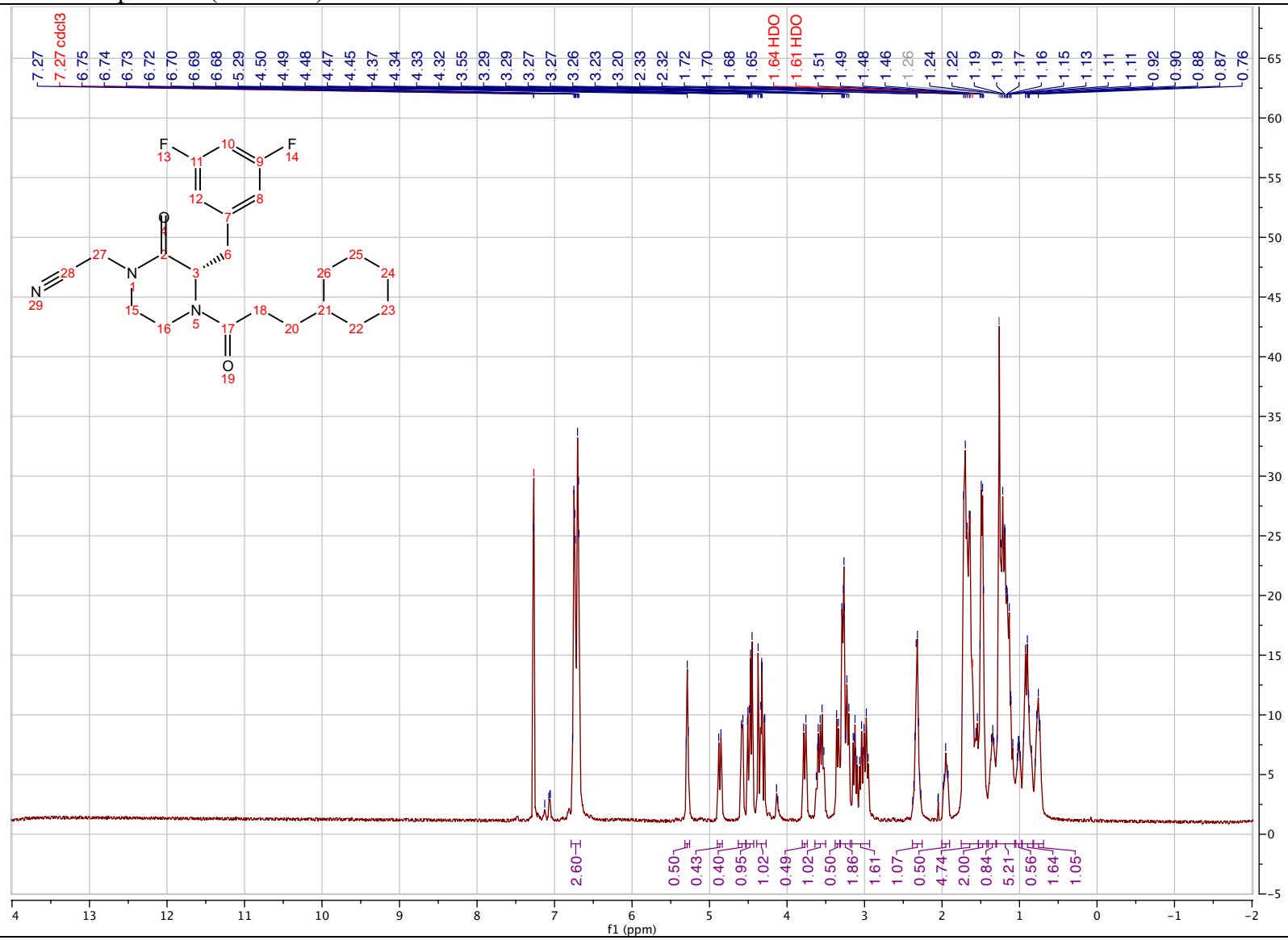
(S)-N-benzyl-2-(4-(3-cyclohexylpropanoyl)-3-(3,5-difluorobenzyl)-2-oxopiperazin-1-yl)-N-ethylacetamide (2.119)

^1H - ^{13}C HSQC NMR spectrum (500 MHz) in $\text{DMSO-}d_6$



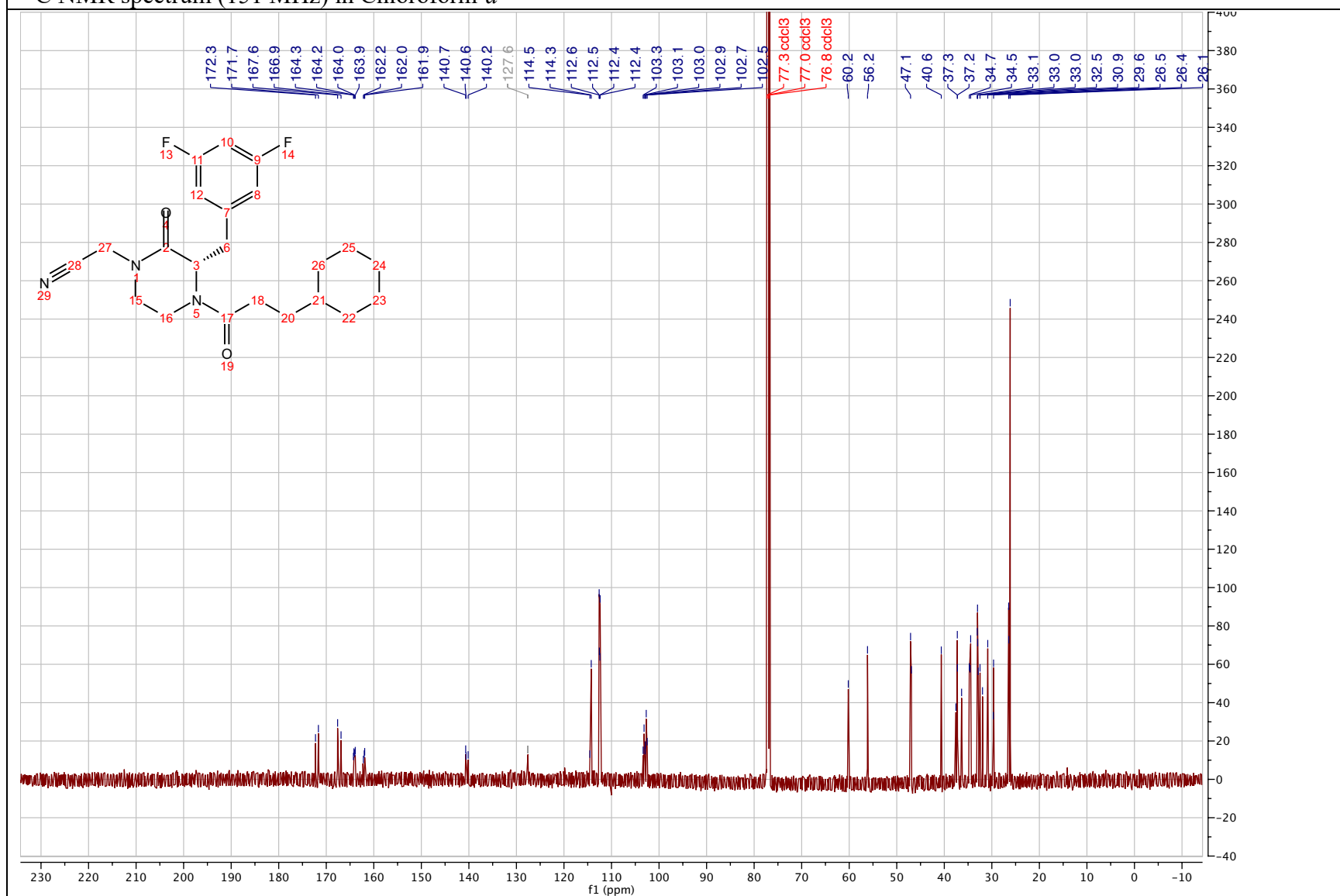
(S)-2-(4-(3-cyclohexylpropanoyl)-3-(3,5-difluorobenzyl)-2-oxopiperazin-1-yl)acetonitrile (2.142)

¹H NMR spectrum (600 MHz) in Chloroform-*d*



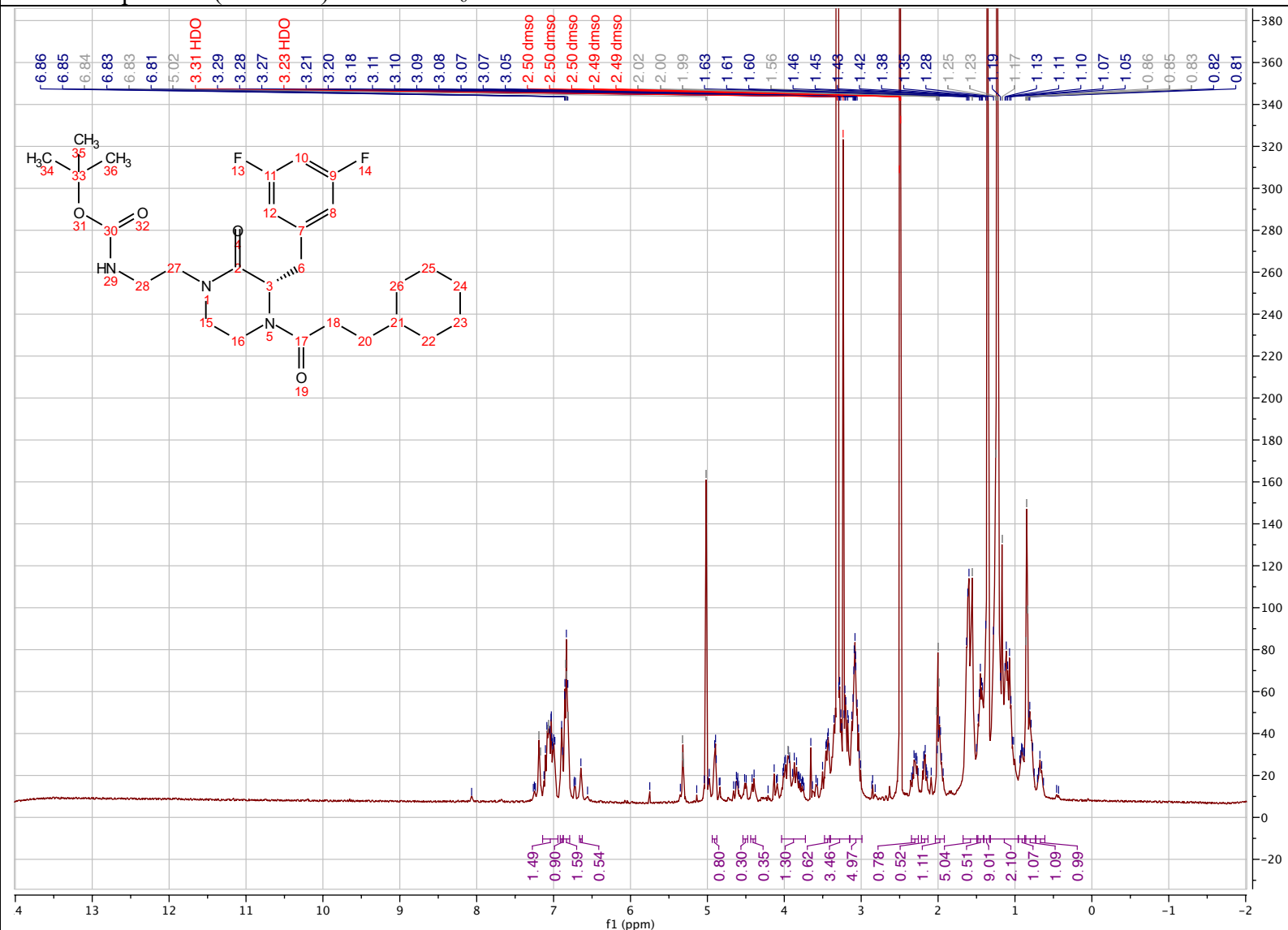
(S)-2-(4-(3-cyclohexylpropanoyl)-3-(3,5-difluorobenzyl)-2-oxopiperazin-1-yl)acetonitrile (2.142)

¹³C NMR spectrum (151 MHz) in Chloroform-*d*



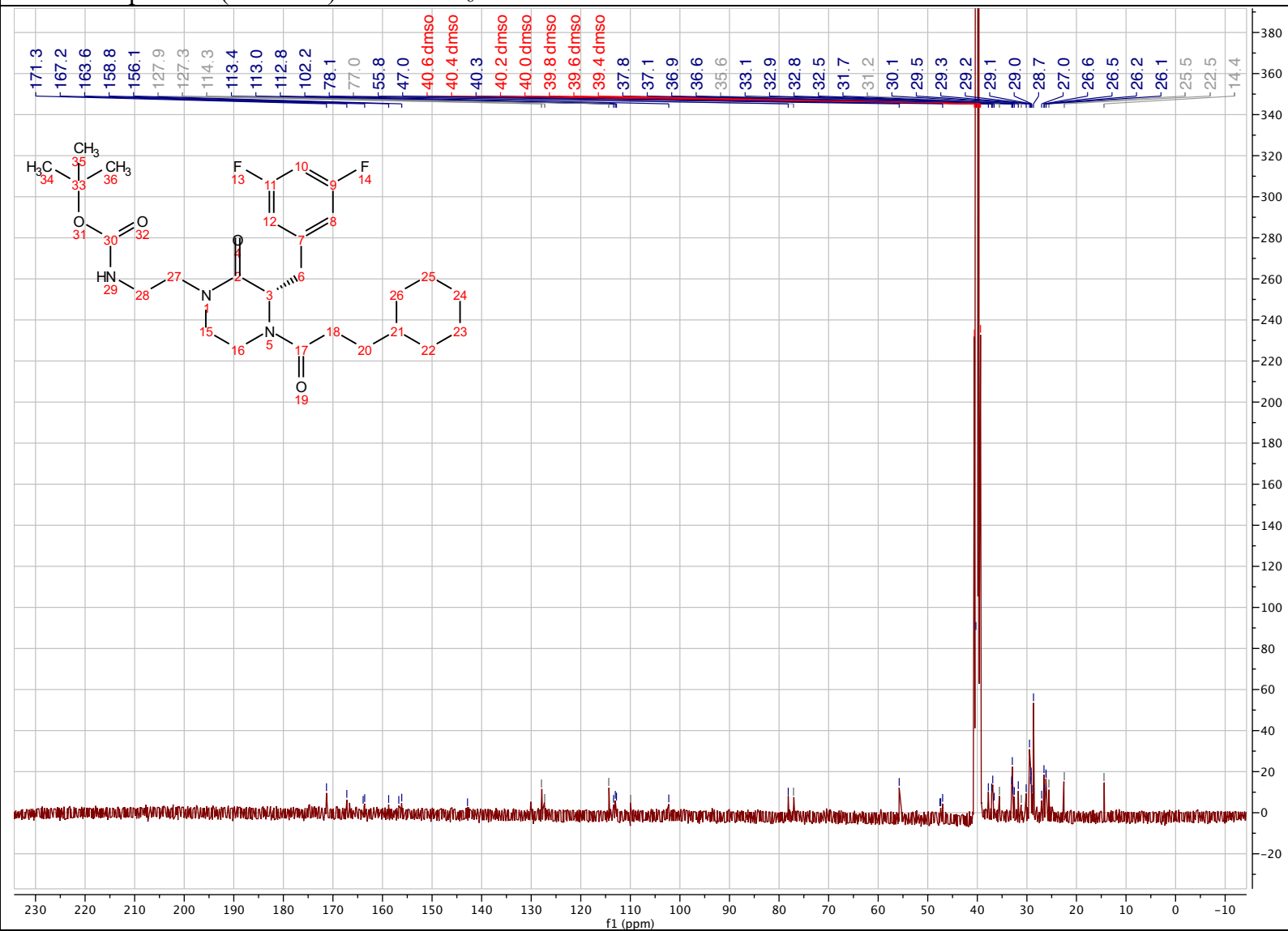
***tert*-butyl (*S*)-(2-(4-(3-cyclohexylpropanoyl)-3-(3,5-difluorobenzyl)-2-oxopiperazin-1-yl)ethyl)carbamate (2.143)**

¹H NMR spectrum (500 MHz) in DMSO-*d*₆



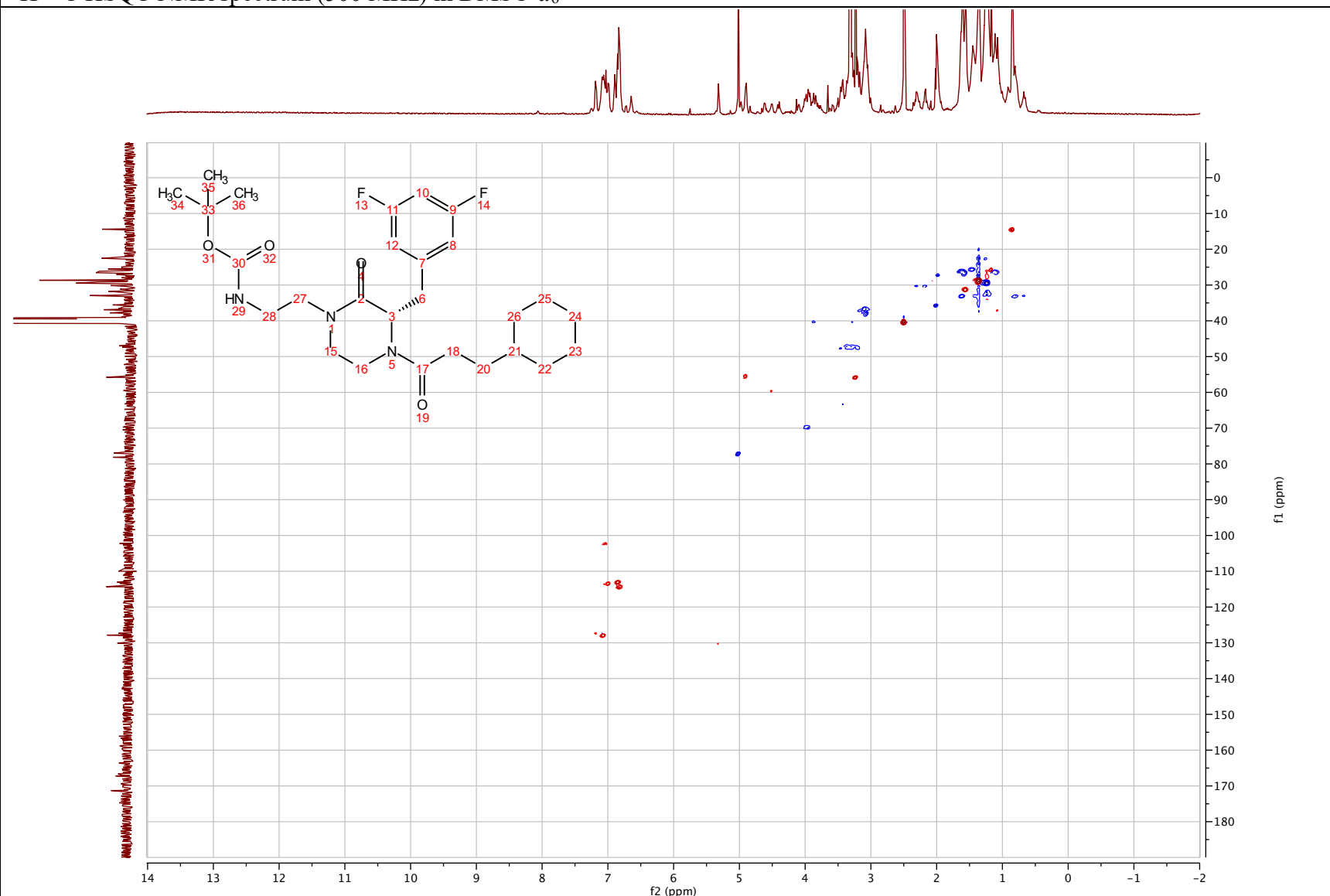
***tert*-butyl (*S*)-(2-(4-(3-cyclohexylpropanoyl)-3-(3,5-difluorobenzyl)-2-oxopiperazin-1-yl)ethyl)carbamate (2.143)**

¹³C NMR spectrum (101 MHz) in DMSO-*d*₆



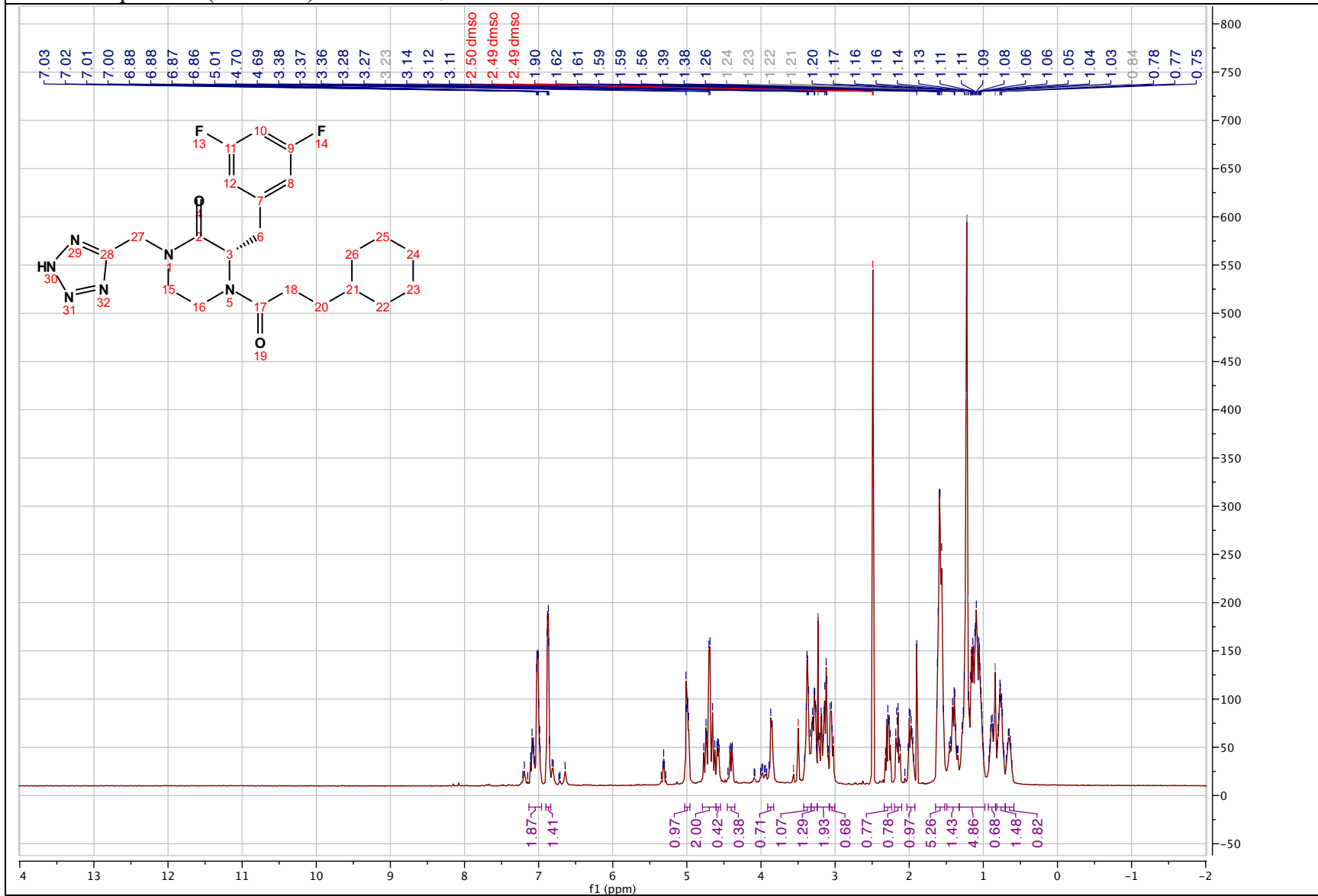
***tert*-butyl (S)-(2-(4-(3-cyclohexylpropanoyl)-3-(3,5-difluorobenzyl)-2-oxopiperazin-1-yl)ethyl)carbamate (2.143)**

^1H - ^{13}C HSQC NMR spectrum (500 MHz) in $\text{DMSO-}d_6$



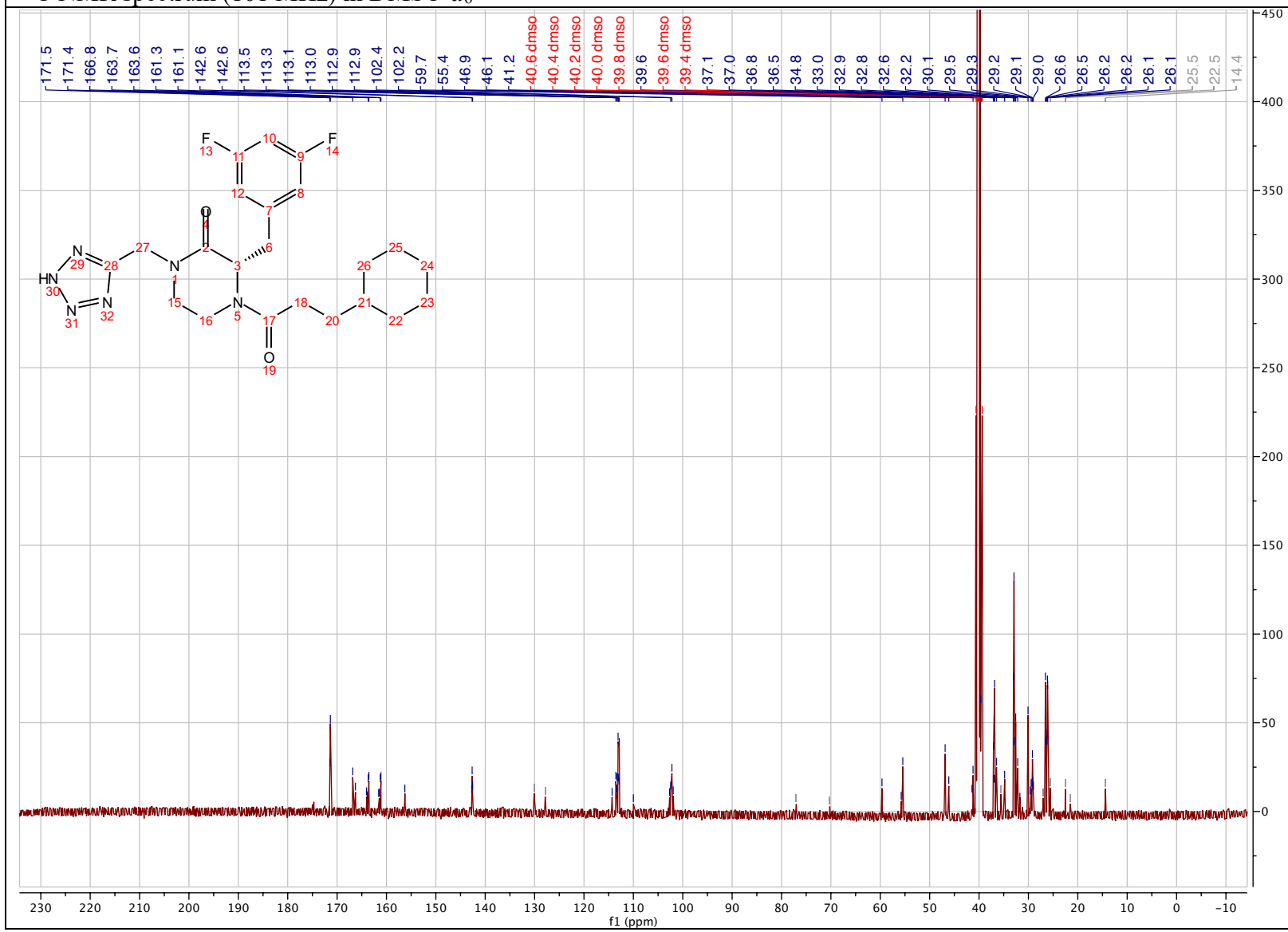
(S)-1-((2H-tetrazol-5-yl)methyl)-4-(3-cyclohexylpropanoyl)-3-(3,5-difluorobenzyl) piperazin-2-one (2.141)

¹H NMR spectrum (500 MHz) in DMSO-*d*₆



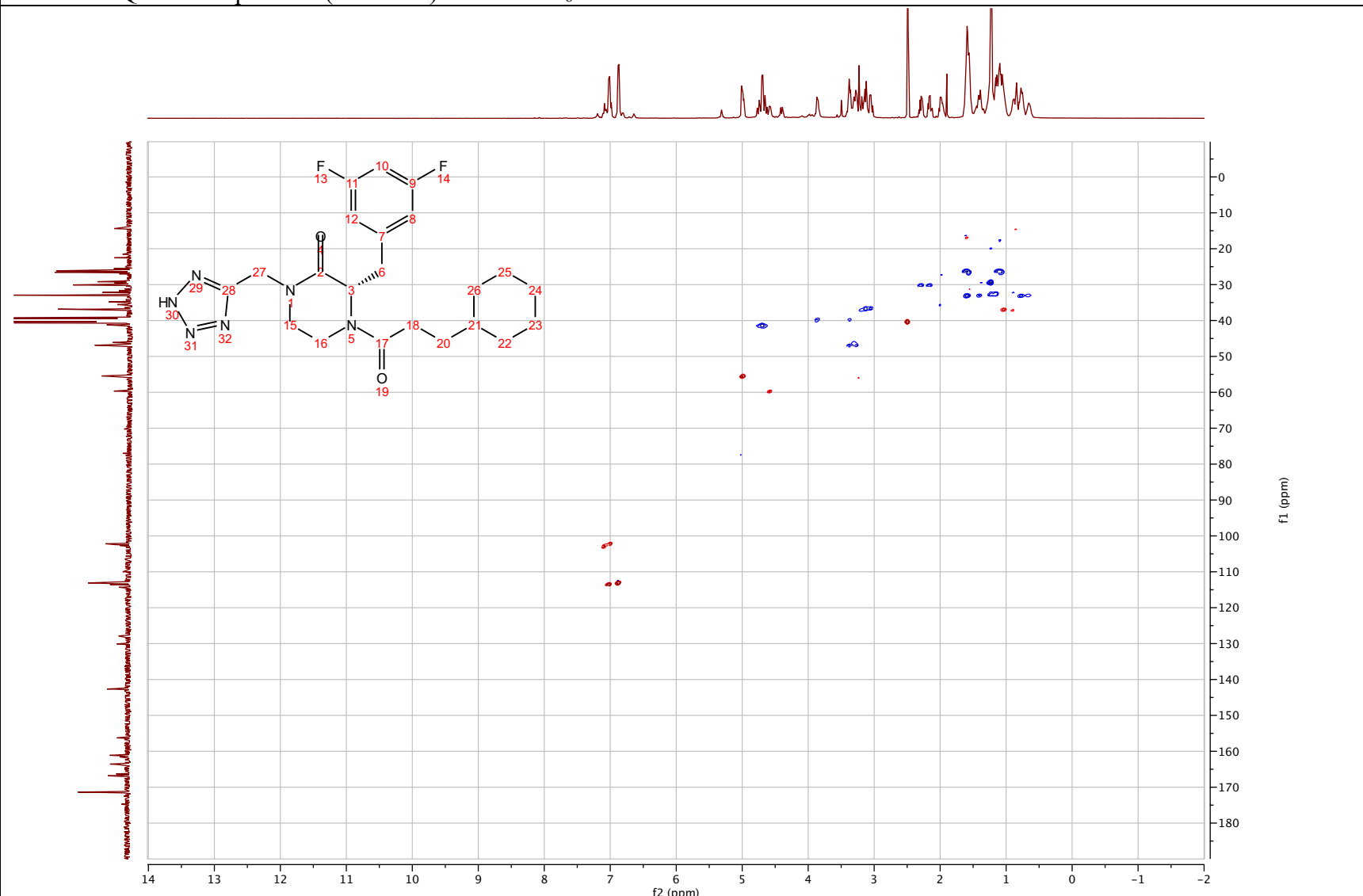
(S)-1-((2H-tetrazol-5-yl)methyl)-4-(3-cyclohexylpropanoyl)-3-(3,5-difluorobenzyl) piperazin-2-one (2.141)

¹³C NMR spectrum (101 MHz) in DMSO-*d*₆



(S)-1-((2H-tetrazol-5-yl)methyl)-4-(3-cyclohexylpropanoyl)-3-(3,5-difluorobenzyl) piperazin-2-one (2.141)

^1H - ^{13}C HSQC NMR spectrum (500 MHz) in $\text{DMSO-}d_6$



1. Pages, J. M.; James, C. E.; Winterhalter, M., The porin and the permeating antibiotic: a selective diffusion barrier in Gram-negative bacteria. *Nat Rev Microbiol* **2008**, *6* (12), 893-903.
2. Schulz, G. E., The Structures of General Porins. **2008**.
3. Hancock, R. E. W.; Tamber, S., Porins of the Outer Membrane of *Pseudomonas aeruginosa*. **2005**, 61-77.
4. Braun, V.; Braun, M., Energy-Coupled Outer Membrane Iron Transporters. **2005**, 213-236.
5. Kadner, R. J.; Chimento, D. P.; Cadieux, N., Structural and Functional Aspects of the Vitamin B12 Receptor BtuB. **2005**, 237-258.
6. Nishino, K.; Latifi, T.; Groisman, E. A., Virulence and drug resistance roles of multidrug efflux systems of *Salmonella enterica* serovar Typhimurium. *Mol Microbiol* **2006**, *59* (1), 126-41.
7. Bogomolnaya, L. M.; Andrews, K. D.; Talamantes, M.; Maple, A.; Ragoza, Y.; Vazquez-Torres, A.; Andrews-Polymenis, H., The ABC-type efflux pump MacAB protects *Salmonella enterica* serovar typhimurium from oxidative stress. *MBio* **2013**, *4* (6), e00630-13.
8. Rouquette-Loughlin, C. E.; Balthazar, J. T.; Shafer, W. M., Characterization of the MacA-MacB efflux system in *Neisseria gonorrhoeae*. *J Antimicrob Chemother* **2005**, *56* (5), 856-60.
9. Lu, S.; Zgurskaya, H. I., MacA, a periplasmic membrane fusion protein of the macrolide transporter MacAB-TolC, binds lipopolysaccharide core specifically and with high affinity. *J Bacteriol* **2013**, *195* (21), 4865-72.
10. Elkins, C. A.; Nikaido, H., Substrate specificity of the RND-type multidrug efflux pumps AcrB and AcrD of *Escherichia coli* is determined predominately by two large periplasmic loops. *Journal of Bacteriology* **2002**, *184* (23), 6490-6498.
11. Sulavik, M. C.; Houseweart, C.; Cramer, C.; Jiwani, N.; Murgolo, N.; Greene, J.; DiDomenico, B.; Shaw, K. J.; Miller, G. H.; Hare, R.; Shimer, G., Antibiotic susceptibility profiles of *Escherichia coli* strains lacking multidrug efflux pump genes. *Antimicrob Agents Chemother* **2001**, *45* (4), 1126-36.
12. Jamshidi, S.; Sutton, J. M.; Rahman, K. M., An overview of bacterial efflux pumps and computational approaches to study efflux pump inhibitors. *Future Med Chem* **2016**, *8* (2), 195-210.
13. Sjuts, H.; Vargiu, A. V.; Kwasny, S. M.; Nguyen, S. T.; Kim, H. S.; Ding, X.; Ornik, A. R.; Ruggerone, P.; Bowlin, T. L.; Nikaido, H.; Pos, K. M.; Opperman, T. J., Molecular basis for inhibition of AcrB multidrug efflux pump by novel and powerful pyranopyridine derivatives. *Proc Natl Acad Sci U S A* **2016**, *113* (13), 3509-14.
14. Abdali, N.; Parks, J. M.; Haynes, K. M.; Chaney, J. L.; Green, A. T.; Wolloscheck, D.; Walker, J. K.; Rybenkov, V. V.; Baudry, J.; Smith, J. C.; Zgurskaya, H. I., Reviving Antibiotics: Efflux Pump Inhibitors That Interact with AcrA, a Membrane Fusion Protein of the AcrAB-TolC Multidrug Efflux Pump. *ACS Infect Dis* **2017**, *3* (1), 89-98.
15. Ghisalberty, D.; Mahamoud, A.; Chevalier, J.; Baitiche, M.; Martino, M.; Pages, J. M.; Barbe, J., Chloroquinolines block antibiotic efflux pumps in antibiotic-resistant *Enterobacter aerogenes* isolates. *Int J Antimicrob Agents* **2006**, *27* (6), 565-9.

16. Li, X. Z.; Plesiat, P.; Nikaido, H., The challenge of efflux-mediated antibiotic resistance in Gram-negative bacteria. *Clin Microbiol Rev* **2015**, *28* (2), 337-418.
17. Bohnert, J. A.; Schuster, S.; Kern, W. V., Pimozide Inhibits the AcrAB-TolC Efflux Pump in Escherichia coli. *Open Microbiol J* **2013**, *7*, 83-6.
18. Aparna, V.; Dineshkumar, K.; Mohanalakshmi, N.; Velmurugan, D.; Hopper, W., Identification of natural compound inhibitors for multidrug efflux pumps of Escherichia coli and Pseudomonas aeruginosa using in silico high-throughput virtual screening and in vitro validation. *PLoS One* **2014**, *9* (7), e101840.
19. Schneiders, T.; Amyes, S. G.; Levy, S. B., Role of AcrR and ramA in fluoroquinolone resistance in clinical Klebsiella pneumoniae isolates from Singapore. *Antimicrob Agents Chemother* **2003**, *47* (9), 2831-7.
20. Ruzin, A.; Visalli, M. A.; Keeney, D.; Bradford, P. A., Influence of transcriptional activator RamA on expression of multidrug efflux pump AcrAB and tigecycline susceptibility in Klebsiella pneumoniae. *Antimicrob Agents Chemother* **2005**, *49* (3), 1017-22.
21. Mazzariol, A.; Zuliani, J.; Cornaglia, G.; Rossolini, G. M.; Fontana, R., AcrAB Efflux System: Expression and Contribution to Fluoroquinolone Resistance in Klebsiella spp. *Antimicrob Agents Chemother* **2002**, *46* (12), 3984-6.
22. Nishino, K.; Yamada, J.; Hirakawa, H.; Hirata, T.; Yamaguchi, A., Roles of TolC-dependent multidrug transporters of Escherichia coli in resistance to beta-lactams. *Antimicrob Agents Chemother* **2003**, *47* (9), 3030-3.
23. Misra, R.; Morrison, K. D.; Cho, H. J.; Khoo, T., Importance of Real-Time Assays To Distinguish Multidrug Efflux Pump-Inhibiting and Outer Membrane-Destabilizing Activities in Escherichia coli. *J Bacteriol* **2015**, *197* (15), 2479-88.
24. Nishino, K.; Yamaguchi, A., Analysis of a complete library of putative drug transporter genes in Escherichia coli. *J Bacteriol* **2001**, *183* (20), 5803-12.
25. Rosenberg, E. Y.; Ma, D.; Nikaido, H., AcrD of Escherichia coli is an aminoglycoside efflux pump. *Journal of Bacteriology* **2000**, *182* (6), 1754-1756.
26. Pletzer, D.; Weingart, H., Characterization of AcrD, a resistance-nodulation-cell division-type multidrug efflux pump from the fire blight pathogen Erwinia amylovora. *BMC Microbiol* **2014**, *14*, 13.
27. Yamasaki, S.; Nagasawa, S.; Hayashi-Nishino, M.; Yamaguchi, A.; Nishino, K., AcrA dependency of the AcrD efflux pump in Salmonella enterica serovar Typhimurium. *J Antibiot (Tokyo)* **2011**, *64* (6), 433-7.
28. Kim, H. B.; Wang, M.; Park, C. H.; Kim, E. C.; Jacoby, G. A.; Hooper, D. C., oqxAB encoding a multidrug efflux pump in human clinical isolates of Enterobacteriaceae. *Antimicrob Agents Chemother* **2009**, *53* (8), 3582-4.
29. Sugawara, E.; Nikaido, H., Properties of AdeABC and AdeIJK efflux systems of Acinetobacter baumannii compared with those of the AcrAB-TolC system of Escherichia coli. *Antimicrob Agents Chemother* **2014**, *58* (12), 7250-7.
30. Magnet, S.; Courvalin, P.; Lambert, T., Resistance-nodulation-cell division-type efflux pump involved in aminoglycoside resistance in Acinetobacter baumannii strain BM4454. *Antimicrob Agents Chemother* **2001**, *45* (12), 3375-80.

31. Gholami, M.; Hashemi, A.; Hakemi-Vala, M.; Goudarzi, H.; Hallajzadeh, M., Efflux Pump Inhibitor Phenylalanine-Arginine Beta-Naphthylamide Effect on the Minimum Inhibitory Concentration of Imipenem in *Acinetobacter baumannii* Strains Isolated From Hospitalized Patients in Shahid Motahari Burn Hospital, Tehran, Iran. *Jundishapur J Microbiol* **2015**, *8* (10), e19048.
32. Pannek, S.; Higgins, P. G.; Steinke, P.; Jonas, D.; Akova, M.; Bohnert, J. A.; Seifert, H.; Kern, W. V., Multidrug efflux inhibition in *Acinetobacter baumannii*: comparison between 1-(1-naphthylmethyl)-piperazine and phenyl-arginine-beta-naphthylamide. *J Antimicrob Chemother* **2006**, *57* (5), 970-4.
33. Beheshti, M.; Talebi, M.; Ardebili, A.; Bahador, A.; Lari, A. R., Detection of AdeABC efflux pump genes in tetracycline-resistant *Acinetobacter baumannii* isolates from burn and ventilator-associated pneumonia patients. *J Pharm Bioallied Sci* **2014**, *6* (4), 229-32.
34. Coyne, S.; Rosenfeld, N.; Lambert, T.; Courvalin, P.; Perichon, B., Overexpression of resistance-nodulation-cell division pump AdeFGH confers multidrug resistance in *Acinetobacter baumannii*. *Antimicrob Agents Chemother* **2010**, *54* (10), 4389-93.
35. Cortez-Cordova, J.; Kumar, A., Activity of the efflux pump inhibitor phenylalanine-arginine beta-naphthylamide against the AdeFGH pump of *Acinetobacter baumannii*. *Int J Antimicrob Agents* **2011**, *37* (5), 420-4.
36. Lin, L.; Ling, B. D.; Li, X. Z., Distribution of the multidrug efflux pump genes, adeABC, adeDE and adeIJK, and class 1 integron genes in multiple-antimicrobial-resistant clinical isolates of *Acinetobacter baumannii*-*Acinetobacter calcoaceticus* complex. *Int J Antimicrob Agents* **2009**, *33* (1), 27-32.
37. Damier-Piolle, L.; Magnet, S.; Bremont, S.; Lambert, T.; Courvalin, P., AdeIJK, a resistance-nodulation-cell division pump effluxing multiple antibiotics in *Acinetobacter baumannii*. *Antimicrob Agents Chemother* **2008**, *52* (2), 557-62.
38. Mamelli, L.; Amoros, J. P.; Pages, J. M.; Bolla, J. M., A phenylalanine-arginine beta-naphthylamide sensitive multidrug efflux pump involved in intrinsic and acquired resistance of *Campylobacter* to macrolides. *Int J Antimicrob Agents* **2003**, *22* (3), 237-41.
39. Akiba, M.; Lin, J.; Barton, Y. W.; Zhang, Q., Interaction of CmeABC and CmeDEF in conferring antimicrobial resistance and maintaining cell viability in *Campylobacter jejuni*. *J Antimicrob Chemother* **2006**, *57* (1), 52-60.
40. Pumbwe, L.; Randall, L. P.; Woodward, M. J.; Piddock, L. J., Evidence for multiple-antibiotic resistance in *Campylobacter jejuni* not mediated by CmeB or CmeF. *Antimicrob Agents Chemother* **2005**, *49* (4), 1289-93.
41. Klancnik, A.; Mozina, S. S.; Zhang, Q., Anti-*Campylobacter* activities and resistance mechanisms of natural phenolic compounds in *Campylobacter*. *PLoS One* **2012**, *7* (12), e51800.
42. Li, X. Z.; Nikaido, H., Efflux-mediated drug resistance in bacteria: an update. *Drugs* **2009**, *69* (12), 1555-623.
43. Masuda, N.; Sakagawa, E.; Ohya, S.; Gotoh, N.; Tsujimoto, H.; Nishino, T., Substrate specificities of MexAB-OprM, MexCD-OprJ, and MexXY-oprM efflux pumps in *Pseudomonas aeruginosa*. *Antimicrob Agents Chemother* **2000**, *44* (12), 3322-7.
44. Fraud, S.; Campigotto, A. J.; Chen, Z.; Poole, K., MexCD-OprJ multidrug efflux system of *Pseudomonas aeruginosa*: involvement in chlorhexidine resistance and induction by membrane-damaging agents dependent upon the AlgU stress response sigma factor. *Antimicrob Agents Chemother* **2008**, *52* (12), 4478-82.

45. Fetar, H.; Gilmour, C.; Klinoski, R.; Daigle, D. M.; Dean, C. R.; Poole, K., mexEF-oprN multidrug efflux operon of *Pseudomonas aeruginosa*: regulation by the MexT activator in response to nitrosative stress and chloramphenicol. *Antimicrob Agents Chemother* **2011**, *55* (2), 508-14.
46. Maseda, H.; Yoneyama, H.; Nakae, T., Assignment of the substrate-selective subunits of the MexEF-OprN multidrug efflux pump of *Pseudomonas aeruginosa*. *Antimicrob Agents Chemother* **2000**, *44* (3), 658-64.
47. Mima, T.; Sekiya, H.; Mizushima, T.; Kuroda, T.; Tsuchiya, T., Gene cloning and properties of the RND-type multidrug efflux pumps MexPQ-OpmE and MexMN-OprM from *Pseudomonas aeruginosa*. *Microbiol Immunol* **2005**, *49* (11), 999-1002.
48. Li, Y.; Mima, T.; Komori, Y.; Morita, Y.; Kuroda, T.; Mizushima, T.; Tsuchiya, T., A new member of the tripartite multidrug efflux pumps, MexVW-OprM, in *Pseudomonas aeruginosa*. *J Antimicrob Chemother* **2003**, *52* (4), 572-5.
49. Morita, Y.; Nakashima, K.; Nishino, K.; Kotani, K.; Tomida, J.; Inoue, M.; Kawamura, Y., Berberine Is a Novel Type Efflux Inhibitor Which Attenuates the MexXY-Mediated Aminoglycoside Resistance in *Pseudomonas aeruginosa*. *Front Microbiol* **2016**, *7*, 1223.
50. Weeks, J. W.; Nickels, L. M.; Ntrel, A. T.; Zgurskaya, H. I., Non-equivalent roles of two periplasmic subunits in the function and assembly of triclosan pump TriABC from *Pseudomonas aeruginosa*. *Mol Microbiol* **2015**, *98* (2), 343-56.
51. Villagra, N. A.; Hidalgo, A. A.; Santiviago, C. A.; Saavedra, C. P.; Mora, G. C., SmvA, and not AcrB, is the major efflux pump for acriflavine and related compounds in *Salmonella enterica* serovar Typhimurium. *J Antimicrob Chemother* **2008**, *62* (6), 1273-6.
52. Gil, F.; Ipinza, F.; Fuentes, J.; Fumeron, R.; Villarreal, J. M.; Aspee, A.; Mora, G. C.; Vasquez, C. C.; Saavedra, C., The ompW (porin) gene mediates methyl viologen (paraquat) efflux in *Salmonella enterica* serovar typhimurium. *Res Microbiol* **2007**, *158* (6), 529-36.
53. Liu, J.; Keelan, P.; Bennett, P. M.; Enne, V. I., Characterization of a novel macrolide efflux gene, mef(B), found linked to sul3 in porcine *Escherichia coli*. *J Antimicrob Chemother* **2009**, *63* (3), 423-6.
54. Yamane, K.; Wachino, J.; Suzuki, S.; Kimura, K.; Shibata, N.; Kato, H.; Shibayama, K.; Konda, T.; Arakawa, Y., New plasmid-mediated fluoroquinolone efflux pump, QepA, found in an *Escherichia coli* clinical isolate. *Antimicrob Agents Chemother* **2007**, *51* (9), 3354-60.
55. Ogawa, W.; Koterasawa, M.; Kuroda, T.; Tsuchiya, T., KmrA multidrug efflux pump from *Klebsiella pneumoniae*. *Biol Pharm Bull* **2006**, *29* (3), 550-3.
56. Tanabe, M.; Szakonyi, G.; Brown, K. A.; Henderson, P. J.; Nield, J.; Byrne, B., The multidrug resistance efflux complex, EmrAB from *Escherichia coli* forms a dimer in vitro. *Biochem Biophys Res Commun* **2009**, *380* (2), 338-42.
57. Lin, M. F.; Lin, Y. Y.; Lan, C. Y., Contribution of EmrAB efflux pumps to colistin resistance in *Acinetobacter baumannii*. *J Microbiol* **2017**, *55* (2), 130-136.
58. Stavri, M.; Piddock, L. J.; Gibbons, S., Bacterial efflux pump inhibitors from natural sources. *J Antimicrob Chemother* **2007**, *59* (6), 1247-60.

59. Su, X. Z.; Chen, J.; Mizushima, T.; Kuroda, T.; Tsuchiya, T., AbeM, an H⁺-coupled *Acinetobacter baumannii* multidrug efflux pump belonging to the MATE family of transporters. *Antimicrob Agents Chemother* **2005**, *49* (10), 4362-4.
60. Xu, X. J.; Su, X. Z.; Morita, Y.; Kuroda, T.; Mizushima, T.; Tsuchiya, T., Molecular cloning and characterization of the HmrM multidrug efflux pump from *Haemophilus influenzae* Rd. *Microbiol Immunol* **2003**, *47* (12), 937-43.
61. Long, F.; Rouquette-Loughlin, C.; Shafer, W. M.; Yu, E. W., Functional cloning and characterization of the multidrug efflux pumps NorM from *Neisseria gonorrhoeae* and YdhE from *Escherichia coli*. *Antimicrob Agents Chemother* **2008**, *52* (9), 3052-60.
62. Allen, F. H.; Baalham, C. A.; Lommerse, J. P. M.; Raithby, P. R.; Sparr, E., Hydrogen-bond acceptor properties of nitro-O atoms: A combined crystallographic database and ab initio molecular orbital study. *Acta Crystallographica Section B-Structural Science* **1997**, *53*, 1017-1024.
63. He, G. X.; Kuroda, T.; Mima, T.; Morita, Y.; Mizushima, T.; Tsuchiya, T., An H⁽⁺⁾-coupled multidrug efflux pump, PmpM, a member of the MATE family of transporters, from *Pseudomonas aeruginosa*. *J Bacteriol* **2004**, *186* (1), 262-5.
64. Srinivasan, V. B.; Rajamohan, G.; Gebreyes, W. A., Role of AbeS, a novel efflux pump of the SMR family of transporters, in resistance to antimicrobial agents in *Acinetobacter baumannii*. *Antimicrob Agents Chemother* **2009**, *53* (12), 5312-6.
65. Leuzzi, A.; Di Martino, M. L.; Campilongo, R.; Falconi, M.; Barbagallo, M.; Marcocci, L.; Pietrangeli, P.; Casalino, M.; Grossi, M.; Micheli, G.; Colonna, B.; Prosseda, G., Multifactor Regulation of the MdtJI Polyamine Transporter in *Shigella*. *PLoS One* **2015**, *10* (8), e0136744.
66. Higashi, K.; Ishigure, H.; Demizu, R.; Uemura, T.; Nishino, K.; Yamaguchi, A.; Kashiwagi, K.; Igarashi, K., Identification of a spermidine excretion protein complex (MdtJI) in *Escherichia coli*. *J Bacteriol* **2008**, *190* (3), 872-8.
67. Ma, C.; Chang, G., Structure of the multidrug resistance efflux transporter EmrE from *Escherichia coli*. *Proc Natl Acad Sci U S A* **2004**, *101* (9), 2852-7.

Chapter 3 Computational Studies and Synthesis of Cyclized Small-Molecule ClpP

Activators

Abstract

The persistent emergence of antimicrobial-resistant bacteria, paired with a dwindling pipeline of therapeutic treatments amplifies the urgency for novel antibacterials. However, antibiotics that exploit new mechanisms of action provide modern challenges to bacteria; and thus, require the development of a completely new resistance regime, potentially lengthening the duration of action. One promising target departing from traditional antibacterial discovery paradigm is caseinolytic protease P (ClpP). Essential in bacterial homeostasis and virulence, this protease can be chemo-activated by natural products such as acyldepsipeptide (ADEP), resulting in uncontrolled protein degradation and subsequent bacterial cell death. Although ADEP exhibit impressive potency against Gram-positive pathogens, its overall low stability and the synthetic challenge that represents the peptidolactone prevent further development as an antibacterial. To structurally simplify ADEP and maintain its potency associated with the peptidolactone, I investigated the introduction of structural constraint to the ADEP bioactive fragment, *N*-heptenoyl-3,5-difluorophenylalanine, via N- to C-terminal cyclization. To understand the conformational behavior of the cyclized ClpP activators ranging from six- to eight-membered ring, I conducted computational studies on the conformational space of each analog. The synthetic work I performed provided methodologies to access the six-membered rings (piperazinones and pyrazinones), the seven-membered ring (1,4-diazepan-2-one), and the eight-membered ring (1,4-diazecan-2-one), and the generation of the corresponding small-molecule ADEP analogs. To evaluate the capacity

of this series to activate ClpP, I employed a fluorescence-based peptide degradation assay. Although all the cyclized analogs were inactive against *Bacillus subtilis* ClpP, the biological results demonstrated that, in conjunction with docking studies, a hydrogen bonding with ADEP and Tyr62 is essential for the chemo-activation of ClpP and conformational alteration of the scaffold cannot overcome the loss of this interaction.

1 Introduction

Regarded as the 20th century “wonder drugs”, antibiotics ushered in an era in which a bacterial infection was no longer considered a death sentence anymore.¹ However, the discovery of antibiotics was also accompanied by the emergence of resistance in bacteria, due to the misuse and over-prescription of antibacterial therapeutics. The same means by which antibiotics affect the survival of bacteria (e.g., disruption of cell wall synthesis, inhibition of protein biosynthesis, interference of bacterial DNA replication or transcription) also result in selective pressures that often drive the emergence of resistant phenotypes.² Achieved by target modification (e.g., upregulation, downregulation, or structural modification), efflux pump overexpression, and enzymatic drug inactivation, antibiotic resistance gives rise to the spread of bacterial strains recalcitrant to therapeutic intervention.³ Consequently, these so-called “superbugs” have become a threat to society as more than 700,000 people die from antibiotic resistant infections every year and this number is expected to reach 10,000,000 by 2050.⁴

In parallel to the emergence of antibiotic resistance, investment and interest (from pharmaceutical companies, particularly) in antibacterial drug discovery programs have dwindled since the 1980s. To magnify the problem, research efforts have largely focused on optimizing known antibiotics to address drug resistance, instead of expanding the scope of therapeutics with new mechanism of action. This paradigm shift created discovery and innovation gaps in the field and only yielded short-lived antibacterials as bacteria quickly acquired resistance against these new generations of current antibiotics. The challenge of discovering and/or developing antibiotics with new mechanisms of action is illustrated by the fact that a new antimicrobial class was last approved by the FDA in 2000, with the oxazolidinone Linezolid. The Pew Trusts have recently

emphasized the need for more antibacterial drug discovery programs by reporting that only 10 out of 43 new antibiotics in clinical development represent a novel drug class or mechanism of action.⁵

A promising avenue diverging from the traditional antibacterial discovery paradigm is the development of compounds exhibiting bactericidal activity by activating a bacterial process rather than inhibiting it. Such therapies relying on activation mechanisms would depart from conventional antibiotics and provide new antibacterial arsenal to treat multidrug resistant bacterial infections. Among the targets eliciting bactericidal activity upon activation, caseinolytic protease P (ClpP) represents an attractive therapeutic strategy and I present, in this chapter, my investigation to optimize a chemotype targeting ClpP via conformational constraint.

1.1 Bacterial Caseinolytic Protease P (ClpP)

Exposure to a broad range of environmental stressors such as extreme fluctuations in temperature, pH and salt concentration, as well as the presence of various antibacterials lead to the disruption of bacterial homeostasis, including abnormal gene expression and protein denaturation.⁶ Proteolysis is a key regulatory mechanism responsible for the turnover of intracellular proteins and ClpP is an example of one such protease that plays a central role in the degradation of damaged or misfolded proteins, short-lived regulatory proteins and virulence factors.⁷⁻¹⁰ Deletion of *clpP* in many pathogenic bacterial species (e.g., *Staphylococcus aureus*, *Streptococcus pneumoniae*, *Listeria monocytogenes*, and *Enterococcus faecalis*) impairs extracellular virulence, biofilm formation and/or bacterial survival.¹¹⁻¹³

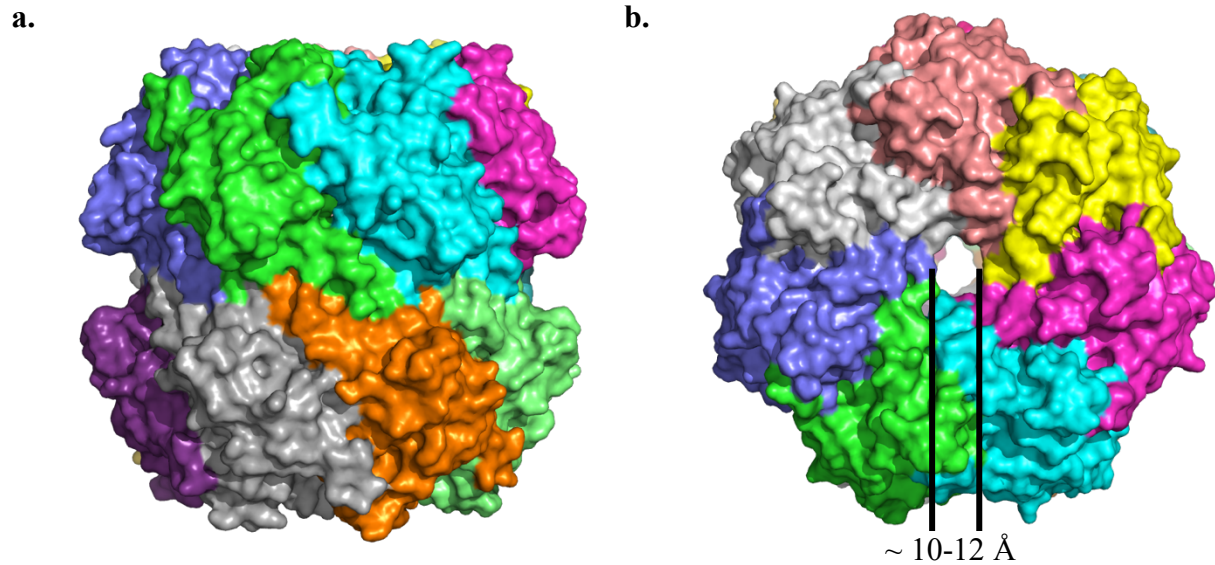
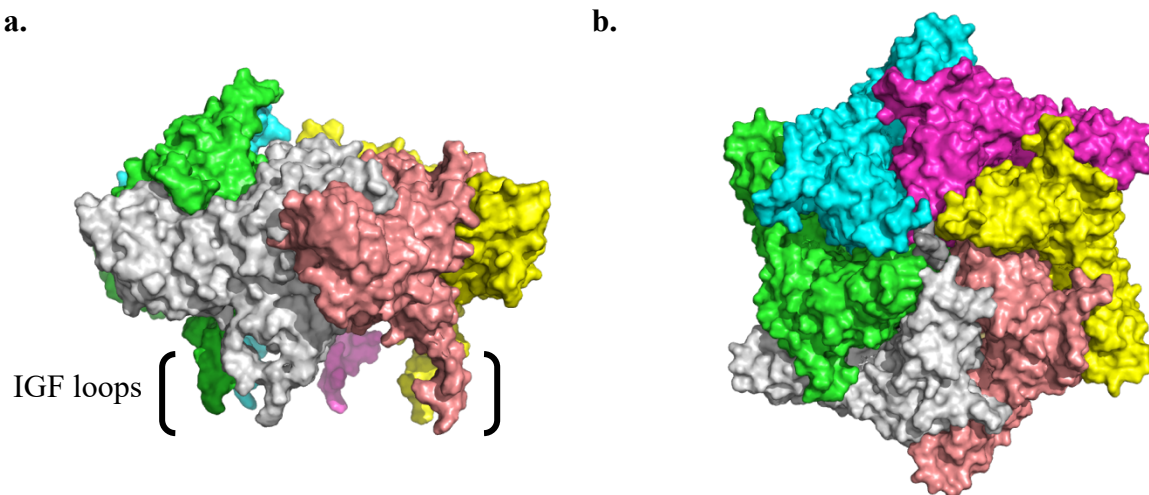


Figure 3.1: Structure of tetradecameric *Escherichia coli* ClpP. (a) Distal and (b) apical views (PDB: 1TYF).

ClpP is a serine protease consisting of 14 subunits organized into two stacked heptameric rings, forming a barrel (**Figure 3.1**) inside of which are located the catalytic residues (Ser-His-Asp).¹¹ The proteolytic activity of ClpP and its substrate selectivity are controlled by structural factors and molecular mechanisms. ClpP activity requires the formation of the tetradecameric barrel-like complex to form the active protease. In the biologically functional tetradecamer, the 14 catalytic triads are secluded from the cytoplasmic environment, protecting the cell from unregulated proteolysis.¹⁴ Substrates access the proteolytic chamber through a channel (10-12 Å in diameter) at the apical surface of ClpP, as depicted in **Figure 3.1b**. The N-terminal region of each ClpP subunit precludes the entrance of folded proteins or large polypeptides into the pore. ClpP alone can only degrade small peptides (<5 amino acids) and larger substrate entry requires the association with Clp-ATPases.¹⁵

ClpP chaperones (e.g., ClpA and ClpX) belong to the AAA+ protein family and are hexameric rings (**Figure 3.2b**) responsible for the recognition of proteins with SsrA degradation

tags.¹⁶ The chaperone ClpX docks between the ClpP monomer interfaces utilizing six protruding IGF loops to engage ClpP (**Figure 3.2a**). This loop motif is named for the Ile268-Gly269-Phe270 sequence that comprise the loop. The IGF loop is known to interact with the side chain of Arg192 in ClpP via hydrogen bonding. The flexibility of the IGF loops is enough to overcome the symmetry mismatch between the hexameric ClpX and the heptameric ClpP (**Figure 3.2d**). The formation of the ClpXP complex triggers a conformational shift in the N-terminal loops of ClpP and opens the pore of the heptameric ring (from 10 to 30 Å in diameter) allowing access to the degradation chamber (**Figure 3.2c**).¹⁷ Upon protein substrate recognition, the chaperone unfolds and translocates the polypeptide chain through the ClpP channel and into the proteolytic chamber in an ATP-dependent process.¹⁴



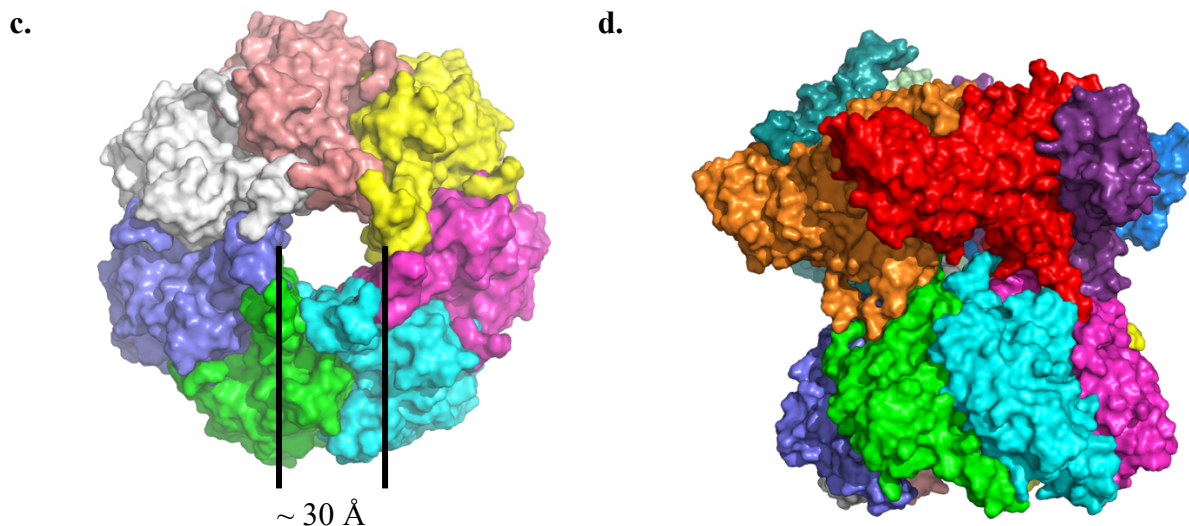


Figure 3.2: Structure of *E. coli* ClpXP complex. (a) Distal and (b) apical views of ClpX alone, (c) apical view of ClpP alone and (d) distal view of hexameric ClpX and heptameric ClpP complex (PDB: 1TYF).

The essential function of ClpP in bacterial homeostasis and virulence makes it an attractive target for the development of antibacterials.

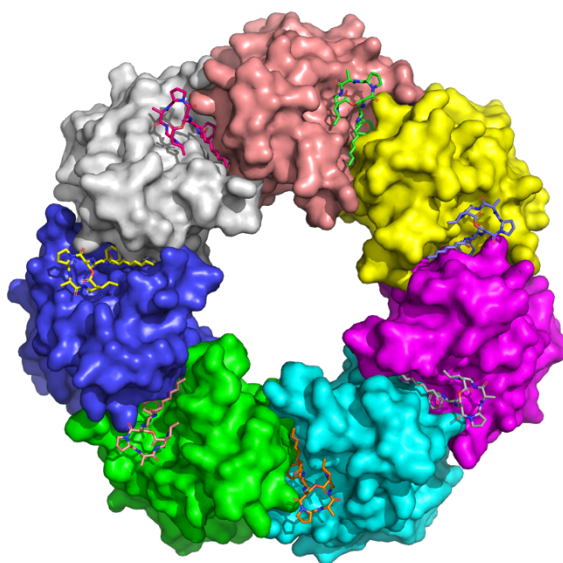
1.2 Chemo-Activation of ClpP

Although the function of ClpP had been known for more than two decades,^{18, 19} it was not considered a potential target until Brotz-Oesterhelt H. et al. identified the natural product acyldepsipeptide (ADEP 1 (**3.1**) in **Figure 3.3b**), from a *Streptococcus hawaiiensis* NRRL 15010 extract,²⁰ and demonstrated the ability of this chemotype to disrupt ClpP proteolytic activity.²¹ Contrary to normal physiological circumstances, ADEP 1 (**3.1**) and its derivatives were found to activate ClpP and induce uncontrolled proteolysis of flexible cytoplasmic polypeptides without the need for Clp-ATPases. This “artificial chemo-activation” of ClpP leads to inhibition of bacterial growth and eventual to cell death.²¹ X-ray crystallography studies revealed that ADEPs binds

competitively to the same hydrophobic pocket as the IGF loops of ClpX, on the apical surface between the interface of ClpP monomers (**Figure 3.3a**).²² As such, the competitive nature of ADEP binding not only results in unregulated peptidolysis, it also results in the inhibition of Clp-ATPases activity and blocks the degradation of typical substrates.²²

Furthermore, the Yang group established that the hydrogen bond between ADEP 1 (**3.1**) and Tyr62 (**Figure 3.3b**) triggers an identical opening of the pore in ClpP tetradecameric complex as that elicited by ClpX.^{9, 17} Upon ADEP 1 (**3.1**) binding, the side chain of Tyr62 is rotated 90° relative to the inactive ClpP causing a “domino effect” that reorients nearby residues and triggers a reordering in the N-terminal loops and a widening of ClpP axial pore. The observation of this effect in *E. coli* ClpP and *Mycobacterium tuberculosis* ClpP1P2, and the high conservation of Tyr62 in different bacterial species suggest this activation mechanism is shared by the whole ClpP family.^{9, 23, 24} The Yang group hypothesized that Tyr62 necessitates the hydrogen bonding with ADEP 1 (**3.1**) to overcome the energy barrier and rotate. By replacing Tyr62 with an alanine residue, they converted *S. aureus* ClpP (SaClpP) into a dysregulated protease able to degrade cell division protein FtsZ *in vivo* and inhibit staphylococcal growth independently of ATPase or ADEP activation. The “self-activation” of SaClpPY62A mutant demonstrated that the removal of the bulk of the tyrosine side chain enables ClpP to dynamically switch between conformations and highlights Tyr62 as a key residue for chemo-activation of ClpP.

a.



b.

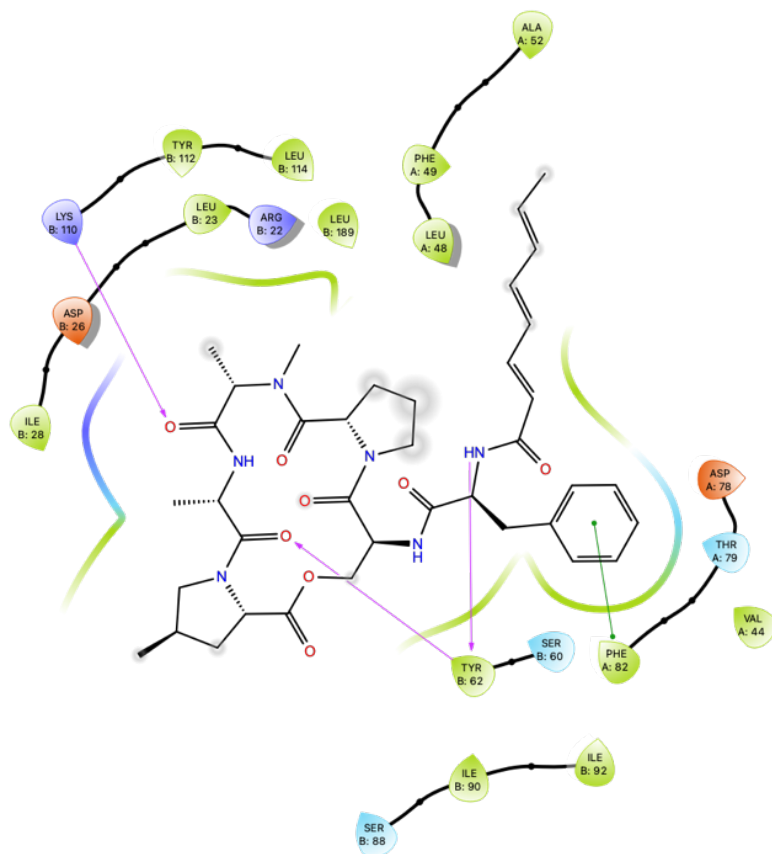


Figure 3.3: Apical view (a) and 2D diagram (b) of the co-crystal structure of ADEP 1 (3.1) bound to ClpP (PDB: 3PTI).

Following the discovery of ADEP 1 (**3.1**) as the first ClpP activator, structural optimization led to ADEP 4 (**3.2**), which exhibits nanomolar activity against various antibiotic-resistant pathogens (**Table 3.1**).

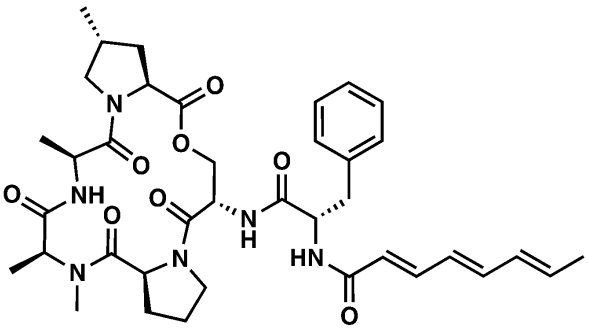
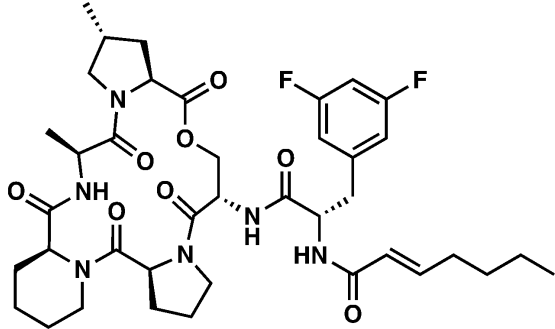
 <p>ADEP 1 (3.1)</p>	 <p>ADEP 4 (3.2)</p>	
Bacterial Strain	IC50 (nM)	
	ADEP 1 (3.1)	ADEP 4 (3.2)
<i>Bacillus subtilis</i> 168	278.2	13.0
<i>Streptococcus pneumoniae</i> 665*	2,225.8	26.0
<i>Streptococcus pyogenes</i> Wacker	556.4	26.0
<i>Enterococcus faecalis</i> ICB 27159	556.4	≤ 13.0
<i>Enterococcus faecium</i> L 4001*	556.4	≤ 13.0
<i>Staphylococcus aureus</i> NRS 119*	8,764.0	65.0

Table 3.1: Antibacterial activity of ADEP 1 (3.1**) and ADEP 4 (**3.2**).** * Resistant phenotype of clinical isolates: penicillin-resistant *Streptococcus pneumoniae* 665, vancomycin-resistant *Enterococcus faecium* L 4001 and methicillin-resistant *Staphylococcus aureus* NRS 119.

As discussed in **Chapter 2 Section 7.1**, the Sello group identified *N*-heptenoyl-3,5-difluorophenylalanine core as a simplified bioactive fragment of ADEP (**3.3**) and produced a series of analogs of fragment **3.4** to elucidate structure-activity relationships (SAR) of the scaffold (**Table 3.2**).²⁵ Among the methyl ester *N*-acyl 3,5-difluorophenylalanine chemotype (i.e., **3.4** – **3.9**, **Table 3.2**), compounds with an acrylamide moiety (i.e., **3.4** – **3.6**, **Table 3.2**) displayed the lowest MICs in *B. subtilis*. Substitution on the C-terminus of *N*-heptenoyl-3,5-

difluorophenylalanine core (i.e., **3.10** – **3.16**, **Table 3.2**) led to the most potent analog of this series, compound **3.16** with a MIC of 5.7 μM and apparent binding constant of 3.9 μM .

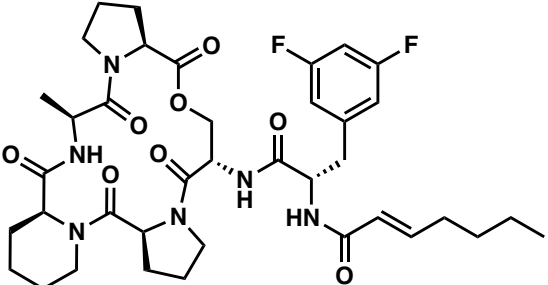
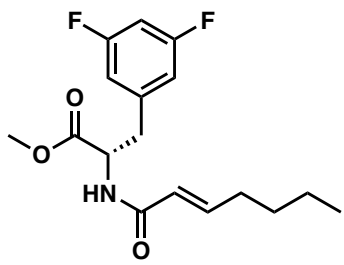
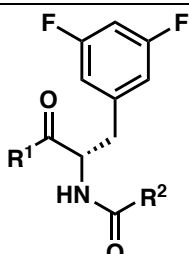

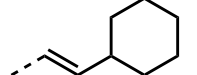
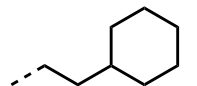
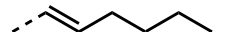
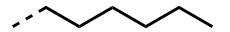
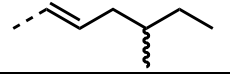
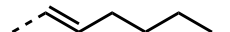
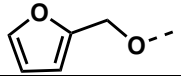
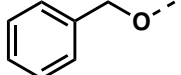
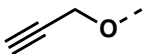
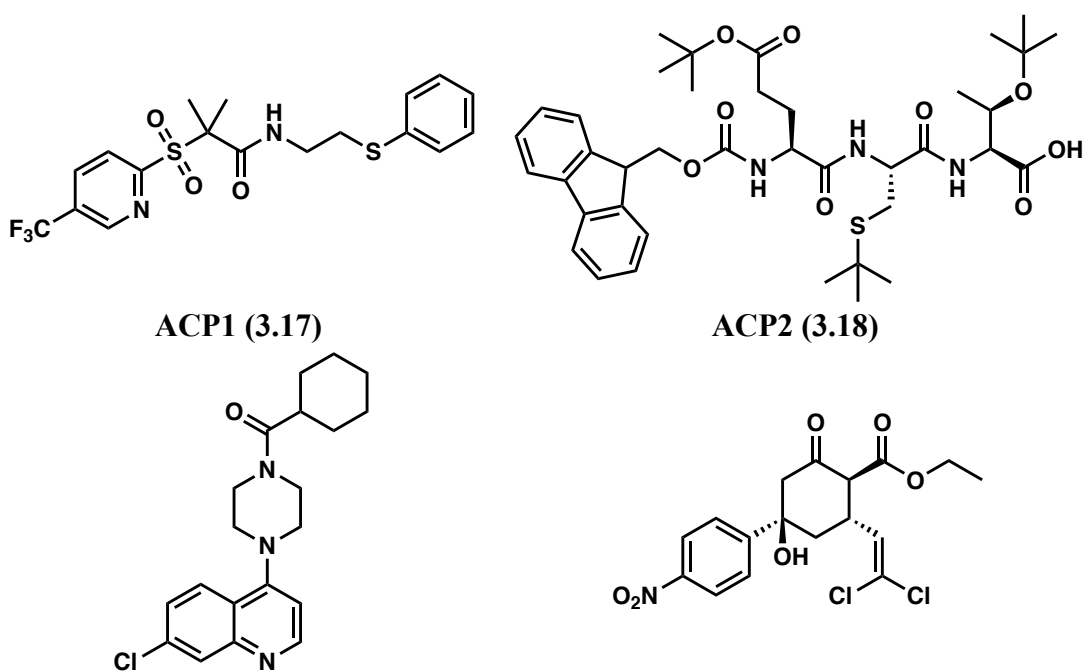
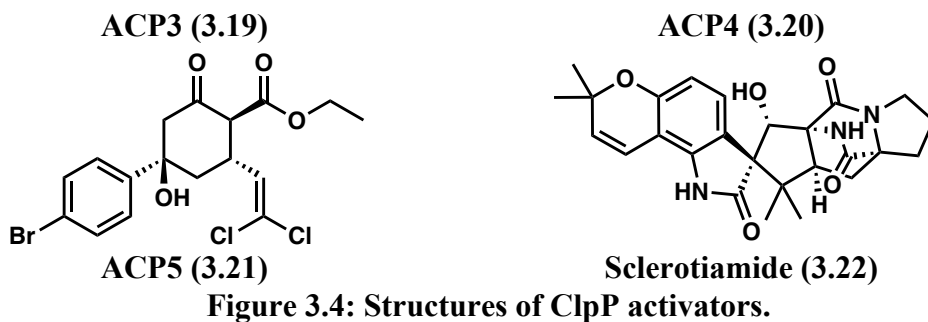
			
3.3		3.4	
			
Compound	R ¹	R ²	MIC in <i>B. subtilis</i> (μM)
3.5	OCH ₃		95.4
3.6			22.7
3.7			362.2
3.4			24.6
3.8			> 390.9
3.9			23.5
3.10	OH		205.6
3.11	NH ₂		103.1
3.12	NHCH ₃		98.7
3.13	N(CH ₃) ₂		189.1
3.14			81.8
3.15			318.8
3.16			5.7

Table 3.2: Derivatives of ADEP and MIC in *B. subtilis*.

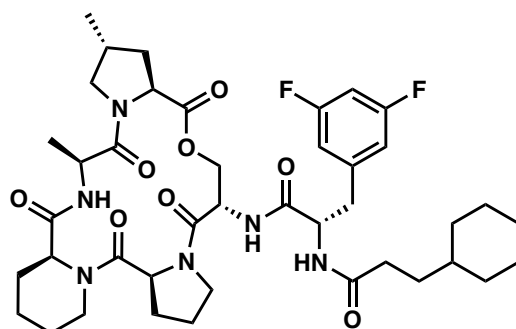
High-throughput screening campaigns have now led to the discovery of different chemotypes capable of activating ClpP. From ~ 65,000 drug-like compounds, small molecules ACP1-5 (**3.17** – **3.21**, **Figure 3.4**) (activators of cylindrical proteases) exhibit micromolar bactericidal activity against different Gram-negative bacteria when co-administered with the membrane permeabilizing agent, polymyxin B nonapeptide.²⁶ In addition, Sclerotiamide (**3.22**) was identified by our group from a fluorescence-based screen of ~ 450 fungal and bacterial secondary metabolites as the first non-peptide-based natural product ClpP activator.²⁷ Despite the interest arising from these structurally diverse ClpP-targeting compounds, the ADEP scaffold remains the most promising lead to develop ClpP activator antibacterials due to the nanomolar activity of ADEP analogs in a wide range of Gram-positive bacteria. Furthermore, the extensive literature on the ADEP scaffold and the corresponding pharmacophore provides the foundation to build upon and investigate important questions.





2 Rationale for the Design of Optimized ADEP Derivatives

2.1 N- to C-terminal Cyclization to Improve Potency and Stability of ADEP Bioactive Fragment



Despite the potent antibacterial activity of the ADEP scaffold, its overall low stability prevents further development as an antibacterial: (1) ADEP 2 (3.23) was degraded up to 90% in ≤ 24 h after incubation in Mueller-Hinton broth;²⁸ (2) The peptidolactone core is susceptible to hydrolysis in basic and acidic aqueous media;²⁹ (3) The acrylamide moiety and the *N*-acyl 3,5-difluorophenylalanine amide bond are metabolically unstable in mouse liver microsomes.³⁰

Proteolytic degradation and fast renal clearance³¹ are major obstacles for peptide drugs³² and the strategies to overcome these issues are often to increase the molecular weight of the peptide

by lipidation, linking larger proteins or pegylation.³³ Despite the success of these strategies, they are more applicable to drugs in a later stage of the pipeline rather than molecules like ADEPs, which are still at an early enough stage of interrogation to implement more traditional medicinal chemistry strategies. As such, modification of the cleavage sites such as N-terminal acetylation, N-methylation, and N- to C-terminal cyclization represent relevant avenues that may lead to address metabolic instability and provide insights for structural optimization.^{34, 35}

Studies by the Batey and Sello group have established that *N*-heptenoyl-3,5-difluorophenylalanine fragment is optimal for ClpP activation.³⁶⁻³⁸ More recently structural optimization of the peptidolactone has been the main focus of research efforts, in particular the stability of the macrocyclic ring.³⁹ However, synthesis of the peptidolactone is tedious and prevents a streamlined medicinal chemistry campaign, thus, structural simplification of the ADEP scaffold is the bottleneck for the advancement of the chemotype toward clinical use. The challenge of “simplifying” the peptidolactone is conserving the structural features which contributes to the potency of ADEP. Not only does the peptidolactone core provide important ligand-protein interactions within ClpP binding pocket, the alanine -NH- is involved in a intramolecular hydrogen bonding with the carbonyl of the C-terminus of 3,5-difluorophenylalanine. This non-covalent interaction has been shown to reduce the entropic penalty of binding by mimicking the bound conformation of ADEP.³⁷ As a consequence, any substitution of the peptidolactone ring with structurally simpler moieties will generally lead to the loss of this intramolecular hydrogen bond and a decrease in potency.²⁵ Therefore, we hypothesized that introducing structural constraint to the *N*-heptenoyl-3,5-difluorophenylalanine fragment through N- to C-terminal cyclization may position important functionalities in an orientation similar to the bound conformation of ADEP. The increased conformational rigidity of such cyclized analogs would reduce the entropic penalty

of binding into ClpP, thus, maintaining the potency of ADEP while being synthetically more tractable.

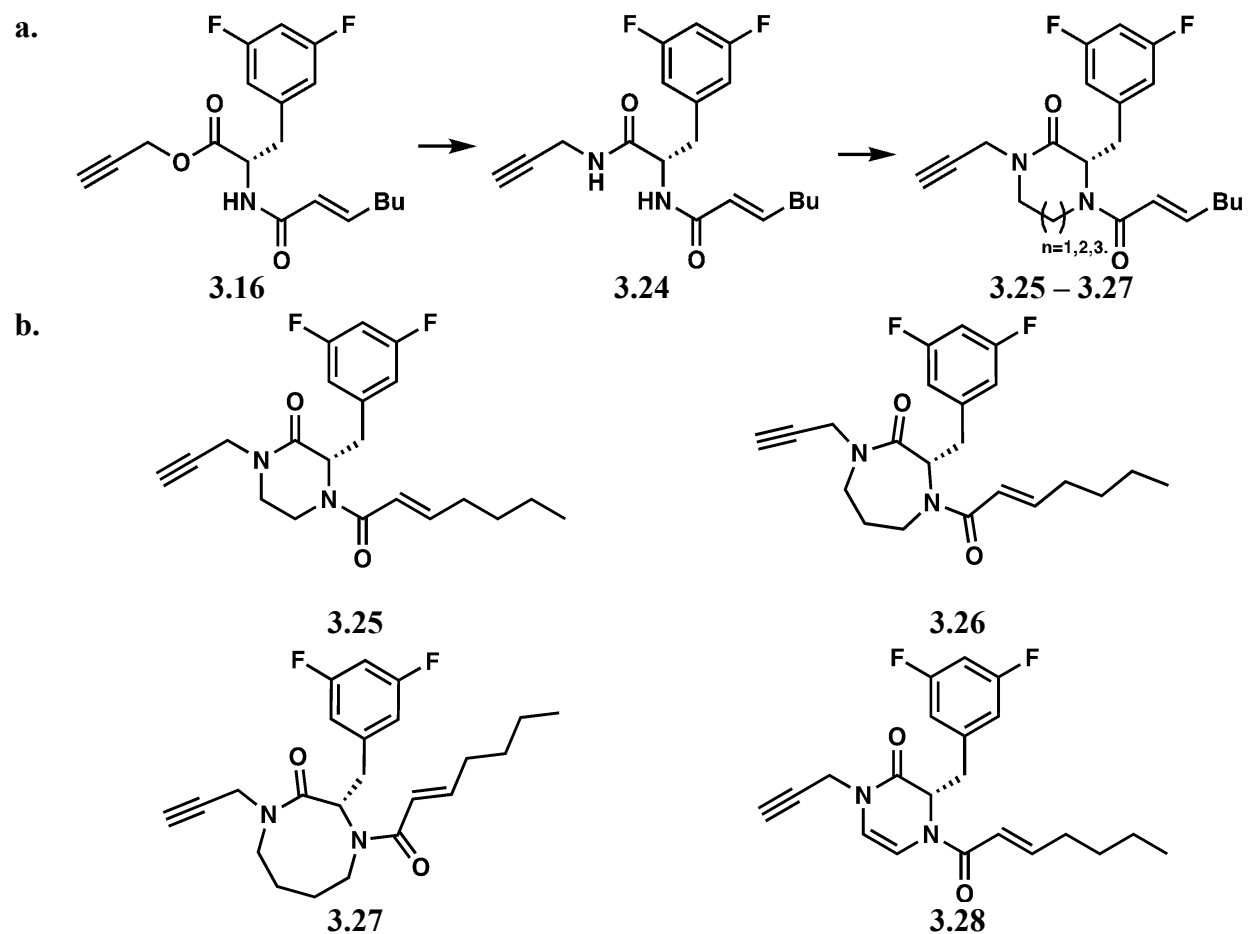


Figure 3.6: Rationale for the N- to C-terminal cyclization (a) and structures of the six- (3.25), seven- (3.26), eight-membered ring (3.27) and pyrazinone (3.28) ClpP activators (b).

In the initial design phase, analog **3.16** was selected as a starting point due to its structural simplicity and its potent binding affinity with ClpP ($K_{app}=3.9 \mu\text{M}$; Hill coefficient: 1.6).²⁵ Amide **3.24** was then envisioned as a more comparable congener to an uncyclized or *seco* analog to ADEPs. This analog also bears two nitrogen handles, which provide the correct valency required for cyclization and functionalization (**Figure 3.6a**). I hypothesized that, if designed properly, the synthesis of cyclized analogs of **3.24** could be achieved for a range of ring sizes (**3.25 – 3.27**,

Figure 3.6b). The pyrazinone analog (**3.28**) was also included in this study, since it can be easily synthesized as it is a precursor for the piperazinone (**3.25**) and the double bond is expected to influence the overall conformation. I envisioned that the specific orientation of the 3,5-difluorobenzyl, propargyl and heptenoyl groups would be determined by the size of the ring. To investigate this hypothesis, I conducted computational studies to assess if the conformations adopted by six- (**3.25**), seven- (**3.26**), eight-membered ring (**3.27**) and pyrazinone (**3.28**) analogs oriented these moieties favorably for binding in the ClpP binding pocket. Following the synthesis of the cyclized ClpP activators, this hypothesis was tested by evaluating their activity with ClpP in a fluorescence-based degradation assay.

2.2 Design of Analogs to Interrogate Alternate Substitutions of ADEP Bioactive Fragment

Although the 3,5-difluorophenylalanine is recognized as the optimal motif for the ADEP scaffold, only two studies have reported SAR for this moiety. As presented in **Table 3.3**, the introduction of a fluorine on the *meta* position (**3.30**) improves the MICs by more than 65-fold in different Gram-positive bacteria (i.e., *S. aureus*, *S. pneumoniae*, *E. faecium* and *E. faecalis*). An additional fluorine on the opposite *meta* position (**3.31**) further improves the MICs up to 2 fold, but inclusion of a third fluorine at the *para* position (**3.32**) is detrimental (15-fold increase). Furthermore, the authors mentioned observing a similar effect on MICs when other halogens and small alkyl groups were substituted to the phenylalanine but did not report the corresponding data. From this trend, Hinzen B. et al. concluded the SAR of the phenylalanine is rather tight and the binding pocket cannot accommodate larger groups.²⁹

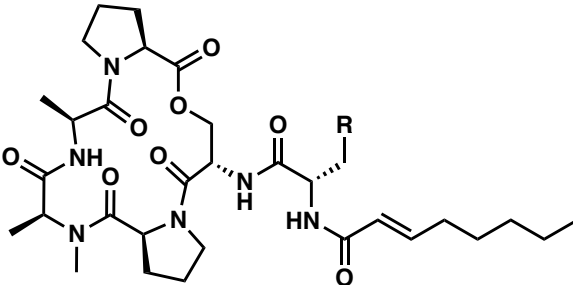
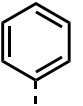
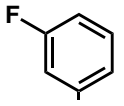
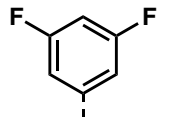
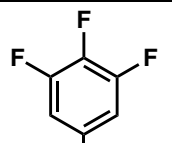
					
Compound	R	MIC (μM)			
		<i>S. aureus</i>	<i>S. pneumoniae</i>	<i>E. faecium</i>	<i>E. faecalis</i>
3.29		>90.3	>90.3	>90.3	>90.3
3.30		1.4	0.34	≤0.17	≤0.17
3.31		0.67	≤0.17	≤0.17	≤0.17
3.32		10.5	2.6	2.6	1.3

Table 3.3: SAR study of the fluorination of the ADEP phenylalanine in Gram-positive bacteria.

In a second SAR study on ADEP (Table 3.4), Batey R. A. et al. substituted the 3,5-difluorobenzyl moiety (3.33) with a pentafluorobenzyl group (3.34), bicyclic rings (3.35 and 3.36) and cyclohexyl group (3.37). Consistent with Hinzen's conclusion, pentafluorination of the benzyl ring (3.34) abolished the antibacterial activity of ADEP in Gram-positive bacteria. In addition, no improvement in MICs was observed with the larger groups (3.35 and 3.36) or the saturated ring (3.37).³⁶ However, the benzothiophenyl (3.35) and cyclohexyl (3.37) analogs maintained micromolar activities indicating that the ClpP binding pocket tolerates larger groups than

anticipated and that exhaustive fluorination might affect the activity of ADEP negatively for reasons outside of steric arguments.

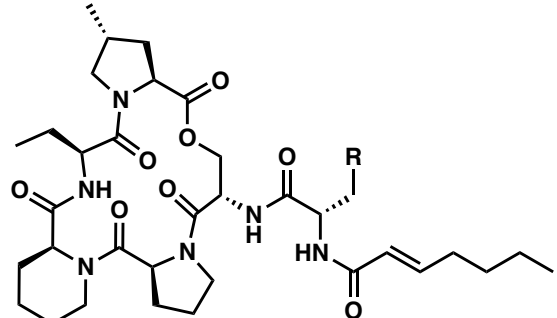
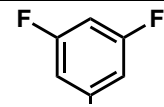
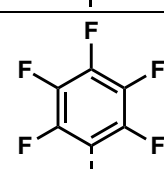
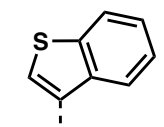
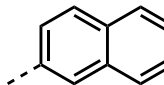
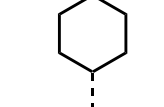
				
Compound	R	MIC (μM)		
		<i>S. aureus</i>	<i>S. pneumoniae</i>	<i>B. subtilis</i>
3.33		0.16	0.08 - 0.16	≤ 0.08
3.34		>152.6	>152.6	152.6
3.35		9.9	9.9	9.9
3.36		>160.2	2.5	160.2
3.37		1.3	0.66	2.7

Table 3.4: SAR study of the substitution of the ADEP phenylalanine in Gram-positive bacteria.

Taken together these SAR studies confirm that the 3,5-difluorophenylalanine is the most favorable moiety in whole-cell assays, but the lack of comparative data (i.e., biochemical assays, binding affinity determinations) and the narrow scope of these studies indicate the lack of

conclusive answers surrounding the 3,5-difluorobenzyl motif and its SAR. Furthermore, the *N*-heptenoyl 3,5-difluorophenylalanine motif was identified by Sello J. K. as an efflux substrate in *Mycobacteria tuberculosis*.⁴⁰ Therefore, further investigations are expected to lead to new observations that may give rise to chemically distinct activators departing from the 3,5-difluorobenzyl motif, and as a result potentially decreasing the efflux susceptibility of such chemotype.

Mutational analysis on the ClpP binding pocket conducted by Houry W. A. et al. demonstrated that the aforementioned ClpP activator ACP5 (**3.21**) also binds in the same pocket as ADEP.²⁶ In addition, my previous computational work further predicted the bromophenyl moiety to fit in the same region as the 3,5-difluorophenylalanine and the bromine was hypothesized to interact with Thr79 (**Figure 3.3b**) via halogen bonding.⁴¹ Therefore, I designed the *para*-Bromo *seco* analog (**3.38**, **Figure 3.7**) to determine: (1) If the binding pocket can accommodate a larger halogen; (2) If a potential halogen bond with Thr79 is accessible and beneficial for ClpP activation. In addition, I designed the tyrosyl *seco* analog (**3.39**) as an alternative moiety to interact with Thr79 via hydrogen bonding.

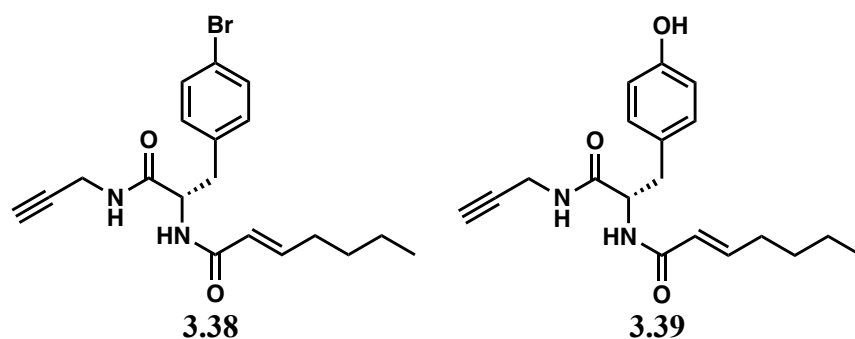


Figure 3.7: Structures of the *para*-Bromo (3.38) and tyrosyl *seco* (3.39) analogs.

As introduced in **Section 1.2**, Tyr62 is involved in a double hydrogen bond with the carbonyl of the depsipeptide alanine and the N-terminus of the phenylalanine of ADEP 1 (**3.1**, **Figure 3.3b**). Since this protein-ligand interaction is critical to trigger the conformational change in Tyr62 leading to the chemo-activation of ClpP.⁹ I hypothesized that the N- to C-terminal cyclization could abolish the hydrogen bond donating character of the N-terminus of the ADEP scaffold and potentially decrease the activity of cyclized analogs. To determine whether the cyclization and the resulting conformational change between compounds **3.25**, **3.26**, **3.27** and **3.28** or the obstruction of the hydrogen bond with Tyr62 is responsible for the possible decrease in activity, I designed the *seco* analog **3.40** (**Figure 3.8**). As the conformation between **3.40** and **3.24** is expected to be similar, I hypothesized that any activity difference between **3.40** and **3.24** in the peptide degradation assay should arise from the methyl group at the N-terminus of the 3,5-difluorophenylalanine preventing the hydrogen bond with Tyr62.

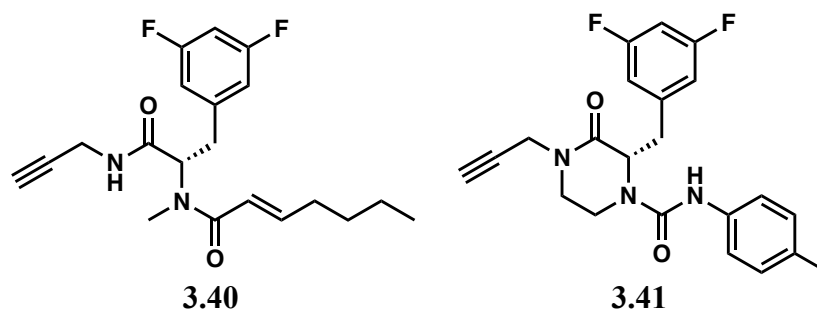


Figure 3.8: Structures of N-methyl *seco* (3.40) and toluyl-urea piperazinone (3.41) analogs.

As discussed in **Chapter 2 Section 7.1**, Lee R. E. et al. reported a new class of ADEP derivatives where the heptenoyl group was replaced by phenyl ureas, improving the metabolic stability of the scaffold. The ureadepsipeptide bearing a toluyl urea (**3.42**, **Figure 3.9**) was also

found to be engaged in an additional hydrogen bond with Tyr62 via crystallography, once again confirming the potential importance of this interaction.³⁰

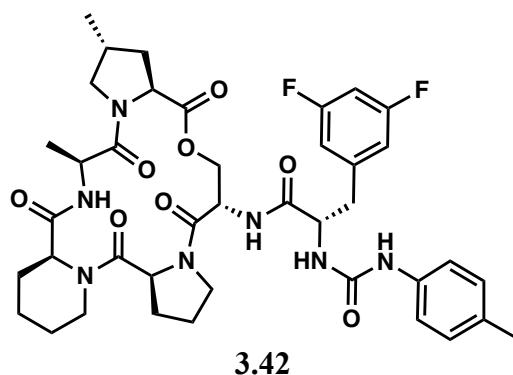


Figure 3.9: Structure of ureadepsipeptide (3.42)

As the loss of the hydrogen bond donor was anticipated to decrease the activity of cyclized analogs, I hypothesized that replacing the heptenoyl group with toluyl urea (**3.41**, **Figure 3.8**) would restore the hydrogen bond with Tyr62 and improve the activity of the series.

3 Computational Studies

3.1 Conformational analysis

The central hypothesis of this project is that the N- to C-terminal cyclization of **3.24** would constraint the core scaffold and lock 3,5-difluorobenzyl, propargyl and heptenoyl groups in an orientation favorable for ClpP binding and provide resistance to esterase and/or peptidase degradation. Varying the ring size of the cyclized core from 6-8 was expected to lead to distinct ground-state conformations of the core ring, leading to slight differences in the projected appendages. To provide a foundational insight into the conformational behavior of the targeted

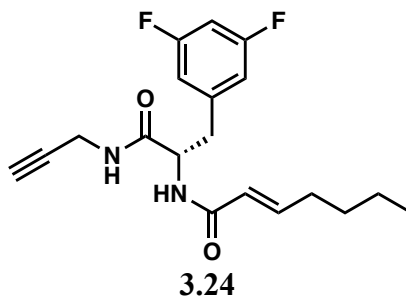
molecules, computational studies were completed to sample the conformational space of each analog.

Compound	Rotatable bond count	Globularity
3.24	9	0.108
3.25	7	0.133
3.26	7	0.084
3.27	7	0.155
3.28	7	0.045

Table 3.5: The number of rotatable bonds and the predicted globularities of analogs 3.24, 3.25, 3.26, 3.27 and 3.28.

First, the flexibility and spatial occupancy of the ClpP analogs were estimated via the number of rotatable bonds and the predicted globularity (i.e., three-dimensionality) respectively, using the eNTRYway platform.⁴² Although cyclized analogs (**3.25 – 3.28**) have a lower number of rotatable bonds, compared to the *seco* analog **3.24**, thus indicating an increased rigidity (**Table 3.5**), this descriptor is inadequate in elucidating the overall flexibility differences between the series of compounds. Similarly, the narrow range of the predicted globularity of **3.24 – 3.28** (0.045 – 0.155, **Table 3.5**) and the absence of correlation between the ring size and the globularity fails to provide any insights into the effect of cyclization or the ring size on the conformational bias of analogs. It is worth noting, however, the predicted globularity decreased 3-fold between **3.25** and **3.28** confirming that the double bond leads to a higher planarity of the structure, as predicted.

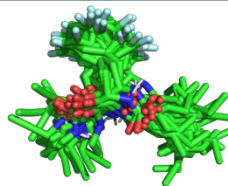
a.



Input Ligand

Hamiltonian Replica Exchange
molecular dynamic simulations

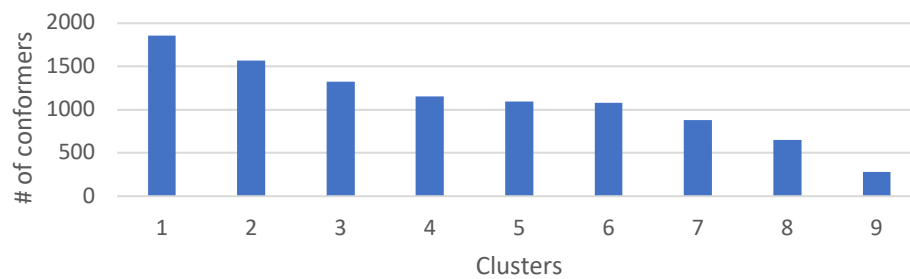
b.



10,000 conformers

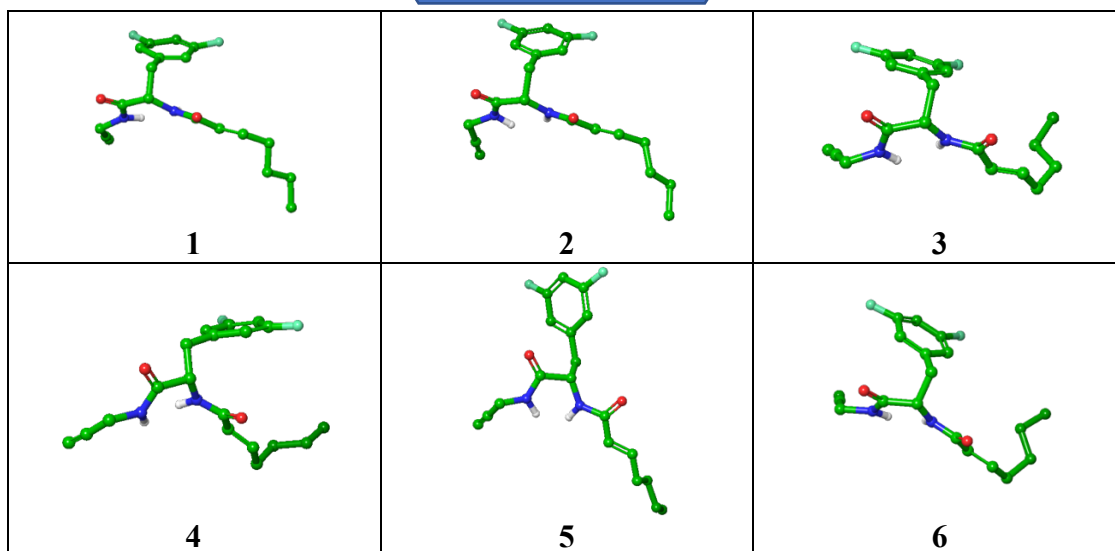
Clusterization

c.



Quantum Mechanics
optimization

d.



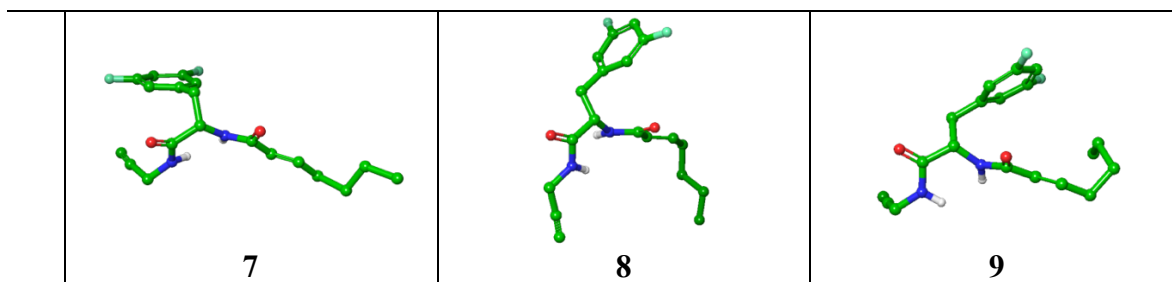


Figure 3.10: Bioactive conformational ensemble pipeline using analog 3.24 as example.

To better investigate the conformational bias of **3.24 – 3.28**, the bioactive conformational ensemble (BCE) server developed by Hospital and Orozco was employed.⁴³ The BCE server (<https://mmb.irbbarcelona.org/BCE/>) works as a fully automated platform for interrogating bioactive ligand conformational space (**Figure 3.10**). Hamiltonian Replica Exchange molecular dynamic simulations are performed in aqueous environment to sample the bioactive conformational space of the molecule (**Figure 3.10b**), and the resulting ~10,000 conformers, representing 95% of the variability of the calculated trajectory, are grouped in clusters (**Figure 3.10c**). Each conformer representative of a cluster is then refined through quantum mechanics calculations, and within the resulting optimized conformational ensemble, each conformer is ranked based on the size of its cluster (**Figure 3.10d**). This approach aims at predicting the bioactive conformations corresponding to the most likely bound conformation of a ligand, these predicted conformations might differ from the most-stable conformation.

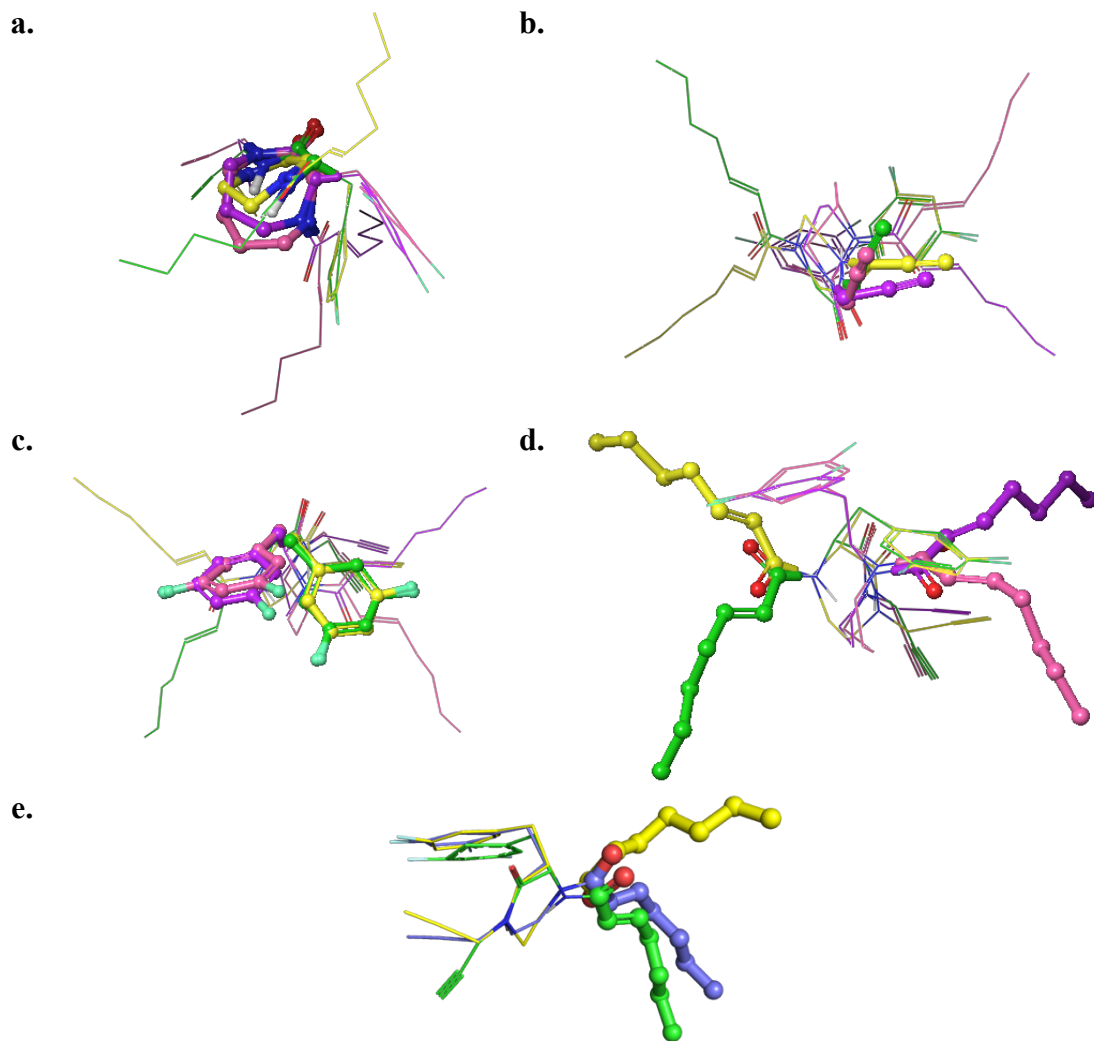


Figure 3.11: Superimposed analogs 3.24 (green), 3.25 (yellow), 3.26 (violet), 3.27 (pink) and 3.28 (blue). The core (a.), propargyl (b.), 3,5-difluorobenzyl (c.) and heptenoyl (d. and e.) are highlighted in licorice and the rest of the structure is represented in lines.

First, I performed a visual analysis of the predicted conformational ensembles of each analog to assess: (1) How the size of the core ring affects the orientation of the appending moieties; (2) What conformations the core rings adopt and the differences based on the size; (3) The range of motion for each analogs.

To qualitatively determine the conformational differences between each analog, the conformer representative of the most populated cluster for **3.24 – 3.28** were aligned according to the backbone of the 3,5-difluorophenylalanine. To facilitate the visual comparison, motifs of

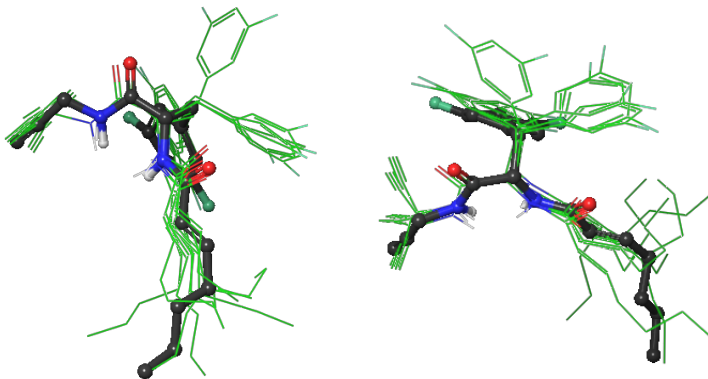
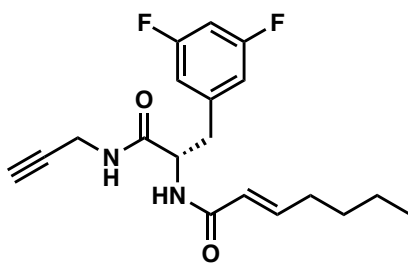
interest were highlighted in licorice and the rest of the structure was represented as lines, as depicted in **Figure 3.11**. Because the C-termini of the 3,5-difluorophenylalanine are constrained and thus overlay well (**Figure 3.11a**), the orientation of the propargyl groups is relatively similar considering it can freely rotate around the carbon adjacent to the terminal alkyne (**Figure 3.11b**). The N-terminal domains of the analogs, however, are shifted out of the plane for both seven- and eight-membered analogs (**Figure 3.11a**) to accommodate the ground-state conformations of the larger ring systems. These leads to a reorientation of the 3,5-difluorobenzyl moiety for both compounds (**Figure 3.11c**). The heptenoyl group produces the most disparate conformations between analogs and the corresponding amide shifts in relation to the α -carbon of the 3,5-difluorophenylalanine: *trans*, *cis*, *cis*, *trans* and *trans* in **3.24**, **3.25**, **3.26**, **3.27** and **3.28** respectively (**Figure 3.11d** and **3.11e**). Although analogs **3.24**, **3.25** and **3.28** overlap to a significant degree (**Figure 3.11e**), the opposite orientation of the heptenoyl group of **3.25** compared to **3.24** and **3.28** highlights the unexpected influence of the pyrazinone double bond on the conformation of **3.28**. The *trans* conformation of the heptenoyl amide is likely and more favorably allows electron delocalization between the π -systems of the pyrazinone and the acrylamide. In summary, the size of the core ring appears to predominantly influence the orientation of the 3,5-difluorobenzyl and heptenoyl groups.

For each analog, a conformer representative of each cluster was aligned according to the backbone of the 3,5-difluorophenylalanine to visualize the conformational space of the clusters (**Figure 3.12**). The core rings were predicted to adopt different conformations depending on the size of the ring (**Figure 3.11a**), but only minor variability is observed between conformers for each analog (**Figure 3.12**). As expected, the planarity of the six-membered ring increases from the piperazinone (**3.25**, **Figure 3.12b**) to the pyrazinone (**3.28**, **Figure 3.12e**) as the pyrazinone double

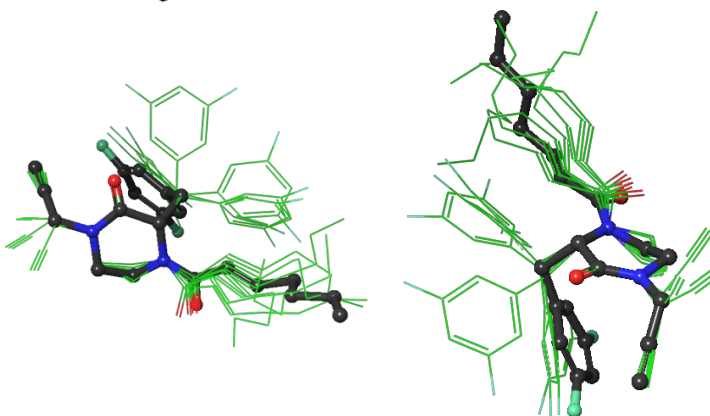
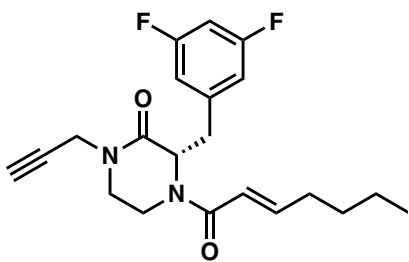
bond expands the π -system by conjugating the internal amide with the heptenoyl amide. In the saturated systems, the planarity is lost as the size of the core ring increases, causing the seven-membered (**3.26**, **Figure 3.12c**) and eight-membered (**3.27**, **Figure 3.12d**) rings to adopt pseudo-chair conformations. Although the motion of the 3,5-difluorobenzyl, propargyl, and aliphatic chain off the heptenoyl tail are not constrained and undergo free rotation, their orientation differs between **3.25**, **3.26**, **3.27** and **3.28**. The 3,5-difluorobenzyl and propargyl moieties were predicted to project to the same face relative to the six-membered ring, whereas the heptenoyl group resides in the same plan as the core ring (**Figure 3.12b** and **3.12e**). However, in the larger 7- and 8-membered systems, the propargyl and heptenoyl groups are on the opposite face relative to the 3,5-difluorobenzyl (**Figure 3.12c** and **3.12d**, respectively).

In summary, qualitative analysis of the conformational ensemble of analogs **3.24** – **3.28** indicated that the size of the core ring appears to predominantly influence the orientation of the 3,5-difluorobenzyl and heptenoyl groups, although 3,5-difluorobenzyl, propargyl, and aliphatic chain off the heptenoyl tail can undergo free rotation. The conformation of the core ring is constrained within each analog, but it evolves from planar (**3.25** and **3.28**) to pseudo-chair (**3.26** and **3.27**). However, this visual analysis did not reflect the extent of which the size of the core ring influences the orientation and flexibility of the appending moieties. Therefore, I used the root-mean square deviation (RMSD) and dihedral angles to quantify such effects.

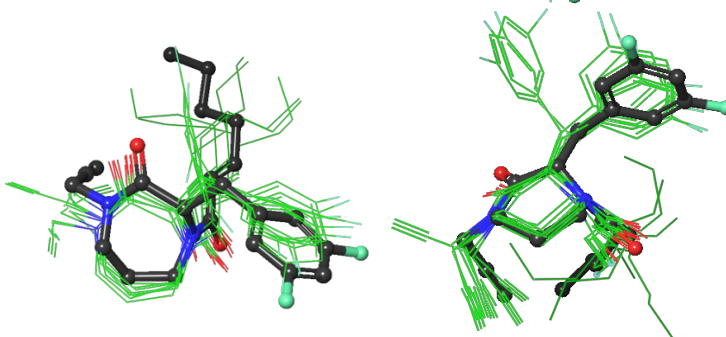
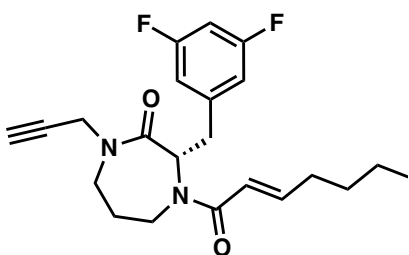
a.



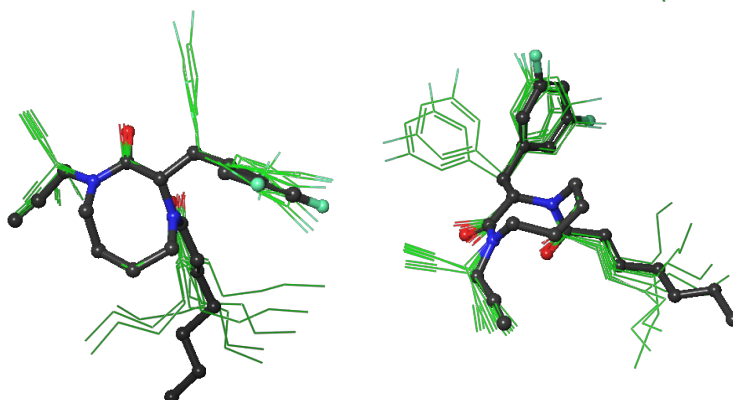
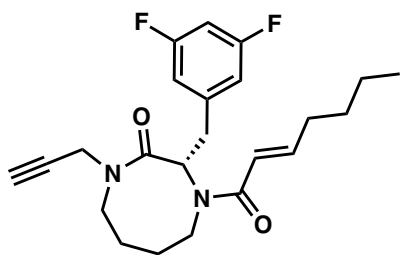
b.



c.



d.



e.

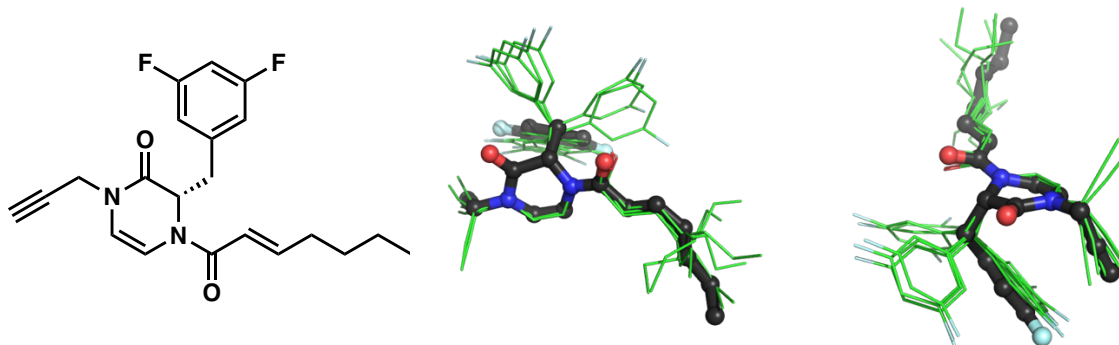


Figure 3.12: Conformational ensemble of analogs 3.24 (a.), 3.25 (b.), 3.26 (c.), 3.27 (d.) and 3.28 (e.). The conformer representative of the most populated cluster is shown in dark gray licorice, and the conformers representative of the less populated cluster are depicted in green lines.

The RMSD, a measure of the average distance between atoms of superimposed structures, was calculated for the conformational ensemble of each analog using Pymol. The conformer representative of the first cluster was used as a reference to determine the RMSD with the other clusters (**Table 3.6**). The weighted average and weighted standard deviation of the RMSD were used as global descriptors of the flexibility of the series of compounds. As observed in **Figure 3.12**, the core ring displays only minor variability within each analog, thus the deviation measured with the RMSD arises from the appended moieties. Since the *seco* analog **3.24** is unconstrained by N- to C-terminal cyclization, it was expected to be more flexible than the cyclized compounds. With the highest weighted average RMSD (1.34 Å, **Table 3.6**) and second most important weighted standard deviation (0.82 Å), the range of motion of **3.24** is indeed predicted to be greater than **3.25**, **3.26** and **3.27**. Although not fully linear, the weighted average RMSD and weighted standard deviation exhibit a descending trend as the size of the core ring increases, suggesting that larger cycles give rise to higher constraint of the substituents attached to the scaffold. In addition, the weighted average RMSD and weighted standard deviation of **3.28** are lower than **3.25**, further validating the observation that the rigidity of pyrazinone ring decreases the overall flexibility of

the structure compared to the piperazinone ring. Although the size of the ring system appears to decrease the overall conformational flexibility, RMSD does not provide information about the orientation and flexibility of each of the appended groups on the scaffold. To gain insight into side chain orientation and flexibility, dihedral angles were then considered.

Compound	3.24		3.25		3.26	
Cluster	Population	RMSD (Å)	Population	RMSD (Å)	Population	RMSD (Å)
1 (Reference)	1857	0	2181	0	2155	0
2	1566	0.43	2022	2.092	1509	0.567
3	1324	0.47	1750	0.26	1507	0.258
4	1157	1.984	1111	1.493	1425	0.307
5	1092	2.112	774	0.584	794	0.963
6	1083	1.67	766	1.372	700	1.039
7	880	1.589	555	2.224	693	0.442
8	652	1.486	497	0.371	632	0.26
9	282	2.414			419	2.259
10						
Weighted Average RMSD (Å)		1.34		1.24		0.60
Weighted Standard Deviation (Å)		0.82		0.86		0.49
Compound	3.27		3.28			
Cluster	Population	RMSD (Å)	Population	RMSD (Å)		
1 (Reference)	1790	0	2587	0		
2	1455	0.3	2164	1.587		
3	1217	0.337	1091	0.259		
4	1217	0.543	967	0.247		
5	1142	1.076	746	0.231		
6	902	0.454	745	0.278		
7	741	1.185	642	1.488		
8	502	2.119	335	0.368		
9	487	0.46	255	0.156		
10			162	2.609		
Weighted Average RMSD (Å)		0.69		0.83		

Weighted Standard Deviation (Å)		0.52		0.70
---------------------------------	--	------	--	------

Table 3.6: Root-mean square deviation (RMSD), weighted average RMSD and weighted standard deviation of the conformational ensemble of analogs 3.24 – 3.28.

To quantify torsional flexibility of **3.24 – 3.28**, the dihedral angles of each moiety displaying orientational variability between conformational clusters were determined. Defined by the angle between two outer bonds within three consecutive bonds, the dihedral angle of each motif was measured in Maestro (Schrodinger) for each cluster and the values were compiled in tables for each analog in the **Appendix**. The dihedral angles of the propargyl, the backbone of 3,5-difluorophenylalanine, the 3,5-difluorobenzyl, the heptenoyl tail, and the heptenoyl amide are represented in histograms in **Figures 3.13 – 3.17** respectively. To illustrate the proportion of the conformers adopting a specific dihedral angle, more populated angles are represented further from the center of the plot. Dihedral angles from the co-crystal structure of ADEP 4 (**3.2**) bound to *S. aureus* ClpP (PDB: 6TTZ) of the same motifs were also calculated and are included in **Figures 3.14 – 3.17** to allow comparison with analogs **3.24, 3.25, 3.26, 3.27** and **3.28**.

In the dihedral histogram for the propargyl group (**Figure 3.13**), changes in orientation do not appear to correlate with the N- to C-terminal cyclization or the increase in the ring size (**3.25, 3.26** and **3.27**). Considering the low bulkiness of the propargyl moiety and its isolated position on the scaffold (opposite to the 3,5-difluorobenzyl and heptenoyl), its torsional motion is likely not affected by structural changes. However, a noticeable spatial proximity between the propargyl and the 3,5-difluorobenzyl moieties in **3.25 (Figure 3.12b)** and **3.28 (Figure 3.12e)**, and heptenoyl and 3,5-difluorobenzyl groups in **3.26 (Figure 3.12c)** could cause the dihedral angle of the propargyl group in these analogs to be predominantly distributed between 70° and 110° (**Figure 3.13**). Whereas the propargyl of **3.24 (Figure 3.12a)** and **3.27 (Figure 3.12d)** is isolated leading

to a more scattered distribution of the dihedral angles. Therefore, the spatial proximity of the appended groups might influence their orientation, but this effect may be only relevant in solution and would not reflect the final orientation of the propargyl moiety upon binding.

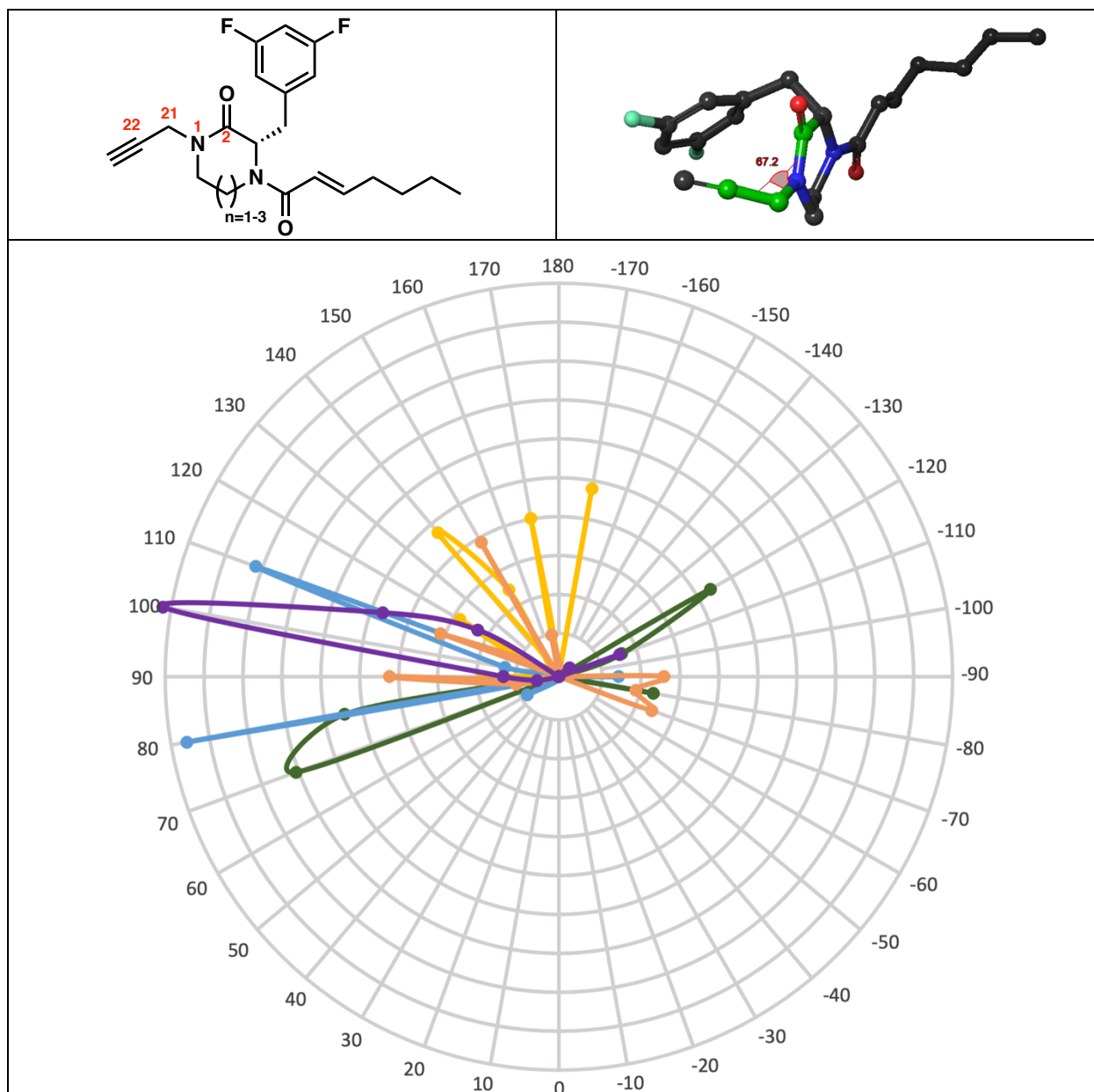
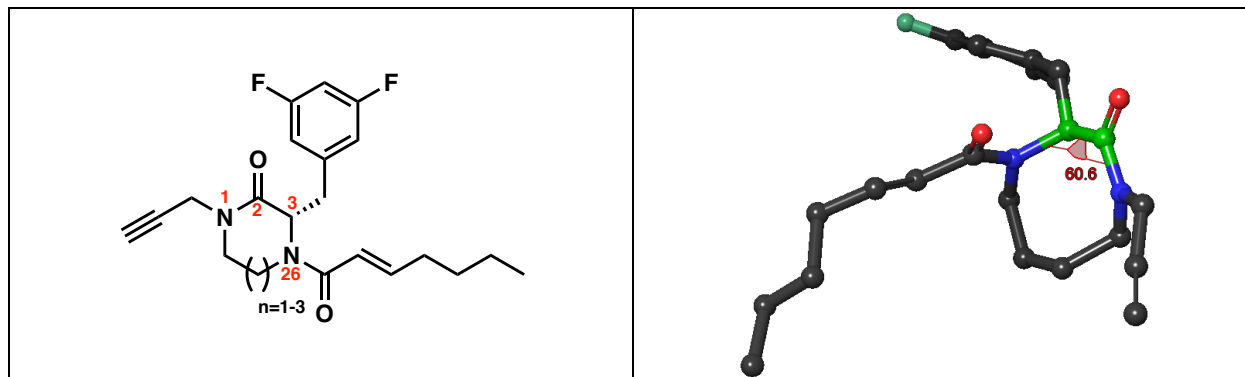


Figure 3.13: Histogram of dihedral angles of the propargyl group in analogs 3.24 (yellow), 3.25 (green), 3.26 (blue), 3.27 (orange) and 3.28 (purple). The dihedral angle was measured for the atoms C22-C21-N1-C2 (labeled in red) and displayed in a 3D representation of 3.25 as an example.

As previously observed in **Figure 3.11a**, the N-terminal domain shifts as the size of the core ring increases, to quantify this effect, the dihedral angle of the 3,5-difluorophenylalanine backbone for each analog was measured. The torsional range of the backbone is limited from 10 to 20° in both *seco* (**3.24**) and cyclized (**3.25**, **3.26**, **3.27** and **3.28**) analogs, as shown in the histogram **Figure 3.14**, confirming the low variability in the conformation adopted by the ring cores. Although the backbone is relatively planar in **3.24**, **3.25** and **3.28**, the dihedral angle of the backbone increases for the seven- (**3.26**) and eight-membered (**3.27**) rings to accommodate the bigger rings and, by doing so, mimics the angle of ClpP-bound ADEP 4 (**3.2**).



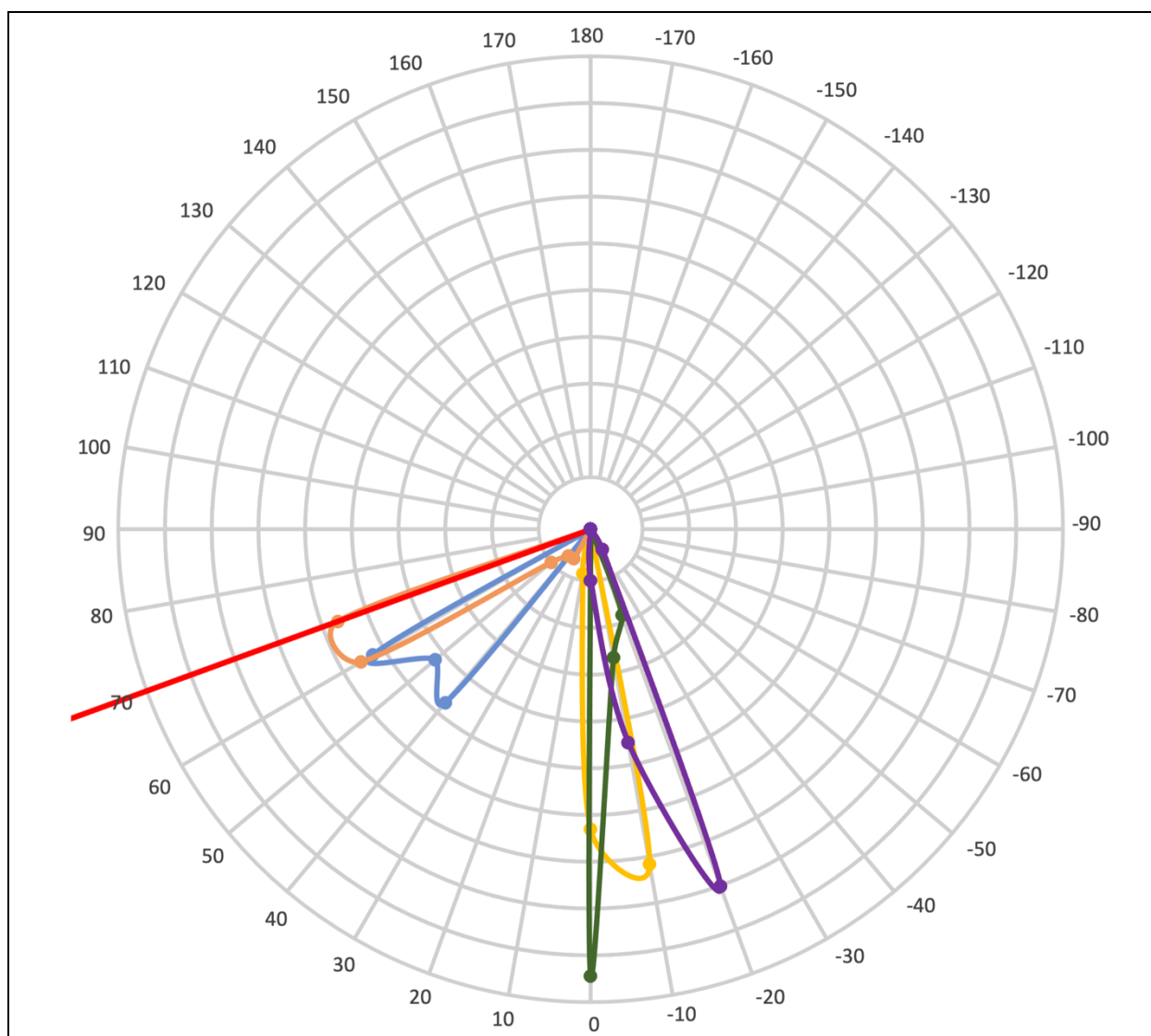
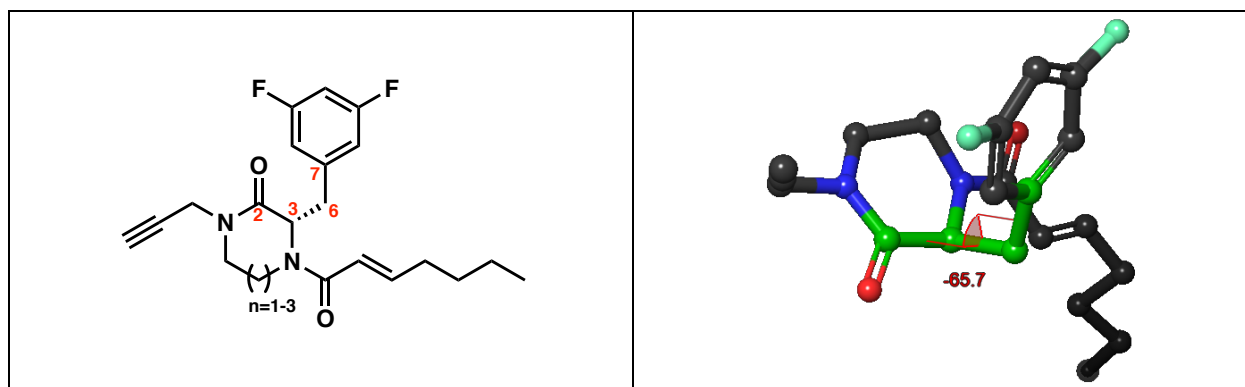


Figure 3.14: Histogram of dihedral angles of the 3,5-difluorophenylalanine backbone in analogs 3.24 (yellow), 3.25 (green), 3.26 (blue), 3.27 (orange) and 3.28 (purple). The dihedral angle was measured for the atoms N1-C2-C3-N26 (labeled in red) and displayed in a 3D representation of **3.27** as an example. The red line in the histogram indicates the dihedral angle of the backbone bond of the cocrystal structure of ADEP 4 (**3.2**) bound to *S. aureus* ClpP (PDB: 6TTZ).

The 3,5-difluorobenzyl appears to be the only moiety whose flexibility decreases as the size of the core ring increases. As depicted in **Figure 3.15**, the dihedral distribution of the conformational ensemble is scattered for analogs **3.24**, **3.25** and **3.28**, and it converges towards 170° with **3.26** and **3.27**. As previously observed (**Figure 3.11c**), the orientation of the 3,5-

difluorobenzyl group changes as the size of the core ring increases (**3.26** and **3.27**). In **Figure 3.15**, the dihedral angle of the bond remains similar following the cyclization from **3.24** to **3.25** and **3.28**. It is once the core increases to seven- (**3.26**) and eight-membered (**3.27**) ring that the dihedral angle shifts by 130° . This reorientation aligns the 3,5-difluorobenzyl moiety of compounds **3.26** and **3.27** with the corresponding angle of ADEP 4 (**3.2**) bound to ClpP. In particular, the distribution of conformers at 170° is more important for **3.27** than **3.26**, suggesting that the eight-membered ring locks the 3,5-difluorobenzyl group in the same conformation as ADEP 4 (**3.2**).



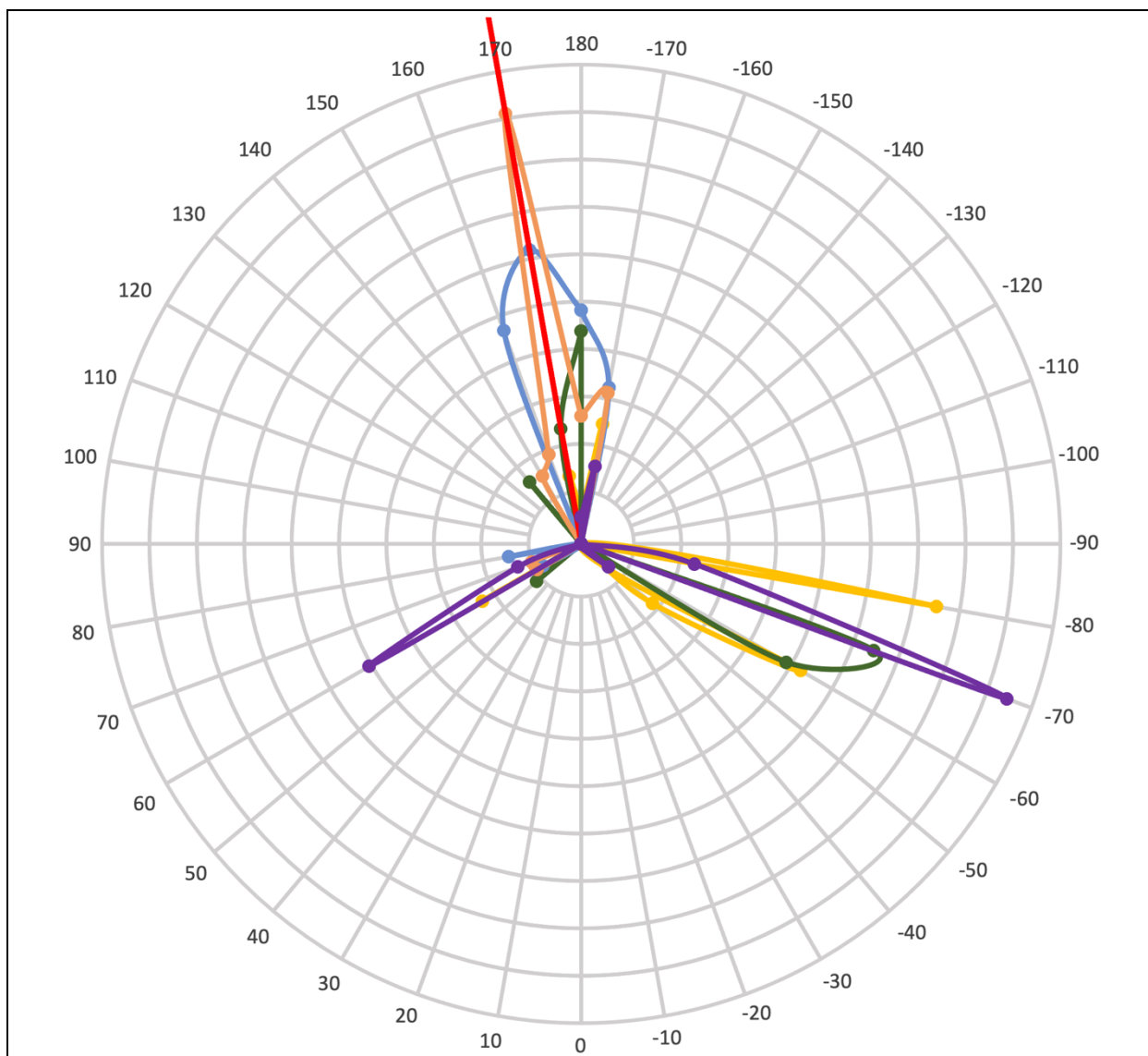
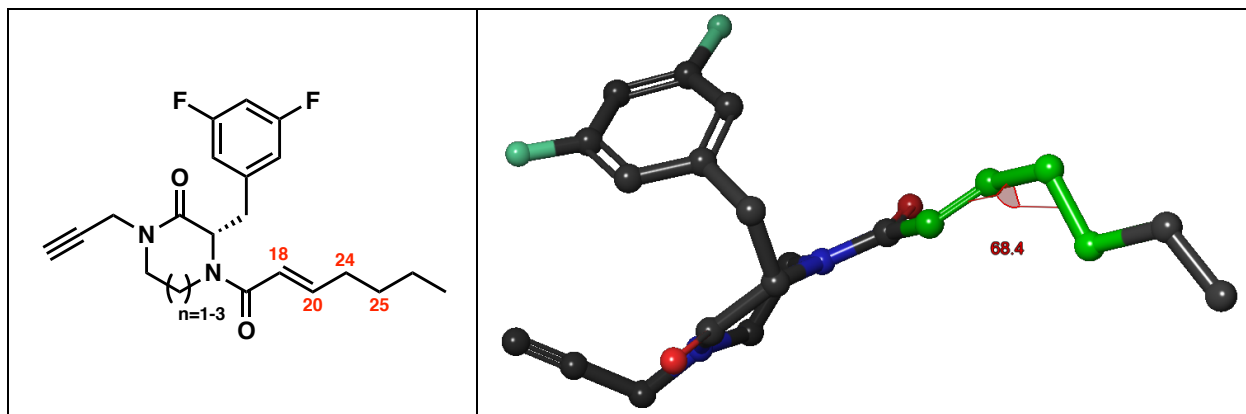


Figure 3.15: Histogram of dihedral angles of the 3,5-difluorobenzyl group in analogs 3.24 (yellow), 3.25 (green), 3.26 (blue), 3.27 (orange) and 3.28 (purple). The dihedral angle was measured for the atoms C2-C3-C6-C7 (labeled in red) and displayed in a 3D representation of 3.25 as an example. The red line in the histogram indicates the dihedral angle of the backbone bond of the cocrystal structure of ADEP 4 (3.2) bound to *S. aureus* ClpP (PDB: 6TTZ).

Although the flexibility of the heptenoyl tail is not altered by the size increase of the core ring as presented in the histogram in **Figure 3.16**, the orientation of the heptenoyl amide is susceptible to the N- to C-terminal cyclization and the increase in the ring size (**Figure 3.17**). The amide of analog 3.24 flips approximately to 180° following the cyclization to a six- (3.25) and

seven-membered (**3.26**) ring. However, the heptenoyl amide of **3.27** switches back to a dihedral angle not only similar to **3.24** but also ADEP 4 (**3.2**). And as discussed above, the conjugated system of **3.28** orients the acrylamide in the same angle as **3.24** and **3.27**.



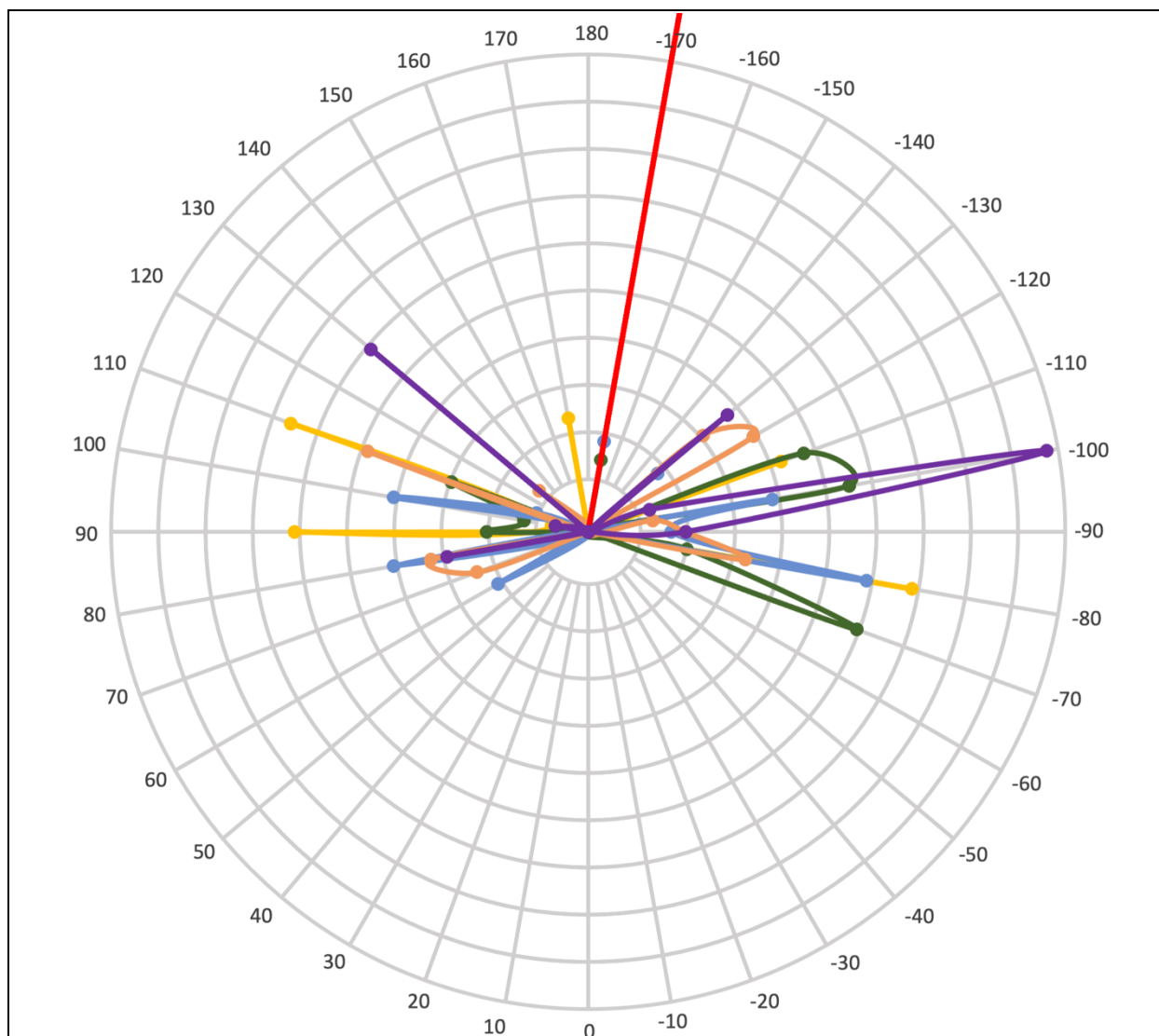


Figure 3.16: Histogram of dihedral angles of the heptenoyl tail in analogs 3.24 (yellow), 3.25 (green), 3.26 (blue), 3.27 (orange) and 3.28 (purple). The dihedral angle was measured for the atoms C18-C20-C24-C25 (labeled in red) and displayed in a 3D representation of **3.25** as an example. The red line in the histogram indicates the dihedral angle of the backbone bond of the cocrystal structure of ADEP 4 (**3.2**) bound to *S. aureus* ClpP (PDB: 6TTZ).

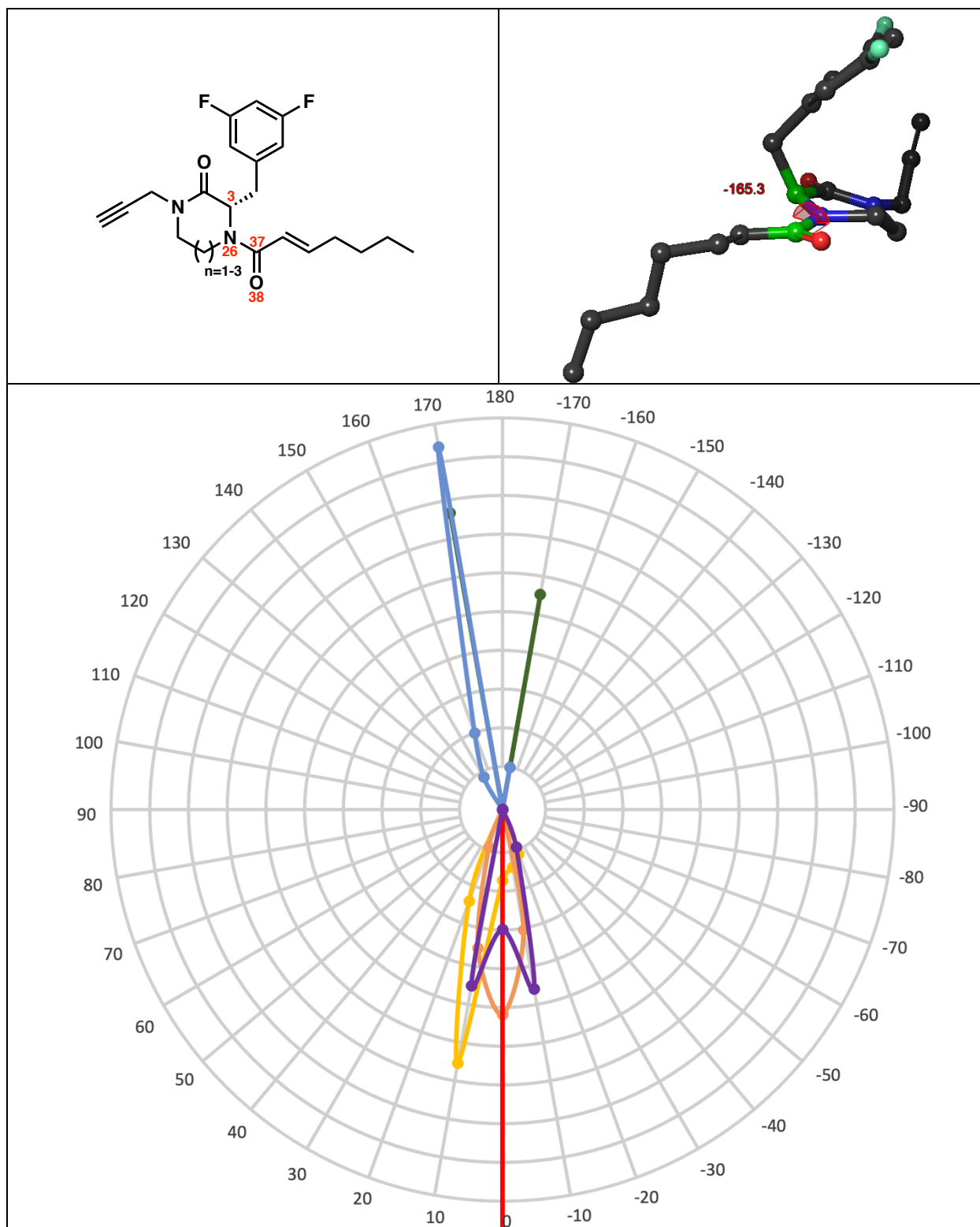


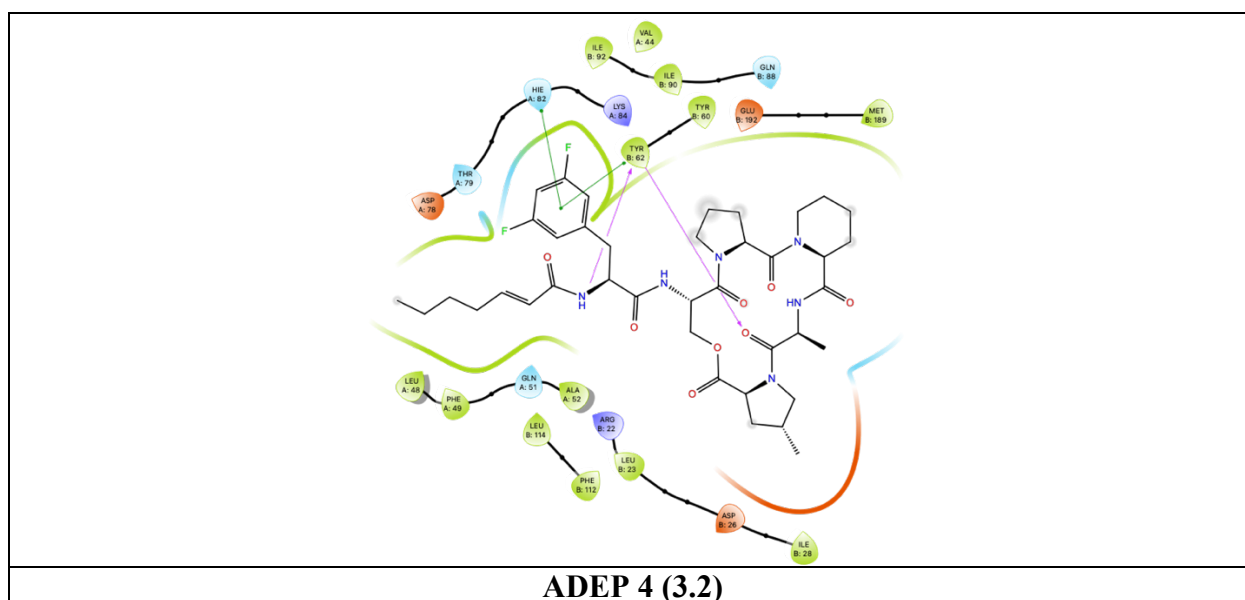
Figure 3.17: Histogram of dihedral angles of the heptenoyl amide in analogs 3.24 (yellow), 3.25 (green), 3.26 (blue), 3.27 (orange) and 3.28 (purple). The dihedral angle was measured for the atoms C3-N26-C37-O38 (labeled in red) and displayed in a 3D representation of 3.25 as

an example. The red line in the histogram indicates the dihedral angle of the backbone bond of the cocrystal structure of ADEP 4 (**3.2**) bound to *S. aureus* ClpP (PDB: 6TTZ).

Using the conformational ensembles of analogs **3.24** – **3.28** generated through the BCE server, this conformational study demonstrated that flexibility of the substituents group of the scaffold, measured via the RMSD, decreases as the size of the core ring increases. However, the 3,5-difluorobenzyl group was the only moiety which orientation was more constrained from six- (**3.25**) to eight-membered (**3.27**) ring, while the degree of motion of propargyl group and heptenoyl tail was unchanged. Interestingly, the backbone core for both *seco* (**3.24**) and cyclized (**3.25** – **3.28**) analogs exhibited minor conformational variability across their respective conformational ensembles. The 3,5-difluorophenylalanine backbone is planar for **3.24**, **3.25** and **3.28**, and the core ring adopts a pseudo-chair conformation as it increases to a seven- (**3.26**) and eight-membered (**3.27**) ring, inducing the 3,5-difluorobenzyl group to reorient by 130°. In addition, the relative orientations of the propargyl, 3,5-difluorobenzyl and heptenoyl groups are dependent on the size of the core ring: (1) The propargyl is projected to the same face as the 3,5-difluorobenzyl in **3.25** but it is projected to the same face as the heptenoyl in **3.26** and **3.27**; (2) The heptenoyl amide either adopts a *cis* conformation (**3.25** and **3.26**) or *trans* (**3.23**, **3.27** and **3.28**). Notably, the conformation of the eight-membered analog **3.27** orients the 3,5-difluorophenylalanine sidechain and backbone, and the heptenoyl amide to mimic how the respective moieties of ADEP 4 (**3.2**) are projected in ClpP upon binding. Consequently, I hypothesized that **3.27** would be the most active of the cyclized ClpP activators series, if the orientation of the appending moieties is sufficient to bind into ClpP. In addition, the comparison between the piperazinone **3.25** and pyrazinone **3.28** indicates that the unsaturation in the core ring leads to a decrease in globularity and flexibility, and changes the heptenoyl amide to the *trans* conformation.

3.2 Docking Studies

Although the conformational study provided *in silico* evidence that N- to C-terminal cyclization of the *seco* analog **3.24** and the increase of the size of the core ring lead to conformations analogous to ClpP-bound ADEP 4 (**3.2**), it remained to be determined if these compounds actually bound to ClpP and elicited a biological response. Prior to synthesizing the compounds, I conducted docking studies of **3.24** – **3.27** to investigate their predicted binding poses in ClpP using Glide (Schrodinger). The results of the docking studies of the *seco* (**3.16** and **3.24**) and the cyclized series (**3.25** – **3.28**) are presented as 2D protein-ligand interaction diagrams in **Figure 3.18** and the docking scores, interactions and RMSD between the N-heptenoyl 3,5-difluorophenylalanine fragment of ADEP 4 (**3.2**) and each compound are summarized in **Table 3.7**.



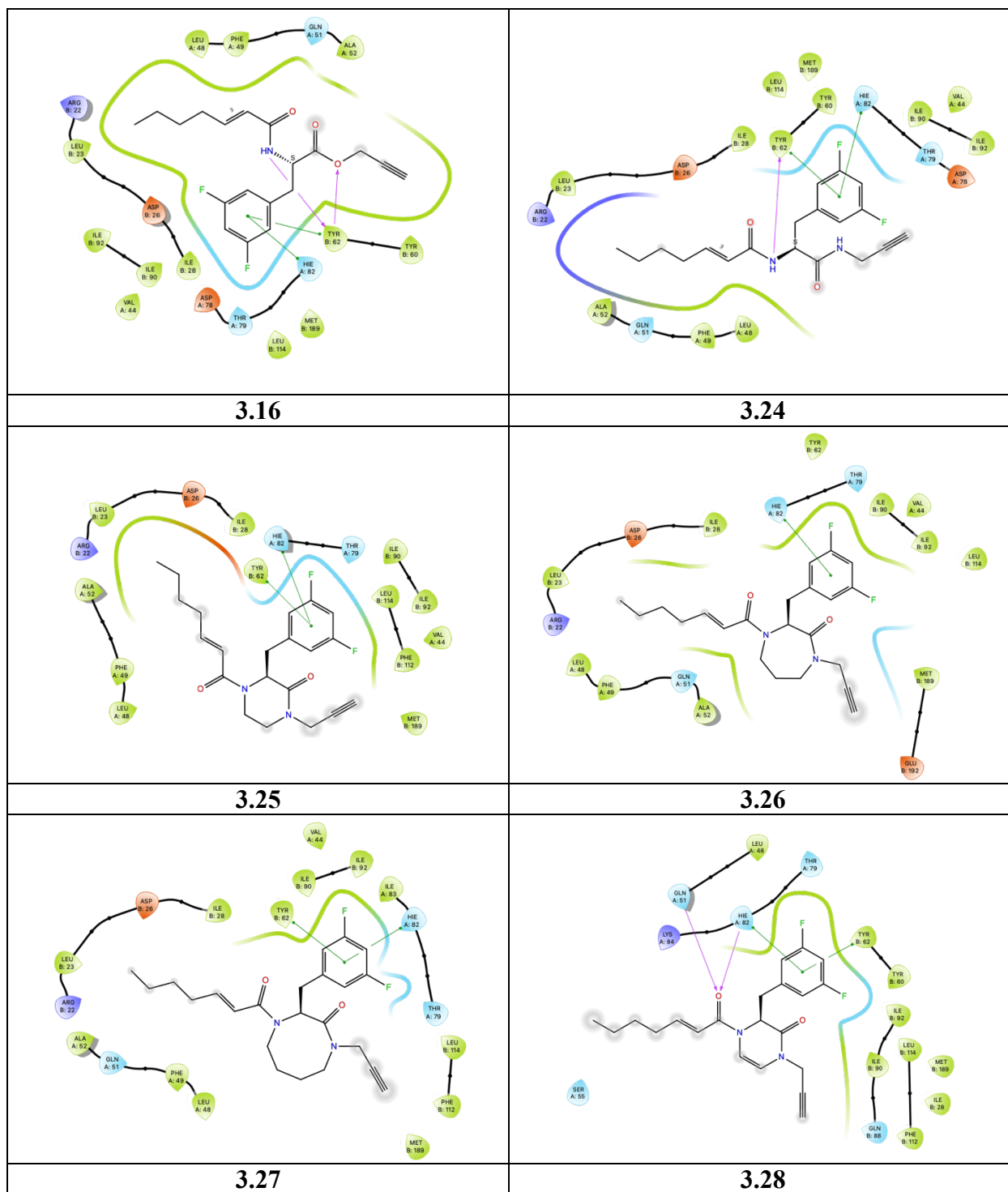


Figure 3.18: 2D protein-ligand interactions diagrams of ADEP 4 (3.2) and analogs 3.16, 3.24, 3.25, 3.26, 3.27 and 3.28.

Using the co-crystal structure of ADEP 4 (**3.2**) bound to ClpP (PDB: 6TTZ), each compound was docked in the ADEP binding pocket of ClpP. To determine the validity of the predicted binding pose, I expected each moiety of the compound to be located in the same position as the corresponding groups in ADEP 4 (**3.2**): (1) The 3,5-difluorobenzyl fits in the hydrophobic sub-pocket composed of Leu48, Tyr62, Thr79, His82 and Leu114, and is engaged in π - π stacking interactions with Tyr62 and His82; (2) The 3,5-difluorophenylalanine N-terminus is involved in a hydrogen bond (H-bond) with Tyr62; (3) The heptenoyl projects into the pocket containing Arg22, Leu23, Asp26, Ile28, Leu48, Phe49, Ala52 and Tyr62; (4) The 3,5-difluorophenylalanine C-terminus and depsipeptide are exposed to solvent and interact with Tyr60, Gln88, Phe112 and Met189.

The binding poses of *seco* analogs **3.16** and **3.24** overlap with ADEP 4 (**3.2**) in great measure, with RMSDs of 1.53 and 1.34 Å, respectively, and the same interactions with Tyr62 and His82 are observed (i.e., H-bond and π - π stacking). Notably, the ester oxygen of **3.16** replaces the depsipeptide alanine carbonyl of ADEP 4 (**3.2**) in the double H-bond with Tyr62. However, this interaction is lost when the ester is changed to the amide in **3.24** (**Figure 3.18**) possibly explaining the decreased docking score of **3.24** compared to **3.16** (**Table 3.7**).

Cyclized analogs **3.25**, **3.26** and **3.27** bind similarly to ADEP 4 (**3.2**), with the 3,5-difluorobenzyl and heptenoyl moieties occupying the same sub-pockets and the core rings and propargyl group being exposed to solvent. The cyclized compounds exhibit similar docking scores, averaging -6.11 kcal/mol. As expected, however, **3.25** – **3.27** are predicted to bind less efficiently than the *seco* analog **3.24**, which is likely explained by the loss of the H-bond with Tyr62. Despite the increased bulk of the larger core ring, the ClpP binding pocket accommodates the cyclized analogs **3.25**, **3.26** and **3.27** independently of the conformation. However, the rigidity of the

pyrazinone ring of **3.28** is detrimental to the docking score, as it appears to interfere with the binding of the heptenoyl group in the same sub-pocket as ADEP 4 (**3.2**).

Compound	Docking score (kcal/mol)	Residues (interaction type)	RMSD with ADEP 4 (Å)
ADEP 4 (3.2)		Tyr62 (H-bond, π - π stacking) His82 (π - π stacking)	
3.16	-8.672	Tyr62 (H-bond, π - π stacking) His82 (π - π stacking)	1.53
3.24	-7.505	Tyr62 (H-bond, π - π stacking) His82 (π - π stacking)	1.34
3.25	-5.690	Tyr62 (π - π stacking) His82 (π - π stacking)	1.27
3.26	-6.450	His82 (π - π stacking)	1.50
3.27	-6.176	Tyr62 (π - π stacking) His82 (π - π stacking)	1.34
3.28	-4.690	Tyr62 (π - π stacking) His82 (π - π stacking)	5.06
3.38	-5.714	Tyr62 (H-bond) His82 (π - π stacking)	2.78
3.39	-7.951	Tyr62 (H-bond, π - π stacking) His82 (π - π stacking) Thr79 (H-bond)	1.14
3.40	-3.552	Tyr62 (π - π stacking) His82 (π - π stacking)	2.78
3.41	-7.016	Tyr62 (π - π stacking) His82 (π - π stacking)	2.12

Table 3.7: Summary of the docking score, protein-ligand interactions and RMSD between the *N*-heptenoyl 3,5-difluorophenylalanine fragment of ADEP 4 (3.2**) and corresponding fragments in compounds **3.16**, **3.24** – **3.28**, **3.38** – **3.41**.**

The *para*-substituted phenylalanine analogs **3.38** and **3.39** exhibited differences in their binding poses (**Figure 3.19**), docking scores and protein-ligand interactions (**Table 3.7**). Despite the similar length in the *para*-substituted benzyl groups (i.e., 4.72 Å for 4-bromobenzyl and 4.68 Å for 4-hydroxybenzyl groups in **3.38** and **3.39** respectively), the 4-bromobenzyl moiety is

displaced by 2.8 Å out of the pocket compared to the 3,5-difluorophenylalanine in ADEP 4 (**3.2**). This predicted displacement results in the decrease of the binding score and the loss of the π - π stacking with Tyr62, suggesting that the activity of analog **3.38** will be lower. In contrast, the ClpP pocket accommodates analog **3.39** in an equivalent pose to ADEP 4 (RMSD = 1.14 Å), and new H-bonds between the tyrosyl group and Thr79, and the backbone carbonyl and Tyr62 are likely the driving features of an improved docking score (-7.951 kcal/mol, **Table 3.7**), which surpasses the parent 3,5-difluorophenylalanine analog **3.24**.

As depicted in **Figure 3.19**, the binding pose adopted by analog **3.40** suggests that the obstruction of the 3,5-difluorophenylalanine N-terminus by a methyl group not only prevents the H-bond with Tyr62 but also induces a 180° flip of the propargyl and heptenoyl groups in the pocket. The low docking score (-3.552 kcal/mol, **Table 3.7**) further confirms the detrimental effect of the methylation on the binding. Interestingly, the cyclized analogs **3.25**, **3.26** and **3.27** are predicted to bind more similarly to ADEP 4 (**3.2**) than **3.40**, despite the equivalent blockage of the 3,5-difluorophenylalanine N-terminus.

The tolyl-urea piperazinone analog **3.41** was predicted to bind to ClpP in a comparable manner to **3.24** and **3.25**, with the tolyl-urea group located in the same sub-pocket as the heptenoyl group, as shown in **Figure 3.19**. The improved docking score relative to **3.25** suggests **3.41** to be capable of binding ClpP, however, contrary to what I had originally predicted, the urea does not form an H-bond with Tyr62.

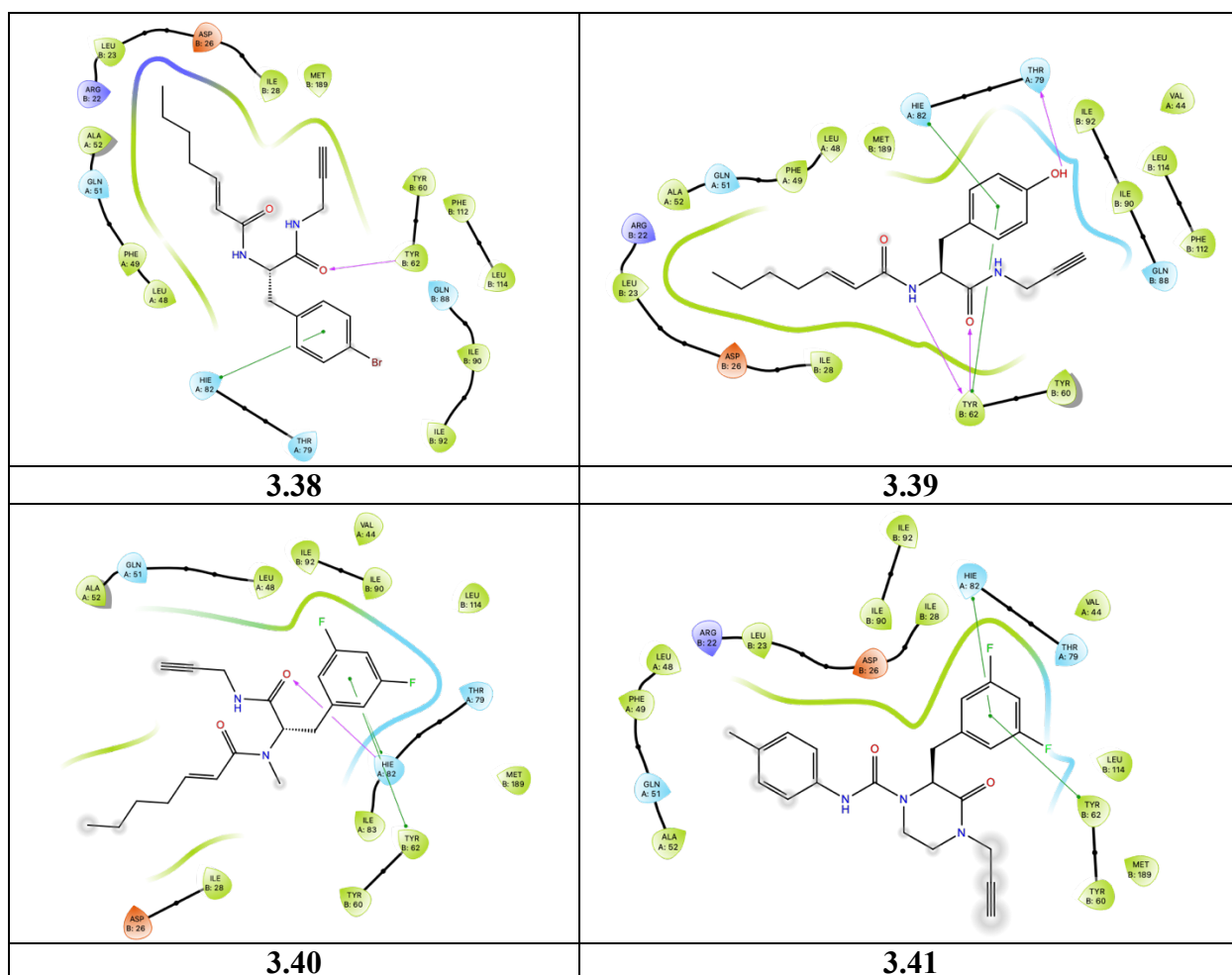


Figure 3.19: 2D protein-ligand interactions diagrams of compounds 3.38 – 3.41.

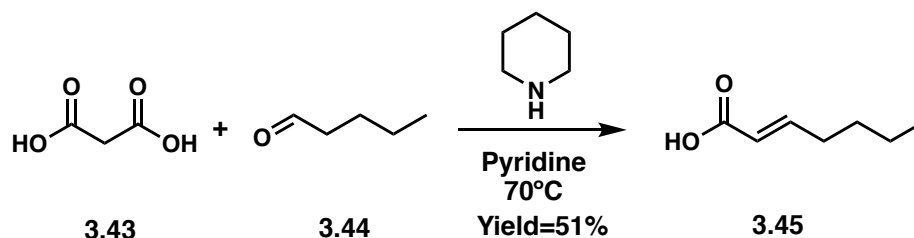
Although the *in silico* conformational studies indicated that each cyclized compound adopts a different conformation based on the size of the core ring and that the orientation of the appended moieties of the eight-membered ring **3.27** is the only analog analogous to ClpP bound ADEP 4, the docking studies predict that **3.24 – 3.27** will all bind to ClpP in a similar manner to ADEP 4 (**3.2**) independently of the size of the core ring. As I expected, cyclization abolishes the H-bond of the 3,5-difluorophenylalanine N-terminus with Tyr62 leading to a decrease in docking score. However, the structural constraint from the cyclization appears to lock the scaffold into a conformation beneficial to the binding, as exemplified by the difference in binding poses between

analogs **3.25** – **3.27** and **3.40**. Furthermore, these docking studies suggest that a tyrosyl group and tolyl-urea could be tolerated as substituents of 3,5-difluorobenzyl and heptenoyl groups respectively.

4 Synthetic Work to Generate *Seco* and Cyclized ClpP Activators

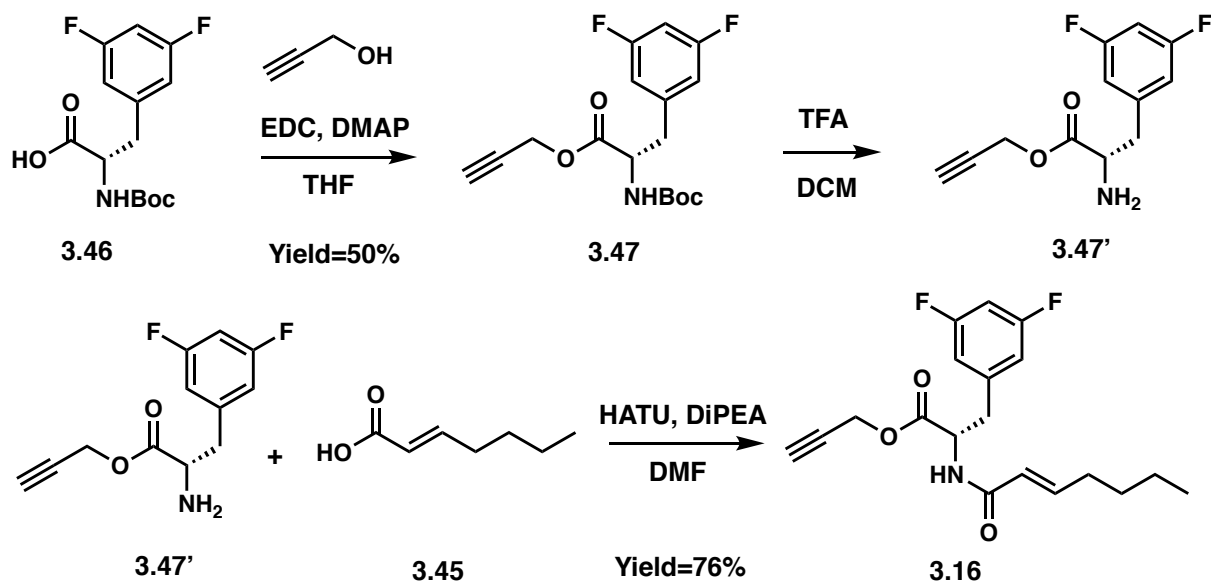
4.1 Synthesis of the *Seco* Analogs

The propargyl ester analog **3.16** was necessary for a direct comparison between published data and the fluorescence-based degradation assays I conducted to evaluate ClpP activation activity. The *seco* propargyl amide **3.24** and methylated analog **3.40** were synthesized as the uncyclized compounds of the series to determine the effect of the N- to C-terminal cyclization on the ability to activate ClpP. To explore the scope of the phenylalanine substitution and test aforementioned hypothesis, the *seco* analogs **3.38** and **3.39** were generated.



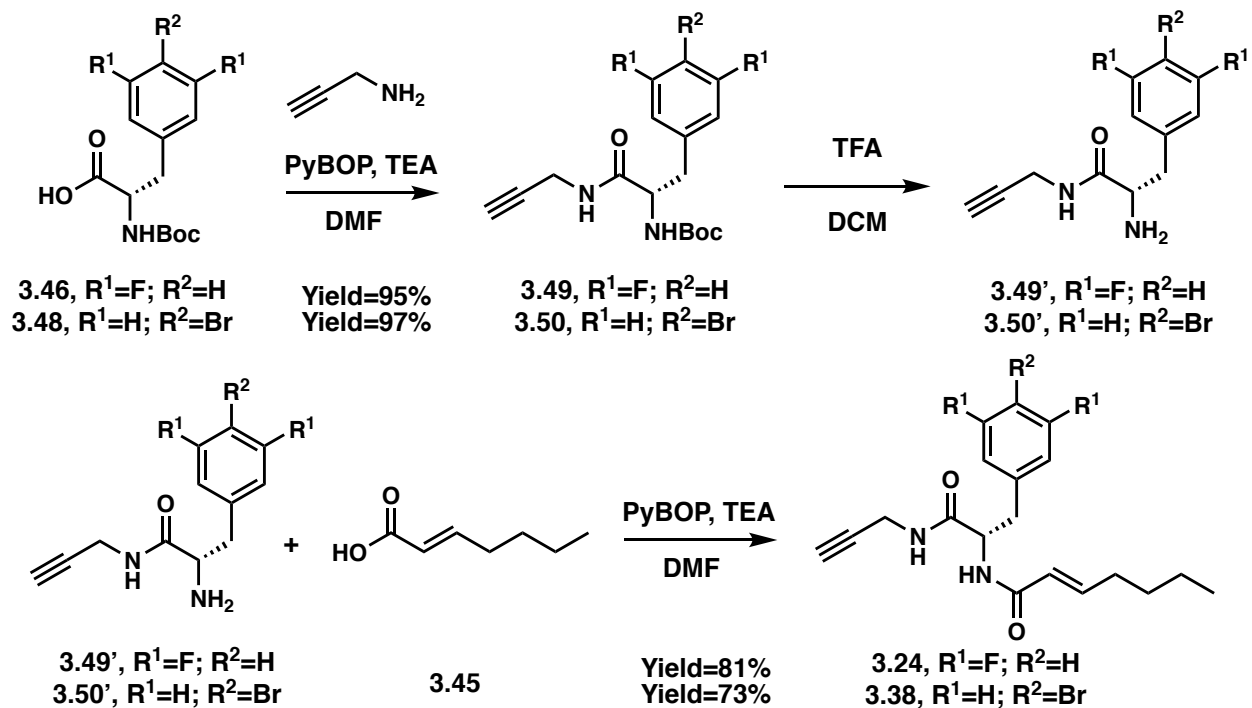
Scheme 3.1: Synthesis of (*E*)-hept-2-enoic acid (**3.45**) via Knoevenagel condensation.

The (*E*)-hept-2-enoic acid (**3.45**) was synthesized through a piperidine-catalyzed Knoevenagel condensation between malonic acid (**3.43**) and valeraldehyde (**3.44**) in pyridine at 70°C in 51% yield (**Scheme 3.1**).



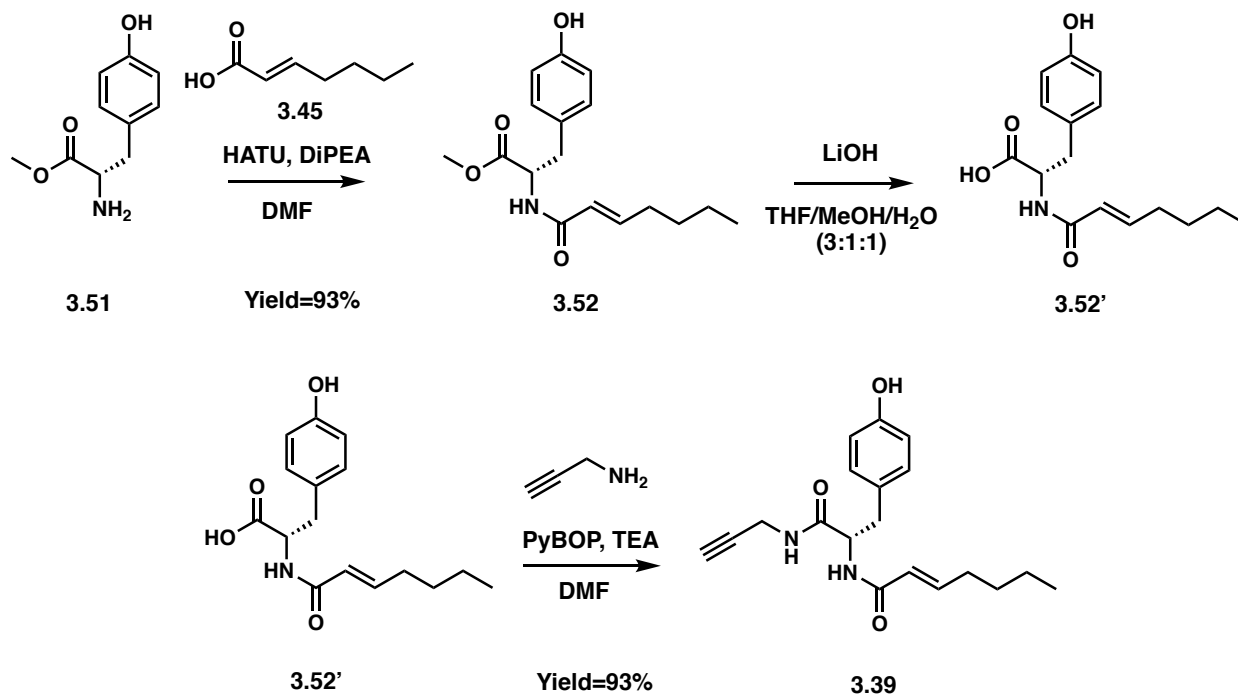
Scheme 3.2: Synthetic route of the propargyl ester analog 3.16.

The esterification of Boc-3,5-difluorophenylalanine **3.46** with propargyl alcohol produced the intermediate **3.47** in 50% yield (**Scheme 3.2**). Following the Boc deprotection of **3.47**, the free amine intermediate **3.47'** was reacted with (*E*)-hept-2-enoic acid (**3.45**) resulting in the *seco* analog **3.16** (yield=76%).



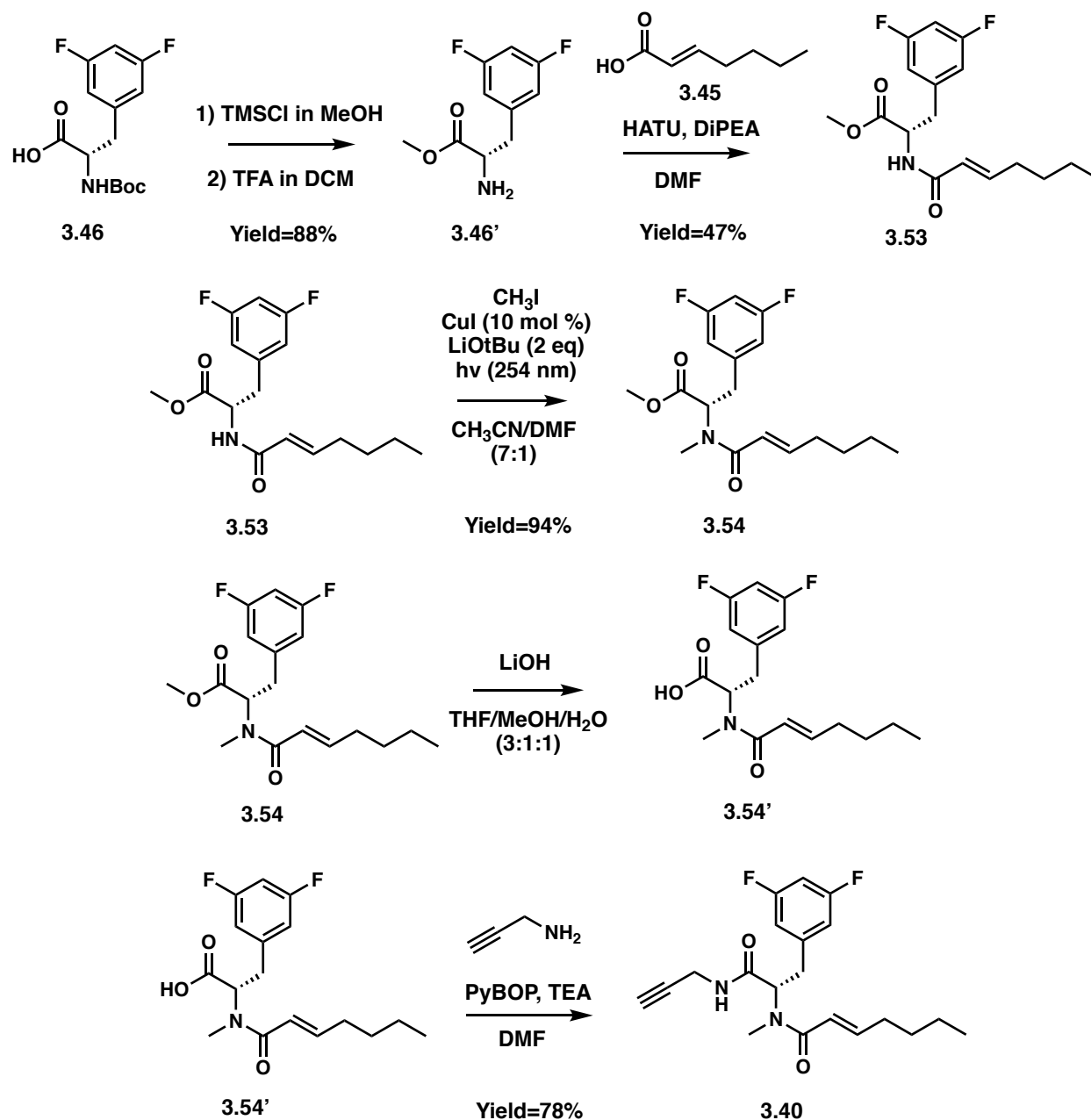
Scheme 3.3: Synthetic route for the *seco* analogs **3.24** and **3.38**.

The *seco* compounds **3.24** and **3.38** were generated by the synthetic route described in **Scheme 3.3**, starting with the amide coupling of the corresponding Boc-phenylalanine **3.46** and **3.48** and propargylamine to afford the intermediates **3.49** and **3.50** in 95% and 93% yield, respectively. The amidation of the deprotected amines **3.49'** and **3.50'** with (*E*)-hept-2-enoic acid (**3.45**) produced **3.24** and **3.38** in 81% and 73% yield, respectively.



Scheme 3.4: Synthetic route for tyrosyl *seco* analog 3.39.

As shown in **Scheme 3.4**, the tyrosyl *seco* analog **3.39** was synthesized by first reacting the methyl ester tyrosine **3.51** with (*E*)-hept-2-enoic acid (**3.45**) to obtain the intermediate **3.52** in 91% yield. After the hydrolysis of **3.52** to the corresponding carboxylic acid, the amide coupling between the propargyl amine and **3.52'** afforded the product **3.39** in 93% yield.



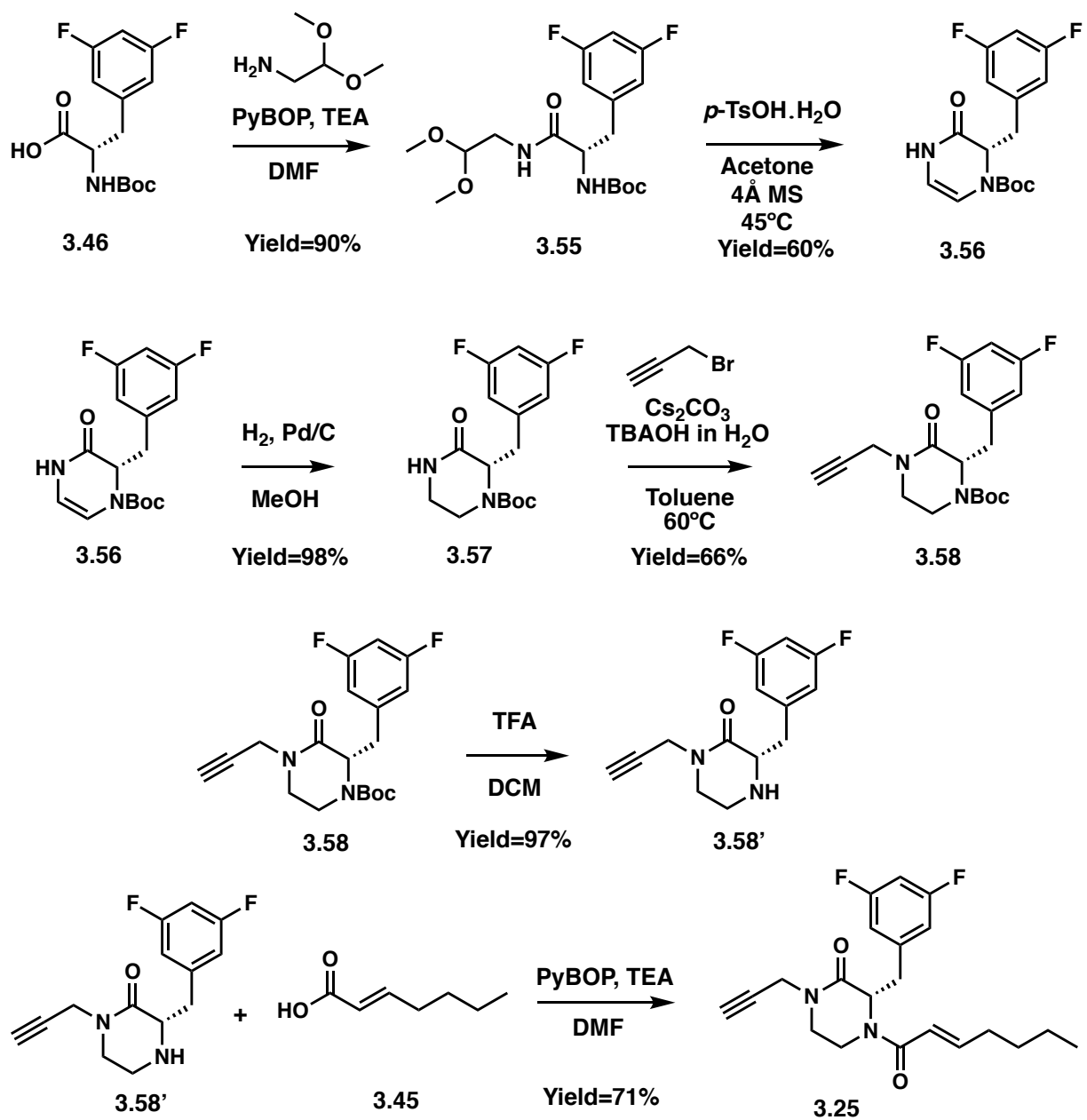
Scheme 3.5: Synthetic route for the N-terminus methylated *seco* analog 3.40.

After the conversion of the Boc-3,5-difluorophenylalanine **3.46** to the methyl ester 3,5-difluorophenylalanine **3.46'**, the amide **3.52** was accessed via the coupling of (*E*)-hept-2-enoic acid (**3.45**) with **3.46'** in 47% yield. The methylation of the 3,5-difluorophenylalanine N-terminus was achieved via the photo-induced copper catalysis in 94% yield. The methylated intermediate

3.54 was then hydrolyzed to the corresponding carboxylic acid and subsequently coupled with propargyl amine to produce compound **3.40** in 87% yield (**Scheme 3.5**).

4.2 Six-Membered Ring Analog Synthesis

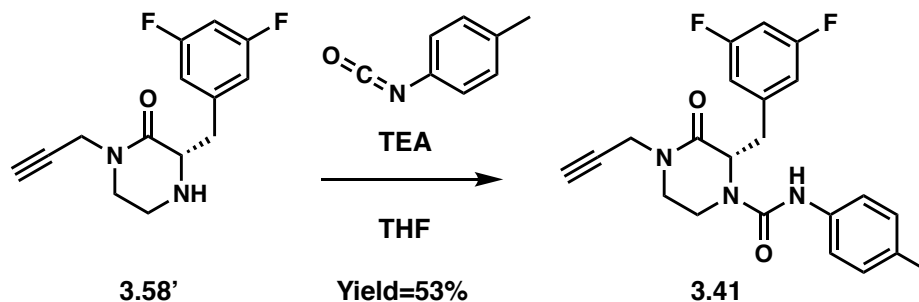
The synthetic route to the piperazinones was previously optimized as detailed in **Chapter 2 Section 8.1**. And **3.28** was accessed by intercepting a synthetic intermediate in the synthesis of **3.25**.



Scheme 3.6: Synthetic route for the six-membered ring analog 3.25.

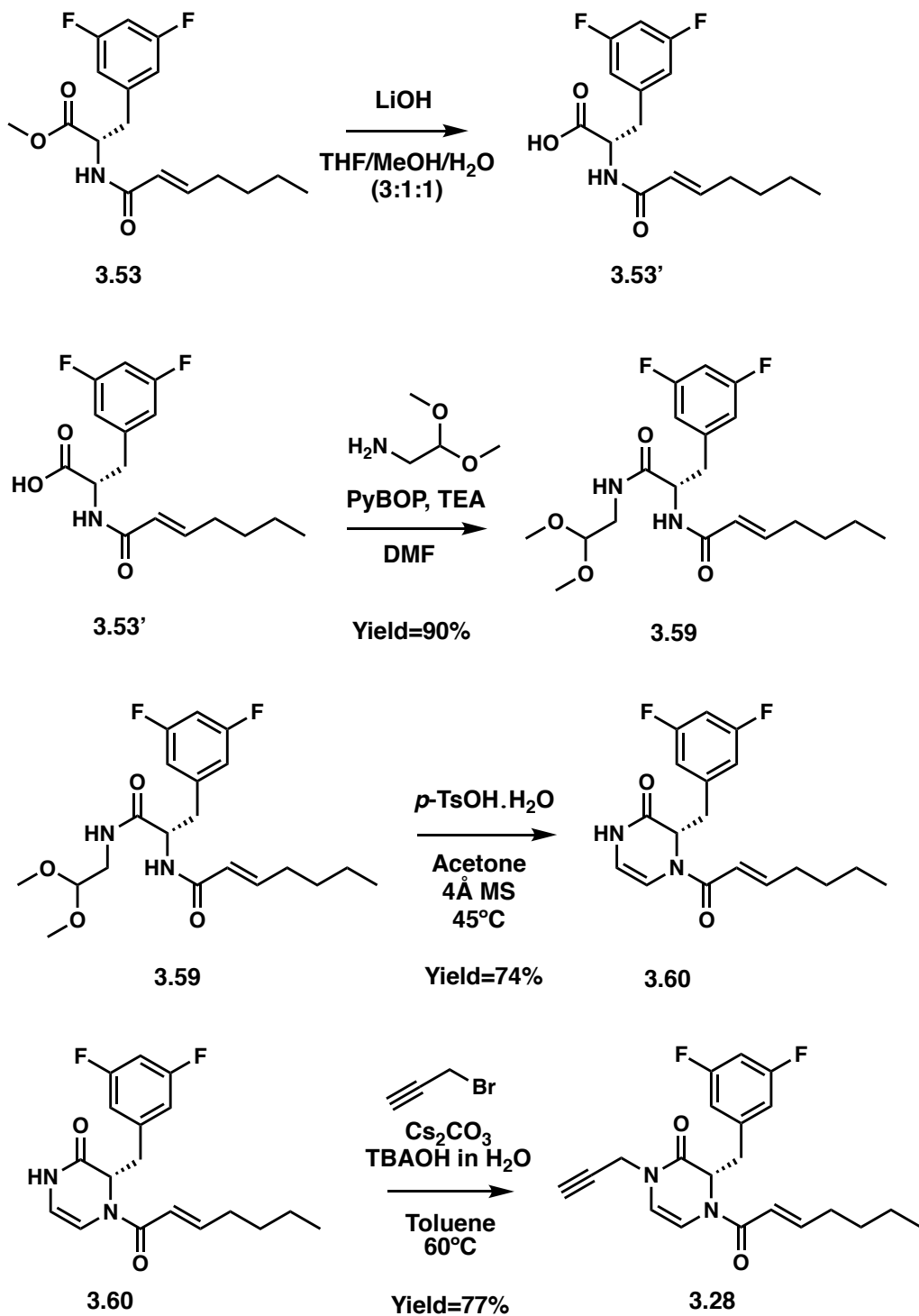
Piperazinone **3.25** was synthesized starting from the coupling of Boc-3,5-difluorophenylalanine **3.46** with aminoacetaldehyde dimethyl acetal to afford the amide intermediate **3.55** in 90% yield. The acetal of **3.55** was deprotected under acidic conditions using para-toluenesulfonic acid monohydrate (*p*-TsOH·H₂O). Subsequent cyclization provided enamine **3.56** in 60% yield. After the hydrogenation of **3.56** to obtain the piperazinone intermediate **3.57**

(Yield = 98%), the propargyl group was installed using phase-transfer catalysis (PTC) to produce the propargyl piperazinone intermediate **3.58** in 66% yield. Following the removal of the Boc group on **3.58**, the synthesis of **3.25** was completed after coupling **3.58'** with (*E*)-hept-2-enoic acid (**3.45**) in 71% yield (Scheme 3.6).



Scheme 3.7: Synthesis of the *para*-tolyl-urea piperazinone analog **3.41**.

The *para*-tolyl-urea piperazinone analog **3.41** was synthesized in 53% yield by reacting *para*-tolyl isocyanate with the piperazinone amine **3.58'** under basic conditions (Scheme 3.7).



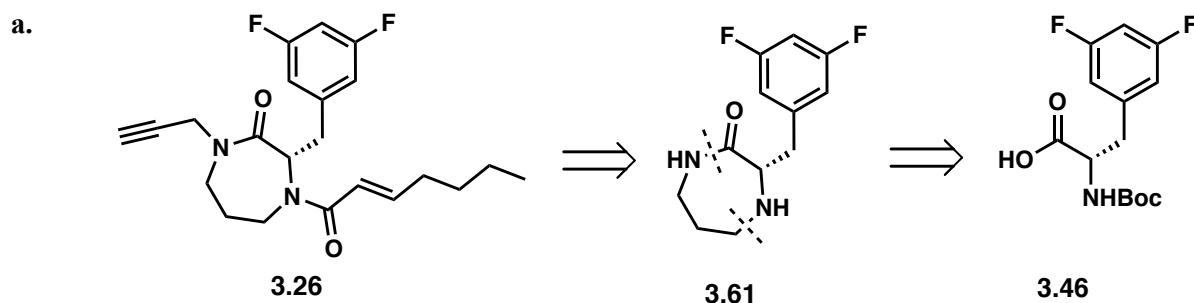
Scheme 3.8: Synthetic route for the pyrazinone analog 3.28.

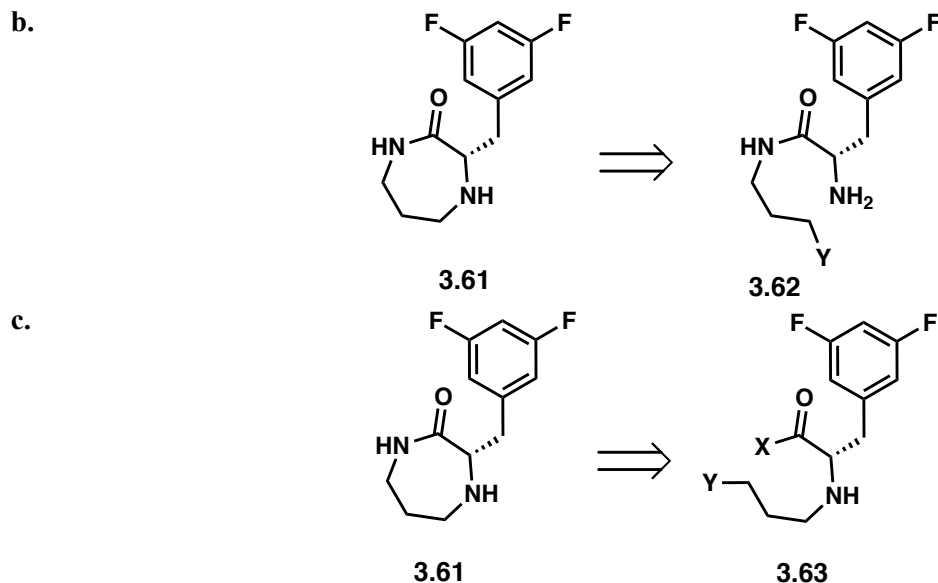
Following the saponification of the methyl ester *N*-heptenoyl 3,5-difluorophenylalanine **3.53**, the resulting carboxylic acid **3.53'** was subjected to aminoacetaldehyde dimethyl acetal under

typical coupling conditions to generate the amide **3.59** in 92% yield (**Scheme 3.8**). Cyclization to the pyrazinone **3.60** was induced under acidic conditions following sequential deprotection of the acetal and intramolecular cyclization (Yield=67%). The propargylation of the pyrazinone amide with previously identified phase transfer catalysis conditions afforded **3.28** in 77% yield.

4.3 Seven-Membered Ring Synthesis

Although a broad range of seven-membered rings containing two nitrogens (i.e., diazepanes) are commonplace in organic chemistry and methodologies have been developed to synthesize them, literature precedent for the synthesis of 1,4-diazepan-2-one (**3.61**, **Scheme 3.9a**) is scarce. Because I selected the 3,5-difluorophenylalanine (**3.46**, **Scheme 3.9a**) as the primary synthon, to set the absolute stereochemistry of the α -carbon from the beginning, the scope of synthetic methods to access **3.26** was further limited. Therefore, two approaches were investigated: (1) Ring-closure from the 3,5-difluorophenylalanine N-terminus (**Scheme 3.9b**) and (2) Ring-closure from the 3,5-difluorophenylalanine C-terminus (**Scheme 3.9c**).





Scheme 3.9: Proposed retrosynthetic scheme for seven-membered ring 3.26 (a), ring-closure from the 3,5-difluorophenylalanine N-terminus approach (b) and ring-closure from the 3,5-difluorophenylalanine C-terminus approach (c).

4.3.1 Ring-closure from the 3,5-Difluorophenylalanine N-Terminus

First, I hypothesized that the formation of the seven-membered ring could occur in a fashion analogous to the synthetic route for the piperazinone **3.57** by simply employing a homologated alkyl acetal group. Therefore, I coupled 3,3-diethoxypropan-1-amine with Boc-3,5-difluorophenylalanine **3.46** to form amide **3.64** (97% yield). Contrary to the transformation of **3.55** into **3.56** (Scheme 3.6), treatment of **3.64** with *p*-TsOH·H₂O (Entry 1, Table 3.8) resulted in the removal of the acetal but failed to promote the formation of the cyclic enamine intermediate **3.65**. Other acidic conditions known to remove acetals were also screened (Entry 2-4, Table 3.8) but none of the conditions employed induced the requisite cyclization.⁴⁴⁻⁴⁶

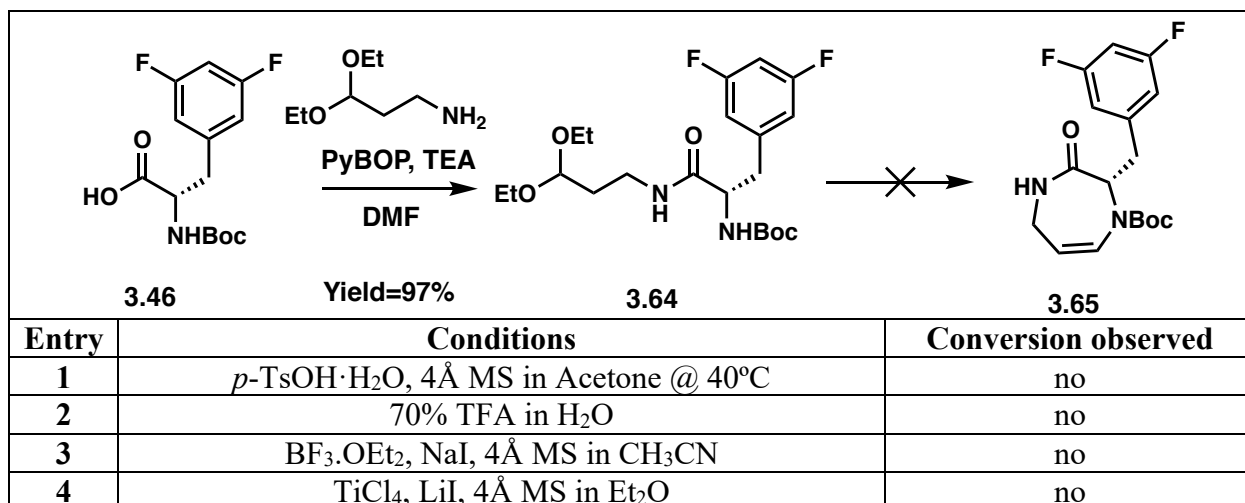
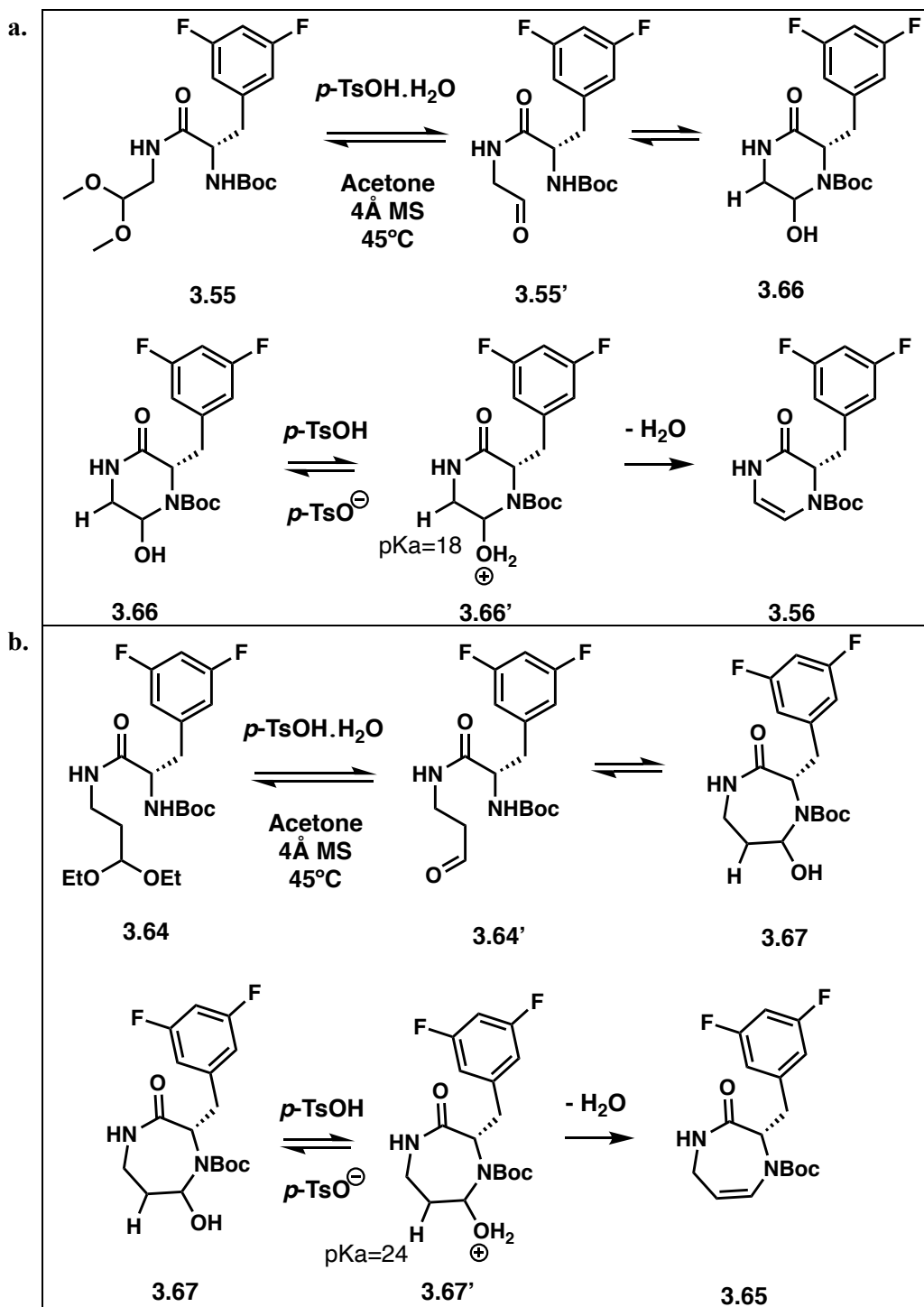


Table 3.8: Acidic conditions screened for the synthesis of the cyclized intermediate 3.65.

From the results of the conditions screened in **Table 3.8**, I concluded that the synthetic strategy used to access piperazinone **3.57** were not applicable to the synthesis of the seven-membered congener. The fact that the cyclization of **3.55** appears to occur promptly after the addition of *p*-TsOH·H₂O suggests that formation of the enamine intermediate **2.56** (**Scheme 3.10**) may provide the “sink” to drive the reaction, a feature not present in the diazepanone formation. Mechanistically (**Scheme 3.10**), as the acetals **3.55** and **3.64** are removed to provide **3.55'** and **3.64'**, respectively, nucleophilic attack by the Boc-protected amine is expected to provide hemiaminals **3.66** and **3.67**. Following the protonation of the hemiaminal alcohol, enamines **3.56** and **3.65** would be formed through the elimination of a water molecule. Since the predicted pK_a of the **3.66'** β-hydrogen (**Scheme 3.10a**) is lower than **3.67'** (**Scheme 3.10b**), pK_a = 18 and 24 respectively, the elimination is more likely to occur in **3.66'** than **3.67'**.⁴⁷ This may provide another explanation for the limitation of employing this approach to access diazepanones.



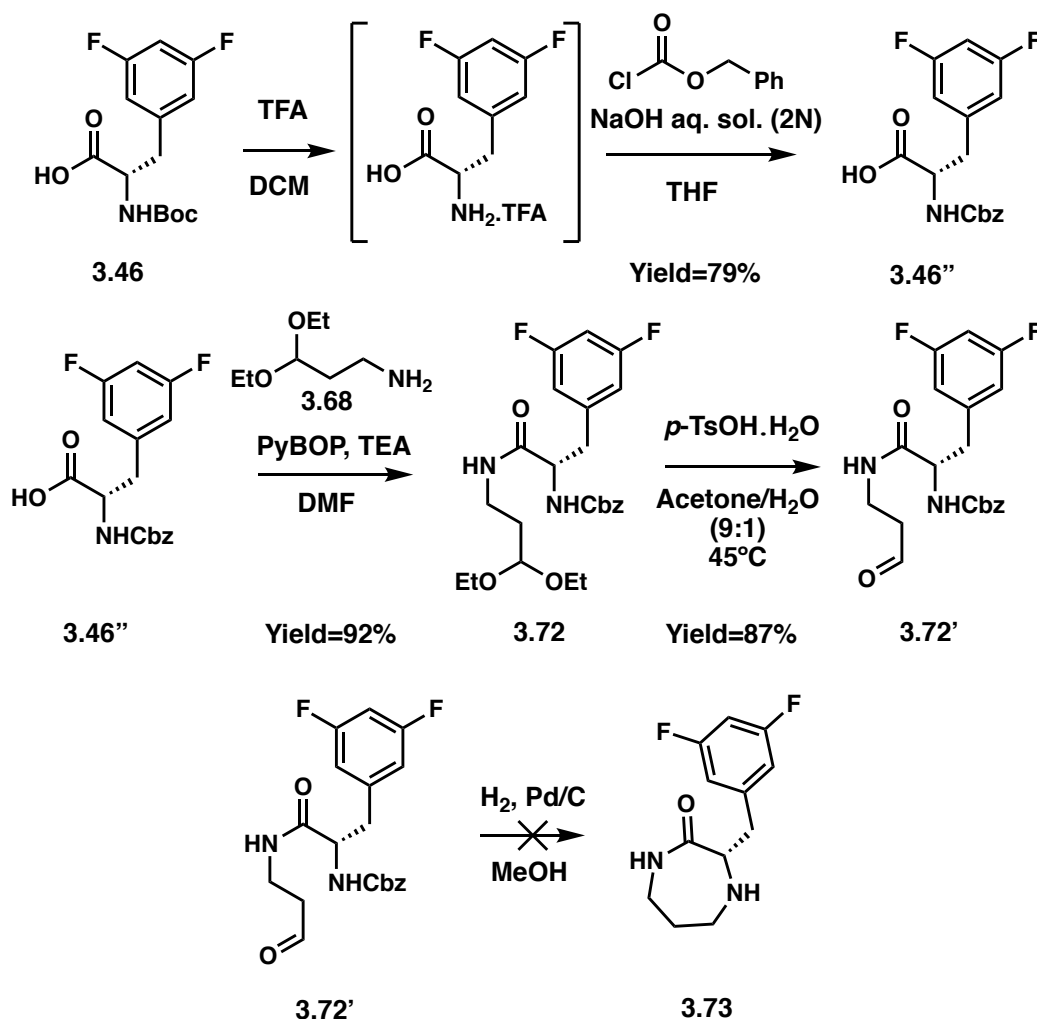
Scheme 3.10: Proposed mechanism for the formation of the enamine intermediates 3.56 and 3.65.

In addition, it is known that the formation of six-membered rings is more favored than for seven-membered ring formation, as the strain energy increases for larger rings.⁴⁸ The strain of this

seven-membered system may preclude the preorganization of the side-chain required for cyclization to occur, thus prohibiting or severely slowing the rate of cyclization. Therefore, I hypothesized that addition of another group to the nitrogen to provide a tertiary amide, may induce a more favorable conformation to promote cyclization by directing the aldehyde more towards the Boc-protected amine. This approach would also reduce the number of steps to produce compound **3.26**.

As shown in **Table 3.9**, the propargyl group was installed on 3,3-diethoxypropan-1-amine **3.68** via mono-alkylation in 23% yield to form amine **3.69**.⁴⁹ The target amide **3.70** was then synthesized by coupling **3.69** to Boc-3,5-difluorophenylalanine **3.46** in 26% yield. Four different conditions were employed in attempts to remove the acetal group and induce the cyclization, but either a complex mixture of products (**Entry 2-4, Table 3.9**) or no conversion to the cyclic intermediate **3.71** (**Entry 1, Table 3.9**) was observed. These results suggested that these conditions are conducive to side-reactions and that installing the propargyl group prior to the cyclization was not sufficient to overcome the issues with conformation and ring strain.

of products limit the practicality of these conditions. Therefore, I designed a synthetic route modeled on the synthesis of a 1,5-diazabicyclo[6,3,0] dodecane amino acid derivative, where the acetal and Boc groups are sequentially removed, allowing for cyclization under hydrogenation conditions (Scheme 3.11).⁵⁰ By first substituting the Boc group with a Cbz group, the 3,5-difluorophenylalanine **3.46''** was reacted with 3,3-diethoxypropan-1-amine **3.68** to produce **3.72** in 92% yield (Scheme 3.11). Following the deprotection of **3.72** under mildly acidic conditions, the resulting aldehyde **3.72'** was exposed to hydrogenation conditions to presumably remove the Cbz group and promote the cyclization, however no cyclized product was observed.

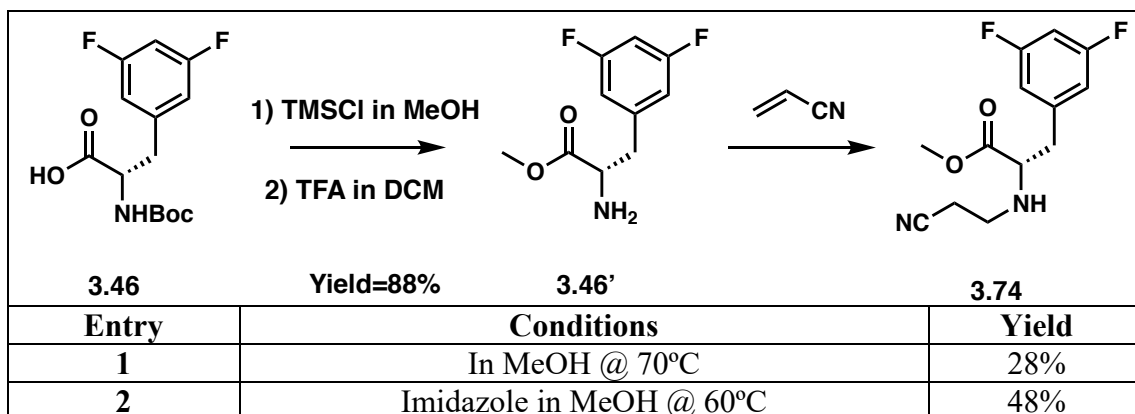


Scheme 3.11: Synthetic route to the 3,5-difluorophenylalanine 1,4-diazepanone **3.73**.

4.3.2 Ring-closure from the 3,5-difluorophenylalanine C-terminus

Due to the lack of success of the synthetic strategies to promote the ring-closure from the 3,5-difluorophenylalanine N-terminus, I then investigated the C-terminus as an alternative locus to form the 1,4-diazepan-2-one ring. This approach is commonly used for the synthesis of medium-sized rings such as ϵ -caprolactams (i.e., seven-membered ring lactam)⁵¹ and 1,4-diazepan-2-one rings.⁵²

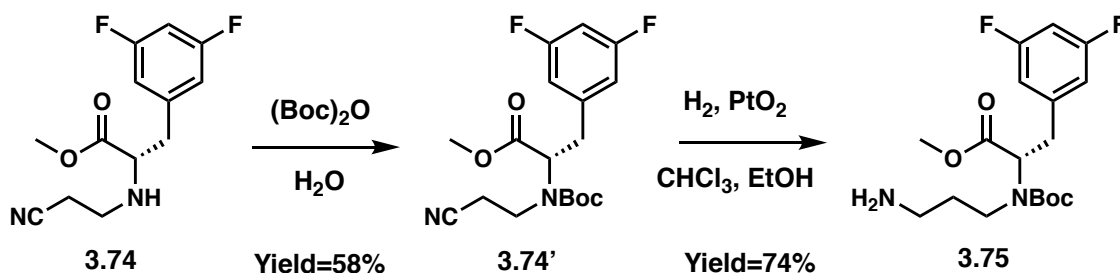
Following the conversion of the Boc 3,5-difluorophenylalanine **3.46** into the methyl ester 3,5-difluorophenylalanine **3.46'**, different conditions for the aza-Michael addition of **3.46'** on acrylonitrile to obtain the adduct **3.74** were attempted. Since the yield of the reaction was not satisfying under reflux conditions in methanol (**Entry 1, Table 3.10**),⁵³ I screened different bases (**Entry 2-6, Table 3.10**) to deprotonate the primary amine of **3.46'** and increase its nucleophilicity. Imidazole was the highest yielding base with 48%, as its conjugate acid can activate the electrophilicity of acrylonitrile by coordinating with the nitrile group. In addition, two transition-metal-based Lewis acids were screened to further increase the yield but no conversion was observed (**Entry 7-10, Table 3.10**).⁵⁴



3	NaOAc in MeOH @ 60°C	24%
4	NaOCH ₃ in MeOH @ 40°C	0%
5	NaOtBu in MeOH @ 50°C	0%
6	Cs ₂ CO ₃ in MeOH @ 40°C	0%
7	Cu(OAc) ₂ in EtOH/H ₂ O @ 25°C	0%
8	Cu(OAc) ₂ in EtOH/H ₂ O @ 60°C	0%
9	FeCl ₃ .6H ₂ O in EtOH/H ₂ O @ 25°C	0%
10	FeCl ₃ .6H ₂ O in EtOH/H ₂ O @ 60°C	0%

Table 3.10: Conditions screening for aza-Michael addition between the amine 3.46' and acrylonitrile.

The product of the aza-Michael addition was Boc-protected and the nitrile group of the intermediate **3.74'** was reduced under hydrogenation condition to generate amine **3.75** in 74% yield.



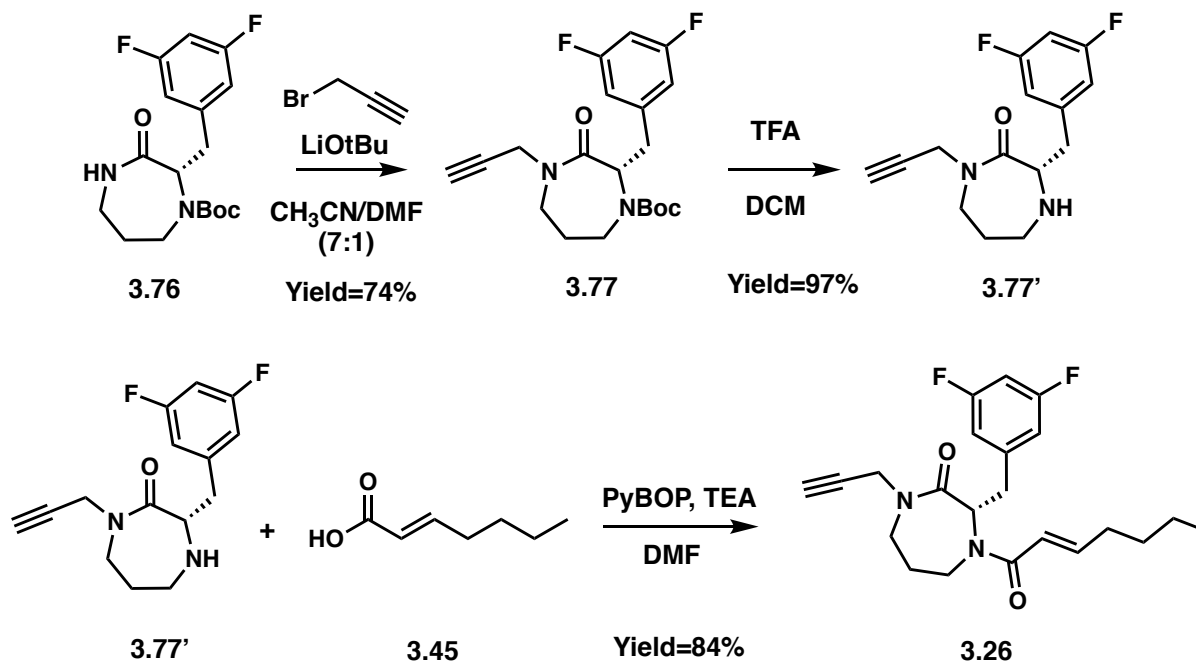
Scheme 3.12: Synthetic route to the 1,4-diazepan-2-one precursor 3.75.

Weber A. E. et al. accessed the 1,4-diazepan-2-one from a precursor similar to **3.75** by employing trimethylaluminum.⁵² However, trimethylaluminum is highly reactive and air sensitive, so I leveraged a bench stable complex of DABCO and trimethylaluminum (DABAL-Me₃) that has been shown to promote the synthesis of a wide range of amides from esters and amines (**Entry 1, Table 3.11**).^{55, 56} DABAL-Me₃ conditions, however, failed to convert **3.75** into the cyclized product **3.76**. I then evaluated aqueous sodium hydroxide (**Entry 2, Table 3.11**) as it is commonly used for lactamization and cyclization occurred in 62% yield.⁵⁷

Entry	Conditions	Concentration of 3.75	Yield
1	DABAL-Me ₃ in Toluene @ 120°C	0.16 mM	0%
2	NaOH (3N aq.) in MeOH @ RT	0.07 M	62%

Table 3.11: Conditions screened for the cyclization of 3.75 into the 1,4-diazepan-2-one 3.76.

As presented in **Scheme 3.13**, the 1,4-diazepan-2-one **3.76** was propargylated using lithium *tert*-butoxide to afford product **3.77** in 74% yield. The targeted seven-membered analog **3.26** was then produced after coupling **3.77'** and (*E*)-hept-2-enoic acid (**3.45**) in 84% yield.



Scheme 3.13: Synthetic route to the seven-membered ring analog 3.26.

4.4 Eight-membered ring synthesis

Although the synthesis of eight-membered fused-ring derivatives such as **3.78** – **3.81** (Figure 3.20) have been reported, no literature precedent exist for 1,4-diazocan-2-one rings.⁵⁸⁻⁶¹ Despite the available methodology for accessing eight-membered ring lactams, the use of Boc-3,5-difluorophenylalanine **3.46** as a precursor for **3.27** limits the applicability of these methodologies.⁶²⁻⁶⁴ Similarly to the synthesis of the seven-membered ring compound **3.26**, I investigated the ring-closure from the 3,5-difluorophenylalanine N-terminus.

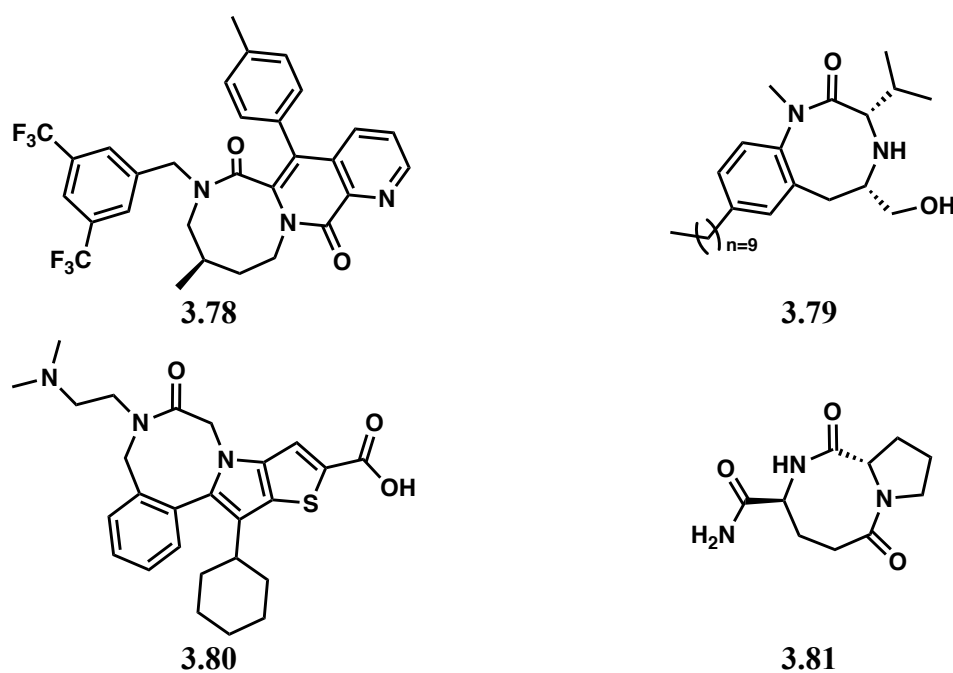


Figure 3.20: Structures of eight-membered fused-ring derivatives.

To install the four-carbon bridge between the C-terminus and N-terminus of 3,5-difluorophenylalanine, Boc-3,5-difluorophenylalanine **3.46** was coupled to 4,4-diethoxybutylamine **3.84** to form amide **3.82** in 94% yield (Table 3.12). Similar to the seven-membered diazepanone synthesis (Table 3.8), utilization of acidic conditions to sequentially

remove the acetal and promote the cyclization were unsuccessful (**Table 3.12**). The ring strain and unfavorable transannular interactions likely prevent the challenging formation of the enamine under these conditions.

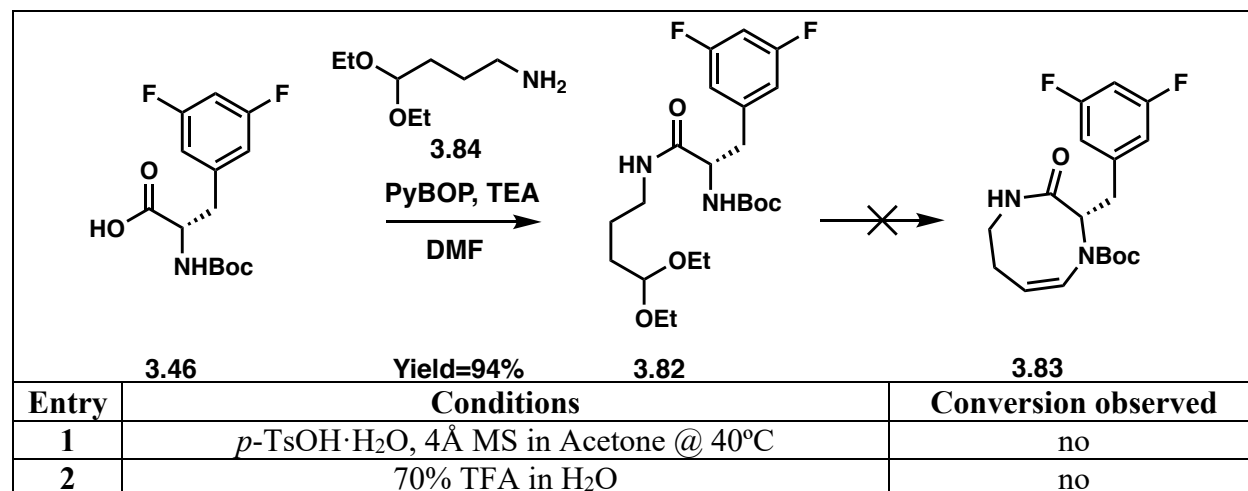


Table 3.12: Acidic conditions screened for the synthesis of the cyclized intermediate **3.83**.

As previously, I evaluated if the propargyl group would aid in orienting the acetal/aldehyde towards the Boc-protected amine to induce the formation of the eight-membered ring. Following the mono-*N*-alkylation of 4,4-diethoxybutylamine **3.84** with propargyl bromide (Yield=48%, **Scheme 3.14**) to provide **3.85**, amide **3.86** was generated by coupling **3.85** and Boc-3,5-difluorophenylalanine **3.46** in 71% yield.

by $\text{NaBH}(\text{OAc})_3$. It would be interesting to assess in the future if this reaction can proceed without the need for $\text{NaBH}(\text{OAc})_3$.

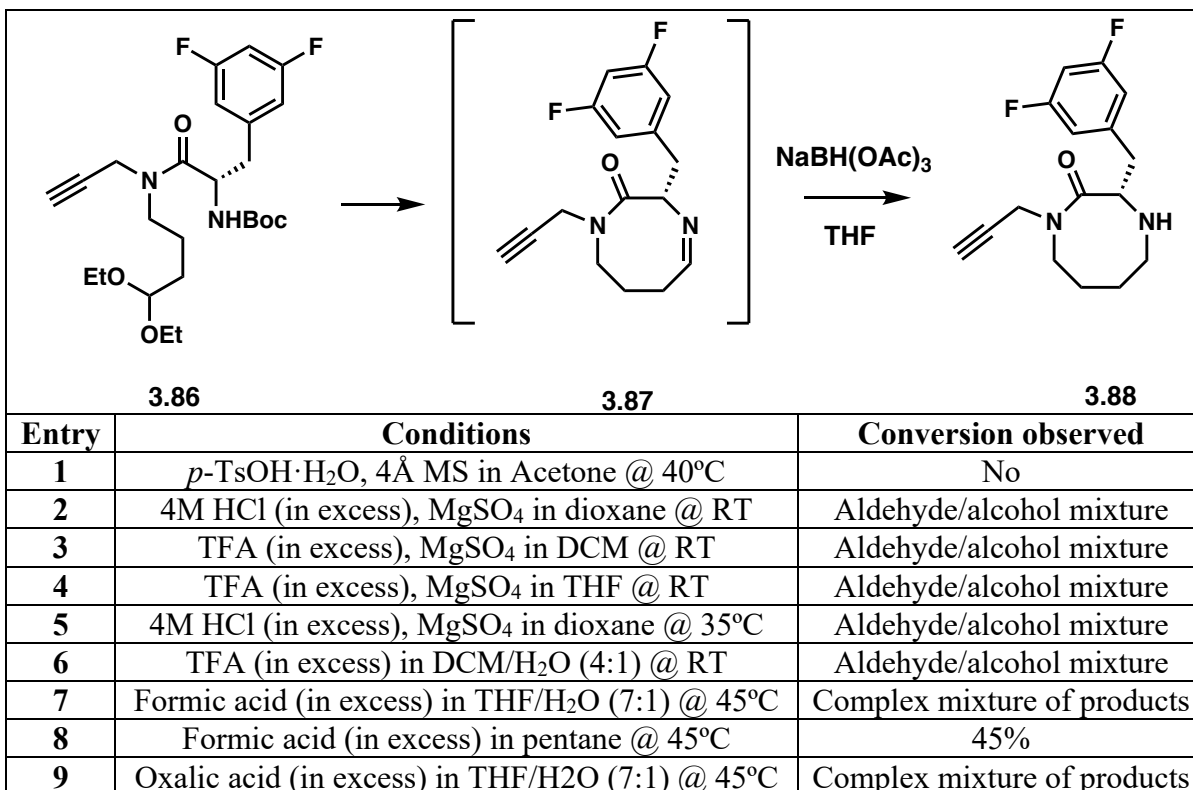
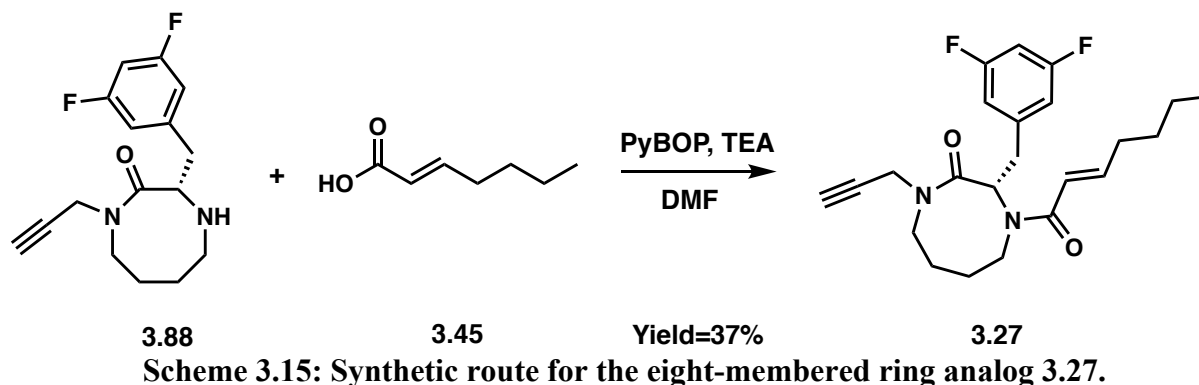


Table 3.13: Summary of the acidic conditions screened for the synthesis of the cyclized intermediate 3.88.

The target eight-membered compound **3.27** was then completed following the coupling between the propargylated 1,4-diazocan-2-one intermediate **3.88** and (*E*)-hept-2-enoic acid (**3.45**) in 37 % yield.



In summary, different methodologies were necessary to synthesize the six- (**3.25**), seven- (**3.26**) and eight-membered (**3.27**) rings. I previously developed and optimized the synthetic route for the piperazinone consisting in the removal of an acetal group under mild acidic conditions to promote the cyclization and the formation of a pyrazinone ring. I modified this synthetic route by installing the heptenoyl group on the 3,5-difluorophenylalanine N-terminus prior to cyclization, and thus, I easily accessed the pyrazinone analog **3.28**. Originally, I hypothesized that I could use a homologated alkyl acetal group to form the seven- and eight-membered rings under the same acidic conditions than for the six-membered ring cyclization. However, this approach was not applicable to the synthesis of the larger rings: (1) The strain energy of the seven- and eight-membered rings hinders the cyclization; (2) The formation of an enamine intermediate similar to the pyrazinone is likely less favorable as the pKa of the carbon adjacent to the acetal group increases preventing the elimination step. Contrary to the six- and eight-membered ring, the seven-membered ring was accomplished via a ring-closure from the 3,5-difluorophenylalanine C-terminus. Although the formation of the eight-membered ring was achieved via the removal of an alkyl acetal group, installation of the propargyl group on the 3,5-difluorophenylalanine C-terminus and harsher acidic conditions were required. This is the first example of a methodology to generate a 1,4-diazocan-2-one ring to be reported and future mechanistic studies will determine: (1) The

role of the propargyl and its utility in the cyclization step; (2) The role of the formic acid in promoting the formation of the cyclized imine intermediate (**3.87**); (3) If the reduction step is necessary, as the formic acid could reduce the imine in a similar fashion to Eschweiler-Clarke and Leuckart-Wallach reactions.

5 Evaluation of the Synthesized Compounds for ClpP Activation

To evaluate the capacity of this series to activate ClpP, I employed a fluorescence-based assay that utilizes an internally quenched fluorogenic ClpP substrate, FITC- β -casein.²⁶ When the tetradecameric form of ClpP is chemo-activated, FITC- β -casein can freely enter axial pores of ClpP and, upon degradation in the catalytic chamber, fluorescence proportional to the activation of ClpP will be released due to FITC cleavage. Because Sello J. K. et al. demonstrated that the *seco* analog **3.16** was the most potent of the ADEP fragment series in growth inhibition assays in a highly ADEP-susceptible wild-type *B. subtilis* AG174, it was implemented as a positive control (100 μ M).²⁵ Compounds **3.24** – **3.28** and **3.38** – **3.41** were screened at two concentrations (250 μ M and 500 μ M) against BsClpP (**Figures 3.21** and **3.22**). The expression and purification of BsClpP was conducted by Dr. Phil Bourne.

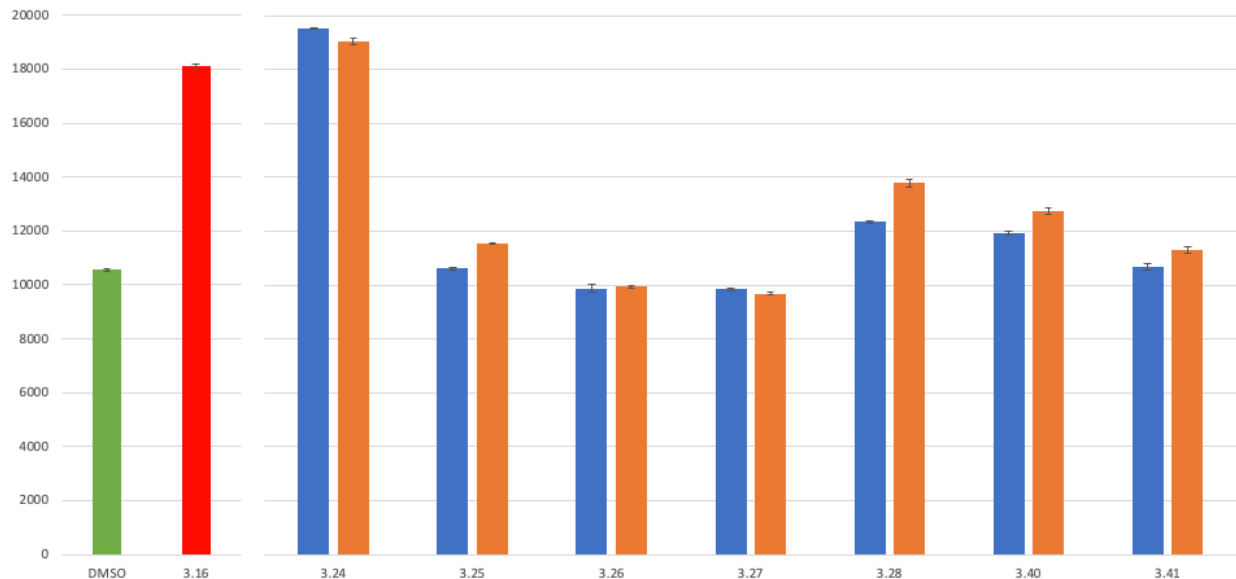


Figure 3.21: Fluorescence results from the FITC- β -casein degradation assay of compounds 3.24 – 3.28, 3.40 and 3.41 with BsClpP. Negative control = DMSO. Positive control = 3.16 (100 μ M). The blue bars represent the fluorescence at 250 μ M and the orange bars represent the fluorescence at 500 μ M.

As shown in **Figure 3.21**, the *seco* analog **3.24** is the strongest ClpP activator of this series and the cyclized six- (**3.25**), seven- (**3.26**), eight-membered ring (**3.27**) and pyrazinone (**3.28**) analogs are inactive at the concentrations tested. In addition, compound **3.40**, the *seco* *N*-terminus methylated analog was also inactive. Therefore, we can conclude that the cyclization, independently of the size of the core ring, abolishes the activity of the *N*-heptenoyl 3,5-difluorophenylalanine scaffold likely by eliminating the H-bond with Tyr62. Furthermore, the replacement of the heptenoyl group with the *p*-tolyl urea moiety failed to re-install activity, suggesting the H-bond with Tyr62 was not restored and confirming the results from the docking study for **3.41**.

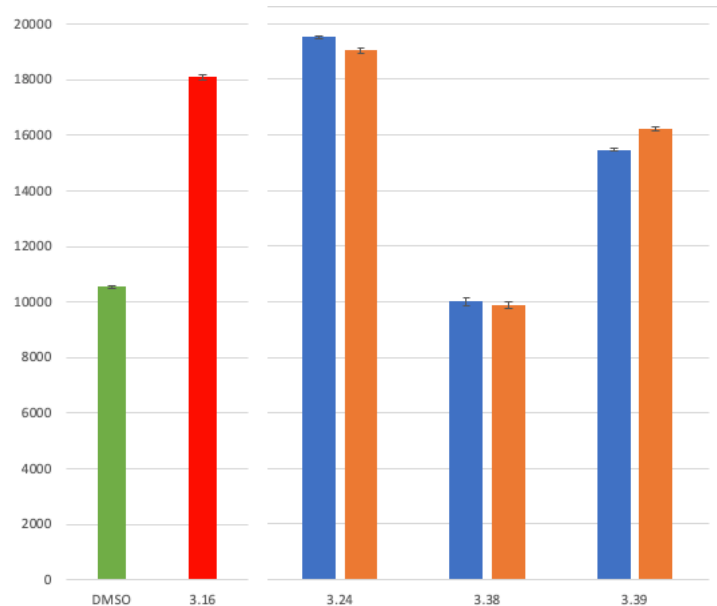


Figure 3.22: Fluorescence results from the FITC- β -casein degradation assay of compounds 3.24, 3.38 and 3.39 with BsClpP. Negative control = DMSO. Positive control = 3.16 (100 μ M). The blue bars represent the fluorescence at 250 μ M and the orange bars represent the fluorescence at 500 μ M.

The fluorescence results of the *para*-substituted phenylalanine analogs **3.38** and **3.39**, presented in **Figure 3.22**, also validated the docking studies: **3.38** was inactive as predicted, likely due to the inability of the binding pocket to accommodate the large bromine atom. The tyrosyl group containing analog (**3.39**) likely establishes an H-bond with Thr79, resulting in a retention of ClpP activation, albeit at a lower level compared to **3.16** and **3.24**. Although **3.39** is not as active as the parent analog **3.24**, it is a new example of a ClpP activator derived from ADEP without the 3,5-difluorobenzyl moiety to be reported, suggesting that further structural optimization is possible.

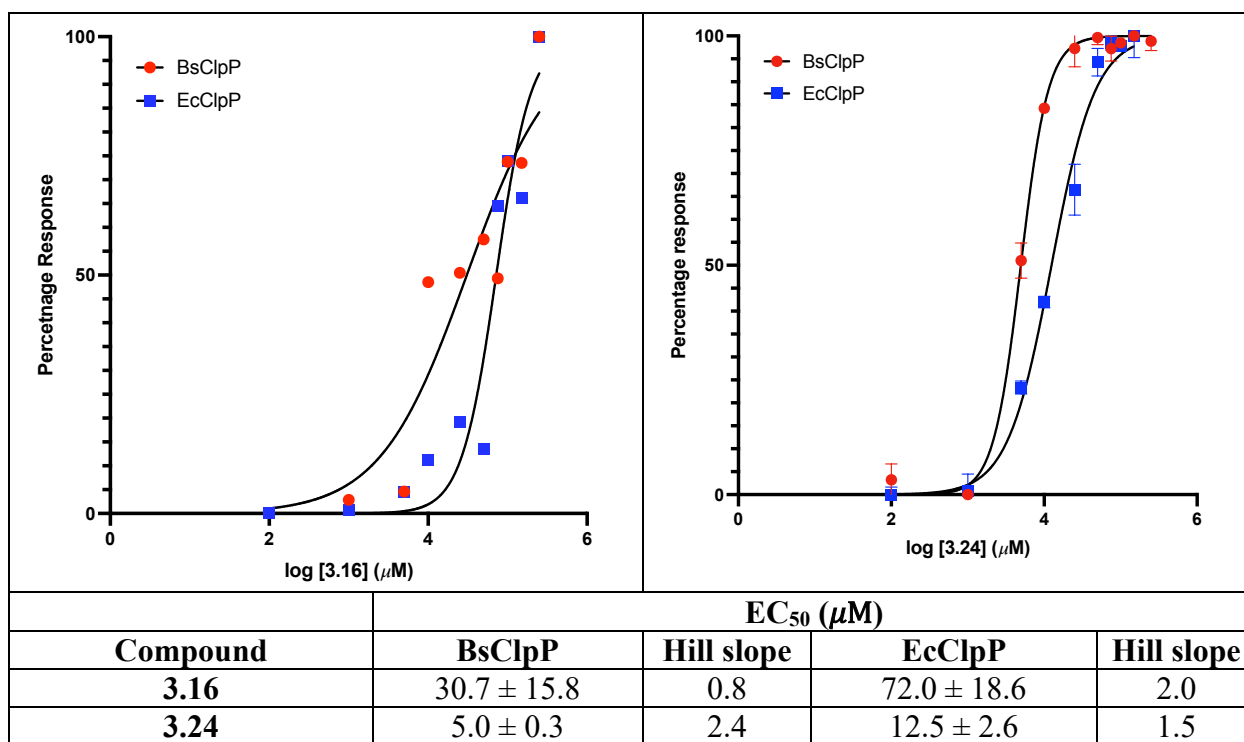


Table 3.14: Dose-response comparison of the *seco* analogs 3.16 and 3.24 for FITC- β -casein degradation with BsClpP and EcClpP.

The half maximal effective concentrations (EC₅₀) of the *seco* analogs **3.16** and **3.24** were determined via dose-dependent degradation of FITC- β -casein with BsClpP and EcClpP, as summarized in **Table 3.14**. The amide analog **3.24** is six-fold more potent than the ester analog **3.26** in both BsClpP and EcClpP suggesting that the amide of the 3,5-difluorophenylalanine C-terminus contributes more to the binding than the docking studies predicted. Although BsClpP and EcClpP are 93% identical, the two-fold difference in EC₅₀ between BsClpP and EcClpP for both **3.16** and **3.24** suggests either that BsClpP is more responsive than EcClpP or a possible selectivity of the scaffold towards Gram-positive bacteria, which was previously observed by Batey R. A. et al.³⁶

6 Conclusion and Future Directions

The drawback from the discovery gap in antibiotic discovery coupled with the emergence of antibiotic-resistant bacteria has made the development of new antibacterial agents particularly challenging. However, antibiotics with new mechanisms of action are a promising avenue towards overcoming the superbug threat and avoiding a global health crisis. Among evolving first-in-class antimicrobials, ClpP activators are good candidates because of the essential functions of ClpP in bacterial homeostasis and virulence. Although ADEP and derivatives are potent ClpP activators, their synthesis is difficult, and their low stability hinders further development.

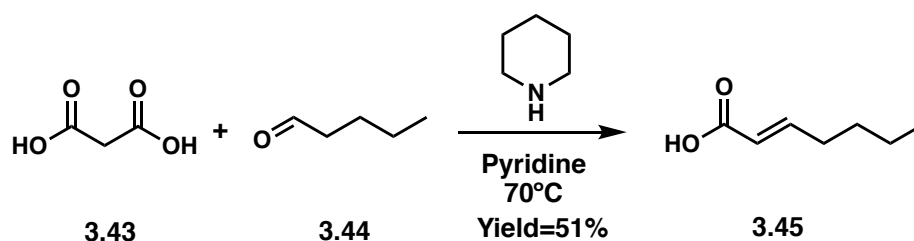
To overcome the issues associated with the ADEP chemotype, I have focused on ADEP bioactive fragment, *N*-heptenoyl 3,5-difluorophenylalanine and investigated the effect of structural constraint via the N- to C-terminal cyclization of the peptidic core on the activation capacity of the chemotype. I assessed the conformational changes associated with the increase in ring size of the central core, from six- to eight-membered cycles using the BCE server. I determined that: (1) The flexibility of appended moieties (i.e., propargyl, 3,5-difluorobenzyl and heptenoyl groups) is only affected in a minor way by the cyclization; (2) The orientations of these groups vary based on the ring size of the central core and notably the conformation adopted by the eight-membered ring orients the 3,5-difluorobenzyl and heptenoyl groups similarly to the corresponding moieties in ClpP-bound ADEP 4; (3) The core rings adopt different conformation based on the size of the ring and little flexibility is predicted.

My synthetic work led to the development of methodologies to access the six-membered rings (piperazinones and pyrazinones), the seven-membered ring (1,4-diazepan-2-one), and the eight-membered ring (1,4-diazecan-2-one), and the generation of the corresponding analogs **3.25**, **3.28**, **3.26** and **3.27**. Despite the potentially favorable conformation for binding to ClpP with less

entropic cost, all of the cyclized analogs were inactive against ClpP. In concordance with the docking studies, the biological results demonstrated the H-bond with ADEP and Tyr62 is essential for the chemo-activation of ClpP and conformational alteration of the scaffold cannot overcome the loss of this interaction. Although the N- to C-terminal ‘bridge’ I employed was aliphatic, opportunities exist to investigate ‘bridges’ that may recapitulate the H-bond with Tyr 62. However, my work led to the discovery of the tyrosyl group as a promising replacement for the 3,5-difluorobenzyl motif and my docking studies suggest that a new H-bond with Thr79 can be leveraged in analog design. This discovery could set the stage for the development of a new ClpP activating chemotypes with increased polarity, and possibly expand the antibacterial activity to Gram-negative bacteria, as more polar antibiotics are known to have a broader spectrum.

7 Experimental Section

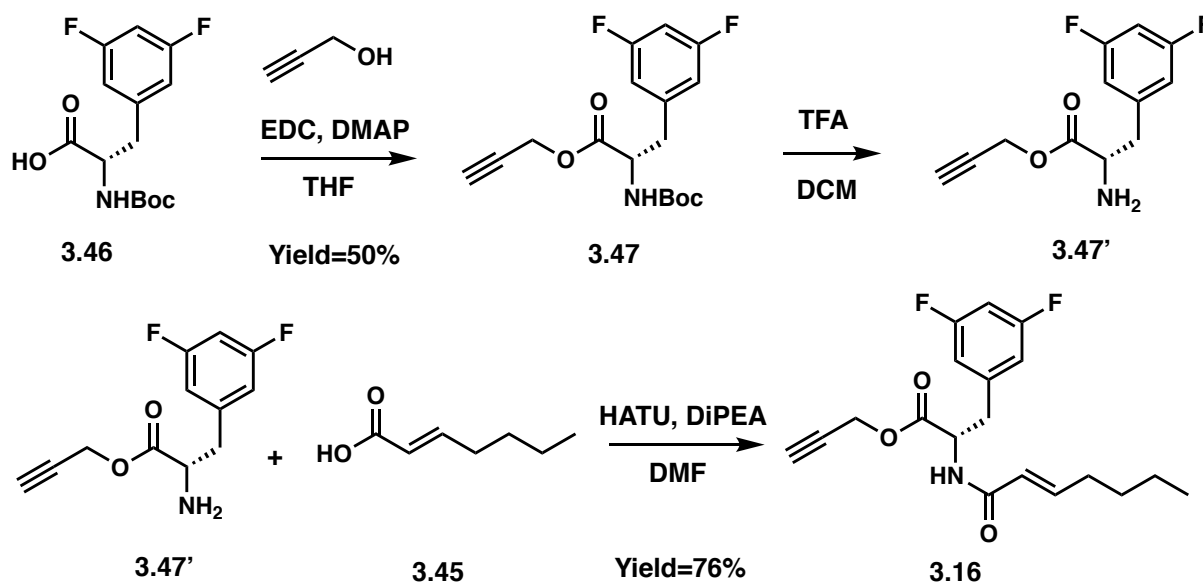
(*E*)-hept-2-enoic acid (3.45):



In a vial, malonic acid **3.43** (500 mg; 4.8 mmol), valeraldehyde **3.44** (647 mg; 5.8 mmol) and piperidine (60 μ L; 0.6 mmol) are dissolved in pyridine (5 mL). The reaction is stirred @ 75°C overnight. The reaction was quenched with 10 mL of concentrated HCl (12 M) in an ice bath. The reaction washed with a saturated solution of copper acetate (20 mL) and the organic layer was extracted with ethyl acetate (EtOAc) (3 times). The organic layers were combined, washed with

brine before being dried over sodium sulfate (Na₂SO₄) and filtered. The filtrate was concentrated in vacuo and purified by flash column chromatography (Silica gel, 0-1 % Methanol (MeOH) in dichloromethane (DCM)) to yield **3.45** (314 mg; Yield=51%) as a clear oil. ¹H NMR (400 MHz, Chloroform-*d*) δ 11.68 (s, 1H), 7.08 (dt, *J* = 15.6, 7.0 Hz, 1H), 5.82 (dt, *J* = 15.6, 1.6 Hz, 1H), 2.23 (qd, *J* = 7.1, 1.6 Hz, 2H), 1.51 – 1.23 (m, 4H), 0.90 (t, *J* = 7.2 Hz, 3H). ¹³C NMR (101 MHz, Chloroform-*d*) δ 172.3, 152.5, 120.6, 32.0, 29.9, 22.2, 13.8.

prop-2-yn-1-yl (*S,E*)-3-(3,5-difluorophenyl)-2-(hept-2-enamido)propanoate (3.16**):**



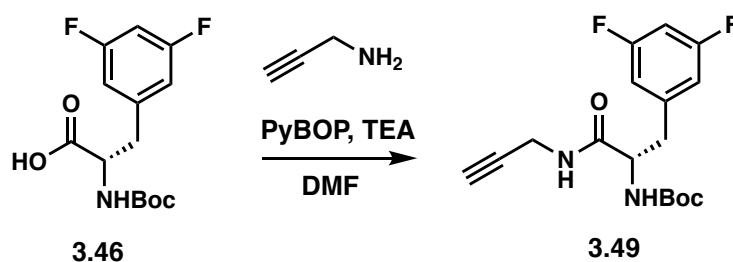
In a vial, Boc-3,5-difluorophenylalanine **3.46** (200 mg; 0.66 mmol), propargyl alcohol (60 μL; 0.9 mmol), 1-Ethyl-3-(3-dimethylaminopropyl)carbodiimide (EDC) (153 mg; 0.8 mmol) and 4-Dimethylaminopyridine (DMAP) (98 mg; 0.8 mmol) were dissolved in 10 mL of dry THF and the reaction mixture was stirred at room temperature (RT) overnight. The reaction was quenched with water (10 mL) and washed with a saturated solution of sodium bicarbonate (NaHCO₃) (20 mL) and the organic layer was extracted with EtOAc (3 times). The organic layers were combined,

washed with brine before being dried over Na₂SO₄ and filtered. The filtrate was concentrated in vacuo and purified by flash column chromatography (Silica gel, 20-50% EtOAc in hexane (Hex)) to yield **3.47** (111 mg; Yield= 50%) as a white solid.

Then, the propargyl ester **3.47** (111 mg; 0.33 mmol) was dissolved in 5 mL of DCM and 1 mL of TFA was added. The reaction mixture was stirred for 3h. After concentration under N₂ flow, the reaction washed with a saturated solution of NaHCO₃ (20 mL) and the organic layer was extracted with EtOAc (3 times). The organic layers were combined, washed with brine before being dried over Na₂SO₄ and filtered. The filtrate **3.47'** was concentrated in vacuo and taken directly to the next step.

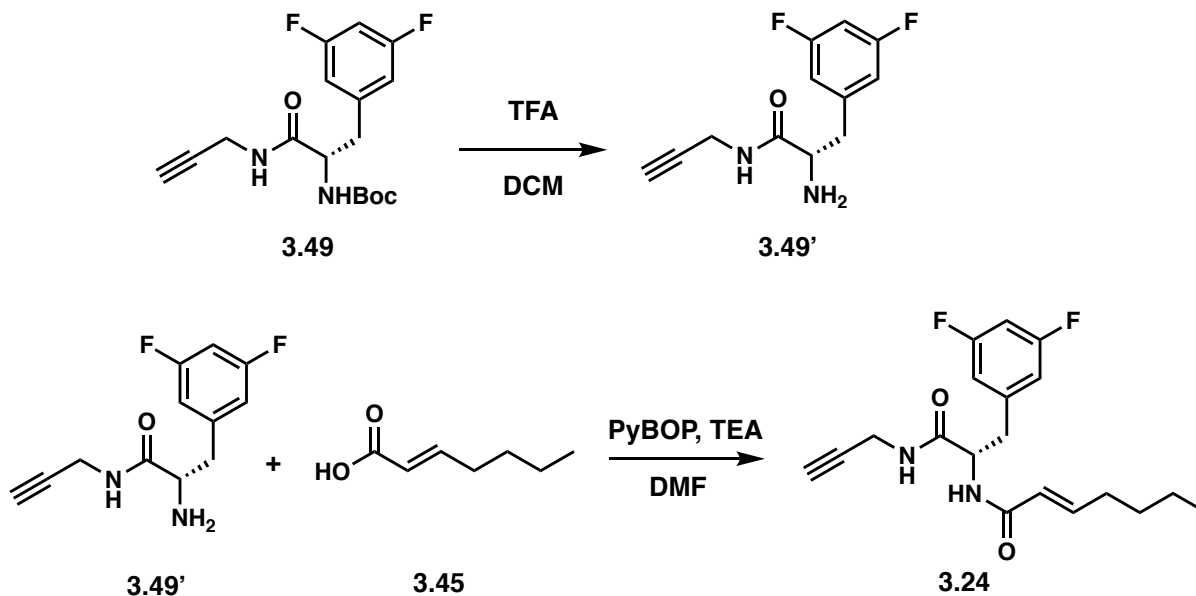
In a vial, the amine **3.47'** (78 mg; 0.33 mmol), (*E*)-hept-2-enoic acid **3.45** (65 mg; 0.5 mmol) and 150 μ L of DiPEA were dissolved in 4 mL of dry DMF. After cooling down the solution to 0°C (ice bath), HATU (152 mg; 0.4 mmol) was added and the reaction mixture was stirred and let warm to room temperature (RT) overnight. The reaction was quenched with water (10 mL) and washed with a saturated solution of NaHCO₃ (20 mL) and the organic layer was extracted with EtOAc (3 times). The organic layers were combined, washed with brine before being dried over Na₂SO₄ and filtered. The filtrate was concentrated in vacuo and purified by flash column chromatography (Silica gel, 20-50% EtOAc in Hex) to yield **3.16** (88 mg; Yield=76%) as a white solid. ¹H NMR (400 MHz, Chloroform-*d*) δ 6.88 (dt, *J* = 15.3, 7.0 Hz, 1H), 6.77 – 6.65 (m, 3H), 5.91 (d, *J* = 7.5 Hz, 1H), 5.79 (dt, *J* = 15.3, 1.6 Hz, 1H), 5.04 – 4.91 (m, 1H), 4.84 (dd, *J* = 15.5, 2.5 Hz, 1H), 4.67 (dd, *J* = 15.5, 2.5 Hz, 1H), 3.26 – 3.12 (m, 2H), 2.58 – 2.52 (m, 1H), 2.19 (qd, *J* = 7.1, 1.6 Hz, 2H), 1.50 – 1.21 (m, 4H), 0.90 (t, *J* = 7.2 Hz, 3H). ¹³C NMR (126 MHz, Chloroform-*d*) δ 170.4, 165.5, 164.0, 163.9, 146.6, 139.4, 122.6, 112.6, 112.5, 112.4, 112.4, 103.0, 102.8, 102.6, 76.6, 76.0, 52.9, 52.7, 37.5, 31.8, 30.2, 22.2, 13.8.

***tert*-butyl (*S*)-3-(3,5-difluorophenyl)-1-oxo-1-(prop-2-yn-1-ylamino)propan-2-yl)carbamate (3.49):**



In a vial, Boc-3,5-difluorophenylalanine **3.46** (100 mg; 0.33 mmol), propargyl amine (35 μ L; 0.4 mmol) and 65 μ L of TEA were dissolved in 4 mL of dry DMF. After cooling down the solution to 0°C (ice bath), PyBOP (208 mg; 0.4 mmol) was added and the reaction mixture was stirred and let warm to RT overnight. The reaction was quenched with water (10 mL) and washed with a saturated solution of NaHCO₃ (20 mL) and the organic layer was extracted with EtOAc (3 times). The organic layers were combined, washed with brine before being dried over Na₂SO₄ and filtered. The filtrate was concentrated in vacuo and purified by flash column chromatography (Silica gel, 20-50% EtOAc in Hex) to yield **3.49** (106 mg; Yield=95%) as a white solid. ¹H NMR (400 MHz, Chloroform-*d*) δ 6.95 – 6.90 (m, 1H), 6.77 – 6.59 (m, 3H), 5.39 (dd, *J* = 17.7, 8.7 Hz, 1H), 4.44 (s, 1H), 4.07 – 3.83 (m, 2H), 3.14 – 2.85 (m, 2H), 2.19 (t, *J* = 2.5 Hz, 1H), 1.36 (d, *J* = 17.6 Hz, 9H).

(*S,E*)-*N*-(3-(3,5-difluorophenyl)-1-oxo-1-(prop-2-yn-1-ylamino)propan-2-yl)hept-2-enamide (3.24):



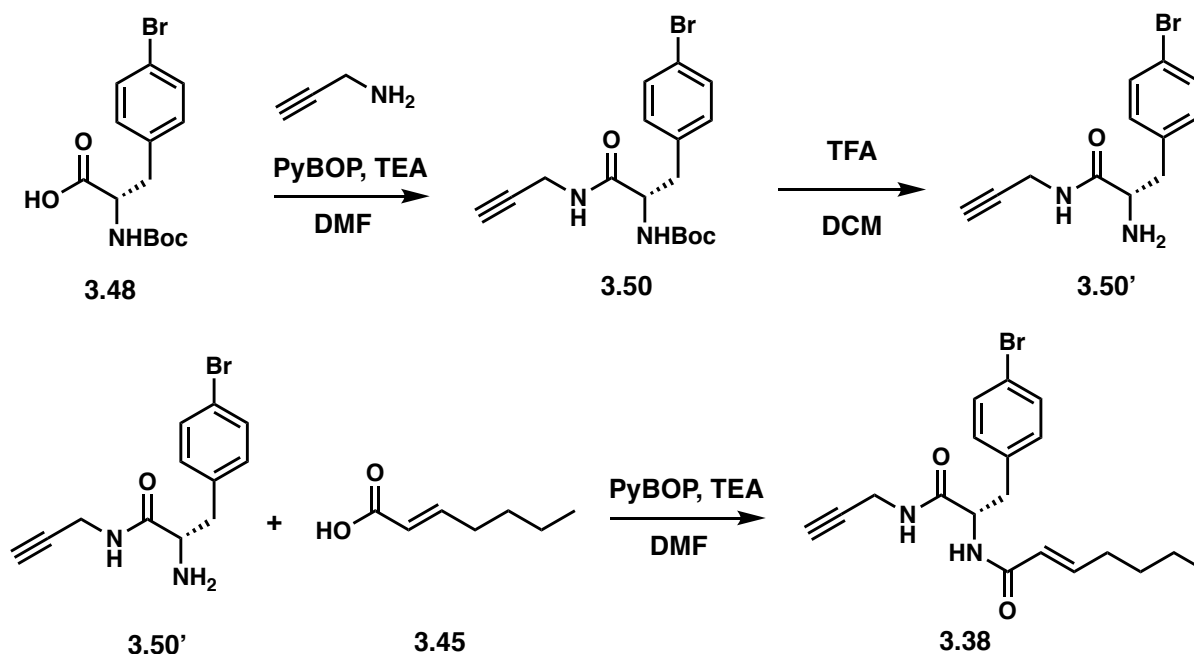
The propargyl amide **3.49** (106 mg; 0.31 mmol) was dissolved in 5 mL of DCM and 1 mL of TFA was added. The reaction mixture was stirred for 3h. After concentration under N₂ flow, the reaction was washed with a saturated solution of NaHCO₃ (20 mL) and the organic layer was extracted with EtOAc (3 times). The organic layers were combined, washed with brine before being dried over Na₂SO₄ and filtered. The filtrate **3.49'** was concentrated in vacuo and taken directly to the next step.

In a vial, the amine **3.49'** (72 mg; 0.3 mmol), *(E)*-hept-2-enoic acid **3.45** (57 mg; 0.45 mmol) and 125 μL of TEA were dissolved in 4 mL of dry DMF. After cooling down the solution to 0°C (ice bath), PyBOP (208 mg; 0.4 mmol) was added and the reaction mixture was stirred and let warm to RT overnight. The reaction was quenched with water (10 mL) and washed with a saturated solution of NaHCO₃ (20 mL) and the organic layer was extracted with EtOAc (3 times). The organic layers were combined, washed with brine before being dried over Na₂SO₄ and filtered. The filtrate was concentrated in vacuo and purified by flash column chromatography (Silica gel, 20-50% EtOAc in Hex) to yield **3.24** (59 mg; Yield=81%) as a white solid. ¹H NMR (400 MHz, Chloroform-*d*) δ 7.33 (t, *J* = 5.3 Hz, 1H), 6.83 (dt, *J* = 15.2, 6.9 Hz, 1H), 6.78 – 6.69 (m, 3H), 6.64

(tt, $J = 9.0, 2.3$ Hz, 1H), 5.81 (dd, $J = 15.3, 1.6$ Hz, 1H), 4.93 (q, $J = 7.4$ Hz, 1H), 4.06 (ddd, $J = 17.5, 5.9, 2.6$ Hz, 1H), 3.84 (ddd, $J = 17.5, 4.9, 2.5$ Hz, 1H), 3.13 – 2.94 (m, 2H), 2.22 – 2.11 (m, 3H), 1.47 – 1.35 (m, 2H), 1.37 – 1.25 (m, 2H), 0.90 (t, $J = 7.2$ Hz, 3H). ^{13}C NMR (101 MHz, Chloroform- d) δ 170.7, 166.1, 164.2, 164.1, 161.7, 161.6, 146.5, 140.3, 140.2, 122.7, 112.5, 112.4, 112.3, 112.2, 102.7, 102.5, 102.2, 78.9, 71.5, 53.8, 38.4, 31.7, 30.2, 29.0, 22.2, 13.8.

(*S,E*)-*N*-(3-(4-bromophenyl)-1-oxo-1-(prop-2-yn-1-ylamino)propan-2-yl)hept-2-enamide

(3.38):



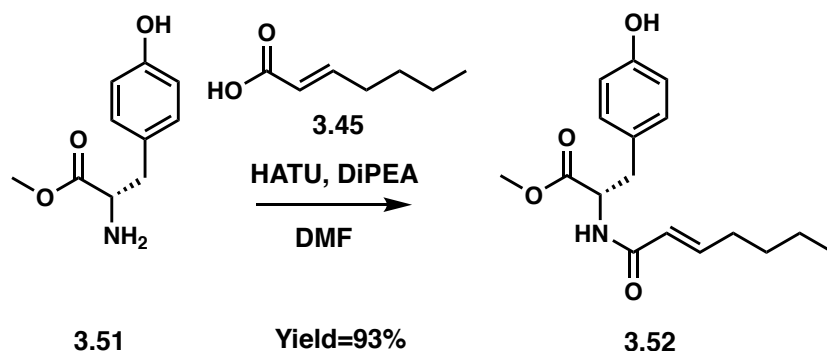
In a vial, Boc-4-bromophenylalanine **3.48** (50 mg; 0.15 mmol), propargyl amine (15 μL ; 0.3 mmol) and 70 μL of TEA were dissolved in 4 mL of dry DMF. After cooling down the solution to 0°C (ice bath), PyBOP (156 mg; 0.3 mmol) was added and the reaction mixture was stirred and let warm to RT overnight. The reaction was quenched with water (10 mL) and washed with a saturated solution of NaHCO_3 (20 mL) and the organic layer was extracted with EtOAc (3 times). The

organic layers were combined, washed with brine before being dried over Na₂SO₄ and filtered. The filtrate was concentrated in vacuo and purified by flash column chromatography (Silica gel, 20-50% EtOAc in Hex) to yield **3.50** (53 mg; Yield=93%) as a white solid.

The propargyl amide **3.50** (53 mg; 0.14 mmol) was dissolved in 5 mL of DCM and 1 mL of TFA was added. The reaction mixture was stirred for 3h. After concentration under N₂ flow, the reaction was washed with a saturated solution of NaHCO₃ (20 mL) and the organic layer was extracted with EtOAc (3 times). The organic layers were combined, washed with brine before being dried over Na₂SO₄ and filtered. The filtrate **3.50'** was concentrated in vacuo and taken directly to the next step.

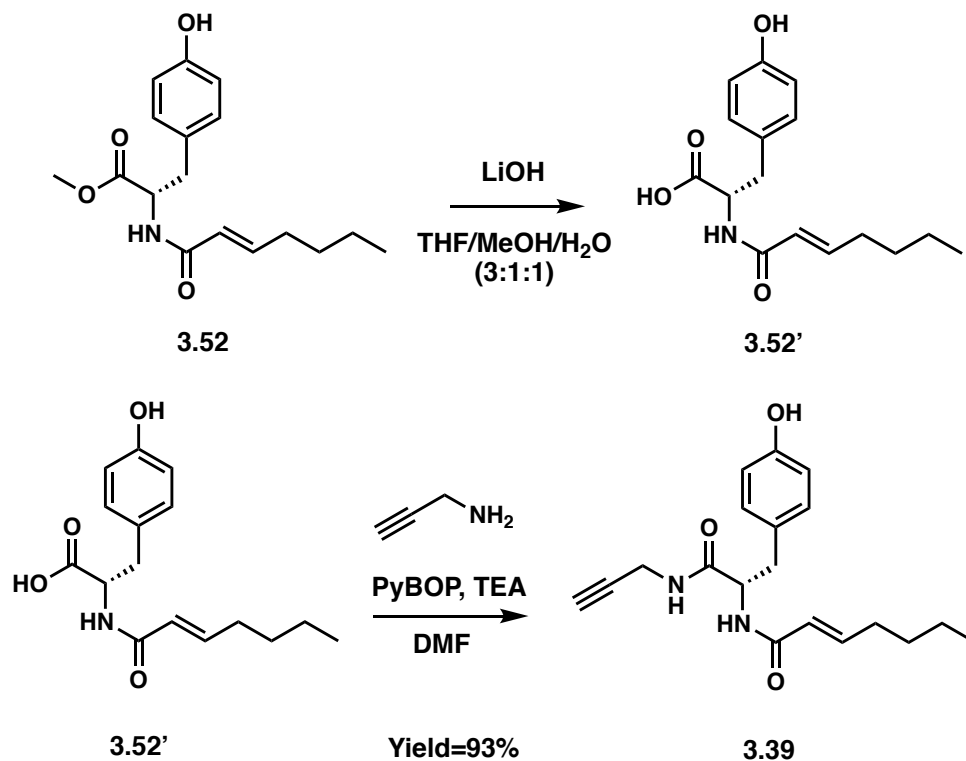
In a vial, the amine **3.50'** (36 mg; 0.13 mmol), (*E*)-hept-2-enoic acid **3.45** (26 mg; 0.2 mmol) and 55 μL of TEA were dissolved in 4 mL of dry DMF. After cooling down the solution to 0°C (ice bath), PyBOP (104 mg; 0.2 mmol) was added and the reaction mixture was stirred and let warm to RT overnight. The reaction was quenched with water (10 mL) and washed with a saturated solution of NaHCO₃ (20 mL) and the organic layer was extracted with EtOAc (3 times). The organic layers were combined, washed with brine before being dried over Na₂SO₄ and filtered. The filtrate was concentrated in vacuo and purified by flash column chromatography (Silica gel, 20-50% EtOAc in Hex) to yield **3.38** (37 mg; Yield=73%) as a white solid. ¹H NMR (500 MHz, Chloroform-*d*) δ 7.43 (d, *J* = 8.1 Hz, 2H), 7.13 – 7.06 (m, 2H), 6.85 (dt, *J* = 14.6, 7.0 Hz, 1H), 6.25 – 6.11 (m, 1H), 6.05 (d, *J* = 8.0 Hz, 1H), 5.77 (dt, *J* = 15.3, 1.5 Hz, 1H), 4.70 (q, *J* = 7.3 Hz, 1H), 4.07 – 3.89 (m, 2H), 3.14 – 3.01 (m, 2H), 2.24 – 2.16 (m, 3H), 1.48 – 1.41 (m, 2H), 1.39 – 1.30 (m, 2H), 0.92 (t, *J* = 7.2 Hz, 3H). ¹³C NMR (126 MHz, Chloroform-*d*) δ 170.3, 162.8, 146.5, 135.4, 131.8, 131.0, 122.7, 121.1, 78.8, 71.7, 54.1, 37.7, 31.7, 30.2, 29.1, 22.2, 13.7.

methyl (*E*)-hept-2-enoyl-*L*-tyrosinate (3.52):



In a vial, the methyl tyrosinate **3.51** (35 mg; 0.15 mmol), (*E*)-hept-2-enoic acid **3.45** (26 mg; 0.2 mmol) and 55 μ L of TEA were dissolved in 4 mL of dry DMF. After cooling down the solution to 0°C (ice bath), PyBOP (104 mg; 0.2 mmol) was added and the reaction mixture was stirred and let warm to RT overnight. The reaction was quenched with water (10 mL) and washed with a saturated solution of NaHCO₃ (20 mL) and the organic layer was extracted with EtOAc (3 times). The organic layers were combined, washed with brine before being dried over Na₂SO₄ and filtered. The filtrate was concentrated in vacuo and purified by flash column chromatography (Silica gel, 1-10% MeOH in DCM) to yield **3.52** (42 mg; Yield=91%) as a white solid. ¹H NMR (300 MHz, Chloroform-*d*) δ 6.99 – 6.78 (m, 3H), 6.72 (d, *J* = 8.1 Hz, 2H), 6.26 – 6.09 (m, 1H), 5.96 (d, *J* = 7.9 Hz, 1H), 5.77 (d, *J* = 15.3 Hz, 1H), 5.00 – 4.80 (m, 1H), 3.73 (s, 3H), 3.17 – 2.89 (m, 2H), 2.21 – 2.10 (m, 1H), 2.08 – 1.96 (m, 1H), 1.47 – 1.20 (m, 4H), 0.95 – 0.82 (m, 3H).

(*S,E*)-*N*-(3-(4-hydroxyphenyl)-1-oxo-1-(prop-2-yn-1-ylamino)propan-2-yl)hept-2-enamide (3.39):

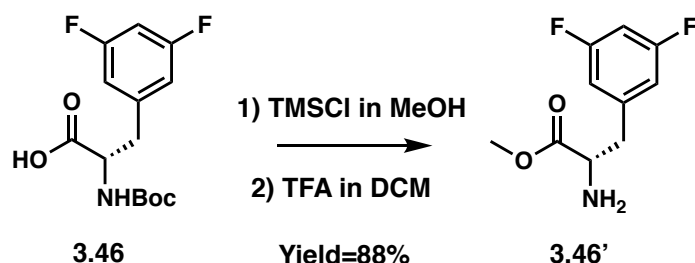


In a vial, the methyl (*E*)-hept-2-enoyl-*L*-tyrosinate **3.52** (42 mg; 0.14 mmol) and lithium hydroxide (LiOH) was dissolved in 10 mL of a mixture of tetrahydrofuran (THF), MeOH and H₂O (3:1:1). After stirring for 10h @ RT, the reaction was quenched with 1N HCl solution (2 mL) and washed with H₂O (20 mL) and the organic layer was extracted with EtOAc (3 times). The organic layers were combined, washed with brine before being dried over Na₂SO₄ and filtered. The filtrate **3.52'** was concentrated in vacuo and taken directly to the next step.

In a vial, the intermediate **3.52'** (22 mg; 0.08 mmol), propargyl amine (5 μL; 0.1 mmol) and 40 μL of TEA were dissolved in 4 mL of dry DMF. After cooling down the solution to 0°C (ice bath), PyBOP (52 mg; 0.1 mmol) was added and the reaction mixture was stirred and let warm to RT overnight. The reaction was quenched with water (10 mL) and washed with a saturated solution of NaHCO₃ (20 mL) and the organic layer was extracted with EtOAc (3 times). The organic layers were combined, washed with brine before being dried over Na₂SO₄ and filtered. The filtrate was concentrated in vacuo and purified by flash column chromatography (Silica gel, 1-10% MeOH in

DCM) to yield **3.39** (24 mg; Yield=93%) as a white solid. ^1H NMR (400 MHz, DMSO- d_6) δ 9.12 (d, J = 3.5 Hz, 1H), 8.46 – 8.39 (m, 1H), 8.06 (d, J = 8.5 Hz, 1H), 7.07 – 6.93 (m, 2H), 6.63 – 6.57 (m, 2H), 6.51 (dt, J = 14.6, 6.9 Hz, 1H), 5.91 (d, J = 15.5 Hz, 1H), 4.48 – 4.29 (m, 1H), 3.82 (ddd, J = 7.9, 5.4, 2.5 Hz, 2H), 3.09 (t, J = 2.5 Hz, 1H), 2.80 (td, J = 16.6, 15.2, 5.3 Hz, 1H), 2.61 (dd, J = 14.0, 9.6 Hz, 1H), 2.08 (q, J = 7.0 Hz, 1H), 2.03 – 1.78 (m, 1H), 1.39 – 1.19 (m, 4H), 0.89 – 0.78 (m, 3H). ^{13}C NMR (101 MHz, DMSO- d_6) δ 171.7, 165.1, 156.2, 143.3, 132.9, 130.5, 128.4, 124.7, 115.3, 81.4, 73.5, 54.6, 37.4, 31.3, 30.4, 28.4, 22.1, 14.2.

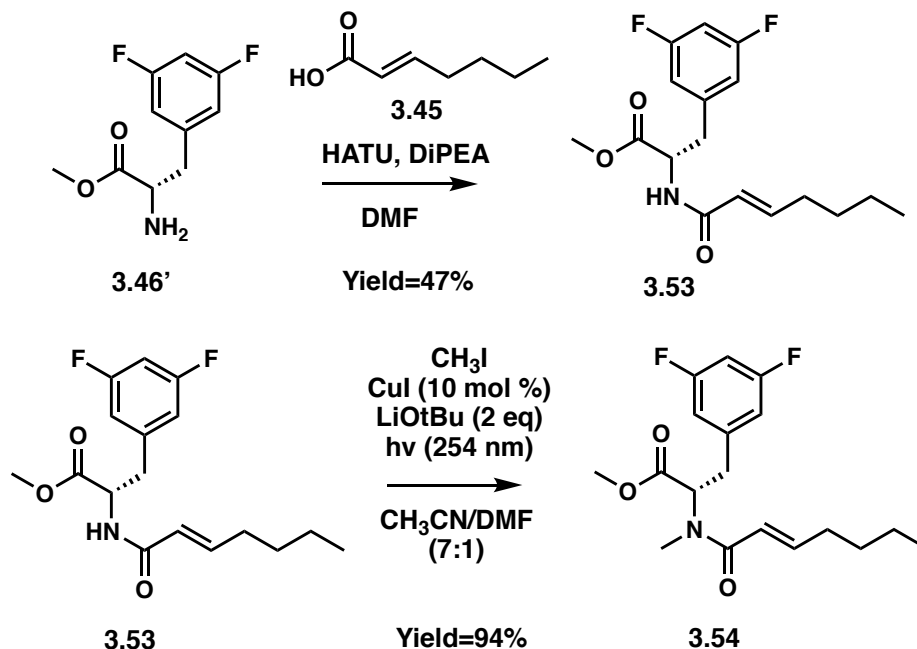
methyl (*S*)-2-amino-3-(3,5-difluorophenyl)propanoate (3.46'**):**



In a vial, Boc-3,5-difluorophenylalanine **3.46** (118 mg; 0.39 mmol) and 150 μL of trimethylsilyl chloride (TMSCl) was stirred for 5 minutes. After adding 5 mL of MeOH the reaction mixture stirred for 10h @ RT. After concentration under N_2 flow, the crude was dissolved in 5 mL of DCM and 1 mL of TFA was added. The reaction mixture was stirred for 3h and then was concentrated under N_2 flow. The reaction was washed with a saturated solution of NaHCO_3 (20 mL) and the organic layer was extracted with EtOAc (3 times). The organic layers were combined, washed with brine before being dried over Na_2SO_4 , filtered and concentrated in vacuo to yield **3.46'** (74 mg; Yield=88%) as a colorless oil. ^1H NMR (400 MHz, Acetonitrile- d_3) δ 6.93 – 6.78 (m, 3H), 3.77 –

3.66 (m, 1H), 3.67 (s, 3H), 3.01 (dd, $J = 13.6, 5.6$ Hz, 1H), 2.89 – 2.77 (m, 1H). ^{13}C NMR (101 MHz, Acetonitrile- d_3) δ 175.1, 164.0, 161.4, 142.7, 112.4, 112.2, 101.6, 55.3, 51.5, 40.1.

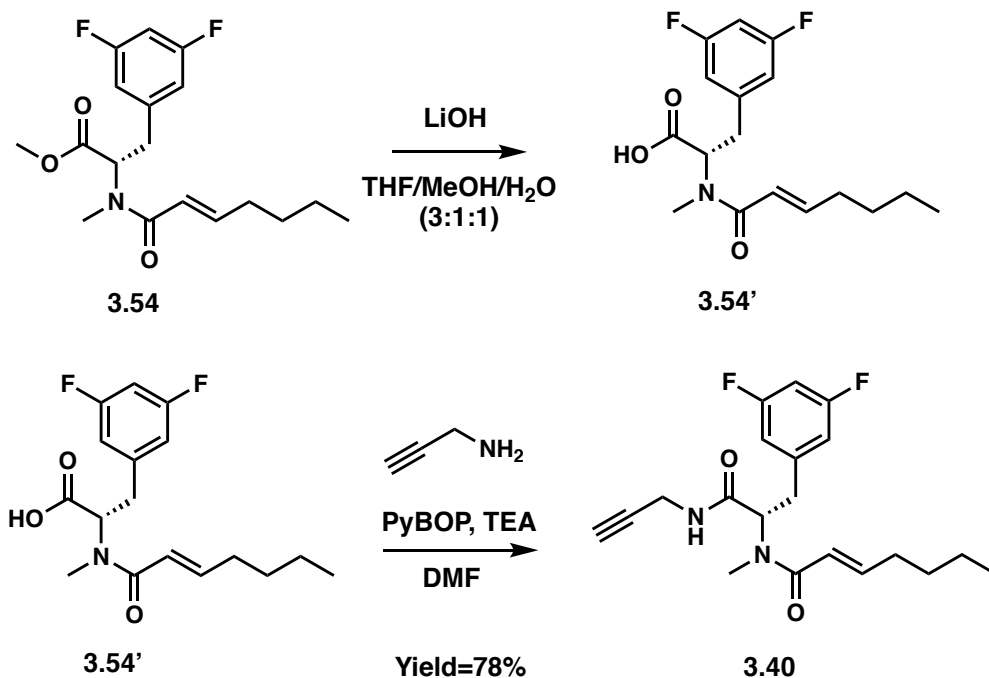
methyl (*S,E*)-3-(3,5-difluorophenyl)-2-(*N*-methylhept-2-enamido)propanoate (3.54**):**



In a vial, the amine **3.46'** (65 mg; 0.3 mmol), (*E*)-hept-2-enoic acid **3.45** (50 mg; 0.4 mmol) and 175 μL of DiPEA were dissolved in 4 mL of dry DMF. After cooling down the solution to 0°C (ice bath), HATU (152 mg; 0.4 mmol) was added and the reaction mixture was stirred and let warm to RT overnight. The reaction was quenched with water (10 mL) and washed with a saturated solution of NaHCO_3 (20 mL) and the organic layer was extracted with EtOAc (3 times). The organic layers were combined, washed with brine before being dried over Na_2SO_4 and filtered. The filtrate was concentrated in vacuo and purified by flash column chromatography (Silica gel, 10-40% EtOAc in Hex) to yield **3.53** (44 mg; Yield=47%) as a yellow oil.

A sealable vial containing the intermediate **3.53** (6 mg; 0.019 mmol), CuI (1 mg; 0.002 mmol) and LiOtBu (3 mg; 0.04 mmol) was evacuated and back-filled with N₂ (3 cycles). A solution of MeI (2.5 μL; 0.04 mmol) in acetonitrile (2.7 mL) and DMF (0.4 mL) was then added to the vial. The reaction mixture was then stirred and irradiated with UVC lamp (254 nm) for 48h. The reaction was quenched with a solution of NH₄OH/NH₄Cl (5 mL) and washed with a saturated solution of NaHCO₃ (20 mL) and the organic layer was extracted with EtOAc (3 times). The organic layers were combined, washed with brine before being dried over Na₂SO₄ and filtered. The filtrate was concentrated in vacuo and purified by flash column chromatography (Silica gel, 10-40% EtOAc in Hex) to yield **3.54** (6 mg; Yield=94%) as a yellow oil. ¹H NMR (400 MHz, Chloroform-*d*) δ 6.91 (dt, *J* = 14.4, 7.1 Hz, 1H), 6.74 (d, *J* = 7.2 Hz, 1H), 6.70 – 6.59 (m, 2H), 6.14 (d, *J* = 15.2 Hz, 1H), 5.16 (dd, *J* = 10.0, 5.6 Hz, 1H), 3.73 (s, 3H), 3.40 – 3.29 (m, 1H), 3.06 (dd, *J* = 14.5, 10.1 Hz, 1H), 2.91 (s, 3H), 2.20 (q, *J* = 7.4, 6.6 Hz, 2H), 1.49 – 1.37 (m, 2H), 1.34 (p, *J* = 7.2 Hz, 2H), 0.90 (dd, *J* = 9.2, 5.3 Hz, 3H).

(*S,E*)-*N*-(3-(3,5-difluorophenyl)-1-oxo-1-(prop-2-yn-1-ylamino)propan-2-yl)-*N*-methylhept-2-enamide (3.40):

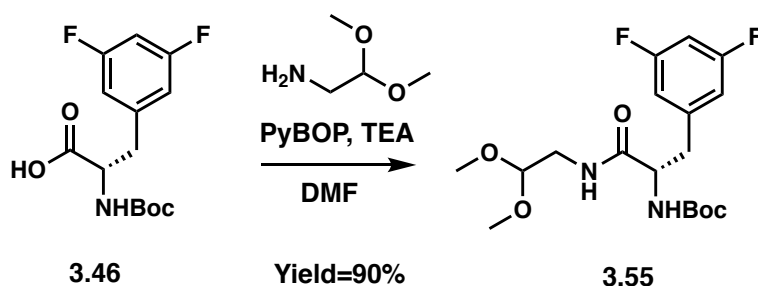


In a vial, the intermediate **3.54** (6 mg; 0.18 mmol) and lithium hydroxide monohydrate (LiOH) (17 mg; 0.4 mmol) was dissolved in 10 mL of a mixture of tetrahydrofuran (THF), MeOH and H₂O (3:1:1). After stirring for 10h @ RT, the reaction was quenched with 1N HCl solution (2 mL) and washed with H₂O (20 mL) and the organic layer was extracted with EtOAc (3 times). The organic layers were combined, washed with brine before being dried over Na₂SO₄ and filtered. The filtrate **53'** was concentrated in vacuo and taken directly to the next step.

In a vial, the intermediate **53'** (6 mg; 0.018 mmol), propargyl amine (3 μL ; 0.04 mmol) and 20 μL of TEA were dissolved in 2 mL of dry DMF. After cooling down the solution to 0°C (ice bath), PyBOP (26 mg; 0.05 mmol) was added and the reaction mixture was stirred and let warm to RT overnight. The reaction was quenched with water (10 mL) and washed with a saturated solution of NaHCO₃ (20 mL) and the organic layer was extracted with EtOAc (3 times). The organic layers were combined, washed with brine before being dried over Na₂SO₄ and filtered. The filtrate was concentrated in vacuo and purified by flash column chromatography (Silica gel, 10-40% EtOAc in Hex) to yield **3.40** (5 mg; Yield=78%) as a colorless oil. ¹H NMR (600 MHz, Chloroform-*d*) δ

6.94 (dt, $J = 14.6, 7.0$ Hz, 1H), 6.74 (d, $J = 7.3$ Hz, 2H), 6.68 – 6.61 (m, 2H), 6.13 (d, $J = 14.9$ Hz, 1H), 5.32 (t, $J = 7.9$ Hz, 1H), 4.05 – 3.93 (m, 2H), 3.32 (dd, $J = 14.5, 7.2$ Hz, 1H), 2.97 (s, 4H), 2.25 – 2.17 (m, 3H), 1.44 (p, $J = 7.4$ Hz, 2H), 1.35 (p, $J = 7.3$ Hz, 2H), 0.91 (t, $J = 7.3$ Hz, 3H).
 ^{13}C NMR (151 MHz, Chloroform- d) δ 169.3, 168.2, 163.7, 162.1, 149.1, 141.0, 119.5, 111.9, 111.8, 111.7, 102.3, 79.1, 71.5, 57.0, 33.3, 32.3, 31.3, 30.3, 29.7, 29.1, 22.2, 13.8.

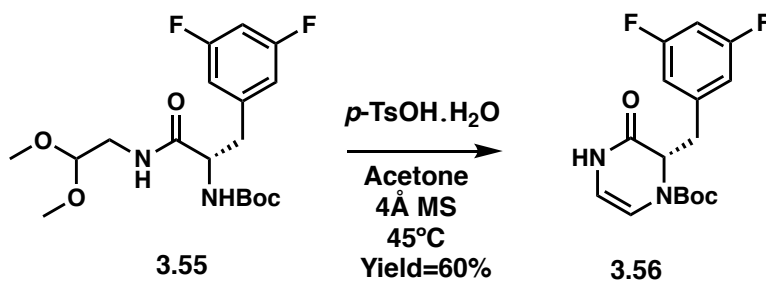
tert-butyl (S)-(3-(3,5-difluorophenyl)-1-((2,2-dimethoxyethyl)amino)-1-oxopropan-2-yl)carbamate (**3.55**):



In a vial, Boc-3,5-difluorophenylalanine **3.46** (100 mg; 0.33 mmol), aminoacetaldehyde dimethyl acetal (80 μL ; 0.66 mmol) and 175 μL of DiPEA were dissolved in 4 mL of dry DMF. After cooling down the solution to 0°C (ice bath), PyBOP (259 mg; 0.498 mmol) was added and the reaction mixture was stirred and let warm to room temperature (RT) overnight. The reaction was quenched with water (10 mL) and washed with a saturated solution of NaHCO_3 (20 mL) and the organic layer was extracted with EtOAc (3 times). The organic layers were combined, washed with brine before being dried over Na_2SO_4 and filtered. The filtrate was concentrated in vacuo and purified by flash column chromatography (Silica gel, 20-50% EtOAc in Hex) to yield **3.55** (114 mg; Yield=89%) as a white solid. ^1H NMR (500 MHz, Acetonitrile- d_3) δ 6.90 (dd, $J = 4.0$ Hz, 2H), 6.84 (tt, $J = 9.5, 2.0$ Hz, 1H), 6.75 (s, 1H), 5.64 (d, $J = 8.6$ Hz, 1H), 4.35 (t, $J = 5.4$ Hz, 1H),

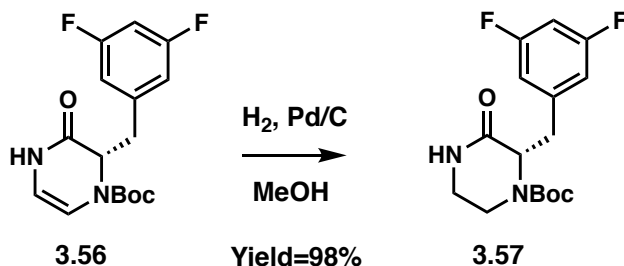
4.31 (td, $J = 8.8, 5.4$ Hz, 1H), 3.34 (d, $J = 3.9$ Hz, 6H), 3.33 – 3.23 (m, 2H), 3.13 (dd, $J = 14.0, 5.4$ Hz, 1H), 2.85 (dd, $J = 13.9, 9.1$ Hz, 1H), 1.37 (s, 9H); ^{13}C NMR (126 MHz, Acetonitrile- d_3) δ 171.0, 163.7, 161.8, 155.3, 142.4, 112.5, 102.3, 101.5, 79.1, 55.2, 53.4, 40.7, 37.6, 27.5.

***tert*-butyl (*S*)-2-(3,5-difluorobenzyl)-3-oxo-3,4-dihydropyrazine-1(*2H*)-carboxylate (3.56):**



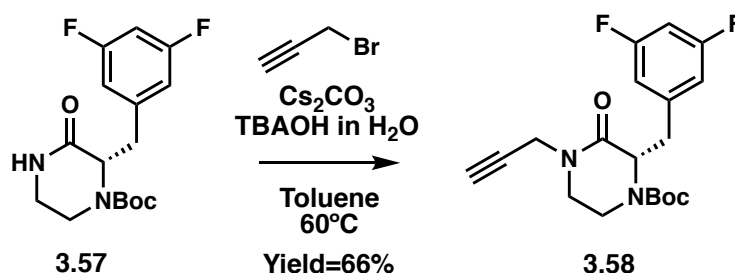
The amide intermediate **3.55** (114 mg; 0.29 mmol), $p\text{TSOH}\cdot\text{H}_2\text{O}$ (50 mg; 0.29 mmol) and 4A molecular sieves were then dissolved in 15 mL of acetone and stirred for 4h at 45°C. The crude was filtered through a celite plug and purified by flash column chromatography (Silica gel, 20-50% EtOAc in Hex) to yield **3.56** (57 mg; Yield= 61%) as a white solid. ^1H NMR (400 MHz, Chloroform- d) δ 8.01 (d, $J = 24.5$ Hz, 1H), 6.74 – 6.63 (m, 3H), 6.25 (dd, $J = 84.7, 5.8$ Hz, 1H), 5.57 (dt, $J = 91.3, 5.3$ Hz, 1H), 4.91 (dt, $J = 63.8, 6.8$ Hz, 1H), 3.04 – 2.83 (m, 2H), 1.45 – 1.23 (m, 9H). ^{13}C NMR (101 MHz, Chloroform- d) δ 166.4, 164.1, 161.6, 151.6, 140.1, 112.6, 108.7, 107.2, 102.4, 82.0, 60.3, 35.6, 27.9.

***tert*-butyl (*S*)-2-(3,5-difluorobenzyl)-3-oxopiperazine-1-carboxylate (3.57):**



In a sealable vial, **3.56** (57 mg; 0.18 mmol) and 50 mg of palladium on carbon (Pd/C) was dissolved in 10 mL of methanol. A balloon of hydrogen was connected to the sealed vial and the reaction mixture was stirred overnight. The crude was concentrated under nitrogen flow and filtered through a celite plug. The filtrate was concentrated in vacuo and purified by flash column chromatography (Silica gel, 40-60% EtOAc in Hex) to yield **3.57** (57 mg; Yield=98%) as a clear oil. ¹H NMR (400 MHz, Chloroform-*d*) δ 7.01 (s, 1H), 6.77 – 6.62 (m, 3H), 4.72 (d, J = 8.0 Hz, 1H), 4.23 – 4.04 (m, 1H), 3.45 – 3.33 (m, 1H), 3.22 (dd, J = 13.7, 4.6 Hz, 1H), 3.15 – 3.05 (m, 2H), 2.88 – 2.75 (m, 1H), 1.32 (s, 9H). ¹³C NMR (101 MHz, Chloroform-*d*) δ 169.8, 164.2, 161.7, 153.5, 141.4, 112.7, 102.2, 80.9, 58.1, 41.3, 37.1, 28.0.

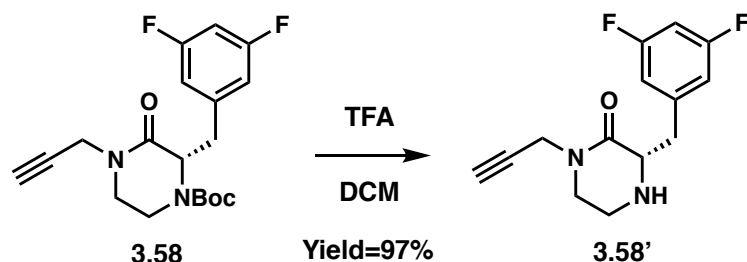
tert-butyl (S)-2-(3,5-difluorobenzyl)-3-oxo-4-(prop-2-yn-1-yl)piperazine-1-carboxylate (**3.58**):



In a 20 mL vial, the piperazinone **3.57** (57 mg; 0.18 mmol), Cs₂CO₃ (115 mg; 0.35 mmol), TBAOH (1M) in H₂O (102 μ L; 0.35 mmol) and in 10 mL of toluene at 60°C. Then the propargyl bromide

solution 80 wt.% in toluene (57 μ L; 0.52 mmol) was added to the reaction mixture and stirred overnight at 60°C. The reaction washed with a saturated solution of NaHCO₃ (20 mL) and the organic layer was extracted with EtOAc (3 times). The organic layers were combined, washed with brine before being dried over Na₂SO₄ and filtered. The filtrate was concentrated in vacuo and purified by flash column chromatography (Silica gel, 20-50% EtOAc in Hex) to yield **3.58** (46 mg; Yield=72%) as a clear oil. ¹H NMR (400 MHz, Chloroform-*d*) δ 6.77 – 6.62 (m, 3H), 4.75 (s, 1H), 4.40 (dd, *J* = 17.3, 2.6 Hz, 1H), 4.11 (dd, *J* = 17.3, 2.5 Hz, 1H), 3.52 – 3.42 (m, 1H), 3.28 – 3.19 (m, 2H), 3.18 – 3.08 (m, 2H), 2.96 – 2.85 (m, 1H), 2.24 (t, *J* = 2.5 Hz, 1H), 1.33 (s, 9H). ¹³C NMR (101 MHz, Chloroform-*d*) δ 167.0, 164.2, 164.1, 161.7, 161.6, 153.4, 141.5, 141.4, 112.7, 112.6, 112.5, 102.5, 102.2, 102.0, 80.9, 77.5, 72.6, 45.7, 35.9, 28.0.

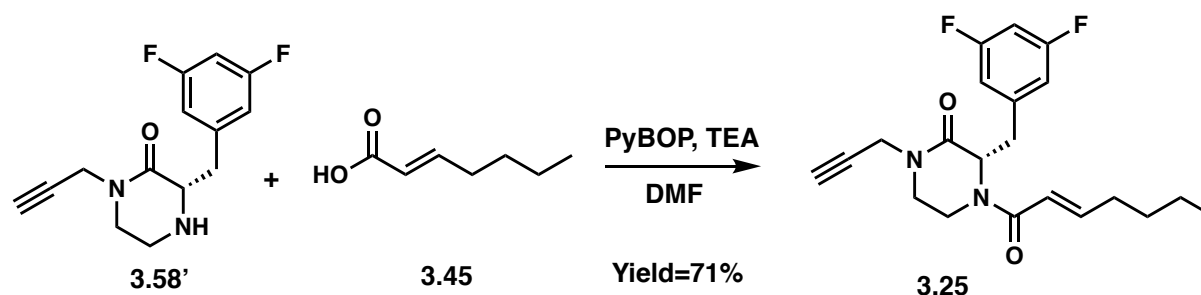
(S)-3-(3,5-difluorobenzyl)-1-(prop-2-yn-1-yl)piperazin-2-one (3.58'):



In a 3-dram vial, the propargyl piperazinone **3.58** (46 mg; 0.13 mmol) was dissolved in 5 mL of DCM and 1 mL of TFA was added. The reaction mixture was stirred for 3h. After concentration under N₂ flow, the reaction washed with a saturated solution of NaHCO₃ (20 mL) and the organic layer was extracted with EtOAc (3 times). The organic layers were combined, washed with brine before being dried over Na₂SO₄ and filtered. The filtrate was concentrated in vacuo and purified by flash column chromatography (Silica gel, 0-4% MeOH in DCM) to yield **3.58'** (45 mg;

Yield=97%) as a yellow oil. ^1H NMR (400 MHz, Chloroform-*d*) δ 6.83 – 6.73 (d, 2H), 6.66 (tt, J = 9.1, 2.4 Hz, 1H), 4.24 (d, J = 2.5 Hz, 2H), 3.61 (dd, J = 9.4, 3.6 Hz, 1H), 3.47 (td, J = 11.1, 10.6, 4.6 Hz, 1H), 3.36 (m, 2H), 3.15 (ddd, J = 12.7, 4.6, 3.0 Hz, 1H), 2.98 (ddd, J = 12.7, 10.2, 4.2 Hz, 1H), 2.87 (dd, J = 13.9, 9.4 Hz, 1H), 2.22 (t, J = 2.6 Hz, 1H). ^{13}C NMR (101 MHz, Chloroform-*d*) δ 168.5, 164.3, 161.7, 142.4, 112.3, 112.1, 102.2, 78.1, 72.2, 60.2, 47.4, 41.9, 38.0, 35.8.

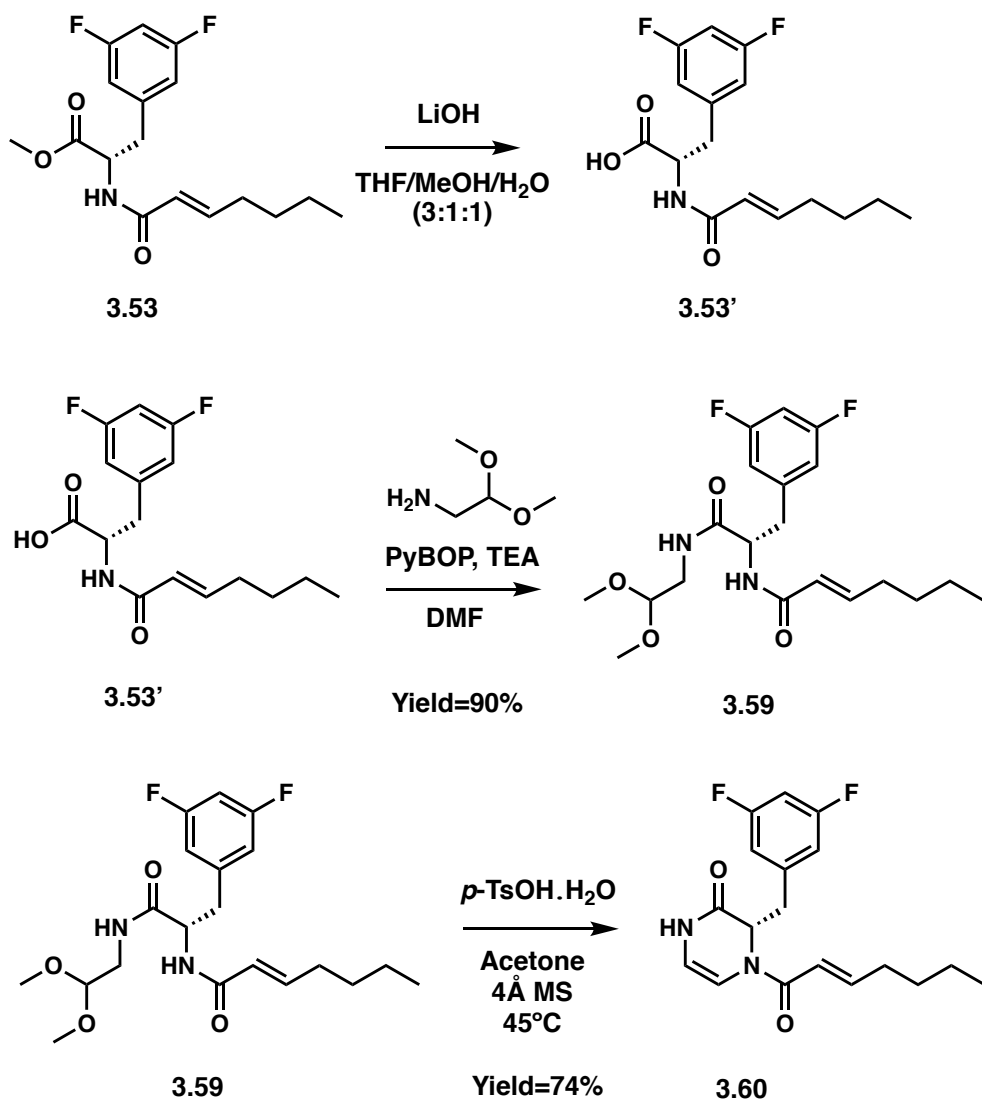
(*S,E*)-3-(3,5-difluorobenzyl)-4-(hept-2-enoyl)-1-(prop-2-yn-1-yl)piperazin-2-one (3.25):



In a vial, the amine **3.58'** (45 mg; 0.17 mmol), (*E*)-hept-2-enoic acid **3.45** (26 mg; 0.2 mmol) and 30 μL of TEA were dissolved in 4 mL of dry DMF. After cooling down the solution to 0°C (ice bath), PyBOP (104 mg; 0.2 mmol) was added and the reaction mixture was stirred and let warm to RT overnight. The reaction was quenched with water (10 mL) and washed with a saturated solution of NaHCO_3 (20 mL) and the organic layer was extracted with EtOAc (3 times). The organic layers were combined, washed with brine before being dried over Na_2SO_4 and filtered. The filtrate was concentrated in vacuo and purified by flash column chromatography (Silica gel, 20-50% EtOAc in Hex) to yield **3.25** (45 mg; Yield=71%) as a colorless oil. ^1H NMR (400 MHz, Acetonitrile-*d*₃) δ 6.84 (t, J = 8.6 Hz, 3H), 6.63 (ddt, J = 71.0, 14.3, 6.9 Hz, 1H), 5.99 (dd, J = 264.4, 15.0 Hz, 1H), 5.16 – 5.00 (m, 0H), 4.70 – 4.60 (m, 1H), 4.28 (ddd, J = 17.5, 8.0, 2.5 Hz, 1H), 4.23 – 4.09 (m, 1H), 4.09 – 3.95 (m, 1H), 3.50 – 3.30 (m, 2H), 3.30 – 3.22 (m, 1H), 3.22 –

3.15 (m, 1H), 3.15 – 2.94 (m, 1H), 2.60 – 2.52 (m, 1H), 2.20 (q, $J = 7.3$ Hz, 1H), 2.05 – 1.96 (m, 1H), 1.47 – 1.27 (m, 2H), 1.27 – 1.17 (m, 2H), 0.95 – 0.80 (m, 3H). ^{13}C NMR (101 MHz, Acetonitrile- d_3) δ 166.7, 165.9, 164.8, 163.9, 161.6, 147.0, 146.4, 133.7, 119.6, 119.0, 117.5, 113.1, 112.9, 112.7, 112.4, 102.5, 102.2, 101.8, 78.3, 72.5, 72.4, 59.3, 56.0, 54.5, 46.0, 45.4, 40.1, 40.0, 37.3, 37.1, 36.2, 35.4, 35.2, 34.8, 34.4, 31.8, 31.5, 30.2, 30.0, 22.0, 13.2.

(*S,E*)-3-(3,5-difluorobenzyl)-4-(hept-2-enoyl)-3,4-dihydropyrazin-2(1*H*)-one (3.60):

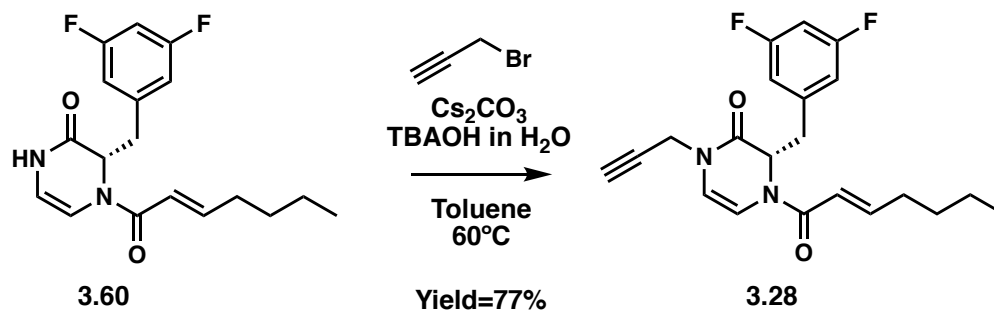


In a vial, the intermediate **3.53** (81 mg; 0.25 mmol) and LiOH (21 mg; 0.5 mmol) was dissolved in 10 mL of a mixture of THF, MeOH and H₂O (3:1:1). After stirring for 10h @ RT, the reaction was quenched with 1N HCl solution (2 mL) and washed with H₂O (20 mL) and the organic layer was extracted with EtOAc (3 times). The organic layers were combined, washed with brine before being dried over Na₂SO₄ and filtered. The filtrate **3.53'** was concentrated in vacuo and taken directly to the next step.

In a vial, **3.53'** (77 mg; 0.25 mmol), aminoacetaldehyde dimethyl acetal (44 mg; 0.3 mmol) and 110 μ L of TEA were dissolved in 2 mL of dry DMF. After cooling down the solution to 0°C (ice bath), PyBOP (182 mg; 0.35 mmol) was added and the reaction mixture was stirred and let warm to RT overnight. The reaction was quenched with water (10 mL) and washed with a saturated solution of NaHCO₃ (20 mL) and the organic layer was extracted with EtOAc (3 times). The organic layers were combined, washed with brine before being dried over Na₂SO₄ and filtered. The filtrate was concentrated in vacuo and purified by flash column chromatography (Silica gel, 20-50% EtOAc in Hex) to yield **3.59** (90 mg; Yield=90%) as a white solid.

The amide intermediate **3.59** (90 mg; 0.23 mmol), pTSA.H₂O (50 mg; 0.29 mmol) and 4A molecular sieves were then dissolved in 15 mL of acetone and stirred for 4h at 45°C. The crude was filtered through a celite plug and purified by flash column chromatography (Silica gel, 20-50% EtOAc in Hex) to yield **3.60** (58 mg; Yield= 74%) as a yellow oil. ¹H NMR (300 MHz, Chloroform-*d*) δ 8.23 (d, *J* = 60.8 Hz, 1H), 7.04 – 6.78 (m, 1H), 6.76 – 6.60 (m, 3H), 6.24 – 6.01 (m, 2H), 5.64 – 5.52 (m, 1H), 5.40 – 5.29 (m, 1H), 3.15 – 2.85 (m, 2H), 2.23 (qd, *J* = 7.1, 1.5 Hz, 1H), 2.08 – 1.95 (m, 1H), 1.74 (s, 0H), 1.53 – 1.19 (m, 4H), 0.97 – 0.79 (m, 3H).

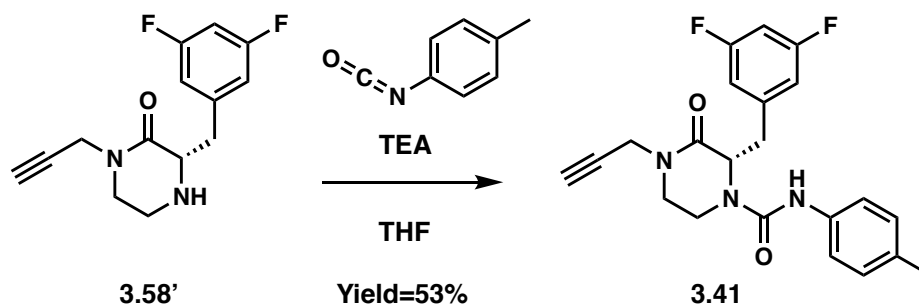
(*S,E*)-3-(3,5-difluorobenzyl)-4-(hept-2-enoyl)-1-(prop-2-yn-1-yl)-3,4-dihydropyrazin-2(1*H*)-one (3.28):



In a 20 mL vial, the piperazinone **3.60** (57 mg; 0.17 mmol), Cs₂CO₃ (115 mg; 0.35 mmol), TBAOH (1M) in H₂O (102 μL; 0.35 mmol) and in 10 mL of toluene at 60°C. Then the propargyl bromide solution 80 wt.% in toluene (40 μL; 0.35 mmol) was added to the reaction mixture and stirred overnight at 60°C. The reaction washed with a saturated solution of NaHCO₃ (20 mL) and the organic layer was extracted with EtOAc (3 times). The organic layers were combined, washed with brine before being dried over Na₂SO₄ and filtered. The filtrate was concentrated in vacuo and purified by flash column chromatography (Silica gel, 20-50% EtOAc in Hex) to yield **3.28** (48 mg; Yield=77%) as a clear oil. ¹H NMR (500 MHz, Acetonitrile-*d*₃) δ 6.92 – 6.76 (m, 3H), 6.76 – 6.59 (m, 1H), 6.62 (d, *J* = 17.9 Hz, 0H), 6.41 (d, *J* = 5.9 Hz, 1H), 6.38 – 6.25 (m, 1H), 6.09 – 6.00 (m, 0H), 5.91 – 5.79 (m, 1H), 5.60 – 5.37 (m, 0H), 5.30 – 5.21 (m, 1H), 4.97 – 4.89 (m, 0H), 4.42 – 4.19 (m, 2H), 3.10 – 2.86 (m, 2H), 2.62 (q, *J* = 2.7 Hz, 1H), 2.26 (q, *J* = 7.2 Hz, 1H), 2.11 – 1.99 (m, 1H), 1.54 – 1.26 (m, 4H), 0.98 – 0.85 (m, 3H). ¹³C NMR (126 MHz, Acetonitrile-*d*₃) δ 169.4, 167.7, 163.7, 148.8, 134.3, 122.1, 119.0, 117.3, 113.0, 108.9, 101.9, 77.9, 72.8, 55.8, 36.9, 35.2, 34.2, 31.8, 30.1, 25.0, 22.0, 13.1.

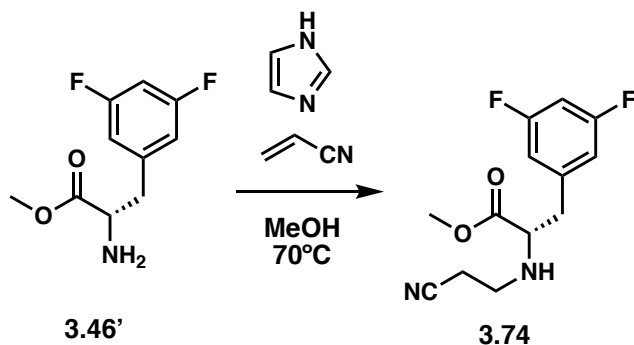
(S)-2-(3,5-difluorobenzyl)-3-oxo-4-(prop-2-yn-1-yl)-N-(p-tolyl)piperazine-1-carboxamide

(3.41):



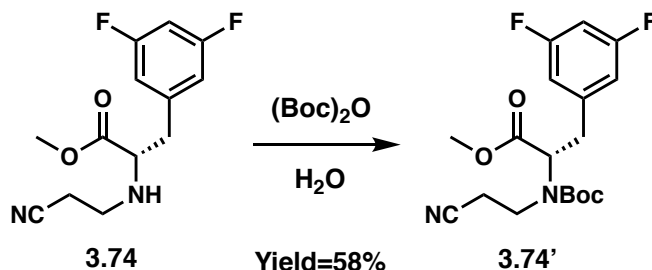
In a vial, the piperazinone amine **3.58'** (13 mg; 0.05 mmol) and 30 μ L of TEA were dissolved in 5 mL of THF. After the addition of *p*-tolyl-isocyanate (5 μ L; 0.04 mmol), the reaction mixture was stirred overnight @ RT. The reaction washed with a saturated solution of NaHCO₃ (20 mL) and the organic layer was extracted with EtOAc (3 times). The organic layers were combined, washed with brine before being dried over Na₂SO₄ and filtered. The filtrate was concentrated in vacuo and purified by flash column chromatography (Silica gel, 20-50% EtOAc in Hex) to yield **3.41** (11 mg; Yield=53%) as a yellow oil. ¹H NMR (500 MHz, Chloroform-*d*) δ 7.05 (d, *J* = 8.0 Hz, 2H), 6.97 (t, *J* = 9.0 Hz, 2H), 6.89 – 6.81 (m, 2H), 6.74 (tt, *J* = 9.4, 3.2 Hz, 1H), 5.89 (d, *J* = 40.0 Hz, 1H), 4.67 (td, *J* = 8.8, 3.7 Hz, 1H), 4.43 (dt, *J* = 17.4, 3.3 Hz, 1H), 4.31 – 4.23 (m, 1H), 4.13 (dd, *J* = 17.4, 2.5 Hz, 1H), 3.61 (td, *J* = 11.5, 4.0 Hz, 1H), 3.40 (ddd, *J* = 12.6, 8.4, 3.9 Hz, 1H), 3.29 (dt, *J* = 12.2, 3.0 Hz, 1H), 3.16 (ddd, *J* = 11.5, 8.7, 2.5 Hz, 1H), 3.09 (tt, *J* = 13.9, 3.2 Hz, 1H), 2.28 (m, 4H). ¹³C NMR (126 MHz, Chloroform-*d*) δ 166.3, 162.2, 154.3, 141.3, 135.5, 133.2, 129.4, 120.0, 112.6, 103.0, 77.3, 72.9, 60.2, 45.5, 37.6, 36.1, 20.7.

methyl (S)-2-((2-cyanoethyl)amino)-3-(3,5-difluorophenyl)propanoate (3.74):



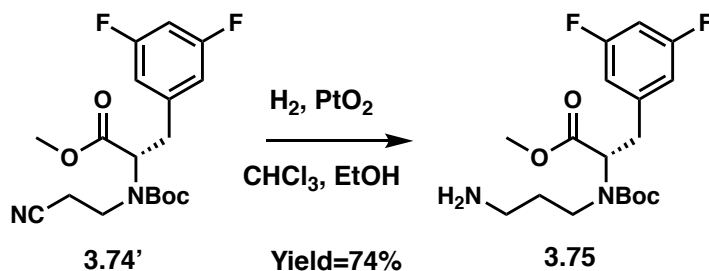
In a vial, the amine **3.46'** (74 mg; 0.34 mmol) and imidazole (68 mg; 1 mmol) were dissolved in 5 mL of MeOH. After stirring for 10 min @ 70°C, acrylonitrile (45 μ L; 0.68 mmol) was added and the reaction mixture was stirred overnight @ 70°C. The reaction was quenched with water (5 mL) and washed with a saturated solution of NaHCO₃ (20 mL) and the organic layer was extracted with EtOAc (3 times). The organic layers were combined, washed with brine before being dried over Na₂SO₄ and filtered. The filtrate was concentrated in vacuo and purified by flash column chromatography (Silica gel, 1-10% MeOH in DCM) to yield **3.74** (44 mg; Yield=48%) as a yellow oil. ¹H NMR (400 MHz, Chloroform-*d*) δ 6.77 – 6.64 (m, 3H), 3.71 (s, 3H), 3.50 (t, *J* = 6.6 Hz, 1H), 3.04 – 2.84 (m, 3H), 2.76 – 2.65 (m, 1H), 2.44 (t, *J* = 6.7 Hz, 2H), 1.72 (s, 1H). ¹³C NMR (101 MHz, Chloroform-*d*) δ 174.0, 164.1, 161.7, 140.8, 118.3, 112.2, 112.0, 102.5, 102.2, 62.1, 52.1, 43.7, 39.3, 19.1.

methyl (S)-2-((tert-butoxycarbonyl)(2-cyanoethyl)amino)-3-(3,5-difluorophenyl)propanoate (3.74'):



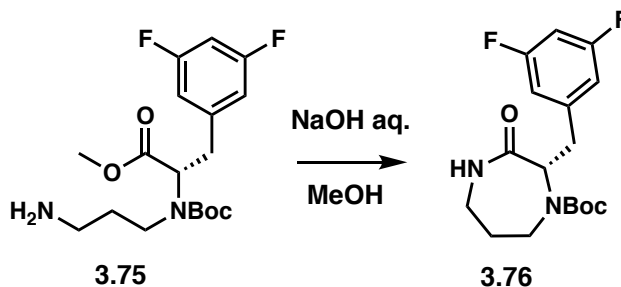
In a vial, the intermediate **3.74** (44 mg; 0.16 mmol) and Di-tert-butyl pyrocarbonate (140 mg; 0.64 mmol) were stirred in 3 mL of H₂O overnight @ RT. The reaction was quenched with water (5 mL) and washed with a saturated solution of NaHCO₃ (20 mL) and the organic layer was extracted with EtOAc (3 times). The organic layers were combined, washed with brine before being dried over Na₂SO₄ and filtered. The filtrate was concentrated in vacuo and purified by flash column chromatography (Silica gel, 1-10% MeOH in DCM) to yield **3.74'** (34 mg; Yield=58%) as a yellow oil. ¹H NMR (500 MHz, Chloroform-*d*) δ 6.76 – 6.69 (m, 3H), 4.31 – 4.13 (m, 1H), 3.79 (d, *J* = 7.8 Hz, 3H), 3.49 (ddt, *J* = 60.4, 14.6, 7.0 Hz, 1H), 3.38 – 3.28 (m, 1H), 3.28 – 3.07 (m, 1H), 3.08 – 2.90 (m, 1H), 2.64 – 2.48 (m, 1H), 2.48 – 2.38 (m, 3H), 1.46 (d, *J* = 12.8 Hz, 9H). ¹³C NMR (126 MHz, cdcl₃) δ 170.7, 164.1, 162.2, 156.1, 154.0, 141.4, 118.0, 111.9, 102.6, 82.0, 62.9, 62.0, 52.6, 45.3, 44.5, 36.2, 35.2, 28.2, 17.4, 16.7.

methyl (S)-2-((3-aminopropyl) (tert-butoxycarbonyl) amino)-3-(3,5-difluorophenyl) propanoate (3.75):



In a sealable vial, **3.74'** (34 mg; 0.09 mmol) and 50 mg of platinum(IV) oxide (PtO₂) was dissolved in 10 mL of a mixture of methanol and chloroform (6:1). A balloon of hydrogen was connected to the sealed vial and the reaction mixture was stirred overnight. The crude was concentrated under nitrogen flow, filtered through a celite plug and concentrated in vacuo to yield **3.75** (32 mg; Yield=74%) as a clear oil. ¹H NMR (500 MHz, Chloroform-*d*) δ 6.82 – 6.66 (m, 3H), 3.99 (s, 1H), 3.76 (s, 3H), 3.47 (s, 1H), 3.35 – 3.25 (m, 2H), 3.18 – 3.09 (m, 2H), 2.98 (s, 1H), 2.66 – 2.59 (m, 1H), 1.89 (s, 2H), 1.43 (s, 9H). ¹³C NMR (126 MHz, cdcl₃) δ 170.5, 164.1, 162.0, 155.9, 141.4, 112.2, 102.6, 82.4, 62.2, 52.8, 45.2, 36.7, 35.9, 28.2, 25.7.

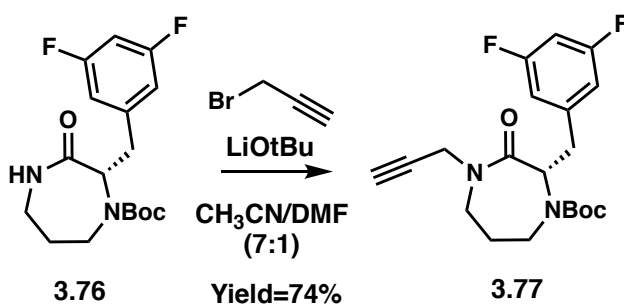
***tert*-butyl (*S*)-2-(3,5-difluorobenzyl)-3-oxo-1,4-diazepane-1-carboxylate (**3.76**):**



In a vial, the amine **3.75** (32 mg; 0.09 mmol) and 80 μL of 1.2M aqueous solution of sodium hydroxide were stirred in 1 mL of MeOH for 3h @ RT. The reaction was dissolved in water (5 mL) and washed with a saturated solution of NaHCO₃ (20 mL) and the organic layer was extracted with EtOAc (3 times). The organic layers were combined, washed with brine before being dried over Na₂SO₄ and filtered. The filtrate was concentrated in vacuo and purified by flash column chromatography (Silica gel, 1-10% MeOH in DCM) to yield **3.76** (18 mg; Yield=62%) as a colorless oil. ¹H NMR (400 MHz, Acetonitrile-*d*₃) δ 6.89 (d, *J* = 6.6 Hz, 2H), 6.79 (tt, *J* = 9.5, 2.4

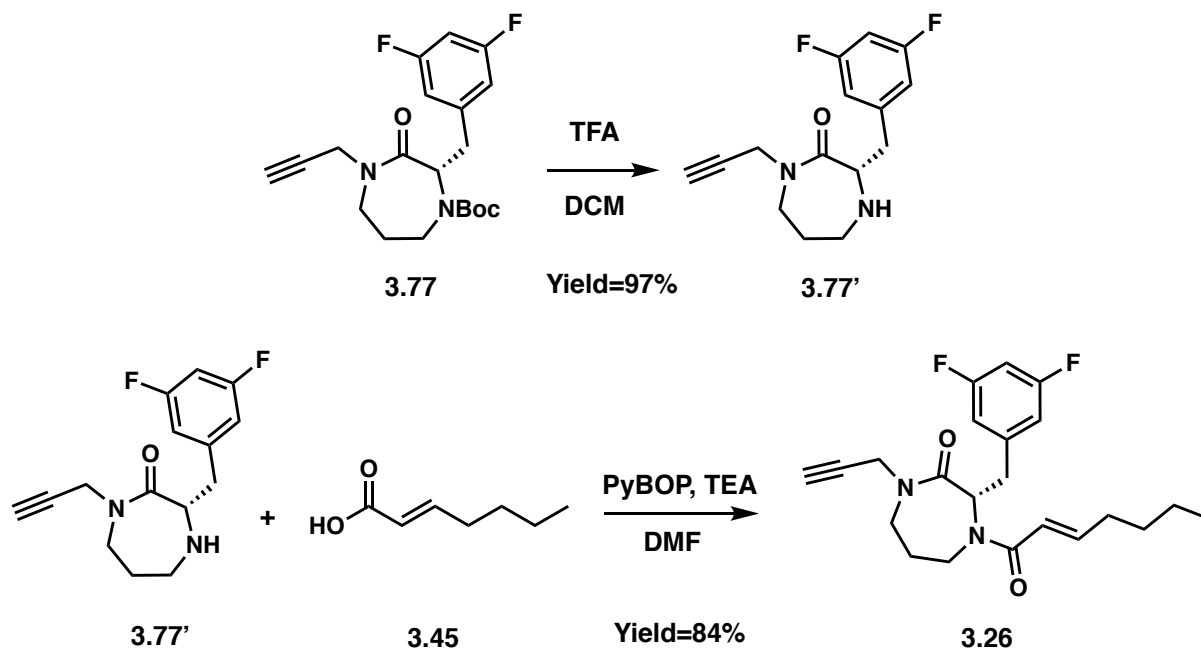
Hz, 1H), 6.22 (s, 1H), 4.79 – 4.70 (m, 1H), 3.54 – 3.44 (m, 1H), 3.35 – 3.20 (m, 2H), 3.20 – 3.07 (m, 3H), 1.90 – 1.79 (m, 1H), 1.78 – 1.65 (m, 1H), 1.39 (s, 9H).

***tert*-butyl (S)-2-(3,5-difluorobenzyl)-3-oxo-4-(prop-2-yn-1-yl)-1,4-diazepane-1-carboxylate (3.77):**



In a vial, the 1,4-diazepan-2-one **3.76** (18 mg; 0.05 mmol) and lithium *tert*-butoxide (LiOtBu) (8 mg; 0.1 mmol) was dissolved in 4 mL of a mixture of dry acetonitrile (CH₃CN) and DMF (7:1) and stirred for 10 min. After the addition of 11 μ L of 80% solution of propargyl bromide in toluene, the reaction mixture was stirred overnight @ RT. The reaction was quenched with water (5 mL) and washed with a saturated solution of NaHCO₃ (20 mL) and the organic layer was extracted with EtOAc (3 times). The organic layers were combined, washed with brine before being dried over Na₂SO₄ and filtered. The filtrate was concentrated in vacuo and purified by flash column chromatography (Silica gel, 10-50% EtOAc in Hex) to yield **3.77** (14 mg; Yield=74%) as a yellow oil. ¹H NMR (500 MHz, Chloroform-*d*) δ 6.81 (d, *J* = 25.9 Hz, 2H), 6.64 (s, 1H), 5.04 – 4.52 (m, 1H), 4.38 (dd, *J* = 17.3, 2.5 Hz, 1H), 4.11 (d, *J* = 17.4 Hz, 1H), 3.69 – 3.59 (m, 1H), 3.57 – 3.48 (m, 1H), 3.47 – 3.26 (m, 3H), 3.24 – 2.99 (m, 1H), 2.22 (s, 1H), 2.04 – 1.75 (m, 2H), 1.47 – 1.29 (m, 9H).

(*S,E*)-3-(3,5-difluorobenzyl)-4-(hept-2-enoyl)-1-(prop-2-yn-1-yl)-1,4-diazepan-2-one (3.26):

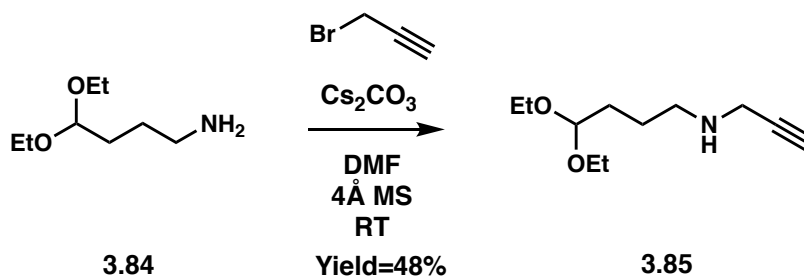


In a 3-dram vial, the propargyl piperazinone **3.77** (14 mg; 0.04 mmol) was dissolved in 5 mL of DCM and 1 mL of TFA was added. The reaction mixture was stirred for 3h. After concentration under N_2 flow, the reaction was washed with a saturated solution of NaHCO_3 (20 mL) and the organic layer was extracted with EtOAc (3 times). The organic layers were combined, washed with brine before being dried over Na_2SO_4 and filtered. The filtrate was concentrated in vacuo and purified by flash column chromatography (Silica gel, 0-4% MeOH in DCM) to yield **3.77'** (10 mg; Yield=97%) as a yellow oil.

In a vial, the amine **3.77'** (10 mg; 0.04 mmol), (*E*)-hept-2-enoic acid **3.45** (8 mg; 0.06 mmol) and 25 μL of DiPEA were dissolved in 2 mL of dry DMF. After cooling down the solution to 0°C (ice bath), PyBOP (31 mg; 0.06 mmol) was added and the reaction mixture was stirred and let warm to RT overnight. The reaction was quenched with water (10 mL) and washed with a saturated solution of NaHCO_3 (20 mL) and the organic layer was extracted with EtOAc (3 times). The

organic layers were combined, washed with brine before being dried over Na₂SO₄ and filtered. The filtrate was concentrated in vacuo and purified by flash column chromatography (Silica gel, 0-50% EtOAc in Hex) to yield **3.26** (11.8 mg; Yield=84%) as a colorless oil. ¹H NMR (500 MHz, Chloroform-*d*) δ 6.83 (dd, *J* = 71.3, 6.1 Hz, 2H), 6.66 (dd, *J* = 39.3, 9.3 Hz, 1H), 5.63 – 5.54 (m, 1H), 5.57 – 5.49 (m, 1H), 5.29 – 5.18 (m, 1H), 4.38 (ddd, *J* = 46.4, 17.3, 2.5 Hz, 1H), 4.12 (ddd, *J* = 49.3, 17.2, 3.1 Hz, 1H), 3.69 – 3.60 (m, 1H), 3.58 – 3.46 (m, 1H), 3.45 – 3.36 (m, 1H), 3.27 (d, *J* = 5.8 Hz, 2H), 3.22 – 3.00 (m, 2H), 2.91 – 2.71 (m, 1H), 2.26 – 2.20 (m, 1H), 2.07 – 2.00 (m, 2H), 2.00 – 1.92 (m, 1H), 1.86 – 1.76 (m, 1H), 1.39 (tq, *J* = 14.3, 7.4 Hz, 2H), 0.95 – 0.80 (m, 3H). ¹³C NMR (101 MHz, Chloroform-*d*) δ 171.0, 169.0, 163.9, 161.4, 142.4, 134.8, 122.3, 112.8, 101.7, 78.5, 72.1, 61.0, 44.0, 37.8, 37.2, 35.4, 34.5, 29.6, 27.4, 22.3, 13.6.

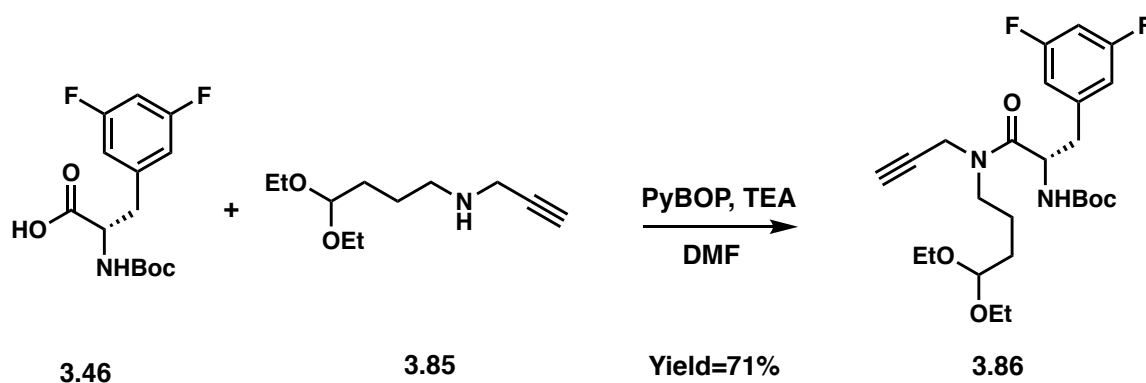
4,4-diethoxy-*N*-(prop-2-yn-1-yl)butan-1-amine (3.85):



In a vial, Cs₂CO₃ (650 mg; 2 mmol) was stirred in 5 mL of dry DMF with 4Å molecular sieves for 10 min. After the addition of 4,4-diethoxybutylamine **3.84** (806 mg; 5 mmol), the reaction mixture was then stirred for 10 min. The propargyl bromide (220 μL; 2 mmol) was introduced and the reaction was stirred overnight @ RT. The reaction mixture was quenched with water (10 mL) and washed with a saturated solution of NaHCO₃ (20 mL) and the organic layer was extracted with EtOAc (3 times). The organic layers were combined, washed with brine before being dried over

Na₂SO₄ and filtered. The filtrate was concentrated in vacuo and purified by flash column chromatography (Silica gel, 0-5% MeOH in DCM) to yield **3.85** (478 mg; Yield=48%) as a yellow oil. ¹H NMR (500 MHz, Chloroform-*d*) δ 4.45 (t, *J* = 5.6 Hz, 1H), 3.58 (dq, *J* = 9.2, 7.0 Hz, 2H), 3.43 (dq, *J* = 9.1, 7.0 Hz, 2H), 3.38 (d, *J* = 2.8 Hz, 4H), 2.52 – 2.45 (m, 2H), 1.63 – 1.55 (m, 2H), 1.53 – 1.44 (m, 2H), 1.14 (t, *J* = 7.2 Hz, 6H).

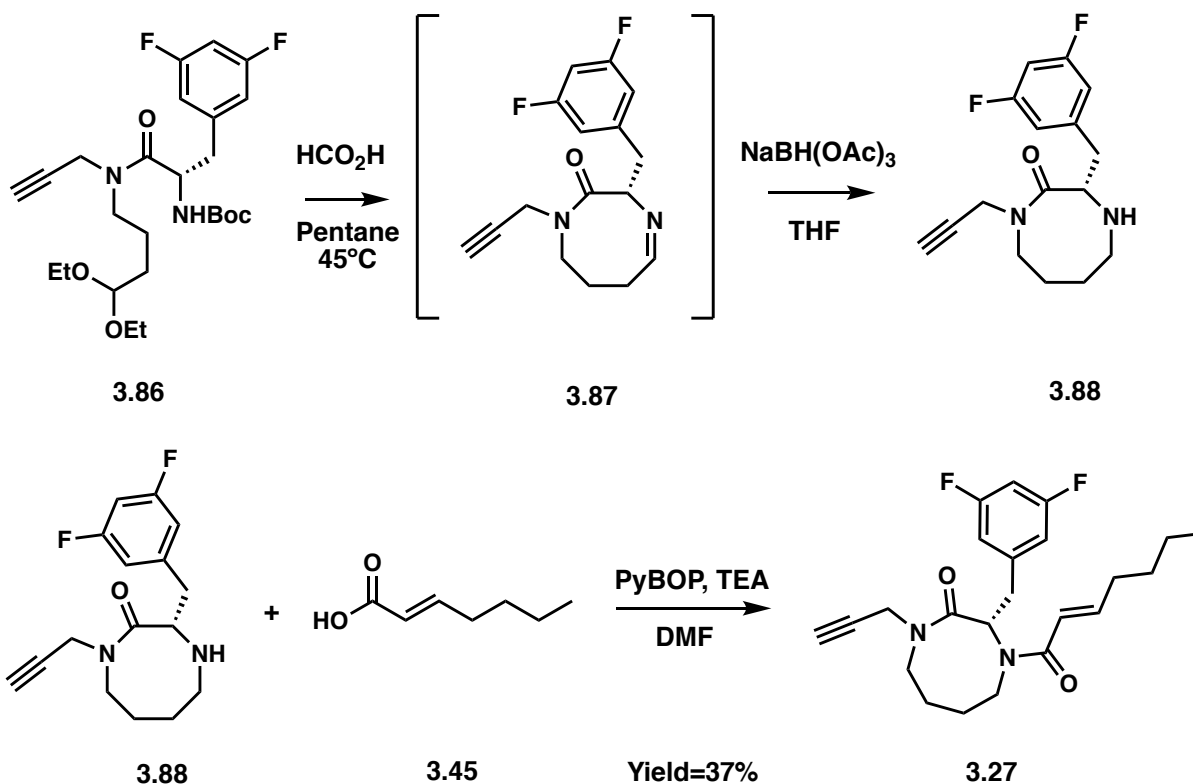
tert-butyl (S)-((4,4-diethoxybutyl)(prop-2-yn-1-yl)amino)-3-(3,5-difluorophenyl)-1-oxopropan-2-yl)carbamate (**3.86**):



In a vial, the amine **3.85** (140 mg; 0.7 mmol), Boc-3,5-difluorophenylalanine **3.46** (170 mg; 0.56 mmol) and 200 μL of TEA were dissolved in 3 mL of dry DMF. After cooling down the solution to 0°C (ice bath), PyBOP (364 mg; 0.7 mmol) was added and the reaction mixture was stirred and let warm to RT overnight. The reaction was quenched with water (10 mL) and washed with a saturated solution of NaHCO₃ (20 mL) and the organic layer was extracted with EtOAc (3 times). The organic layers were combined, washed with brine before being dried over Na₂SO₄ and filtered. The filtrate was concentrated in vacuo and purified by flash column chromatography (Silica gel, 0-50% EtOAc in Hex) to yield **3.86** (191 mg; Yield=71%) as a white solid. ¹H NMR (400 MHz, Chloroform-*d*) δ 6.78 – 6.67 (m, 2H), 6.62 (tt, *J* = 9.1, 2.6 Hz, 1H), 5.44 (dd, *J* = 23.6, 8.9 Hz, 1H),

4.83 – 4.67 (m, 1H), 4.46 – 4.27 (m, 2H), 3.83 (dt, $J = 18.4, 2.9$ Hz, 1H), 3.64 – 3.51 (m, 2H), 3.49 – 3.31 (m, 3H), 3.31 – 3.14 (m, 1H), 3.02 (ddd, $J = 36.8, 13.4, 6.9$ Hz, 1H), 2.85 (dt, $J = 13.1, 6.3$ Hz, 1H), 2.23 (dt, $J = 33.9, 2.5$ Hz, 1H), 1.64 – 1.41 (m, 4H), 1.34 (d, $J = 5.4$ Hz, 9H), 1.14 (td, $J = 7.1, 2.4$ Hz, 6H).

(*S,E*)-3-(3,5-difluorobenzyl)-4-(hept-2-enoyl)-1-(prop-2-yn-1-yl)-1,4-diazocan-2-one (3.27):



In a vial, **3.86** (22 mg; 0.05 mmol) was dissolved in 10 mL of pentane and 8 mL of formic acid was added and the reaction mixture was stirred @ 45°C for 6 hours. After concentrating the reaction mixture under N_2 flow, the reaction was washed with a saturated solution of NaHCO_3 (20 mL) and the organic layer was extracted with EtOAc (3 times). The organic layers were combined, washed with brine before being dried over Na_2SO_4 and filtered. The filtrate was concentrated in

vacuo and redissolved in 4 mL of THF. Following the addition of NaBH(OAc)₃ (30 mg; 0.15 mmol) and 100 mg of MgSO₄, the reaction mixture was stirred overnight @ RT. The reaction was quenched with a saturated solution of NH₄Cl (2 mL) and washed with a saturated solution of NaHCO₃ (20 mL) and the organic layer was extracted with EtOAc (3 times). The organic layers were combined, washed with brine before being dried over Na₂SO₄ and filtered. The filtrate was concentrated in vacuo and taken to the next step.

In a vial, the amine **3.88** (~6 mg; 0.02 mmol), (*E*)-hept-2-enoic acid **3.45** (6 mg; 0.05 mmol) and 30 μL of TEA were dissolved in 3 mL of dry DMF. After cooling down the solution to 0°C (ice bath), PyBOP (26 mg; 0.05 mmol) was added and the reaction mixture was stirred and let warm to RT overnight. The reaction was quenched with water (10 mL) and washed with a saturated solution of NaHCO₃ (20 mL) and the organic layer was extracted with EtOAc (3 times). The organic layers were combined, washed with brine before being dried over Na₂SO₄ and filtered. The filtrate was concentrated in vacuo and purified by flash column chromatography (Silica gel, 0-50% EtOAc in Hex) to yield **3.26** (3 mg; Yield=37%) as a colorless oil. ¹H NMR (500 MHz, Chloroform-*d*) δ 6.86 (d, *J* = 7.8 Hz, 2H), 6.72 (d, *J* = 31.4 Hz, 1H), 6.62 (t, *J* = 9.2 Hz, 1H), 5.50 (t, *J* = 6.6 Hz, 1H), 5.42 (dt, *J* = 14.6, 6.3 Hz, 1H), 4.33 – 4.25 (m, 1H), 4.17 – 4.09 (m, 1H), 3.73 – 3.61 (m, 2H), 3.46 (dd, *J* = 13.7, 7.2 Hz, 1H), 3.39 (d, *J* = 11.4 Hz, 1H), 3.20 – 3.12 (m, 2H), 3.09 (t, *J* = 7.5 Hz, 1H), 3.02 – 2.94 (m, 0H), 2.91 (dd, *J* = 13.8, 5.9 Hz, 1H), 2.24 (s, 1H), 2.07 – 1.97 (m, 3H), 1.79 (s, 2H), 1.71 – 1.61 (m, 1H), 1.40 (dq, *J* = 13.9, 7.3, 6.6 Hz, 2H), 0.97 – 0.88 (m, 3H). ¹³C NMR (101 MHz, Chloroform-*d*) δ 171.2, 170.0, 168.0, 134.7, 122.1, 112.8, 112.5, 110.0, 101.8, 77.2, 72.3, 57.8, 44.6, 42.9, 38.2, 37.0, 35.6, 34.5, 31.9, 23.7, 22.7, 22.3, 14.1. HRESI *m/z* 403.2204 (C₂₃H₂₈F₂N₂O₂ + H⁺ requires 403.2192)

8 Bioactivity Evaluation

8.1 ClpP Protein Purification

Two different *E. coli* cell strains were used for overexpression. *E. coli* ClpP (EcClpP) was overexpressed in BLR (DE3) *E. coli* cells and *Bacillus subtilis* ClpP (BsClpP) was overexpressed in BL21 (DE3) *E. coli* cells from New England Biolabs. Overexpression and purification conditions for both proteins were similar. Overnight cultures were used to inoculate 4 X 1 L LB-broth, which were grown at 37 °C while shaking at 250 rpm to OD600 = 0.7-1.0. Prior to induction, the cultures were cooled to ~18 °C. 1000x IPTG was then added to a final concentration of 1 mM IPTG. ClpP was expressed for 12-16 h at 18 °C while shaking at 180 rpm. Cells were harvested by centrifugation for 15 min at 10,000 g and the pellet was resuspended in ~10 mL Buffer A (50 mM Tris-Cl pH = 8.0, 300 mM NaCl, 10% glycerol) per 1g pellet. The cells were lysed with an Avestin C3 Emulsiflex and the resulting lysate was clarified by centrifugation for 45 min at 28,850 g. The filtrate was loaded onto a 5 mL HP HisTrap Column (GE Healthcare), and washed with 5% Buffer B (Buffer A + 500 mM Imidazole) for 20 column volumes before stepwise elution (15%, 30%, 45%, 70%, 100% Buffer B) using a GE Healthcare Lifesciences AKTA FPLC. Fractions were pooled and exchanged into the storage buffer (25 mM HEPES pH = 7.5, 5 mM MgCl₂, 100 mM KCl, 1 mM DTT, 10% glycerol) with a 16/60 S-300 HiPrep Sephacryl SEC (GE Healthcare). Purified protein solutions were concentrated with 50 kDa MWCO Amicon centrifugal concentrator to ~4.5 mg/mL. Final protein concentration was determined with a standard Bradford assay, and >95% purity was confirmed by SDS-PAGE gel analysis. Protein solution aliquots were flash-frozen with liquid N₂ and stored at -80 °C.

8.2 FITC-Casein Degradation Assay

A 250 nM tetradecameric EcClpP or BsClpP in buffer A (25 mM Tris-HCl, pH 7.5, and 100 mM KCl) was incubated with compounds (100, 250 and 500 μ M) at 37 °C for 15 min in flat bottom, nonbinding, nonsterile, white polystyrene 96-well plates (Corning 3990). After the preincubation period, 10 μ L of a 19.2 μ M FITC- β -casein solution in buffer A was added to each assay well to give a final assay concentration of 1.92 μ M FITC- β -casein and final assay volume of 100 μ L. Assay plates were incubated at 37 °C, and hydrolysis of the fluorogenic substrate was monitored via an i-TECAN Infinite M200 plate reader (excitation: 485 nm; emission: 538 nm). Readings were taken every hour for 5 h.

9 Bibliography

1. Bud, R., Antibiotics: the epitome of a wonder drug. *BMJ* **2007**, *334 Suppl 1*, s6.
2. Gentry, E. J., Antibiotics and Antimicrobial Agents. In *Foye's Principles of Medicinal Chemistry*, Health, W. K., Ed. 2012; pp 1073-1124.
3. Reygaert, W. C., An overview of the antimicrobial resistance mechanisms of bacteria. *AIMS Microbiol* **2018**, *4* (3), 482-501.
4. O'Neill, J., Tackling Drug-Resistant Infections Globally: Final Report and Recommendations. *The Review on Antimicrobial Resistance* **2016**.
5. <https://www.pewtrusts.org/en/research-and-analysis/data-visualizations/2014/antibiotics-currently-in-clinical-development>.
6. Frees, D.; Gerth, U.; Ingmer, H., Clp chaperones and proteases are central in stress survival, virulence and antibiotic resistance of *Staphylococcus aureus*. *Int J Med Microbiol* **2014**, *304* (2), 142-9.
7. Sauer, R. T.; Bolon, D. N.; Burton, B. M.; Burton, R. E.; Flynn, J. M.; Grant, R. A.; Hersch, G. L.; Joshi, S. A.; Kenniston, J. A.; Levchenko, I.; Neher, S. B.; Oakes, E. S.; Siddiqui, S. M.; Wah, D. A.; Baker, T. A., Sculpting the proteome with AAA(+) proteases and disassembly machines. *Cell* **2004**, *119* (1), 9-18.

8. Nagpal, J.; Tan, J. L.; Truscott, K. N.; Heras, B.; Dougan, D. A., Control of protein function through regulated protein degradation: biotechnological and biomedical applications. *J Mol Microbiol Biotechnol* **2013**, *23* (4-5), 335-44.
9. Ni, T.; Ye, F.; Liu, X.; Zhang, J.; Liu, H.; Li, J.; Zhang, Y.; Sun, Y.; Wang, M.; Luo, C.; Jiang, H.; Lan, L.; Gan, J.; Zhang, A.; Zhou, H.; Yang, C. G., Characterization of Gain-of-Function Mutant Provides New Insights into ClpP Structure. *ACS Chem Biol* **2016**, *11* (7), 1964-72.
10. Raju, R. M.; Goldberg, A. L.; Rubin, E. J., Bacterial proteolytic complexes as therapeutic targets. *Nat Rev Drug Discov* **2012**, *11* (10), 777-89.
11. Brotz-Oesterhelt, H.; Sass, P., Bacterial caseinolytic proteases as novel targets for antibacterial treatment. *Int J Med Microbiol* **2014**, *304* (1), 23-30.
12. Bhandari, V.; Wong, K. S.; Zhou, J. L.; Mabanglo, M. F.; Batey, R. A.; Houry, W. A., The Role of ClpP Protease in Bacterial Pathogenesis and Human Diseases. *ACS Chem Biol* **2018**, *13* (6), 1413-1425.
13. Moreno-Cinos, C.; Goossens, K.; Salado, I. G.; Van Der Veken, P.; De Winter, H.; Augustyns, K., ClpP Protease, a Promising Antimicrobial Target. *Int J Mol Sci* **2019**, *20* (9).
14. Baker, T. A.; Sauer, R. T., ClpXP, an ATP-powered unfolding and protein-degradation machine. *Biochim Biophys Acta* **2012**, *1823* (1), 15-28.
15. Alexopoulos, J. A.; Guarne, A.; Ortega, J., ClpP: a structurally dynamic protease regulated by AAA+ proteins. *J Struct Biol* **2012**, *179* (2), 202-10.
16. Flynn, J. M.; Neher, S. B.; Kim, Y.-I.; Sauer, R. T.; Baker, T. A., Proteomic Discovery of Cellular Substrates of the ClpXP Protease Reveals Five Classes of ClpX-Recognition Signals. *Molecular Cell* **2003**, *11* (3), 671-683.
17. Fei, X.; Bell, T. A.; Jenni, S.; Stinson, B. M.; Baker, T. A.; Harrison, S. C.; Sauer, R. T., Structures of the ATP-fueled ClpXP proteolytic machine bound to protein substrate. *Elife* **2020**, *9*.
18. Maurizi, M. R.; Thompson, M. W.; Singh, S. K.; Kim, S. H., Endopeptidase Clp: ATP-dependent Clp protease from Escherichia coli. *Methods Enzymol* **1994**, *244*, 314-31.
19. Wang, J.; Hartling, J. A.; Flanagan, J. M., The Structure of ClpP at 2.3 Å Resolution Suggests a Model for ATP-Dependent Proteolysis. *Cell* **1997**, *91* (4), 447-456.
20. Michel, K. H.; Kastner, R. E. A54556 antibiotics and process for production thereof. 1985.
21. Brotz-Oesterhelt, H.; Beyer, D.; Kroll, H. P.; Endermann, R.; Ladel, C.; Schroeder, W.; Hinzen, B.; Raddatz, S.; Paulsen, H.; Henninger, K.; Bandow, J. E.; Sahl, H. G.; Labischinski, H., Dysregulation of bacterial proteolytic machinery by a new class of antibiotics. *Nat Med* **2005**, *11* (10), 1082-7.
22. Lee, B. G.; Park, E. Y.; Lee, K. E.; Jeon, H.; Sung, K. H.; Paulsen, H.; Rubsamen-Schaeff, H.; Brotz-Oesterhelt, H.; Song, H. K., Structures of ClpP in complex with acyldepsipeptide antibiotics reveal its activation mechanism. *Nat Struct Mol Biol* **2010**, *17* (4), 471-8.
23. Schmitz, K. R.; Carney, D. W.; Sello, J. K.; Sauer, R. T., Crystal structure of Mycobacterium tuberculosis ClpP1P2 suggests a model for peptidase activation by AAA+ partner binding and substrate delivery. *Proc Natl Acad Sci U S A* **2014**, *111* (43), E4587-95.
24. Li, D. H.; Chung, Y. S.; Gloyd, M.; Joseph, E.; Ghirlando, R.; Wright, G. D.; Cheng, Y. Q.; Maurizi, M. R.; Guarne, A.; Ortega, J., Acyldepsipeptide antibiotics induce the formation of a structured axial channel in ClpP: A model for the ClpX/ClpA-bound state of ClpP. *Chem Biol* **2010**, *17* (9), 959-69.

25. Carney, D. W.; Compton, C. L.; Schmitz, K. R.; Stevens, J. P.; Sauer, R. T.; Sello, J. K., A simple fragment of cyclic acyldepsipeptides is necessary and sufficient for ClpP activation and antibacterial activity. *Chembiochem* **2014**, *15* (15), 2216-20.
26. Leung, E.; Datti, A.; Cossette, M.; Goodreid, J.; McCaw, S. E.; Mah, M.; Nakhamchik, A.; Ogata, K.; El Bakkouri, M.; Cheng, Y. Q.; Wodak, S. J.; Eger, B. T.; Pai, E. F.; Liu, J.; Gray-Owen, S.; Batey, R. A.; Houry, W. A., Activators of cylindrical proteases as antimicrobials: identification and development of small molecule activators of ClpP protease. *Chem Biol* **2011**, *18* (9), 1167-78.
27. Lavey, N. P.; Coker, J. A.; Ruben, E. A.; Duerfeldt, A. S., Sclerotiamide: The First Non-Peptide-Based Natural Product Activator of Bacterial Caseinolytic Protease P. *J Nat Prod* **2016**, *79* (4), 1193-7.
28. Famulla, K.; Sass, P.; Malik, I.; Akopian, T.; Kandror, O.; Alber, M.; Hinzen, B.; Ruebsamen-Schaeff, H.; Kalscheuer, R.; Goldberg, A. L.; Brotz-Oesterhelt, H., Acyldepsipeptide antibiotics kill mycobacteria by preventing the physiological functions of the ClpP1P2 protease. *Mol Microbiol* **2016**, *101* (2), 194-209.
29. Hinzen, B.; Raddatz, S.; Paulsen, H.; Lampe, T.; Schumacher, A.; Habich, D.; Hellwig, V.; Benet-Buchholz, J.; Endermann, R.; Labischinski, H.; Brotz-Oesterhelt, H., Medicinal chemistry optimization of acyldepsipeptides of the enopeptin class antibiotics. *ChemMedChem* **2006**, *1* (7), 689-93.
30. Griffith, E. C.; Zhao, Y.; Singh, A. P.; Conlon, B. P.; Tangallapally, R.; Shadrick, W. R.; Liu, J.; Wallace, M. J.; Yang, L.; Elmore, J. M.; Li, Y.; Zheng, Z.; Miller, D. J.; Cheramie, M. N.; Lee, R. B.; LaFleur, M. D.; Lewis, K.; Lee, R. E., Ureadepsipeptides as ClpP Activators. *ACS Infect Dis* **2019**, *5* (11), 1915-1925.
31. Werle, M.; Bernkop-Schnurch, A., Strategies to improve plasma half life time of peptide and protein drugs. *Amino Acids* **2006**, *30* (4), 351-67.
32. Pollaro, L.; Heinis, C., Strategies to prolong the plasma residence time of peptidedrugs. *MedChemComm* **2010**, *1* (5), 319-324.
33. Muttenthaler, M.; King, G. F.; Adams, D. J.; Alewood, P. F., Trends in peptide drug discovery. *Nat Rev Drug Discov* **2021**, *20* (4), 309-325.
34. Erak, M.; Bellmann-Sickert, K.; Els-Heindl, S.; Beck-Sickinger, A. G., Peptide chemistry toolbox - Transforming natural peptides into peptide therapeutics. *Bioorg Med Chem* **2018**, *26* (10), 2759-2765.
35. Craik, D. J.; Fairlie, D. P.; Liras, S.; Price, D., The future of peptide-based drugs. *Chem Biol Drug Des* **2013**, *81* (1), 136-47.
36. Goodreid, J. D.; Janetzko, J.; Santa Maria, J. P., Jr.; Wong, K. S.; Leung, E.; Eger, B. T.; Bryson, S.; Pai, E. F.; Gray-Owen, S. D.; Walker, S.; Houry, W. A.; Batey, R. A., Development and Characterization of Potent Cyclic Acyldepsipeptide Analogues with Increased Antimicrobial Activity. *J Med Chem* **2016**, *59* (2), 624-46.
37. Carney, D. W.; Schmitz, K. R.; Truong, J. V.; Sauer, R. T.; Sello, J. K., Restriction of the conformational dynamics of the cyclic acyldepsipeptide antibiotics improves their antibacterial activity. *J Am Chem Soc* **2014**, *136* (5), 1922-9.
38. Carney, D. W.; Schmitz, K. R.; Scruse, A. C.; Sauer, R. T.; Sello, J. K., Examination of a Structural Model of Peptidomimicry by Cyclic Acyldepsipeptide Antibiotics in Their Interaction with the ClpP Peptidase. *Chembiochem* **2015**, *16* (13), 1875-1879.

39. Li, Y.; Lavey, N. P.; Coker, J. A.; Knobbe, J. E.; Truong, D. C.; Yu, H.; Lin, Y. S.; Nimmo, S. L.; Duerfeldt, A. S., Consequences of Depsipeptide Substitution on the ClpP Activation Activity of Antibacterial Acyldepsipeptides. *ACS Med Chem Lett* **2017**, *8* (11), 1171-1176.
40. Compton, C. L.; Carney, D. W.; Groomes, P. V.; Sello, J. K., Fragment-Based Strategy for Investigating and Suppressing the Efflux of Bioactive Small Molecules. *ACS Infect Dis* **2015**, *1* (1), 53-8.
41. Avila, Q. Design and Synthesis of New ClpP Activators: Towards the Development of a Computationally Guided Approach. University of Oklahoma, 2016.
42. Richter, M. F.; Drown, B. S.; Riley, A. P.; Garcia, A.; Shirai, T.; Svec, R. L.; Hergenrother, P. J., Predictive compound accumulation rules yield a broad-spectrum antibiotic. *Nature* **2017**, *545* (7654), 299-304.
43. Zivanovic, S.; Bayarri, G.; Colizzi, F.; Moreno, D.; Gelpi, J. L.; Soliva, R.; Hospital, A.; Orozco, M., Bioactive Conformational Ensemble Server and Database. A Public Framework to Speed Up In Silico Drug Discovery. *J Chem Theory Comput* **2020**, *16* (10), 6586-6597.
44. Mandal, A. K.; Shrotri, P. Y.; Ghogare, A. D., Boron Trifluoride Etherate/Iodide Ion, a Novel Reagent for the Non-Aqueous Conversion of Acetals to Carbonyl Compounds. *Synthesis* **1986**, *1986* (03), 221-222.
45. Balme, G.; Gore, J., Conversion of acetals and ketals to carbonyl compounds promoted by titanium tetrachloride. *The Journal of Organic Chemistry* **2002**, *48* (19), 3336-3338.
46. Peng, H.; Carrico, D.; Thai, V.; Blaskovich, M.; Bucher, C.; Pusateri, E. E.; Sebt, S. M.; Hamilton, A. D., Synthesis and evaluation of potent, highly-selective, 3-aryl-piperazinone inhibitors of protein geranylgeranyltransferase-I. *Org Biomol Chem* **2006**, *4* (9), 1768-84.
47. Roszak, R.; Beker, W.; Molga, K.; Grzybowski, B. A., Rapid and Accurate Prediction of pKa Values of C-H Acids Using Graph Convolutional Neural Networks. *J Am Chem Soc* **2019**, *141* (43), 17142-17149.
48. Casadei, M. A.; Galli, C.; Mandolini, L., Ring-Closure Reactions .22. Kinetics of Cyclization of Diethyl (Omega-Bromoalkyl)Malonates in the Range of 4-Membered to 21-Membered Rings - Role of Ring Strain. *Journal of the American Chemical Society* **1984**, *106* (4), 1051-1056.
49. Castillo, J.-C.; Orrego-Hernández, J.; Portilla, J., Cs₂CO₃-Promoted Direct N-Alkylation: Highly Chemoselective Synthesis of N-Alkylated Benzylamines and Anilines. *European Journal of Organic Chemistry* **2016**, *2016* (22), 3824-3835.
50. Peng, Y.; Sun, H.; Wang, S., Design and synthesis of a 1,5-diazabicyclo[6,3,0] dodecane amino acid derivative as a novel dipeptide reverse-turn mimetic. *Tetrahedron Letters* **2006**, *47* (27), 4769-4770.
51. Nubbemeyer, U., Synthesis of medium-sized ring lactams. *Stereoselective Heterocyclic Synthesis Iii* **2001**, *216*, 125-196.
52. Biftu, T.; Feng, D.; Qian, X.; Liang, G. B.; Kieczkowski, G.; Eiermann, G.; He, H.; Leiting, B.; Lyons, K.; Petrov, A.; Sinha-Roy, R.; Zhang, B.; Scapin, G.; Patel, S.; Gao, Y. D.; Singh, S.; Wu, J.; Zhang, X.; Thornberry, N. A.; Weber, A. E., (3R)-4-[(3R)-3-Amino-4-(2,4,5-trifluorophenyl)butanoyl]-3-(2,2,2-trifluoroethyl)-1,4-diazepan-2-one, a selective dipeptidyl peptidase IV inhibitor for the treatment of type 2 diabetes. *Bioorg Med Chem Lett* **2007**, *17* (1), 49-52.
53. Häkkinen, M. R.; Keinänen, T. A.; Khomutov, A. R.; Auriola, S.; Weisell, J.; Alhonen, L.; Jänne, J.; Vepsäläinen, J., Synthesis of novel deuterium labelled derivatives of N-alkylated polyamines. *Tetrahedron* **2009**, *65* (2), 547-562.

54. Xu, L.-W.; Li, L.; Xia, C.-G., Transition-Metal-Based Lewis Acid Catalysis of Aza-Type Michael Additions of Amines to α,β -Unsaturated Electrophiles in Water. *Helvetica Chimica Acta* **2004**, *87* (6), 1522-1526.
55. Dubois, N.; Glynn, D.; McNally, T.; Rhodes, B.; Woodward, S.; Irvine, D. J.; Dodds, C., On DABAL-Me₃ promoted formation of amides. *Tetrahedron* **2013**, *69* (46), 9890-9897.
56. Lee, D. S.; Amara, Z.; Poliakoff, M.; Harman, T.; Reid, G.; Rhodes, B.; Brough, S.; McNally, T.; Woodward, S., Investigating Scale-Up and Further Applications of DABAL-Me₃ Promoted Amide Synthesis. *Organic Process Research & Development* **2015**, *19* (7), 831-840.
57. Hartman, G. D.; Kuduk, S. Azepane derivatives and methods of treating hepatitis B infections. 2019.
58. Natsugari, H.; Ikeura, Y.; Kamo, I.; Ishimaru, T.; Ishichi, Y.; Fujishima, A.; Tanaka, T.; Kasahara, F.; Kawada, M.; Doi, T., Axially chiral 1,7-naphthyridine-6-carboxamide derivatives as orally active tachykinin NK(1) receptor antagonists: synthesis, antagonistic activity, and effects on bladder functions. *J Med Chem* **1999**, *42* (19), 3982-93.
59. Kozikowski, A. P.; Wang, S.; Ma, D.; Yao, J.; Ahmad, S.; Glazer, R. I.; Bogi, K.; Acs, P.; Modarres, S.; Lewin, N. E.; Blumberg, P. M., Modeling, chemistry, and biology of the benzolactam analogues of indolactam V (ILV). 2. Identification of the binding site of the benzolactams in the CRD2 activator-binding domain of PKCdelta and discovery of an ILV analogue of improved isozyme selectivity. *J Med Chem* **1997**, *40* (9), 1316-26.
60. Martin Hernando, J. I.; Ontoria, J. M.; Malancona, S.; Attenni, B.; Fiore, F.; Bonelli, F.; Koch, U.; Di Marco, S.; Colarusso, S.; Ponzi, S.; Gennari, N.; Vignetti, S. E.; Del Rosario Rico Ferreira, M.; Habermann, J.; Rowley, M.; Narjes, F., Optimization of thienopyrrole-based finger-loop inhibitors of the hepatitis C virus NS5B polymerase. *ChemMedChem* **2009**, *4* (10), 1695-713.
61. Mazurov, A. A.; Andronati, S. A.; Korotenko, T. I.; Sokolenko, N. I.; Dyadenko, A. I.; Shapiro, Y. E.; Gorbatyuk, V. Y.; Voronina, T. A., Design of a novel cognitive enhancer (8S, 10aS)-8-carbamoyl-1,2,3,6,7,8,9,10a-octahydro-5H,10H-pyrrolo[1,2-a][1,4]diazocin-5,10-dione. *Bioorganic & Medicinal Chemistry Letters* **1996**, *6* (21), 2595-2600.
62. Wu, A.; Feng, Q.; Sung, H. H. Y.; Williams, I. D.; Sun, J., Synthesis of Eight-Membered Lactams through Formal [6+2] Cyclization of Siloxy Alkynes and Vinylazetidines. *Angew Chem Int Ed Engl* **2019**, *58* (20), 6776-6780.
63. Zhou, Y.; Wei, Y. L.; Rodriguez, J.; Coquerel, Y., Enantioselective Organocatalytic Four-Atom Ring Expansion of Cyclobutanones: Synthesis of Benzazocinones. *Angew Chem Int Ed Engl* **2019**, *58* (2), 456-460.
64. Hill, J. E.; Matlock, J. V.; Lefebvre, Q.; Cooper, K. G.; Clayden, J., Consecutive Ring Expansion and Contraction for the Synthesis of 1-Aryl Tetrahydroisoquinolines and Tetrahydrobenzazepines from Readily Available Heterocyclic Precursors. *Angew Chem Int Ed Engl* **2018**, *57* (20), 5788-5791.
65. Eschweiler, W., *Ber. Dtsch. Chem. Ges.* **1905**, *38*, 880.
66. Clarke, H. T.; Gillespie, H. B.; Weisshaus, S. Z., *J. Am. Chem. Soc.* **1933**, *55*, 4571.
67. Webers, V. J.; Bruce, W. F., The Leuckart reaction; a study of the mechanism. *J Am Chem Soc* **1948**, *70* (4), 1422-4.

Appendix – Chapter 3

Computational Studies

The dihedral angle of the flexible bonds of analogs **3.24** – **3.28** were measured for each their corresponding conformers (each representative of a cluster) predicted by the bioactive conformational ensemble (BCE) server (<https://mmb.irbbarcelona.org/BCE/>) using the measuring tools in Schrodinger.

Cluster	Dihedral angle				
	Propargyl C24-C23-N13-C11	Backbone N13-C11-C10-N12	3,5-difluorobenzyl C11-C10-C9-C3	Heptenoyl C17-C18-C19-C20	C10-N12-C34-O35
1	169.4	-11.7	-78.8	-77.2	7.7
2	-168.5	-3.6	-78.9	-110.8	5.1
3	119.6	-1.7	-62.9	110.5	-4.1
4	145.7	3.6	-170.9	90.2	18.0

5	138.5	-13.2	61.5	107.2	-6.1
6	139.4	-10.3	-59.8	94.2	5.9
7	90.5	-13.6	-50.1	166.0	-16.1
8	-173.6	5.5	173.9	-81.5	16.0
9	83.4	-2.5	176.8	102.7	12.8

Table 3.15: Summary of the dihedral angles of the conformer ensemble of analog 3.24.

Cluster	Dihedral angle				
	Propargyl C22-C21-N1-C2	Backbone N1-C2-C3-N26	3,5-difluorobenzyl C3-C6-C7-C12	Heptenoyl C18-C20- C24-C25	C3-N26-C37- O38
1	67.2	-2.1	-65.7	68.4	-165.3
2	-117.9	2.7	178.1	-97.7	166.9
3	80.2	1.3	-62.6	-111.2	172.0
4	-75.4	-9.1	165.0	110.4	-165.6
5	-104.5	-14.0	-70.2	88.3	168.9
6	76.7	-19.2	143.0	-83.8	-176.8
7	73.5	-17.2	53.9	-175.7	172.9
8	72.4	0.5	-60.8	103.4	171.6

Table 3.16: Summary of the dihedral angles of the conformer ensemble of analog 3.25.

Cluster	Dihedral angle				
	Propargyl C10-C9-N1-C7	Backbone N1-C7-C6-N5	3,5-difluorobenzyl C7-C6-C17-C18	Heptenoyl C13-C15-C16-C26	C6-N5-C31-O32
1	81.4	41.6	163.7	-79.9	172.2
2	83.5	57.9	-172.1	101.9	161.3
3	105.0	45.4	169.6	81.5	173.9
4	104.5	57.4	176.6	-97.6	172.8
5	113.0	48.6	178.9	64.4	-174.5
6	82.8	56.9	82.8	-167.2	169.9
7	-91.8	35.0	174.5	-128.1	152.0
8	95.6	52.7	170.0	-91.1	172.4
9	64.1	40.4	59.0	110.4	174.0

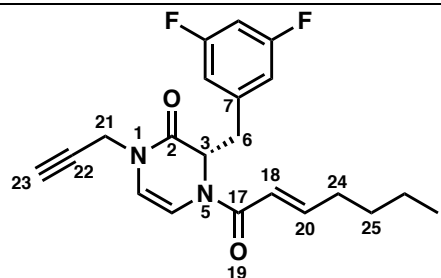
Table 3.17 Summary of the dihedral angles of the conformer ensemble of analog 3.26.

Cluster	Dihedral angle				
	Propargyl C11-C10-N1-C8	Backbone N1-C8-C7-N6	3,5-difluorobenzyl C8-C7-C13-C14	Heptenoyl C24-C25-C26-C27	C7-N6-C40-O41

1	152.5	60.6	170.2	108.1	-13.4
2	107.3	74.0	-179.5	-118.1	-3.8
3	-93.9	66.4	174.3	-78.8	-2.6
4	91.7	68.5	175.1	79.7	9.8
5	-73.6	57.0	174.3	-130.5	-1.8
6	-81.4	64.6	163.7	67.0	14.6
7	86.1	50.1	154.2	-85.2	16.3
8	82.5	37.9	68.2	-97.7	6.1
9	166.1	30.0	60.4	126.5	-9.3

Table 3.18 Summary of the dihedral angles of the conformer ensemble of analog 3.27.

Cluster	Dihedral angle				
	Propargyl C22-C21-N1-C2	Backbone N1-C2-C3-N5	3,5-difluorobenzyl C2-C3-C6-C7	Heptenoyl C18-C20-C24-C25	C3-N5-C17-O19
1	100.8	-16.6	-66.1	-98.2	11.5
2	107.6	-8.1	64.0	126.9	-8.7
3	95.7	-19.0	-76.7	76.9	-1.3
4	103.4	-7.0	-66.9	-102.4	-6.8
5	-108.6	-19.2	-65.3	-88.5	-15.3
6	117.2	-4.8	-169.7	-128.3	5.3
7	86.4	-23.1	72.6	-133.7	-3.8
8	116.0	-25.7	-51.5	-109.0	-2.1
9	77.9	-21.3	-179.3	96.9	-5.5



10	-126.0	-18.7	62.5	-106.1	-0.9
----	--------	-------	------	--------	------

Table 3.19: Summary of the dihedral angles of the conformer ensemble of analog 3.28.

FITC-Casein Degradation Assay Data

	Buffer	BsClpP + DMSO (-)	BsClpP + 16 (+) (100 uM)	BsClpP + 23 (500uM)	BsClpP + 23 (250uM)	BsClpP + 25 (500uM)
0h	994	9051	11337	11595	11600	10041
1h	1003	9282	15580	16410	16564	10620
2h	981	9543	16543	17496	17801	10852
3h	1012	10068	17397	18447	18747	11213
4h	1005	10550	18098	19031	19522	11526
	BsClpP + 25 (250uM)	BsClpP + 26 (500uM)	BsClpP + 26 (250uM)	BsClpP + 27 (500uM)	BsClpP + 27 (250uM)	BsClpP + 38 (500uM)
0h	9535	8861	8870	8626	8708	8789
1h	9836	9108	9083	8972	9132	9273
2h	9966	9403	9357	9250	9313	9564
3h	10384	9589	9495	9405	9599	9703
4h	10605	9937	9868	9687	9850	9881
	BsClpP + 38 (250uM)	BsClpP + 40 (500uM)	BsClpP + 40 (250uM)	BsClpP + 39 (500uM)	BsClpP + 39 (250uM)	BsClpP + 38 (250uM)
0h	9418	9094	9182	9592	9562	9418
1h	9470	10617	10204	13464	12760	9470
2h	9558	11340	10631	14545	13715	9558
3h	9946	12201	11336	15445	14737	9946
4h	10002	12725	11935	16203	15468	10002

	BsClpP + 41 (500uM)	BsClpP + 41 (250uM)	BsClpP + 28 (500uM)	BsClpP + 28 (250uM)		
0h	10057	10140	9867	9100		
1h	10507	9812	11360	10266		
2h	10701	9984	12170	10994		
3h	11045	10333	13159	11695		
4h	11306	10659	13775	12334		

Table 3.20: Fluorescence measured for FITC-casein degradation assay with BsClpP, and DMSO (negative control) and compounds 16 (positive control), 23, 25, 26, 27, 28, 38, 39, 40 and 41. Each fluorescence presented is the average fluorescence for a triplicate. Fluorescence was monitored via an i-TECAN Infinite M200 plate reader (excitation: 485 nm; emission: 538 nm; gain: 120).

	Buffer	BsClpP + DMSO (-)	BsClpP + 16 (100 nM)	BsClpP + 16 (1 uM)	BsClpP + 16 (5 uM)	BsClpP + 16 (10 uM)
0h	18751.67	18340.67	18524.66667	20892.33333	13413	20825.33
2h	15092.33	16328.67	16512.66667	16747.66667	12869.33	22707.33
4h	13389.33	14893.33	14806.66667	14307.33333	14989	21399.67
6h	13647.67	15570.67	15451.33333	15885.66667	16150.33	22783.33
	BsClpP + 16 (25 uM)	BsClpP + 16 (50 uM)	BsClpP + 16 (75 uM)	BsClpP + 23 (100 uM)	BsClpP + 16 (150 uM)	BsClpP + 16 (250 uM)
0h	22495.33	22451	14132.33	20889.33	24180	26978
2h	23115.67	23885.67	16470.67	26525.33	28049	32428
4h	22137.67	22879.33	21076.67	26021.33	25271.67	29837.33
6h	23081.33	24141	22904.67	26602.33	26562.33	30566
	EcClpP + DMSO (-)	EcClpP + ADEP (+)	EcClpP + 16 (100 nM)	EcClpP + 16 (1 uM)	EcClpP + 16 (5 uM)	EcClpP + 16 (10 uM)
0h	17649.33	29008.67	18646.33	18414.33	18940	18857.67
2h	17215.33	33079.67	17323	17576	17418.67	18370.33
4h	14753.67	33877.33	14704.33	14911.33	15478	16364.67
6h	15110.33	35696.67	15201.67	15304	15817.33	16696.33
	EcClpP + 16	EcClpP + 16	EcClpP + 16	EcClpP + 16	EcClpP + 16	EcClpP + 16

	(25 uM)	(50 uM)	(75 uM)	(100 uM)	(150 uM)	(250 uM)
0h	13289.33	7802.333	22684.67	22822	13521.67	23210
2h	13211.33	7770	24083.33	24570.33	16251.67	25688.33
4h	17014.33	15416.33	22203.33	23348.67	20842	27091.67
6h	17760	17008.67	23790.33	25049.67	24027.67	28524.33

Table 3.21: Fluorescence measured for FITC-casein degradation assay with BsClpP and EcClpP, and DMSO (negative control), ADEP (positive control) and compound 16. Each fluorescence presented is the average fluorescence for a triplicate. Fluorescence was monitored via an i-TECAN Infinite M200 plate reader (excitation: 485 nm; emission: 538 nm; gain: 120).

	Buffer	BsClpP + DMSO (-)	BsClpP + 23 (100 nM)	BsClpP + 23 (1 uM)	BsClpP + 23 (5 uM)	BsClpP + 23 (10 uM)
0h	14182	15082.67	16718	16078.33	15754.67	19574.67
2h	13815.33	14277.67	15651	14365.67	20813	26873.67
4h	13831.67	14414.67	15259	14513	23251.67	29812
6h	13252	13767.67	14643.33	14021	23825	30206.67
	BsClpP + 23 (25 uM)	BsClpP + 23 (50 uM)	BsClpP + 23 (75 uM)	BsClpP + 23 (100 uM)	BsClpP + 23 (150 uM)	BsClpP + 23 (250 uM)
0h	20784.33	20510	21275.67	21410.67	21834.33	21122.67
2h	29495.67	30145.67	30122	30016	30486	30204.67
4h	32483	32762	32831.33	33027.33	33094	32883
6h	32712	33165.33	32707	32944.33	33237.33	33019
	EcClpP + DMSO (-)	EcClpP + ADEP (+)	EcClpP + 23 (100 nM)	EcClpP + 23 (1 uM)	EcClpP + 23 (5 uM)	EcClpP + 23 (10 uM)
0h	13434	21264.67	14819.67	14619.67	15411.67	18528
2h	14379.67	27880.33	14223.33	14467.67	17710.67	20242.67
4h	14649.33	29952.67	14412	14667	18127.67	21220.67
6h	14092.67	29773	13983	14136.67	18029.67	21261.67
	EcClpP + 23 (25 uM)	EcClpP + 23 (50 uM)	EcClpP + 23 (75 uM)	EcClpP + 23 (100 uM)	EcClpP + 23 (150 uM)	

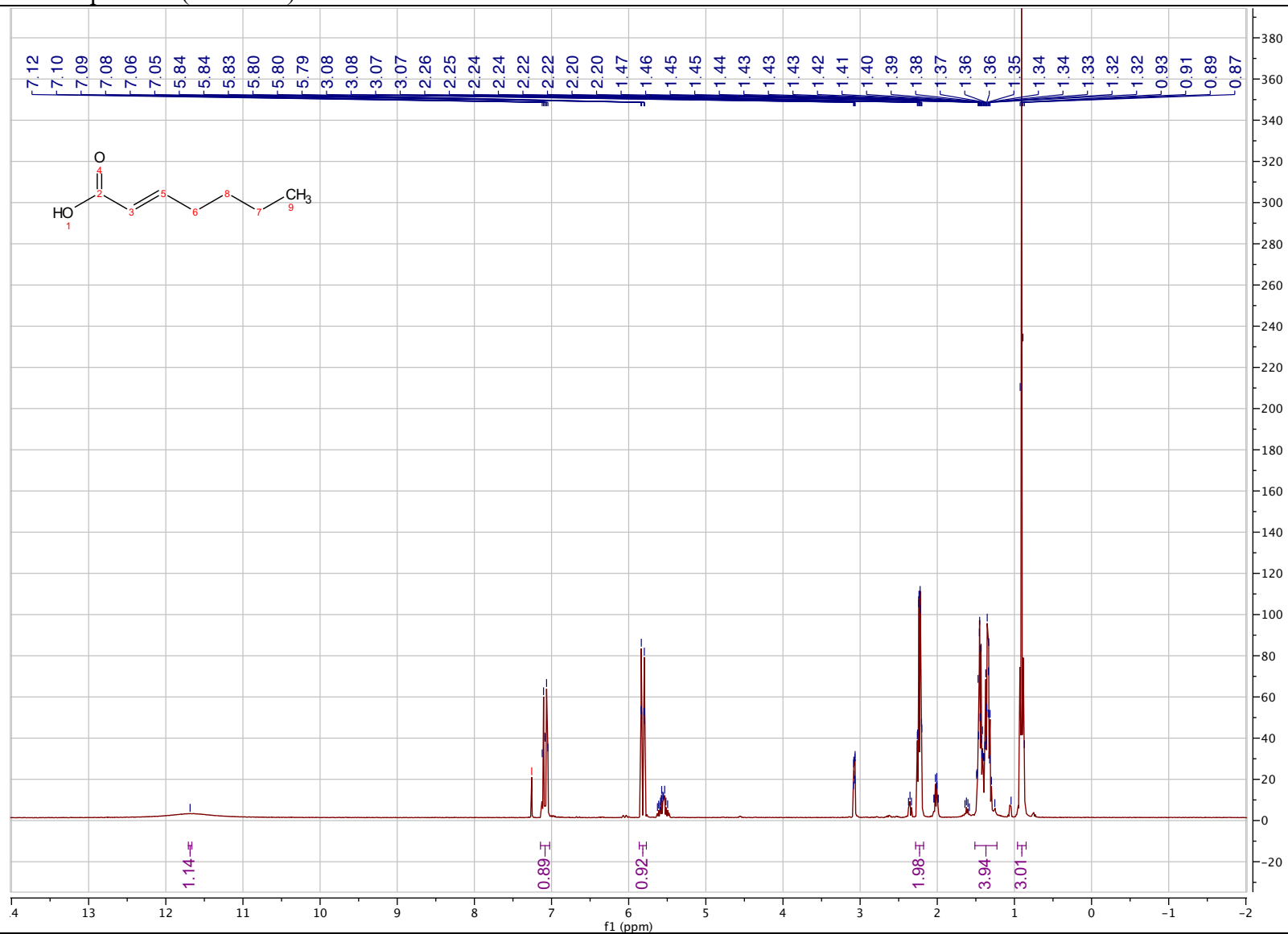
0h	20500	23760.67	23605	23403.33	23587.33	
2h	24615	28713.33	29524.67	29241.67	29616.33	
4h	25744.33	30731	31610.67	31114.33	31700	
6h	25510	30330	31050.67	30924.33	31320.33	

Table 3.22: Fluorescence measured for FITC-casein degradation assay with BsClpP and EcClpP, and DMSO (negative control), ADEP (positive control) and compound 23. Each fluorescence presented is the average fluorescence for a triplicate. Fluorescence was monitored via an i-TECAN Infinite M200 plate reader (excitation: 485 nm; emission: 538 nm; gain: 120).

Spectra

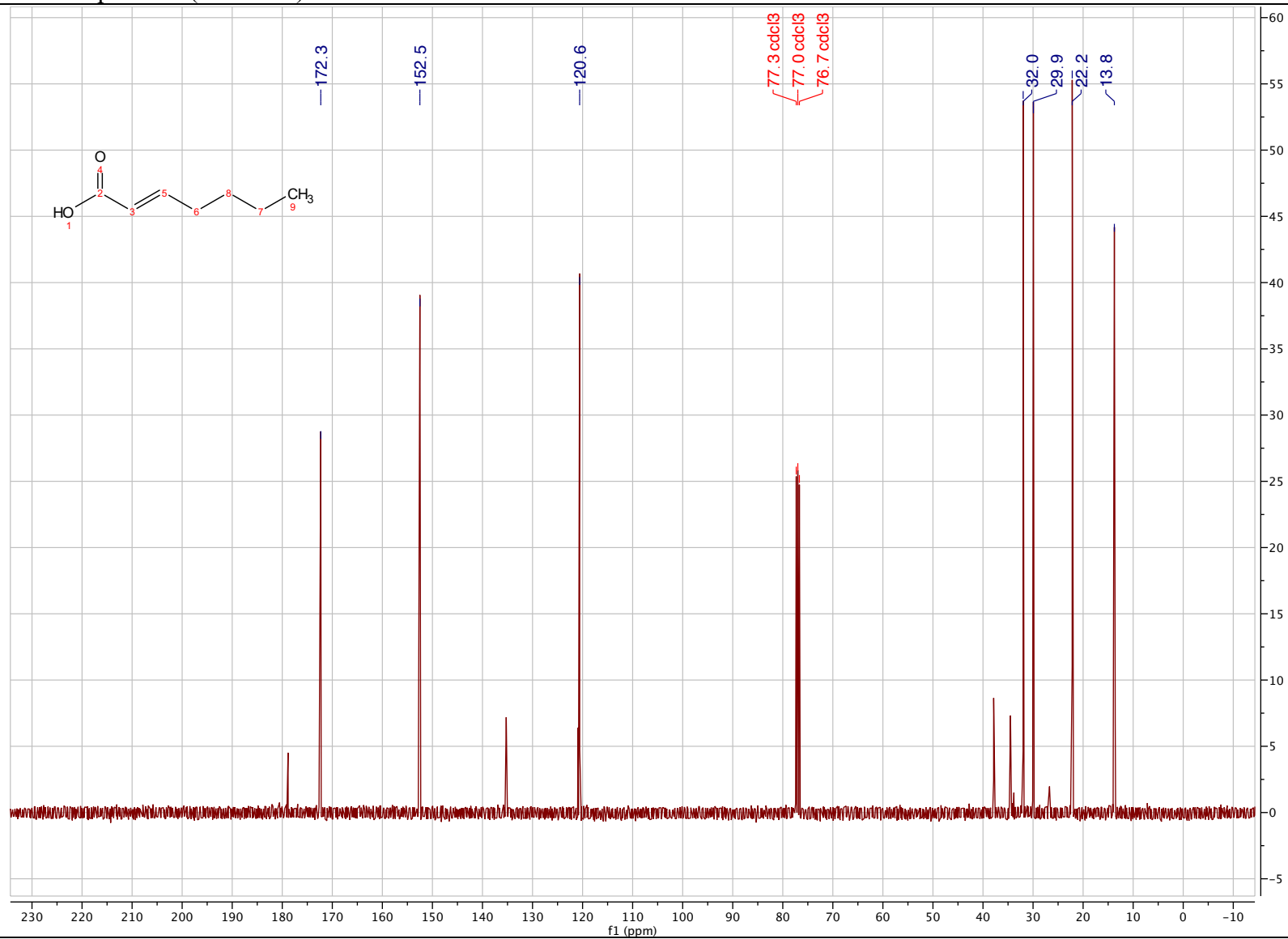
(E)-hept-2-enoic acid (3.45)

¹H NMR spectrum (400 MHz) in Chloroform-*d*



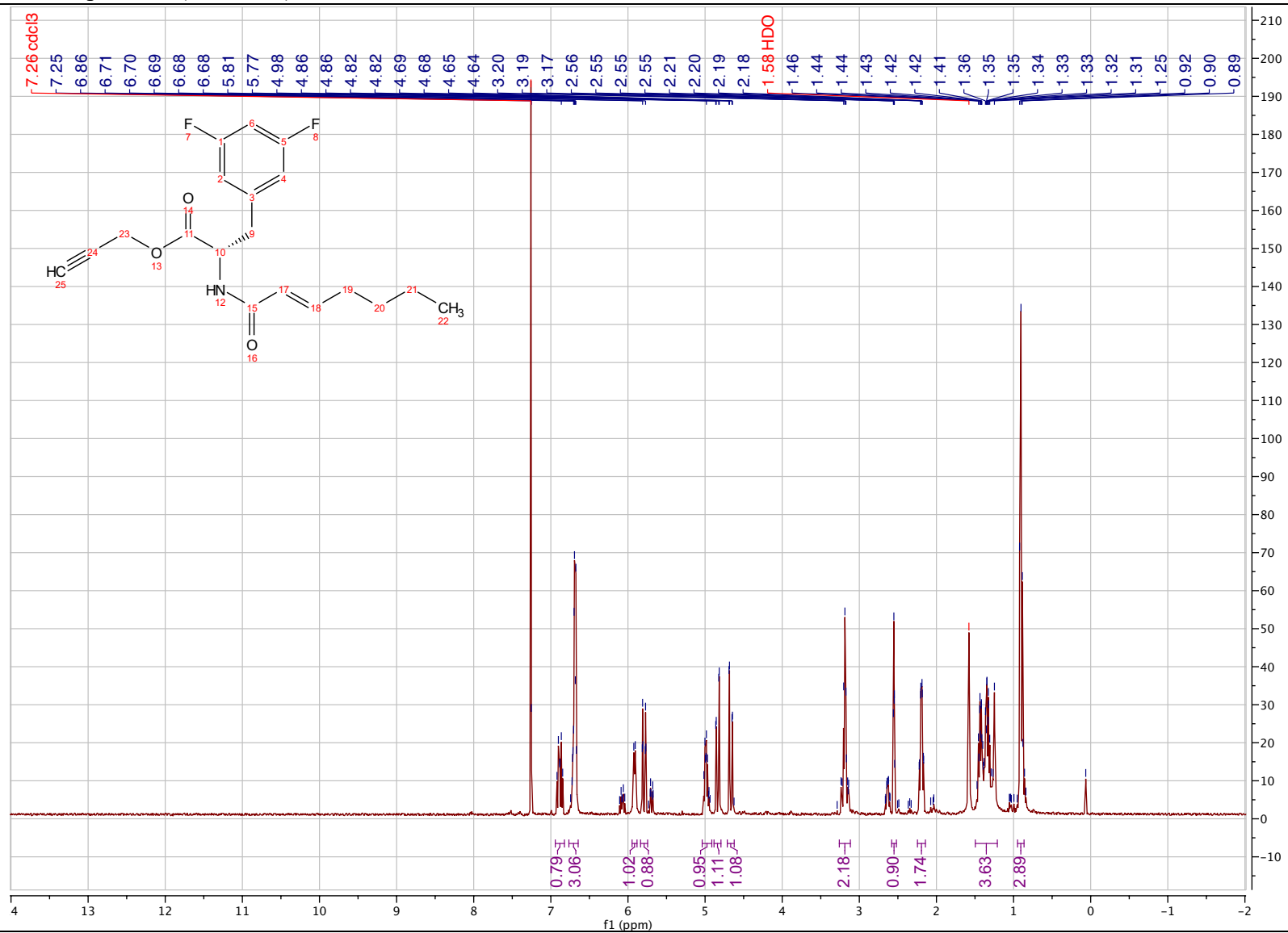
(E)-hept-2-enoic acid (3.45)

^{13}C NMR spectrum (101 MHz) in Chloroform-*d*



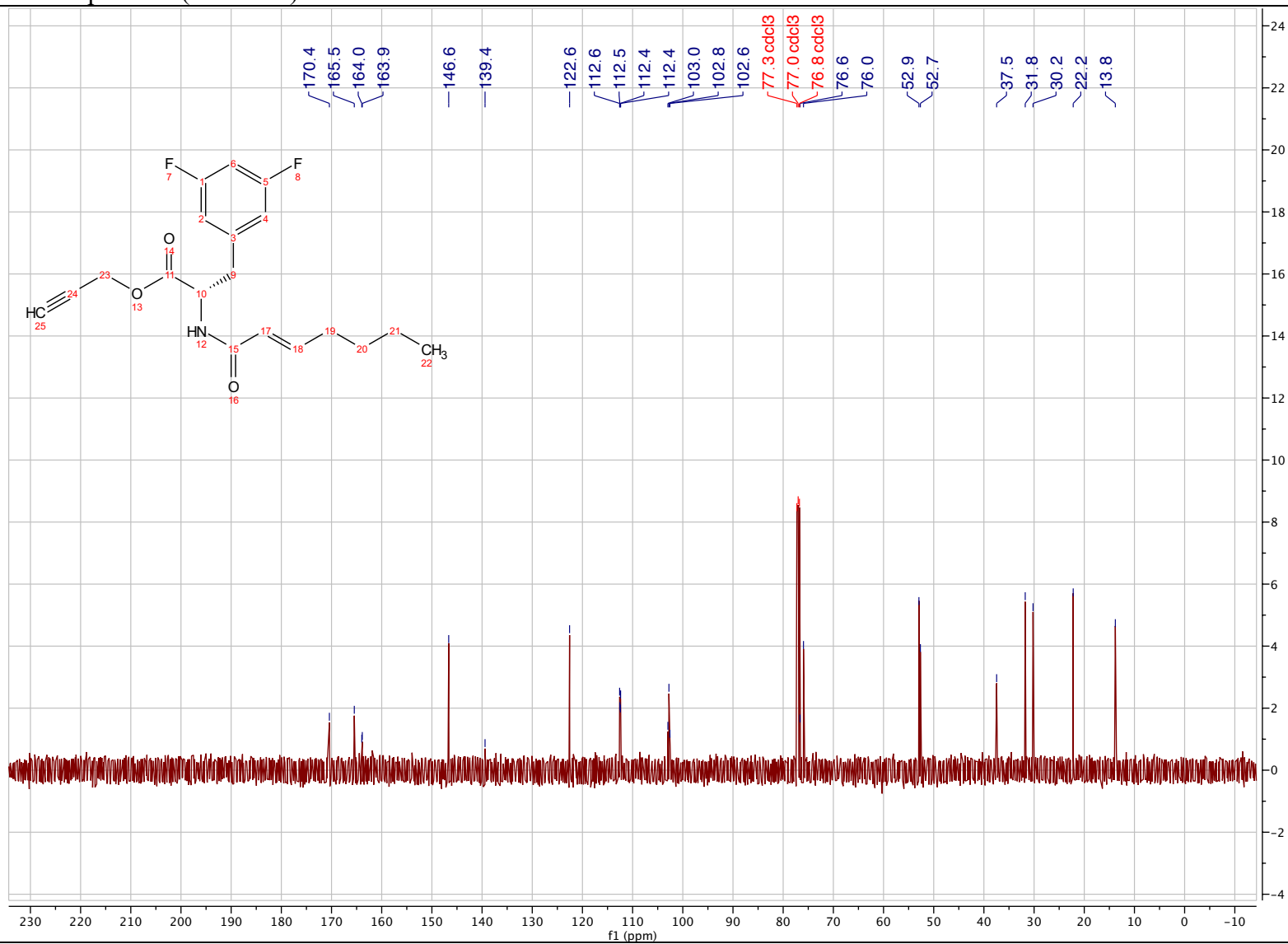
prop-2-yn-1-yl (*S,E*)-3-(3,5-difluorophenyl)-2-(hept-2-enamido)propanoate (3.16)

¹H NMR spectrum (400 MHz) in Chloroform-*d*



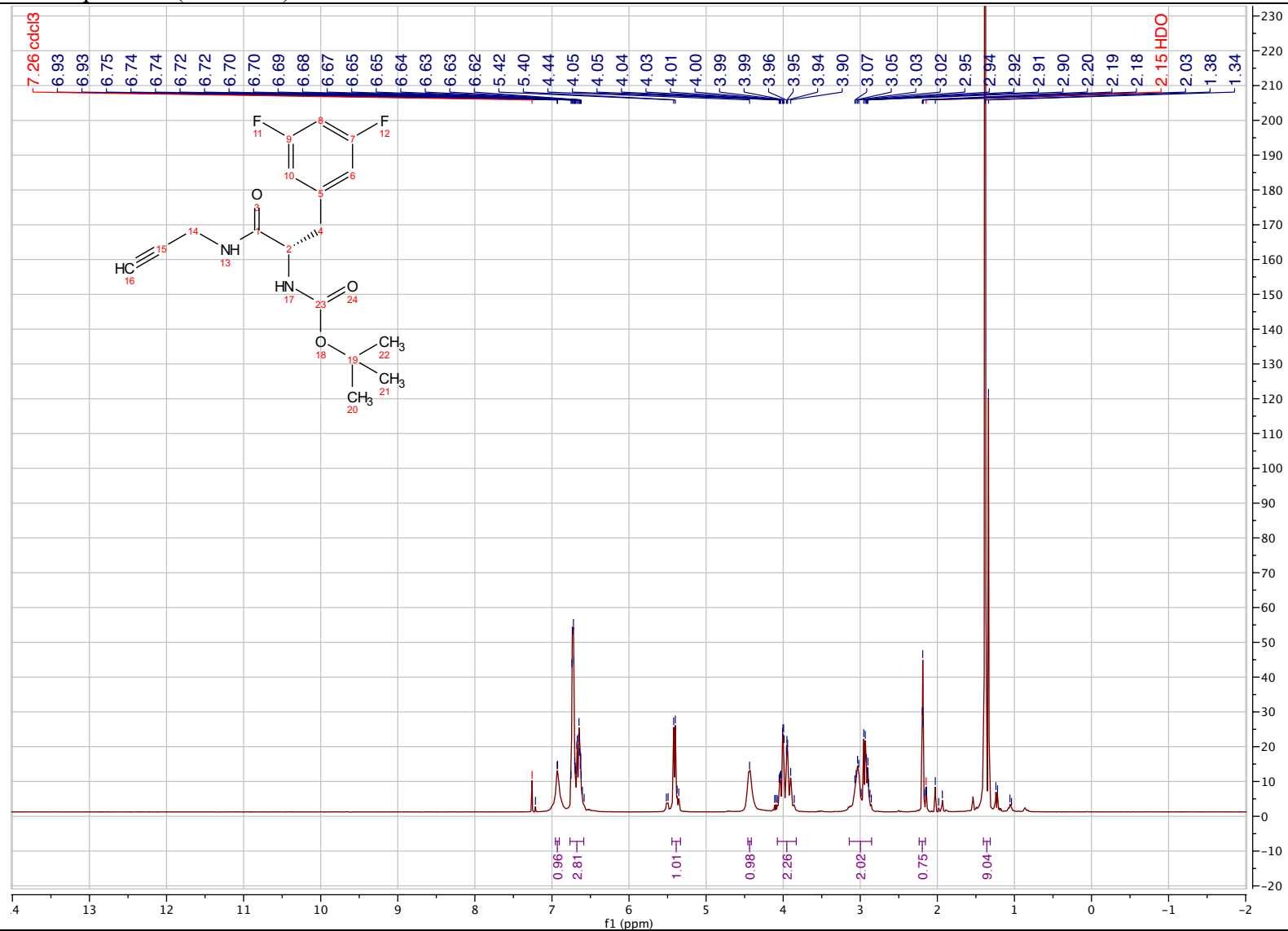
prop-2-yn-1-yl (*S,E*)-3-(3,5-difluorophenyl)-2-(hept-2-enamido)propanoate (3.16)

^{13}C NMR spectrum (101 MHz) in Chloroform-*d*



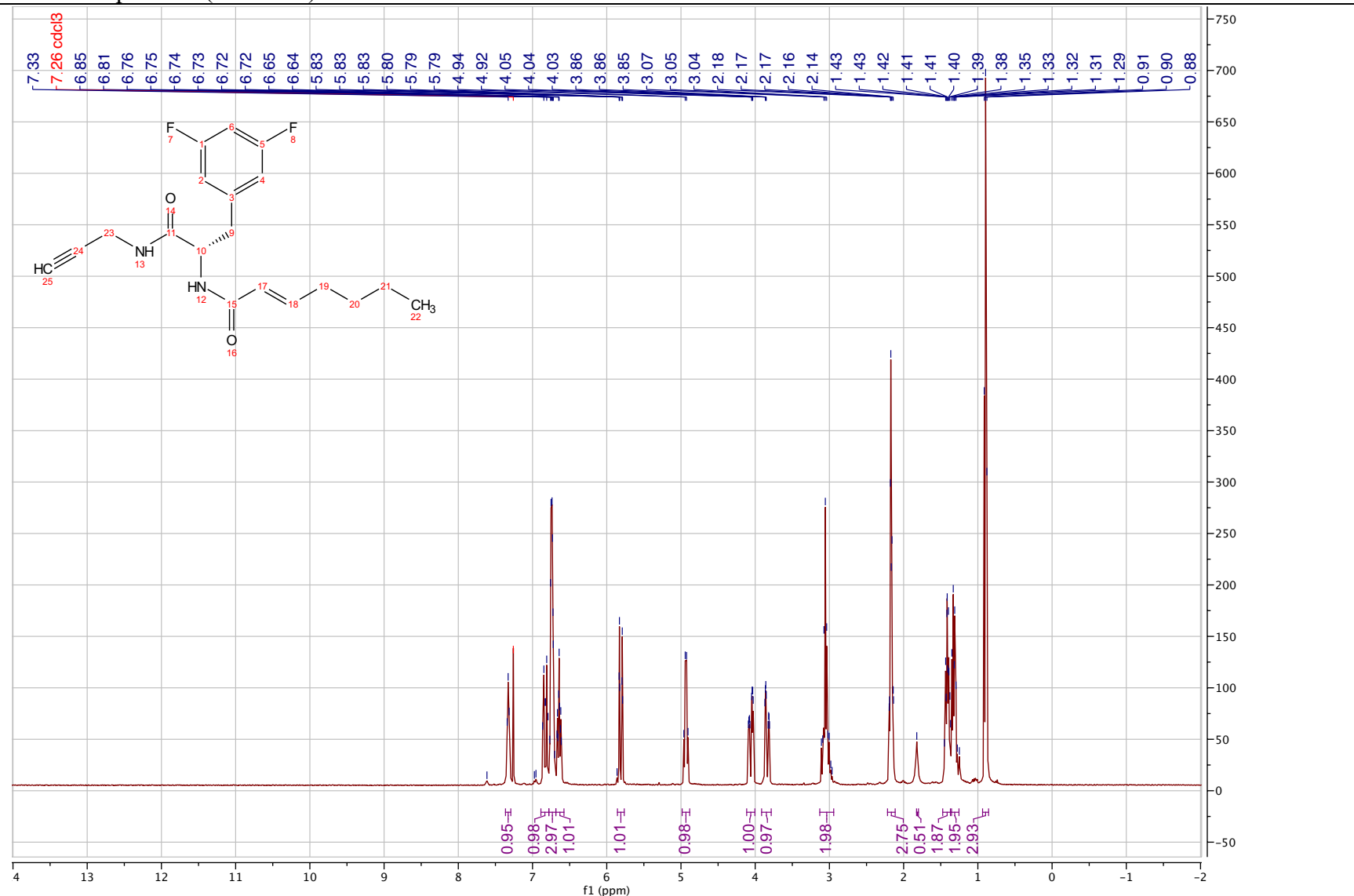
***tert*-butyl (*S*)-(3-(3,5-difluorophenyl)-1-oxo-1-(prop-2-yn-1-ylamino)propan-2-yl)carbamate (3.49)**

¹H NMR spectrum (400 MHz) in Chloroform-*d*



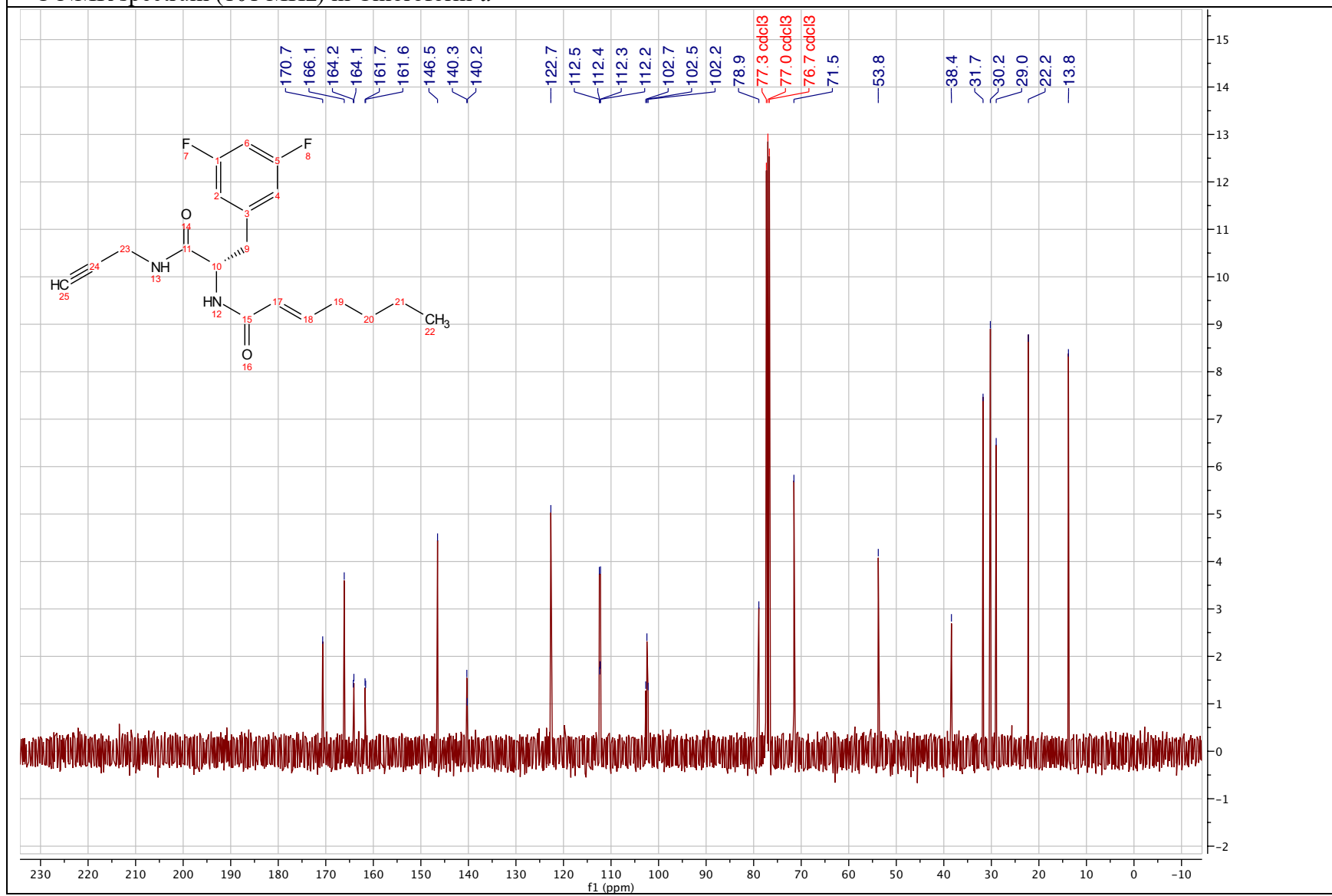
(*S,E*)-*N*-(3-(3,5-difluorophenyl)-1-oxo-1-(prop-2-yn-1-ylamino)propan-2-yl)hept-2-enamide (3.24)

¹H NMR spectrum (400 MHz) in Chloroform-*d*



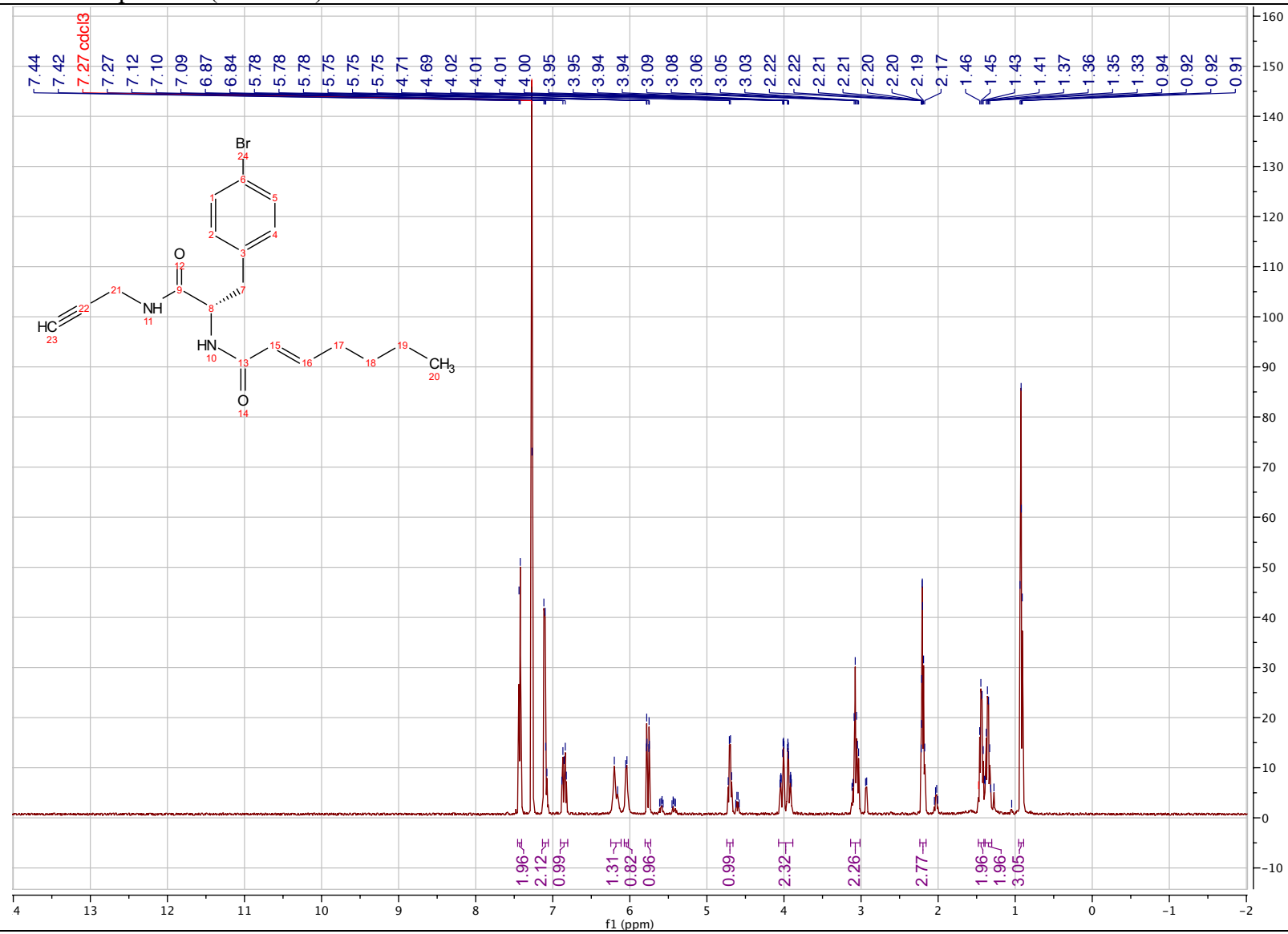
(*S,E*)-*N*-(3-(3,5-difluorophenyl)-1-oxo-1-(prop-2-yn-1-ylamino)propan-2-yl)hept-2-enamide (3.24)

^{13}C NMR spectrum (101 MHz) in Chloroform-*d*



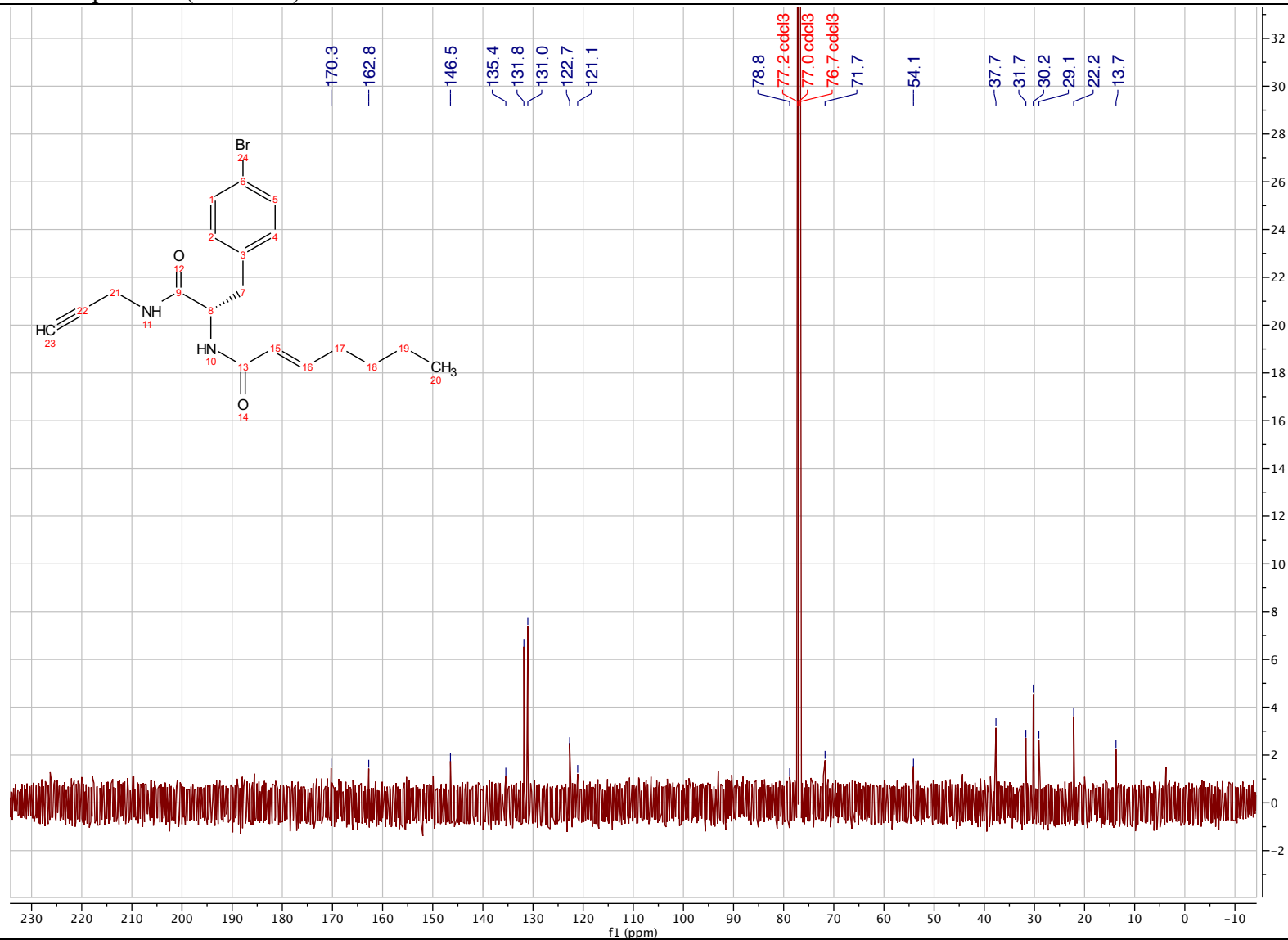
(*S,E*)-*N*-(3-(4-bromophenyl)-1-oxo-1-(prop-2-yn-1-ylamino)propan-2-yl)hept-2-enamide (3.38)

¹H NMR spectrum (400 MHz) in Chloroform-*d*



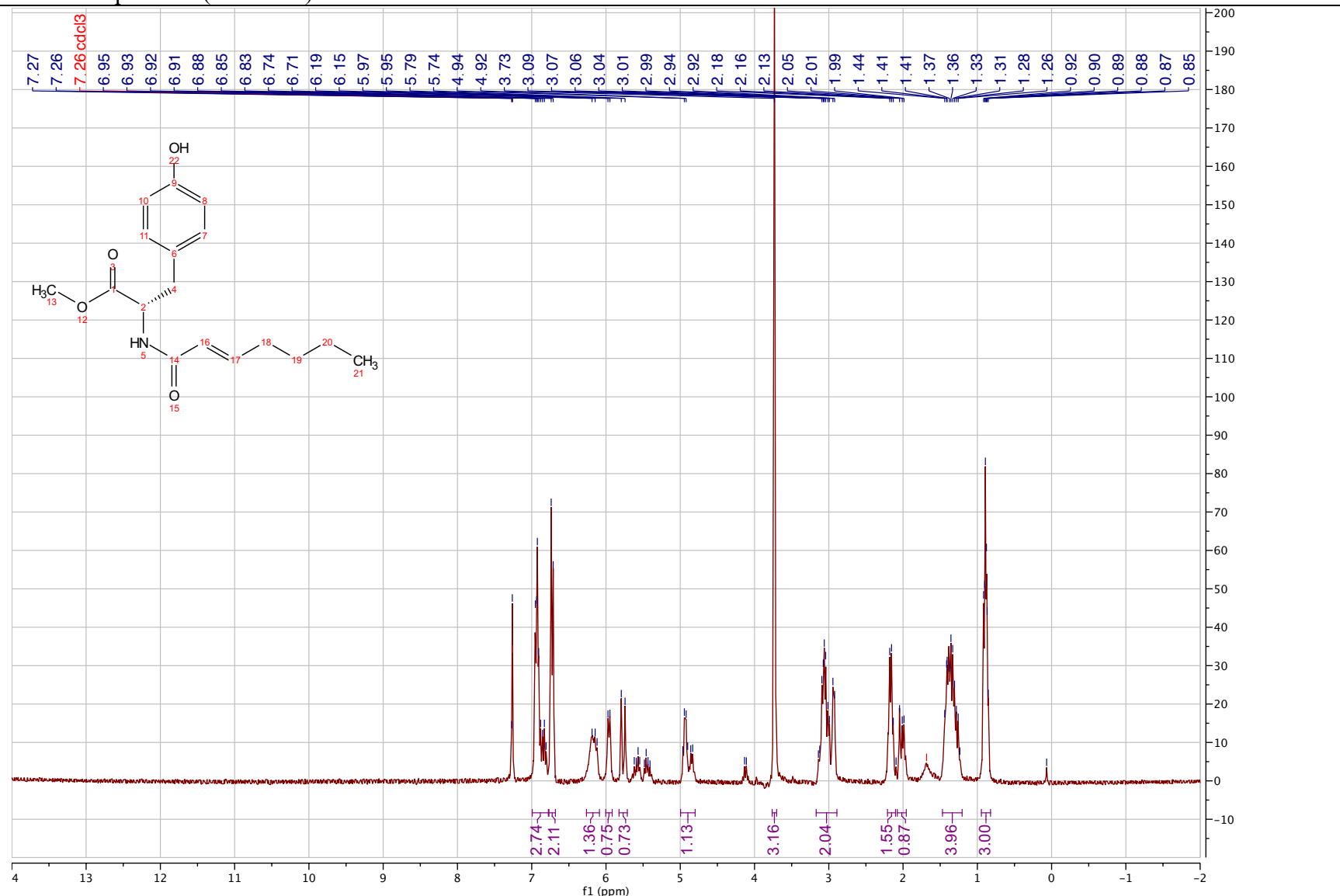
(*S,E*)-*N*-(3-(4-bromophenyl)-1-oxo-1-(prop-2-yn-1-ylamino)propan-2-yl)hept-2-enamide (3.38)

¹³C NMR spectrum (101 MHz) in Chloroform-*d*



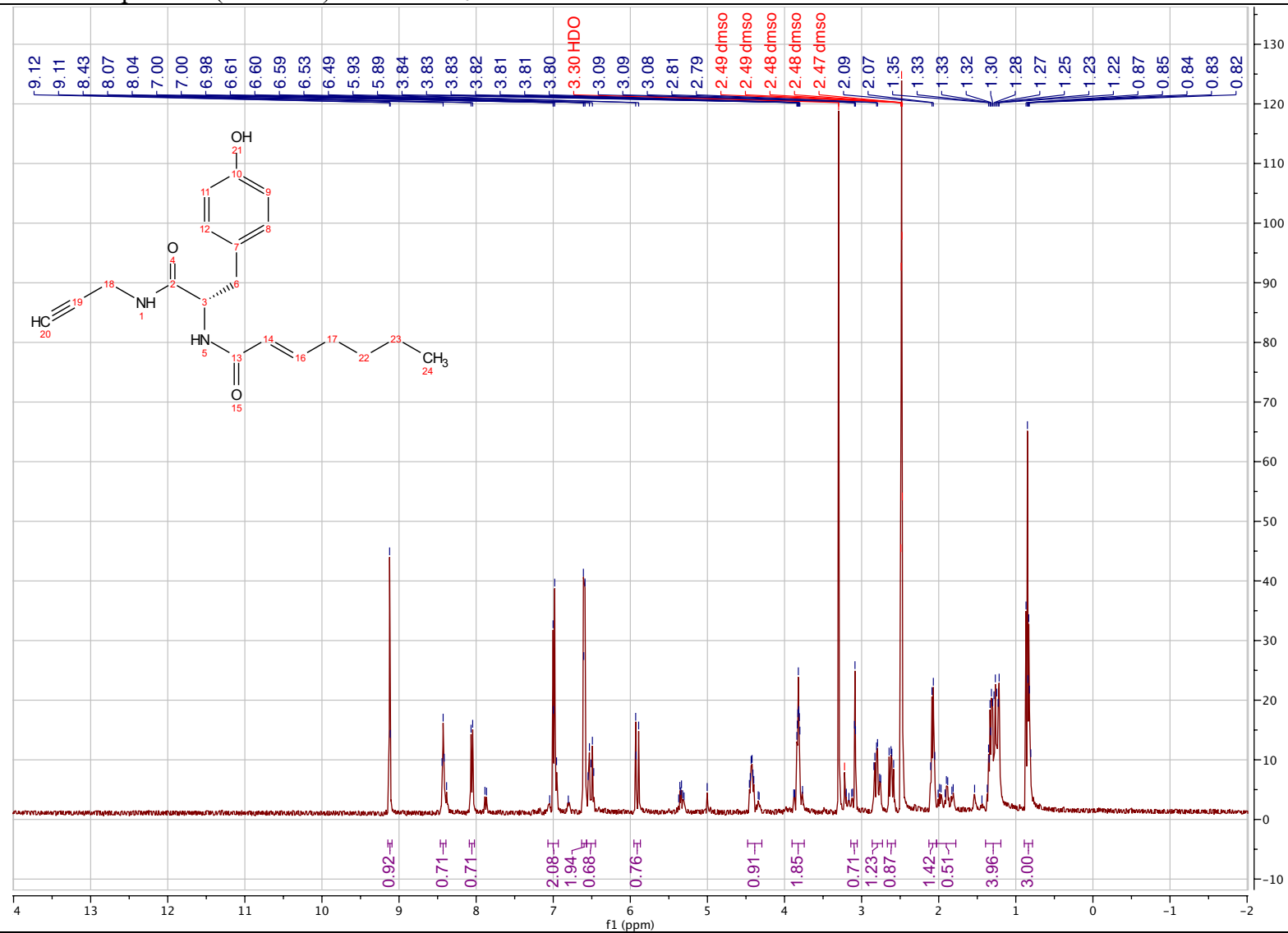
methyl (*E*)-hept-2-enoyl-*L*-tyrosinate (3.52)

¹H NMR spectrum (300 MHz) in Chloroform-*d*



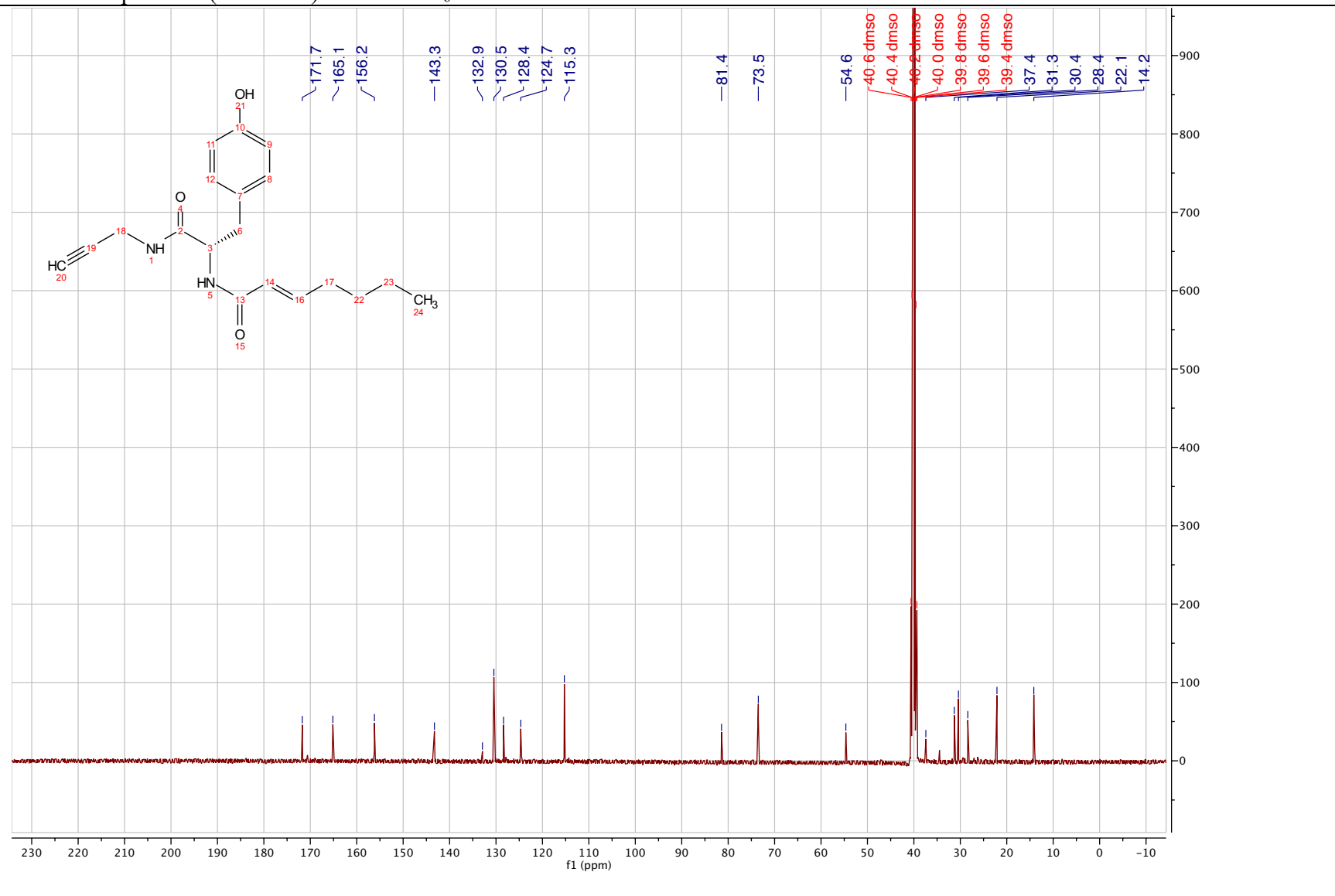
(*S,E*)-*N*-(3-(4-hydroxyphenyl)-1-oxo-1-(prop-2-yn-1-ylamino)propan-2-yl)hept-2-enamide (3.39)

¹H NMR spectrum (400 MHz) in DMSO-*d*₆



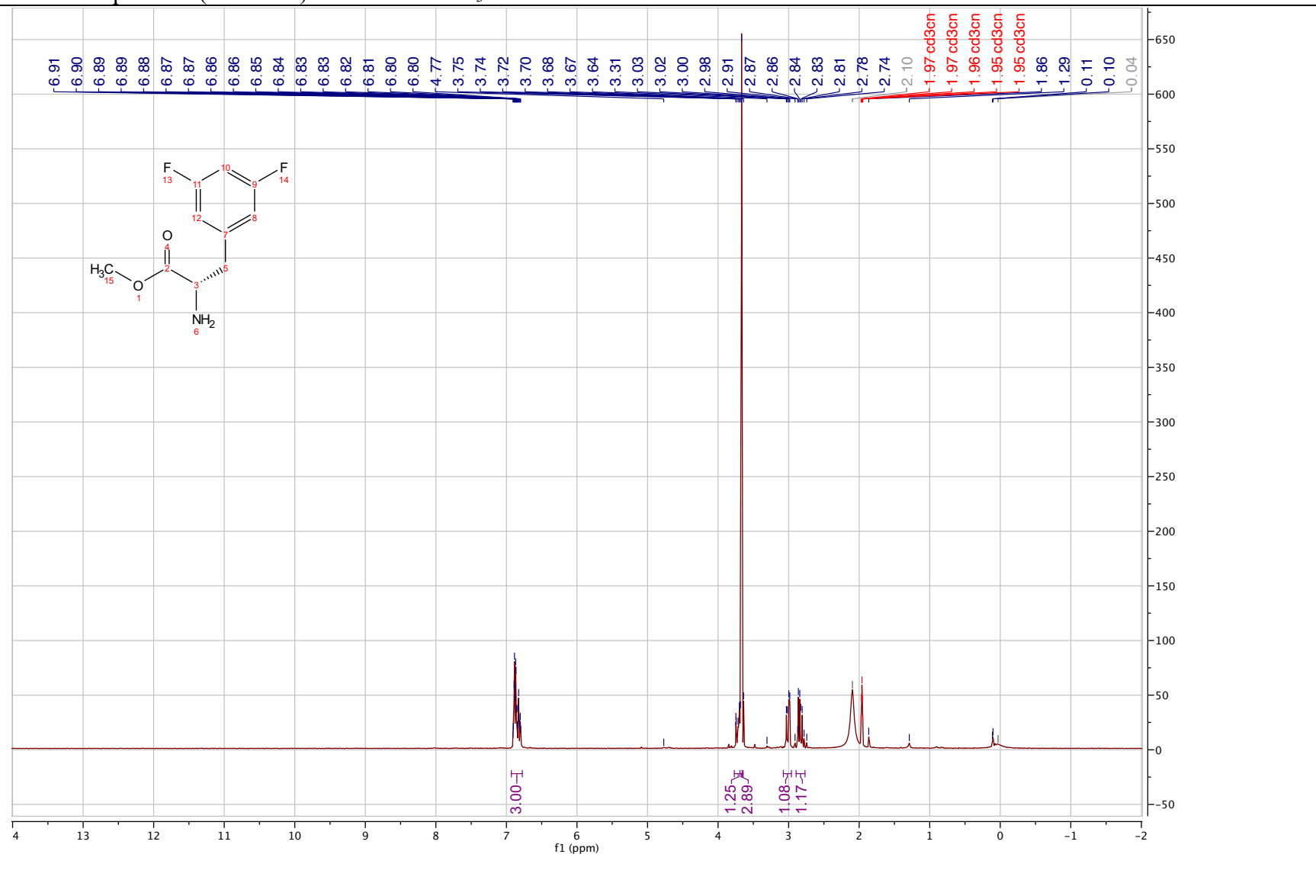
(*S,E*)-*N*-(3-(4-hydroxyphenyl)-1-oxo-1-(prop-2-yn-1-ylamino)propan-2-yl)hept-2-enamide (3.39)

¹³C NMR spectrum (101 MHz) in DMSO-*d*₆



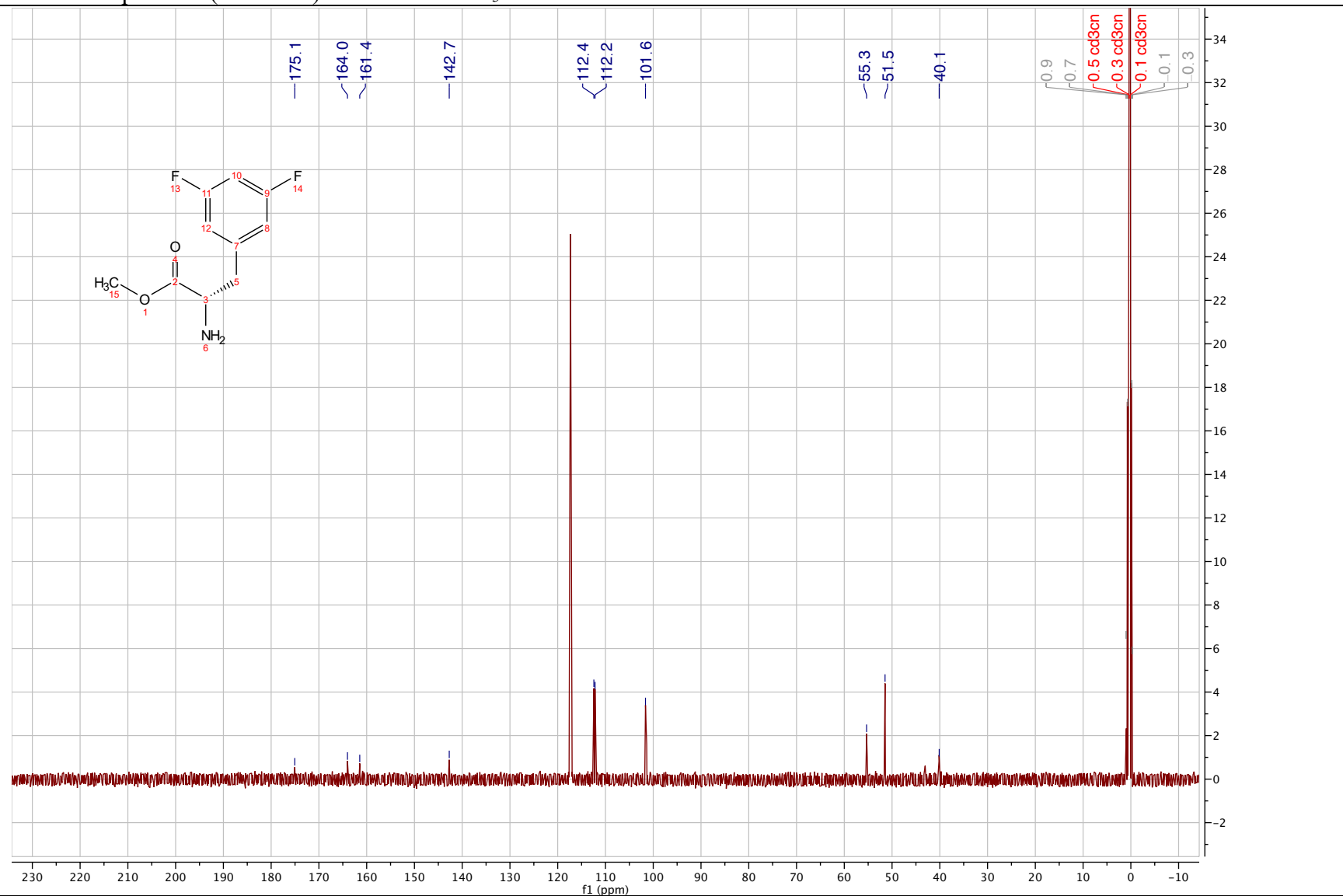
methyl (*S*)-2-amino-3-(3,5-difluorophenyl)propanoate (3.46')

¹H NMR spectrum (400 MHz) in Acetonitrile-*d*₃



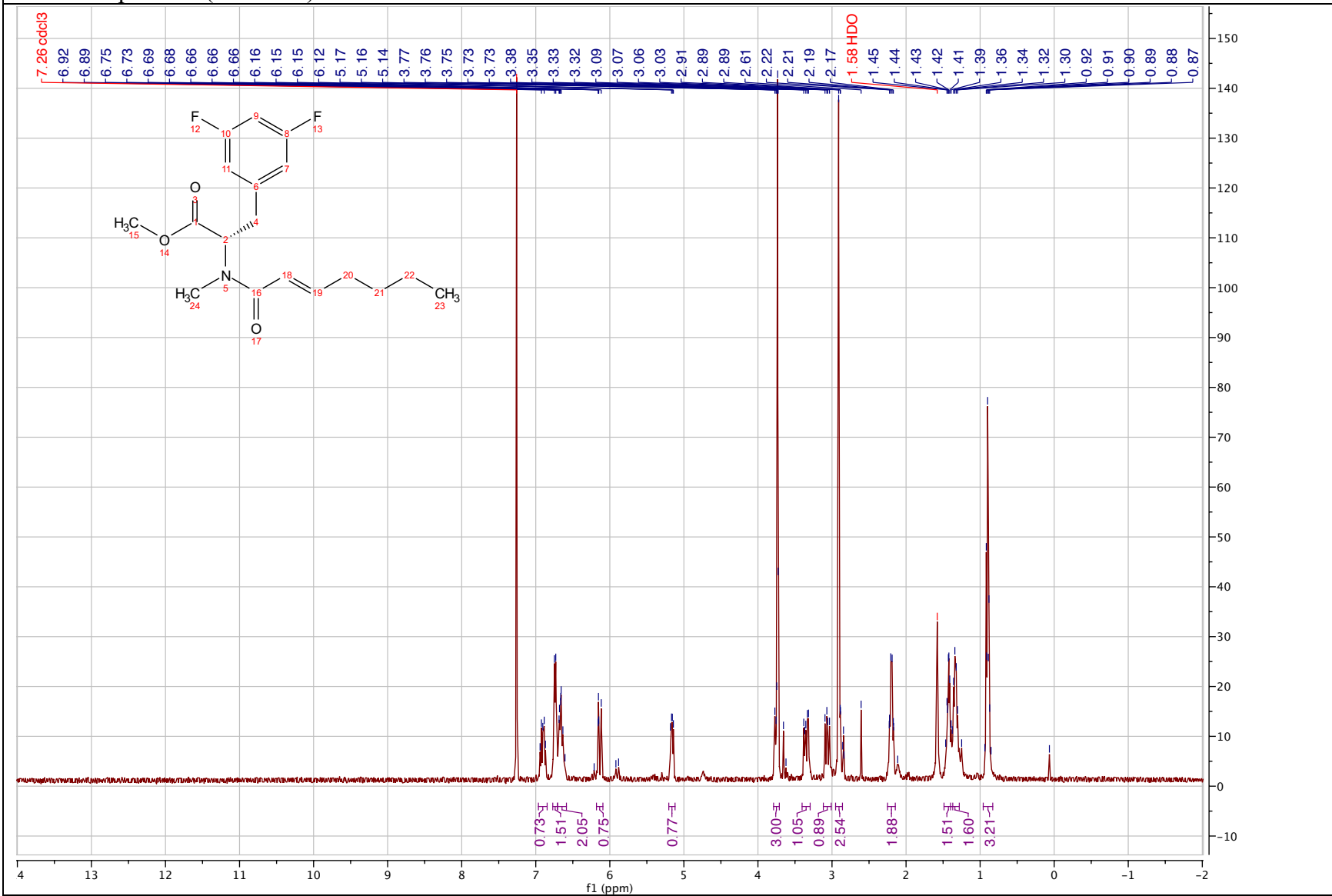
methyl (*S*)-2-amino-3-(3,5-difluorophenyl)propanoate (3.46')

¹³C NMR spectrum (101 MHz) in Acetonitrile-*d*₃



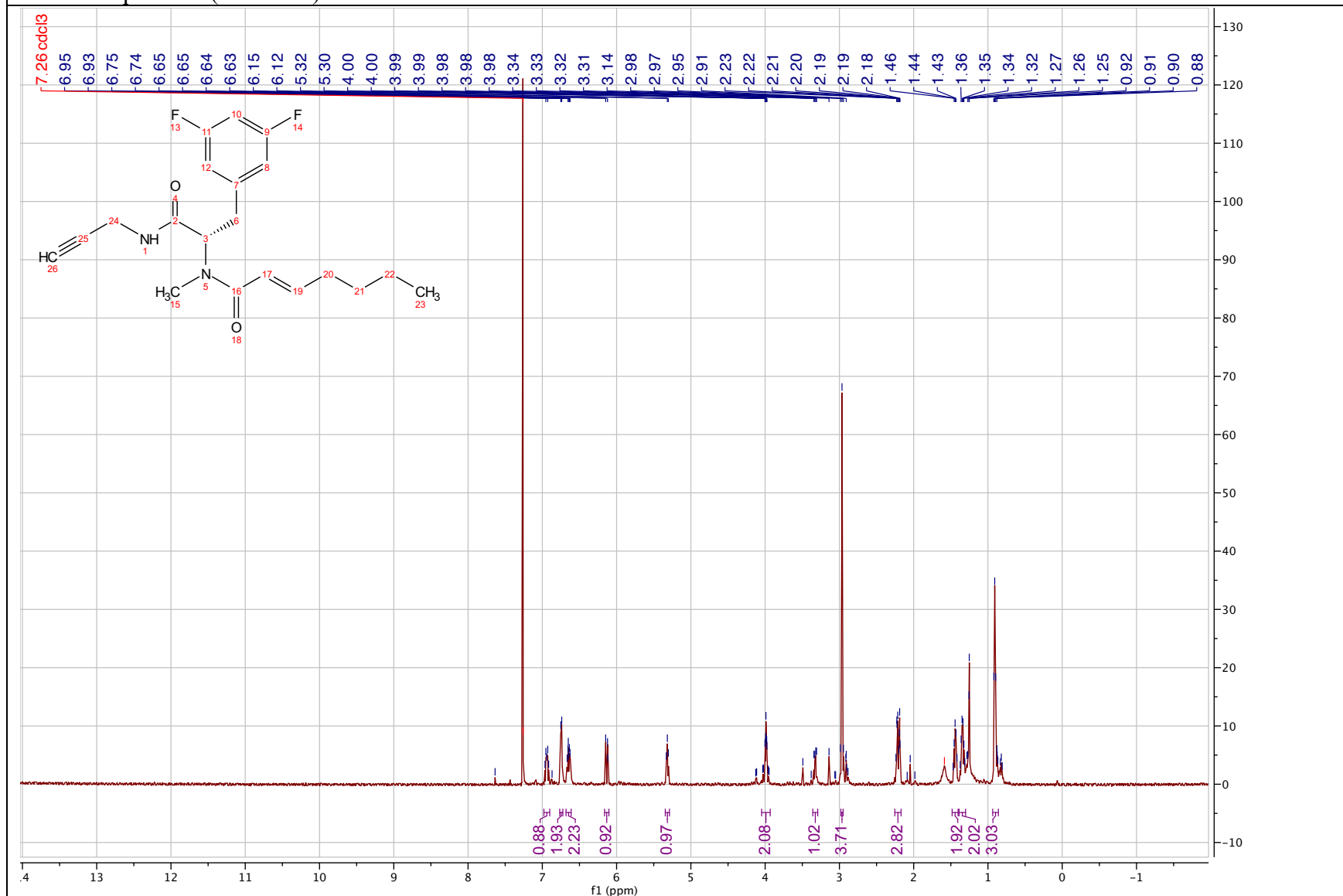
methyl (*S,E*)-3-(3,5-difluorophenyl)-2-(*N*-methylhept-2-enamido)propanoate (3.54)

¹H NMR spectrum (400 MHz) in Chloroform-*d*



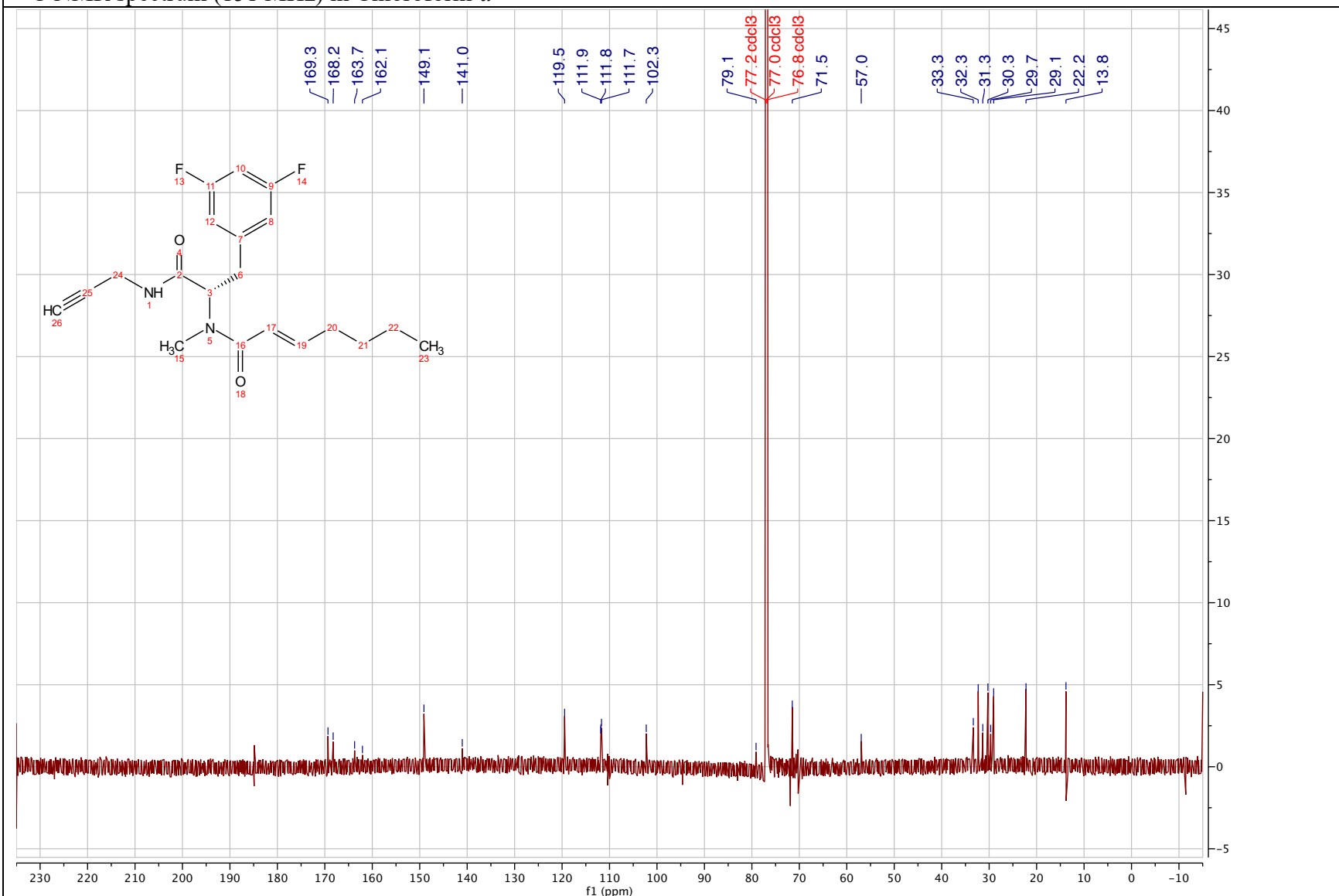
(*S,E*)-*N*-(3-(3,5-difluorophenyl)-1-oxo-1-(prop-2-yn-1-ylamino)propan-2-yl)-*N*-methylhept-2-enamide (3.40)

¹H NMR spectrum (600 MHz) in Chloroform-*d*



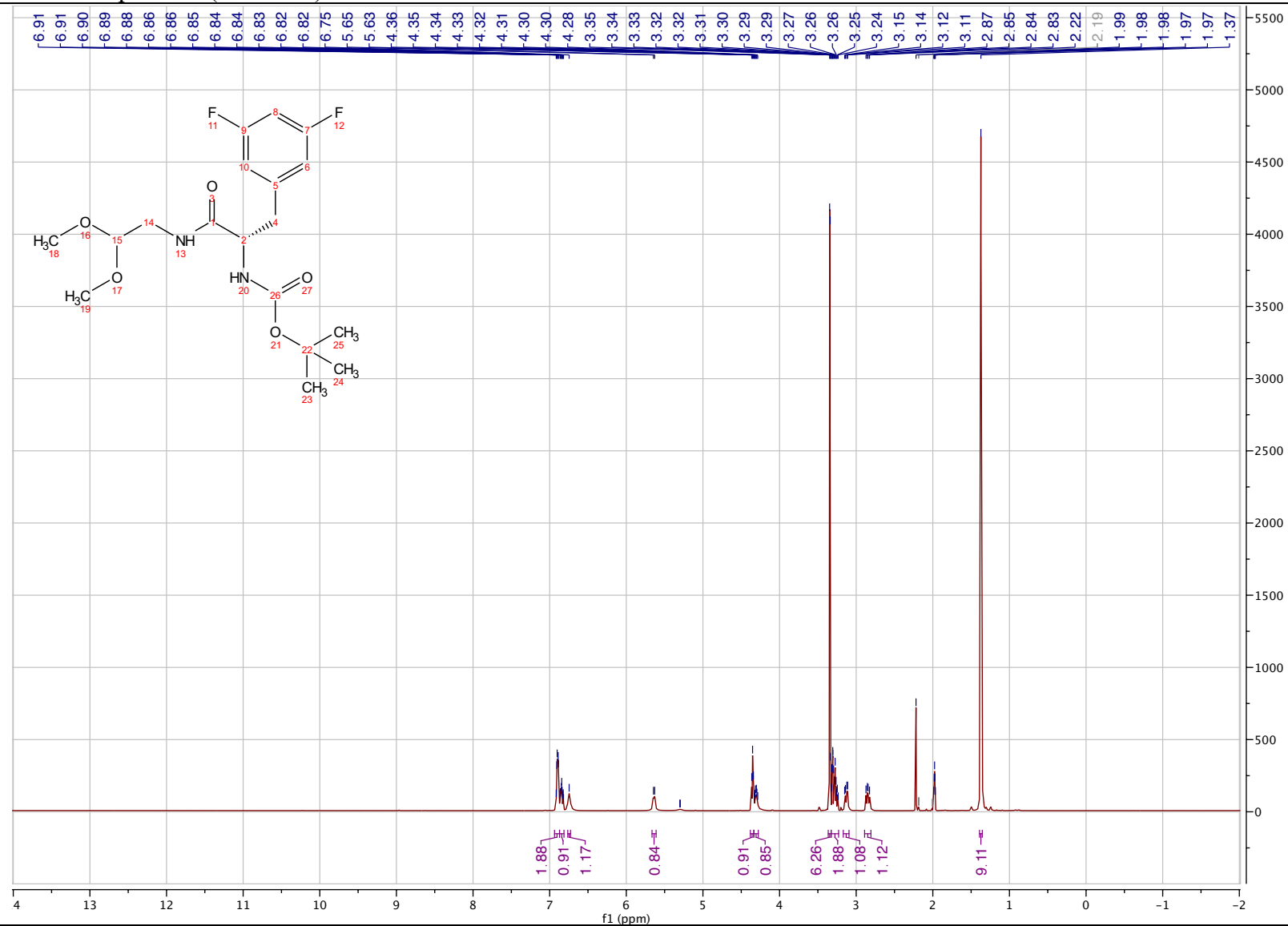
(*S,E*)-*N*-(3-(3,5-difluorophenyl)-1-oxo-1-(prop-2-yn-1-ylamino)propan-2-yl)-*N*-methylhept-2-enamide (3.40)

¹³C NMR spectrum (151 MHz) in Chloroform-*d*



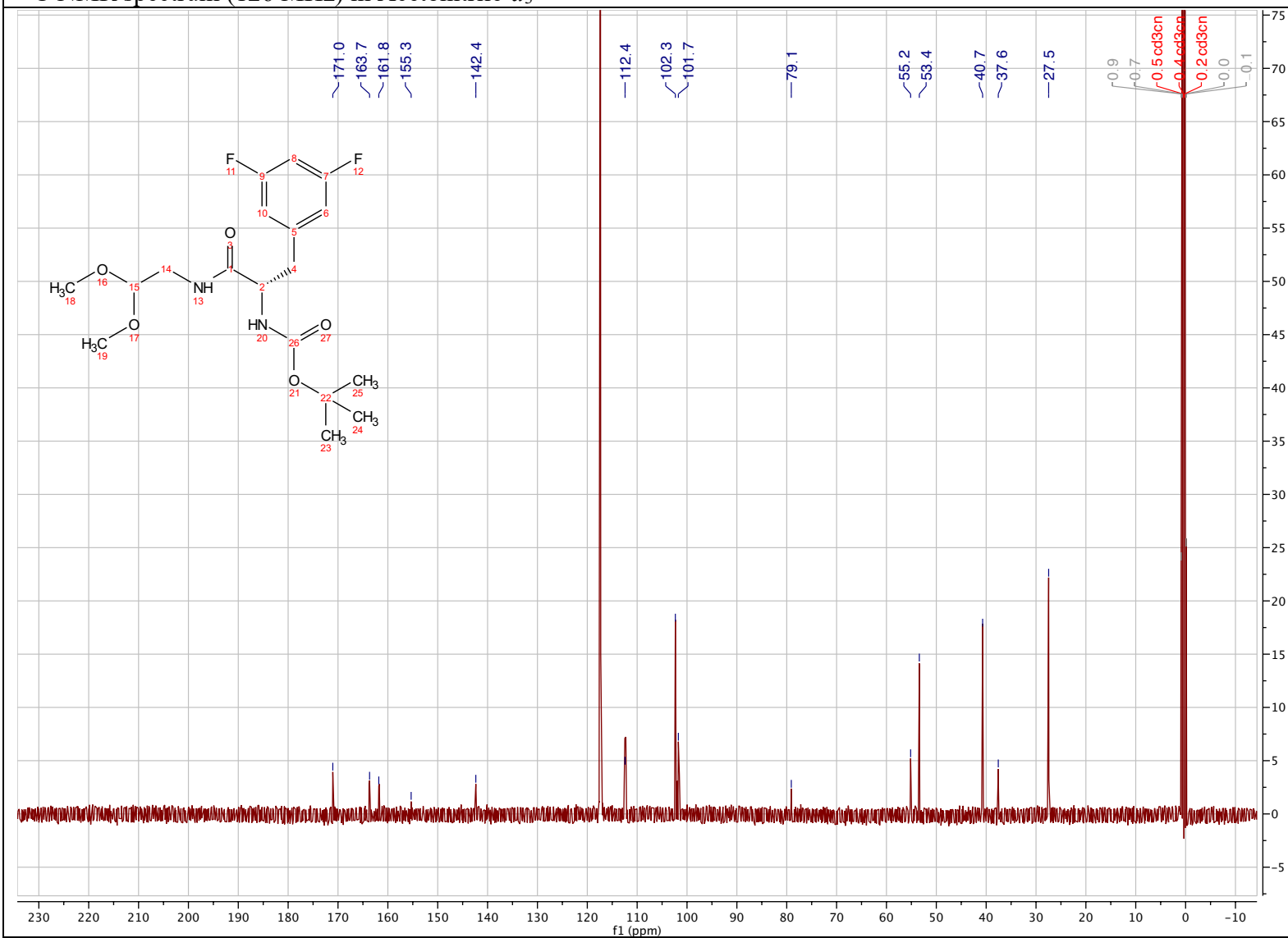
***tert*-butyl (*S*)-(3-(3,5-difluorophenyl)-1-((2,2-dimethoxyethyl)amino)-1-oxopropan-2-yl)carbamate (3.55)**

¹H NMR spectrum (500 MHz) in Acetonitrile-*d*₃



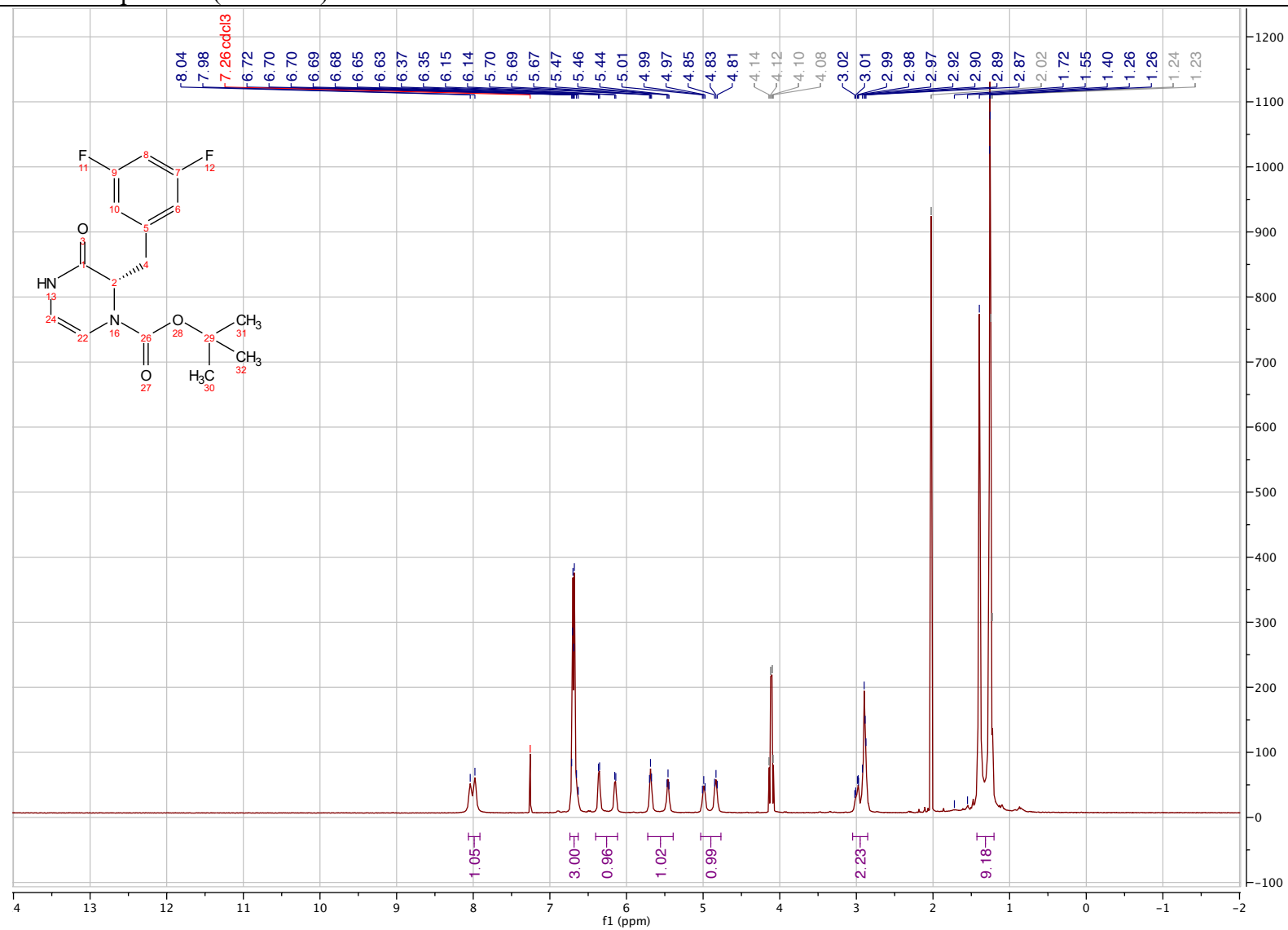
***tert*-butyl (*S*)-(3-(3,5-difluorophenyl)-1-((2,2-dimethoxyethyl)amino)-1-oxopropan-2-yl)carbamate (3.55)**

^{13}C NMR spectrum (126 MHz) in Acetonitrile- d_3



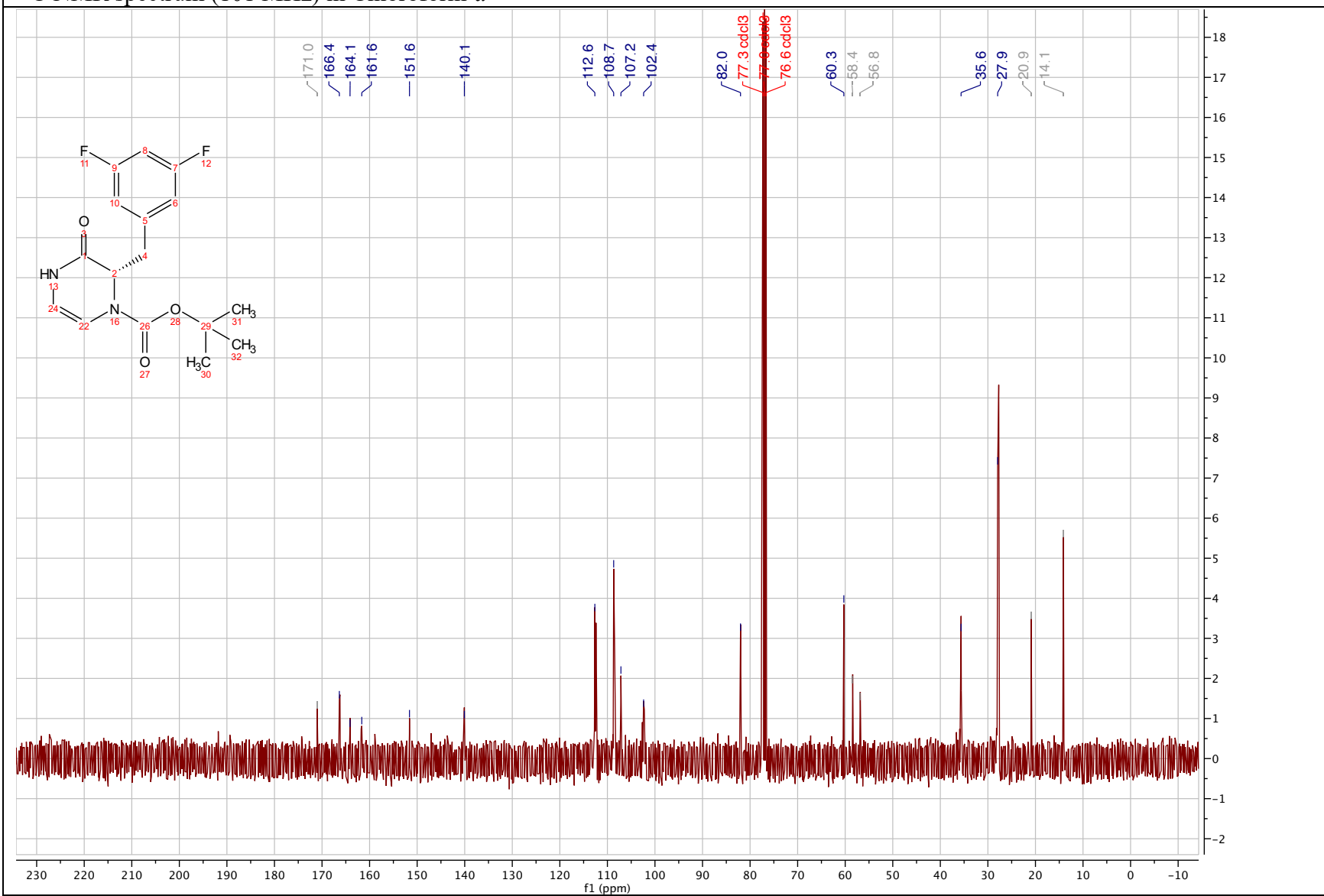
***tert*-butyl (*S*)-2-(3,5-difluorobenzyl)-3-oxo-3,4-dihydropyrazine-1(2*H*)-carboxylate (3.56)**

¹H NMR spectrum (400 MHz) in Chloroform-*d*



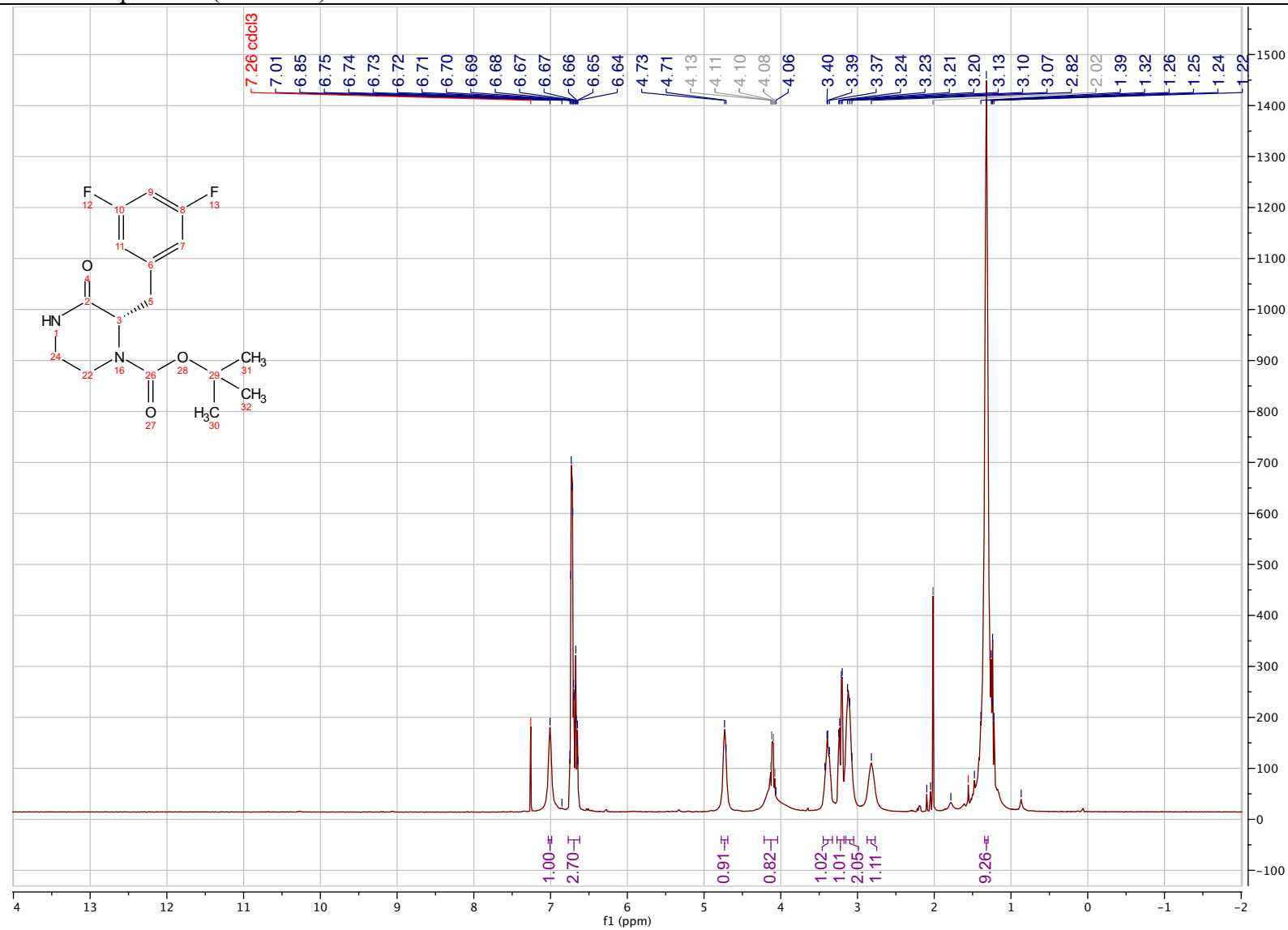
***tert*-butyl (*S*)-2-(3,5-difluorobenzyl)-3-oxo-3,4-dihydropyrazine-1(2*H*)-carboxylate (3.56)**

¹³C NMR spectrum (101 MHz) in Chloroform-*d*



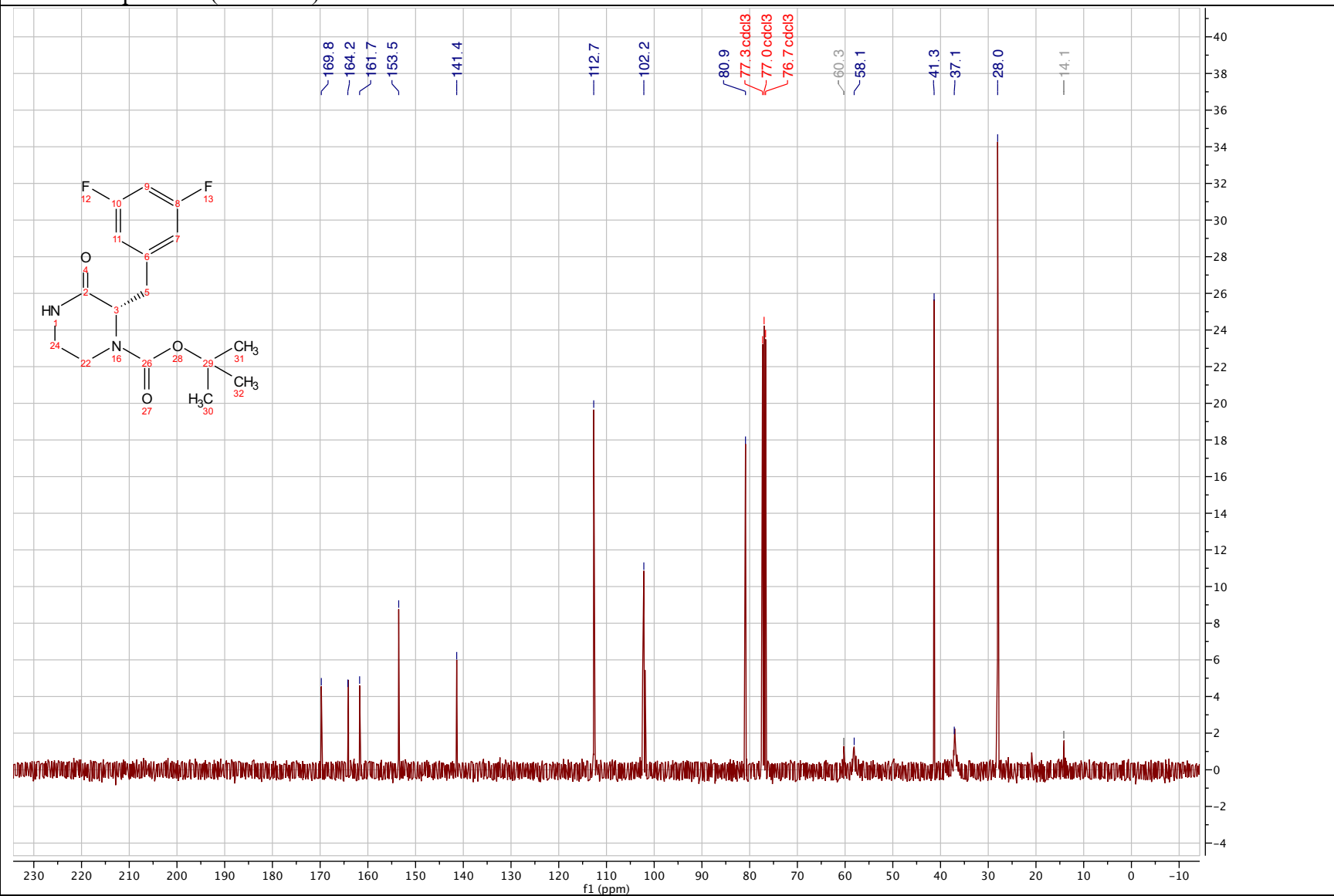
***tert*-butyl (*S*)-2-(3,5-difluorobenzyl)-3-oxopiperazine-1-carboxylate (3.57)**

¹H NMR spectrum (400 MHz) in Chloroform-*d*



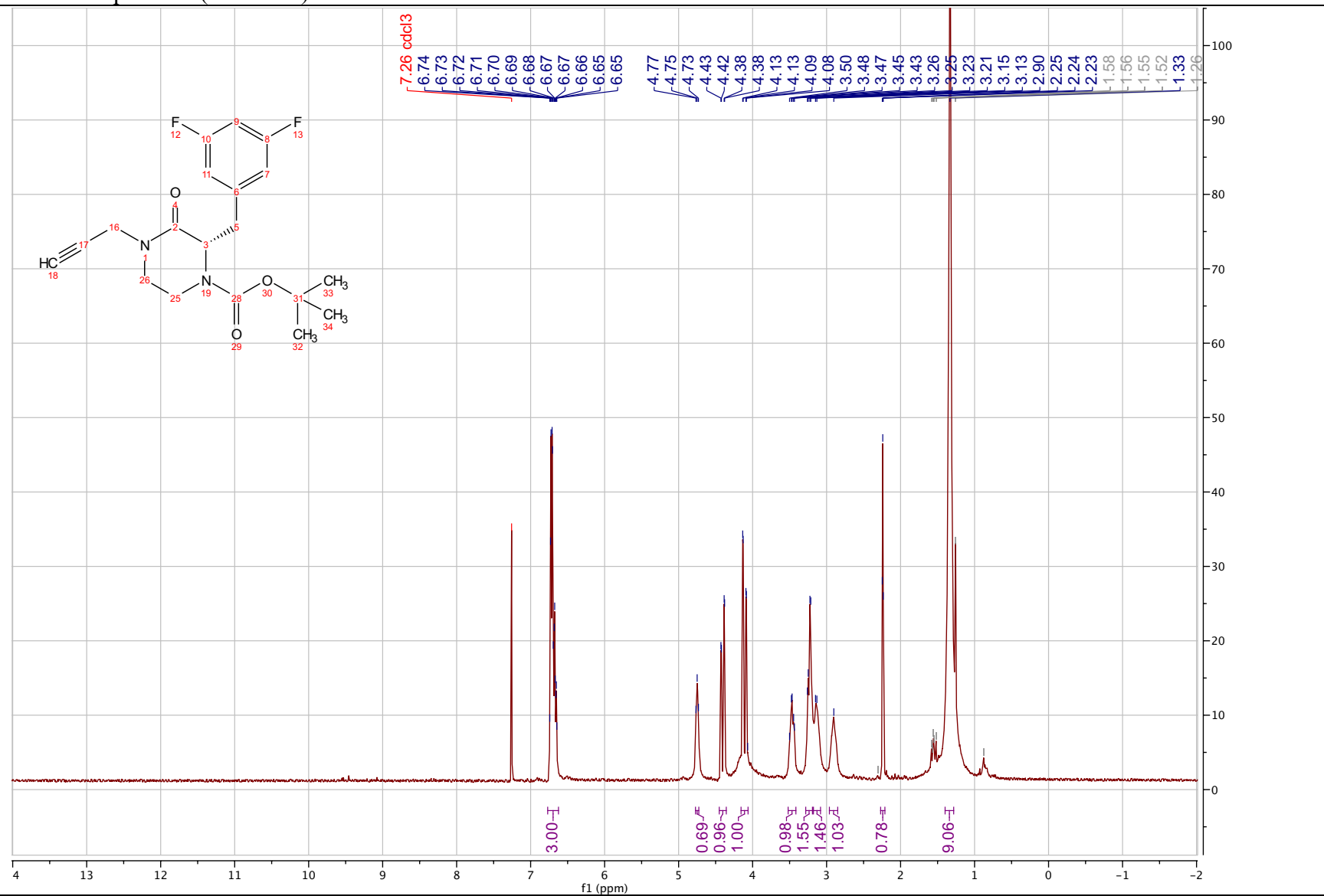
***tert*-butyl (*S*)-2-(3,5-difluorobenzyl)-3-oxopiperazine-1-carboxylate (3.57)**

^{13}C NMR spectrum (101 MHz) in Chloroform-*d*



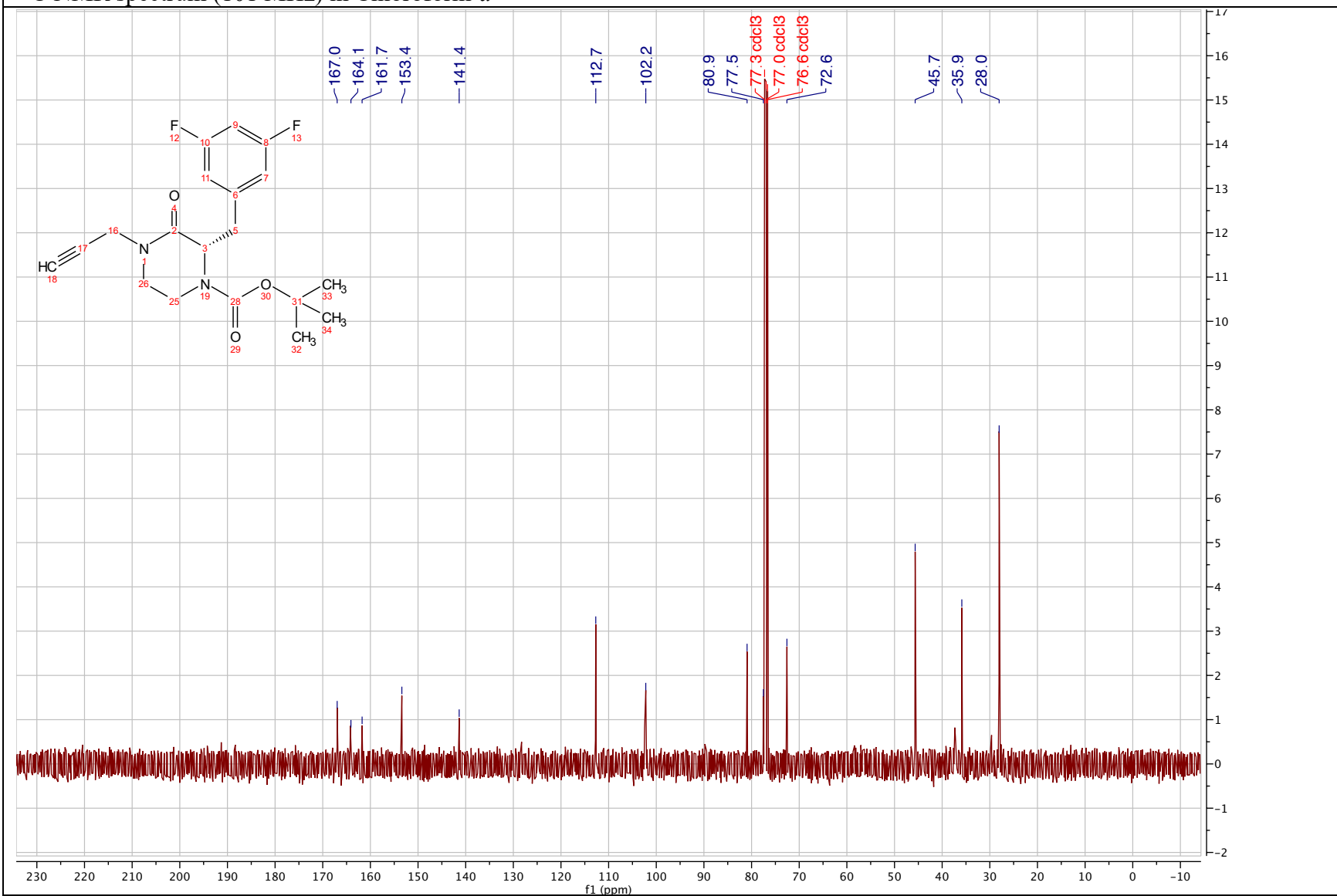
***tert*-butyl (*S*)-2-(3,5-difluorobenzyl)-3-oxo-4-(prop-2-yn-1-yl)piperazine-1-carboxylate (3.58)**

¹H NMR spectrum (400 MHz) in Chloroform-*d*



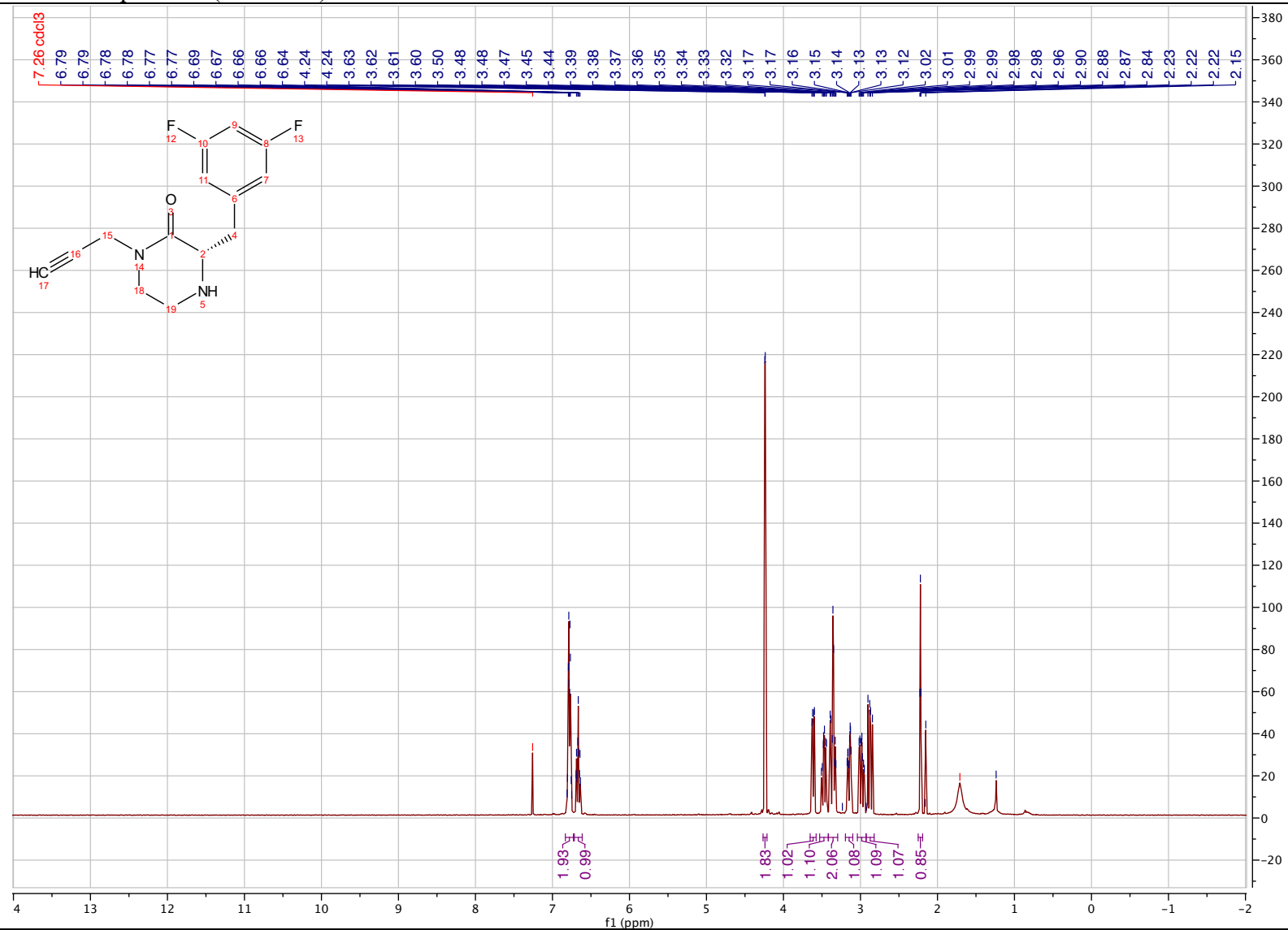
***tert*-butyl (*S*)-2-(3,5-difluorobenzyl)-3-oxo-4-(prop-2-yn-1-yl)piperazine-1-carboxylate (3.58)**

¹³C NMR spectrum (101 MHz) in Chloroform-*d*



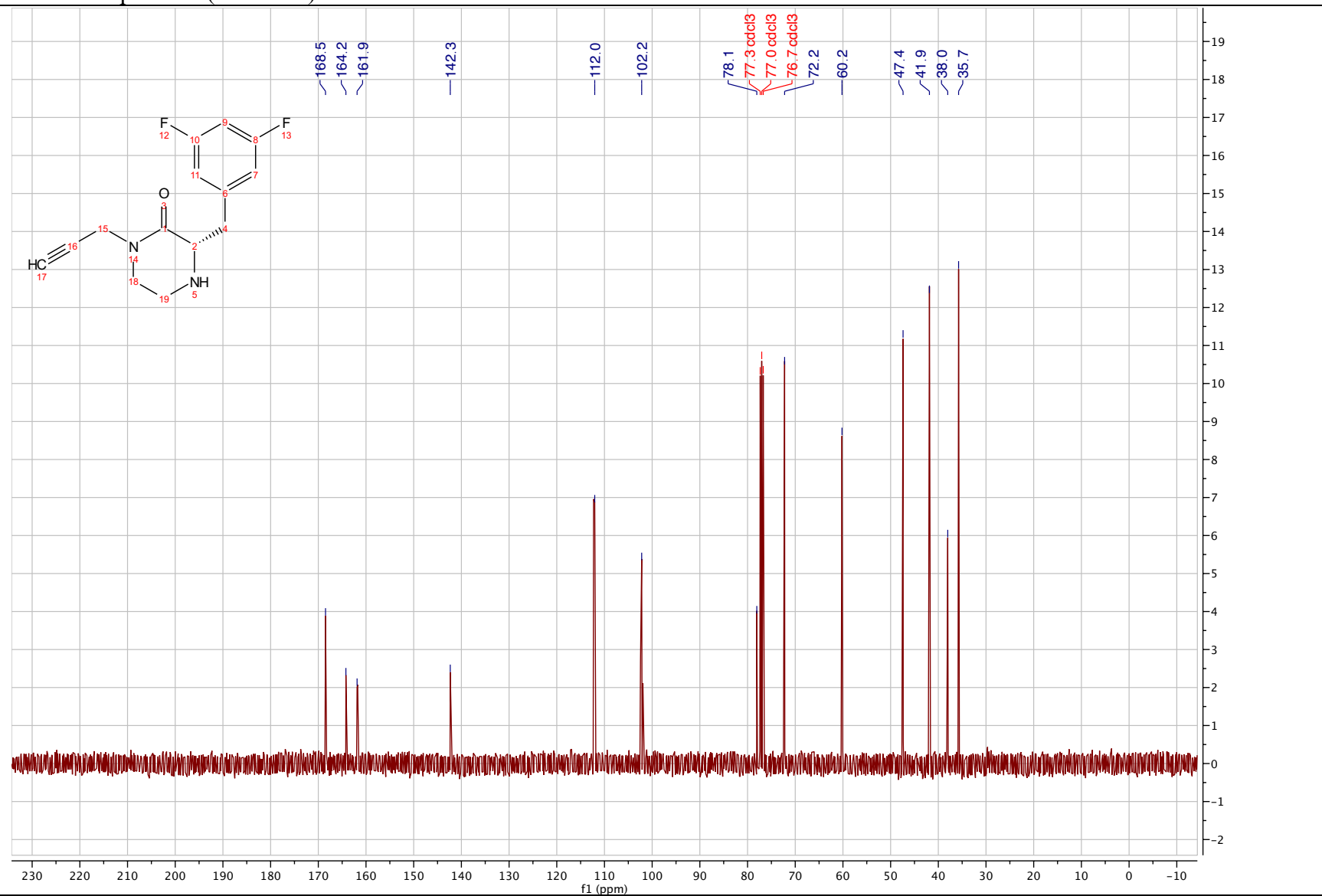
(S)-3-(3,5-difluorobenzyl)-1-(prop-2-yn-1-yl)piperazin-2-one (3.58')

¹H NMR spectrum (400 MHz) in Chloroform-*d*



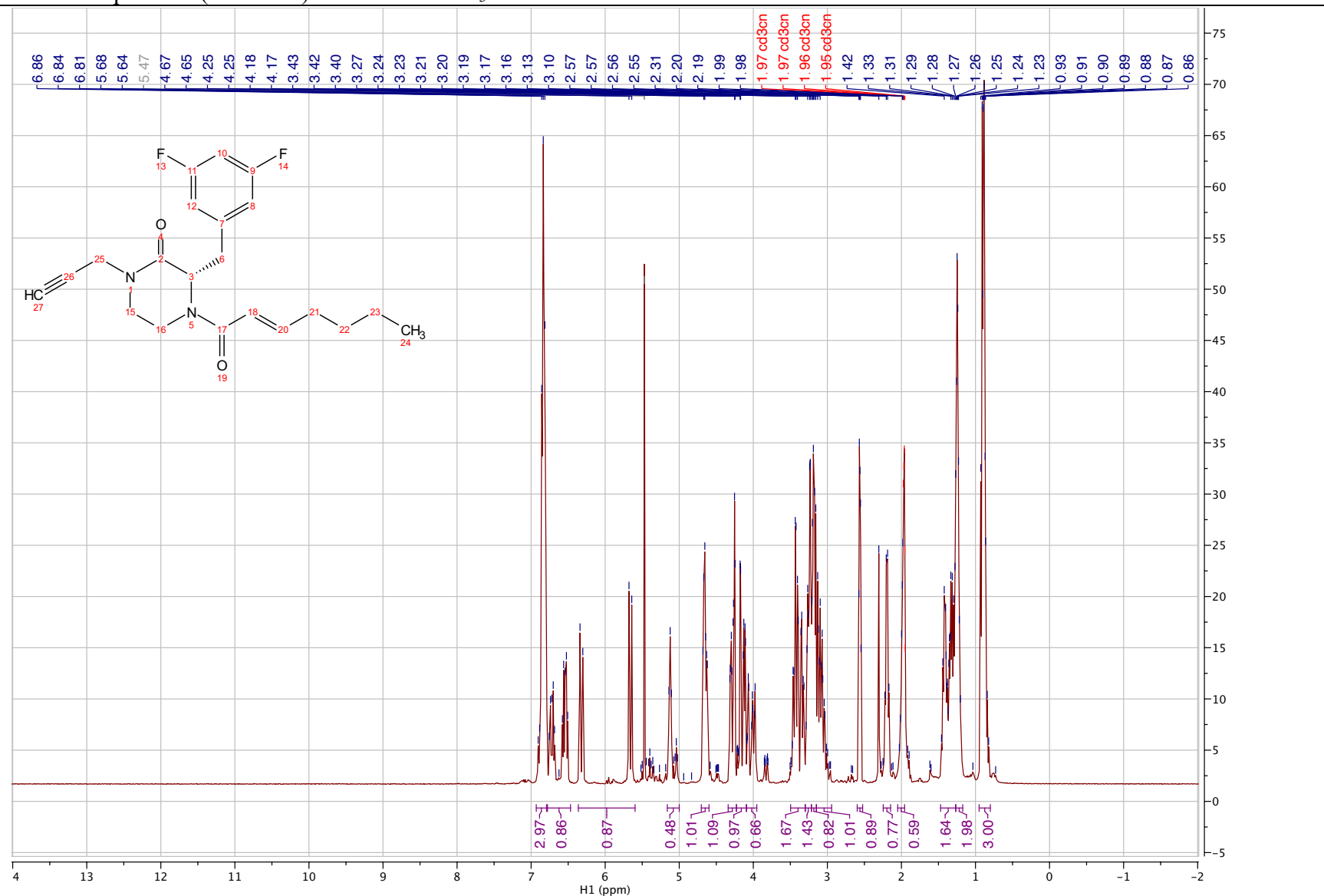
(S)-3-(3,5-difluorobenzyl)-1-(prop-2-yn-1-yl)piperazin-2-one (3.58')

^{13}C NMR spectrum (101 MHz) in Chloroform-*d*



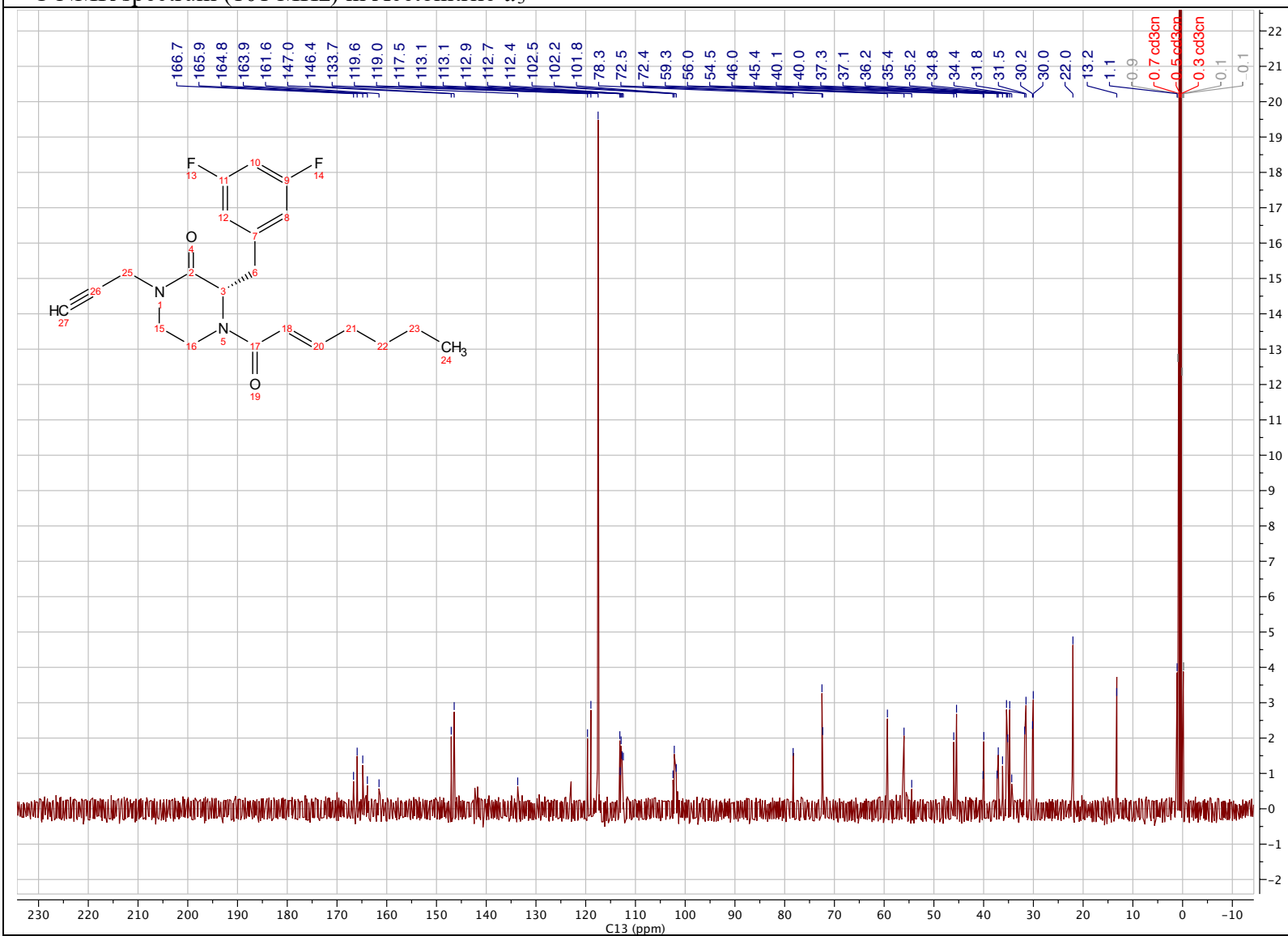
(*S,E*)-3-(3,5-difluorobenzyl)-4-(hept-2-enyl)-1-(prop-2-yn-1-yl)piperazin-2-one (3.25)

¹H NMR spectrum (400 MHz) in Acetonitrile-*d*₃



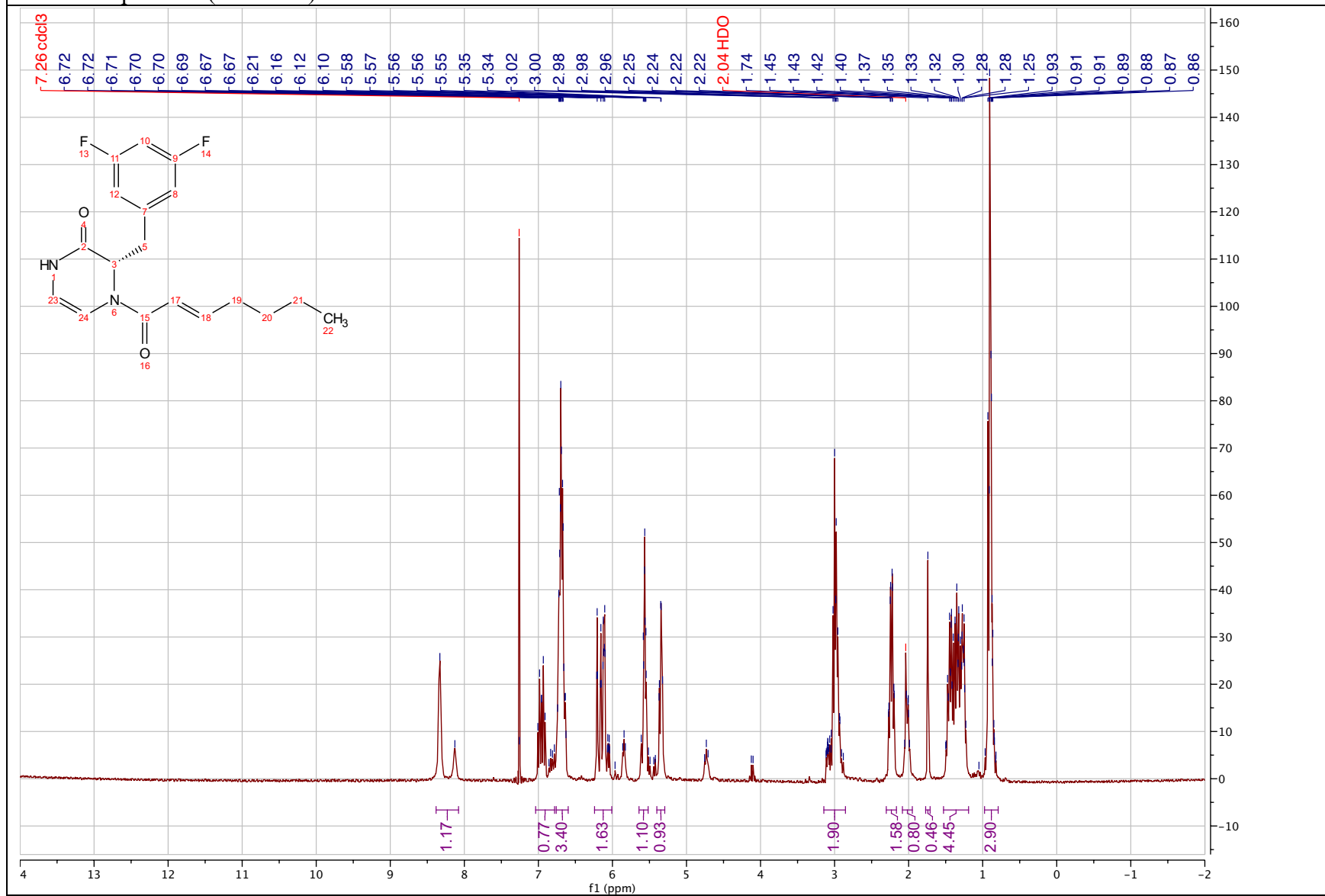
(*S,E*)-3-(3,5-difluorobenzyl)-4-(hept-2-enyl)-1-(prop-2-yn-1-yl)piperazin-2-one (3.25)

¹³C NMR spectrum (101 MHz) in Acetonitrile-*d*₃



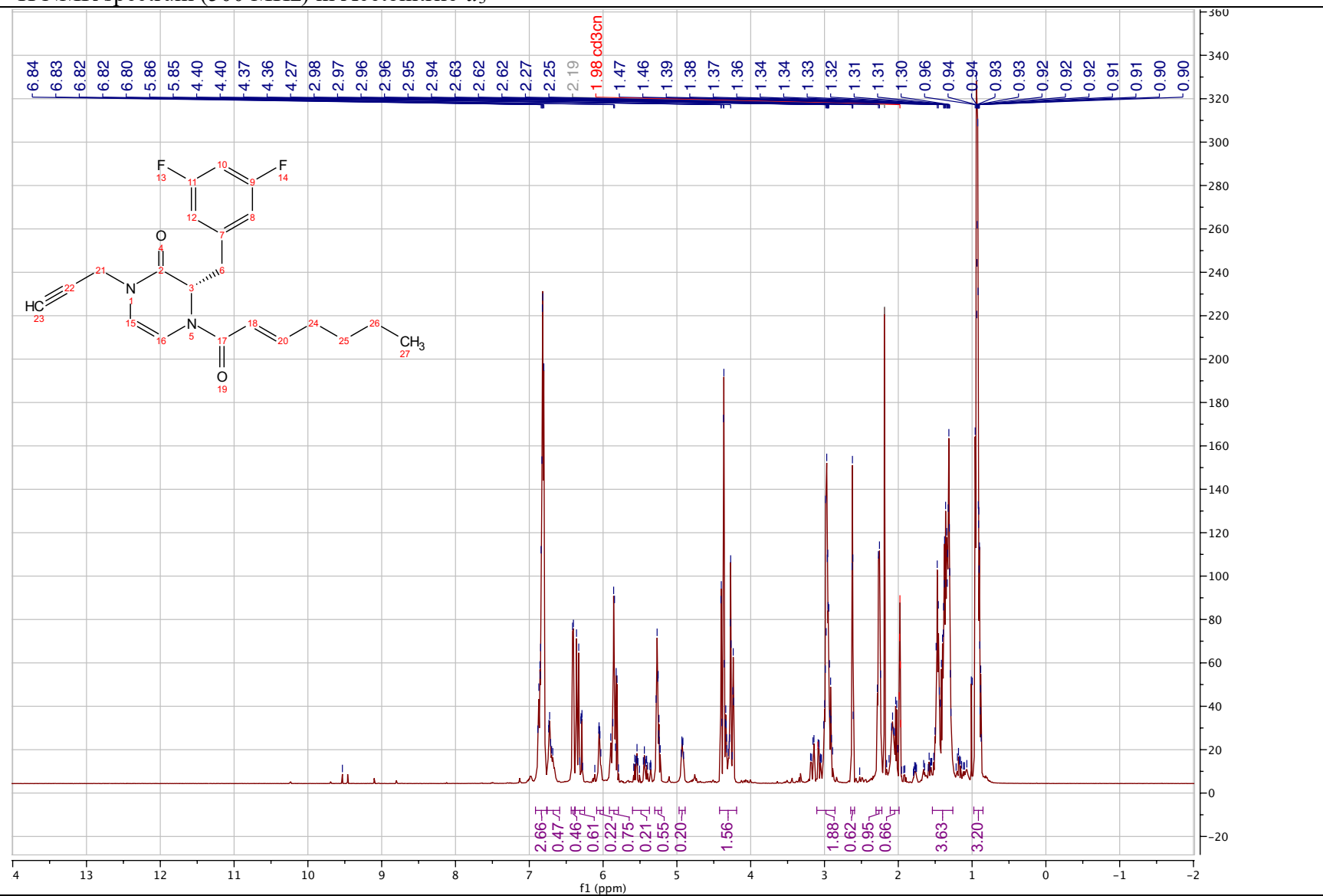
(*S,E*)-3-(3,5-difluorobenzyl)-4-(hept-2-enyl)-3,4-dihydropyrazin-2(1*H*)-one (3.60)

¹H NMR spectrum (300 MHz) in Chloroform-*d*



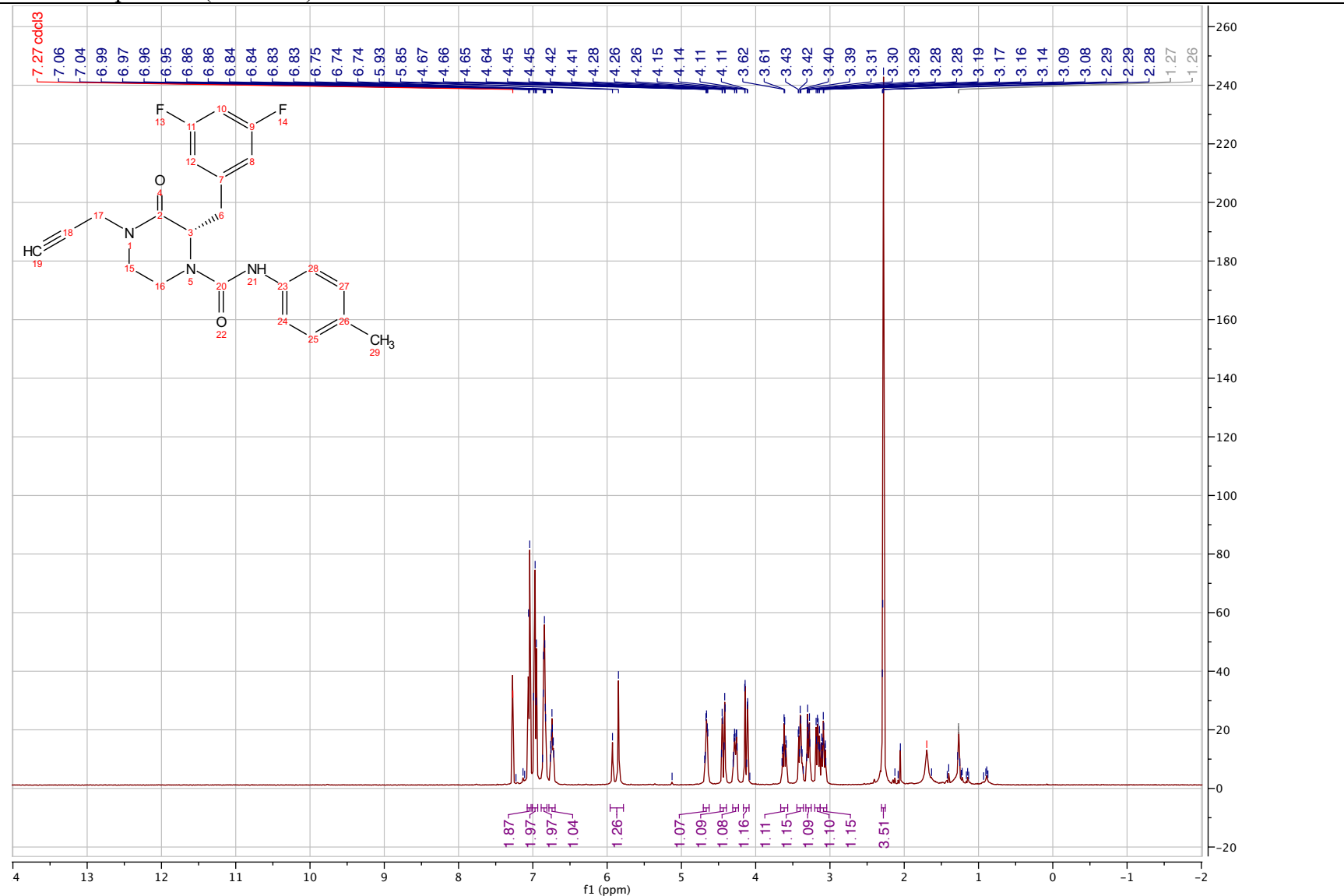
(*S,E*)-3-(3,5-difluorobenzyl)-4-(hept-2-enoyl)-1-(prop-2-yn-1-yl)-3,4-dihydropyrazin-2(1*H*)-one (3.28)

¹H NMR spectrum (500 MHz) in Acetonitrile-*d*₃



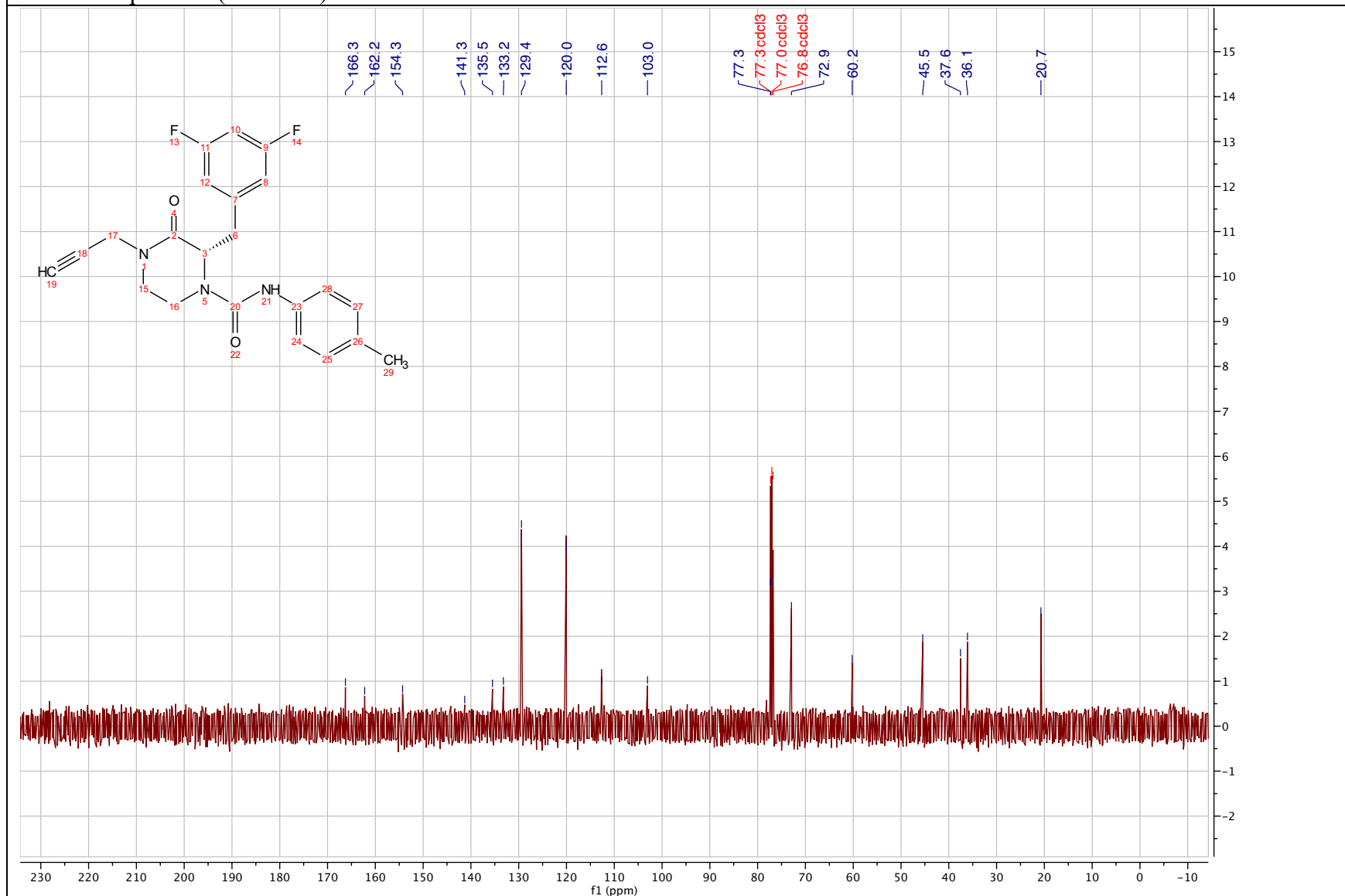
(S)-2-(3,5-difluorobenzyl)-3-oxo-4-(prop-2-yn-1-yl)-N-(p-tolyl)piperazine-1-carboxamide (3.41)

¹H NMR spectrum (500 MHz) in Chloroform-*d*



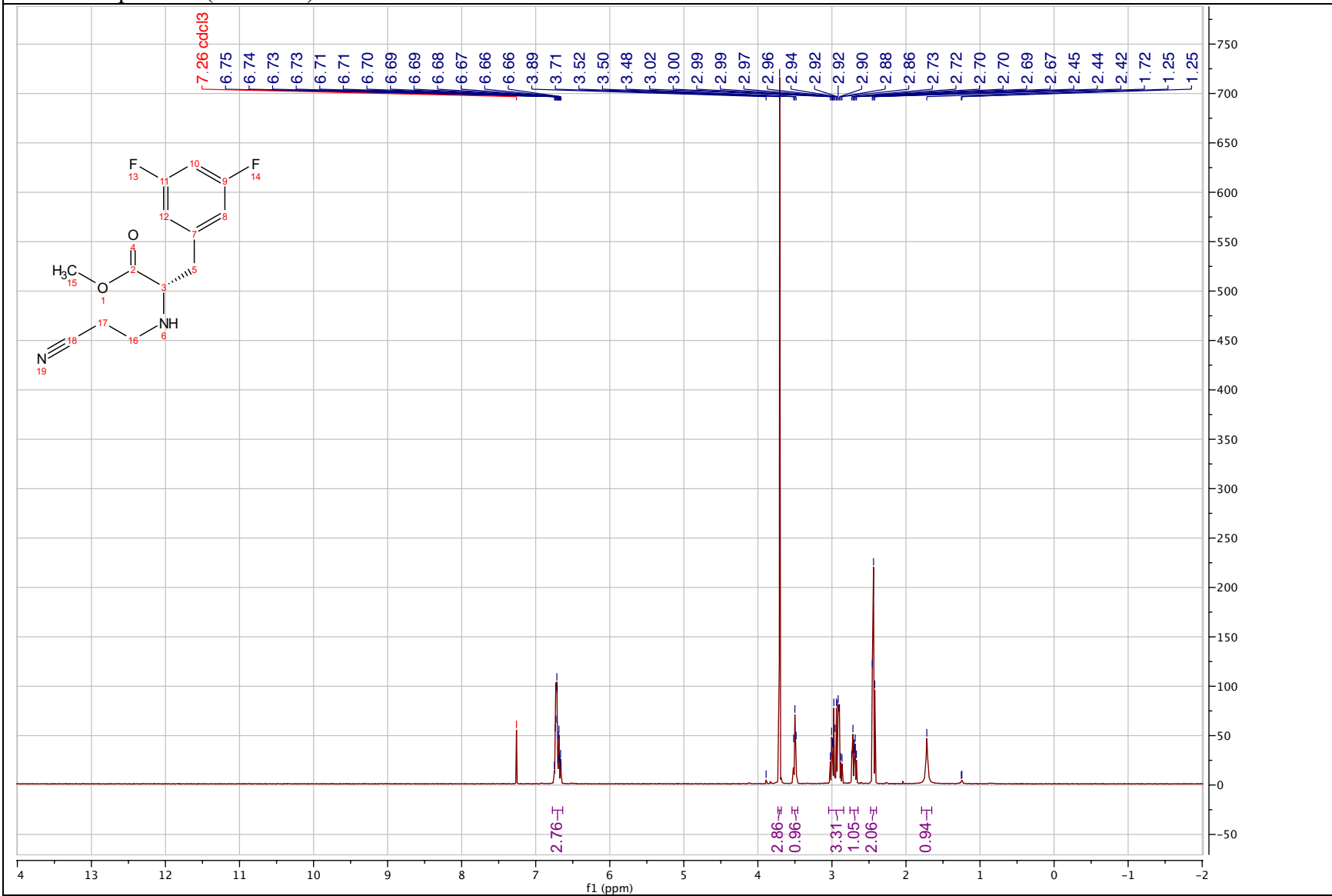
(S)-2-(3,5-difluorobenzyl)-3-oxo-4-(prop-2-yn-1-yl)-N-(p-tolyl)piperazine-1-carboxamide (3.41)

¹³C NMR spectrum (126 MHz) in Chloroform-*d*



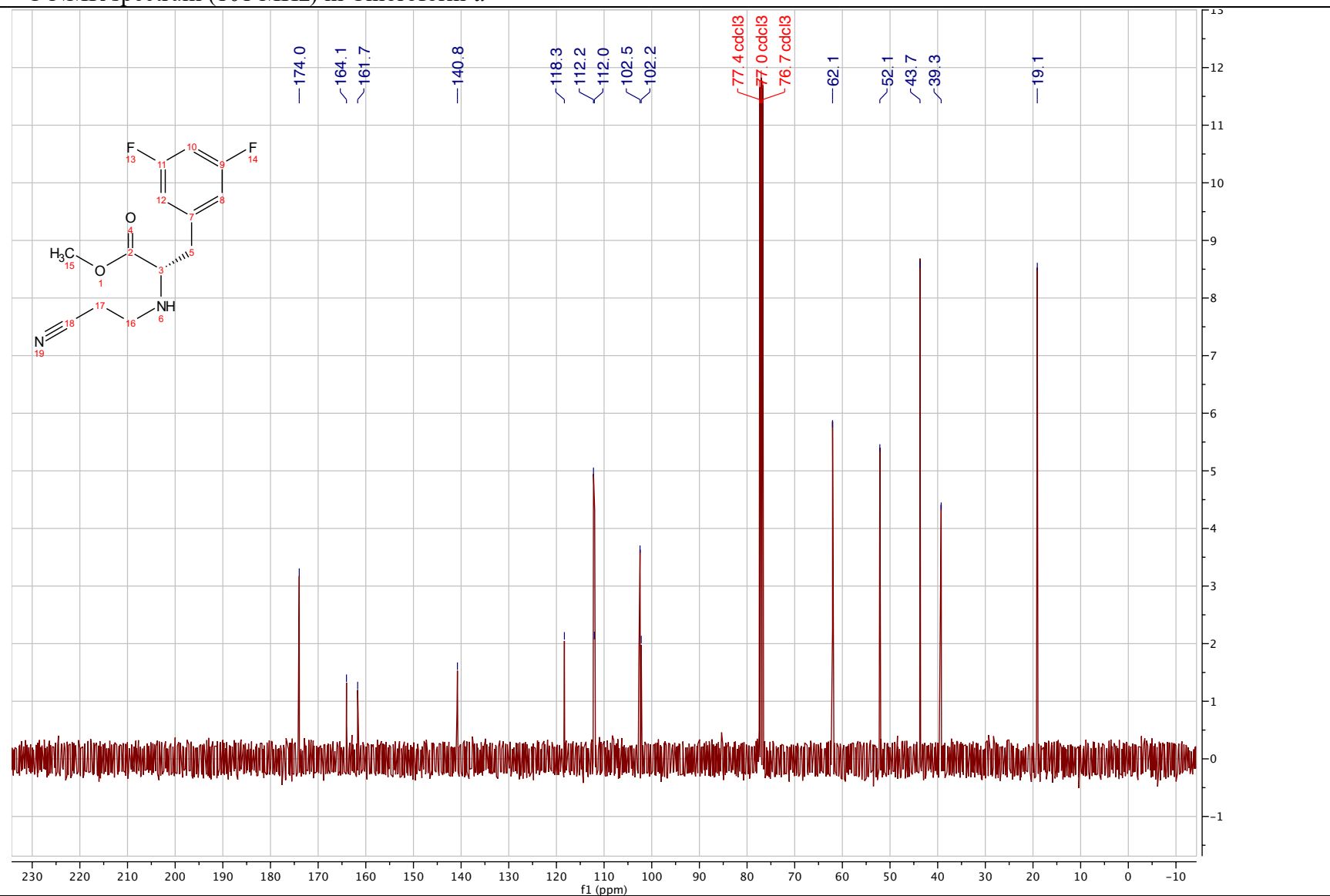
methyl (*S*)-2-((2-cyanoethyl)amino)-3-(3,5-difluorophenyl)propanoate (3.74)

¹H NMR spectrum (400 MHz) in Chloroform-*d*



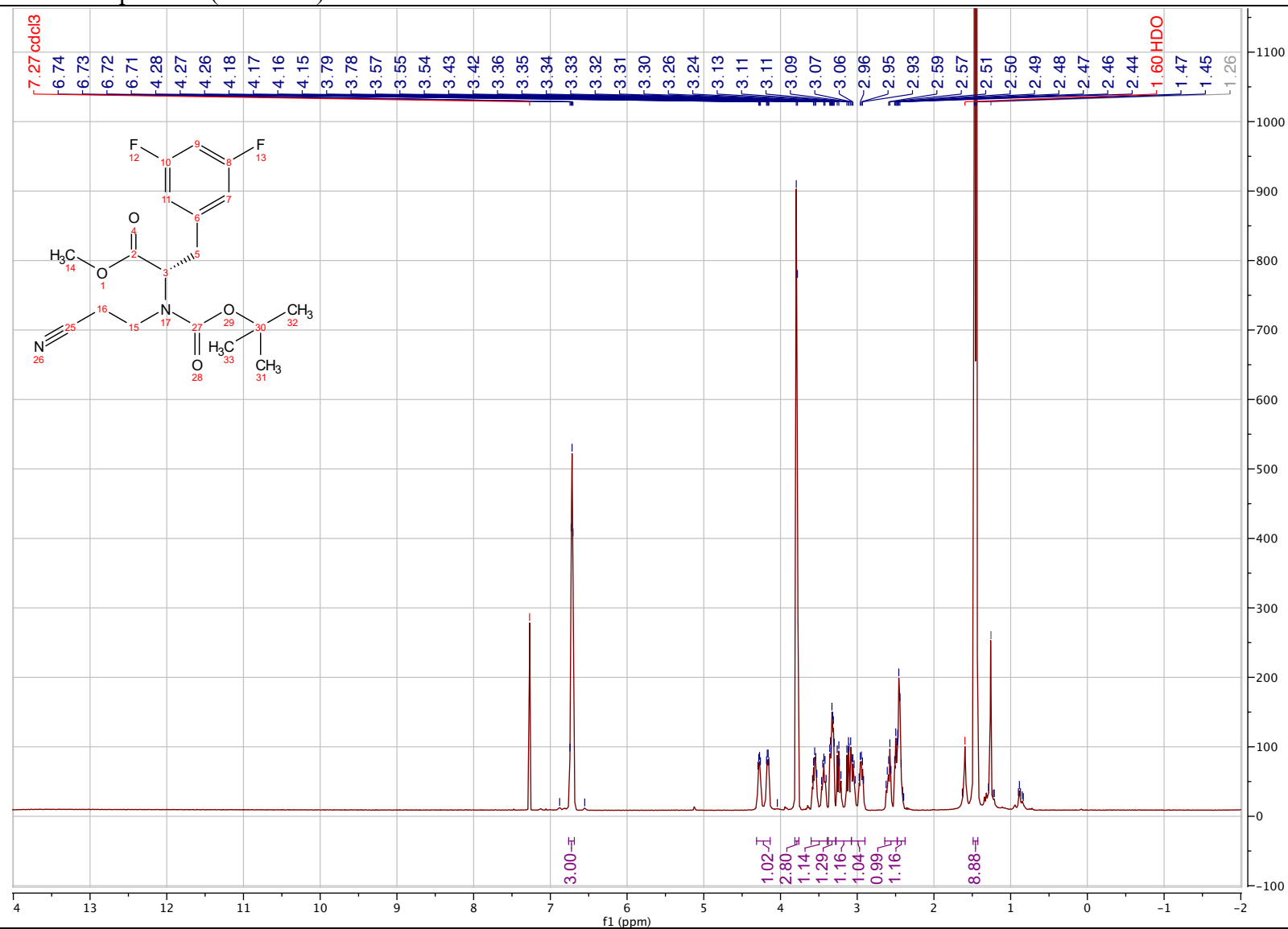
methyl (*S*)-2-((2-cyanoethyl)amino)-3-(3,5-difluorophenyl)propanoate (3.74)

¹³C NMR spectrum (101 MHz) in Chloroform-*d*



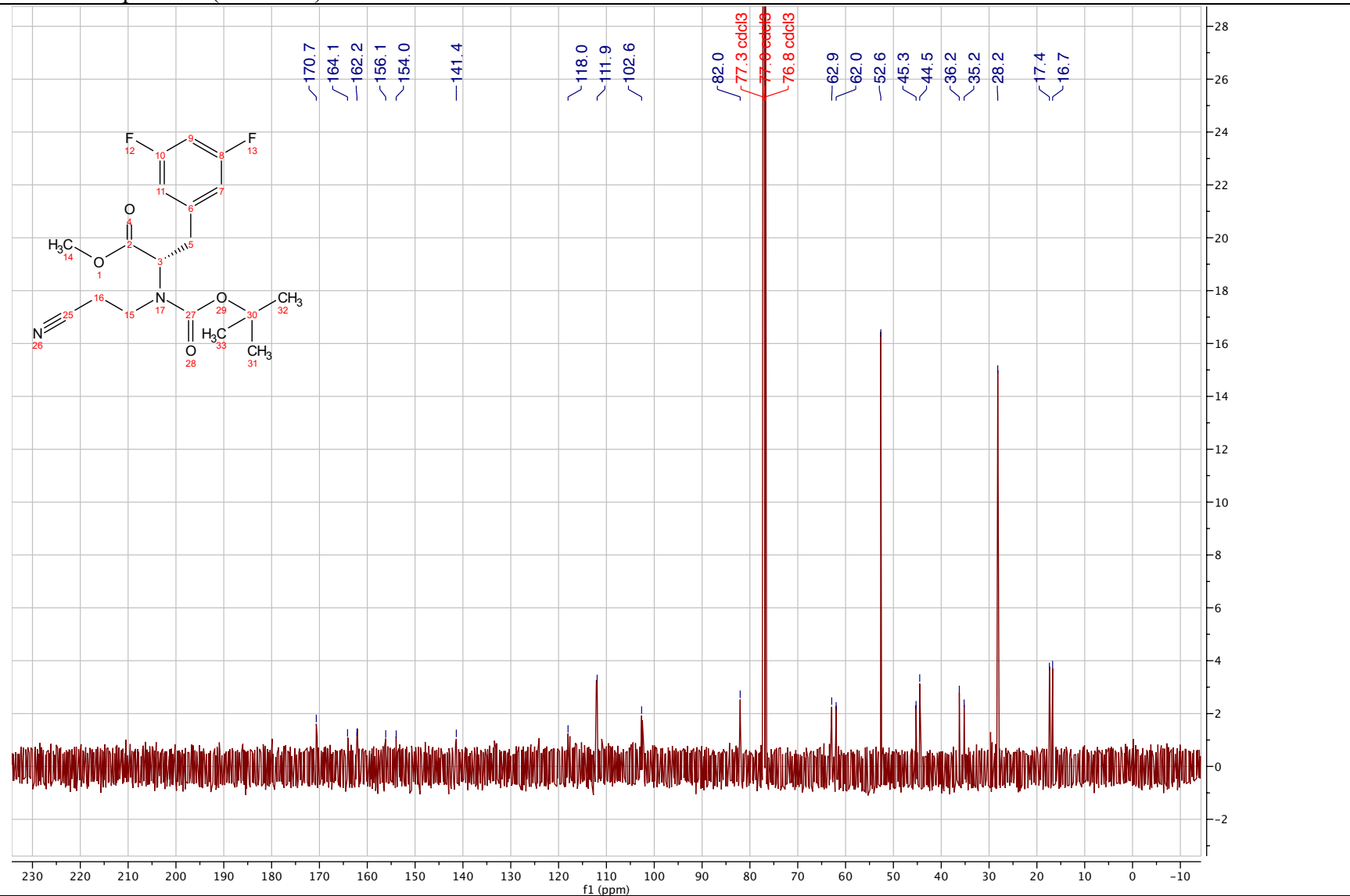
methyl (*S*)-2-((*tert*-butoxycarbonyl)(2-cyanoethyl)amino)-3-(3,5-difluorophenyl)propanoate (3.74')

¹H NMR spectrum (400 MHz) in Chloroform-*d*



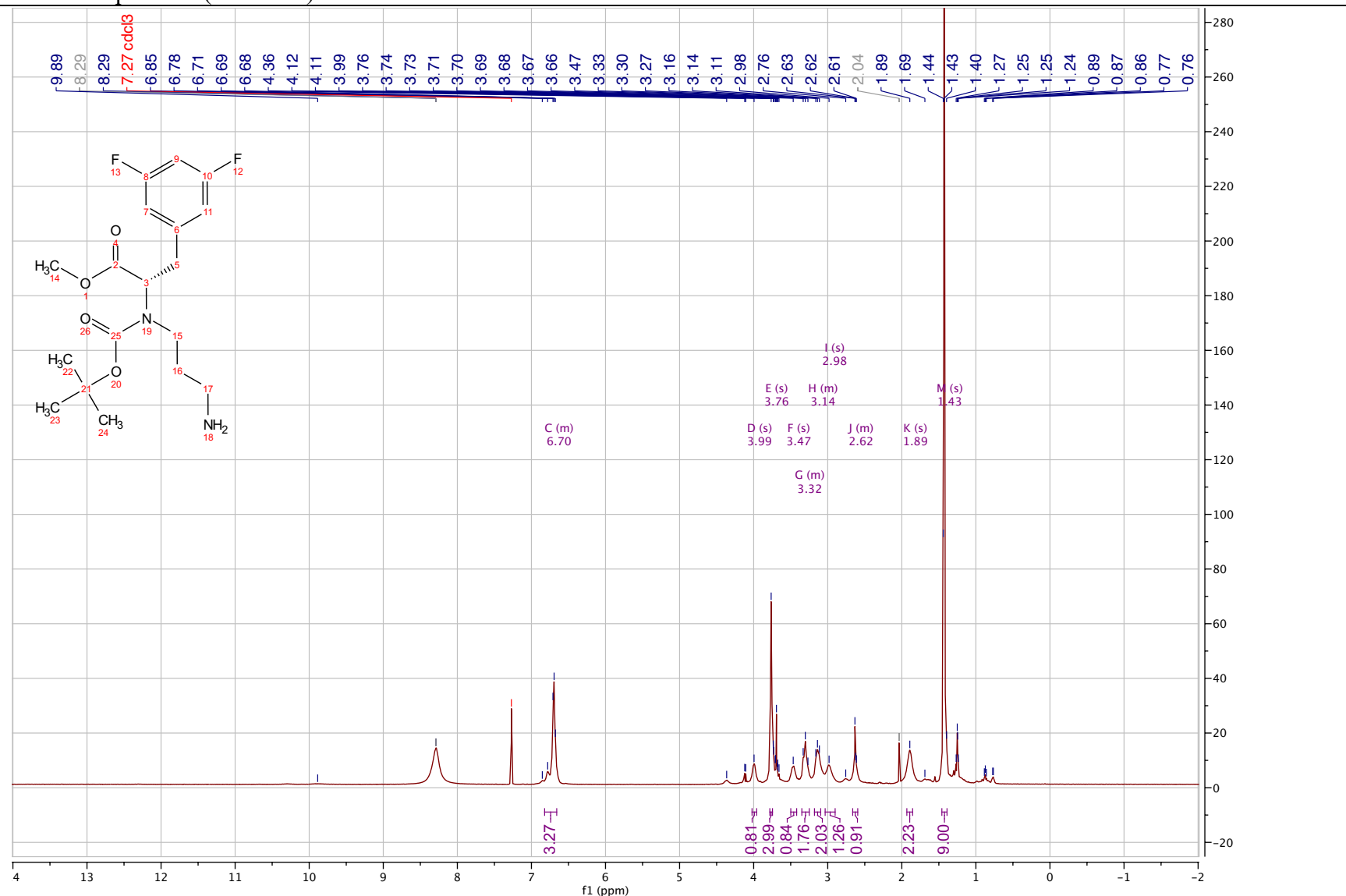
methyl (*S*)-2-((*tert*-butoxycarbonyl)(2-cyanoethyl)amino)-3-(3,5-difluorophenyl)propanoate (3.74')

¹³C NMR spectrum (101 MHz) in Chloroform-*d*



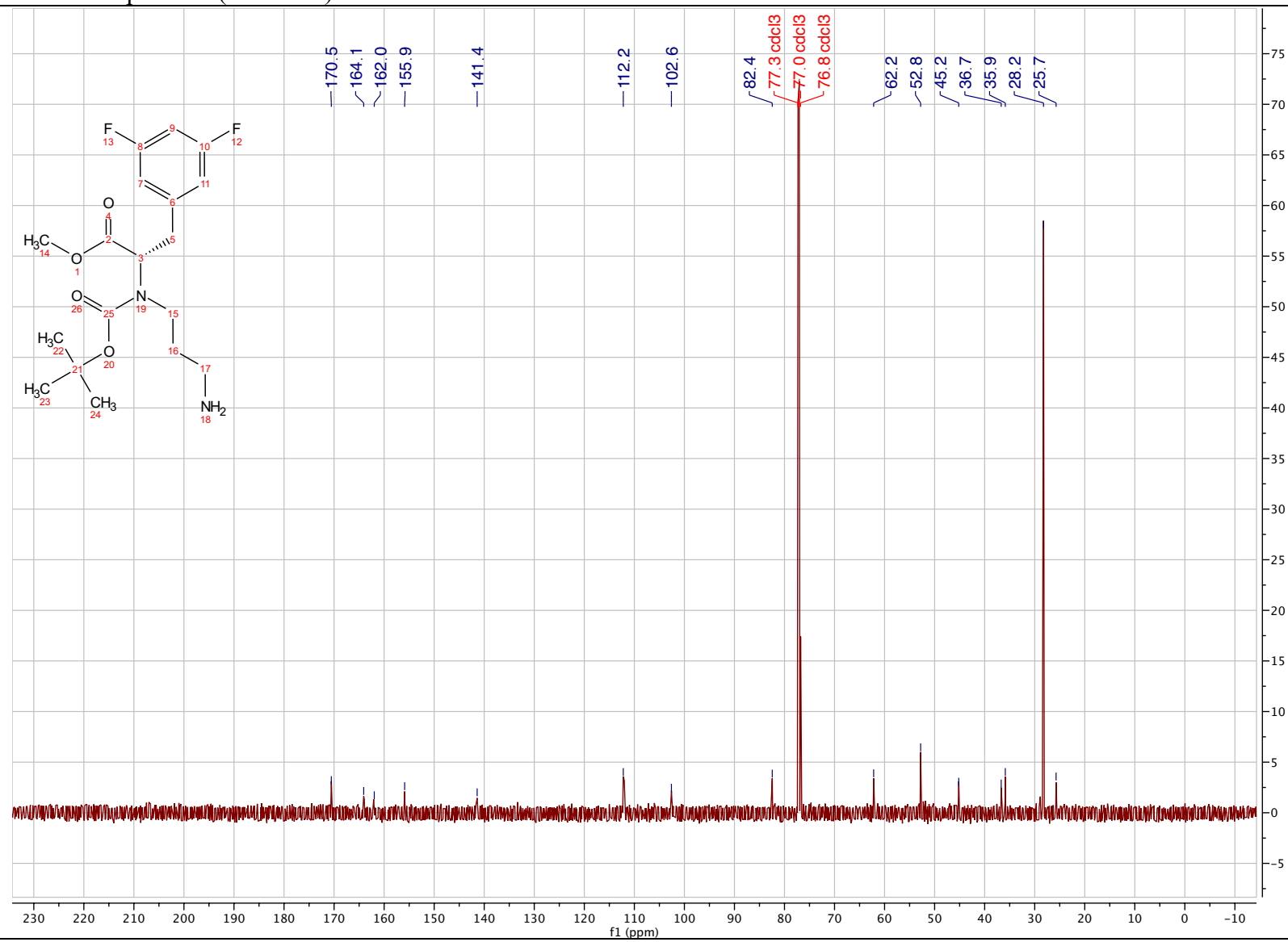
methyl (*S*)-2-((3-aminopropyl) (*tert*-butoxycarbonyl) amino)-3-(3,5-difluorophenyl) propanoate (3.75)

¹H NMR spectrum (400 MHz) in Chloroform-*d*



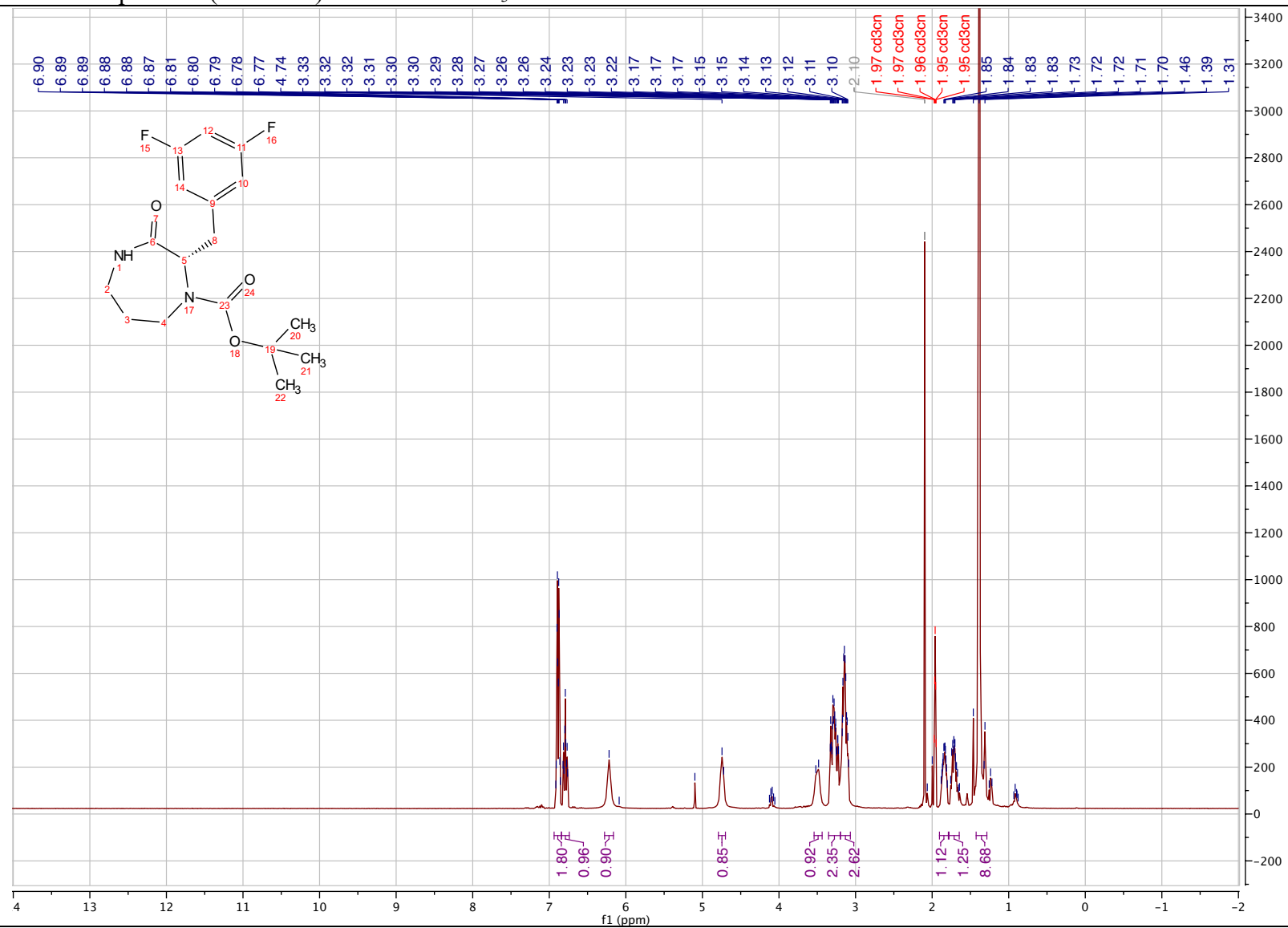
methyl (*S*)-2-((3-aminopropyl) (*tert*-butoxycarbonyl) amino)-3-(3,5-difluorophenyl) propanoate (3.75)

¹³C NMR spectrum (101 MHz) in Chloroform-*d*



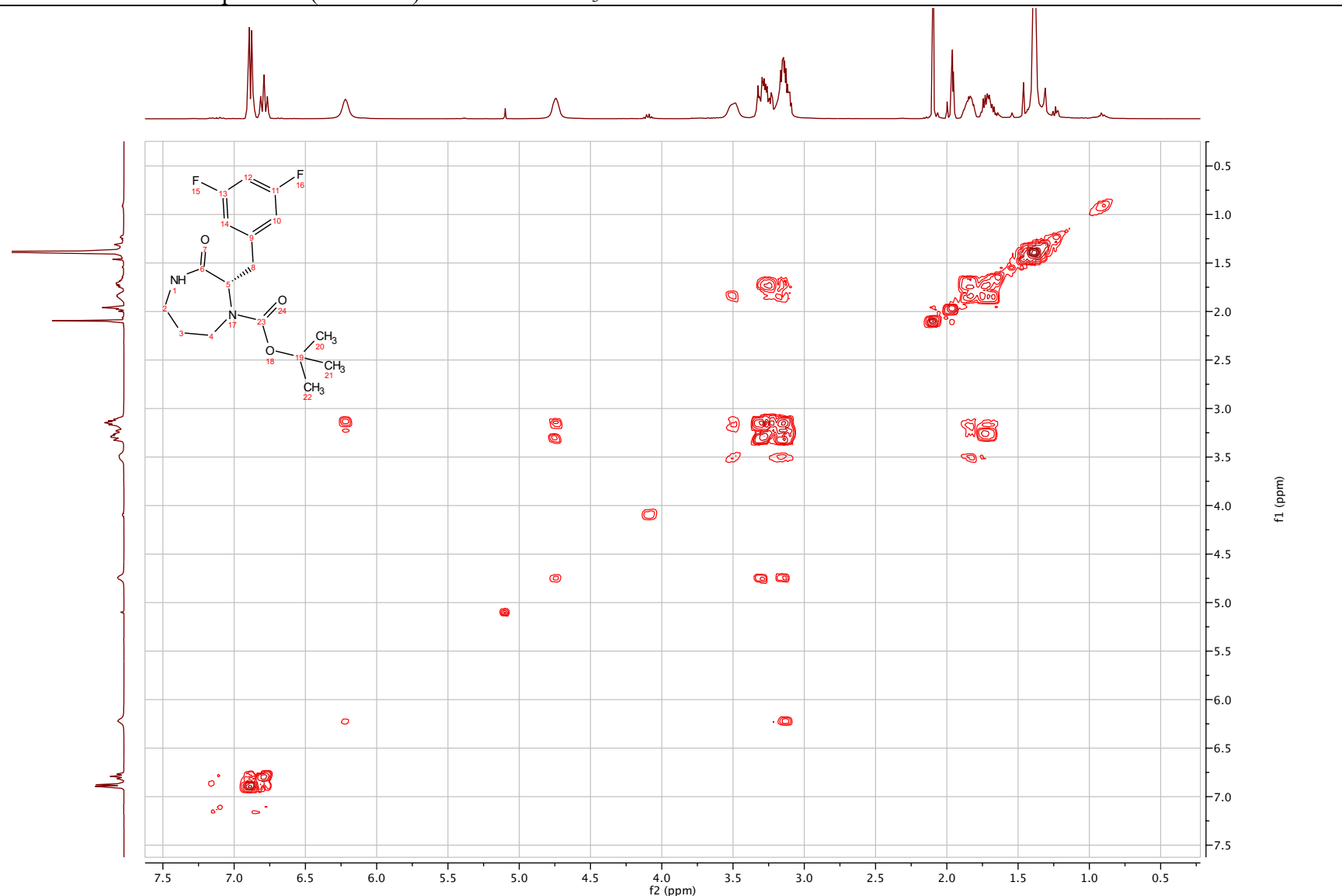
***tert*-butyl (*S*)-2-(3,5-difluorobenzyl)-3-oxo-1,4-diazepane-1-carboxylate (3.76)**

¹H NMR spectrum (400 MHz) in Acetonitrile-*d*₃



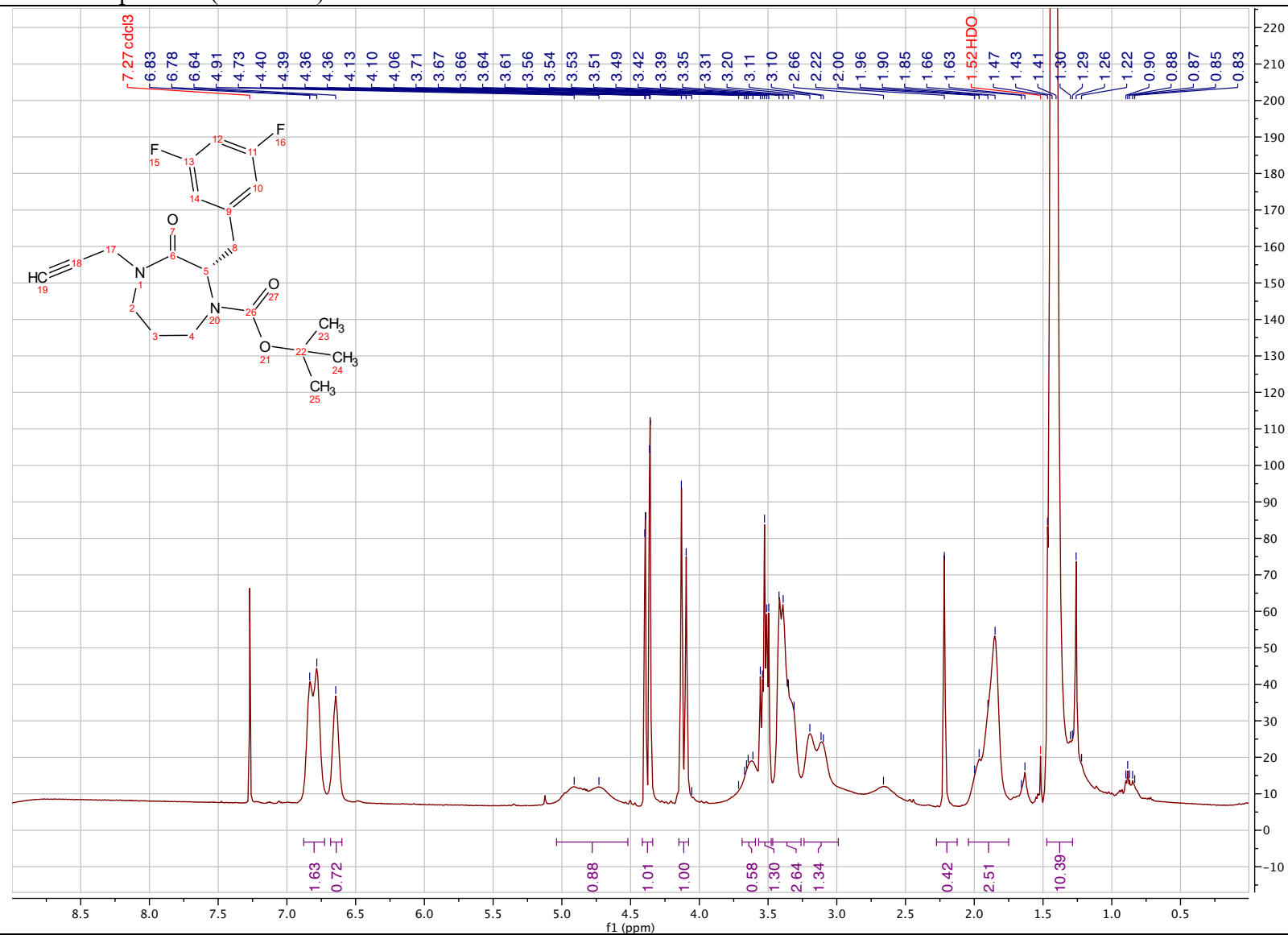
***tert*-butyl (*S*)-2-(3,5-difluorobenzyl)-3-oxo-1,4-diazepane-1-carboxylate (3.76)**

¹H-¹H COSY NMR spectrum (400 MHz) in Acetonitrile-*d*₃



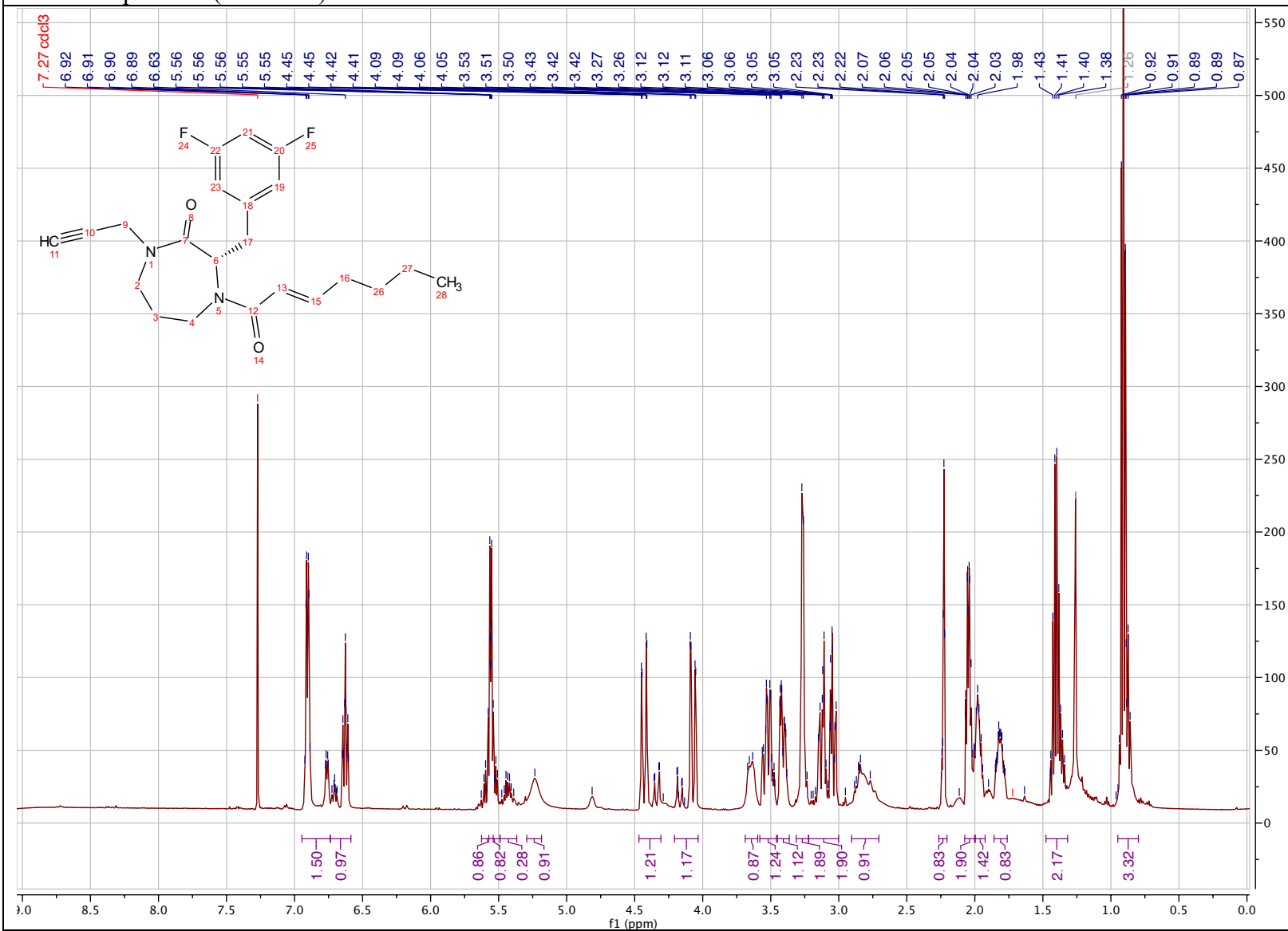
***tert*-butyl (*S*)-2-(3,5-difluorobenzyl)-3-oxo-4-(prop-2-yn-1-yl)-1,4-diazepane-1-carboxylate (3.77)**

¹H NMR spectrum (400 MHz) in Chloroform-*d*



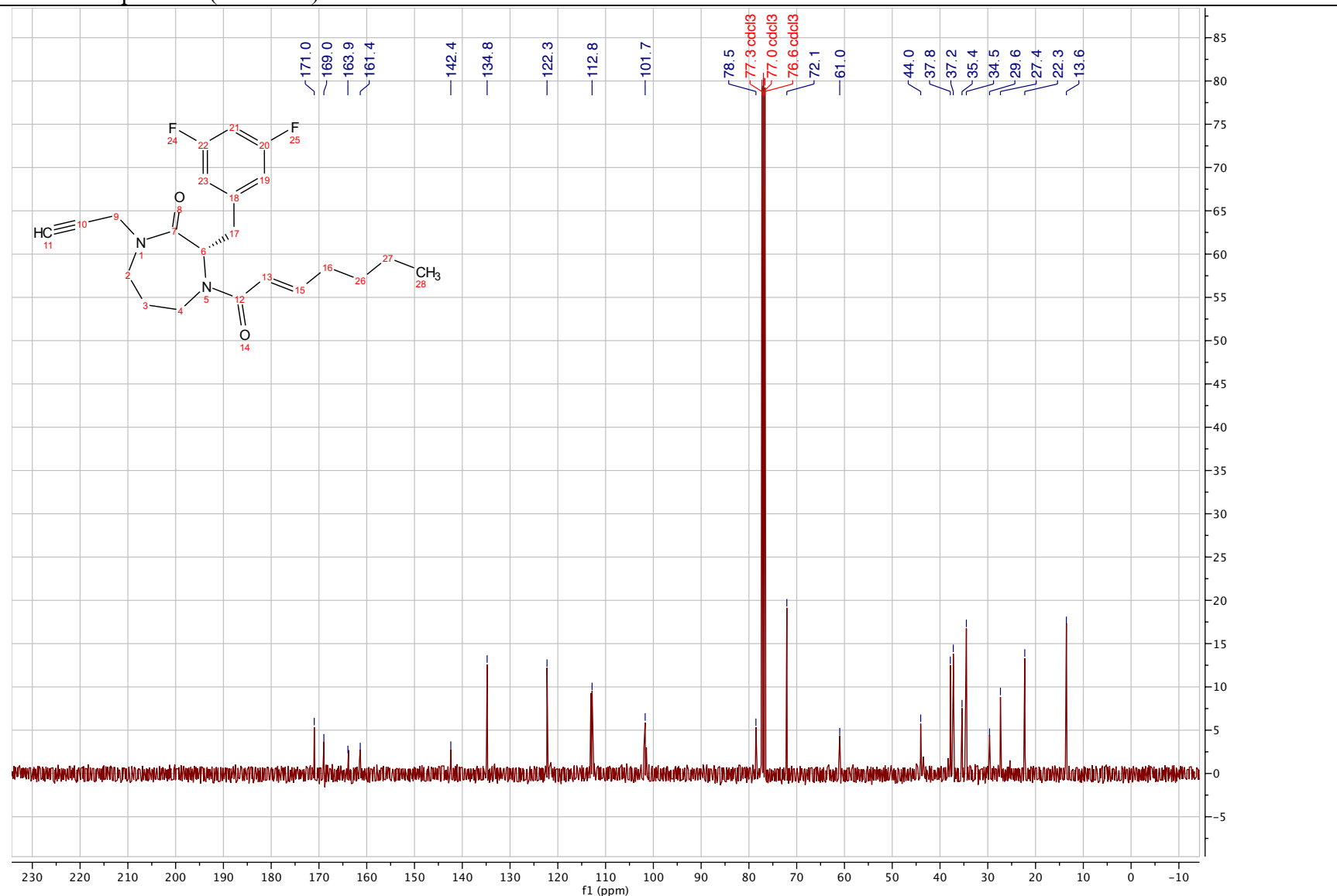
(*S,E*)-3-(3,5-difluorobenzyl)-4-(hept-2-enyl)-1-(prop-2-yn-1-yl)-1,4-diazepan-2-one (3.26)

¹H NMR spectrum (500 MHz) in Chloroform-*d*



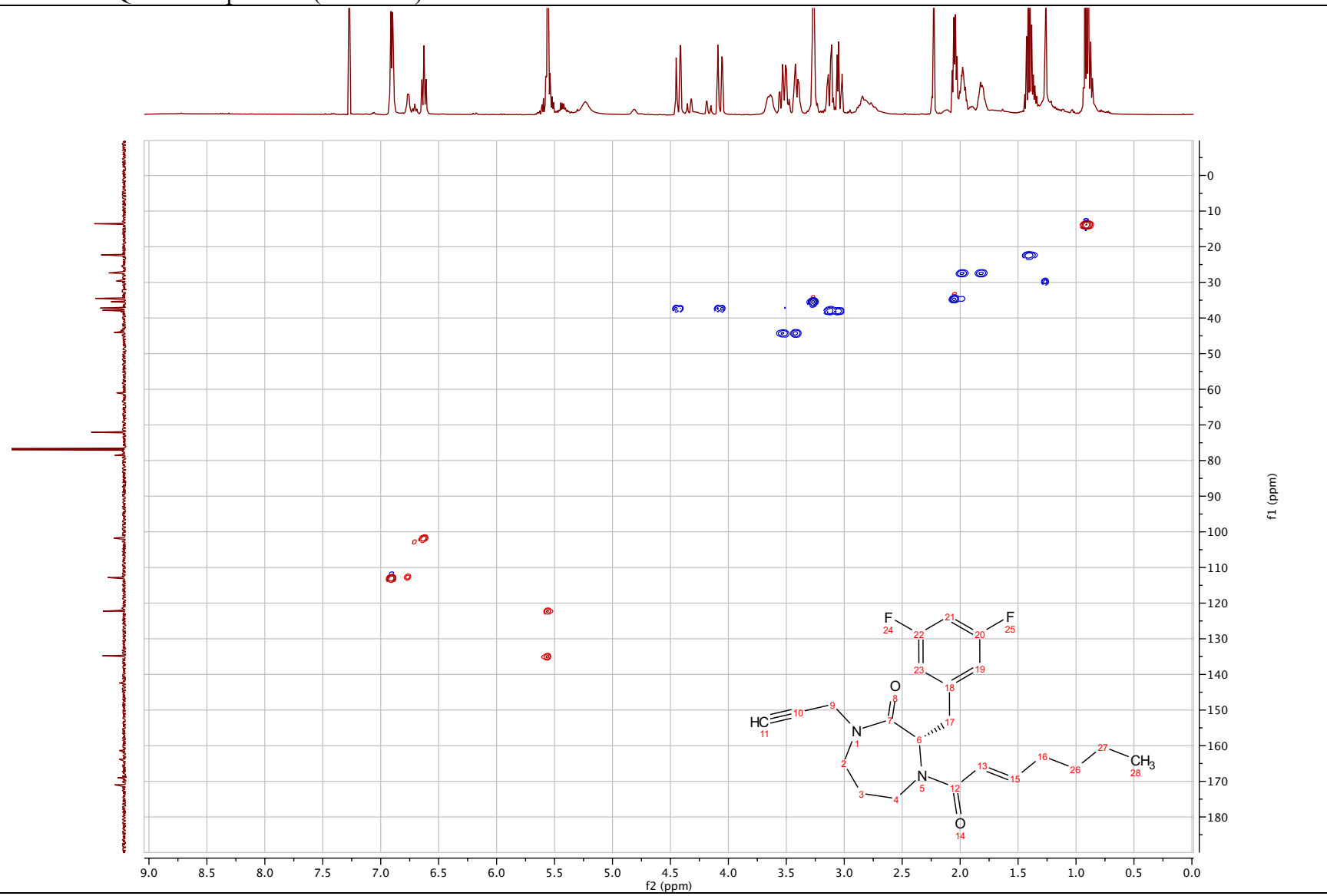
(*S,E*)-3-(3,5-difluorobenzyl)-4-(hept-2-enoyl)-1-(prop-2-yn-1-yl)-1,4-diazepan-2-one (3.26)

¹³C NMR spectrum (126 MHz) in Chloroform-*d*



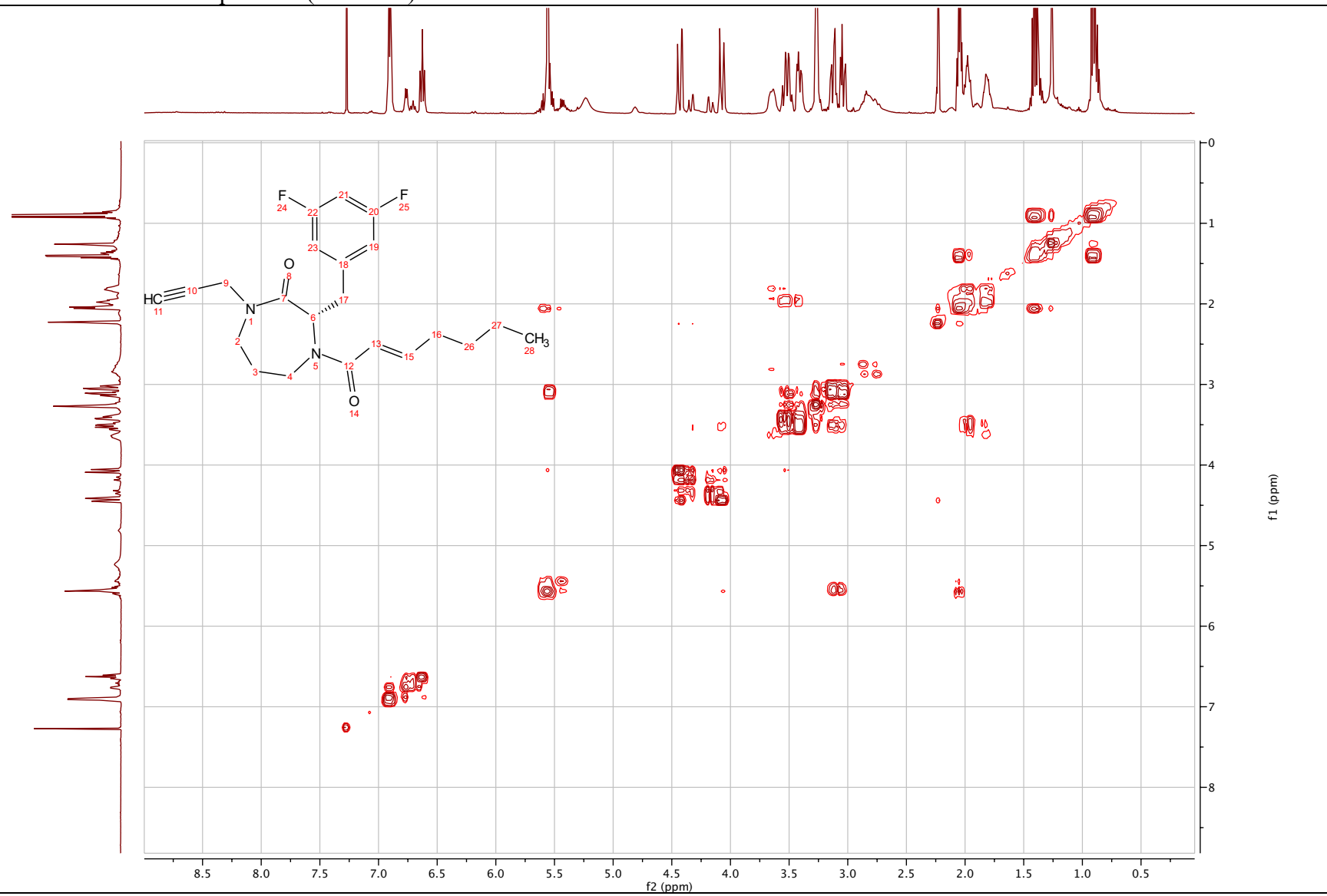
(*S,E*)-3-(3,5-difluorobenzyl)-4-(hept-2-enoyl)-1-(prop-2-yn-1-yl)-1,4-diazepan-2-one (3.26)

^1H - ^{13}C HSQC NMR spectrum (500 MHz) in Chloroform-*d*



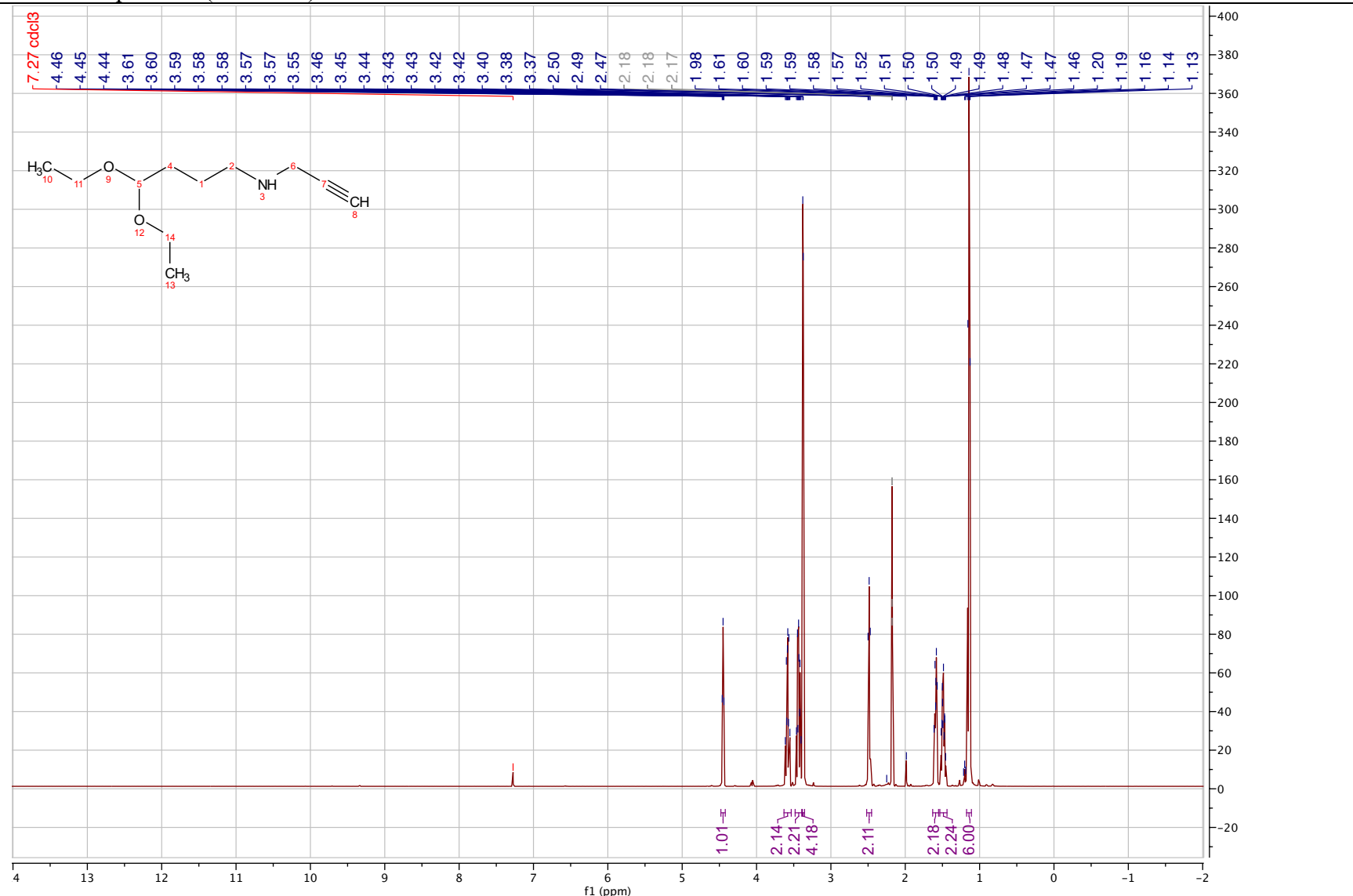
(*S,E*)-3-(3,5-difluorobenzyl)-4-(hept-2-enyl)-1-(prop-2-yn-1-yl)-1,4-diazepan-2-one (3.26)

¹H-¹H COSY NMR spectrum (500 MHz) in Chloroform-*d*



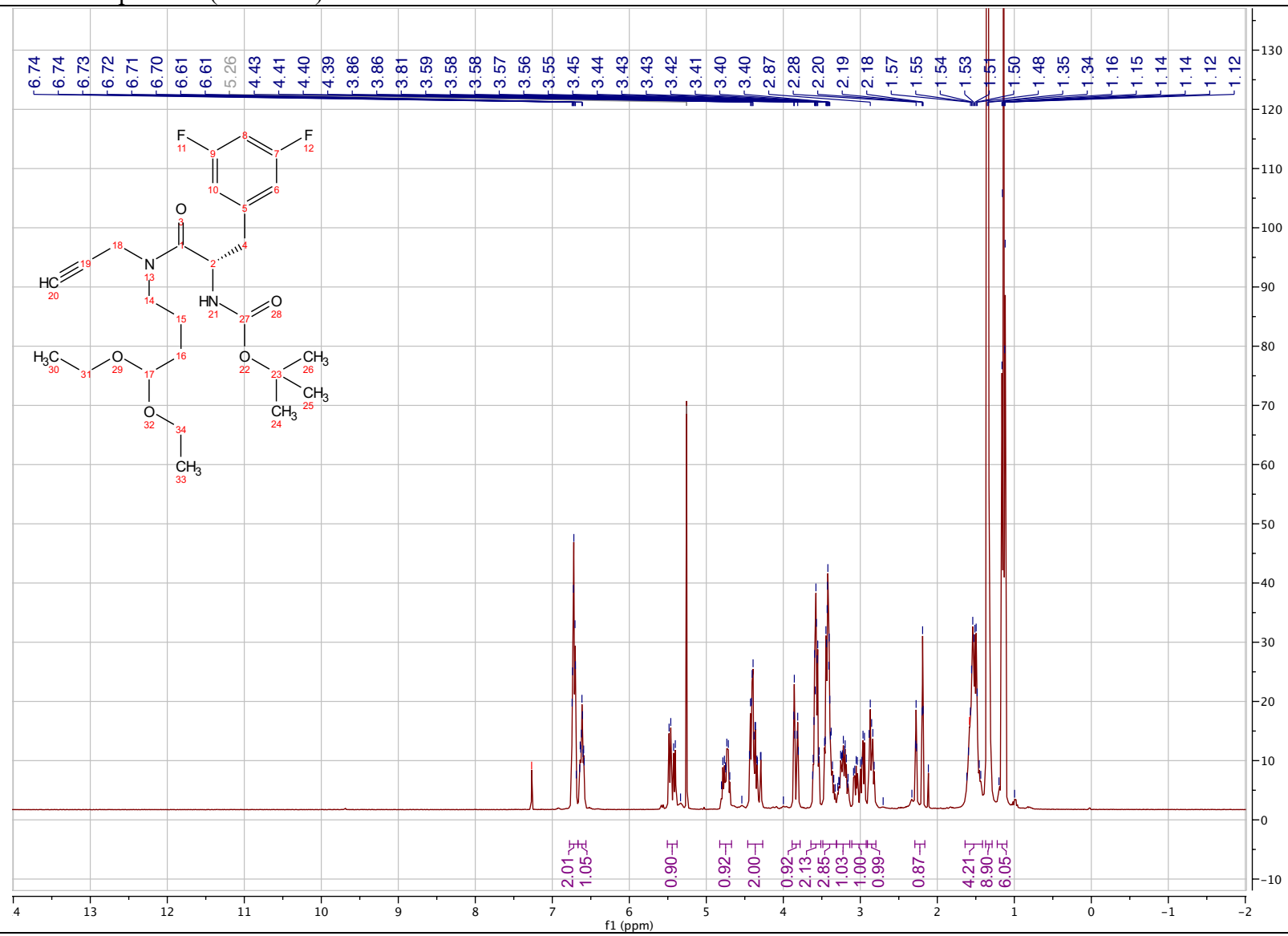
4,4-diethoxy-N-(prop-2-yn-1-yl)butan-1-amine (3.85)

¹H NMR spectrum (500 MHz) in Chloroform-*d*



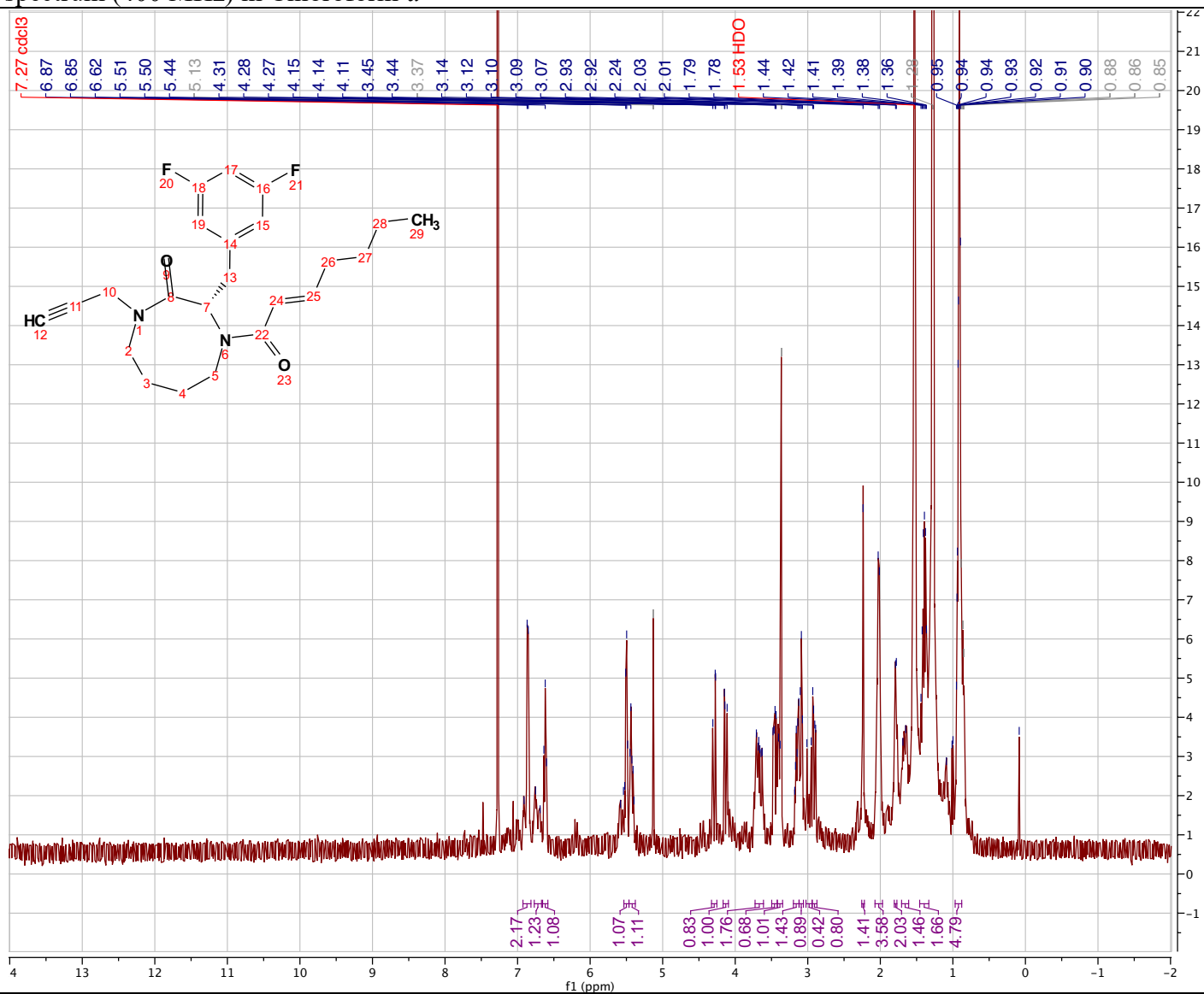
***tert*-butyl (*S*)-1-((4,4-diethoxybutyl)(prop-2-yn-1-yl)amino)-3-(3,5-difluorophenyl)-1-oxopropan-2-yl)carbamate (3.86)**

¹H NMR spectrum (400 MHz) in Chloroform-*d*



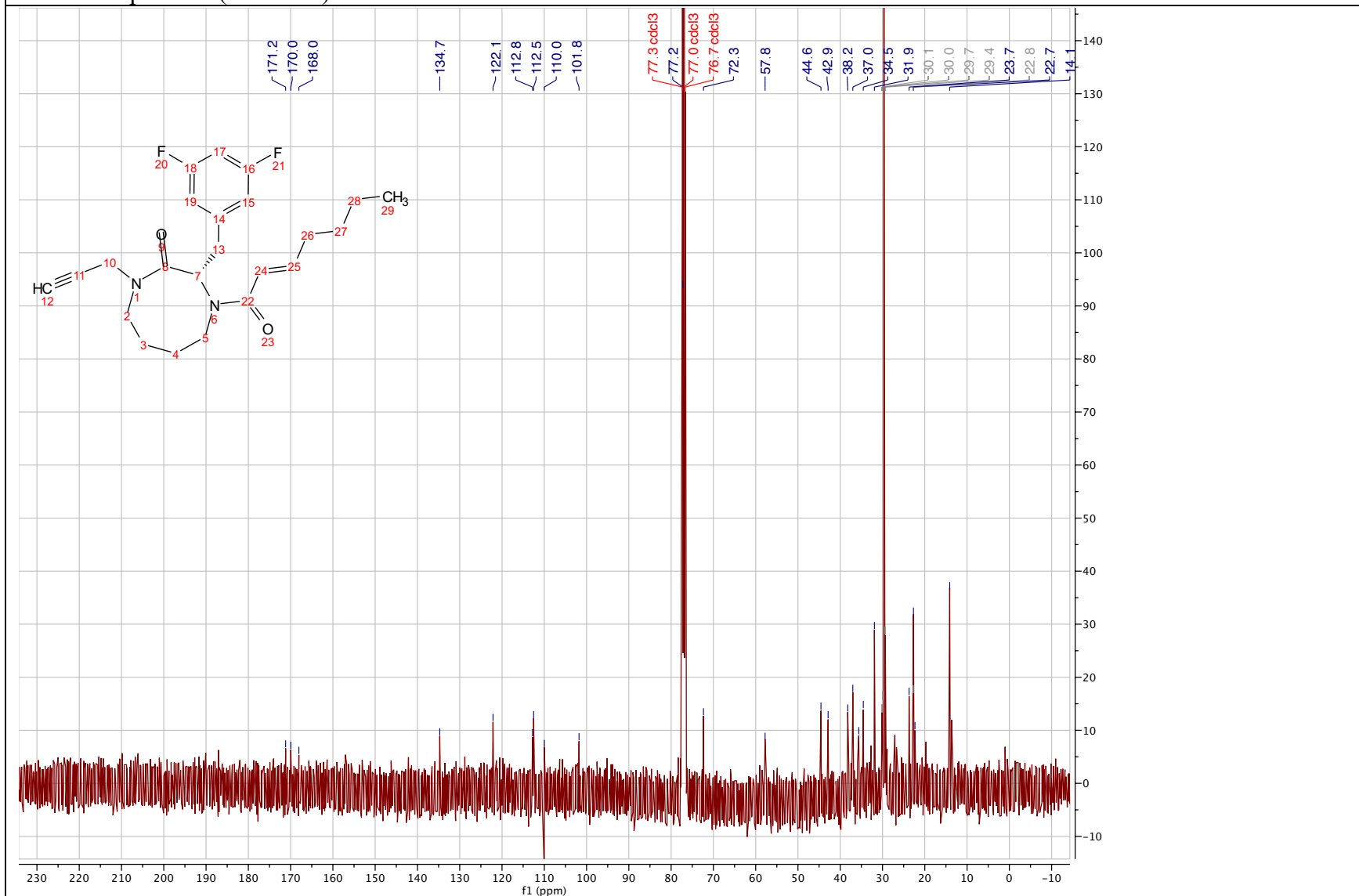
(*S,E*)-3-(3,5-difluorobenzyl)-4-(hept-2-enoyl)-1-(prop-2-yn-1-yl)-1,4-diazocan-2-one (3.27)

¹H NMR spectrum (400 MHz) in Chloroform-*d*



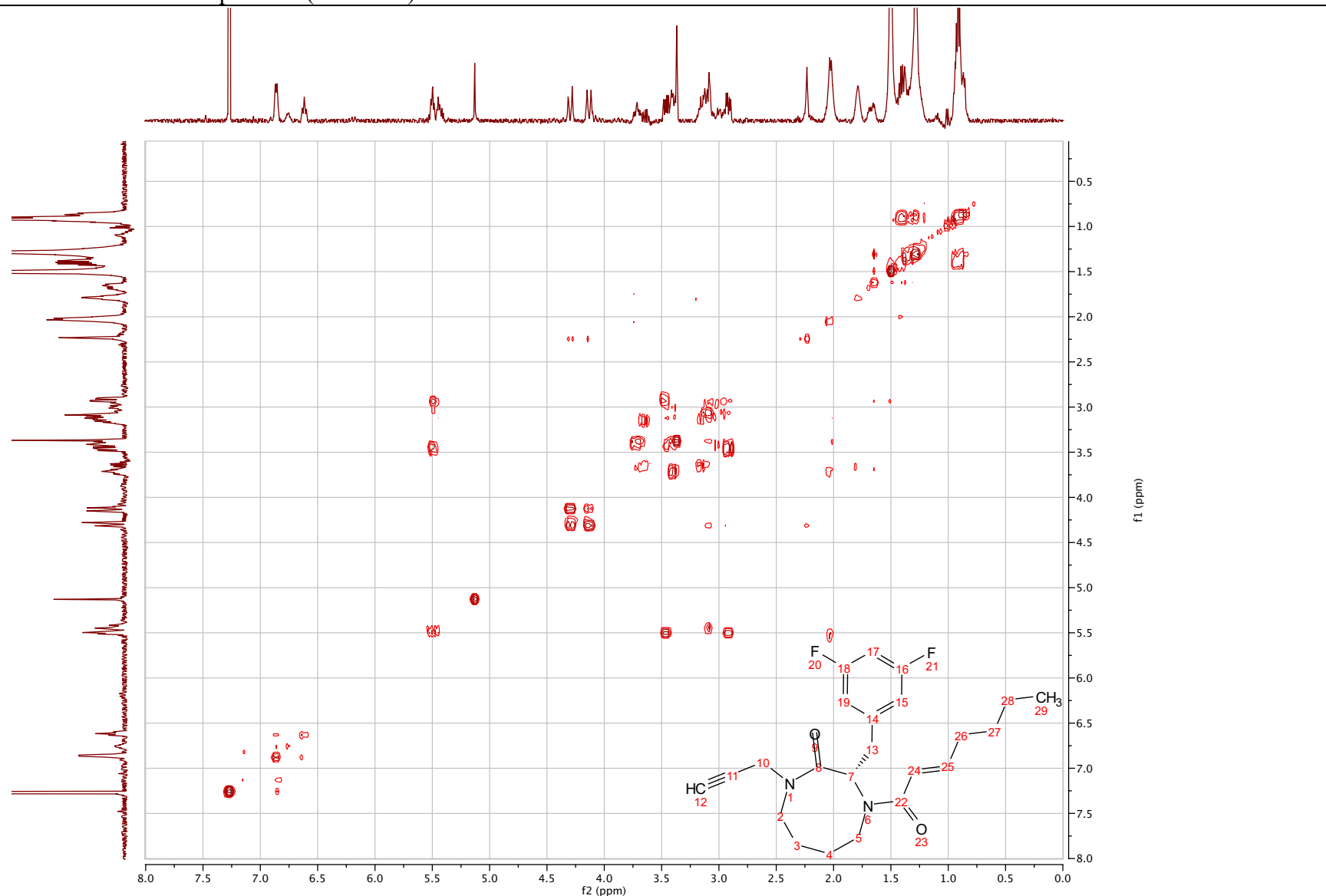
(*S,E*)-3-(3,5-difluorobenzyl)-4-(hept-2-enyl)-1-(prop-2-yn-1-yl)-1,4-diazocan-2-one (3.27)

^{13}C NMR spectrum (101 MHz) in Chloroform-*d*



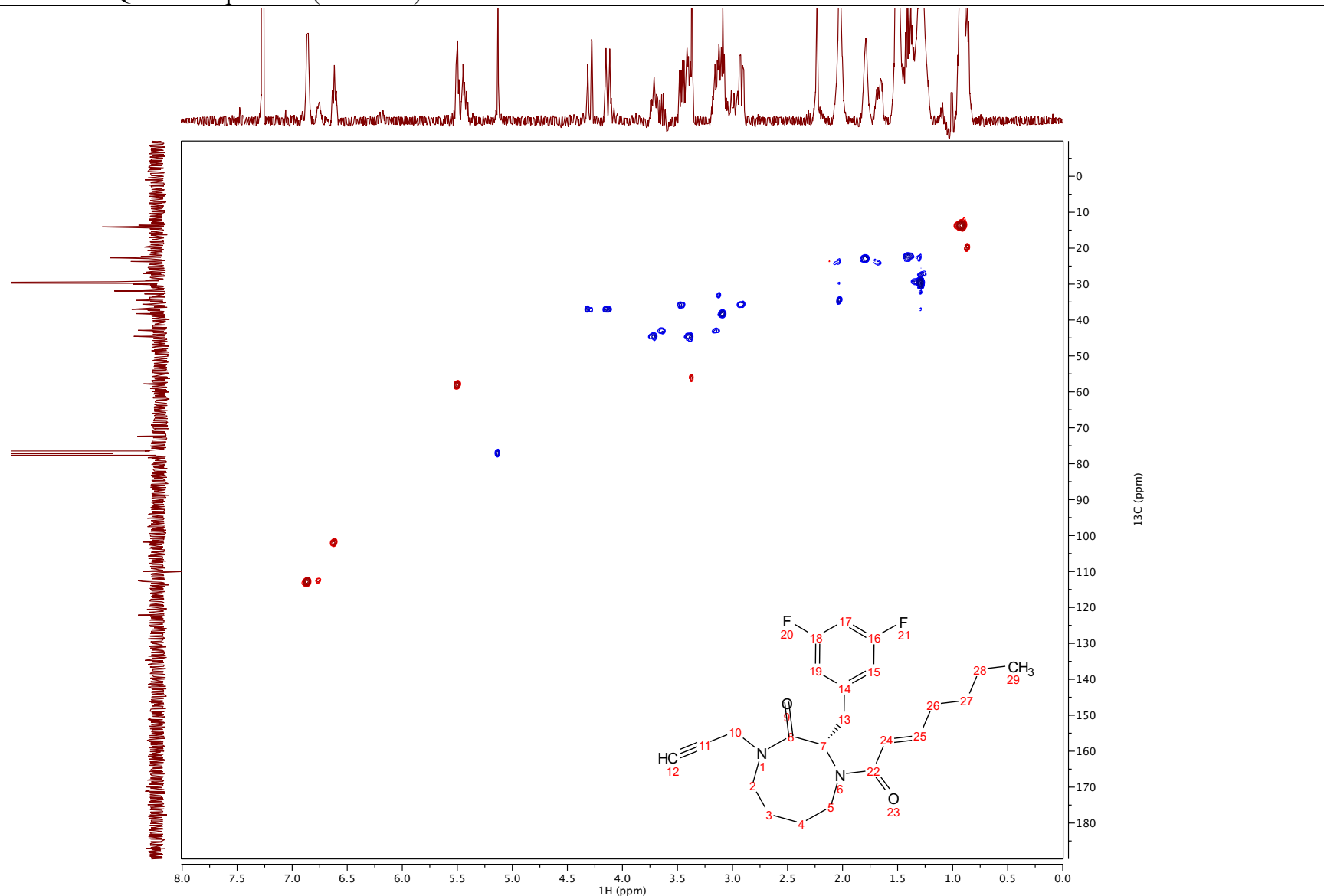
(*S,E*)-3-(3,5-difluorobenzyl)-4-(hept-2-enyl)-1-(prop-2-yn-1-yl)-1,4-diazocan-2-one (3.27)

¹H-¹H COSY NMR spectrum (500 MHz) in Chloroform-*d*



(*S,E*)-3-(3,5-difluorobenzyl)-4-(hept-2-enoyl)-1-(prop-2-yn-1-yl)-1,4-diazocan-2-one (3.27)

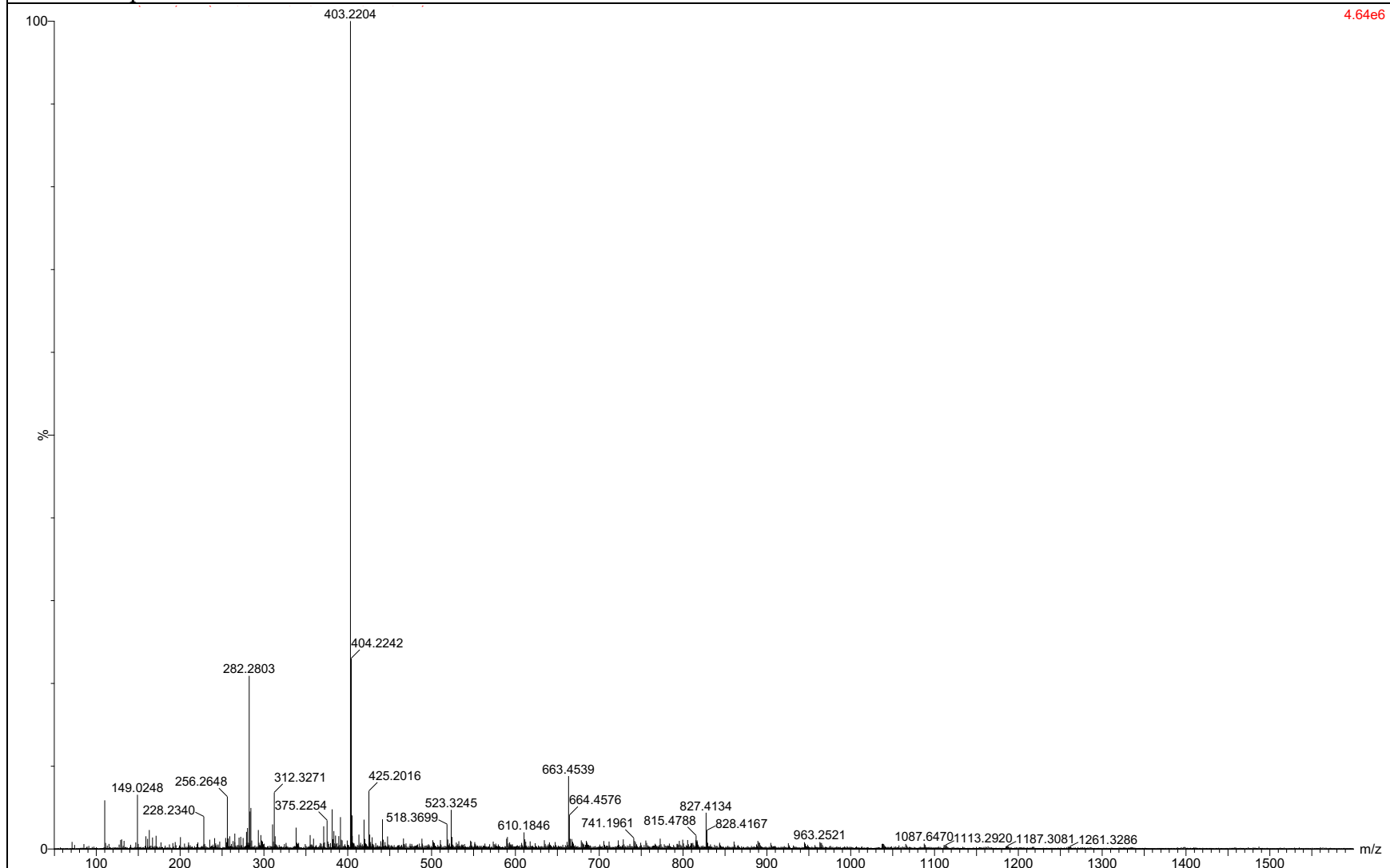
^1H - ^{13}C HSQC NMR spectrum (500 MHz) in Chloroform-*d*



(*S,E*)-3-(3,5-difluorobenzyl)-4-(hept-2-enoyl)-1-(prop-2-yn-1-yl)-1,4-diazocan-2-one (3.27)

HRESI + spectrum

4.64e6



Chapter 4 Design and Synthesis of Peptidomimetic Non-Covalent SARS-CoV-2 Main Protease Inhibitors

Abstract

The COVID-19 pandemic culminated in more than 470 million cases and six million deaths worldwide since the outbreak of SARS-CoV-2 in December 2020. These numbers along with our individual experience during the last two years make the need for antiviral treatments for coronaviruses indisputable. As the pandemic was taking hold, Jessi Gardner, Katelyn Stevens and I investigated four structurally diverse scaffolds for potential non-covalent SARS-CoV-2 Main protease (Mpro) inhibitors. Among these four scaffolds I designed by leveraging existing literature on Mpro inhibitors and hits from a large-scale crystallographic fragment screen by Diamond Light Source, I conducted docking studies to validate a piperazine scaffold. Although the piperazine scaffold was not pursued because of its poor binding to Mpro, it informed the design of a substituted piperazinone scaffold. Docking studies indicated that this scaffold engaged in multiple protein-ligand interactions with Mpro resulting in good docking scores. Since the piperazinone ring is the result of a N- to C-terminal cyclization of a “peptidic” scaffold, I also conducted docking studies of an “uncyclized” peptidic series of analogs to compare the impact of the cyclization on the binding. Although the docking score of these analogs was weaker, I synthesized a preliminary library of piperazinone and peptidic potential Mpro inhibitors setting the stage for biochemical evaluation against SARS-CoV-2 Mpro.

1 Introduction

As SARS-CoV-2 spread across the country and the number of cases increased, many campuses on the coasts closed down in early March 2020. Not only did this first wave of COVID-19 cases represent the propagation of a virus we would quickly become acquainted with, but it also demonstrated how we perceived this inexorable event that would leave us in a perpetual state of limbo. On March 16th, 2020, the University of Oklahoma reported its first COVID-19 cases, prompting a temporary closure of the Norman campus. However, due to the growing coronavirus outbreak, this temporary closure inevitably turned into a shutdown on March 24th, requiring us to stop any experiments and bringing progress in the Department of Chemistry and Biochemistry to a halt. Like many other researchers, we left our laboratory and stayed home not knowing when we would be able to go back.

Even though the new coronavirus variant stalled wet chemistry lab experiments, it did not break our scientific spirit. On March 29th, the Office of the Vice President for Research and Partnerships (OVPRP) opened applications for a Rapid Response Research Seed Grant to address the COVID-19 pandemic. With our knowledge of medicinal chemistry and our determination to go back to the lab, Jessi Gardner, Katelyn Stevens and I seized this opportunity to contribute to the pressing need for therapeutic leads – a research endeavor that countless other scientists would be involved in. Capitalizing on our expertise on bacterial proteases (i.e., caseinolytic protease P), we decided to focus on developing inhibitors of SARS-CoV-2 main protease (Mpro). Our strategy was two-fold: (1) Expand the chemical space of SARS-CoV-2 protease inhibitors by collaborating with the Scripps Research Institute (TSRI) to screen a portion of our lab legacy collection in

phenotypic viral replication inhibition assays and (2) Design and synthesize new Mpro inhibitors through *de novo in silico* approaches.

2 Coronaviruses

Coronaviruses are responsible for respiratory and enteric diseases in animals (e.g., porcine transmissible gastroenteritis virus (TGEV), avian infectious bronchitis virus (IBV), and bovine coronavirus (BCoV)) and in humans (e.g., HCoV 229E, NL63, OC43, and HKU1).¹ Human coronaviruses are the second leading cause of the common cold after rhinoviruses and are endemic globally.² Coronaviruses have been believed to only cause mild upper respiratory tract infections until late 2002 when several hundred cases of severe acute respiratory syndrome (SARS) were reported in China. Although SARS originates from horseshoe bats, human-to-human transmission was the primary means of spread, which occurred through close contact or infectious droplets and aerosols.^{1,3} The basic reproductive rate (R_0)¹ was estimated to be 2.4.⁴ A majority of cases arose through nosocomial transmission as substantial virus shedding follows the onset of symptoms, when patients are already in hospital settings.⁵ After an average incubation period of 5 days, patients start displaying influenza-like symptoms (i.e., fever over 38°C, myalgia, sore throat and gastrointestinal symptoms), which were then followed by coughing and often hypoxia requiring

¹ The basic reproduction rate (R_0) is a metric used to estimate the transmissibility of a pathogen in the population and is defined as the average number of secondary transmissions from one infected person.

ventilation in 10-20% of cases.⁶ Even though SARS-CoV was primarily detected in the kidney, liver and small intestine, the lung is the organ the most severely affected. By July 2003, the World Health Organization (WHO) declared the SARS pandemic over, which accounted for 8,096 confirmed cases, including 774 deaths across 27 countries (mortality rate = 9.6%).^{6, 7}

In June 2012, a novel coronavirus emerged in Saudi Arabia designated as Middle East respiratory syndrome (MERS). Even though cases of MERS have been reported from around the world, the major outbreaks occurred in the Arabian Peninsula and South Korea, amounting to 2,519 people contracting MERS with a 34% mortality rate.^{1, 6} With a R0 of 0.69, MERS is less transmissible than SARS, and its spread arose from contact between infected people or contact with infected dromedary camels, which are considered to be the intermediate reservoir.^{1, 8} However, MERS, which has an incubation period averaging 7 days, is more severe. In addition to fever, cough, myalgia, fatigue, vomiting and diarrhea, patient condition deteriorates rapidly resulting in an acute respiratory infection and, for >50% of cases, acute renal damage (6.6% in SARS patients).^{1, 9}

In a 2018 annual review, the World Health Organization (WHO) produced a list of diseases for which no vaccine or efficacious drug are available and are thus capable of causing a public health emergency. On this list are SARS and MERS. Notably, a so-called Disease X is also included on the list and is caused by an unidentified pathogen or a known pathogen with new epidemiological characteristics.¹⁰ The following year, cases of “pneumonia” were first reported in the Wuhan, China, which were then attributed to a new virus, SARS-CoV-2. The origins of the SARS-CoV-2 are yet to be determined and cases are suspected to have occurred in France and Italy as early as November 2019. The rapid spread across China, and eventually the world, prompted the WHO to declare SARS-CoV-2 a global pandemic on March 11th 2020.¹¹

Despite its similarities with MERS and SARS in particular, this virus differs in its higher transmissibility ($R_0 = 2.5$), milder symptoms and lower mortality rate (6.6%).^{4, 12} These distinct characteristics are what propelled this coronavirus from infecting thousands, for SARS and MERS, to infecting millions. Similar to the predecessor viruses, SARS-CoV-2 is predominantly transmitted to humans by respiratory aspirates and droplets arising from person to person proximity. While the peak of SARS viral load occurs 6-11 days after symptom onset, SARS-CoV-2 viral load is at its highest at the onset of symptoms. Consequently, mitigation of transmission is more challenging as quarantine of COVID-19 patients and determination of direct contacts needs to be carried out swiftly. Furthermore, the significant proportion of mildly affected or asymptomatic people, although hard to quantify, represents an additional factor bolstering the spread of the virus.⁴

3 Biochemistry and Replication Cycle of Coronavirus

In reference to the spike proteins projecting from the spherical virion surface, the name of coronavirus is derived from the Latin *corona*, meaning crown. Coronaviruses are part of the enveloped viruses *Coronaviridae* family and are characterized by a positive-stranded RNA genome of about 30 kb in length.^{7, 13} The recent coronaviruses are closely related, SARS-CoV-2 shares 79.5% and 50% genomic homology with SARS-CoV and MERS-CoV, respectively.¹⁴

The spike proteins have a key role in the cellular entry and viral replication of coronaviruses, they consist of two subunits. Involved in the recognition and binding to the host receptors, the S1 subunit contains the receptor binding domain, and the S2 subunit is responsible for the fusion with the host membrane.¹⁵ The angiotensin-converting enzyme 2 (ACE2) is the main

receptor of SARS-CoV and SARS-CoV-2 and is expressed on the surface of cells of the lungs, heart, kidneys, small intestine and olfactory neuroepithelium.^{1,16} Due to an insertion of four amino acid residues on the S1/S2 boundary, SARS-CoV-2 has an affinity 10-20 times higher for ACE2 than SARS-CoV, which likely accounts for the increased transmissibility of SARS-CoV-2.¹⁷ In contrast, the major host receptor for MERS-CoV is dipeptidyl peptidase 4 (DPP4), which is not only expressed in the respiratory tract, gastrointestinal tract, heart, kidney and olfactory neuroepithelium (similarly to ACE2), but also in the liver, thymus, prostate and bone marrow.¹⁸ The increased biodistribution of DPP4 leads to the heightened severity and acute renal damage observed in MERS.

The genome of coronaviruses consists of 7 to 14 open reading frames (ORFs) encoding for two polyproteins, four structural proteins and additional accessory proteins involved in interfering with the host innate immune response. Upon binding with the host receptor, the spike protein undergoes a conformational change inducing the fusion of the viral envelope with either the host plasma membrane or endosomal membrane. Subsequently, the viral RNA is released into the cytoplasm and uncoated for the translation of two ORFs (ORF1a and ORF1b) into the polyproteins (pp1a and pp1ab) constituting the viral replicase-transcriptase complex, and the remaining ORFs are transcribed into a nested set of sub genomic mRNAs.¹ The two proteases present in pp1a, the papain-like protease (PLpro) and the main protease (Mpro) – also known as 3C-like protease – auto catalytically cleave the polyproteins to produce 16 non-structural proteins (nsps).¹⁹ The resulting nsps include a RNA-dependent RNA polymerase (RdRp), a helicase (Hel) and an exonuclease (ExoN) which prevents the accumulation of detrimental mutations in the RNA genome.⁶ Assembled from nsps, the viral replicase-transcriptase complex is compartmentalized in double-membrane vesicles derived from the rough endoplasmic reticulum (ER) to organize viral

replication and evade replicating RNA from antiviral host cell response.²⁰ At the ER–Golgi intermediate compartment, the newly translated spike, envelop, membrane and nucleocapsid proteins, from sub genomic mRNAs, are then exported to the site of virus assembly to combine with genomic RNA to form virion particles. Finally, the nascent viruses are released following the fusion of the virion-containing vesicles with the host plasma membrane.⁶

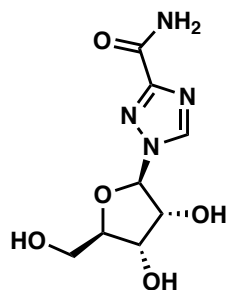
4 Rationale for the Selection of SARS-CoV-2 Target

Considering the time-constrained nature of this research project and the limited information about SARS-CoV-2, we chose to target SARS-CoV-2 main protease (Mpro) as we could build our medicinal chemistry campaign upon the existing body of knowledge on SARS-CoV Mpro. Hereafter, I review the different drugs investigated to treat COVID-19 and our rationale to select Mpro from the pool of target under investigation.

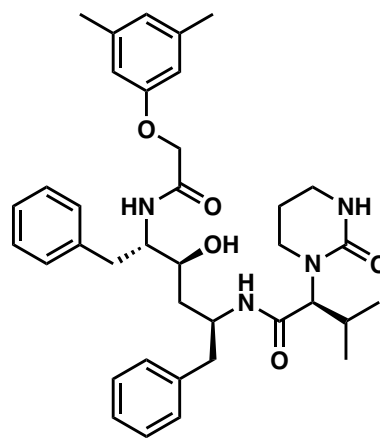
4.1 Repurposing Drugs to Treat COVID-19

In the wake of SARS and MERS, researchers and healthcare professionals have explored different therapies. However, no therapeutic treatments have been approved and clinical data lack clear efficacy, as these treatments are often administered in combination, or due to the absence of control groups. Since the SARS and MERS epidemic, several antiviral therapies have been under investigation. The broad-spectrum antiviral Ribavirin (**4.1**) has been used for both SARS and MERS in combination with corticosteroids, interferons, or with the HIV protease inhibitors Lopinavir (**4.2**) and Ritonavir (**4.3**), but the efficacy of these therapies remains unclear.⁶

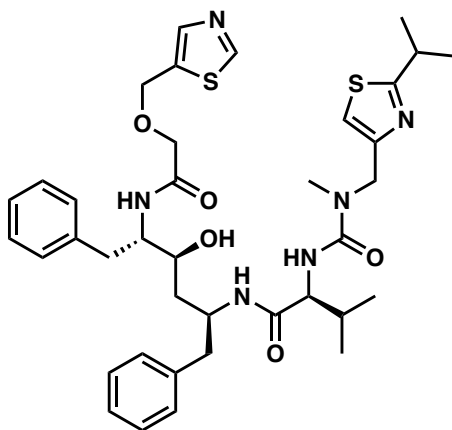
Convalescent plasma and antibody therapy were alternate approaches under consideration to treat MERS in particular. Despite promising *in vitro* and *in vivo* results, they did not translate to clinical use.²¹⁻²³



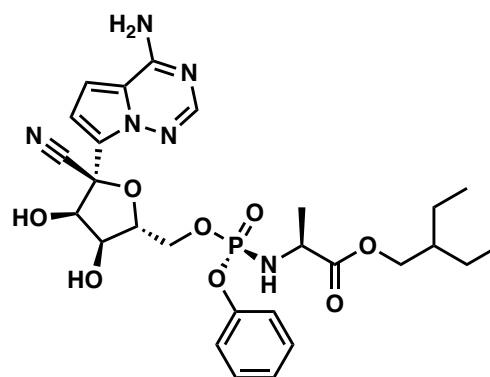
Ribavirin (4.1)



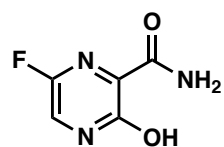
Lopinavir (4.2)



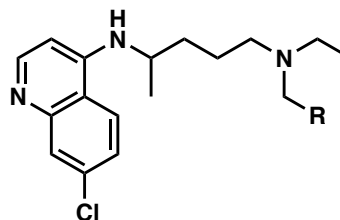
Ritonavir (4.3)



Remdesivir (4.4)

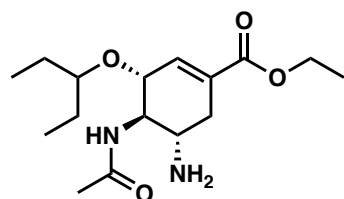


Favipiravir (4.5)

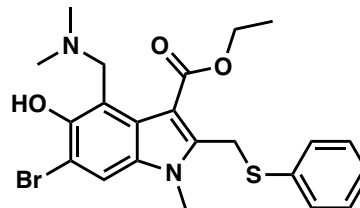


R = CH₃ Chloroquine (4.6)

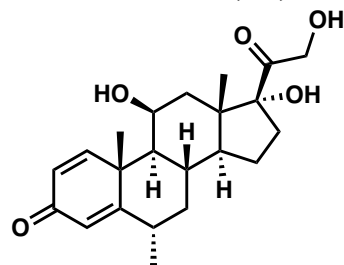
R = OH Hydroxychloroquine (4.7)



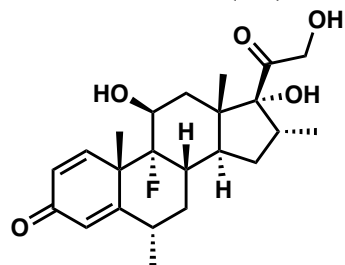
Oseltamivir (4.8)



Umifenovir (4.9)



Methylprednisolone (4.10)



Dexamethasone (4.11)

Figure 4.1: Antivirals under investigation for SARS, MERS and COVID-19.

Originally developed as a treatment against Ebola, Remdesivir (4.4) is a broad-spectrum antiviral agent that inhibits RNA-dependent RNA polymerase and the Food and Drug Agency (FDA) approved an ‘emergency use authorization’ for patients with severe COVID-19 in May 2020.^{24, 25} When administered intravenously, Remdesivir (4.4) demonstrated improvement of recovery time by 31% but did not reduce the mortality rate. However, adverse effects have been reported such as hepatotoxicity, nausea and acute respiratory failure in over 10% of patients.²⁴ Favipiravir (4.5) is another promising selective inhibitor of RNA-dependent RNA polymerase, as preliminary clinical data showed improvement in viral clearance and reduction of symptoms (i.e., fever, cough and respiratory problems) against COVID-19.²⁶ However, the positive effect on the recovery rate was predominantly observed in non-critical COVID-19 patients and further clinical trials are underway to assess the potential of Favipiravir in more advanced patients.^{27, 28} Early hope and publicity around chloroquine (4.6) and hydroxychloroquine (4.7) prompted the FDA to allow emergency use for patients hospitalized with COVID-19 on March 28, 2020. Although the lack of anti-viral effect against COVID-19, combined with the risk of heart arrhythmias led reconsideration

by the FDA who issued a safety warning regarding the use of chloroquine and hydroxychloroquine for COVID-19 due to associated risks.^{29, 30} Other antiviral agents such as Oseltamivir (**4.8**), Umifenovir (**4.9**), Lopinavir-Ritonavir (**4.2/4.3**) and Ribavirin (**4.1**) failed to improve outcomes in COVID-19 patients.³¹⁻³⁴ An alternative avenue for COVID-19 therapies is the use of corticosteroids in order to limit lung damage by reducing systemic inflammation.³² While the glucocorticoid methylprednisolone (**4.10**) lacked clear clinical efficacy, dexamethasone (**4.11**) was found to decrease the mortality rate, in particular among patients on ventilators.^{35, 36}

4.2 Current Research to Target SARS-CoV-2

Despite the efforts to repurpose drugs for the treatment of COVID-19, the FDA has not approved any therapeutic treatment for COVID-19 as of the writing of this dissertation. Given that SARS-CoV-2 and SARS-CoV share 79.5% sequence identity and 94.6% sequence identity in ORF1a/b, previous research on SARS-CoV have the potential to translate to SARS-CoV-2.^{14, 37} Specifically, two distinct avenues for therapeutic development for SARS-CoV and SARS-CoV-2 have been under investigation: blocking virus entry and inhibition of the replication-transcription complex.

4.2.1 Blocking Virus Entry

Because of its crucial role in viral entry into the host cell, the SARS-CoV-2 spike glycoprotein represents an attractive target. Following the recognition of the S protein by the ACE2 receptor, host proteases promote virus–host cell membrane fusion by cleaving the spike protein.¹⁵

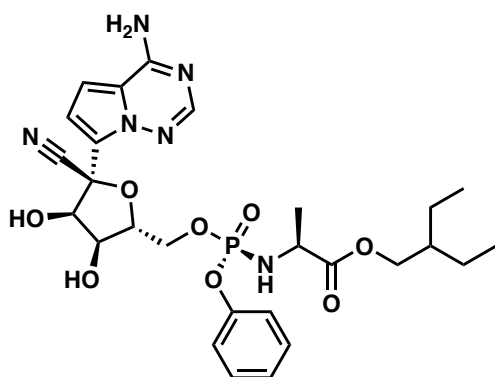
Although different human proteases are involved in the virion endocytosis, the transmembrane serine protease 2 (TMPRSS2) is a promising target, as studies showed that inhibition reduced the entry of SARS-CoV-2. Camostat mesylate is a serine protease inhibitor approved for clinical use in Japan, and recently, it has demonstrated *in vitro* activity against TMPRSS2 and blocked virus entry.³⁸ Because of the lack of crystal structures combined with the challenge of selectively inhibiting a host protease, TMPRSS2 is not an accessible drug target. Even though preventing the entry of the virus is an intuitive therapeutic avenue, the high probability of mutations in the S protein along with the difficulty of selectively targeting human ACE2 receptor and proteases pose significant roadblocks.

4.2.2 Inhibition of the Replication-Transcription Complex

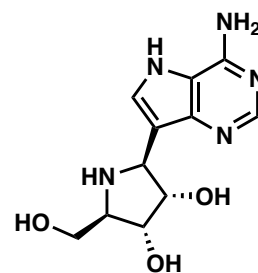
4.2.2.1 Targeting RNA-Dependent RNA Polymerase

Alternatively, the non-structural proteins involved in the replication-transcription complex represent promising targets, as they are highly conserved, and no human counterpart exist. RNA-Dependent RNA Polymerase (RdRp) is one such protein, responsible for replication and transcription of viral RNA genome with 96% sequence identity between SARS-CoV and SARS-CoV-2.³⁹ Among viral polymerase inhibitors there are two main categories, the nucleoside inhibitors (NIs), which target the RdRp substrate site, and the non-nucleoside inhibitors (NNIs), which interact with allosteric binding sites.⁴⁰ So far, the repurposing of known broad spectrum NIs has shown some encouraging clinical results in treating COVID-19 patients, while no NNIs have been reported to display antiviral activity against SARS-CoV-2 infections.⁴⁰ Leveraging the structural similarity with nucleobases, NIs inhibit RdRp activity via substrate recognition and their

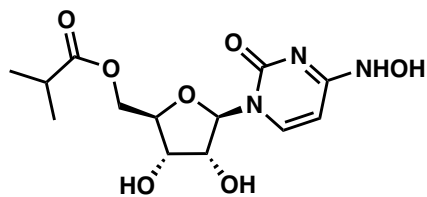
incorporation disrupts the nascent RNA structure or lead to lethal mutagenesis. RdRp inhibitor candidates can be classified as adenine (Remdesivir, **4.4** and Galidesivir, **4.12**, **Figure 4.2**), guanine (Favipiravir, **4.5**, **Figure 4.2**), and cytosine (EIDD-2801, **4.13**, **Figure 4.2**) analogs.^{41, 42} Despite the apparent druggability of RdRp and the extensive structural data available, this target remains underexplored in the context of SARS-CoV-2.⁴⁰ In addition, the proofreading activity of exonuclease decreases the efficacy of the nucleotide analogs by removing mismatches.⁴³ Therefore, RdRp does not appear to be an ideal target for the type of short medicinal chemistry project we wanted to conduct.



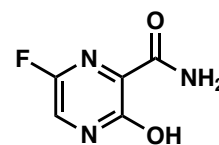
Remdesivir (4.4)



Galidesivir (4.12)



EIDD-2801 (4.13)



Favipiravir (4.5)

Figure 4.2: SARS-CoV-2 RdRp inhibitors under investigation.

4.2.2.2 Targeting Papain-like Protease and Main Protease

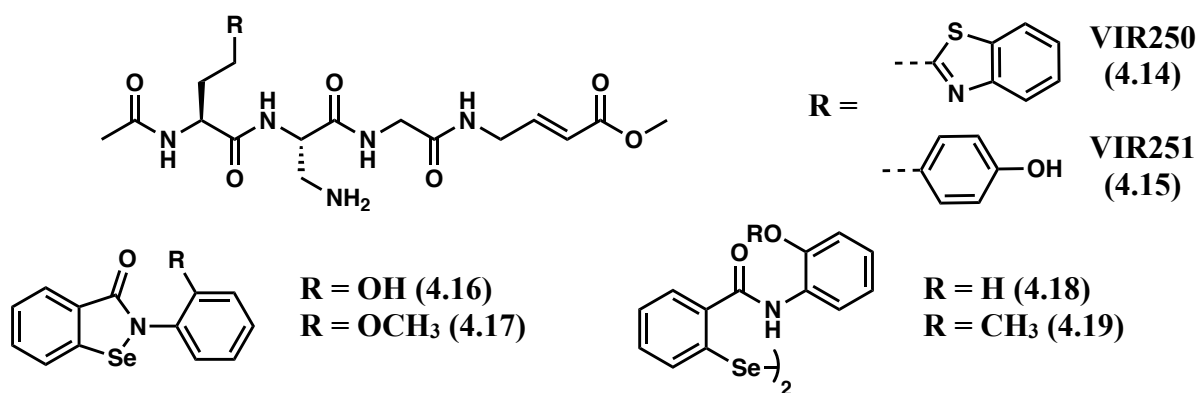
As mentioned above, SARS-CoV-2 encodes for 2 cysteine proteases the papain-like protease (PLpro) and the main protease (Mpro). The main function of these proteases is to cleave

the polyproteins (pp1a and pp1ab) into structural and non-structural proteins necessary for the viral replication. Interestingly, no human proteases sharing similar cleavage specificity have been identified, making inhibition of PLpro and Mpro promising targets for antiviral therapy.⁴⁴⁻⁴⁶ Even though Mpro processes pp1a/pp1ab in more sites than PLpro, (11 versus 3, respectively), the proteolytic activity of PLpro extends to ubiquitin and the ubiquitin-like interferon-induced gene 15 (ISG15). On one hand, this additional proteolytic function on host cell proteins make PLpro a compelling target as it interferes with the innate immune response against viral infection by preventing the production of important cytokines.⁴⁷ On the other hand, inhibition of PLpro introduces a risk for inhibiting host-cell deubiquitinases, leading to potential detrimental side effects.⁴⁸ Because PLpro is less conserved than Mpro between SARS-CoV and SARS-CoV-2, 83% and 96% sequence identity respectively, it is unclear if SARS-CoV PLpro inhibitors are active against the SARS-CoV-2 counterpart.

Inhibition of either Mpro or PLpro can be achieved by targeting the catalytic cysteine-histidine dyad and two main strategies have been employed: (1) Inhibition by covalent modification of the cysteine; (2) Non-covalent inhibition of the dyad. Covalent inhibition of Mpro and/or PLpro relies on the nucleophilic attack of cysteine on an electrophilic reactive group and, based on the nature of the “warhead”, the bond can be reversible (e.g., ketone, aldehyde, α -fluoro ketone, α -ketoamide) or irreversible (e.g., michael acceptor, epoxide, aza-epoxide, heterocyclic esters).⁴⁹

A prominent approach to inhibit proteases is to introduce a warhead into a peptidic substrate. As such, the high selectivity of the inhibitor promotes the binding to the protease active site, consequently allowing the cysteine to attack the electrophilic moiety. On this basis, Rut W. et al. developed two tetrapeptides with a vinyl ester warhead, VIR250 (**4.14, Figure 4.3**) and

VIR251 (**4.15**, **Figure 4.3**), displaying an IC_{50} value of approximately $10 \mu\text{M}$ against SARS-CoV and SARS-CoV-2 PLpro.^{40, 50} So far, a limited amount of non-peptidomimetic PLpro inhibitors have been discovered. Notably, the seleno-organic compounds (**4.16**, **4.17**, **4.18** and **4.19**, **Figure 4.3**) have been reported to irreversibly inhibit SARS-CoV-2 PLpro at a submicromolar IC_{50} .⁵¹ Alternatively, the deubiquitinase function of PLpro has been targeted with naphthalene-based compounds, such as GRL-0617 (**4.21**, **Figure 4.3**), through non-covalent interactions with a distal pocket of the active site. However, GRL-0617 (**4.21**) demonstrated IC_{50} and EC_{50} values in the low micromolar range.⁵² Recently, Shen Z. et al reported compounds XR8-23 (**4.22**, **Figure 4.3**) and XR8-24 (**4.23**, **Figure 4.3**), which exhibit improved inhibitory and antiviral activity in biochemical and cell-based assays, compared to the parent molecule, GRL-0617 (**4.21**).⁵³ Despite the potential of PLpro as an antiviral target, it has been less studied relatively to Mpro and no potent inhibitors are yet available in the clinic. Consequently, Mpro represents a more tractable target and one that we gravitated towards for this research project.



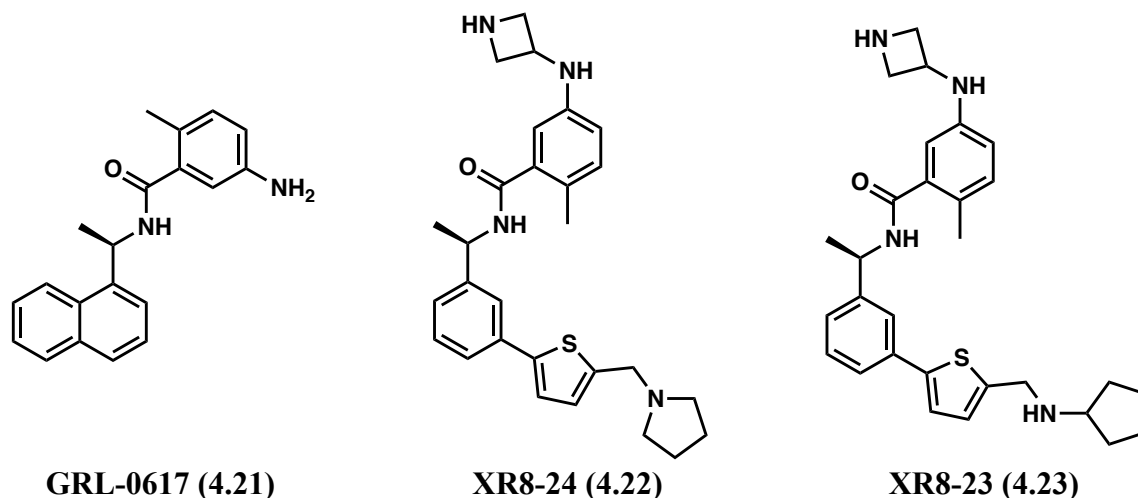


Figure 4.3: SARS-CoV-2 PLpro inhibitors under investigation.

In its active form, Mpro is organized as a dimer with each monomer comprising three domains: domains 1 (residues 10-99) and 2 (residues 100-182) are six-stranded antiparallel β -barrels and domain 3 (residues 198-303) is a cluster of five α -helices (**Figure 4.4**).⁵⁴ Dimerization occurs through a salt-bridge between N-terminal residues of each parent monomer with the domain 2 of the other monomer (**Figure 4.5**) and this interaction is essential for the active conformation of the substrate-binding site.⁵⁵ The active site of Mpro is located in a cleft between domains 1 and 2 and consists of five sub-pockets, as determined by the binding of the native polyprotein substrate (**Figure 4.6**). The proteolytic cleavage of polyprotein substrates occurs at Leu-Gln↓(Ser, Ala, Gly) (↓ indicates the cleavage site). This site is conserved in main proteases of other coronaviruses and enteroviruses, but this specificity has not been observed for human proteases.^{44-46, 56}

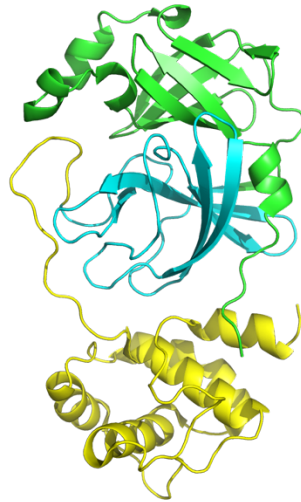


Figure 4.4: Mpro monomer. Domain 1 in green, Domain 2 in cyan and Domain 3 in yellow.

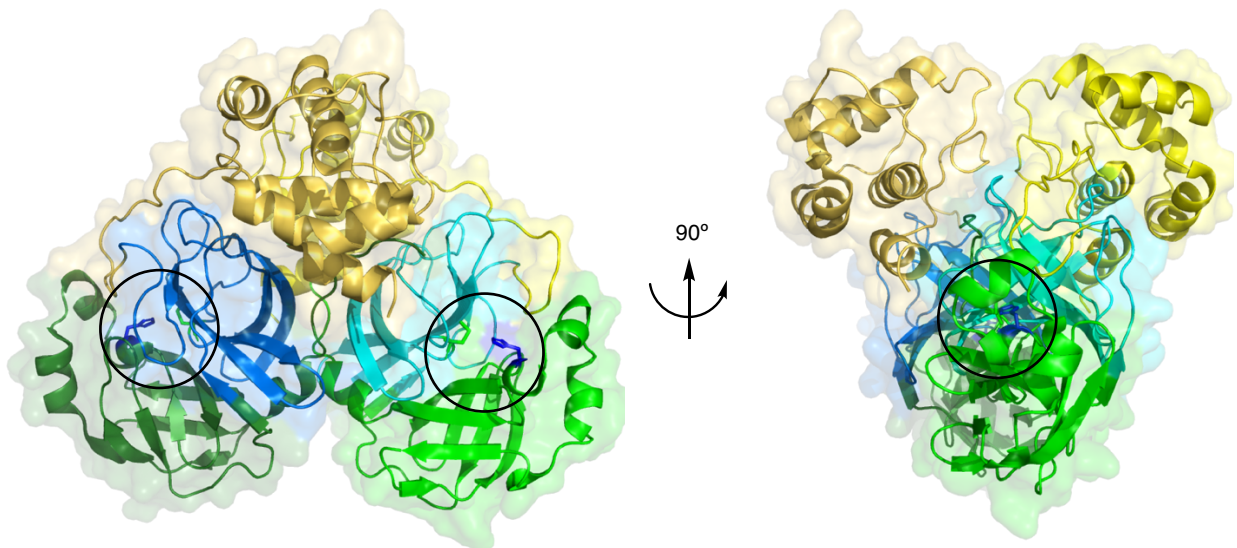
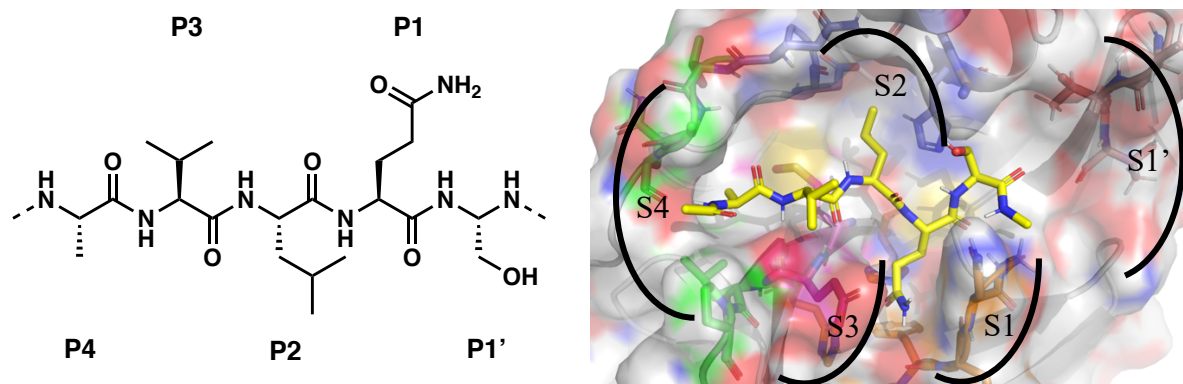


Figure 4.5: Structure of dimeric SARS-CoV-2 Mpro. The catalytic dyad is circled in black highlighting Cysteine 145 in green and Histidine 41 in marine blue (PDB: 1UK4).

a.

b.



c.

Subsite	S1'	S1	S2	S3	S4
Residues subsite	Thr24 Thr25 Thr26 Gly143 Cys145	Phe140 Phe140(bb) Leu141(bb) Asn142 Glu166 His163 His172	His41 Met49 Met165 Asp187(bb) Gln189	Met165 Glu166 (bb) Leu167 Pro168	Gln189 Thr190 Ala191 Gln192
Residue substrate	P1'	P1	P2	P3	P4

Figure 4.6: SARS-CoV-2 Mpro active site pocket. (a) Representative example of SARS-CoV-2 protein substrate. (b) Surface representation of the active site of SARS-CoV-2 Mpro bound to a protein substrate.⁵⁷ (c) Summary table of SARS-CoV-2 Mpro residues for each subsite of the binding pocket. (bb) = backbone.

The development of covalent inhibitors has demonstrated that it is an effective approach enzyme inhibition, despite the presumed risks associated with reactive electrophilic moieties in biological systems.⁵⁸ The design of such inhibitors is based on the structure of polyprotein segment binding in the active site of Mpro and several covalent SARS-CoV-2 Mpro inhibitors have been reported with low micromolar to nanomolar IC₅₀s and EC₅₀s.^{46, 59, 60} As exemplified in **Figure 4.7**, these newly developed compounds share the same core structure: the “warhead” (denoted X in **Figure 4.7**) is oriented in the subsite S1' to be attacked by Cys145; the (S)- γ -lactam ring is a rigid bioisotere of glutamine and occupies the S1 site; the S2 site can accommodate a large and hydrophobic residue; the terminal substituent is often an aryl or heteroaryl group involved in hydrogen bonding with the residues of the S4 subsite.⁶⁰

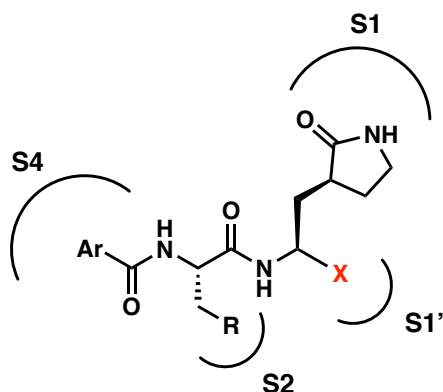
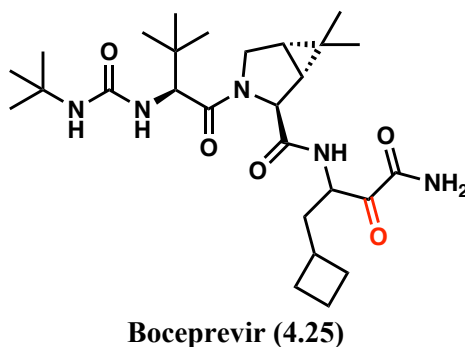
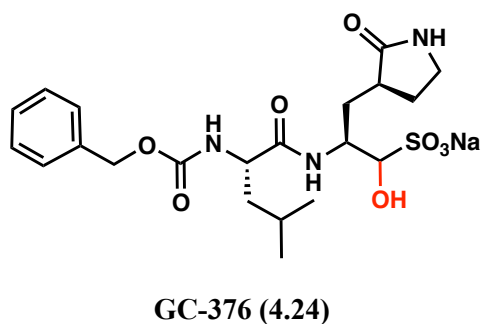
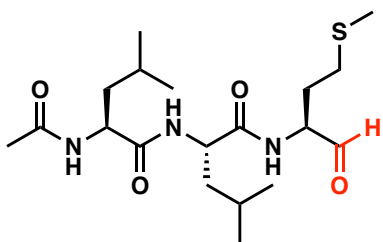


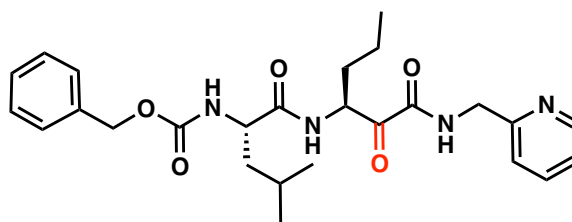
Figure 4.7: General structure of covalent SARS-CoV-2 Mpro inhibitors.

Drug repurposing has been a one of the main avenues to quickly identify novel antiviral therapies for COVID-19. Being as repurposed drugs are already FDA-approved, and have a known safety and pharmacokinetic profile, follow-up studies can be expedited for clinical use. A significant study by Ma C. et al reported four drugs with SARS-CoV-2 Mpro inhibitory activity (**Figure 4.8**): (1) GC-376 (**4.24**), a veterinary drug, with IC_{50} of $0.03 \mu\text{M}$ and EC_{50} of $3.37 \mu\text{M}$; (2) Boceprevir (**4.25**), a hepatitis C drug, with IC_{50} of $4.13 \mu\text{M}$ and EC_{50} of $1.90 \mu\text{M}$; (3) Calpain inhibitor II (**4.26**) showing IC_{50} of $0.97 \mu\text{M}$ and EC_{50} of $2.07 \mu\text{M}$; (4) Calpain inhibitor XII (**4.27**) displaying IC_{50} of $0.45 \mu\text{M}$ and EC_{50} of $0.49 \mu\text{M}$.⁶¹





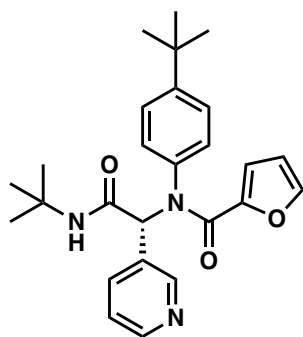
Calpain inhibitor II (4.26)



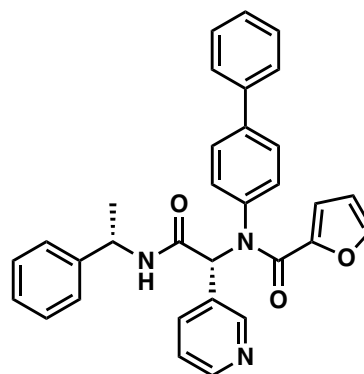
Calpain inhibitor XII (4.27)

Figure 4.8: Reversible covalent SARS-CoV-2 Mpro inhibitors. The functional groups in red are the warheads.

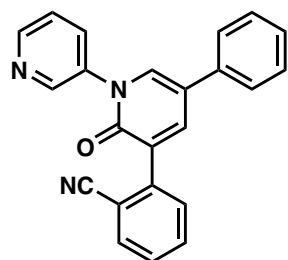
Even though the development of covalent inhibitors has shown some successes as described above, its counterpart approach, the identification of non-covalent inhibitors, has yielded compounds active against SARS-CoV-2 Mpro as well. From a structure-based design study of ML188 (4.28, non-covalent, **Figure 4.9**) and Calpain inhibitor XII (4.27, covalent, **Figure 4.8**), Kitamura N. et al utilized an Ugi multi-component reaction to produce a library of 40 compounds. This approach expedited SAR studies and produced compound 4.29 which inhibits the proteolytic activity of SARS-CoV-2 Mpro ($IC_{50} = 0.31 \mu M$) and SARS-CoV-2 viral replication ($EC_{50} = 1.27 \mu M$).⁶²



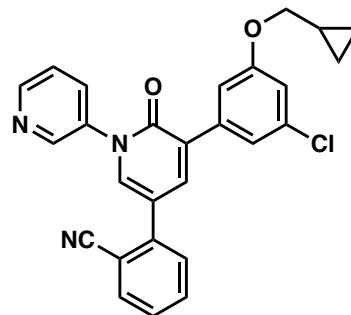
ML188 (4.28)



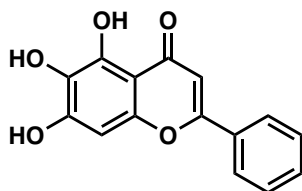
4.29



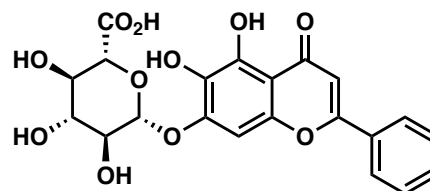
Perampanel (4.30)



4.31



Baicalein (4.32)



Baicalin (4.33)

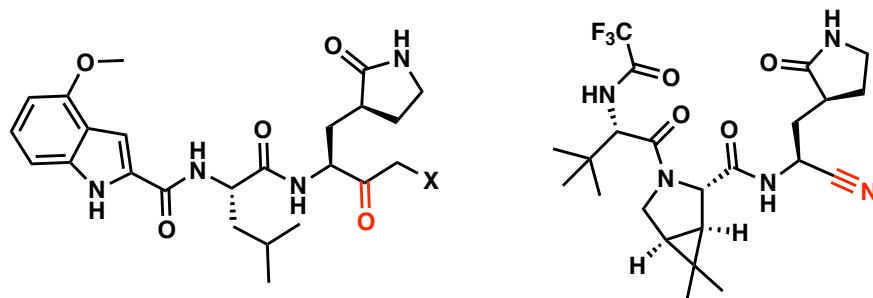
Figure 4.9: Non-covalent SARS-CoV-2 Mpro inhibitors.

Separately, a virtual screen of 2000 drugs resulted in the identification of 14 small molecules, out of which Perampanel (**4.30**, **Figure 4.9**), an anti-epileptic drug with micromolar inhibitory activity against Mpro, was selected for further redesign. Free-energy perturbation (FEP) calculations of the predicted pose of **4.30** in complex with Mpro directed the structural optimization, leading to compound **4.31** with a 100-fold increase in the inhibitory activity against SARS-CoV-2 Mpro. In addition, **4.31** displayed an EC_{50} of 1 μ M in a cell-based assay and no cytotoxicity against Vero E6 and normal human bronchial epithelial cells (up to 100 μ M).⁶³

Illustrating the structural diversity of chemotypes with inhibitory activity against SARS-CoV-2 Mpro, the flavone Baicalein (**4.32**, **Figure 4.9**) and its glucuronide analogue Baicalin (**4.33**, **Figure 4.9**) have shown IC_{50} s of 0.94 μ M and 6.41 μ M, respectively.⁶⁴ The low micromolar antiviral activity (EC_{50} = 1.69 μ M) and the lack of toxicity (CC_{50} > 200 μ M) paired with its existing

use as an adjuvant therapy for hepatitis and influenza fever make Baicalein a promising antiviral candidate.^{65, 66}

Following the SARS pandemic, Pfizer discovered PF-07304814 (**4.34**, **Figure 4.10**), a phosphate prodrug that is converted *in vivo* by alkaline phosphatase enzymes into the active compound PF-00835231 (**4.35**, **Figure 4.10**). Even though PF-07304814 (**4.34**) acts as a broad-spectrum coronavirus reversible covalent inhibitor and demonstrated potent antiviral activity *in vivo*, the sudden decline of the SARS outbreak put the project on hold.⁶⁷ The COVID-19 crisis allowed Pfizer to resurrect PF-07304814 (**4.34**) and the clinical trial started September 2020. This candidate, however, requires intravenous administration, restricting its use to hospital settings and the predicted effective dose (i.e., 500mg/day) is high. In April 2021, Pfizer revealed a promising alternative Mpro inhibitor, PF-07321332 (**4.36**). Following the Emergency Use Authorization issued by the FDA, PF-07321332 (**4.36**) “boosted” with Ritonavir (**4.3**) is available in a pill form for the treatment of patients over the age of 12 with mild to moderate COVID-19 and at high risk of severe symptoms.⁶⁸ Although PF-07321332 (**4.36**) was unknown to us when we started this research project, the success of the drug development program validates our rationale to choose SARS-CoV-2 Mpro as the target to pursue.



PF-07304814 (prodrug) X = PO₄H₂ (**4.34**) PF-07321332 (**4.36**)
PF-00835231 (drug) X = OH (**4.35**)

Figure 4.10: Pfizer's reversible covalent SARS-CoV-2 Mpro inhibitors.

5 Design of SARS-CoV-2 Mpro Non-Covalent Inhibitors

5.1 Structural Analysis of Mpro Non-covalent Inhibitors

As mentioned, covalent Mpro inhibitors have been extensively studied and numerous compounds based on a common scaffold (**Figure 4.7**) have been developed, with an inhibitor having reached patients, PF-07321332 (**4.36**, **Figure 4.10**). In contrast, non-covalent Mpro inhibitors remain in the early stage of drug development even though diverse hit scaffolds have been identified. We decided to focus our efforts on the design and synthesis of non-covalent inhibitors of SARS-CoV-2 Mpro.

Notably, a peptidomimetic core has been the subject of structural optimization to improve potency against SARS-CoV Mpro and recently SARS-CoV-2 Mpro. The original hit of this chemotype, ML188 (**4.28**, **Figure 4.9**) exhibited IC_{50} of 11.23 μ M and 10.96 μ M against Mpro of SARS-CoV and SARS-CoV-2, respectively. In contrast to the (S)- γ -lactam ring of covalent Mpro inhibitors (**Figure 4.7**), which acts as a hydrogen bond donor with His163, the pyridyl group of ML188 (**4.28**) acts as a hydrogen bond acceptor (**Figure 4.11**). ML188 (**4.28**) is engaged in two additional hydrogen bonds: (1) The oxygen atoms of the furyl amide provide a bifurcated interaction with the Gly-143 backbone; (2) The backbone of Glu166 interacts the carbonyl of the *tert*-butyl amide (**Figure 4.11**).⁶⁹ The 4-*tert*-butylanilido group and *tert*-butyl amide occupy the S2 and S3 subsites, respectively, without participating in specific interactions with the pocket. This observation prompted a follow-up study focusing on the S2 and S3 subsites, resulting in analog **4.29** (**Figure 4.11**). Substitution of the *tert*-butyl group of the terminal amide with α -methylbenzyl moiety on the terminal amide accessed the S2 and S3 pockets. Due to the chirality and hydrophobic nature of the α -methylbenzyl moiety, the benzyl ring is projected towards S2 leading to an

intramolecular π - π stacking with the first phenyl of the biphenyl substituent. The authors proposed that through this intramolecular π - π stacking, the biphenyl group projects deeper into the S2 pocket, potentially contributing to the improved inhibitory activity of **4.29**, $IC_{50} = 0.27 \mu\text{M}$ and $IC_{50} = 0.31 \mu\text{M}$ in enzymatic assay against Mpro of SARS-CoV and SARS-CoV-2, respectively.⁶²

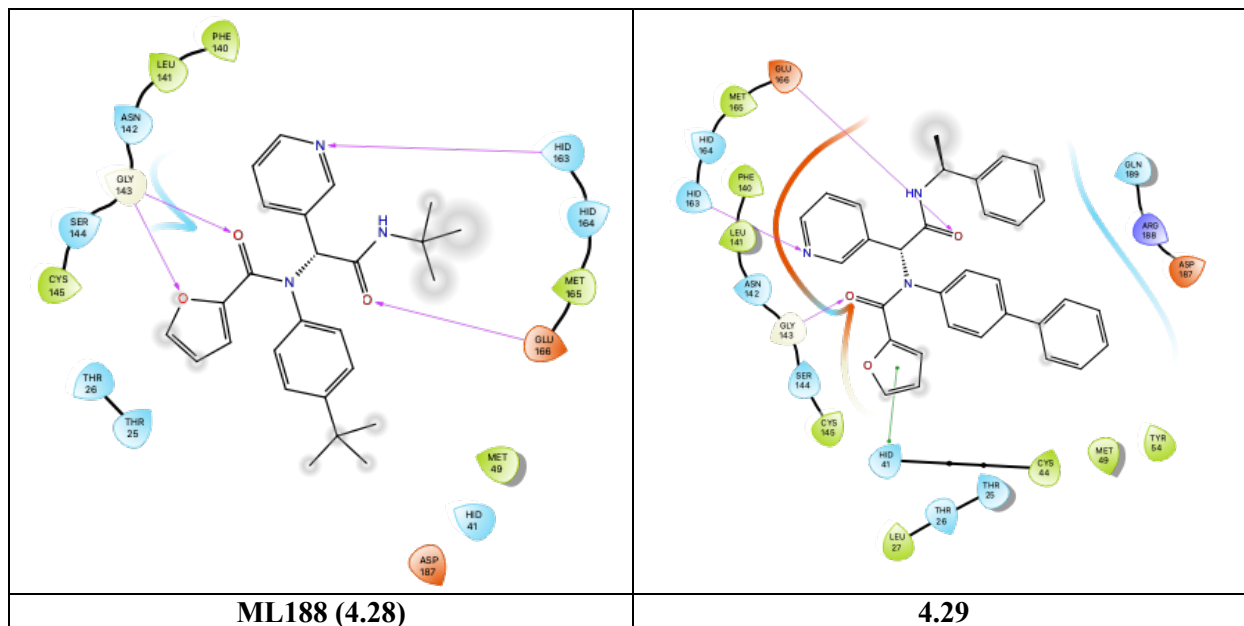


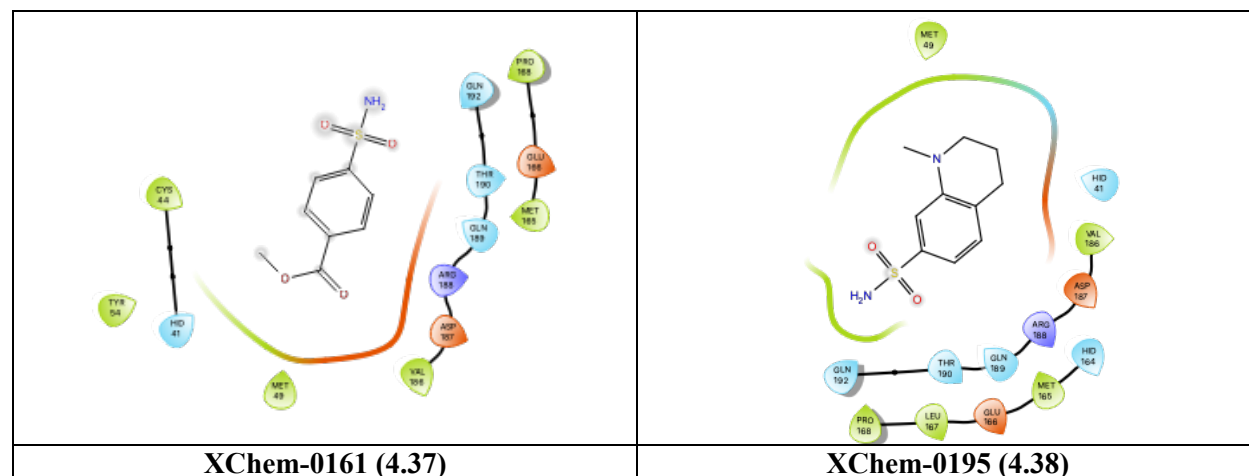
Figure 4.11: 2D ligand interaction diagram of the co-crystal structure of ML188 (4.28) in SARS-CoV Mpro (PDB: 3V3M) and 4.29 in SARS-CoV-2 Mpro (PDB: 7KX5).

5.2 Structural Analysis of XChem Fragment Library

As the scientific community focused on addressing the COVID-19 crisis, a plethora of new resources and data became available setting the stage for us to contribute to the research effort. In particular, the United Kingdom's national synchrotron, Diamond Light Source, produced an apo-structure of SARS-CoV-2 Mpro (PDB: 6YB7) and conducted a large-scale crystallographic fragment screen against the coronavirus protein. From the 1500-crystal experiment, 74 hits were identified, which included 22 non-covalent and 48 covalent hits in the active site of Mpro, and 3

hits in the dimer interface.⁶⁸ This gave me the opportunity to design novel inhibitors by merging fragments or improving upon known scaffolds by introducing moieties from these screening hits. Even though these fragments were shown to bind to the active site of Mpro, no enzymatic assay has been conducted. Therefore, an important caveat for the analysis of the hits was to recognize that I was pursuing known binders with unknown activity.

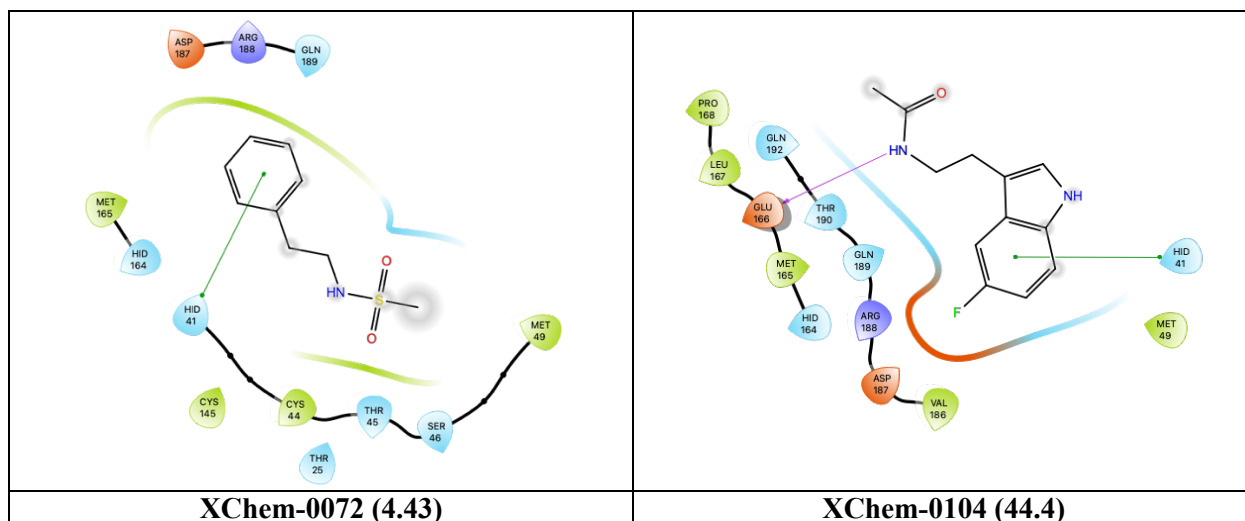
Among the 22 non-covalent hits, one fragment (XChem-0991 – **4.42**) was not considered as the molecular weight was under 100 g/mol. In addition, XChem-0991 (**4.42**) along with XChem-0161 (**4.37**), -0195 (**4.38**), -0354 (**4.39**), -0395 (**4.40**) and -0946 (**4.41**) (**Table 4.1**) were excluded because no relevant interactions between this fragment and the binding pocket was reported (i.e., hydrogen bonding, π - π stacking, ...).



(His41)	XChem-0387 (4.46)* XChem-1077 (4.48)*		XChem-1249 (4.49)
S3 (Glu166-bb)		XChem-0107 (4.50)** XChem-1093 (4.55)	XChem-0104 (4.44) XChem-0874 (4.47)

Table 4.2: Summary of the binding subsites of the 16 XChem hits. * denotes the binding of fragments in S1' without interacting with the backbone of Gly143 via hydrogen bonding. ** denotes the binding of fragments in S3 without interacting with the backbone of Glu166 via hydrogen bonding.

A majority of hits interact with His41 through T-shaped π - π stacking or hydrophobic contact, suggesting that they have an inhibitory potential as this residue is critical for the proteolytic activity of Mpro. Therefore, observation of this key interaction from a number of fragments informed us of moieties (i.e., phenyl, indolyl, pyridyl, thiophenyl) conducive to the binding in the S2 pocket (Table 4.3).



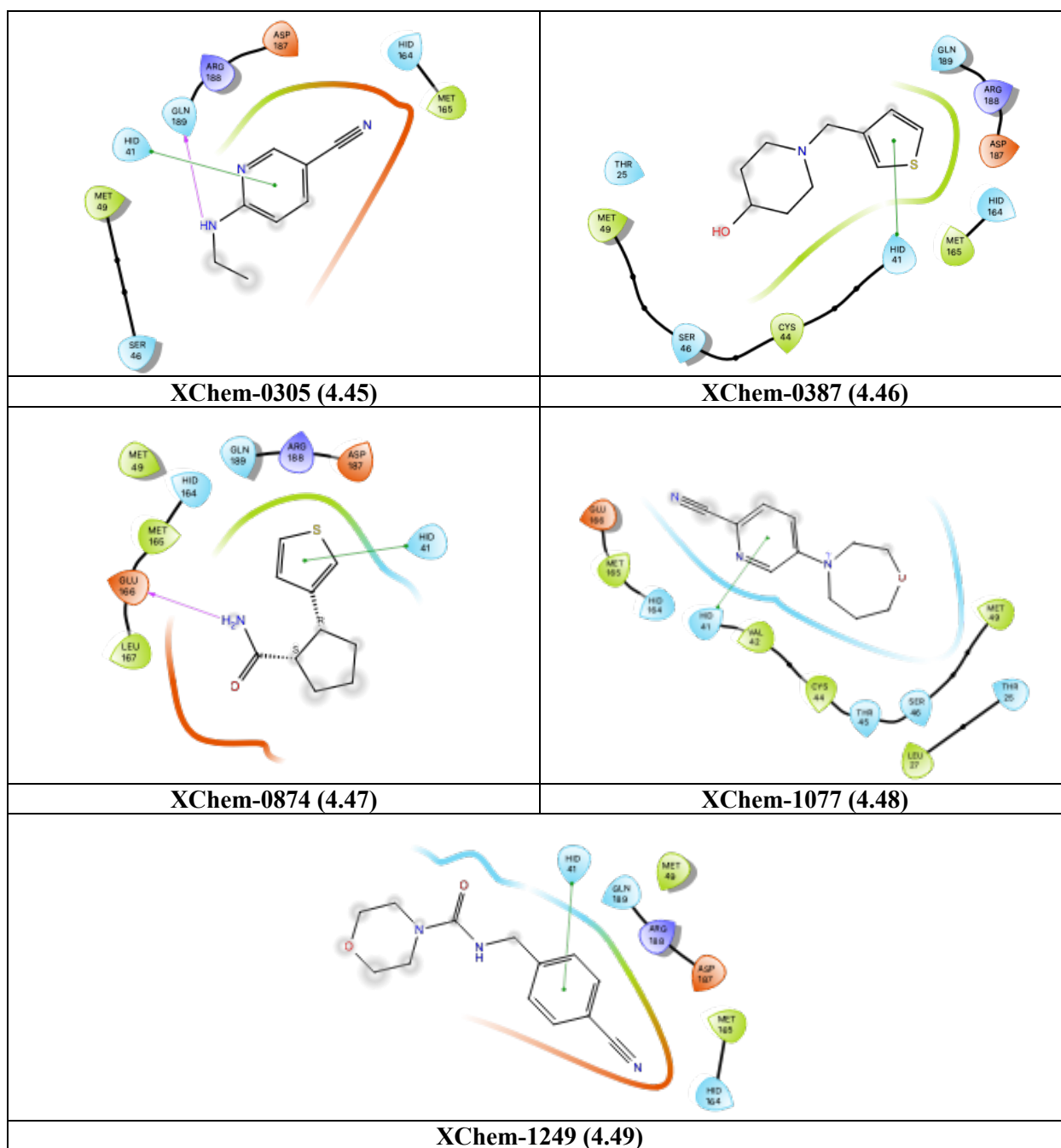
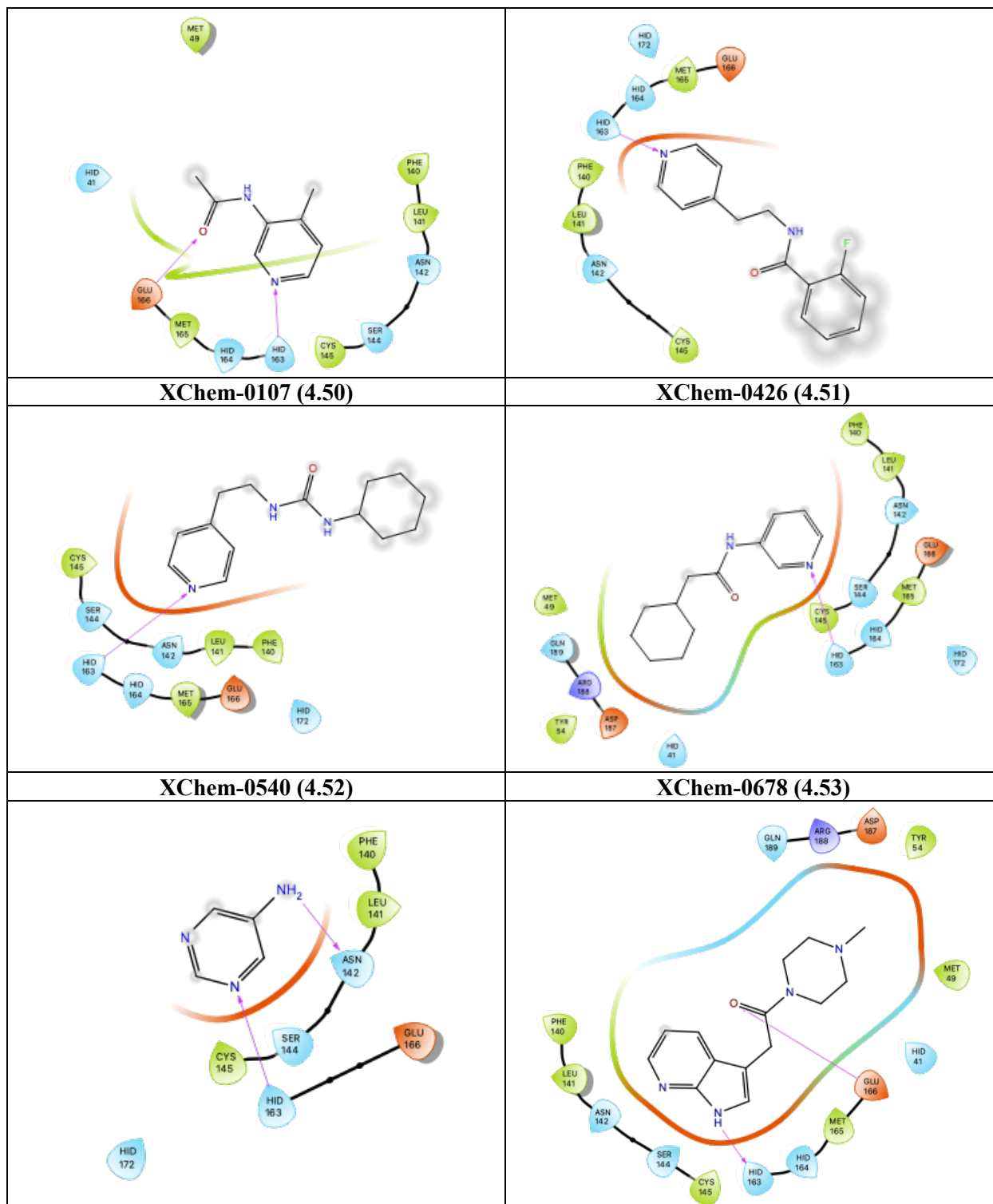


Table 4.3: 2D ligand interaction diagrams of the co-crystal structure of XChem-0072 (4.43), -0104 (4.44), -0305 (4.45), -0387 (4.46), -0874 (4.47), -1077 (4.48) and -1249 (4.49) in SARS-CoV-2 Mpro (S2 subsite).

As shown in **Table 4.4** and **4.5**, His163 is another important residue with which nine XChem fragments are engaged in a hydrogen bonding with a pyridyl group (i.e., XChem-0107 (4.50), -0426 (4.51), -0434 (4.57), -0678 (4.53) and -0540 (4.52)) or a nitrogen containing

heterocyclic ring (i.e., pyrimidyl, isoxazolyl, 7-azaindolyl, phenolic group of XChem-0995 (4.54), -0397 (4.56), -1093 (4.55), -0967 (4.58), respectively) predominating.



XChem-0995 (4.54)	XChem-1093 (4.55)
-------------------	-------------------

Table 4.4: 2D ligand interaction diagram of the co-crystal structure of XChem-0107 (4.50), -0426 (4.51), -0540 (4.52), -0678 (4.53), -0995 (4.54) and -1093 (4.55) in SARS-CoV-2 Mpro (S1 subsite).

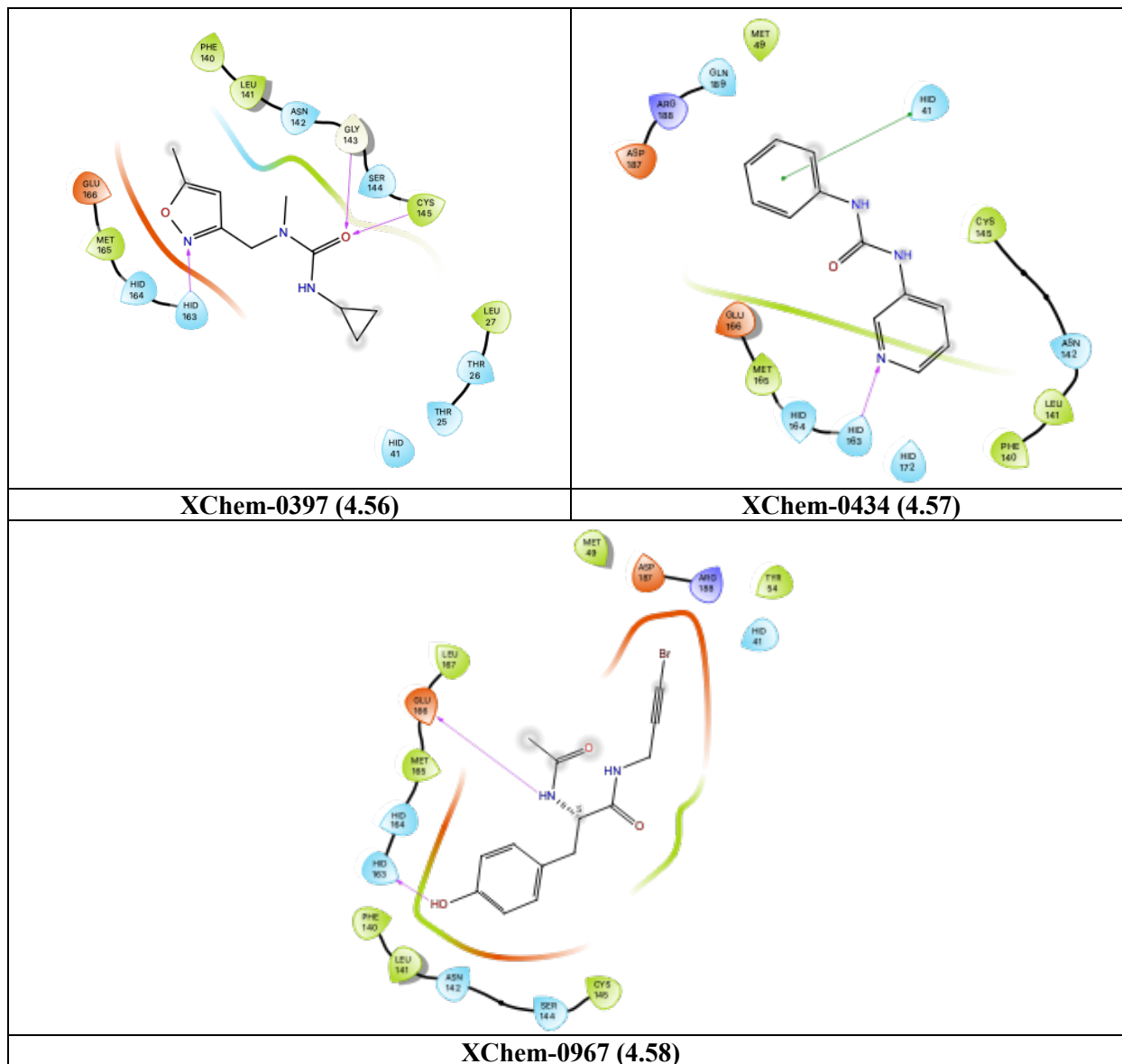


Table 4.5: 2D ligand interaction diagram of the co-crystal structure of XChem-0397 (4.56), -0434 (4.57) and -0967 (4.58) in SARS-CoV-2 Mpro.

The binding poses of the fragments XChem-0397 (4.56), -0434 (4.57) and -0967 (4.58) span multiple pockets, providing us with a framework to design Mpro inhibitor scaffolds. The urea

XChem-0397 (**4.56**) occupies the S1 and S1' subsites and interacts via hydrogen bonding with His163, Gly143 and Cys145. The other urea-containing fragment XChem-0434 (**4.57**) interacts with His163 and His41 in the S1 and S2 pockets, respectively. Tyrosine-based XChem-0967 (**4.58**) spans the S1, S2 and S3 sites by acting as hydrogen bond donor with His163 and the Glu166 backbone, and the bromopropynyl is in the vicinity of His41 but is unclear if a π - π stacking interaction is occurring.

The XChem fragment library combined with the data of non-covalent peptidomimetic Mpro inhibitors informed us of the key residues and design strategies to pursue: (1) His41, one of two amino acids of the catalytic dyad, is central to Mpro proteolytic activity and its inhibition looks to be possible by leveraging of T-shaped π - π stacking; (2) Hydrogen bonding with His163 provides a prevalent interaction in the S1 subsite; (3) Hydrogen bonding with the NHs of Gly143 and Glu166 backbone provide interactions with S1' and S3 respectively. These three observations/hypotheses taken from previous studies acted as design principles in our *de novo* ligand design.

5.3 Design of SARS-CoV-2 Mpro Non-Covalent Inhibitor Chemotypes

Due to the nature of this project (short duration, limited funding, restricted lab access, etc.) I took into account these additional criteria when designing analogs: (1) The synthetic route should require a limited number of steps; (2) The synthetic methods should be known and employ common reagents; (3) The building blocks should be affordable and chemically stable; (4) The scaffold should have multiple substitution sites; (5) The scaffold should span multiple subsites of the binding pocket.

5.3.1 Design of the Urea Scaffold

Ureas are commonly found in drugs and are known to improve aqueous solubility and permeability, due to the presence hydrogen bond donor and acceptor, and to introduce conformational constraint, due the delocalization of nonbonded electrons on nitrogens into the central carbonyl group, orienting the substituents in different angles.⁷⁰ Although XChem-0397 (**4.56**) only occupies the subsites S1 and S1' of the Mpro active site, the methyl group of the urea is projected towards S2 and S3 offering the opportunity to the explore the rest of the binding site. In contrast, the binding pose of the other two urea-containing fragments (XChem-0434 (**4.57**) and XChem-0540 (**4.52**)) prevented further structural optimization, as their nitrogens are oriented outside the pocket. I proposed three modifications to the scaffold (**4.59**, **Figure 4.12**): (1) The substitution of the methyl-isoxazole with pyridine was expected to improve the hydrogen bond accepting capacity of the nitrogen⁷¹; (2) Introduction of a larger substituent than the isopropyl group would allow additional interactions with residues of S1'; (3) The methyl group of the urea core was considered a useful handle to introduce aryl groups to explore the S3 and possibly S4 subsites.

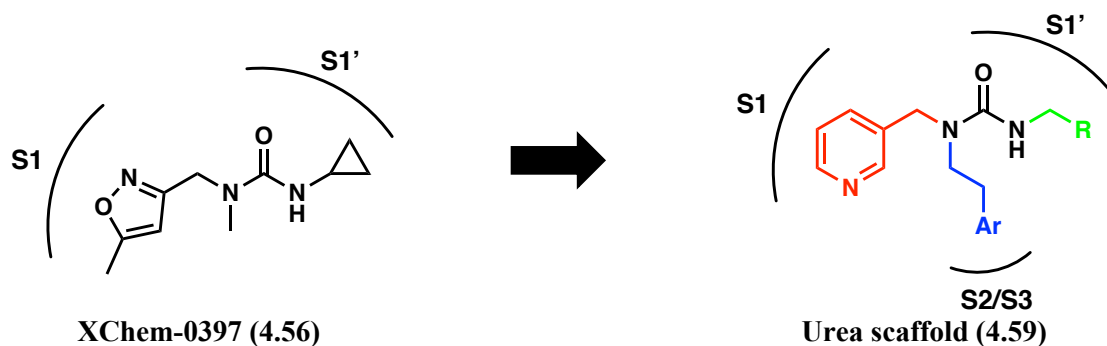


Figure 4.12: Representation of the rationale for the design of the urea scaffold 4.59 from XChem-0397 (4.56).

5.3.2 Design of the Tyrosine Scaffold

Even though XChem-0967 (4.58) is involved in the same hydrogen bonding with His163 as other fragments or inhibitors, no tyrosine-containing Mpro inhibitors has been reported. Consequently, the development of a scaffold with a tyrosine core would provide a novel chemotype of non-covalent Mpro inhibitor. A library of tyrosine analogs could be produced in a straight-forward fashion via protection and deprotection of the tyrosine core and amide coupling, allowing the screening of a broad range of moieties. The acetamide could be replaced with substituted alkyl arenes in order to provide residues capable of spanning both the S3 and S4 subsites of Mpro (4.60, Figure 4.13). Due to the likely toxicity of the bromopropynyl group,⁷² I hypothesized that the substitution with an aromatic functionality would be a suitable alternative and would provide π - π stacking interaction with His41.

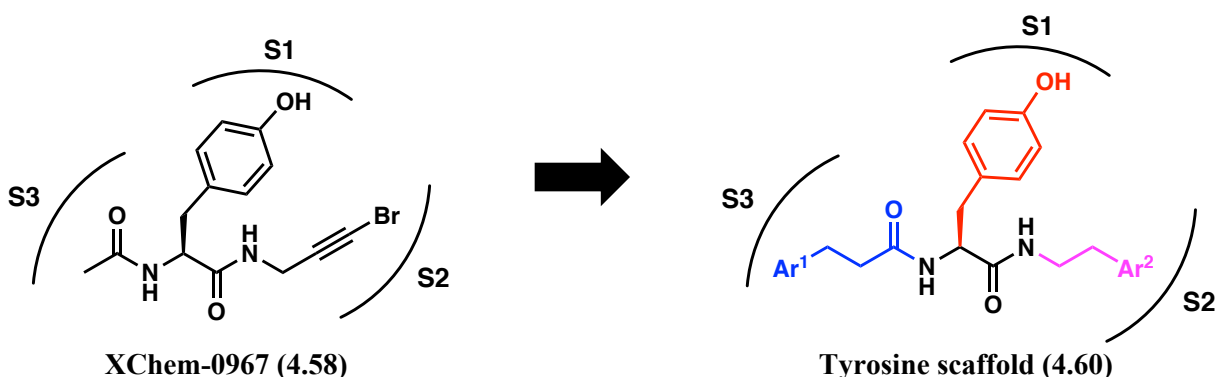
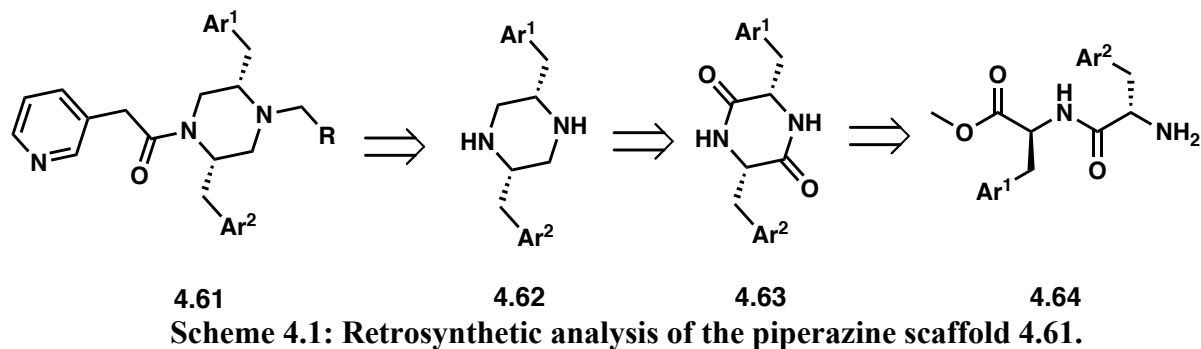


Figure 4.13: Representation of the rationale for the design of the tyrosine scaffold 4.60 from XChem-0967 (4.58).



5.3.4 Design of the ML188-Like Scaffold

As previously mentioned, the peptidomimetic scaffold of ML188 (**4.28**) has been subject to several studies and resulted in submicromolar inhibitory activity against Mpro.^{62,69} However, a significant part of the chemical space of the chemotypes remains to be investigated, particularly for the S1', S2 and S3 pockets. Even though the furyl amide is critical for the hydrogen bonding contact with Gly143, the known toxicity associated with furans prompted the pursuit of a less reactive moiety capable of maintaining the hydrogen bond ability.⁷³ Previously reported peptidomimetic compounds have been synthesized through an Ugi four-component coupling and only anilines have been used employed as building blocks of the aryl group occupying the S2 subsite. Therefore, I proposed to use benzylamines to introduce a flexible aromatic group capable of interacting with His41 via π - π stacking (**4.65**, **Figure 4.15**). Following the suggestion by Kitamura et al., the extension of the aryl group occupying S3 towards S4 was expected to lead to the improvement of the enzymatic inhibition.

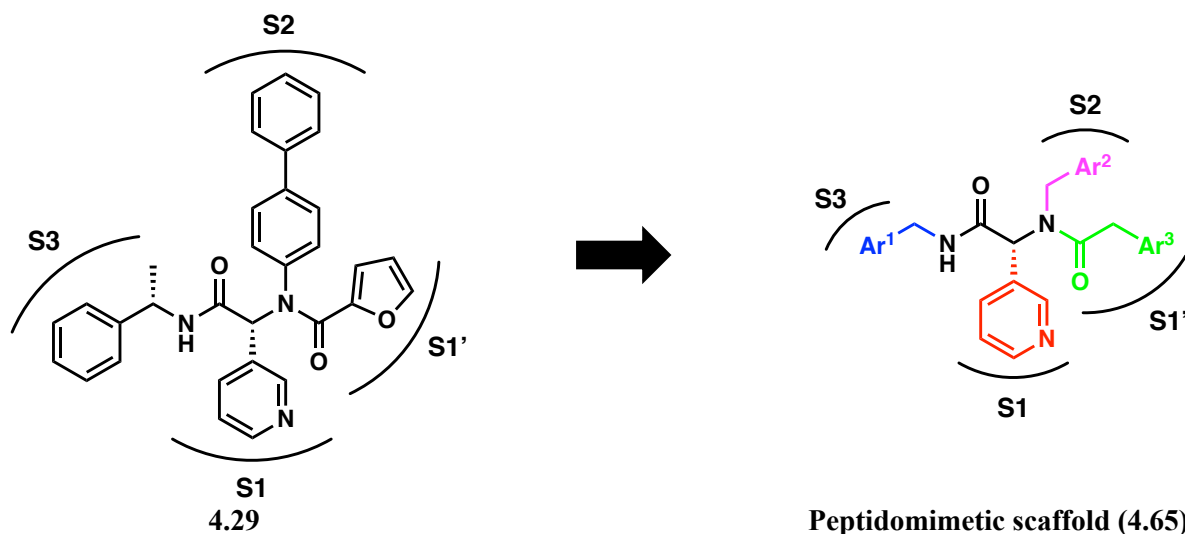


Figure 4.15: Representation of the rationale for the design of the peptidomimetic scaffold (4.65) from 4.29.

5.4 Computational Studies the Piperazine Scaffold

Although molecular modeling of the binding site of Mpro and XChem fragments provided useful insights to design the scaffolds discussed above, further investigation was required to determine if these designed scaffolds would be expected to bind to Mpro pocket. *In silico* methods such as docking studies are powerful to predict how small molecules might bind to a pocket of interest (binding pose) and how well they bind to it (docking score), and potential protein-ligand interactions can be identified. These docking studies enable the selection and prioritization of *in silico* hits from a screening of a large number of ligands. Among the four proposed scaffolds, I directed my attention on the piperazine scaffold for the following computational work to identify a library of small molecules to synthesize. Jessi Gardner worked on the ML188-like scaffold and Katelyn Stevens on the urea and tyrosine scaffolds. Due to the short duration of this project and restricted lab access, I started the synthesis of the piperazine scaffold **4.61** in parallel of the computational studies.

5.4.1 Computational Methods

The Schrödinger software suite was used to prepare and optimize the protein and ligands, and to conduct the docking studies. Briefly, the co-crystal structure of ML188 (**4.28**) with SARS-CoV Mpro (PDB: 3V3M) were selected for the docking studies for the following reasons: (1) The scaffold I was targeting was in size range of ML188 (~400 g/mol); (2) The protonation state of the His163 imidazole of this protein structure enables the hydrogen bonding with the pyridyl group of the scaffold. The protein structure was refined with the ‘Protein Preparation Wizard’ to add hydrogens, assign hydrogen bonds, fill missing sidechains, and minimize the protein structure. The ligands were minimized using the OPLS_2005 force field and the protonation state of the molecules were generated at a pH = 7.4. The minimized ligands were docked in the binding pocket with ‘Glide’ at the extra precision (XP) level and the state penalties were added to the docking score.

5.4.2 Predictive Model for the Mpro Inhibition Activity

Recently, Barzilay and Collins developed a deep neural network capable of predicting molecules with antibacterial activity against *Escherichia coli* and successfully discovered a molecule structurally divergent from conventional antibiotics, halicin, which is active against a range of drug-resistant Gram-negative bacteria.⁷⁴ Following the COVID-19 crisis, Barzilay and Collins applied the approach to SARS-CoV-2 and trained a model to predict the inhibitory activity of molecules against Mpro using the data from PubChem assay AID1706. Briefly, AID1706

comprises a dataset from a QFRET-based high throughput screening assay of more than 290,000 compounds from the MLPCN library tested in singlicate at a concentration of 6 μM .⁷⁵ Due to the imbalance between positive and negative hits, 0.1% and 99.9% respectively, a class balance approach (where each training batch samples an equal number of positive and negative molecules) was employed to provide more accurate predictive model, ‘SARS – Balanced’ model. The values returned by the model correspond to the predicted probability of molecules to inhibit SARS-CoV-2 Mpro and range from 0 to 1.

In my computational study, the ‘SARS – Balanced’ model was used to give additional weight to the following docking studies, the examined ligands were part of the ‘test set’ and the AID1706 compounds were the ‘training set’.⁶⁸ In order to assess the accuracy of the model’s prediction, the aforementioned Mpro inhibitors and XChem hits were processed as shown in **Table 4.6** and **4.7**, respectively. The values returned by the model represent the probability a molecule is to inhibit Mpro, but it is not proportional to IC_{50} , as shown in **Table 4.6**, due to the single concentration used for the HTS assay. Consequently, the values from the ‘SARS – Balanced’ model has a qualitative not quantitative connotation and can provide further indication if a molecule can inhibit Mpro independently from the docking studies results. Notably, the prediction value appeared to reflect IC_{50} differences within chemotypes: ML188 (**4.28**) > **4.29**; Perampanel (**4.30**) > **4.31**; Baicalein (**4.32**) > Baicalin (**4.33**). Therefore, the SARS – Balanced model has the potential to give an indication of the probability of inhibition Mpro, insight not provided by docking.

Name	SARS-CoV-2 IC_{50} (μM)	SARS – Balanced prediction (AU)
GC-376 (4.24)	0.03	0.253
Boceprevir (4.25)	4.13	0.291
Calpain inhibitor II (4.26)	0.97	0.179
Calpain inhibitor XII (4.27)	0.45	0.399

PF-00835231 (4.35)	0.0069	0.277
ML188 (4.28)	11.23	0.714
4.29	0.31	0.851
Perampanel (4.30)	100	0.468
4.31	0.120	0.487
Baicalein (4.32)	0.94	0.482
Baicalin (4.33)	6.41	0.475

Table 4.6: Probability of Mpro inhibition of know Mpro inhibitors predicted by ‘SARS – Balanced’.

As presented in **Table 4.7**, no correlation could be made between the binding subsites where the XChem hits are located and the SARS-Balanced model prediction values because this model is established on the basis of inhibitory activity instead of binding. As fragments, the XChem hits are less likely to induce inhibitory activity within the range of the active AID1706 compounds.

XChem hits	Binding subsites				SARS – Balanced prediction (AU)
	S1'	S1	S2	S3	
0161 (4.37)					0.280
0195 (4.38)					0.246
0354 (4.39)					0.121
0395 (4.40)					0.137
0946 (4.41)					0.374
0991 (4.42)					0.240
0072 (4.43)					0.120
0104 (4.44)					0.233
0305 (4.45)					0.120
0387 (4.46)					0.065
0874 (4.47)					0.138
1077 (4.48)					0.112
1249 (4.49)					0.092
0107 (4.50)					0.240
0426 (4.51)					0.247
0540 (4.52)					0.074
0678 (4.53)					0.104
0995 (4.54)					0.236
1093 (4.55)					0.148
0397 (4.56)					0.071
0434 (4.57)					0.329

0967 (4.58)					0.198
-------------	--	--	--	--	-------

Table 4.7: Probability of Mpro inhibition of XChem-fragment predicted by ‘SARS – Balanced’.

In the following docking studies, SARS – Balanced model prediction values were included along with the docking score to inform the design and the selection of analogs to investigate.

5.4.3 Docking Studies

Using the original co-crystal structure of ML188 (**4.28**) with SARS-CoV Mpro (PDB: 3V3M), XChem-1093 (**4.55**) was docked to determine if our docking method could reproduce a similar binding pose. The root-mean-square deviation (RMSD) between the initial ligand and the docked ligand was 0.1758 Å, suggesting that the docking method was reliable and could be further employed for our docking studies. As shown in **Table 4.8**, XChem-1093 (**4.55**) is engaged in two hydrogen bonds with His163 and the backbone of Glu166 resulting in a docking score of -5.950 kcal/mol. In the subsequent docking studies, the designed compounds were considered as good candidates to synthesize under the following criteria: (1) Since the proposed compounds bear a pyridyl group, the predicted binding pose had to exhibit a hydrogen bond between His163 and the pyridyl group; (2) The predicted binding score should be more negative than that of XChem-1093 (**4.55**) by more than 0.1 kcal/mol; (3) The binding pose should demonstrate additional protein-ligand interactions; (4) The predicted probability of Mpro inhibitory activity by SARS – Balanced model should be higher than that of XChem-1093 (**4.55**) by at least 0.01 AU. Consequently, this multifactor approach avoided relying only on the docking score as it often does not equate binding with inhibitory activity.

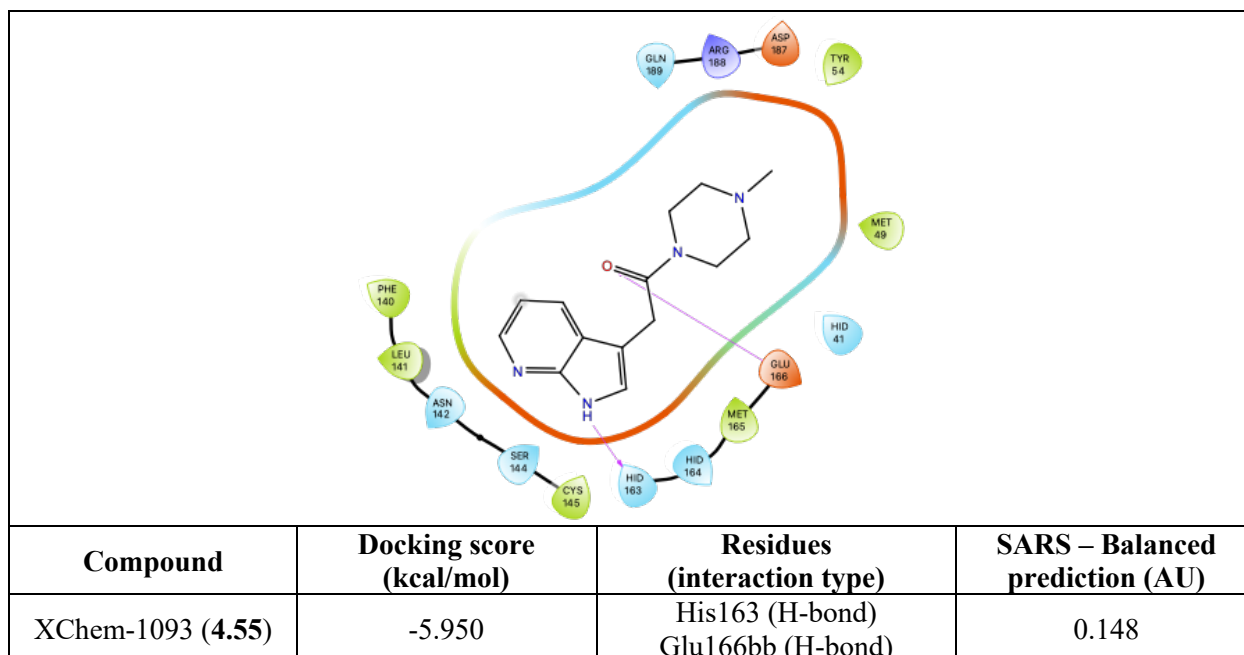
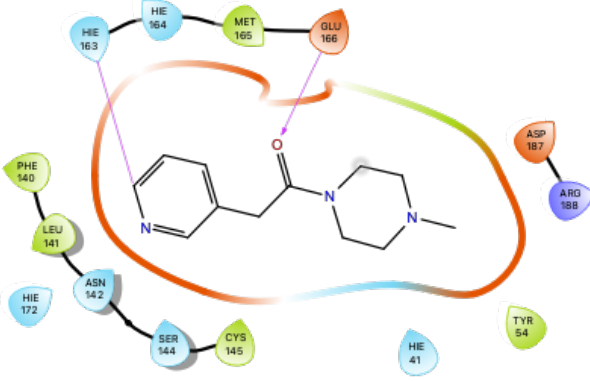


Table 4.8: Structural representation of compound XChem-1093 (4.55) in SARS-CoV-2 Mpro pocket. The 2D ligand interaction diagram of the binding pose of 4.55 in SARS-CoV-2 Mpro (PDB: 3V3M) was predicted by Glide.

5.4.3.1 Investigation of the Piperazine as a Scaffold for Mpro Inhibitors

The first objective of the docking studies was to validate the piperazine **4.61** as a viable scaffold to generate a library of Mpro inhibitors. Starting with XChem-1093 (**4.55**), I employed a sequential buildup method to incrementally introduced structural features of **4.61** (i.e., pyridine, aryl groups on the piperazine bridges and substituents on the piperazine nitrogen) to determine the impact of each proposed substitution on the predicted binding.

Even though the substitution from the 7-azaindole to pyridine decreased the predicted binding affinity and probability of Mpro inhibition, the hydrogen bonds with His163 and the backbone of Glu166 were maintained (**4.66**, **Table 4.9**). Combined with the fact that the pyridyl group is prevalent among non-covalent Mpro inhibitors, I considered that the binding and the inhibitory activity of the following designed analogs would not be eliminated by this substitution.



Compound	Docking score (kcal/mol)	Residues (interaction type)	SARS – Balanced prediction (AU)
4.66	-4.538	His163 (H-bond) Glu166bb (H-bond)	0.118

Table 4.9: Structural representation of compound 4.66 in SARS-CoV-2 Mpro pocket. The 2D ligand interaction diagram of the binding pose of **4.66** in SARS-CoV-2 Mpro (PDB: 3V3M) was predicted by Glide.

Upon introduction of the two benzyl groups on the piperazine core, the binding pose of the scaffold was not significantly altered and the docking score of **4.67** improved to -5.074 kcal/mol (**Table 4.10**). Similarly, the predicted probability of Mpro inhibition had nearly tripled relative to **4.66**. Although one benzyl moiety was engaged with His41 in a T-shaped π - π stacking, the other occupied the S1' subsite but was not predicted to interact with any residues. The distance of the pyridyl-His163 hydrogen bond was increased from 2.96 to 3.44 Å, beyond the distance range of the typical interaction. In addition, the carbonyl of the piperazine amide was not in the vicinity of the Glu166 backbone anymore for the second hydrogen bond. Although a new π - π stacking interaction was formed between one of the benzyl group and His41, the bulkiness resulting from the benzyl groups appeared to have a detrimental effect on the other protein-ligand interactions but not the predicted affinity. Taken together these data did not provide conclusive evidence that the dibenzyl piperazine was a suitable scaffold for Mpro inhibition.

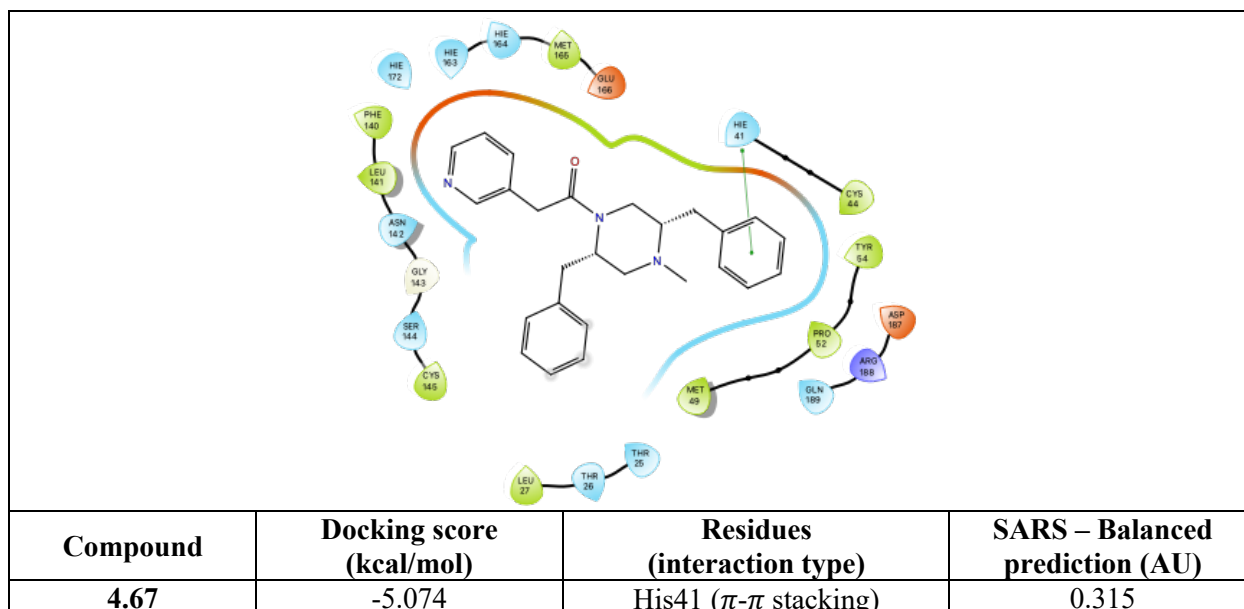


Table 4.10: Structural representation of compound 4.67 in SARS-CoV-2 Mpro pocket. The 2D ligand interaction diagram of the binding pose of 4.67 in SARS-CoV-2 Mpro (PDB: 3V3M) was predicted by Glide.

Although the proposed dibenzyl piperazine analog **4.67** (Table 4.10) did not satisfy the aforementioned criteria in regard to the ligand-protein interactions, the docking score and predicted probability of Mpro inhibition were sufficient to not abandon the dibenzyl piperazine scaffold yet. I hypothesized that structural modifications of the 2-pyridylacetamide could restore the necessary hydrogen bond with His163 and improve the docking score.

I first removed the carbonyl amide of **4.67** resulting in analog **4.68**. This amide not only reduces the flexibility of the piperazine but also reduces the conformational freedom of the pyridyl moiety, I hypothesized that the carbonyl functionality might prevent the hydrogen bond with His163 in **4.67**. Although the docking score of **4.68** was improved, the pyridyl-His163 hydrogen bond was not restored and **4.68** adopted an inadequate binding pose. Compared to **4.67**, the ligand **4.68** was rotated 90° clockwise and the pyridine occupied the S2 subsite and the previous binding

pyridylethyl group was not tolerated in S1 because of the length of the pyridine-piperazine linker. Therefore, I examined the impact of shortening the chain between the pyridine and the piperazine on the binding pose of the piperazine scaffold. The docking of **4.69**, as shown in **Table 4.12**, predicted the restoration of the pyridine-His163 hydrogen bond as it adopted a similar pose as **4.67**. This resulted in the opposite benzyl group engaging with His41 in T-shaped π - π stacking. The benzyl adjacent to the methyl group, however, occupied the S3 pocket and clashed with the sidechain of Gln192, likely explaining the lower predicted affinity compared to **4.67**. Therefore, shortening the chain between the pyridine and the piperazine was beneficial but the presence of two benzyl groups on the piperazine core led to steric clashes.

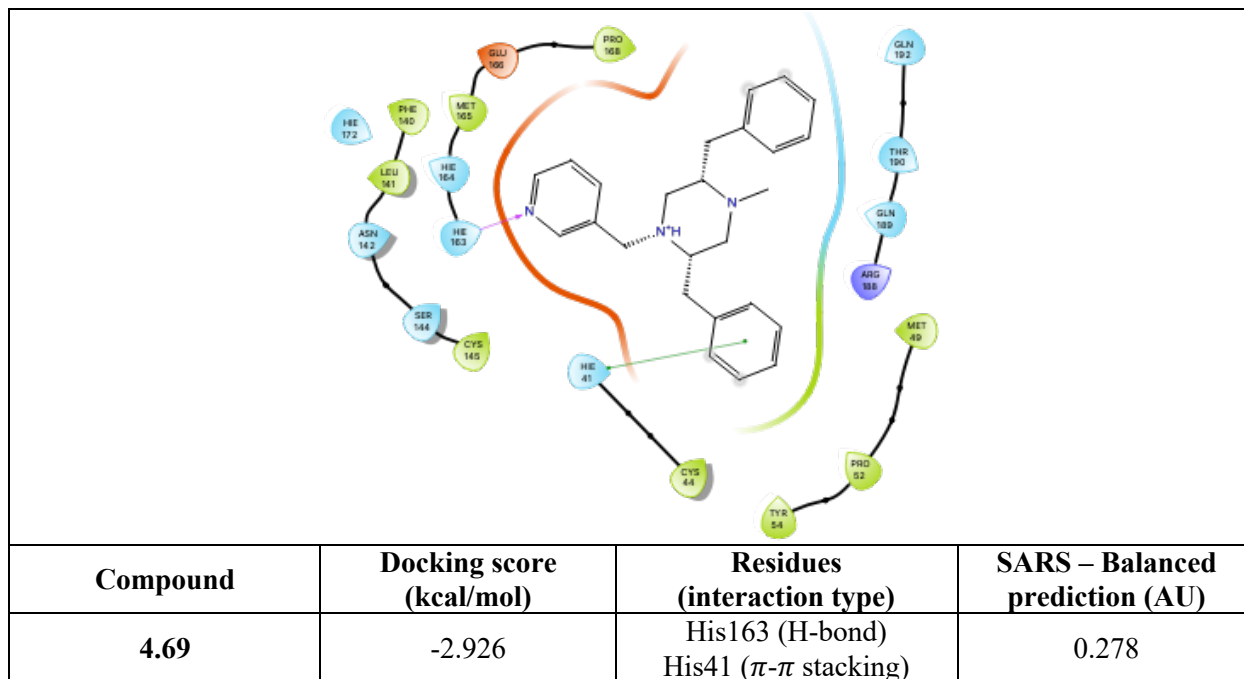


Table 4.12: Structural representation of compound 4.69 in SARS-CoV-2 Mpro pocket. The 2D ligand interaction diagram of the binding pose of **4.69** in SARS-CoV-2 Mpro (PDB: 3V3M) was predicted by Glide.

The docking studies of the dibenzyl piperazine analogs (i.e., **4.66**, **4.67**, **4.68** and **4.69**) indicated that: (1) The pyridyl group could be substituted for the 7-azaindole without significant detrimental effects to the docking score; (2) Although one of the benzyl groups could engage in a π - π stacking interaction with His41, the bulk of the two moieties led to steric clashes with Mpro active site; (3) The pyridine-piperazine linker could diverge from the initial scaffold **4.61** to promote the essential pyridine-His163 hydrogen bond. Consequently, I decided to redirect from the dibenzyl piperazine scaffold to pursue an alternative avenue for the **4.61** chemotype.

Even though substitution on both of the ethylene bridges of the piperazine core was possible, several challenges were envisioned: (1) The use of identical substituents on the piperazine core revealing a symmetrical chemotype that would likely suffer from unfavorable interactions with an asymmetrical binding pocket; (2) Although possible, asymmetrical substitution of the piperazine core would lead to challenging selective functionalization of the piperazine nitrogens (**4.62**, **Scheme 4.1**). Therefore, I decided to use **4.66** as a starting point to explore different mono-substitutions on the piperazine core.

First, the carbonyl linker between the pyridine and the piperazine was replaced with a methylene, which conserved the binding pose as demonstrated by the superposition of **4.66** and **4.70** (**Table 4.13**). However, its docking score was worse than **4.70** (-3.595 kcal/mol, **Table 4.14**), likely due to the absence of the hydrogen bond with the backbone of Glu166 compared to **4.66**. With the shorter methylene bridge, the piperazine is closer to S1, leaving more space for substituents to be accommodated in S2. From this pyridylmethylpiperazine core **4.70**, substitutions on the piperazine (i.e., ethylene bridges and nitrogen) were investigated to determine which position could improve protein-ligand interactions.

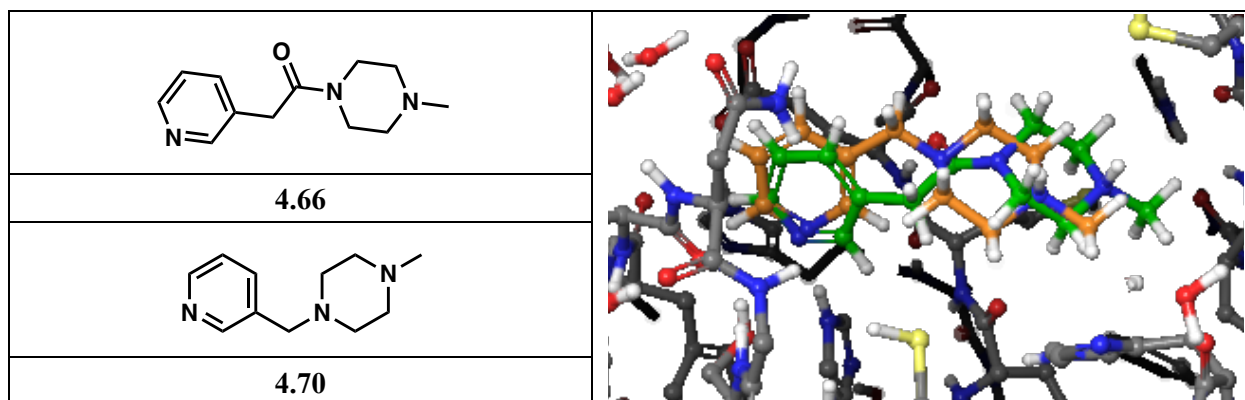
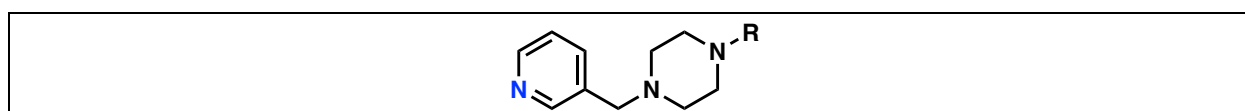


Table 4.13: Superposition of 4.66 and 4.70 docked to SARS-CoV-2 Mpro. On the right, the 3D representation of the binding poses of **4.66** (green) and **4.70** (orange) in SARS-CoV-2 Mpro (PDB: 3V3M) were predicted by Glide.

First, the methylamine moiety on **4.70** was subjected to structural exploration to identify aromatic rings that could be accommodated in S2 subsite, targeting in particular His41. The docking studies indicated that the majority of substituted benzyl piperazines (i.e., **4.71**, **4.73**, **4.74**, **4.76**, **4.78**, **Table 4.14**) did not bind in the expected conformation with the pyridine occupying the S1 subsite, with the exception of analogs with benzyl bearing electro-withdrawing group (i.e., **4.72** and **4.75**, **Table 4.14**). Despite superior predicted binding affinity and probability of inhibition of Mpro, the benzyl moieties of the latter compounds do not interact with His41. In addition, bulkier aryl groups such as biphenyl on **4.76** prevented adequate binding but, interestingly, the naphthalene on **4.77** improved the predicted binding affinity but did not access additional protein-ligand interactions. The docking studies of this series of aryl piperazine suggested that the substitution on the methylamine moiety was not beneficial for access π - π stacking interaction with His41.



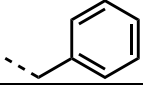
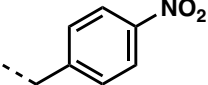
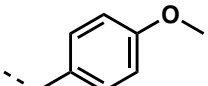
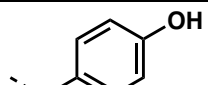
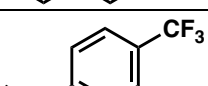
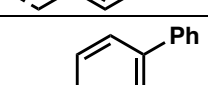
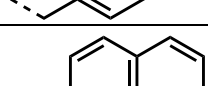
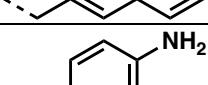
R	Compound	Docking score (kcal/mol)	Residues (interaction type)	SARS – Balanced prediction (AU)
--CH ₃	4.70	-3.595	His163 (H-bond)	0.131
	4.71	No binding	n/a	0.199
	4.72	-4.129	His163 (H-bond)	0.251
	4.73	No binding	n/a	0.146
	4.74	No binding	n/a	0.138
	4.75	-4.634	His163 (H-bond)	0.406
	4.76	No binding	n/a	0.329
	4.77	-5.878	His163 (H-bond)	0.332
	4.78	No binding	n/a	0.253

Table 4.14: Summary of the docking studies of the aryl piperazine series in SARS-CoV-2 Mpro (PDB: 3V3M). The docking score and protein-ligand interactions were predicted by Glide and SARS – Balanced model predicted the probability of Mpro inhibition. The binding poses of the ligands were considered not adequate (No binding) when the pyridyl group was not engaged in a H-bond with His163.

Although the substitution on the methylamine moiety with aryl groups failed to provide analogs with additional protein-ligand interactions, I considered that further investigating the functionalization of this position on the piperazine core was beneficial, as the secondary amine is a convenient synthetic handle. As discussed above, peptidic covalent inhibitors have been extensively studied, leading to potent compounds that exhibit high complementarity with the Mpro active site. For example, moieties such as N-carboxybenzyl protected (Cbz) amino acids have demonstrated improvement of Mpro inhibitory activity via the interaction of the benzyloxy group

with S4 (TG-0205221 (**4.79**) in **Figure 4.16**).⁷⁶ As depicted in **Scheme 4.2**, I hypothesized that a hybrid of **4.70** and TG-0205221 (**4.79**) would result in potent non-covalent inhibitors with high complementarity to the Mpro binding pocket. Supposing that the piperazine core could act as a bioisostere to the cyclohexyl alanine backbone, the pyridylmethylpiperazine coupled to Cbz-protected amino acids would occupy the S1/S2 and S3/S4 sites (**Scheme 4.2**), respectively.

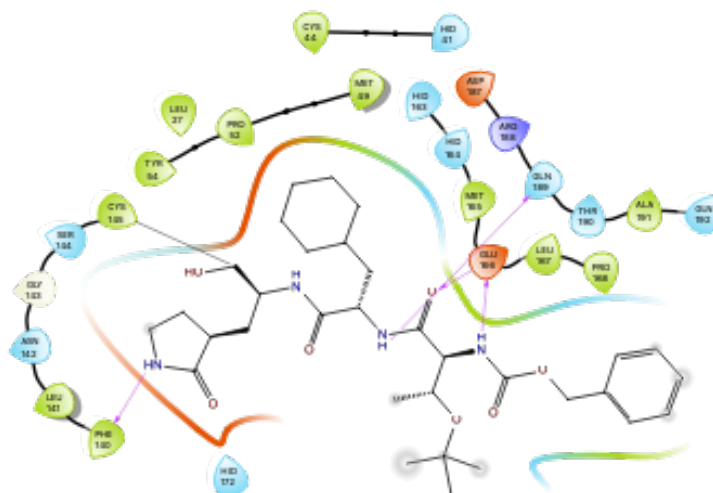
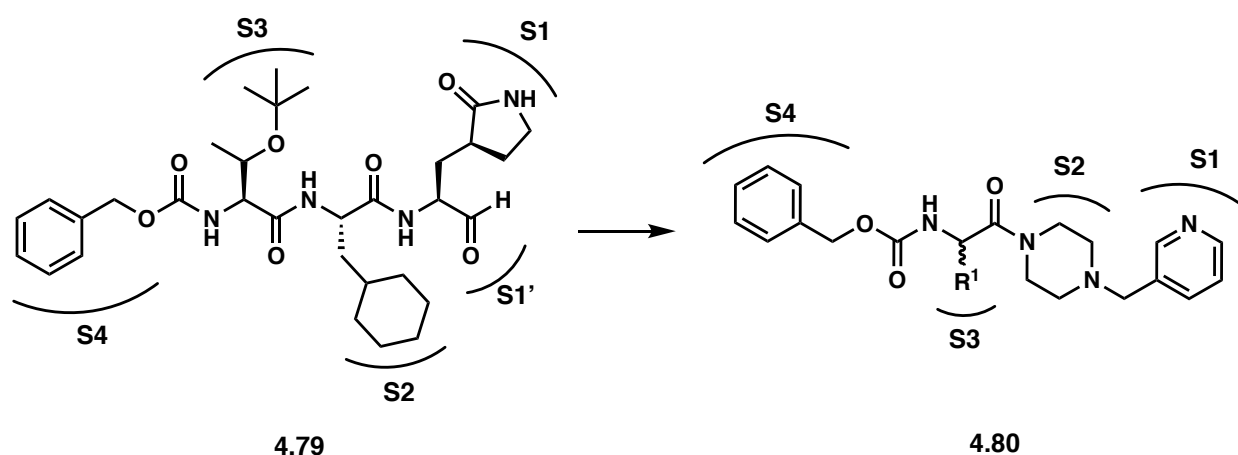
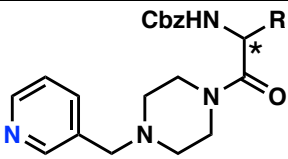
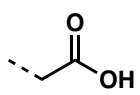
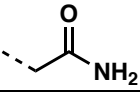
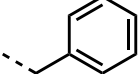


Figure 4.16: 2D ligand interaction diagram of the co-crystal structure of TG-0205221 (**4.79**) with SARS-CoV Mpro (PDB: 2GX4).



Scheme 4.2: Rationale for the design of the amino acid piperazine series (**4.80**) from TG-0205221 (**4.79**).

Although the sidechain of *tert*-butyl threonine occupies the S3 subsite, it is solvent exposed and does not interact with residues of the pocket (**Figure 4.16**). Therefore, the objectives of the following docking studies (**Table 4.15**) were (1) to determine if Cbz-protected piperazine compounds (**4.80**) were predicted to bind in Mpro and (2) to identify amino acid sidechains tolerated by the pocket. **Table 4.15** summarizes the amino acid sidechains examined with both R and S stereochemistry along with the docking scores, interactions with residues and predicted probability of inhibition of Mpro. Overall, none of the screened compounds bound to Mpro with the benzyloxy group in the S4 subsite and only five maintained the pyridine-His163 hydrogen bond. The results of the docking studies suggested that the functionalization of the piperazine with Cbz-protected amino acids does not establish protein-ligand interactions with S4 and S3 subsites. Due to structural constraint, the piperazine likely prevents the adequate binding of the pyridyl and is not a good bioisostere of the cyclohexyl alanine backbone in this context. From these docking studies (**Table 4.14** and **4.15**), the substitution of the methylamine of the piperazine appeared not to be a good avenue for improving the binding of the piperazine scaffold **4.70**. Therefore, I shifted my focus of the functionalization of the ethylene bridge of the piperazine core **4.70**.

				
R	Compound*	Docking score (kcal/mol)	Residues (interaction type)	SARS – Balanced prediction (AU)
	4.81 (R)	-1.108	His163 (H-bond) Gln189 (H-bond)	0.230
	4.82 (S)	No binding	n/a	0.237
	4.83 (R)	No binding	n/a	0.349
	4.84 (S)	No binding	n/a	0.360
	4.85 (R)	No binding	n/a	0.468
	4.86 (S)	No binding	n/a	0.477

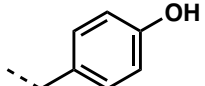
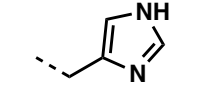
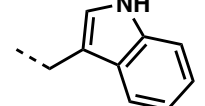
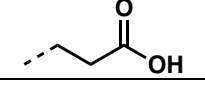
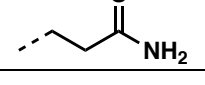
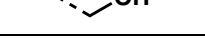
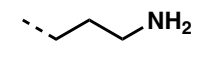
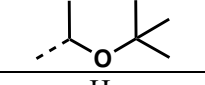
	4.87 (R)	No binding	n/a	0.435
	4.88 (S)	No binding	n/a	0.444
	4.89 (R)	No binding	n/a	0.381
	4.90 (S)	-5.744	His163 (H-bond) Gln189 (H-bond)	0.390
	4.91 (R)	No binding	n/a	0.645
	4.92 (S)	No binding	n/a	0.652
	4.93 (R)	No binding	n/a	0.337
	4.94 (S)	No binding	n/a	0.345
	4.95 (R)	No binding	n/a	0.337
	4.96 (S)	-3.525	His163 (H-bond)	0.337
	4.97 (R)	No binding	n/a	0.231
	4.98 (S)	-4.916	His163 (H-bond)	0.237
	4.99 (R)	-2.05	His163 (H-bond) Gln189 (H-bond)	0.287
	4.100 (S)	No binding	n/a	0.287
	4.101 (R)	No binding	n/a	0.383
	4.102 (S)	No binding	n/a	0.374
H	4.103	No binding	n/a	0.263

Table 4.15: Summary of the docking studies of the amino acid piperazine series in SARS-CoV-2 Mpro (PDB: 3V3M). The docking score and protein-ligand interactions were predicted by Glide and SARS – Balanced model predicted the probability of Mpro inhibition. The binding poses of the ligands were considered not adequate (No binding) when the pyridyl group was not engaged in a H-bond with His163. * The absolute stereochemistry of the chiral center of each analog is indicated by R or S.

Although docking studies suggested that the two benzyl groups of **4.67**, **4.68** and **4.69** were detrimental to the binding pose, a π - π stacking interaction was formed between one of the benzyl and His41. Therefore, I investigated the introduction of one benzyl group on the ethylene bridge of the piperazine core and its effect on the binding in the active site of Mpro. A positional scanning approach was used to define the optimal position of the benzyl functionality on the piperazine ring: (1) The enantiomers **4.104** and **4.105** with the benzyl group adjacent to the methylamine of the piperazine were referred as *trans*; (2) The enantiomers **4.106** and **4.107** with the benzyl group adjacent to the pyridylmethylamine of the piperazine were referred as *cis*. As presented in **Table**

4.16, these four analogs have a better docking score than the unsubstituted piperazine **4.70** and the dibenzyl piperazine **4.69**, suggesting that introduction of one benzyl group was favorable to the binding. Even though the *trans* isomers (**4.104** and **4.105**) have a similar predicted binding affinity and are both engaged in a hydrogen bond with His163, only the R stereoisomer **4.104** had the benzyl moiety engaged in a π - π stacking interaction with His41. Conversely, the S stereoisomer of the *cis* ligands (**4.107**) was able to access the same contact. Notably, the four analogs displayed a comparable binding pose regardless of the position of the substituent as depicted in **Figure 4.17**. These preliminary docking studies indicated that the monobenylation of piperazine scaffold elicited a better docking score relative to unsubstituted piperazine **4.70** and the benzyl group was engaged in a π - π stacking interaction with His41 based on the configuration of the chiral center. Despite the improvement of the docking score by this substitution, the predicted probability of Mpro inhibition remained low.

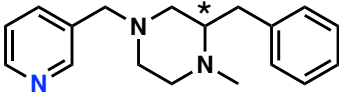
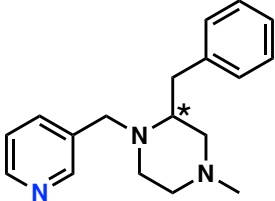
			
Compound*	Docking score (kcal/mol)	Residues (interaction type)	SARS – Balanced prediction (AU)
4.104 (R)	-5.071	His163 (H-bond) His41 (π - π stacking)	0.176
4.105 (S)	-5.076	His163 (H-bond)	0.171
			
Compound*	Docking score (kcal/mol)	Residues (interaction type)	SARS – Balanced prediction (AU)
4.106 (R)	-4.744	His163 (H-bond)	0.173
4.107 (S)	-5.256	His163 (H-bond) His41 (π - π stacking)	0.178

Table 4.16: Summary of the docking studies of the monobenzylated piperazine series in SARS-CoV-2 Mpro (PDB: 3V3M). The docking score and protein-ligand interactions were

predicted by Glide and SARS – Balanced model predicted the probability of Mpro inhibition. *
The absolute stereochemistry of the chiral center of each analog is indicated by R or S.

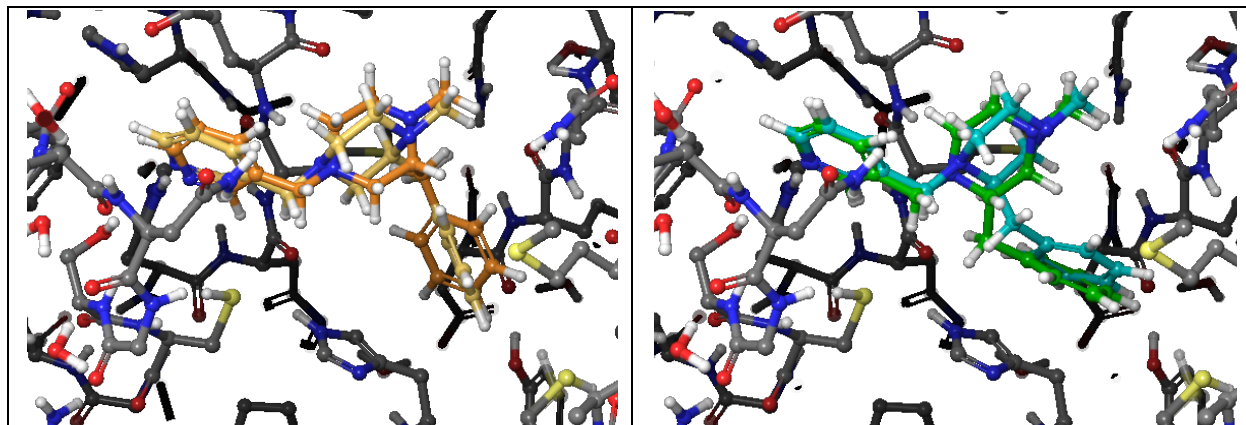
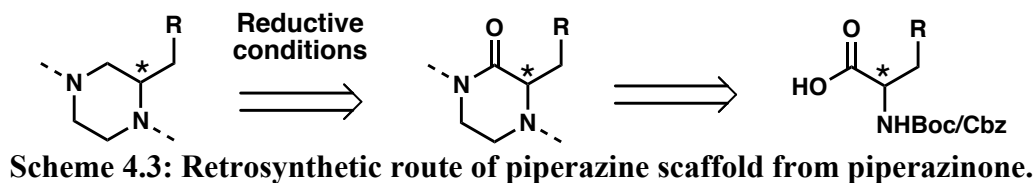


Figure 4.17: Superposition of the monobenzylated piperazine series docked to SARS-CoV-2 Mpro. The 3D representation of the binding poses of **4.104** (left, orange), **4.105** (left, yellow), **4.106** (right, cyan), **4.107** (right, green) in SARS-CoV-2 Mpro (PDB: 3V3M) was predicted by Glide.

In my approach to the design of Mpro inhibitors, I predominantly relied on docking studies to select a scaffold, but the synthetic tractability of a scaffold was also a main concern. Although enantioselective methodologies to synthesize substituted piperazine have been developed,⁷⁷ I envisioned the synthesis of the monosubstituted piperazine scaffold via the reduction of a piperazinone as shown in **Scheme 4.3**. Because of my familiarity with the preparation of piperazinones from protected amino acids, I would be able to easily generate analogs with the stereochemistry of the chiral center set from the beginning. A common practice in the Duerfeldt lab is to evaluate important synthetic intermediates in biochemical assays along with “final compounds” because these intermediates are valuable analogs in of themselves. As a result of using the proposed synthetic route, piperazinone intermediates would be easily accessible analogs. To assess the potential of the piperazinone scaffold for Mpro inhibition, I conducted docking studies of the monobenzylated piperazinone analogs (**4.108** – **4.111**) and the results are presented

in **Table 4.17**. Similar to the monobenzylated piperazine series, a positional scanning approach was employed and the docking of *cis* and *trans* enantiomers was interrogated.



The predicted docking scores and probabilities of Mpro inhibition of the piperazinone analogs (**4.108** – **4.111**) were moderately improved compared to the piperazine series (**4.104** – **4.107**) (**Table 4.17** and **4.16**, respectively). In addition, while the piperazine series shared relatively similar binding poses (**4.104** – **4.107**, **Figure 4.17**), the piperazinone ligands exhibited diverging binding poses (**4.108** – **4.111**, **Figure 4.18**). As presented in **Table 4.17**, the *trans* isomers (**4.108** and **4.109**) form two hydrogen bonds, between the pyridyl group and His163, and between the piperazinone carbonyl and the backbone of Glu166. However, only **4.109** is engaged in a π - π stacking interaction between His41 and its benzyl group. Because of the R configuration of **4.108**, the methyl group blocks the contact between the benzyl and His41, while the methyl of **4.109** is solvent exposed (**Figure 4.18**). This π - π stacking interaction with His41 likely explains the 0.64 kcal/mol difference in docking score between **4.108** and **4.109**. In contrast, the *cis* piperazinones, **4.110** and **4.111**, were predicted to engage in fewer (i.e., hydrogen bonding with His163) or no interactions with Mpro pocket, respectively. In addition, **4.111** did not bind in the expected conformation, it is rotated 90° clockwise as the pyridyl and benzyl group occupy the S2 and S1 subsites, respectively. In conclusion, the piperazinone was revealed to be a better scaffold than the piperazine as hydrogen bond between the carbonyl and Glu166 backbone likely improved the docking score. The positional scanning approach led to the identification of **4.109** as the best

candidate of the series, with a docking score and additional protein-ligand interactions with Mpro pocket (i.e., π - π stacking interaction with His41). It is also synthetically more tractable than the piperazine scaffold because the methodology has been established.

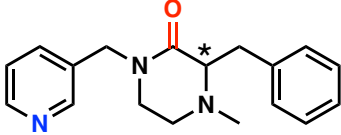
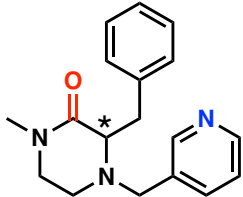
			
Compound*	Docking score (kcal/mol)	Residues (interaction type)	SARS – Balanced prediction (AU)
4.108 (R)	-5.149	His163 (H-bond) Glu166bb (H-bond)	0.194
4.109 (S)	-5.790	His163 (H-bond) His41 (π - π stacking) Glu166bb (H-bond)	0.186
			
Compound *	Docking score (kcal/mol)	Residues (interaction type)	SARS – Balanced prediction (AU)
4.110 (R)	-6.067	His163 (H-bond)	0.185
4.111 (S)	No binding	n/a	0.193

Table 4.17: Summary of the docking studies of the monobenzylated piperazinone series in SARS-CoV-2 Mpro (PDB: 3V3M). The docking score and protein-ligand interactions were predicted by Glide and SARS – Balanced model predicted the probability of Mpro inhibition. * The absolute stereochemistry of the chiral center (denoted by *) of each analog is indicated by R or S at the end of the name.

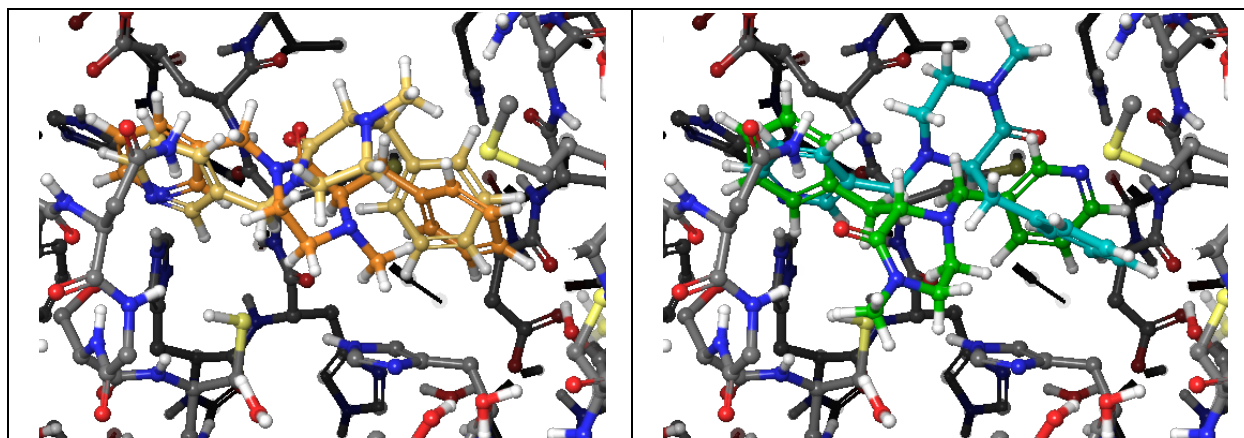


Figure 4.18: Superimposition of the monobenzylated piperazinone series docked to SARS-CoV-2 Mpro. The 3D representation of the binding poses of **4.108** (left, orange), **4.109** (left, yellow), **4.110** (right, cyan), **4.111** (right, green) in SARS-CoV-2 Mpro (PDB: 3V3M) was predicted by Glide.

Starting with **4.55** as an initial hit, I investigated the effect of structural modifications on the docking score, binding pose and probability to inhibit Mpro via a sequential buildup method. Although these docking studies led to invalidate the proposed dibenzyl piperazine scaffold **4.61**, they provided key design information: (1) The 7-azaindole of **4.55** could be replaced by a pyridyl group without significant impacting the docking score; (2) While steric clashes arose from dibenylation of the piperazine core (**4.67** – **4.69**), monobenylation (**4.104** – **4.107**) elicited a π - π stacking interaction with His41; (3) A shorter pyridine-piperazine linker promoted the essential pyridine-His163 hydrogen bond (**4.69** and **4.70**); (4) Functionalization of the methylamine of the piperazine core failed to produce ligand able to interact with residues in S2 subsite. However, piperazinone, a precursor of piperazine, was identified as a superior scaffold as the carbonyl can engage in a hydrogen bond with the backbone of Glu166 improving the docking score. A positional scanning approach determined **4.109** as the best ligand of the piperazinone series as the benzyl group at the *trans* position on the piperazinone interacts with His41 via π - π stacking. Although the docking score of **4.109** was not improved compared to **4.55**, I considered it as a promising

scaffold to design Mpro inhibitors and the known synthetic methodology would allow for rapid generation of analogs to evaluate in biochemical assays.

5.4.3.2 Design of Piperazinone Mpro Inhibitors

Further investigation was needed to determine which position of **4.109** could be subject to substitution (i.e., methylamine, α -carbon of the piperazinone carbonyl, ethylene bridge) to produce a library of analogs. Although docking studies of substituted methylamine failed to provide piperazine analogs binding in the expected conformation (**Table 4.14** and **4.15**), the hydrogen bonding between the piperazinone carbonyl and the backbone of Glu166 shifted the piperazinone core in Mpro binding pocket opening S2 subsite for substituents. I used an unsubstituted pyridylmethylpiperazinone core to interrogate substitution on the methyl position and determine if this substitution was tolerated on the piperazinone scaffold compared to the piperazine. The unsubstituted pyridylmethylpiperazinone core was chosen for the docking studies instead of **4.109** because previous docking studies showed that dibenylation of the core scaffold was detrimental to the binding. Therefore, the removal of the benzyl group on **4.109** would prevent any potential steric clashes and allow the identification of the optimal substituent on the methylamine group.

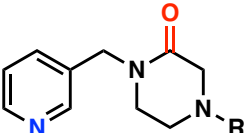
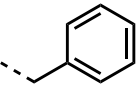
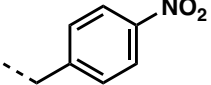
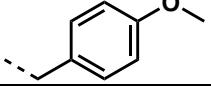
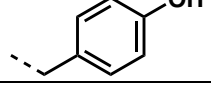
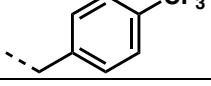
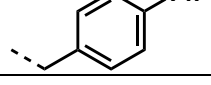
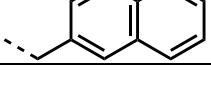
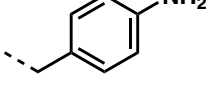
The results of the docking studies of piperazinone analogs with different substituted benzyl, aryl group and various piperazinone-phenyl linkers are summarized in **Table 4.18**. The methyl piperazinone **4.112** and cyclopropyl piperazinone **4.126** show lower predicted binding affinity and probability of Mpro inhibition compared to aryl piperazinone analogs. Among the eight aryl and substituted benzyl piperazinones (**4.113** – **4.120**), the benzyl piperazinone **4.113** was revealed to have one of the best docking score and is engaged in two hydrogen bonds with His163 and Asn142,

and face-to-face π - π stacking with His41. Notably, the trifluoromethylbenzyl analog **4.117** had the best predicted docking score and probability of Mpro inhibition of the series but it only interacts with His163. Furthermore, the benzyl piperazinone substituted with hydrogen bond donors (**4.116** and **4.120**) make hydrogen bonds deep in the S2 subsite with the backbone of Asp187. The compounds **4.121** – **4.125** and **4.127** were used to determine if the piperazinone-phenyl linker could be optimized to improve docking score or interact with additional residues. However, no such improvement was observed, and only **4.125** and **4.127** maintained the hydrogen bonding with His163. These results suggested that the methylene linker was the most favorable.

The orientation of the piperazinone appeared to be determined by the substitution of the methylamine. In analogs with benzyl groups tolerated by the pocket (**4.113**, **4.116** and **4.120**), the carbonyl is projected toward the S1' subsite and interacts with the side chain of Asn142. In contrast, the carbonyl of compounds with substituents other than benzyl groups (**4.112**, **4.124**, **4.126** and **4.117**) is projected toward S3 and interacts with the backbone of Glu166. Interestingly, the docking scores of the ligands interacting with Asn142 (**4.113**, **4.116** and **4.120**) were better than of the group (**4.112**, **4.124**, **4.126** and **4.117**) interacting with the backbone of Glu166.

These docking studies indicated that the benzyl piperazinone **4.113** is the best ligand of this series as it is predicted to engage in two hydrogen bonds with His163 and Asn142, and π - π stacking with His41 resulting in a docking score of -6.114 kcal/mol. In addition, none of the piperazinone-phenyl linkers investigated provided an improvement in docking score or additional interactions compared to **4.113**. Although the benzyl groups in **4.109** and **4.113** both interact with His41, the benzyl moiety of **4.109** is engaged in a T-shaped π - π stacking with His41, while the benzyl of **4.113** is face-to-face. This difference likely arose from the location of the benzyl group on the α -carbon of the piperazinone carbonyl for **4.109** and the piperazinone amine for **4.113**. This

site difference also appeared to influence the orientation of the piperazinone core, as the carbonyl of **4.109** is projected toward S3 and interacts with the backbone of Glu166, and the carbonyl of **4.113** is projected toward the S1' subsite and interacts with the side chain of Asn142. Taken together, the interactions between **4.113** and Mpro likely improved the docking score by 0.32 kcal/mol, suggesting that the benzyl group is more beneficial to the binding on the piperazinone amine. As such, it offered an opportunity to interrogate the substitution on the α -carbon of the piperazinone.

				
R	Compound	Docking score (kcal/mol)	Residues (interaction type)	SARS – Balanced prediction (AU)
--CH ₃	4.112	-3.529	Glu166bb (H-bond)	0.124
	4.113	-6.114	His163 (H-bond) His41 (π - π stacking) Asn142 (H-bond)	0.197
	4.114	-5.017	His163 (H-bond)	0.261
	4.115	No binding	n/a	0.160
	4.116	-6.007	Asn142 (H-bond) Asp187bb (H-bond)	0.153
	4.117	-6.182	His163 (H-bond)	0.433
	4.118	No binding	n/a	0.337
	4.119	-6.010	His163 (H-bond) His41 (π - π stacking)	0.345
	4.120	-5.847	His163 (H-bond) His41 (π - π stacking) Asn142 (H-bond) Asp187bb (H-bond)	0.256

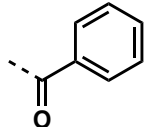
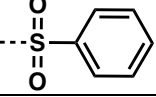
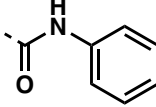
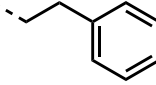
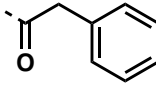
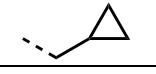
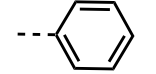
	4.121	No binding	n/a	0.265
	4.122	-5.587	His41 (π - π stacking) Gln189 (H-bond)	0.234
	4.123	No binding	n/a	0.260
	4.124	-3.127	Glu166bb (H-bond)	0.185
	4.125	-5.677	His163 (H-bond) His41 (π - π stacking)	0.238
	4.126	-3.345	His163 (H-bond) Glu166bb (H-bond)	0.097
	4.127	-5.262	His163 (H-bond) His41 (π - π stacking) Glu166bb (H-bond)	0.246

Table 4.18: Summary of the docking studies of the unsubstituted piperazinone series in SARS-CoV-2 Mpro (PDB: 3V3M). The docking score and protein-ligand interactions were predicted by Glide and SARS – Balanced model predicted the probability of Mpro inhibition.

Since the α -carbon of the piperazinone is oriented towards the S1' subsite of Mpro, as shown in **Figure 4.19**, I hypothesized that substituents on this position could target the solvent-exposed residues Gly143, and Thr24, Thr25 and Thr26. To test this hypothesis, I run docking studies of a series of piperazinone analogs with amino acid sidechains in R and S configuration and the results are summarized in **Table 4.19**.

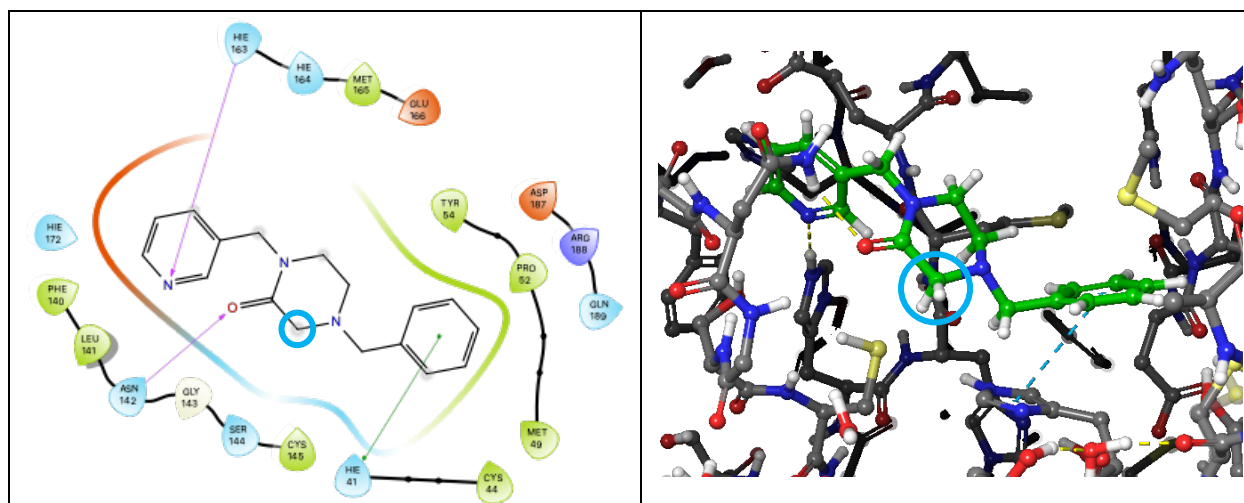
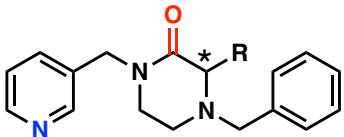
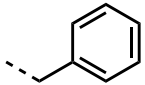
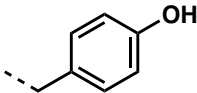
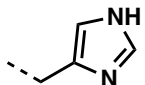
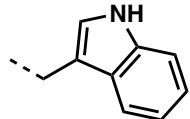


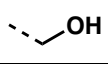
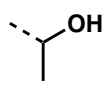
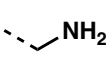
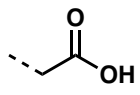
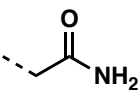
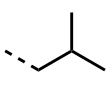
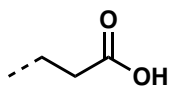
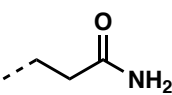
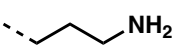
Figure 4.19: Structural representations of 4.113 in SARS-CoV-2 Mpro pocket. The 2D ligand interaction diagram is on the left and, on the right, the 3D representation of the binding pose of 4.113 in SARS-CoV-2 Mpro (PDB: 3V3M) was predicted by Glide. The blue circle highlights the α -carbon of the piperazinone.

With the exception of the Tryptophane (4.134 and 4.135) and Serine (4.136 and 4.137) piperazinones, the introduction of amino acid sidechain improved the docking score compared to the unsubstituted analog, 4.113. Notably, the binding pose vary based on the configuration of the α -carbon: (1) The R configuration of eight ligands (4.132, 4.134, 4.136, 4.138, 4.140, 4.144, 4.150 and 4.152) shifts the pyridyl nitrogen away from His163 preventing the important hydrogen bonding, whereas the S isomers (4.133, 4.135, 4.137, 4.139, 4.141, 4.145, 4.151 and 4.153) interact with His163; (2) The R stereoisomers 4.128, 4.130 and 4.146 are engaged in a hydrogen bond with the backbone of Glu166 in the S3 pocket, but the corresponding S analogs 4.129, 4.131 and 4.147 adopt the opposite orientation towards the S1' subsite.

The results of these docking studies (Table 4.19) indicated that the substituted piperazinone series: (1) Has an overall improved docking score compared to the unsubstituted piperazinones (Table 4.18), any of the piperazine analogs and the XChem fragment 4.55; (2) Maintained the pyridine-His163 hydrogen bonding and the benzyl-His41 π - π stacking,

particularly the R isomers; (3) Established additional hydrogen bondings with S1' subsite residues (e.g., Asn142 and Gly143); (4) Is predicted to inhibit Mpro (SARS – Balanced model) in a greater probability than the other studied scaffolds. Although the docking scores of R analogs tend to be moderately better than the S counterparts, I considered S substituted piperazinone compounds for synthesis and biochemical evaluation as they more reliably engage in the critical hydrogen bonding with His163. As such I chose to pursue the synthesis of the compounds **4.129**, **4.143**, **4.145**, **4.149**, **4.151** and **4.153** for their good docking score, the predicted protein-ligand interactions and adequate predicted Mpro inhibition.

				
R	Name*	Docking score (kcal/mol)	Residues (interaction type)	SARS – Balanced prediction (AU)
H	4.113	-6.114	His163 (H-bond) His41 (π - π stacking) Asn142 (H-bond)	0.197
	4.128 (R)	-6.357	His163 (H-bond) His41 (π - π stacking) Glu166bb (H-bond)	0.359
	4.129 (S)	-7.012	His163 (H-bond) Asn142 (H-bond)	0.348
	4.130 (R)	-7.315	His163 (H-bond) Glu166bb (H-bond)	0.300
	4.131 (S)	-7.325	His163 (H-bond) Thr26bb (H-bond)	0.290
	4.132 (R)	-6.620	His41 (π - π stacking) Asn142 (H-bond) Thr26bb (H-bond)	0.245
	4.133 (S)	-6.463	His163 (H-bond) His41 (π - π stacking) Asn142 (H-bond) Thr26bb (H-bond)	0.254
	4.134 (R)	-5.565	His41 (π - π stacking)	0.520
	4.135 (S)	-5.785	His163 (H-bond)	0.508

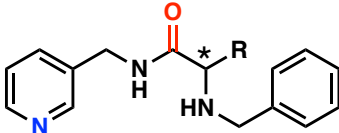
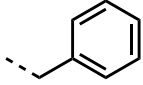
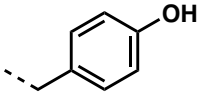
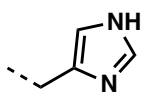
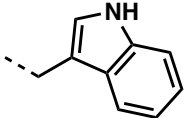
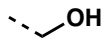
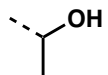
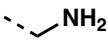
	4.136 (R)	No binding	n/a	0.165
	4.137 (S)	No binding	n/a	0.171
	4.138 (R)	-7.777	His41 (π - π stacking) Asn142 (H-bond)	0.177
	4.139 (S)	-7.301	His163 (H-bond) His41 (π - π stacking) Asn142 (H-bond)	0.190
	4.140 (R)	No binding	n/a	0.217
	4.141 (S)	-6.674	His163 (H-bond) Asn142 (H-bond)	0.225
	4.142 (R)	-7.108	His163 (H-bond) His41 (π - π stacking) Asn142 (H-bond) Gly143 (H-bond)	0.252
	4.143 (S)	-6.930	His163 (H-bond) His41 (π - π stacking) Asn142 (H-bond) Gly143 (H-bond)	0.263
	4.144 (R)	-7.809	His41 (π - π stacking) Asn142 (H-bond) Gly143 (H-bond)	0.263
	4.145 (S)	-7.053	His163 (H-bond) His41 (π - π stacking) Asn142 (H-bond) Gly143 (H-bond)	0.275
	4.146 (R)	-6.385	His163 (H-bond) His41 (π - π stacking) Glu166bb (H-bond)	0.196
	4.147 (S)	-6.611	His163 (H-bond) His41 (π - π stacking) Asn142 (H-bond)	0.204
	4.148 (R)	-7.585	His163 (H-bond) His41 (π - π stacking) Asn142 (H-bond) Gly143 (H-bond)	0.250
	4.149 (S)	-7.444	His163 (H-bond) His41 (π - π stacking) Asn142 (H-bond) Gly143 (H-bond)	0.258
	4.150 (R)	-8.269	His41 (π - π stacking) Asn142 (H-bond) Gly143 (H-bond)	0.236
	4.151 (S)	-8.117	His163 (H-bond) His41 (π - π stacking) Asn142 (H-bond) Gly143 (H-bond)	0.244
	4.152 (R)	-7.147	Asn142 (H-bond) His41 (π - π stacking) Thr26bb (H-bond)	0.204
	4.153 (S)	-6.488	His163 (H-bond)	0.197

			His41 (π - π stacking) Asn142 (H-bond)	
--	--	--	--	--

Table 4.19: Summary of the docking studies of the substituted piperazinone series in SARS-CoV-2 Mpro (PDB: 3V3M). The docking score and protein-ligand interactions were predicted by Glide and SARS – Balanced model predicted the probability of Mpro inhibition. * The absolute stereochemistry of the chiral center (denoted by *) of each analog is indicated by R or S at the end of the name.

As discussed in **Chapter 2** and **3**, the N- to C-terminal cyclization of a peptidic core reduces the conformational flexibility of the scaffold and influences the orientation of the appending moieties. Since the piperazinone scaffold was determined to be the best candidate to generate a library of analogs, I considered this was an opportunity to interrogate the effect of cyclization on inhibitory activity against Mpro by comparing the piperazinone scaffold and its uncyclized peptidic counterpart. Therefore, a series of uncyclized peptidic analogs of **4.113** and **4.128 – 4.153** were the subject of the docking studies presented in **Table 4.20**. The objective of this investigation was to determine if the structural constraint resulting from the ethylene bridge of the piperazinone is favorable or detrimental to the binding in Mpro.

Taken together, the results of the docking studies (**Table 4.20**) indicates that peptidic analogs generally have a lower predicted binding affinity and probability of Mpro inhibition than their piperazinone counterparts. Compared to the piperazinone series, the binding poses of the peptidic compounds are less affected by the configuration of the α -carbon. In aggregate, the docking studies suggest that the higher flexibility of the peptidic scaffold allow protein-ligand interactions for a broader range of ligands relative to the piperazinone scaffold. However, the improved flexibility of the peptidic scaffold may increase the entropic cost of binding in Mpro pocket, resulting in a lower predicted binding affinity.

				
R	Compound*	Docking score (kcal/mol)	Residues	SARS – Balanced prediction (AU)
H	4.154	-6.010	His163 (H-bond) His41 (π - π stacking) Asn142 (H-bond) Gly143 (H-bond)	0.156
	4.155 (R)	No binding	n/a	0.279
	4.156 (S)	-6.406	His163 (H-bond) His41 (π - π stacking) Glu166bb (H-bond)	0.286
	4.157 (R)	-6.184	His163 (H-bond) Glu166bb (H-bond) Asp187bb (H-bond)	0.258
	4.158 (S)	-6.577	His41 (π - π stacking) His163 (H-bond) Glu166bb (H-bond) Met49bb (H-bond)	0.264
	4.159 (R)	-5.821	His163 (H-bond) Asn142 (H-bond) Thr26bb (H-bond)	0.205
	4.160 (S)	-5.644	His41 (π - π stacking) His163 (H-bond)	0.211
	4.161 (R)	-6.466	His41 (π - π stacking) His163 (H-bond) Glu166bb (H-bond)	0.471
	4.162 (S)	No binding	n/a	0.464
	4.163 (R)	-6.529	His41 (π - π stacking) His163 (H-bond) Asn142 (H-bond) Gly143 (H-bond)	0.137
	4.164 (S)	-6.540	His41 (π - π stacking) His163 (H-bond) Asn142 (H-bond) Gly143 (H-bond)	0.141
	4.165 (R)	-6.677	His163 (H-bond) Asn142 (H-bond)	0.142
	4.166 (S)	-6.692	His41 (π - π stacking) His163 (H-bond) Asn142 (H-bond) Gly143 (H-bond)	0.151
	4.167 (R)	No binding	n/a	0.187
	4.168 (S)	-6.775	His41 (π - π stacking) His163 (H-bond) Asn142 (H-bond)	0.191
	4.169 (R)	-6.788	His41 (π - π stacking)	0.223

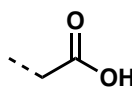
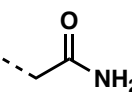
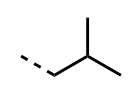
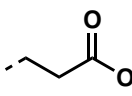
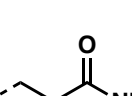
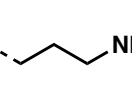
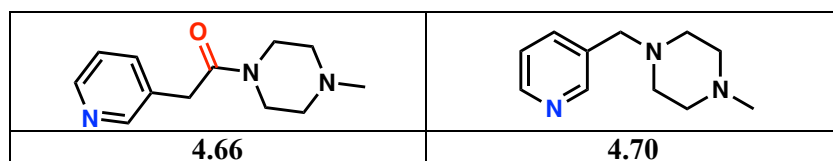
			His163 (H-bond) Asn142 (H-bond) Gly143 (H-bond) Cys145 (H-bond)	
	4.170 (S)	No binding	n/a	0.230
	4.171 (R)	-7.700	His41 (π - π stacking) His163 (H-bond) Asn142 (H-bond) Gly143 (H-bond) Thr26bb (H-bond)	0.228
	4.172 (S)	-7.942	His41 (π - π stacking) His163 (H-bond) Asn142 (H-bond) Gly143 (H-bond) Thr26bb (H-bond)	0.237
	4.173 (R)	-5.870	His41 (π - π stacking) His163 (H-bond)	0.138
	4.174 (S)	-6.484	His41 (π - π stacking) His163 (H-bond) Asn142 (H-bond)	0.141
	4.175 (R)	-6.765	His163 (H-bond) His164 (H-bond) Glu166bb (H-bond) Cys145 (H-bond)	0.212
	4.176 (S)	-6.987	His163 (H-bond) His41 (π - π stacking) Asn142 (H-bond) Gly143 (H-bond) Cys145 (H-bond) Glu166bb (H-bond)	0.217
	4.177 (R)	-6.278	His163 (H-bond) His41 (π - π stacking) Asn142 (H-bond) Gly143 (H-bond)	0.204
	4.178 (S)	-7.262	His163 (H-bond) Glu166bb (H-bond) Gln189 (H-bond)	0.208
	4.179 (R)	-6.296	His163 (H-bond) His41 (π - π stacking) Asn142 (H-bond) Thr26bb (H-bond)	0.158
	4.180 (S)	-6.993	His163 (H-bond) His41 (π - π stacking) Gly143 (H-bond)	0.161

Table 4.20: Summary of the docking studies of the substituted peptidic series in SARS-CoV-2 Mpro (PDB: 3V3M). The docking score and protein-ligand interactions were predicted by Glide and SARS – Balanced model predicted the probability of Mpro inhibition. * The absolute stereochemistry of the chiral center (denoted by *) of each analog is indicated by R or S at the end of the name.

In summary, the dibenzyl piperazine scaffold, that was designed from the XChem fragment **4.55**, was invalidated by my docking studies due to the poor binding in Mpro pocket and the encountered synthetic challenges. However, the results from the docking studies provided an alternative rationale for the design of the substituted piperazinone scaffold. The investigation of this scaffold indicated that: (1) The docking score surpassed the ones of the piperazine scaffold and **4.55**; (2) Substituents on the α -carbon of the piperazinone led to additional protein-ligand interactions with residues of the S1' subsite (i.e., Asn142 and Gly143); (3) The benzyl group on the piperazinone amine was more beneficial to the binding than on the α -carbon and led to a π - π stacking interaction with His41; (4) The probability for Mpro inhibition (SARS – Balanced model) was higher than the piperazine scaffold and **4.55**. As the piperazinone scaffold was determined to be the best candidate for the design of Mpro inhibitors, it was an opportunity to examine the role of the N- to C-terminal cyclization on the inhibitory activity of the scaffold by comparing uncyclized peptidic analogs. Therefore, I selected a set of the ligands (**Table 4.21**) used in these docking studies for synthesis and biochemical evaluation, to (1) validate the rationale developed in these computational studies (i.e., **4.66**, **4.70**, **4.113**) and (2) assess the effect of the conformational constraint on the inhibitory activity against Mpro of *in silico* piperazinone hits (i.e., **4.126**, **4.143**, **4.145**, **4.149**, **4.151** and **4.153**) relative to their peptidic counterparts (i.e., **4.154**, **4.156**, **4.170**, **4.172**, **4.176**, **4.178** and **4.180**).



4.113	4.154
4.129	4.156
4.143	4.170
4.145	4.172
4.149	4.176
4.151	4.178
4.153	4.180

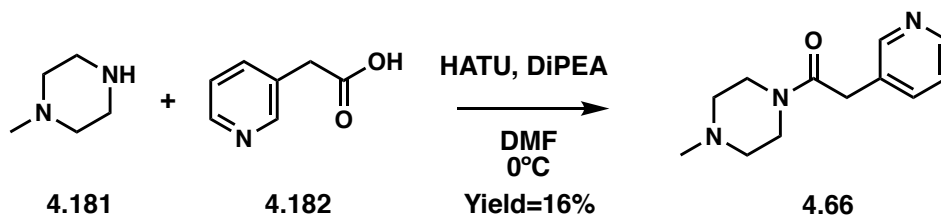
Table 4.21: Summary of the library of compounds to synthesize.

6 Synthesis of the Library of Mpro Inhibitors

Due to the time constrained nature of this project and the limited access to the laboratory, the computational studies and the synthetic work were conducted in parallel. As such I started with the development of a methodology to access the piperazine scaffold. However, the conclusions drawn from the docking studies which led to invalidate the piperazine prompted me to pivot and use the previously optimized methodology for the synthesis of piperazinones to generate the analogs from **Table 4.21**. Hereafter, I present the synthetic work I produced throughout this project to generate a preliminary set of compounds targeting SARS-CoV-2 Mpro.

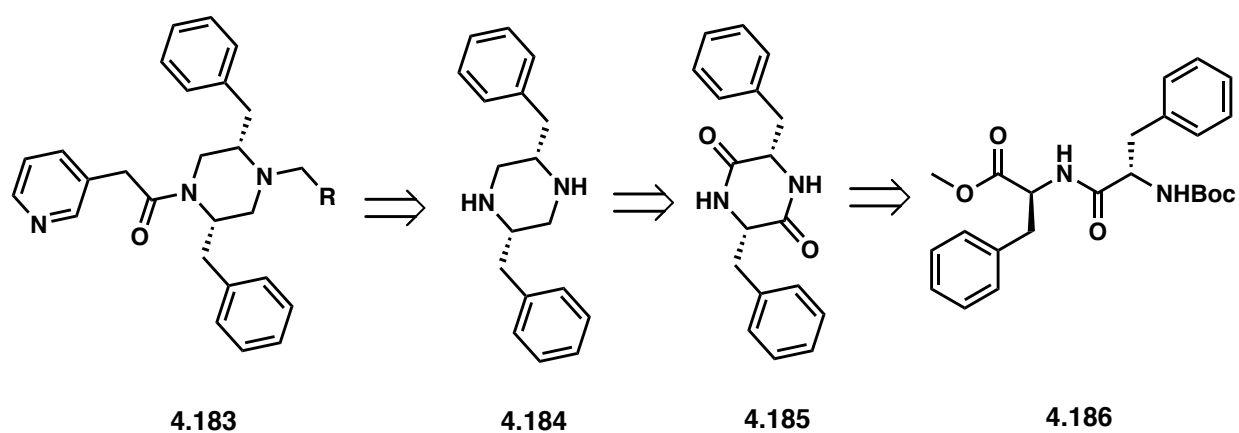
6.1 Synthesis of the Piperazine Mpro Inhibitors

Because I started the rationale for the design of the piperazinone series with the XChem fragment **4.55**, it was important to evaluate its inhibitory activity against Mpro to establish a benchmark for the rest of the compounds. However, the 2-(7-azaindole) acetic acid was not available at the time in our reactant library. Therefore, the pyridyl analog **4.66** was prepared instead as the “benchmark” compound with the 2-(pyridine-3-yl) acetic acid **4.182** and 1-methylpiperazine **4.181** in 16% yield.



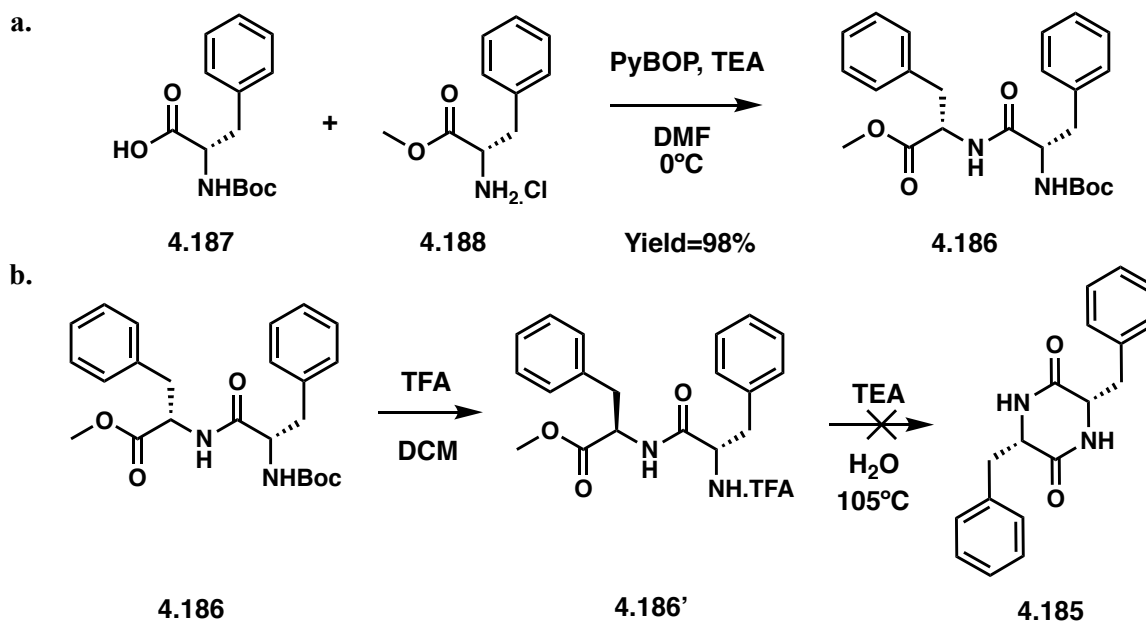
Scheme 4.4: Synthetic route for the piperazine analog **4.66**.

At this stage of the project, I was conducting docking studies on the dibenzyl piperazine scaffold **4.183** and, in parallel, I was investigating the methodology to synthesize the scaffold from the diketopiperazine **4.185** (Scheme 4.5).



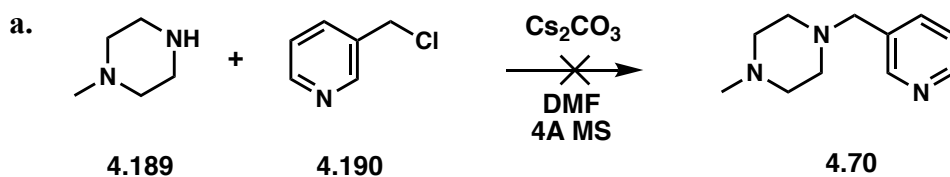
Scheme 4.5: Retrosynthetic analysis of the piperazine scaffold 4.183.

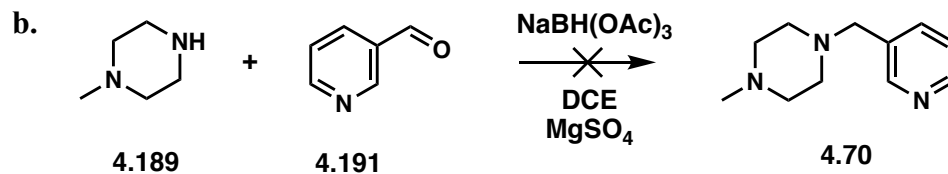
As depicted in **Scheme 4.5**, I proposed to access the diketopiperazine **4.185** from the diphenylalanine **4.186** which was prepared from the amide coupling of the phenylalanines **4.187** and **4.187** in 98% yield (**Scheme 4.6a**). However, the cyclization of the deprotected diphenylalanine **4.186'** did not yield the desired product **4.185**.⁷⁸ For this reason and the results of the docking studies on this scaffold, I pivoted to the synthesis of the piperazinone scaffold.



Scheme 4.6: Synthetic route for the diphenylalanine 4.186 (a) and dibenzyl diketopiperazine (b).

Although the dibenzyl piperazine series was not pursued, the piperazine **4.70** was instrumental for the design process of the piperazinone scaffold and evaluating its inhibitory activity against Mpro could validate my rationale for the design of the piperazinone series built from **4.70**. However, the different synthetic routes examined failed to produce **4.70**. First, the use of methylpiperazine was expected to yield **4.70** in one step via N-alkylation (**Scheme 4.7a**) or reductive amination (**Scheme 4.7b**). Although partial conversion of chloromethylpyridine **4.190** and nicotinaldehyde **4.191** was observed by thin layer chromatography (TLC), the product was lost following the purification step due to the significant polarity of **4.70**.





Scheme 4.7: Synthetic routes for 4.70 from methylpiperazine.

Then I explored an alternative route starting with a reductive amination of Boc-piperazine **4.192** and nicotinaldehyde **4.191** which afforded the intermediate **4.193** in 67% yield. Although the synthesis of **4.193** was more tractable, I encountered the same purification challenges when I employed methylation conditions (Entry 1 and 2, Table 4.22) on the deprotected pyridylpiperazine intermediate **4.193'**.

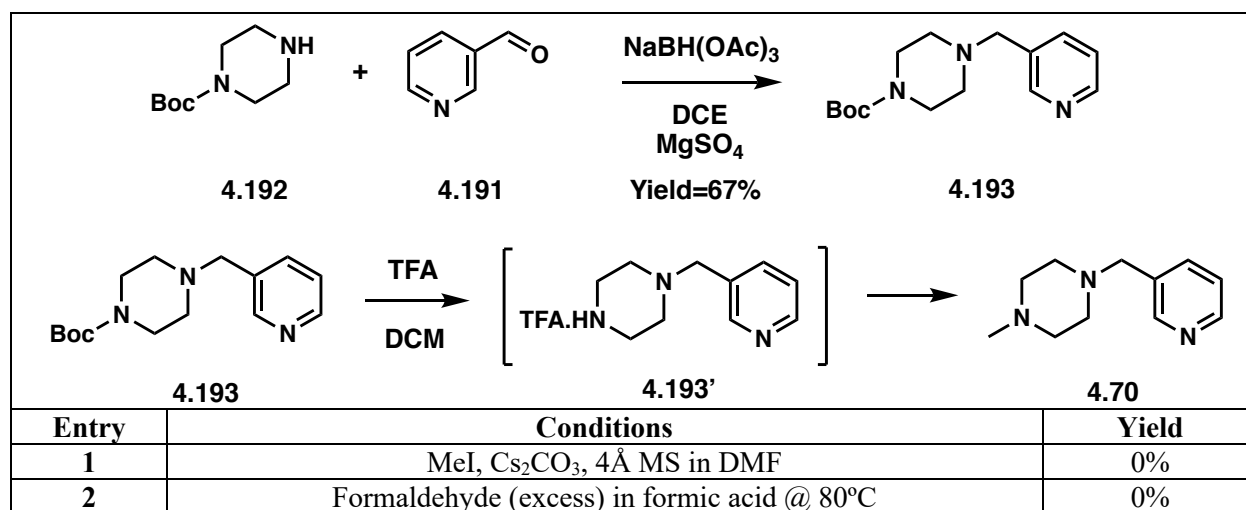
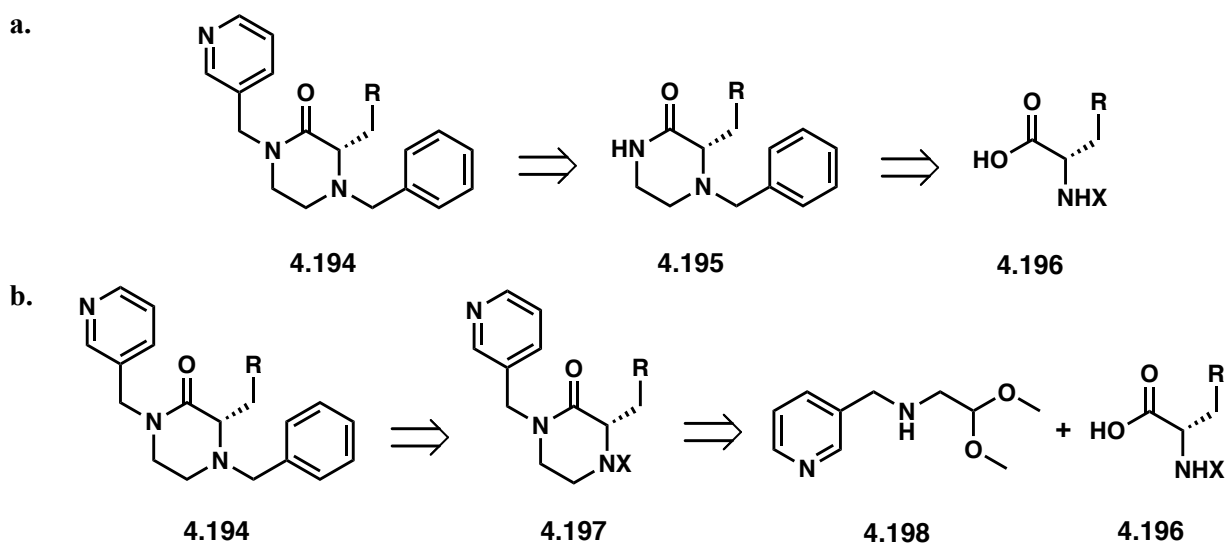


Table 4.22: Synthetic route for 4.70 from Boc-piperazine.

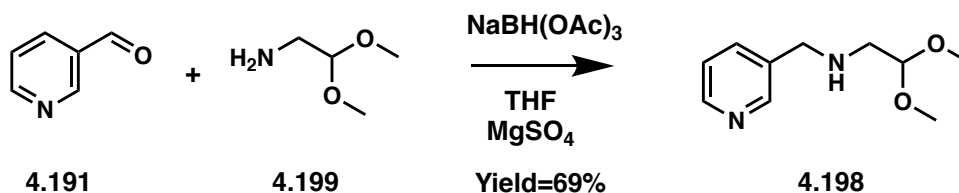
6.2 Synthesis of the Piperazinone Mpro Inhibitors

Although I have previously presented a synthetic route for the piperazinone scaffold comprising the formation of the piperazinone ring followed by the N-alkylation of the secondary

amide, I needed to adapt it in accordance with the reactants employed for the generation of this library. I anticipated that, if the piperazinone **4.195** (Scheme 4.8a) was formed first, N-alkylation of the piperazinone amide with chloromethylpyridine **4.190** would be challenging as: (1) **4.190** might not be compatible with the methodologies used in Chapter 2; (2) Competitive N-alkylation with the tertiary amine on the piperazinone or with the sidechain of the amino acids (e.g., **4.145**, **4.151** and **4.153**) are possible. Therefore, I proposed the incorporation the methylpyridyl group into the aminoacetaldehyde dimethyl acetal via reductive amination (Scheme 4.9), to avoid these potential pitfalls as depicted in Scheme 4.8b.

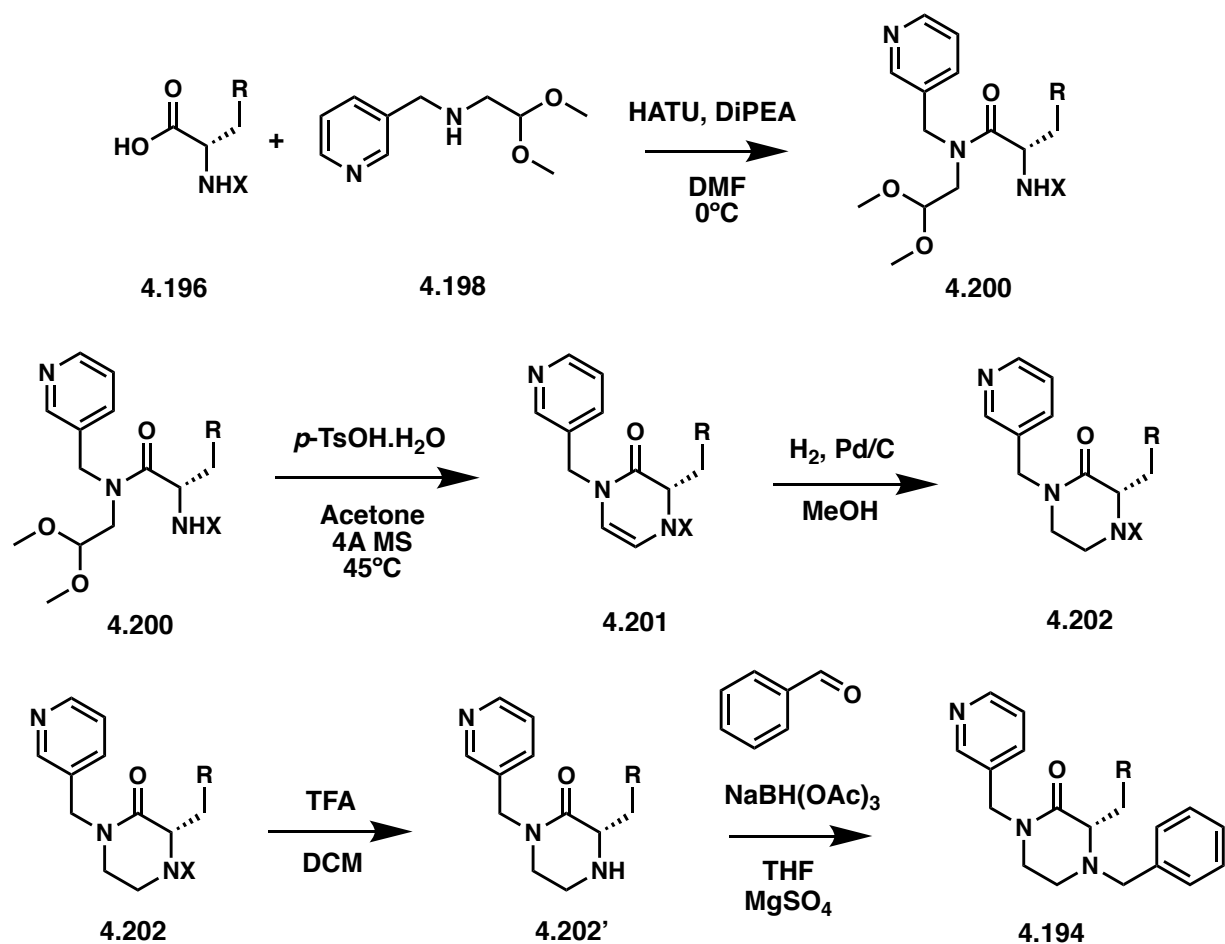


Scheme 4.8: Retrosynthetic schemes for the piperazinone scaffold.



Scheme 4.9: Synthetic route for the preparation of 4.198.

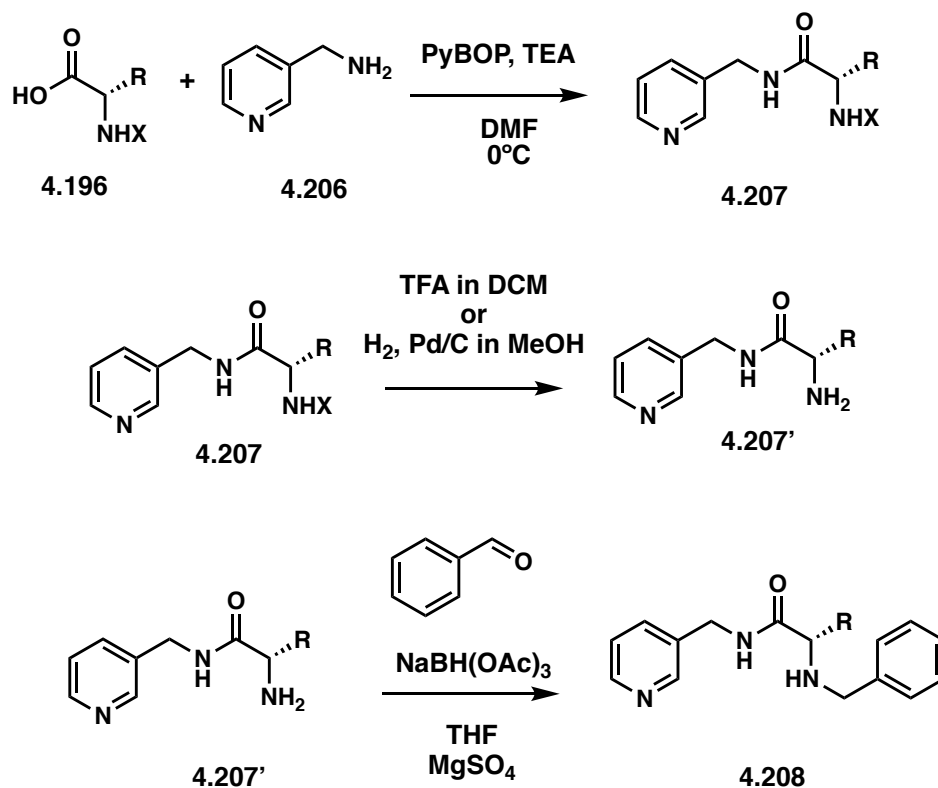
The piperazinone compound **4.113** was synthesized following the synthetic route presented in **Scheme 4.10**. Briefly, the amine **4.198** was coupled with a Boc- or Cbz-protected L-amino acid **4.196** to afford the amide **4.200**. As previously described, the removal of the dimethyl acetal under acidic conditions promoted the intramolecular cyclization of **4.200** to the enamine **4.201**. Following hydrogenation of **4.201**, the piperazinone **4.202** was deprotected with trifluoroacetic acid (TFA) and the final product **4.194** was obtained via reductive amination with benzaldehyde. Although **4.113** was easily accessed from the Boc-glycine, the use of different amino acids revealed to be more challenging than anticipated. Therefore, further optimization of this synthetic route is needed to produce piperazinone analogs.



Scheme 4.10: Synthetic route to the substituted piperazinone scaffold **4.194**. The N-terminus protecting group (denoted by X) is either Boc or Cbz group.

6.3 Synthesis of the Peptidic Mpro Inhibitors

As shown in **Scheme 4.11**, the peptidic compounds **4.156**, **4.180** and **4.178** were synthesized as follows. The amide coupling of pyridyl methanamine **4.206** and Boc- or Cbz-protected L amino acid **4.196** afforded the amide **4.207** and the Boc- or Cbz-group was deprotected via treatment with TFA or hydrogenation conditions, respectively. The reductive amination of benzaldehyde and the amine **4.207'** yielded the final product **4.208**.



Scheme 4.11: Synthetic route to the substituted piperazinone scaffold 4.208. The N-terminus protecting group (denoted by X) is either Boc or Cbz group.

7 Conclusion and Future Directions

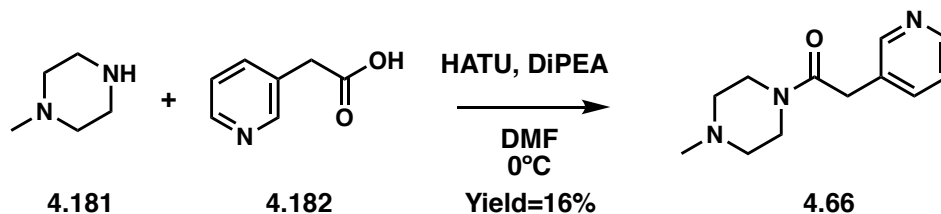
Although the COVID-19 pandemic was a cataclysmic event, it was an opportunity for us to harness the medicinal chemistry we acquired in the Duerfeldt lab and contribute to the research effort taking place around the world. Considering the time constraint of the project and the limited access to the lab, we reviewed the existing literature on SARS-CoV and decided to target Mpro. This choice was later comforted by the emergency use authorization by the FDA of PF-07321332 (4.36) “boosted” with Ritonavir (4.3) in a pill form. Thanks to the existing body of knowledge on Mpro and the XChem fragment hits, I designed four structurally distinct scaffolds of potential non-covalent Mpro inhibitors.

The docking studies I performed led to invalidate the original dibenzyl piperazine scaffold, but they provided useful insights to design the piperazinone scaffold. Compared with the XChem hit **4.55** I used to build my rationale, piperazinone analogs improved in their docking score and probability to inhibit Mpro (SARS – Balanced model). Furthermore, the piperazinone accessed new protein-ligand interactions (i.e., π - π stacking with His41, hydrogen bonds with Asn142 and Gly143) via substitution of the α -carbon.

As discussed in **Chapter 2** and **3**, N- to C-terminal cyclization of a peptidic scaffold introduces conformational constraint and influences the orientation of appending moieties. Therefore, this project provided an opportunity to interrogate the effect of such cyclization and the related conformational changes on the inhibitory activity against Mpro by contrasting a piperazinone library with its uncyclized peptidic counterpart. The preliminary set of potential Mpro inhibitors I synthesized set the stage for future biochemical evaluation and further optimization of the piperazinone synthetic route will determine the applicability of the N- to C-terminal cyclization approach beyond ClpP activation.

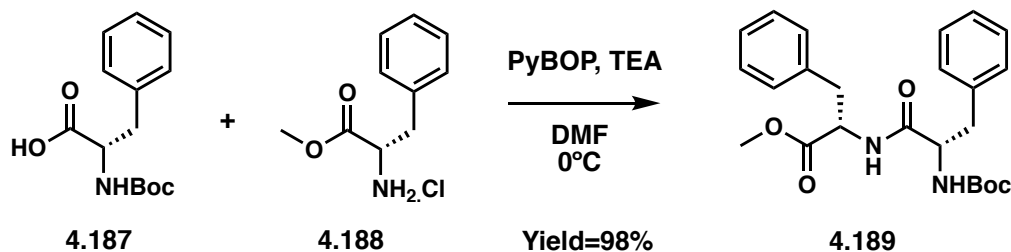
8 Experimental Section

1-(4-methylpiperazin-1-yl)-2-(pyridin-3-yl) ethan-1-one (**4.66**):



In a 3-dram vial, 1-methylpiperazine **4.181** (0.5 mmol, 60 μ L), 2-(pyridin-3-yl) acetic acid **4.182** (0.5 mmol, 87 mg) and N, N-Diisopropylethylamine (DiPEA) (1.5 mmol, 250 μ L) were dissolved in 4 mL of dry dimethylformamide (DMF). After the reaction mixture was cooled down to 0°C (ice bath) HATU was added (0.6 mmol, 228 mg). The reaction was stirred and let warm to room temperature (RT) overnight. The reaction was quenched with water (4 mL) and washed with a saturated solution of sodium bicarbonate (NaHCO₃) (20 mL) and the organic layer was extracted with ethyl acetate (EtOAc) (3 times). The organic layers were combined, washed with brine before being dried over sodium sulfate (Na₂SO₄) and filtered. The filtrate was concentrated in vacuo and purified by flash column chromatography (Silica gel, 2-10% methanol (MeOH) in dichloromethane (DCM)) to yield **4.66** (18 mg; Yield=16%) as a red oil. ¹H NMR (400 MHz, Chloroform-*d*) δ 8.51 (dd, *J* = 4.9, 1.6 Hz, 1H), 8.48 (d, *J* = 2.3 Hz, 1H), 7.62 (dt, *J* = 7.9, 2.0 Hz, 1H), 7.28 (dd, *J* = 7.9, 4.9 Hz, 1H), 3.71 (s, 2H), 3.66 (t, *J* = 5.2 Hz, 2H), 3.54 – 3.47 (m, 2H), 2.38 (t, *J* = 5.2 Hz, 2H), 2.35 – 2.30 (m, 2H), 2.28 (s, 3H). ¹³C NMR (101 MHz, Chloroform-*d*) δ 168.3, 149.9, 148.3, 136.6, 130.8, 123.5, 77.3, 77.0, 76.7, 54.9, 54.5, 45.9, 41.8, 37.6.

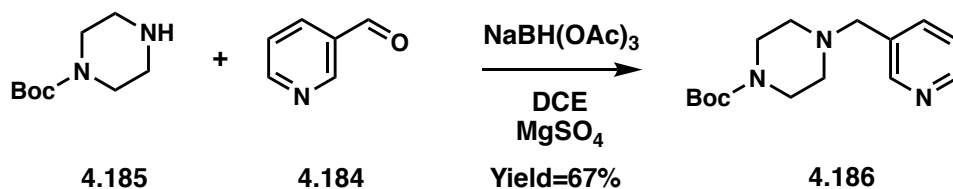
methyl (*tert*-butoxycarbonyl)-*L*-phenylalanyl-*L*-phenylalaninate (4.189**):**



In a 3-dram vial, (*tert*-butoxycarbonyl)-*L*-phenylalanine **4.187** (0.75 mmol, 200 mg), methyl ester *L*-phenylalanine hydrochloride **4.188** (0.75 mmol, 162 mg) and triethylamine (TEA) (3 mmol, 410

μL) were dissolved in 4 mL of dry DMF. After the reaction mixture was cooled down to 0°C (ice bath) PyBOP was added (1 mmol, 520 mg). The reaction was stirred and let warm to RT overnight. The reaction was quenched with water (4 mL) and washed with a saturated solution of NaHCO_3 (20 mL) and the organic layer was extracted with EtOAc (3 times). The organic layers were combined, washed with brine before being dried over Na_2SO_4 and filtered. The filtrate was concentrated in vacuo and purified by flash column chromatography (Silica gel, 20-50% EtOAc in Hexane) to yield **4.189** (313 mg; Yield=98%) as a white solid. ^1H NMR (500 MHz, Chloroform-*d*) δ 7.31 – 7.17 (m, 8H), 7.05 – 6.99 (m, 2H), 6.55 (d, $J = 7.7$ Hz, 1H), 5.15 (d, $J = 8.1$ Hz, 1H), 4.84 – 4.76 (m, 1H), 4.45 – 4.37 (m, 1H), 3.65 (s, 3H), 3.12 – 2.99 (m, 4H), 1.40 (s, 9H). ^{13}C NMR (126 MHz, Chloroform-*d*) δ 171.5, 171.0, 155.3, 136.6, 135.7, 129.4, 129.3, 128.6, 128.5, 127.1, 126.9, 80.0, 53.3, 52.3, 38.3, 38.0, 28.3.

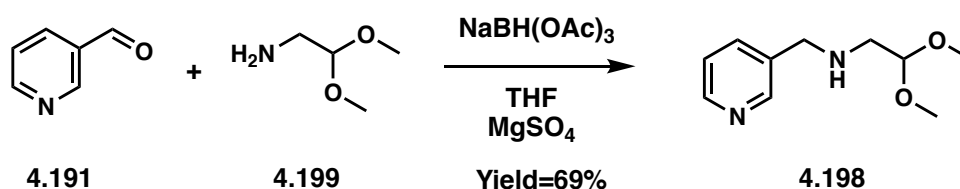
***tert*-butyl 4-(pyridin-3-ylmethyl) piperazine-1-carboxylate (4.186):**



In a 3-dram vial, *tert*-butyl piperazine-1-carboxylate **4.185** (1 mmol, 186 mg), nicotinaldehyde **4.184** (1.1 mmol, 110 μL) and 50 mg of MgSO_4 were dissolved in dry 4 mL of 1,2-Dichloroethane (DCE) and stirred for 10 min. NaBH(OAc)_3 (1.5 mmol, 318 mg) was then added and the reaction mixture was stirred overnight. The reaction was quenched with a saturated solution of ammonium chloride (4 mL) and washed with a saturated solution of NaHCO_3 (20 mL). The organic layer was extracted with EtOAc (3 times) and then were combined, washed with brine before being dried

over Na₂SO₄ and filtered. The filtrate was concentrated in vacuo and purified by flash column chromatography (Silica gel, 2-10% MeOH in DCM) to yield **4.186** (187 mg; Yield=67%) as a white solid. ¹H NMR (400 MHz, Methanol-*d*₄) δ 8.50 (d, *J* = 2.0 Hz, 1H), 8.44 (dd, *J* = 4.9, 1.6 Hz, 1H), 7.84 (dt, *J* = 7.9, 2.0 Hz, 1H), 7.41 (ddd, *J* = 7.9, 4.9, 0.9 Hz, 1H), 3.58 (s, 2H), 3.42 (t, *J* = 5.1 Hz, 4H), 2.41 (t, *J* = 5.0 Hz, 4H), 1.44 (s, 9H). ¹³C NMR (101 MHz, Methanol-*d*₄) δ 154.9, 149.5, 147.6, 137.9, 134.0, 123.8, 79.8, 59.3, 52.4, 48.3, 48.0, 47.8, 47.6, 47.4, 47.2, 47.0, 27.3.

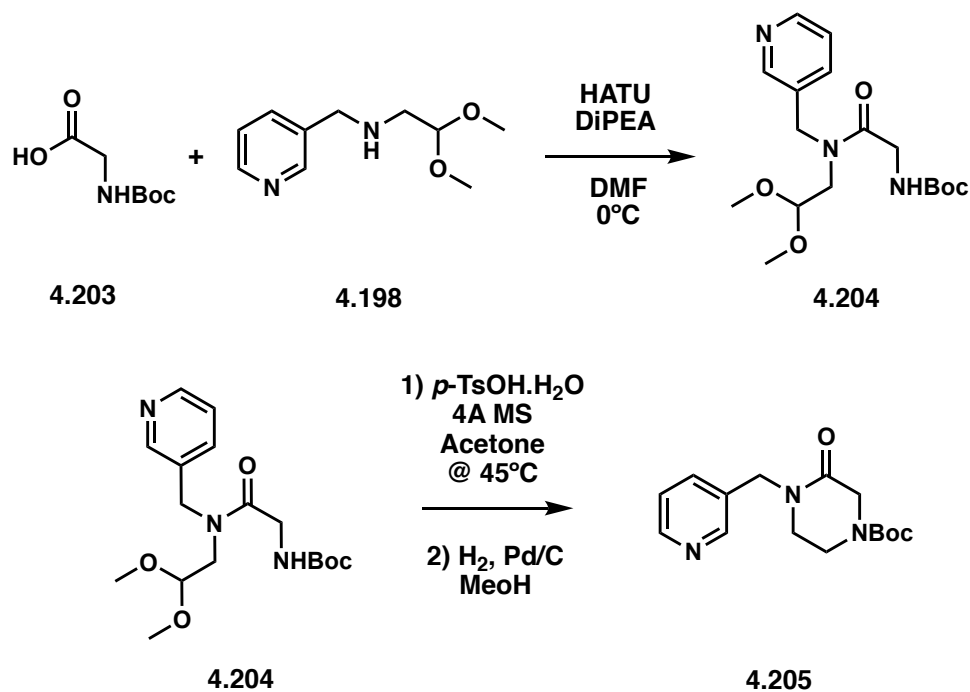
2,2-dimethoxy-*N*-(pyridin-3-ylmethyl) ethan-1-amine (4.198):



In a 3-dram vial, nicotinaldehyde **4.191** (1.0 mmol, 94 μL), aminoacetaldehyde dimethyl acetal **4.199** (1.1 mmol, 120 μL) and 120 mg of MgSO₄ were dissolved in dry 4 mL of tetrahydrofuran (THF) and stirred for 10 min. NaBH(OAc)₃ (1.5 mmol, 318 mg) was then added and the reaction mixture was stirred overnight. The reaction was quenched with a saturated solution of ammonium chloride (4 mL) and washed with a saturated solution of NaHCO₃ (20 mL). The organic layer was extracted with EtOAc (3 times) and then were combined, washed with brine before being dried over Na₂SO₄ and filtered. The filtrate was concentrated in vacuo and purified by flash column chromatography (Silica gel, 2-10% MeOH and 10% CH₃CN in DCM) to yield **4.198** (136 mg; Yield=69%) as a yellow oil. ¹H NMR (400 MHz, Chloroform-*d*) δ 8.57 – 8.52 (m, 1H), 8.52 – 8.46 (m, 1H), 7.71 – 7.63 (m, 1H), 7.29 – 7.21 (m, 1H), 4.47 (td, *J* = 5.4, 0.9 Hz, 1H), 3.81 (s, 2H),

3.36 (d, $J = 1.0$ Hz, 6H), 2.73 (dd, $J = 5.5, 0.9$ Hz, 2H). ^{13}C NMR (101 MHz, Chloroform- d) δ 149.7, 148.6, 135.86, 135.2, 123.4, 103.7, 77.4, 77.1, 76.8, 54.1, 51.1, 50.4.

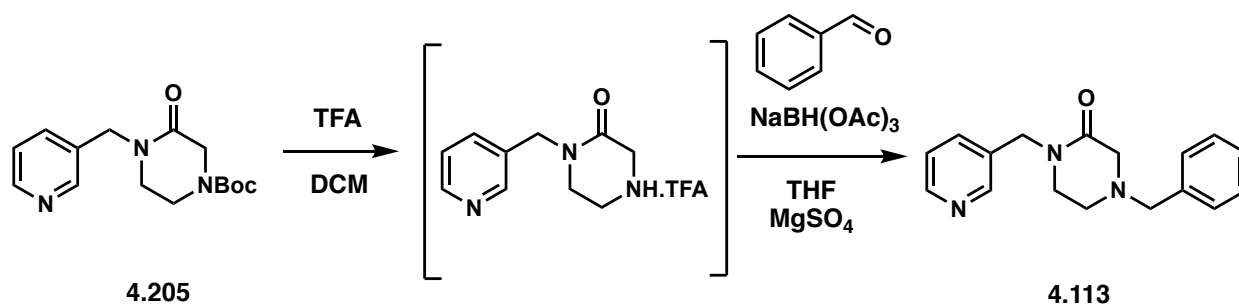
***tert*-butyl 3-oxo-4-(pyridin-3-ylmethyl) piperazine-1-carboxylate (4.205):**



In a 3-dram vial, **4.198** (0.86 mmol, 168 mg), Boc-glycine **4.203** (0.57 mmol, 100 mg) and DIPEA (0.86 mmol, 298 μL) were dissolved in 2 mL of dry DMF. After the reaction mixture was cooled down to 0°C (ice bath) HATU was added (0.86 mmol, 326 mg). The reaction was stirred and let warm to RT overnight. The reaction was quenched with water (4 mL) and washed with a saturated solution of NaHCO_3 (20 mL) and the organic layer was extracted with EtOAc (3 times). The organic layers were combined, washed with brine before being dried over Na_2SO_4 and filtered. The filtrate was concentrated in vacuo and purified by flash column chromatography (Neutral alumina, 0-2% MeOH in DCM) to yield the amide intermediate **4.204** (198 mg; Yield=98%) as a white solid. **4.204** (0.56 mmol, 198 mg), $p\text{-TsOH}\cdot\text{H}_2\text{O}$ (1.1 mmol, 200 mg) and 4A molecular

sieves were then dissolved in 15 mL of acetone and stirred for 4h at 45°C. The crude was filtered through a celite plug and was taken directly to the next step. In a sealable vial, the crude (94 mg) and palladium on carbon (35 mg) was dissolved in 10 mL of MeOH. A balloon of hydrogen was connected to the sealed vial and the reaction mixture was stirred overnight. The crude was concentrated under nitrogen flow and filtered through a celite plug. The filtrate was concentrated in vacuo and purified by flash column chromatography (Neutral alumina, 2-4% MeOH in DCM) to yield **4.205** (198 mg; Yield=98%) as a white solid. ¹H NMR (400 MHz, Chloroform-*d*) δ 8.53 (dd, *J* = 4.8, 1.6 Hz, 1H), 8.51 – 8.49 (m, 1H), 7.66 – 7.59 (m, 1H), 7.29 – 7.25 (m, 1H), 4.60 (s, 2H), 4.13 (s, 2H), 3.59 (t, *J* = 5.4 Hz, 2H), 3.27 (t, *J* = 5.5 Hz, 2H), 1.44 (s, 9H).

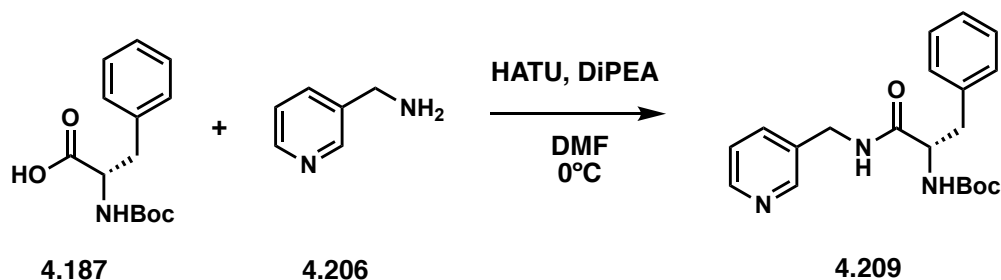
4-benzyl-1-(pyridin-3-ylmethyl) piperazin-2-one (**4.113**):



In a 3-dram vial, 183 was dissolved in 10 mL of DCM and 4 mL of TFA was added. The reaction mixture was stirred overnight. After concentration under N₂ flow, the crude was taken directly to the next step. In a 3-dram vial, the crude (0.05 mmol, 10 mg), benzaldehyde (0.05 mmol, 6 μL) and ~100 mg of MgSO₄ were dissolved in dry 4 mL of THF and stirred for 10 min. NaBH(OAc)₃ (0.1 mmol, 22 mg) was then added and the reaction mixture was stirred overnight. The reaction was quenched with a saturated solution of ammonium chloride (4 mL) and washed with a saturated solution of NaHCO₃ (20 mL). The organic layer was extracted with EtOAc (3 times) and then were

combined, washed with brine before being dried over Na₂SO₄ and filtered. The filtrate was concentrated in vacuo and purified by flash column chromatography (Silica gel, 0-4% MeOH and 10% CH₃CN in DCM) to yield **4.113** (15 mg; Yield=87%) as an oil. ¹H NMR (400 MHz, Methanol-*d*₄) δ 8.48 (d, *J* = 2.3 Hz, 1H), 8.45 (dd, *J* = 4.9, 1.7 Hz, 1H), 7.76 (dt, *J* = 7.9, 2.0 Hz, 1H), 7.40 (dd, *J* = 7.9, 4.9 Hz, 1H), 7.36 – 7.29 (m, 4H), 7.26 (dtd, *J* = 10.8, 5.7, 2.8 Hz, 1H), 4.62 (s, 2H), 3.58 (s, 2H), 3.35 – 3.31 (m, 2H), 3.18 (s, 2H), 2.71 (dd, *J* = 6.3, 4.8 Hz, 2H). ¹³C NMR (101 MHz, Methanol-*d*₄) δ 168.3, 148.5, 147.9, 136.6, 133.1, 129.0, 128.5, 128.1, 127.2, 123.9, 61.1, 56.4, 48.7, 48.2, 48.0, 47.8, 47.6, 47.4, 47.2, 46.9, 46.8, 46.2.

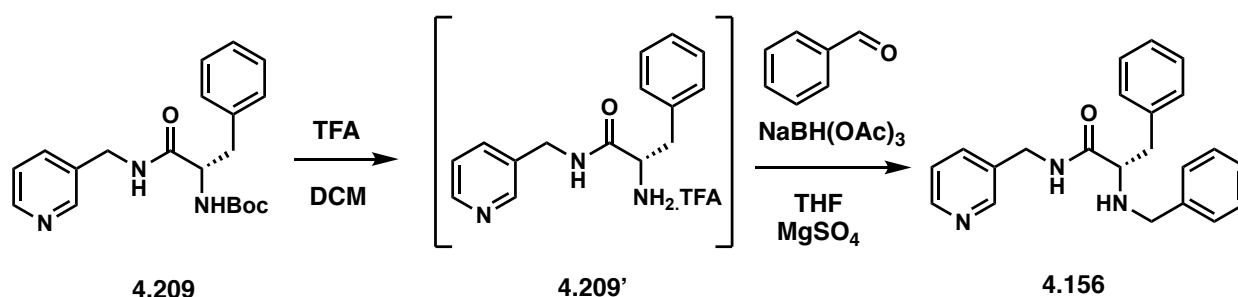
tert-butyl (*S*)-(1-oxo-3-phenyl-1-((pyridin-3-ylmethyl) amino) propan-2-yl) carbamate (**4.209**):



In a 3-dram vial, pyridin-3-ylmethanamine **4.206** (0.36 mmol, 37 μL), Boc-*L*-phenylalanine **4.187** (0.3 mmol, 80 mg) and DiPEA (0.9 mmol, 157 μL) were dissolved in 2 mL of dry DMF. After the reaction mixture was cooled down to 0°C (ice bath) HATU was added (0.36 mmol, 137 mg). The reaction was stirred and let warm to RT overnight. The reaction was quenched with water (4 mL) and washed with a saturated solution of NaHCO₃ (20 mL) and the organic layer was extracted with EtOAc (3 times). The organic layers were combined, washed with brine before being dried over Na₂SO₄ and filtered. The filtrate was concentrated in vacuo and purified by flash column

chromatography (Neutral alumina, 2-4% MeOH in DCM) to yield **4.209** (98 mg; Yield=92%) as a white solid. ¹H NMR (400 MHz, Acetone-*d*₆) δ 8.49 (s, 1H), 8.44 (d, *J* = 4.8 Hz, 1H), 7.86 (s, 1H), 7.59 (d, *J* = 7.9 Hz, 1H), 7.24 (m, 6H), 6.17 (d, *J* = 8.5 Hz, 1H), 4.40 (m, 3H), 3.16 (dd, *J* = 13.7, 5.8 Hz, 1H), 2.99 – 2.91 (m, 2H), 1.33 (s, 9H).

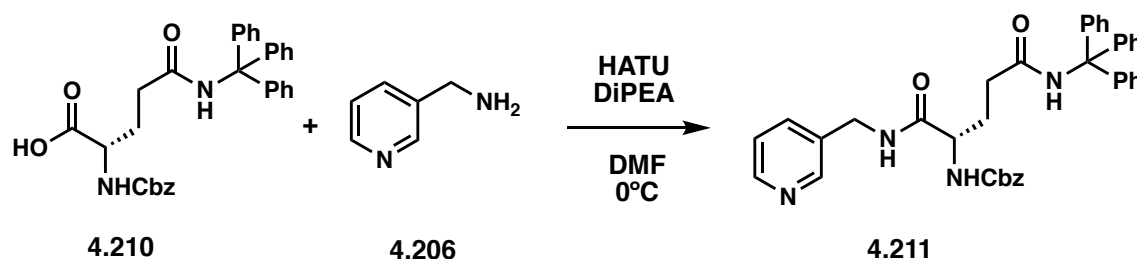
(*S*)-2-(benzylamino)-3-phenyl-*N*-(pyridin-3-ylmethyl) propenamide (4.156):



In a 3-dram vial, **4.209** was dissolved in 10 mL of DCM and 4 mL of TFA was added. The reaction mixture was stirred overnight. After concentration under N₂ flow, the crude was taken directly to the next step. In a 3-dram vial, the crude (0.05 mmol, 13 mg), benzaldehyde (0.05 mmol, 6 μL) and ~100 mg of MgSO₄ were dissolved in dry 4 mL of THF and stirred for 10 min. NaBH(OAc)₃ (0.1 mmol, 22 mg) was then added and the reaction mixture was stirred overnight. The reaction was quenched with a saturated solution of ammonium chloride (4 mL) and washed with a saturated solution of NaHCO₃ (20 mL). The organic layer was extracted with EtOAc (3 times) and then were combined, washed with brine before being dried over Na₂SO₄ and filtered. The filtrate was concentrated in vacuo and purified by flash column chromatography (Silica gel, 0-4% MeOH and 10% CH₃CN in DCM) to yield **4.156** (15 mg; Yield=87%) as an oil. ¹H NMR (400 MHz, Methanol-*d*₄) δ 8.40 (d, *J* = 4.9 Hz, 1H), 8.36 (s, 1H), 7.55 – 7.48 (m, 1H), 7.36 – 7.28 (m, 1H), 7.27 – 7.14 (m, 8H), 7.14 – 7.10 (m, 2H), 4.37 (d, *J* = 15.1 Hz, 1H), 4.26 (d, *J* = 15.0 Hz, 1H),

3.70 (d, $J = 13.1$ Hz, 1H), 3.58 (d, $J = 13.1$ Hz, 1H), 3.39 (td, $J = 7.1, 1.3$ Hz, 1H), 2.97 – 2.84 (m, 2H). ^{13}C NMR (101 MHz, Methanol- d_4) δ 174.9, 148.2, 147.4, 139.2, 137.3, 136.2, 135.0, 128.9, 128.1, 128.0, 127.9, 126.8, 126.3, 123.7, 63.1, 51.5, 48.2, 48.0, 47.8, 47.6, 47.4, 47.1, 46.9, 39.1, 39.1.

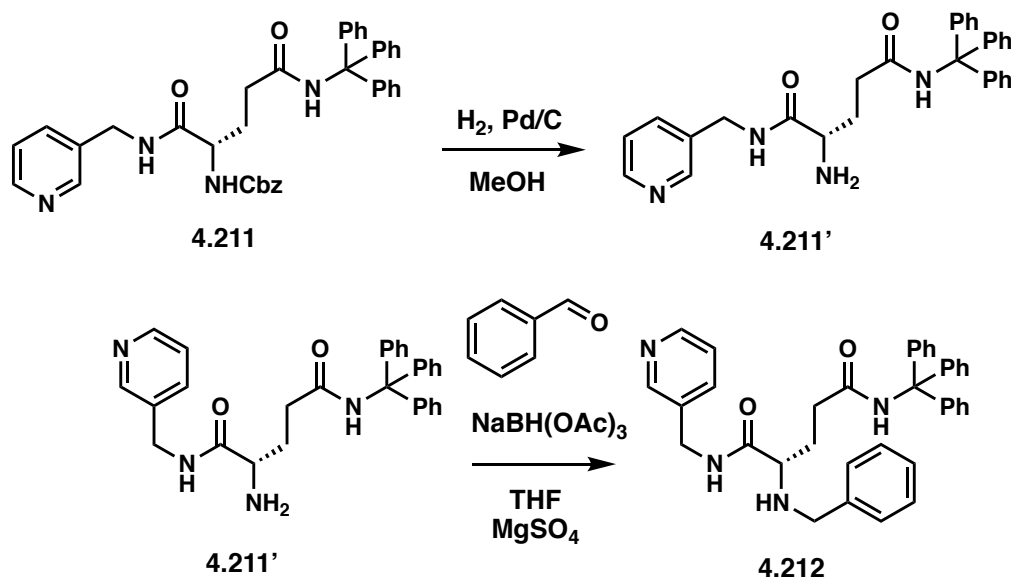
benzyl (*S*)-(1,5-dioxo-1-((pyridin-3-ylmethyl) amino)-5-(tritylamino) pentan-2-yl) carbamate (4.211):



In a 3-dram vial, pyridin-3-ylmethanamine **4.206** (0.36 mmol, 37 μL), *N*⁵-trityl-*L*-glutamine **4.210** (0.3 mmol, 157 mg) and DiPEA (0.9 mmol, 157 μL) were dissolved in 2 mL of dry DMF. After the reaction mixture was cooled down to 0°C (ice bath) HATU was added (0.36 mmol, 137 mg). The reaction was stirred and let warm to RT overnight. The reaction was quenched with water (4 mL) and washed with a saturated solution of NaHCO_3 (20 mL) and the organic layer was extracted with EtOAc (3 times). The organic layers were combined, washed with brine before being dried over Na_2SO_4 and filtered. The filtrate was concentrated in vacuo and purified by flash column chromatography (Neutral alumina, 2-4% MeOH in DCM) to yield **4.211** (150 mg; Yield=82%) as a white solid. ^1H NMR (400 MHz, Chloroform- d) δ 8.46 (d, $J = 3.5$ Hz, 2H), 7.55 (d, $J = 7.8$ Hz, 1H), 7.39 – 7.10 (m, 21H), 6.99 (s, 1H), 6.00 (d, $J = 7.1$ Hz, 1H), 5.12 –

5.01 (m, 2H), 4.31 (d, $J = 5.8$ Hz, 2H), 4.06 (q, $J = 6.7$ Hz, 1H), 2.60 – 2.49 (m, 1H), 2.43 – 2.32 (m, 1H), 2.10 – 1.99 (m, 1H), 1.92 (dt, $J = 14.1, 6.5$ Hz, 1H).

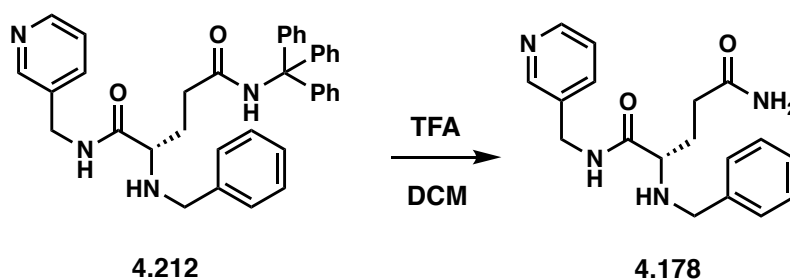
(*S*)-2-(benzylamino)-*N*¹-(pyridin-3-ylmethyl)-*N*⁵-tritylpentanediamide (4.212):



In a sealable 3-dram vial, **4.211** (0.3 mmol 150 mg) and palladium on carbon (80 mg) was dissolved in 10 mL of MeOH. A balloon of hydrogen was connected to the sealed vial and the reaction mixture was stirred overnight. The crude was concentrated under N₂ flow, filtered through a celite plug and taken directly to the next step. In a 3-dram vial, the crude (0.1 mmol, 48 mg), benzaldehyde (0.15 mmol, 15 μ L) and ~100 mg of MgSO₄ were dissolved in dry 4 mL of THF and stirred for 10 min. NaBH(OAc)₃ (0.2 mmol, 42 mg) was then added and the reaction mixture was stirred overnight. The reaction was quenched with a saturated solution of ammonium chloride (4 mL) and washed with a saturated solution of NaHCO₃ (20 mL). The organic layer was extracted with EtOAc (3 times) and then were combined, washed with brine before being dried over Na₂SO₄ and filtered. The filtrate was concentrated in vacuo and purified by flash column chromatography

(Silica gel, 0-8% MeOH and 10% CH₃CN in DCM) to yield **4.212** (32 mg; Yield=56%) as an oil. ¹H NMR (500 MHz, Methanol-*d*₄) δ 8.48 (d, *J* = 2.2 Hz, 1H), 8.41 (dd, *J* = 4.9, 1.5 Hz, 1H), 7.75 (d, *J* = 8.0 Hz, 1H), 7.36 (d, *J* = 7.1 Hz, 2H), 7.34 – 7.26 (m, 4H), 7.26 – 7.18 (m, 15H), 5.10 (q, *J* = 12.3 Hz, 2H), 4.46 – 4.32 (m, 2H), 4.10 (dd, *J* = 9.4, 4.9 Hz, 1H), 2.44 (qdd, *J* = 15.0, 8.3, 6.5 Hz, 2H), 2.06 – 1.98 (m, 1H), 1.83 (dtd, *J* = 14.4, 8.7, 5.9 Hz, 1H). ¹³C NMR (126 MHz, Methanol-*d*₄) δ 173.8, 172.8, 147.9, 147.3, 144.5, 136.1, 135.1, 128.6, 128.1, 127.7, 127.6, 127.3, 126.4, 123.8, 70.2, 66.4, 54.8, 48.1, 47.9, 47.8, 47.6, 47.4, 47.3, 47.1, 40.1, 32.4, 27.5.

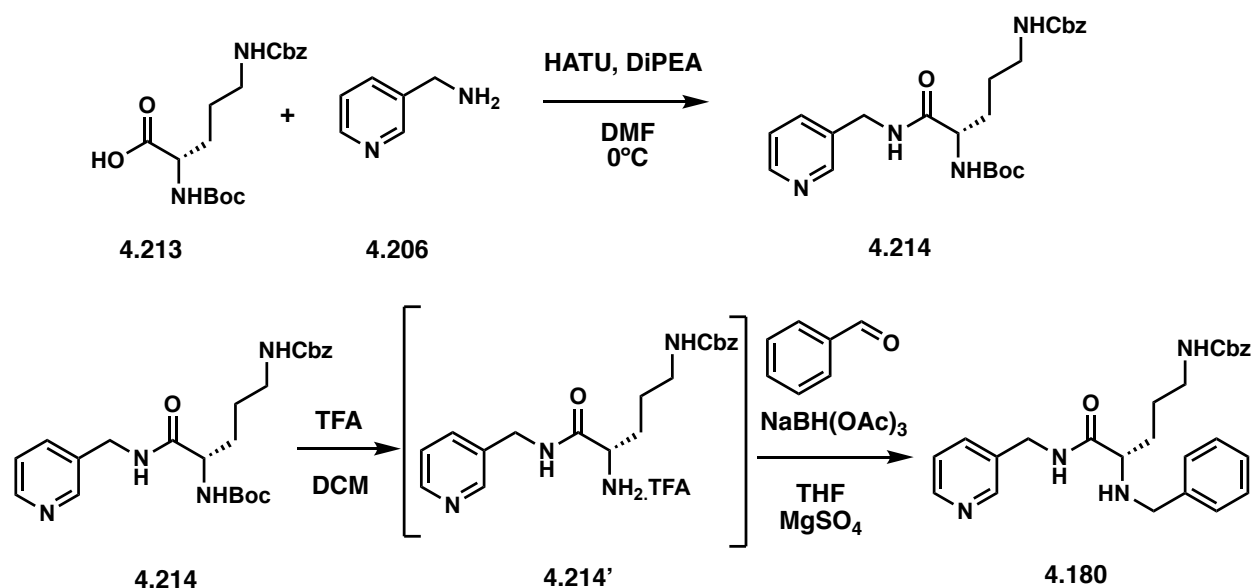
(S)-2-(benzylamino)-N¹-(pyridin-3-ylmethyl)pentanediamide (4.178):



In a 3-dram vial, **4.212** (32 mg, 0.06 mmol) was dissolved in 10 mL of DCM and 4 mL of TFA was added. The reaction mixture was stirred overnight. After concentration under N₂ flow, the crude was washed with a saturated solution of NaHCO₃ (20 mL). The organic layer was extracted with EtOAc (3 times) and then were combined, washed with brine before being dried over Na₂SO₄ and filtered. The filtrate was concentrated in vacuo and purified by flash column chromatography (Silica gel, 0-10% MeOH and 10% CH₃CN in DCM) to yield **4.212** (3 mg; Yield=15%) as an oil. ¹H NMR (400 MHz, DMSO-*d*₆) δ 8.50 – 8.40 (m, 2H), 7.61 (d, *J* = 7.8 Hz, 1H), 7.47 (d, *J* = 7.8 Hz, 1H), 7.37 – 7.30 (m, 3H), 7.33 – 7.25 (m, 2H), 7.26 – 7.22 (m, 1H), 7.09 – 7.02 (m, 1H), 6.84 – 6.77 (m, 0H), 6.74 (s, 1H), 5.03 – 4.98 (m, 2H), 4.32 – 4.26 (m, 2H), 4.00 – 3.91 (m, 1H), 2.14

– 2.04 (m, 1H), 1.90 – 1.84 (m, 1H), 1.78 – 1.66 (m, 1H), 1.57 – 1.50 (m, 1H), 1.47 – 1.39 (m, 1H). ¹³C NMR (101 MHz, DMSO-*d*₆) δ 174.0, 172.3, 156.4, 149.0, 148.5, 137.4, 135.3, 135.3, 128.8, 128.2, 128.2, 123.8, 65.9, 55.1, 40.1, 32.0, 28.0.

benzyl (*S*)-(4-(benzylamino)-5-oxo-5-((pyridin-3-ylmethyl)amino)pentyl)carbamate (4.180):



In a 3-dram vial, pyridin-3-ylmethanamine **4.206** (0.16 mmol, 17 μ L), N- α -Cbz-N- ϵ -Boc-L-lysine **4.213** (0.11 mmol, 40 mg) and DiPEA (0.33 mmol, 57 μ L) were dissolved in 2 mL of dry DMF. After the reaction mixture was cooled down to 0°C (ice bath) HATU was added (0.16 mmol, 62 mg). The reaction was stirred and let warm to RT overnight. The reaction was quenched with water (4 mL) and washed with a saturated solution of NaHCO₃ (20 mL) and the organic layer was extracted with EtOAc (3 times). The organic layers were combined, washed with brine before being dried over Na₂SO₄ and filtered. The filtrate was taken to the next step. In a 3-dram vial, **4.214** (48 mg) was dissolved in 10 mL of DCM and 4 mL of TFA was added. The reaction mixture was stirred overnight. After concentration under N₂ flow, the crude was taken directly to the next

step. In a 3-dram vial, the crude (0.05 mmol, 18 mg), benzaldehyde (0.05 mmol, 6 μ L) and ~100 mg of MgSO₄ were dissolved in dry 4 mL of THF and stirred for 10 min. NaBH(OAc)₃ (0.1 mmol, 22 mg) was then added and the reaction mixture was stirred overnight. The reaction was quenched with a saturated solution of ammonium chloride (4 mL) and washed with a saturated solution of NaHCO₃ (20 mL). The organic layer was extracted with EtOAc (3 times) and then were combined, washed with brine before being dried over Na₂SO₄ and filtered. The filtrate was concentrated in vacuo and purified by flash column chromatography (Silica gel, 0-8% MeOH and 10% CH₃CN in DCM) to yield **4.180** (10 mg; Yield=45%) as an oil. ¹H NMR (400 MHz, Acetonitrile-*d*₃) δ 8.51 (d, *J* = 2.3 Hz, 1H), 8.46 (dd, *J* = 4.8, 1.7 Hz, 1H), 7.69 – 7.59 (m, 2H), 7.42 – 7.32 (m, 4H), 7.36 – 7.27 (m, 5H), 7.30 – 7.21 (m, 1H), 5.72 (s, 1H), 5.05 (s, 2H), 4.38 (d, *J* = 6.2 Hz, 2H), 3.72 (d, *J* = 13.3 Hz, 1H), 3.64 (d, *J* = 13.3 Hz, 1H), 3.13 – 3.04 (m, 3H), 1.70 – 1.48 (m, 4H). ¹³C NMR (101 MHz, Acetonitrile-*d*₃) δ 174.5, 149.0, 148.3, 140.4, 135.1, 135.1, 128.4, 128.3, 128.2, 127.8, 127.6, 126.9, 123.4, 65.8, 61.6, 51.9, 40.0, 30.6.

9 Bibliography

1. Burrell, C. J. H., C. R.; Murphy, F. A., Coronaviruses. *Fenner and White's Medical Virology* **2017**, 437-446.
2. Paules, C. I.; Marston, H. D.; Fauci, A. S., Coronavirus Infections-More Than Just the Common Cold. *JAMA* **2020**, *323* (8), 707-708.
3. Drexler, J. F.; Corman, V. M.; Drosten, C., Ecology, evolution and classification of bat coronaviruses in the aftermath of SARS. *Antiviral Res* **2014**, *101*, 45-56.
4. Petersen, E.; Koopmans, M.; Go, U.; Hamer, D. H.; Petrosillo, N.; Castelli, F.; Storgaard, M.; Al Khalili, S.; Simonsen, L., Comparing SARS-CoV-2 with SARS-CoV and influenza pandemics. *The Lancet Infectious Diseases* **2020**, *20* (9), e238-e244.
5. Peiris, J. S.; Chu, C. M.; Cheng, V. C.; Chan, K. S.; Hung, I. F.; Poon, L. L.; Law, K. I.; Tang, B. S.; Hon, T. Y.; Chan, C. S.; Chan, K. H.; Ng, J. S.; Zheng, B. J.; Ng, W. L.; Lai, R. W.; Guan, Y.; Yuen, K. Y.; Group, H. U. S. S., Clinical progression and viral load in a community outbreak of coronavirus-associated SARS pneumonia: a prospective study. *Lancet* **2003**, *361* (9371), 1767-72.
6. de Wit, E.; van Doremalen, N.; Falzarano, D.; Munster, V. J., SARS and MERS: recent insights into emerging coronaviruses. *Nat Rev Microbiol* **2016**, *14* (8), 523-34.
7. Marra, M. A.; Jones, S. J.; Astell, C. R.; Holt, R. A.; Brooks-Wilson, A.; Butterfield, Y. S.; Khattra, J.; Asano, J. K.; Barber, S. A.; Chan, S. Y.; Cloutier, A.; Coughlin, S. M.; Freeman, D.; Girm, N.; Griffith, O. L.; Leach, S. R.; Mayo, M.; McDonald, H.; Montgomery, S. B.; Pandoh, P. K.; Petrescu, A. S.; Robertson, A. G.; Schein, J. E.; Siddiqui, A.; Smailus, D. E.; Stott, J. M.; Yang, G. S.; Plummer, F.; Andonov, A.; Artsob, H.; Bastien, N.; Bernard, K.; Booth, T. F.; Bowness, D.; Czub, M.; Drebot, M.; Fernando, L.; Flick, R.; Garbutt, M.; Gray, M.; Grolla, A.; Jones, S.; Feldmann, H.; Meyers, A.; Kabani, A.; Li, Y.; Normand, S.; Stroher, U.; Tipples, G. A.; Tyler, S.; Vogrig, R.; Ward, D.; Watson, B.; Brunham, R. C.; Kraiden, M.; Petric, M.; Skowronski, D. M.; Upton, C.; Roper, R. L., The Genome sequence of the SARS-associated coronavirus. *Science* **2003**, *300* (5624), 1399-404.
8. Breban, R.; Riou, J.; Fontanet, A., Interhuman transmissibility of Middle East respiratory syndrome coronavirus: estimation of pandemic risk. *Lancet* **2013**, *382* (9893), 694-9.
9. Zhu, Z.; Lian, X.; Su, X.; Wu, W.; Marraro, G. A.; Zeng, Y., From SARS and MERS to COVID-19: a brief summary and comparison of severe acute respiratory infections caused by three highly pathogenic human coronaviruses. *Respir Res* **2020**, *21* (1), 224.
10. Mehand, M. S.; Al-Shorbaji, F.; Millett, P.; Murgue, B., The WHO R&D Blueprint: 2018 review of emerging infectious diseases requiring urgent research and development efforts. *Antiviral Res* **2018**, *159*, 63-67.
11. Carrat, F.; Figoni, J.; Henny, J.; Desenclos, J. C.; Kab, S.; de Lamballerie, X.; Zins, M., Evidence of early circulation of SARS-CoV-2 in France: findings from the population-based "CONSTANCES" cohort. *Eur J Epidemiol* **2021**.
12. Hu, T.; Liu, Y.; Zhao, M.; Zhuang, Q.; Xu, L.; He, Q., A comparison of COVID-19, SARS and MERS. *PeerJ* **2020**, *8*, e9725.
13. Rota, P. A.; Oberste, M. S.; Monroe, S. S.; Nix, W. A.; Campagnoli, R.; Icenogle, J. P.; Penaranda, S.; Bankamp, B.; Maher, K.; Chen, M. H.; Tong, S.; Tamin, A.; Lowe, L.; Frace, M.; DeRisi, J. L.; Chen, Q.; Wang, D.; Erdman, D. D.; Peret, T. C.; Burns, C.; Ksiazek, T. G.;

- Rollin, P. E.; Sanchez, A.; Liffick, S.; Holloway, B.; Limor, J.; McCaustland, K.; Olsen-Rasmussen, M.; Fouchier, R.; Gunther, S.; Osterhaus, A. D.; Drosten, C.; Pallansch, M. A.; Anderson, L. J.; Bellini, W. J., Characterization of a novel coronavirus associated with severe acute respiratory syndrome. *Science* **2003**, *300* (5624), 1394-9.
14. Lu, R.; Zhao, X.; Li, J.; Niu, P.; Yang, B.; Wu, H.; Wang, W.; Song, H.; Huang, B.; Zhu, N.; Bi, Y.; Ma, X.; Zhan, F.; Wang, L.; Hu, T.; Zhou, H.; Hu, Z.; Zhou, W.; Zhao, L.; Chen, J.; Meng, Y.; Wang, J.; Lin, Y.; Yuan, J.; Xie, Z.; Ma, J.; Liu, W. J.; Wang, D.; Xu, W.; Holmes, E. C.; Gao, G. F.; Wu, G.; Chen, W.; Shi, W.; Tan, W., Genomic characterisation and epidemiology of 2019 novel coronavirus: implications for virus origins and receptor binding. *Lancet* **2020**, *395* (10224), 565-574.
15. Ou, X.; Liu, Y.; Lei, X.; Li, P.; Mi, D.; Ren, L.; Guo, L.; Guo, R.; Chen, T.; Hu, J.; Xiang, Z.; Mu, Z.; Chen, X.; Chen, J.; Hu, K.; Jin, Q.; Wang, J.; Qian, Z., Characterization of spike glycoprotein of SARS-CoV-2 on virus entry and its immune cross-reactivity with SARS-CoV. *Nat Commun* **2020**, *11* (1), 1620.
16. Yang, X.; Yu, Y.; Xu, J.; Shu, H.; Xia, J. a.; Liu, H.; Wu, Y.; Zhang, L.; Yu, Z.; Fang, M.; Yu, T.; Wang, Y.; Pan, S.; Zou, X.; Yuan, S.; Shang, Y., Clinical course and outcomes of critically ill patients with SARS-CoV-2 pneumonia in Wuhan, China: a single-centered, retrospective, observational study. *The Lancet Respiratory Medicine* **2020**, *8* (5), 475-481.
17. Walls, A. C.; Park, Y. J.; Tortorici, M. A.; Wall, A.; McGuire, A. T.; Velesler, D., Structure, Function, and Antigenicity of the SARS-CoV-2 Spike Glycoprotein. *Cell* **2020**, *181* (2), 281-292 e6.
18. Memish, Z. A.; Perlman, S.; Van Kerkhove, M. D.; Zumla, A., Middle East respiratory syndrome. *The Lancet* **2020**, *395* (10229), 1063-1077.
19. Snijder, E. J.; Decroly, E.; Ziebuhr, J., The Nonstructural Proteins Directing Coronavirus RNA Synthesis and Processing. *Adv Virus Res* **2016**, *96*, 59-126.
20. Knoops, K.; Kikkert, M.; Worm, S. H.; Zevenhoven-Dobbe, J. C.; van der Meer, Y.; Koster, A. J.; Mommaas, A. M.; Snijder, E. J., SARS-coronavirus replication is supported by a reticulovesicular network of modified endoplasmic reticulum. *PLoS Biol* **2008**, *6* (9), e226.
21. Houser, K. V.; Gretebeck, L.; Ying, T.; Wang, Y.; Vogel, L.; Lamirande, E. W.; Bock, K. W.; Moore, I. N.; Dimitrov, D. S.; Subbarao, K., Prophylaxis With a Middle East Respiratory Syndrome Coronavirus (MERS-CoV)-Specific Human Monoclonal Antibody Protects Rabbits From MERS-CoV Infection. *J Infect Dis* **2016**, *213* (10), 1557-61.
22. ter Meulen, J.; Bakker, A. B. H.; van den Brink, E. N.; Weverling, G. J.; Martina, B. E. E.; Haagmans, B. L.; Kuiken, T.; de Kruif, J.; Preiser, W.; Spaan, W.; Gelderblom, H. R.; Goudsmit, J.; Osterhaus, A. D. M. E., Human monoclonal antibody as prophylaxis for SARS coronavirus infection in ferrets. *The Lancet* **2004**, *363* (9427), 2139-2141.
23. Tang, X. C.; Agnihothram, S. S.; Jiao, Y.; Stanhope, J.; Graham, R. L.; Peterson, E. C.; Avnir, Y.; Tallarico, A. S.; Sheehan, J.; Zhu, Q.; Baric, R. S.; Marasco, W. A., Identification of human neutralizing antibodies against MERS-CoV and their role in virus adaptive evolution. *Proc Natl Acad Sci U S A* **2014**, *111* (19), E2018-26.
24. Ledford, H., Hopes rise for coronavirus drug remdesivir. *Nature* **2020**.
25. Kupferschmidt, K., WHO launches global megatrial of the four most promising coronavirus treatments. *Science* **2020**.
26. Coomes, E. A.; Haghbayan, H., Favipiravir, an antiviral for COVID-19? *J Antimicrob Chemother* **2020**, *75* (7), 2013-2014.

27. Cai, Q.; Yang, M.; Liu, D.; Chen, J.; Shu, D.; Xia, J.; Liao, X.; Gu, Y.; Cai, Q.; Yang, Y.; Shen, C.; Li, X.; Peng, L.; Huang, D.; Zhang, J.; Zhang, S.; Wang, F.; Liu, J.; Chen, L.; Chen, S.; Wang, Z.; Zhang, Z.; Cao, R.; Zhong, W.; Liu, Y.; Liu, L., Experimental Treatment with Favipiravir for COVID-19: An Open-Label Control Study. *Engineering (Beijing)* **2020**, *6* (10), 1192-1198.
28. Chen, C.; Zhang, Y.; Huang, J.; Yin, P.; Cheng, Z.; Wu, J.; Chen, S.; Zhang, Y.; Chen, B.; Lu, M.; Luo, Y.; Ju, L.; Zhang, J.; Wang, X., Favipiravir versus arbidol for COVID-19: a randomized clinical trial. *medRxiv* **2020**.
29. Magagnoli, J.; Narendran, S.; Pereira, F.; Cummings, T.; Hardin, J. W.; Sutton, S. S.; Ambati, J., Outcomes of hydroxychloroquine usage in United States veterans hospitalized with Covid-19. *medRxiv* **2020**.
30. Geleris, J.; Sun, Y.; Platt, J.; Zucker, J.; Baldwin, M.; Hripsak, G.; Labella, A.; Manson, D. K.; Kubin, C.; Barr, R. G.; Sobieszczyk, M. E.; Schluger, N. W., Observational Study of Hydroxychloroquine in Hospitalized Patients with Covid-19. *N Engl J Med* **2020**, *382* (25), 2411-2418.
31. Sanders, J. M.; Monogue, M. L.; Jodlowski, T. Z.; Cutrell, J. B., Pharmacologic Treatments for Coronavirus Disease 2019 (COVID-19): A Review. *JAMA* **2020**, *323* (18), 1824-1836.
32. Yousefi, B.; Valizadeh, S.; Ghaffari, H.; Vahedi, A.; Karbalaei, M.; Eslami, M., A global treatments for coronaviruses including COVID-19. *J Cell Physiol* **2020**, *235* (12), 9133-9142.
33. Li, Y.; Xie, Z.; Lin, W.; Cai, W.; Wen, C.; Guan, Y.; Mo, X.; Wang, J.; Wang, Y.; Peng, P.; Chen, X.; Hong, W.; Xiao, G.; Liu, J.; Zhang, L.; Hu, F.; Li, F.; Zhang, F.; Deng, X.; Li, L., An exploratory randomized, controlled study on the efficacy and safety of lopinavir/ritonavir or arbidol treating adult patients hospitalized with mild/moderate COVID-19 (ELACOI). *medRxiv* **2020**.
34. Lian, N.; Xie, H.; Lin, S.; Huang, J.; Zhao, J.; Lin, Q., Umifenovir treatment is not associated with improved outcomes in patients with coronavirus disease 2019: a retrospective study. *Clin Microbiol Infect* **2020**, *26* (7), 917-921.
35. Group, R. C.; Horby, P.; Lim, W. S.; Emberson, J. R.; Mafham, M.; Bell, J. L.; Linsell, L.; Staplin, N.; Brightling, C.; Ustianowski, A.; Elmahi, E.; Prudon, B.; Green, C.; Felton, T.; Chadwick, D.; Rege, K.; Fegan, C.; Chappell, L. C.; Faust, S. N.; Jaki, T.; Jeffery, K.; Montgomery, A.; Rowan, K.; Juszczak, E.; Baillie, J. K.; Haynes, R.; Landray, M. J., Dexamethasone in Hospitalized Patients with Covid-19 - Preliminary Report. *N Engl J Med* **2020**.
36. Ledford, H., Coronavirus breakthrough: dexamethasone is first drug shown to save lives. *Nature* **2020**, *582* (7813), 469.
37. Morse, J. S.; Lalonde, T.; Xu, S.; Liu, W. R., Learning from the Past: Possible Urgent Prevention and Treatment Options for Severe Acute Respiratory Infections Caused by 2019-nCoV. *ChemBiochem* **2020**, *21* (5), 730-738.
38. Hoffmann, M.; Kleine-Weber, H.; Schroeder, S.; Kruger, N.; Herrler, T.; Erichsen, S.; Schiergens, T. S.; Herrler, G.; Wu, N. H.; Nitsche, A.; Muller, M. A.; Drosten, C.; Pohlmann, S., SARS-CoV-2 Cell Entry Depends on ACE2 and TMPRSS2 and Is Blocked by a Clinically Proven Protease Inhibitor. *Cell* **2020**, *181* (2), 271-280 e8.
39. Kirchdoerfer, R. N.; Ward, A. B., Structure of the SARS-CoV nsp12 polymerase bound to nsp7 and nsp8 co-factors. *Nat Commun* **2019**, *10* (1), 2342.

40. Cannalire, R.; Cerchia, C.; Beccari, A. R.; Di Leva, F. S.; Summa, V., Targeting SARS-CoV-2 Proteases and Polymerase for COVID-19 Treatment: State of the Art and Future Opportunities. *J Med Chem* **2020**.
41. Shannon, A.; Le, N. T.; Selisko, B.; Eydoux, C.; Alvarez, K.; Guillemot, J. C.; Decroly, E.; Peersen, O.; Ferron, F.; Canard, B., Remdesivir and SARS-CoV-2: Structural requirements at both nsp12 RdRp and nsp14 Exonuclease active-sites. *Antiviral Res* **2020**, *178*, 104793.
42. Agostini, M. L.; Andres, E. L.; Sims, A. C.; Graham, R. L.; Sheahan, T. P.; Lu, X.; Smith, E. C.; Case, J. B.; Feng, J. Y.; Jordan, R.; Ray, A. S.; Cihlar, T.; Siegel, D.; Mackman, R. L.; Clarke, M. O.; Baric, R. S.; Denison, M. R., Coronavirus Susceptibility to the Antiviral Remdesivir (GS-5734) Is Mediated by the Viral Polymerase and the Proofreading Exoribonuclease. *mBio* **2018**, *9* (2).
43. Ferron, F.; Subissi, L.; Silveira De Morais, A. T.; Le, N. T. T.; Sevajol, M.; Gluais, L.; Decroly, E.; Vonrhein, C.; Bricogne, G.; Canard, B.; Imbert, I., Structural and molecular basis of mismatch correction and ribavirin excision from coronavirus RNA. *Proc Natl Acad Sci U S A* **2018**, *115* (2), E162-E171.
44. Anand, K.; Ziebuhr, J.; Wadhwani, P.; Mesters, J. R.; Hilgenfeld, R., Coronavirus main proteinase (3CLpro) structure: basis for design of anti-SARS drugs. *Science* **2003**, *300* (5626), 1763-7.
45. Chuck, C. P.; Chow, H. F.; Wan, D. C.; Wong, K. B., Profiling of substrate specificities of 3C-like proteases from group 1, 2a, 2b, and 3 coronaviruses. *PLoS One* **2011**, *6* (11), e27228.
46. Zhang, L.; Lin, D.; Kusov, Y.; Nian, Y.; Ma, Q.; Wang, J.; von Brunn, A.; Leyssen, P.; Lanko, K.; Neyts, J.; de Wilde, A.; Snijder, E. J.; Liu, H.; Hilgenfeld, R., alpha-Ketoamides as Broad-Spectrum Inhibitors of Coronavirus and Enterovirus Replication: Structure-Based Design, Synthesis, and Activity Assessment. *J Med Chem* **2020**, *63* (9), 4562-4578.
47. Baez-Santos, Y. M.; St John, S. E.; Mesecar, A. D., The SARS-coronavirus papain-like protease: structure, function and inhibition by designed antiviral compounds. *Antiviral Res* **2015**, *115*, 21-38.
48. Hilgenfeld, R., From SARS to MERS: crystallographic studies on coronaviral proteases enable antiviral drug design. *FEBS J* **2014**, *281* (18), 4085-96.
49. Pillaiyar, T.; Manickam, M.; Namasivayam, V.; Hayashi, Y.; Jung, S. H., An Overview of Severe Acute Respiratory Syndrome-Coronavirus (SARS-CoV) 3CL Protease Inhibitors: Peptidomimetics and Small Molecule Chemotherapy. *J Med Chem* **2016**, *59* (14), 6595-628.
50. Rut, W.; Lv, Z.; Zmudzinski, M.; Patchett, S.; Nayak, D.; Snipas, S. J.; El Oualid, F.; Huang, T. T.; Bekes, M.; Drag, M.; Olsen, S. K., Activity profiling and structures of inhibitor-bound SARS-CoV-2-PLpro protease provides a framework for anti-COVID-19 drug design. *bioRxiv* **2020**.
51. Węglarz-Tomczak, E.; Tomczak, J. M.; Giurg, M.; Burda-Grabowska, M.; Brul, S., Discovery of potent inhibitors of PL_p roC oV2 by screening a library of selenium-containing compounds. *bioRxiv* **2020**.
52. Freitas, B. T.; Durie, I. A.; Murray, J.; Longo, J. E.; Miller, H. C.; Crich, D.; Hogan, R. J.; Tripp, R. A.; Pegan, S. D., Characterization and Noncovalent Inhibition of the Deubiquitinase and deISGylase Activity of SARS-CoV-2 Papain-Like Protease. *ACS Infect Dis* **2020**, *6* (8), 2099-2109.
53. Shen, Z.; Ratia, K.; Cooper, L.; Kong, D.; Lee, H.; Kwon, Y.; Li, Y.; Alqarni, S.; Huang, F.; Dubrovskiy, O.; Rong, L.; Thatcher, G. R.; Xiong, R., Potent, Novel SARS-CoV-2 PLpro Inhibitors Block Viral Replication in Monkey and Human Cell Cultures. *bioRxiv* **2021**.

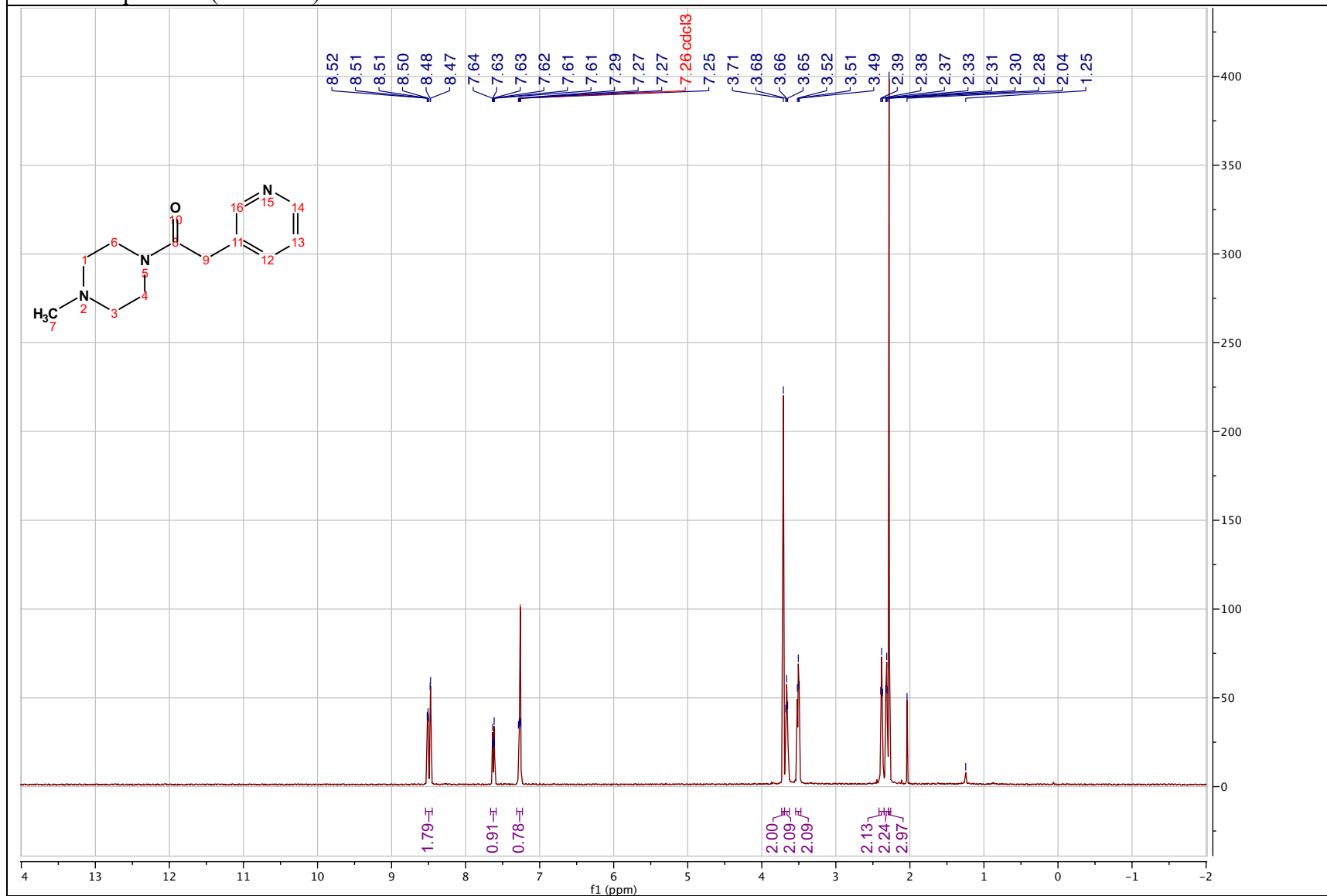
54. Yang, H.; Yang, M.; Ding, Y.; Liu, Y.; Lou, Z.; Zhou, Z.; Sun, L.; Mo, L.; Ye, S.; Pang, H.; Gao, G. F.; Anand, K.; Bartlam, M.; Hilgenfeld, R.; Rao, Z., The crystal structures of severe acute respiratory syndrome virus main protease and its complex with an inhibitor. *Proc Natl Acad Sci U S A* **2003**, *100* (23), 13190-5.
55. Anand, K.; Palm, G. J.; Mesters, J. R.; Siddell, S. G.; Ziebuhr, J.; Hilgenfeld, R., Structure of coronavirus main proteinase reveals combination of a chymotrypsin fold with an extra alpha-helical domain. *EMBO J* **2002**, *21* (13), 3213-24.
56. Wu, A.; Wang, Y.; Zeng, C.; Huang, X.; Xu, S.; Su, C.; Wang, M.; Chen, Y.; Guo, D., Prediction and biochemical analysis of putative cleavage sites of the 3C-like protease of Middle East respiratory syndrome coronavirus. *Virus Res* **2015**, *208*, 56-65.
57. Suarez, D.; Diaz, N., SARS-CoV-2 Main Protease: A Molecular Dynamics Study. *J Chem Inf Model* **2020**, *60* (12), 5815-5831.
58. Sutanto, F.; Konstantinidou, M.; Domling, A., Covalent inhibitors: a rational approach to drug discovery. *RSC Med Chem* **2020**, *11* (8), 876-884.
59. Jin, Z.; Du, X.; Xu, Y.; Deng, Y.; Liu, M.; Zhao, Y.; Zhang, B.; Li, X.; Zhang, L.; Peng, C.; Duan, Y.; Yu, J.; Wang, L.; Yang, K.; Liu, F.; Jiang, R.; Yang, X.; You, T.; Liu, X.; Yang, X.; Bai, F.; Liu, H.; Liu, X.; Guddat, L. W.; Xu, W.; Xiao, G.; Qin, C.; Shi, Z.; Jiang, H.; Rao, Z.; Yang, H., Structure of M(pro) from SARS-CoV-2 and discovery of its inhibitors. *Nature* **2020**, *582* (7811), 289-293.
60. Dai, W.; Zhang, B.; Jiang, X. M.; Su, H.; Li, J.; Zhao, Y.; Xie, X.; Jin, Z.; Peng, J.; Liu, F.; Li, C.; Li, Y.; Bai, F.; Wang, H.; Cheng, X.; Cen, X.; Hu, S.; Yang, X.; Wang, J.; Liu, X.; Xiao, G.; Jiang, H.; Rao, Z.; Zhang, L. K.; Xu, Y.; Yang, H.; Liu, H., Structure-based design of antiviral drug candidates targeting the SARS-CoV-2 main protease. *Science* **2020**, *368* (6497), 1331-1335.
61. Ma, C.; Sacco, M. D.; Hurst, B.; Townsend, J. A.; Hu, Y.; Szeto, T.; Zhang, X.; Tarbet, B.; Marty, M. T.; Chen, Y.; Wang, J., Boceprevir, GC-376, and calpain inhibitors II, XII inhibit SARS-CoV-2 viral replication by targeting the viral main protease. *Cell Res* **2020**, *30* (8), 678-692.
62. Kitamura, N.; Sacco, M. D.; Ma, C.; Hu, Y.; Townsend, J. A.; Meng, X.; Zhang, F.; Zhang, X.; Kukuljac, A.; Marty, M. T.; Schultz, D.; Cherry, S.; Xiang, Y.; Chen, Y.; Wang, J., An expedited approach towards the rationale design of non-covalent SARS-CoV-2 main protease inhibitors with in vitro antiviral activity. *bioRxiv* **2020**.
63. Zhang, C. H.; Stone, E. A.; Deshmukh, M.; Ippolito, J. A.; Ghahremanpour, M. M.; Tirado-Rives, J.; Spasov, K. A.; Zhang, S.; Takeo, Y.; Kudalkar, S. N.; Liang, Z.; Isaacs, F.; Lindenbach, B.; Miller, S. J.; Anderson, K. S.; Jorgensen, W. L., Potent Noncovalent Inhibitors of the Main Protease of SARS-CoV-2 from Molecular Sculpting of the Drug Perampanel Guided by Free Energy Perturbation Calculations. *ACS Cent Sci* **2021**, *7* (3), 467-475.
64. Su, H. X.; Yao, S.; Zhao, W. F.; Li, M. J.; Liu, J.; Shang, W. J.; Xie, H.; Ke, C. Q.; Hu, H. C.; Gao, M. N.; Yu, K. Q.; Liu, H.; Shen, J. S.; Tang, W.; Zhang, L. K.; Xiao, G. F.; Ni, L.; Wang, D. W.; Zuo, J. P.; Jiang, H. L.; Bai, F.; Wu, Y.; Ye, Y.; Xu, Y. C., Anti-SARS-CoV-2 activities in vitro of Shuanghuanglian preparations and bioactive ingredients. *Acta Pharmacol Sin* **2020**, *41* (9), 1167-1177.
65. Su, H.; Yao, S.; Zhao, W.; Li, M.; Liu, J.; Shang, W.; Xie, H.; Ke, C.; Gao, M.; Yu, K.; Liu, H.; Shen, J.; Tang, W.; Zhang, L.; Zuo, J.; Jiang, H.; Bai, F.; Wu, Y.; Ye, Y.; Xu, Y., Discovery of baicalin and baicalein as novel, natural product inhibitors of SARS-CoV-2 3CL protease in vitro. *bioRxiv* **2020**.

66. Li, M.; Shi, A.; Pang, H.; Xue, W.; Li, Y.; Cao, G.; Yan, B.; Dong, F.; Li, K.; Xiao, W.; He, G.; Du, G.; Hu, X., Safety, tolerability, and pharmacokinetics of a single ascending dose of baicalein chewable tablets in healthy subjects. *J Ethnopharmacol* **2014**, *156*, 210-5.
67. Boras, B.; Jones, R. M.; Anson, B. J.; Arenson, D.; Aschenbrenner, L.; Bakowski, M. A.; Beutler, N.; Binder, J.; Chen, E.; Eng, H.; Hammond, J.; Hoffman, R.; Kadar, E. P.; Kania, R.; Kimoto, E.; Kirkpatrick, M. G.; Lanyon, L.; Lendy, E. K.; Lillis, J. R.; Luthra, S. A.; Ma, C.; Noell, S.; Obach, R. S.; O'Brien, M. N.; O'Connor, R.; Ogilvie, K.; Owen, D.; Pettersson, M.; Reese, M. R.; Rogers, T.; Rossulek, M. I.; Sathish, J. G.; Stepan, C.; Ticehurst, M.; Updyke, L. W.; Zhu, Y.; Wang, J.; Chatterjee, A. K.; Mesecar, A. D.; Anderson, A. S.; Allerton, C., Discovery of a Novel Inhibitor of Coronavirus 3CL Protease as a Clinical Candidate for the Potential Treatment of COVID-19. *bioRxiv* **2020**.
68. <https://www.diamond.ac.uk/covid-19/for-scientists/Main-protease-structure-and-XChem.html>.
69. Jacobs, J.; Grum-Tokars, V.; Zhou, Y.; Turlington, M.; Saldanha, S. A.; Chase, P.; Egger, A.; Dawson, E. S.; Baez-Santos, Y. M.; Tomar, S.; Mielech, A. M.; Baker, S. C.; Lindsley, C. W.; Hodder, P.; Mesecar, A.; Stauffer, S. R., Discovery, synthesis, and structure-based optimization of a series of N-(tert-butyl)-2-(N-arylamido)-2-(pyridin-3-yl) acetamides (ML188) as potent noncovalent small molecule inhibitors of the severe acute respiratory syndrome coronavirus (SARS-CoV) 3CL protease. *J Med Chem* **2013**, *56* (2), 534-46.
70. Ghosh, A. K.; Brindisi, M., Urea Derivatives in Modern Drug Discovery and Medicinal Chemistry. *J Med Chem* **2020**, *63* (6), 2751-2788.
71. Nobeli, I.; Price, S. L.; Lommerse, J. P. M.; Taylor, R., Hydrogen bonding properties of oxygen and nitrogen acceptors in aromatic heterocycles. *Journal of Computational Chemistry* **1997**, *18* (16), 2060-2074.
72. Mons, E.; Jansen, I. D. C.; Loboda, J.; van Doodewaerd, B. R.; Hermans, J.; Verdoes, M.; van Boeckel, C. A. A.; van Veelen, P. A.; Turk, B.; Turk, D.; Ovaa, H., The Alkyne Moiety as a Latent Electrophile in Irreversible Covalent Small Molecule Inhibitors of Cathepsin K. *J Am Chem Soc* **2019**, *141* (8), 3507-3514.
73. Peterson, L. A., Reactive metabolites in the biotransformation of molecules containing a furan ring. *Chem Res Toxicol* **2013**, *26* (1), 6-25.
74. Stokes, J. M.; Yang, K.; Swanson, K.; Jin, W.; Cubillos-Ruiz, A.; Donghia, N. M.; MacNair, C. R.; French, S.; Carfrae, L. A.; Bloom-Ackermann, Z.; Tran, V. M.; Chiappino-Pepe, A.; Badran, A. H.; Andrews, I. W.; Chory, E. J.; Church, G. M.; Brown, E. D.; Jaakkola, T. S.; Barzilay, R.; Collins, J. J., A Deep Learning Approach to Antibiotic Discovery. *Cell* **2020**, *180* (4), 688-702 e13.
75. National Center for Biotechnology Information. PubChem Bioassay Record for AID 1706, Source: The Scripps Research Institute Molecular Screening Center. <https://pubchem.ncbi.nlm.nih.gov/bioassay/1706>. Accessed May 3, 2021.
76. Yang, S.; Chen, S. J.; Hsu, M. F.; Wu, J. D.; Tseng, C. T.; Liu, Y. F.; Chen, H. C.; Kuo, C. W.; Wu, C. S.; Chang, L. W.; Chen, W. C.; Liao, S. Y.; Chang, T. Y.; Hung, H. H.; Shr, H. L.; Liu, C. Y.; Huang, Y. A.; Chang, L. Y.; Hsu, J. C.; Peters, C. J.; Wang, A. H.; Hsu, M. C., Synthesis, crystal structure, structure-activity relationships, and antiviral activity of a potent SARS coronavirus 3CL protease inhibitor. *J Med Chem* **2006**, *49* (16), 4971-80.
77. Gettys, K.; Ye, Z.; Dai, M., Recent Advances in Piperazine Synthesis. *Synthesis* **2017**, *49* (12), 2589-2604.

78. Tullberg, M.; Grøtli, M.; Luthman, K., Efficient synthesis of 2,5-diketopiperazines using microwave assisted heating. *Tetrahedron* **2006**, *62* (31), 7484-7491.

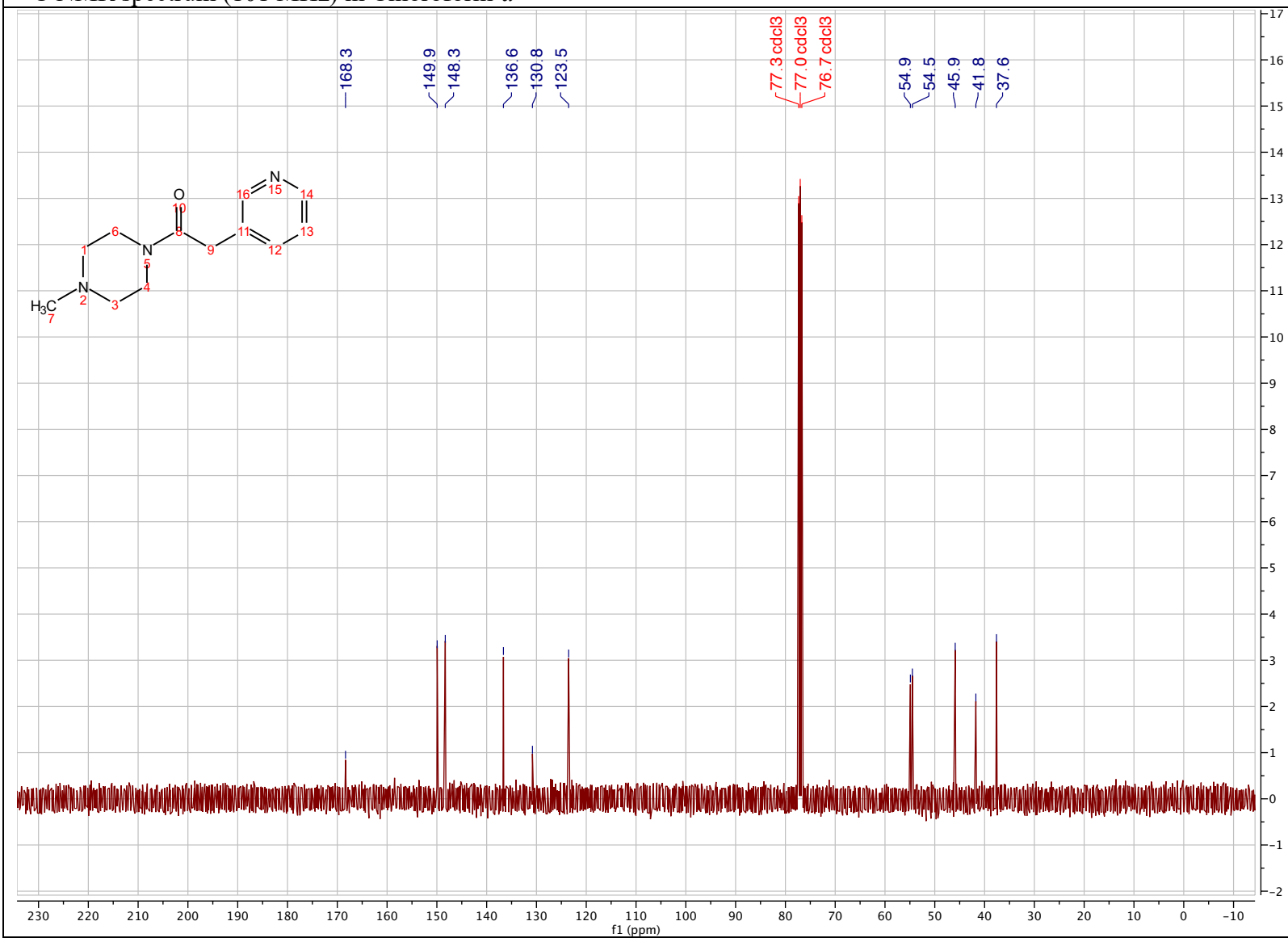
1-(4-methylpiperazin-1-yl)-2-(pyridin-3-yl) ethan-1-one (4.66)

¹H NMR spectrum (400 MHz) in Chloroform-*d*



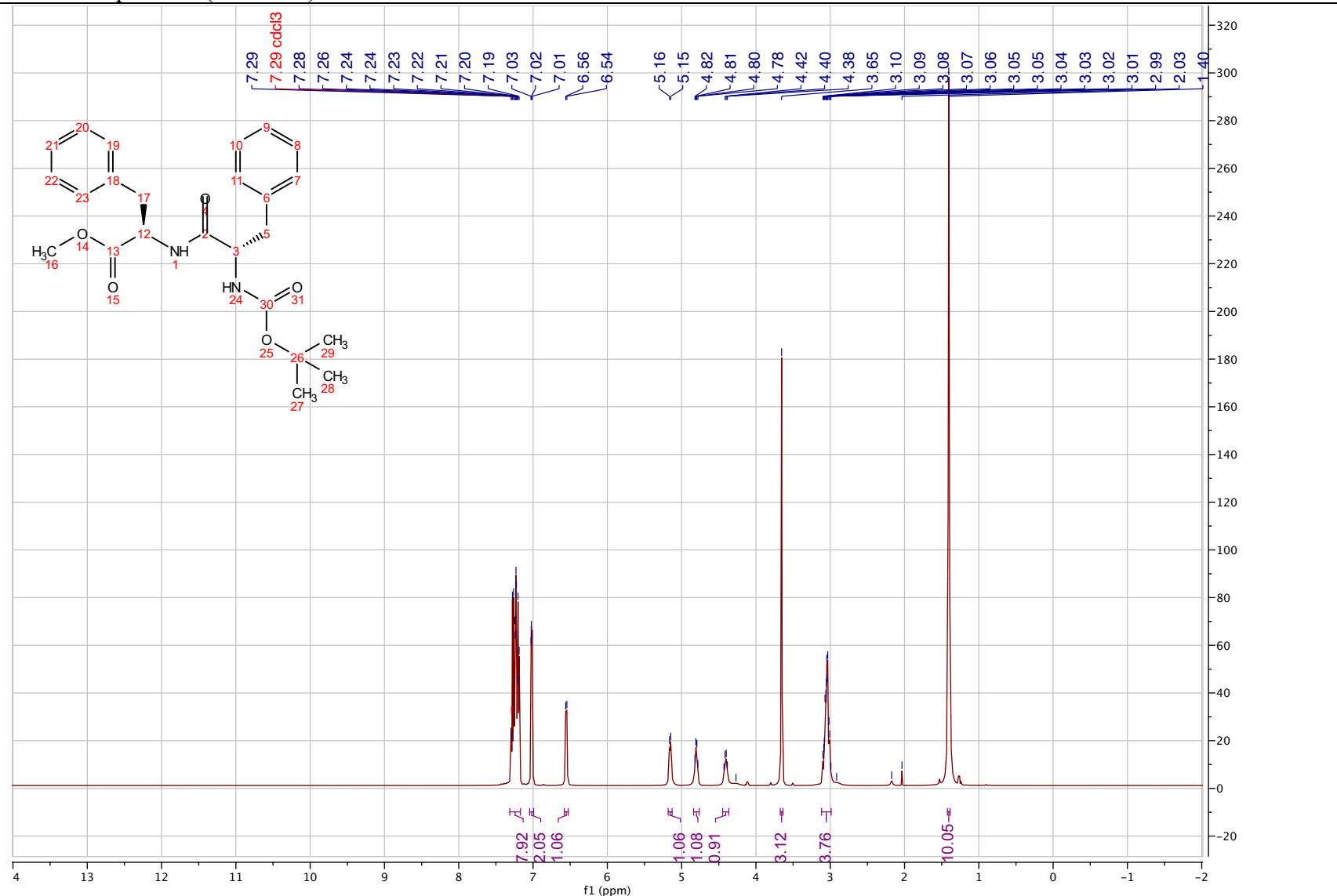
1-(4-methylpiperazin-1-yl)-2-(pyridin-3-yl) ethan-1-one (4.66)

^{13}C NMR spectrum (101 MHz) in Chloroform-*d*



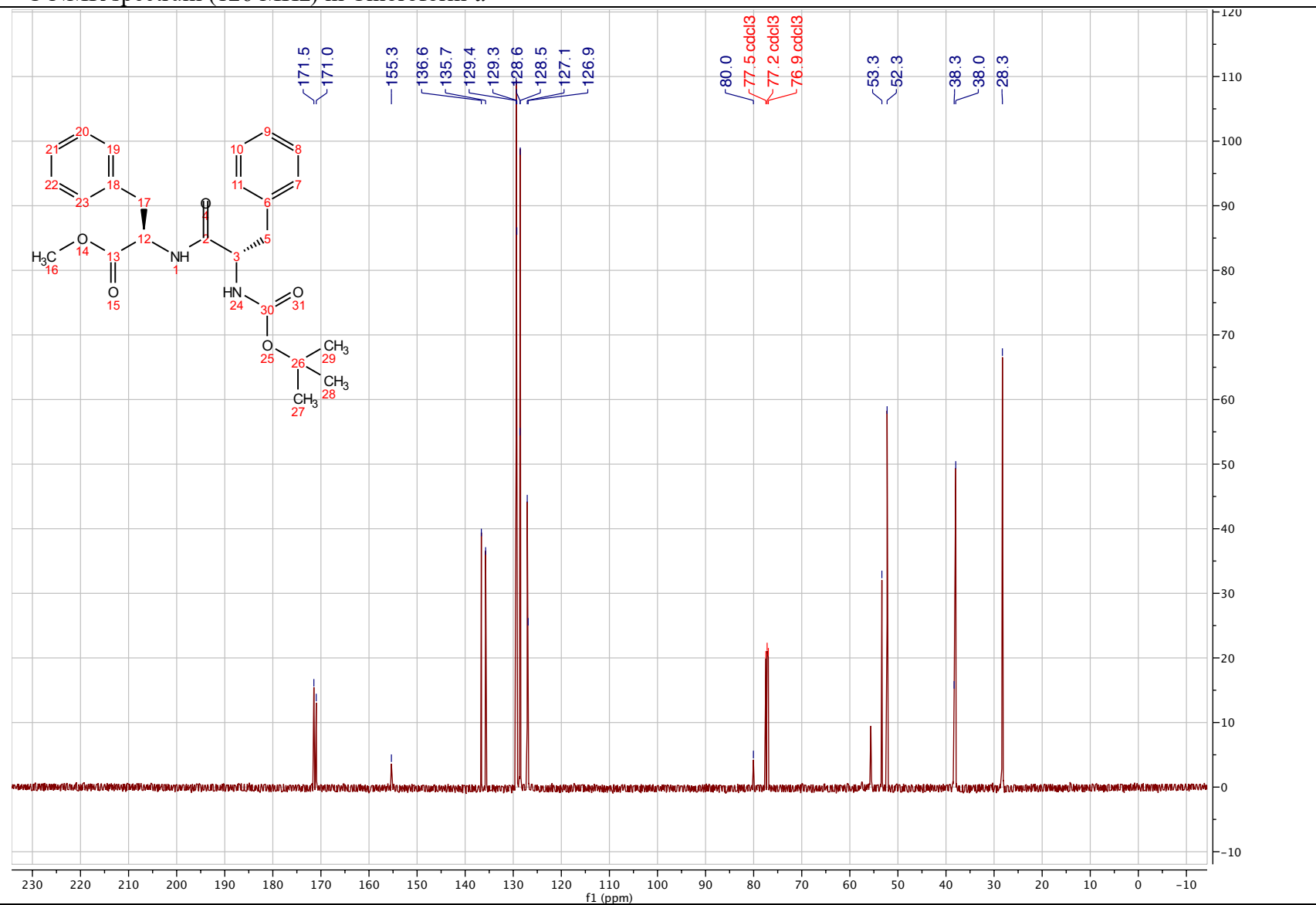
methyl (*tert*-butoxycarbonyl)-*L*-phenylalanyl-*L*-phenylalaninate (4.189)

¹H NMR spectrum (500 MHz) in Chloroform-*d*



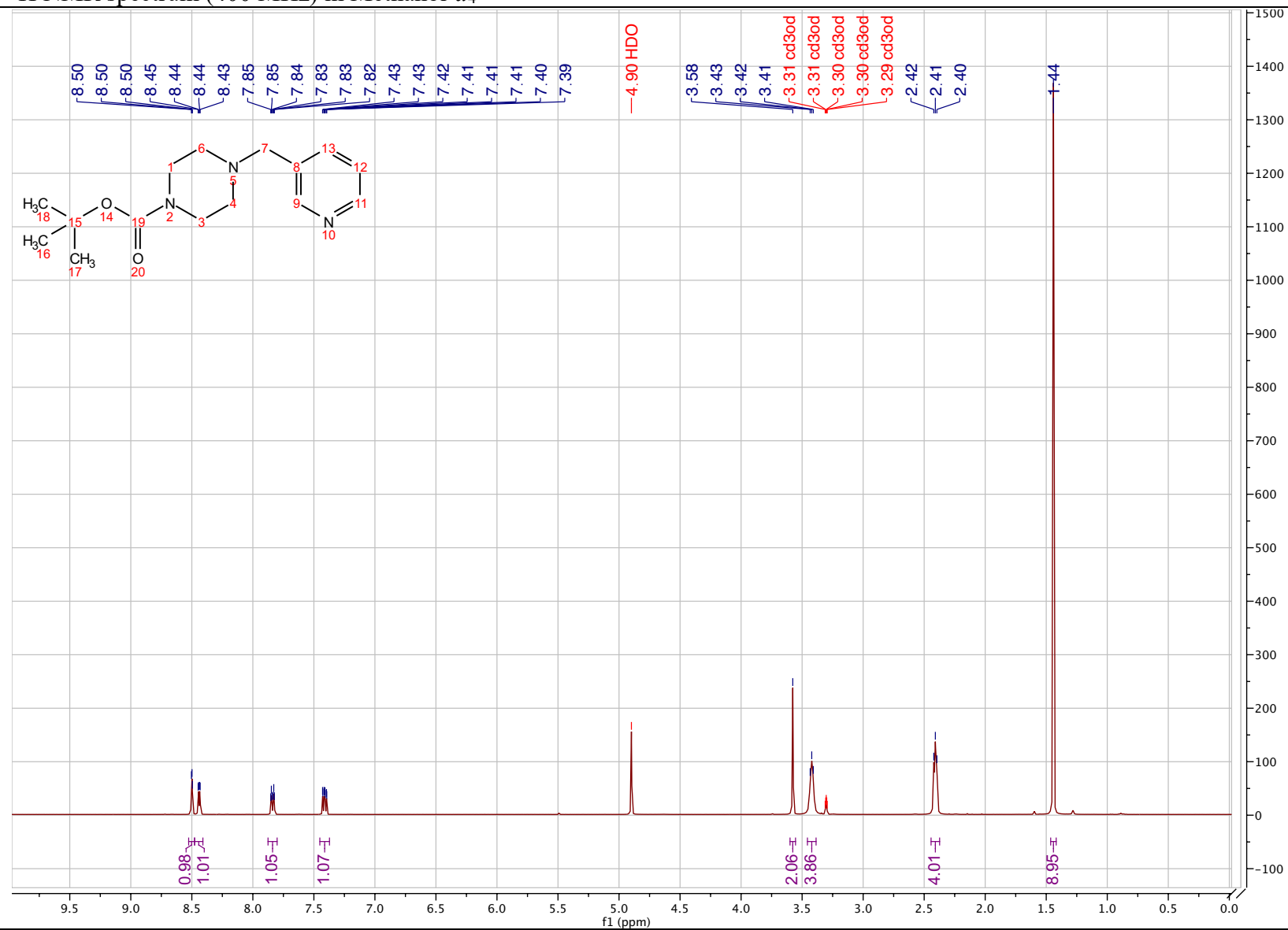
methyl (*tert*-butoxycarbonyl)-*L*-phenylalanyl-*L*-phenylalaninate (4.189)

¹³C NMR spectrum (126 MHz) in Chloroform-*d*



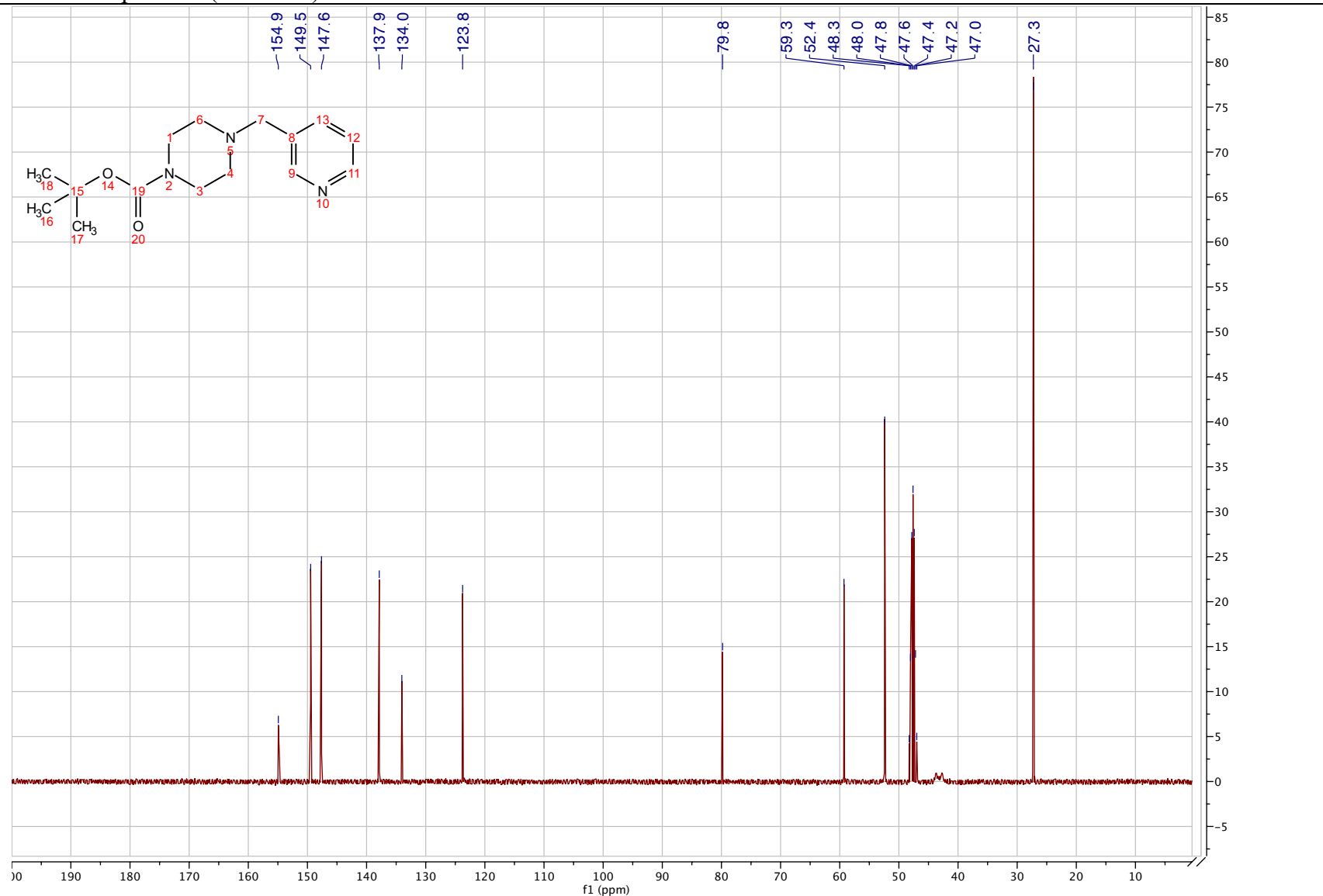
***tert*-butyl 4-(pyridin-3-ylmethyl) piperazine-1-carboxylate (4.186)**

¹H NMR spectrum (400 MHz) in Methanol-*d*₄



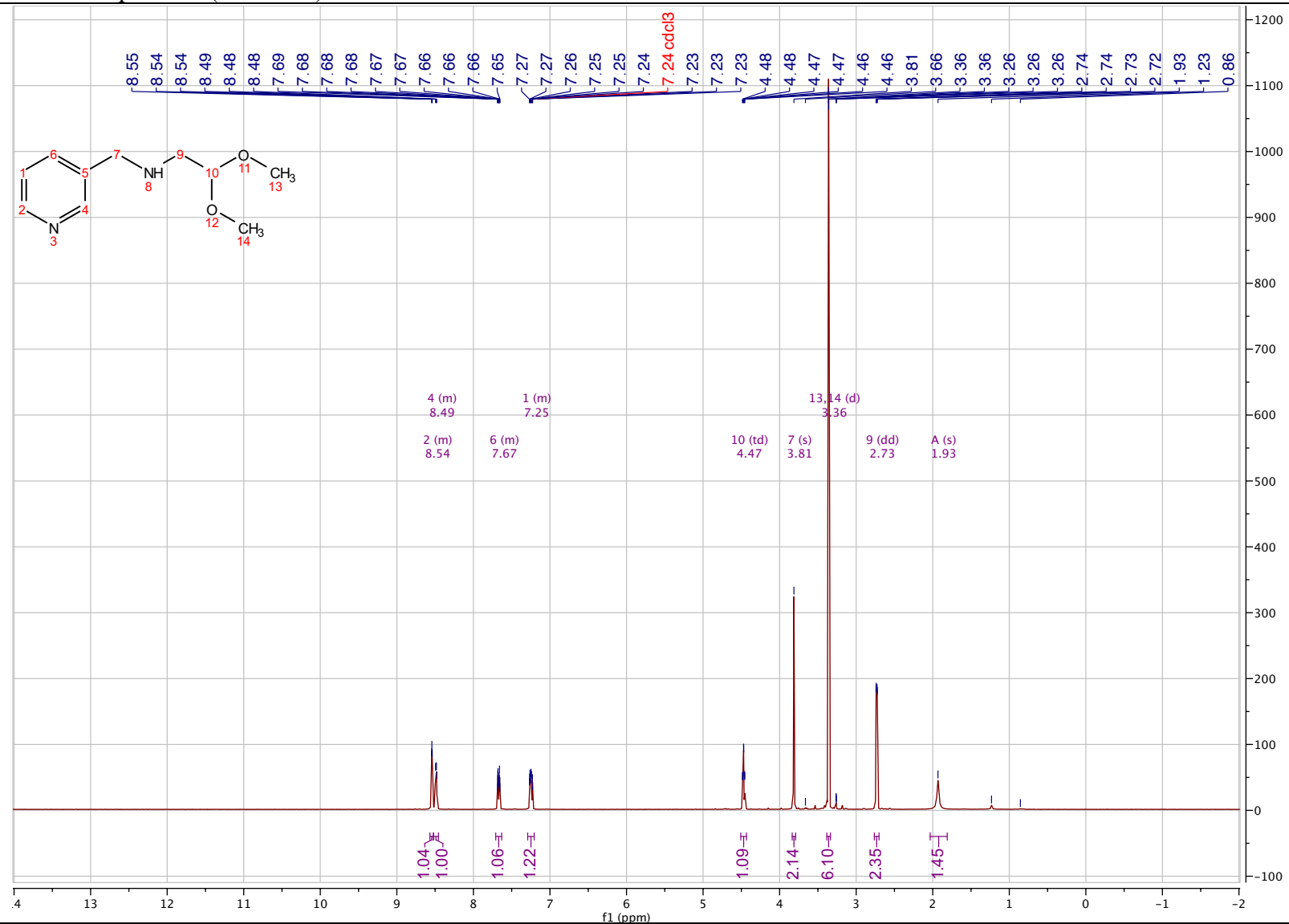
***tert*-butyl 4-(pyridin-3-ylmethyl) piperazine-1-carboxylate (4.186)**

¹³C NMR spectrum (101 MHz) in Methanol-*d*₄



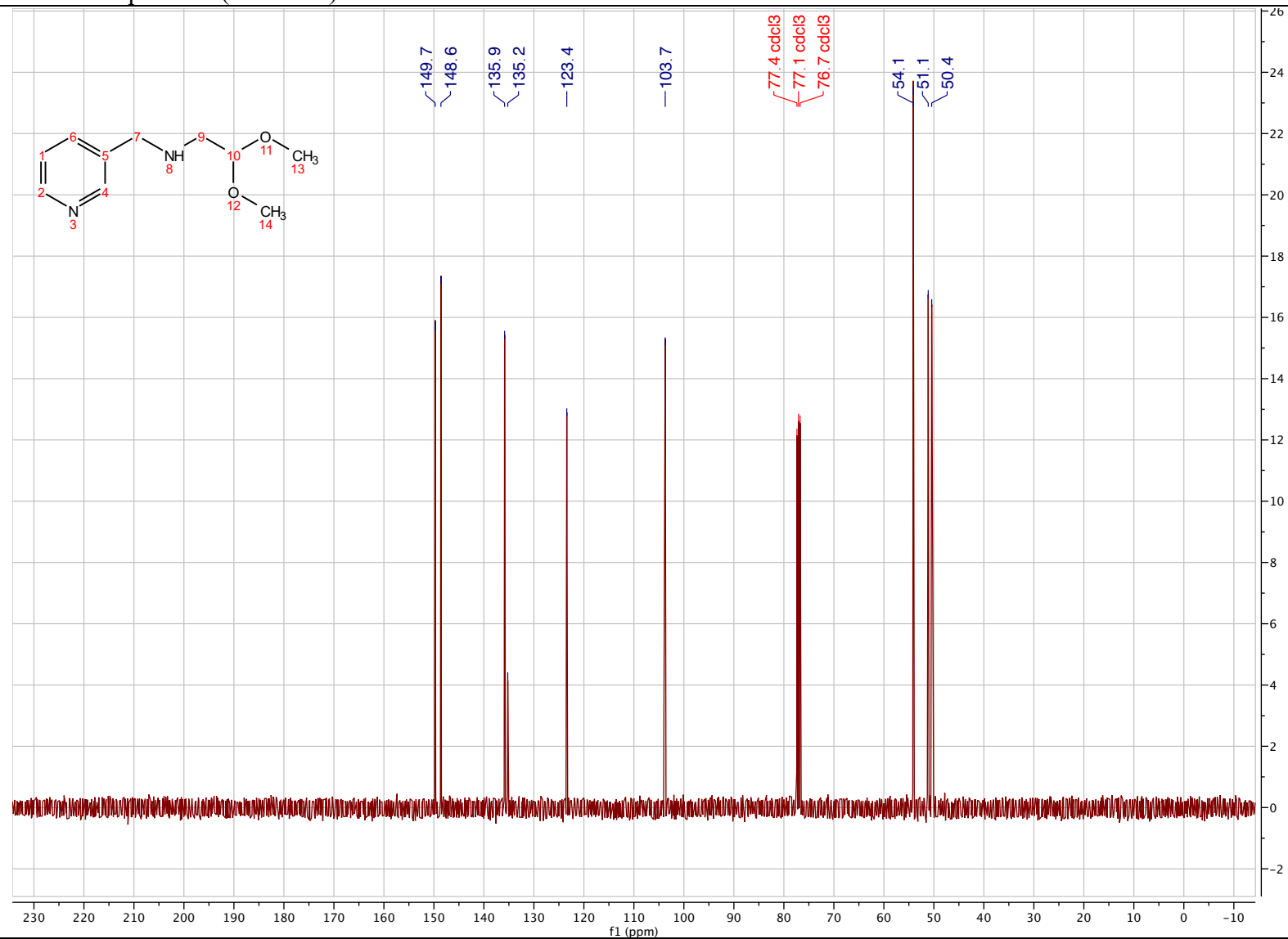
2,2-dimethoxy-N-(pyridin-3-ylmethyl) ethan-1-amine (4.198)

¹H NMR spectrum (400 MHz) in Chloroform-*d*



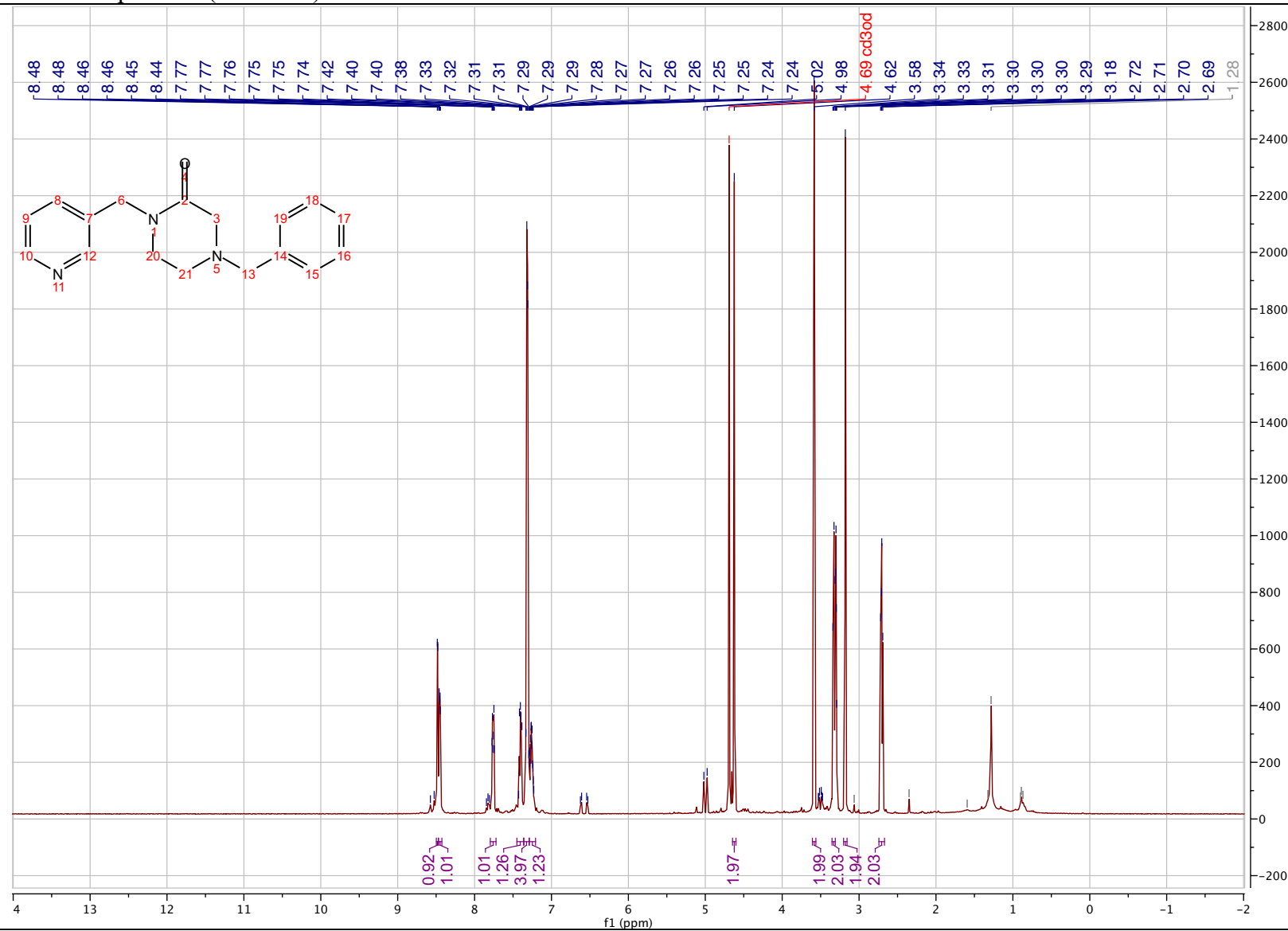
2,2-dimethoxy-N-(pyridin-3-ylmethyl) ethan-1-amine (4.198)

^{13}C NMR spectrum (101 MHz) in Chloroform-*d*



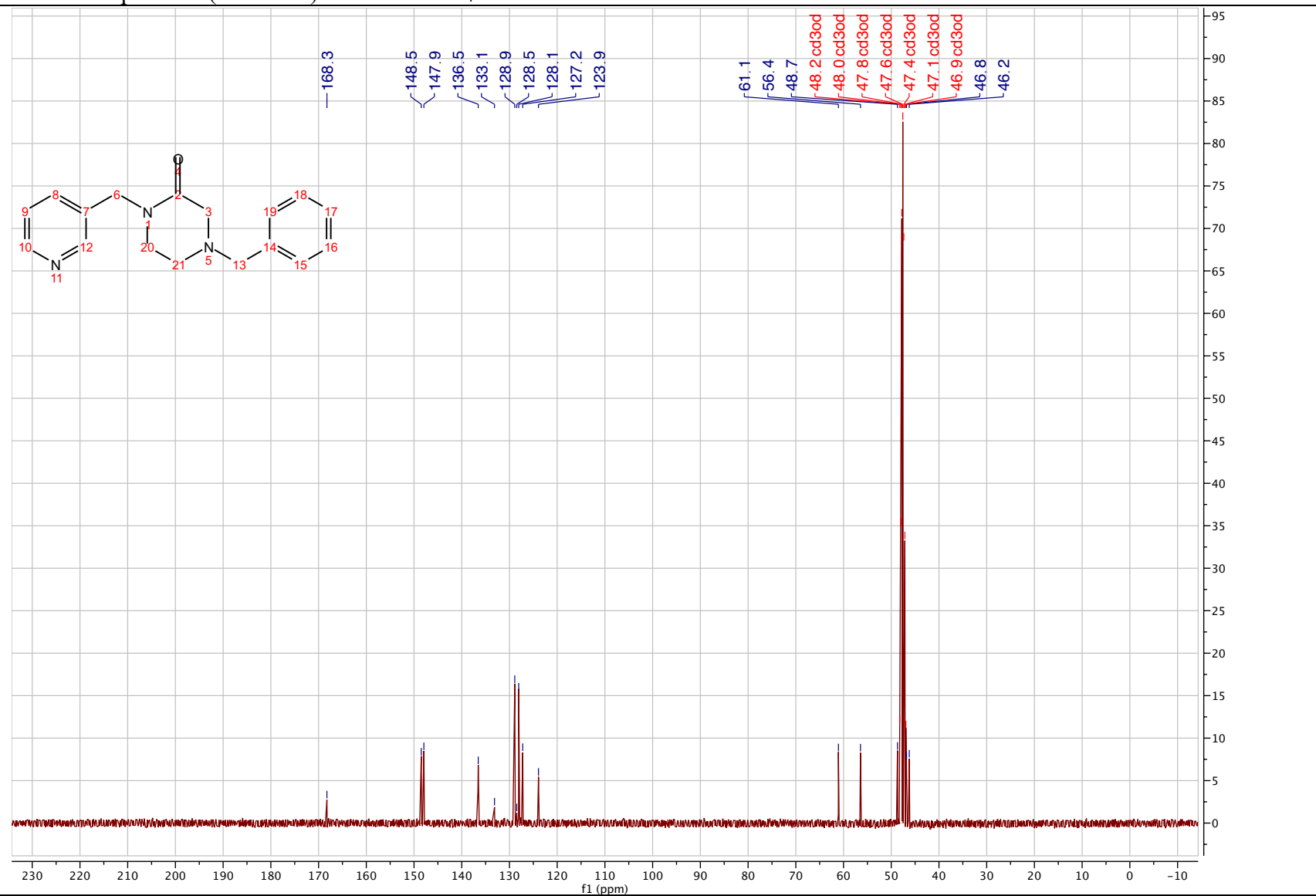
4-benzyl-1-(pyridin-3-ylmethyl) piperazin-2-one (4.113)

¹H NMR spectrum (400 MHz) in Methanol-*d*₄



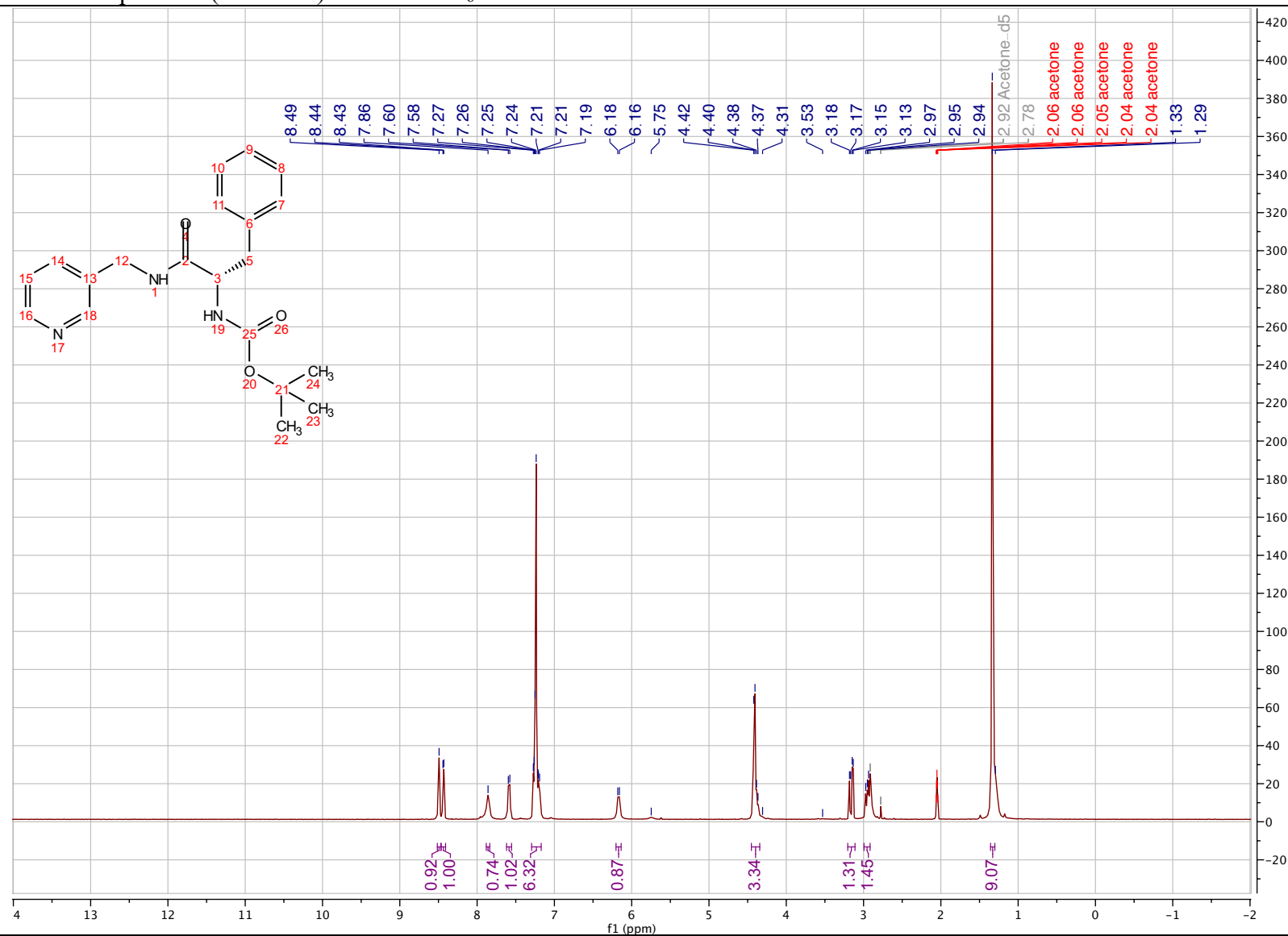
4-benzyl-1-(pyridin-3-ylmethyl) piperazin-2-one (4.113)

^{13}C NMR spectrum (101 MHz) in Methanol- d_4



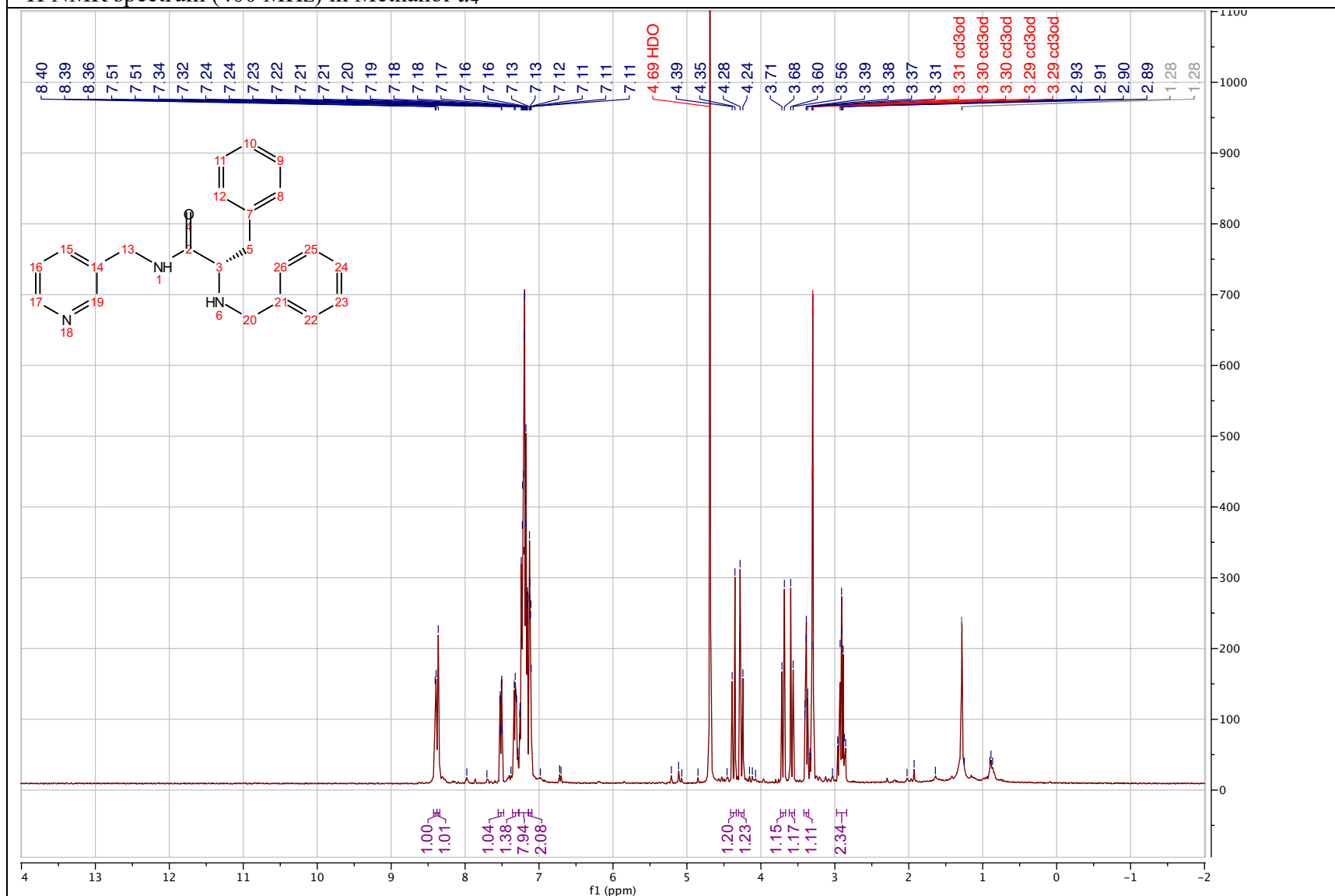
***tert*-butyl (*S*)-(1-oxo-3-phenyl-1-((pyridin-3-ylmethyl) amino) propan-2-yl) carbamate (4.209)**

¹H NMR spectrum (400 MHz) in Acetone-*d*₆



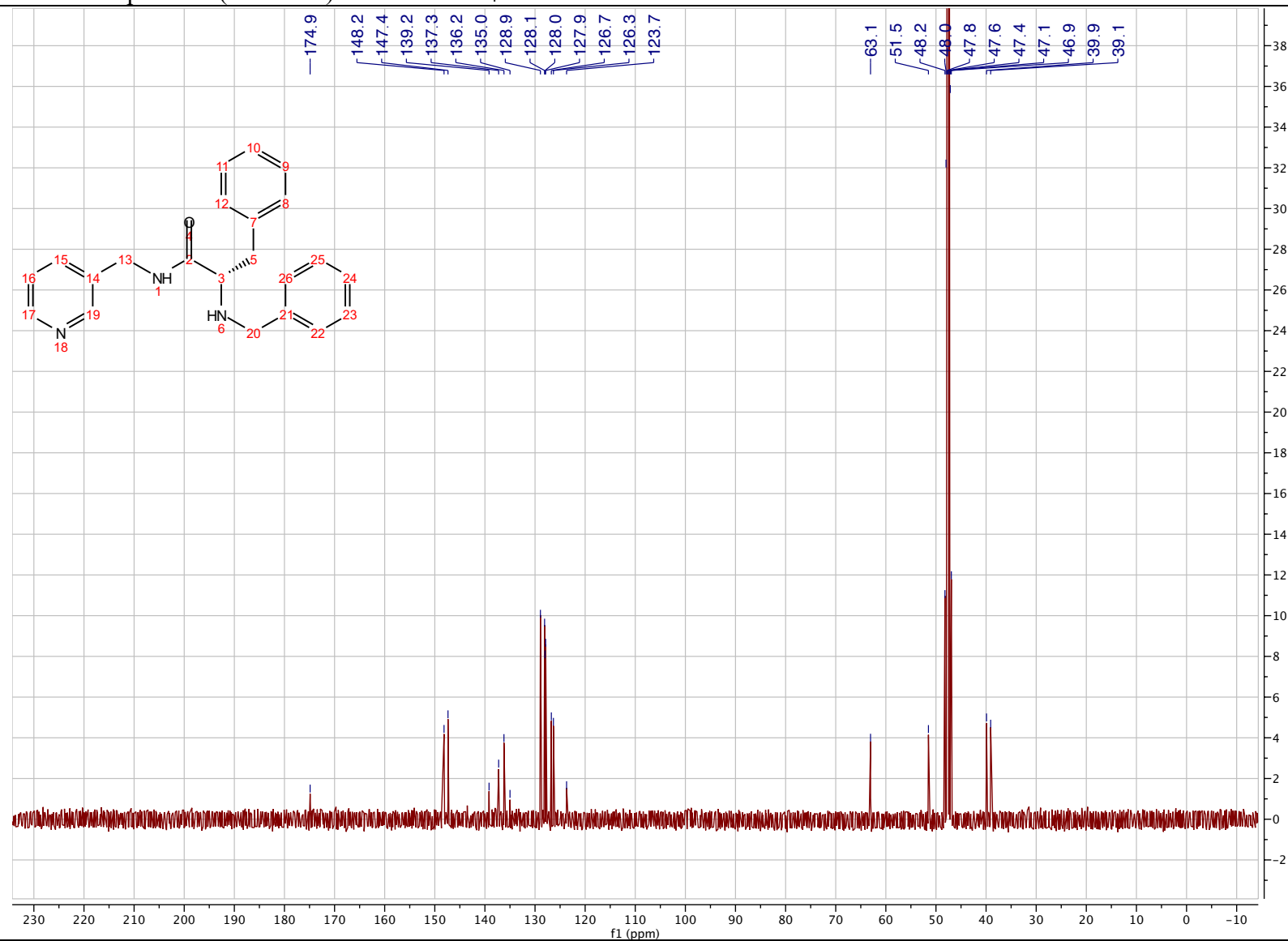
(S)-2-(benzylamino)-3-phenyl-N-(pyridin-3-ylmethyl) propenamide (4.156)

¹H NMR spectrum (400 MHz) in Methanol-*d*₄



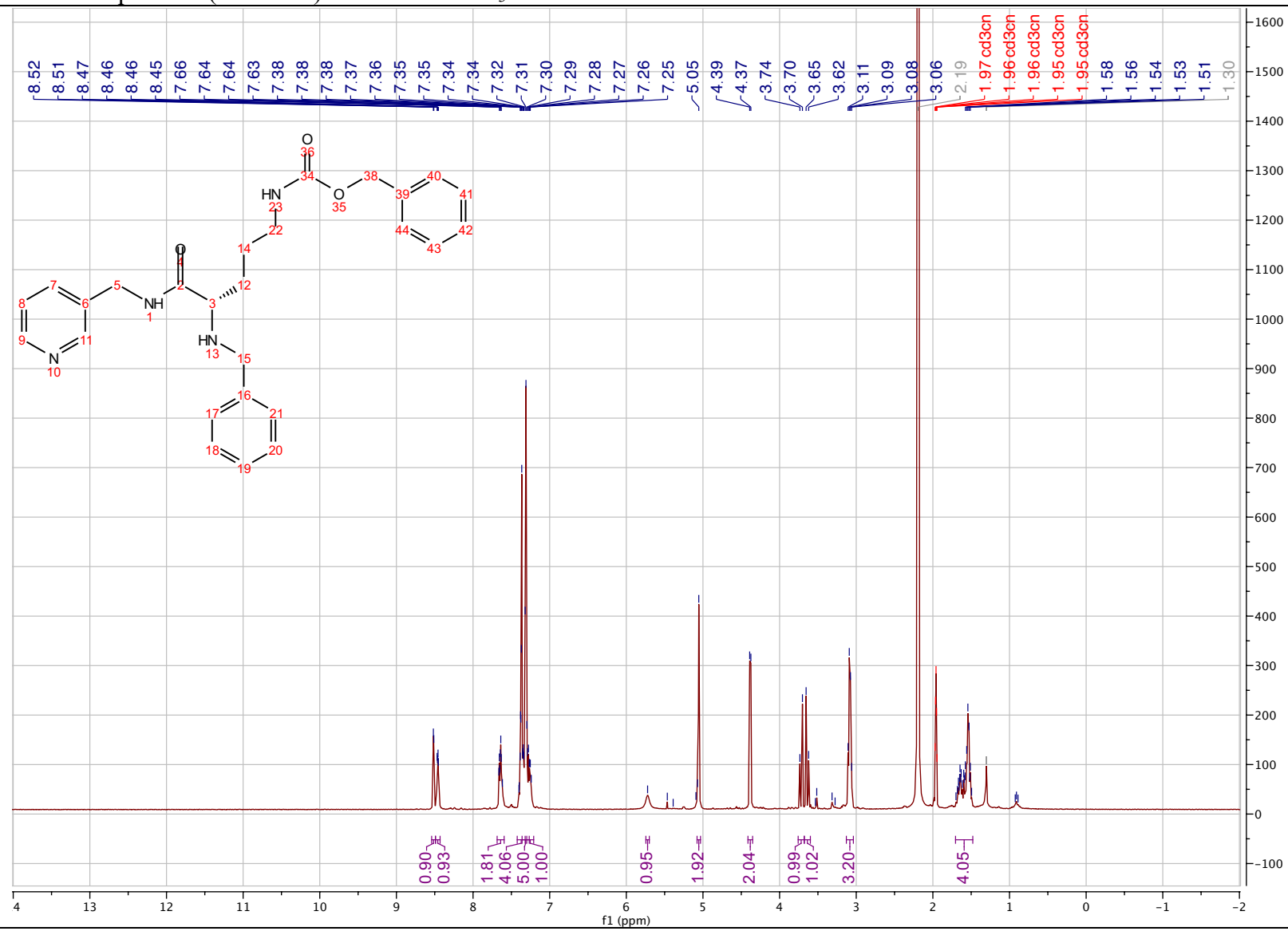
(S)-2-(benzylamino)-3-phenyl-N-(pyridin-3-ylmethyl) propenamide (4.156)

^{13}C NMR spectrum (101 MHz) in Methanol- d_4



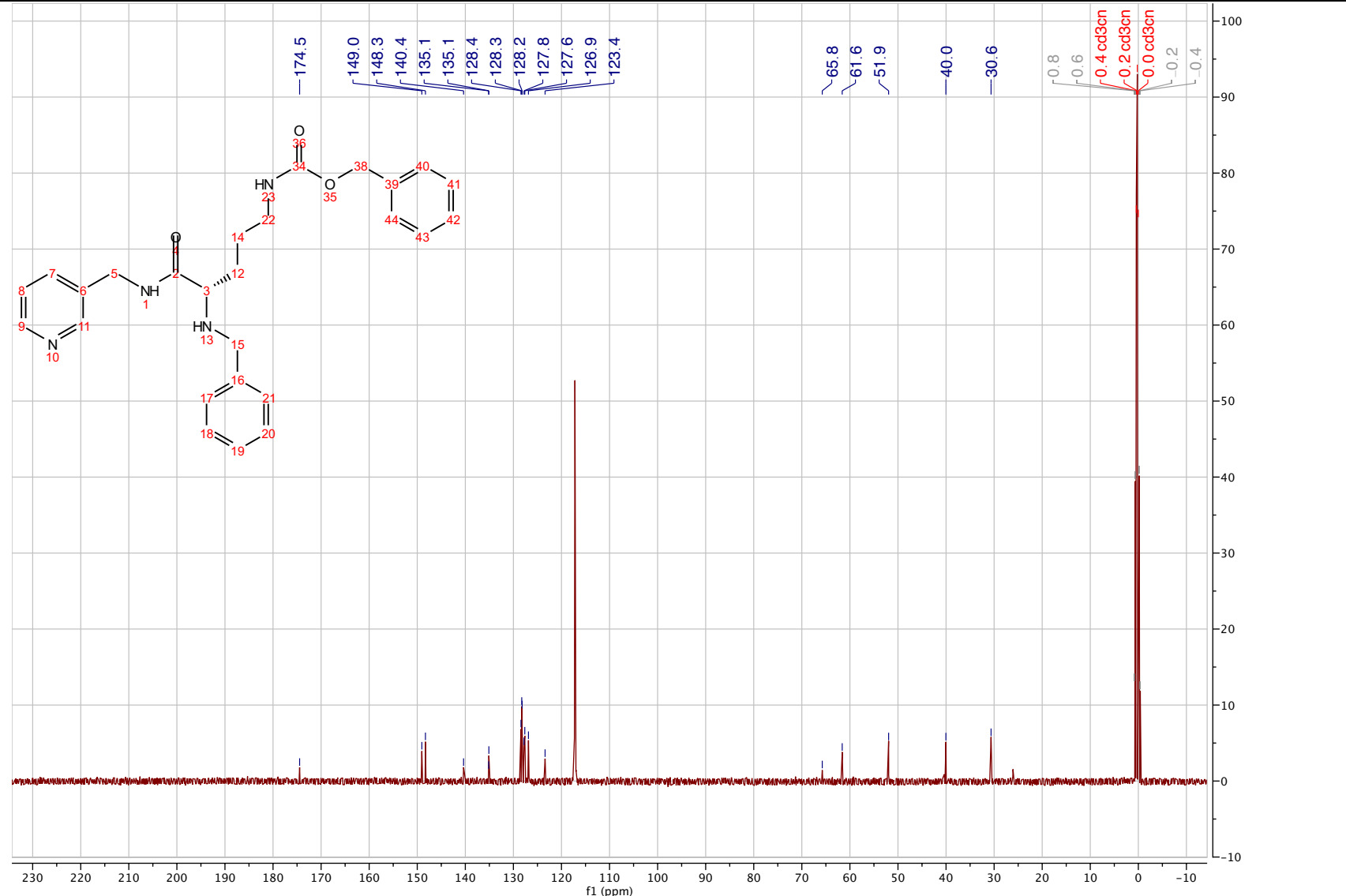
benzyl (S)-4-(benzylamino)-5-oxo-5-((pyridin-3-ylmethyl)amino)pentyl)carbamate (4.180)

¹H NMR spectrum (400 MHz) in Acetonitrile-*d*₃



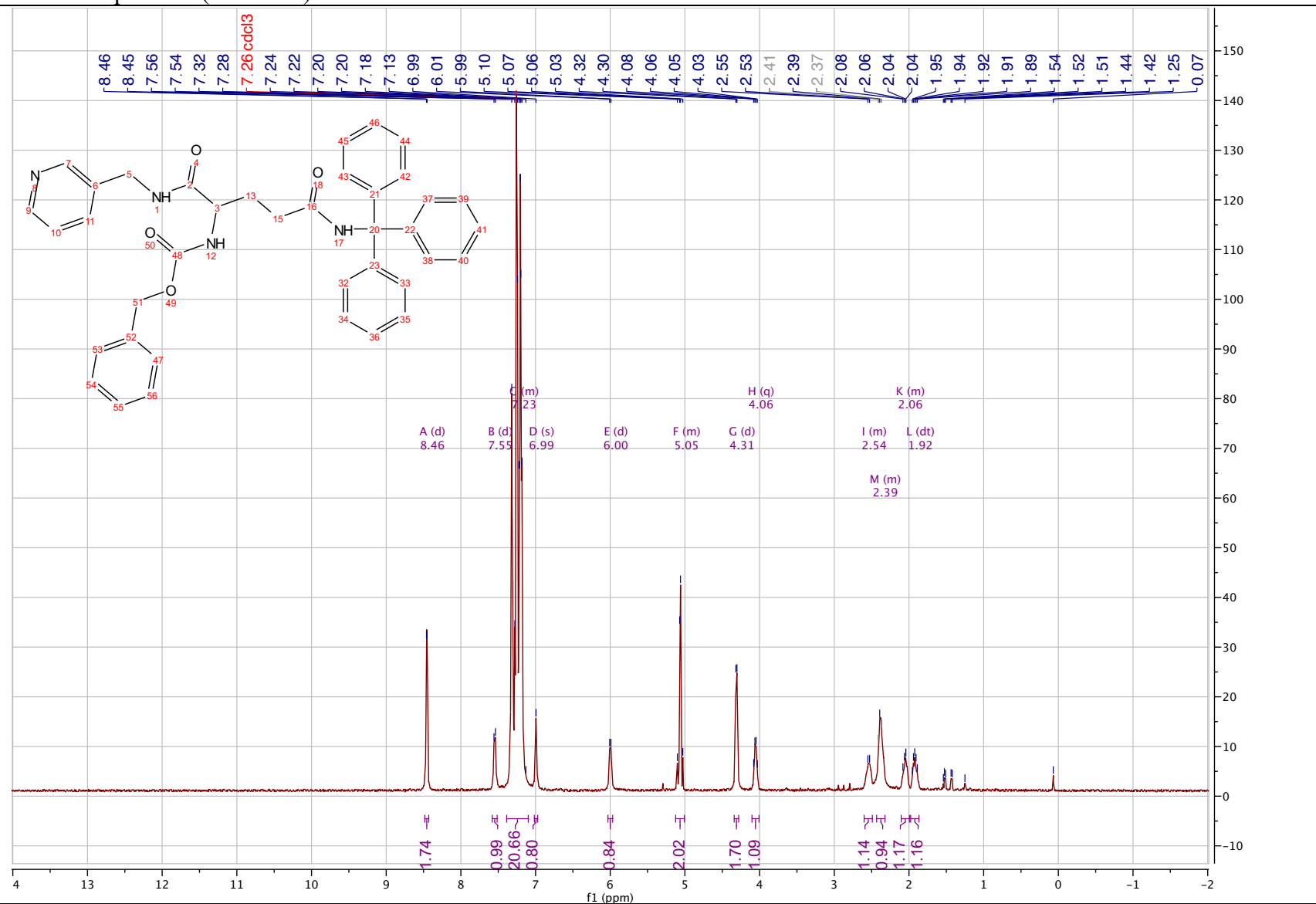
benzyl (S)-4-(benzylamino)-5-oxo-5-((pyridin-3-ylmethyl)amino)pentyl)carbamate (4.180)

¹H NMR spectrum (400 MHz) in Acetonitrile-*d*₃



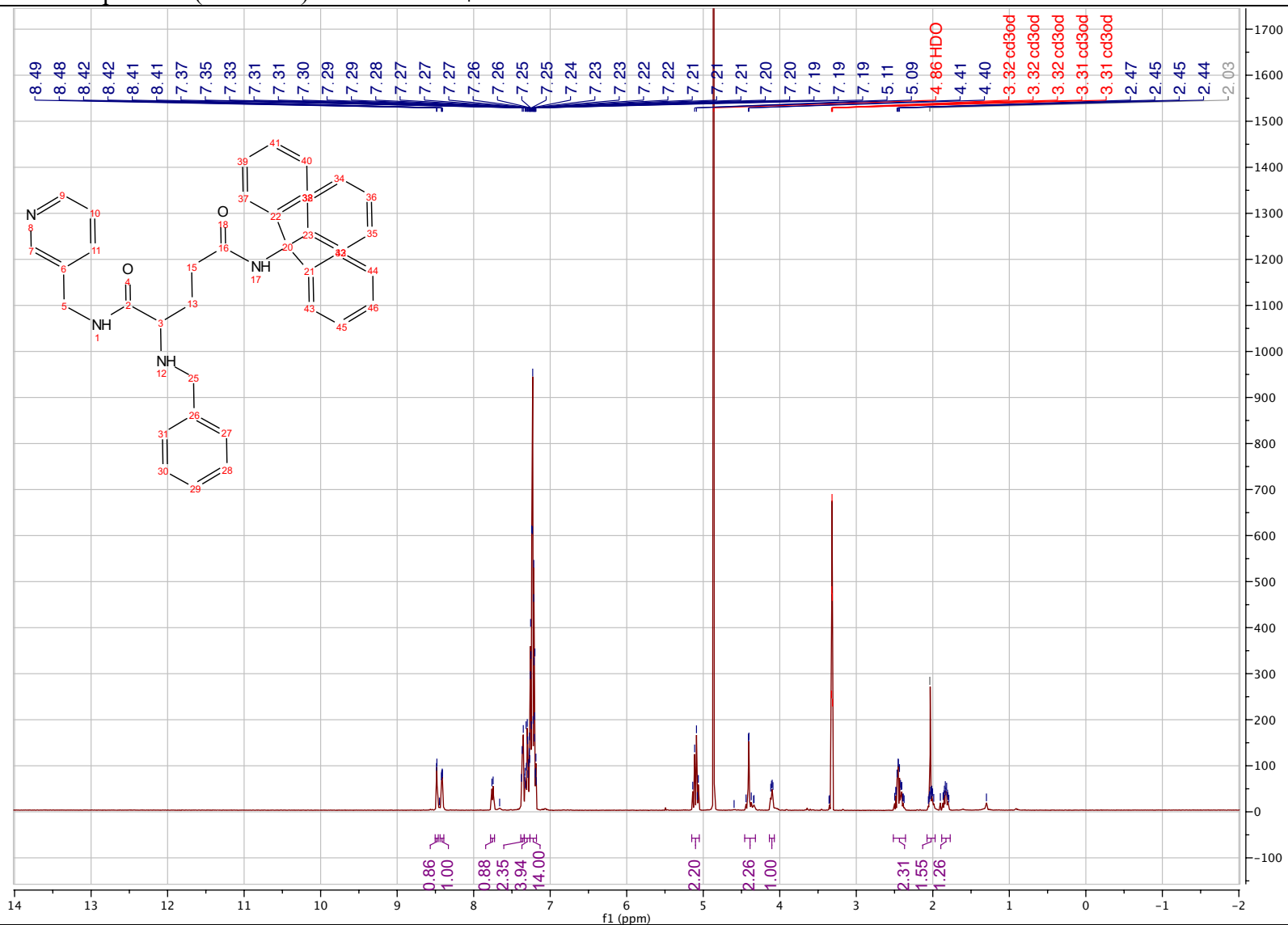
benzyl (S)-(1,5-dioxo-1-((pyridin-3-ylmethyl) amino)-5-(tritylamino) pentan-2-yl) carbamate (4.211)

¹H NMR spectrum (400 MHz) in Chloroform-d



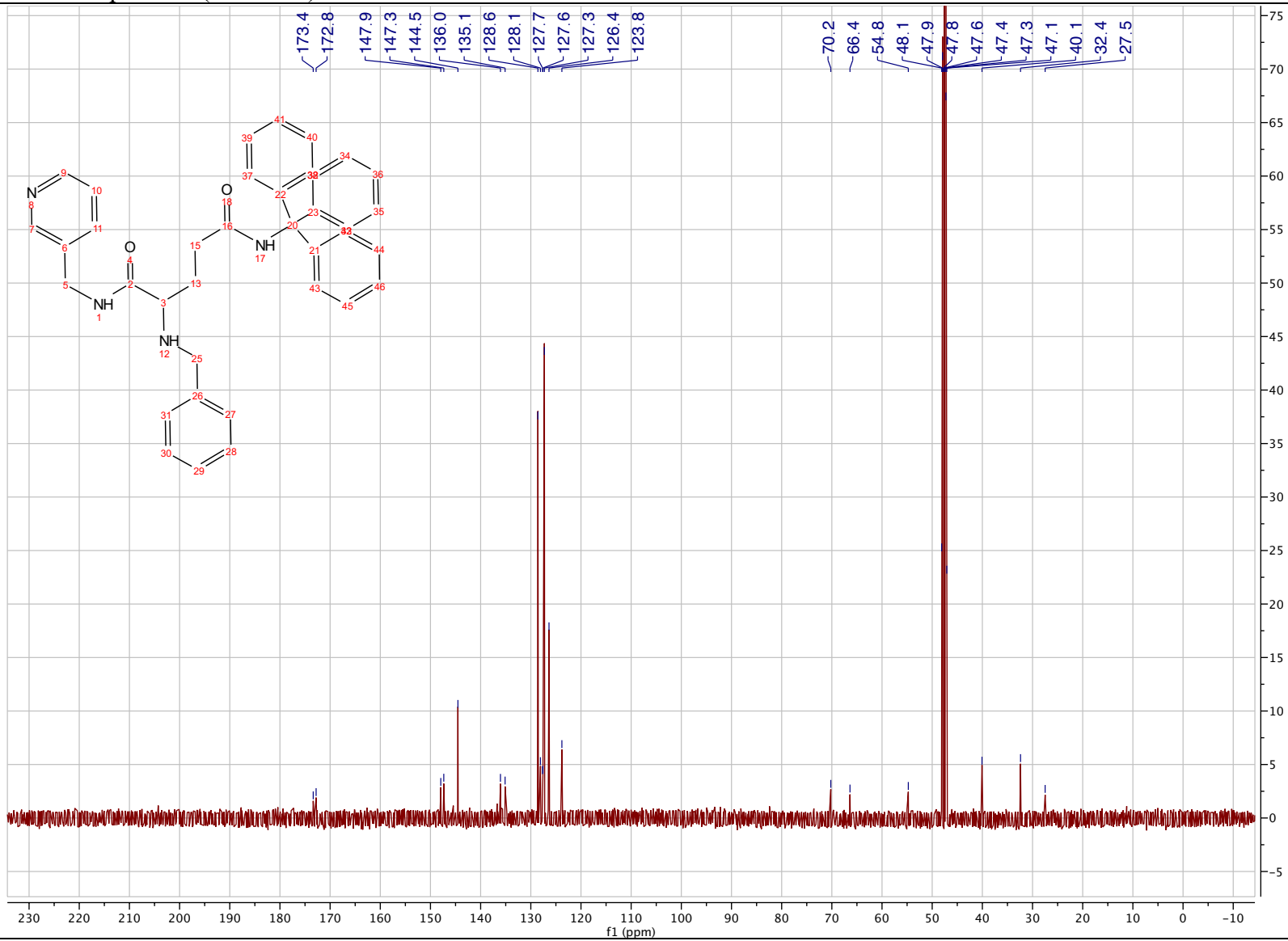
(S)-2-(benzylamino)-N¹-(pyridin-3-ylmethyl)-N⁵-tritylpentanediamide (4.212)

¹H NMR spectrum (400 MHz) in Methanol-*d*₄



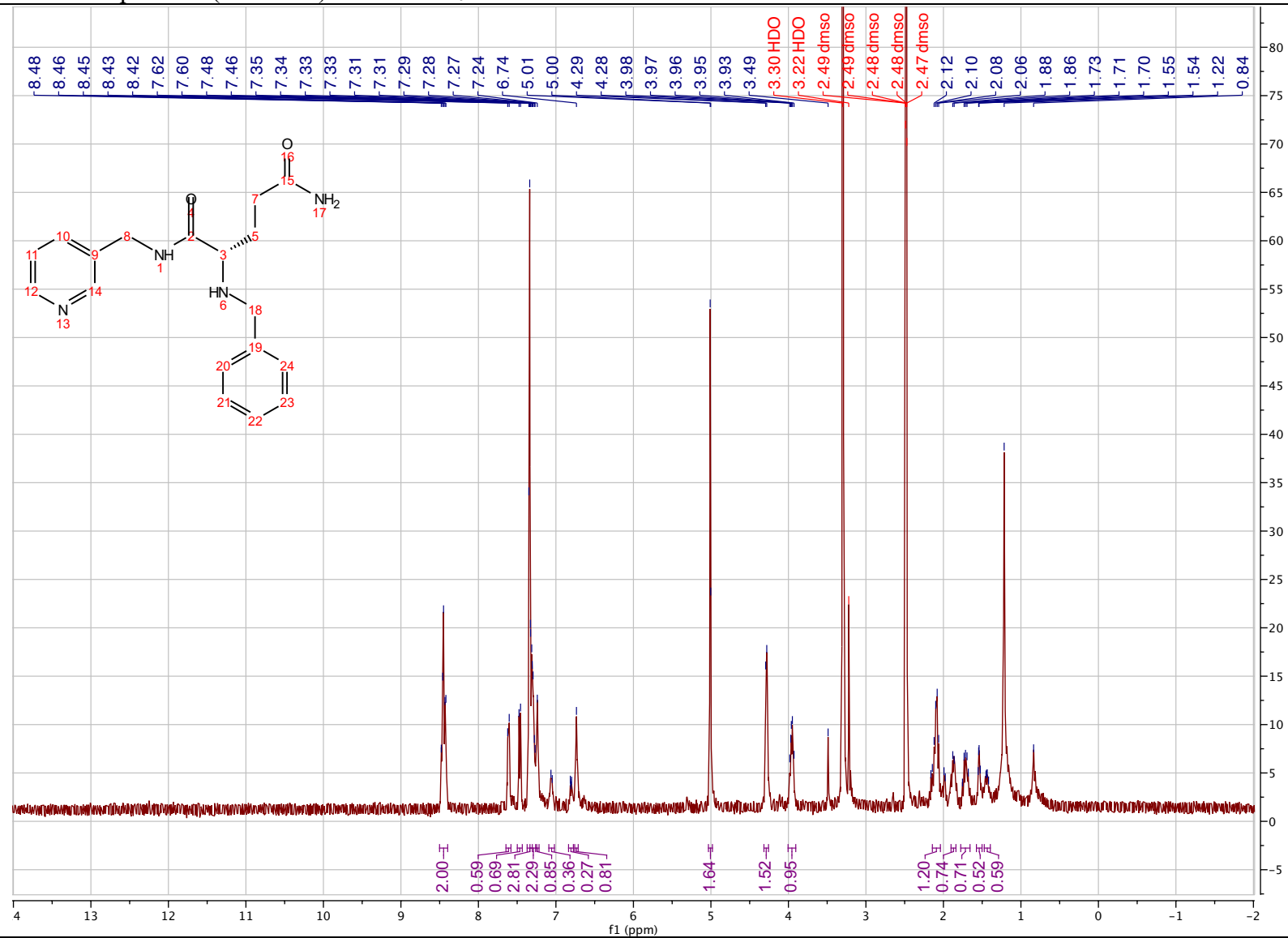
(S)-2-(benzylamino)-N¹-(pyridin-3-ylmethyl)-N⁵-tritylpentanediamide(4.212)

¹³C NMR spectrum (400 MHz) in Methanol-*d*₄



(S)-2-(benzylamino)-N¹-(pyridin-3-ylmethyl)pentanediamide

¹H NMR spectrum (400 MHz) in DMSO-*d*₆



(S)-2-(benzylamino)-N¹-(pyridin-3-ylmethyl)pentanediamide

¹³C NMR spectrum (400 MHz) in DMSO-d₆

